Ibrahim Dincer · Adnan Midilli
Haydar Kucuk *Editors*

Progress in Sustainable Energy Technologies: Generating Renewable Energy

Springer

Progress in Sustainable Energy Technologies: Generating Renewable Energy

Volume 1

Ibrahim Dincer • Adnan Midilli • Haydar Kucuk
Editors

Progress in Sustainable Energy Technologies: Generating Renewable Energy

Springer

Editors
Ibrahim Dincer
Department of Mechanical Engineering
University of Ontario Institute
of Technology (UOIT)
Oshawa
Canada

Haydar Kucuk
Department of Mechanical Engineering
Recep Tayyip Erdoğan University
Rize
Turkey

Adnan Midilli
Department of Mechanical Engineering
Recep Tayyip Erdoğan University
Rize
Turkey

ISBN 978-3-319-07895-3 ISBN 978-3-319-07896-0 (eBook)
DOI 10.1007/978-3-319-07896-0
Springer Cham Heidelberg New York Dordrecht London

Library of Congress Control Number: 2014941874

Printed on acid-free paper

Springer is part of Springer Science+Business Media (www.springer.com)

Preface

Renewable energy sources are of vital importance for future of humanity due to the issues and problems caused by mainly fossil-based energy systems and applications. Renewable energy sources are treated as sustainable energy sources while fossil fuels are considered unsustainable. This fact has attracted many researchers, scientists, practicing engineers, etc. to work on tirelessly and develop better renewable energy-based technologies for a sustainable future. The study domain is quite diverse, covering many engineering disciplines, such as mechanical, civil, physical, chemical, biotechnology, environmental, industrial, geological, electrical, etc. and non-engineering areas, such as chemistry, biology, physics, mathematics, business, informational technology, economy, medicine, etc.

Everyone agrees that sustainable energy technologies are necessary for solving current and potentially future energy problems and achieve environmentally benign solutions. This volume primarily concerns the largest energy domain under sustainable energy technologies, covering all relevant disciplinary areas, ranging from current problems, projections, new concepts, modeling, experiments and measurements to simulations, and discusses recent research findings on solar energy, wind energy, biomass, geothermal energy, hydro energy, wave energy, hydrogen production, fuel cells, energy storage, heat pump, integrated energy systems, etc.

This volume includes some invited contributions and the selected papers from the 11th International Conference on Sustainable Energy technologies (SET-2012) held in Vancouver, Canada on September 2–5, 2012. The conference had a multidisciplinary nature, covering main areas of sustainable energy technologies, and aimed to provide a forum for researchers, scientists, engineers and practitioners from all over the world to exchange information, to present high-quality research results and new developments in the wide domain covered by sustainable energy technologies, and discussed the future direction and priorities in the field.

In conclusion, the editors of this volume gratefully acknowledge the assistance provided by Dr. Ugur Akbulut in reviewing and revising several chapters, checking for consistency and finalizing them for publication. The editors also register their sincere appreciation to the authors for their contributions which have made this

unique book possible. Furthermore, Dr. Dincer acknowledges the support provided by the Turkish Academy of Sciences in Ankara, Turkey.

Oshawa, ON, Canada Ibrahim Dincer
Rize, Turkey Adnan Midilli
Rize, Turkey Haydar Kucuk

Contents

Contributors

Ali H. Abedin Golder Associates Ltd., Mississauga, Ontario, Canada

Naeem Abas Department of Electrical Engineering, COMSATS Institute of Information Technology, Islamabad, Pakistan

Morteza Abdolzadeh Faculty of Mechanical Engineering, Kerman graduate university of technology, Kerman, Iran

Canan Acar Faculty of Engineering and Applied Science, University of Ontario Institute of Technology, Oshawa, ON, Canada

Nishant Aggarwal Mechanical Department, NIT, Kurukshetra, Haryana, India

Pouria Ahmadi Faculty of Engineering and Applied Science, University of Ontario Institute of Technology (UOIT), Oshawa, ON, Canada

Syed Ahmed Mechatronic Systems Engineering, School of Engineering Science, Simon Fraser University, Surrey, BC, Canada

Chouder Aissa Centre de Développement des Energies Renouvelables Route de l'observatoire, Bouzaréah, Algiers

Betul Akyurek Energy Systems Engineering Department, Bahcesehir University, BesiktasIstanbul, Turkey

Loay Aldabbagh Mechatronics Engineering Department, College of Engineering, Mosul University, Mosul, Iraq

Mohammed Al-Hussein NSERC Industrial Research Chair in the Industrialization of Building ConstructionDepartment of Civil and Environmental Engineering Hole School of Construction, University of Alberta, Edmonton, Canada

M. Al Ali Faculty of Engineering and Applied Science, University of Ontario Institute of Technology (UOIT), Oshawa, ON, Canada

Mohammed Al-Khawaja Faculty of Engineering, Qatar University, Doha, Qatar

Lobna Altorkmany Department of Engineering Sciences and Mathematics, Luleå University of Technology, Luleå, Sweden

Hadj Arab Amar Centre de Développement des Energies Renouvelables Route de l'observatoire, Bouzaréah, Algiers

Majid Amidpour Mechanical Engineering Faculty, K.N. Toosi University of Technology, Tehran, Iran

Ulvi Arslan Institute of Materials and Mechanics in Civil Engineering, Technical University Darmstadt (TUD), Darmstadt, Germany

Mohammad Reza Azmi Islamic Azad University-Science and Research Branch, Tehran, Iran

H. Barzegaravval Board Member of Energy Optimization R&D Group, Tehran, Iran

Ali Behbahaninia Mechanical Engineering Faculty, K.N. Toosi University of Technology, Tehran, Iran

Filippo Busato Department of Management and Engineering, University of Padua, Vicenza, Italy

Luma M. Diab Department of Mechanical and Industrial Engineering, Qatar University, Doha, Qatar

Ibrahim Dincer Department of Mechanical Engineering, University of Ontario Institute of Technology (UOIT), Oshawa, ON, Canada

Rami Salah El-Emam Faculty of Engineering and Applied Science, University of Ontario Institute of Technology, Oshawa, ON, Canada

Faculty of Engineering, Mansoura University, Mansoura, Egypt

Andi Erwin Eka Putra Department of Mechanical Engineering, Hasanuddin University Tamalanrea, Makassar, Indonesia

Cherfa Farida Centre de Développement des Energies Renouvelables Route de l'observatoire, Bouzaréah, Algiers

Hasan Ufuk Gökçe Department of Civil and Environmental Engineering Hole School of Construction, University of Alberta, Edmonton, Canada

Mohamed Gadalla Department of Mechanical Engineering, American University of Sharjah, Sharjah, United Arab Emirates

Hamed Shakouri Ganjavi Department of Industrial and Systems Engineering, Collage of Engineering, University of Tehran, Tehran, Iran

Mark Gillott University of Nottingham, Nottingham, UK

Hooman Golchoobian Mechanical Engineering Faculty, K.N. Toosi University of Technology, Tehran, Iran

Rebecca Gough Loughborough University, Loughborough, UK

Mustafa Gul Department of Civil and Environmental Engineering Hole School of Construction, University of Alberta, Edmonton, Canada

Philip Hall Division of Engineering, The University of Nottingham Ningbo China, Ningbo, China

Thomas Hamacher Institute for Energy Economy and Application Technology (IfE), Technische Universität München, Munich, Arcisstr. 21, Germany

Seyed M. Hashemi Department of Aerospace Engineering, Ryerson University, Toronto, ON, Canada

Ferri Hassani Department of Mining Metals and Materials Engineering, McGill University, Montreal, QC, Canada

Arash Hatami Department of Industrial Engineering, University College of Engineering, University of Tehran, Tehran, Iran

Hanzade Haykiri-Acma Chemical and Metallurgical Eng. Faculty, Department of Chemical Engineering, Istanbul Technical University, MaslakIstanbul, Turkey

Mehdi Hosseini Faculty of Engineering and Applied Science, University of Ontario Institute of Technology, Oshawa, 2000 Simcoe St. North, ON, Canada

Heiko Huber CDM Smith Consult GmbH, Alsbach, Germany

Ishtiaq Hussain National Center for Physics, Islamabad, Pakistan

Mohammed Hussain Mechatronic Systems Engineering, School of Engineering Science, Simon Fraser University, Surrey, BC, Canada

Aghil Iranmanesh Department of Mechanical Engineering, Ferdowsi University of Mashhad, Mashhad, Iran

M. F. Ismail Department of Mechanical Engineering, University of British Columbia, Vancouver, Canada

Anand S. Joshi Department of Mechanical Engineering, CMR Institute of Technology, Bangalore, Karnataka, India

Muhyiddine Jradi Department of Architecture and Built Environment, Faculty of Engineering, University of Nottingham, Nottingham, UK

Abdeladim Kamel Centre de Développement des Energies Renouvelables Route de l'observatoire, Bouzaréah, Algiers

Kerkouche Karim Centre de Développement des Energies Renouvelables Route de l'observatoire, Bouzaréah, Algiers

M. T. H. Khan Industrial and Systems Engineering, Wayne State University, Detroit, MI, USA

Nasrullah Khan Department of Electrical Engineering, COMSATS Institute of Information Technology, Islamabad, Pakistan

Dinesh Khanduja Mechanical Department, NIT, Kurukshetra, Haryana, India

Mohamad Kharseh Faculty of Engineering, Qatar University, Doha, Qatar

Erik Kjeang Mechatronic Systems Engineering, School of Engineering Science, Simon Fraser University, Surrey, BC, Canada

Seama Koohi-Fayegh University of Ontario Institute of Technology, Faculty of Engineering and Applied Science, Oshawa, ON, Canada

Kourosh Malek Mechatronic Systems Engineering, School of Engineering Science, Simon Fraser University, Surrey, BC, Canada

National Research Council, Vancouver, BC, Canada

Chemistry Department, Simon Fraser University, Burnaby, BC, Canada

Pratin Kullavanijaya Pilot Plant Development and Training Institute, King Mongkut's University of Technology Thonburi (Bang Khun Thian), Bangkok, Thailand

Chun Kwong Lee Department of Mechanical Engineering, University of Hong Kong, Hong Kong, China

Renato Lazzarin Department of Management and Engineering, University of Padua, Vicenza, Italy

Edward Lester School of Chemical and Environmental Engineering, The University of Nottingham, Nottingham, UK

Xinming Li Department of Civil and Environmental Engineering Hole School of Construction, University of Alberta, Edmonton, Canada

Benziada Mébrouk Centre Développement Energies Renouvelables, Bouzaréah, Alger, Algérie

Kourosh Malek Mechatronic Systems Engineering, School of Engineering Science, Simon Fraser University, Surrey, BC, Canada

National Research Council, Vancouver, BC, Canada

Chemistry Department, Simon Fraser University, Burnaby, BC, Canada

M. Malik Faculty of Engineering and Applied Science, University of Ontario Institute of Technology (UOIT), Oshawa, ON, Canada

Robinson L. Manfro Escola de Química, Universidade Federal do Rio de Janeiro (UFRJ), Centro de Tecnologia, Rio de Janeiro, Brazil

Abdulkarym Mayere Institute of Sustainable Energy Technology, University of Nottingham, Nottingham, UK

Mozaffar Ali Mehrabian Department of Mechanical Engineering, Shahid Bahonar University of Kerman, Kerman, Iran

Mozzafar Ali Mehrabian Faculty of Mechanical Engineering, Shahid Bahonar University of Kerman, Kerman, Iran

David Morrow Hydraft Development Services Inc., Edmonton, Canada

Shinobu Mukasa Department of Engineering for Production and Environment, Ehime University Matsuyama, Ehime, Japan

3 Bunkyo-cho, Matsuyama, Ehime, Japan

Farayi Musharavati Department of Mechanical and Industrial Engineering, Qatar University, Doha, Qatar

Hong Nam Lam Department of Mechanical Engineering, University of Hong Kong, Hong Kong, China

Neven Ninic Faculty of Electrical Engineering, Mechanical Engineering and Naval Architecture, University of Split, Split, Croatia

Sandro Nizetic Faculty of Electrical Engineering, Mechanical Engineering and Naval Architecture, University of Split, Split, Croatia

Shinfuku Nomura Department of Engineering for Production and Environment, Ehime University Matsuyama, Ehime, Japan

3 Bunkyo-cho, Matsuyama, Ehime, Japan

Marco Noro Department of Management and Engineering, University of Padua, Vicenza, Italy

Seyed Hadi Nourbakhsh Faculty of Industrial Engineering, University of Tehran, Tehran, Iran

Raheleh Nowzari Mechanical Engineering Department, Eastern Mediterranean University, Famagusta, Turkey

Abdeen Omer Department of Architecture and Built Environment, University of Nottingham, Nottingham, UK

Siddig Omer Department of Architecture and Built Environment, University of Nottingham, Nottingham, UK

E. Oralli Faculty of Engineering and Applied Science, University of Ontario Institute of Technology (UOIT), Oshawa, ON, Canada

Hasan Ozcan Faculty of Engineering and Applied Science, University of Ontario Institute of Technology, Oshawa, ON, Canada

Somboon Pitayarangsarit T.C.M. Environment Ltd, Samutprakarn, Thailand

Omid Pourali Mechanical Engineering Faculty, K.N. Toosi University of Technology, Tehran, Iran

S. Rahnamayan Faculty of Engineering and Applied Science, University of Ontario Institute of Technology (UOIT), Oshawa, ON, Canada

T. A. H. Ratlamwala Faculty of Engineering and Applied Science, University of Ontario Institute of Technology, Oshawa, ON, Canada

SZABIST, 90 and 100 Clifton Campus, Karachi, Sindh, Pakistan

Bale V. Reddy Faculty of Engineering and Applied Science, University of Ontario Institute of Technology, Oshawa, ON, Canada

Behnaz Rezaie Faculty of Engineering and Applied Science, University of Ontario Institute of Technology, Oshawa, ON, Canada

Nielson F. P. Ribeiro Escola de Química, Universidade Federal do Rio de Janeiro (UFRJ), Centro de Tecnologia, Rio de Janeiro, Brazil

Saffa Riffat Department of Architecture and Built Environment, Faculty of Engineering, University of Nottingham, Nottingham, UK

Saffa Riffat Institute of Sustainable Energy Technology, University of Nottingham, Nottingham, UK

Costanzo Robert Engineering Department, City of Surrey, Surrey, BC, Canada

Lars Rose Mechatronic Systems Engineering, School of Engineering Science, Simon Fraser University, Surrey, BC, Canada

National Research Council, Vancouver, BC, Canada

Materials Engineering Department, University of British Columbia, Vancouver, BC, Canada

Marc A. Rosen Faculty of Engineering and Applied Science, University of Ontario Institute of Technology (UOIT), Oshawa, ON, Canada

Bouchakour salim Centre de Développement des Energies Renouvelables Route de l'observatoire, Bouzaréah, Algiers

Karl Schoensteiner Institute for Energy Economy and Application Technology (IfE), Technische Universität München, Munich, Arcisstr. 21, Germany

Salman Kheirabadi Shahvali Faculty of Industrial Engineering, University of Tehran, Tehran, Iran

Tanzia Sharmin Department of Civil and Environmental Engineering Hole School of Construction, University of Alberta, Edmonton, Canada

Mahmoud Shatat Institute of Sustainable Energy Technology, University of Nottingham, Nottingham, UK

Kaiqi Shi Division of Engineering, The University of Nottingham Ningbo China, Ningbo, China

Jianzhong Song Southeast University, School of Energy and Environment, Nanjing, China

Academy of Southeast University, Changshu Applied Technology, Changshu, China

Mariana M. V. M. Souza Escola de Química, Universidade Federal do Rio de Janeiro (UFRJ), Centro de Tecnologia, Rio de Janeiro, Brazil

Pouyan Talebizadeh Amirkabir University of Technology, Tehran, Iran

Hiromichi Toyota Department of Engineering for Production and Environment, Ehime University Matsuyama, Ehime, Japan

3 Bunkyo-cho, Matsuyama, Ehime, Japan

Pablo Tuza Escola de Química, Universidade Federal do Rio de Janeiro (UFRJ), Centro de Tecnologia, Rio de Janeiro, Brazil

Fehmi Gorkem Uctug Energy Systems Engineering Department, Bahcesehir University, BesiktasIstanbul, Turkey

Markus Wagner Institute for Energy Economy and Application Technology (IfE), Technische Universität München, Munich, Arcisstr. 21, Germany

Chinnapong Wangnai Pilot Plant Development and Training Institute, King Mongkut's University of Technology Thonburi (Bang Khun Thian), Bangkok, Thailand

Jennifer White University of Nottingham, Nottingham, UK

Tao Wu Division of Engineering, The University of Nottingham Ningbo China, Ningbo, China

Qikuang Yao Southeast University, School of Energy and Environment, Nanjing, China

Serdar Yaman Chemical and Metallurgical Eng. Faculty, Department of Chemical Engineering, Istanbul Technical University, MaslakIstanbul, Turkey

Jiefeng Yan Division of Engineering, The University of Nottingham Ningbo China, Ningbo, China

Can Yang Southeast University, School of Energy and Environment, Nanjing, China

Yijun Yuan ISAW technology Corporation, Hangzhou, China

Sayem Zafar Department of Mechanical Engineering, American University of Sharjah, Sharjah, United Arab Emirates

Xiaosong Zhang Southeast University, School of Energy and Environment, Nanjing, China

Academy of Southeast University, Changshu Applied Technology, Changshu, China

Haitao Zhao Division of Engineering, The University of Nottingham Ningbo China, Ningbo, China

M. A. Zobaer Department of Mechanical Engineering, Bangladesh University of Engineering and Technology (BUET), Dhaka, Bangladesh

About the Editors

Prof. Dr. Ibrahim Dincer is a full professor of Mechanical Engineering and programs director in the faculty of Engineering and Applied Science at University of Ontario Institute of Technology. Renowned for his pioneering works, he has authored and co-authored many books and book chapters, over 800 refereed journal and conference papers, and numerous technical reports. He has chaired many national and international conferences, symposia, workshops, and technical meetings. He is the founding chair/co chair of various well-established international conferences, including the International Exergy, Energy, and Environment Symposium. He has delivered over 200 keynote and invited lectures. He is an active member of various international scientific organizations and societies, and serves as Editor-In-Chief for International Journal of Energy Research, International Journal of Exergy, and International Journal of Global Warming, as well as associate editor, regional editor, and editorial board member on various prestigious international journals. He is a recipient of several research, teaching, and service awards, including the Premier's Research Excellence award in Ontario, Canada, in 2004. He has made innovative contributions to the understanding and development of exergy analysis of advanced energy systems for his so-called five main pillars: (1) better efficiency, (2) better cost-effectiveness, (3) better environment, (4) better sustainability, and (5) better energy security. He was the chair of a new technical group in ASHRAE named Exergy Analysis for Sustainable Buildings.

Prof. Dr. Haydar Kucuk is Associate Professor at Mechanical Engineering Department and Associate Dean of Engineering Faculty at the Recep Tayyip Erdoğan University. He teaches graduate and undergraduate courses in the fields of thermodynamics, fluid mechanics and heat transfer. His research interests involve numerical heat transfer and fluid flow, drying and drying models, energy and exergy analysis, economic analysis and sustainability and thermodynamics. He serves as referee for international prestigious journals. He has participated in national and international research projects as a researcher. He has contributed as technical chair in The Sixth International Exergy, Energy and Environment Symposium.

Prof. Dr. Adnan Midilli Midilli is a full professor of Mechanical Engineering in Engineering Faculty of Recep Tayyip Erdoğan University, Rize, Turkey. He is

an active member of various international scientific organizations and societies, and serves as editorial board member on various prestigious international journals. He is a recipient of several national research awards. He has been working to be researcher in the national and international research projects. His research interest includes sustainable energy technologies, sustainable development, thermodynamic design and modeling.

Chapter 1
Comparative Study of Effect of Cloudiness/ Haziness Factor on the Quality of Solar Radiation

Anand S. Joshi, Ibrahim Dincer and Bale V. Reddy

Abstract In this chapter, the effect of cloudiness/haziness factor on the quality of solar radiation is analysed. First, the solar radiation is predicted and compared with the experimental observations and then, the exergy of solar radiation is calculated and analysed based on various models. The effect of cloudiness/haziness factor is plotted in the form of graphs. Other factors affecting the solar radiation, namely, atmospheric transmittance, perturbation factor and background diffuse radiation are also discussed briefly. It is found that for lower values of cloudiness/haziness factor, the solar energy is more and vice versa. Also, lower the cloudiness/haziness factor better would be the intensity of solar radiation.

Keywords Solar energy · Radiation · Cloudiness/Haziness factor · Exergy · Quality

1.1 Introduction

Unarguably, solar energy is the immense source of energy that can fulfill the increasing energy demand of the world. Its appropriate application for useful purposes is also very important. Generally, solar energy can be utilized in two ways, they are, photovoltaic and solar thermal applications. On one hand, thermal application of solar energy is at its maturity these days as most of the solar thermal devices possess good energy and exergy efficiencies. On the other hand, photovoltaic possesses more challenge to scientists and engineers because of relatively lower efficiencies and hence, presents more scope for possible improvement.

A. S. Joshi (✉)
Department of Mechanical Engineering, CMR Institute of Technology,
132 AECS layout, IT park Road, Bangalore, Karnataka 560037, India
e-mail: anandsj75@rediffmail.com

I. Dincer
Department of Mechanical Engineering, University of Ontario Institute of Technology (UOIT),
2000 Simcoe Street North, Oshawa ON L1H 7K4, Canada
e-mail: ibrahim.dincer@uoit.ca

B. V. Reddy
Faculty of Engineering and Applied Science, University of Ontario Institute of Technology,
2000 Simcoe Street North, Oshawa ON L1H 7K4, Canada

I. Dincer et al. (eds.), *Progress in Sustainable Energy Technologies: Generating Renewable Energy,* DOI 10.1007/978-3-319-07896-0_1,

The performance of the system depends upon the behaviour of the solar energy incident on it. In other words, the quality of the solar energy, rather, exergy of solar radiation affects the performance of a solar based system.

Solar energy is measured in terms of global radiation which is the sum of beam and diffuse radiations. The exergy of solar radiation majorly depends upon the beam radiation as beam radiation has the photonic energy that can be converted into useful work. Diffuse radiation can be useful for some purposes like low potential heating. For photovoltaic application, a good quality global radiation is necessary that should be rich in beam radiation and should have less diffuse radiation. In other words, presence of higher diffuse radiation deteriorates the quality (exergy) of the global radiation.

Exergy of solar radiation depends upon some parameters like, geographical position (altitude and latitude of the place), weather conditions, sky conditions and ambient temperature. For higher altitudes, the global radiation received is higher as compared to lower altitudes. The reason is that, at lower altitudes the amount of background diffuse radiation is high due to the presence of various objects/obstacles (like walls, buildings, trees etc.). This higher background diffuse radiation in the global radiation reduces the exergy of solar radiation. Different weather conditions also affect the magnitude of solar radiations. The relative altitude of sun in winters and summers also plays an important role in terms of intensity of solar light. In winters the magnitude is less as compared to summers ending up in less exergy in the winter season. In rainy season, although the magnitude is comparatively high, the intermittency due to clouds still affects the performance of various systems. The air mass which is the ratio of the optical distance travelled by the solar radiation in the terrestrial region at a given time to the optical distance travelled by the solar radiation when sun is at zenith, is also an important parameter which affects the quality of sunlight. In mornings and evenings the air mass is high as compared to noon when the air mass is least, that is, nearly one. Higher the air mass is, lower would be the solar radiation.

Another important parameter is cloudiness/haziness factor. Suspension of fine dust particles and other impurities in terrestrial region (sky) of earth interrupt solar radiation by absorption, adsorption, scattering, reflection, refraction etc. The cloudiness/haziness factor is a parameter by which the clearness of sky can be measured. If sky is clear (also called blue sky), the solar radiation incident on the earth's surface would be more as compared to when sky is cloudy. A detailed study of cloudiness/haziness factor is done in the later sections. Other parameters that affect the solar radiation are atmospheric transmittance, perturbation factor and background diffuse radiation. The cloudiness/haziness factor and atmospheric transmittance are important to predict the beam radiation on a horizontal surface where as the perturbation factor and background diffuse radiation are responsible to predict diffuse radiation. The effect of atmospheric transmittance, perturbation factor and background diffuse radiation on solar radiation prediction is also discussed in detail.

The application of solar energy depends on certain parameters like surrounding conditions, ambient temperature and the intensity of radiation. Surrounding conditions majorly depend upon the presence of so called obstacles which can increase background diffuse radiation. Ambient temperature is important especially for the

Table 1.1 Cloudiness/haziness factor for different months. (Tiwari [8])

Region ▼	Month											
	1	2	3	4	5	6	7	8	9	10	11	12
Mountain	1.8	1.9	2.1	2.2	2.4	2.7	2.7	2.7	2.5	2.1	1.9	1.8
Flat land	2.2	2.2	2.5	2.9	3.2	3.4	3.5	3.3	2.9	2.6	2.3	2.2
City	3.1	3.2	3.5	3.9	4.1	4.2	4.3	4.2	3.9	3.6	3.3	3.1

photovoltaic applications as PV panels loses efficiency (electrical conversion efficiency) when heated and if the ambient temperature is also high, it does not allow panels to cool down naturally because of low temperature gradient between panel and the ambient. Performance of the system improves with the quality of solar radiation, i.e., exergy of solar radiation. Many researchers and scientists gave different models to evaluate the exergy of solar radiations namely, Petela [1], Jetter [2], Spanner [3], Saitoh [4], Zamfirescu and Dincer [5], Joshi et al. [6] etc. In the following sections the effect of cloudiness/haziness factor on solar radiation is analysed using Joshi and Tiwari model [7]. Further, a critical analysis of exergy of solar radiation from each of the above said models is done for a case study.

1.2 Methodology

Now we discuss the cloudiness/haziness factor and its application to evaluate the solar radiation in this section. Later the exergy of the solar radiation is calculated by using the cloudiness/haziness factor and various models.

Cloudiness/Haziness Factor

As the name suggests, cloudiness/haziness factor is a parameter to know the clearness of the sky [7–10]. Joshi and Tiwari [7] and Singh and Tiwari [9] have evaluated cloudiness/haziness factor for different climatic conditions of India based on the past data obtained from Indian Meteorological Department (IMD), India. As discussed earlier, the cloudiness/haziness factor influences the solar radiation incident on earth, therefore it is important to know how it affects the latter. Tiwari [8] has given cloudiness/haziness factor for different months and regions for India. The different regions were mountain, flat land and city as shown in Table 1.1.

It is interesting to see that for any particular month, the highest value for the factor is in city region and the lowest is in mountain region. The value for flat land region is in between the values for other two regions. The two reasons for the higher values in city region may be (i) the presence of objects like buildings, bridges, trees and other civil structures that may interrupt the incident solar radiation and (ii) the air pollution due to automobiles, industries, power plants, oil industries etc. that may deteriorate the quality of the air in city as compared to flat land and mountain

regions. Joshi and Tiwari [7] have conducted the experimental study of the cloudiness/haziness factor for New Delhi climatic condition and theoretical study for some other cities namely Bangalore, Jodhpur, Mumbai and Srinagar in India [11]. Table 1.2 shows the results of Joshi and Tiwari [7] for the climatic conditions of New Delhi. The hourly solar radiation data for past 11 years have been adopted from IMD. The climate is classified into four different types of sky conditions based on real irradiation namely a, b, c and d according to the ratio of daily diffuse radiation to the daily global radiation and the number of sunshine hours [7]. A day is said to be a clear or, blue sky day (type 'a') if the above ratio is less than or equal to 0.25 and the number of sunshine hours is more than or equal to 9. The hazy day (type 'b') is defined for the ratio between 0.25 and 0.50 and number of sunshine hours between 7 and 9. For partially hazy and cloudy day, that is, type 'c', the ratio is between 0.5 and 0.75 and the number of sunshine hours is between 5 and 7. Type 'd' or cloudy day is defined for the ratio more than or equal to 0.75 and the number of sunshine hours less than or equal to 5. It can be seen from Table 1.2 that the cloudiness/haziness factor increases from winters (January–February) to summers (May–June) and then decreases from summers to winters (November–December) for all the four types of the days. This is because in winters the sky is clear due to the presence of moisture in the atmosphere as compared to summers when the atmosphere is dry thereby allows suspension of more dust particles in the atmosphere. Also the cloudiness/haziness factor is least for type 'a' condition and maximum for the type 'd' condition for any month. In other words the cloudiness/haziness factor increases from type 'a' to type 'd'. Therefore, one can understand the significance of the cloudiness/haziness factor as lower the cloudiness/haziness factor clearer would be the sky conditions.

Table 1.3 shows the cloudiness/haziness factor and other parameters based on the horizontal solar radiation experimentally measured at New Delhi [7].

A careful observation reveals that the cloudiness/haziness factors for clear day condition (type 'a') in Table 1.2 resembles the values of flat land or mountain region in Table 1.1. This is because the IMD records solar radiation data on high rise towers and in big fields, for example, airports, which possess the same effect as that of flat land and/or mountain regions. Comparing Tables 1.1 and 1.3 shows that the cloudiness/haziness factors are higher (Table 1.3) and similar to the values of city region of Table 1.1. This is because Joshi and Tiwari [7] have conducted experiments in city region only. It is evident from the above discussion that the values for cloudiness/haziness factor change for different regions so that the intensity of solar radiation. To evaluate the solar radiation for a particular region, one should use the values of the cloudiness/haziness factor and other parameters accordingly. After identifying the values of the parameters the horizontal beam and diffuse radiation can be forecasted by the model of Joshi and Tiwari [7] which is given here to explain the methodology:

The terrestrial beam radiation (S_{HB}) received on horizontal surface is expressed as

$$S_{HB} = S_{ON} \exp\left[\frac{-T_R}{0.9 + 9.4\cos\theta_z} + \alpha\right]\cos\theta_z = S_N \cos\theta_z \tag{1.1}$$

Table 1.2 Parameters on horizontal surface for sunshine hours = 10 for all four weather type of days for New Delhi

Type of day	Parameters	Month											
		Jan	Feb	Mar	Apr	May	Jun	Jul	Aug	Sep	Oct	Nov	Dec
a	T_R	2.25	2.79	2.85	2.72	3.54	2.47	2.73	2.58	2.53	1.38	0.62	0.72
	α	0.07	0.10	0.17	0.23	0.16	0.28	0.37	0.41	0.29	0.47	0.59	0.54
	K_1	0.47	0.39	0.33	0.28	0.20	0.27	0.41	0.40	0.23	0.21	0.21	0.28
	K_2	−13.17	−6.25	5.61	38.32	65.04	31.86	−40.57	−55.08	39.92	32.77	30.62	9.73
b	T_R	2.28	2.78	2.89	3.15	5.44	4.72	5.58	5.43	3.23	4.56	0.19	1.83
	α	0.15	0.13	0.14	0.17	0.16	0.20	0.24	0.18	0.31	0.22	1.14	0.42
	K_1	0.51	0.54	0.49	0.46	0.45	0.45	0.53	0.39	0.37	0.42	0.35	0.40
	K_2	−21.77	−28.26	−9.22	−11.55	1.54	23.99	−51.61	9.46	14.07	−9.50	17.47	−0.07
c	T_R	5.88	6.36	6.11	7.77	9.20	10.54	7.13	7.97	5.51	5.01	4.93	3.23
	α	0.27	0.37	0.37	0.31	0.07	0.06	0.41	0.51	0.49	1.26	1.06	0.64
	K_1	0.39	0.36	0.33	0.35	0.56	0.48	0.47	0.35	0.39	0.36	0.31	0.43
	K_2	−14.73	−7.97	10.87	20.45	−56.00	−0.37	−52.27	47.70	35.64	−0.68	13.06	−7.04
d	T_R	7.47	8.97	10.77	11.18	13.69	12.47	8.21	8.58	9.40	7.24	4.30	4.02
	α	0.96	1.04	0.24	0.07	0.07	0.61	1.26	1.10	0.84	1.29	1.43	1.70
	K_1	0.35	0.30	0.43	0.49	0.48	0.46	0.43	0.43	0.41	0.36	0.31	0.38
	K_2	−25.89	−6.48	−36.46	−44.07	−42.58	−62.66	−56.75	−61.08	−27.09	3.90	20.10	−11.78

Table 1.3 Parameters for the prediction of solar radiation. (Adopted from [7])

Sunshine hours	Parameters	Months					
		Jan	Feb	Mar	Apr	May	Jun
8 (9 am−4 pm)	T_R	3.92	5.19	6.95	7.11	7.63	7.25
	α	0.05	0.07	0.04	0.06	−0.00	0.01
	K_1	0.27	0.23	0.19	0.18	0.18	0.15
	K_2 (W/m^2)	1.17	1.67	2.76	−1.15	−1.12	−3.54

where, T_R is cloudiness/haziness factor, α is atmospheric transmittance factor for beam radiation for lumped atmosphere, S_N (W/m^2) is the normal terrestrial solar radiation at the ground level, θ_z is zenith angle (degree) and S_{ON} (W/m^2) is extraterrestrial radiation.

S_{ON} is given by,

$$S_{ON} = S_{SC}\left[1.0 + 0.033\cos\left(360n/365\right)\right] \tag{1.2}$$

where, S_{SC} and n are solar constant (1367 W/m^2) and day of the year (i.e. for January 1, $n=1$). For calculation, the recommended average values of n for different months are used (Duffie and Beckman [12]).

The terrestrial diffuse radiation (S_{HD}) on horizontal surface can be written as

$$S_{HD} = K_1(S_{ON} - S_N)\cos\theta_z + K_2 \tag{1.3}$$

where, K_1 is perturbation factor and K_2 (W/m^2) is background diffuse radiation for diffuse radiation [9].

The cloudiness/haziness factor and atmospheric transmittance of Eq. (1.1) and the perturbation factor and background diffuse radiation of Eq. (1.3) can be obtained by linear regression analysis for known hourly data of beam and diffuse radiations. The linear regression analysis to obtain cloudiness/haziness factor and atmospheric transmittance of Eq. (1.1) is discussed in brief here:

Equation 1.1 can be rewritten as,

$$\frac{S_{HB}}{S_{ON}.\cos\theta_z} = \exp\left[\frac{-T_R}{0.9 + 9.4\cos\theta_z} + \alpha\right]$$

The above equation after taking natural log becomes

$$\ln\left[\frac{S_{HB}}{S_{ON}.\cos\theta_z}\right] = \frac{-T_R}{0.9 + 9.4\cos\theta_z} + \alpha$$

Above equation is a standard straight line equation as

$$Y = MX + C$$

where, $Y = \ln\left[\frac{S_{HB}}{S_{ON}\cos\theta_z}\right]$; $X = \left[\frac{1}{0.9 + 9.4\cos\theta_z}\right]$; $M = -T_R$ and $C = \alpha$

The values for above parameters are shown in Table 1.2 for New Delhi which are evaluated by using the hourly beam and diffuse radiation data for past 11 years provided by Indian Meteorological Department (IMD).

By using the above equations for the given values of the parameters described, beam and diffuse radiation can be calculated. The sum of beam and diffuse radiations gives the (S_T) global radiation on the horizontal surface.

Exergy of Solar Radiation

The quality of solar radiation often refers to its usability. How much energy of solar radiation we can use or what is the maximum usability of the solar radiation defines the availability of useful solar energy for a particular application. The limit of maximum usage of energy of solar radiation is known as exergy of solar radiation. The exergy of solar radiation depends upon its intensity, sun's temperature and the ambient temperature. Sun's temperature (5777 K) is almost constant throughout the year where as ambient temperature changes. Many scientists have tried to quantify the exergy of solar radiation namely, Petela [1], Jeter [2], Spanner [3], Saitoh et al. [4], Zamfirescu and Dincer [5], Joshi et al [6], Bejan [13], Santarelli and Macagno [14]. The exergy of solar radiation, in simple words, is the part of solar energy that can completely be utilized in useful purposes. The remaining part is known as exergy destruction due to irreversibility and it is bound to get wasted. To analyse the performance of any solar based system based on second law efficiency, the exergy of solar radiation is an important parameter without which the exergy analysis cannot be performed. Therefore, it becomes necessary to evaluate the exergy of solar radiation. The global solar radiation can be calculated by the model presented in the previous section. Once the global radiation (S_T) is available, the exergy rate of solar irradiance, $\dot{E}x_{solar}$ (W/m^2), can be evaluated approximately as (Jeter [2], Bejan [13], Santarelli and Macagno [14]):

$$\dot{E}x_{solar} = \left(1 - \frac{T_{amb.}}{T_{sun}}\right) S_T \tag{1.4}$$

which is probably the simplest model that has a thermodynamic term in the parenthesis which resembles the Carnot cycle efficiency of a fictitious heat engine between sun and earth.

The exergy rate of solar irradiance, can also be calculated by using Petela's [1] model as,

$$\dot{E}x_{solar} = \left[1 + \left(\frac{1}{3}\right)\left(\frac{T_{amb}}{T_{sun}}\right)^4 - \left(\frac{4}{3}\right)\left(\frac{T_{amb}}{T_{sun}}\right)\right] S_T \tag{1.5}$$

Saitoh et al. [4] have adopted an approach by assuming a flat 95 % of the solar radiation as the exergy of the solar radiation which is given as,

$$\dot{E}x_{solar} = 0.95 S_T \tag{1.6}$$

Zamfirescu and Dincer [5] have also proposed a model to calculate exergy of solar radiation as,

$$\dot{E}x_{solar} = \left[1 - \left(\frac{T_{amb}}{T_{sun}}\right)\left(\frac{S_{sc}}{S_T}\right)\right] S_T \tag{1.7}$$

The above model works well for the given range of solar radiation that is, $500 \geq S_T \geq 1000\,\mathrm{W/m^2}$.

Spanner [3] also gave a model to calculate exergy of solar radiation which is as follows,

$$\dot{E}x_{solar} = \left[1 - \left(\frac{4}{3}\right)\left(\frac{T_{amb}}{T_{sun}}\right)\right] S_T \tag{1.8}$$

Recently Joshi et al. [6] have proposed a new method to calculate exergy of solar radiation based on the photonic energy available on earth for a given solar intensity, wavelength of the visible spectrum and ambient temperature. The model looks simple and is as follows,

Energy of a photon can be given as,

$$E_{Ph}(\lambda) = \left(\frac{hc}{\lambda}\right) \tag{1.9}$$

where h is Planck's Constant (6.626×10^{-34} J s), c is speed of light (2.998×10^8 m/s), λ is wavelength of visible spectrum (nm).

To calculate the photonic energy falling on earth, the rate of photons falling is important. Following Markvart [15], the number of photons (N_{ph}) falling per second on one square centimeter area on earth for a clear sky day is 4.4×10^{17} (for per square meter area on earth it is 4.4×10^{21}). Assuming the solar radiation as the solar constant (1367 W/m^2) for a clear day, the number of photons falling per second on per square meter area can be calculated for a given solar radiation by multiplying it (solar radiation) with a factor $((4.4 \times 10^{21})/1367)$. The rate of photonic energy (W/m^2), thus, can be calculated by multiplying the number of photons (N_{ph}) falling per second per square meter area on earth and the energy of a photon and can be given as,

$$\dot{E}n_{Ph}(\lambda) = E_{Ph}(\lambda) \times N_{Ph} \tag{1.10}$$

where, N_{Ph} can be calculated as,

$$N_{Ph} = \left(\frac{4.4 \times 10^{21}}{1367}\right) S_T \tag{1.11}$$

Once the photonic energy is known, the available photonic exergy, $\dot{E}x_{Ph}\,(\mathrm{W/m^2})$, can be calculated by multiply it with a thermodynamic term, $(1-(T_{amb}/T_{sun}))$ as suggested by Marti and Luque [16] and can be given as,

$$\dot{E}x_{Ph}(\lambda) = \dot{E}n_{Ph}(\lambda) \times \left(1 - \frac{T_{amb}}{T_{sun}}\right) = \left(\frac{hc}{\lambda}\right) N_{Ph} \left(1 - \frac{T_{amb}}{T_{sun}}\right) \tag{1.12}$$

Here, three key terms are: (i) energy of a photon, (ii) number of photons falling per second per meter square on earth for a given solar radiation intensity and, (iii) a thermodynamic term same as the Carnot cycle efficiency of a fictitious heat engine working between the sun and the earth's ambient temperatures. The third term is useful to limit the maximum useful work/energy (that is, exergy) that can be drawn from the given high and low temperatures. Therefore, Eq. (1.12) is dependent on wavelength of the visible spectrum, number of photons falling per second on per square meter on earth for a given solar intensity and ambient temperature. Once the above variables of Eqs. (1.10–1.12) are known; the exergy of the solar radiation can be calculated.

In the next section, the models presented in the current section for global solar radiation and exergy of solar radiation forecasting is applied to some real climatic conditions.

1.3 Case Study

For a case study, New Delhi climatic condition is chosen and data for monthly average solar radiation on horizontal surface and ambient temperature (Table 1.4) and the parameters used in Eqs. (1.1–1.3) (Table 1.3) for winter (January) and summer (June) seasons are adopted from Joshi and Tiwari [7]. Two pyranometers have been used to measure the global and diffuse radiations. The first has been used to measure hourly global radiation and second one for hourly diffuse radiation with the help of shading ring. The pyranometers have been connected to a computer through a data logger for hourly readings. Both pyranometers have been calibrated at regular intervals of three months so that any corrections due to moisture/dust/starch deposition on cover can be taken into account. The ring has been adjusted at regular intervals to give complete shadow over pyranometer. The ambient temperature was measured by using a calibrated thermometer. The average value for day of the month (n) used in the Eq. (1.2) is adopted from Duffie and Beckman [12] as 17 and 167 for January and June respectively. As mentioned earlier, the January and June months are chosen as representative of winter and summer seasons respectively. As mentioned earlier, the types of days, that is, a, b, c and d signify clear (blue sky) day, hazy day, partially hazy and cloudy day and completely cloudy day respectively.

Table 1.4 Monthly average hourly global experimental and theoretical (predicted) solar radiations, photonic energy, ambient temperature and exergy from solar radiation for January and June

Month	Time (hour)	Amb. temp	Solar radiation (W/m^2)		Photonic energy (W/m^2)	Exergy from solar radiation (W/m^2)					
			Exp	Theo		Petela [1]	Jeter [2]	Spanner [3]	Zamfirescu and Dincer [5]	Joshi et al. [6]	Saitoh [4]
January	9:00	11.00	264.25	268.62	263.53	251.05	255.41	251.05	201.38	250.57	255.19
	10:00	15.00	411.27	444.01	435.59	414.55	421.86	414.55	375.82	413.87	421.81
	11:00	17.00	517.48	575.69	564.79	537.24	546.78	537.24	507.04	536.42	546.91
	12:00	18.00	579.85	644.11	631.91	600.93	611.65	600.93	575.21	600.06	611.9
	1:00	18.00	576.18	640.86	628.72	597.91	608.57	597.91	571.97	597.04	608.82
	2:00	19.00	520.45	566.34	555.61	528.25	537.70	528.25	497.21	527.52	538.03
	3:00	19.00	400.43	429.77	421.63	400.86	408.03	400.86	360.64	400.30	408.28
	4:00	19.00	256.38	252	247.23	235.05	239.26	235.05	182.87	234.72	239.4
June	9:00	37.00	445.1	449.55	441.03	417.45	425.42	417.45	376.16	417.36	427.07
	10:00	38.00	595.24	596.17	584.88	553.47	564.06	553.46	522.54	553.37	566.36
	11:00	42.00	686.67	700.49	687.22	649.67	662.28	649.67	625.92	649.73	665.47
	12:00	43.00	715.8	749.45	735.25	694.9	708.43	694.9	674.64	695.01	711.98
	1:00	45.00	700.78	737.37	723.40	683.36	696.76	683.36	662.09	683.56	700.5
	2:00	46.00	630.63	665.63	653.02	616.72	628.86	616.72	590.11	616.94	632.35
	3:00	43.00	585.64	542.73	532.45	503.23	513.03	503.23	467.92	503.31	515.59
	4:00	42.00	345.87	384.88	377.59	356.95	363.88	356.95	310.3	356.99	365.63

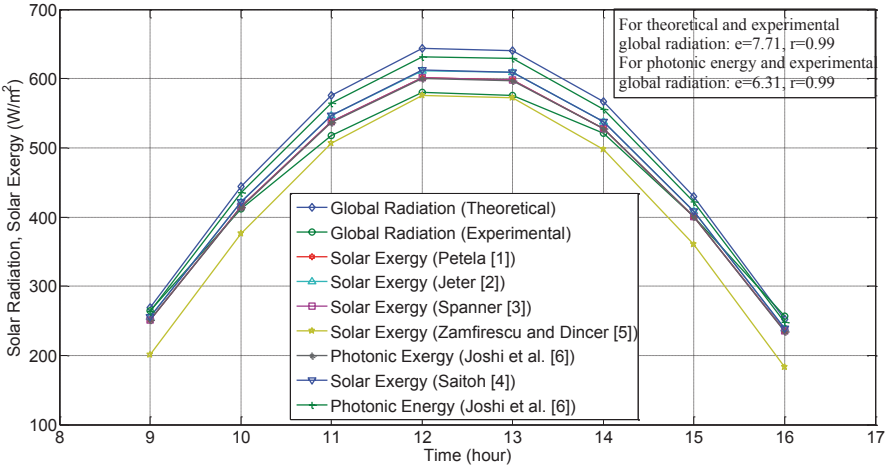

Fig. 1.1 Comparison of experimental and predicted solar radiations and exergy of predicted solar radiation for January ($n = 17$)

The above said data and Eqs. (1.1–1.3) are used to evaluate the solar radiation for a particular month and then by using Eqs. (1.5–1.12), the exergy of the solar radiation is calculated by various models presented. The predicted monthly average global radiations for January and June are compared with the measured monthly average global radiation. The photonic energy is also evaluated and compared with the monthly average global radiation for January and June. Effect of T_R, α, K_1 and K_2 is evaluated on the exergy of the solar radiation by varying one parameter at a time and keeping others constant.

1.4 Results and Discussion

Figure 1.1 shows the predicted solar radiation based on the values of T_R, α, K_1 and K_2 for the month of January and June. As discussed above, the average day of the month is taken as 17 for January and 167 for June following Duffie and Beckman [12]. The theoretical and experimental results of global solar radiations are in fairly well agreement with root mean square of standard deviation and regression coefficient as 7.71 % and 0.99 respectively for January (Fig. 1.1) and 5.51 % and 0.98 respectively for June (Fig. 1.2). Therefore for the exergy of solar radiation calculation, theoretical (predicted) solar radiation is used. The photonic energy, by using Eq. (1.10) is also calculated and compared with the experimental global radiation for January and June and it is found that they are in fair agreement with root mean square of standard deviation and regression coefficient as 6.31 % and 0.99 for January and 5.04 % and 0.98 for June respectively. It should be noted that the photonic energy is calculated by using the theoretical global radiation and a reasonable value

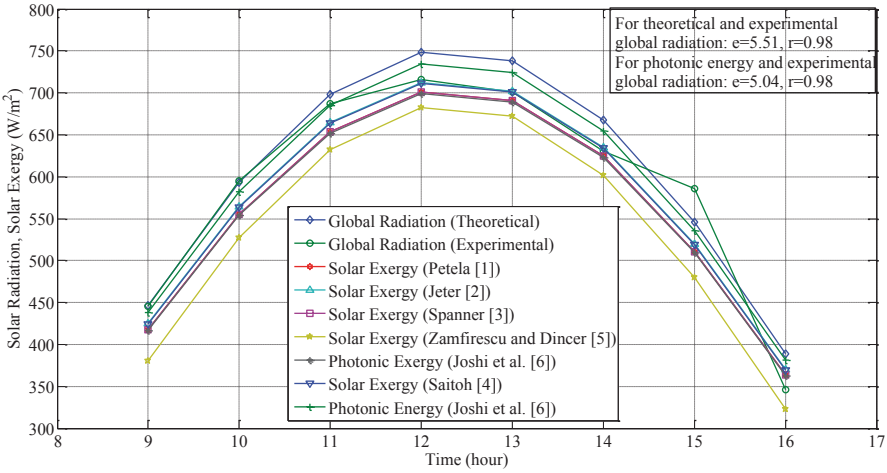

Fig.1.2 Comparison of experimental and predicted solar radiations and exergy of predicted solar radiation for June ($n=167$)

of wavelength, that is, 650 nm, for which the root mean square of standard deviation for photonic energy and experimental solar radiation is the least.

The exergy of solar radiation using different models is also given in the Figs. 1.1 and 1.2 for January and June respectively. It is evident from the same figures that Petela's [1] and Spanner's [3] models give same results till the fifth place after decimal. This is because the fourth order term in the Petela's [1] model (Eq. 1.5) is the only different term from the Spanner's [3] model (Eq. 1.8) and due to its extremely small numerical value, it makes a difference only after fifth decimal place in the exergy of solar radiation. Joshi et al.'s [6] model also gives almost same values as that of the two models discussed above. Jeter's [2] and Saitoh's [4] models give slightly higher values and Zamfirescu and Dincer's [5] model gives lower values than the three models discussed, namely, Petela's [1], Spanner's [3] and Joshi et al.'s [6].

Table 1.4 shows the monthly average hourly global experimental and theoretical solar radiation and exergy of solar radiation evaluated by the various models presented in Section 1.2.2 for January and June. Photonic energy is also calculated by using the theoretical solar radiations and presented in the same table. The experimental solar radiation data is obtained for New Delhi from Joshi and Tiwari [7] whereas the theoretical solar radiation is evaluated by using the values of T_R, α, K_1 and K_2 given for clear sky condition and city region (Table 1.3). A comparison of the results obtained by different models with the solar radiation is given in Table 1.5.

By keeping the value of hourly solar radiation as 1, the exergy is evaluated in fraction corresponding to each model. It is evident from the same table that the Petela's [1] model gives the average exergy fraction as 0.932397 and 0.927448 for January and June respectively whereas Jeter's [2] model gives slightly higher

Table 1.5 Exergy as a fraction of solar radiation for January and June

Month	Time (hour)	Solar radiation in fraction	Exergy as a fraction of solar radiation					
			Petela [1]	Jeter [2]	Spanner [3]	Zamfirescu and Dincer [5]	Joshi et al. [6]	Saitoh [4]
January	9:00	1	0.934584	0.950814	0.934582	0.749690	0.932801	0.950000
	10:00	1	0.933663	0.950121	0.933661	0.846434	0.932121	0.950000
	11:00	1	0.933203	0.949775	0.933201	0.880739	0.931782	0.950000
	12:00	1	0.932973	0.949602	0.932970	0.893039	0.931612	0.950000
	1:00	1	0.932973	0.949602	0.932970	0.892498	0.931612	0.950000
	2:00	1	0.932742	0.949429	0.932740	0.877934	0.931442	0.950000
	3:00	1	0.932742	0.949429	0.932740	0.839144	0.931442	0.950000
	4:00	1	0.932742	0.949429	0.932740	0.725671	0.931442	0.950000
Average		***1***	***0.933203***	***0.949775***	***0.933201***	***0.838144***	***0.931782***	***0.950000***
June	9:00	1	0.928599	0.946313	0.928596	0.836748	0.928385	0.950000
	10:00	1	0.928369	0.946140	0.928366	0.876500	0.928215	0.950000
	11:00	1	0.927448	0.945447	0.927445	0.893541	0.927536	0.950000
	12:00	1	0.927218	0.945274	0.927215	0.900180	0.927366	0.950000
	1:00	1	0.926757	0.944928	0.926754	0.897903	0.927027	0.950000
	2:00	1	0.926527	0.944755	0.926524	0.886544	0.926857	0.950000
	3:00	1	0.927218	0.945274	0.927215	0.862160	0.927366	0.950000
	4:00	1	0.927448	0.945447	0.927445	0.806241	0.927536	0.950000
Average		***1***	***0.927448***	***0.945447***	***0.927445***	***0.869977***	***0.927536***	***0.950000***

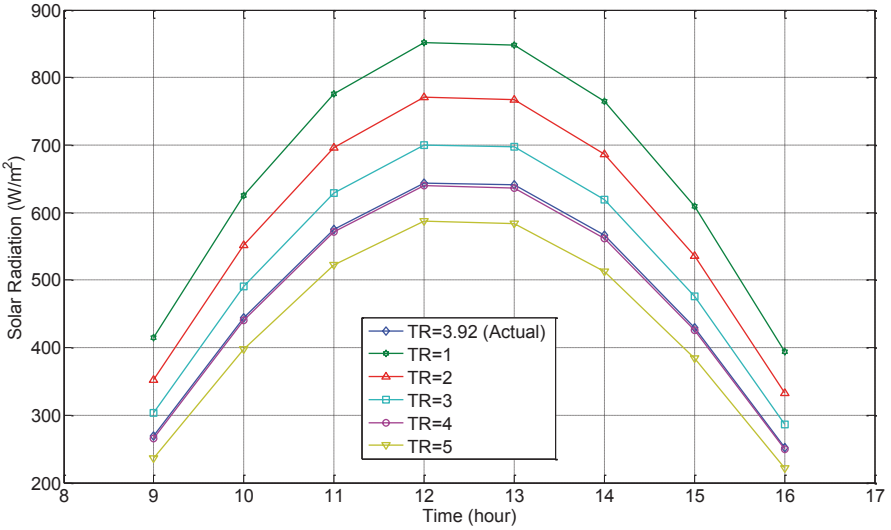

Fig. 1.3 Effect of cloudiness/haziness factor on solar radiation

exergy fraction (0.949175 and 0.945438 for January and June respectively) as compared to the Petela's [1] and Spanner's [3] (0.932395 and 0.927445 for January and June respectively) models. Zamfirescu and Dincer's [5] model gives average exergy fraction 0.835925 and 0.869963 whereas Joshi et al.'s [6] model gives 0.931188 and 0.927538 for January and June respectively. Saitoh's [4] model gives exergy fraction at a flat rate, that is, 0.95. As discussed earlier, Petela's [1] and Spanner's [3] models give almost identical values; identical up to fifth decimal place and only sixth decimal place is different. The variation in Zamfirescu and Dincer's [5] model is highest as compared to any other model. By critical examination of the results of Zamfirescu and Dincer's [5] model, one can infer that the variation in the values is less for the higher solar radiations and it is more when the solar radiation is less. In other words, the model gives closer results same as other models for higher solar radiations and for lower solar radiations, the difference in the values is more. Joshi et al.'s [6] model (Eq. 1.12) based on photonic energy is also comparable with other models. Though it gives the upper and lower limits (for details see [6]) of exergy of the solar radiation for different wavelengths of visible spectrum (400–700 nm), but a reasonable value of the exergy has been calculated for comparatively long wavelength. As discussed earlier, a reasonable value of wavelength, i.e., 650 nm is adopted following Joshi et al. [6].

The effect of various parameters used in Eqs. (1.1–1.3), are shown in Figs. 1.3, 1.4, 1.5 and 1.6. These figures are drawn by varying one parameter at a time and keeping others constant so as to obtain the effect of each parameter individually on the quality of solar radiation. A higher value of solar radiation obtained by varying the various parameters directly relates to the higher amount of exergy in it.

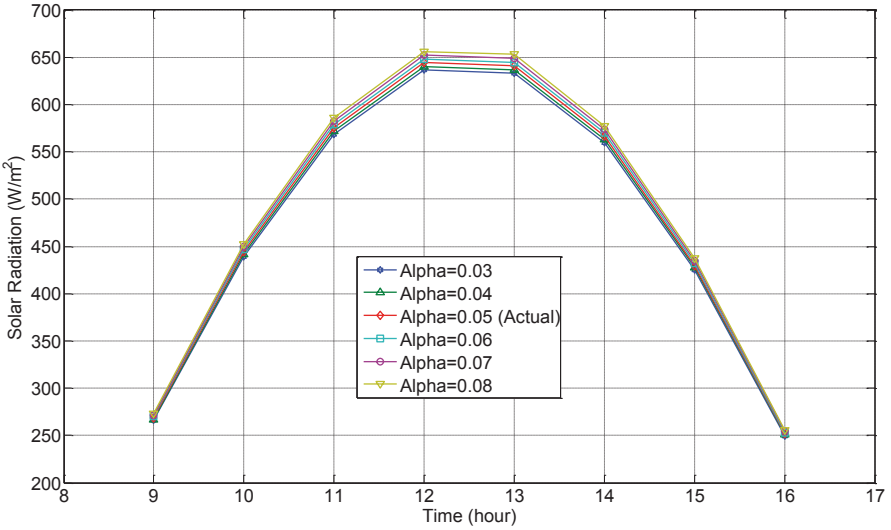

Fig. 1.4 Effect of atmospheric transmittance on solar radiation

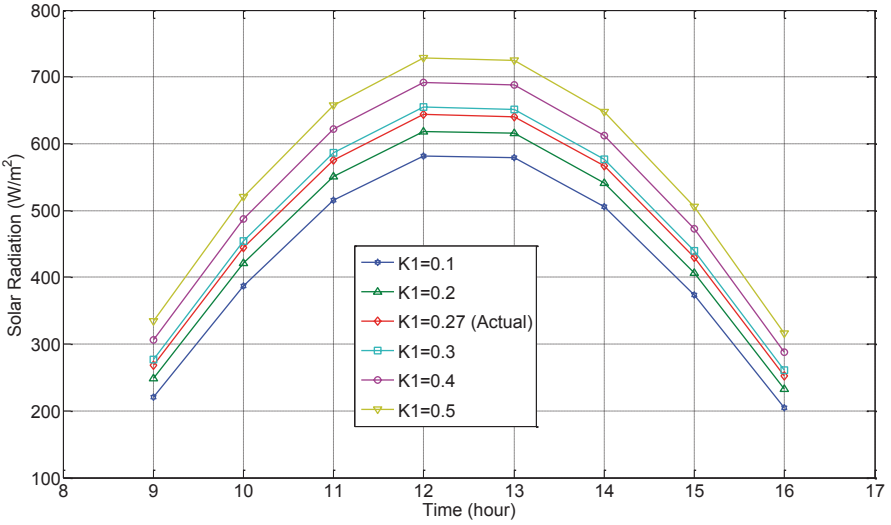

Fig. 1.5 Effect of perturbation factor on solar radiation

Figure 1.3 shows the effect of cloudiness/haziness factor on the quality of solar radiation. Quality here relates to the intensity of solar radiation. The figure shows the intensity of solar radiation for different cloudiness/haziness factors starting from 1 to 5 with an increment of 1. The measured average solar radiation (at $T_R = 3.92$)

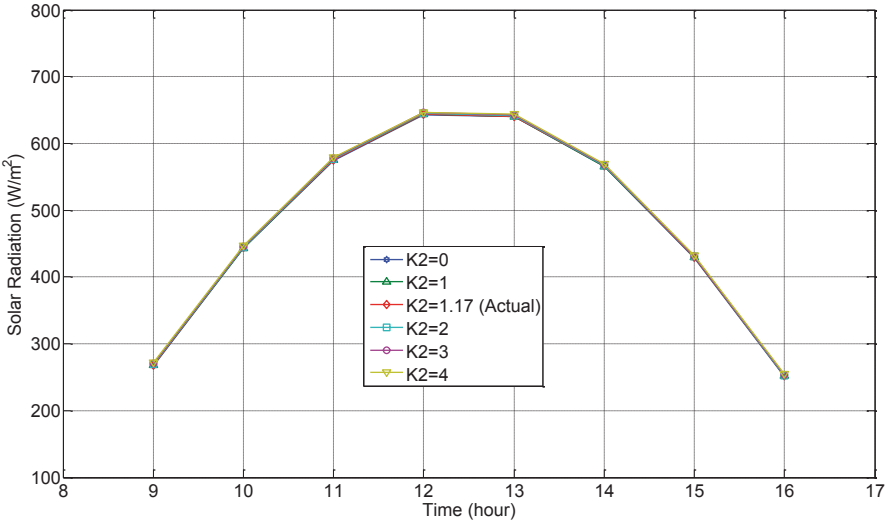

Fig. 1.6 Effect of background diffuse radiation on solar radiation

for clear sky and city condition for January is also shown in same figure for comparison. The solar radiation varies from a minimum of 410–400 W/m^2 in the morning and evening at 9 am and 4 pm respectively to a maximum of 850 W/m^2 in the afternoon at 12 pm and 1 pm for $T_R = 1$. For $T_R = 2$, radiation varies from a minimum of 350 to a maximum of 760 W/m^2 at 9 am and 12 pm respectively. Similarly, for $T_R = 3$, solar radiation varies from 300 to 700 W/m^2 and for $T_R = 4$, it varies from 370 to 640 W/m^2 which is almost same for the variation of solar radiation for $T_R = 3.92$. For $T_R = 5$ the variation is least, that is, from 240 to 590 W/m^2. A careful observation reveals that at 12 pm the highest solar radiation is for $T_R = 1$ and the lowest is for $T_R = 5$. It is clear from the same figure that higher cloudiness/haziness factor relates to poor quality or less intensity of the solar radiation. When the cloudiness/haziness factor is reduced from 3.92 to 3 and 1, which means reducing the value by 25 and 75 %, it resulted in an increase in the solar radiation from 8 to 31 % respectively. This can be seen from Fig. 1.3 between 12 and 1 pm. Also when the cloudiness/haziness factor is increased by 25 %, a reduction of almost 9 % in the solar radiation can be seen in the same figure between 12 and 1 pm. A higher value of T_R may be obtained as a consequence of heavy suspension of dust particles in the sky (Joshi [11]).

The effect of atmospheric transmittance on solar radiation is shown in Fig. 1.4. Variation in solar radiation is plotted for different atmospheric transmittance from 0.03 to 0.08. The solar radiation corresponding to the atmospheric transmittance for January, that is, 0.05 is also shown in same figure for comparison. When atmospheric transmittance increases from 0.05 to 0.08 that means, an increase of 60 % in the atmospheric transmittance, it results in the increase of solar radiation from 640 to 660 W/m^2 between 12 and 1 pm, that is, an increase of 3.13 % only. Similarly,

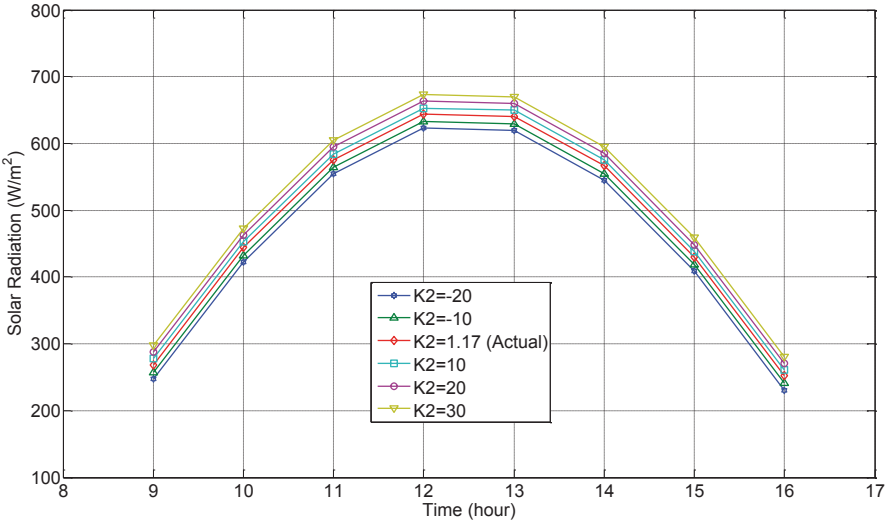

Fig. 1.7 Effect of background diffuse radiation at higher magnitudes on solar radiation

when atmospheric transmittance is decreased from 0.05 to 0.03, that means, a decrease of 40 % in the atmospheric transmittance, it resulted in the decrease of solar radiation from 640 to 630 W/m^2 between 12 and 1 pm, that is, a decrease of 1.56 % only. Therefore it can be said that the effect of atmospheric transmittance on solar radiation is not as significant as that of cloudiness/haziness factor.

The effect of perturbation factor can be seen from Fig. 1.5. It can be said that the increased values of K_1 ensures increased values of solar radiation. An average value of solar radiation (at $K_1 = 0.27$) for clear sky condition for January is also shown in same figure.

A decrease in perturbation factor from 0.3 to 0.1 that is when the perturbation factor is reduced by 2/3rd, there is a decrease of 11 % in the solar radiation and when it is increased by 2/3rd that is from 0.3 to 0.5, there is an increase of 12 % in the solar radiation between 12 and 1 pm. The effect of perturbation factor on solar radiation is also not as significant as that of cloudiness/haziness factor.

If the increase or decrease in the magnitude of K_2 is made 10–20 times than that of its actual value, the effect on solar radiation is evident. This is shown in Fig. 1.7. It can be seen from the same figure that if the background diffuse radiation is increased by almost 30 times its actual value (1.17 W/m^2), an increase of only 5 % in solar radiation is observed at 12 pm. An increased value of background diffuse radiation is responsible for the higher global radiation but it can affect only at higher magnitudes. However, it is not of much use as far as application of solar radiation is concerned as it increases diffuse radiation only and hence, a lower value is desirable. It can be said that the effect of background diffuse radiation on solar radiation is the least and that of the cloudiness/haziness factor is the most amongst the four parameters.

Conclusions

Various models are presented to evaluate the exergy of the solar radiation. Once the cloudiness/haziness factor, atmospheric transmittance of sky, perturbation factor and background diffuse radiation are established, the global solar radiation and exergy of solar radiation can be predicted for a particular location. The following concluding remarks can be drawn from the above study:

- Cloudiness/haziness factor is an important parameter to evaluate the quality of the solar radiation and hence the exergy of the solar radiation.
- A lower value of cloudiness/haziness factor is desirable to have more exergy of the solar radiation.
- Higher values of atmospheric transmittance, perturbation factor and background diffuse radiation result in higher solar radiation but the last parameter only increases the diffuse radiation as a composition of global radiation hence a lower value of it is desirable.
- The effect of cloudiness/haziness factor on solar radiation is highest in comparison to the other parameters namely atmospheric transmittance, perturbation factor and background diffuse radiation.
- All models give reasonably close results for the exergy of solar radiation.
- Photonic approach is comparable with the other models as it gives closer value of exergy of solar radiation for a reasonable value of comparatively long wavelength.

Nomenclature

c	Speed of light $(2.998\times10^{8}\,\mathrm{m/s})$
e	Root mean square of percentage deviation (%)
$E_{ph}(\lambda)$	Energy of a photon (J)
$\dot{E}n_{ph}(\lambda)$	Rate of photonic energy (W/m^2)
$\dot{E}x_{ph}(\lambda)$	Rate of photonic exergy (W/m^2)
$\dot{E}x_{solar}$	Exergy rate of solar radiation (W/m^2)
h	Planck's Constant $(6.626\times10^{-34}\,\mathrm{Js})$
K_1	Perturbation factor
K_2	Background diffuse radiation (W/m^2)
n	Day of the month/year (Example, for 1st January, $n=1$)
N_{ph}	Number of photons falling per second per unit area on earth (1/s m^2)
r	Linear coefficient of correlation (dimensionless)
S_{HB}	Horizontal beam solar radiation (W/m^2)
S_{HD}	Horizontal diffuse solar radiation (W/m^2)
S_N	Normal terrestrial solar radiation at the ground level (W/m^2)
S_{ON}	Extraterrestrial radiation (W/m^2)
S_T	Hourly measured total solar irradiation (W/m^2)
S_{SC}	Solar constant (1367 W/m^2)
T_{amb}	Ambient air temperature (°C)
T_{sun}	Sun Temperature (5777 K)
T_R	Cloudiness/haziness factor

α Atmospheric transmittance
θ_z Zenith angle (degree)
λ Wavelength of visible spectrum $(400\text{nm} \le \lambda \le 700\text{nm})$ of solar radiation (nm)

Acknowledgement The authors acknowledge the financial support provided by the Natural Sciences and Engineering Research Council of Canada.

References

1. Petela R (2003) Exergy of undiluted thermal radiation. Sol Energy 74(6):469–488
2. Jeter SJ (1981) Maximum conversion efficiency for the utilization of direct solar radiation. Sol Energy 26:231–236
3. Spanner DC (1964) Introduction to thermodynamics. Academic Press, London
4. Saitoh H, Hamada Y, Kubota H, Nakamura M, Ochifuji K, Yokoyama S (2003) Field experiments and analyses on a hybrid solar collector. Appl Therm Eng 23:2089–2105
5. Zamfirescu C, Dincer I (2009) How much exergy one can obtain from incident solar radiation? J Appl Phys 105:044911
6. Joshi AS, Dincer I, Reddy BV (2009) Thermodynamic assessment of photovoltaic systems. Sol Energy 83:1139–1149
7. Joshi AS, Tiwari GN (2007) Evaluation of solar radiation and its application for photovoltaic/thermal air collector for Indian composite climate. Int J Energy Res 31:811–828
8. Tiwari GN (2002) Solar energy: fundamentals, design, modeling and applications. Narosa Publishing House/CRC Press, New Delhi/Washington
9. Singh HN, Tiwari GN (2005) Evaluation of cloudiness/haziness factor for composite climate. J Energy 20:1589–1601
10. Linke F (1922) Transmission coefficient and turbidity factor. J Beitraege Phys Fr Atom 10:91–103
11. Joshi AS (2006) PhD thesis. Evaluation of cloudiness/haziness factor and its application for photovoltaic thermal (PV/T) system for Indian climatic conditions, IIT Delhi, New Delhi, India
12. Duffie JA, Beckman WA (1991) Solar engineering of thermal processes, 2nd edn. Wiley Interscience, New York, pp 1–14
13. Bejan A (1998) Advanced engineering thermodynamics. Wiley, Chichester
14. Santarelli M, Macagno SA (2004) A thermo economic analysis of a PV hydrogen system feeding the energy requests of a residential building in an isolated valley of the Alps. Energy Convers Manage 45(3):427–451
15. Markvart T (2003) Solar electricity, 2 edn. Wiley, Chichester
16. Marti' A, Luque A (2004) Next generation photovoltaics high efficiency through full spectrum utilization. Institute of Physics Publishing Ltd., Bristol

Chapter 2
Investigation of a Renewable Energy-Based Integrated System for Baseload Power Generation

Mehdi Hosseini, Ibrahim Dincer and Marc A. Rosen

Abstract A renewable energy-based integrated system is proposed for baseload power generation. Wind, solar, and biomass options are considered. The electric power produced by wind turbines, a photovoltaic (PV) system, and fuel cells is fed to the power grid. The surplus electricity produced by the integrated energy system is stored in forms of compressed air and hydrogen. When required, the compressed air is heated in a combustion process and expanded in a gas turbine for further power generation. The hydrogen produced by the electrolysis process is fed to a solid oxide fuel cell (SOFC) system for electricity generation. The system is analyzed with energy and exergy methods, and results are presented for monthly power generation, compressed air energy storage (CAES) and compression, and hydrogen production and consumption rates. Moreover, exergoeconomic analyses are performed based on the unit exergy cost of the electricity produced by the integrated system. The round-trip efficiency of the CAES system is 60 % without considering heat recovery potentials. The overall energy and exergy efficiencies of the integrated system are 37.0 and 31.9 %, respectively. Results of the exergoeconomic analyses show that the unit cost of electricity generated by the Wind-CAES system is 7 ¢/kWh, while it is 89 and 17 ¢/kWh for the photovoltaic-hydrogen-solid oxide fuel cell and the biomass-solid oxide fuel cell-gas turbine systems, respectively.

Keywords Renewable · Integrated energy system · Energy · Exergy · Solar · Wind · Biomass · Fuel cell

M. Hosseini (✉) · M. A. Rosen
Faculty of Engineering and Applied Science, University of Ontario Institute of Technology, 2000 Simcoe St. North, ON L1H 7K4, Canada
e-mail: mehdi.hosseini@uoit.ca

I. Dincer
Department of Mechanical Engineering, University of Ontario Institute of Technology (UOIT), 2000 Simcoe Street North, Oshawa ON L1H 7K4, Canada
e-mail: ibrahim.dincer@uoit.ca

I. Dincer et al. (eds.), *Progress in Sustainable Energy Technologies: Generating Renewable Energy,* DOI 10.1007/978-3-319-07896-0_2,

2.1 Introduction

Renewable energy resources (e.g. wind and solar) cannot produce steady electric power, due to their intermittent characteristics. Wind speed and direction change almost constantly due to weather conditions, and solar irradiance reaching the surface of the earth is dependent on geographical location, time of the day, and clearness of the sky. However, proper design of wind turbines (variable speed power generators, appropriate pitching and tilting) makes them capable of producing a fixed-rated power over a course of wind speed range. No matter how sophisticated are the wind turbine control systems, the power output of a wind park depends on the wind speed. Therefore, when utilizing wind turbines in a baseload power plant, the intermittent power output of the wind park must be compensated. One solution is using energy storage systems, and example of which is compressed-air energy storage (CAES). During the period of excess power generation by the wind park, a CAES system can convert and store the surplus electricity in the form of compressed air.

Another option for overcoming the intermittent behavior of wind energy in generating constant rated power is hydrogen storage. According to Yang and Aydin [1], the excess power output of wind turbines can be utilized in water electrolysers for hydrogen production and storage. Once the hydrogen is stored in an appropriate high-pressure vessel, it can be used in a combustion engine, fuel cell, or water-cooled burner to produce high-quality steam for space heating, or to drive a turbine to generate electric power. In large scale baseload power generation, the size of the hydrogen tanks will be significantly large, and work of compression will be considerable.

Batteries, as small scale power generation systems, could be a good option to store the excess generated electricity by the wind turbine(s) and meet the demand when needed. However, in large scale scenarios (baseload power), batteries are very bulky, expensive, and require continuous maintenance. CAES seems promising, since the compressed air is stored in abandoned mines or underground salt caverns. CAES utilizes the familiar gas turbine cycle, with a simple modification. When integrated with wind turbines, excess generated electricity by the wind turbines is consumed by the compressors to compress ambient air, which is stored in the salt cavern or the abandoned mine.

Solar energy systems can also benefit from energy storage. The surplus electric power output of a solar photovoltaic (PV) system can be utilized for hydrogen production, which can be stored in hydrogen tanks for later use. Integrated wind and solar energy-based systems can help reduce greenhouse gas emission rates, if designed for baseload power production. This is achieved through diminishing the use of fossil fuels for electricity generation. Further, Ashraf, et al. [2] report that solar photovoltaic systems have great potential in grid-connected power generation, due to their simplicity of installation, operation and maintenance, and being carbon emission free electricity generation systems.

However, not all the renewable energy resources are emission free. Unlike wind and solar that produce almost no greenhouse gases (GHGs), biomass is a renewable energy resource that releases carbon containing gases when used. For example, a solid-oxide fuel cell-micro gas turbine (SOFC-GT) system integrated with biomass

gasification releases 741 g/kWh of CO_2 [3]. This level of gross emission is comparable to the carbon dioxide emission by a fossil fuel power plant, 617 g/kWh.

Renewable energy-based systems can be integrated to increase renewable energy utilization. Depending on the available renewable resources, different configurations can be proposed. In this study, an integrated renewable energy-based system is proposed to supply baseload electric power. The system utilizes wind, solar, and biomass as the renewable energy resources. Basedload wind energy is the subject of the work by Greenblatt, et al. [4]. The economic feasibility of a wind-CAES system is investigated and compared with gas and wind-gas power plants. The CAES system is used to store the surplus generated electricity by the wind turbines. For one set of input assumptions, i.e. $ 5/GJ effective natural gas price and 650 W/m^2 wind resource, the wind-CAES is the most expensive (6 ¢/kWh) system. This result is obtained for a compressed air energy storage system with a 169 h storage capacity.

Residential applications of photovoltaic electricity generation systems can be grid-connected and grid-independent. In both cases energy storage systems may be required to increase renewable energy utilization and/or to achieve higher power reliability. Widén, et al. [5] present options for improving PV capability in load following scenarios, considering the following options: PV array orientation, demand-side management (DSM) and electricity storage. They apply the available methods to a PV system for residential applications, and conclude that energy storage is more efficient than DSM and photovoltaic orientation methods if high PV penetration is desired. Castillo-Cagigal, et al. [6] present active demand-side management (ADSM) analysis for a grid-connected residential PV system in Spain. The ADSM method basically controls the power load variations between the electricity generation/supplying systems and the demand. The presented experimental set up is connected to the local electricity grid, and takes advantage of lead-acid battery storage.

Solar PV systems also can be used for large-scale, baseload power generation, as pointed out by Radchik, et al. [7].They state that intermittency of solar power output is a major factor in economic development of baseload PV systems. They propose market-based solutions for baseload PV electricity generation systems integrated with virtual non-intermittent generators, i.e. gas-fired power plants. This provides a financially attractive option for integrating a solar generator into existing electricity markets.

Solid oxide fuel cells are capable of operating with such fuels as natural gas, hydrogen, and syngas. The latter is produced with biomass gasification, and can be directly used after post-processing in SOFCs [3]. Colpan, et al. [8] investigate effects of gasification medium on systems integrating biomass gasification and SOFCs. Steam gasification is found to have a higher exergy efficiency, relative to air gasification. Also, the results show that a higher electricity generation rate (in the SOFC) is achieved with steam as the biomass gasification medium. Exergy, a measure of the quality of energy, is a concept that helps with identifying sources of irreversibility in a system or a process flow [9]. Exergy combines with economics to form exergoeconomics, which is used for evaluating the costs related to unit exergy flows and system products [9].

In the present study an integrated renewable energy-based system is investigated for baseload power generation. The integrated system utilizes wind, solar and

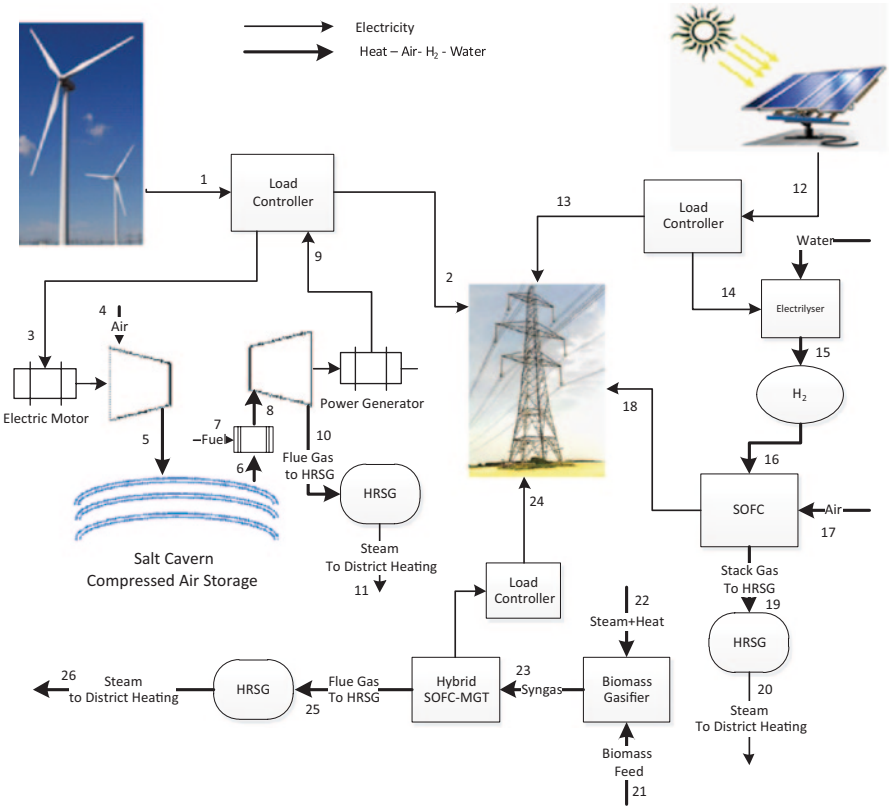

Fig. 2.1 Simplified schematic of grid-integrated renewable combined heat and power system for a district

biomass as the renewable energy resources. Energy and exergy methods are used to analyze the system electric power generation and thermal energy output. Moreover, carbon emission rates are calculated on a per kWh basis. Economic analyses are combined with exergy concepts to perform exergoeconomic analyses of the system, providing information regarding unit cost of electricity production of the electric power generation components.

2.2 System Description

The renewable-based integrated energy system contains three different power generation systems, each utilizing a renewable energy resource. As shown in Fig. 2.1, wind, solar and biomass are the renewable energy resources.

The integrated system is meant to supply the baseload electric power of a district, and the system components are selected so the wind park has the greatest share in

meeting the power demand. The operation of each sub-system of the integrated system is described below.

Wind-CAES

The power output of the wind park (point 1) is fed to a load controller. The controller decides if the power output should be delivered to the grid (point 2) or to the CAES system (point 3). When the electric power output of the wind park is more than the demand, the surplus electricity is fed to the CAES system. The compressor consumes the surplus electricity to pressurize ambient air (point 4) in two steps. First, the ambient air is compressed to a medium pressure (pressure ratio of r_c), and is cooled in the heat-exchanger. The heat removed from the compressed air in the heat exchanger can be used for district heating, or can be stored in a thermal storage system. The medium pressure, low temperature air enters the next compressor for further compression. During the compression process it gains energy. To decrease the required volume for storage, the high pressure compressed air is cooled in the second heat exchanger, and stored in underground salt caverns (point 5).

If the power output of the wind park is less than the demand, the gas turbine operates, extracting compressed air (point 6) from the salt cavern. The compressed air enters a combustion process with natural gas (point 7), and is fed to the gas turbine (point 8) for electric power generation (point 9). To increase efficiency, the gas turbine exhaust gas (point 10) is fed to the heat recovery steam generator (HRSG) for low pressure steam generation (point 11). The generated steam is stored in a thermal energy storage system. Due to the intermittency of power generation by the gas turbine, an advantageous way to utilize the generated steam is energy storage, as it gives more flexibility in meeting part of the thermal demand of the district. The compressor must produce enough compressed air so there is a net positive amount of stored air in the salt cavern throughout the year, considering air consumption by the gas turbine.

PV-H_2-FC System

The photovoltaic-hydrogen-solid oxide fuel cell (PV-H_2-FC) is considered to supply a small part of the electricity demand (5 MW). This decision is made due to the high land use of the photovoltaic system (5.9 m^2/kWe). The electricity output of the PV system depends on solar irradiance, which is related to climate. It is possible to size the PV system so that electricity generated during day time exceeds demand, and surplus electricity can be harvested and stored as hydrogen gas. Thus the PV system generates as much electricity as needed to meet the electricity demand. The intermittent characteristic of solar energy is overcome by the hydrogen–fuel cell system. The electrolyser utilizes the surplus electricity of the PV system (point 13) during times of the day when PV output exceeds the electricity demand of the grid. The

electrolyser splits water (point 14) into hydrogen and oxygen (point 15). Interest in the substitution of fossil fuels with hydrogen is growing; however hydrogen storage is a challenge in developing sustainable energy systems. Hydrogen can be stored and transported in bulk as a compressed gas or liquid, and new storage methods are under development. These storage methods require significant inputs through compression and liquefaction processes, and require high-tech storage tanks. In contrast, on-site utilization of hydrogen eliminates most of these difficulties. In the system illustrated in Fig. 2.1, hydrogen is produced in an electrolyser installed at the PV-H_2-FC site. Therefore, there is no need for long term storage of hydrogen, because it is consumed by the fuel cell system on demand. Moreover, with proper sizing of system components, high pressure compressed gas is not required. The stored hydrogen is fed (point 16) to the SOFC system for electricity generation (point 18).

Solid oxide fuel cells are capable of generating baseload electric power. In addition, the high temperature exhaust gases leaving the fuel cell stack (point 19) can be used for space heating or hot water production in a heat utilization unit. Since the fuel cell is in operation only when required, the heat gained by the heat utilization unit is stored in a thermal energy storage system (point 20).

Biomass-SOFC-GT System

The integrated system includes a biomass gasification unit, an SOFC, a gas turbine and a heat recovery unit. Wood dust or crop waste is used as biomass in the biomass gasification unit (point 21). To improve the performance of the gasification process, the moisture content of the biomass feed is controlled via a biomass dryer. Various drying methods are available, among which direct steam biomass drying has the higher exergy efficiency. The superheated steam is supplied by the heat recovery steam generator. The gasification process occurs in the presence of pressurized steam (point 22). The product syngas (point 23) is fed to the fuel cell system for power generation (point 24). The gases leaving the fuel cell stack enter the combustion chamber of the micro gas turbine, and the gas turbine cascade for further electricity generation. The biomass-SOFC-GT system is assumed to supply a fixed portion of the electricity demand of the grid. This means that, in contrast to the wind-CAES and PV-H_2-FC systems, the biomass-SOFC-GT system has steady, not-intermittent, operation. The SOFC-GT exhaust gas feeds a heat recovery steam generator (point 25) for further renewable energy utilization. The generated steam is fed to the thermal storage system for thermal management (point 26).

Thermal Energy Storage

The heat recovered from the gas turbine flue gas of the CAES and SOFC-GT systems is stored in the form of hot water in thermal energy storage systems. The hot water is used for hot water usage or space heating.

2.3 Energy and Exergy Analyses

The main components of the integrated system are considered in the energy and exergy analyses. Their energy and exergy flows are illustrated in the following section.

Wind Park

Wind energy is a cubic function of wind speed. Therefore, any fluctuation in the wind speed leads to a significant change in its available energy. Wind turbines are usually in operation 80% of the year, and produce nearly 30% of their nominal power capacity throughout the year [10]. Wind power density (W/m^2) is an index quantifying the level of wind resource, and can be related to the cube of wind speed and the Weibull distribution function. The efficiency of wind turbines is limited to a maximum of 59%, known as the Betz limit [10].

Power output of the wind turbine is a function of wind speed, blade geometry and turbine efficiency, and can be expressed as

$$\dot{W}_{\mathrm{wt}} = \frac{\pi}{8} C_{\mathrm{p}} \rho D^2 v^3 \tag{2.1}$$

Here, C_{p} is the wind turbine efficiency, which is related to aerodynamics characteristics of the blades [11]. Due to the quality of electric power output of the wind turbine, the energy and exergy efficiencies are the same; therefore, the exergy destruction rate of the wind turbine is calculated using:

$$\dot{I}_{\mathrm{wt}} = \left(\frac{1}{C_p} - 1 \right) \dot{W}_{\mathrm{wt}} \tag{2.2}$$

Compressed Air Energy Storage System

Compressor

The energy and exergy balances for the CAES compressor and intercoolers, respectively, follow:

$$(\dot{m}_{\mathrm{air}} h_{\mathrm{air}})_{\mathrm{in}} + (\dot{m}_{\mathrm{air}} w_{\mathrm{C}})_{\mathrm{in}} = (\dot{m}_{\mathrm{air}} h_{\mathrm{air}})_{\mathrm{out}} \tag{2.3}$$

$$(\dot{m}_{\mathrm{air}} ex_{\mathrm{air}})_{\mathrm{in}} + (\dot{m}_{\mathrm{air}} w_{\mathrm{C}})_{\mathrm{in}} = (\dot{m}_{\mathrm{air}} ex_{\mathrm{air}})_{\mathrm{out}} + \dot{I}_{\mathrm{c}} \tag{2.4}$$

The enthalpy of air is calculated as $\Delta h = c_p \Delta T$, where ΔT is obtained using the isentropic relations for the compressor:

$$T_{\text{out}} = T_{\text{in}}\left[1+\frac{1}{\eta_{\text{c}}}\left(r_{\text{c}}^{\frac{\gamma_{\text{air}}-1}{\gamma_{\text{air}}}}-1\right)\right] \tag{2.5}$$

For a compression ratio r_c and a known inlet air temperature, the compressor outlet temperature is calculated. The specific work of compression can thus be calculated as follows:

$$w_{\text{c}} = (h_{\text{air}})_{\text{in}} - (h_{\text{air}})_{\text{out}} \tag{2.6}$$

In Eq. 2.4, exergy of the inlet air to the compressor is zero, considering the ambient conditions be the same as the reference environment. The balances for the air intercoolers are as follows:

$$(\dot{m}_{\text{air}} h_{\text{air}})_{\text{in}} + (\dot{m}_{\text{cw}} h_{\text{cw}})_{\text{in}} = (\dot{m}_{\text{air}} h_{\text{air}})_{\text{out}} + (\dot{m}_{\text{cw}} h_{\text{cw}})_{\text{out}} \tag{2.7}$$

$$(\dot{m}_{\text{air}} ex_{\text{air}})_{\text{in}} + (\dot{m}_{\text{cw}} ex_{\text{cw}})_{\text{in}} = (\dot{m}_{\text{air}} ex_{\text{air}})_{\text{out}} + (\dot{m}_{\text{cw}} ex_{\text{cw}})_{\text{out}} + \dot{I}_{\text{intercooler}} \tag{2.8}$$

where subscript cw in Eqs. 2.7 and 2.8 represents the cooling water, removing heat from the compressed air.

Gas Turbine

The energy and exergy balances for the gas turbine of the CAES system, respectively, follow:

$$(\dot{m}_{\text{air}} h_{\text{air}})_{\text{in}} + (\dot{m}_{\text{fuel}} LHV_{\text{CH}_4})_{\text{in}} = (\dot{m}_{\text{gas}} w_{\text{T}})_{\text{out}} + (\dot{m}_{\text{gas}} h_{\text{gas}})_{\text{out}} \tag{2.9}$$

$$(\dot{m}_{\text{air}} ex_{\text{air}})_{\text{in}} + (\dot{m}_{\text{fuel}} ex_{\text{CH}_4})_{\text{in}} = (\dot{m}_{\text{gas}} w_{\text{GT}})_{\text{out}} + (\dot{m}_{\text{gas}} ex_{\text{gas}})_{\text{out}} + \dot{I}_{\text{GT}} \tag{2.10}$$

The enthalpy of the combustion gases is calculated as $h = c_{p,g} T$, where T is obtained using the isentropic relations for the gas turbine:

$$T_{\text{out}} = T_{\text{in}}\left[1+\frac{1}{\eta_{\text{GT}}}\left(r_{\text{T}}^{\frac{\gamma_{\text{g}}-1}{\gamma_{g}}}-1\right)\right] \tag{2.11}$$

The air and gas specific heats are functions of gas molar fractions, and temperature.

Energy and Exergy Efficiencies of the Wind-CAES System

The main output of the integrated renewable energy-based system is baseload electric power. The system takes advantage of heat recovery to increase renewable energy utilization. Since the energy resources are renewable, and therefore intermittent, the recovered heat is stored as hot water in thermal energy storage systems. The inputs to the Wind-CAES section of the integrated system are wind and natural gas. The overall energy and exergy efficiencies follow:

$$\eta_{\text{wind-CAES}} = \frac{W_{\text{demand}} + Q_{\text{HRSG}} + (\Delta m \cdot h)_{\text{stored air}}}{E_{\text{Wind}} + (m \cdot LHV)_{\text{CH}_4}} \tag{2.12}$$

$$\psi_{\text{wind-CEAS}} = \frac{W_{\text{demand}} + Ex_{\text{q,HRSG}} + (\Delta m \cdot ex_{\text{ph}})_{\text{stored air}}}{Ex_{\text{Wind}} + (m \cdot ex)_{\text{CH}_4}} \tag{2.13}$$

Here, $P_{\text{demand}}, Ex_{\text{q,HRSG}}, and\, \Delta m_{\text{stored air}}$ account for the total annual electric energy demand of the wind park, the total annual heat recovery from the overall CAES system, and the difference between production and consumption of compressed air on a yearly basis, respectively. The energy inputs in the denominator of the efficiency equations are also considered on a yearly basis. The notations in Eq. 2.13 explain the exergy terms using the same concepts.

PV-H_2-FC system

The mathematical model and energy and exergy analysis equations for the PV-H_2-FC system are presented by the authors elsewhere [12].

The PV cell power output is a function of its terminal voltage and current, which are dependent on solar irradiance and ambient temperature:

$$\dot{W}_{\text{PV}} = IV \tag{2.14}$$

The difference between PV electric power output and the grid electric power demand is

$$\Delta \dot{W}_{\text{PV}} = \dot{W}_{\text{PV}} - \dot{W}_{\text{demand}} \tag{2.15}$$

If $\Delta \dot{W}_{\text{PV}} > 0$, the PV system produces more power than the demand, and the surplus electricity is fed to the electrolyser for hydrogen production. If $\Delta \dot{W}_{\text{PV}} < 0$, the SOFC produces power to make up for the power difference between the PV and the grid.

Energy and Exergy Efficiencies of the PV-H_2-FC System

The energy input to the hybrid PV-fuel cell system is solar irradiance. Although solar energy is not available during night hours and cloudy days, the system operates solely on solar energy, thanks to the storage options considered in the integrated system. The main output of the system is electricity, which is fed to the grid. Heat recovery from the SOFC stack gas is another output of the system. The integrated system is sized to supply the electricity demand throughout the year. Therefore, the storage tank size should always contain enough hydrogen to feed the fuel cell, when required. On a year round basis, hydrogen production is set to be more than hydrogen consumption. Thus, the remaining hydrogen in the storage tank is another output of the system. The overall energy and exergy efficiencies of the hybrid PV-fuel cell system can be written as follows:

$$\eta_{\text{PV-fuel cell}} = \frac{W_{demand} + Q_{\text{HRSG}} + \Delta m_{\text{H}_2} LHV}{E_{\text{solar}}} \tag{2.16}$$

$$\psi_{\text{PV-fuel cell}} = \frac{W_{\text{demand}} + Ex_{\text{q,HRSG}} + \Delta m_{\text{H}_2} ex_{\text{ch,H}_2}}{Ex_{\text{solar}}} \tag{2.17}$$

In Eq. 2.16, W_{demand} is the annual electricity demand in kWh, Q_{HRSG} is the total heat recovery from the fuel cell stack gas, Δm_{H_2} is the difference between production and consumption of hydrogen on a yearly basis, and E_{solar} is the annual solar energy received by the PV system. The notations in Eq. 2.17 apply to the exergy terms similarly.

Biomass Gasification and SOFC-GT

Details of the modeling and thermodynamic analysis of the hybrid SOFC-GT system integrated with biomass gasification are presented by the authors elsewhere [13]. The electric power output of the biomass-SOFC-GT system is expressible as

$$\dot{W}_{\text{SOFC-MGT}} = \dot{W}_{\text{SOFC}} \eta_{\text{conv}} + \dot{W}_{\text{MGT}} - \dot{W}_{\text{airC}} - \dot{W}_{\text{consumption}} \tag{2.18}$$

where η_{conv} is DC/AC power converter, and $\dot{W}_{\text{airC}}$ and $\dot{\text{W}}_{\text{consumption}}$ are air compressor and internal consumption, respectively.

The energy and exergy balances can be written as follows:

$$(\dot{m}ex)_{\text{biomass}} + \dot{E}x_{\text{steam}} + \dot{E}x_{Q} = \dot{W}_{\text{SOFC-MGT}} + \dot{E}x_{\text{out}} + \dot{I}_{\text{biomas-SOFC-MGT}} \tag{2.19}$$

Here, $\dot{E}x_{\text{steam}}$ is the exergy rate of steam entering the gasifier, $\dot{E}x_{\text{Q}}$ is the gasification thermal exergy rate, and $\dot{E}x_{\text{out}}$ is the exergy rate of the flue gas of the SOFC-GT cycle, which is released to the environment.

Accounting for the heat recovered in the HRSG, the total efficiencies of the SOFC-GT CHP system are

$$\eta_{\text{biomass-SOFC-GT}} = \frac{W_{\text{demand}} + Q_{\text{HRSG}}}{(m \cdot LHV)_{\text{biomass}} + E_{\text{Steam}} + Q_{\text{gasifier}} + E_{\text{gas-cleaning}}} \tag{2.20}$$

$$\psi_{\text{biomass-SOFC-GT}} = \frac{W_{\text{demand}} + \text{Ex}_{\text{Q,HRSG}}}{(m.ex)_{\text{biomass}} + Ex_{\text{Steam}} + Ex_{\text{Q}} + Ex_{\text{gas-cleaning}}} \tag{2.21}$$

Overall Energy and Exergy Efficiencies of the Integrated Renewable Energy-Based System

The overall energy and exergy efficiencies of the integrated renewable energy-based system for baseload power generation follow:

$$\eta_{\text{wind-PV-biomass}} = \frac{W_{\text{demand}} + Q_{\text{HRSG}} + \Delta m_{\text{H}_2} LHV_{\text{H}_2}}{E_{\text{solar}} + E_{\text{Wind}} + (m \cdot LHV)_{\text{biomass}}} \tag{2.22}$$

$$\psi_{\text{wind-PV-biomass}} = \frac{W_{\text{demand}} + Ex_{\text{q,HRSG}} + \Delta m_{\text{H}_2} ex_{\text{ch,H}_2}}{Ex_{\text{solar}} + Ex_{\text{Wind}} + (m \cdot ex)_{\text{biomass}}} \tag{2.23}$$

Here, W_{demand}, $Ex_{\text{q,HRSG}}$, and Δm_{H_2} account for the total annual electric energy demand, thermal exergy recovery from all the available waste heat sources, and the difference between production and consumption of hydrogen on a yearly basis, respectively.

Exergoeconomic Analysis

In economic calculations of energy systems, unit costs based on energy are conventionally used. Since these systems are incur losses that can be better quantified based on exergy concepts, the use of exergy based unit costs better distribute costs among outputs. The combination of exergy analysis and economic calculations represents a useful tool for optimization of energy systems, and forms the basis of the relatively new field of exergoeconomics. The exergy model calculates the exergy content of each point in the system, and the economic model accounts for all costs

relevant to capital, operation and maintenance (O&M) of the system. In the exergoeconomic models, each exergy stream has a cost. Thus, the cost of exergy of all inlet streams plus the capital and O&M costs equals to the cost of exergy of all exiting streams [9].

The exergoeconomic factor *f* relates the costs associated with exergy destruction and exergy losses to the levelized capital costs. The exergoeconomic factor of component k, f_k, is defined as

$$f_k = \frac{\dot{Z}_k}{\dot{Z}_k + c_{F,k}(\dot{I}_k + \dot{E}x_{loss})} \tag{2.24}$$

where $c_{F,k}$ is the unit cost of exergy of fuel provided to the component. The values of the exergoeconomic factor fall between zero and one. A small value for *f* suggests that the system needs to be improved in terms of irreversibility, although this may require capital cost investments. Higher values for *f* signify that, no matter how efficient the component is, its purchase cost is significantly high. The concepts of exergoeconomic analysis discussed in this section are applied to the components of the integrated systems.

2.4 Assumptions and Data

The modeling and analyses are performed based on the following assumptions and data.

- Transient behavior of the systems is not considered, although the weather data has transient characteristics.
- The wind turbine power output is 3.5 MW, with a $ 700/kW capital cost [4].
- The CAES system is considered to have 168 h of air storage capacity.
- The equivalent natural gas price (natural gas plus carbon dioxide emission price) is $ 5/GJ.
- The compression pressure range for the parametric study is 81, 64, and 49 bar.
- The expansion pressure range for the parametric study is 64, 49 and 36 bar.
- Hourly wind speed data of Port Colbourne, Ontario, Canada [14] are used for wind power calculations.
- Hourly solar irradiance data of Toronto [15], Ontario, Canada are used for PV power calculations.
- The reference environment state, taken as similar to the ambient condition, for the exergy analysis is set to 1 bar and 298 K.

Economic and exergoeconomic analyses are performed based on data presented in Table 2.1.

Table 2.1 Unit cost of components

Component	Wind turbine	Air compressor	Gas turbine	PV	SOFC	Electrolyser	Bio-SOFC-GT
Capital cost, $/kW	700[a]	175[a]	185[a]	5400[b]	2300[c]	590[d]	3800[e]

[a] Data adapted from Greenblatt et al. (2007)
[b] Data adapted from SunPower Corporation (2012), N. Enbar (2010)
[c] Data adapted from Braun et al. (2011), McIlveen-Wright et al. (2011)
[d] Data adapted from state-of-the-art hydrogen production (2009)
[e] Data adapted from McIlveen-Wright et al. (2011)

2.5 Results and Discussion

The investigation of the integrated renewable energy-based baseload power generation system is performed for 5 MW solar PV and 25 MW biomass-SOFC-GT power outputs. Since each sub-power generation system is independent from the rest, the results are presented separately. In this section the results of modeling, and energy and exergy economic analyses of the systems are presented. When discussing the monthly performance of the Wind-CAES system, the compression ratio of the compressor stages is set to 8, while the expansion ratio of each stage of the gas turbine is considered to be 6. The pressure difference between the compressed air storage system and the gas turbine operating pressure is regulated by a pressure regulator, considering the pressure losses in the pathways and pipelines [4].

Wind-CAES system

The Wind-CAES system power output accounts for 94% of the baseload power supply. However, since wind power is inherently intermittent, the shares of the wind park and the CAES systems in providing the grid with electricity vary. Power penetration is the ratio of the electricity provided by the system to the electric power demand. Power penetrations for the wind park and the CAES system are shown in Fig. 2.2. There is no specific trend to the shares of the two power supply systems, since they strongly depend on the wind resource. However, the wind park plays a major role in the Fall-Winter months.

Figure 2.2 also shows that power penetration of the wind park for some months of the year is more than 100%. During these months, the power output of the wind park exceeds the demand; however, the CAES system is fully charged, so there is no need to compress air with the electricity. In some analyses, the wind park excess electricity is dissipated or used for space heating, unless there is the possibility of selling the electricity to the grid.

The CAES system is charged (refilled with compressed air) when the wind park power output exceeds the electricity demand. It is discharged when there is a need for power production otherwise met by the gas turbine. Therefore, the charging/

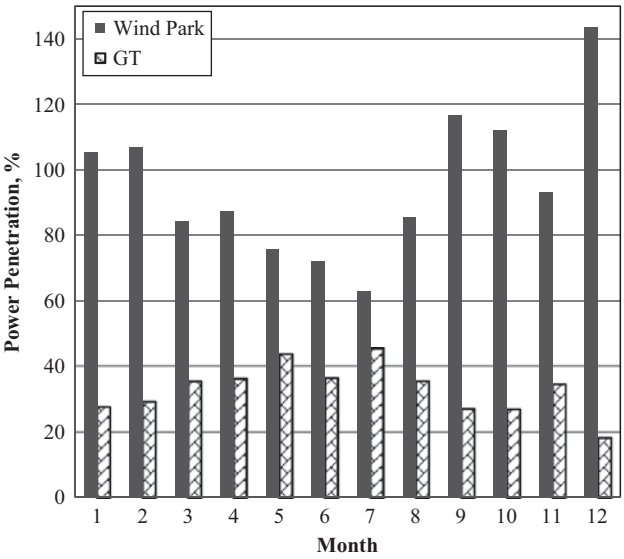

Fig. 2.2 Monthly power penetration of wind park and gas turbine sites ($r_c = 8$, $r_{GT} = 6$, $h_s = 168$)

discharging rates change as illustrated in Fig. 2.3. The system component (wind turbines, air compressor, gas turbine) capacities are selected to maintain a net positive quantity of stored air in the cavern throughout the year. The data in Fig. 2.3 is presented in million kg of compressed air per month, to quantify the differences between storage and consumption for each month.

Wind-CAES systems are generally not carbon emission-free power generation plants. In fact, if the compressed air is heated by combustion, some levels of carbon and other greenhouse gas emissions are released. In this paper, the compressed air undergoes a combustion process with methane. Figure 2.4 illustrates monthly changes in fuel consumption and carbon dioxide emissions. They are proportional to the gas turbine operation and the need for excess power generation.

With the performance of the Wind-CAES system described, a parametric study is performed considering changes in the compressor and gas turbine pressure ratios. For a fixed storage cavern pressure at 64 bar (implying a compressor stage pressure ratio of 8, since two compression stages are considered), the change in the wind power penetration is shown in Fig. 2.5, for various gas turbine pressure ratios. Figure 2.5 shows that the wind park penetration decreases as the gas turbine pressure ratio increases.

A higher pressure ratio in the gas turbine results in a higher specific power output. Therefore, fewer wind turbines are required for the wind park, and the share of the gas turbine in meeting the electricity demand increases (Fig. 2.6).

The gas turbine expansion ratio impacts the capacity of the main components of the Wind-CAES system, which affects related system costs. The unit cost of electricity is a function of the system total capital and maintenance costs and the total generated power by the system during its lifetime. Figure 2.7 shows that

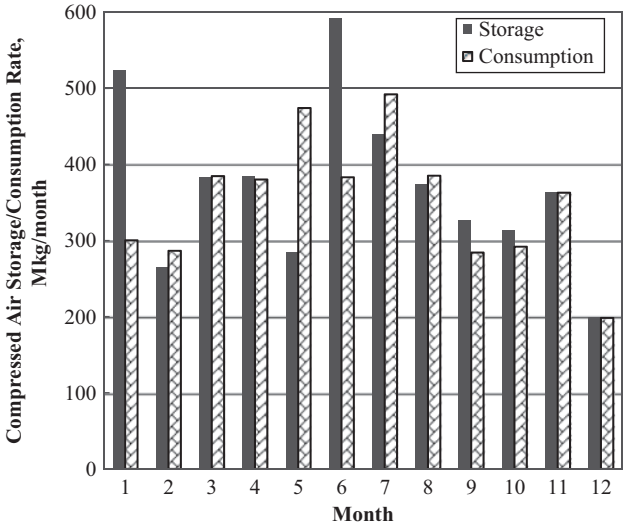

Fig. 2.3 Charging and discharging phases of the compressed air storage system (r_c=8, r_{GT}=6, h_s=168)

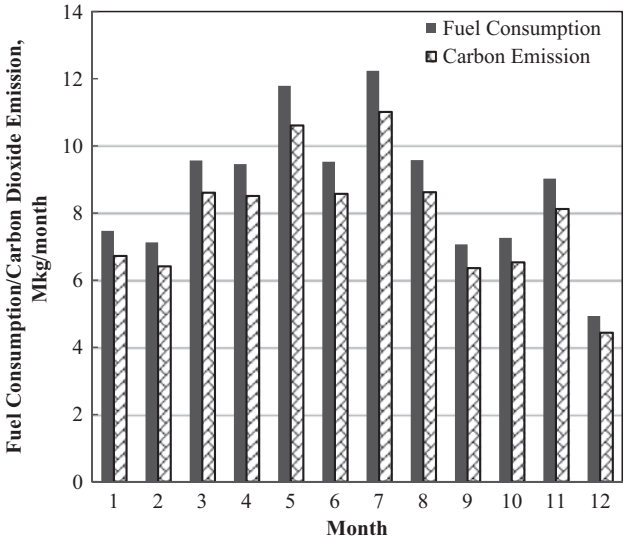

Fig. 2.4 Fuel consumption and carbon dioxide emission rates (r_c=8, r_{GT}=6, h_s=168)

increasing the GT expansion ratio decreases the unit cost of generated electricity by the Wind-CAES system. According to Fig. 2.7, the unit cost of electricity drops from 7.4 to 7.0 ¢/kWh as the GT expansion ratio increases from 6 to 8. For a fixed GT capacity, a higher specific power output leads to lower air and fuel consumption. A decrease in the fuel consumption due to the increase in turbine

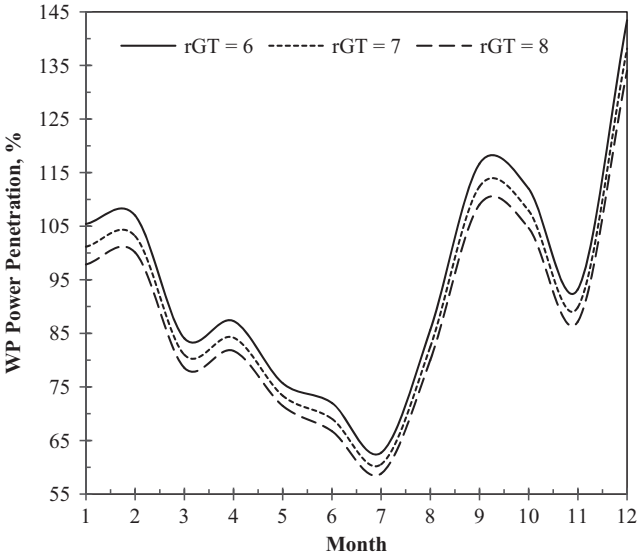

Fig. 2.5 Monthly power penetration of wind park with various GT expansion ratios (r_c=8, h_s=168)

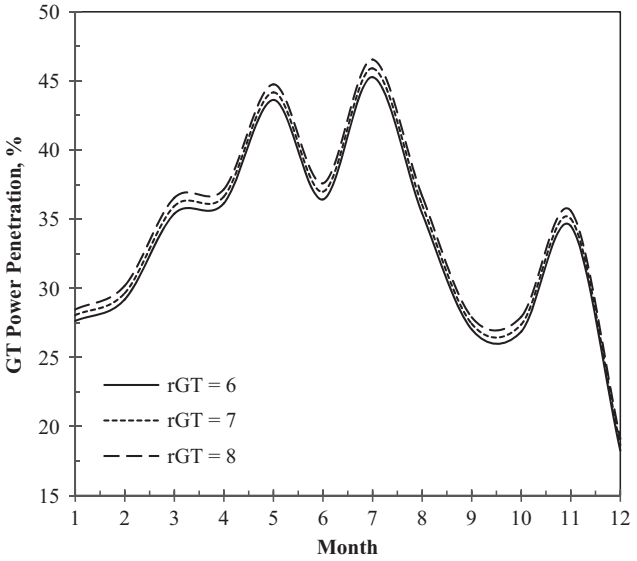

Fig. 2.6 Monthly power penetration of GT for various GT expansion ratios (r_c=8, h_s=168)

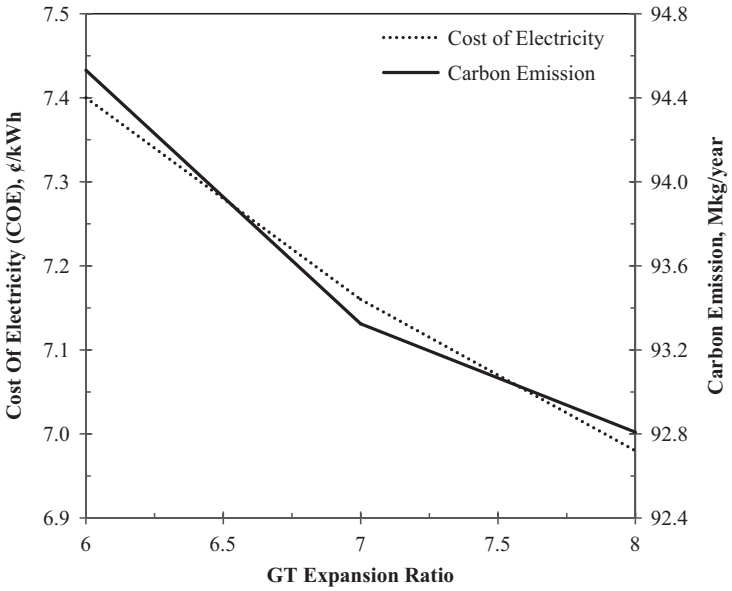

Fig. 2.7 Cost of electricity (COE) and annual carbon emission vs. GT expansion ratio (r_c=8, h_s=168)

Table 2.2 Effect of gas turbine expansion ratio of the overall energy and exergy efficiencies of the Wind-CAES system (r_c=8, h_s=168)

Gas turbine expansion ratio	6	7	8
Wind-CAES energy efficiency, %	37.17	37.90	37.60
Wind-CEAS exergy efficiency, %	32.83	33.86	34.73

expansion ratio results in a reduction in the yearly carbon dioxide emissions, as also illustrated in Fig. 2.7.

Moreover, decreasing the pressure difference between the gas turbine inlet pressure and the pressure of the air storage cavern (i.e., increasing the gas turbine expansion ratio), increases the overall energy and exergy efficiencies of the Wind-CAES system, as observed in Table 2.2.

As discussed in Fig. 2.6 and illustrated in Fig. 2.8, the GT power output increases if the pressure of the air entering the turbine cascade is closer to the compressed air pressure (decreasing the level of pressure loss in the air cavern). Also, Fig. 2.7 shows that the annual carbon emission rate decreases with increasing gas turbine pressure ratio. However, since the share of the wind park in providing the grid with electricity decreases, the specific carbon dioxide emission in g/kWh increases. A trade-off between decreasing electricity generation cost and carbon emission can be the objective for an optimization problem.

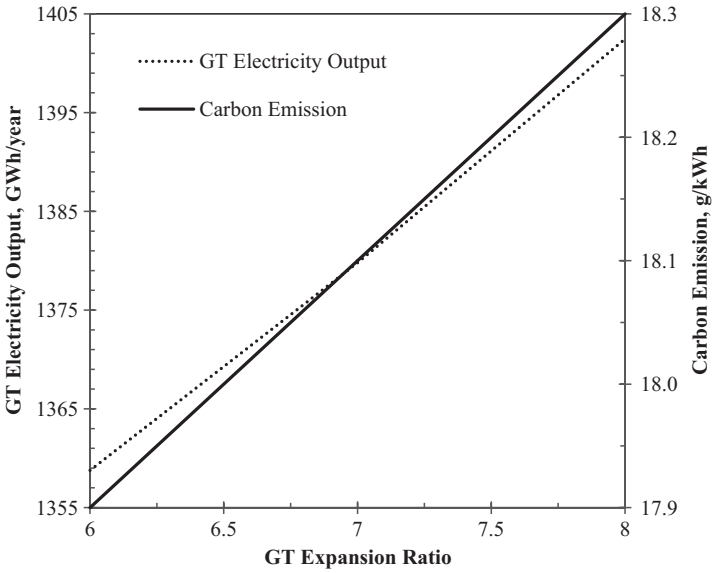

Fig. 2.8 GT electric power output and carbon emission per unit of Wind-CAES electric power vs. GT expansion ratio ($r_C = 8$, $h_s = 168$)

The exergoeconomic method is used to calculate the unit cost of exergy of the system components. Here, the unit cost of generated electricity by the gas turbine is presented. The compressed air pressure affects the electricity cost of the Wind-CAES system, mainly due to the changes in the system components' capacities. The variation of the unit cost of GT electricity output with a change in the pressure of the stored air and the expansion ratio of the gas turbine is shown in Fig. 2.9. The highest price is for the case when the difference between the compressed air pressure and the turbine inlet pressure is a maximum. Figure 2.9 shows that if there is no pressure difference between the storage system and the gas turbine inlet pressure, the unit cost of GT electricity output is a minimum.

PV-H_2-FC System

Hydrogen is produced by water electrolysis, using surplus generated electricity by the PV system, and is consumed by the solid oxide fuel cell when the PV power is below the demand.

The production/consumption pattern depends on the temporal variation of the solar irradiance. Figure 2.10 shows that more hydrogen is produced during high irradiance months (spring-summer) than Fall-Winter months. But, the SOFC consumes more hydrogen during low solar irradiance months. The system components are sized to have positive cumulative hydrogen in the storage tank throughout the year. The hydrogen production/consumption pattern is observed to be proportional

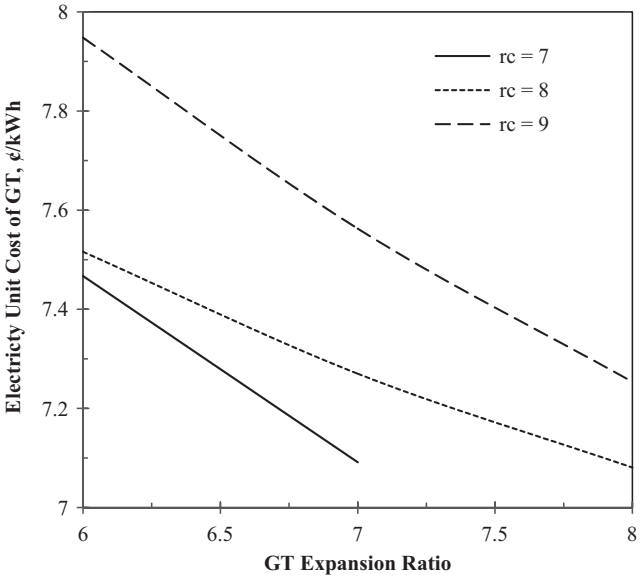

Fig. 2.9 Variation of GT unit cost of electric exergy with the compressed air pressure ratio and the gas turbine expansion ratio

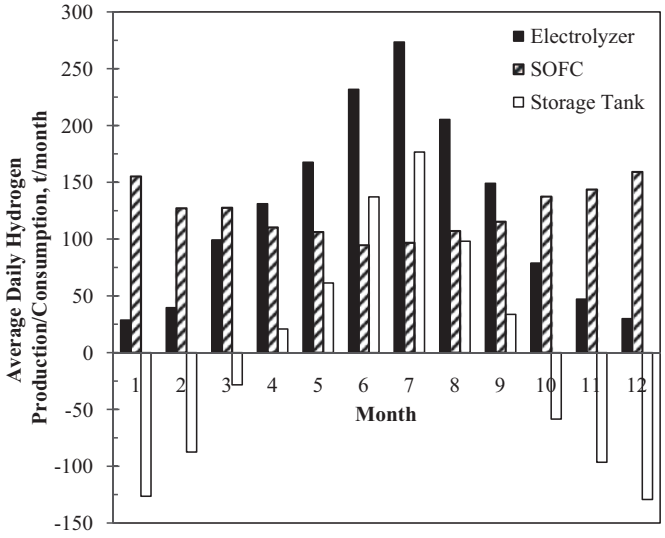

Fig. 2.10 Monthly flow rate of hydrogen production/consumption

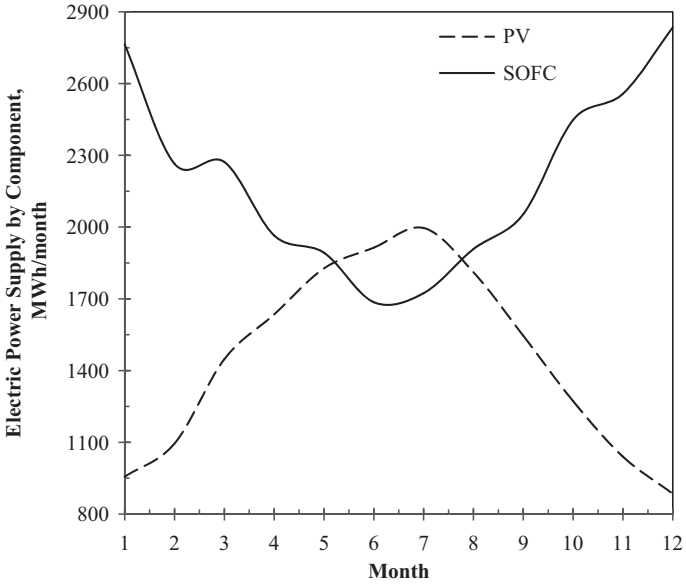

Fig. 2.11 PV and SOFC share in electric power supply

to the PV and fuel cell power outputs (see Fig. 2.11). A better understanding of the PV and fuel cell shares in power production can be observed in Fig. 2.12. The power penetration of the PV system exceeds that of the fuel cell in Spring-Summer months, and exhibits an opposite trend in Fall-Winter months.

A graphical illustration of the contributions of the PV-H_2-FC system main components to the total exergy destruction (Fig. 2.13) shows that the PV accounts for almost 85% of the annual exergy destruction. This is mainly associated with internal irreversibility.

Since the performance of the PV-H_2-FC system depends on the weather condition, for the exergoeconomic analysis, the unit cost of exergy of the products of the main components are determined on a monthly basis. Figure 2.14 shows that during the months with high solar irradiance, the cost of generated electricity by the PV and fuel cell systems is minimal. The PV electricity generation is significantly below its rated power during Fall-Winter months, causing a significant increase in the unit costs of the products.

Although the fuel cell operates closer to its nominal capacity during this period of time, the generated electricity is still expensive due to the higher price for hydrogen production in months with low solar irradiance.

Integrated Renewable Energy-based Power Generation System

PV has a very low exergoeconomic factor, demonstrating its high level of exergy destruction, according to Table 2.3. The SOFC in the PV-H_2-FC system has the min-

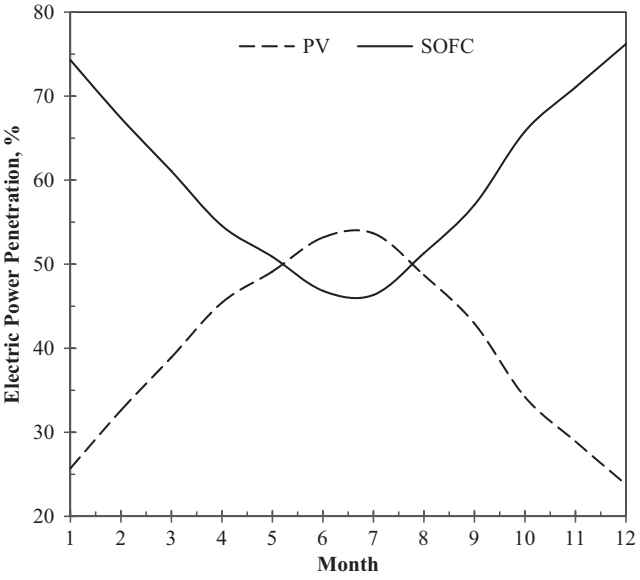

Fig. 2.12 Electric power penetration of PV and SOFC system in meeting the demand

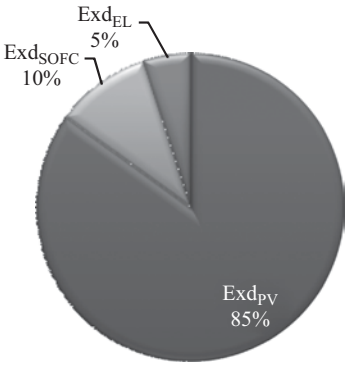

Fig. 2.13 Annual exergy destruction breakdown for the main components of the PV-H_2-FC system

imum exergoeconomic factor due to its high exergy destruction and low capacity factor. The exergoeconomic factors of the other main components of the integrated renewable energy-based system are also presented in Table 2.3.

Table 2.4 provides information regarding heat recovery potential from the components of the integrated system. Moreover, the ratios of the heat recovered to the electric power input (output) of the components are presented. Table 2.4 shows that there is a good potential for heat recovery from the compressed air during compression and storage of air in the CAES system. The extent of heat recovery from the SOFC-GT system integrated with biomass gasification is significant, since heat can be recovered from the gasification process, the fuel cell and the micro gas turbine.

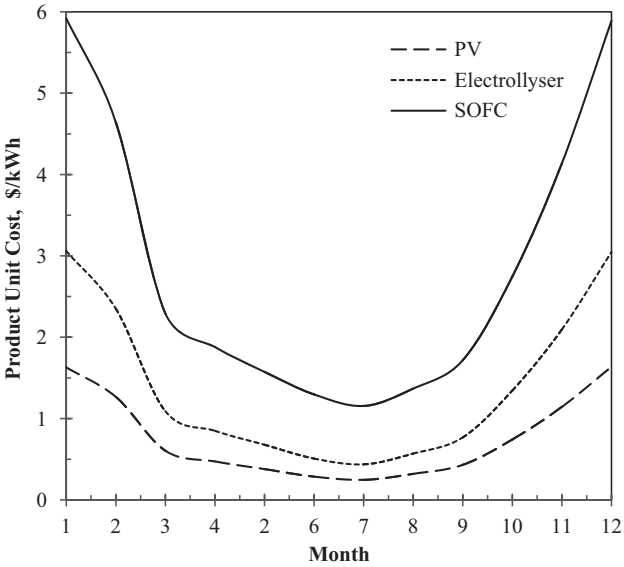

Fig. 2.14 Unit cost of exergy for PV-H_2-FC components' products

Table 2.3 Exergoeconomic factor for the main components of the integrated CHP system

Component	PV-H_2-FC			Wind-CAES			Biomass-SOFC-GT
	PV system	Electrolyser	SOFC	Wind park	Air compressor	Gas turbine	
Exergoeconomic factor	0.33	0.36	0.12	0.62	0.55	0.89	0.17

Table 2.4 Heat recovery from the integrated system components

Component	CAES[a]		PV-H_2-FC	Biomass-SOFC-GT
	Air	GT		
Heat recovery, GWh/y (GWh*th*/GWh*e*)	246.8 (0.3)	118.0 (0.1)	11.6 (0.3)	148.7 (0.7)
Energy consumption, GWh/y	817.3	1458.8	12.0[b]	687.0 (biomass)
Electric power output, GWh/y		1358.8	43.8	219.0

[a] $r_c = 8$, $h_s = 168$, $r_{GT} = 6$

[b] Energy for pre-heating the hydrogen feed to the SOFC

The round-trip efficiency of the CAES system can be calculated as $\frac{1358.8}{1458.8+817.3} = 60\%$ without considering heat recovery potentials. If the electrical equivalent of the heat recovered from the compression and expansion processes is considered (assuming 50% efficiency of a thermal power plant to calculate the equivalent electric energy for heat), the round-trip energy efficiency is 68%.

Table 2.5 Energy and exergy flows and efficiencies of the integrated system components

	Wind-CEAS	PV-H_2-FC	Biomass-SOFC-GT	Integrated system
E_{inlet}, GWh/y	13,600.0	614.0	609.7	14,823.7
E_{outlet}, GWh/y	5060.0	55.5	367.9	5483.4
η, %	37.2	9.0	60.3	37.0
Ex_{inlet}, GWh/y	13,900.0	568.6	646.45	15,115.3
Ex_{outlet}, GWh/y	4490.0	51.9	274.2	4816.1
ψ,%	32.3	9.1	42.4	31.9

Table 2.6 Unit cost of generated electricity by each sub-system of the integrated system

Sub-system	Wind-CAES	PV-H_2-FC	Integrated biomass-SOFC-GT
Unit cost of electricity, ¢/kWh	7.4[a]	89[b]	17[c]

[a] r_c=8, h_s=168, r_{GT}=6, P_{GT}=470 MW
[b] P=5 MW
[c] P=25 MW, TIT=1300 K, T_{stack}=1173 K

The total energy and exergy flows in the integrated renewable energy-based system are listed in Table 2.5. These values are reported for each sub-system and for the overall system, separately. Values of energy and exergy efficiencies are reported. Table 2.5 shows that the overall energy and exergy efficiencies of the integrated system are 37.0 and 31.9 %, respectively. A lower exergy value of recovered heat is the main reason for the lower overall exergy efficiency, compared to the energy efficiency.

Each sub-system of the integrated renewable energy-based system generates electricity, however with a different unit cost of electricity. Table 2.6 reports the electricity generation cost by the integrated system. Results of the exergoeconomic analyses show that the unit cost of electricity generated by the Wind-CAES system is 7 ¢/kWh, while it is 89 and 17 ¢/kWh for the PV-H_2-SOFC and the biomass-SOFC-GT systems, respectively.

Conclusions

Integrated renewable energy-based systems have the potential for baseload power generation. The novel integrated system presented in this study utilizes wind, solar and biomass energy resources, and provides 500 MW baseload power. The performance of the integrated system depends on weather conditions and the system component design parameters. For a 64 bar compressed air pressure, and a 36 bar gas turbine inlet air pressure, 356 3.5-MW rated power wind turbines are required to generate 470 MW baseload power. The compressed air storage will have a volume 3.3×10^3 m^3 in and an energy storage capacity of 79 GWh (i.e., 7 days storage capacity at the gas turbine rated power).

The lower the pressure difference between the compressed air in the cavern and the gas turbine inlet air pressure, the fewer are the wind turbines required in the Wind-CAES system. This results in higher penetration for the gas turbine.

The results also show that 5.35×10^5 PV modules (covering 0.66 Mm^2 of land) are required to generate 5 MW of baseload electric power. The capacity of the SOFC of the PV-H_2-FC system is 5 MW with 11.6 GWh*th* annual heat-recovery potential. The PV system accounts for almost 85% of the annual exergy destruction, due to its internal irreversibility.

Nomenclature

c_p	specific heat at constant pressure, kJ/kg.K
Cp	wind turbine effectiveness
D	diameter, m
ex	specific exergy, kJ/kg
Ex	exergy flow, kJ
$\dot{E}x$	exergy flow rate, kW
f	exergoeconomic factor
h	specific enthalpy, kJ/kg
I	electric current, A
$\dot{I}$	exergy destruction rate, kW
LHV	lower heating value, kJ/kg
$\dot{m}$	mass flow rate, kg/s
Q	thermal energy, kJ
$\dot{Q}$	heat flow rate, kW
r	compression ratio, bar/bar
SC	steam to carbon ratio
T	temperature, K
v	velocity, m/s
V	voltage, V
w	specific work, kJ/kg
W	electric energy, kWh (kJ)
$\dot{W}$	electric power, kW
$\dot{Z}$	levelized capital cost rate, $/s

Greek Letters

ρ	density, kg/m^3
η	energy efficiency, %
ψ	exergy efficiency, %
γ	specific heat ratio

Subscripts

airC	air compressor
c	compressor
ch	chemical exergy
conv	electricity converter
cw	cooling water

CH_4	methane
DH	district heating heat demand
F	fuel
g	gas
GT	gas turbine
in	inlet flow
intercooler	air inter-cooler in the compressor
out	outlet flow
ph	physical exergy
Q	thermal energy
wt	wind turbine

Acronyms

AC	alternating current
CAES	compressed air energy storage
DC	direct current
HRSG	heat recovery steam generator
GT	gas turbine
SOFC	solid oxide fuel cell
PV	photovoltaic
PV-H_2- FC	photovoltaic-hydrogen-fuel cell

References

1. Yang W-J, Aydin O (2001) Wind energy–hydrogen storage hybrid power generation. Int J Energy Res 25:449–463
2. Ashraf I, Chandra A, Sodha MS (2004) Techno-economic and environmental analysis for grid interactive solar photovoltaic power system of Lakshadweep islands. Int J Energy Res 28 1033–1042
3. Hosseini M, Dincer I, Rosen MA (2012) Thermodynamic analysis of a cycle integrating a solid oxide fuel cell and micro gas turbine with biomass gasification. 11th International conference on sustainable energy technologies (SET 2012) Vancouver, 2–5 Sept, 2012
4. Greenblatt JB, Succar S, Denkenberger DC, Williams RH, Socolow RH (2007) Baseload wind energy: modeling the competition between gas turbines and compressed air energy storage for supplemental generation. Energy Policy 35 1474–1492
5. Widén J, Wäckelgård E, Lund PD (2009) Options for improving the load matching capability of distributed photovoltaics: methodology and application to high-latitude data. Sol Energy 83 1953–1966
6. Castillo-Cagigal M, Caamaño-Martín E, Matallanas E, Masa-Bote D Gutiérrez A, Monasterio-Huelin F, Jiménez-Leube J (2011) PV self-consumption optimization with storage and active DSM for the residential sector. Sol Energy, 85 2338–2348
7. Radchik A, Skryabin I, Maisano J, Novikov A, Gazarian T (2013) Ensuring long term investment for large scale solar power stations: hedging instruments for green power. Sol Energy, 98(B) 167–179
8. Colpan CO, Hamdullahpur F, Dincer I, Yoo Y (2010) Effect of gasification agent on the performance of solid oxide fuel cell and biomass gasification systems. Int J Hydrogen Energy, 35 5001–5009
9. Bejan A, Tsatsaronis G, Moran M (1996) Thermal design and optimization. Wiley, New York

10. Munteanu I, Bratcu AI, Cutululis NA, Ceanga E (2008) Optimal control of wind energy systems toward a global approach. Springer, London
11. Şahin AD, Dincer I, Rosen MA (2006) Thermodynamic analysis of wind energy. Int J Energy Res 30 553–566
12. Hosseini M, Dincer I, Rosen MA (2013) Hybrid solar–fuel cell combined heat and power systems for residential applications: energy and exergy analyses. J Power Sour 221 372–380
13. Hosseini M, Dincer I, Rosen MA (2012) Steam and air fed biomass gasification: comparisons based on energy and exergy. Int J Hydrogen Energy 37 16446–16452
14. NCDIA (2011) Daily data report of Port Colborne, environment Canada. http://www.climate.weatheroffice.gc.ca/climateData/canada_e.html. Accessed 18 Apr 2013
15. UTM (2012) Weather data, University of Toronto Mississauga, University of Toronto Mississauga. http://www.utm.utoronto.ca. Accessed 12 June 2012

Chapter 3
Investigation of Organic Rankine Cycle Performance with Variable Mixture Composition

H. Barzegaravval and Ibrahim Dincer

Abstract The present study deals with a comprehensive thermodynamic modeling of a renewable energy-based organic Rankine cycle (ORC). In this regard, two different cases are chosen to investigate the effect of mixture composition on the cycle performance in terms of exergy efficiency. While one cycle responses negatively to the mixture variation, another shows an increase in cycle performance and hence, efficiency. In addition, this study reveals that using a variable mixture composition can provide a wide range of working conditions for design purposes. The effects of working fluid composition on the turbine and pump works and exergy efficiency of the cycle are investigated, and the results are discussed as well. The exergy efficiency drops by about 0.002 in the first case, but increases by about 0.01 in the second case. It appears that temperature ratios can act like indicators of the cycle performance.

Keywords Thermodynamics · Exergy · Efficiency · Mixture Composition · Organic Rankine Cycle · Working fluid

3.1 Introduction

Organic Rankine Cycles (ORCs) are widely preferred over conventional power generating cycles to recover exergy from low-grade heat sources. Their applications widely range from small residential buildings to geothermal and industrial low temperature heat recovery systems. Extreme present Vast sources of lowtemperature waste heat streams provides many applications for ORCs. These cycles are used in a large variety of configurations with diverse working fluids.

ORCs have been investigated by various researchers in the area of resources, configurations, and multi-generation cycles. For example, Husband et al. [1]

H. Barzegaravval (✉)
Board Member of Energy Optimization R&D Group, Tehran, Iran
e-mail: hasan.barzegar.a@gmail.com

I. Dincer
Department of Mechanical Engineering, University of Ontario Institute of Technology (UOIT), 2000 Simcoe Street North, Oshawa ON L1H 7K4, Canada
e-mail: ibrahim.dincer@uoit.ca

I. Dincer et al. (eds.), *Progress in Sustainable Energy Technologies: Generating Renewable Energy,* DOI 10.1007/978-3-319-07896-0_3,

studied the feasibility of a solar organic Rankine cycle with scroll compressor. Yang [2] studied an ORC-solar-hydrogen storage system. The ORC-solar combination under investigation was capable of producing electricity to fulfill the electricity demand and produce hydrogen. Mago et al. [3] performed analysis the exergetic performance analysis of the MT-ORC cycle with various working fluids like R113, R123, R245fa, and R236fa. They showed that MT-ORC cycles with small micro-turbines have better performance than the larger conventional turbines. They also concluded that R113 resulted in a higher efficiency compared to other noted fluids. Preibinger et al. [4] investigated a double staged biomass fired ORC and showed that the working fluid in lower temperature cycle had a greater effect on the efficiency than higher temperature cycle. Note that a different working fluid results in different working temperature and pressure limits and cycle efficiency. The fluid properties have strong effects on the cycle working condition, designing and performance. Some recent studies have focused on selection and optimization of working fluid parameters. The parameters like thermodynamic properties (e.g., T, s), saturated vapor slope, boiling and condensing temperature, critical temperature and pressure and etc. are proposed as important parameters in fluid selection. A useful review on this area of research is given in [5]. Their authors reviewed the performance of ORCs working with 35 different fluids. The cost, environmental impacts, thermodynamic and physical properties are among the characteristics which fluids are compared based on. The results presented mainly in terms of latent heat for 35 working fluids.

The performance of ORCs, heat pumps and cooling systems are greatly dependent on the thermophyscial properties of the working fluid [6]. To study working fluid's effects, various concepts and methods are chosen. Hung et al. [7] categorized working fluid's in three main groups: isentropic, dry and wet fluids. The parameters selected for investigations were temperatures and qualities at different points as well as efficiency. They summarized the results by showing that fluids with sharp saturated curves on T-s diagrams have better efficiencies. Also they concluded that fluids which provide higher temperatures in evaporator and lower temperatures in condenser results in a more efficient system. Chi-Ron Kuo et al. [8] studied the effects of various working fluids. Various fluid properties, such as Jakob number and condensing and boiling temperature are considered. "Figure of merit" was taken as an important parameter to represent the performance of the cycle is shown to be inversely related to this parameter. Thermoeconomic analysis of various working fluids was considered by Stijepovic et al. [9], and their study led to a development of strategy for working fluid selection. Important working fluid parameters are introduced and their effects on the cycle performance were studied.

Rayegan and Tao [10] investigated working fluid effects on the performance of the ORC for solar application. The Refprop 8.0 data base was used, and working fluids were compared based on their molecular components and thermodynamic diagrams. Eleven fluids were proposed for solar applications, and their results showed that changing working fluid can enhance the collector efficiency and hence, total cycle performance significantly. They concluded that with high molecular complexity the higher efficiencies can be obtained in general.

Guo et al. [11] investigated geothermal transcritical organic Rankine cycle performance using different working fluids. Their results showed that R125 represents the best thermodynamics and economic performance. Also they added that R143a and R32 showed improvement in performance while the source temperature rose above 100°C.

In general, the working fluids affect other cycle characteristics like heat exchangers area. The effect of working fluid on the performance and heat transfer area in solar collectors are investigated by Delgado-Torres and Garcia-Rodriguez [12] comparing 12 different working fluids. Saturated vapor slope for different working fluids was considered for comparison as well as the resulted area and efficiency for different cycle configurations was analyzed.

ORCs are divided into low-, medium- and high-temperature cycles. Temperature limits can change the fluid category and selection criteria. The effects of various working fluids for high temperature organic Rankine cycles were studied by Lai et al. [13]. The BACK-ONE and PC-SAFT equations of state were used for modeling, and a pinch analysis was used for heat exchanger performance investigation. Their results showed that cyclopentane is the best working fluid considering thermal efficiency of the cycle, heat and volume flow rates. Heat transfer area and efficiency of the cycle working with different fluids were studied by Lakew and Bolland [14]. At low temperatures, significant changes in performance and heat exchangers surface area were observed in their studies for different working fluids.

Although there have extensive works presented on pure fluid effects on the ORCs, the few studies have been done on the effect of using mixtures instead of pure fluids. Zamfirescu and Dincer [15] used water-amonia as working fluid. They considered a Rankine cycle using an expander instead of boiler which removes the pinch point and in addition to binary fluid effect, matched the temperature profiles in heat exchangers better. The cycle was compared with different organic Rankine and Kalina cycle and showed better performance. They reported a 7 % improvement in the cycle exergy efficiency compared to other cycles usingl steam only. Kim et al. [16] analyzed ammonia-water Rankine and regenerative Rankine cycles. The effect of ammonia mass concentration was studied. They concluded that regenerative cycles are generally better, and the efficiency can reach to a maximum at the lowest allowable ammonia concentration which decreases with turbine inlet pressure increase. Mathematical modeling of an ORC using different pure fluid and a mixture was investigated by Li et al. [17]. The effects of working fluid as well evaporator temperature were studied. They concluded that mixture type working fluids result in a lower efficiency, but it provides a wider range for fluid selection. Chen et al. [18] used zeotropic mixture composition for a supercritical ORC. Their results show that exergy efficiency for the cycle improved significantly by using the mixture. Supercritical condition at evaporator and non-constant condensation were proposed to be the reasons for efficiency increase.

In the present paper, we extensively study how mixture composition variations affect the performance of the cycles, temperatures and heat transfer phenomena in heat exchangers. In order to show that such mixture effects can be positive or negative, depending on the type of fluids and their thermophysical properties and operating conditions, two cases are considered and modeled. The present results are

then utilized for comparison and performance assessment. The temperature ratios are used as a performance indicator for comparison. Also, the fluids are selected based on the volatility. Some specific objectives of this are then given as follows:

- To investigate the effect of mixture composition on the temperatures and exergy efficiency of the cycle.
- To present the effects of working conditions on the mixtures.
- To introduce key parameters for evaluating the mixture effects on the cycle performance.
- To demonstrate how using mixtures can provide a wide continues range of performance parameters and temperatures for better designs.
- To study the effect of adding more volatile fluids on the performance of the cycle.

To ensure the correctness of the developed code, the present simulation program is validated by using some experimental data taken from Pei et al. [19]. The specifications of the second case are chosen based on the cycle as presented in the work of Akkaya and Sahin [20].

3.2 Thermodynamic Aspects of Potential Mixture

The thermodynamic behaviors of mixtures fundamentally differ from pure fluid behavior. Regarding pure fluid cases, mixtures go through variable temperature-compositions equilibrium states during phase changes in constant pressure. This characteristic introduces two important set of state points called, bubble and dew points. Bubble points and dew points concepts are shown in Fig. 3.1. Suppose that a mixture goes through the vertical line from liquid to superheated equilibrium states, with 0.5 mol R11 and 0.5 mol R113. The lower bound of the 2 phase regions introduces bubble line and the upper bound, represents the dew points. For the specified composition, conjunction of the vertical line and bubble and dew point curves represent the bubble point and dew point temperatures for the mixture respectively.

Among equations and models for mixtures properties estimations, third order equations are of the special interest, due to their simplicity and two phase estimations abilities. The complete set of state equations can be found in the related literatures [21]. The critical properties of mixtures are functions of mixture compositions and critical parameters of individuals in compositions. So, with constant working pressures it will be crucial to choose appropriate fluids which their critical properties (temperatures specially) do not differ largely. This will ensure the presence of two-phase behavior for mixture in normal and common conditions of the cycle.

To better understand the thermodynamics of mixtures especially phase equilibrium it is essential to start with a state equation. A state equation has the general form as follows:

$$P = f\left(T, V\right) \tag{3.1}$$

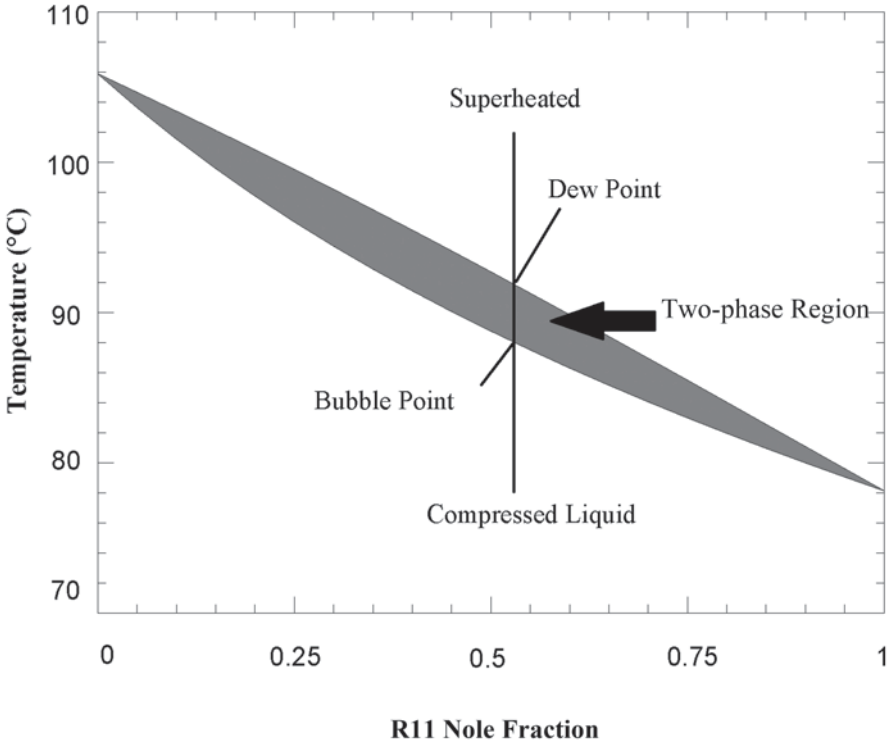

Fig. 3.1 Bubble and dew point and thermodynamic phase equilibrium for a double component mixture REFPROP [22]

where the function *f* has essential parameters which represent the nature of the fluid molecules and its molecular structure. Such parameters are critical temperature and pressure and intermolecular models constants. The intermolecular constants depends on the type of the state equation which is used and the fluid. Among these constants, acentric factor is most famous and widely applied in many models.

Using the state equation, various properties can be calculated. For example, entropy is written in the integral form as follows:

$$S^* = \int_{\infty}^{V} \left[\left(\frac{\partial P}{\partial T} \right)_V - \frac{R}{V} \right] dV + Rln\left(\frac{V}{V^0} \right) \tag{3.2}$$

In many applications two phase thermodynamics is encountered. For a simple fluid in which gas and liquid phases are in equilibrium, Gibbs function is minimized. For the phase change without reaction this equilibrium condition leads to equality of fugacity for each phase [21]:

$$f_i^v = f_i^l \quad i = 1, \ldots, n \tag{3.3}$$

For a mixture thermodynamic state equation is a function of composition as well as temperature and volume:

$$P = f\left(T, V, X\right) \tag{3.4}$$

Here, the Quasi-Pure fluid model is usually used with equations of states to evaluate the fluid thermodynamic properties. The mixing rules are chosen based on the state function to estimate the equivalent Quasi-Pure fluid specifications like critical temperature, pressure and acentric factor. The calculation of two or multiphase properties for mixtures is complicated and time consuming. In two phase region, the composition of each phase changes with temperature and pressure, and the specific algorithms, like flash algorithm, is used to determine each phase composition and the vapor or liquid fraction (quality). These algorithms for equilibrium phases are founded on the equality of fugacity as like as pure fluid calculations. For specified types of molecules and compositions, mixing rules and proper state functions are evaluated through experimental or semi experimental correlations which provide more accurate data. The softwares and programs, like REFPROP [22], use such improved models beside general methods for more accurate and reliable data.

3.3 Cycle Description and Problem Definition

Here, two different cases are studied, to show the effect of mixture composition on the efficiency and performance of cycles. The first case which is used for validation of the simulation code and procedure is constructed for evaporator, condenser, turbine and pump as main parts. A schematic of the cycle is shown in Fig. 3.2. Hot oil is used to assist the heat source in evaporator and water flow serve the cooling duty in condenser. A separator is utilized to prevent liquid particles from reaching the turbine. This case is used for validation and the effect of composition variation on the exergy efficiency of the cycle is also investigated. The results of this study may strongly be affected by the cycle configuration and working condition. To show this, another cycle (Case II) is simulated and investigated. The flow diagram of this cycle is shown in Fig. 3.3. An ORC bottoming an SOFC integrated cycle is chosen. The hot flue gases are considered as the heat source, which exchange energy with working fluid. The results show that in case I efficiency reduced when mixture was used but in case II efficiency increased. The performance data for cases I and II are presented in Table 3.1. The main working fluid is also specified for the cycles.

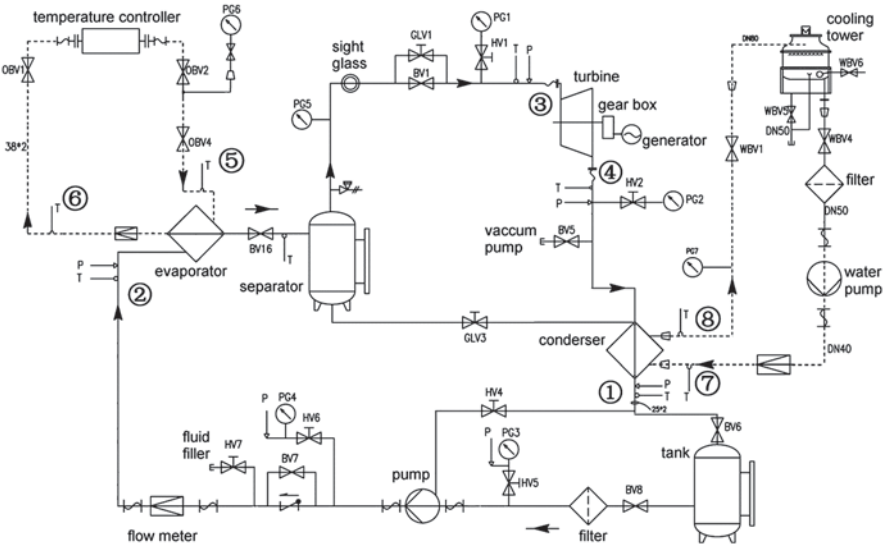

Fig. 3.2 Flow diagram of the organic Rankine cycle used for validation as case I [19]

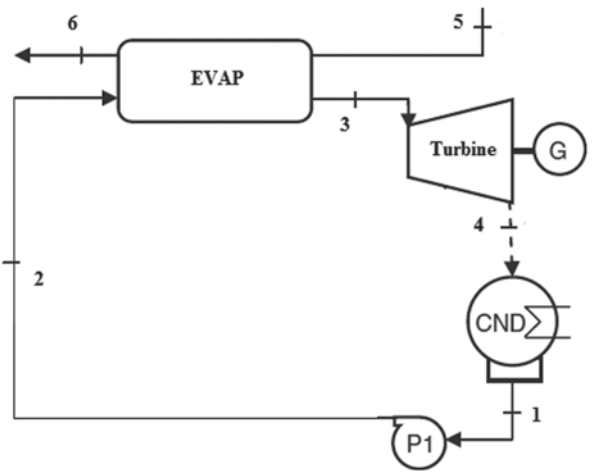

Fig. 3.3 Flow diagram of the cycle for case II [20]

3.4 Analysis

The analyses of the both cycles are performed using thermodynamic laws, and the necessary properties are evaluated using REFPROP software. The simulation procedure for both cases is the same. For turbine we write:

$$h_{out} = h_{in} - \eta_{is} \times \left(h_{in} - h_{out_{is}} \right) \tag{3.5}$$

Table 3.1 Cases I and II operating data [19, 20]

	Case I	Case II
P_1	103 kPa	36.5 kPa
P_2	550 kPa	500 kPa
P_3	455 kPa	500 kPa
P_4	107 kPa	36.5 kPa
$\eta_{Turbine}$	0.625	0.85
η_{Pump}	0.18	0.7
Working Fluid	R123	R113

$$\dot{W}_{Turbine} = \dot{m}_{mix} \times \left(h_{in} - h_{out}\right) \tag{3.6}$$

Here, the inlet and outlet conditions of hot stream in evaporator in both cases are known. The conditions at evaporator outlet are superheated and known. For state 3 in both cases one may write

$$T_3 = T_{bubble} + \Delta T_{superheat} \tag{3.7}$$

The degree of superheat $\Delta T_{superheat}$ is assumed to be 10° for both cases. The evaporator heat balance may lead to the following equation for mass flow rate:

$$\dot{m}_{mix} = \frac{(\dot{m} \times (h_{in} - h_{out}))_{hot\ stream}}{\left(h_{out} - h_{in}\right)_{cold\ stream}} \times \eta_{evap} \tag{3.8}$$

The pumps are modeled like turbines through the balance equations with isentropic efficiency as follows:

$$h_{out} = h_{in} + \left(h_{out_{is}} - h_{in}\right) \Big/ \eta_{is} \tag{3.9}$$

$$\dot{W}_{Pump} = \dot{m}_{mix} \times \left(h_{out} - h_{in}\right) \tag{3.10}$$

Thermodynamic state at the condenser outlet is assumed to be in saturated liquid state or for mixture at dew point. So, the heat removed in condenser is calculated as

$$\dot{Q}_{cond} = \dot{m}_{mix} \times \left(h_{in} - h_{out}\right)_{mix} \tag{3.11}$$

To evaluate the effect of mixture composition on heat exchangers performance, a minimum temperature difference between cold and hot streams is defined and calculated as follows:

$$\Delta T_{mean} = \frac{\int (T_{hot} - T_{cold})dh}{\int dh} \tag{3.12}$$

Table 3.2 Comparison between simulation results and experimental data for case I

	Simulation	Experiment [19]
T_1	28.423 ˚C	28.2 ˚C
T_2	29.93 ˚C	29.8 ˚C
T_4	72.55 ˚C	72.5 ˚C
$W_{Turbine}$	1.357 kW	1.36 kW
Cycle Efficiency	0.066	0.068
Condenser Heat Loss	16.74 kW	16.8 kW

where *dh* is infinitesimal heat transfer between cold and hot streams.

The exergy efficiency of the cycle is evaluated using the following formula:

$$\eta_{ex} = \frac{\dot{W}_{Turbine} - \dot{W}_{Pump}}{\left(\dot{E}x_{in} - \dot{E}x_{out}\right)_{hot\ stream}} \tag{3.13}$$

3.5 Validation

As mentioned earlier, case I is used for model validation. The following assumptions are made for analysis and simulation:

- Turbine and pump are considered adiabatic.
- R123 mass flow rate is 0.083 kg/s according to the experiment.
- Condenser outlet condition is saturated liquid.
- All the pressures are assumed to be same based on the experimental data as presented in Table 3.1.
- The efficiencies of turbine and pumps are given in Table 3.1.

In addition, the simulation and experimental data are listed and compared in Table 3.2.

3.6 Case I: Results and Discussion

The working fluid in case I is a combination of R113, R123, and R114. As previously said, R123 is the main fluid. R113 and R114 are chosen to show the effect of components volatility. The first additive has higher critical temperature and boiling temperature than the main fluid. In return, R114 has lower critical and boiling temperature than R123. The temperatures at points 1 and 3 in Fig. 3.1 are normalized using following definitions:

$$Tr_1 = \frac{T_1}{T_4} \tag{3.14}$$

$$Tr_2 = \frac{T_3}{T_4} \tag{3.15}$$

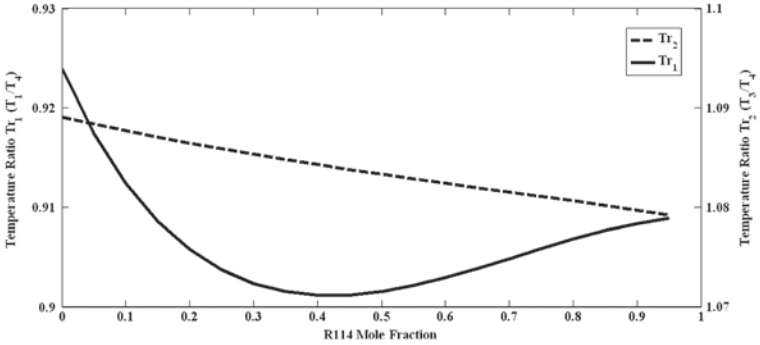

Fig. 3.4 Temperature ratios variations vs. R114 mol fraction for case I

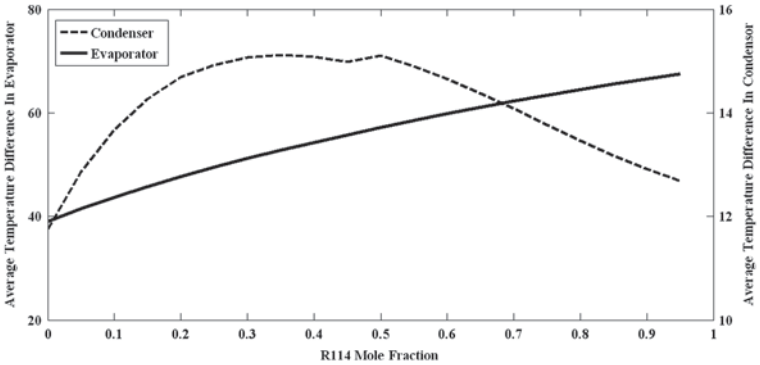

Fig. 3.5 Changes in mean temperature difference in condenser and evaporator with R114 mol fraction for case I

Firstly, R114 is added to R123. Figure 3.4 shows how temperature ratios are changed while contribution of R114 in the composition varies. Tr_2 decreases due to reduction in bubble point temperature in evaporator. Tr_1 shows a minimum at 0.4 and then increases.

The mean temperature difference between hot and cold flow flows in heat exchangers presents the exergy efficiency of the heat transfer phenomena. The lower the temperature difference in heat exchangers the higher the exergy efficiencies. Figure 3.5 represents the variations of mean temperature difference in evaporator and condenser. ΔT_{mean} in evaporator increases due to a large decrease in evaporator inlet temperature and bubble point temperature. However, condenser shows a different behavior. Mean temperature difference increases and then decreases. These tendencies are matched with temperature ratio variations in Fig. 3.4.

Turbine and pump works are shown in Fig. 3.6. Turbine power behaves similar to Tr_1, as decreased firstly and then increased at minimum. The decrease in turbine work is due to reduction in inlet temperature as shown in Fig. 3.7 mass flow

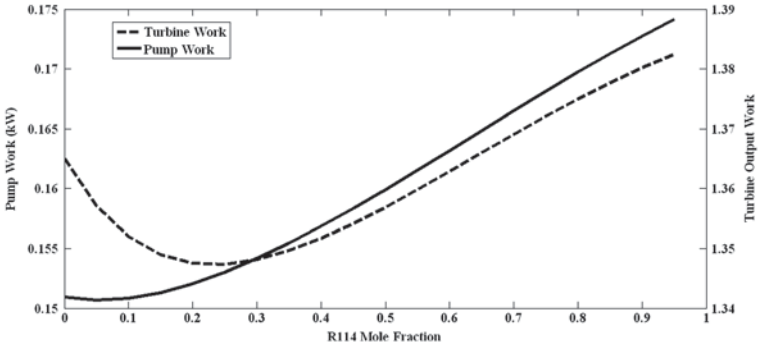

Fig. 3.6 The turbine and pump work rates versus R114 mol fraction for case I

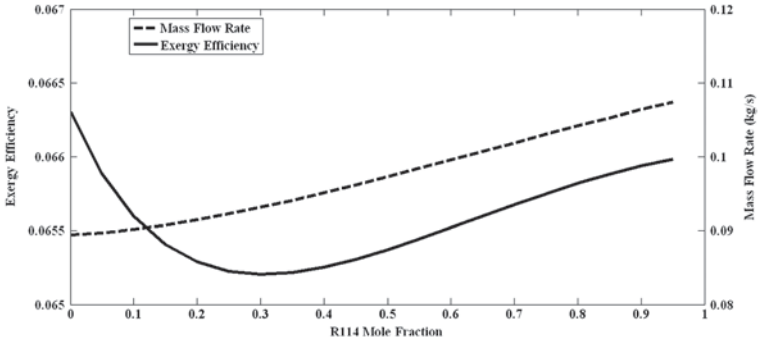

Fig. 3.7 Mass flow rate and exergy efficiency in function of R114 mol fraction changes for case I

rate increases ad results in more output work in turbine. Pump work increases for increase in mass flow rate. Exergy efficiency presents a similar trend in as temperature ratios variations especially Tr_1. Firstly reduced and then increases but to a lower value than its original value with R123 as working fluid.

The effect of a less volatile additive is investigated using R113 in addition to R123. Figure 3.8 shows the temperature ratios variations. Both ratios are falling down but around 0.8 as Tr_1 increases. The mean temperature differences in evaporator decrease due to an increase in inlet and outlet temperatures. The mean temperature difference in condenser first increases and then decreases. These variations are shown in Fig. 3.9.

The turbine and pump works are presented in Fig. 3.10. The turbine work decreases firstly and finally increases up to 0.8. The pump work increases with an increase in mass flow rate. As shown in Fig. 3.11, the exergy efficiency is a function of Tr_1 and turbine work, and it decreases first and tends to increase later.

Triple mixture composition effects on mass flow rate and exergy efficiency are shown in Figs. 3.12 and 3.13. In addition, the mean temperature differences in

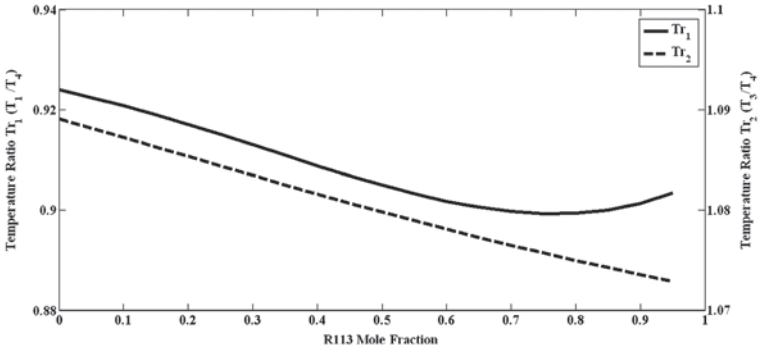

Fig. 3.8 Effect of R113 mole fraction changes on temperature ratios for case I

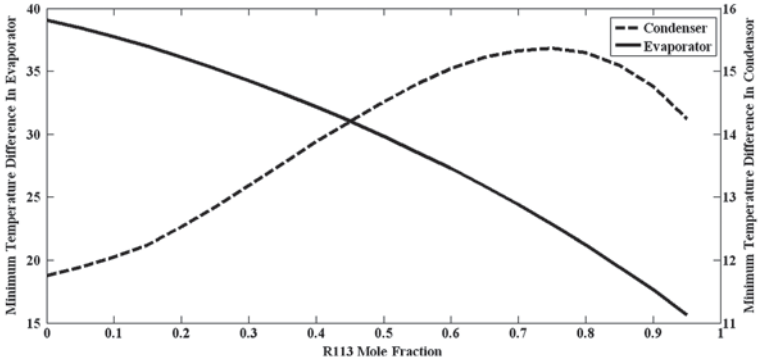

Fig. 3.9 Variations of mean temperature difference in evaporator and condenser with R113 mole fraction for case I

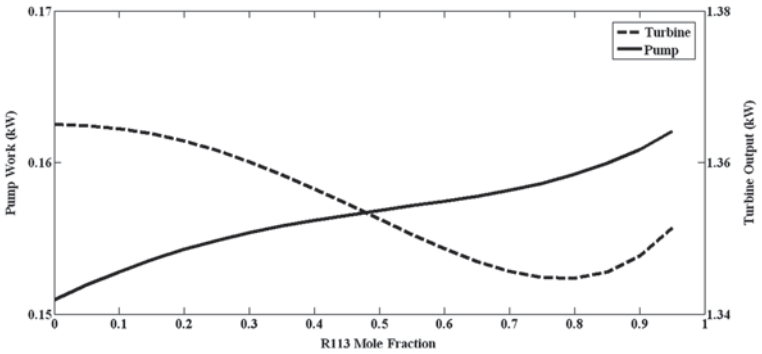

Fig. 3.10 The turbine and pump work rate changes with R113 mol fraction variations for case I

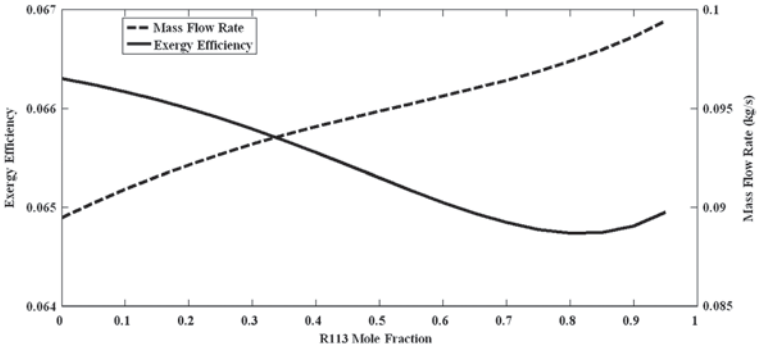

Fig. 3.11 Mass flow rate and exergy efficiency variations vs. R113 mole fraction for case I

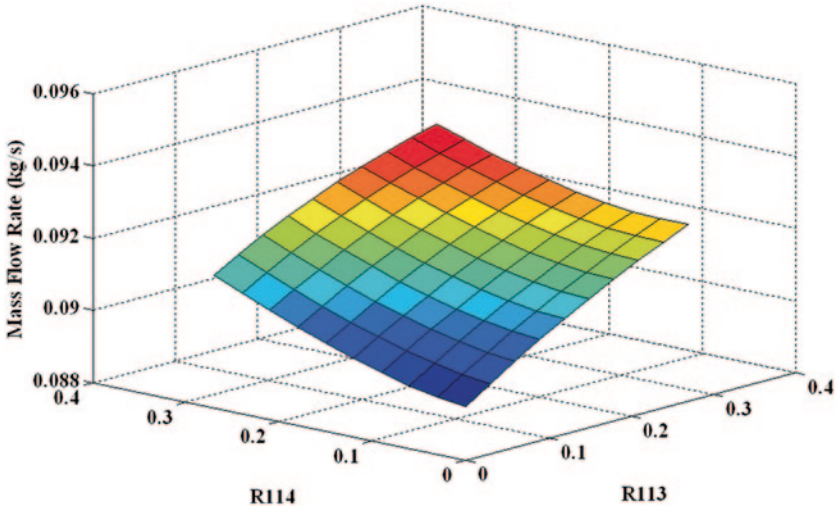

Fig. 3.12 Case I: Composition effect on the mixture mass flow rate

evaporator and condenser have a strong effect on exergy efficiency of the cycle as shown in Fig. 3.14.

3.7 Case II: Results and Discussion

In case II, R113 is the main working fluid. R11, which is more volatile, is added to the main fluid. The effects of R11 mol fraction variations on temperature ratios are shown in Fig. 3.15. Both temperature ratios increase while R11 mol fraction

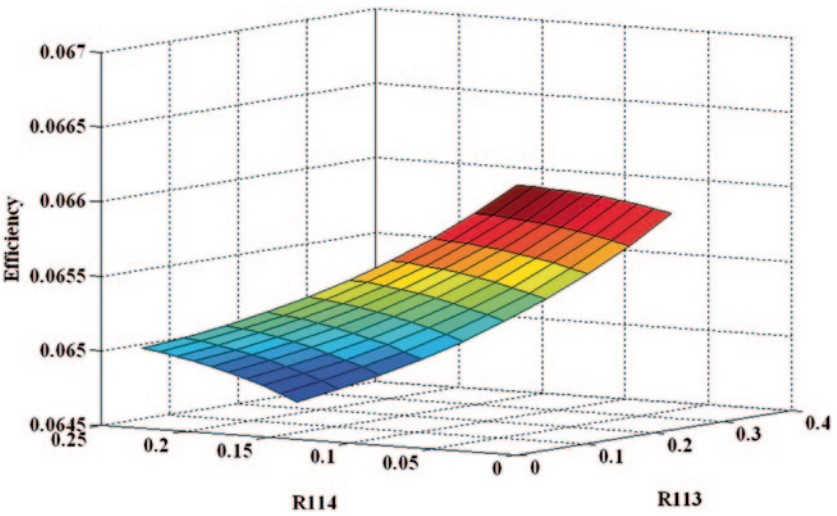

Fig. 3.13 Case I: Composition variations effects on the cycle exergy efficiency

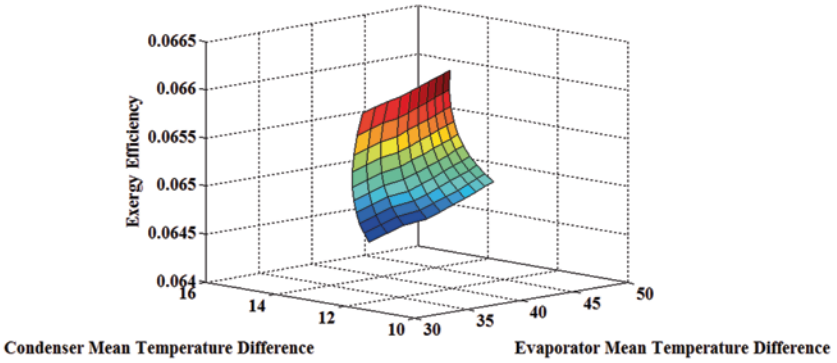

Fig. 3.14 Case I: Exergy efficiency vs. evaporator and condenser mean temperature difference

increases, which shows a different trend from the previous case. As it is presented in Fig. 3.16, the mean temperature difference in condenser decreases except for a narrow region of low R11 concentration. The temperature at evaporator outlet, the decreases due to reduction in saturated vapor temperature. So, increase in temperature ratio Tr_2 means that turbine outlet temperature decreases more than turbine inlet temperature. In addition, R11 reduces the saturation liquid temperature at condenser exit. So, a rise in temperature ratio Tr_1 is observed due to a significant decrease in turbine outlet temperature, and these effects cause the mean temperature difference in condenser to decrease.

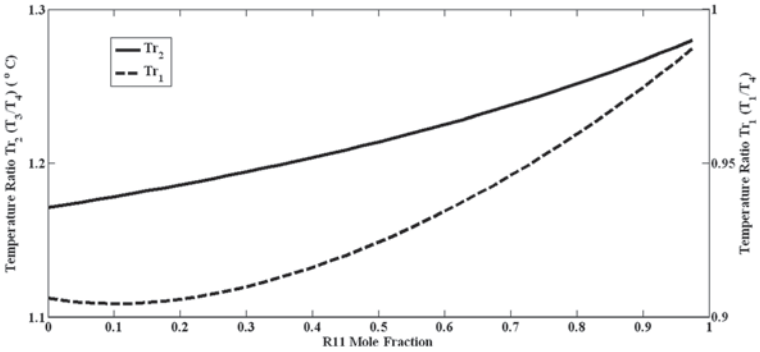

Fig. 3.15 Temperature ratio variations vs. R114 mol fraction for case II

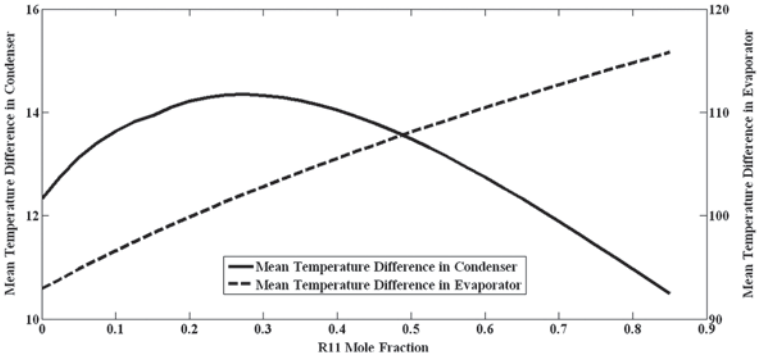

Fig. 3.16 Mean temperature difference in evaporator and condenser vs. R11 mol fraction changes for case I

If the temperature at the turbine exit falls significantly, there is an expectation for an increase in the turbine output work. Actually, turbine work reaches to higher values and the pump work reduces significantly due to reduction in mass flow rate. These effects are shown in Figs. 3.17 and 3.18.

So, there is an expectation for efficiency increase in this case. The exergy efficiency rises while mass flow rate decreases. The results for both cases show that temperature ratios have significant roles in the performance of the cycles. Tr_1 shows the degree of superheat at turbine outlet and the amount of heat released to the coolant in condensers. So the lower Tr_1 results in less heat loss and higher efficiency. Tr_2 is more complicated. While it increases there might be a positive or negative change in mass flow rate. However, when Tr_2 increases work per mass unit passing the turbine will increases due to higher temperature reduction or enthalpy drop in turbine.

In addition to the changes in efficiency and work, there is another benefit in using mixtures which is that the mixtures essentially provide a wide range of temperatures and working conditions for designing purpose. This helps improve flexibility and reliability of working fluids.

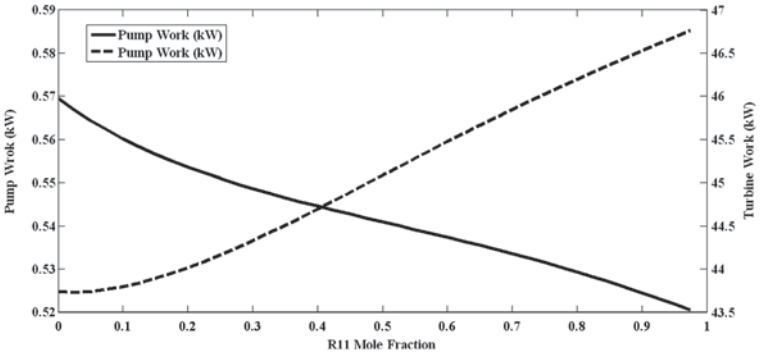

Fig. 3.17 The turbine and pump works in function of R11 mol fraction for case II

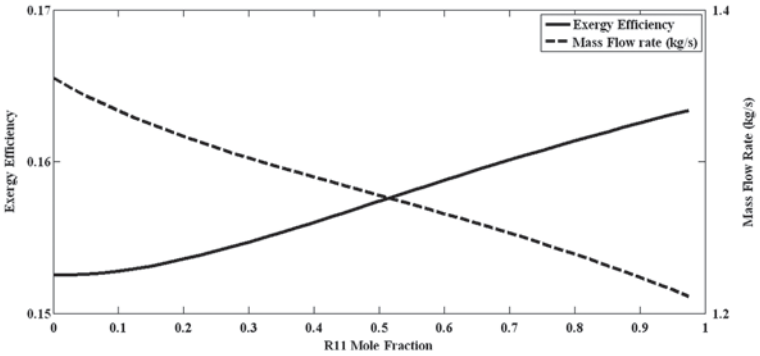

Fig. 3.18 Exergy efficiency and mass flow rate variations vs. R11 mol fraction for case II

Conclusions

The effect of mixture composition on the cycle performance is investigated. Using mixtures instead of pure fluid may have positive or negative effects on the cycle efficiency. The results show that adding more volatile fluids may increase the efficiency. The temperature ratios are important representatives of the cycle performance. Also, the mean temperature differences in evaporators and condensers, which are a function of mixture composition and temperature ratios, show how efficient heat transfer procedures are. In summary, the following concluding remarks may be extracted:

- The effect of using mixtures is depended on the base working fluid, additives and working conditions, like pressures.
- The temperature ratios have significant effect on the cycle performance. Tr_1 shows the temperature drop across the turbine and Tr_2 presents the heat loss in condenser. The results show that turbine output work may increase about 2 kW and efficiency may rise about 1 % for case II.

- The mean temperature differences in condenser tend to decrease as Tr_1 increases. This results in higher efficiency in condenser.
- The mean temperature differences in evaporator increases when more volatile fluid is used and decreases when less volatile fluid is used as addition to the base fluid.

Finally, using mixtures provides a wider range of working conditions. This helps achieve better operating cycles.

Nomenclature

$\dot{E}x$	Exergy Flow Rate(kW)
f	Fugacity
h	Specific Enthalpy (kJ/kg)
n	Number of components in mixture
P	Pressure (kPa)
$\dot{Q}$	Heat Rate (kW)
R	Universal Gas Constant, kJ/kg °K
S	Specific Entropy (kJ/kg °K)
T	Temperature (K or °C)
Tr	Temperature Ratio
V	Volume
$\dot{W}$	Power or Work Rate (kW)
X	Mixture Mole Fractions Vector

Greek Letters

η	Efficiency

Subscripts

cold	Cold stream
evap	Evaporator
ex	Exergetic
hot	Hot stream
is	Isentropic
in	Inlet
mix	Mixture
out	Outlet

Superscripts

0	Ideal Gas Property
*	Departure Function
v	Vapor
l	Liquid

Acronyms

LHV	Lower heating value

References

1. Husband WW, Beyene A (2008) Low-grade heat-driven Rankine cycle, a feasibility study. Int J Energy Res 32:1373–1382
2. Yang W-J, Kuo C-H, Aydin O (2001) A hybrid power generation system: solar-driven Rankine engine–hydrogen storage. Int J Energy Res 25:1107–1125
3. Mago Pedro J, Rogelio L (2012) Energetic and exergetic analysis of waste heat recovery from a microturbine using organic Rankine Cycles. Int J of Energy Res Rev 37:888–898
4. Preibinger M, Heberle F, Brüggemann D (2012) Thermodynamic analysis of double-stage biomass fired organic Rankine cycle for micro-cogeneration. Int J of Energy Res Rev 36:944–952
5. Chen H, Goswami DY, Stefanakos EK (2010) A review of thermodynamic cycles and working fluids for the conversion of low-grade heat. Renew Sustain Energy Rev 14:3059–3067
6. Zamfirescu C, Dincer I (2009) Performance investigation of high-temperature heat pumps with various BZT working fluids. Thermochimica Acta 488:66–77
7. Hung TC, Wang SK, Kuo CH, Pei BS, Tsai KF (2010) A study of organic working fluids on system efficiency of an ORC using low-grade energy sources. Energy 35:1403–1411
8. Kuo C-R, Hsu S-W, Chang K-H, Wang C-C (2011) Analysis of a 50 kW organic Rankine cycle system. Energy 36:5877–5885
9. [9]Stijepovic MZ, Linke P, Papadopoulos AI, Grujic AS (2012) On the role of working fluid properties in organic Rankine Cycle performance. Appl Therm Eng 36:406–413
10. Rayegan R, Tao YX (2011) A procedure to select working fluids for Solar Organic Rankine Cycles (ORCs). Renew Energy 36:659–670.
11. Guo T, Wang H, Zhang S (2011) Comparative analysis of natural and conventional working fluids for use in transcritical Rankine cycle using low-temperature geothermal source. Int J of Energy Res 35:530–544
12. Delgado-Torres AM, García-Rodríguez L (2010) Analysis and optimization of the low-temperature solar organic Rankine cycle (ORC). Energy Convers Management 51:2846–2856
13. Lai NA, Wendland M (2011) Fischer Johann (2011) Working fluids for high-temperature organic Rankine cycles. Energy 36:199–211
14. Lakew AA, Bolland O (2010) Working fluids for low-temperature heat source. Appl Therm Eng 30:1262–1268
15. Zamfirescu C, Dincer I (2008) Thermodynamic analysis of a novel ammonia–water trilateral Rankine cycle. Thermochimica Acta 477:7–15
16. Kim KH, Han CH, Kim K (2012) Effects of ammonia concentration on the thermodynamic performances of ammonia–water based power cycles. Thermochimica Acta 530:7–16
17. Li W, Feng X, Yu LJ, Xu J (2011) Effects of evaporating temperature and internal heat exchanger on organic Rankine cycle. Appl Therm Eng 31:4014–4023
18. Chen H, Goswami DY, Rahman Muhammad M, Stefanakos EK (2011) A supercritical Rankine cycle using zeotropic mixture working fluids for the conversion of low-grade heat into power. Energy 36:549–555
19. Pei G, Li J, Li Y, Wang D, Ji J (2011) Construction and dynamic test of a small-scale organic rankine cycle. Energy 36:3215–3223
20. Akkaya AV, Sahin B (2009) A study on performance of solid oxide fuel cell-organic Rankine cycle combined system. Int J Energy Res 39:553–564
21. Poling BE, Prausnitz Jm, O'connell JP (2001) The properties of gases and liquids: 5th edn. Mc Grow Hill Inc.
22. NIST REFPROP Software. http://www.nist.gov

Chapter 4
Comparative Performance Assessment of Two Geothermal-Based Integrated Systems for Hydrogen Production

T. A. H. Ratlamwala and Ibrahim Dincer

Abstract In this paper, we conduct a comparative performance assessment study between a conventional electrolyzer and a steam methane reformer (SMR) to investigate which one provides a better option from energy, exergy and sustainability perspectives. The power to both systems is provided by a quintuple flash power plant running on a geothermal source. The quintuple flash power plant is selected due to its capability of producing power in an efficient and environmentally-benign manner. The results show that increasing the ambient temperature increases the overall system exergy efficiency of the first system (consisting of an electrolyzer) from 51.7 to 60.8 % while this remains almost constant at 6.8 % for the second system (containing SMR). The amount of hydrogen produced by the electrolyzer and SMR vary varies from 3.9 to 65.3 L/s and 365 to 426.5 L/s, respectively, with a rise in the geothermal source temperature. With increase in the geothermal source temperature, the exergy efficiencies vary from 54.2 to 62.1 % for the first system and 6.6 to 7.6 % for the second system. Furthermore, the first system is much more sustainable compared to the second system.

Keywords Geothermal power · Energy · Exergy · Efficiency · Power plant · Hydrogen production

T. A. H. Ratlamwala (✉)
Faculty of Engineering and Applied Science, University of Ontario Institute of Technology, 2000 Simcoe Street North, Oshawa, ON L1H 7K4, Canada
e-mail: tahir.ratlamwala@uoit.ca

SZABIST, 90 and 100 Clifton Campus, Karachi, Sindh, Pakistan

I. Dincer
Department of Mechanical Engineering, University of Ontario Institute of Technology (UOIT), 2000 Simcoe Street North, Oshawa ON L1H 7K4, Canada
e-mail: ibrahim.dincer@uoit.ca

I. Dincer et al. (eds.), *Progress in Sustainable Energy Technologies: Generating Renewable Energy,* DOI 10.1007/978-3-319-07896-0_4,

4.1 Introduction

The negative effects of extensive use of fossil fuels to meet energy demands have started appearing in every part of the world. Problems ranging from ozone layer depletion to a rise in sea levels have become major concerns for countries around the world. It is believed that fossil fuels are the main culprit to these problems as combustion of fossil fuels results in emissions of harmful gases such as CO_2, NOx, SOx etc. Furthermore, the finite pool of fossil fuel resources demands the introduction of new energy sources to substitute conventional resources and create a more sustainable future.

A very promising energy resource that can help reduce dependence on fossil fuels is geothermal option. Geothermal energy is considered to be a clean source of energy as it is extracted from the Earth's crust and when used has no greenhouse gas emissions [1–3]. The use of geothermal energy is dependent on the source temperature, and therefore geothermal resources are divided into three categories: high-temperature source, medium-temperature source, and low-temperature sources [4]. High-temperature geothermal source are best suited for power generation using flash systems [5], moderate-temperature sources can be utilized to produce power using organic Rankine cycles or to provide heating or cooling using absorption technology, and low-temperature sources are best suited for direct use such as heating. Power can be produced using geothermal steam with the help of three existing power production technologies: dry steam, flash/binary, and flash-system power plants [6]. Studies carried out by [7, 8] for comparison of multi-flash systems showed that double flash system resulted in better energetic and exergetic efficiencies compared to single flash system, hence hinting towards an increase in efficiency with an increase in number of flash units. However, when it comes to producing hydrogen, electrolysis of water and steam methane reforming (SMR) are considered to be very mature and well-developed technologies. Dufour et al. [9] stated that at present 96% of hydrogen is produced using SMR.

The use of hydrogen as an energy source for fuel cells holds great potential due to its high efficiency and zero green house gas emissions. The use of hydrogen as a fuel makes the energy generation process eco-friendly because the by-product of this process is water and steam. In the future, the role of hydrogen may become more important, as some researchers suggest that the world's energy systems may undergo a transition to an era in which the main energy carriers will be hydrogen [10–12].

The main objective of this contribution is to conduct a comparative performance assessment study between two integrated systems. A parametric study is performed to investigate the effect of variation in ambient temperature and geothermal source temperature on the amount of power produced, rate of hydrogen produced, energy and exergy efficiencies, and sustainability indexes.

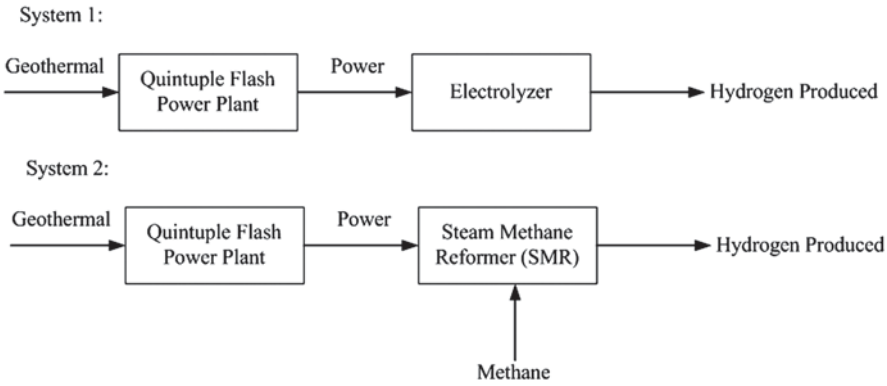

Fig. 4.1 Schematic of the integrated systems

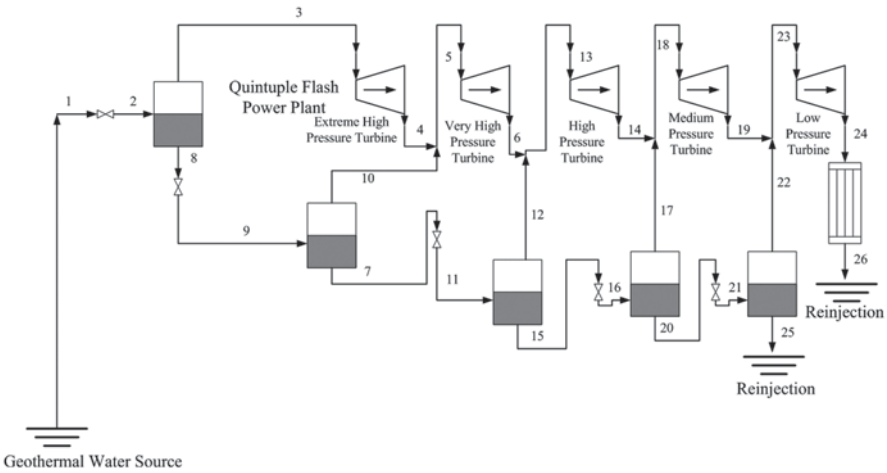

Fig. 4.2 Schematic of quintuple-flash system

4.2 System Description

Here, two integrated systems namely quintuple-flash integrated with electrolyzer (system 1) and quintuple-flash integrated with SMR (system 2) are studied as shown schematically in Fig. 4.1. The first step in both systems is power production using the geothermal quintuple-flash system as shown in Fig. 4.2. In quintuple-flash systems, geothermal water enters at high pressure and temperature at state 1. The pressure of the geothermal water is than dropped subsequently using an expansion valve, which helps in generating steam. The steam is then collected from the top of the separator and is supplied to the turbine at

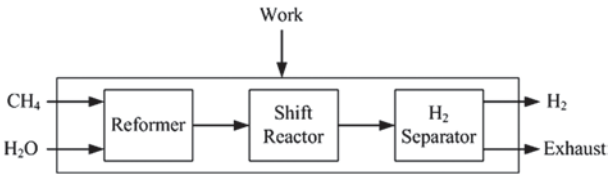

Fig. 4.3 Schematic of steam methane reformer

state 3. In the turbine, the steam expands to generate power and leaves at state 4. From the separator, liquid water is collected at state 8 and is passes through the second expansion valve where its pressure drops (state 9). The steam generated is then collected from the top part of the second separator (state 10), which later combines with steam at state 4 leaves at state 5 to enter a second turbine. In the second turbine, steam entering at state 5 expands and generates power. The liquid geothermal water collected from the bottom of the second separator (state 7) then passes through a third expansion valve. This process is repeated until streams 25 and 26 are re-injected into the geothermal well. The power produced by the quintuple-flash power plant is supplied to the electrolyzer (system 1) and the SMR (system 2). In the electrolyzer, power is used to break apart water molecules to produce hydrogen. In the SMR, methane is compressed to increase its pressure and water is then pumped to match the pressure of the methane. Methane and steam then passes through the reformer, shift reactor, and hydrogen separation system as showing in Fig. 4.3. The hydrogen produced in these systems can later be used to produce heat and power using a Proton Exchange Membrane Fuel Cell (PEMFC). The exhaust gases produced by the SMR are released to the environment.

4.3 Energy and Exergy Analyses

The energy and exergy balance equations presented in this paper are written for the main system components. The software Engineering Equation Solver (EES) is used for the thermodynamic analyses of all processes. In the simulation, pure methane is supplied as a fuel in addition to pure water. The following assumptions are made for the analysis:

- The electrolyzer and SMR efficiency are assumed to be 56 %
- The losses in pipes and connections are negligible.
- The ambient temperature and pressure are 291.2 K and 100 kPa, respectively.
- The heat exchangers are modeled using a prescribed effectiveness and a minimum temperature difference between inlet and outlet streams.
- The parasitic losses are taken to be 20 %.

The detailed energy and exergy analyses of both integrated systems studied in this paper are carried out. The power produced by the turbines is calculated using

$$\dot{W}_{turb} = \dot{m}_3(h_3 - h_4) + \dot{m}_5(h_5 - h_6) + \dot{m}_{13}(h_{13} - h_{14}) + \dot{m}_{18}(h_{18} - h_{19}) + \dot{m}_{23}(h_{23} - h_{24}) \tag{4.1}$$

The exergetic content at state 1 is found using

$$\dot{E}x_1 = \dot{m}_1((h_1 - h_0) - T_0(s_1 - s_0)) \tag{4.2}$$

The same formulation is used to the calculate exergy rate at each state. The parasitic losses are also considered and defined as

$$\dot{W}_{parasitic} = 0.2(\dot{W}_{turb}) \tag{4.3}$$

The actual net power that can be obtained from the quintuple flash plant running on geothermal is expressed as

$$\dot{W}_{net} = \dot{W}_{turb} - \dot{W}_{parasitic} \tag{4.4}$$

The rate of hydrogen produced by the electrolyzer is calculated by

$$\eta_{elec} = \frac{\dot{m}_{H_2 elec} \times LHV_{H_2}}{\dot{W}_{elec}} \tag{4.5}$$

where $\eta_{elec} = 56\%$ and $\dot{W}_{elec} = \dot{W}_{net}$.

The rate of hydrogen produced by the SMR is calculated by

$$\eta_{SMR} = \frac{\dot{m}_{H_2 SMR} \times LHV_{H_2}}{\dot{W}_{SMR} + \dot{m}_{CH_4} \times LHV_{CH_4}} \tag{4.6}$$

where $\eta_{SMR} = 56\%$ and $\dot{W}_{SMR} = \dot{W}_{net}$.

The exergetic content of the hydrogen is obtained by

$$\dot{E}x_{H_2} = \dot{m}_{H_2}\left[ex_{H_2,ch} + ex_{H_2,ph}\right] \tag{4.7}$$

where $ex_{H_2,ch} = \dfrac{235.153 \times 1000}{MW_{H_2}}$ and $ex_{H_2,ph} = \left[(h_{H_2} - h_0) - T_0(s_{H_2} - s_0)\right]$.

The exergetic content of the supplied methane is obtained by

$$\dot{E}x_{CH_4} = \dot{m}_{CH_4}\left[ex_{CH_4,ch} + ex_{CH_4,ph}\right] \tag{4.8}$$

where $ex_{CH_4,ch} = \dfrac{830.212 \times 1000}{MW_{CH_4}}$ and $ex_{CH_4,ph} = \left[(h_{H_2} - h_0) - T_0(s_{H_2} - s_0)\right]$.

The quintuple flash system energy efficiency is defined as

$$\eta_{en,qf} = \frac{\dot{W}_{net}}{\dot{m}_1 h_1 - (\dot{m}_{25} h_{25} + \dot{m}_{26} h_{26})} \tag{4.9}$$

The quintuple flash system exergy efficiency is defined as

$$\eta_{ex,qf} = \frac{\dot{W}_{net}}{\dot{E}x_1 - (\dot{E}x_{25} + \dot{E}x_{26})} \tag{4.10}$$

The overall energy and exergy efficiencies of system 1 are found by

$$\eta_{en,sys,elec} = \frac{\dot{m}_{H_2 elec} \times LHV_{H_2} + \dot{Q}eva}{\dot{m}_1 h_1 - (\dot{m}_{25} h_{25} + \dot{m}_{26} h_{26})} \tag{4.11}$$

$$\eta_{ex,sys,elec} = \frac{\dot{E}x_{H_2 elec}}{\dot{E}x_1 - (\dot{E}x_{25} + \dot{E}x_{26})} \tag{4.12}$$

The overall energy and exergy efficiencies of system 2 are found by

$$\eta_{en,sys,SMR} = \frac{\dot{m}_{H_2 SMR} \times LHV_{H_2}}{\dot{m}_1 h_1 - (\dot{m}_{25} h_{25} + \dot{m}_{26} h_{26}) + \dot{m}_{CH_4} \times LHV_{CH_4}} \tag{4.13}$$

$$\eta_{ex,sys,SMR} = \frac{\dot{E}x_{H_2 SMR}}{\dot{E}x_1 - (\dot{E}x_{25} + \dot{E}x_{26}) + \dot{E}x_{CH_4}} \tag{4.14}$$

The sustainability index for system 1 is defined as

$$SI = \frac{\dot{E}x_1}{\dot{E}x_{dest,tot,elec}} \tag{4.15}$$

The sustainability index for system 2 is defined as

$$SI = \frac{\dot{E}x_1 + \dot{E}x_{CH_4}}{\dot{E}x_{dest,tot,SMR}} \tag{4.16}$$

4.4 Results and Discussion

In this paper, a comparative study is conducted to observe the effect of variation in operating parameters on the performance and sustainability of two systems namely quintuple flash power plant integrated with electrolyzer (system 1) and quintuple flash power plant integrated with SMR (as system 2).

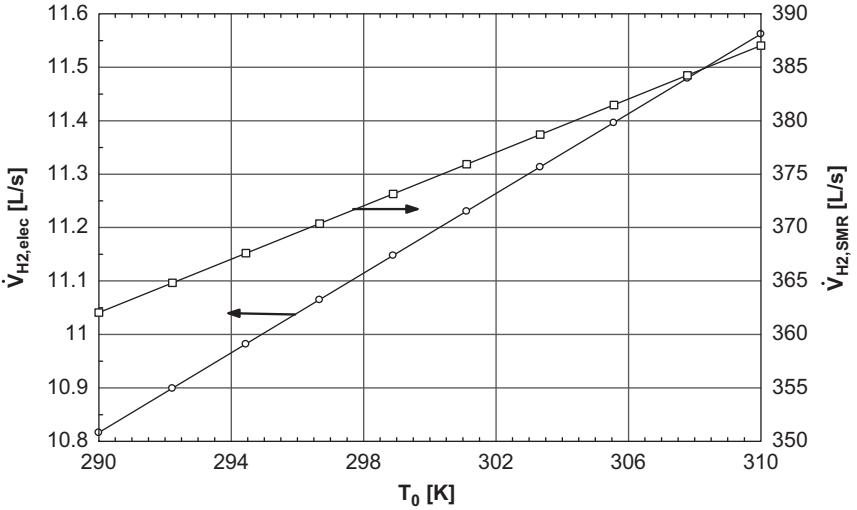

Fig. 4.4 Effect of ambient temperature on rate of hydrogen production

Effect of Ambient Temperature

The ambient temperature plays a critical role in performance determination of many systems, especially those working on the principle of temperature difference (e.g., geothermal systems). The effect of a rise in the ambient temperature on rate of hydrogen produced by system1 and system 2 is presented in Fig. 4.4. The rate of hydrogen produced by system 1 and system 2 increases from 10.8 to 11.6 L/s and 362.1 to 387 L/s respectively, with a rise in ambient temperature from 290 to 310 K. This behavior is observed because a rise in ambient temperature results in lower heat loss from the geothermal power plant to the environment based on temperature difference. As the rate of heat loss from the power plant to the environment decreases, the power production capability of the power plant and the hydrogen production capacity increases. It is also observed that system 2 generates far more hydrogen compared to system 1 for the same amount of power input. Figure 4.5 illustrates the effect of a rise in ambient temperature on the exergy efficiencies. It is observed that with rise in ambient temperature the exergy efficiency of the quintuple-flash system, system 1 and system 2 vary from 47 to 55.4%, 51.7 to 60.8%, and 6.7 to 6.8%, respectively. The results show that a rise in the ambient temperature affects the performance of the quintuple-flash system and system 1 but the performance of system 2 remains constant. It is also observed that system 1 has a much higher efficiency compared to system 2. This indicates that it is more beneficial to apply system 1 as opposed to system 2. The effect of a rise in the ambient temperature on the sustainability of both systems is presented in Fig. 4.6. It can be seen that the sustainability index of system 1 increases from 2.4–2.8, but remains constant for

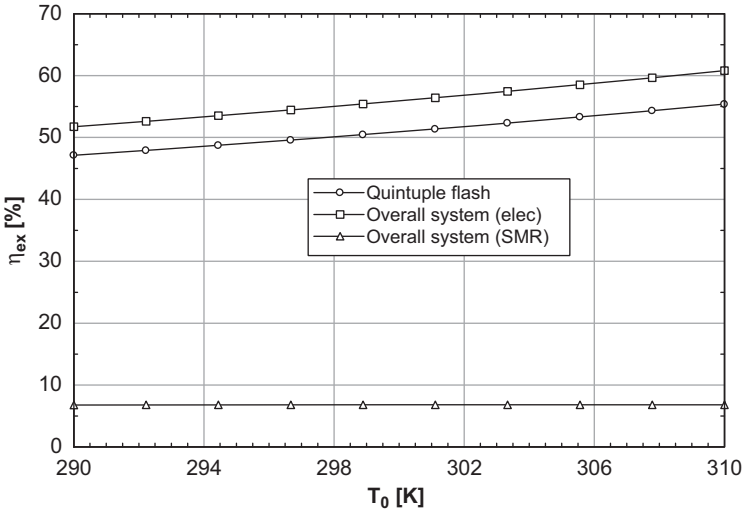

Fig. 4.5 Effect of ambient temperature on exergy efficiencies

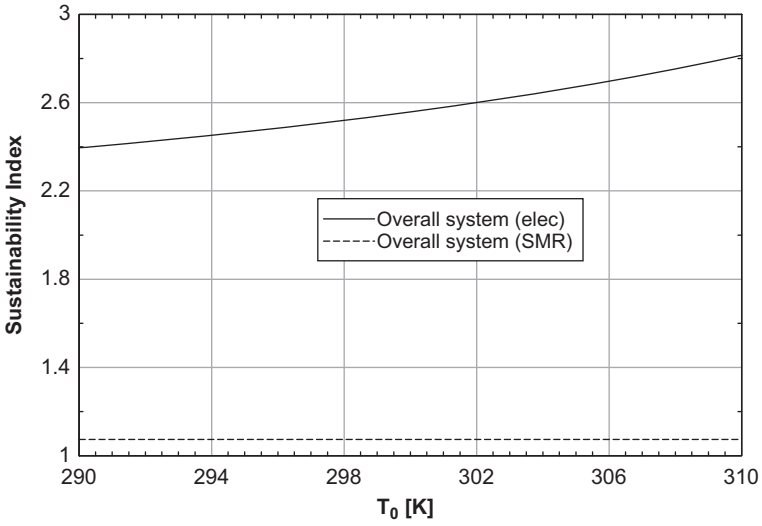

Fig. 4.6 Effect of ambient temperature on sustainability index

system 2 at 1.0. Sustainability index is calculated using input exergy to the system and exergy destructed by the system. This index helps to visualize how sustainable a process is from an exergy perspective. The results show that system 1 is far more sustainable than system 2.

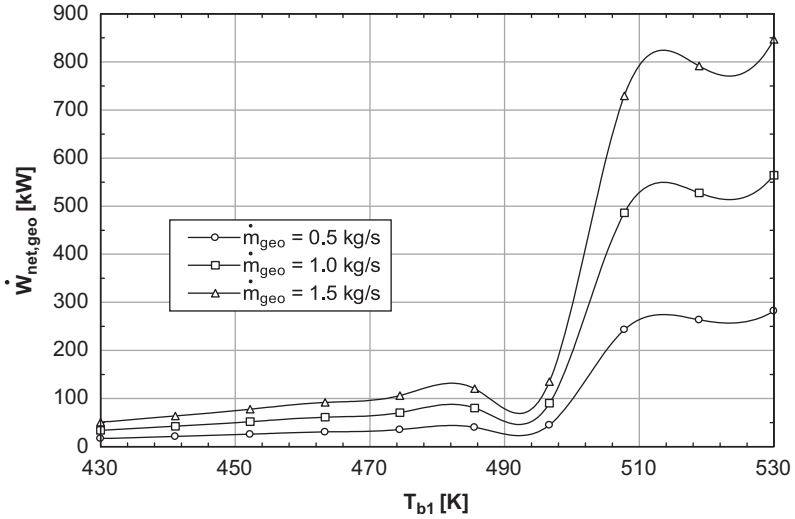

Fig. 4.7 Effect of geothermal source temperature on net power production

Effect of Geothermal Source Temperature

As mentioned earlier, the geothermal source temperature plays a major role in the utilization of a geothermal energy system. Figure 4.7 illustrates the effect of an increase in geothermal source temperature on the net power produced by the power plant. It can be seen that the net power produced varies from 16.95 to 846.7 kW with an increase in the source temperature from 430 to 530 K and a variation in the mass flow rate of geothermal water from 0.5 to 1.5 kg/s. It can be seen that for each mass flow rate there are several local minima and local maxima that occur with an increase in source temperature. The results show that the maximum amount of net power for each of the mass flow rates is produced when the geothermal source temperature is 530 K. Figure 4.8 portrays the effect of an increase in the geothermal source temperature on the rate of hydrogen production by system 1 and system 2. The rate of hydrogen produced by system 1 and system 2 varies from 4.0 to 65.4 L/s and 365 to 426.5 L/s, respectively, with an increase in the geothermal source temperature and for geothermal water mass flow rate of 1.0 kg/s. As with net power production, the rate of hydrogen produced by both systems show several local minima and local maxima but a geothermal source temperature of 530 K provides the best results. Furthermore, system 2 leads to higher rates of hydrogen production compared to system 1. The effect of an increase in the geothermal source temperature on energy efficiency is shown in Fig. 4.9. It is observed that the energy efficiency of the quintuple-flash system, system 1 and system 2 vary from 12.2 to 20.4 %, 6.9 to 11.4 %, and 51.9 to 35.08 %, respectively, with an increase in the geothermal source temperature. The

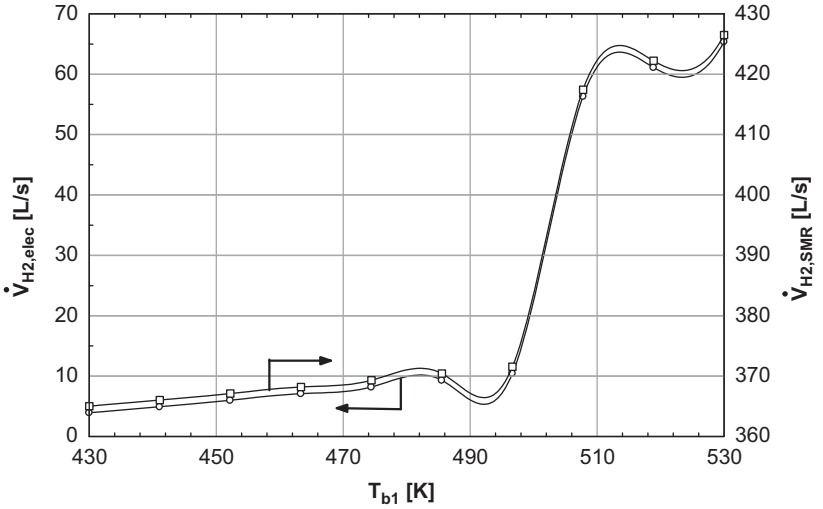

Fig. 4.8 Effect of geothermal source temperature on rate of the hydrogen production

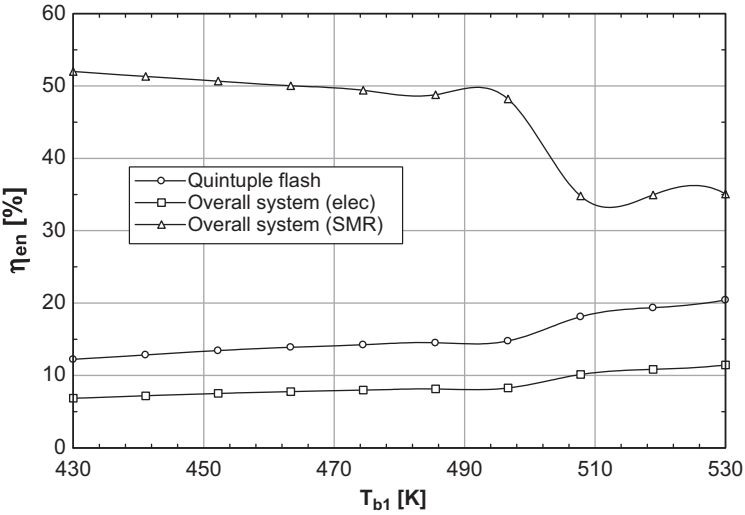

Fig. 4.9 Effect of geothermal source temperature on energy efficiencies

exergy efficiency of the quintuple flash system, system 1 and system 2 is found to be varying from 49.4 to 56.61 %, 54.2 to 62.2 %, and 6.7 to 7.7 %, respectively, as shown in Fig. 4.10. It can be seen that from an energy perspective, system 2 has the best efficiency but from an exergy perspective system 2 has the lowest efficiency. Due to higher exergy content of methane, the exergy efficiency of system

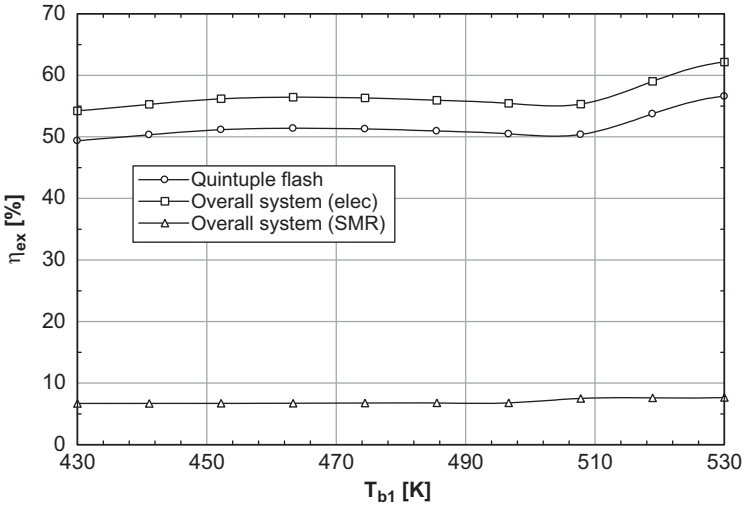

Fig. 4.10 Effect of geothermal source temperature on exergy efficiencies

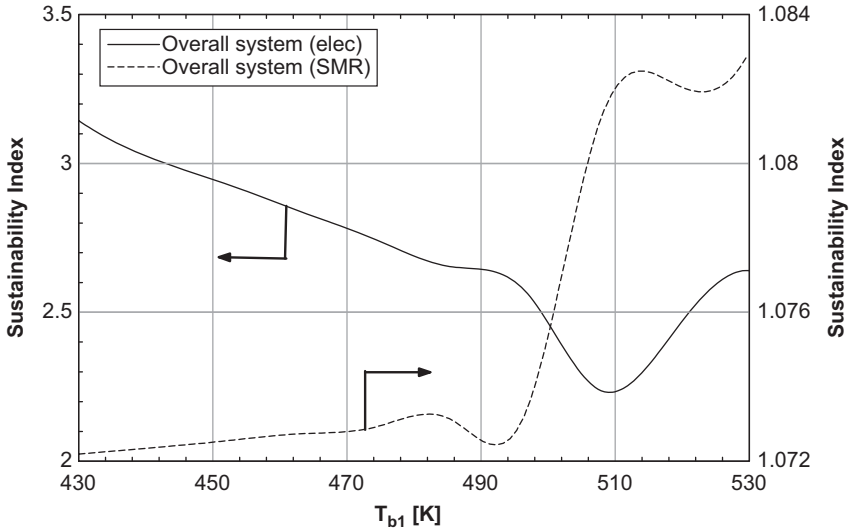

Fig. 4.11 Effect of geothermal source temperature on the sustainability index

2 drops compared to the exergy efficiency of system 1. Figure 4.11 illustrates the effect of an increase in the geothermal source temperature on the sustainability index of systems 1 and 2. The sustainability index of systems 1 and 2 varies from 3.14 to 2.64 and 1.07 to 1.08, respectively. The results show that the sustainability index of system 1 drops while the index for system 2 remains constant with an

increase in geothermal source temperature. It is also observed that the sustainability index of system 1 is three times higher than system 2, indicating that system 1 is far more sustainable than system 2 from an exergy perspective.

Conclusions

In this paper, we presented a comparative performance assessment of two systems namely a quintuple-flash system integrated with an electrolyzer and quintuple-flash system integrated with SMR. A parametric study is conducted to investigate the effect of varying the ambient temperature and geothermal source temperature on the amount of power produced, rate of hydrogen produced, energy and exergy efficiencies, and sustainability index. It is observed that a rise in ambient temperature leads to an increase in the rate of hydrogen production by systems 1 and 2 from 10.8 to 11.6 L/s, and 362.1 to 387 L/s, respectively. It is also observed that a rise in ambient temperature changes the exergy efficiency of the quintuple flash system, system 1 and system 2 vary from 47 to 55.4 %, 51.7 to 60.8 %, and 6.7 to 6.8 %, respectively. The sustainability index of systems 1 and 2 varies from 3.14 to 2.64 and 1.07 to 1.08, respectively, with an increase in geothermal source temperature. The results show that although system 2 produces far more hydrogen compared to system 1, it has a much lower exergy efficiency. Also, the sustainability index of system 1 is much higher compared to system 2, which shows that system 1 is far more sustainable than system 2.

Nomenclature

$\dot{E}x$	Exergy rate, kW
h	Specific enthalpy, kJ/kg
$\dot{m}$	Mass flow rate, kg/s
MW	Molecular weight, kg/kmol
s	Specific entropy, kJ/kg K
SI	Sustainability index
T	Temperature, K
$\dot{W}$	Work rate, kW

Greek Letters

η	Efficiency

Subscripts

ch	Chemical
CH_4	Methane
$dest$	Destruction
$elec$	Electrolyzer

en	Energy
ex	Exergy
H_2	Hydrogen
net	Net output
ph	Physical
qf	Quintuple flash
SMR	Steam methane reforming
tot	Total
turb	Turbine
1…26	State numbers
0	Ambient or reference condition

Acronyms

LHV	Lower heating value
SMR	Steam methane reforming

Acknowledgement The authors gratefully acknowledge the financial support provided by the Ontario Research Excellence Fund.

References

1. Erdogdu E (2009) A snapshot of geothermal energy potential and utilization in Turkey. Renew Sustain Energy Rev 13:2535–2543
2. Phillips J (2010) Evaluating the level and nature of sustainable development for a geothermal power plant. Renew Sustain Energy Rev 14:2414–2425
3. Gunerhan GG, Kocar G, Hepbasli A (2001) Geothermal energy utilization in Turkey. Int J Energy Res 25:769–784
4. Coskun C, Oktay Z, Dincer I (2011) Modified exergoeconomic modeling of geothermal power plants. Energy 36:6358–6366
5. Alicilar A, Dogan M, Guru M (1995) Optimization of a double stage flash system. Int J Energy Res 19:169–179
6. Coskun C, Oktay Z, Dincer I (2011) Performance evaluations of a geothermal power plant. Appl Therm Eng 31:4074–4082
7. Yari M (2010) Exergetic analysis of various types of geothermal power plants. Renew Energy 35:112–121
8. Bodvardson G, Eggers DE (1972) The exergy of thermal water. Geothermics 1:93–95
9. Dufour J, Serrano DP, Galvez JL, Moreno J, Garcia C (2009) Life cycle assessment of processes for hydrogen production: environmental feasibility and reduction of greenhouse gases emissions. Int J Hydrog Energy 34:1370–1376
10. Turner J (2008) Renewable hydrogen production. Int J Energy Res 32:379–407
11. Dincer I (2007) Environmental and sustainability aspects of hydrogen and fuel cell systems. Int J Energy Res 31:29–55
12. Ratlamwala TAH, El-Sinawi AH, Gadalla MA, Aidan A (2012) Performance analysis of a new designed PEM fuel cell. Int J Energy Res 36:1121–1132

Chapter 5
Exergetic Optimization of Two Renewable Energy Based Tri-generation Systems Using Genetic Algorithm

M. Malik, M. Al Ali, Ibrahim Dincer and S. Rahnamayan

Abstract In the present study, two renewable energy based tri-generation systems are considered. Optimization has been done using genetic algorithm in order to optimize the objective function, which is the maximization of overall exergy efficiency of system. Biomass and solar are the main sources of energy for both systems, respectively. Energy and exergy efficiencies are defined with or without considering tri-generation and the effect of tri-generation over single generation has been analyzed. The optimum value of objective function, which is the exergy efficiency of the system, is found to be equal to 36.18% for biomass operated system and 70.68% for solar operated system. Further, a parametric study has been conducted in order to observe the effect of variation in different parameters on the efficiency of the system.

Keywords Renewable energy · Exergy · Biomass · Solar · Trigeneration · Optimization

5.1 Introduction

Energy is the first and basic need of a developing country. A cursory look at the history of development of human civilization will make it abundantly clear that energy forms the backbone of the world's progress. With the increase of world population

M. Malik (✉) · M. A. Ali · S. Rahnamayan
Faculty of Engineering and Applied Science, University of Ontario Institute of Technology (UOIT), 2000 Simcoe Street North, Oshawa, ON L1 H 74K Canada
e-mail: Monu.malik@uoit.ca

M. A. Ali
e-mail: Mohammed.AlAli@uoit.ca

I. Dincer
Department of Mechanical Engineering, University of Ontario Institute of Technology (UOIT), 2000 Simcoe Street North, Oshawa ON L1H 7K4, Canada
e-mail: Ibrahim.dincer@uoit.ca

S. Rahnamayan
e-mail: Shahryar.Rahnamayan@uoit.ca

I. Dincer et al. (eds.), *Progress in Sustainable Energy Technologies: Generating Renewable Energy,* DOI 10.1007/978-3-319-07896-0_5,

and the rise in living standards, world energy demands are also increasing steadily at a fast rate. Renewable energy can make a substantial contribution to overcome the energy crisis. It is in this context that the role of renewable energy needs to be seen. Also more attention has been given to improve the design of energy system in order to increase the efficiency of the system. Renewable energy is available in various forms in nature like solar, wind, geothermal, biomass, hydro, ocean current, tides and wave which can be utilized as primary sources of energy input to any system. These all renewable resources are important as they are non-exhaustible source of high quality energy and at the same time it is also important to utilize them with high energy efficiency.

A trigeneration system is a novel approach to increase the efficiency of any system by utilizing the waste energy. A trigeneration system is a thermal system that produces three different commodities from one or more primary energy sources. The products can be electrical power, heating, and cooling. The Organic Rankine Cycle (ORC) is a potential subsystem that can be used in trigeneration systems for electrical power production. ORC is suitable for a low- or medium-temperature energy source [1]. Moreover, when a high-temperature energy source is available a steam Rankine cycle can be integrated more efficiently.

A number of studies have been previously done by various researchers on trigeneration to improve the performance of the systems. Three trigeneration systems were presented by Al-Sulaiman et al. [2] using solar, biomass or SOFC as the primary energy source to produce electricity, heating and cooling. According to a study conducted by Zamfirescu et al. [3] energy efficiency of concentrated solar power (CSP) can be increased from 15–20 to 80 % through cogeneration by recovering the heat which is normally rejected by heat engine. Granovskii et al. [4] studied the exergetic performance of a cogeneration system that integrates a gas turbine with a SOFC and its found that efficiency can be raised up to 66 % by cogeneration. The efficiency of a system is greatly depends on the input and output parameters. In order to enhance the performance of a system, these parameters should be carefully selected to find the optimum value.

Optimization is a reasonable solution, in order to find out the optimum value of parameter for maximizing the system's performance. Many researchers use optimization techniques to enhance the performance of their system. Ahmadi and Dincer [5] have performed an exergoenvironmental analysis and optimization of a cogeneration plant system using Multimodal Genetic Algorithm (MGA) in order to minimize the running cost of a project and found 9.80 % improvement in objective function. While Ahmadi et al. [6] have done a multi-objective optimization of combined cycle power plants using an evolutionary algorithm. In another study, Dincer et al. [7] have conducted performance assessment and optimization of a novel integrated multigeneration system for residential buildings and concluded that there is 60 % increase in system efficiency with optimization and multigeneration. All these studies show that optimization techniques and cogeneration systems are very effective in improving the performance of a complicated system.

In the present paper, two renewable energy based systems are selected for optimization. The primary energy inputs to both these systems are biomass and solar radiations, respectively. The main objective of this study is to optimize the solar and biomass systems exergetically using genetic algorithm and to find the effect

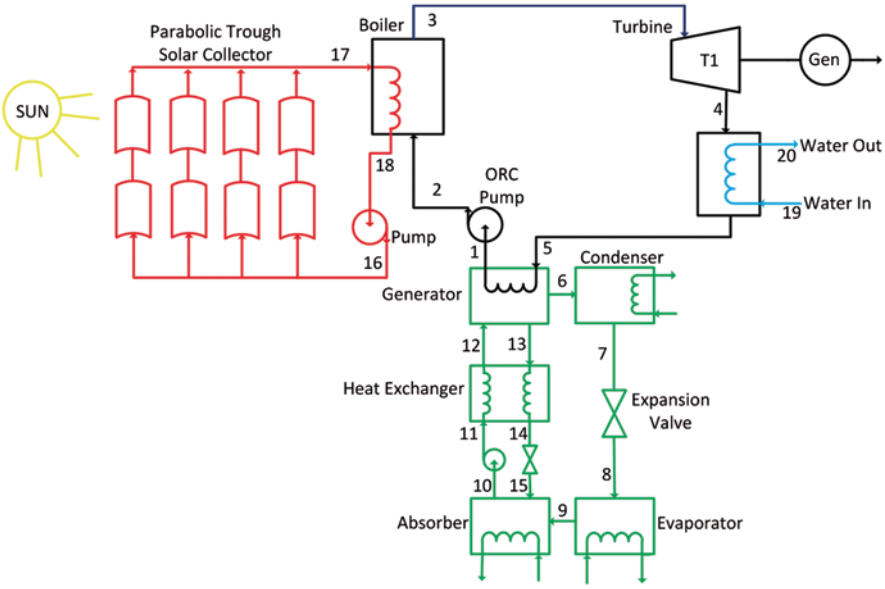

Fig. 5.1 A complete layout of the integrated solar system

of trigeneration and variation in variant parameters over objective function, which results maximization of the overall exergy efficiency.

5.2 Systems Description

In the current study, two trigeneration systems are studied and assessed in terms of energy and exergy efficiencies. Both systems are similar in term of the output but different in terms of energy input (energy source). In one system, the primary energy source is solar energy, where the energy from sun is collected by using concentrated parabolic trough solar collector, whereas in the other system the primary energy source is pine sawdust type biomass having 10% moisture content. These systems are combined with the ORC and single effect absorption chiller system separately as shown in Figs. 5.1 and 5.2, respectively. Recent research efforts have been made to examine the feasibility of these two renewable energy sources and they are still ongoing. The systems considered consist of an ORC as a prime mover to produce the electrical power, a heat exchanger to supply the heating load, and single effect absorption chiller to supply the cooling load. In both systems, there are two common cycles [2]: ORC and single effect absorption chiller cycle.

In case of solar operated system, a heat transfer fluid (HTF) is pumped to the parabolic trough solar collector at point 16, where it absorbs the concentrated solar energy from solar collector. This high temperature HTF enters to the boiler at point

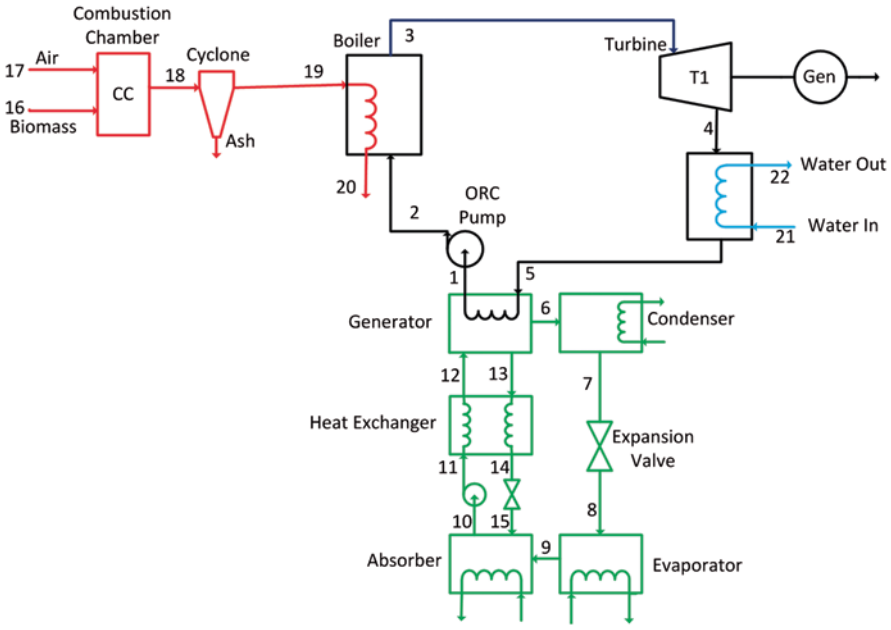

Fig. 5.2 A complete layout of the integrated biomass system

17, where it transfers the heat to the ORC working fluid and exits the boiler at point 18 and again pumps to solar collector.

The ORC working fluid exits the boiler at high temperature and pressure at point 3 and enters to ORC turbine and expands through the turbine to produce the mechanical power. This mechanical power is used to rotate the electrical generator which is connected to the turbine and converted into electrical power. Then, the working fluid exits the turbine at point 4 at low pressure and medium temperature and enters to the heat exchanger, where it supply the heat to the cold water entering to the heat exchanger at point 19 and hot water exit the heat exchanger at point 20. After that, the organic fluid enters the absorption chiller generator at point 5 as saturated vapor and transfers the remaining heat to the mixture of $LiBr - H_2O$ and leaves the absorption chiller generator as liquid at point 1. Then, the working fluid is transfer to the boiler at a high pressure through an ORC pump at point 2 and the cycle remains continuing. This ORC cycle is same for both the systems, there is only a few changes in state point, as in case of biomass operated system, point 19 and 20 are replace with point 21 and 22, and the process remains the same.

The heat rejected at absorption chiller generator from ORC working fluid is the input energy to the single- effect absorption chiller. The flow streams transport among the components of this chiller cycle as either water or a mixture of $LiBr - H_2O$. As a result of the input heat into the absorption chiller generator, water evaporates from the mixture of the $LiBr - H_2O$ and enters the condenser in vapor form at point

6. In the condenser, water vapor rejects the heat to a cooling source and exits the condenser in liquid form at point 7. After that, the water passes through an expansion valve and enters the evaporator at low temperature and pressure at point 8. In evaporator, heat from cooling load is absorbed by cold water and is converted into vapors. These water vapors exits from the evaporator and enters to the absorber at point 9, where it is mixed with strong solution of $LiBr - H_2O$ and is converted into weak solution of $LiBr - H_2O$.

This weak solution of $LiBr - H_2O$ exits the absorber at point 10 and is pumped to the heat exchanger at point 11, where it absorbs heat from strong solution of $LiBr - H_2O$ and enters to the absorption chiller generator at higher temperature. This mixture is heated in the absorption chiller generator and part of the water from the mixture evaporates and exits the absorption chiller generator in vapor form at point 6 leaving behind a strong solution of $LiBr - H_2O$. This strong solution of $LiBr - H_2O$ enters to the heat exchanger at point 13 and transfers the heat to the week solution of $LiBr - H_2O$ and exits the heat exchanger at point 14. Then passes through an expansion valve where its temperature and pressure drop and enters to the absorber at point 15 and is mixed with water vapor and this process remains continuing, which is the same for both systems.

In case of biomass operated system, air and pin saw dust type biomass enter to combustion chamber at point 16 and 17, respectively, as shown in Fig. 5.2. After combustion in combustion chamber (CC) air and biomass leaves the CC in form of high temperature gas at point 18 and enters to cyclone, where ash is removed from high temperature gas. This high temperature gas enters to the boiler at point 19 and transfers the energy to the ORC working fluid (n-octane) and exits to the atmosphere at a low temperature. Rest of the process and system is similar to solar operated system, which is discussed earlier.

5.3 Energy and Exergy Analyses

The thermodynamic modeling of biomass and solar systems were presented in [8, 9], respectively. The thermodynamic modeling applied to the single-effect absorption chiller is similar to the approach used by Refs. [10–12]. To carry out the analysis, some assumptions are made as follows:

- The systems operate at steady state flow process.
- The pressure changes are neglected except in the pumps, blowers, turbine and expansion valves.
- The ambient conditions T_0 and P_0 are assumed to be 298 K and 101.325 kPa, respectively.
- The efficiencies for all pump, compressor and turbine are taken as 85 % [13].
- The changes in kinetic and potential energies are negligible.
- No mass losses take place in the system.
- The incoming solar radiations are taken as constant.

In thermodynamics, it is important to write mass and energy balances under the first law of thermodynamics as follows:

$$\sum_{in} \dot{m} = \sum_{out} \dot{m} \tag{5.1}$$

$$\dot{Q} - \dot{W} = \sum_{out} \dot{m}\left(h + \frac{V^2}{2} + gz\right) - \sum_{in} \dot{m}\left(h + \frac{V^2}{2} + gz\right) \tag{5.2}$$

where, $\dot{m}$, $\dot{Q}$ and $\dot{W}$ are the mass flow rate, heat transfer to the system, and work done by the system, respectively.

Unlike energy, exergy is not conserved. The exergy balance of a control volume system is defined as

$$\sum_{k} \dot{Q}_k \left(1 - \frac{T_0}{T_k}\right) + \sum_{i} \dot{m}_i ex_i + \dot{W} + \sum_{e} \dot{m}_e ex_e + \dot{E}x_{Dest} \tag{5.3}$$

where T, ex and $\dot{E}x_{Dest}$ are temperature, specific exergy and exergy destruction rates, respectively. The subscript k is the property value at state k and the subscript 0 is the value of a property at the reference environment. The physical specific exergy, ex, at a given state is defined as:

$$ex = (h - h_0) - T_0(s - s_0) + \frac{V^2 - V_0^2}{2} + g(z - z_0) \tag{5.4}$$

The chemical exergy of ideal gas mixtures is defined as [14]

$$\overline{ex}_{ch} = \sum x_k \overline{ex}^{k}_{ch} + RT_0 \sum x_k ln(x_k) \tag{5.5}$$

where $\overline{ex}^{k}_{ch}$ is the standard chemical exergy for gas k.

For the biomass system, the following composition has been used as fuel at combustion chamber:

$$C_x H_y O_z + \omega H_2O + \lambda(O_2 + 3.76N_2) \rightarrow aCO_2 + bH_2O + cN_2 \tag{5.6}$$

Chemical composition of biomass is calculated from the method specified by Ahmadi et al. [15]. To find out the physical exergy of fuel, lower heating value (LHV) of fuel is needed to be calculated, which is define as:

$$\overline{LHV}_{dry} = \frac{400,000 + 100,600y - \frac{z}{1 + 0.5y}(117,600 + 100,600y)}{12 + y + 16z} \tag{5.7}$$

It is assumed that biomass contain some moisture content which affects the LHV value of the fuel

$$\overline{LHV}_{Mois} = (1-\mu_m - H_u) \times \overline{LHV}_{dry} - 2500 H_u \tag{5.8}$$

where μ_m and H_u are mineral matter and moisture contents in biomass, respectively. To assist in determining the chemical exergy of fuels, Szargut et al. [16] provided values of the exergy to energy ratio:

$$\phi = \frac{ex_f}{LHV} \tag{5.9}$$

For a chemical Formula $C_\alpha H_\beta N_\gamma O_\delta$ the value of ϕ can be calculated from given below relation [16]:

$$\phi = 1.0401 + 101728\frac{\beta}{\alpha} + 0.0432\frac{\delta}{\alpha} + 0.2169\frac{\gamma}{\alpha}\left(1 - 2.062\frac{\beta}{\alpha}\right) \tag{5.10}$$

The exergy destruction at combustion chamber can be calculated using the following equation.

$$\dot{m}_{16} ex_{16} + \dot{m}_{17} ex_{17} = \dot{m}_{18} ex_{18} + \dot{Q}_{L17}\left(1 - \frac{T_{s17}}{T_0}\right) + \dot{E}x_{cc}^{Dest} \tag{5.11}$$

The exergy destruction at the boiler:

$$\dot{m}_2 ex_2 + \dot{m}_{19} ex_{19} = \dot{m}_{20} ex_{20} + \dot{m}_3 ex_3 + \dot{Q}_{L20}\left(1 - \frac{T_{s20}}{T_0}\right) + \dot{E}x_{Boiler}^{Dest} \tag{5.12}$$

The exergy destruction at ORC heat exchanger:

$$\dot{m}_4 ex_4 + \dot{m}_{21} ex_{21} = \dot{m}_5 ex_5 + \dot{m}_{22} ex_{22} + \dot{Q}_{L21}\left(1 - \frac{T_{s21}}{T_0}\right) + \dot{E}x_{Boiler}^{HE_{ORC}} \tag{5.13}$$

In the absorption chiller cycle the exergetic COP is calculated as:

$$\dot{E}_{COP_{Chiller}} = \frac{\dot{m}_8 (h_9 - h_8)\left(1 - \frac{T_0}{T_{s_{eva}}}\right)}{\dot{m}_5 (h_5 - h_1)\left(1 - \frac{T_0}{T_{s_{gen}}}\right)} \tag{5.14}$$

The energy efficiency for the biomass operated trigeneration system is defined as

$$\eta = \frac{\dot{W}_{net} + \dot{Q}_{cool} + \dot{Q}_{heat}}{\dot{m}_{bio} \times LHV_{moist} + \dot{m}_{air} h_{air}} \tag{5.15}$$

Whereas the energy efficiency for the solar operated trigeneration system is defined as

$$\eta = \frac{\dot{W}_{net} + \dot{Q}_{cool} + \dot{Q}_{heat}}{\dot{Q}_{in}}, \tag{5.16}$$

where

$$\dot{Q}_{in} = \eta_{solar} \times A_p \times R_a \times Col_r \times Col_c \tag{5.17}$$

Whereas, in case of single generation, energy and exergy efficiency are calculated without considering $\dot{Q}_{cool}$ and $\dot{Q}_{heat}$ for both solar and biomass operated systems.

5.4 Optimization

Optimization is an essential tool for many engineering designs. Using that, one can find an optimum design without the need to examine all possible cases (i.e., exhaustive search). Several optimization methods have been proposed in the literature. Each method has own advantages and limitations. In Engineering Equations Solver (EES), genetic algorithm is one of the optimization methods which can be used. For the trigeneration systems considered in this study, the genetic algorithm is the appropriate one since it provides a good design solution for these complicated systems.

Optimization by Genetic Algorithm In last two decades, optimization algorithms have been improved significantly and have received increasing attention by the research communities as well as the industries. Genetic algorithm (GA) is an optimization technique based on natural genetics. GA was developed by Holland to understand the adaptive processes of natural systems [17]. GA proved to be a robust optimization technique to solve black-box non-convex and nonlinear problems efficiently. The term robust denotes the ability of the GA for finding the global optimum, or a near-optimal solution, for any optimization problem and keeping a good solution even if there is a small change (uncertainty) in the input parameters.

The basic steps for the GA are described as follow. An initial set of candidate solutions are created uniform randomly and each single candidate solution is converted into a string that is coded (chromosome). The size of the population may vary from tens to several hundreds. Increasing the population size does not necessarily result candidate solution improvement, a good number for population size can be determined after several trail runs. Then, each candidate solution is tested and evaluated on the objective function to show how good a solution is (fitness value). After that, the selection criterion is applied to conduct the crossover and mutation operations. Next, when a new population is created after applying the mentioned genetic operations; it replaces the old population. A stopping criterion is utilized for the algorithm to decide whether to continue with another iteration or stop. The number of generations is considered as the stopping criteria, a good number of generation is in

Table 5.1 Input data for solar and biomass operated systems

Input data for biomass	
Biomass type	Pine sawdust
Moisture content in the fuel (% wt)	10%
Ultimate analysis (% wt dry basis)	
Carbon (C)	50.54%
Hydrogen (H)	7.08%
Oxygen(O)	41.11%
Sulfur	0.57%
Input data for solar	
Solar collector	Parabolic trough
Intensity of solar radiation (Ra)	800
Number of rows (Col_r)	7
Collector in each row (Col_c)	50
L	12.57 m
w	5.76 m
Overall efficiency of the solar system (η_{solar})	52.5%

the range of 200–500 [17], depending on the dimension and complexity of problem to be solved. The candidate solutions should be coded when doing the operations, but decoded when evaluating the fitness values.

Objective Function The objective function in the current study is defined as the overall exergy efficiency of the trigeneration system. Trigeneration systems are well-connected systems and by changing one variable, the whole system is affected. Exergy efficiency is defined as the total useful exergy output over the exergy input supplied to the system. In these trigeneration systems, the useful outputs are power, heating and cooling, while the input for the biomass operated system is pine sawdust biomass and solar radiations in case of solar operated system. The generalized objective function (fitness function) for both systems can be defined as follows:

$$\psi = \frac{\dot{W}_{net} + \dot{E}x_c + \dot{E}x_h}{\dot{E}x_{in}} \tag{5.18}$$

where

$$\dot{W}_{net} = \dot{W}_T - \dot{W}_P \tag{5.19}$$

$$\dot{E}x_c = \dot{Q}_c \left(1 - \frac{T_0}{T_c}\right) \tag{5.20}$$

$$\dot{E}x_h = \dot{Q}_h \left(1 - \frac{T_0}{T_h}\right) \tag{5.21}$$

Table 5.2 Box constrains

Variables range
Overall efficiency of solar system $\leq 60\%$
$0 < P_3 < 100$ MPa
$260\,^{\circ}C < T_{HTF} < 593\,^{\circ}C$
$COP_{chiller} \leq 0.9$
$-56.77\,^{\circ}C < T_{n-octane} < 477\,^{\circ}C$
$0.05 < MC < 0.4$
Adiabatic flame temperature $\leq 2165\,^{\circ}C$
$6.02 \leq$ Air fuel ratio ≤ 7

where $\dot{W}_{net}$, $\dot{Q}_c$, $\dot{Q}_h$, and $\dot{E}x_{in}$ are the net output power from the system, cooling load, heating load, and exergy input to the system, respectively. The exergy input depends on the energy source of the system, for the biomass trigeneration system, the exergy input is defined as

$$\dot{E}x_{in(bio)} = \dot{E}x_{biofuel} + \dot{E}x_{air} \tag{5.22}$$

where

$$\dot{E}x_{biofuel} = \dot{E}x_{ph} + \dot{E}x_{ch} \tag{5.23}$$

Whereas for the solar system the exergy input is defined as

$$\dot{E}x_{in(solar)} = \dot{Q}_{in}\left(1 - \frac{T_0}{T_{sun}}\right) \tag{5.24}$$

Decision Variables and Constrains There are many parameters which can affect the performance and efficiency of a trigeneration system. These parameters (decision variables) should be chosen carefully to save optimization time and to improve process to find the optimal design. To eliminate any thermodynamic or manufacturing problems, constrains must be specified accordingly. In this study some of the decision variables are selected based on Ref. [14]. The constrains and decision variables with their optimum values are given in Tables 5.2 and 5.3, respectively.

5.5 Results and Discussion

In the present study, two tri-generation systems which are different in terms of primary energy source are considered for optimization. Objective function which represents overall exergy efficiency is defined. Modeling of both systems has been done using engineering equation solver (ESS). The input data for the biomass and solar systems are listed in Table 5.1. Decision variables for each system have been

Table 5.3 Optimum values resulted by GA

Decision variable	Biomass	Solar
$\dot{m}_2$	2.002	5.061
$\dot{m}_{10}$	14.62	15.45
$\dot{m}_{21}$	1.509	–
P_2	2092	1965
P_4	47.02	47.12
T_0	30	27.76
T_3	439.5	453
T_4	152.6	105.8
T_{18}	1883	–
T_{22}	60.06	–
T_{13}	–	83.49
T_{16}	–	279.7
COP	0.7542	0.8848
η_{tri}	57.59%	77.01%
Objective unction (ψ_{tri})	36.18%	70.42%

carefully selected. Most of the decision variables are same in both systems except two or three, since primary energy source is different in both systems. To find the maximum exergy efficiency some constrains are defined and the range of the constraints are selected properly. Parameter studies are conducted to analyze the effects of the change in ambient temperature, ORC turbine input and output temperatures and mass flow rate, heat transfer fluid (HTP) temperature on energy and exergy efficiencies of the ORC cycle and the whole system. Also, calculations have been performed to find out the exergy destruction at major components. Furthermore,

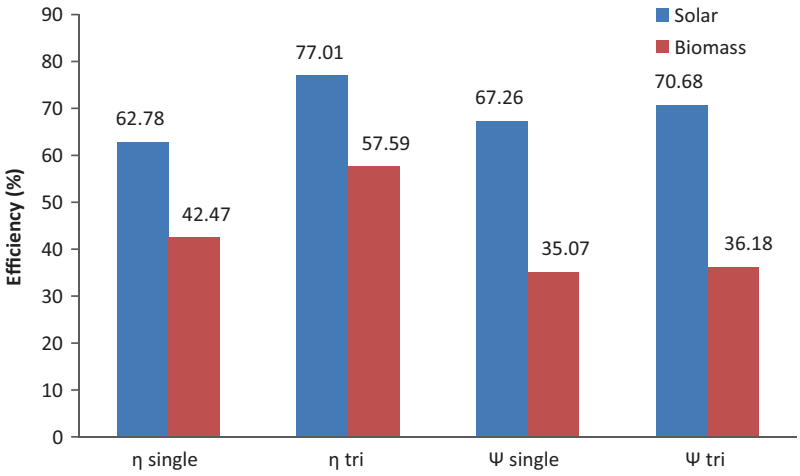

Fig. 5.3 Comparison of the energy and exergy efficiencies of biomass and solar systems

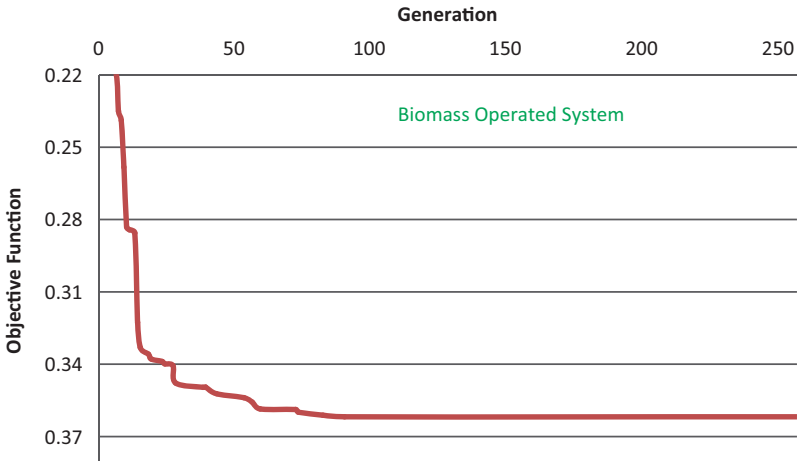

Fig. 5.4 Variation of the objective function with the number of generation for the biomass system

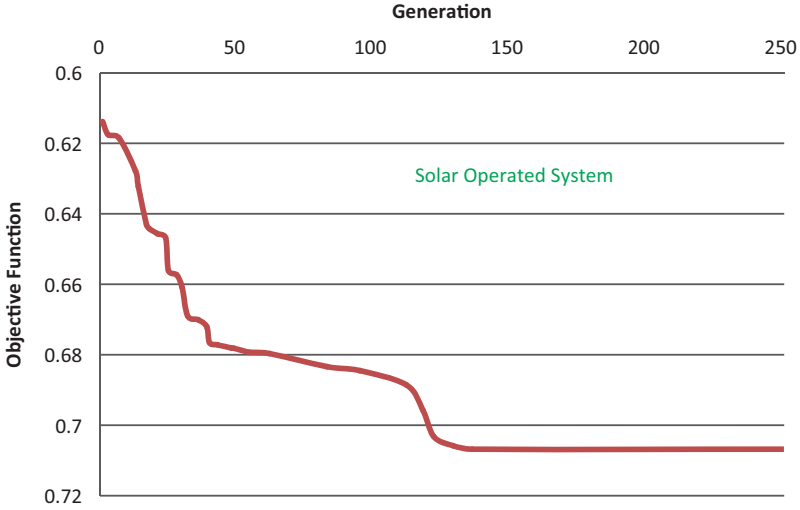

Fig. 5.5 Variation of the objective function with the number of generation for the solar system

the calculations have been done to obtain the properties like temperature, pressure, mass flow rate, enthalpy, entropy and exergy and to observe how the properties are varying at variant points in the system. These properties are given in Tables 5.5 and 5.6 for the biomass and solar system, respectively.

Optimization Results In this section, the optimization results for both systems have been discussed in detail. As it has been already explained, single objective

optimization is applied on both systems in order to find out the maximum possible exergy efficiency using genetic algorithm. The objective function, maximization of exergy efficiency of each tri-generation system, has been modeled for the optimization. The optimization process has been done using genetic algorithm in EES software. For both systems, the number of generation has been set to 256 generations for each run and it is found that the optimum value of exergy efficiency for the biomass system is 36.18 % and found after 90 generations as shown in Fig. 5.4. On the other hand, in case of solar, the optimum value of exergy efficiency is 70.68 % and found after 136 generatiosn as shown in Fig. 5.5. The population size has been set to 32 with the maximum mutation rate of 0.0875. These parameters are set the same for both systems. The energy efficiency of tri-generation system in case of biomass is found to be equal to 57.59 %, whereas in case of solar, it is found to equal to 77.01 %. Energetic and exergetic values of COP for the absorption chiller cycle in case of biomass operated system with respect to the optimum value of the objective function is found to be equal to 0.7542 and 0.5097, respectively, whereas in case of solar system, it is found to be equal to 0.8848 and 0.5293, respectively.

The optimum values of the decision variables for both systems are given in Table 5.3. From these results, it is found that the value of the inlet pressure P_2 for both systems and outlet pressure P_3 for both systems at ORC turbine are very close. The inlet pressure P_2 at ORC turbine in the biomass is equal to 2092 kPa, whereas in the solar system it's equal to 1965 kPa. In the same manner, the outlet pressure P_3 is equal to 47.02 kPa and 47.12 kPa in biomass and solar operated system, respectively. The ORC turbines in both systems have different operating condition and input parameter, which lead to different power production. The power output from ORC turbine in the biomass operated system is equal to 2067 kW, whereas in case of solar it is equal to 6680 kW. One point should be accounted and taken care of that the objective of the current study is to optimize/maximize the exergy efficiencies of both systems, not getting the maximum power output from ORC turbine. Also, as the energy input to both ORC turbines are different, so it is worthless to compare their outputs, but the system having higher exergy efficiency is the best one.

Effect of Tri-Generation Over Single Generation By the definition of tri-generation systems, it is clear that in case of tri-generation, the system produces three outputs by using one or more primary energy inputs. The main reason for using a tri-generation system in place of a normal single generation system is to increase the overall efficiency of the given system. However, one point should be considered, converting a simple system into tri-generation is associated with a high initial cost, so before converting a simple system into tri-generation, calculation should be done in order to find out the effects of tri-generation over a simple system in terms of efficiency and initial cost.

In the current study, in order to see the effect of tri-generation over single generation, energy and exergy efficiency are calculated for a single generation system by neglecting the heating and cooling output and considering the same primary energy input for both systems. Results show that energy and exergy efficiencies

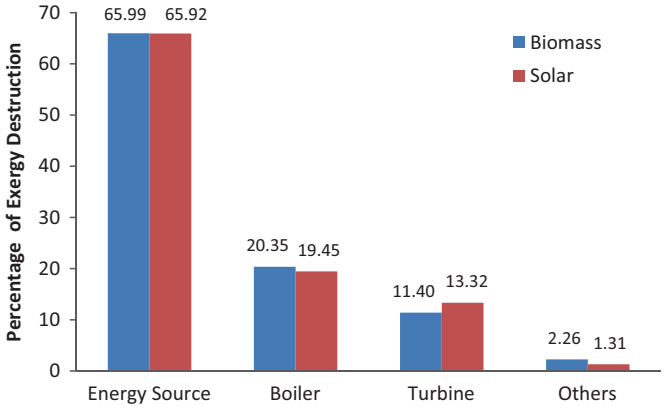

Fig. 5.6 Exergy destruction in major components of the systems

are decreased from 57.59 to 42.47% and from 36.18 to 35.07%, respectively, for the biomass system, whereas in the case of solar, energy and exergy efficiencies decrease from 77.01 to 62.78% and from 70.68 to 67.26%, respectively, as shown in Fig. 5.3. So, the results show that while using tri-generation system, the effect on energy efficiency is quite significant, while the effect on exergy efficiency is marginally good.

Comparison in Both Systems in Terms of Efficiency and Exergy Destruction The solar and biomass systems are same in terms of the type of outputs, but different in terms of their primary source of energy input. Both systems uses renewable energy sources and produce power output from ORC turbine, hot water from heat exchanger and chilling effect from absorption chiller system. So, it's important to compare the two systems in order to conclude about the more efficient system.

In Term of Efficiency From the results, it is found that, a system that have the solar as its primary energy source is more efficient as compared to a system that have the biomass as the primary energy source, both energetically and exergetically, whether its single generation or tri-generation. The energy and exergy efficiencies of the solar system are greater than biomass system's by 19.42 and 34.5%, respectively, in case of tri-generation system, whereas in case of single generation system, energy and exergy efficiencies of solar operated system is more by 20.31 and 32.19% respectively as shown in Fig. 5.3. So, from the results it can be concluded that solar system is more efficient in term of exergy as compared to energy generated by the biomass operated system.

In Term of Exergy Destruction As known, according to the 2nd law of thermodynamics there is no such a system that can convert 100% of the heat into work; therefore, there are always some losses to the surrounding. In the current study, assumption has been taken that there is no heat loss to the surrounding from ORC turbine and pipes, but still there is exergy destruction at ORC turbine, combustion chamber, boiler, solar system and other parts in both systems. In order to compare

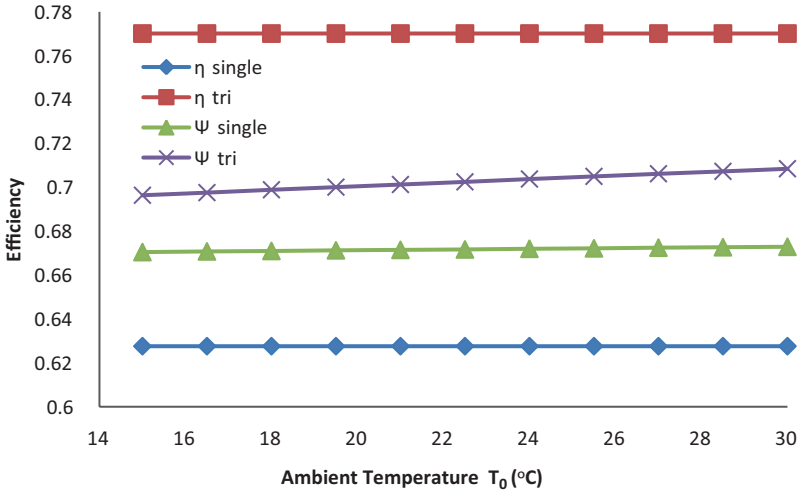

Fig. 5.7 Effect of the reference environment on the energy and exergy efficiencies of the solar system

the exergy losses in both systems, exergy destruction at all major components is calculated and their percentage values are plotted for both systems as shown in Fig. 5.6. From the calculations, it is found that the maximum exergy destruction is found to be at the energy sources, which is combustion chamber (i.e., 65.99%) in case of biomass system and solar collector part (i.e., 65.92%) in case solar operated system. After that, the maximum exergy destruction is found to be at the boiler with 20.35 and 19.45% for the turbine, followed by 11.50 and 13.32% at ORC turbine for the biomass and solar system, respectively, whereas negligible exergy destruction is found at other component, which is 1.31 and 2.26% for solar and biomass operated system, respectively. While comparing the exergy destruction between both systems, it can be seen from Fig. 5.6 that percentage of exergy destruction is almost same at each component for both systems. So, both systems are almost the same in term of percentage of exergy destruction.

Parameter Analysis Parameter analysis of a system is very important, as the performance of any system is mainly dependent upon the various parameters. Any variation in a parameter will certainly change the outputs and efficiencies of a system. In the present study, a parameter study has been done for both systems in order to observe the effect of changes in various parameters like ambient temperature, input and output temperature and mass flow rate at ORC turbine, mass flow rate of biomass and air at CC and outlet temperature at CC, solar radiation and overall efficiency of solar system on exergetic and energetic efficiency of the system.

Effect of Ambient Temperature on System Ambient temperature plays an important role in determining the performance of any system. Any variations in the environmental conditions can increase or decrease the performance of a system. In the current study, the optimum value of the ambient temperature is equal to 27.76 °C

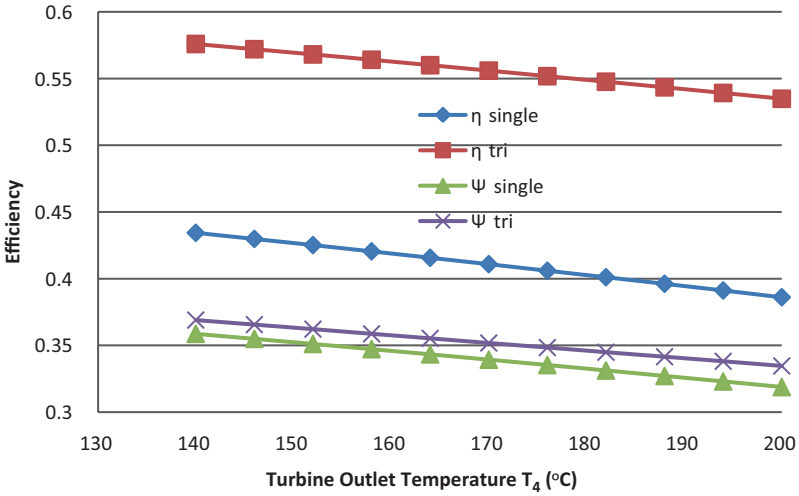

Fig. 5.8 Effect of ORC turbine outlet temperature on the energy and exergy for the biomass system

for the solar system and 30 °C for biomass system, while keeping the constant at 101.325 kpa for both systems. Calculations have been done to observe the effect of the change in ambient temperature on energy and exergy efficiencies of single and tri-generation system by varying ambient temperature from 15 °C to 30 °C. In case of solar operated system, the result shows that exergy efficiency is increasing from 69.64 to 70.85 % in case of tri-generation, whereas increasing from 67.05 to 67.29 % in case of single generation system, when the ambient temperature increase from 15 °C to 30 °C, while negligible effect is found on energy efficiency as shown in Fig. 5.7. The same pattern is found in case of biomass operated system for energy and exergy efficiencies with respect to the ambient temperature.

Effect of ORC Turbine Inlet and Outlet Temperature and Pressures on System Efficiency Output power from any turbine basically depends upon the inlet and outlet temperatures and pressure of turbine. From the calculation it has been observed that both exergy and energy efficiencies of the system increase with increase in inlet temperatures of ORC turbine temperature, while decrease with increase in turbine outlet temperatures. Fig. 5.8 shows that in case of biomass operated system, when turbine outlet temperature (TOT) increases from 140 to 200 °C, the energy efficiency of tri-generation system decreases from 57.59 to 53.48 %, whereas in single generation system it decrease from 43.44 to 38.61 %. Also, the exergy efficiency of tri-generation system decreases from 36.9 to 33.46 %, whereas in single generation system it decreases from 35.87 to 31.88 %. Same pattern is found in case of solar operated system. Furthermore, the calculation has been done by changing the turbine inlet and outlet pressures for both systems and it has been found that there is negligible effect of variation in inlet and outlet pressures on overall energy and exergy efficiency.

Table 5.4 Thermodynamic properties of n-octane

Substance name	n-octane
Mol. formula	C_8H_{18}
Mol. weight	114.231
Freeze point (°C)	−56.77
Boiling point (°C)	125.68
Crit. temp. (°C)	295.68
Crit. pressure (bar)	24.86
Crit. volume(cm^3/mol)	492.1
Crit. density(g/cm^3)	0.2322
Crit. compressibility	0.259
Acentric factor	0.396

Table 5.5 Optimum states for biomass resulted by GA

State No.	Temperature (C^o)	Pressure (kPa)	Mass flow (kg/s)	Enthalpy (kJ/kg.K)	Entropy (kJ/kg.K)	Exergy (kJ/kg)
0	29.8	101.3	–	10.74	0.03579	0
1	85	28.92	2.002	140.5	0.4346	8.992
2	85	1950	2.002	142.1	0.4252	13.42
3	438.5	1950	2.002	1824	2.755	990.1
4	153.9	28.92	2.002	612.2	1.709	94.87
5	85	28.92	2.002	469.2	1.346	61.57
6	78.2	7.424	0.2158	2646	8.471	80.96
7	40.11	7.424	0.2158	168	0.5737	−5.669
8	1.5	0.6812	0.2158	168	0.6116	−17.12
9	1.5	0.6812	0.2158	2503	9.114	−256.5
10	34	0.6812	14.84	90.43	0.1952	81.68
11	34	7.424	14.84	90.43	0.1952	81.68
12	71.64	7.424	14.84	166	0.4249	87.66
13	80	7.424	14.84	185.6	0.4665	94.71
14	41.36	7.424	14.84	109	0.2378	19585
15	36.06	0.6812	14.84	109	0.2048	0
16	29.8	101.3	0.3	–	–	2944
17	29.8	101.3	1.63	303.4	5.7	0
18	1882	101.3	1.93	2447	7.892	2944
19	1882	101.3	1.93	2447	7.892	2944
20	120	101.3	1.93	394.3	5.974	21.97
21	29.8	101.3	1.519	124.9	0.4338	0
22	60.21	101.3	1.519	285.2	0.8337	39.12

Effect of Mass Flow Rate in ORC on Efficiency In both systems, n-octane is used as working fluid in organic Rankine cycle. Properties of n-octane can be found in [18] and given in Table 5.4. The calculation has been done in order to see the effect of mass flow rate of n-octane on overall efficiencies of both systems and results show that overall efficiency of both the system decrease with increase in mass flow rate for same energy input. Fig. 5.10 shows that, in case of biomass operated system, when mass flow rate increases from 0.5 to 3.5 kg/s, the tri-generation energy and exergy efficiencies decrease from 66.29 to 48.91% and from 46.18

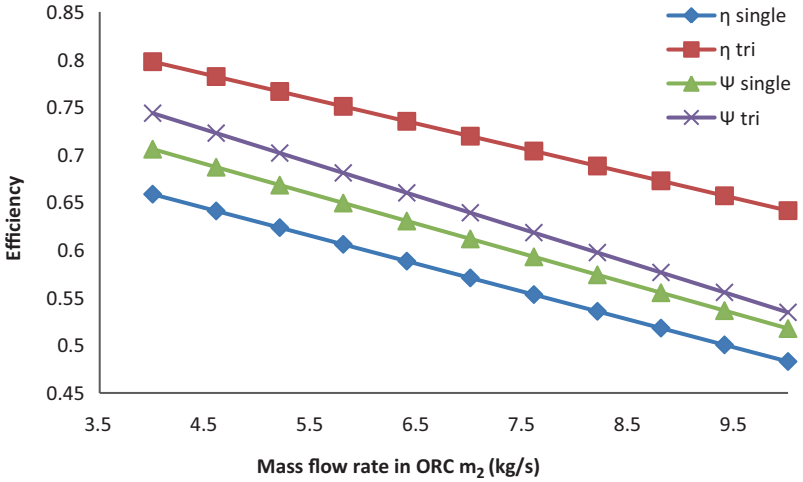

Fig. 5.9 Effect of mass flow rate in ORC on efficiency for solar system

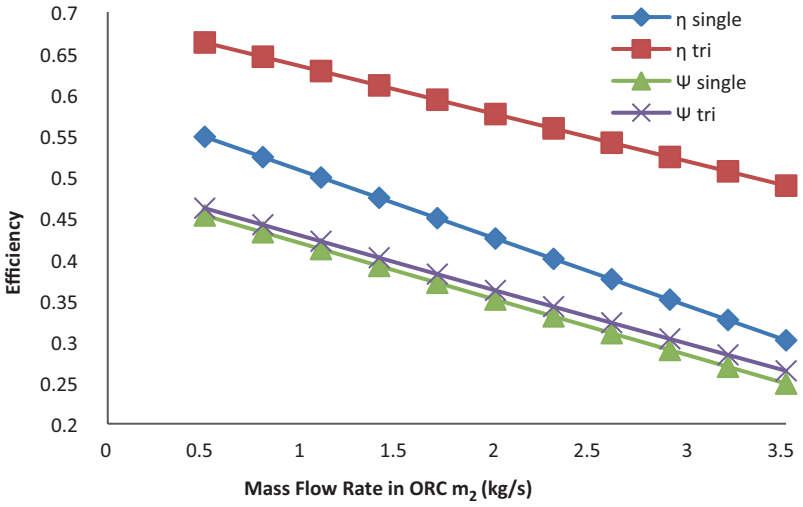

Fig. 5.10 Effect of mass flow rate in ORC on efficiency for biomass system

to 26.43 % respectively, while single generation energy and exergy efficiencies decrease from 54.84 to 30.13 % and from 45.29 to 24.88 % respectively. The reason behind is the same, as the mass flow rate increases, the temperature of working fluid decreases, which further decrease the specific enthalpy and entropy on which energy and exergy values are dependent. But the mass flow at which efficiency is the maximum which can't be used due to temperature limitation of working fluid.

Table 5.6 Optimum states for solar resulted by GA

State No.	Temperature (C^o)	Pressure (kPa)	Mass flow (kg/s)	Enthalpy (kJ/kg.K)	Entropy (kJ/kg.K)	Exergy (kJ/kg)
0	27.76	101.3	–	6.154	0.02062	0
1	80	47.12	5.061	140.5	0.5319	12.03
2	85	1965	5.061	142.1	0.4251	14.25
3	453	1965	5.061	1415	2.821	566.9
4	105.8	47.12	5.061	508.8	1.417	82.57
5	95	47.12	5.061	423.3	1.198	63.09
6	78.2	7.424	0.6303	2646	8.471	98.23
7	40.11	7.424	0.6303	168	0.5737	4.551
8	1.5	0.6812	0.6303	168	0.6116	-15.93
9	1.5	0.6812	0.6303	2503	9.114	-237.9
10	34	0.6812	15.45	90.43	0.1952	77.1
11	34.19	7.424	15.45	90.8	0.1964	77.12
12	72.55	7.424	15.45	167.8	0.4302	83.78
13	83	7.424	14.82	196.6	0.4729	99.88
14	42.08	7.424	14.82	118.2	0.2359	92.63
15	38.98	0.6812	14.82	118.2	0.2172	98.26
16	279.7	101.3	35	29.5	0.05385	45.7
17	483	101.3	35	337.1	0.5279	495.9
18	279.7	101.3	35	29.5	0.05385	45.7
19	27.7	101.3	3	116.1	0.4046	0
20	60	101.3	3	174.1	0.8311	70.32

On the same pattern, Fig. 5.9 shows that, in case of solar operated system, when mass flow rate increase from 4 to 10 kg/s, the tri-generation energy and exergy efficiency decrease from 79.78 to 64.14% and from 74.37 to 53.46% respectively and in the same pattern for single generation. The reason behind this is same as in case of biomass operated system. The optimum value of mass flow rate with respect to optimum value of objective function is found to be equal to 2.002 and 5.061 kg/s for biomass and solar operated system, respectively.

Effect of CC Outlet Temperature and Mass Flow Rate of Biomass on Efficiencies In case of biomass operated system, the outlet temperature of air at CC depends on the adiabatic flame temperature of the biomass, which is further dependent on the percentages of carbon, hydrogen and other molecules present in the biomass. In the present study, the adiabatic flame temperature is found to be equal to 2165 °C. For the current study the value of air and biomass ratio (air-fuel) is taken as 6.33. Figure 5.12 shows that the tri-generation energy and exergy efficiency are increase from 40.39 to 57.55% and from 21.98 to 36.15%, with increase in air temperature at outlet of CC from 1400 to 1880 °C while the single generation energy and exergy efficiencies are increased from 25.27 to 42.43% and from 20.86 to 35.04%. The optimum value of air temperature at outlet of CC is found 1881 °C. Figure 5.11 shows the effect of the mass flow rate of biomass over the energy and exergy efficiencies and results are very interesting. From results, it is found that energy and exergy efficiency are increasing drastically with the increase of mass flow rate

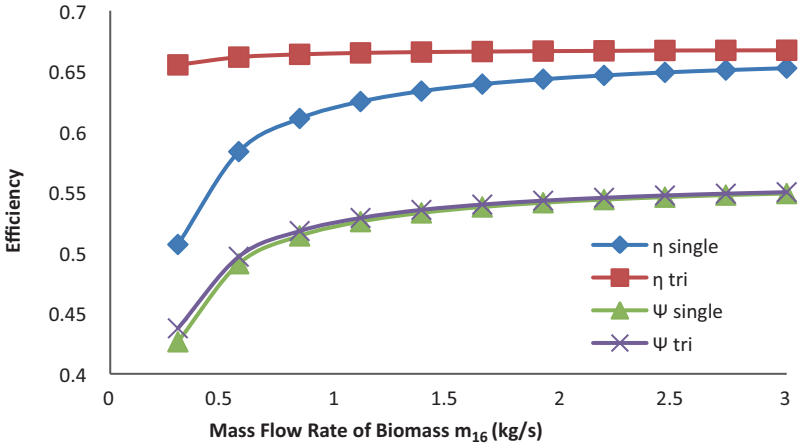

Fig. 5.11 Effect of mass flow rate of biomass on efficiencies

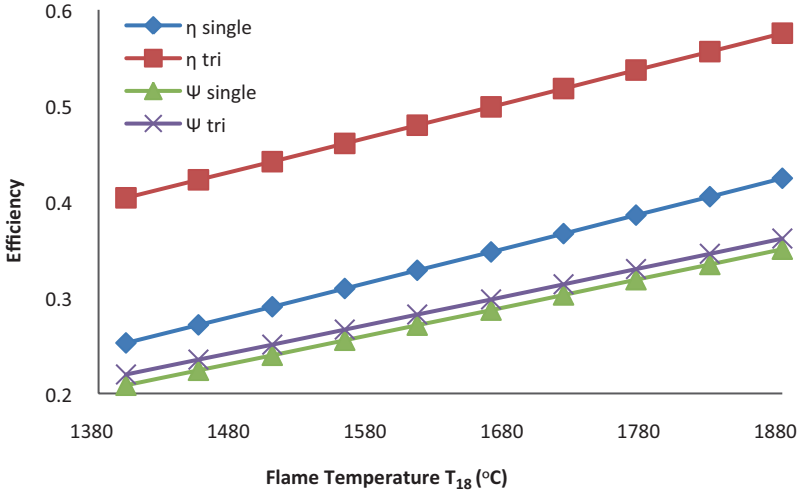

Fig. 5.12 Effect of CC outlet temperature on efficiencies

of the biomass up to a certain limit and then after that it is almost constant with increase in mass flow rate of biomass. Tri-generation energy and exergy efficiency are increasing from 74.49 to 78.25% and from 51.29 to 64.69% respectively; and the same pattern is found for single generation energy and exergy efficiencies.

Effect of Change in Solar Radiation and Solar System Efficiency in Solar Operated System During the day time, the intensity of solar radiation constantly varies, depending on the weather conditions. So, in order to calculate the effect of the

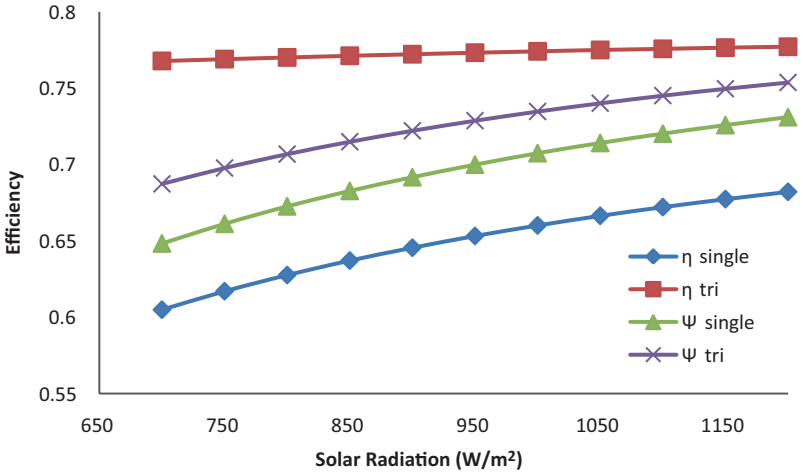

Fig. 5.13 Effect of change in solar radiation on energy and exergy efficiency in solar operated system

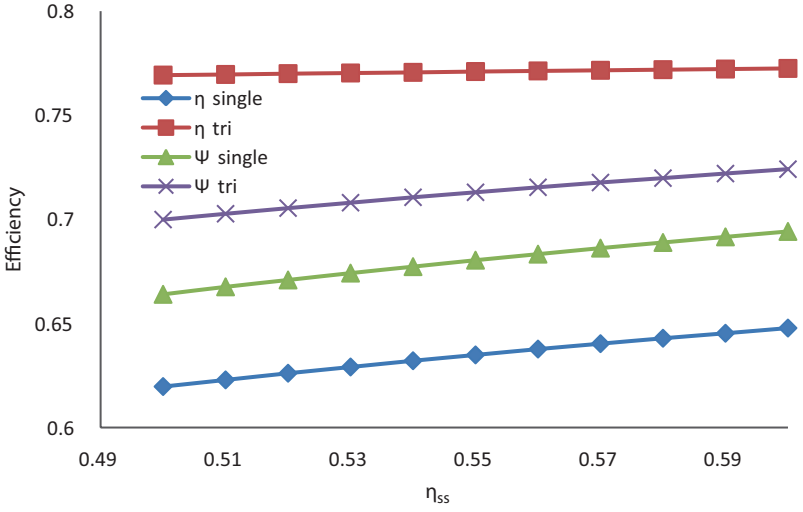

Fig. 5.14 Variation in energy and exergy efficiencies with respect to change in solar system efficiency

change in solar radiation on the efficiency of the system, calculation has been conducted by varying the intensity of the solar radiation from 700 to 1220 W/m^2. Figure 5.13 presents that tri-generation energy and exergy efficiency increase from 76.78 to 77.71 % and from 68.73 to 75.37 % respectively, with increase in intensity of solar radiation and the same pattern is found in case of single generation. For the simplicity, the overall efficiency of whole solar system has been selected (52.2 %)

and in order to see the effect of it on the overall energy and exergy efficiency, calculation has been done by varying the efficiency of solar system from 50 to 60%. Fig. 5.14 shows that the tri-generation energy and exergy efficiencies increasing almost linearly from 76.93 to 77.25% and from 69.99 to 72.41% respectively with increasing in the efficiency of the solar system. Similarly, the single generation energy and exergy efficiencies increase from 76.73 to 77.25% and from 66.4 to 69.42%, respectively.

Conclusions

In the present study two tri-generation systems are considered for optimization and objective function which is the overall exergy efficiency is optimized using genetic algorithm. The optimum value of exergy efficiency in biomass operated system in found to be 36.18%, while it is higher in solar operated system and equal to 70.68%. By comparing single and tri-generation system, it is found that the exergy efficiency in biomass operated system is increased by 1.11% and by 3.42% in the solar operated system in tri-generation over single generation. From this study it has been observed that any change in the parameters can significantly affect the energy and exergy efficiencies of the system and also tri-generation and optimization approaches are novel way to enhance the efficiency of a system.

Nomenclature

A_p	aperture area of collector, m^2
Col_c	collector in each row
Col_r	number of rows
CoP	coefficient of performance
en	specific energy, kJ/kg
ex	specific exergy, kJ/kg
$\dot{E}x$	exergy rate, kW
g	gravity of acceleration, m/s^2
h	specific enthalpy, kJ/kg
H_u	moisture content in biomass
L	length of collector, m
LHV	lower Heating value of fuel, kW
$\dot{m}$	mass flow rate, kg/s
P	pressure, kPa
$\dot{Q}$	heat transfer rate, kW
R_a	intensity of solar radiation, W/m^2
s	specific entropy, kJ/kg K.
T	temperature, K
v	specific volume, m^3/kg
V	velocity, m/s
w	width of collector, m

w,a,b,c	stoichiometric constant in biomass combustion reaction in Eq. (5.6) (moles)
$\dot{W}_P$	pump work Input, kW
$\dot{W}_T$	turbine work output, kW
x_k	number of molecules of gas k (molecules)
y,z	constant in Eq. (5.7) related to number of atoms of hydrogen and oxygen in biomass
z	elevation difference, m

Greek Letters

α	number of atoms of carbon,
β	hydrogen,
δ	nitrogen and
γ	oxygen in biomass (atoms/mole)
η	energy efficiency
Ψ	exergy efficiency
μ_m	mineral matter content in biomass
ϕ	exergy to energy ration of fuel

Subscripts

bio	biomass
Cc	combustion
ch	chemical
cool	cooling
Dest	destruction
e	exit
eva	evaporator
gen	generator
heat	heating
HE	heat exchanger
HTF	heat transfer fluid
i	inlet
L	loss
mois	moisture
ORC	organic Rankine cycle
ph	physical
s	source
ss	solar system
single	single generation
tri	tri-generation
x,y,z	number of atoms of carbon, hydrogen and oxygen in biomass(atoms/molecule)
1…22	state numbers
0	ambient or reference condition

References

1. Hung T, Shai T, Wang S (1997) A review of organic Rankine cycles (ORCs) for the recovery of low-grade waste heat. Energy 22:661–667
2 Al-Sulaiman F, Hamdullahpur F, Dincer I (2011) Performance comparison of three trigeneration systems using organic Rankine cycles. Energy 36:5741–5754
3. Zamfirescu C, Dincer I, Stern M, Wagar W (2012) Exergetic, environmental and econom nalyses of small-capacity concentrated solar-driven heat engines for power and heat cogeneration. Int J Energy Res 36:397–408
4. Granovskii M, Dincer I, Rosen MA (2009) Exergetic performance analysis of a gas turbine cycle integrated with solid oxide fuel cells. ASME 131(2): doi:10.1115/1.3185348
5. Ahmadi P, Dincer I (2010) Exergoenvironmental analysis and optimization of a cogeneration plant system using multimodal genetic algorithm (MGA). Energy 35(12):5161–5172
6. Ahmadi P, Dincer I, Rosen MA (2011) Exergy, exergoeconomic and environmental analyses and evolutionary algorithm based multi-objective optimization of combined cycle power plants. Energy 36:5886–5898
7. Dincer I, Ahmadi P, Rosen MA (2013) Performance assessment and optimization of a novel integrated multigeneration system for residential buildings. Energy Build 67:568–578
8. Al-Sulaiman FA, Hamdullahpur F, Dincer I (2011) Greenhouse gas emission and exergy assessments of an integrated organic rankine cycle with a biomass combustor for combined cooling, heating and power production. Appl Therm Eng 31:439–446
9. Sulaiman FAAl, Hamdullahpur F, Dincer I (2012) Performance assessment of a novel system using parabolic trough solar collectors for combined cooling, heating, and power production. Renew Energy 48:161–172
10. Herold KE Radermarcher R, Klein SA (1996) Absorption chillers and heat pumps. CRC. ISBN - 9780849394270
11. ASHRAE Handbook Fundamentals (2005) American Society of Heating, Refrigerating and Air Conditioning Engineers, Atlanta, GA
12. Mehrabian M, Shahbeik A (2005) Thermodynamic modelling of a single-effect LiBr-H_2O absorption refrigeration cycle. ProQuest Sci J 219: 261–273
13. Cengel YA, Boles MA, KanogËlu M (2007) Thermodynamics: an engineering approach. McGraw-Hill, New York
14. Dincer I, Rosen MA (2012) Exergy: energy, environment and sustainable development. Newnes
15. Ahmadi P, Dincer I, Rosen MA (2013) Development and assessment of an integrated biomass-based multi-generation energy system. Energy 56(1): 155–166
16. Szargut J, Morris DR, Steward FR (1988) Energy analysis of thermal. chemical, and metallurgical processes. Hemisphere Publishing Corporation
17. Talbi EG (2009) Metaheuristics: from design to implementation. Wiley, New York
18. Yaws CL (1999) Chemical properties handbook: physical, thermodynamic, environmental, transport, safety, and health related properties for organic and inorganic chemicals. McGraw-Hill, New York

Chapter 6
Performance Evaluation of Integrated Energy Systems

Pouria Ahmadi, Ibrahim Dincer and Marc A. Rosen

Abstract The current literature on integrated energy systems for various applications is discussed and how energy systems are integrated for multigeneration purposes is explained. Three integrated energy systems, including renewable and non-renewable ones, are considered to enhance the analyses. A micro-gas turbine integrated system is selected as the non-renewable system while biomass and ocean thermal energy conversion based energy systems are considered as the renewable options. Exergy analysis is conducted to determine the irreversibilities in each component and the system performance. Furthermore, economic and environmental impact assessments of the systems are conducted, and the results are presented for each integrated system. The results show that the integrated energy systems have higher exergy efficiency compared to single generation unit and that the integration results in reduction of greenhouse gases emission. The performances of the three systems are compared, and the results show that the choice and benefits of integrated systems strongly depends on the priorities of the designers and engineers.

Keywords Energy · Exergy · Efficiency · Integrated energy system

6.1 Introduction

Energy use is directly linked to well-being and prosperity across the world. Meeting the growing demand for energy in a safe and environmentally responsible manner is an important challenge. A key driver of energy demand is the human desire to sustain and improve ourselves, our families and our communities. There are around 7 billion people on Earth and population growth will likely lead to an increase in energy demand, which depends on the adequacy of energy resources. Increasing population

I. Dincer (✉)
Department of Mechanical Engineering, University of Ontario Institute of Technology (UOIT), 2000 Simcoe St. North, Oshawa, ON L1H 7K4, Canada
e-mail: ibrahim.dincer@uoit.ca

P. Ahmadi · M. A. Rosen
Faculty of Engineering and Applied Science, University of Ontario Institute of Technology (UOIT), 2000 Simcoe St. North, Oshawa, ON L1H 7K4, Canada

I. Dincer et al. (eds.), *Progress in Sustainable Energy Technologies: Generating Renewable Energy,* DOI 10.1007/978-3-319-07896-0_6,

and economic development in many countries are having serious implications for the environment, because energy generation processes (e.g., generation of electricity, heating, cooling, and shaft work for transportation and other applications) emit pollutants, many of which are harmful to ecosystems. Burning fossil fuels results in the release of large amounts of greenhouse gases, particularly carbon dioxide.

Energy exists in several forms, e.g. light, heat, and electricity. Concerns exist regarding limitations to easily accessible supplies of energy resources and the contribution of energy processes to global warming as well as other environmental concerns such as air pollution, acid precipitation, ozone depletion, forest destruction, and radioactive emissions [1]. There are various alternative energy options to fossil fuels, including solar, geothermal, hydropower, wind and nuclear energy. The use of many of the available natural energy resources is limited due to their reliability, quality and energy density. Nuclear energy has the potential to contribute a significant share of large scale energy supply without contributing to climate change. Advanced technologies, aimed at mitigating global warming, are being proposed and tested in many countries. Among these technologies, multigeneration processes, including trigeneration, can make important contributions due to their potential for high efficiencies as well as low operating costs and pollution emissions per energy output. Issues like fossil fuel depletion and climate change amplify the advantages and significance of efficient multigeneration energy systems.

Global warming, which is one the facets of global climate change, refers to an increase in the average temperature of the atmosphere and oceans, which appears to have occurred in recent decades and is projected to continue. The drivers of climate change are generally agreed to be changes in the atmospheric concentrations of greenhouse gases (GHGs) and aerosols. According to the Intergovernmental Panel on Climate Change (IPCC), most of the increase in global average temperatures since the mid-twentieth century is linked to the observed increase in anthropogenic GHG concentrations. A greenhouse gas is a gas in an atmosphere that absorbs and emits radiation within the thermal infrared range [2]. This process is the fundamental cause of the greenhouse effect.

The primary greenhouse gases in the Earth's atmosphere are water vapor, carbon dioxide, methane, nitrous oxide, and ozone. The greenhouse effect is a process by which thermal radiation from a planetary surface is absorbed by atmospheric greenhouse gases, and is re-radiated in all directions. Since part of this re-radiation is back towards the surface and the lower atmosphere, it results in an elevation of the average surface temperature above what it would be in the absence of the gases [2]. Global warming is agreed by many to be a direct effect of GHG emissions, which have increased notably over the last century.

Human activity since the Industrial Revolution has increased the amount of greenhouse gases in the atmosphere, leading to increased radioactive forcing from CO_2, methane, tropospheric ozone, chlorofluorocarbons (CFCs) and nitrous oxide. The effect of greenhouse gases on global warming is assessed using an index called global warming potential (GWP), which is a measure of how much a given mass of GHG contributes to global warming relative to a reference gas (usually CO_2) for which the GWP is set to 1. For a 100-year time horizon, GWPs of CO_2, CH_4 and

N_2O are reported to be 1, 25 and 298, respectively [3]. Using this index, one can calculate the equivalent CO_2 emissions by multiplying the emission of a GHG by its GWP. The main causes of global warming are as follows [3]:

- Carbon dioxide emissions from fossil fuel burning power plants.
- Carbon dioxide emissions from burning gasoline for transportation.
- Methane emissions from animals, agriculture such as rice paddies, and from Arctic sea beds.
- Deforestation, especially tropical forests for wood, pulp, and farmland.
- Use of chemical fertilizers on croplands.

CO_2 is widely believed to be a significant cause of global warming. The literature shows that concentrations of CO_2 and methane have increased by 36 and 148 % respectively since 1750 [3]. Fossil fuel combustion is responsible for about three-quarters of the increase in CO_2 from human activity over the past 20 years. The rest of this increase is caused mostly by changes in land use, particularly deforestation. The main source of CO2 emissions is fossil fuel-based electricity generation units, which account for about 32 % of the total CO2 emissions. The next largest source of CO2 emissions are caused by heating and cooling, which account for about 33 % of total CO_2 emissions, followed by emissions from cars and trucks, which account for 23 % of total global CO_2 emissions, and other major transportation, which accounts for 12 % [3]. Hence, about 65 % of the total CO_2 emissions are attributable to electricity generation and heating and cooling, both of which are directly associated with energy needs of human beings.

Cogeneration, or combined heat and power (CHP), represents a relatively simple, integrated multigeneration energy system involving the use of waste or other heat from electricity generation to produce heating. The overall energy efficiency of a cogeneration system, defined as the part of the fuel converted to both electricity and useful thermal energy, is typically 40–50 % [4] but can be much higher. Recently, researchers have extended CHP to trigeneration, a system for the simultaneous production of heating, cooling and electricity from a common energy source. Trigeneration often utilizes the waste heat of a power plant to improve overall thermal performance [5], and is suitable for some energy markets.

The benefits of integrating energy systems became prominent with the application of cogeneration for heat and electricity production. In this simple energy system, waste or other heat is used to produce either cooling or heating. In general, cogeneration is the production of heat and electricity in one process using a single energy source, which often yields considerable reductions in input energy compared to separate processes. Cogeneration is often associated with the combustion of fossil fuels, but can also be carried out using certain renewable energy sources, nuclear energy, and waste thermal energy (obtained directly or by burning waste materials). The recent trend has been to use cleaner fuels for cogeneration, such as natural gas. The strong long-term prospects for cogeneration in global energy markets are related to its ability to provide significant operational, environmental and financial benefits. The product thermal energy from cogeneration can be used for domestic hot water heating, space heating, pool heating, laundry heating processes

and absorption cooling. The more the product heat from cogeneration can be used in existing systems, the more financially attractive the system is. Cogeneration helps overcome a drawback of many conventional electrical and thermal systems: significant heat losses, which detract greatly from efficiency [5]. Heat losses are reduced and efficiency is increased when cogeneration is used to supply heat to various applications and facilities.

The overall energy efficiency of a cogeneration system is the percent of the fuel converted into both electricity and useful thermal energy. Recently, researchers have extended CHP to have more output purposes. In this regard, trigeneration energy systems have become more suitable for energy markets. Trigeneration is the simultaneous production of heating, cooling and electricity from a common energy source. Trigeneration utilizes the waste or other heat of a power plant to improve overall thermal performance, often utilizing the free energy available from waste energy. In a trigeneration system, waste heat from the plant's prime mover (e.g, gas turbine or diesel engine or Rankine cycle [6]), sometimes with temperature enhancement, drives heating and cooling devices. The heat can be used for space heating, domestic hot water production or steam production for process heating. The heat can also be used for cooling, by driving an absorption chiller. Several studies on trigeneration have been conducted in the last few years, likely due to its benefits and plans for applications. Trigeneration can be applied widely, e.g., in chemical and food industries, airports, shopping centres, hotels, hospitals, and houses. Figure 1.1 illustrates a trigeneration energy system, consisting of the following three major parts:

- A power generation unit, i.e. a prime mover, such as a gas turbine.
- A cooling unit, such as a single-effect absorption chiller.
- A heating unit, such as a boiler or heat recovery steam generator.

The following processes occur in a trigeneration plant:

- Mechanical power is produced via a generator unit, such as a gas turbine.
- The mechanical power is used to drive an electrical generator.
- Waste heat exits the mechanical generator unit directly or via heated materials like exhaust gases.

As shown in Fig. 6.1, with a single prime mover we can produce heating, cooling and electricity simultaneously. Recently, researchers have extended trigeneration to produce more products like hot water, hydrogen and potable water using a single prime mover via multigeneration.

The efficiencies for multigeneration energy systems can be higher than those for either trigeneration or CHP because of the additional products (hydrogen, potable and hot water, etc.). Figures 6.2 and 6.3 illustrate two multigeneration energy systems. The system in Fig. 6.2 produces electricity, cooling, heating, hot water and hydrogen. To produce hydrogen, an electrolyzer is used, which is driven by part of the electricity generated by a solar concentrating collector. Hot water enters the electrolyzer and is reacted electrochemically to split its molecules into hydrogen and oxygen. The heating system is composed of two parts, one for hot water

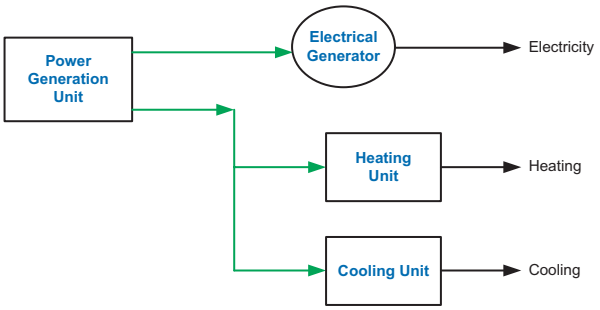

Fig. 6.1 A typical trigeneration energy system [5]

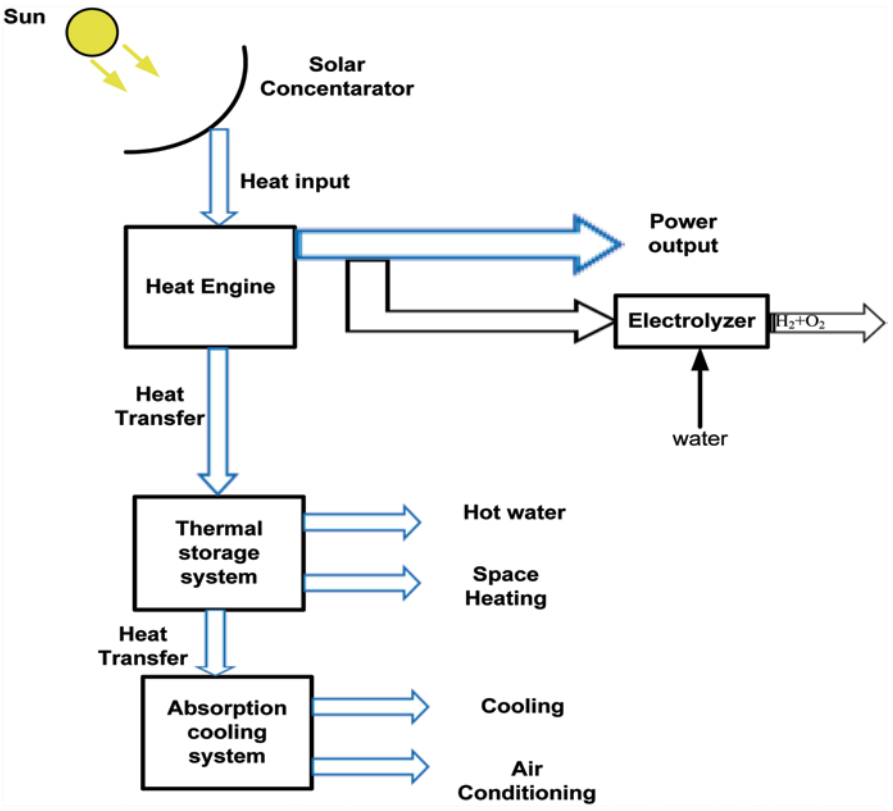

Fig. 6.2 A multigeneration energy system for producing electricity, cooling, heating, hot water and hydrogen [7]

production and another for space heating. Heat rejected from the storage system enters the absorption cooling system to produce cooling and air conditioning. If the system is extended to produce potable water, a desalination system must be used, and such a multigeneration energy system is shown in Fig. 6.3. In this case, a portion of the heat produced by the solar concentrator is used to run a desalination

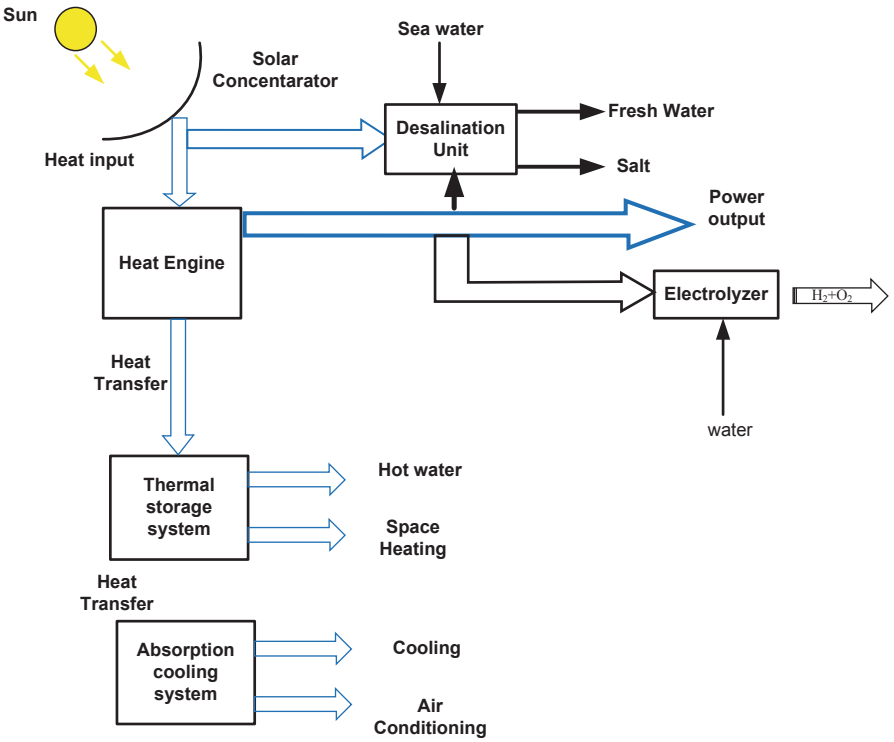

Fig. 6.3 A multigeneration energy system for producing electricity, cooling, heating, hot water, hydrogen and fresh water [7]

system, while part of the electricity generated by the power unit drives the pumps. Other parts of the system are the same as in Fig. 6.2. These two figures are representative of typical multigeneration energy systems that use only solar energy as an input. Other configurations that combine renewable and conventional energy sources are also possible, and are discussed subsequently.

Benefits of Integrated Energy Systems

There are many benefits of integrated energy systems, including higher plant efficiency, reduced thermodynamic losses and wastes, reduced operating costs, reduced greenhouse gas emissions, better use of resources, shorter transmission lines, fewer distribution units, multiple generation options, increased reliability, and less grid failure [7]. These benefits are discussed below. Integrated systems improve the overall efficiency of the plant and reduce the operating costs. The overall efficiency of conventional power plants that use fossil fuel with a single prime mover is usually less than 40%. That is, more than 60% of the heating value of the fuel energy entering a conventional power plant is lost. On the other hand, the overall efficiency of a conventional power plant that produces electricity and heat separately is around 60% or more [8].

However, with the utilization of the waste heat from the prime mover, the efficiency of multigeneration plants could reach up to 80% [9]. In a multigeneration plant, the waste heat from the electricity generation unit is used to operate the cooling and heating systems without the need for extra fuel, unlike a conventional power plant that requires extra energy resources. Thus, a multigeneration plant uses less energy to produce the same output as a conventional plant, and has correspondingly lower operating costs.

Integrated systems also reduce GHG emissions. Since a multigeneration energy system uses less fuel to produce the same output compared to a conventional power plant, a multigeneration plant emits less GHGs. Although the GHG emissions from multigeneration plants are less than conventional plants, there are some limitations of using multigeneration plants in a distributed manner because of their on-site gas emissions. Another important benefit of using multigeneration energy systems is that they reduce costs and energy losses due to the fact that they need fewer electricity transmission lines and distribution units. The conventional production of electricity is usually from a centralized plant that is generally located far from the end user. The losses from transmission and distribution of electricity from a centralized system to the user can be about 9% [8].

These benefits have encouraged researchers and designers to develop multigeneration energy systems. The improvement in efficiency is often an important factor in implementing a multigeneration energy system. Further assessments before selecting multigeneration plants, such as evaluations of initial capital and operating costs, are needed to ensure efficient and economic multigeneration plant construction and performance [8].

Multigeneration Energy Systems

A multigeneration energy system usually refers to a system with more than three different purposes from the same source of input energy (the prime mover). These purposes can include electricity, cooling, heating, hot water, hydrogen and fresh water. These systems should be considered for residential application, power plants and other places where numerous useful outputs are required. It must be noted that the location and requirements of its application are major factors the design of a multigeneration energy system. For example, in a place where the need for fresh water is vital, a multigeneration system meant to address the need must prioritize this purpose. In the literature, there are few studies on focused on optimizing multigeneration energy systems. These systems are have the potential to help address global warming.

It is worth mentioning that different methods are available to achieve each purpose of multigeneration energy systems; this is why the application of each subsystem is very important in meeting the system's requirements. Figure 6.6 shows a practical multigeneration energy system to produce electricity, cooling, power and domestic hot water that works based on a gas turbine Brayton cycle. In order to produce saturated steam in this multigeneration system, a dual pressure heat

recovery steam generator (HRSG) is used. High pressure saturated steam enters a steam turbine to produce electricity while lower pressure steam works as an absorption chiller heat input into the generator. In order to produce the cooling demand, a single effect absorption chiller with Li-Br water as working fluid is employed. Saturated liquid leaves the generator, which is then used to heat up water using a domestic water heater. According to the concept of a Rankine cycle, the condenser rejects an amount of heat. This heat could be considered either for the space heating application or for a thermochemical water splitting cycle to produce hydrogen. As illustrated in Fig. 6.4, where the fuel is just injected into the combustion chamber, it is observed that this system has less environmental impact compared to GT cycles, CHP systems and trigeneration energy systems. The reason is due to this fact that waste heat from GT and CHP systems is used to produce cooling and heating applications. Energy efficiency of this cycle can exceed 70 %. This multigeneration system could be used to produce hydrogen, another valuable purpose. In this case, a part of the produced electricity could be used to drive an electrolyzer to produce hydrogen, which could then be used for either hybrid electric vehicles or to produce electricity using a fuel cell. As shown in Fig. 6.5, flue gases leave the HRSG at a temperature around 150 °C. To increase the efficiency of this multigeneration system, the energy of these flue gases could be utilized in a heat exchanger and produce more electricity and cooling by using an ejector refrigeration system. With this configuration, the efficiency of the system could be higher than 85 %.

Figure 6.5 shows another multigeneration energy system for production of electricity, heating, cooling and fresh water. A photovoltaic solar panel is selected to use solar energy in order to run triple effect absorption to provide cooling. A triple effect absorption cooling system is also considered for the cooling demand of the system, and a desalination unit is applied to produce fresh water. In addition, Figs. 6.4 and 6.5 demonstrate the significant potential of multigeneration energy systems. There are many more options in the design multigeneration energy systems, which are discussed in detail in the following sections.

6.2 Review of Recent Advances

Various studies associated with CHP and trigeneration energy systems have been reported in the literature, although comprehensive studies of multigeneration energy systems are rare. Because of the environmental concerns and technological developments in the last decade, both the need and the capability of producing multipurpose energy solutions have been amplified considerably. The related papers, their aims, method of analysis and brief conclusions are presented in this section. We have tried to focus on the most recent studies regarding combined heat and power (CHP), trigeneration and multigeneration energy systems. Since there are several papers about CHP and trigeneration systems, the literature has been categorized based on thermodynamic modeling, exergy, exergoeconomic and exregoenvironmental analyses and optimization.

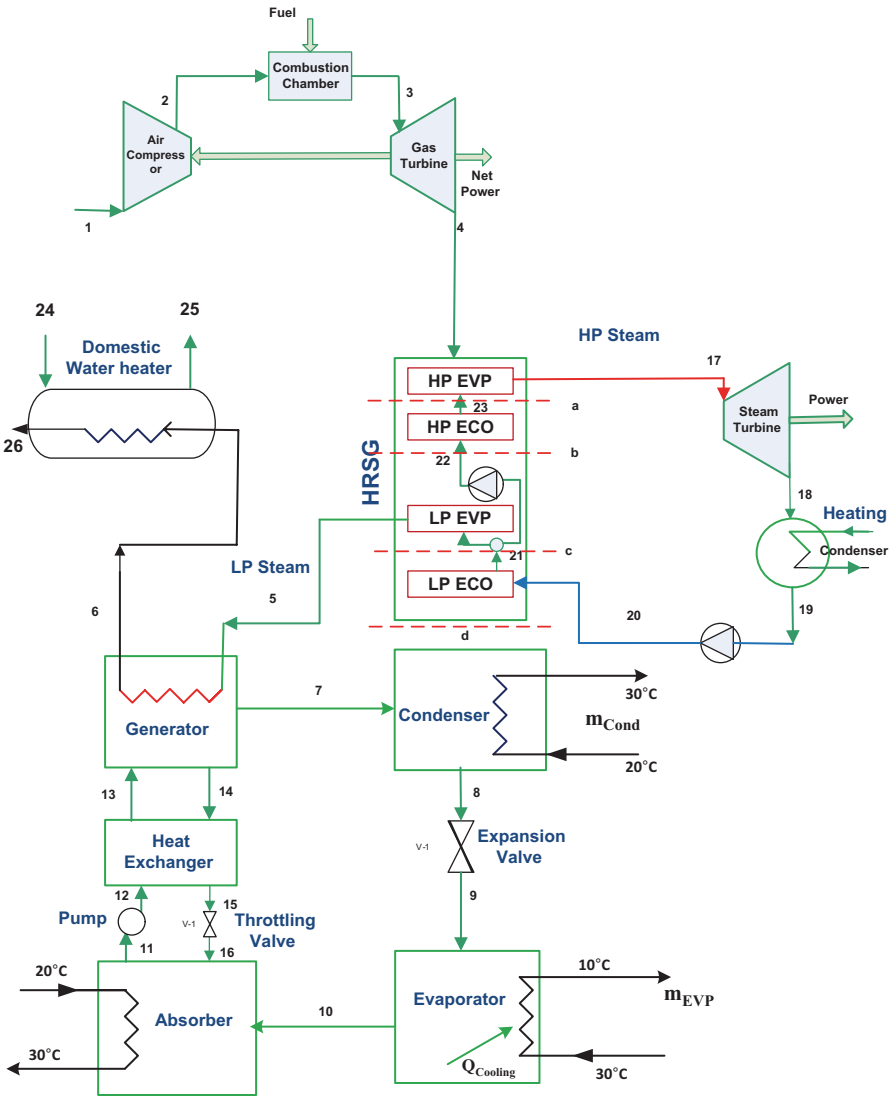

Fig. 6.4 Schematic of a multigeneration system for electricity, heating, cooling and hot water [5]

Cogeneration Heat and Power (CHP) Systems

An integrated energy system produces several useful outputs from one or more kinds of energy inputs. The main purposes of energy integration are usually to increase efficiency and sustainability of the system and to reduce environmental impact and cost of the system. Such systems often provide significant potential for

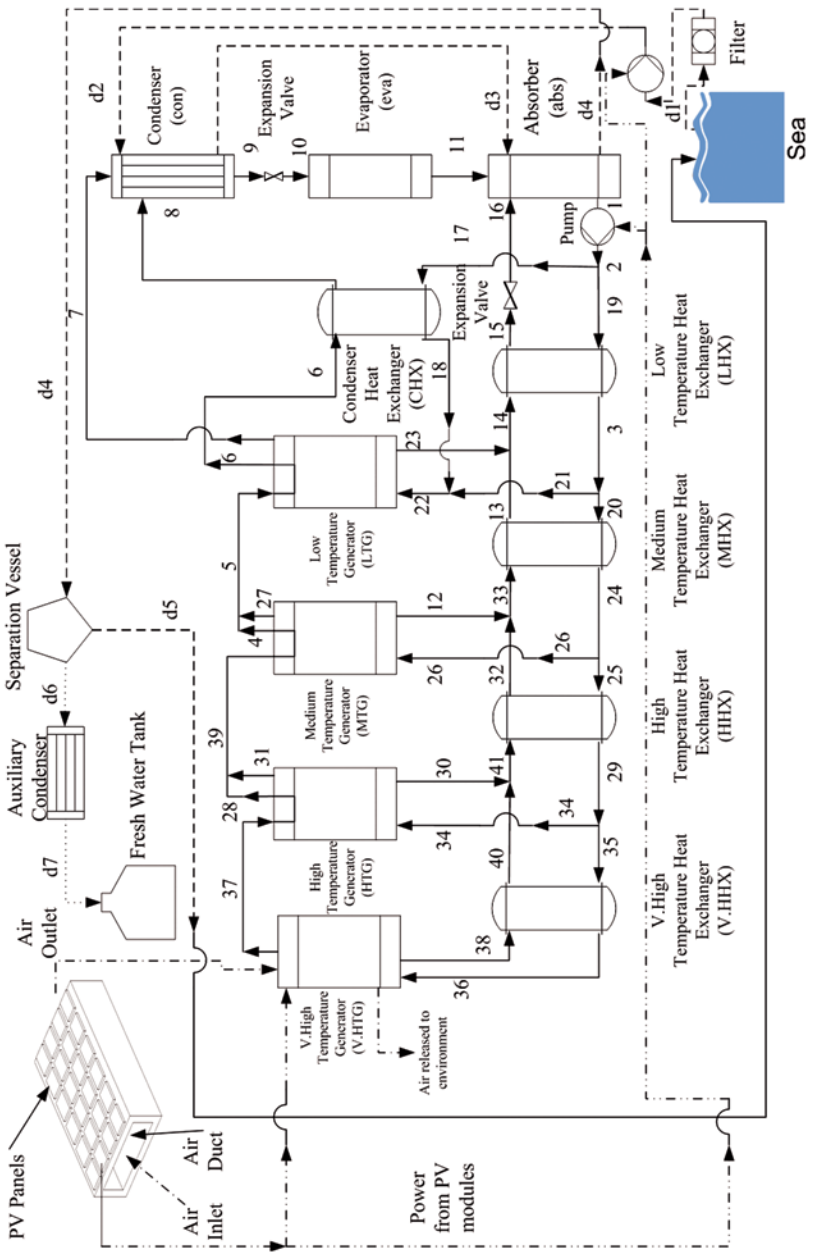

Fig. 6.5 Schematic diagram of a multigeneration energy system including desalination [10]

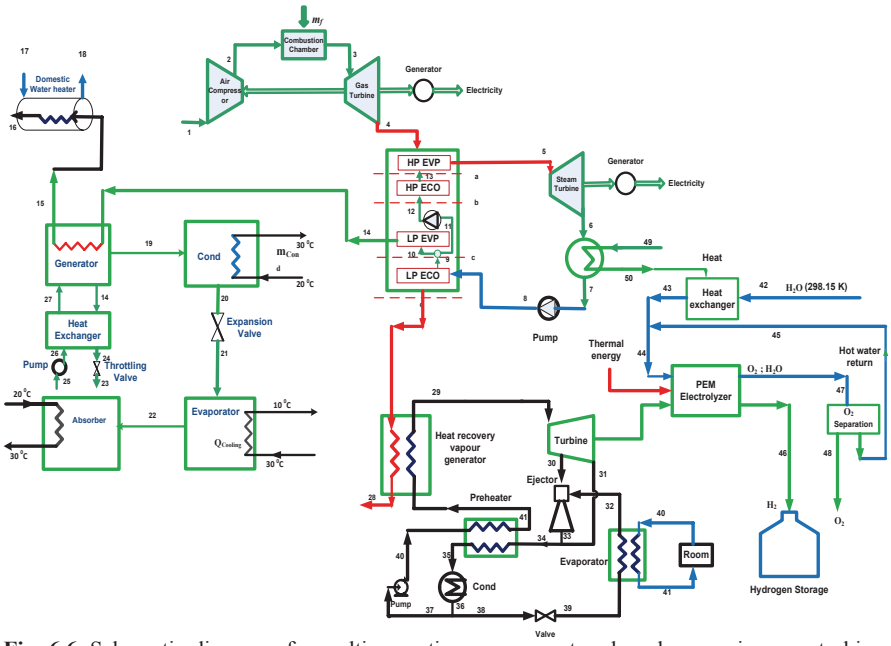

Fig. 6.6 Schematic diagram of a multigeneration energy system based on a micro gas turbine, a dual pressure heat recovery steam generator, an absorption chiller, and an ejector refrigeration cycle [5]

global warming mitigation. Multigeneration energy system as a potential example of integrated system can possibly produce some useful outputs including electricity, heating, cooling, hot water, fresh water and hydrogen. Cogeneration, or CHP, represents a relatively simple process that produces two commodities in an integrated fashion, including the use of waste heat from electricity generation to produce heating. The overall energy efficiency of a cogeneration system, defined as the part of the fuel energy content converted to both electricity and useful thermal energy, is typically 40–50 % and, in some cases, higher [11, 12, 13].

A micro-scale building cooling, heating and power (BCHP) system with an adsorption chiller was experimentally studied by Huangfu et al. [14]. The authors observed the performance of an adsorption chiller under different heating conditions. They concluded that there was an almost linear relation between the adsorption chiller and the change in hot water inlet temperature for the two investigated models. Mago et al. [15] analyzed and optimized the use of CHP-ORC systems for small commercial buildings. In another study, Mago et al. [16] reported on the evaluation of the potential emission reductions from the use of CHP systems in different commercial buildings. Mago and Hueffed [17] evaluated a turbine-driven combined cooling, heating and power (CCHP) system for large office buildings under various operating strategies, and explored the use of carbon credits to show how the possible reduction in carbon dioxide emissions via a CCHP system could translate into economic benefits.

Bianchi et al. [18] studied the performance analysis of an integrated CHP system with thermal and electric energy storage for residential application. Athanasovici et al. [4] proposed a unified comparison method for the thermodynamic efficiency of CHP plants, and used this method to compare various separate and combined energy production processes. Havelsky [19] analyzed the problem of efficiency evaluation of systems for combined heat, cold and electricity production, and developed equations for energy efficiency and primary energy savings. The energy analysis of trigeneration plants with heat pumps was examined by Miguez et al. [20, 21]. They concluded that the heat pump is important for plant efficiency enhancement.

Khaliq et al. [9] carried out an exergy analysis of a combined electrical power and refrigeration cycle, as well as a parametric study of the effects of exhaust gas inlet temperature, pinch point and gas composition on energy and exergy efficiencies, electricity to cold ratio, and exergy destruction rate for a cogeneration system and its components. Cihan et al. [22] carried out energy and exergy analyses for a combined cycle located in Turkey and suggested modifications to decrease the exergy destruction in combined cycle power plants (CCPPs). Their results showed that combustion chambers, gas turbines and HRSGs are the main sources of irreversibilities, representing over 85 % of the overall exergy losses.

Barelli et al. [23] conducted an exergetic analysis of a residential CHP system based on a PEM fuel cell. They also conducted a complete parametric study to see the effect of fuel cell design parameters such as temperature, pressure and relative humidity on the system performance. Bingol et al. [24] reported the exergy based performance analysis of high efficiency polygeneration systems for sustainable building applications. El-Emam and Dincer [25] conducted the energy and exergy analyses of a CHP system with a molten carbonate fuel cell (MCFC) and a gas turbine system. They performed a parametric study by changing some design parameters of the system in order to assess the system performance. The results showed that the maximum output work of the MCFC is estimated to be 314 kW for an operating temperature of 650 °C. The overall energy and exergy efficiencies achieved for this system were 43 and 38 %, respectively.

Akkaya et al. [26] conducted the exergy analysis for a hybrid CHP system using a SOFC and a gas turbine and performed a parametric study. The results showed that a design based on an exergy performance coefficient criterion has considerable advantage in terms of entropy generation rate. Al-Sulaiman et al. [27] demonstrated an efficiency gain of more than 22 % using a trigeneration plant compared with a power cycle (SOFC and organic Rankine cycle). They also determined the maximum efficiencies of 74 % for the trigeneration plant, 71 % for heating cogeneration, 57 % for cooling cogeneration and 46 % for net electricity generation, and concluded that exergy analysis is a significant tool for both CHP and trigeneration cycles.

In recent decades, exergoeconomics and thermoeconomics have been increasingly utilized by researchers, combining thermodynamics with economics. Many such studies have been reported, especially for power generation and cogeneration (CHP). Rosen and Dincer [28] performed an exergoeconomic analysis of a coal fired electricity generating station, and found the ratio of thermodynamic loss rate to the capital cost to be a significant parameter in evaluating plant performance that

may allow thermodynamics and economics to be successfully traded-off in plant designs. Ahmadi et al. [29] carried out energy, exergy and exergoeconomic analyses of a steam power plant in Iran, and considered the effect of the load variations and ambient temperature on component exergy destruction rate. The results showed that energy losses are mainly associated with the condenser, where the energy loss rate to the environment was 307 MW, while the boiler energy loss rate was only 68 MW. However, the irreversibility rate of the boiler was significantly higher than the irreversibility rates of the other components. Exergy and exergoeconomic analyses of CHP plants [30–32] have demonstrated the usefulness of these methods for thermal systems.

Trigeneration Systems

Trigeneration commonly utilizes waste or other heat from a power plant to improve overall thermal performance, often utilizing the free energy available via waste energy. In a trigeneration system, waste heat from the plant's prime mover (e.g., gas turbine, diesel engine, or Rankine cycle [6]), sometimes with temperature enhancement, drives heating and cooling devices. The heat can be used for space heating, domestic hot water production, or to produce steam for process heating. The heat can also be used for cooling, by driving an absorption chiller. Pospisil et al. [33] performed an energy analysis of a trigeneration system and compared cogeneration and trigeneration plants for a typical building. The results showed that cogeneration can increase the efficiency by about 31 % while trigeneration systems increase efficiency by about 39% compared to a single generation system. Al-Sulaiman et al. [34] reported the performance comparison of three trigeneration systems using organic Rankine cycles. The systems they considered consist of SOFC-trigeneration, biomass-trigeneration, and solar-trigeneration. Martins et al. [35] studied the thermodynamic performance assessment of a trigeneration cycle considering the influence of operational variables. Calva et al. [36] studied the thermal integration of trigeneration systems. They focused on trigeneration schemes where a gas turbine is used as a prime mover for power production and cooling is generated by a typical compression refrigeration system. Huang et al. [37] reported a biomass fuelled trigeneration system in selected buildings. This trigeneration system consisted of an internal combustion (IC) engine integrated with biomass gasification. In their system the gas generated by the biomass gasifier was used to provide electricity for a typical building using an IC engine. The waste heat is then recovered from the engine cooling system and exhaust gases are utilized to supply hot water for space heating; excess heat was also used to drive an absorption cooling system.

Rocha et al. [38] studied the performance tests of two small trigeneration pilot plants. The first system was based on a 30 kW natural gas powered micro turbine, and the second used a 26 kW natural gas powered IC engine coupled with an electrical generator as a prime mover. They also used an ammonia water absorption refrigeration chiller for producing chilled water. Huicochea et al. [39] carried out a

thermodynamic analysis of a trigeneration system consisting of a micro gas turbine and a double effect absorption chiller. The system consisted of a microturbine to produce electrical power, a double effect absorption water LiBr chiller for air conditioning and a heat exchanger to produce hot water.

Chicco and Mancarella [40] proposed some energy indicators to assess the fuel efficiency of a trigeneration plant. Chicco and Mancarella [41] applied these energy indicators to introduce a planning criterion called equivalent gas price. Aghahosseini et al. [42] reported the thermodynamic analysis of an integrated gasification and Cu-Cl cycle for trigeneration of hydrogen, steam and electricity. They used Aspen HYSYS to simulate the system. The results showed that using oxygen instead of air for the gasification process, in which oxygen is provided by the integrated Cu-Cl cycle, led to a 20 % increase in the hydrogen content of produced syngas. Minciuc et al. [43] presented a method for analyzing trigeneration systems and established limits for the best performance of gas turbine trigeneration with absorption chilling from a thermodynamic point of view.

Moya et al. [44] studied the performance assessment of a trigeneration system consisting of a micro gas turbine and an air cooled, indirect fired, ammonia water absorption chiller. They also conducted a parametric study by changing some major design parameters, including variation of output power of the micro gas turbine, ambient temperature for the absorption unit, chilled water outlet temperature and thermal oil inlet temperature. Velumani et al. [45] proposed a new integrated trigeneration system consisting of a micro gas turbine, a solid oxide fuel cell and a single effect absorption chiller. The results showed that the energy efficiency of this cycle is about 70 %.

Buck and Fredmann [46] studied the performance of a trigeneration plant based on a micro turbine assisted by a small solar tower. They conducted an economic analysis on the use of single and double effect absorption chillers. The authors recommended using the double effect chiller since it showed better thermal performance and lower operating cost compared to the single effect absorption chiller.

Exergy is a useful tool for determining the location, type and true magnitude of exergy losses, which appear in the form of either exergy destructions or waste exergy emissions [47]. Therefore, exergy can assist in developing strategies and guidelines for more effective use of energy resources and technologies. Recently, exergy analysis has become increasingly popular for analyzing thermal systems. Some studies have applied exergy analyses to CHP and trigeneration energy systems based on IC engines. Santo et al. [48] conducted the energy and exergy analyses of a IC engine based trigeneration system under two operating strategies for buildings. They presented a computational hourly profile method that combined fittings from the literature and actual data from manufacturer into a single algorithm curve in order to obtain the mathematical representations of physical phenomena and thermodynamic properties. The developed simulation method was used to predict the performance of a given cogeneration concept under two operational strategies.

Ebrahimi et al. [49] carried out energy and exergy analyses of a micro steam CCHP cycle for a residential building. They analyzed a trigeneration energy system consisting of a steam turbine and an ejector refrigeration system to provide

the cooling load for residential buildings. They also optimized the system using a genetic algorithm to determine its maximum overall efficiency. The exergy analysis results revealed that the greatest exergy destruction rate takes place in the steam generator for both summer and winter seasons.

Khaliq [50] conducted an exergy analysis for a trigeneration system. The system studied consisted of a gas turbine cycle, a single pressure heat recovery steam generator to provide heating and a single effect Li-Br absorption chiller to provide sufficient cooling. He also conducted a comprehensive parametric study to investigate the effects of compressor pressure ratio, gas turbine inlet temperature, combustion chamber pressure drop, and evaporator temperature on the exergy destruction rate in each component, first law efficiency, electrical to thermal energy ratio, and second law efficiency of the system. The exergy analysis results indicated that that maximum exergy destruction rate occurred in the combustion and steam generation process, which represented over 80 % of the total exergy destruction rate in the overall system.

Kong et al. [51] conducted energy and economic analyses of a trigeneration plant using a Stirling engine as a prime mover with a conventional plant with a separate production of cooling, heating and power. They concluded that the trigeneration plant with the Stirling engine can save more than 33 % of the primary energy compared to the conventional plant. Ziher and Poredos [52] addressed the economics of using a trigeneration plant in a hospital. They calculated the cooling, heating, and power price per kWh on a monthly basis for 1 year. In order to obtain the cooling capacity, the authors suggested that the use of steam absorption and compression chillers with a cold storage system in the plant. Ahmadi et al. [6] carried out an exergoenvironmental analysis of a trigeneration system based on a micro gas turbine and an organic Rankine cycle (ORC), and performed a parametric study involving the main design parameters of the trigeneration system.

Temir and Bilge [53] studied a thermoeconomic analysis of a trigeneration system that produces electrical power with a natural gas fed reciprocating engine and that yields absorption cooling by making use of the system's exhaust gases. Ehyaei and Mozafari [54] performed energy, economic and environmental impact assessment ofa micro gas turbine employed for on-site combined heat and power production, and examined the optimization of the micro turbine application to meet the electrical, heating and cooling loads of a building. Mago and Hueffed [18] evaluated a turbine driven combined cooling, heating and power (CCHP) system for large office buildings under various operating strategies, and explored the use of carbon credits to show how the possible reduction in carbon dioxide emissions via a CCHP system could translate into economic benefits. Ozgener et al. [55] developed an exergoeconomic model for a vertical ground source heat pump (GSHP) residential heating system. They calculated the ratio of thermodynamic loss rate to capital cost values to be in the range of 0.18–0.43, and provided a linear correlation between the value of this parameter and ambient temperatures. They also drew attention to the compressor as the component where the most exergy destruction occurred.

Ozgener and Hepbasli [56] conducted an exergoeconomic analysis for a solar assisted ground source heat pump heating system with a 50 m vertical and 32 mm

nominal diameter U bend ground heat exchanger. They determined that the total exergy loss values were between 0.010and 0.480 kW and found the largest energy and exergy losses in the greenhouse compressor. Moreover, they have calculated the ratio of thermodynamic loss rate to capital cost values to be in the range of 0.035–1.125.

Many reports in the literature consider environmental aspects of thermal systems. Dincer [57] and Dincer and Rosen [47] considered the environmental and sustainability aspects of hydrogen and fuel cell systems. The exergetic and environmental aspects of drying systems have also been examined [17]. Ahmadi and Dincer [4] conducted an exergoenvironmental optimization of a CHP system using a genetic algorithm, and a sensitivity analysis of how optimized design parameters vary with the fuel cost. A thermodynamic analysis of post-combustion CO_2 capture in a natural gas fired power plant has been reported by Amrolahi et al. [58]. Petrakopoulou et al. [59] studied exergoeconomic and exergoenvironmental analyses of a combined cycle power plant with chemical looping technology. This research provided an evaluation of chemical looping combustion technology from an economic and environmental perspective by comparing it with a reference plant, a combined cycle power plant that includes no CO_2 capture.

For various reasons, it is important to optimize processes so that an objective function is maximized or minimized. For example, the output, profit, productivity, product quality, etc., may be maximized, or the cost per item, investment, energy input, etc., may be minimized. The success and growth of industries today is strongly based on their ability to optimize designs and systems. With the advent in the recent years of new materials, such as composites and ceramics, and new manufacturing processes, several traditional industries (e.g., steel) have faced significant challenges and, in some cases, diminished in size, while many new fields have emerged. It is important to exploit new techniques for product improvement and cost reduction in traditional and new industries. Even in an expanding area, such as consumer electronics, the prosperity of a company is closely connected to its ability to apply optimization to new and existing process and system designs. Consequently, engineering design, which has always been important, has become increasingly coupled with optimization [47].

Energy engineering is a field where optimization plays a particularly important role. Engineers involved in thermal energy engineering, for instance, are required to answer the questions such as

- What processes or equipment should be selected for a system, and how should the parts be arranged for the best outcome?
- What are the best characteristics for the components (e.g., size, capacity, cost)?
- What are the best process parameters (e.g., temperature, pressure, flow rate and composition) of each stream interacting with the system?

In order to answer such questions, engineers are required to formulate an appropriate optimization problem. Proper formulation is usually the most important and sometimes the most difficult step in optimization. To formulate an optimization problem, there are numerous elements that need to be defined, including system boundaries, optimization criteria, decision variables and objective functions.

Sahoo [60] carried out an exergoeconomic analysis and optimization of a cogeneration system which produces 50 MW of electricity and 15 kg/s of saturated steam at 2.5 bar. He optimized the unit using exergoeconomic principles and evolutionary programming, and showed that the cost of electricity production is 9.9 % lower for the optimum case in terms of exergoeconomics compared to a base case. Sayyaadi and Sabzaligol [61] performed an exergoeconomic optimization of a 1000 MW light water nuclear power generation system using a genetic algorithm and considering ten decision variables, and showed that the fuel cost of the optimized system is greater than that for a base case. Shortcomings in the optimized system are compensated by larger monetary savings in other economic sectors. Haseli et al. [62] found the optimum temperatures in a shell and tube condenser with respect to exergy. The optimization problem in that study considered condensation of the entire vapor flow and was solved with sequential quadratic programming (SQP).

Saayaadi and Nejatolahi [63] analyzed cooling tower assisted vapor compression refrigeration machines with respect to total exergy destruction rate and total product cost objective functions. They used energy and exergy analyses for the thermodynamic model and incorporated Total Revenue Requirement (TRR) for the economic model. They have optimized the system with respect to single objective thermodynamic, single objective economic and multi-objective criteria. For the multi-objective optimization, they selected final solutions from the Pareto frontier curve. Finally, they compared the results obtained from the three optimizations and calculated that the percentage deviation from ideal results for thermodynamic and economic criteria is 40 % for thermodynamically optimized system, 83 % for economically optimized system and 23 % for the multi-objective optimized system and therefore determined that the multi-objective optimization satisfies the generalized engineering criteria more than the other two single-objective optimized designs.

Ahmadi et al. [64] conducted a comprehensive exergy, exergoeconomic and environmental impact analyses and a multi-objective optimization for combined cycle power plants (CCPPs) with respect to the exergy efficiency, total cost rate and CO_2 emissions of the overall plant. They determined that the largest exergy destructions occurred in the CCPP combustion chamber and that increasing the gas turbine inlet air temperatures decreases the CCPP cost of exergy destruction. They derived the expression for the Pareto optimal point curves for the determined exergy efficiency range and concluded that the increase in total cost per unit exergy efficiency is considerably high after exergy efficiencies over 57 % and therefore a point below this should be chosen on the Pareto optimal curve.

Sayyaadi and Babaelahi [65] analyzed a liquefied natural gas re-liquefaction plant with respect to multi-objective approach which simultaneously considers exergy and exergoeconomic objectives. They used MATLAB multi-objective optimization algorithm of NSGA-II, which is based on the Genetic Algorithm, and obtained Pareto optimal frontier to find the Pareto optimal solutions. They compared the final optimal system with the base case and found that the exergetic efficiency in the multi-objective optimum design is 11 % higher than that of the exergoeconomic optimized system, while the total product cost of the multi-objective optimal design is 16.7 % higher than that of the exergoeconomic optimal system.

Ghaebi et al. [66] conducted the exergoeconomic optimization of a trigeneration system for heating, cooling and power production purpose based on total revenue requirement (TRR) method and using evolutionary algorithm. The system studied consists of an air compressor, a combustion chamber, a gas turbine, a dual pressure heat recovery steam generator and an absorption chiller in order to produce cooling, heating and power. The economic model used in their research was the TRR and the cost of the total system product was defined as our objective function and optimized using a genetic algorithm technique.

Kavvadias and Maroulis [67] investigated the multi-objective optimization of a trigeneration plant. This optimization was carried out on technical, economical, energetic and environmental performance indicators in a multi-objective optimization framework. The results showed that trigeneration plants can be more economically attractive, energy efficient and environmental friendly than conventional cogeneration plants. Al-Sulaiman et al. [68] studied the thermoeconomic optimization of three trigeneration systems using organic Rankine cycles. The three systems considered were SOFC-trigeneration, biomass-trigeneration, and solar-trigeneration systems. The results showed that solar based trigeneration system has the highest net available exergy as compared to the other two systems. Therefore, it has the highest potential to have the highest exergy if the solar collector performance is improved.

Wang et al. [69] conducted multi-objective optimization of an organic Rankine cycle (ORC) for low grade waste heat recovery using evolutionary algorithm. The multi-objective optimization of the ORC with R134a as the working fluid was conducted in order to achieve the system optimization design from both thermodynamic and economic aspects using non-dominated sorting genetic algorithm (NSGA-II). The decision variables considered for multi-objective optimization were turbine inlet pressure, turbine inlet temperature, pinch temperature difference, approach temperature difference and condenser temperature difference are selected as the decision variables.

Shirazi et al. [70] conducted a comprehensive thermodynamic modeling and multi-objective optimization of an internal reforming solid oxide fuel cell gas turbine hybrid system. They validated the model using available data in the literature. They used genetic algorithm to optimize the system. In the multi-objective optimization procedure, the exergy efficiency and the total cost rate of the system (including the capital and maintenance costs, operational cost and social cost of air pollution for CO, NO_x, and CO_2) were considered as objective functions. They also performed sensitivity analyses of the variation of each objective function with major design parameters of the system.

Multigeneration Energy Systems

Hosseini et al. [71] conducted a comprehensive thermodynamic model for an integrated energy system. The system studied consists of a gas turbine, a SOFC fuel cell, a single pressure HRSG and a multi effect desalination to produce electricity,

heating, cooling and fresh water. They also performed a comprehensive parametric study to see the effect of some major design parameters on the system performance. The results showed that the integrated system could increase the system efficiency by about 25 % compared to a single generation system.

Ahmadi et al. [6] studied a new integrated trigeneration energy system consisting of a gas turbine, a double pressure heat recovery steam generator and a single effect absorption chiller and an organic Rankine cycle. They also performed a parametric study to see the variation of exergy efficiency, cooling and heating load and cost of environmental impact. The results of this study demonstrated that system performance is notably affected by the compressor pressure ratio, the gas turbine inlet temperature and the gas turbine isentropic efficiency.

Ratlamwala et al. [72] studied a performance assessment of an integrated PV/T and triple effect cooling system for hydrogen and cooling production. The also conducted a comprehensive parametric study on the effect of average solar radiation for different months, operating time of the electrolyzer, inlet air temperature and PV area module on the power production and hydrogen production rate. In another study, Ratlamwala et al. [73] analyzed the performance of a novel integrated geothermal system for multigeneration, based on a geothermal double flash power generating unit, an ammonia water quadruple effect absorption unit and an electrolyzer system for cooling, heating, power, hot water and hydrogen production. Increasing the geothermal source temperature, pressure and mass flow rate was observed to increase the output power and hydrogen production rate.

Ozturk and Dincer [74] conducted a thermodynamic analysis of a solar based multigeneration system with hydrogen production. The solar based multigeneration considered for this analysis consists of four main sub systems: Rankine cycle, organic Rankine cycle, absorption cooling and heating, and hydrogen production and utilization. The exergy efficiency and exergy destruction rate for the subsystems and the overall system show that the parabolic dish collectors have the highest exergy destruction rate among constituent parts of the solar-based multigeneration system.

Dincer and Zamfirescu [7] performed energy and exergy analyses of renewable-energy-based multigeneration, considering several options for producing such products as electricity, heat, hot water, cooling, hydrogen, and fresh water. Ahmadi et al. [75] studied the exergo-environmental analysis of an integrated organic Rankine cycle for polygeneration to produce electricity, heating, cooling and hot water. The system analyzed consists of a gas turbine cycle, an organic Rankine cycle (ORC), a single effect absorption chiller and a domestic water heater. The exergy efficiency of the trigeneration system is found to be higher than that of typical combined heat and power systems or gas turbine cycles. The results also indicate that carbon dioxide emissions for the trigeneration system are less than for the aforementioned systems. The exergy results show that combustion chamber has the largest exergy destruction of the cycle components, due to the irreversible nature of its chemical reactions and the high temperature difference between the working fluid and flame temperature.

Ahmadi et al. [76] studied a thermodynamic modeling and assessment of an integrated biomass-based multigeneration energy system. They analyzed a new multigeneration system based on a biomass combustor, an organic Rankine cycle (ORC), an absorption chiller and a proton exchange membrane electrolyzer to produce hydrogen, and a domestic water heater for hot water production, is proposed and thermodynamically assessed. Also, they conducted exergy analysis to determine the irreversibilities in each component and the system performance. In addition, an environmental impact assessment of the multigeneration system was performed, and the potential reduction in CO_2 emissions when the system shifts from power generation to multigeneration are investigated.

Ahmadi et al. [8] carried out an exergy-based optimization of a multigeneration energy system. They considered a multigeneration energy system with a gas turbine as the prime mover to produce electricity, heating, cooling and domestic hot water, and applied a multi-objective evolutionary based optimization to find the best design parameters of the system considering exergy efficiency and total cost of the system as two objective functions.

The research reported to date suggests that multigeneration is often advantageous for mitigating global warming and increasing efficiency. However, complete energy, exergy, and environmental impact assessments of a multigeneration based on micro gas turbine and ejector refrigeration system, biomass based multigeneration system and ocean thermal energy conversion based multigeneration system have not been reported in the literature. Also, a fast and elitist non-dominated sorting genetic algorithm (NSGA-II) based multi-objective optimization for such complex systems has not been used yet in such research.

6.3 Descriptions of Case Studies

In this section, three novel multigeneration energy systems are modeled, analyzed and compared. The system products include electricity, heating, cooling, hot water, fresh water and hydrogen, and various sources of energy are considered like heat source from conventional to renewable energy sources.

Case study I: Multigeneration System Based on Gas Turbine Prime Mover

A gas turbine is mature and advantageous prime mover for many reasons, so it is used in one of the multigeneration energy systems considered here. This system is comprised of five subsystems (see Fig. 6.6).Electricity is produced by a gas turbine and a steam turbine while cooling is produce based on two different cycles, a single effect absorption chiller and an ejector refrigeration cycle. To produce hydrogen, a

PEM electrolyzer is used driven by electricity produced by the ejector. A domestic water heater uses the energy from the absorption generator. A more complete explanation of each subsystem is given below.

Figure 6.6 illustrates an integrated multigeneration system containing a compressor, a combustion chamber (CC), a gas turbine, a double pressure heat recovery steam generator (HRSG) to produce superheated steam, a single effect absorption chiller, a heat recovery vapor generator (HRVG) to produce ORC vapor that is driven by heat from flue gases from the HRSG, an organic Rankine cycle (ORC) ejector refrigeration system, a PEM electrolyzer for hydrogen production and a domestic water heater for hot water production. Air at ambient conditions enters the air compressor at point 1 and exits after compression (point 2). The hot air enters the combustion chamber (CC) into which fuel is injected, and hot combustion gases exit (point 3) and pass through a gas turbine to produce shaft power. The hot gas expands in the gas turbine to point 4. Hot flue gases enter the double pressure HRSG to provide high and low pressure steam at points 5 and 14. High pressure steam enters the steam turbine to generate shaft power while the low pressure steam enters the generator of the absorption system to provide the cooling load of the system. The low pressure line leaving the generator has adequate energy for use in a domestic water heater that provides hot water at 50 °C. Furthermore, flue gases leaving the HRSG at point *C* enter a heat recovery vapor generator to provide electricity and cooling. Since the flue gases have a low temperature, around 160 °C, an ORC cycle is used, consisting of an ORC turbine to generate electricity and a steam ejector to provide the system cooling load. These flue gases enter the HRVG at point *d* to produce saturated vapor at point 29, which leaves the HRVG at point 28. Saturated vapor at point 29 enters the ORC turbine and work is produced. The extraction turbine and ejector play important roles in this combined cycle. The high pressure and temperature vapor is expanded through the turbine to generate power, and the extracted vapor from the turbine enters the supersonic nozzle of the ejector as the primary vapor. The stream exiting the ejector (point 33) mixes with turbine exhaust (point 31) and is cooled in the preheater and enters the condenser where it becomes a liquid by rejecting heat to the surroundings. Some of the working fluid leaving the condenser enters the evaporator after passing through the throttle valve (point 39), and the remainder flows back to the pump (point 37). The ORC pump increases the pressure (point 40), and high pressure working fluid is heated in the preheater (point 41) before entering the HRVG. The low pressure and temperature working fluid after the valve (point 39) enters the evaporator, providing a cooling effect for space cooling. Some of the electricity is considered for residential applications while some directly drives a PEM electrolyzer to produce hydrogen. In this analysis, waste heat is used as a heat source to stimulate the multigeneration system and R123 is selected as the working fluid because it is a non-toxic, non-flammable and non-corrosive refrigerant with suitable thermophysical characteristics.

Case study II: Biomass Based Multigeneration System

Renewable energy is a source of energy which comes from natural resources such as sunlight, wind, rain, tides, waves, geothermal heat and biomass. These are naturally replenished when used. Biomass, as a renewable energy source, is biological material from living, or recently living, organisms [77].

Comprehensively, biomass comprises all the living matter present on Earth and, as an energy source, biomass can either be used directly, or converted into other energy products such as biofuels [77]. Currently, biomass resources are mainly used in the production of heating, cooling and electricity. Direct combustion of biomass with coal is the most common method of conversion and provides the greatest potential for large scale utilization of biomass energy in the near term [78]. Other thermochemical conversion technologies such as gasification and pyrolysis are technically feasible and potentially efficient, compared to combustion, for power generation. However, these technologies either lack of maturity and reliability or are not economically viable for large scale utilization [79]. Biomass based cogeneration systems are studied over many years by numerous researchers for various industries (e.g., sugar, rice, palm oil, paper and wood) as a means of waste disposal and energy recovery [80].

Figure 6.7 illustrates an integrated multigeneration system containing a biomass combustor, an ORC cycle to produce electricity, a double-effect absorption chiller for cooling, a heat exchanger for heating, a proton exchange membrane (PEM) electrolyzer to produce hydrogen, a domestic water heater to produce hot water and a reverse osmosis (RO) desalination to produce fresh water. Pine sawdust is used as the biomass fuel and burned in a biomass combustor. The heat from the biomass combustor is input to the ORC cycle. The waste heat from the ORC is utilized to produce steam in the heating process via the heat exchanger, and to produce cooling using a double-effect absorption chiller. To have an efficient ORC, its working fluid should have a high critical temperature so that the waste heat can be used more efficiently [75]. A typical organic fluid used in ORCs is n-octane, which has a relatively high critical temperature (569 K) [76]. This organic fluid is selected here as the working fluid of the ORC. The ORC cycle produces electricity, part of which is used for residential applications depending on electricity needs of the building, and the remainder of which drives a PEM electrolyzer for hydrogen production and RO desalination to produce fresh water. The hydrogen and fresh water are stored in a hydrogen tank and fresh water tank respectively. Since the flue gases leaving the ORC evaporator still have energy, they are utilized to produce hot water in a domestic water heater.

As shown in Fig. 6.7 biomass enters the combustor at point 30 and air enters at point 29. Hot flue gases leave the biomass combustor at point 31 and then enter a cyclone to remove the ash. Hot flue gases without ash enter an ORC evaporator to produce steam at point 27 to rotate the ORC turbine blades and produce shaft work. The high-pressure and temperature vapor at point 27 is expanded through the turbine to generate power, and the extracted vapor from the turbine enters the heat exchanger for the heating process. Saturated vapor leaves the heating process unit

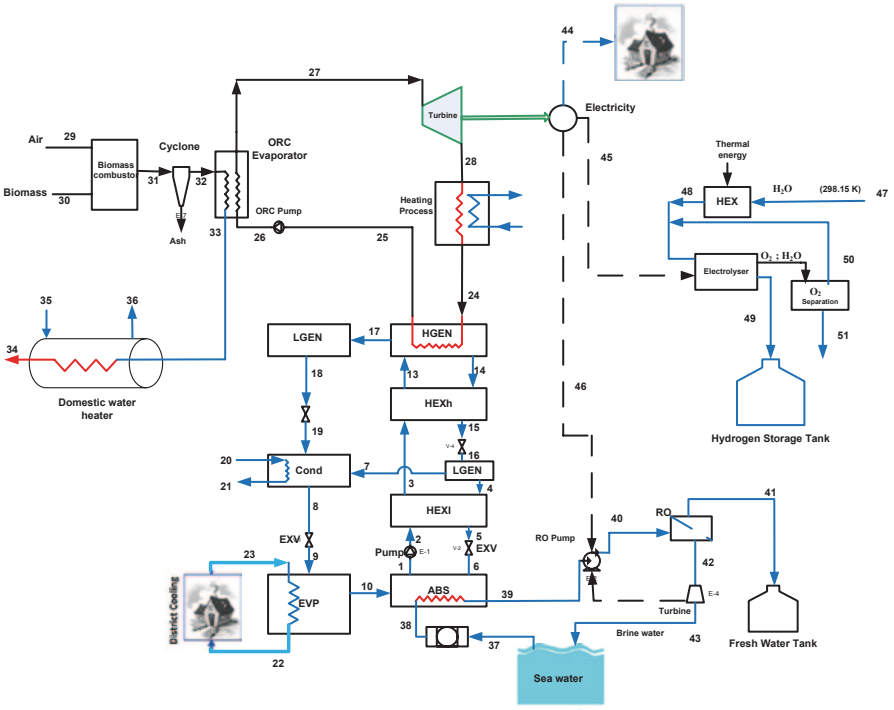

Fig. 6.7 Schematic of biomass based a multigeneration energy system for the provision of heating, cooling, electricity, hydrogen, fresh water and hot water [5]

at point 24. This saturated steam enters the generator of the double-effect absorption system to provide the cooling load of the system. Saturated liquid leaves the absorption generator and enters the ORC pump at point 25. ORC pump increase the pressure of ORC working fluid and high pressure ORC fluid enters the ORC evaporator at point 26 to close the ORC power generation unit. Since flue gases leaving the ORC evaporator still have energy, a domestic water heater is used to utilize the energy of the hot gases at point 33. Water enters the domestic water heater at point 35 and hot water leave the domestic water heater at point 36. Reverse osmosis (RO) desalination is used to produce fresh water as shown right bottom side of Fig. 6.9.

Sea water at point 37 enters a filter to remove dissolved species and then passes through the absorber of the double-effect absorption chiller to increase the temperature to improve the efficiency of the OR desalination unit. A high pressure RO pump is used to increase the pressure of the water. High pressure sea water leaves the RO pump and enters the RO unit at point 40. Fresh water is produced at point 41 and stored in a fresh water tank for the later use while high pressure brine water enters a hydraulic turbine to reduce the pressure and generate electricity. Finally, low pressure brine water leaves the RO unit and sends back to the sea. The cooling load of the system is provided by a double-effect absorption chiller. Weak Li-Br solution at point a is pumped through an high pressure solution leaves the pump at point 2 then

passes through a high temperature heat exchanger to increase the temperature. High temperature weak solution then enters the high temperature heat exchanger at point 3 and the high temperature weak solution enters the high temperature generator. In high temperature generator water is removed from the solution and the strong solution sends back to the absorber after passing through the high and low temperature heat exchangers. On the other side, vapor leaves the high temperature generator at point 17 and enters the low temperature generator. The refrigerant steam produced by the low pressure generator is condensed by the cooling water and then enters the expansion valve at point 8 to reduce the pressure and enters the evaporator at point 9. This low pressure vapor enters the evaporator and saturated vapor leaves the evaporator at point 10 and enters the absorber. The absorption heat is removed by the sea water entering the absorber at point 38 to improve the efficiency of the RO desalination unit.

Case Study III: Integrated Ocean Thermal Energy Conversion Multigeneration System

A large amount of solar energy is stored as heat in the surface waters of the world's oceans, providing a source of renewable energy. Ocean thermal energy conversion (OTEC) is a process for harnessing this renewable energy in which a heat engine operates between the relatively warm ocean surface, which is exposed to the sun, and the colder (about 5 °C) water deeper in the ocean, in order to produce electricity. OTEC usually incorporates a low-temperature Rankine cycle engine which boils a working fluid such as ammonia to generate a vapor which turns the turbine to generate electricity, and then is condensed back into a liquid in a continuous process. 80 % of the energy that is received from the sun by the earth is stored in the world's oceans [81, 82], and many regions of the world have access to this OTEC resource. OTEC can produce fuels by using its product electricity to produce hydrogen, which can be used in hydrogen fueled cars as well as in the development of synthetic fuels. For a small city, millions of tons of CO_2 are generated annually through fossil fuel use while with OTEC the value is zero, during the operation of devices. OTEC has a potential to replace some fossil fuel use, perhaps via OTEC ships travelling the seas of the world.

An OTEC system utilizes low-grade energy and has a low energy efficiency (approximately 3–5 %). Therefore, achieving a high electricity generating capacity with OTEC requires the use of large quantities of seawater, and a correspondingly, large amounts of pumping power. These factors have negative impact on the cost-effectiveness of this technology and therefore OTEC is not commercially viable today. In order to improve the effectiveness and economics of OTEC cycles, it is proposed to integrate them with industrial operations so that, apart from generating electricity, they could be used for fresh water production, air conditioning and refrigeration, cold water agriculture, aquaculture and mariculture, and hydrogen

production [81]. Potential markets for OTEC have been identified, most of which are in the Pacific Ocean, and about 50 countries are examining its implementation as a sustainable source of energy and fresh water, including India, Korea, Palau, Philippines, the U.S. and Papua New Guinea [83]. In 2001, as a result of cooperation between Japan and India, a 1-MW OTEC plant was built in India [83], and others are planned to be constructed in the near future [84].

Considerable research has been directed to the development of OTEC recently. Uehara [85–87] conducted numerous theoretical and experimental studies on the major components of an OTEC plant, and showed that ammonia is a suitable working fluid for an OTEC plant employing a closed organic Rankine cycle (ORC). The energy efficiency of the Rankine cycle in an OTEC plant is usually limited to around 5 % due to the small temperature differences between surface water and deep water of the ocean. Thus, in order to improve the efficiency of OTEC, other thermodynamic cycles such as the Kalina cycle and the Uehara cycle that use an ammonia–water mixture as the working fluid are being considered [88]; they are reported to have better energy efficiencies than a Rankine cycle at the same temperature difference [88]. Increasing in the temperature difference between the hot heat source and the cold heat sink can improve the efficiency of OTEC plants, as can the integration of OTEC with other energy technologies. Saitoh and Yamada [88] proposed a conceptual design of a multiple Rankine-cycle system using both solar thermal energy and ocean thermal energy in order to improve the cycle efficiency.

Figure 6.8 shows a schematic diagram of an integrated OTEC system equipped with a flat plate and PV/T solar collector, a reverse osmosis (RO) desalination unit, a single effect absorption chiller and PEM electrolyzer. This integrated system uses the warm surface seawater to evaporate a working fluid such as ammonia or a Freon refrigerant, which drives an ORC turbine to produce electricity, which in turn is used to drive a PEM electrolyzer to produce hydrogen. After passing through the turbine, the vapor is condensed in a heat exchanger that is cooled by cold deep seawater. The working fluid is then pumped back through the warm seawater heat exchanger, and the cycle is repeated continuously. Warm surface water is pumped from the ocean surface at point 1. A warm surface pump increases the pressure where the high pressure warm water enters a flat plate collector at point 2 to increase its temperature. Water enters an evaporator at point 3 and after a heat exchange with the ORC fluid, leaves the evaporator at point 4 where it is flushed back to the ocean surface.

A PV/T solar panel is considered to provide the cooling load of the system. Air enters the PV/T panel at point 41 and, after absorbing the sun's heat using its panels, its temperature increases. Next, the hot air leaves the PV/T at point 40 and enters the absorption chiller generator in order to run the chiller. The electricity generated by PV/T is directed to derive a RO desalination plant to produce fresh water. In this multigeneration system, a provision of the electricity generated by OTEC plant is used to produce hydrogen using a PEM electrolyzer at point 22. The produced hydrogen is stored in a hydrogen storage tank for later usage.

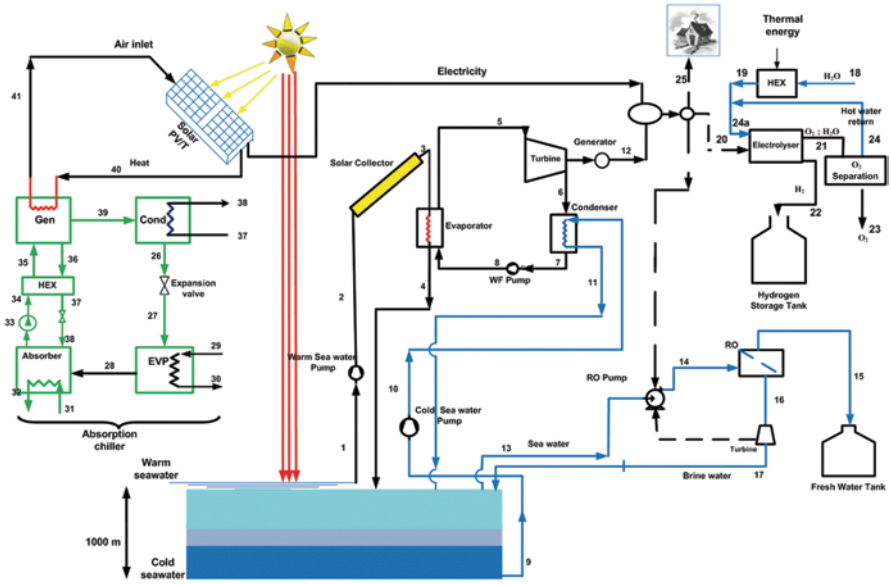

Fig. 6.8 Schematic of an integrated renewable based multigeneration energy system for the provision of cooling, electricity, hydrogen, fresh water [5]

6.4 Exergy Analyses

Exergy analysis can help develop strategies and guidelines for more efficient and effective use of energy, and is utilized to study various thermal processes, especially power generation, CHP, trigeneration and multigeneration. The exergy of a substance is often divided into four components. Two common ones are physical and chemical exergy. The two others, kinetic and potential exergy, are assumed to be negligible here, as elevation changes are small and speeds are relatively low [29, 47, 76]. Physical exergy is defined as the maximum useful work obtainable as a system interacts with an equilibrium state. Chemical exergy is associated with the departure of the chemical composition of a system from its chemical equilibrium and is considered important in processes involving combustion and other chemical changes [88–90]. Through the second law of thermodynamics, the following exergy rate balance is written as

$$\dot{E}x_Q + \sum_i \dot{m}_i ex_i = \sum_e \dot{m}_e ex_e + \dot{E}x_W + \dot{E}x_D \tag{6.1}$$

where subscripts i and e denote the control volume inlet and outlet flow, respectively, $\dot{E}x_D$ is the exergy destruction rate and other terms are given as follows:

$$\dot{E}x_Q = \left(1 - \frac{T_0}{T_i}\right)\dot{Q}_i \tag{6.2}$$

$$\dot{E}x_w = \dot{W} \tag{6.3}$$

$$ex = ex_{ph} + ex_{ch} \tag{6.4}$$

Here, $\dot{E}x_Q$ is the exergy rate of heat transfer crossing the boundary of the control volume at absolute temperature T, the subscript 0 refers to the reference environment conditions and $\dot{E}x_W$ is the exergy rate associated with shaft work. Also, ex_{ph} is defined as follows:

$$ex_{ph} = (h - h_0) - T_0(s - s_0) \tag{6.5}$$

The specific chemical exergy for gas mixtures is defined as follows [90]:

$$ex_{mix}^{ch} = \left[\sum {}_{i=1}^{n} x_i ex_i^{ch} + RT_0 \sum {}_{i=1}^{n} x_i \ln x_i\right] \tag{6.6}$$

The above equation cannot be used to evaluate fuel exergy. Here, fuel exergy is approximated with the following simplification [29, 90]:

$$\xi = \frac{ex_f}{LHV_f} \tag{6.7}$$

The ratio of chemical exergy to LHV_f is usually close to unity for common gaseous fuels, e.g., $\xi_{CH_4} = 1.06$, $\xi_{H_2} = 0.985$

For a general gaseous fuel with composition C_xH_y, the following experimental correlation can be used for ξ [90]:

$$\xi = 1.033 + 0.0169\frac{y}{x} - \frac{0.0698}{x} \tag{6.8}$$

Exergy Analysis of System I

Here, the exergy of each flow is calculated at all states and the changes in exergy are determined for each major component. The exergy destructions for all components in this multigeneration system are shown in Table 6.1. Since in this multigeneration energy system, a combustion reaction occurs in combustion chamber, it is important to calculate the chemical exergy where combustion takes place and where the solution is not real such as LiBr solution. Chemical exergy is equal to the maximum amount of work that can be obtained when a substance is brought from the reference-environment state to the dead state by a process including heat transfer and exchange of substances only with the reference environment. The maximum work

Table 6.1 Expressions for exergy destruction rates for components of system I

Component	Exergy destruction rate expression
Air compressor	$\dot{E}x_{D,AC} = \dot{E}x_1 - \dot{E}_2 - \dot{W}_{AC}$
Combustion chamber (CC)	$\dot{E}x_{D,CC} = \dot{E}x_2 + \dot{E}x_f - \dot{E}x_3$
Gas turbine (GT)	$\dot{E}x_{D,GT} = \dot{E}x_3 - \dot{E}x_4 - \dot{W}_{GT}$
HRSG	$\dot{E}x_{D,HRSG} = \dot{E}x_4 + \dot{E}x_8 - \dot{E}x_5 - \dot{E}x_c$
Steam turbine (ST)	$\dot{E}x_{D,ST} = \dot{E}x_5 - \dot{E}x_6 - \dot{W}_{ST}$
Steam condenser	$\dot{E}x_{D,Cond} = \dot{E}x_6 + \dot{E}x_{49} - \dot{E}x_7 - \dot{E}x_{50}$
Pump	$\dot{E}x_{D,P} = \dot{E}x_7 - \dot{E}x_8 + \dot{W}_P$
Heat recovery vapor generator	$\dot{E}x_{D,HRVG} = \dot{E}x_c + \dot{E}x_{41} - \dot{E}x_{28} - \dot{E}x_{29}$
ORC turbine	$\dot{E}x_{D,ORCT} = \dot{E}x_{29} - \dot{W}_{ORC} - \dot{E}x_{30} - \dot{E}x_{31}$
Ejector	$\dot{E}x_{D,Ejector} = \dot{E}x_{30} + \dot{E}x_{32} - \dot{E}x_{33}$
Preheater	$\dot{E}x_{D,PRH} = \dot{E}x_{34} + \dot{E}x_{40} - \dot{E}x_{35} - \dot{E}x_{41}$
ORC pump	$\dot{E}x_{D,ORCPump} = \dot{E}x_{37} + \dot{W}_{ORC} - \dot{E}x_{40}$
ORC condenser	$\dot{E}x_{D,Cond} = \dot{E}x_{35} - \dot{E}x_{36} - \dot{E}x_{Q,Cond}$
ORC evaporator	$\dot{E}x_{D,EVP} = \dot{E}x_{39} + \dot{E}x_{40} - \dot{E}x_{32} - \dot{E}x_{41}$
ORC expansion valve	$\dot{E}x_{D,EXV} = \dot{E}x_{38} - \dot{E}x_{39}$
Domestic water heater	$\dot{E}x_{D,DWH} = \dot{E}x_{15} + \dot{E}x_{17} - \dot{E}x_{16} - \dot{E}x_{18}$
PEM electrolyzer	$\dot{E}x_{D,PEM} = \dot{E}x_{42} + \dot{W}_{PEM} - \dot{E}x_{46} - \dot{E}x_{47} + \dot{E}x_Q$
Absorption condenser	$\dot{E}x_{D,Cond} = \dot{E}x_{19} - \dot{E}x_{20} - \dot{E}x_Q$
Absorption expansion valve	$\dot{E}x_{D,EXV} = \dot{E}x_{20} - \dot{E}x_{21}$
Absorption evaporator	$\dot{E}x_{D,EVP} = \dot{E}x_{21} - \dot{E}x_{22} + \dot{E}x_Q$
Absorber	$\dot{E}x_{D,Abs} = \dot{E}x_{22} + \dot{E}x_{23} - \dot{E}x_{25} - \dot{E}x_Q$
Absorption pump	$\dot{E}x_{D,P} = \dot{E}x_{25} + \dot{W}_P - \dot{E}x_{26}$
Absorption heat exchanger	$\dot{E}x_{D,HEX} = \dot{E}x_{26} + \dot{E}x_{14'} - \dot{E}x_{24} - \dot{E}x_{27}$
Absorption generator	$\dot{E}x_{D,Gen} = \dot{E}x_{14} + \dot{E}x_{27} - \dot{E}x_{15} - \dot{E}x_{14'} - \dot{E}x_{19}$

is attained when the process is reversible. Alternatively, chemical exergy can also be viewed as the exergy of a substance that is at the reference-environment state.

Chemical exergy is also equivalent to the minimum amount of work necessary to produce a substance at the reference-environment state from the constituents in the reference environment. Chemical exergy has two main parts, reactive exergy resulting from the chemical reactions necessary to produce species which do not exist as stable components in the reference environment, and concentration exergy resulting from the difference between the chemical concentration of a species in a system and its chemical concentration in the reference environment [47]. The concentration part is related to the exergy of purifying or diluting a substance, such as separating oxygen from air.

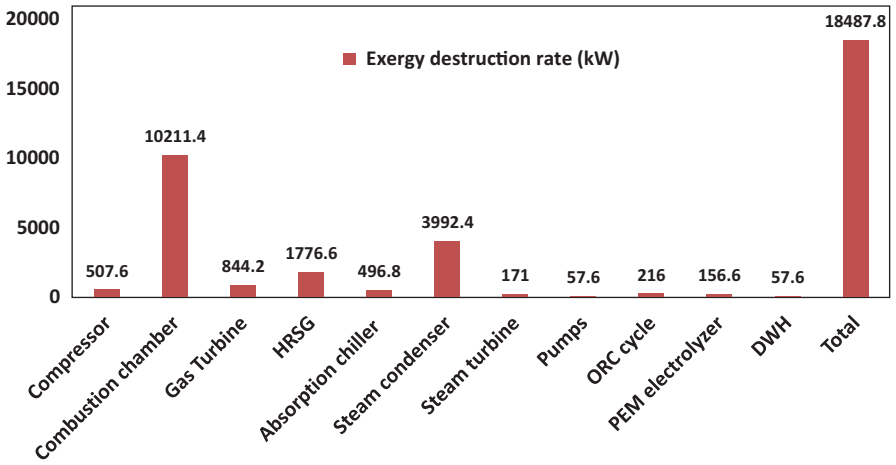

Fig. 6.9 Exergy destruction rates for the gas turbine multigeneration system and its components

As shown in Fig. 6.9, combustion reaction occurs in combustion chamber where the energy of fuel is converted to increase the temperature at gas turbine inlet temperature. Since chemical component of the gasses leaving the combustion chamber differ from the one in the reference environment, we should use chemical exergy of mixture to calculate the chemical exergy at at point 3 in Fig. 6.6.Therefore, we should first define the partial pressures and molar fractions of various constituents of air.

Exergy Analysis of System II

Here, the exergy of each flow is calculated at all states and the changes in exergy are determined for each major component. The exergy destructions for all components in this multigeneration system (Fig. 6.7) are listed in Table 6.2.

The exergy efficiency, defined as the product exergy output divided by the exergy input [47], can be expressed for the ORC power generation unit, the CHP unit and the multigeneration system as follows:

$$\psi_{ORC} = \frac{\dot{W}_{net,ORC}}{\dot{E}x_{biomass}} \tag{6.9}$$

$$\psi_{CHP} = \frac{\dot{W}_{net,ORC} + \dot{E}x_{heating}}{\dot{E}x_{biomass}} \tag{6.10}$$

$$\psi_{multi} = \frac{\dot{W}_{net,ORC} + \dot{E}x_{heating} + \dot{E}x_{cooling} + \dot{E}x_{H_2} + \dot{E}x_{36} + \dot{E}x_{41}}{\dot{E}x_{biomass}} \tag{6.11}$$

Table 6.2 Expressions for exergy destruction rates for components of system II

Component	Exergy destruction rate expression
Combustor	$\dot{E}x_{D,Comb} = \dot{E}x_{29} + \dot{E}x_{30} - \dot{E}x_{31}$
ORC evaporator	$\dot{E}x_{D,Evp} = \dot{E}x_{32} + \dot{E}x_{26} - \dot{E}x_{27} - \dot{E}x_{33}$
ORC turbine	$\dot{E}x_{D,T} = \dot{E}x_{27} - \dot{W}_T - \dot{E}x_{28}$
Heating process	$\dot{E}x_{D,heat} = \dot{E}x_{28} - \dot{E}x_Q - \dot{E}x_{24}$
ORC pump	$\dot{E}x_{D,P} = \dot{E}x_{25} + \dot{W}_P - \dot{E}x_{26}$
Absorption condenser	$\dot{E}x_{D,Cond} = \dot{E}x_{19} + \dot{E}x_{20} - \dot{E}x_8 - \dot{E}x_{21} + \dot{E}x_7$
Expansion valves	$\dot{E}x_{D,Exv} = \dot{E}x_{18} - \dot{E}x_{19} + \dot{E}x_8 - \dot{E}x_9 + \dot{E}x_{15} - \dot{E}x_{16} + \dot{E}x_5 - \dot{E}x_6$
Absorption evaporator	$\dot{E}x_{D,Evp} = \dot{E}x_9 + \dot{E}x_{21} - \dot{E}x_{23} - \dot{E}x_{10}$
Absorber	$\dot{E}x_{D,Abs} = \dot{E}x_{10} + \dot{E}x_6 + \dot{E}x_{38} - \dot{E}x_1 - \dot{E}x_{39}$
Absorption pump	$\dot{E}x_{D,P} = \dot{E}x_1 + \dot{W}_P - \dot{E}x_2$
Absorption heat exchanger I	$\dot{E}x_{D,HExI} = \dot{E}x_2 + \dot{E}x_4 - \dot{E}x_3 - \dot{E}x_5$
Absorption heat exchanger h	$\dot{E}x_{D,HExh} = \dot{E}x_3 + \dot{E}x_{14} - \dot{E}x_{13} - \dot{E}x_{15}$
High temperature absorption generator	$\dot{E}x_{D,Genh} = \dot{E}x_{24} + \dot{E}x_{13} - \dot{E}x_{14} - \dot{E}x_{17} - \dot{E}x_{25}$
Low temperature absorption generator	$\dot{E}x_{D,GenL} = \dot{E}x_{17} - \dot{E}x_{18} - \dot{E}x_Q$
PEM electrolyzer	$\dot{E}x_{D,PEM} = \dot{E}x_{22} + \dot{W}_{PEM} - \dot{E}x_{24} - \dot{E}x_{23}$
Domestic hot water heater	$\dot{E}x_{D,DWH} = \dot{E}x_{33} + \dot{E}x_{35} - \dot{E}x_{36} - \dot{E}x_{34}$
RO pump	$\dot{E}x_{D,ROPump} = \dot{E}x_{39} + \dot{W}_P - \dot{E}x_{40}$
RO desalination unit	$\dot{E}x_{D,ROdesalination} = \dot{E}x_{40} - \dot{E}x_{41} - \dot{E}x_{42}$
RO hydraulic turbine	$\dot{E}x_{D,hturbine} = \dot{E}x_{42} - \dot{W}_T - \dot{E}x_{43}$

where

$$\dot{E}x_{heating} = \dot{Q}_{cond}\left(1 - \frac{T_0}{T_{cond}}\right) \tag{6.12}$$

$$\dot{E}x_{cooling} = \dot{Q}_{cooling}\left(\frac{T_0 - T_{EVP}}{T_{EVP}}\right) \tag{6.13}$$

$$\dot{E}x_{H_2} = \dot{m}_{H_2} ex_{H_2} \tag{6.14}$$

$$\dot{E}x_{35} = \dot{m}_{35}(h_{35} - h_0) - T_0(s_{35} - s_0) \tag{6.15}$$

Also, $\dot{E}x_{biomass}$ is the exergy of biomass, defined as [24]:

$$\dot{E}x_{biomass} = \dot{m}_{biomass}\beta LHV_{mois} \tag{6.16}$$

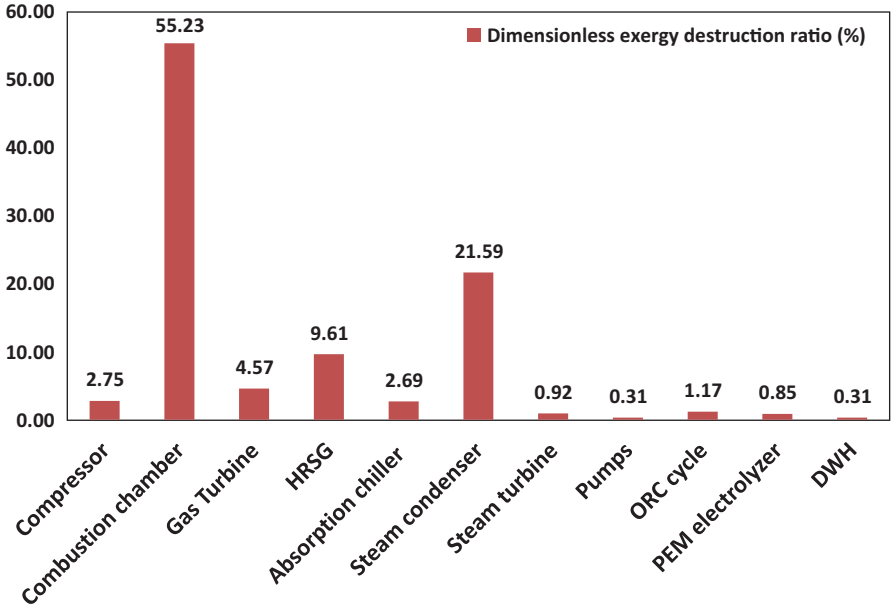

Fig. 6.10 Dimensionless exergy destruction ratio for the multigeneration system I and its components

Here, β is defined as

$$\beta = \frac{1.0414 + 0.0177\left(\frac{\mathrm{H}}{\mathrm{C}}\right) - 0.3328\left(\frac{\mathrm{O}}{\mathrm{C}}\right)\left\{1 + 0.0537\left(\frac{\mathrm{H}}{\mathrm{C}}\right)\right\}}{1 - 0.4021\left(\frac{\mathrm{O}}{\mathrm{C}}\right)} \tag{6.17}$$

Exergy Analysis of System III

The exergy destructions for all components in multigeneration system III (Fig. 6.10) are shown in Table 6.3.The exergy efficiency is defined as the product exergy output divided by the exergy input. According to Yamada et al. [88], the exergy efficiency of the ORC power generation cycle in an OTEC system is given as

$$\psi_{Power} = \frac{\dot{W}_{net}}{\dot{E}x_m} = \frac{\dot{W}_{net,OTEC}}{\dot{E}x_{in,WS} + \dot{E}x_{in,CS}} \tag{6.18}$$

$$\psi_{CHP} = \frac{\dot{W}_{net,OTEC} + \dot{W}_{PV/T}}{\dot{E}x_{in,WS} + \dot{E}x_{in,CS} + \dot{E}x_{Sun}} \tag{6.19}$$

Table 6.3 Expressions for exergy destruction rates for components of system III

Component	Exergy destruction rate expression
Warm sea water pump	$\dot{E}x_{D,P} = \dot{E}x_1 + \dot{W}_P - \dot{E}x_2$
Cold sea water pump	$\dot{E}x_{D,P} = \dot{E}x_9 + \dot{W}_P - \dot{E}x_{10}$
Solar collector	$\dot{E}x_{D,collector} = \dot{E}x_2 + \dot{E}x_{sun} - \dot{E}x_3$
Turbine	$\dot{E}x_{D,T} = \dot{E}x_5 - \dot{W}_T - \dot{E}x_6$
Condenser	$\dot{E}x_{D,Cond} = \dot{E}x_6 + \dot{E}x_{10} - \dot{E}x_7 - \dot{E}x_{11}$
WF pump	$\dot{E}x_{D,P} = \dot{E}x_7 + \dot{W}_P - \dot{E}x_8$
Solar PV/T	$\dot{E}x_{D,collector} = \dot{E}x_{41} + \dot{E}x_{sun} - \dot{E}x_{40}$
Absorption condenser	$\dot{E}x_{D,Cond} = \dot{E}x_{39} - \dot{E}x_{26} - \dot{E}x_Q$
Absorption expansion valves	$\dot{E}x_{D,EXV} = \dot{E}x_{26} + \dot{E}x_{37} - \dot{E}x_{27} - \dot{E}x_{38}$
Absorption evaporator	$\dot{E}x_{D,EVP} = \dot{E}x_{27} - \dot{E}x_{29} + \dot{E}x_Q$
Absorber	$\dot{E}x_{D,Abs} = \dot{E}x_{28} + \dot{E}x_{38} + \dot{E}x_{31} - \dot{E}x_{32} - \dot{E}x_{33}$
Absorption pump	$\dot{E}x_{D,P} = \dot{E}x_{33} + \dot{W}_P - \dot{E}x_{34}$
Absorption heat exchanger	$\dot{E}x_{D,HEX} = \dot{E}x_{34} + \dot{E}x_{36} - \dot{E}x_{35} - \dot{E}x_{37}$
Absorption generator	$\dot{E}x_{D,Gen} = \dot{E}x_{35} + \dot{E}x_{40} - \dot{E}x_{41} - \dot{E}x_{33} - \dot{E}x_{36}$
PEM electrolyzer	$\dot{E}x_{D,PEM} = \dot{E}x_{29} + \dot{W}_{PEM} - \dot{E}x_{22} - \dot{E}x_{21}$
RO pump	$\dot{E}x_{D,RO\ Pump} = \dot{E}x_{13} + \dot{W}_P - \dot{E}x_{14}$
RO desalination unit	$\dot{E}x_{D,RO\ desalination} = \dot{E}x_{14} - \dot{E}x_{10} - \dot{E}x_{15}$
RO hydraulic turbine	$\dot{E}x_{D,h\ turbine} = \dot{E}x_{16} - \dot{W}_T - \dot{E}x_{17}$

$$\psi_{multi} = \frac{\dot{W}_{net,ORC} + \dot{W}_{PV/T} + \dot{E}x_{cooling} + \dot{E}x_{H_2} + \dot{E}x_{22}}{\dot{E}x_{in,\,WS} + \dot{E}x_{in,\,CS} + \dot{E}x_{Sun}} \tag{6.20}$$

where

$$\dot{E}x_{in,WS} = \dot{m}_{in,WS}\left[(h_{WS,in} - h_0) - T_0(s_{WS,in} - s_0)\right] \tag{6.21}$$

$$\dot{E}x_{in,CS} = \dot{m}_{in,CS}\left[(h_{CS,in} - h_0) - T_0(s_{CS,in} - s_0)\right] \tag{6.22}$$

Here, the reference-environment state is taken to be $P_0 = 1.01$ bar and $T_0 = 298.15$ K.

6.5 Results and Discussion

In order to enhance the understanding of the system's performance, it is important to use several analyses to see how this performance varies with design parameters. In this section, the results of thermodynamic modeling, exergy, economic and environmental impact assessment, and optimization are explained. Exergy analysis can help develop strategies and guidelines for more efficient and effective use of energy, and is utilized to study various thermal processes, especially power generation, CHP, trigeneration and multigeneration. The exergy analysis includes the determination of the exergy destruction rate and exergy efficiency of each component in the system and also determines the overall exergy efficiency of the multigeneration system. Exergy analysis also helps to identify and quantify the source of irreversibilities in the systems that are associated with each component. Economic analysis shows the total cost rate of the system, cost of each component, cost of electricity and cost of environmental impacts.

Exergy Analysis of System I

The exergy analysis results are summarized in Fig. 6.9, and show that the highest exergy destruction occurs in the combustion chamber (CC), mainly due to the irreversibilities associated with combustion and the large temperature difference between the air entering the CC and the flame temperature. The condenser in the Rankine cycle exhibits the next largest exergy destruction, mainly due to the temperature difference between two fluid streams passing through it, but also due to the pressure drop across the device.

Figure 6.10 shows for each component the dimensionless exergy destruction ratio. This measure is useful for prioritizing exergy losses in an intuitive manner. Both exergy destruction and the dimensionless exergy destruction ratio are higher in the combustor than in other components, suggesting that it would likely be worthwhile to focus improvement efforts on this component. Moreover, the results show that the absorption cycle does not exhibit significant exergy destructions, in part because it does not directly utilize fuel energy but instead uses steam produced by the HRSG.

In order to better understand the system performance, energy and exergy efficiency of each subsystem are calculated (see Fig. 6.10). It is seen that energy and exergy efficiencies are higher for the multigeneration system compared to other cycles when it is not configured in an integrated manner. It is also seen that both energy and exergy efficiencies for the multigeneration system are almost double those of a power generation system, mainly due to an increase in the numerator of exergy efficiency.

Table 6.4 Parameter values from modeling and energy and exergy analyses of the system II

Parameter	Unit	Value
Biomass flow rate, $\dot{m}_f$	kg/s	0.30
Heating load, $\dot{Q}_{Heating}$	kW	2383
Cooling load, $\dot{Q}_{Cooling}$	kW	2560
Net output power, $\dot{W}_{Net}$	kW	500.47
Exergy efficiency, ψ	%	28.82
Absorption chiller COP	–	1.63
ORC mass flow rate, $\dot{m}_{ORC}$	kg/s	4.84
Hydrogen production mass flow rate, $\dot{m}_{H_2}$	kg/day	2
Hot water mass flow rate, $\dot{m}_{HW}$	kg/s	0.78
Fresh water mass flow rate, $\dot{m}_{fresh}$	Kg/s	1.93
Specific CO_2 emission, ε	kg/MWh	358
Total cost rate	$/h	476
Cost of environmental impact	$/h	48.47
Total exergy destruction rate	kW	5393
Power to cooling ratio	–	0.19
Power to heating ratio	–	0.20

Exergy Analysis of Case Study II

Table 6.4 lists the thermodynamic specifications of the multigeneration system, including heating and cooling loads, the electricity generated by the turbines, the COP of the absorption chiller, and the mass flow rates of biomass, hydrogen and hot water. The analysis described earlier is used to evaluate output parameters including exergy efficiency and exergy destruction rate of the components in the system considered, as well as the carbon dioxide emissions in kg/MWh. These parameters are examined while varying the ORC evaporator pinch point temperature, the ORC pump inlet temperature, the turbine inlet pressure and the biomass mass flow rate. The exergy efficiency and CO_2 emissions are calculated for three cases: electrical power, cogeneration and multigeneration. The exergy analysis results are summarized in Fig. 6.12, and show that the highest exergy destruction occurs in the combustor, mainly due to the irreversibilities associated with combustion and the large temperature difference between the air entering the combustor and the flame temperature. The double-effect absorption chiller heat exhibits the next largest exergy destruction, mainly due to the temperature difference between two fluid streams passing through all heat exchangers as the pressure drop across the device.

Table 6.5 Input data for the system simulation of OTEC system

Parameter	Value	Parameter	Value
Turbine isentropic efficiency, η_T	0.80	Warm seawater mass flow rate (kg/s)	150
Generator mechanical efficiency, η_G	0.90	Cold sea water mass flow rate (kg/s)	150
Working fluid pump isentropic efficiency, η_{WFP}	0.78	Cold sea water pipe length (m)	1000
Seawater pumps isentropic efficiency, η_P	0.80	Cold seawater pipe inner diameter (m)	0.70
Ambient temperature (°C)	25	Warm sea water pipe length (m)	50
Solar radiation incident on collector surface, I (W/m^2)	700	Warm sea water pipe length (m)	0.70
Warm sea water temperature, T_{WSI} (°C)	22	Solar collector effective area (m^2)	5000
Cold sea water temperature at depth of 1000 m, T_{CSI} (°C)	4	Electrolyzer working temperature (°C)	80
PV/T solar collector length (m)	1.2	PV/T solar collector width (m)	0.54
Absorption chiller evaporator temperature (°C)	5	OTEC evaporator pinch point temperature (°C)	3
Sea water salinity (ppm)	36000	PV/T air mass flow rate (kg/s)	2

Exergy Analysis Results for Case Study III

In order to conduct the simulation, input data are required. For each subsystem certain reliable data are inputted to the simulation code in order to determine the outputs. Table 6.5 lists the input parameters for the OTEC system simulation. In addition, Table 6.6 lists the parameter used to simulate the PEM electrolyzer. Table 6.7 lists the thermodynamic specifications of the multigeneration system, including cooling load, the electricity generated by the turbines, the COP of the absorption chiller, and the mass flow rates of biomass, hydrogen, hot water and fresh water production.

The exergy analysis results are summarized in Fig. 6.13, and show that the highest exergy destruction occurs in the solar collectors, mainly due to the irreversibilities associated with the high temperature of sun which creates high exergy input. Moreover, the temperature difference between the solar cell and inlet air temperature results in a significant entropy generation. The OTEC Rankine cycle exhibits the next largest exergy destruction, mainly due to the temperature difference between two fluid streams passing through the components, along with the pressure drop across the device Fig. 6.11.

Table 6.6 Input parameters used to model PEM electrolysis

Parameter	Value
P_{o_2} (atm)	1.0
P_{H_2} (atm)	1.0
T_{PEM} (°C)	80
$E_{\text{act,a}}$ (kJ/mol)	76
$E_{\text{act,c}}$ (kJ/mol)	18
λ_{a}	14
λ_{c}	10
D (μm)	100
J_a^{ref} (A/m^2)	1.7×10^5
J_c^{ref} (A/m^2)	4.6×10^3
F (C/mol)	96,486

Table 6.7 Parameter values resulting from energy and exergy analyses of the system III

Parameter	Value
Net power output, $\dot{W}_{net}$ (kW)	72.49
Exergy efficiency, Ψ (%)	0.37
Sustainability Index, *SI*	1.29
Total exergy destruction rate, $\dot{E}x_{D,tot}$ (kW)	1351
Hydrogen production rate, $\dot{m}_{H_2}$ (kg/hr)	0.26
Cooling load (kW)	105
Fresh water mass flow rate (kg/s)	0.23
Total cost rate ($/h)	176.35
PEM electrolyzer exergy efficiency, Ψ_{PEM} (%)	56.32
Warm surface pump power, $\dot{W}_{WS}$ (kW)	1.39
Cold surface pump power, $\dot{W}_{CS}$ (kW)	3.34
Working fluid pump power, $\dot{W}_{WF}(kW)$	1.12

Figure 6.13 shows the dimensionless exergy destruction ratio for each component. This measure is useful for prioritizing exergy losses in an intuitive manner. Both exergy destruction and the dimensionless exergy destruction ratio are higher in solar collectors than in any other component, suggesting that it would likely be worthwhile to focus improvement efforts on this component. Moreover, the results show that, the absorption cycle and RO desalination unit do not exhibit significant exergy destructions, since it does not directly utilize fuel energy but uses heat produced by the PV/T and work instead.

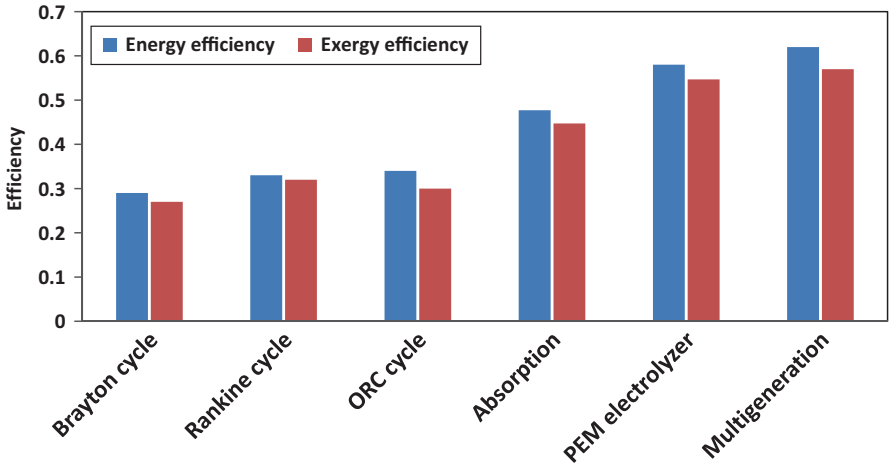

Fig. 6.11 Energy and exergy efficiency for the subsystems of the multigeneration system I

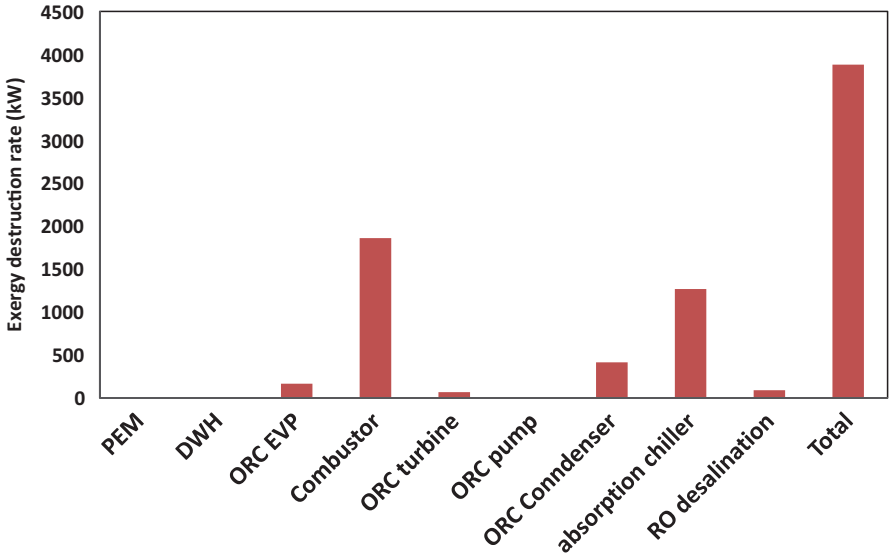

Fig. 6.12 Exergy destruction rates for the multigeneration system II and its components

6.6 Comparison and generalization

In this section, the comprehensive thermodynamic modelling, exergy analyses, environmental impact assessments, and multi-objective optimization of three newly proposed multigeneration systems for heating, cooling, electricity generation,

Table 6.8 Comparison of three novel multigeneration systems

Parameter	$\dot{W}_{net}$ (kW)	$\dot{Q}_{heat}$ (kW)	$\dot{Q}_{cooling}$ (kW)	H_2 (kg/h)	$\dot{m}_{DWH}$ (kg/s)	$\dot{m}_{FW}$ (kg/s)	$\dot{Z}_{tot}$ ($/h)	Ψ	CO_2 (kg/kWh)
System I	11038	5788	1262	1.25	3.58	NA	1090	0.60	132
System II	500	2383	2560	0.08	0.8	1.9	476	0.3	0.36
System III	73	NA	105	0.2	NA	0.2	152	0.37	0

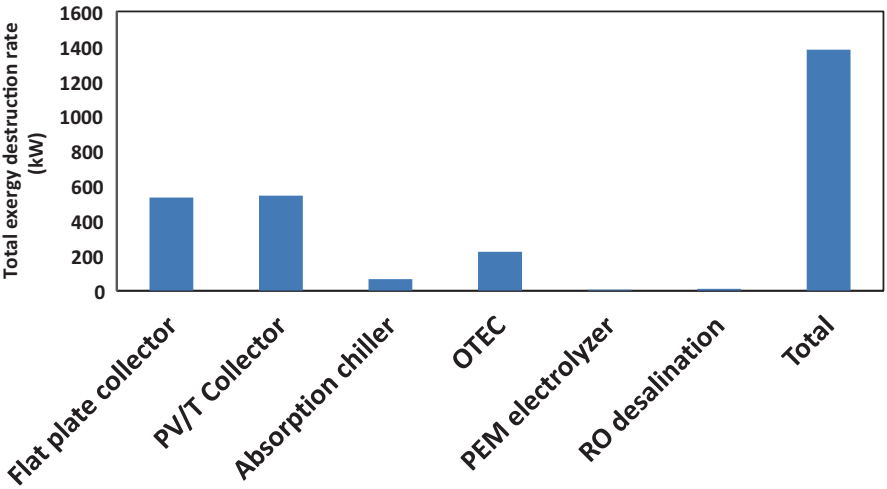

Fig. 6.13 Exergy destruction rates for the Integrated OTEC based multigeneration system and its components

hydrogen, hot water and fresh water productions are reported for insights they provide. Since these three systems have different prime movers, the comparison needs different criteria. Table 6.8 lists the useful outputs of each multigeneration energy system. This data shows that although the net power output of system I is much higher than that of alternative systems, the CO_2 emissions and total cost rate are higher compared to other systems fig. 6.14.

Since the capacity of each system is different, it is difficult to meaningfully compare them. One approach is to normalize each system and then compare them. In order to normalize the cost, the total cost rate of each system is divided by the energy of useful outputs and the final cost per kWh of products is compared. The following equations are used to normalize the cost:

$$C_{System} = \frac{\dot{Z}_{tot,I}}{\sum \dot{W}_{net} + \sum \dot{Q}_{heat} + \sum \dot{Q}_{cooling} + \dot{E}n_{H_2} + \dot{E}n_{DWH} + \dot{E}n_{FW}} \tag{6.23}$$

Here,

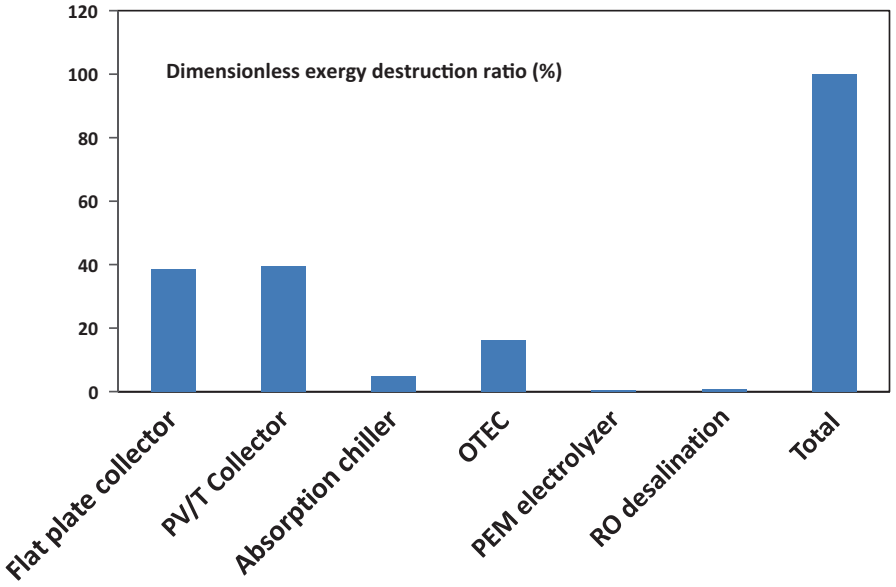

Fig. 6.14 Dimensionless exergy destruction ratio for the multigeneration system III and its components

Table 6.9 Comparison of normalized cost for each multigeneration system

Name of system	Normalized cost ($/kWh)
System I (Gas turbine based)	0.06
System II (Biomass based)	0.08
System III (OTEC based)	0.71

En_{H_2} is the energy of hydrogen production, En_{DWH} is the energy of hot water at 60 °C and En_{FW} is the energy of fresh water production. Table 6.9 lists the normalized cost for each multigeneration system. The results show that the normalized cost of the gas turbine multigeneration energy system is less those other systems; however, the CO_2 emissions are relatively high. By contrast, the normalized cost of the integrated OTEC multigeneration system is higher than the other two, but does not have any CO_2 emissions at all. In conclusion, the comparison between multigeneration systems strongly depends on the stated priorities of the designers and engineers. For example, if the priority is to have a system without any emissions and the location is close to the sea, the OTEC system is the best choice. If the plant is going to be installed in a rural area with sufficient biomass, the second multigeneration system is preferred. In addition, the amount of each useful output can help designers to decide which system they should select. For instance, the gas turbine multigeneration system can provide 10 MW of electricity, while OTEC system can only provide 100 kW of electricity.

In summary, the comparison of systems indicates that there are several criteria to be considered before undertaking the design of a multigeneration energy system:

- Location of the plant.
- Electricity, heating and cooling requirements of the system.
- Budget for the system.
- Environmental concerns and global warming mitigation.
- Availability and cost of fuel for each system component.

Concluding Remarks

The comprehensive thermodynamic modeling and exergy analyses of newly proposed integrated energy systems for heating, cooling, electricity generation, hydrogen and hot water production have provided useful insights. Three different integrated multigeneration systems depending on location, energy resource availability and cost are selected and analyzed. This chapter provides several interesting results on using multigeneration energy systems to increase the overall efficiency of the plant and to provide the needs. These outcomes of this chapter can assist designers in developing more energy efficient systems in an integration fashion. Integrated energy systems have the potential to reduce environmental impacts of the systems and mitigate the global warming which eventually results in the better sustainability. Micro-gas turbine integrated system results show that the combustion chamber, steam condenser and HRSG are the main sources of irreversibility, with the high exergy destruction attributable to the high temperature difference for heat transfer in both devices and the reaction in the combustion chamber. In addition, the multigeneration cycle exhibits less CO_2 and CO emissions than micro gas turbine and CHP cycles.

The results of biomass based integrated system show that the combustor and ORC evaporator are the two main sources of irreversibility, with the highest exergy destruction rate due to the high temperature difference of heat transfer in both devices and the reaction in the combustor. System performance is notably affected by pinch point temperature, ORC turbine inlet pressure, and ORC pump inlet temperature. The results of ocean thermal energy conversion integrated energy systems show that system performance is notably affected by warm surface mass flow rate, solar radiation intensity, condenser temperature, PV/T collector length, PV/T collector width, PV/T inlet air mass flow rate and evaporator pinch point temperature difference (*PP*). Both exergy destruction and the dimensionless exergy destruction ratio are higher in solar collectors than in other components, suggesting that it would be worthwhile to focus efforts on improving this component.

Nomenclature

c_p	specific heat at constant pressure, kJ/kg°C
ex	specific exergy, kJ/kg
$\dot{E}x_D$	exergy destruction rate, kW

J	current density, A/m^2
J_o	exchange current density, A/m^2
J_i^{ref}	pre-exponential factor, A/m^2
L	length, m
h	specific enthalpy, kJ/kg
$\dot{m}$	mass flow rate, kg/s
$\dot{N}$	molar mass flow rate, mol/s
T	temperature (°C)
P	pressure, kPa
$\dot{Q}$	heat transfer rate, kW
R	gas constant, kJ/kg K
R_{PEM}	proton exchange membrane resistance, Ω
s	specific entropy, kJ/kg K
V	voltage potential, V
V_0	reversible potential, V
V_{act}	activation overpotential, V
$V_{act,a}$	anode activation overpotential, V
$V_{act,c}$	cathode activation overpotential, V
$\dot{W}$	work rate (kW)

Greek Letters

η	energy efficiency
λ_a	water content at the anode-membrane interface, Ω^{-1}
λ_c	water content at the cathode-membrane interface, Ω^{-1}
$\lambda(x)$	water content at location x in the membrane, Ω^{-1}
σ_{PEM}	proton conductivity in PEM (s/m)
$\sigma(x)$	local ionic PEM conductivity (s/m)
Ψ	exergy efficiency
ω	entertainment ratio

Subscripts

a	anode
c	cathode
CHP	combined heat and power
D	destruction
EXV	expansion valve
HRVG	heat recover vapor generator
HW	hot water
Multi	multigeneration
ORC	organic Rankine cycle
PRH	preheater
tot	total
WF	working fluid
Cond	Condenser

Superscripts

. rate

References

1. Dincer I (2000) Renewable energy and sustainable development: a crucial review. Renew Sustain Energy Rev 4:157–175
2. Ozgur Colpan C, Dincer I, Hamdullahpur F (2009) The reduction of greenhouse gas emissions using various thermal systems in a landfill site. Int J Global Warming 1:89–105
3. Spahni R, Chappellaz J, Stocker TF, Loulergue L, Hausammann G, Kawamura K, Flückiger J, Schwander J, Raynaud D, Masson-Delmotte V (2005) Atmospheric methane and nitrous oxide of the late Pleistocene from Antarctic ice cores Science 310:1317–1321
4. Ahmadi P, Dincer I (2010) Exergoenvironmental analysis and optimization of a cogeneration plant system using Multimodal Genetic Algorithm (MGA). Energy 35:5161–5172
5. Ahmadi P (2013) Modeling, analyses and optimization of integrated energy systems for multigeneration purposes Ph.D Disertation. University of Ontario Institute of Technology, Canada
6. Ahmadi P, Rosen MA, Dincer I (2011) Greenhouse gas emission and exergo-environmental analyses of a trigeneration energy system. Int J Greenh Gas Control 5:1540–1549
7. Dincer I, Zamfirescu C (2012) Renewable-energy-based multigeneration systems. Int J Energy Res 36:1403–1415
8. Ahmadi P, Rosen MA, Dincer I (2012) Multi-objective exergy-based optimization of a polygeneration energy system using an evolutionary algorithm. Energy 46:21–31
9. Khaliq A, Kumar R, Dincer I (2009) Performance analysis of an industrial waste heat-based trigeneration system. Int J Energy Res 33:737–744
10. Ratlamwala T, Dincer I, Gadalla M (2012) Energy and exergy analyses of an integrated solar-based desalination quadruple effect absorption system for freshwater and cooling production. Int J Energy Res 37:1569–1579
11. Horlock JH (2003) Advanced gas turbine cycles. Pergamon Press Oxford, UK.
12. Haseli Y, Dincer I, Naterer G (2008) Thermodynamic modeling of a gas turbine cycle combined with a solid oxide fuel cell. Int J Hydrog Energy 33:5811–5822
13. Srinivas N, Deb K (1994) Muiltiobjective optimization using nondominated sorting in genetic algorithms. Evolut Comput 2:221–248
14. Huangfu Y, Wu J, Wang R, Xia Z (2007) Experimental investigation of adsorption chiller for micro-scale BCHP system application. Energy Build 39:120–127
15. Mago PJ, Hueffed A, Chamra LM (2010) Analysis and optimization of the use of CHP–ORC systems for small commercial buildings. Energy Build 42:1491–1498
16. Mago PJ, Smith AD (2012) Evaluation of the potential emissions reductions from the use of CHP systems in different commercial buildings. Build Environ 53:74–82
17. Mago PJ, Hueffed AK (2010) Evaluation of a turbine driven CCHP system for large office buildings under different operating strategies. Energy Build 42:1628–1636
18. Bianchi M, De Pascale A, Melino F (2013) Performance analysis of an integrated CHP system with thermal and electric energy storage for residential application. Appl Energy
19. Havelský V (1999) Energetic efficiency of cogeneration systems for combined heat, cold and power production. Int J Refrig 22:479–485
20. Mıguez J, Murillo S, Porteiro J, Lopez L (2004) Feasibility of a new domestic CHP trigeneration with heat pump: I. Design and development. Appl Therm Eng 24:1409–1419
21. Porteiro J, Mıguez J, Murillo S, Lopez L (2004) Feasibility of a new domestic CHP trigeneration with heat pump: II. Availability analysis. Appl Therm Eng 24:1421–1429

22. Cihan A, Hacıhafızoglu O, Kahveci K (2006) Energy–exergy analysis and modernization suggestions for a combined-cycle power plant. Int J Energy Res 30:115–126
23. Barelli L, Bidini G, Gallorini F, Ottaviano A (2011) An energetic–exergetic analysis of a residential CHP system based on PEM fuel cell. Appl Energy 88:4334–4342
24. Bingöl E, Kılkış B, Eralp C (2011) Exergy based performance analysis of high efficiency poly-generation systems for sustainable building applications. Energy Build 43:3074–3081
25. El-Emam RS, Dincer I (2011) Energy and exergy analyses of a combined molten carbonate fuel cell–Gas turbine system. Int J Hydrog Energy 36:8927–8935
26. Akkaya AV, Sahin B, Huseyin Erdem H (2008) An analysis of SOFC/GT CHP system based on exergetic performance criteria. Int J Hydrog Energy 33:2566–2577
27. Al-Sulaiman FA, Dincer I, Hamdullahpur F (2010) Energy analysis of a trigeneration plant based on solid oxide fuel cell and organic Rankine cycle. Int J Hydrog Energy 35:5104–5113
28. Rosen MA, Dincer I (2003) Exergoeconomic analysis of power plants operating on various fuels. Appl Therm Eng 23:643–658
29. Ameri M, Ahmadi P, Hamidi A: Energy, exergy and exergoeconomic analysis of a steam power plant (2009) A case study. Int J Energy Res 33:499–512
30. Balli O, Aras H, Hepbasli A (2007) Exergetic performance evaluation of a combined heat and power (CHP) system in Turkey. Int J Energy Res 31:849–866
31. Balli O, Aras H, Hepbasli A (2008) Exergoeconomic analysis of a combined heat and power (CHP) system. Int J Energy Res 32:273–289
32. Kwak HY, Byun GT, Kwon YH, Yang H (2004) Cost structure of CGAM cogeneration system. Int J Energy Res 28:1145–1158
33. Pospisil J, Fiedler J, Skala Z, Baksa M (2006) Comparison of cogeneration and trigeneration technology for energy supply of tertiary buildings. WSEAS Trans Heat Mass Transf 1:262–267
34. Al-Sulaiman FA, Hamdullahpur F, Dincer I (2011) Performance comparison of three trigeneration systems using organic rankine cycles. Energy 36:5741–5754
35. Martins L, Fábrega F, d'Angelo J (2012) Thermodynamic performance investigation of a trigeneration cycle considering the influence of operational variables. Procedia Eng 42:2061–2070
36. Calva ET, Núnez MP, Toral M (2005) Thermal integration of trigeneration systems. Appl Therm Eng 25:973–984
37. Huang Y, Wang Y, Rezvani S, McIlveen-Wright D, Anderson M, Hewitt N (2011) Biomass fuelled trigeneration system in selected buildings. Energy Convers Manage Â52:2448–2454
38. Rocha M, Andreos R, Simões-Moreira J (2012) Performance tests of two small trigeneration pilot plants. Appl Therm Eng Â41:84–91
39. Huicochea A, Rivera W, Gutiérrez-Urueta G, Bruno JC, Coronas A (2011) Thermodynamic analysis of a trigeneration system consisting of a micro gas turbine and a double effect absorption chiller. Appl Therm Eng 31:3347–3353
40. Chicco G, Mancarella P (2005) Planning aspects and performance indicators for small-scale trigeneration plants. In Future Power Systems, 2005 International Conference on p 6
41. Chicco G, Mancarella P (2006) Planning evaluation and economic assessment of the electricity production from small-scale trigeneration plants. WSEAS Trans Power Syst 1:393–400
42. Aghahosseini S, Dincer I, Naterer G (2011) Integrated gasification and Cu–Cl cycle for trigeneration of hydrogen, steam and electricity. Int J Hydrog Energy 36:2845–2854
43. Minciuc E, Le Corre O, Athanasovici V, Tazerout M, Bitir I (2003) Thermodynamic analysis of tri-generation with absorption chilling machine. Appl Therm Eng 23:1391–1405
44. Moya M, Bruno J, Eguia P, Torres E, Zamora I, Coronas A (2011) Performance analysis of a trigeneration system based on a micro gas turbine and an air-cooled, indirect fired, ammonia–water absorption chiller. Appl Energy 88:4424–4440
45. Velumani S, Enrique Guzmán C, Peniche R, Vega R (2010) Proposal of a hybrid CHP system: SOFC/microturbine/absorption chiller. Int J Energy Res 34:1088–1095
46. Buck R, Friedmann S (2007) Solar-assisted small solar tower trigeneration systems. Transactions-american society of mechanical engineers. J Sol Energy Eng 129:349

47. Dincer I, Rosen MA (2012) Exergy: energy, environment and sustainable development. 2nd Edition, Elsevier Science
48. Santo D (2012) Energy and exergy efficiency of a building internal combustion engine trigeneration system under two different operational strategies. Energy Build 53:28–38
49. Ebrahimi M, Keshavarz A, Jamali A (2012) Energy and exergy analyses of a micro-steam CCHP cycle for a residential building. Energy Build 45:202–210
50. Khaliq A (2009) Exergy analysis of gas turbine trigeneration system for combined production of power heat and refrigeration. Int J Refrig 32:534–545
51. Kong X, Wang R, Huang X (2004) Energy efficiency and economic feasibility of CCHP driven by stirling engine. Energy Convers Manage 45:1433–1442
52. Ziher D, Poredos A (2006) Economics of a trigeneration system in a hospital. Appl Therm Eng 26:680–687
53. Temir G, Bilge D (2004) Thermoeconomic analysis of a trigeneration system. Appl Therm Eng 24:2689–2699
54. Ehyaei M, Mozafari A (2010) Energy, economic and environmental (3E) analysis of a micro gas turbine employed for on-site combined heat and power production. Energy Build 42:259–264
55. Ozgener O, Hepbasli A (2005) Exergoeconomic analysis of a solar assisted ground-source heat pump greenhouse heating system. Appl Therm Eng 25:1459–1471
56. Ozgener O, Hepbasli A, Ozgener L (2007) A parametric study on the exergoeconomic assessment of a vertical ground-coupled (geothermal) heat pump system. Build Environ 42:1503–1509
57. Dincer I (2007) Environmental and sustainability aspects of hydrogen and fuel cell systems. Int J Energy Res 31:29–55
58. Amrollahi Z, Ertesvåg IS, Bolland O (2011) Thermodynamic analysis on post-combustion CO capture of natural-gas-fired power plant. Int J Greenh Gas Control 5:422–426
59. Petrakopoulou F, Boyano A, Cabrera M, Tsatsaronis G (2011) Exergoeconomic and exergoenvironmental analyses of a combined cycle power plant with chemical looping technology. Int J Greenh Gas Control 5:475–482
60. Sahoo P (2008) Exergoeconomic analysis and optimization of a cogeneration system using evolutionary programming. Appl Therm Eng 28:1580–1588
61. Sayyaadi H, Sabzaligol T (2009) Exergoeconomic optimization of a 1000 MW light water reactor power generation system. Int J Energy Res 33:378–395
62. Haseli Y, Dincer I, Naterer G (2008) Optimum temperatures in a shell and tube condenser with respect to exergy. Int J Heat Mass Transf 51:2462–2470
63. Sayyaadi H, Nejatolahi M (2011) Multi-objective optimization of a cooling tower assisted vapor compression refrigeration system. Int J Refrig 34:243–256
64. Ahmadi P, Dincer I, Rosen MA (2011) Exergy, exergoeconomic and environmental analyses and evolutionary algorithm based multi-objective optimization of combined cycle power plants. Energy 36:5886–5898
65. Sayyaadi H, Babaelahi M (2011) Multi-objective optimization of a joule cycle for re-liquefaction of the liquefied natural gas. Appl Energy 88:3012–3021
66. Ghaebi H, Saidi M, Ahmadi P (2012) Exergoeconomic optimization of a trigeneration system for heating, cooling and power production purpose based on TRR method and using evolutionary algorithm. Appl Therm Eng 36:113–125
67. Kavvadias K, Maroulis Z (2010) Multi-objective optimization of a trigeneration plant. Energy Policy 38:945–954
68. Al-Sulaiman FA, Dincer I, Hamdullahpur F (2013) Thermoeconomic optimization of three trigeneration systems using organic Rankine cycles: Part I–Formulations. Energy Convers Manage 59:199–208
69. Wang J, Yan Z, Wang M, Li M, Dai Y (2013) Multi-objective optimization of an organic Rankine cycle (ORC) for low grade waste heat recovery using evolutionary algorithm. Energy Convers Manage 71:146–158

70. Shirazi A, Aminyavari M, Najafi B, Rinaldi F, Razaghi M (2012) Thermal–economic–environmental analysis and multi-objective optimization of an internal-reforming solid oxide fuel cell–gas turbine hybrid system. Int J Hydrog Energy
71. Hosseini M, Dincer I, Ahmadi P, Avval HB, Ziaasharhagh M (2011) Thermodynamic modelling of an integrated solid oxide fuel cell and micro gas turbine system for desalination purposes. Int J Energy Res 37:426–434
72. Ratlamwala T, Gadalla M, Dincer I (2011) Performance assessment of an integrated PV/T and triple effect cooling system for hydrogen and cooling production. Int J Hydrog Energy 36:11282–11291
73. Ratlamwala T, Dincer I, Gadalla M (2012) Performance analysis of a novel integrated geothermal-based system for multi-generation applications. Appl Therm Eng 40:71–79
74. Ozturk M, Dincer I (2012) Thermodynamic analysis of a solar-based multi-generation system with hydrogen production. Appl Therm Eng 51:1235–1244
75. Ahmadi P, Dincer I, Rosen MA (2012) Exergo-environmental analysis of an integrated organic Rankine cycle for trigeneration. Energy Convers Manage 64:447–453
76. Ahmadi P, Dincer I, Rosen MA (2013) Development and assessment of an integrated biomass-based multi-generation energy system. Energy 56:155–166
77. Cohce M, Dincer I, Rosen M (2011) Energy and exergy analyses of a biomass-based hydrogen production system. Bioresour Technol 102:8466–8474
78. Hughes EE, Tillman DA (1998) Biomass cofiring: status and prospects 1996. Fuel Process Technol 54:127–142
79. Lian Z, Chua K, Chou S (2010) A thermoeconomic analysis of biomass energy for trigeneration. Appl Energy 87:84–95
80. Mujeebu M, Jayaraj S, Ashok S, Abdullah M, Khalil M (2009) Feasibility study of cogeneration in a plywood industry with power export to grid. Appl Energy 86:657–662
81. Tchanche BF, Lambrinos G, Frangoudakis A, Papadakis G (2011) Low-grade heat conversion into power using organic Rankine cycles—a review of various applications. Renew Sustain Energy Rev 15:3963–3979
82. Faizal M, Rafiuddin Ahmed M (2011) On the ocean heat budget and ocean thermal energy conversion. Int J Energy Res 35:1119–1144
83. Meegahapola L, Udawatta L, Witharana S (2007) The Ocean Thermal Energy Conversion strategies and analysis of current challenges. In Industrial and Information Systems, 2007 ICIIS 2007 International Conference on 123–128
84. Esteban M, Leary D (2012) Current developments and future prospects of offshore wind and ocean energy. Appl Energy 90:128–136
85. Uehara H, Nakaoka T (1984) OTEC using plate-type heat exchanger (using ammonia as working fluid). Trans Jpn Soc Mech Engineers 50:1325–1333
86. Uehara H, Ikegami Y (1990) Optimization of a closed-cycle OTEC system. J Sol Energy Eng (USA) 112(4):247–256
87. Uehara H, Miyara A, Ikegami Y, Nakaoka T (1996) Performance analysis of an OTEC plant and a desalination plant using an integrated hybrid cycle. J Sol Energy Eng 118(2):115–122
88. Yamada N, Hoshi A, Ikegami Y (2009) Performance simulation of solar-boosted ocean thermal energy conversion plant. Renew Energy 34:1752–1758
89. Cengel YA, Boles MA, Kanoğlu M (2011) Thermodynamics: an engineering approach. McGraw-Hill New York, USA
90. Bejan A, Tsatsaronis G, Moran M (1995) Thermal design and optimization. Wiley-Interscience New York, USA

Chapter 7
Performance Assessment of a Two–stage Heat Pump–Drying System

Canan Acar and Ibrahim Dincer

Abstract In this study, energy and exergy analyses of a two–stage heat pump–drying system are conducted, and the performance of the overall system is then evaluated. The system has two cycles: a heat pump and a drying cycle. The working fluid of the heat pump and the drying cycles are R-134 A and air, respectively. The two–stage heat pump consists of two evaporators; one operates at high pressures while the other one operates at lower pressures for additional cooling and dehumidification of the drying air. After the condenser, two sub–coolers are used for additional heating. Also, the exergy destruction rates, energy and exergy efficiencies of each unit, cycle, and the overall system are calculated. Each unit and cycle's exergy destruction rate is investigated to identify the corresponding unit's relative irreversibility, and as a result, potential points to improve the system's exergetic performance. Parametric studies are conducted to understand the effect of ambient temperature on exergy efficiencies and exergy destruction rates of each unit, cycle, and the overall system. The selection and design of these to reduce exergy destruction, and as a result, increase the exergy efficiency of the system by minimizing irreversibilities is discussed in this study. Furthermore, the effect of air mass flow rate on system COP is studied. The initial results with 0.5 kg/s air flow rate at ambient temperature and pressure of 5 °C and 1 atm gives energy and exergy efficiencies of 62 % and 35 %, respectively. The COP of the system is calculated to be about 3.8.

Keywords Heat pump · Drying · Two–stage evaporator · Exergy · Efficiency

C. Acar (✉)
Faculty of Engineering and Applied Science, University of Ontario Institute of Technology, 2000 Simcoe Street North, Oshawa, ON L1H 7K4, Canada
e-mail: Canan.Acar@uoit.ca

I. Dincer
Department of Mechanical Engineering, University of Ontario Institute of Technology (UOIT), 2000 Simcoe Street North, Oshawa ON L1H 7K4, Canada
e-mail: ibrahim.dincer@uoit.ca

I. Dincer et al. (eds.), *Progress in Sustainable Energy Technologies: Generating Renewable Energy,* DOI 10.1007/978-3-319-07896-0_7,

7.1 Introduction

Drying is one of the most energy intensive processes used in many industrial processes. Despite providing several advantages such as lighter weight for transportation and less space for long time storage, drying consumes up to 70 and 50 % of all the energy used in the wood and textile industries, respectively [1]. Fossil fuels, biomass, and electricity are the major primary energy sources of commonly used air conductive industrial driers. Reducing/recovering the heat losses during the drying process is an important step to minimize energy consumption and greenhouse gas emissions. Heat pump assisted drying systems make it possible to recover significant amounts of energy, minimize waste and save up to 50 % of the primary energy used [2, 3].

Some of the advantages of heat pump dryers can be listed as exhaust gas energy recovery and drying gas temperature and humidity control [4, 5]. Controlling the drying conditions to meet the precise requirements of a wide range of products is critical especially when the product quality is an important parameter of the drying process [6, 7]. Another advantage of the heat pump dryer systems is that any conventional dryer, regardless of their primary energy source, can be used in a heat pump dryer system. Heat pumps can convert latent heat into sensible heat, which makes them an exceptional option when heat recovery in a drying process is an important issue [8, 9]. Table 7.1 compares hot air and vacuum drying to heat pump driers. The key advantages of heat pump driers listed on Table. 7.1 can be summarized as: high SMER (Specific Moisture Extraction Ratio), improved quality of drying at low temperatures, a broad range of drying conditions, improved control of operation for high-value products, and reduced energy consumption.

In 1981, Perry [10] proposed a system which uses a heat pump with two evaporators, one at high and one at low pressures, in conjunction with a drying system. In his system, the high pressure evaporator provided sensible heat cooling and the low pressure evaporator is used to remove latent heat. At first, the idea was not accepted widely since the control of a single evaporator system is much easier and the new system was thought to be a complicated concept. Later, Chua and Chou developed, built, and tested Perry's concept for drying agricultural products [2, 11, 12]. Li and Su [13] state that a refrigerating system with two evaporators shows better performance than the one with a single evaporator. All the previous work on two-evaporator systems concluded that from the thermodynamic viewpoint, a two-evaporator system provides larger surface area for heat transfer, which minimizes the compressor work within the cycle.

In this study, it is aimed to conduct a comprehensive exergy analysis and an exergetic performance assessment of a two–stage heat pump–drying system, which was previously developed by Chua and Chou [2]. The performance evaluation of the overall system is performed based on the energy and exergy analyses of every component within the system. Performance of the system is investigated for various environmental parameters via parametric studies. In the end, recommendations for better performance in terms of environmental and sustainability issues are provided.

Table 7.1 Comparison of hot air, vacuum, and heat pump drying systems. (Adapted from [8])

Parameter	Hot air drying	Vacuum drying	Heat pump drying
SMER (kg water/kW-h)	0.12–1.28	0.72–1.2	1.0–4.0
Drying efficiency (%)	35–40	<70	95
Operating temperature range (°C)	40–90	30–60	10–65
Operating RH range (%)	Variable	Low	10–65
Capital cost level	Low	High	Moderate
Running cost level	High	Very high	Low

7.2 System Description

The two-stage evaporator heat pump-dryer system investigated in this study is shown in Fig. 7.1. The system, based on Chua and Chou's design [2] has one high and one low pressure evaporators, two subcoolers, one condenser, one compressor, two expansion valves, one accumulator, and one drier. The units of the overall system are listed along with their unit numbers in Table 7.2.

The summary of each stream, along with their corresponding stream number, component, mass flow rate (kg/s), temperature (°C), pressure (kPa), and state is listed in Table 7.3. The overall system analysis is conducted based on the data presented in Table 7.3. The selected refrigerant, R–134 A, is used in the heat pump cycle where air is the part of the drying cycle. Further explanation on mass, energy, entropy, and exergy balances as well as efficiency equations are provided in the next section.

7.3 System Analysis

The thermodynamic performance of the heat pump-dryer system is evaluated by conducting quantitative energy and exergy analyses, and calculating efficiencies and sustainability indexes. The thermodynamic properties of all the states and the thermodynamic balance equations are solved by using the EES software for detailed performance analysis.

The potential and kinetic energy changes during the course of operation are neglected within the system. All processes are assumed to be steady state steady flow. There are no chemical reactions, heat transfer and pressure drop in tubing connecting the components, valves, and the neat transfer with the environment are negligible. Isentropic efficiency of the compressor is 95 %. The condenser and expansion valve is assumed to be 100 % energy efficient. The change in specific heat of air, water, and the refrigerant with respect to the change in temperature is neglected. All equipment except condenser, subcoolers, evaporators and dryer are adiabatic.

The conservation of mass in a control volume of any system can be described in its general form as follows:

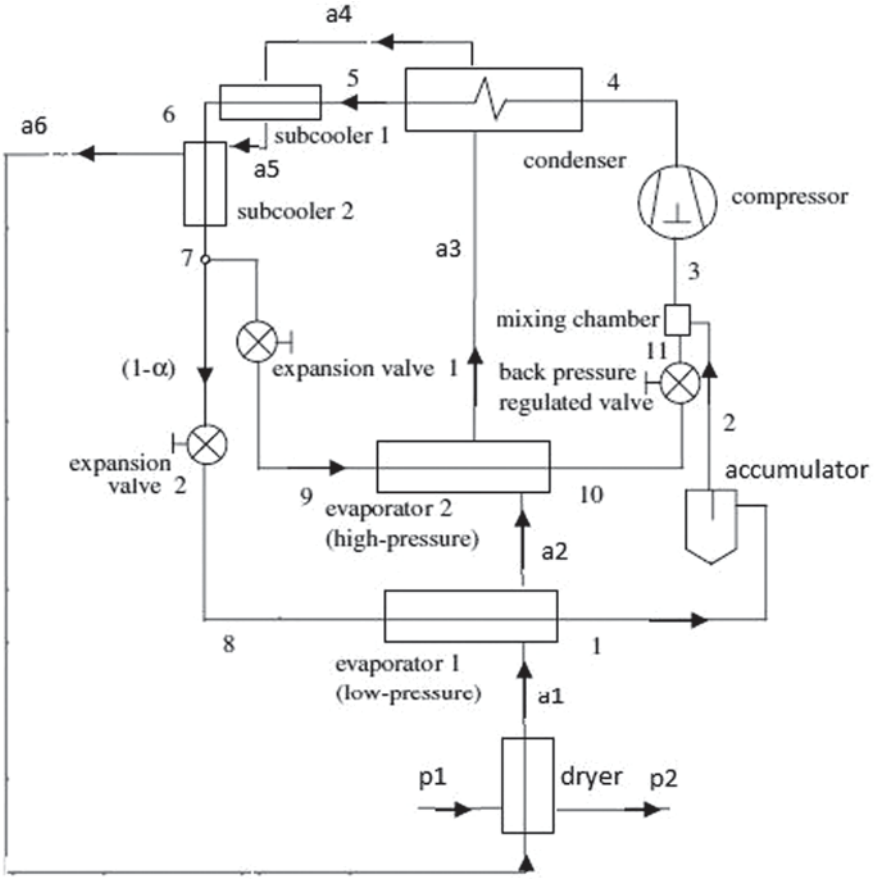

Fig. 7.1 Schematic of the refrigerant and air cycle of the heat pump dryer system proposed by Chua and Chou [2]

$$\frac{dm_{cv}}{dt} = \sum \dot{m}_{in} - \sum \dot{m}_{out} \tag{7.1}$$

where m and $\dot{m}$ are the mass and mass flow rate, and the subscripts "*cv*", "*in*" and "*out*" indicate the control volume and the inlet and outlet of the control volume, respectively. During the steady state operation, the mass balance equation (MBE) can be written as

$$\sum \dot{m}_{in} = \sum \dot{m}_{out} \tag{7.2}$$

Similarly, the steady state energy, entropy, and exergy balance equations can be written as

Table 7.2 List of units used in the heat pump dryer system

Units	
1	Compressor
2	Condenser
3	Subcooler 1
4	Subcooler 2
5	Expansion Valve 1 (EV1)
6	Expansion Valve 2 (EV2)
7	Low Pressure Evaporator (LPE)
8	High Pressure Evaporator (HPE)
9	Back Pressure Regulated Valve (BPRV)
10	Accumulator
11	Mixing chamber
12	Dryer

$$\sum \dot{E}_{in} = \sum \dot{E}_{out} \tag{7.3}$$

$$\sum \dot{S}_{in} + \dot{S}_{gen} = \sum \dot{S}_{out} \tag{7.4}$$

$$\sum \dot{E}x_{in} = \sum \dot{E}x_{out} + \dot{E}x_{dest} \tag{7.5}$$

Table 7.3 Summary of each stream along with their component and properties

Stream	Component	$\dot{m}$ (kg/s)	T (°C)	P (kPa)	State
1	R-134A	0.0429	7.45	500	Gas
2	R-134A	0.0429	7.45	500	Gas
3	R-134A	0.066	7.45	500	Gas
4	R-134A	0.066	83.48	2500	Liquid
5	R-134A	0.066	61.35	2500	Liquid
6	R-134A	0.066	56.35	2500	Liquid
7	R-134A	0.066	51.35	2500	Liquid
8	R-134A	0.0429	0.1148	500	VLE[a]
9	R-134A	0.0231	23.4	1000	VLE[a]
10	R-134A	0.0231	23.4	1000	Gas
11	R-134A	0.0231	7.45	500	Gas
a1	Air	0.5	28.05	101.3	Gas
a2	Air	0.5	25.27	101.3	Gas
a3	Air	0.5	23.6	101.3	Gas
a4	Air	0.5	44.21	101.3	Gas
a5	Air	0.5	45.17	101.3	Gas
a6	Air	0.5	46.08	101.3	Gas

[a] *VLE* Vapor-liquid equilibrium

Here, $\dot{E}$ is the rate of energy input and "*in*" and "*out*"represent the inlet and outlet of the control volume, respectively. This input can be in the form of heat ($\dot{Q}$), work ($\dot{W}$), or an inlet/outlet stream. The rate of energy carried by a stream (e.g. stream *i*) is expressed as

$$\dot{E}_i = \dot{m}_i h_i \tag{7.6}$$

The subscript *i* denotes the "stream i" and *h* represent the specific enthalpy (kJ/kg) of the corresponding stream. Similarly, $\dot{S}$ in Eq. 7.4 is the rate of entropy input (subscript *in*), output (subscript *out*), or generation (subscript *gen*). The rate of entropy carried by a stream (e.g. stream *i*) based on its specific entropy content *s* is written as

$$\dot{S}_i = \dot{m}_i s_i \tag{7.7}$$

The term Ex in Eq. 7.5 represents the rate of exergy flow where the subscript *dest* refers to the rate of exergy destruction, which describes the system irreversibility. The steady state exergy balance can be more specifically written as

$$\sum \dot{m}_{in} ex_{in} + \sum \dot{E}x_{\dot{Q}_{in}} + \sum \dot{E}x_{\dot{W}_{in}} = \sum \dot{m}_{out} ex_{out} + \sum \dot{E}x_{\dot{Q}_{out}} + \sum \dot{E}x_{\dot{W}_{out}} + \dot{E}x_{dest} \tag{7.8}$$

The exergy transfer rate associated with work $(\dot{E}x_{\dot{Q}})$ is equal to the rate of work $(\dot{W})$. For the heat transfer rate $(\dot{Q})$, the maximum rate of conversion from thermal energy to useful work, which describes the thermal exergy flow, can be stated as follows:

$$\dot{E}x_{\dot{Q}} = \dot{Q}\left(1 - \frac{T_0}{T}\right) \tag{7.9}$$

The term $(1-T_0/T)$ is the dimensionless exergetic temperature, which is equal to the Carnot efficiency working between the environmental temperature at T_0 and the operating temperature *T*. Exergy of a flow of matter can be defined as the maximum amount of work obtainable when the flow is brought from its initial state to the dead state during a process of interaction with its environment. The exergy associated with a stream flow is composed of four main components: physical (ex^{ch}), chemical (ex^{ch}), kinetic (ex^{ke}) and potential (ex^{pe}). In this study, all potential and kinetic energy, and chemical exergy changes are neglected. Thus, the specific exergy of a flow is caused by physical processes involving only thermal interaction with the environment to bring the flow from its initial condition to the environmental state which is defined by T_0 and P_0. The following equation describes the specific physical exergy components:

$$ex = (h - h_0) - T_0(s - s_0) \tag{7.10}$$

where h and h_0 are specific enthalpies, and s and s_0 are the specific entropies at the defined and the reference environment states, respectively.

The amount of exergy leaving the control volume must be less than the input exergy as a result of the exergy destruction within the process/system. The rate of exergy destruction, which appears as $\dot{E}x_{dest}$ in the general exergy balance equation, is proportional to the rate of entropy generation:

$$\dot{E}x_{dest} = \mathrm{T}_0 \dot{S}_{gen} \tag{7.11}$$

Exergy analysis acknowledges that, although energy cannot be created or destroyed, it can be degraded in quality, eventually reaching a state in which it is in complete equilibrium with the surroundings and hence of no further use for performing tasks [14]. The energy and exergy efficiencies of the system units are listed in Table 7.4. The relative irreversibility (RI) and sustainability index (SI) of a unit (e.g. unit i) can be written as

$$RI_i = \frac{\dot{E}x_{dest,i}}{\dot{E}x_{dest}} \tag{7.12}$$

$$SI_i = \frac{1}{1-\psi_i} \tag{7.13}$$

Overall COP and energy and exergy efficiency equations can be written as

$$COP = \frac{Condenser\ Load(\dot{E}_3 - \dot{E}_4)}{Compressor(\dot{W}_1)} \tag{7.14}$$

$$\eta = \frac{\dot{Q}_2}{\dot{W}_1} \tag{7.15}$$

$$\psi = \frac{\dot{Q}_2\left(1-\frac{T_0}{T}\right)}{\dot{W}_1} \tag{7.16}$$

7.4 Results and Discussion

In order to study the heat pump-dryer system energetically and exergetically, each stream is defined by its state, components, temperature and pressure. After the states are defined, the specific enthalpy, entropy, exergy and energy and exergy flow rates of each stream are calculated (either from initial data on Table 7.5 or via balance Eq. 2–11). The input data presented in Table 7.5 is based on the model developed by Chua and Chou [2]. Reference state is taken to be 20 °C and 101.3 kPa, respectively. The thermodynamic properties of air, water, and R-134 A are found using the Engineering Equation Solver (EES) software package. The exergy, energy, RI (relative

Table 7.4 Energy and exergy efficiencies of system units

Units	Energy efficiency	Exergy efficiency
1	$\eta_1 = \frac{\dot{E}_4 - \dot{E}_3}{\dot{W}_1}$	$\psi_1 = \frac{\dot{E}x_4 - \dot{E}x_3}{\dot{W}_1}$
2	$\eta_2 = \frac{\dot{E}_{a4} - \dot{E}_{a3}}{\dot{E}_4 - \dot{E}_5}$	$\psi_2 = \frac{\dot{E}x_{a4} - \dot{E}x_{a3}}{\dot{E}x_4 - \dot{E}x_5}$
3	$\eta_3 = \frac{\dot{E}_{a5} - \dot{E}_{a4}}{\dot{E}_5 - \dot{E}_6}$	$\psi_3 = \frac{\dot{E}x_{a5} - \dot{E}x_{a6}}{\dot{E}x_5 - \dot{E}x_6}$
4	$\eta_4 = \frac{\dot{E}_{a6} - \dot{E}_{a5}}{\dot{E}_6 - \dot{E}_7}$	$\psi_3 = \frac{\dot{E}x_{a6} - \dot{E}x_{a5}}{\dot{E}x_6 - \dot{E}x_7}$
5	$\eta_5 = \frac{\dot{E}_9}{\dot{E}_7 \alpha}$	$\psi_5 = \frac{\dot{E}x_9}{\dot{E}x_7 \alpha}$
6	$\eta_6 = \frac{\dot{E}_8}{\dot{E}_7 (1-\alpha)}$	$\psi_6 = \frac{\dot{E}x_8}{\dot{E}x_7 (1-\alpha)}$
7	$\eta_7 = \frac{\dot{E}_1 - \dot{E}_8}{\dot{E}_{a1} - \dot{E}_{a2}}$	$\psi_7 = \frac{\dot{E}x_1 - \dot{E}x_8}{\dot{E}x_{a1} - \dot{E}x_{a2}}$
8	$\eta_8 = \frac{\dot{E}_{10} - \dot{E}_9}{\dot{E}_{a2} - \dot{E}_{a3}}$	$\psi_8 = \frac{\dot{E}x_{10} - \dot{E}x_9}{\dot{E}x_{a2} - \dot{E}x_{a3}}$
9	$\eta_9 = \frac{\dot{E}_{11}}{\dot{E}_{10}}$	$\psi_9 = \frac{\dot{E}x_{11}}{\dot{E}x_{10}}$
10	$\eta_{10} = \frac{\dot{E}_2}{\dot{E}_1}$	$\psi_{10} = \frac{\dot{E}x_2}{\dot{E}x_1}$
11	$\eta_{11} = \frac{\dot{E}_3}{\dot{E}_2 + \dot{E}_{11}}$	$\psi_{11} = \frac{\dot{E}x_3}{\dot{E}x_2 + \dot{E}x_{11}}$

irreversibility), and SI (sustainability index) data of each unit and the overall system are presented and discussed in this section. The energy and exergy efficiencies and corresponding COP values are also introduced.

Table 7.6 summarizes the energy input/output (either work or heat), exergy efficiency, rate of exergy destruction, relative irreversibility (RI) and sustainability index (SI) of each unit. From Table 7.6, it can be seen that the lowest exergy efficiency, which is around 37 % occurs in the high pressure evaporator (37 %), followed by low pressure evaporator (41 %), and condenser (59 %). Similarly, exergy is largely destructed in the low pressure evaporator (0.9 kW), condenser (0.83 kW), and high pressure evaporator (0.7 kW). The system uses 2.808 kW of electrical energy to run the compressor. Overall, the energy and the exergy efficiencies of the system are 62 and 35 %, respectively. The total exergy destruction rate is 3.96 kW and the sustainability index of the overall system is 1.54.

The relative irreversibilities of the heat pump-dryer system units are presented in Fig. 7.2. As discussed earlier Unit 7, low pressure evaporator, has the highest irreversibility (24 %), due to the high exergy destruction rates of this unit. Condenser,

Table 7.5 Input data for the system. (Adapted from [2])

m_r	Refrigerant mass flow rate (kg/s)	0.066
m_a	Air mass flow rate (kg/s)	0.5
α	The mass ratio of the refrigerant sent to HP evaporator	0.35
T_3	Compressor inlet temperature (K)	280.6
P_3	Compressor inlet pressure (kPa)	500
ΔT_{SC1}	Degree of subcooling in Subcooler 1 (K)	5
ΔT_{SC2}	Degree of subcooling in Subcooler 2 (K)	5
T_0	Ambient temperature (K)	278.15
P_0	Ambient pressure (kPa)	101.33

Table 7.6 Exergy efficiency, heat and work input/output, rate of exergy destruction, RI, and SI of the major units of the heat pump-dryer system

Unit		Ψ_i (%)	$\dot{Q}$ (kW)	$\dot{W}$ (kW)	$\dot{E}x_{d\,est}$ (kW)	RI (%)	SI
1	Compressor	84		2.808	0.37	10	6.2
2	Condenser	59	10.73[a]		0.83	22	2.42
3	Subcooler 1	79	0.5[a]		0.02	0	4.78
4	Subcooler 2	87	0.48[a]		0.01	0	7.49
5	Expansion Valve 1 (EV1)	94			0.06	2	17.51
6	Expansion Valve 2 (EV2)	85			0.07	2	6.61
7	Low Pressure Evaporator (LPE)	41	6.24[b]		0.9	24	1.68
8	High Pressure Evaporator (HPE)	37	3.42[b]		0.7	19	1.58
9	Back Pressure Regulated Valve	72			0.17	5	3.51
12	Dryer	66	8.52[b]		0.42	11	2.9

[a] Heat rejected
[b] Heat input

Unit 2, follows Unit 7 with 22% irreversibility. And Unit 8, high pressure evaporator has 19% irreversibility. About 64% of the exergy destruction of the overall system is caused by the operation of HPE, LPE, and the condenser, combined.

The irreversibilities in the evaporators and the condenser occur due to the temperature differences between the two heat exchanger fluids, pressure losses, flow imbalances and heat transfer with the environment. Since compressor power depends strongly on the inlet and outlet pressures, any heat exchanger improvements that reduce the temperature difference will reduce compressor power by bringing the condensing and evaporating temperatures closer together.

From a design standpoint, compressor irreversibility can be reduced independently. Recent advances in the heat pump market have led to the use of scroll compressors. Replacing the reciprocating compressor by a scroll unit can increase cooling effectiveness. The only way to eliminate the throttling loss is to replace the capillary tube (the expansion device) with an isentropic turbine (an isentropic expander) and to recover some shaft work from the pressure drop. The compressor irreversibility is partly due to the large degree of superheat achieved at the end of

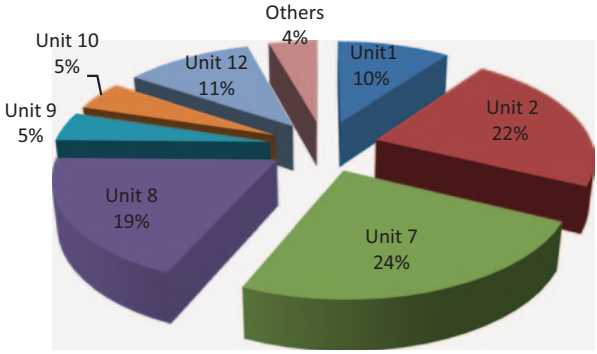

Fig. 7.2 Relative irreversibilities of the heat pump-dryer system units (others include subcoolers, expansion valves, and the mixing chamber)

the compression process, leading to large temperature differences associated with the initial phase of heat transfer. The mechanical–electrical losses are due to imperfect electrical, mechanical and isentropic efficiencies and emphasize the need for careful selection of this equipment, since components of inferior performance can considerably reduce overall system performance.

The sustainability indexes of the heat pump-dryer system units as well as the overall system are shown in Fig. 7.3. The average SI value of the subcoolers (Units 3 and 4) and expansion valves (Units 5 and 6) are taken as basis when constructing Fig. 7.3. It should be noted that the accumulator (Unit 10) and the mixing chamber (Unit 11) are assumed to be 100% efficient. Therefore, their SI is not evaluated. Since the system components (i.e. valves, pipes, etc.) are assumed to be reversible and all the losses are neglected, the expansion valves have very high SI (meaning high exergy efficiencies) compared to the other system units. The high exergy losses of the condenser (Unit 2), low (Unit 7) and high pressure evaporators (Unit 8) can be seen in Figure as low sustainability indexes. Overall, the system has an SI of 1.54.

Initially the system is studied at an ambient temperature of 5 °C, to further investigate the effect of ambient temperature on the performance of the system, the exergy destruction rates and efficiencies of selected units and the overall system at different ambient temperatures are presented in Fig. 7.4, 7.5 and 7.6.

From Fig. 7.4, it can be seen that the exergy destruction rate of compressor (Unit 1) decreases by 0.05 kW as the ambient temperature increased from 0 to 25 °C. Similarly, with increasing ambient temperature, the rate of exergy destruction caused by the low (Unit 7) and high pressure (Unit 8) evaporators decreased by around 0.06 kW within the given interval. On the other hand, as the ambient temperature increased from 0 to 25 °C, the exergy destruction rate at the condenser (Unit 2) increased by 0.07 kW, this amount increased by about 0.03 kW at the dryer (Unit 12). This difference can be explained by the inlet and outlet temperature and pressures of the streams associated with each unit. As exergy flow of a stream decreases as it gets closer to ambient conditions, increasing ambient temperature affects each stream differently; some of the streams' exergy flow rate increases while some of them decrease by varying ambient temperature.

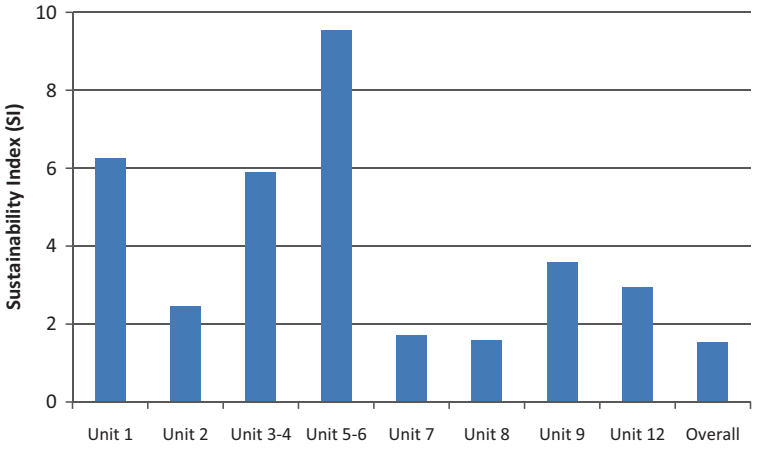

Fig. 7.3 Sustainability indexes of the heat pump-dryer system units and the overall system

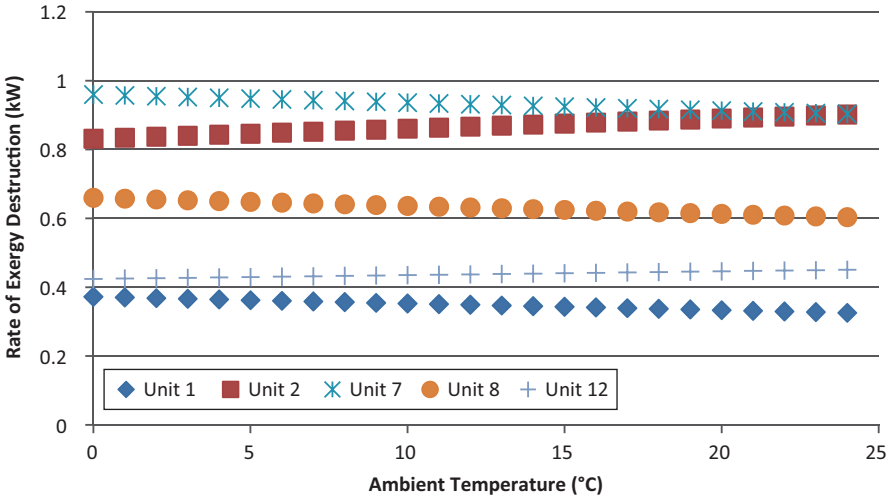

Fig. 7.4 Effect of ambient temperature on the exergy destruction rates of the major units of the system

Again, the effect of ambient temperature is observed differently on selected units. As ambient temperature increased within the given ambient temperature interval from 0 to 25 °C, the exergy efficiency of the compressor (Unit 1) increased by 1.60 %. Similarly, the exergy efficiency the low (Unit 7) and high pressure (Unit 8) evaporators increased by 1.7 %. On the other hand, under the same circumstances, the exergy efficiency of the condenser (Unit 2) and the dryer (Unit 12) decreased by around 10 %.

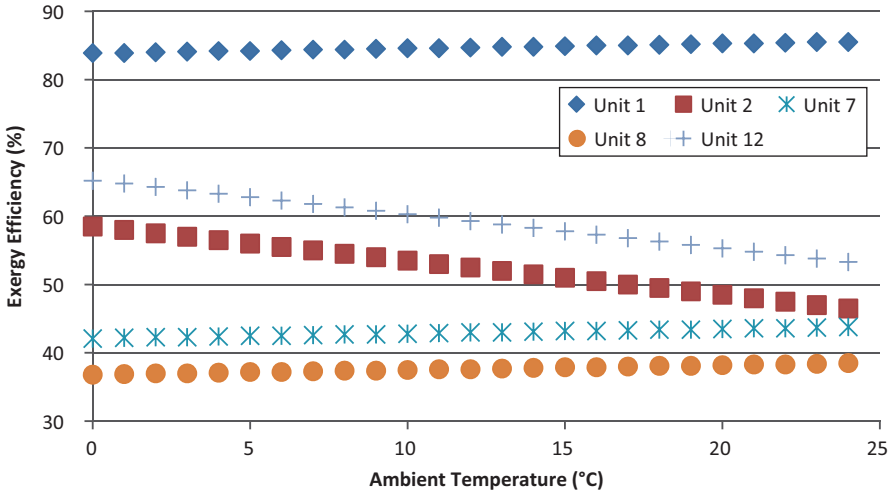

Fig. 7.5 Effect of ambient temperature on exergy efficiencies of the major units of the system

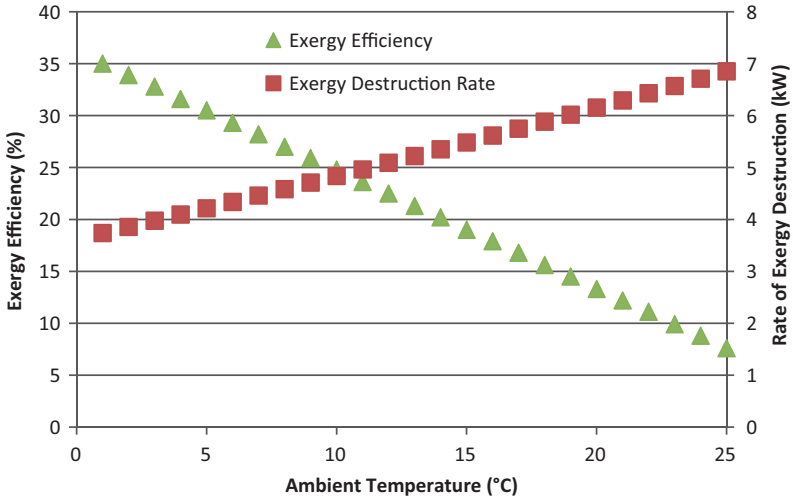

Fig. 7.6 Effect of ambient temperature on exergy efficiencies and destruction rates of the overall system

Figure 7.6 presents the effect of the ambient temperature on the overall system performance. As ambient temperature increased from 0 to 25 °C, the total rate of exergy destruction of the overall system increased from around 3.7 kW to about 6.8 kW. On the other hand, the overall exergy efficiency decreased from around 35 to about 10 %. The overall system's performance change with respect to the change in ambient temperature is similar to the performance change of the condenser and the dryer.

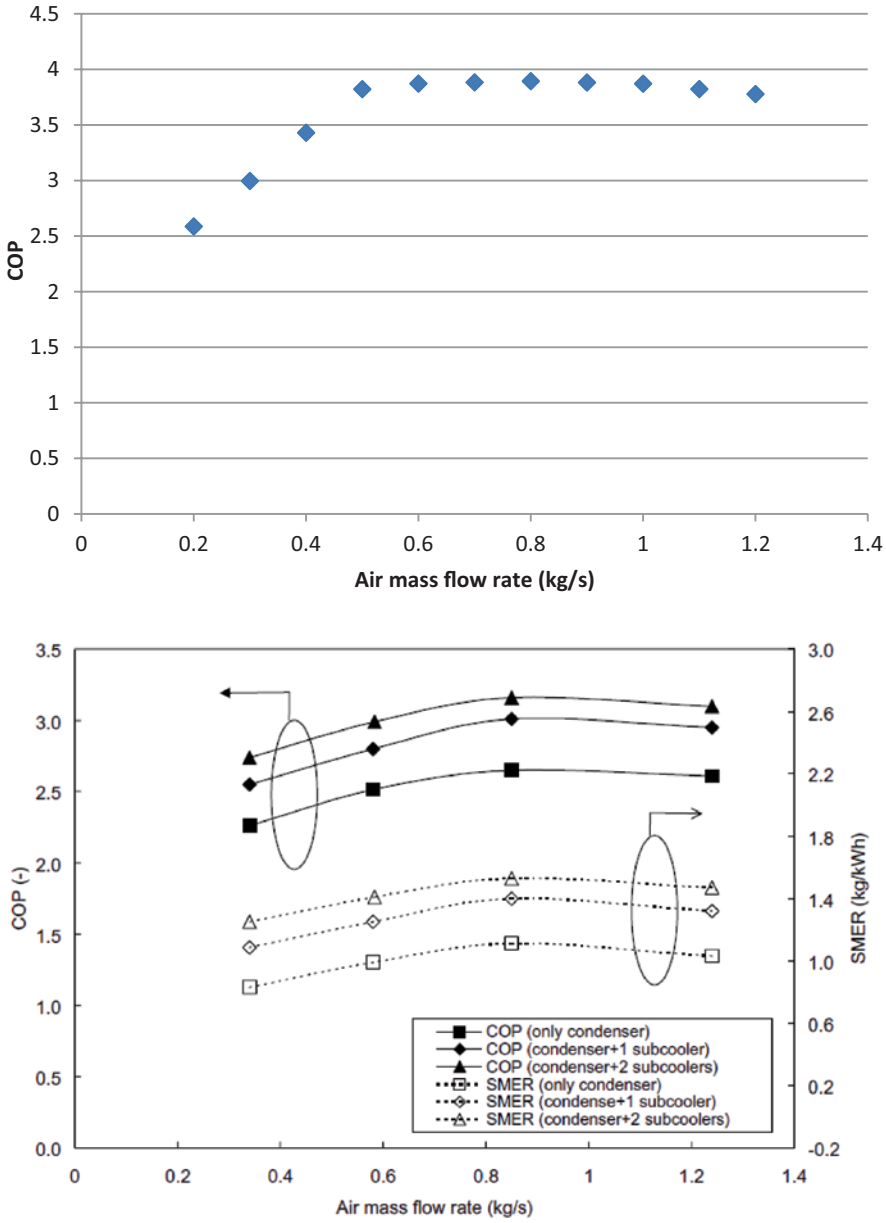

Fig. 7.7 Impact of air mass flow rate on the overall system performance, COP (*top*) and the results of Chuo and Chou's [2] study (*bottom*)

Initially, the system is considered to work with a drying air mass flow rate of 0.5 kg/s. Given the conditions introduced in Table 7.5, the COP of the system is calculated to be 3.82. The effect of air mass flow rate on COP is investigated and

the results are presented in compared to the data provided by Chua and Chou [2]. The results are shown in Fig. 7.7. When the COP (condenser + 2 subcoolers) data of Chuo and Chou is compared to the findings of this study, it can be seen that both results are parallel to each other. This study shows a slight increase in COP compared to Chuo and Chou [2], which can be explained by the assumptions made during the course of this study. First, neglecting the heat losses throughout the system increased the entire system's energy efficiency. Also, the expansion valves are assumed to be an ideal. Therefore, any losses are neglected and the expansion valves are taken as isenthalpic. Furthermore, any heat loss and pressure drop in the tubing connecting the components and valves are neglected. Taking these factors into account could decrease the energy and exergy efficiencies significantly.

Taking the exergy efficiencies into account provided a better insight about the model. Based on the parametric studies and exergy analyses, a better optimum operating condition can be picked for the proposed two stage heat pump-drying system.

Conclusions

In this study, exergy destruction and exergy efficiency concepts are studied to consider irreversibilities in a two stage heat pump-dryer system to address the consequences of non-conservation of exergy. Defining the exergy efficiency and determining the destructions for the heat pump and drying systems and the system's exergetic performance provide significant information about "the availability of work" lost in different units and at different ambient temperatures. For the direct benefit of industry in particular and society in general, it is important that the potential benefits of exergy be exploited. Heat is lost to the environment throughout the entire heat pump cycle. The pipes and components of the heat pump system cannot be perfectly insulated. However, proper insulation of the entire system including all subunits, pipes, and valves can improve the energy and exergy efficiencies strongly. The losses due to equipment inefficiencies (compressor, pumps, mechanical drive, and waste heat) also decrease both energy and exergy efficiencies. A careful selection of the equipment and material can also increase both the energy and exergy efficiencies. The specific findings of this study can be summarized as follows:

- At an ambient temperature and pressure of 5 °C and 1 atm, the overall system has an energy and exergy efficiency of 62 and 35 %, respectively. The overall rate of exergy destruction is 3.96 kW.
- The largest contributors to overall destruction are low pressure evaporator (0.9 kW), condenser (0.83 kW), and high pressure evaporator (0.7 kW).
- The overall rate of exergy destruction increases and the exergy efficiency decreases with increasing ambient temperature.

Exergy efficiency of the overall system can be improved by finding and analyzing the points of irreversibility of the process. Irreversibility could be caused by the temperature difference of the heat exchanger fluids, pressure drops, flow imbalances, and lack of recovering latent heat because of the high temperature difference of inlet and outlet fluids. Reducing the temperature difference brings evaporator and condensing temperatures together increases the amount of heat recovered per amount of work provided to the system.

Nomenclature

E	Energy (kJ)
$\dot{E}$	Energy flow rate (kW)
ex	Specific exergy (kJ/kg)
Ex	Exergy (kJ)
$\dot{E}x$	Exergy flow rate (kW)
h	Specific enthalpy (kJ/kg)
m	Mass (kg)
$\dot{m}$	Mass flow rate (kg/s)
P	Pressure (kPa)
Q	Heat (kJ)
$\dot{Q}$	Heat transfer rate (kW)
S	Specific entropy (kJ/kg-K)
S	Entropy (kJ/K)
$\dot{S}$	Entropy flow rate (kW/K)
t	Time (s)
T	Temperature (K)
W	Work (kJ)
$\dot{W}$	Work transfer rate (kW)

Greek Symbols

α	Mass ratio of the refrigerant sent to HPE
Δ	Change
η	Energy efficiency
Ψ	Exergy efficiency

Subscript and Superscripts

Ch	Chemical
cv	Control volume
dest	Destruction
en	Energy
ex	Exergy
gen	Generation
in	Inlet stream
ke	Kinetic
out	Outlet stream

pe	Potential
ph	Physical
°	Standard state
0	Reference state

Acronyms

BPRV	Back Pressure Regulated Valve
COP	Coefficient of Performance
EES	Engineering Equation Solver
EV	Expansion Valve
GHG	Greenhouse Gas
HPE	High Pressure Evaporator
LP	Low Pressure Evaporator
RH	Relative Humidity
RI	Relative Irreversibility
SI	Sustainability Index
SMER	Specific Moisture Extraction Ratio
VLE	Vapor-liquid Equilibrium

References

1. Mujumbar AS (2007) Handbook of industrial drying. Taylor & Francis Group, New York
2. Chua KJ, Chou SK (2005) A modular approach to study the performance of a two-stage heat pump system for drying. Appl Therm Eng 25:1363–1379
3. Strumillo C (2006) Perspectives on development in drying. Dry Technol 24:1059–1068
4. Lubis IL, Kanoglu M, Dincer I, Rosen MA (2011) Thermodynamic analysis of a hybrid geothermal heat pump system. Geothermics 40(3):233–238
5. Zamfirescu C, Dincer I, Naterer G (2009) Performance evaluation of organic and titanium based working fluids for high-temperature heat pumps. Thermochimica Acta 496(1–2):18–25
6. Artnaseaw TS, Benjapiyaporn C (2010) Drying characteristics of shiitake mushroom and jinda chili during vacuum heat pump drying. Food Bioproducts Process 88(2–3):105–114
7. Artnaseaw, TS, Benjapiyaporn C (2010) Development of a vacuum heat pump dryer for drying chilli. Biosyst Eng 105(1):130–138
8. Perera CO, Rahman MS (1997) Heat pump dehumidifier drying of food. Trends Food Sci Technol 8:75–79
9. Zamfirescu C, Dincer I (2009) Performance investigation of high-temperature heat pumps with various BZT working fluids. Thermochimica Acta 488(1–2):66–77
10. Perry EJ (1981) Drying by Cascade Heat Pumps. Inst Refrig Manage (1)1–8
11. Chua KJ (2000) Dynamic modelling, experimentation, and optimization of heat pump drying for agricultural products. Ph.D. thesis, National University of Singapore, Department of Mechanical Engineering
12. Chua KJ, Chou SK, Ho JC, Hawlader NA (2002) Heat pump drying: recent developments and future trends. Dry Technol 20(8):1579–1610
13. Li CJ, Su CC (2003) Experimental study of a series-connected two-evaporator refrigerating system with propane (R-290) as the refrigerant. Appl Therm Eng 23:1503–1514
14. Dincer I, Rosen MA (2013) Exergy, 2nd edn. Elsevier, Oxford

Chapter 8
Comparative Assessment of Nuclear Based Hybrid Sulfur Cycle and High Temperature Steam Electrolysis Systems Using HEEP

Hasan Ozcan, Rami Salah El-Emam and Ibrahim Dincer

Abstract Hydrogen is one of the most promising alternatives as a replacement for the fossil fuels, since it can be produced by several methods using numerous sources. Sustainable production of hydrogen is highly dependent on the energy source utilized. Nuclear and renewable energy resources are considered as the best candidates for sustainable hydrogen production. Although there are numerous methods possible for hydrogen production, cost and economic factors play a crucial role in the feasibility and applicability of such plants. In this study, cost assessment of nuclear hydrogen production methods can be comparatively evaluated using Hydrogen Economy Evaluation Programme (HEEP) provided by International Atomic Energy Agency (IAEA). HEEP software is a user friendly cost estimation package, including various nuclear reactor options, as well as hydrogen generation, storage and transportation facilities. Rather than the existing data, HEEP offers user defined options from energy source to end user. Futhermore, hybrid sulfur (HyS) thermochemical cycle and high temperature steam electrolysis (HTSE) hydrogen generation systems are compared using high temperature reactors by considering storage and transportation options. The results show that the cost of hydrogen from HyS is 20% lower than that of HTSE. HTSE requires more power consumption than HyS cycle, which has the highest impact of plant and production costs.

Keywords Nuclear hydrogen production · Cost estimation · HyS · HTSE · HEEP · IAEA

H. Ozcan (✉) · R. S. El-Emam
Faculty of Engineering and Applied Science, University of Ontario Institute of Technology, 2000 Simcoe Street North, Oshawa, ON L1H 7K4, Canada
e-mail: Hasan.Ozcan@uoit.ca

R. S. El-Emam
Faculty of Engineering, Mansoura University, Mansoura, Egypt
e-mail: Rami.Elemam@uoit.ca

I. Dincer
Department of Mechanical Engineering, University of Ontario Institute of Technology (UOIT), 2000 Simcoe Street North, Oshawa ON L1H 7K4, Canada
e-mail: ibrahim.dincer@uoit.ca

I. Dincer et al. (eds.), *Progress in Sustainable Energy Technologies: Generating Renewable Energy,* DOI 10.1007/978-3-319-07896-0_8,

Table 8.1 Cost of hydrogen from various energy sources (Adapted from [3])

Source	Process	Hydrogen amount (kg H_2/day)	Cost ($/kg)	Reference
Natural gas	SMR	341,448	2.33	[6]
Nuclear	S-I	723,000	2.45	[7]
Solar	S-I	86,400	7.53	[8]
Wind	CE	50,000	6.61	[9]
Biomass	Gasification	139,700	1.99	[10]
Coal	Gasification	281,100	1.25	[11]

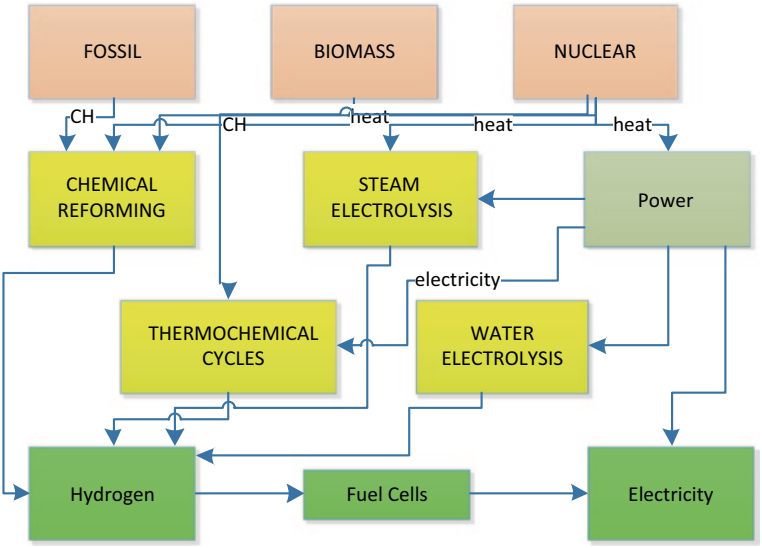

Fig. 8.1 Pathways for nuclear hydrogen generation (Adapted from [5])

8.1 Introduction

Sustainable production of any form of energy is based on clean and non-polluting resources. Renewable energy sources can be considered as the most suitable resources for clean energy production. However, cost of the energy produced from most renewable sources can be relatively higher than fossil fuel based energy production methods, since these systems are not as mature, and have higher capital costs, and possess higher capital costs [1, 2]. Nuclear energy is already a mature method for power and heating production and can be one of the most suitable sources for sustainable hydrogen production with relatively lower hydrogen production cost. Table 8.1 presents the costs and rates for hydrogen production from various energy resources [3]. Some of the hydrogen production methods from different sources are represented in Fig. 8.1.

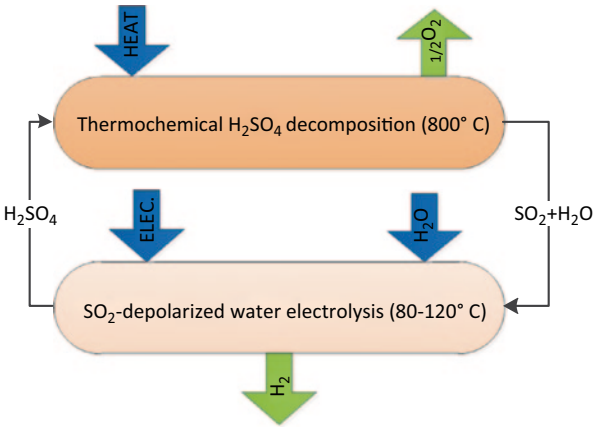

Fig. 8.2 Flow diagram of hybrid Sulfur thermochemical process

Thermochemical processes are characterized by chemical reactions, where water is indirectly split into oxygen and hydrogen with low electricity requirement. The Hybrid Sulfur (HyS) cycle is one of the simplest thermochemical water splitting processes, including only two reactions [4, 5]. Fig 8.2 shows the process of HyS cycle with respect to chemical reactions. First, high grade heat (T~800 °C) drives the thermochemical reaction for the decomposition of sulfuric acid. Second, SO_2-depolarized water splitting takes place with electrical work input for a temperature range of 80–120 °C. Simple water electrolysis theoretically consumes 1.229 V for splitting 1 mol of water, where HyS needs only 0.158 V electrical input.

The practical electricity consumption of electrochemical HyS step is around 0.6 V, which makes this system promising compared to other proposed hybrid cycles. High temperature steam electrolysis process can be considered as the reverse process of solid oxide fuel cells where the electrical energy demand can be decreased by around 24 % than the conventional water electrolysis at higher temperatures up to 1000 °C. Since thermal energy provided by nuclear power plants is cheaper than electricity, considerable savings are possible with this process [5]. A simple schematic of the HTSE process is represented in Fig. 8.3.

Overall hydrogen generation efficiency of nuclear hydrogen production plants starts from 25 %, where the nuclear plant efficiency is assumed to be between 33 and 40 %. Depending on the hydrogen production plant, overall efficiency of the plant may drastically decrease relative to the energy content used by the hydrogen generation plant. Conventional electrolysis (CE) is one of the most efficient hydrogen generation methods of those which are completely dependent on electrical energy input. Hybrid thermochemical processes decrease the power consumption, however the efficiency of such cycles are lower than that of CE. Thus, comparative cost assessment methods are of importance for an overall observation of economy of proposed methods. Maximum temperature requirement of the hydrogen production methods are important to specify which method is suitable for a particular nuclear reactor type. Table 8.2 summarizes this required information with temperature ranges and their coolant.

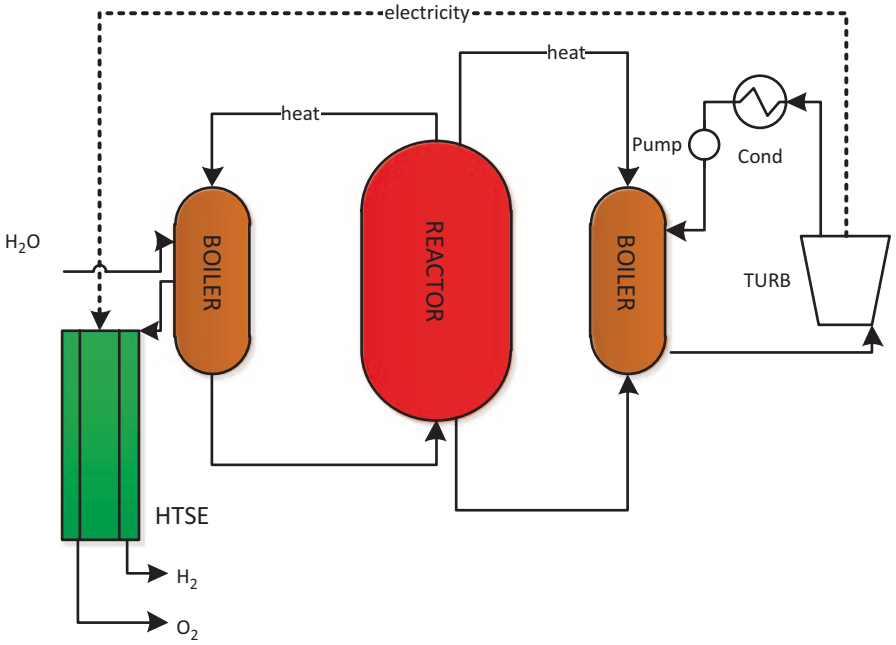

Fig. 8.3 A simplified diagram of nuclear HTSE process

In this study, HEEP software is utilized to estimate the cost of hydrogen from S-I cycle and HTSE system combined with a high temperature nuclear reactor. Hydrogen storage and transportation are also considered to estimate the cost from energy source to end user. The results are comparatively evaluated and discussed in order to specify the best cost effective method for the considered cases. The results are also compared and validated with in the literature to show how HEEP software compares to detailed studies.

8.2 HEEP Software and Utilization

The HEEP software is a newly released program for evaluation and economic analysis of large scale nuclear hydrogen production with storage and transportation options [12,13]. Some hydrogen production methods, such as low and high temperature electrolysis, thermo-electro-chemical hydrogen production, and steam methane reforming can be comparatively evaluated in terms of economics. Capacities, total capital cost, initial and annual fuel costs, etc. are included for cost estimation [14]. Some technical features of the HEEP software are summarized in Table 8.3.

The HEEP includes quick cost estimate features by providing general techno-economic inputs for the plants. Capital costs, O&M costs, decommissioning costs,

Table 8.2 Nuclear reactors and their characteristics for hydrogen generation (Adapted from [5])

Reactor type	Coolant	Reactor coolant temperature (°C)	Reactor size range (MWt)	Hydrogen production route
Light water reactors (PWR, AP, EPR)	Light water	280–325	2000–4080	Water electrolysis
Heavy-water reactors (CANDU, ACR)	Heavy water	310–319	2000–3200	Water electrolysis
Supercritical water reactor (S-LWR, CANDU, SCWR)	Light water	430–625	1600–2540	Water electrolysis, thermochemical
Liquid metal fast reactors (SFR, LFR)	Sodium: lead: lead bismuth	500–800	45–3000	Water electrolysis, thermochemical CH4 reforming
Molten salt reactors (AHTR)	Salts	750–1000	900–2400	Water & steam electrolysis, thermochemical CH4 reforming
Gas-fast reactors (GFR)	Helium	850	600–2400	Water & steam electrolysis, thermochemical CH4 reforming
High-temp. reactors (HTGR, VHTR)	Helium	750–950	100–600	Water & steam electrolysis, thermochemical CH4 reforming

initial and annual fuel feeds and thermal ratings of the nuclear plant are provided as inputs. One can use the library included in HEEP, or can use an existing data by updating the HEEP database for later use. All types of nuclear hydrogen production options, as well as storage and transportation can be adapted in the software. A captured image from main page of the HEEP software for data initialization is shown in Fig. 8.4.

More technical and introductive information about HEEP software, including cost components (Capital or fixed cost, operational costs, decommissioning cost), and execution module for levelized cost of hydrogen production can be found elsewhere [12–15]. The calculation of levelized hydrogen cost is made by HEEP as the ratio of sum of present value of generated hydrogen, storage, and transportation to present value of gross hydrogen generated [14].

$$C_{H2} = \frac{E_{NPP}(t_0) + E_{H2GP}(t_0) + E_{H2T}(t_0)}{G_{H2}(t_0)} \tag{8.1}$$

Table 8.3 Technical features of HEEP (Adapted from [15])

Nuclear plant	Hydrogen plant	Hydrogen storage plant	Transportation
Thermal rating	Co-located or away from NPP	Compression, liquefaction, metal hydride storing	Pipeline, vehicle transportation option
Heat for hydrogen plant	Heat consumption	Storage capacity	Transportation distance
Electricity rating	Electricity required	Electricity requirement	Fuel/electricity costs
Plant efficiency	Number of units	Capital cost	Other costs
Unit numbers	Capital cost	Compressor operating cost	Decommissioning cost
Capital costs	Energy usage cost	Other costs	
O&M costs	Other costs	Decommissioning cost	
Fuel costs	Decommissioning cost		
Decommissioning costs			
Annual fuel feed			
Types (HTRK, PBR, PMR)			

where *E, C and G* refer to expenditures, and subscripts NPP, H2GP, and H2T refer to nuclear power plant, hydrogen generation and storage, and hydrogen transportation, respectively.

The present value of expenditures is calculated with the following definition:

$$E(t_0) = \sum_{t\_i}^{t\_f} \frac{CI_t(t_0)}{(1+r)^{t-t_0}} + \sum_{t\_i}^{t\_f} \frac{R_t}{(1+r)^{t-t_0}} + \sum_{t\_i}^{t\_f} \frac{DC_t}{(1+r)^{t-t_0}} \tag{8.2}$$

Here, *CI, R and DC* refer to capital investment expenditures, Facility running expenditures, and decommissioning expenditures for the year *t*, respectively. Subscript *0* is for the base year, and defined *r* is real discount rate. The present value of the gross hydrogen generation for the time to is written as follows:

$$G_{H2}(t_0) = \sum_{t\_i}^{t\_f} \frac{G_{H2}(t_0)}{(1+r)^{t-t_0}} \tag{8.3}$$

Other details of execution module of HEEP software can be found in elsewhere [13–15]. Two different cases are proposed as case studies to investigate and perform the cost assessment of hydrogen production using HEEP. The motivation behind this comparison is that both hydrogen production plants are hybrid and require both electrical and heat input. High Temperature Gas Cooled Reactor (HTGR) is considered as the Nuclear Power Plant (NPP) with different capacities for the two proposed cases based on the hydrogen generation plant (HG) to be integrated. For Case I, HyS is considered as HG plant, while HTSE is integrated with NPP with Case II. Table 8.4 summarizes of the two cases considered in this study. In Case

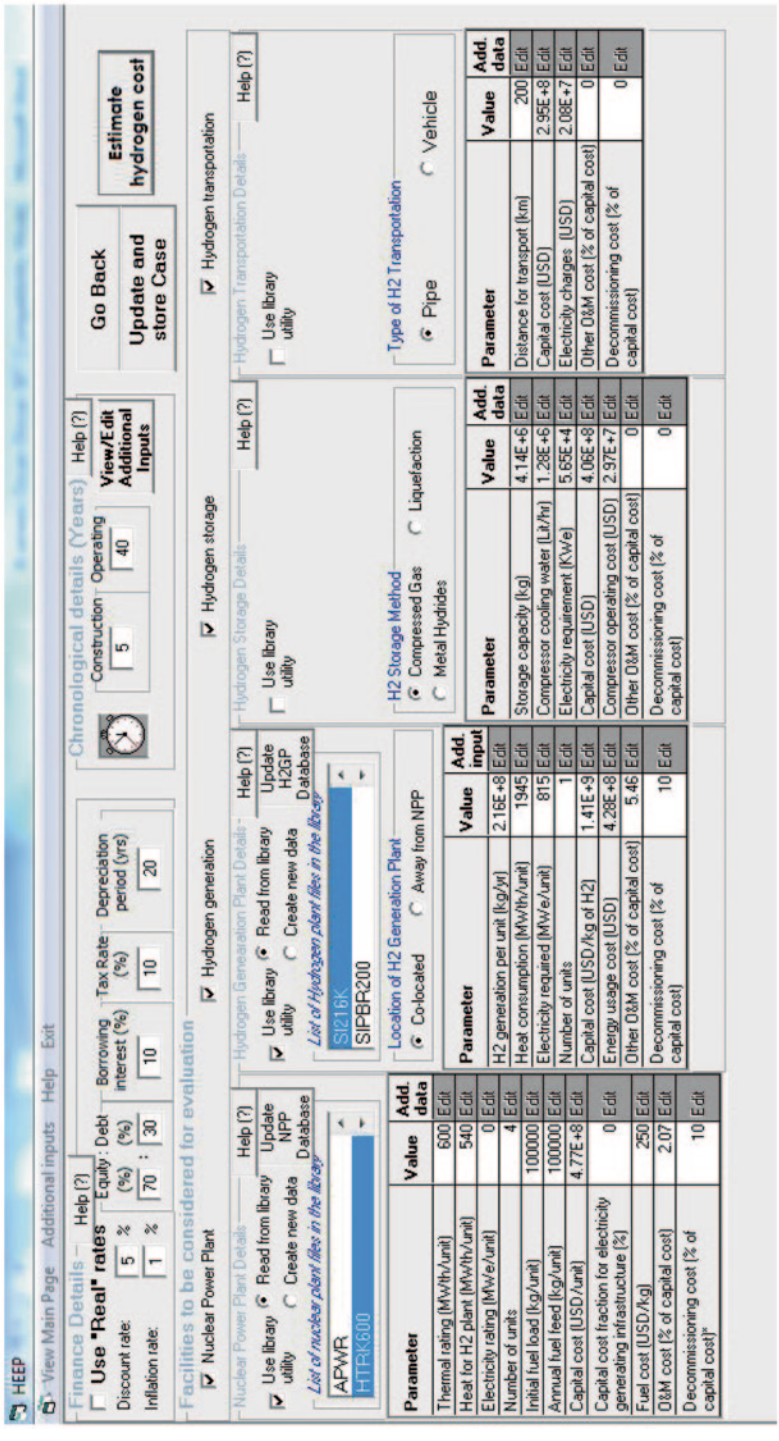

Fig. 8.4 A captured image from main page of HEEP software

Table 8.4 Capacity and thermal specifications of the considered cases of nuclear power plant and hydrogen generation plant

	CASE I	CASE II
Nuclear power plant	HTGR	HTGR
Thermal rating per unit (MW_{th})	835	1191
Number of units	2	2
Capital cost (M$/unit)	730	1080
O&M cost (%)	1.79	1.79
Fuel cost ($/kg)	275	275
Hydrogen Generation Plant	HyS	HTSE
Hydrogen generation (ton/year)	126,000	126,000
Number of units	1	1
Thermal-hydrogen efficiency (%)	45	40
Thermal energy consumption (MW_{th}/unit)	743	800
Electric energy required (MW_e/unit)	323	272
Capital cost (M$)	667	673
O&M cost (%)	4.46	5.5

Currency is CAD$

I, two units of capacity of 835 MW_{th} are used to provide the required thermal and electric load of HyS unit which are 742.9 MW_{th} and 323 MW_e, respectively. For Case II, the capacity of the two HTGR units is considered as 1191 MW_{th} to satisfy 412 MW_{th} and 788 MW_e of thermal and electric demand of the HTSE unit. Other operating parameters and data about the NPP and HG performance and operation are listed in Table 8.5.

8.3 Results and Discussion

For performing a complete assessment, comparative analysis considers different Hydrogen Storage (HS) technologies. Compressed Gas (CG), Liquefaction (LQ) and metal hydride (MH) technologies are introduced to be integrated with the production unit in for the two proposed cases. Also, transportation with pipeline of CG stored hydrogen is integrated with the system to investigate the effect of the travelled distance of transportation on the hydrogen production cost. Table 8.5 shows different parameters that are considered in the analyses of the system units. The plant construction and other time period parameters and financial data considered in the analysis are shown in Table 8.6.

As a comparative assessment for all the presented analyses performed in this study, Fig. 8.5 gives the cost of hydrogen production and cost share of different system units for the two proposed cases. Results are discussed and illustrated in details later on with more specific comparative figures to show the effect of each unit and its percentage effect on the final cost of hydrogen production.

From Fig. 8.6, the calculations shows hydrogen costs of 2 and 2.85 CAD$/kg for Cases I and II, respectively, when considering NPP-HG system integration with no storage or transportation units. The results in this figure also illustrate the share

Table 8.5 Operating parameters for the proposed systems

Nuclear power plant and hydrogen production plant	
Nuclear power plant efficiency (%)	40
Heat exchanger effectiveness (%)	86
Production	
Hydrogen production rate (kg/s)	4
Water consumption, L/kg H_2	9
Storage	
Hydrogen storage period (h)	168
Unit cost of cooling water for storage ($/ML)	0.00022
O&M cost for hydrogen storage (%)	5
Liquefaction	
Cooling water flow rate of Liquefaction, L/kg H_2	209
Daily Boil-off rate (%)	0.1
Metal hydride	
Specific heating power, MJ/kg H_2	23.26
Hydride cooling, L/kg H_2	209
Pipelines transportation	
Pipe equivalent radius (mm)	125
Inlet pressure of Hydrogen (bar)	53.2
Delivery pressure (bar)	50.0
Temperature of hydrogen (K)	293
Friction factor (-)	0.01
Decommissioning cost (%)	1
O&M cost (%)	1

Table 8.6 Time and financial parameters in the proposed study

General cost and operating parameters	
Depreciation period (year)	20
Construction period (year)	3
Operation life time/Return period (year)	50
Cooling before decommissioning (year)	1
Decommissioning (year)	9
Fuel cooling (year)	2
Waste cooling (year)	2
Unit cost of grid electricity (c$/kWh)	6.6
Capacity factor (%)	90
availability factor (%)	100
Discount rate (%)	5
Inflation rate (%)	1.2
Interest rate (%)	10
Tax rate (%)	10
Equity:debt	70:30

of cost from NPP and HG for each case considering same hydrogen production capacity. The cost of hydrogen production is generally higher for Case II due to the larger electric power demand for HTSE versus HyS, which is made apparent by the share of HG plant in the cost for each case. This also reflects on the cost share of

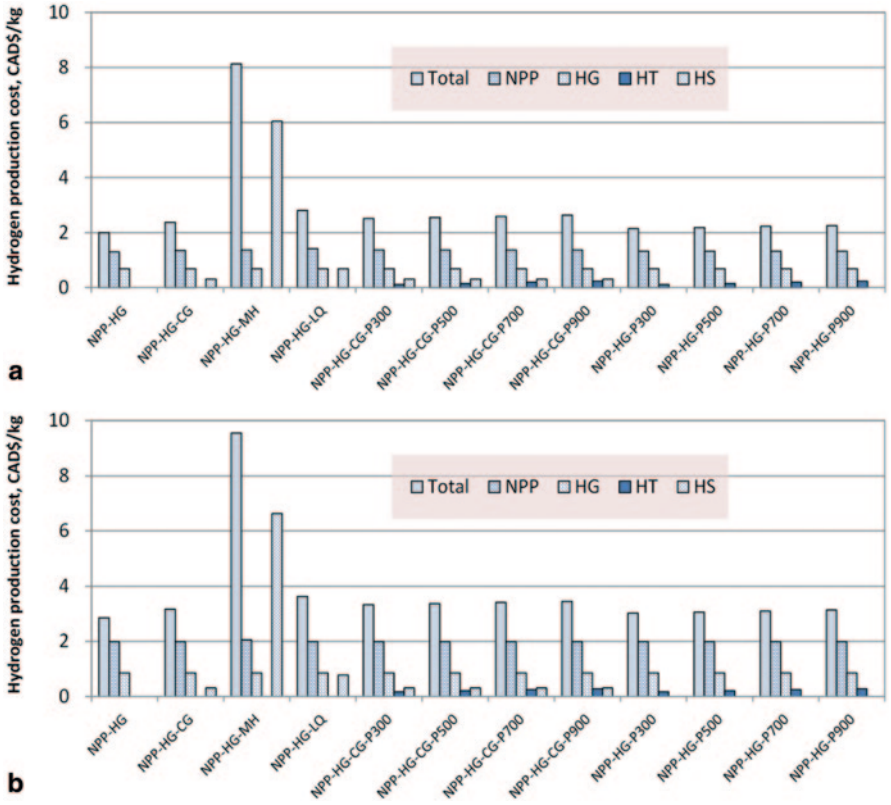

Fig. 8.5 Assessment of hydrogen production cost for the two considered cases **a** Case I, **b** Case II

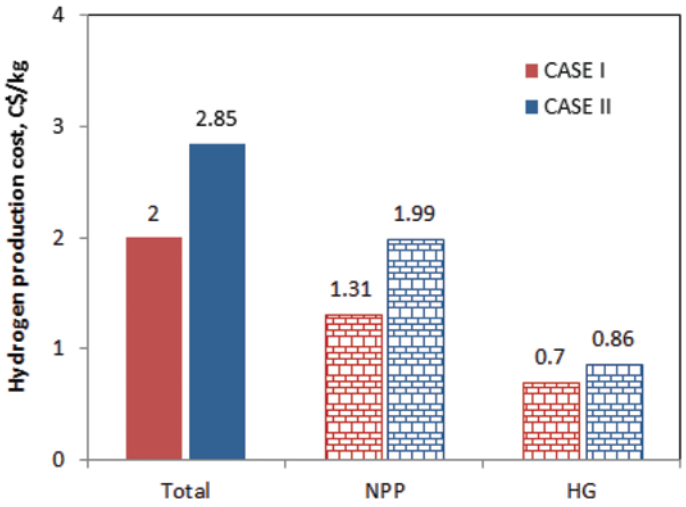

Fig. 8.6 Total cost and share of hydrogen production cost of NPP and HG for the proposed cases

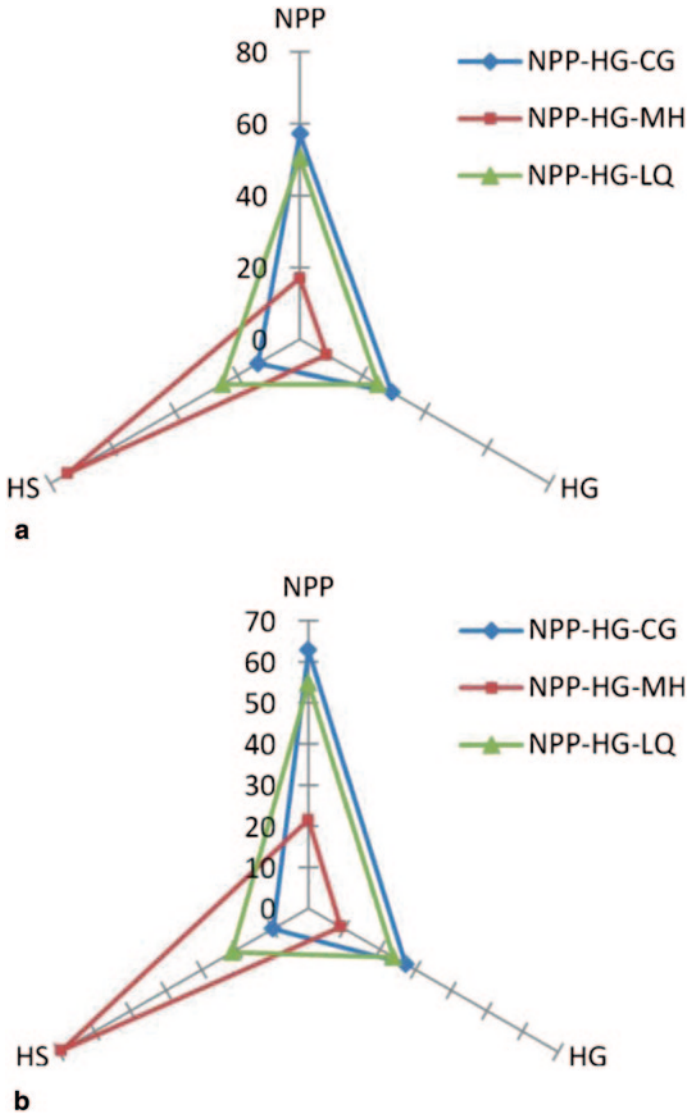

Fig. 8.7 Percentage of share of cost for the system plants for a) Case I, b) Case II, at different hydrogen storage scenarios

NPP which is higher for Case II, as more electric power generation is required to be supplied from the NPP.

Three different scenarios of hydrogen storage options are considered in the comparative analysis of Case I and Case II, as shown in Figs. 8.7 and 8.8. The results in Fig. 8.7 show the percentage of cost breakdown with respect the cost share of NPP, HG and HS. In Fig. 8.8, total cost of hydrogen production is presented for the three

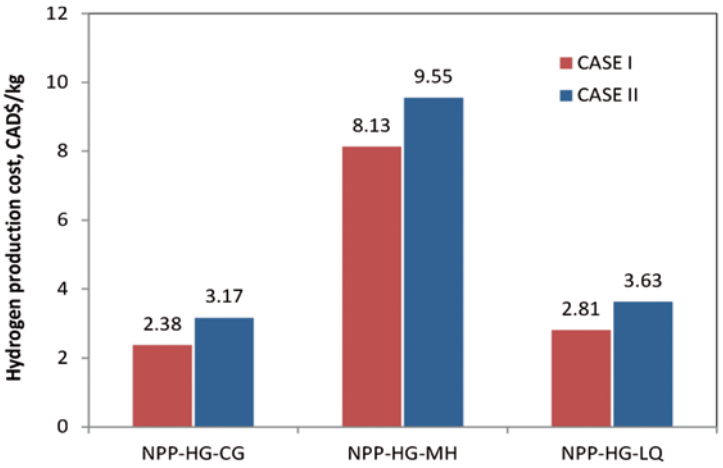

Fig. 8.8 Total hydrogen production cost comparison for different storage scenarios for the proposed cases

different storage cases. From the presented results, it can be seen that Case I experience lower cost for all storage options, which is due to the same reasons discussed earlier in Fig. 8.6.

The results shown in Fig. 8.9 highlight the effect of transportation distance for two different cases: with compressed gas storage of the produced hydrogen, and without a storage option. Results indicate that integration of hydrogen storage increases production costs by an average of 20 cents per kg of hydrogen. Furthermore, increasing travel distance from 300 km to 900 km is associated with an average cost increase of 11 cents. It can be also seen from the presented results that increasing the travelling distance from 300 to 900 km caused an average increase of 11 cents in the cost. Figure 8.10 shows the cost share of pipelines as transportation option at different travelled distance.

Conclusions

In this study, comparative cost assessment of two nuclear hydrogen production plants has been conducted using the HEEP software package, provided by IAEA. The first cases differ primarily in terms of hydrogen generation plants, namely hybrid sulfur and high temperature steam electrolysis. Heat and power source is considered as high temperature nuclear reactor for both cases. Various options for hydrogen storage and transportation is also included for the comparative assessment of cases. The following implications can be deduced from the proposed cases.

- Cost of hydrogen for the HyS integrated nuclear plant is 20% lower than HTSE integrated plant. This outcome is strongly dependent on higher electrical energy

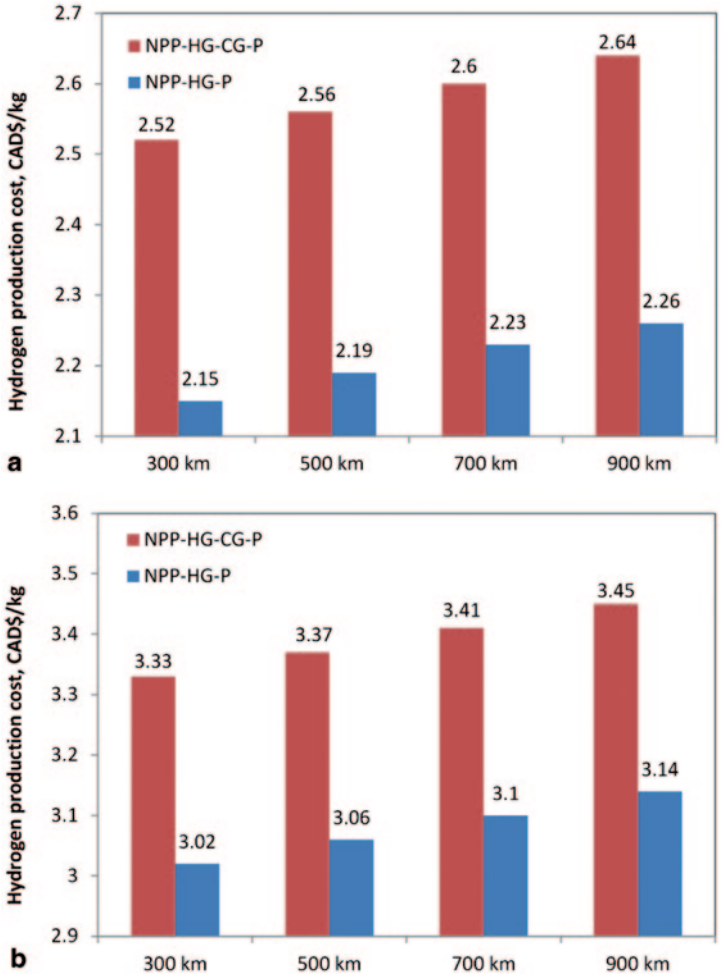

Fig. 8.9 Hydrogen production cost considering NPP-HG-CG-P and NPP-HG-P for **a** Case I, **b** Case II

requirement of HTSE plant. Hydrogen cost for the nuclear hydrogen production for HyS cycle is 2 CAD$/kg, and 2.85 CAD$ for HTSE system.

- Capital, operational and maintenance costs of HTSE unit are slightly higher than those of HyS cycle. This is due to continuous high grade heat requirement of the HTSE system resulting with lower efficiencies, and higher operational costs.
- Cost of hydrogen drastically increases when metal hydride storage is considered as the hydrogen storage option. Although metal hydrides are the best option to store larger amount of hydrogen than gas compression and liquefaction, expensive material processing brings relatively high capital cost. Capital cost

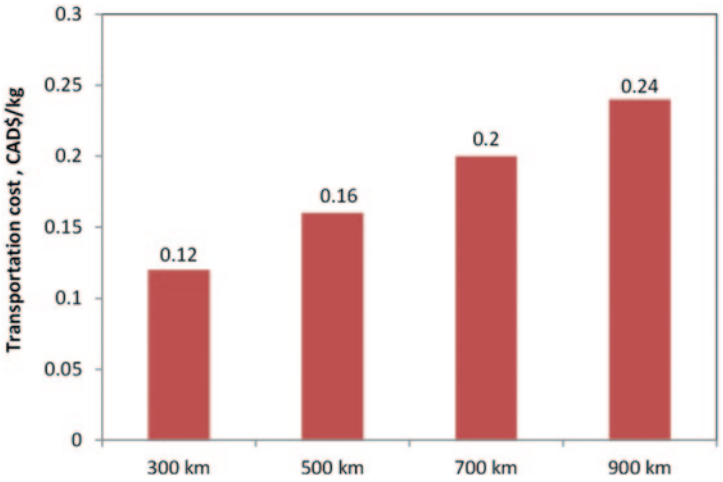

Fig. 8.10 Transportation cost considering pipeline transportation of compressed hydrogen for different pipeline lengths

of metal hydride storage system is 3340 M$, where it is 54.9 and 10.9 M$ for liquefaction and gas compression, respectively.

- Pipeline transportation is the best option for delivering hydrogen to end user with low investment costs than that of vehicle transportation, and zero greenhouse gas emissions. When direct pipeline transportation of generated hydrogen is considered, 7% increase in hydrogen cost is observed for 300 km pipeline length. This value can go up to 13% at 900 km. When compressed gas is fed to pipeline, hydrogen cost drastically increases due to additional investment cost of hydrogen compression plant.
- Nuclear power plant accommodates 65.5% of total hydrogen cost for the nuclear HyS cycle, where it is 69.8% for nuclear HTSE system. This is due to higher electricity requirement of HTSE system. Required electricity is also supplied by converting thermal load into electricity at lower efficiencies at a conventional steam turbine, and resulting in higher annual fuel load and bigger reactor size.

In summary, HEEP software is a user friendly cost evaluation program which compiles and provides economic data for various nuclear reactor types and hydrogen generation plant. It also provides a user defined option for systems that do not exist in the library of the software. An extended library is currently under development by the IAEA for the HEEP software package, including a larger database for all types of nuclear hydrogen generation options.

Nomenclature

AHTR	Advanced high temperature reactor
CANDU	Canada deuterium-uranium
CE	Conventional electrolysis

CG Compressed gas
EPR European pressurized reactor
HEEP Hydrogen economy evaluation program
HG Hydrogen generation
HTGR High temperature reactor
HTSE High temperature steam electrolysis
HyS Hybrid Sulfur
IAEA International Atomic Energy Agency
LFR Lead-cooled fast reactor
LQ Liquefaction
LWR Light water reactor
MH Metal hydride
NPP Nuclear power plant
O&M Operational & Maintenance
P Pipeline
PWR Pressurized water reactor
SCWR Supercritical water-cooled reactor
SFR Sodium-cooled fast reactor
S-LWR Super light water reactor
SMR Steam methane reforming
VHTR Very high temperature reactor

References

1. Holladay JD, Hu J, King DL, Wang Y (2009) An overview of hydrogen production technologies. Catalysis Today 139:244–60
2. Dincer I, Zamfirescu C (2012) Sustainable hydrogen production options and role of AIHE. Int J Hydrog Energy 37:16266–16286
3. Bartels JR, Pate MB, Olson NK (2010) An economic survey of hydrogen production from conventional and alternative energy sources. Int J Hydrog Energy 35:8371–8384
4. Gorensek MB (2011) Hybrid sulfur cycle flowsheets for hydrogen production using high-temperature gas-cooled reactors. Int J Hydrog Energy 36:12725–12741
5. Yan XL, Hino R (2011) Nuclear hydrogen production handbook. CRC, New York
6. Doe Hydrogen, Fuel Cells Records (2012) http://www.hydrogen.energy.gov/pdfs/12024_h2_production_cost_natural_gas.pdf. Accessed 14 April 2014
7. Schultz K (2003) Use of modular helium reactor for hydrogen production. World Nuclear Annual Symposium, 1–11
8. Giaconia A, Grena R, Lanchi M, Liberatore R, Tarquini P (2007) Hydrogen/methanol production by sulfur-iodine thermochemical cycle powered by combined solar/fossil energy. Int J Hydrog energy 32:469–481
9. Kroposki B, Levene J, Harrison K (2006) Electrolysis: information and opportunities for electric power utilities. http://www.nrel.gov/docs/fy06osti/40605.pdf. Accessed 14 April 2014
10. National Renewable Energy Laboratory (2009) http://www.hydrogen.energy.gov/pdfs/46612.pdf. Accessed 18 April 2014
11. Gouse SW, Gray D, Tomlinson G (1993) Integration of fossil and renewable energy technologies to mitigate carbon dioxide. Energy Conv Manage 34:1023–1030

12. Internatioanl Atomic Energy Agency (IAEA) (1999), Hydrogen as an energy carrier and its production from nuclear power. Vienna, IAEA-TECDOC-1085.
13. Khamis I (2010) HEEP: a new tool for the economic evaluation of hydrogen economy. Int J Hydrog Energy 35:8398–8406
14. HEEP user manual (2012) Available online http://www.iaea.org/NuclearPower/HEEP/. Accessed 18 April 2014
15. Khamis I (2011) HEEP: an overview of the IAEA HEEP software and international programmes on hydrogen production using nuclear energy. Int J Hydrog Energy 36:4125–4129

Chapter 9
Thermodynamic Analysis of a Cycle Intergrating a Solid-Oxide Fuel Cell and Micro Gas Turbine with Biomass Gasification

Mehdi Hosseini, Marc A. Rosen and Ibrahim Dincer

Abstract An integrated solid-oxide fuel cell-micro gas turbine system with biomass gasification is investigated based on energy and exergy. The system consists of a biomass gasification system, a solid-oxide fuel cell (SOFC), a micro gas turbine (MGT), and a heat recovery steam generator (HRSG). Various parameters are determined for the integrated system, including syngas molar fraction, and heat input to the gasifier. Moreover, exergy flows and exergy destruction rates of major components of the system are calculated. The maximum energy and exergy efficiencies of the gasification system are 65.7 and 84.8 %, respectively. These values for the SOFC-MGT cycle with biomass gasification are reported as 58.3 and 69.6 %. The variations of syngas molar fraction and mass flow rate, gasifier exergy destruction, and CO_2 emissions with the steam to carbon (SC) ratio are investigated. The results show that there is an optimum value for the SC ratio at which the syngas mass flow rates and the gasification energy efficiency reach a maximum. The CO_2 emission, which is an important factor for the sustainability of the system, increases by 19.4 % as the value of the SC ratio increases. Increasing the gasification temperature, from 800 to 1000 °C, reduces the energy and exergy efficiencies of the total integrated system by 7.90 %, mainly by increasing the required heat input to the gasifier.

Keywords Biomass gasification · Solid oxide fuel cell · Micro gas turbine · Energy · Exergy

M. Hosseini (✉) · M. A. Rosen
Faculty of Engineering and Applied Science, University of Ontario Institute of Technology, 2000 Simcoe St North, Oshawa, ON L1H 7K4 Canada
e-mail: Mehdi.Hosseini@uoit.ca

M. A. Rosen
e-mail: Marc.Rosen@uoit.ca

I. Dincer
Department of Mechanical Engineering, University of Ontario Institute of Technology (UOIT), 2000 Simcoe Street North, Oshawa, ON L1H 7K4, Canada
e-mail: ibrahim.dincer@uoit.ca

I. Dincer et al. (eds.), *Progress in Sustainable Energy Technologies: Generating Renewable Energy,* DOI 10.1007/978-3-319-07896-0_9,

9.1 Introduction

Solid oxide fuel cells (SOFCs) are capable of producing electric power and heat in an integrated cycle. They can be integrated with micro gas turbines (MGTs) and heat recovery steam generators (HRSGs) to increase electricity and heat generation [1]. For instance, Motahar and Alemrajabi [2] report an exergy analysis of an integrated SOFC-GT cycle with and without steam injection to the combustion chamber of the gas turbine. They propose the use of the gas turbine flue gas in an HRSG and inject the produced steam in the combustion chamber. The exergy efficiency of the integrated system is seen to increase by 12 % with steam injection. Moreover, they report the effects of compression ratio, current density, and the HRSG pinch point on system performance. Energy and exergy analyses of a hybrid fuel cell-gas turbine combined heat and power (CHP) system are reported by Akkaya et al. [3]. For exergetic performance evaluation, exergy efficiency, exergy output and exergy loss rate of the system are considered. Methane is used as the fuel and the molar fractions of the by-product species are reported for each point in the system [3]. In other systems, hydrogen, methane, and natural gas can be used as the fuel, but the integrated SOFC-MGT cycles are analyzed independent of the fuelling processes. Nevertheless, SOFCs can operate with different types of fuels, thanks to their internal reforming capability and high resistivity to carbon poisoning. However, higher hydrocarbons require pre-reforming or cracking before entering the fuel cell stack, because they decompose at conditions higher than the stack temperature [4].

With the increased attention on mitigation of carbon dioxide emission and other environmental considerations, the use of renewable energy resources in power generation is receiving much attention. Biomass can be used directly (direct burning) or indirectly (as a biofuel) to generate electricity [5]. Biomass gasification has been demonstrated to be a feasible and promising technology in the future energy market [6]. The gas mixture product of biomass gasification contains several species, depending on the process type and operational conditions. Stoichiometric calculations can help determine the products of reaction [7]. Abuadala and Dincer [8] consider the use of biomass gasification product gas as the fuel feed to a SOFC, as a potential, integrated application. In the present work, we consider a similar system in which the product gas is fed to the fuel cell stack after gas cleaning and CO_2 removal. The aim is to improve understanding of its performance, and this is accomplished by performing a parametric study of the effect of steam to carbon (SC) ratio on the performance of the SOFC-MGT cycle integrating biomass gasification. The variations in molar fraction and lower heating value (LHV) of the syngas (a mixture of H_2 and CO), and the gasification process exergy destruction and energy and exergy efficiencies are reported, as the steam to carbon ratio changes.

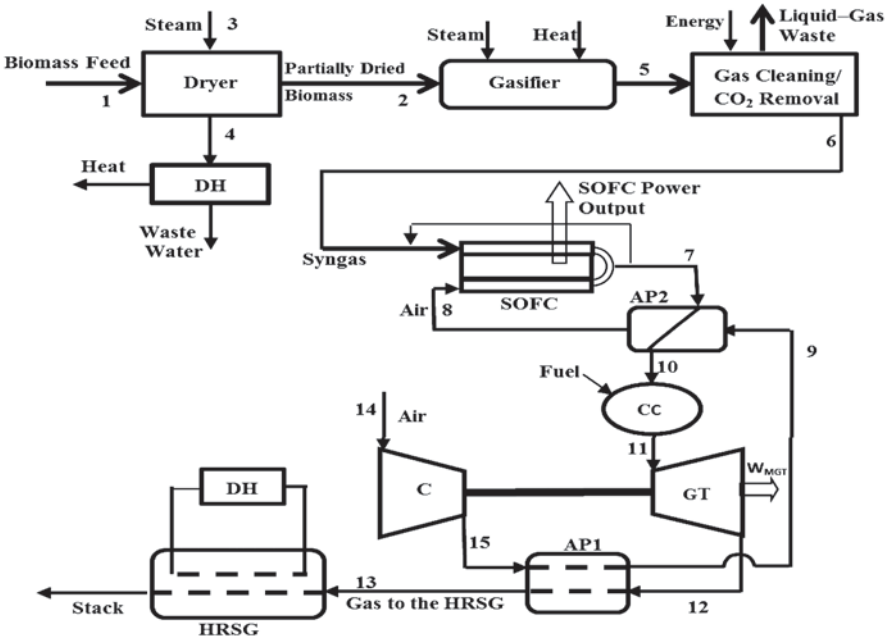

Fig. 9.1 Schematic of the integrated SOFC-MGT with biomass gasification

9.2 System Description

The integrated system includes a biomass gasification unit, an SOFC, a micro gas turbine and a heat recovery unit. Each of these systems consists of components, illustrated in Fig. 9.1, in which processes occur. Sawdust is fed to the biomass dryer before entering the gasifier. In the analyses, a direct-steam drying process is considered to remove 50% of the biomass moisture content. In the gasifier, biomass is converted to a mixture of gases in the presence of superheated steam. Biomass gasification is an endothermic process, and the gasification system is considered to be indirectly heated by an external heat source.

The product gas mixture leaving the gasifier contains CO, H_2, CH_4, CO_2, H_2O, N_2, and C. The lower heating value (LHV) of the product gas is strongly dependant on the mixture composition. Moreover, downstream components in the integrated system are affected by the gas properties. Therefore, gas cleaning and CO_2 removal are added to the system. With these post-gasification processes, the product syngas consists of CO, H_2, and CH_4 and is fed to the solid oxide fuel cell for power production.

The basic electrochemical reactions taking place in a SOFC stack are given by [1, 9]

$$CH_4 + H_2O \leftrightarrow 3H_2 + CO \tag{9.1}$$

$$CO + H_2O \leftrightarrow H_2 + CO_2 \tag{9.2}$$

$$H_2 + \frac{1}{2}O_2 \rightarrow H_2O \tag{9.3}$$

Characteristic curves of SOFCs are obtained based on the equilibrium constants and reaction rates of Eq. 9.1–9.3. The oxygen ions are formed in the cathode side of the fuel cell and pass through the electrolyte to the anode. The electrochemical reaction between hydrogen and oxygen ions releases electrons, which pass through an external electric circuit providing the power output of the SOFC. To avoid cell starvation, only a certain percent of the syngas reacts with oxygen ions in the anode. This is specified by fuel utilization factor. The by-product of the electrochemical reactions leaves the fuel cell stack with a temperature between 800 to 1000 °C. Also, the by-product contains some non-reacted syngas. In order to recover the energy from the SOFC exhaust gas, an afterburner is utilized to burn the remaining syngas and provide the micro gas turbine with the required input energy. Therefore, the by-product gas leaving the fuel cell anode side mixes with the air from the cathode side. The combustion process in the afterburner produces a high-enthalpy gas which can be used in the MGT for electric power generation. Before the combustion gas enters the micro gas turbine, it is utilized to preheat the air entering the fuel cell stack. The combustion chamber of the micro gas turbine is used to fix the turbine inlet temperature (TIT). The combustion gases enter the MGT, produce mechanical energy, and leave the MGT with a temperature between 550 and 750 °C, depending on the compressor pressure ratio. The mechanical energy of the MGT is converted into electricity in the generator. The MGT flue gas has a significant amount of energy, which is recovered in the heat recovery steam generator. The flue gas enters the HRSG and transfers its energy to the water flowing inside the tubes of the HRSG. Unless applied for power generation purposes, most HRSGs produce saturated steam for steam utilizing units.

9.3 Analyses

Biomass Gasification System

Superheated steam is used as the gasification medium in the gasifier. Sawdust is gasified in the presence of steam according to the following overall chemical equation:

$$C_aH_bO_cN_d + SC \times H_2O(steam) + \dot{Q}_{\text{gasifier}} \rightarrow n_1CO + n_2H_2 + n_3CH_4 + n_4CO_2 + n_5H_2O + n_6N_2 + n_7C \tag{9.4}$$

Minimization of the Gibbs Free Energy is used [7, 10]to obtain the reaction coefficients (n_1 to n_7). To calculate the gasifier heat input, the steady-state energy balance is used:

$$\dot{n}_{\mathrm{mb},2}\left(h^{f}_{\mathrm{mb},2}+\overline{h}_{\mathrm{mb},2}-h^{0}_{\mathrm{mb},2}\right)+\dot{n}_{\mathrm{s}}\left(h^{f}_{\mathrm{s}}+\overline{h}_{\mathrm{s}}-h^{0}_{\mathrm{s}}\right)+\dot{Q}_{\mathrm{gasifier}}=\left[\sum\nolimits_{\mathrm{i}=1}^{7}\dot{n}_{\mathrm{i}}\left(h^{f}_{\mathrm{i}}+\overline{h}_{\mathrm{i}}-h^{0}_{\mathrm{i}}\right)\right]_{\mathrm{p}} \tag{9.5}$$

Here, $h^{f}_{\mathrm{mb},2}$ is the enthalpy of formation of biomass, which is affected by the moisture content of the biomass, $\overline{h}-h^{0}$ is the sensible heat of the material relative to the reference state, which is the ambient condition. Further, "mb" refers to moist biomass and "s" to steam. Also, $\dot{n}$ denotes the molar flow rate of the species in the reaction, and the subscript "i" refers to the product species. The enthalpy of formation and the sensible heat of the product gas, a gas mixture, are calculated based on the data and approach presented by Borgnakke and Sonntag [11].

A steady-state exergy balance for the gasifier follows:

$$\dot{E}x_{\mathrm{mb},2}+\dot{E}x_{\mathrm{s}}+\dot{E}x_{\mathrm{Q}}=\dot{E}x_{\mathrm{p}}+\dot{I}_{\mathrm{gasifier}} \tag{9.6}$$

The biomass dryer and district heating unit are parts of the gasification system. The necessary energy and exergy balance equations, which lead to the calculation of steam input to the dryer and heat flow rate of the district heating unit, are presented in a previous paper [10]. Considering these two components, the total energy and exergy efficiencies respectively of the gasification system can be obtained:

$$\eta_{\mathrm{gasification}}=\frac{\dot{m}_{\mathrm{syngas}}\times LHV_{\mathrm{syngas}}+\dot{Q}_{\mathrm{DH}}}{\dot{m}_{\mathrm{biomass}}\times LHV_{\mathrm{biomass}}+\dot{E}n_{\mathrm{Steam}}+\dot{Q}_{\mathrm{gasifier}}+\dot{E}n_{\mathrm{gas-cleaning}}} \tag{9.7}$$

$$\psi_{\mathrm{gasification}}=\frac{\dot{m}_{\mathrm{syngas}}\times ex_{\mathrm{syngas}}+\dot{E}x_{\mathrm{q,DH}}}{\dot{m}_{\mathrm{biomass}}\times ex_{\mathrm{biomass}}+\dot{E}x_{\mathrm{Steam}}+\dot{E}x_{\mathrm{Q}}+\dot{E}x_{\mathrm{gas-cleaning}}} \tag{9.8}$$

In Eqs. 9.7–9.8, steam use is considered for both the dryer and the gasifier.

SOFC-MGT System

Colpan et al. [12] present a model for the electrochemical reaction in the SOFC. Their model considers a mixture of H_2, CO and CH_4 as the syngas fuel. In the present paper, the same gas species are used in the fuel cell. The electric power output of the fuel cells stack can be expressed as

$$\dot{W}_{\mathrm{SOFC}}=V\times i\times A_{\mathrm{cell}}\times N_{\mathrm{SOFC}} \tag{9.9}$$

where V is the output voltage, i is the current density, A_{cell} is the single cell active area, and N_{SOFC} is the total number of cells in the stack.

The modeling of the afterburner and the combustion chamber is based on combustion reactions of the remaining syngas in the fuel cell exhaust gas and the gas turbine inlet temperature. The gas turbine and the compressor are modeled based on isentropic relations and isentropic efficiencies. Therefore, the compressor outlet air temperature is obtained as follows [13]:

$$T_{\text{oc}} = T_{\text{ic}} \left\{ 1 + \frac{1}{\eta_{\text{c}}} \left(\left[rc \right]^{\frac{\gamma_{\text{a}} - 1}{\gamma_a}} - 1 \right) \right\} \tag{9.10}$$

where T_{oc} and T_{ic} are the compressor outlet and inlet air temperatures, η_{c} is the compressor isentropic efficiency, is the compression ratio, and γ_{a} is the specific heat ratio of air.

A similar relation is used to calculate the exhaust gas temperature of the gas turbine:

$$T_{\text{oMGT}} = T_{\text{TIT}} \left\{ 1 - \eta_{\text{MGT}} \left(1 - \left[rc \right]^{\frac{\gamma_{\text{g}} - 1}{\gamma_g}} \right) \right\} \tag{9.11}$$

Here, T_{oc} and T_{ic} are the gas turbine outlet and inlet gas temperatures, η_{MGT} is the MGT isentropic efficiency, *rc* is the compression ratio, and γ_{g} is the specific heat ratio of gas. The temperatures are calculated to obtain the specific work quantities of the compressor and the gas turbine.

The gases leaving the MGT are fed to the HRSG to produce steam for steam/hot water utilization purposes. Accounting for the heat recovered in the HRSG, the total efficiencies of the SOFC-MGT CHP system are

$$\eta_{\text{SOFC-MGT CHP}} = \frac{\dot{W}_{\text{SOFC}} + \dot{W}_{\text{MGT}} + \dot{Q}_{\text{HRSG}}}{\dot{m}_{\text{fuel,SOFC-MGT}} \cdot LHV_{\text{syngas}}} \tag{9.12}$$

$$\psi_{\text{SOFC-MGT CHP}} = \frac{\dot{W}_{\text{SOFC}} + \dot{W}_{\text{MGT}} + \dot{E}x_{\text{Q,HRSG}}}{\dot{m}_{\text{fuel,SOFC-MGT}} \cdot ex_{\text{syngas}}} \tag{9.13}$$

Assumptions and Data Use

The following assumptions are made in the analyses of the integrated SOFC-MGT system with biomass gasification:

- The system operates at steady-state.
- All gases are considered ideal.
- Heat losses to the environment from the system boundary are considered negligible.

Table 9.1 Input parameters for the gasification system

Parameter	Value
Dryer	
Biomass feed rate (kg/s)	0.011[a]
Superheated steam pressure (bar)	3
Superheated steam temperature (°C)	200
Moisture fraction of feed biomass ($kg_{moisture}$/kg_{WB})	0.5[b]
Gasifier	
Steam pressure (bar)	10[b]
Steam temperature (°C)	400
Steam to carbon ratio, SC	2[b]

[a] This flow rate is equivalent to 36 kg/hr of biomass
[b] Adapted from [7]

Table 9.2 Input parameters for the SOFC system

Parameter	Value
Compressor inlet air temperature (T_0) (°C)	25
Air compressor is entropic efficiency, %	85[a]
Fuel compressor is entropic efficiency, %	87[a]
Stack outlet temperature (°C)	1000[b]
Activation area (cm^2)	834[b]
Cell current density (A/cm^2)	0.350
Fuel utilization factor	0.850[b]
Compressor pressure ratio, rc	9
AP1 outlet temperature (Point 9 in Fig. 9.1) (°C)	527

[a] Adapted from [15]
[b] Adapted from [3, 12]

Table 9.3 Input parameters for the MGT–HRSG system

Parameter	Value
Micro Gas Turbine	
MGT is entropic efficiency	0.93[a]
Turbine inlet temperature (K)	1400
Heat Recovery Steam Generator	
Pinch point temperature difference (°C)	10
Outlet steam pressure (bar)	10

[a] Adapted from [15]

- Pressure drops along the system are considered negligible.
- Gasification takes place in equilibrium.
- The sawdust biomass has a chemical formula $C_{4.643}H_{6.019}O_{2.368}N_{0.021}$ [14].

Tables 9.1, 9.2 and 9.3 list the input parameters for the analyses of the integrated system.

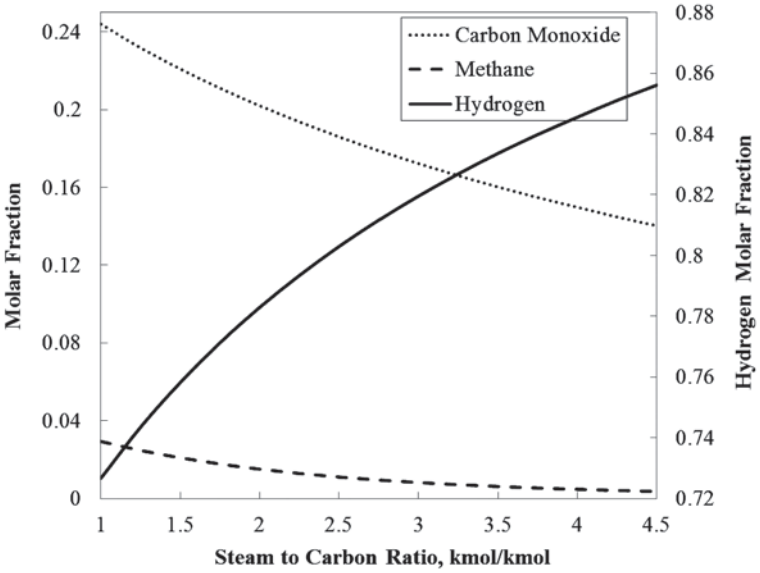

Fig. 9.2 Variation of molar fractions of syngas species with steam to carbon ratio

9.4 Results and Discussion

The effect of steam to carbon ratio on the syngas species molar fraction is shown in Fig. 9.2. When SC varies from 1 to 4.5 the hydrogen molar fraction increases 17.8%, while the carbon monoxide and methane molar fractions decrease by 42.5 and 87.7%, respectively. These significant changes in the molar fraction result in the variation of the total mass flow rate of the syngas with SC shown in Fig. 9.3. At SC = 2, the syngas mass flow rate reaches its maximum value, after which it reduces gradually. The lower heating value of the syngas is calculated based on molar fraction of each species in the mixture. The trade-off between the variations of molar fractions with the SC results in the final variation of LHV is illustrated in Fig. 9.3.

The gasification heat requirement and exergy destruction rate are affected by the steam to carbon ratio. Introducing more steam to the gasifier decreases the need for external heat for the gasification process. The steam acts as the gasification medium and its energy content is used by the gasification process. With more steam entering the gasifier, more energy is introduced and the required heat input decreases. According to Fig. 9.4, increasing the gasification temperature results in an increase in the heat requirement of the gasifier. Although, the heat requirement of the gasifier varies significantly with the change in temperature, the gasification process exergy destruction rate does not seem to be affected noticeably. This is shown in Fig. 9.5, in which the exergy destruction rate is observed to decrease with increasing steam to carbon ratio.

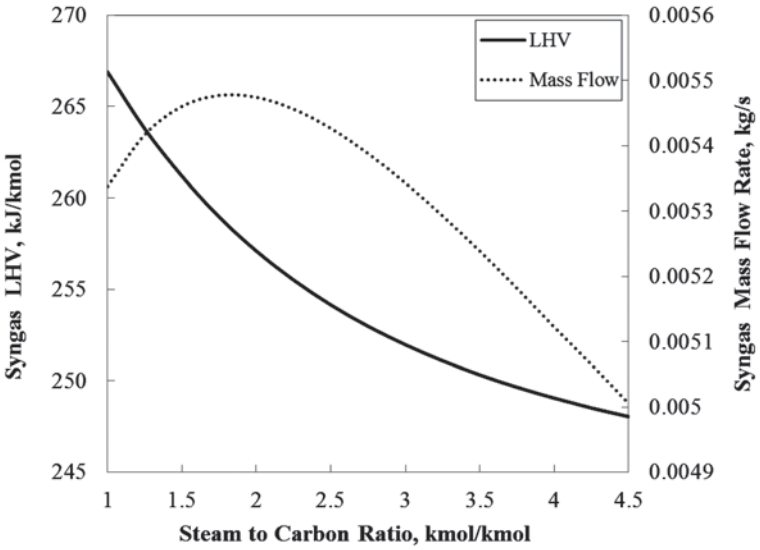

Fig. 9.3 Variation of syngas lower heating value and mass flow rate with steam to carbon ratio

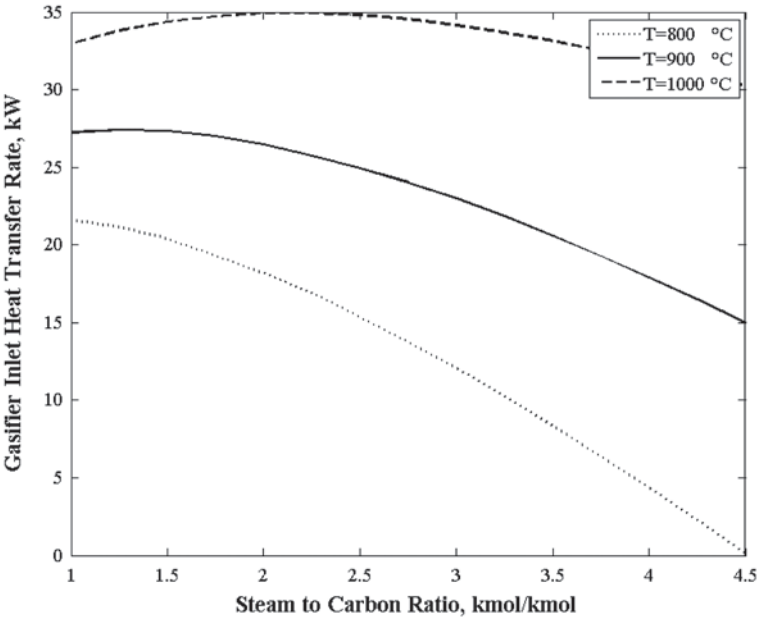

Fig. 9.4 Effect of steam to carbon ratio on the gasifier heat requirement rate for various gasification temperatures

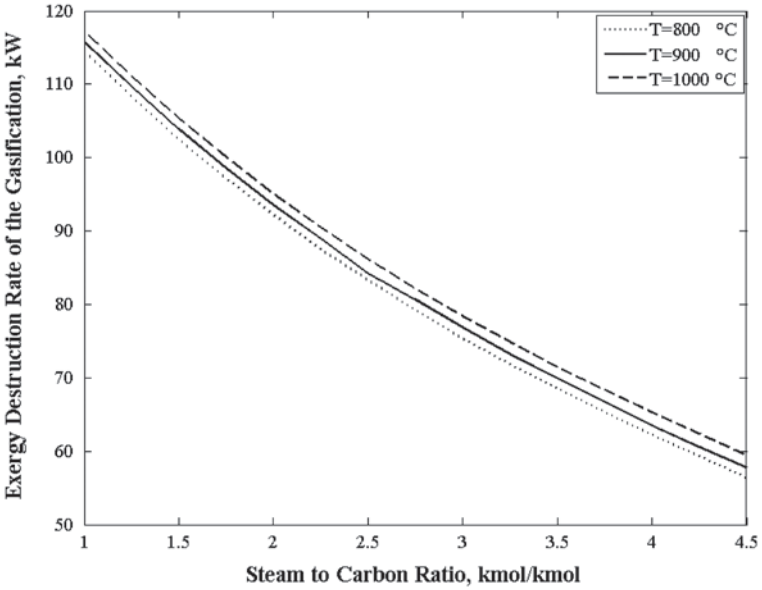

Fig. 9.5 Gasification exergy destruction rate vs. steam to carbon ratio for various gasifier temperatures

Energy and exergy efficiencies of biomass gasification are obtained using Eqs. 7 and 8. The variations of these efficiencies with SC and the gasifier temperature are illustrated in Figs. 9.6 and 9.7, respectively.

Fig. 9.6 shows that for a gasifier temperature of 800 °C, the total energy efficiency of the gasification process reaches its maximum value of 65.6 % at SC = 2. With further increase in the gasification medium into the gasifier, the energy efficiency drops, reaching 62.4 % for SC = 4.5. Increasing the gasification temperature reduces the total energy efficiency, as seen in Fig. 9.6. The gasification exergy efficiency exhibits a similar trend as the energy efficiency. However, the maximum value occurs at higher SC values. Higher values are achieved for efficiencies based on exergy compared to energy, because the exergy of heat is less than its energy. Since heat is an input to the gasification process, the denominator of the efficiency definition for exergy is less than that for energy.

The SOFC-MGT power output varies as a result of the change in the syngas LHV, as do the total energy and exergy efficiencies of the integrated SOFC-MGT system with biomass gasification. These variations are illustrated in Figs. 9.8 and 9.9.

According to the results in Fig. 9.2, the molar fraction of both CO and CH_4 decrease with increasing steam to carbon ratio. These two constituents are the source of CO_2 production in the SOFC-MGT cycle. However, by introducing more steam to the gasifier, the rate of CO_2 production increases, which results in an overall increase in the CO_2 emission of the integrated SOFC-MGT cycle with biomass gasification (Fig. 9.10).

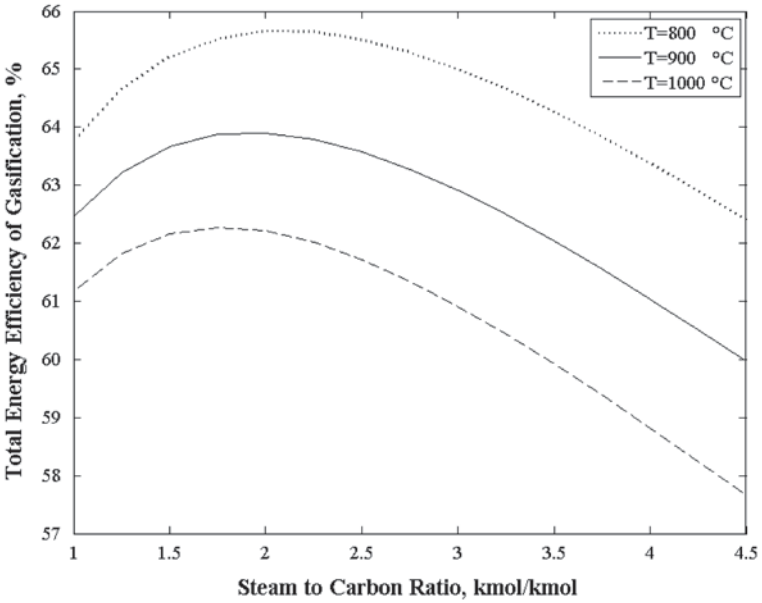

Fig. 9.6 Total energy efficiency of sawdust gasification vs. steam to carbon ratio, for various gasifier temperatures

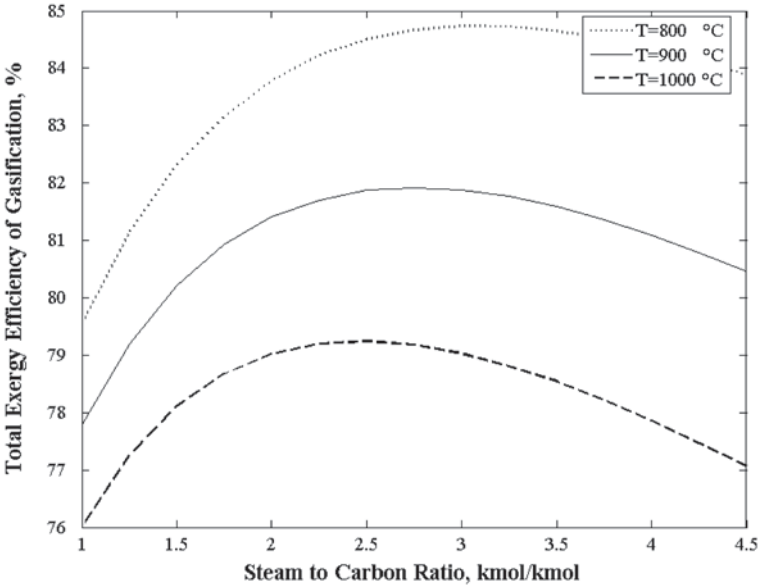

Fig. 9.7 Total exergy efficiency of sawdust gasification vs. steam to carbon ratio, for various gasifier temperatures

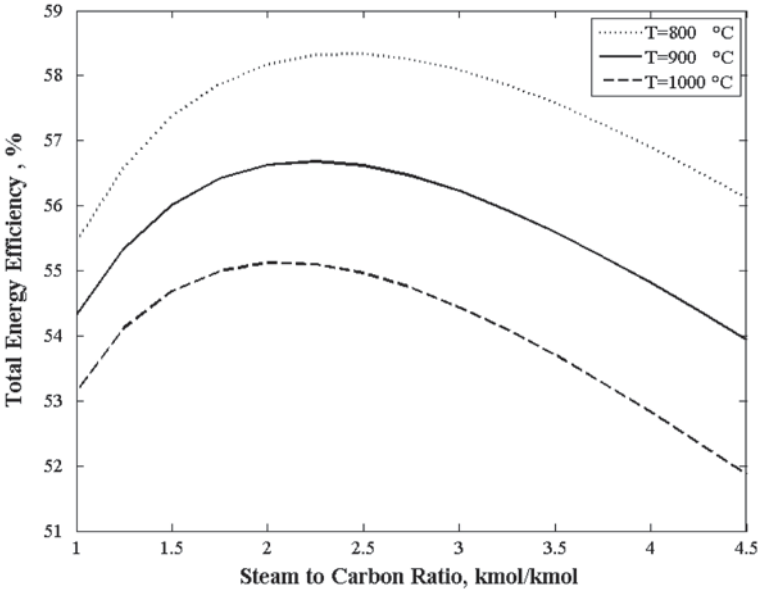

Fig. 9.8 Variation of total energy efficiency with SC for gasifier at various temperatures

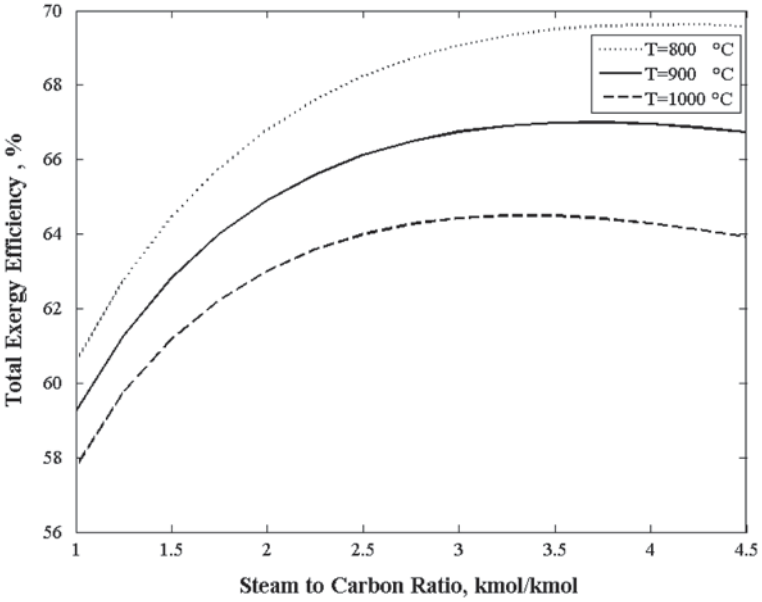

Fig. 9.9 Variation of total exergy efficiency with SC for gasifier at various temperatures

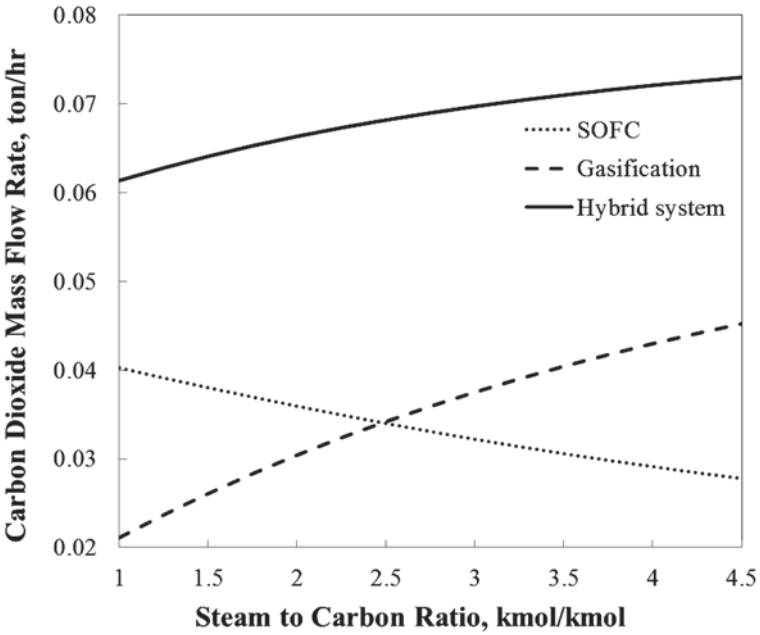

Fig. 9.10 Variation of carbon dioxide emission with steam to carbon ratio

Conclusions

Energy and exergy analyses were performed for an SOFC-MGT cycle with biomass gasification. The integrated system performance varies by introducing more steam to the gasifier. Although the hydrogen molar fraction in the product syngas of sawdust biomass gasification increases by 17.8% with the change in steam to carbon ratio from 1 to 4.5, the carbon monoxide and methane molar fractions decrease by 42.5 and 87.7%, respectively. The gasification process is sensitive to the steam to carbon ratio of the gasifier, and the mass flow rate of the product syngas reaches its maximum value at SC = 2. However, the LHV of the product syngas reduces by 7.05% when SC increases from 1.0 to 4.5. For a gasifier temperature of 800 °C, the energy efficiency of the gasification process reaches the maximum value of 65.5%, although the exergy efficiency varies slightly differently. By introducing more steam to the gasifier, the rate of CO_2 production increases, which results in an overall increase in the CO_2 emission of the integrated SOFC-MGT cycle with biomass gasification.

Nomenclature

ex	specific exergy, kJ/kg
$\dot{E}x$	exergy flow rate, kW
h	specific enthalpy, kJ/kg

h_f	enthalpy of formation, kJ/kmol
i	current density, A/cm^2
$\dot{I}$	exergy destruction rate, kW
LHV	lower heating value, kJ/kg
$\dot{m}$	mass flow rate, kg/s
n	reaction coefficient
$\dot{n}$	molar flow rate, kmol/s
N	number of cells in the SOFC
$\dot{Q}$	heat flow rate, kW
rc	compression ratio
SC	steam to carbon ratio
T	temperature,°C
$\dot{W}$	electric power, kW

Greek Letters

η	energy efficiency, %
ψ	exergy efficiency, %
γ	specific heat ratio

Subscripts

0	ambient or standard condition
a	air
c	compressor
$cell$	SOFC cell
ex	exergy
g	gas
i	species
ic	compressor inlet
mb	moist biomass
MGT	micro-gas turbine
oc	compressor outlet
$oMGT$	MGT outlet
DH	district heating heat demand
p	product gas
Q	heat
s	surface or steam
TIT	turbine inlet temperature
WB	wet biomass

Superscripts

*	reference condition

Acronyms

SOFC solid oxide fuel cell
MGT micro gas turbine
HRSG heat recovery steam generator

Acknowledgment The authors gratefully acknowledge the support provided by the Natural Sciences and Engineering Research Council of Canada.

References

1. Chan SH, Ho HK, Tian Y (2002) Modelling of simple hybrid solid oxide fuel cell and gas turbine power plant. J Power Sour 109:111–120
2. Motahar S, Alemrajabi AA (2009) Exergy based performance analysis of a solid oxide fuel cell and steam injected gas turbine hybrid power system. Int J Hydrog Energy 34:2396–2407
3. Akkaya AV, Sahin B, Huseyin Erdem H (2008) An analysis of Sofc/Gt Chp system based on exergetic performance criteria. Int J Hydrog Energy 33:2566–2577
4. Hawkes AD, Aguiar P, Croxford B, Leach MA, Adjiman CS, Brandon NP (2007) Solid oxide fuel cell micro combined heat and power system operating strategy: options for provision of residential space and water heating. J Power Sour 164:260–271
5. Tock L, Maréchal F (2012) Co-production of hydrogen and electricity from lignocellulosic biomass: process design and thermo-economic optimization. Energy 45:339–349
6. Tock L, Gassner M, Maréchal F (2010) Thermochemical production of liquid fuels from biomass: thermo-economic modeling, process design and process Integration analysis. Biomass Bioenerg 34:1838–1854
7. Basu P (2010) Biomass gasification and pyrolysis: practical design and theory. Elsevier, Oxford
8. Abuadala A, Dincer I (2012) A review on biomass-based hydrogen production and potential applications. Int J Energy Res 36:415–455
9. Hosseini, M, Dincer I, Ahmadi P, Avval HB, Ziaasharhagh M (2013) Thermodynamic modelling of an integrated solid oxide fuel cell and micro gas turbine system for desalination purposes. Int J Energy Res 37:426–434
10. Hosseini M, Dincer I, Rosen MA (2012) Steam and air fed biomass gasification: comparisons based on energy and exergy. Int J Hydrog Energy 37:16446–16452
11. Borgnakke C, Sonntag RE (2008) Fundamentals of thermodynamics. Wiley, Hoboken
12. Colpan CO, Dincer I, Hamdullahpur F (2007) Thermodynamic modeling of direct internal reforming solid oxide fuel cells operating with syngas. Int J Hydrog Energy 32:787–795
13. Hosseini M, Ziabasharhagh M (2010) Energy and exergy analysis of a residential sofc-gt/absorption chiller system. ECOS 2010, Lausanne 5:411–418
14. Rao MS, Singh SP, Sodha MS, Dubey AK, Shyam M (2004) Stoichiometric, mass, energy and exergy balance analysis of countercurrent fixed-bed gasification of post-consumer residues. Biomass Bioenerg 27:155–171
15. Dincer I, Rosen MA, Zamfirescu C (2009) Exergetic performance analysis of a gas turbine cycle integrated with solid oxide fuel cells. J Energy Res Technol 131:032001–0320011

Chapter 10
Exergy Analysis of Scroll-Based Rankine Cycles with Various Working Fluids

E. Oralli and Ibrahim Dincer

Abstract In this study the possibility of converting scroll compressor into expander is investigated. Refrigeration equipment manufacturers produce scroll compressors massively for refrigeration and air conditioning applications. It is shown here that, through appropriate modeling, catalog data of scroll compressors can be used to predict the operation in reverse, as expanders. The modification of the geometry with respect to rolling angle and involute angles are necessary to use scroll compressor as expanders in heat engines. If no modifications are made to the scroll compressor, the efficiency of the Rankine cycle will result low because the built-in volume ratio is not adapted to the cycle configuration for the same pressure and temperature levels in the expanders. A low capacity scroll compressor is selected from a refrigeration equipment manufacturer and using the equations for modeling of positive displacement compressors and the compressor manufacturer data for nominal operation, isentropic efficiency, built-in volume ratio and the flow coefficient of the scroll machine are determined. After these determinations, the expander model has been used to predict the operation of the same scroll machine in reverse as it without and modification of the geometry. The resulting Rankine cycle is non-realizable with a low exergy efficiency of 50 % since the sink temperature for the cycle is far below the normal environmental temperature. In order to run a feasible Rankine cycle with the selected expander, without changing the scroll geometry and the working fluid, the upper pressure and temperature must be increased. It is found that by increasing the pressure and temperature at the expander intake to supercritical value, that is 68 bar and 264 °C, the cycle becomes realizable and achieves an exergy efficiency of 61 %, respectively.

Keywords Scroll compressor · Eexpander · Rankine cycle · Heat engines · Exergy · Efficiency

E. Oralli (✉)
Faculty of Engineering and Applied Science, University of Ontario Institute of Technology (UOIT), 2000 Simcoe Street North, Oshawa, ON L1H 74K, Canada
e-mail: Emre.Oralli@uoit.ca

I. Dincer
Department of Mechanical Engineering, University of Ontario Institute of Technology (UOIT), 2000 Simcoe Street North, Oshawa, ON L1H 74K, Canada
e-mail: ibrahim.dincer@uoit.ca

I. Dincer et al. (eds.), *Progress in Sustainable Energy Technologies: Generating Renewable Energy,* DOI 10.1007/978-3-319-07896-0_10,

10.1 Introduction

The Rankine cycle is a closed power cycle that has been used for more than 150 years for the heat pumps. A Rankine cycle describes a model of steam powered heat engine for the power plants generally have four components, namely, condenser, boiler, pump and expander. Working fluid is heated by boiler where it becomes high-pressure vapor, it is then introduced in to expander to produce power by rotating generator. The low temperature working fluid from expander cooled and condensed in a heat exchanger and pumped to be able to perform the same process for power generation.

The Rankine cycle has an advantage of the small amount of work required to pump a liquid and the amount of energy that can be extracted from latent heat. An ORC differs from the basic Rankine cycle in that the working fluid is organic. Saleh et al. [1] modeled 31 different working fluids in different ORC configurations. Types of organic working fluids modeled included alkanes, fluorinated alkanes, ethers and fluorinated ethers. These fluids can behave differently when used in an ORC and it is important to discuss the different configurations and working fluid characteristics together. Organic working fluids have performance advantages over water-steam at low power levels but these advantages disappear at 300 kW or more because of the poor heat transfer properties of organic fluids.

Organic fluids should be considered since they have additional properties such as boiling temperature, latent heat, critical point, and stability temperature which are all important in ensuring good thermodynamic performance. Fraas [2] mentions it also has effects on the expander type used as in the case of small turbines a high molecular weight is desired to maintain a high and optimal Reynolds number. A low critical point is useful when *s*-type cycles are considered. Boiling temperature and stability temperature are important when choosing a fluid for the heat source.

Working fluid should also be considered in terms of environment and inhabitants beyond thermodynamic performance. Therefore global warming potential (GWP), ozone-layer depletion potential (ODP), toxicity, flammability, material compatibility and atmospheric lifetime are also important factors. Hung [3] mentioned that refrigerants have a low toxicity in general.

All HCFC refrigerants are scheduled to be phased out by 2030 as all countries agree in 2009, World Climate Conference and most CFCs are already prohibited. This makes these fluids poor choices as long term candidates for working fluids.

It can be observed that most fluids with simpler molecules have lower critical temperatures and also tended to be w- or i- types. Hung [3] and Schuster et al. [4] found that complex molecules have higher critical temperatures in comparison and tend to be d-fluid.

Saleh et al. [1] showed that fluids with low critical temperatures had a low thermal efficiency when evaporated at subcritical conditions. He found that the low critical point of organic fluids makes the supercritical ORC a practical solution.Saleh et al. [1] also noticed that superheating w- and i- fluids is increasing the thermal efficiency. Through the use of both superheat and regenerator, more significant gains can be achieved. Mago et al. [5] observed that d-working fluids show a decrease in

thermal efficiency with superheat. They both noted that superheat would cause an increase in irreversibility and for maximum performance the cycle should be operated at saturated conditions.

Saleh et al. [1] recommended R236ea, R245ca, R245fa, R600, R600a, R601a, RE134, and RE245 as working fluids in ORCs and stated that fluids with higher boiling temperatures showed better performance. Borsukiewicz-Gozdur and Nowak [6] recommended both R245fa and R235ea as working fluids. Mago et al. [5] concluded that *d*-working fluids such as R113, R123, R245ca, R245fa, and isobutene achieved better performance than *w*-working fluids such as R134a and propane.

The irreversibilities such as friction and leakage losses in the cycle cause reduction of cycle efficiency and of useful work output. Friction and leakage losses from expander contribute the highest portion of the irreversibilities with pressure drops and inefficiencies from the heat exchanger. The improvements regarding the geometry of the scroll machine will directly affect the cycle efficiency not only because of reducing the leakages but also to obtain appropriate built-in ratio for the compression/expansion process.

ORC has inherent irreversibilities as many processes. The losses may come in the form of friction-heat loses in the expander and pump. This is accounted in the isentropic efficiencies of each device. Valves, pipes and pressure drops are other sources. Hung [3] stated that the largest source of irreversibility in the system is caused by the evaporator. The mismatch between the working fluid and the heat source causes this type of loss. Larjola [7] showed that the organic working fluids due to their low latent heat match the source temperature profile better than water-steam.

There are crucial studies thesis studies, research papers and project results presented on ORCs in general and something specific to scroll compressors and expanders and their use [8–28]. There are some practical solutions to reduce losses for ORC. The liquid entering the pump should be sub-cooled to prevent cavitation. The fluid should be superheated when using turbines with w-type working fluids to prevent droplet formation during expansion. It is a known fact that the quality at the turbine exit can be kept at 90%. Both cavitation and high speed droplets will corrode the pump and expander.

There are a limited number of ways to improve the thermal efficiency of the cycle after the cycle configuration and fluid have been specified. Increasing the average high side temperature or decreasing the average low side temperature is one of the approaches that can be used. The high side temperature is fixed in low temperature heat recovery and decreasing the condenser temperature below atmospheric conditions is not practical. Other approaches include increasing the isentropic efficiencies of the pump and expander. The pump work is significantly less than the expander work in a Rankine cycle. Therefore improvement of the efficiency of the expander will provide the greatest degree of cycle improvement.

Badr et al. [8] modeled an ORC and performed a sensitivity study to show which of these parameters had the greatest effect on thermal efficiency. They varied the isentropic expander efficiency, evaporator temperature, and condenser temperature. They modeled both a basic and regenerative ORC with R113 as the working fluid.

The evaporator temperature and the expander efficiency are both important parameters in optimizing a ORCs performance. They noted that the expander efficiency was the most important parameter in low temperature energy recovery and that great care should be taken during expander selection in order to increase cycle efficiency.

Scroll machine is first invented in 1905 by Croux (1905) [as discussed in detail in 22, 25] and main characteristics, working principle has been known since then for more than a century. But it took almost 70 years for the industry to provide machine tools with small enough tolerances to be able to manufacture scroll pairs. Since then development and technical studies have been growing regarding environmentally friend working fluid search, possible heat engine applications and improvement of geometry to reduce leakages for an efficient compression and expansion process.

Scrolls can be categorized into two types; compliant and kinematically constrained. Constrained scrolls are fixed in their position. They can be constrained radially, axially, or both. Commonly they are composed of three cranks that are separated by 120° [9]. The three cranks are then linked to a common shaft. It is because of this additional gearing that the scroll and shaft can have different speeds [10]. Manufacturing tolerances are a critical parameter in the effective sealing of constrained scrolls. A compliant scroll in contrast is not constrained and uses a centrifugal effect to keep the orbiting scroll in continuous contact with the fixed scroll. Compliant scrolls require lubrication to operate efficiently without causing significant wear. Constrained scrolls in contrast can operate without lubrication.

The scroll expander is a positive displacement device and is commonly used as a compressor in vapor compression cycles. Common to all positive displacement devices it has a fixed volumetric ratio. Compared to the aforementioned positive displacement expansion devices it has the most complicated geometry. It is made up of two involute curves in opposing directions. They are called the orbiting and fixed scrolls. The fixed scroll does not move and the orbiting scroll always keeps its orientation while it orbits around the shafts center.

An advantage of compliant scrolls over constrained types is that they can provide better radial and flank sealing. The scroll wraps are only separated by an oil film. They also have the advantage of being tolerant of liquids which allows them to increase the gap size if excessive pressure builds up inside the device [9].

In constrained scrolls a low friction material is used to form a tip seal between the plates which resists radial leakage. Only the tight tolerances between wraps minimize the amount of flank leakage. This sealing can be improved by using oil which acts as a gap filler. Peterson et al. [9] mentioned that constrained scrolls that operate as expanders have a tendency to washout this oil. When they operate as compressors it is swept in.

The primary modes of loss are both leakage and friction. Peterson et al. [9] determined that the poor performance of constrained scroll expanders was caused by excessive leakage. Lemort et al. [11] created a semi-empirical model for the performance of a scroll expander. They concluded that internal leakage is the largest contributing factor in efficiency loss. The lesser but second largest contributor was mechanical losses. Other publications have also concluded that leakage is the primary cause for decreased performance [10].

In constrained scroll expanders internal leakage can be controlled to an extent by increasing the speed of the expander. This is why their efficiency increases with speed [12] because of the time the vapor has to escape decreases. There is a point where increasing the speed will have a negative impact on performance. At excessive speeds frictional losses will become noticeable.

Scroll expanders have demonstrated high performance over a variety of working conditions. They consistently achieve isentropic efficiencies over 50% and have achieved efficiencies as high as 83%. They also have demonstrated good partial load performance [4].

Scroll geometry is one of the key components affecting the scroll machine efficiency defining chamber areas and volumes. The parameters to describe scroll geometry have to be understood to generate equations for volume and area of the expander chambers as a function of angle in terms of obtaining specific characteristics of the working fluid. The shape of the scroll expander is an involute of a circle with a constant distance of wraps.

The geometry of the scroll machine was defined by Halm [13]. The goal of the geometrical modeling is to define pocket volumes for intake, expansion and discharge chambers as a function of orbiting angle (θ) to obtain volume-angle functions. The orbiting angle describes the number of turns of the orbiting scroll around the fixed scroll for a complete cycle of expansion. The study of Wang et al. [14] evaluates the chamber volumes as a function of orbiting angle throughout the compression process in a scroll machine. In his thesis analytic expressions calculated for scroll compressor is converted for the expander operation to use in organic Rankine cycle application since they are reversible machines.

In order to define the position of fixed and orbiting scroll, conjugancy of the scroll profiles is given by Bush and Beagle [15]. Calculation of the chamber volumes between the fixed and orbiting scroll with respect to orbiting angle for suction, compression/expansion and discharge is investigated by Hirano et al. [16] and Yanagisawa et al. [17]. In this thesis the expressions given by Wang et al. [14] have been used to generate the expander model.

In this study, the feasibility of converting a scroll compressor into an expander as to be used in heat recovery Rankine cycle of low capacity is modeled. The specific objectives of this work are given as follows:

- To characterize the scroll machine in the expander mode and investigate the effect of scroll geometry on the ORC exergy efficiency.
- To evaluate the geometric parameters of the scroll expander by optimization process to reduce the leakage loss caused by the gaps between the fixed and orbiting scroll and between the scrolls and plates which will ensure appropriate built-in volume ratio for the cycle.
- To select an appropriate organic working fluid such as R404a, Toluene, R123, R141b, R134a and NH_3 which will ensure suitable temperature and pressure range to make the cycle realizable when converting scroll compressor to an expander.

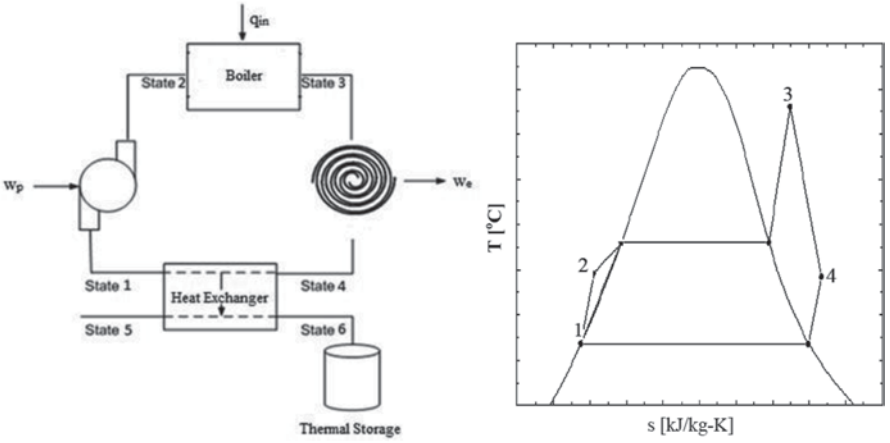

Fig. 10.1 Rankine cycle configuration and T-s diagram of a general organic Rankine cycle

10.2 System Description

Here, an exergy analysis of the Organic Rankine Cycle (ORC) is conducted. The performance of an ORC will be analyzed for different working fluids under diverse working conditions using the first law of thermodynamics. There will be assumptions regarding the system as follows: steady-state conditions, no pressure drop in the evaporator, condenser and pipes and isentropic efficiencies for the turbine and pump. The heat engine to produce electrical power with ORC is shown in Fig. 10.1. There are four different processes in ORC as can be observed from Fig. 5.6: process 1–2 (constant-pressure transfer of heat), process 2–3 (expansion process), process 3–4 (constant-pressure heat transfer), and process 4–1 (pumping process).A *T-s* diagram of the typical ORC is given in Fig. 10.1.

10.3 Analysis

The geometrical model and volume expressions for the chambers will be used to model the thermodynamic process of the working fluid from the beginning of suction ($\theta = 0$) to the end of the discharge process ($\theta = 2\pi$ rad)

The first law of thermodynamics for the control volume with a mass balance can be applied to calculate the temperature, mass and pressure in the working chambers with respect to orbiting angle.

The conservation of energy for a control volume is:

$$\frac{dE_{cv}}{dt} = \dot{Q} + \dot{W} + \sum \dot{m}_{su}\left(h + \frac{V^2}{2} + gz\right)_{su} - \sum \dot{m}_{ex}\left(h + \frac{V^2}{2} + gz\right)_{ex} \tag{10.1}$$

where $\frac{dE_{cv}}{dt}$ is the rate of total internal energy increase (W), $\dot{Q}$ is the heat transfer rate (W), $\dot{W}$ is the power output from expander (W), $\dot{m}$ is the inflow or outflow rate (kg/s), $h+\frac{V^2}{2}+g$ is the total enthalpy (J/kg).

The mass balance for the control volume is:

$$\frac{dM}{dt}=\sum\dot{m}_{su}-\sum\dot{m}_{ex} \tag{10.2}$$

The total energy of the control volume E_{cv} can be reduced to internal energy U_{cv} neglecting kinetic and potential energies.The left side of the conservation of energy equation can be written as

$$\frac{dE_{cv}}{dt}=\frac{dU_{cv}}{dt}=m\frac{du}{dt}+u\frac{dm}{dt} \tag{10.3}$$

The change of the specific internal energy u for the control volume is

$$du=C_v dT+\left[T\left(\frac{\partial P}{\partial T}\right)_v-P\right]dv \tag{10.4}$$

The specific internal energy u can be written as $u=h-Pv$, where h is the specific enthalpy, such that Eq. (10.3) can be written as

$$\frac{dU_{cv}}{dt}=mC_v\frac{dT}{dt}+T\left(\frac{\partial P}{\partial T}\right)_v\left(\frac{dV}{dt}-V\frac{dm}{dt}\right)-P\frac{dV}{dt}+h\frac{dm}{dt} \tag{10.5}$$

Uniform pressure and temperature can be assumed for each control volume and the work term $\dot{W}=\frac{\partial W}{\partial t}$ on the right hand side of Eq. (10.1) can be expressed as

$$\dot{W}=-P\frac{dV}{dt} \tag{10.6}$$

The first law of thermodynamics for the control volume becomes

$$mC_v\frac{dT}{dt}+T\left(\frac{\partial P}{\partial T}\right)_v\left(\frac{dV}{dt}-V\frac{dm}{dt}\right)+h\frac{dm}{dt}=\dot{Q}+\sum\dot{m}_{in}h_{in}-\sum\dot{m}_{out}h_{out} \tag{10.7}$$

Equation (10.7) can be arranged to

$$\frac{dT}{dt} = \frac{1}{mC_v}\{-T\left(\frac{\partial P}{\partial T}\right)_v\left[\frac{dV}{dt} - v\left(\dot{m}_{in} - \dot{m}_{out}\right)\right] - \sum \dot{m}_{in}\left(h - h_{in}\right) + \dot{Q}\} \tag{10.8}$$

by applying mass balance Eq. (10.2) for $h=h_{out}$. The temperature change with respect to orbiting angle can be obtained from Eq. (10.8) if angular speed w is expressed as

$$w = \frac{d\theta}{dt} \tag{10.9}$$

Substituting Eq. (10.9) in to Eq. (10.8) yields

$$\frac{dT}{d\theta} = \frac{1}{mC_v}\{-T\left(\frac{\partial P}{\partial T}\right)_v\left[\frac{dV}{dt} - \left(v/w\right)\left(\dot{m}_{in} - \dot{m}_{out}\right)\right] - \sum (\dot{m}_{in}/w)\left(h - h_{in}\right) + \left(\dot{Q}/w\right)\}$$

And the mass balance equation becomes

$$\frac{dM}{d\theta} = \left(\sum \dot{m}_{in}/w\right) - \left(\sum \dot{m}_{ex}/w\right) \tag{10.10}$$

In Eq. (10.8), the independent variables temperature T and mass m should be integrated for the first order differential equation. Applying the mass balance Eq. (10.10) and the equation of temperature distribution with respect to orbiting angle (10.9) the thermophysical properties in each chamber can be evaluated as a function of the orbiting angle (θ).

There are different types of heat transfer mechanisms in a scroll compressor including between:

1. The shell of the scroll compressor and the fluid in suction
2. The fluid and motor, oil, scrolls (electromechanical losses)
3. The shell of the scroll compressor/expansion and the fluid in discharge
4. The fluid and the ambient

It can be assumed that the wall of the temperature is constant at T_w through the thickness of the fluid to be able to present the heat transfer and conservation of energy equations. The steady state balance for the wall can be given as

$$\dot{Q}_{ex} - \dot{Q}_{su} - \dot{Q}_{amb} - \dot{W}_{\text{loss}} = 0 \tag{10.11}$$

The suction heat transfer assuming constant envelope temperature for the isothermal heat exchanger and uniform wall temperature is

$$\dot{Q}_{su} = \dot{m}c_p\left(T_{su,1} - T_{su}\right) = \varepsilon_{su}\dot{m}c_p\left(T_w - T_{su}\right) = \left[1 - e^{\left(-\frac{AU_{su}}{\dot{M}c_p}\right)}\right]\dot{m}c_p\left(T_w - T_{su}\right) \tag{10.12}$$

The discharge heat transfer under the same conditions and assumptions:

$$\dot{Q}_{ex} = \dot{m}c_p\left(T_{ex} - T_{ex,1}\right) = \varepsilon_{su}\dot{m}c_p\left(T_{ex} - T_w\right) = \left[1 - e^{\left(-\frac{AU_{su}}{\dot{M}c_p}\right)}\right]\dot{m}c_p\left(T_{ex} - T_w\right) \tag{10.13}$$

where AU_{su} can be written in terms of nominal heat transfer coefficient ($AU_{su,\,n}$) which is given by Dewitt (2002) to develop the model for a turbulent flow through a pipe by the the Reynolds number as follows:

$$AU_{su} = AU_{su,n}(\dot{m} / \dot{m_n})^{0.8} \tag{10.14}$$

The ambient heat transfer can be evaluated by the following equation introducing a global heat transfer coefficient (AU_{amb}):

$$\dot{Q}_{amb} = AU_{amb}\left(T_w - T_{amb}\right) \tag{10.15}$$

After defining the properties of the fluid and the volume of the chambers as a function of the orbiting angle there is a need to develop a model to analyze and describe the main features of the machine regarding the energy and exergy efficiencies and fluid flow characteristics with a limited number of parameters.

The model proposed by Winandy et al. [18] was modified to be able to predict the characteristics of the flow and the thermodynamic process of the scroll machine converting from scroll compressor to scroll expander and to improve the modeling of heat pump systems.

The schematic representation of the evolution of the refrigerant through the scroll machine is given for both the compressor and expander case in Fig. 10.2. In this study the heat up in suction and cool down in discharge are not taken into account considering the compression and expansion process of the refrigerant in a scroll machine.

The compression process can be decomposed into two parts:

1. Isentropic compression (1→2s)
2. Isochoric pressure rising (2s→2a)

The expansion process can be decomposed into two parts:

1. Isentropic expansion (1→2s)
2. Constant volume pressure rebuild (2s→2a)

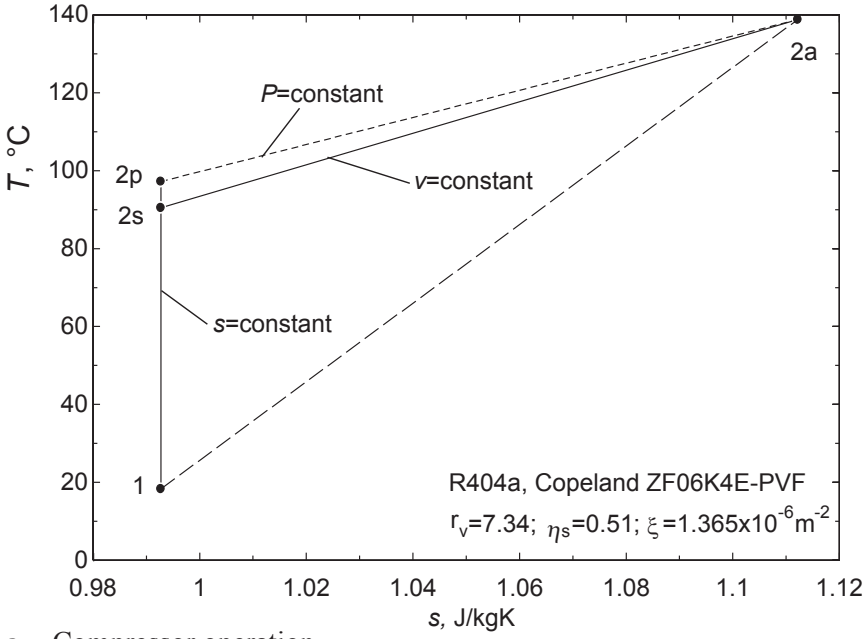

a Compressor operation

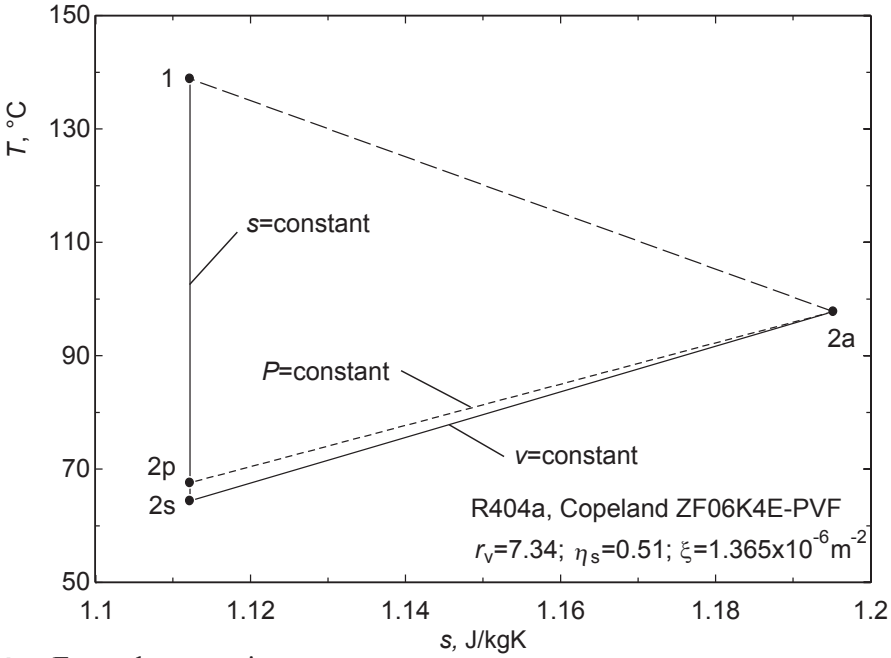

b Expander operation

Fig. 10.2 Compression and expansion processes determined by simplified model

The equations describing the thermodynamic model will be given in terms of heat transfer, the internal leakage and pressure drop to describe the compression and expansion processes separately.

Figure 10.2 introduces the scroll machine models functioning as compressor (a) and expander (b). Assume that a low pressure gas is to be compressed (Fig. 10.2a) from state 1. The compression process in positive displacement compressors implies closing the volume of gas in a compression chamber, which reduces its volume according to the built-in volume ratio. One assume that no leakages and no heat transfer occurs during the theoretical compression process represented from state 1 to state 2s as an isentropic one. The amount of work required for this part of compression process is denoted Ws.

In real compression processes the gas does not evolve isentropically and more work is consumed. The additional work is in fact transformed into heat that increases the entropy and enthalpy of the gas. Therefore, after the isentropic process 1–2s it follows an isochoric process with rising pressure driven by heat addition. The added heat originates from the input work, which is partially destroyed such that $Q = W_{in} - W_s$ (see Fig. 10.2a). After the isochoric process the working fluid achieves state 2a. Eventually a part of the discharged gas flows back to suction as leakage flow. The leakage flow rate can be estimated from energy balance applied to simplified model. The energy balance can be written as it follows, in the compressor case. The isentropic compression work is

$$\dot{W}_s = \left(\dot{m} + \dot{m}_{leak}\right)\left(h_{2s} - h_1\right) \tag{10.16}$$

where $\dot{m}$ is the net mass flow rate, and $\dot{m}_{leak}$ represents the internal leakage flow rate. The summation $\dot{m} + \dot{m}_{leak}$ is the mass flow rate actually circulated through the compressor. In order to compensate the irreversibilities (leakages and heat exchange) more work input is needed to drive the compressor, such that $\dot{W}_{in} = \dot{W}_s + \dot{Q}$. Assuming that most of the irreversibilities are due to leakage flows, it becomes possible to calculate the leakage flow rate from an energy balance:

$$\dot{Q} = \dot{W}_{in} - \dot{W}_s = \left(\dot{m} + \dot{m}_{leak}\right)\left(h_{2a} - h_{2s}\right) = \dot{m}_{leak}\left(h_{2a} - h_1\right). \tag{10.17}$$

Therefore, noting also that $v_{2a} = v_{2s}$ one solves for $\dot{m}_{leak}$ and obtains

$$\frac{\dot{m}_{leak}}{\dot{m}} = \frac{h_{2a} - h_{2s}}{h_{2s} - h_1}. \tag{10.18}$$

A leakage flow coefficient $\zeta = C_f A_{leak}$ can be determined if one solves volume equation for known pressure difference across the compressor

$$\dot{m}_{leak} = \zeta\sqrt{P_{2a}/v_{2a} - P_1/v_1} \tag{10.19}$$

where C_f is the specific flow coefficient per average leakage area A_{leak}.

The simplified model for the expander is introduced in Fig. 10.2b. In this case, a part of the main flow by-passes the expander and dissipates power as it flows over the expander's "flow resistance"; this is the leakage flow, $\dot{m}_{\text{e,leak}}$. The expansion process according to the simplified model, evolves first isentropically from state 1 to 2s followed by, a constant volume pressure rebuild 2s–2a. At the reverse operation—as expander—a reasonable assumption is to consider that the leakage coefficient remains the same. Therefore, denoting expander's states with index "e" one has the following equations can be written for the expander to apply for the thermodynamic modeling.

$$\begin{cases} v_{\text{e,2a}} = v_{\text{e,2s}} \\ \dot{m}_{\text{e,leak}} = \zeta \sqrt{\dfrac{P_{\text{e,1}}}{v_{\text{e,1}}} - \dfrac{P_{\text{e,2a}}}{v_{\text{e,2a}}}} \\ \dot{W}_{\text{e,s}} = \left(\dot{m}_{\text{e}} - \dot{m}_{\text{e,leak}}\right)\left(h_{\text{e,1}} - h_{\text{e,2s}}\right) \\ \dot{Q}_{\text{e,diss}} = \dot{m}_{\text{e,leak}}\left(h_{\text{e,1}} - h_{\text{e,2s}}\right) \\ \dot{W}_{\text{e,out}} = \dot{W}_{\text{e,s}} - \dot{Q}_{\text{e,diss}} = \dot{m}_{\text{e}}\left(h_{\text{e,1}} - h_{\text{e,2a}}\right) \end{cases} . \tag{10.20}$$

From Eq. (10.20) one can determine the ratio

$$\frac{\dot{m}_{\text{e}}}{\dot{m}_{\text{e,leak}}} = 2 \times \frac{h_{\text{e,1}} - h_{\text{e,2s}}}{h_{\text{e,2a}} - h_{\text{e,2s}}}, \tag{10.21}$$

which is important for calculating the mass flow rate through the expander.

Pump Process 1→2 in Fig. 10.1b implies an increase in the pressure resulting from using the pump. The driving mechanism of the ORC is the pump since it ensures the circulation.

The energy balance equation for the pump is

$$\dot{m}_1 h_1 + \dot{W}_p = \dot{m}_2 h_2 \tag{10.22}$$

The entropy balance equation for the pump is

$$\dot{m}_1 s_1 + \dot{S}_{gen} = \dot{m}_2 s_2 \tag{10.23}$$

The exergy balance equation for the pump is

$$\dot{E}x_1 + \dot{W}_{in} = \dot{E}x_2 + \dot{E}x_d \tag{10.24}$$

$$\text{Where } \dot{E}x_1 = \dot{m}_1 h_1 - \dot{m}_0 h_0 - T_0 \dot{m}_1 \left(s_1 - s_0\right) \tag{10.25}$$

The pump power can be expressed as

$$\dot{W}_p = \frac{\dot{W}_{p,ideal}}{\eta_p} = \frac{\dot{m}\left(h_1 - h_{2s}\right)}{\eta_p} \tag{10.26}$$

where $\dot{W}_{p,ideal}$ is the ideal work that should be supplied for the pump, η_p is the isentropic efficiency of the pump, $\dot{m}$ is the flow rate of the working fluid, h_1 and h_{2s} are the inlet and outlet enthalpies of the refrigerant for the ideal case.

The actual specific enthalpy can be given as

$$h_2 = h_1 - \frac{\dot{W}_p}{\dot{m}} \tag{10.27}$$

The exergy destruction rate for the uniform flow can be expressed as

$$\dot{E}x_d = T_0 \frac{dS}{dt} = T_0 \dot{m} \left[\sum s_{exit} - \sum s_{inlet} + \frac{ds_{system}}{dt} + \sum_j \frac{q_j}{T_j} \right] \tag{10.28}$$

where j represents the heat transfer for different reservoirs. Applying the steady-state conditions $(\frac{ds_{system}}{dt}) = 0$ Eq. (10.28) becomes

$$\dot{E}x_d = T_0 \frac{dS}{dt} = T_0 \dot{m} \left[\sum s_{exit} - \sum s_{inlet} + \sum_j \frac{q_j}{T_j} \right] \tag{10.29}$$

And the exergy destruction rate for the pump is

$$\dot{E}x_{d,p} = T_0 \dot{m} \left(s_2 - s_1 \right) \tag{10.30}$$

where s_1 and s_2 are the specific entropies of the working fluid at the inlet and exit of the pump for the actual conditions.

Boiler The pressure of the working fluid stays constant during the heat addition process in boiler. The boiler heats the working fluid at the pump outlet to the turbine inlet condition, which can be saturated or superheated vapor.

The energy balance equation for the boiler is

$$\dot{m}_2 h_2 + \dot{Q}_{in} = \dot{m}_3 h_3 \tag{10.31}$$

The entropy balance equation for the boiler is

$$\dot{m}_2 s_2 + \frac{\dot{Q}_{in}}{T_H} + \dot{S}_{gen} = \dot{m}_3 s_3 \tag{10.32}$$

The exergy balance equation for the boiler is

$$\dot{E}x_2 + \dot{Q}_{in}\left(1 - \frac{T_0}{T_H}\right) = \dot{E}x_3 + \dot{E}x_d \tag{10.33}$$

The heat transfer rate from the boiler into the working fluid is given by

$$\dot{Q}_b = \dot{m}\left(h_3 - h_2\right) \tag{10.34}$$

where h_3 and h_2 are the enthalpies of the working fluid at the exit and inlet of the boiler. Using Eq. (10.28), the boiler exergy destruction rate can be determined as

$$\dot{E}x_{d,b} = T_0 \dot{m}\left[\left(s_3 - s_2\right) - \frac{h_3 - h_2}{T_H}\right] \tag{10.35}$$

where s_3 and s_2 are the specific entropies of the working fluid at the inlet and exit of the boiler and T_H is the temperature of the high temperature heat source.

Expander In the expander, the superheated or saturated vapor working fluid passes through the scrolls of the expander to rotate the shaft to generate mechanical power. The pressure decreases in the expansion process due to the volume increase of the chambers between the fixed and orbiting scroll.

The energy balance equation for the expander is

$$\dot{m}_3 h_3 = \dot{m}_4 h_4 + \dot{W}_e \tag{10.36}$$

The entropy balance equation for the expander is

$$\dot{m}_3 s_3 + \dot{S}_{gen} = \dot{m}_4 s_4 \tag{10.37}$$

The exergy balance equation for the expander is

$$\dot{E}x_3 = \dot{W}_e + \dot{E}x_4 + \dot{E}x_d \tag{10.38}$$

The expander power can be given as

$$\dot{W}_e = \dot{W}_{e,ideal}\eta_e = \dot{m}\left(h_3 - h_2\right)\eta_e \tag{10.39}$$

where $W_{e,ideal}$ is the ideal power of the expander, η_e the expander isentropic efficiency, and h_3 and h_{4s} the enthalpies of the working fluid at the inlet and outlet of the expander for the ideal case. The actual specific enthalpy of the working fluid at the expander exit is

$$h_4 = h_3 - \frac{\dot{w}_e}{m} \tag{10.40}$$

And the exergy destruction rate for expander is

$$\dot{E}x_{d,e} = T_0 \dot{m}(s_4 - s_3) \tag{10.41}$$

where T_0 is the ambient temperature which can be assumed as 298.15 K, s_3 and s_4 are the specific entropies of the working fluid at the inlet and exit of the expander for the actual conditions.

Condenser The low pressure and temperature working fluid leaving the expander rejects latent heat to the environment or condenser coolant by heat exchanger through a constant-pressure phase change process.

The energy balance equation for the condenser is

$$\dot{m}_4 h_4 + = \dot{Q}_{out} + \dot{m}_1 h_1 \tag{10.42}$$

The entropy balance equation for the condenser is

$$\dot{m}_4 s_4 + \dot{S}_{gen} = \dot{m}_1 s_1 + \frac{\dot{Q}_{out}}{T_L} \tag{10.43}$$

The exergy balance equation for the condenser is

$$\dot{E}x_4 = \dot{Q}_{out}\left(1 - \frac{T_0}{T_L}\right) + \dot{E}x_1 + \dot{E}x_d \tag{10.44}$$

The condenser heat rate, $\dot{Q}_c$, which is the rate of latent heat rejection from the condensing working fluid, can be expressed as

$$\dot{Q}_c = \dot{m}(h_1 - h_4) \tag{10.45}$$

The condenser exergy destruction rate can be determined from Eq. (10.28) as follows

$$\dot{E}x_{d,c} = T_0 \dot{m}(s_1 - s_4) - \frac{h_1 - h_4}{T_L} \tag{10.46}$$

Table 10.1 Scroll expander and Rankine cycle parameters with various working fluids

Working fluid	φ_e rad	r_v	V_{suc} ml/rev	P_{max} bar	T_{max} °C
R404a	27	3.0	54	38	139
R404a	57[a]	7.3	128	68	264
R141b	33	3.8	68	30	178
R141b	69[a]	9.2	161	54	338
NH_3	57[a]	7.3	128	60	173
NH_3	29	3.3	61	33.5	91
R134a	57[a]	7.3	128	40	170
R134a	28	3.1	59	22.3	89.4
R123	185[a]	25	447	21	230
R123	90	10.6	206	11.7	121
Toluene	725[a]	100	1790	20	273
Toluene	352	42.4	824	11.1	143

[a] No modification of scroll geometry

where s_1 and s_4 are the specific entropies of the working fluid at the inlet and exit of the condenser, and T_L is the temperature of the low-temperature reservoir where the heat is rejected for $T_1 > T_c > T_0$.

Total Cycle Exergy Destruction The total exergy destruction can be obtained by adding Eqs. (10.30, 10.35, 10.41, and 10.46) as follows:

$$\dot{E}x_{d,cycle} = \sum_j \dot{E}x_{d,j} = \dot{E}x_{d,p} + \dot{E}x_{d,b} + \dot{E}x_{d,e} + \dot{E}x_{d,c} \tag{10.47}$$

$$\dot{E}x_{d,cycle} = \dot{m}T_0\left[\left(-\frac{h_3 - h_2}{T_H}\right) - \left(\frac{h_1 - h_4}{T_L}\right)\right] \tag{10.48}$$

Cycle Exergy Efficiency The second-law exergy efficiency can be calculated using the following equation

$$\eta_{ex} = \frac{\dot{W}_{net}}{\dot{Q}_{in}\left[1 - \left(\frac{T_o}{T_H}\right)\right]} \tag{10.49}$$

10.4 Results and Discussion

Several working fluids for Rankine cycle were investigated. For each studied case the expander geometry has been adjusted with respect to the rolling angle only. The rolling angle and Rankine cycle parameters were determined by a trial and error method. The results are summarized in Table 10.1 where 6 working fluids were investigated. The working fluid is originally used for the scroll compressor, R404a

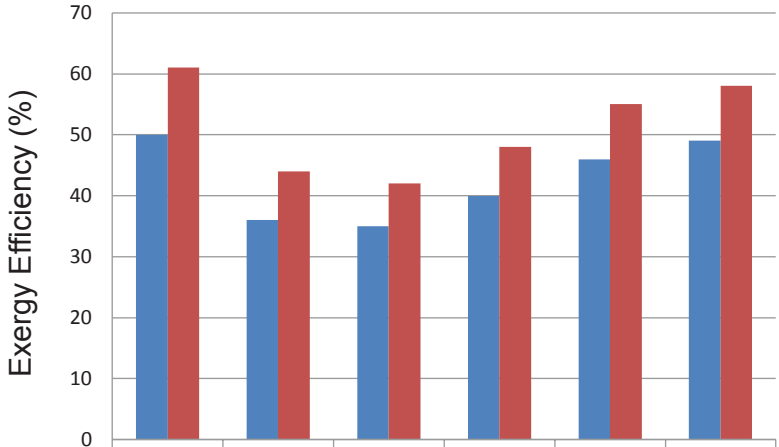

	R404a	R141b	NH3	R134a	R123	Toluene
nonmodified	50	36	35	40	46	49
modified	61	44	42	48	55	58

Fig. 10.3 Exergy efficiency of the cycle for the modified and nonmodified geometry

that gave the best performance. Two cases were analyzed with R404a. In the first case the rolling angle has been reduced to 27 rad. The corresponding built-in pressure ratio in this case becomes 3.0. In this situation, a supercritical Rankine cycle has been implemented for a maximum pressure and temperature values of 38 bar and 139 °C. The corresponding exergy efficiency is 61 %. The cycle configuration offers a good opportunity for internal heat regeneration between streams 2–3 and 5–1. For this reason, the resulted efficiency is exceptionally high.

Second-law analysis is performed and corresponding exergy efficiencies are evaluated for modified and nonmodified scroll geometries with different organic fluids and the results are given in Fig. 10.3. The configuration with R404a involves modifications of the scroll geometry. This configuration is described above achieves 49 % exergy efficiency by using Toluene as a working fluid. The other working fluid that shows a good performance is R123a; however, Table 10.1 shows that the rolling angle is very high which results in a less compact design with 46 % exergy efficiency. Toluene requires an expansion ratio of 100, leading to a massive expander with 725 rad rolling angle, which is not practical. All other studied fluids show lower exergy efficiency and therefore appear to be less attractive for implementation.

Table 10.1 indicates that if no modifications are made to the scroll machine, the appropriate choice of working fluid for Rankine cycle is R134a because the resulted exergy efficiency is good (40 %) and the maximum level of pressure and temperature in the system does not require modification of the housing. If modification of the housing is to be considered only with respect to maximum pressure and temperature but not to the scroll geometry modifications, then the original working fluid can be used. In this case, the pressure that needed to be withstood is more than triple and the temperature is 100 °C higher, while the exergy efficiency is 49 % for

Toluene. The best results are obtained with R404a and the built-in ratio is reduced from 7.3 to 3. The scroll rolling angle is 27 rad, the temperatures and pressures in the system are reasonably low and are suitable for low temperature heat engine and the exergy efficiency will reach 61 %. It can be observed from Fig. 10.3 that the exergy efficiencies of the Rankine cycle is strongly depended on the scroll expander geometry.

For all the organic working fluids, the exergy efficiency can be improved by modifying the geometry in order to be able to calculate the most appropriate built-in volume ratio for the scroll machine. The rolling angle is the most important geometric parameter since it defines the length of the scroll and the number of loops through the expansion process. Built-in volume ratio of the scroll expander is modified with respect to the rolling angle and influence of the modified geometry on the efficiency is evaluated for different working fluids as shown in Fig. 10.3. It can be observed that exergy efficiencies are expected higher than energy efficiencies because of the temperature difference between sink and source times heat input term at the denominator in Eq. (10.49).

The optimum rolling angle of the scroll expander for each organic fluid is evaluated and results are given in Table 10.1 to obtain an appropriate built in volume ratio for the best possible cycle exergy efficiency. The results are provided in Fig. 10.3, and the modified geometry is shown by the columns labeled in red. R404a clearly gives the best result for the modified geometry and the exergy efficiency is increased from 50 to 61 % (see Fig. 10.3). R123 and Toluene are the other working fluids which have relatively higher exergy efficiencies compared to other organic fluids for the modified and unmodified cases of the scroll expander geometry as can be observed in the figures.

Figure 10.4 illustrates the percentage of the exergy destruction in each component with respect to the total system exergy destruction for both configurations. Figure 10.4 demonstrates that the evaporator is the component with the highest exergy destruction contribution (76 %) followed by the expander with 22.1 % for the ORC that has an expander with a rolling angle of 57°. For the ORC with modified expander, the evaporator is still the highest contributor to the total exergy destruction of the system, contributing 81.2 % of the total exergy destruction. However, the exergy destruction in the expander reduced from 22.1 to 17.3 % by using expander with the rolling angle of 27°. This exergy reduction is mainly due to reduced leakage which is implied by the rolling angle geometric modification that accounts for 4.8 % of the exergy destruction.

Figure 10.5 illustrates the percentage of the exergy destruction in each component with respect to the total system exergy destruction for both configurations. Figure 10.5 demonstrates that the evaporator is the component with the highest exergy destruction contribution (75.3 %) followed by the expander with 23.2 % for the ORC with expander rolling angle of 69°. For the ORC with modified expander, the evaporator is still the highest contributor to the total exergy destruction of the system contributing 78.7 % of the total destruction. However, the exergy destruction in the expander is reduced from 23.2 to 19.8 % by using expander with the rolling angle of 33°. This exergy reduction is mainly due to reduced leakage which is im-

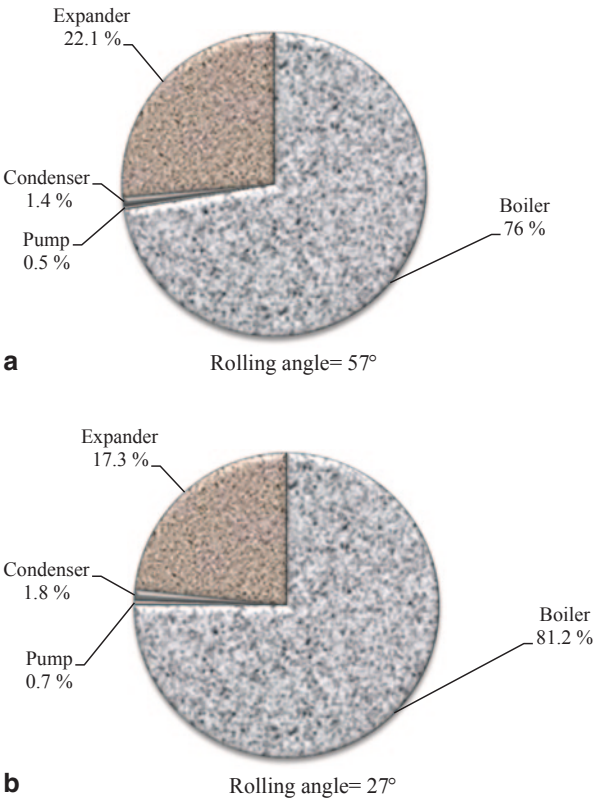

Fig. 10.4 Percentage of the exergy destruction in each component for R404a. **a** $\varphi_e = 57°$ and **b** $\varphi_e = 27°$

plied by rolling angle geometric modification that accounts for 3.4% of the exergy destruction.

Figure 10.6 illustrates the percentage of the exergy destruction in each component with respect to the total system exergy destruction for both configurations. It clearly demonstrates that the evaporator is the component with the highest exergy destruction contribution (74.59%) followed by the expander with 24.4% for the ORC with expander rolling angle of 57°. For the ORC with modified expander, the evaporator is still the highest contributor to the total exergy destruction of the system contributing 77.07% of the total destruction. However, the exergy destruction in the expander reduced from 24.4 to 20.7% in comparison by using expander with the rolling angle of 28°. This exergy reduction is mainly due to decreased leakage destruction which is implied by geometric modification in rolling angle that accounts for 3.7% of exergy destruction.

Figure 10.7 illustrates the percentage of the exergy destruction in each component with respect to the total system exergy destruction for both configurations. Figure 10.7 demonstrates that the evaporator is the component with the highest exergy destruction contribution (72.41%) followed by the expander with 26.29% for the ORC with expander rolling angle of 57°. For the ORC with modified expander,

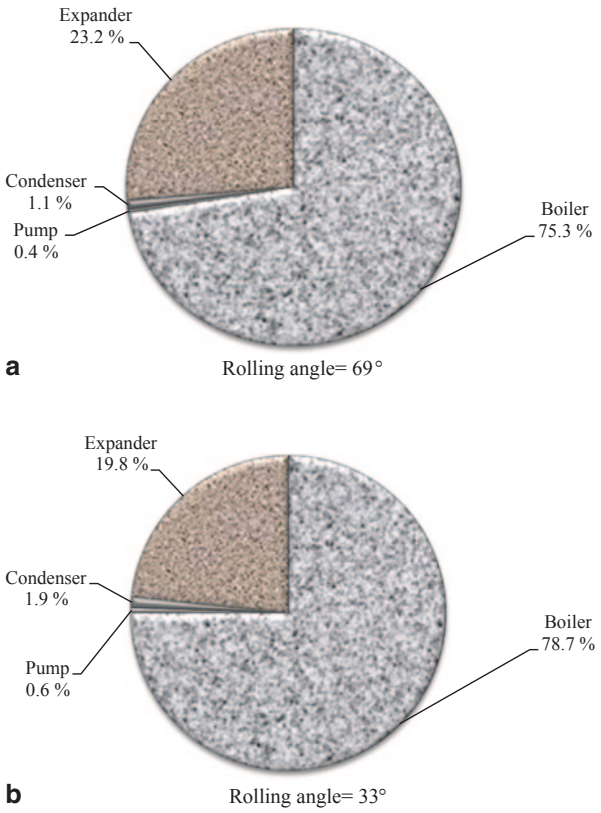

Fig. 10.5 Percentage of the exergy destruction in each component for R141b. **a** $\varphi_e = 69°$ and **b** $\varphi_e = 33°$

the evaporator is still the highest contributor to the total exergy destruction of the system contributing 75.02% of the total destruction. However, the exergy destruction in the expander reduced from 26.29 to 23.37% in comparison by using expander with the rolling angle of 28°. This exergy reduction is mainly due to decreased leakage destruction which is implied by geometric modification in rolling angle that accounts for 2.92% of exergy destruction.

Figure 10.8 shows the exergy wheel graph of ORC using R404a as an organic fluid that has an expander rolling angle of 57°. It can be observed that boiler and the expander have the highest contribution of exergy destructions with 3.02 and 0.55 kW, respectively.

Figure 10.9 shows the exergy wheel graph of ORC for R404a using an organic fluid and expander rolling angle of 27°. It can be from the figure that boiler and expander have the highest contribution of exergy destructions with 3.02 and 0.43 kW, respectively. It can be observed that exergy destruction in the expander is reduced from 0.55 to 0.43 kW by decreasing the rolling angle of expander from 57° to 27° and therefore the exergy output from the expander is increased from 2.6 to 2.72 kW.

Figure 10.10 shows the exergy wheel graph of ORC for R141b as an organic fluid and expander rolling angle of 69°. It can be observed that boiler and expander

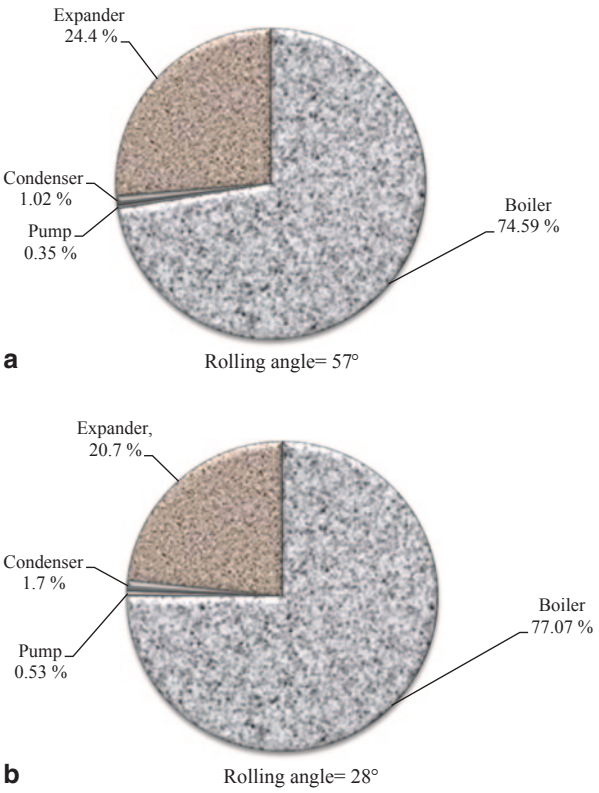

Fig. 10.6 Percentage of the exergy destruction in each component for R134a. **a** $\varphi_e = 57°$ and **b** $\varphi_e = 28°$

have the highest contribution of exergy destructions with 3.02 and 0.74 kW, respectively.

Figure 10.11 shows the exergy wheel graph of ORC for R141b as an organic fluid and expander rolling angle of 33°. It can be from the figure that boiler and expander have the highest contribution of exergy destructions with 3.02 and 0.62 kW, respectively. It can be observed that exergy destruction in the expander is reduced from 0.74 to 0.62 kW by decreasing the rolling angle of expander from 69° to 33° and therefore the exergy output from the expander is increased from 2.41 to 2.53 kW.

Figure 10.12 shows the exergy wheel graph of ORC for R134a as an organic fluid and expander rolling angle of 57°. It can be observed that boiler and expander have the highest contribution of exergu destructions with 3.02 and 1.02 kW, respectively.

Figure 10.13 shows the exergy wheel graph of ORC for R134a as an organic fluid and expander rolling angle of 28°. It can be from the figure that boiler and expander have the highest contribution of exergy destructions with 3.02 and 0.88 kW, respectively. It can be observed that exergy destruction in the expander is reduced from 1.02 to 0.88 kW by decreasing the rolling angle of expander from 57° to

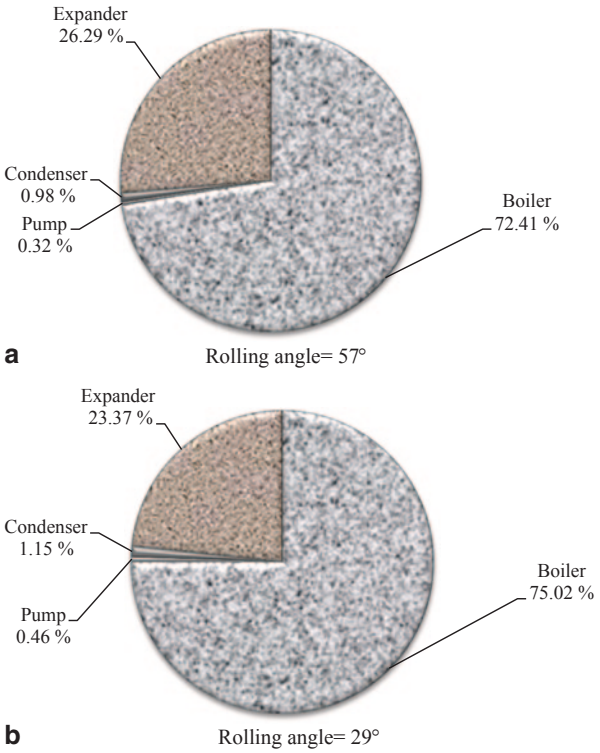

Fig. 10.7 Percentage of the exergy destruction in each component for NH_3. **a** $\varphi_e = 57°$ and **b** $\varphi_e = 29°$

28° and therefore the exergy output from the expander is increased from 2.13 to 2.27 kW.

Figure 10.14 shows the exergy wheel graph of ORC for NH_3 as an organic fluid and expander rolling angle of 57°. It can be observed that boiler and expander have the highest contribution of exergu destructions with 3.02 and 1.23 kW, respectively.

Figure 10.15 shows the exergy wheel graph of ORC for NH_3 as an organic fluid and expander rolling angle of 29°. It can be from the figure that boiler and expander have the highest contribution of exergy destructions with 3.02 and 1.07 kW, respectively. It can be observed that exergy destruction in the expander is reduced from 1.23 to 1.07 kW by decreasing the rolling angle of expander from 57° to 29° and therefore the exergy output from the expander is increased from 1.92 to 2.08 kW.

The effect of increased rolling angle on the exergy efficiency of the cycle is given in Fig. 10.16. Some fluids were omitted from the figure in order to analyze easily. It can be observed that the second-law efficiencies decrease for all the fluids with the increment of the rolling angle. In order to be able to obtain an optimum built-in volume ratio for the scroll machine, rolling angle should be decreased to the value that the rate of increase for the net work output from the scroll expander over the total heat input from the boiler has reached to the maximum value for the supercritical temperature condition at the expander inlet. The number of rotations

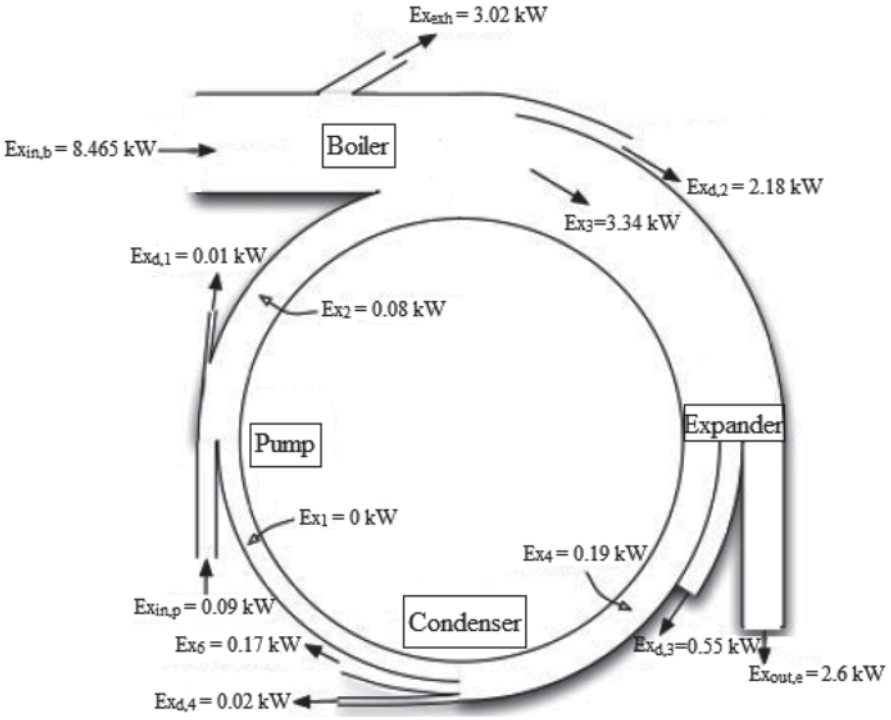

Fig. 10.8 Exergy wheel diagram for R404a and $\varphi_e = 57°$

of the orbiting scroll with respect to the fixed scroll is limited by the rolling angle. The produced shaft power will be lower for reduced rolling angles, however the efficiency will increase until the optimum built-in volume ratio is obtained for the scroll expander through the optimization process.

Figure 10.17 shows the variation of the system irreversibility with respect to the boiler outlet temperature for the temperature range changes from saturation temperature to critical temperature for the organic fluids considered. It can be observed that the total system irreversibility increases with the increment of the boiler outlet temperature for all the fluids. The results show the importance of second-law analysis. According to the results of the energy analysis, the energy efficiency is approximately constant with the boiler outlet temperature. However, combining the first- and second-law analyses shows the best case scenario is obtained when the fluid is operated at saturated conditions before the expander. That means the same energy efficiency with the lower rate of irreversibility can be achieved for the superheated refrigerant if the working fluid is sent to expander at saturated conditions. Figure 10.22 shows how the system with higher (R404a) and lower (NH_3) energy efficiencies present the lower and higher irreversibilities. Among all the fluids considered in this study, R134a shows the highest irreversibility.

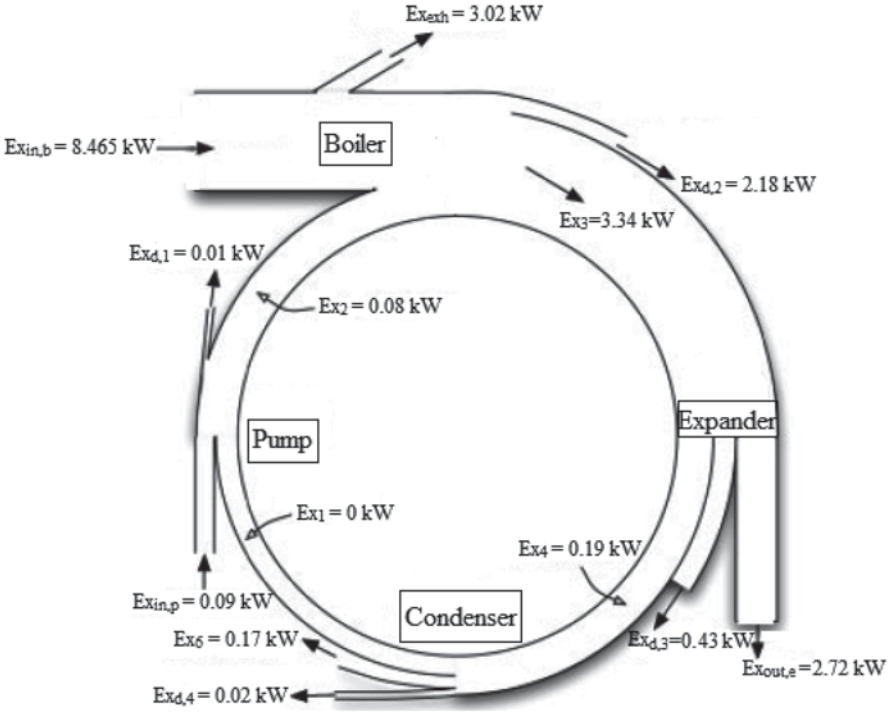

Fig. 10.9 Exergy wheel diagram for R404a and $\varphi_e = 27°$

Figure 10.18 shows the effect of the expander inlet temperature on the system second-law efficiency. It can be concluded for all the fluids that the exergy efficiency decreases with the boiler outlet temperature due to heat transfer at the boiler. It can be observed that exergy efficiency decreases with the increment in the temperature difference between the boiler inlet and outlet. These results agree with the results presented in Fig. 10.17, because an increment in the system irreversibility yields a decrease in the system exergy efficiency.

Figure 10.18 is plotted by assuming the temperatures of the fluids are constant at their saturation temperature at the boiler inlet. Boiler outlet temperature has been increased to the critical temperature to see the effect of temperature difference between boiler inlet and outlet on the cycle exergy efficiency. For temperatures between 430 and 525 K, R404a shows the best exergy efficiency; for a range of temperatures 400–430 K, Toluene shows the best efficiency; R123 and R2141b present the best exergy efficiency for temperatures between 380 and 400 K. R134a shows the best efficiencies for a temperature range of 360–380 K and NH_3 for a temperature range of 330–360 K, whereas NH_3 shows the low exergy efficiency among all the evaluated fluids. The effect of the isentropic efficiency of the expander on the second law efficiency was not investigated since it remained constant at 0.8, but it could be predicted that the increase of the expander isentropic efficiency will

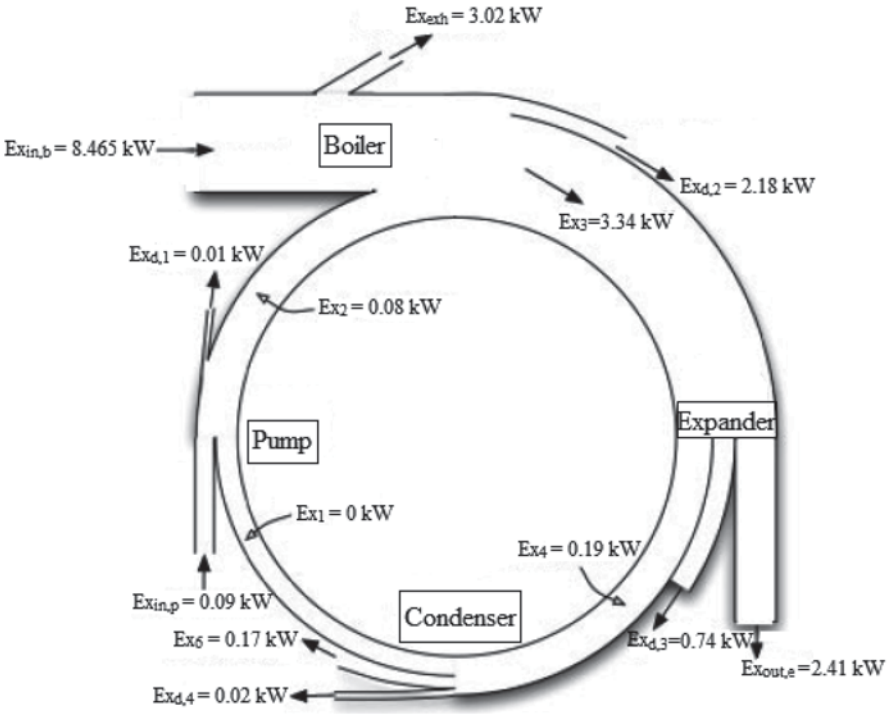

Fig. 10.10 Exergy wheel diagram for R141b and $\varphi_e = 69°$

represent higher exergy efficiencies for the cycle because of the lower irreversibility associated with the expander.

Figure 10.19 shows the total specific irreversibility versus the expander inlet pressure. It can be observed how the irreversibility increases with the increment of the expander pressure for all the fluids. R404a and Toluene show the highest and lowest irreversibilities respectively.

The variation of the mass flow rate needed to generate the same power output with the expander inlet pressure is shown in Fig. 10.20. Using the same conditions given in Fig. 10.18 and a fixed power output of 1.7 kW the figure is generated. It can be observed that the mass flow rate needed decreases with the increment of an expander inlet pressure. The reason is due to the increase in the net work output of the cycle with the increment of the expander inlet pressure. These results agree well with the results obtained from Fig. 10.18, because an increment of the net work represents an increase in the cycle exergy efficiency. R141b requires the highest mass flow rate for the pressure range from 0.5 to 4.0 MPa and R134a needs the lowest mass flow rate for the expander inlet pressure of 2 MPa and above.

Figure 10.21 shows the irreversibility rates for each fluid for the case analyzed in Fig. 10.18. It can be observed from the figure that the rate of irreversibility is higher for low pressures and decreases with the increment in the expander inlet pressure.

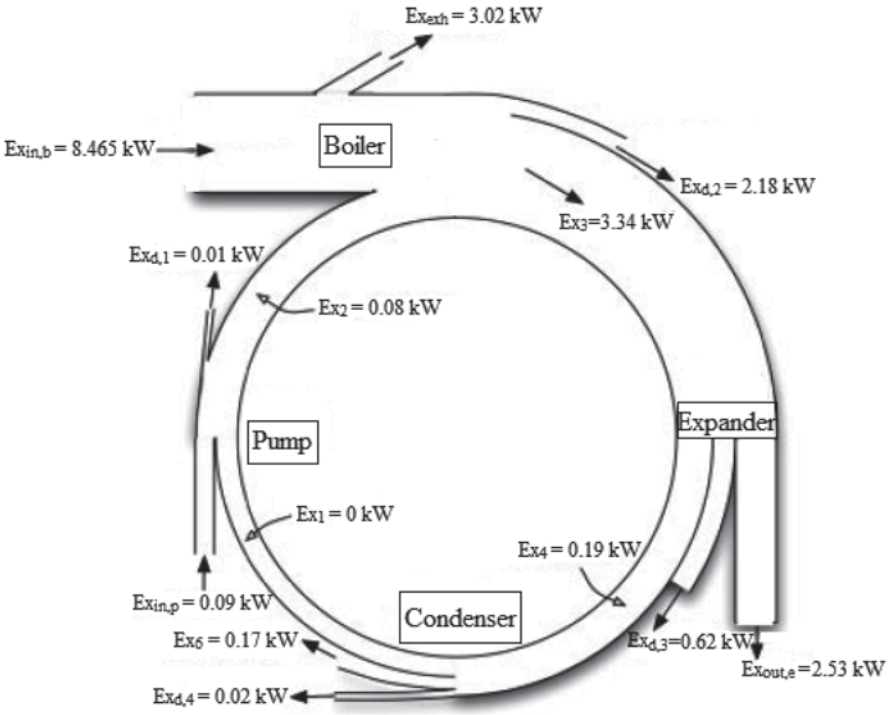

Fig. 10.11 Exergy wheel diagram for R141b and $\varphi_e = 33°$

Increment in the irreversibility occurs for high expander inlet pressure at 2 MPa or above. R404a and R134a show the lowest and the highest irreversibility rates for the expander inlet pressures which ranges from 0.5 to 3.5 MPa among other organic working fluids.

Figure 10.22 illustrates the exergy efficiency of the system with the condenser outlet temperature for R404a, R134a and NH_3. It can be observed that the exergy efficiency decreases with the increment of the condenser outlet temperature for all fluids. It can be indicated from Figs. 10.21 and 10.22 that ORC will be more suitable in places with low ambient temperature in terms of heat transfer in order to obtain higher exergy efficiencies.

The evaporator temperature and the expander efficiency are both important parameters in optimizing a ORCs performance. They noted that the expander efficiency was the most important parameter in low temperature energy recovery and that great care should be taken during expander selection in order to increase cycle efficiency.

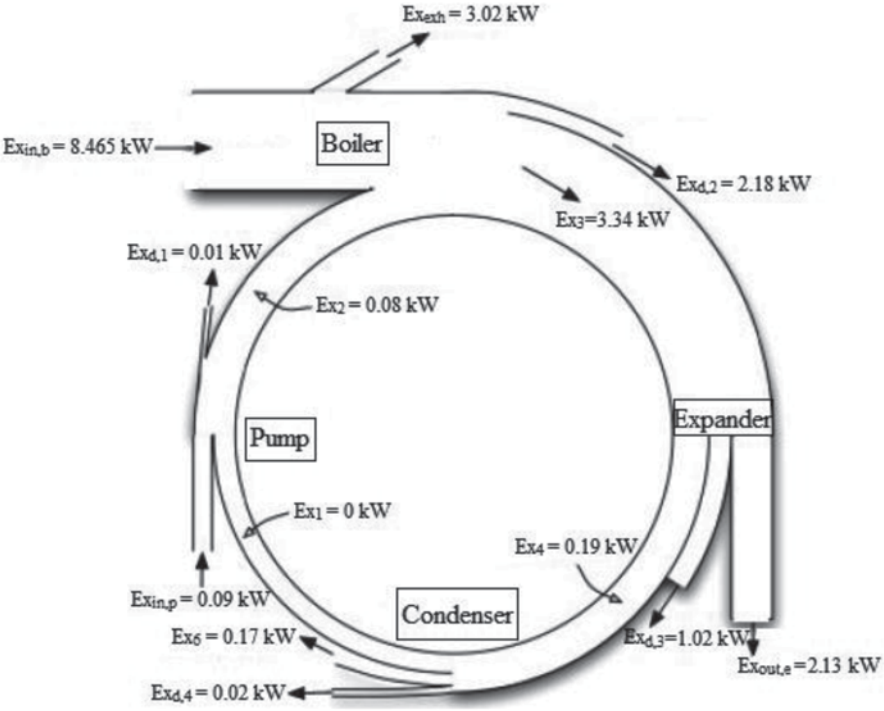

Fig. 10.12 Exergy wheel diagram for R134a and $\varphi_e = 57°$

Conclusions

In this study, several working fluids for a Rankine cycle are investigated for the modified scroll geometry. A Parametric study is performed in order to evaluate the influence of the geometric and thermodynamic parameters on the cycle performance. Some concluding remarks can be drawn from this study as follows:

- The rolling angle of the scroll machine should be modified in order to obtain an appropriate built-in volume ratio.
- Exergy efficiency of the Rankine cycle is strongly depended on the geometry of the scroll expander. Built-in volume ratio of the scroll expander is modified with respect to rolling angle and influence of the modified geometry on the efficiency is evaluated for different working fluids.
- It is possible to improve the efficiency of the cycle by adjusting the scroll geometry for all fluids. R404a clearly gives the best results for the modified geometry and the exergy efficiency is increased to 61 % from 50 %. It can be said that the rolling angle should be reduced to have an optimum built-in volume ratio for the cycle in terms of appropriate temperature and pressure range that will ensure higher energy and exergy efficiency.

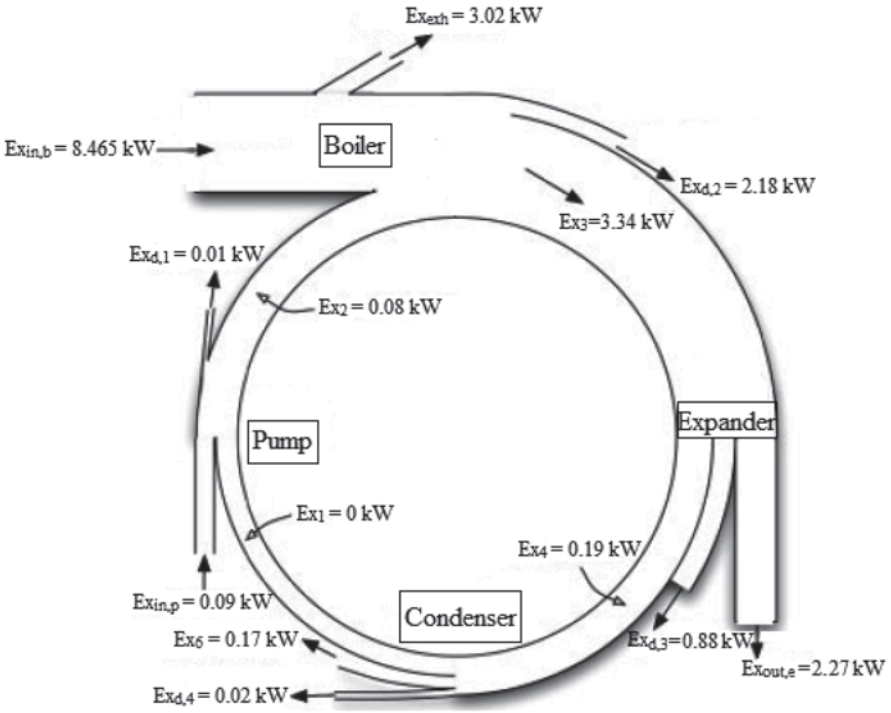

Fig. 10.13 Exergy wheel diagram for R134a and $\varphi_e = 28°$

- Percentage of the exergy destroyed in each component with respect to the total system exergy destruction is calculated for different scroll geometries and organic fluids. R404a with rolling angle of 33° gave the best results for the ORC that the evaporator is the component with the highest exergy destruction contribution (75.3 %) followed by the expander with 23.2 % for the ORC with expander rolling agle of 69°. For the ORC with modified expander, the evaporator is still the highest contributor to the total exergy destruction of the system contributing 78.7 % of the total destruction. However, the exergy destruction in the expander reduced from 23.2 to 19.8 % in comparison by using expander with the rolling angle of 33°. This exergy reduction is mainly due to decreased leakage loss which is implied by geometric modification in rolling angle that accounts for 3.4 % of exergy destruction.
- Organic fluids need to be superheated as the cycle thermal efficiency remains approximately constant when the inlet temperature of the expander is increased. However using the second-law analysis it can be said that superheating organic fluids increase the irreversibility. Therefore organic fluids must be operated at saturated conditions to reduce the total irreversibility of the system.

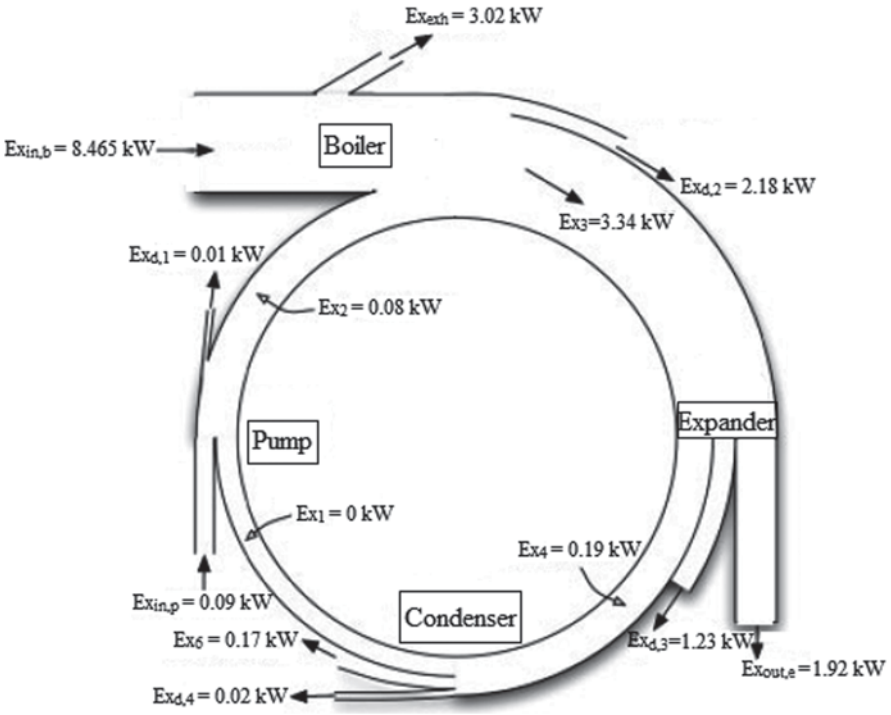

Fig. 10.14 Exergy wheel diagram for NH_3 and $\varphi_e = 57°$

- The thermal efficiency of ORC increases when the condenser temperature is decreased. Therefore using ORC in locations with low ambient temperature will be more effective.
- The procedure can be applied for the conversion of scroll compressors use in reverse, as expanders for Rankine cycles applications. Through an appropriate modeling, scroll compressors can be used to predict the operation in reverse, as expanders. If no modifications are made to the scroll compressor, the efficiency of the Rankine cycle will result low because the built-in volume ratio is not adapted to the cycle configuration for the same pressure and temperature levels in the expanders.

Nomenclature

A	area, m^2
c_p	specific heat at constant pressure, J/kg.K
c_v	specific heat at constant volume, J/kg.K
C_d	discharge coefficient
C_f	specific flow coefficient
D	diameter, m
E	total internal energy, J

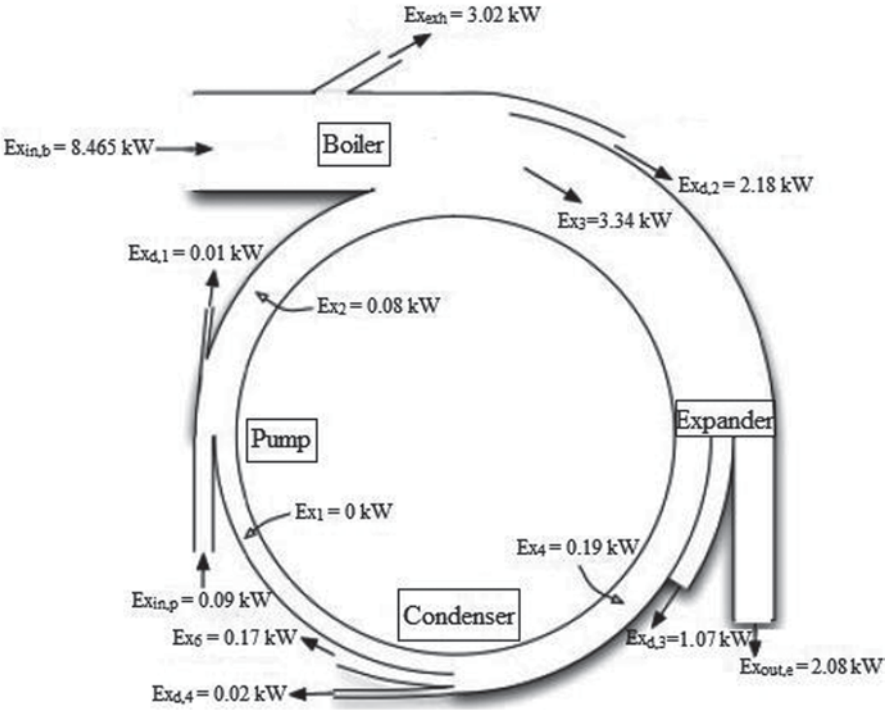

Fig. 10.15 Exergy wheel diagram for NH_3 and $\varphi_e = 29°$

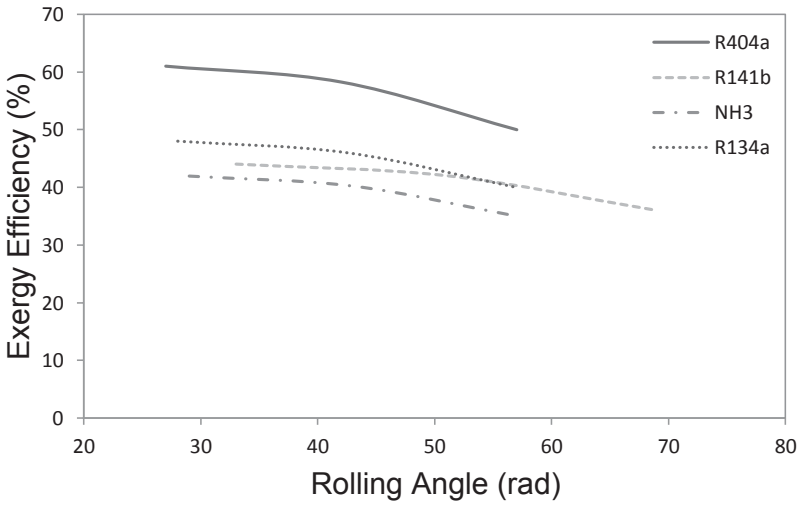

Fig. 10.16 Variation of the exergy efficiency with the rolling angle of the scroll machine

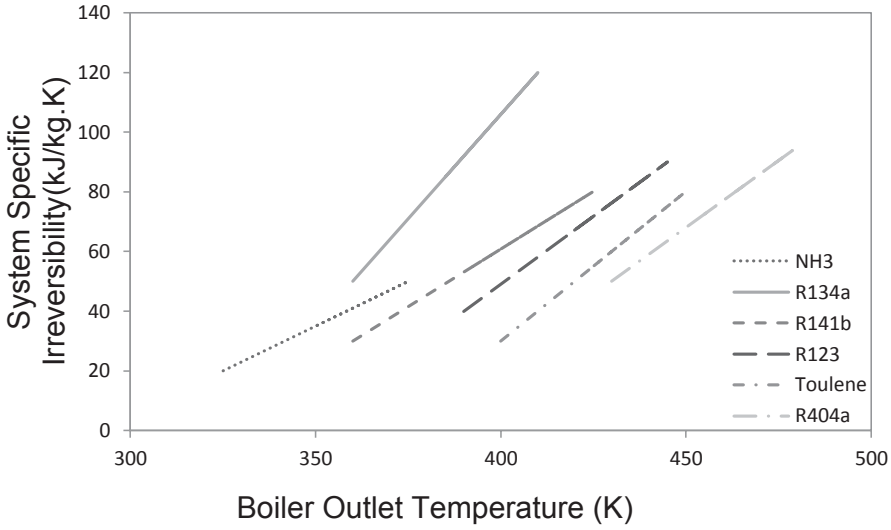

Fig. 10.17 Variation of the system irreversibility with the expander inlet temperature

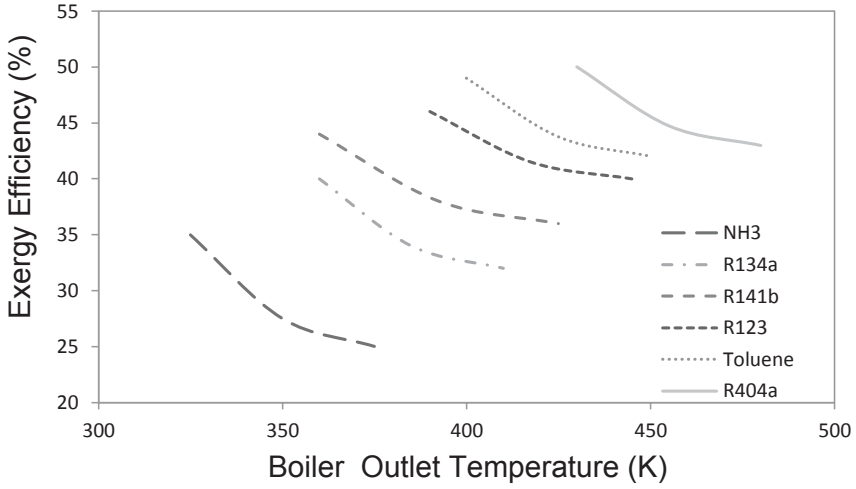

Fig. 10.18 Variation of the system second-law efficiency with expander inlet temperature

Ex	exergy, J
$\dot{E}x$	exergy rate, J/s
g	gravity of earth, m/s^2
h	specific enthalpy, J/kg
h_c	convective heat transfer coefficient, W/m^2-K

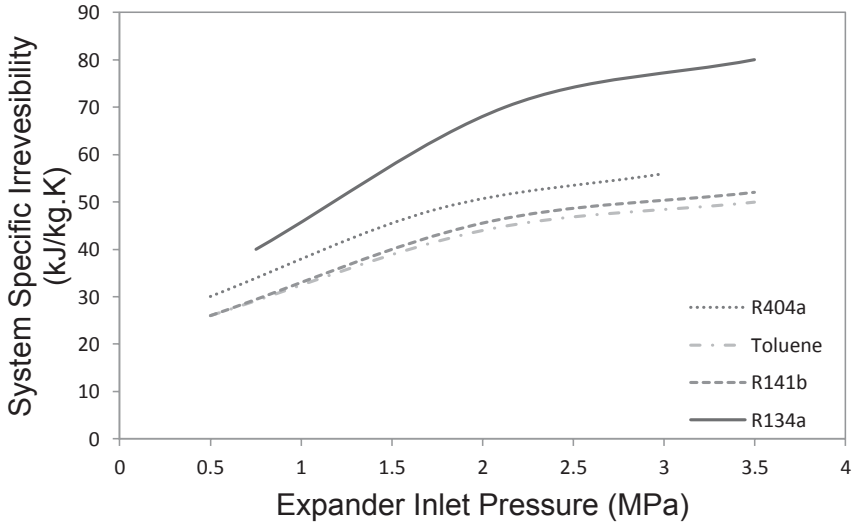

Fig. 10.19 Variation of the system irreversibility with the expander inlet pressure

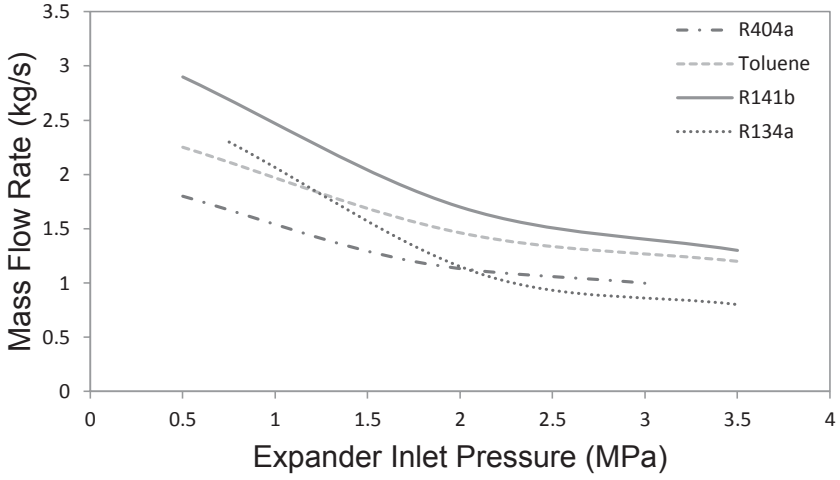

Fig. 10.20 Variation of the mass flow rate with the expander inlet pressure

h_s	scroll height, m
k	specific heat ratio
L	length, m
m	mass, kg
$\dot{m}$	mass flow rate, kg/s

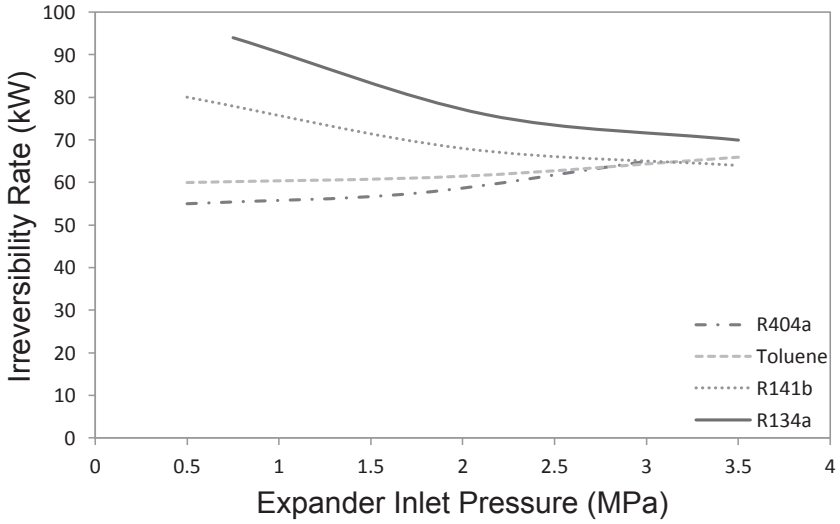

Fig. 10.21 Variation of the irreversibility rate with the expander inlet pressure

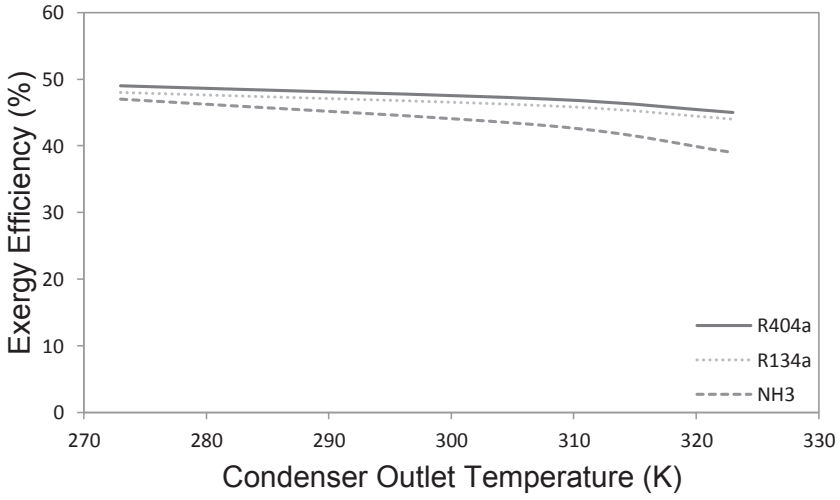

Fig. 10.22 Variation of the exergy efficiency with the condenser outlet temperature

N	rotational speed, Hz
P	pressure, Pa
Q	heat, J
$\dot{Q}$	heat rate, J/s
r	radius, m

r_b	radius of the basic circle of the scroll, m
r_o	orbiting radius of the rotating scroll, m
r_v	built-in volume ratio
s	specific entropy, J/kg-K
t	scroll thickness, m
T	temperature,°C
u	specific internal energy, J/kg
U	internal energy, J
v	velocity, m/s
v	specific volume, m^3/kg
V	volume, m^3
V_{ed}	expander discharge chamber volume, m^3
V_{ee}	expander expansion chamber volume, m^3
V_{ei}	expander intake chamber volume, m^3
W	work, J
$\dot{W}$	work rate, J/s
W_{in}	total work input to the compressor, J
W_{out}	net work output from the expander, J
W_s	total work output for the expander, J
z	height, m

Greek Letters

v	specific volume, m^3/kg
w	rotational speed, rad/s
ξ	leakage flow coefficient
δ	gap, m
Δ	difference
ε	effectiveness
η	efficiency
θ	orbiting angle, rad
ρ	density, kg/m^3
φ	involute angle, rad
φ_e	rolling angle (involute ending angle), rad
$\varphi_{i,s}$	starting angle of the inner involute, rad
φ_{i0}	initial angle of the inner involute, rad
$\varphi_{o,s}$	starting angle of the outer involute, rad
φ_{o0}	initial angle of the outer involute, rad

Subscripts

a	actual
amb	ambient
b	base circle
c	Curvature
conj	Conjugate
cp	Compressor

CV	control volume
d	discharge
diss	dissipated
e	expansion
en	ending
ex	exergy
exh	exhaust
exp	expander
fix	fixed
i	initial
l	low
leak	leakage
loss	mechanical loss
mot	motor
o	outer, orbiting radius
orb	orbiting
plen	plenum
rad	radial
s	isentropic
su	supply
suc	suction

References

1. Saleh B, Koglbauer G, Wendland M, Fischer J (2007) Working fluids for low-temperature organic Rankine cycles. Energy 32(7):1210–1221
2. Fraas A (1982) Engineering evaluation of energy systems. McGraw-Hill, New York
3. Hung T (2001) Waste heat recovery of organic rankine cycle using dry fluids. Energy Convers Manage 42(5):539–553
4. Schuster A, Karellas S, Aumann R (2010) Efficiency optimization potential in supercritical organic Rankine cycles. Energy 35(2):1033–1039
5. Mago PJ, Chamra LM, Somayaji C (2007) Performance analysis of different working fluids for use in organic Rankine cycles. Proc Inst Mech Eng Part A: J Power Energy 221(3):255–263
6. Borsukiewicz-Gozdur A, Nowak W (2007) Comparative analysis of natural and synthetic refrigerants in application to low temperature Clausius–Rankine cycle. Energy 32(4):344–352
7. Larjola J (1995) Electricity from industrial waste heat using high-speed organic rankine cycle (ORC). Int J Prod Econ 41(1):227–235
8. Badr O, O'Callaghan PW, Hussein M, Probert SD (1984) Multi-vane expanders as prime movers for low-grade energy organic Rankine-cycle engines. Appl Energy 16(2):129–146
9. Peterson RB, Wang H, Herron T (2008) Performance of a small-scale regenerative Rankine power cycle employing a scroll expander. Proc Inst Mech Eng Part A: J Power Energy 222(3):271–282
10. Kim HJ, Ahn JM, Park I, Rha PC (2007) Scroll expander for power generation from a low-grade steam source. Proc Ins Mec Eng Part A: J Power Energy 221(5):705–711
11. Lemort V, Quoilin S, Cuevas C, Lebrun J (2009) Testing and modeling a scroll expander integrated into an Organic Rankine cycle. Appl Therm Eng 29(14):3094–3102

12. Xiaojun G, Liansheng L, Yuanyang Z, Pengcheng S (2004) Research on a scroll expander used for recovering work in a fuel cell. Int J Thermodyn 7(1):1–8
13. Halm, NP (1997) Mathematical modeling of scroll compressors. Master Thesis Purdue University
14. Wang B, Li X, Shi W (2005) A general geometrical model of scroll compressors based on discretional initial angles of involute. Int J Refrig 28:958–966
15. Bush JW, Beagle WB (1992) Derivation of general relationship governing the conjugacy of scroll profiles. Proceedings of International Compressor Engineering Conference at Purdue, pp 1079–1088
16. Hirano T, Matsumura N, Takeda K (1988) Development of high efficiency scroll compressors for air conditioners. Proceedings of International Compressor Engineering Conference at Purdue, pp 65–74
17. Yanagisawa T, Fukuta M, Ogi Y, Hikichi T (2001) Performance of an oil-free scroll type air expander. Proc. of the ImechE Conf. Trans. on compressors and their systems pp 167–174
18. Winandy E, Saavedra CO, Lebrun J (2002) Experimental analysis and simplified modelling of a hermatic scroll refrigeration compressor. Appl Therm Eng 22:107–120
19. Chen Y, Halm NP, Groll EA, Braun JE (2002) Mathematical modeling of scroll compressors-part I: compression process modeling. Int J Refrig 25:731–750
20. DeBlois RL, Stoeffler RC (1988) Instrumentation and data analysis techniques for scroll compressor. Proceedings of the International Compressor Engineering Conference at Purdue, pp 182–188
21. Gravesen J, Henriksen C (2001) The geometry of the scroll compressor. SIAM Rev 43:113–126
22. Harada J (2010) Development of a small scale scroll expander. Master Thesis, Oregon State Uni
23. Ishii N, Fukushima M, Sano K, Sawai K (1986) A study on dynamic behavior of a scroll compressor. Proceedings of International Compressor Engineering Conference at Purdue, pp 901–916
24. Oralli E (2010) Conversion of a scroll compressor to an expander for Organic Rankine cycle: modeling and analysis. Master Thesis, University of Ontario Institute of Technology
25. Quoilin S (2007) Experimental study and modeling of a low temperature Rankine cycle for small scale cogeneration. Master Thesis, University of Liege, Belgium
26. Quoilin S, Lemort V, Lebrun J (2010) Experiment study and modeling of an Organic Rankine cycle using scroll expander. Appl Energy 87:1260–1268
27. Zamfirescu C, Dincer I (2008) Thermodynamic analysis of a novel ammonia-water trilateral Rankine cycle. ThemochimicaActa 477:7–15
28. Zhang B, Peng X, He Z, Xing Z, Shu P. (2007) Development of a double acting free piston expander for power recovery in transcritical CO_2 cycle. Appl Therm Eng 27(8):1629–1636

Chapter 11
Thermochemical Energy Storage Systems: Design, Assessment and Parametric Study of Effects of Charging Temperature

Ali H. Abedin and Marc A. Rosen

Abstract Thermal energy storage (TES) is an advanced technology that can enhance energy systems by reducing environmental impact and increasing efficiency. Thermochemical TES is an emerging method which permits more compactness storage through greater energy storage densities. The design of thermochemical energy storage systems is complex and requires appropriate consideration of many factors. Generally, many criteria need to be evaluated by engineers in engineering design such as cost, environmental impact, safety, reliability, efficiency, size, and maintenance. These factors need to be considered in designing thermochemical TES systems. In this study, some important factors related to design concepts of thermochemical TES systems are considered and preliminary design conditions for them are investigated. Parametric studies are carried out for the thermochemical storage systems to investigate the effects of charging temperature on the efficiency and behavior of thermochemical storage systems. The results show that the charging and overall energy and exergy efficiencies for both closed and open loop systems decrease by increasing the charging temperature.

Keywords Thermal energy storage · Thermochemical energy storage · Parametric study · Exergy · Efficiency

11.1 Introduction

Thermal energy storage is defined as the temporary holding of thermal energy in the form of hot or cold substances for later utilization. There are three main types of TES: sensible, latent and thermochemical. Sensible TESs store energy by changing

M. A. Rosen (✉)
Faculty of Engineering and Applied Science, University of Ontario Institute of Technology, 2000 Simcoe Street North, Oshawa, Ontario L1H 7K4, Canada
e-mail: marc.rosen@uoit.ca

A. H. Abedin
Golder Associates Ltd., 6925 Century Avenue, Suite #100, Mississauga, Ontario L5N 7K2, Canada
e-mail: ali.hajiabedin@gmail.com

I. Dincer et al. (eds.), *Progress in Sustainable Energy Technologies: Generating Renewable Energy,* DOI 10.1007/978-3-319-07896-0_11,

the temperature of the storage medium (water, brine, rock, soil, etc.). Latent TESs store energy through phase change (e.g., cold storage via water/ice and heat storage by melting paraffin waxes). In thermochemical energy storage, energy is stored after a dissociation reaction and then recovered in a chemically reversed reaction. Thermochemical energy storage has a higher storage density than other TES types, reducing the mass and space requirements for the storage. Thermochemical TES systems experience thermochemical interactions with their surroundings, including heat transfer after and before a chemical process. Generally, many criteria need to be evaluated in engineering design such as cost, environmental impact, safety, reliability, efficiency, size, and maintenance. These factors need to be considered in designing thermochemical TES systems. Usually, difficulties and complexities exist in design processes and need to be analyzed carefully.

The key objective in designing a thermochemical storage system is to charge and discharge the storage in a controlled and optimal way, including having an appropriate overall efficiency. Designing such systems necessitates the application of engineering thermodynamics, heat and mass transfer, fluid mechanics, economics, reaction kinetics, and other subjects.

In order to understand the relation among various parameters affecting the performance of a thermochemical energy storage system, parametric analyses can be performed. Two of the most important parameters to assess the performance of a thermochemical storage system are its energy and exergy efficiencies. Various factors identified in the design section can influence both the energy and exergy efficiencies of a storage system. Each thermochemical energy storage system is based on a working pair reaction for which the corresponding reaction has unique conditions, e.g. operating temperature and pressure, and enthalpy of reaction. Properties of thermochemical materials, e.g. durability and cyclic behavior, are other factors that have significant effects on the performance of thermochemical storage systems. The design of thermochemical energy storage systems is investigated in this study. Some important factors related to design concepts of thermochemical TES systems are considered and preliminary design conditions for them are investigated. Also, parametric studies are carried out for the thermochemical storage systems to investigate the effects of selected parameters on the efficiency and behavior of thermochemical storage systems.

11.2 Key Factors in Design of a Thermochemical Storage System

Systems design for thermochemical energy storage, like for general thermal systems of many types, requires that two main categories be considered [1]: component and system design.

Component Design A reactor design for the thermochemical process is selected in this section.

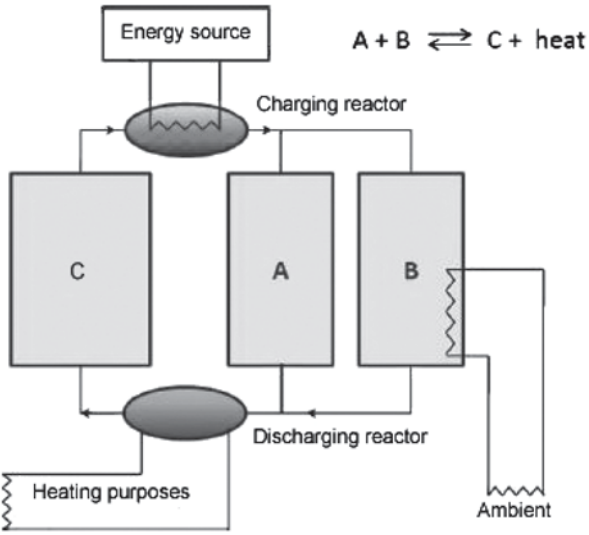

Fig. 11.1 Separate reactors in thermochemical TES systems. (Adapted from [4, 5])

Reactor There are two types of design concepts for reactors in thermochemical TES systems:

- Separate reactors (Fig. 11.1): Thermochemical material C absorbs energy from an energy resource and is converted to components A and B, which are separately stored. Separate reactors are suitable for long-term storage, e.g. seasonal storage when large storage capacity is required.
- Integrated reactors (Fig. 11.2): Since component B is a solid after the charging process, it can be stored in the same reactor as the thermochemical material C, avoiding the need for a space to store it.

System Design Closed and Open Loop Thermochemical Energy Storage Closed loop and open loop thermochemical systems have been investigated. Briefly, open systems operate at the atmospheric pressure and water vapor is the working fluid, which is released to the ambient environment. In an open system the gaseous working fluid is directly released to the environment and therefore normally only water is a possible candidate as the working fluid. Materials in open systems must be nontoxic and non-flammable. In closed loop systems, internal substances are separate from the heat transport stream and can provide higher output temperatures than open systems in heating applications. The charging process usually requires higher temperatures for closed rather than open systems [2]. A closed loop thermochemical TES system, with water is one of reactants, is illustrated as Fig. 11.3, and an open loop thermochemical TES system in Fig. 11.4.

Thermochemical Material Material selection is a key element that significantly affects the performance of thermochemical storage systems. Some key factors to be considered in selecting thermochemical material for a thermochemical storage system can be listed as follows [3, 4]:

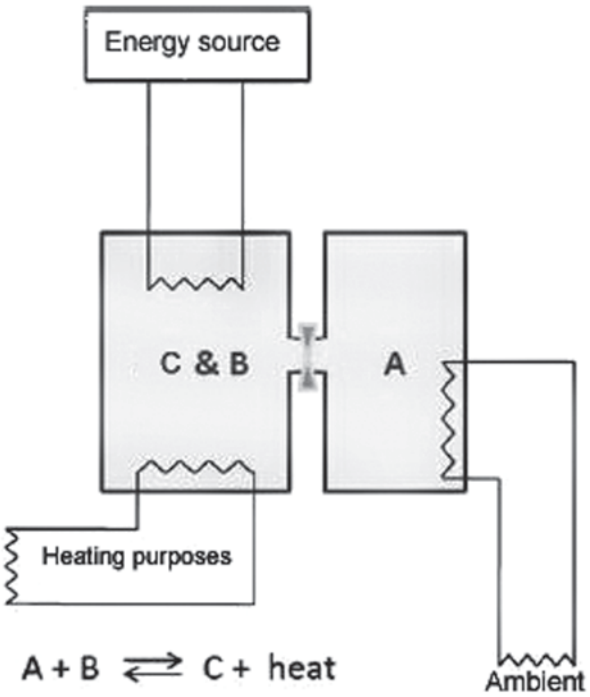

Fig. 11.2 Integrated reactors in thermochemical TES systems. (Adapted from [4, 5])

- High storage density at the operating conditions
- Low charging time, which results in higher system efficiency as well
- Suitable availability
- High thermal conductivity and high heat transfer rate from material to heat exchangers
- Environmentally friendly, non toxic, non flammable; low global warming potential (GWP) and ozone depletion potential (ODP)
- Non corrosive, which improves the effective life of components in thermochemical TES systems
- Low cost
- Good cyclic behaviour (reversibility with little degradation over large numbers of cycles) as well as thermal and chemical stability under operating conditions
- Low temperature heat source required for the evaporation during discharging period
- Easy to handle and transport

Cyclic Behaviour of Thermochemical Materials The durability of thermochemical materials should be examined under repetitive cycles to demonstrate their operability. With an increasing number of thermochemical cycles, a thermochemical material degrades and its behaviour may change. The heat of dissociation (recovered heat) and the overall efficiency of the storage system may decrease over time and numbers of cycles. A study has been performed [6] for a magnesium oxide/

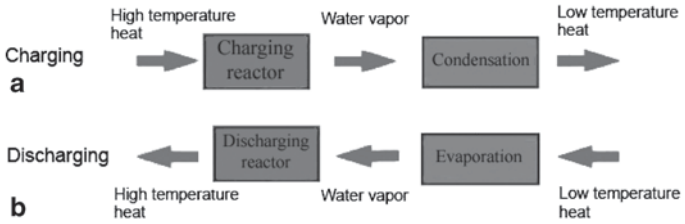

Fig. 11.3 Charging (**a**) and discharging (**b**) process in closed thermochemical TES. (Adapted from [4])

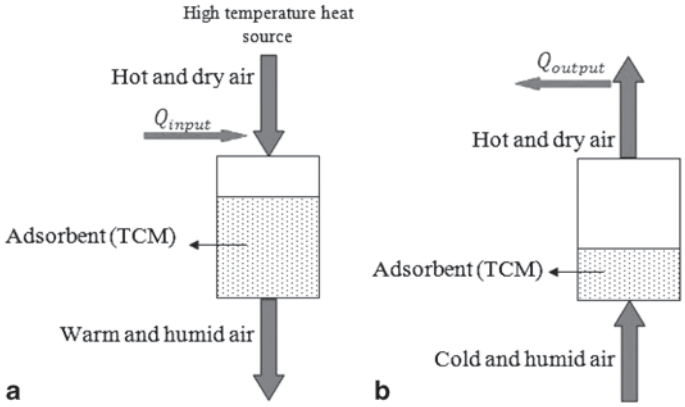

Fig. 11.4 Charging (**a**) and discharging (**b**) process in open thermochemical TES. (Adapted from [7])

water reaction system for a heat pump and the durability of the materials under repetitive reactions has been investigated. Three types of MgO were chosen for the experiment: MgO material using ultra-fine magnesium oxide powder as the precursor (UFP-Mg), MgO material using common magnesium hydroxide as the precursor (Com-Mg), and MgO using magnesium ethoxide as the precursor (Eth-Mg). Twenty-four cycles of charging and discharging were performed on the three types of magnesium oxide and UFP-Mg was found to have the highest durability with repeated cycles.

11.3 Parametric Study of Effect of Charging Temperature on Efficiency of Thermochemical Energy Storage Systems

Parametric studies can be carried out for thermochemical storage systems to investigate the effects of selected parameters on efficiencies and behaviour of storage systems. In this section the effects are examined of varying charging temperature on charging and overall energy efficiencies and exergy efficiencies.

Energy Efficiency As mentioned previously, charging temperature can affect the efficiency of a thermochemical storage system. This effect is investigated for closed and open thermochemical energy storages, using illustrative examples. Energy and exergy efficiencies are considered in this subsection.

Closed Loop Thermochemical Energy Storage To illustrate the analysis of closed thermochemical TES, an existing system is considered for which experimental data have been reported [8]. The system considered integrates a flat plate solar collector and a chemical process using bromide strontium as the reactant and water as the working fluid. The storage reaction can be expressed as

$$SrBr_2 \cdot H_2O + 5H_2O \leftrightarrow SrBr_2 \cdot 6H_2O + 5\Delta H \tag{11.1}$$

Where $\Delta H = 3732$ kJ/kg H_2O. In this reaction, $SrBr_2 \cdot H_2O$ and $SrBr_2 \cdot 6H_2O$ and are in the solid phase and H_2O is in the vapour phase which is condensed and stored in a separate tank. Data are available for the heating operation (floor heating) during the mid-seasons of fall and spring. The system is comprised of two heat transfer loops: one between a plate-type heat exchanger and solar panels, and another between the heat exchanger and the building floor. The mass of $SrBr_2 \cdot H_2O$ is 171.3 kg and the mass of exchanged water in the reactor is 57.9 kg. The water (working fluid) flows at a rate of 6 L/min. The total volume of the prototype reactor is 1 m^3 and the system is able to store 60 kWh in heating capacity. Various thermodynamic constraints apply for the reactive pair and for mid-season conditions: the maximum output temperature of the flat-plate solar collector is 80 ℃, the temperature of the external environment is 7 ℃, the inlet temperature for floor heating is 35 ℃, the solid/gas equilibrium temperature for the dehydration phase is 43 ℃, and the solid/gas equilibrium temperature for the hydration phase is 43 ℃. Also, during charging and discharging, the energy changes are equal in magnitude, i.e. $\Delta H_c = -\Delta H_d$, as are the exergy changes, i.e. $\Delta \in_c = -\Delta \in_d$. In this system, the energy efficiencies of the charging and overall processes are dependent on the charging temperature according to the following expressions, respectively:

$$\eta_c = \frac{\Delta H_c}{m_c C_p (T_1 - T_2)} \tag{11.2}$$

$$\eta_o = \frac{m_d C_p (T_4 - T_3)}{m_c C_p (T_1 - T_2)} \tag{11.3}$$

Here, T_1 is the charging temperature supplied by solar energy. In efficiency calculations T_1 has been assumed to be 70 ℃ but the maximum theoretical output temperature of the flat-plate solar collector can be 80 ℃ [8]. In this analysis T_1 varies from 70 to 80 ℃ and other parameters are held constant. So, the values of charging and overall energy efficiencies relative to different values of T_1 can be evaluated. The terms m_d, C_p, T_2, T_3, T_4 and ΔH_c have been evaluated earlier [9] as $m_c = 14{,}866$ kg, and $m_d = 15{,}055$ kg, $T_2 = 50$ °C, $T_3 = 25$ °C, $T_4 = 35$ °C, $C_p = 4.183$ kJ/kg K, and

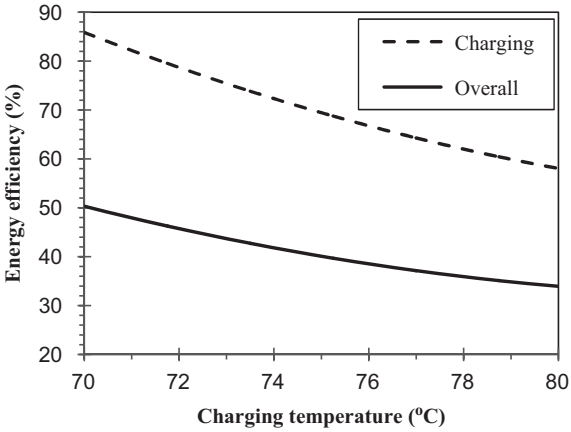

Fig. 11.5 Charging and overall energy efficiencies vs. charging temperature in closed loop thermochemical TES case study

$\Delta H_c = 1{,}080{,}414$ kJ. The effect of varying charging temperature on the charging and overall energy efficiencies is illustrated in Fig. 11.5. This figure shows that the charging and overall energy efficiencies for the closed loop thermochemical TES case study decrease with increasing charging temperature.

Open Loop Thermochemical Energy Storage To illustrate the analysis of an open thermochemical TES system, we consider an existing system for which experimental data have been reported. Here, we consider an open sorption thermochemical storage system, which has been utilized in a school in Munich, Germany since 1996. This system is connected to the Munich district heating system, and heats a school building in winter and cools a jazz club in summer. The school building and jazz club are also connected to the district heating system. The storage system is connected to a combined air, radiator and floor heating system [7]. The thermochemical TES contains 7000 kg of zeolite 13X beads. Zeolite 13X is non-toxic and non-flammable and can be handled easily. The maximum air flow through the zeolite storage is 6000 m^3/h [10]. The heating mode of the system (applicable during winter) is investigated in this study. An energy storage density of 135 kWh/m^3 (0.5 GJ/m^3) can be obtained in the heating mode of the storage [11]. In this case study, the energy efficiencies of the charging and overall processes are dependent on the charging temperature according to the following expressions, respectively:

$$\eta_c = \frac{\Delta H_{ds}}{m_c C_p (T_1 - T_2)} = \frac{useful\ output\ energy}{input\ energy} \tag{11.4}$$

$$\eta_o = \frac{Q_{rec}}{m_c C_p (T_1 - T_2)} \tag{11.5}$$

Here, T_1 is the charging temperature supplied by district heating system. In efficiency calculations T_1 is assumed 130 ℃ but the maximum theoretical output temperature of the district heating system can be 180 ℃ [7]. In this analysis, the effect of varying

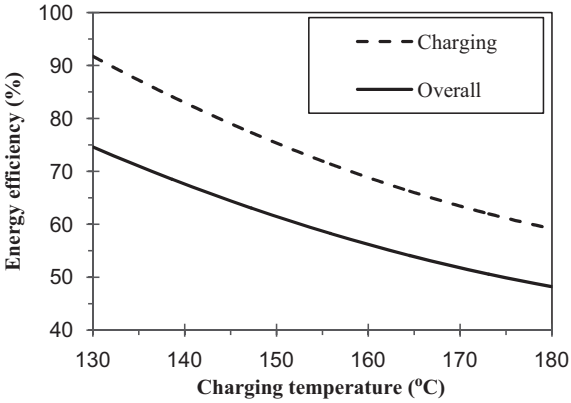

Fig. 11.6 Charging and overall energy efficiencies vs. charging temperature in open loop thermochemical TES case study

charging temperature is considered and T_1 varies from 130 to 180 ℃. The effect of varying charging temperature on other parameters is neglected and as a result, other parameters are held constant. So, the values of charging and overall energy efficiencies relative to different values of T_1 can be evaluated. The terms m_c, C_p, T_2, and have been evaluated previously [9] as $m_c = 59{,}400$ kg, $T_2 = 40$ °C, $C_p = 1.006$ kJ/kg K, useful input energy = 5,040,000 kJ and recovered energy = 4,738,457 kJ. The discharging duration is 14 h in this system. Figure 11.6 shows that the charging and overall energy efficiencies decrease with increasing charging temperature.

Exergy Efficiency

Closed Loop Thermochemical Energy Storage In the closed loop thermochemical energy storage case study, the exergy efficiencies of the charging and overall processes are expressed as follows:

$$\psi_c = \frac{Exergy\ stored\ in\ charging\ reaction}{Exergy\ input} \tag{11.6}$$

$$\psi_o = \frac{Exergy\ recovered}{Exergy\ input} \tag{11.7}$$

where

$$Exergy\ input = m_c\left[h_1 - h_2 - T_0(s_1 - s_2)\right] \tag{11.8}$$

Here, the exergy stored and the exergy recovered have been calculated previously and the exergy input is dependent on T_1 because h_1 and s_1 are dependent on T_1 Values of the charging and overall exergy efficiencies for various values of T_1 have been evaluated. Other parameters have been evaluated before [9] as, mc = 14,866 kg, $T_0 = 25$ °C, $T_2 = 50$ °C, $h_2 = 209.4$ kJ/kg, $s_2 = 0.7037$ kJ/kg K, the exergy stored and

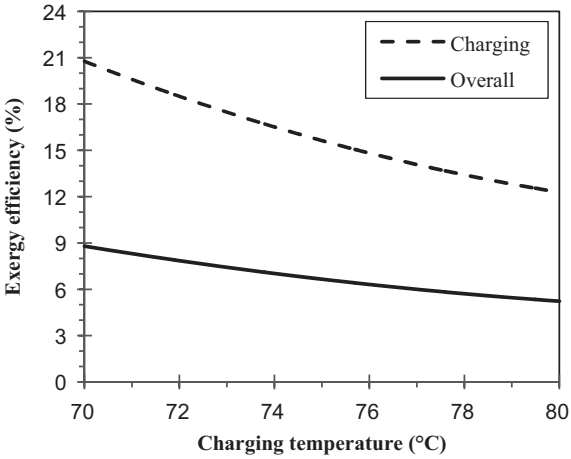

Fig. 11.7 Charging and overall exergy efficiencies vs. charging temperature in closed loop thermochemical TES case study

exergy recovered have been calculated as exergy stored in reaction = 32,275 kJ and exergy recovered = 11,682 kJ.

The effect of charging temperature on the charging and overall exergy efficiencies is illustrated in Fig. 11.7. As shown in this figure, the charging and overall exergy efficiencies in closed loop thermochemical TES case study decrease with increasing the charging temperature.

Open Loop Thermochemical Energy Storage Using the same methodology for the open loop thermochemical storage case study, the charging and overall exergy efficiencies can be evaluated for various charging temperatures. Here, the exergy stored and the exergy recovered have been calculated and exergy input is dependent on T_1 because h_1 and s_1 are dependent on T_1 Charging and overall exergy efficiencies for various values of T_1 can be evaluated. Other parameters have been evaluated before [9] as $m_c = 59{,}400$ kg, $T_2 = 25\,°C$, $h_2 = 404.5$ kJ/kg, $s_2 = 6$ kJ/kg k, exergy stored in desorption = 794,847 kJ and exergy recovered by air = 218,696 kJ.

The effect of varying charging temperature on the charging and overall exergy efficiencies for an open loop thermochemical TES considered in the case study (Fig. 11.8). This figure shows that the charging and overall exergy efficiencies decrease with increasing charging temperature.

11.4 Further Discussion

The parametric studies in this study describe the effect charging temperature on efficiencies through illustrative examples. The effect of varying charging temperature on the overall energy and exergy efficiencies is shown in Figs. 11.5, 11.6, 11.7 and 11.8. The results show that the charging and overall energy and exergy efficiencies

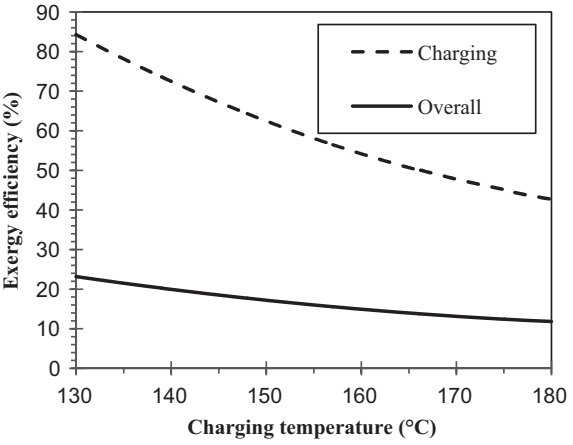

Fig. 11.8 Charging and overall exergy efficiencies vs. charging temperature in open loop thermochemical TES case study

for both closed and open loop systems decrease by increasing the charging temperature. Comparing the results between energy and exergy efficiencies in closed and open loop case studies shows that the charging and overall energy/exergy of the closed loop case has less reduction relative to the corresponding efficiencies in the open loop case. Furthermore, exergy efficiencies (charging and overall) in both case studies have more reduction relative to the corresponding energy efficiencies. The charging temperature is of importance in designing a thermochemical energy storage. Achieving appropriate efficiencies is a key factor in enhancing thermochemical storage systems and in optimizing designs.

Conclusions

Some important factors related to preliminary design concepts of thermochemical energy storage systems are investigated in this study. Since thermochemical energy storage systems are undergoing research and experimentation, much information needed for design is lacking. The design of these systems is complex and requires consideration on many factors, e.g., economic, efficiency, environmental, and engineering aspects. Further research is needed to improve understanding of the scientific and engineering characteristics of these systems including material selection, durability of the storage system, energy savings, costs, etc. Such information can help efforts to improve various design aspects relating to the performance and implementation of these systems. Parametric analyses of closed and open loop thermochemical energy storage case studies have been performed in this study. The effect of charging temperature on efficiencies of the storage system has been investigated. The charging temperature can affect overall and charging energy and exergy efficiencies of the storage system. The results show that efficiencies decrease with increasing charging temperature.

Nomenclature

Cp	specific heat at constant pressure (kJ/kg K)
E	energy (kJ)
h	specific enthalpy (kJ/kg)
m	mass of working fluid (kg)
M	mass of reactant (kg)
n	number of moles (−)
Q	heat (kJ)
s	specific entropy (kJ/kg K)
T	temperature (°C or K)

Greek Symbols

ΔH	enthalpy change of reaction (kJ)
ΔE	energy accumulation (kJ)
$\Delta \in$	exergy accumulation (kJ)
$\in$	exergy (kJ)
η	energy efficiency (−)
ψ	exergy efficiency (−)

Subscript and Superscripts

0	reference environment
c	charging
d	discharging
ds	desorption
o	overall

Acronyms

TES	Thermal Energy Storage
GWP	Global Warming Potential
ODP	Ozone Depletion Potential

Acknowledgement The authors gratefully acknowledge the financial support provided by the Natural Sciences and Engineering Research Council of Canada.

References

1. Bejan A, Tsatsaronis G, Moran M (1996) Thermal design and optimization. Wiley, New York
2. Hauer A, Lavemann E (2007) Open absorption systems for air conditioning and thermal energy consumption. In: Paksoy HÖ (ed) Thermal energy storage for sustainable energy storage. Springer, Netherlands, pp 429–444
3. International Energy Agency Solar Heating and Cooling Program (IEA-SHC) (2008) Advanced storage concepts for solar and low energy buildings, Annex text, Task 32, Subtask B: Chemical and Sorption, February 2008

4. Edem N'Tsoukpe K, Liu H, Pierres NLe, Luo L (2009) A review on long-term sorption solar energy storage. Renew Sustain Energy Rev 13:2385–2396
5. Zondag HA, Kalbasenka A, van Essen M, Bleijendaal L, Van Helden W, Krosse L (2008) First studies in reactor concepts for thermochemical storage. Proc. Eurosun 2008, 1st International Conference on Solar Heating, Cooling and Buildings, 7–10 October, Lisbon, Portugal
6. Kato Y, Kobayashi K, Yoshizawa Y (1998) Durability of repetitive reaction of magnesium oxide/water reaction system for a heat pump. Appl Therm Eng 18:85–92
7. Hauer A (2002) Thermal energy storage with zeolite for heating and cooling applications, Proc. 3rd Workshop of Annex 17 ECES IA/IEA, 1–2 October, Tokyo, Japan
8. Mauran S, Lahmidi H, Goetz V (2008) Solar heating and cooling by a thermochemical process: first experiments of a prototype storing 60 kWh by a solid/gas reaction. Solar Energy 82:623–636
9. Haji Abedin A, Rosen MA (2011) Closed and open thermochemical energy storage: energy- and exergy-based comparisons. Energy 41:83–92
10. Hauer A (2007) Sorption theory for thermal energy storage. In: Paksoy HÖ (ed) Thermal energy storage for sustainable energy consumption. Part VI. Springer, Netherlands, pp 393–408
11. Fischer S, Hauer A (1998) Space heating and cooling with a thermochemical storage system in the district heat net of Munich. Proc. IEA Annex 10, Phase Change Materials and Chemical Reactions for Thermal Energy Storage, Second Workshop, November, Sofia, Bulgaria

Chapter 12
Thermodynamic Assessment of Seasonal Stratified Thermal Storage

Behnaz Rezaie, Bale V. Reddy and Marc A. Rosen

Abstract District energy (DE) and thermal energy storage (TES) are two energy technologies that can enhance the efficiency of energy systems. Also, DE and TES can help address global warming and other environmental problems. In this study, a stratified TES is assessed using exergy analysis, to improve understanding of the thermodynamic performance of the stratified TES, and to identify energy and exergy behavioural trends. The analysis is based on the Friedrichshafen DE system, which incorporates seasonal TES, and which uses solar energy and fossil fuel. The overall energy and exergy efficiencies for the Friedrichshafen TES are found to be 60 and 19 % respectively, when accounting for thermal stratification. It is also found that stratification does not improve the performance of the TES notably. Considering the TES as stratified and fully mixed does not significantly affect the overall performance of the Friedrichshafen TES because, for this particular case, temperatures are very close whether the TES is treated as stratified or fully mixed.

Keywords Renewable energy · Thermal energy storage · District energy · Waste heat · Friedrichshafen district heating system

12.1 Introduction

Much research is being undertaken to address environmental problems through, e.g., using renewable energy to reduce greenhouse gas (GHG) emissions and using energy resources intelligently. For instance, Robbins [1] describes various practical approaches to reduce GHG emissions, while Rosen [2] describes methods to combat global warming through non-fossil fuel energy alternatives. Also, Dincer

B. Rezaie (✉) · B. V. Reddy · M. A. Rosen
Faculty of Engineering and Applied Science, University of Ontario Institute of Technology, 2000 Simcoe Street North, Oshawa, ON, L1H 7K4, Canada
e-mail: Behnaz.Rezaie@uoit.ca

B. V. Reddy
e-mail: Bale.Reddy@uoit.ca

M. A. Rosen
e-mail: Marc.Rosen@uoit.ca

I. Dincer et al. (eds.), *Progress in Sustainable Energy Technologies: Generating Renewable Energy,* DOI 10.1007/978-3-319-07896-0_12,

[3] proposes environmental measures such as energy conservation, renewable energy use and cleaner technologies. One way to increase the efficiency of energy resource utilization is the use of more efficient equipment [4] and recovery of industrial waste heat for useful tasks [5].

District energy systems can use renewable energy (e.g., solar thermal energy) and waste heat as energy sources, and facilitate intelligent integration of energy systems. District energy offers many advantages for society [6]. Rezaie and Rosen [7] describe DE technology and its potential enhancement. TES is an important complement to solar energy systems, for increasing the fraction of incident solar energy ultimately used. Incorporating TES in DE systems can reduce thermal losses, resulting in increased efficiency for the overall thermal system. Kharseh and Nordell [8] interpret TES as a bridge to close the gap between the energy demand of a DE system and the energy supply to the DE system. Large seasonal TES systems have been built in conjunction with DE systems [9].

The Friedrichshafen DE system uses district heating assisted with solar energy and seasonal TES, and is a project within the "Solarthermie 2000" program in Germany. This DE system is used as the case study in this investigation, which aims to assess the performance of the TES in the Friedrichshafen DE system by the exergy method, accounting for the thermally stratified nature of the TES. Exergy analysis is a method for assessing and improving the efficiency of energy systems and reducing the associated environmental impact [10, 11]. Exergy analysis can help increase efficiency and reduce thermodynamic losses in DE systems [12]. This work complements ongoing work by the authors in which the Friedrichshafen TES is thermodynamically analyzed neglecting stratification.

12.2 Methodology

This research focuses on thermodynamic modeling and analysis of the TES in a DE system. Energy and exergy balances and merit measures for TES are described and applied to the TES in the Friedrichshafen DE system. The Friedrichshafen DE system is shown in Fig. 12.1.

Energy and exergy balances for a thermal system can be written respectively as [9]:

$$\text{Energy input} - \text{Energy output} = \text{Energy accumulation} \tag{12.1}$$

$$\text{Exergy input} - \text{Exergy output} - \text{Exergy destruction} = \text{Exergy accumulation where} \tag{1 2.2}$$

$$\text{Energy output} = \text{Product energy output} + \text{Waste energy output} \tag{12.3}$$

$$\text{Exergy output} = \text{Product exergy output} + \text{Waste exergy output} \tag{12.4}$$

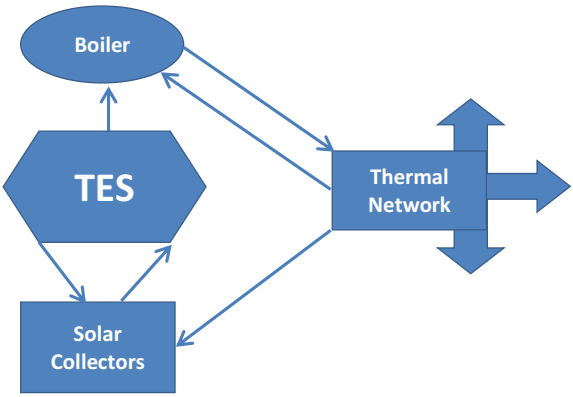

Fig. 12.1. Simplified illustration of the Friedrichshafen DE system, showing flows of energy

The energy transferred to a TES is not distributed uniformly when mixing is limited, because vertical thermal stratification develops and the temperature of the storage medium varies spatially. Careful management and utilization of stratification can increase the efficiency and effectiveness of a TES by increasing the exergy stored and recovered.

A stratified TES can be modelled as having a linear temperature distribution model [9, 13]. In such instances, the mixed temperature of the TES T_m can be written as

$$T_m = \frac{(T_t + T_b)}{2} \tag{12.5}$$

Where T_t is the temperature at the top of the TES, and T_b is the temperature at the bottom. The equivalent temperature of a mixed TES which has the similar exergy as the stratified TES T_e can be expressed as:

$$T_e = \exp\left\{\left[T_t(\ln T_t - 1) - T_b(\ln T_b - 1)\right]/(T_t - T_b)\right\} \tag{12.6}$$

Then, the energy of the stratified TES can be expressed:

$$E = E_m = m\, C_p (T_m - T_0) \tag{12.7}$$

Where E_m denotes the energy of the fully mixed storage, m the mass of the water in the TES, C_p is the specific heat at constant pressure of the storage fluid, and T_0 is the reference-environment temperature. The energy of the stratified and fully mixed storage is the same. Similarly, the exergy of the stratified TES can be expressed as:

$$Ex = E - mC_p T_0 \ln (T_e/T_0) \tag{12.8}$$

while the exergy for the fully mixed storage can be written as:

$$Ex_m = E - mC_p T_0 \ln (T_m/T_0) \tag{12.9}$$

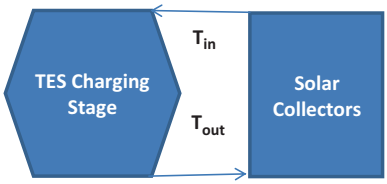

Fig. 12.2 Charging stage of the TES, where stored energy is provided by solar energy

The exergy of the stratified tank differs from that of the fully mixed tank, which can be expressed as:

$$Ex - Ex_m = mC_pT_0 \ln (T_m / T_e) \tag{12.10}$$

An important assumption here relates to the thermal stratification of the TES. Three temperatures are measured in the TES, and the performance of the TES during the charging, storing and discharging is determined accounting for spatial variations in TES temperature.

Energy and exergy analyses for different seasons are determined for the TES during its three operating stages: charging, storing, and discharging.

TES Charging Stage

A simplified model of the TES charging stage is illustrated in Fig. 12.2. The extra energy generated by solar collectors in the charging stage is directed to the TES. Water with the lowest temperature, at the bottom of the TES, flows to the solar panels where it is heated and returns to the top of the TES where the temperature is highest.

The general energy balance in Eqs. (12.1) and (12.2) can be expressed for the charging phase as:

$$\text{Net energy input} - \text{Heat loss} = \text{Energy accumulated in TES} \tag{12.11}$$

$$Q_{in\text{-}TES} - Q_{loss\text{-}TES} = \Delta U_c \tag{12.12}$$

where $Q_{in\text{-}TES}$ represents net energy input to the TES, $Q_{loss\text{-}TES}$ the TES energy loss, and ΔU_c the energy accumulated in the TES during charging, i.e.,

$$\Delta U_c = m\, C_v\, \Delta T_e \tag{12.13}$$

Here, ΔT_e is the equivalent temperature difference of the TES water in a certain period of time (defined here as one month), and C_v the specific heat at constant volume of the storage fluid. Also, the storage mass m is expressible as:

$$m = \rho\, V \tag{12.14}$$

where ρ denotes the density of water in the TES at its temperature and V the volume of the TES.

Heat is transferred by a flow of water to the TES. The mass of the flowing water is determined as follows:

$$m_c = \frac{Q_{in-TES}}{C_p(T_{in} - T_{out})} \tag{12.15}$$

where m_c is the mass of water transferring energy to the TES during charging, and T_{in} and T_{out} denote the TES inlet and outlet temperatures respectively.

The energy efficiency of the Friedrichshafen TES for charging can be written as:

$$\eta_c = \frac{\text{Energy accumulated by TES}}{\text{Energy input}} = \frac{\Delta U_c}{Q_{in-TES}} \tag{12.16}$$

An exergy balance for the DE system can be written with Eqs. (12.2) and (12.4) as:

$$\text{Exergy input} - \text{Exergy destruction} - \text{Exergy loss} = \text{Exergy accumulation} \tag{12.17}$$

$$\text{Exergy input} = m_c\left[h_{in} - h_{out} - T_0(s_{in} - s_{out})\right] \tag{12.18}$$

Where h_{in} and h_{out} is the specific enthalpy of the inlet and outlet water to/from the TES respectively, and s_{in} and s_{out} denote the specific entropy of inlet and outlet water to/from the TES respectively. Also,

$$\text{Exergy loss charging} = Q_{\text{loss-TES}}\left(1 - \frac{T_0}{T_e}\right) \tag{12.19}$$

$$\text{Exergy accumulation} = Ex_f - Ex_i = m\left[u_f - u_i - T_0(s_f - s_i)\right] \tag{12.20}$$

Where u_f and u_i are specific internal energy at the final and initial states of the TES respectively, s_f and s_i are the final and initial specific entropy of the TES. T_0 and T_e are in K. Furthermore,

$$\text{Exergy destruction} = m_c[h_{in} - h_{out} - T_0(s_{in} - s_{out})] - Q_{\text{loss-TES}}\left(1 - \frac{T_0}{T_e}\right) - m\left[u_f - u_i - T_0(s_f - s_i)\right] \tag{12.21}$$

The exergy efficiency ψ_c of the TES during the charging stage is expressible as:

$$\psi_c = \frac{\text{Exergy accumulated in TES}}{\text{Exergy input}} \tag{12.22}$$

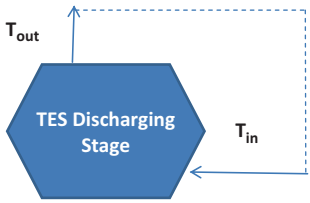

Fig. 12.3 TES discharging stage, where stored energy is transferred to the DE system

TES storing stage

The storing stage is the interim stage for a TES to store energy without charging or discharging. An energy balance for storing stage is as follows:

$$-\text{Energy loss} = \text{energy accumulation} \tag{12.23}$$

and the energy efficiency of the storing period η_s can be written as:

$$\eta_s = \frac{\text{Energy accumulation in TES during charging and storing}}{\text{Energy accumulation in TES during charging}} \tag{12.24}$$

An exergy balance for the storing stage can be expressed as:

$$-\text{Exergy loss} - \text{Exergy destruction} = \text{Exergy accumulation} \tag{12.25}$$

and the exergy efficiency of storing period ψ_s as:

$$\psi_s = \frac{\text{Exergy accumulation in TES during charging and storing}}{\text{Exergy accumulation in TES during charging}} \tag{12.26}$$

TES Discharging Stage

During the discharge stage (see Fig. 12.3), stored energy in the TES is recovered for use in the Friedrichshafen DE system. The dotted line in Fig. 12.3 represents the cycle of water from the TES through other components of DE system. Here, Q_{rec} denotes the recovered energy from the TES, $Q_{loss\text{-}TES}$ the heat loss from the TES and ΔU_d the energy accumulation of the TES during discharging, expressible as:

$$\Delta U_d = m\, C_v\, \Delta T_m \tag{12.27}$$

During discharging, ΔU_d takes on a negative value.

Heat exits the TES via a water cycle. The outlet water flow mass can be evaluated as:

$$m_d = \frac{Q_{rec}}{C_p (T_{out} - T_{in})} \tag{12.28}$$

where m_d is the mass of the transfer fluid, and T_{in} and T_{out} denotes temperature of the inlet/outlet in/from the TES respectively.

The energy efficiency of the TES during discharging is:

$$\eta_d = \frac{\text{Useful energy recovered by TES}}{\text{Total energy stored by TES}} = \frac{Q_{rec}}{Q_{rec} + Q_{loss-d}} \tag{12.29}$$

Where $Q_{loss\text{-}d}$ is the heat loss during the discharge stage and Q_{rec} is as defined earlier.

An exergy balance for the TES in the DE system can be expressed with Eqs. (12.3) and (12.4) as follows:

$$\begin{aligned} &-(\text{Exergy recovered} + \text{Exergy loss}) - \text{Exergy destruction} \\ &= \text{Exergy accumulated} \end{aligned} \tag{12.30}$$

$$Ex_{rec} = m_d \left[h_{out} - h_{in} - T_0 (s_{out} - s_{in}) \right] \tag{12.31}$$

Here, Ex_{rec} denotes the recovered exergy, h_{out} and h_{in} are the specific enthalpy of the TES outlet and inlet water respectively, and s_{out} and s_{in} represent the specific entropy of outlet and inlet water from/to the TES respectively. Also,

$$\text{Exergy loss} = Q_{loss\text{-}TES} \left(1 - \frac{T_0}{T_e} \right) \tag{12.32}$$

$$\text{Exergy accumulation} = Ex_f - Ex_i = m\left[u_f - u_i - T_0 (s_f - s_i) \right] \tag{12.33}$$

$$\begin{aligned} \text{Exergy destruction} = {} & m_d \left[h_{out} - h_{in} - T_0 (s_{out} - s_{in}) \right] - Q_{loss\text{-}TES} \left(1 - \frac{T_0}{T_e} \right) \\ & - m[u_f - u_i - T_0 (s_f - s_i)] \end{aligned} \tag{12.34}$$

Where u_f and u_i are the final and initial states internal energy of the TES respectively, other parameters are defined already.

The exergy efficiency ψ_d of the TES during can be expressed as:

$$\psi_d = \frac{\text{Exergy recovered from TES}}{\text{Exergy accumulated in TES}} \tag{12.35}$$

TES Overall Cycle

An overall energy balance for the TES of the DE system can be expressed as:

Energy input − (Energy recovered + Heat loss) = Energy accumulation

$$\sum Q_{in-TES} - \left(\sum Q_{rec} + \sum Q_{loss} \right) = \sum \Delta U_c \tag{12.36}$$

and the overall energy efficiency η_o of the TES can be written as:

$$\eta_o = \frac{\text{Energy recovered from TES during discharging}}{\text{Energy input to TES during charging}} = \frac{\sum Q_{rec}}{\sum Q_{in-TES}} \quad (12.37)$$

Similarly, we can express an overall exergy balance for the TES of the DE system as:

Exergy input − (Exergy recovered + Exergy loss) − Exergy destruction = Exergy accumulation

$$\sum Ex_{in-TES} - \left(\sum Ex_{rec} + \sum Ex_{loss}\right) - \sum Ex_{dest} = \sum Ex_{ace} \quad (12.38)$$

and the overall exergy efficiency ψ_o of the TES as:

$$\psi_o = \frac{\text{Exergy recovered from TES during discharging}}{\text{Exergy input to TES during charging}} = \frac{\sum E_{X_{rec}}}{\sum E_{X_{in-TEX}}} \quad (12.39)$$

Description Friedrichshafen DE System and Its TES

Nuβbicker-Lux and Schmidt [14, 15] report that the first phase of the Friedrichshafen DE system included a hot water TES made of reinforced concrete with a volume of 12,000 m^3 which served 280 apartments in multi-family houses and a daycare, and included flat plate solar collectors with an area of 2700 m^2. Solar heat provided 24% of the total heat demand for district heating. In the second phase, built in 2004, district heating was expanded to a second set of apartments comprising 110 units, and 1350 m^2 of solar collector area was added to the system. Also, two gas condensing boilers were installed to cover the energy demand for district heating during periods when insufficient energy is available via the solar collectors and thermal storage.

The Friedrichshafen DE system contains two natural gas boilers, solar thermal collectors mostly on building roofs, a central solar heating plant with seasonal heat storage (CSHPSS), heat exchangers to transfer heat between the thermal network and solar collectors, and the thermal network which distributes heat to consumers, as well as pipes, pumps and valves. Water is the heat storage media and the heat transport media circulating in the Friedrichshafen system.

Historical temperature data for the Friedrichshafen DE system [14, 15] are presented in Fig. 12.4. Also, data for a typical annual period follows:

- Return water (circulating media) from thermal network temperature: 55.4 °C
- Measured TES heat loss: 421 MWh
- Storage efficiency: 60%
- Thermal energy yield of solar collectors: 1200 MWh

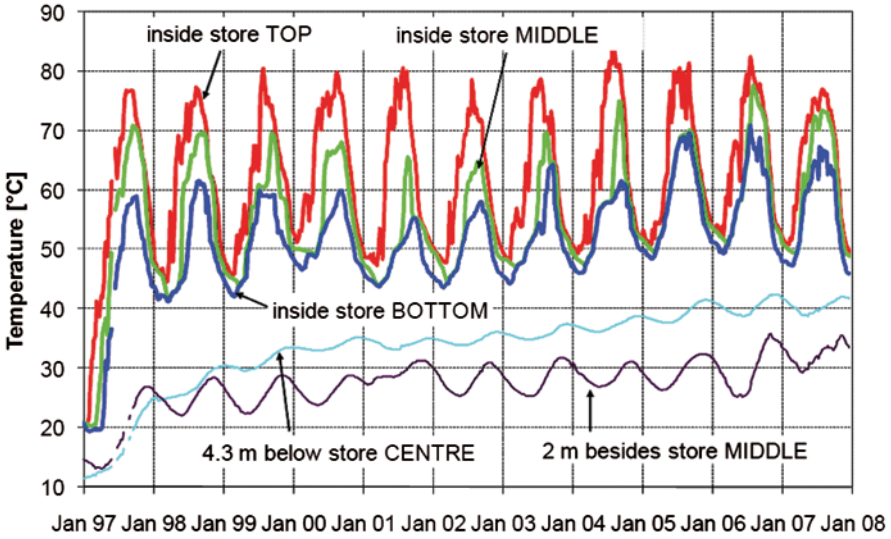

Fig. 12.4 Historical variation of temperatures in and near the TES in the Friedrichshafen DE system. (Nuβbicker et al. [14], printed by permission)

- Solar heat input to district heating network: 803 MWh
- Overall heat delivery to district heating network: 3017 MWh
- Heat delivered by gas bolilers: 2310 MWh
- Solar fraction: 26%
- Maximum temperature in TES: 81 °C (at top)

Note that the temperature of the return water is reported as an annual average, although in the reality the return temperature varies depending on the time of day and season. The temperature and mass flow rate of the water, the building profile, and weather conditions affect the return temperature. Nonetheless, the temperature of the return water is considered constant here to simplify the calculations in this preliminary study, thereby permitting the main objective of assessing the role of the TES to be more clearly illustrated.

Also, Lottner and Mangold [16] and Fisch and Kubler [17] report that the temperature of thermal network (T) in average all over the year is 70 °C.

For simplicity, it is assumed here, based on a similar thermal system reported by Zhai et al. [18], that heat losses in pipelines are negligible.

12.3 Results and Discussion

Energy and Exergy Parameters

The year 2006 is considered in the present analysis because it appears to be a typical year. Consequently, TES temperature for each season are taken from Fig. 12.4 for

Table 12.1 TES, soil and ambient temperatures during the year 2006. (Sources: Rezaie et al. [14, 19, 20], and Tutiepo [19] and Nuβbicker et al. [14]

Season/Solar generation	Month	TES temp. (top) (°C)	TES temp. (center) (°C)	TES temp. (bottom) (°C)	T_0 (°C)	Soil temp. (°C)	ΔT (T_{ave}—soil temp.) (°C)	$Q_{loss\text{-}TES}$ (MWh)
Spring/376.07 MWh	Mar.	60	56	52	3.4	26	30	32.6
	Apr.	70	61	56	9.9	25	36	39.1
	May	80	69	60	13.7	25	44	47.7
Summer/473.33 MWh	Jun.	83	74	63	19.8	26	48	52.1
	Jul.	82	76	67	19.7	28	48	52.1
	Aug.	87	74	66	16.1	31	43	46.7
Fall/233.42 MWh	Sept.	74	65	58	17.9	34	31	33.6
	Oct.	60	59	50	13.0	35	24	26.0
	Nov.	54	52	51	6.6	34	18	19.5
Winter/116.76 MWh	Dec.	51	50	48	2.7	32	19	20.6
	Jan.	54	52	50	–2.6	30	22	23.9
	Feb.	55	54	51	0.3	29	25	27.1
							Σ=388	*Σ=421*

ΔT is temperature difference between TES center temperature and soil temperature, $Q_{loss\text{-}TES}$ is TES heat loss in each month (estimation is explained in the text)

that year. Monthly temperatures in and near the TES for 2006 are listed in Table 12.1, along with the monthly environment temperature [19]. The total energy loss of the TES during 2006, reported to be 421 MWh, needs to be broken down by month. Note that TES in the Friedrichshafen DE system is built in the ground, so heat loss is mostly between the TES and the surrounding soil. Data are available of the soil temperature 4.3 m under the TES. Here, this temperature is assumed for TES heat losses in all directions. Because the volume of underground Friedrichshafen TES is large at 12,000 m^3, most of the TES is deep in the ground. Since the temperature of the ground is almost constant at a depth of 10 m, the majority of surrounding soil is thus at a constant temperature, so we use a single ground temperature in all directions here for simplicity. The temperature difference between the TES and the soil 4.3 m below the TES is calculated for each month. The soil temperature is read from Fig. 12.4 and listed in Table 12.1. Table 12.1 also contains the breakdown by month and season of the received solar energy, estimated by Rezaie et al. [20], is also illustrated in Table 12.1.

Also, the sum of the monthly differences between the centre TES temperature and the soil temperature for the year is 388 °C; these values are used as weighting factors in determining the monthly breakdown of the TES annual heat loss. That is, the energy loss for each month is calculated by multiplying its temperature difference by the ratio 421 MWh/388 °C. For example, the TES heat loss for March is determned to be:

$$Q_{loss\text{-}TES} = 421(30/388) = 32.6 \text{ MWh (for March)}$$

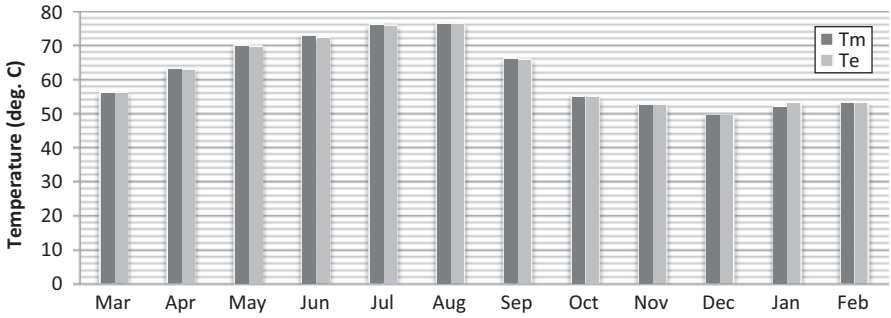

Fig. 12.5 Monthly values for the effective temperature and fully mixed temperature for the TES in the Friedrichshafen DE system for 2006

Table 12.2 Energy and exergy parameters for the Friedrichshafen TES in 2006 during charging, accounting for stratification

Energy					Exergy				
Month	ΔU_c (MWh)	Q_{in}-TES (MWh)	m_c (t)	η_c	Ex_{in-c} (MWh)	Ex_{loss-c} (MWh)	ΔEx_{acc-c} (MWh)	Ex_{dest} (MWh)	ψ_c
March	40.92	73.47	7,890.24	0.56	46.48	5.2	13.26	28.02	0.29
April	94.38	133.44	81,89.29	0.71	56.98	6.16	20.27	30.55	0.36
May	93.97	141.71	6,087.83	0.66	42.45	7.81	3.72	30.93	0.09
June	41.04	93.13	4,000.99	0.44	30.33	7.98	3.25	19.10	0.11
July	41.60	93.68	4,471.59	0.44	37.71	8.38	6.25	23.08	0.17
August	6.00	52.66	2,154.44	0.11	18.45	8.04	9.55	0.87	0.52
Total	317.91	588.09	n/a	n/a	231.38	43.38	74.44	113.55	n/a

ΔU_c Energy accumulation in TES, $Q_{in\text{-}TES}$ Energy input to TES, m mass of water transferring energy, η_c Energy efficiency of TES, $Ex_{in\text{-}c}$ Exergy input to TES, $Ex_{loss\text{-}c}$ Exergy loss from TES, $\Delta Ex_{acc\text{-}c}$ Exergy accumulation in TES, Ex_{dest} Exergy destruction for TES, ψ_c Exergy efficiency of TES

Values for T_e and T_m are determined using Eqs. (12.5) and (12.6) and values for T_b and T_t are listed in Table 12.1. Monthly values of T_e and T_m for the Friedrichshafen TES in 2006 are depicted in Fig. 12.5.

Energy and exergy parameters for the TES, evaluated with Eqs. (12.12)–(12.22) during charging months, accounting for thermal stratification, are listed in Table 12.2. There, the average temperature for the TES charging stage is assumed fixed at 72 °C (for which $C_p = 4.19$ kJ/kg K).

The TES in the Friedrichshafen DE system provides energy for the DE system when the top temperature of the TES is higher than 55.4 °C; otherwise the TES does not provide heating. Thus, from Table 12.1, November, December, January, and February are months when the TES is not used for heating in the Friedrichshafen DE system since in these months $T_{TES} < 55.4$ °C. Therefore, in Table 12.3 the rows of November, December, January, and February are not shown. From March to August, ΔU_c and $Q_{in\text{-}TES}$ for each month are positive, which means the energy of the TES is increasing every month compared to the previous month. This pattern is repeated

Table 12.3 Energy and exergy parameters for the Friedrichshafen TES in 2006 during discharging, accounting for stratification

Energy					Exergy				
Month	ΔU_d (MWh)	Q_{rec} (MWh)	m_d (t)	η_d	Ex_{rec} (MWh)	Ex_{loss-d} (MWh)	ΔEx_{acc-d} (MWh)	Ex_{dest} (MWh)	ψ_d
Sep.	−142.11	175.75	8,118.37	0.84	−24.70	4.76	72.89	43.50	0.34
Oct.	−148.93	174.97	32,681.50	0.87	−18.52	3.33	32.75	10.90	0.57
Total	−291.04	350.72	n/a	n/a	−43.15	8.09	105.63	54.39	n/a

ΔU_d Energy accumulation in TES, Q_{rec} Energy recovered by TES, m_d mass of water transferring energy, η_d Energy efficiency of TES, Ex_{rec} Exergy recovered by TES, Ex_{loss-d} Exergy loss from TES, ΔEx_{acc-d} Exergy accumulation in TES, Ex_{dest} Exergy destruction for TES, ψ_d Exergy efficiency of TES

in the exergy section: from March to August the exergy level is increasing relative to the previous month. So, March to August is the charging stage of the TES. The energy and exergy efficiencies of the stratified TES for the overall charging stage are determined using Eqs. (12.16) and (12.22) to be 54 and 24%, respectively.

In the storing stage energy loss is equal to energy accumulation. Since the Friedrichshafen DE system TES is not adiabatic, there are always heat losses from the TES. The first month after the charging stage (September), the energy loss exceeds the energy input. Hence, the TES directly shifts from the charging stage to the discharging stage and there is no storing stage for the Friedrichshafen DE system.

It is seen that for September and October ΔU_d has a negative value, meaning the TES is losing energy compared to the previous month as it discharges energy to the Friedrichshafen DE system. The change in TES exergy is also negative during September and October. Energy and exergy parameters for the stratified TES during the two discharging months, evaluated using Eqs. (12.27)–(12.34), are listed in Table 12.3. For the overall discharging stage, energy and exergy efficiencies are evaluated with Eqs. (12.29) and (12.35) for the TES in the Friedrichshafen DE system, accounting for stratification, as 85 and 41%, respectively. As noted earlier, the TES does not heat the Friedrichshafen DE system from November to February.

For the stratified TES, the overall energy efficiency η_o is determined with Eq. (12.37) to be 60% and the overall exergy efficiency ψ_o is determined with Eq. (39) to be 19%.

Comparison of Exergy Parameters for Fully Mixed and Stratified Storage

Exergy and energy parameters are determined considering thermal stratification as well as assuming the simpler model of a fully mixed tank at a uniform temperature. The TES energy contents for both situations are the same, but the exergy differs. The difference in the TES exergy content for fully mixed and stratified conditions is Eqs. (12.8) and (12.9) for several months (see Fig. 12.6). The differences are small, in line with the fact that the differences between effective temperatures and fully mixed temperature in Fig. 12.5 are also small.

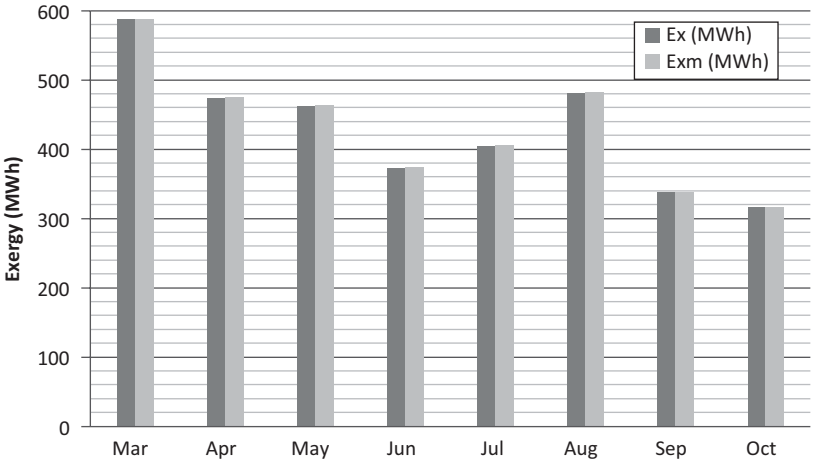

Fig. 12.6 Comparison of exergy contents of the Friedrichshafen TES for fully mixed and stratified conditions

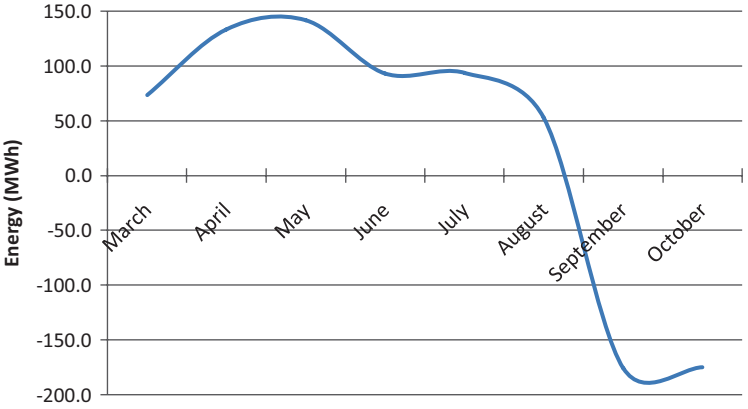

Fig. 12.7 Annual variation in energy content of the TES in the Friedrichshafen DE system

The results suggest that accounting for stratification or simplifying by assuming a fully mixed tank does not significantly affect thermodynamic analyses for the Friedrichshafen TES. This result is likely applicable to other TESs where thermal stratification is not great.

Comparison of Energy and Exergy Performance

The variation in energy content in the Friedrichshafen TES over an annual period is shown Fig. 12.7. In the charging stage, the energy is increasing in the TES, and in

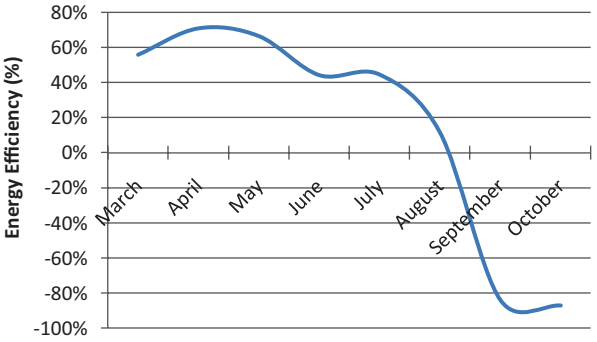

Fig. 12.8. Annual variation in energy efficiency of the TES in the Friedrichshafen DE system

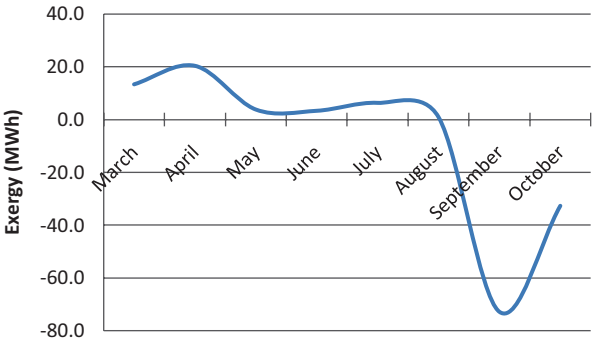

Fig. 12.9 Annual variation in exergy accumulation in the TES in the Friedrichshafen DE system, accounting for thermal stratification

the discharging stage the TES is losing the energy (reflected by negative values in the diagram) as it releases energy to the Friedrichshafen DE system.

The variation in energy efficiency in the Friedrichshafen TES over an annual period is shown Fig. 12.8. The energy efficiency is positive during charging and negative during discharging. The negative value is related to direction, and means the TES is discharging stored energy to the DE system. Figures 12.7 and 12.8 exhibit similar trends. Note that the negative portions of Figs. 12.7, 12.8, 12.9 and 12.10 indicate the behaviour of the TES during discharging whereas the positive portions are for charging. In the charging stage, the TES is accumulating energy and in discharging stage it is releasing energy.

The variation in the exergy accumulation in the TES in the Friedrichshafen DE system over a year is shown in Fig. 12.9. The exergy content of the TES increases during charging, and decreases during discharging as the accumulated exergy is released to the Friedrichshafen DE system. Note in Fig. 12.9 that the exergy accumulation decreases slightly from May to July since the ambient temperature increases and exergy is calculated based on a reference-environment temperature. The variation in exergy efficiency in the Friedrichshafen TES over an annual period is shown Fig. 12.10, which exhibits a similar trend to Fig. 12.9.

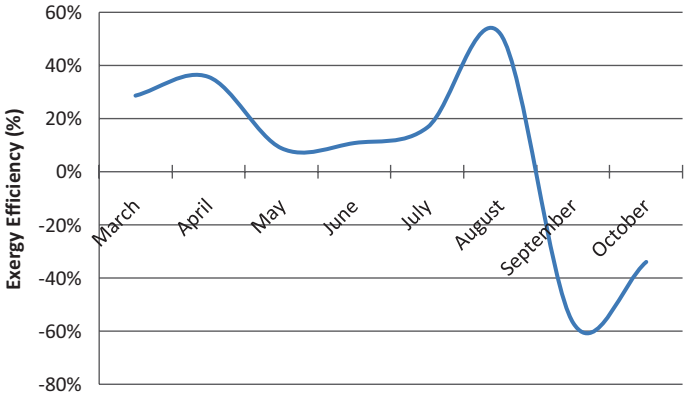

Fig. 12.10 Annual variation in exergy efficiency of the TES in the Friedrichshafen DE system, accounting for thermal stratification

Conclusions

The TES in the Friedrichshafen DE system has been analyzed, accounting for thermal stratification. Energy and exergy are input to the TES during charging when surplus energy and exergy are harvested by solar collectors, mainly in the spring and summer, and the stored energy and exergy are subsequently discharged to the Friedrichshafen DE system. The overall energy and exergy efficiencies of the stratified TES in the DE system are 60 and 19 %, respectively.

The analysis results (e.g., energy and exergy contents and efficiencies) for the TES in the Friedrichshafen DE system when stratification is accounted for are similar to those when a fully mixed assumption is applied. The results suggest that accounting for stratification or simplifying by assuming a fully mixed tank does not significantly affect thermodynamic analyses for TESs with moderate thermal stratification, as is the case for the Friedrichshafen TES.

Nomenclature

C_v	Specific heat at constant volume, kJ/kg °C
m	Mass, kg
Q_g	Energy input to boilers, kJ
$Q_{loss\text{-}TES}$	Heat loss from TES, kJ
Q_s	Solar energy, kJ
Q_{TN}	Energy demand of thermal networks, kJ
$T_{ave\text{-}TES}$	Average temperature of TES, °C
T_{max}	Maximum temperature of TES, °C
T_{min}	Minimum temperature of TES, °C
T_{return}	Temperature of returning circulating water from thermal network, °C
U	Internal energy of storage, kJ
U_c	Internal energy of storageduring charging, kJ

U_d Internal energy of storageduring discharging, kJ
V Volume of natural gas, m^3
ρ Density, kg/m^3

Acknowledgement Financial support was provided by the Natural Sciences and Engineering Research Council of Canada, and is gratefully acknowledged.

References

1. Robbins J (2010) The new good life: living better than ever in an age of less. Random house LLC
2. Rosen MA (2009) Combating global warming via non-fossil fuel energy options. Int J Global Warming 1(1):2–28
3. Dincer I (2003) On energy conservation policies and implementation practices. Int J Energy Res 27(7):687–702
4. Patil A, Ajah A, Herder P (2009) Recycling industrial waste heat for sustainable district heating: a multi-actor perspective. Int J Environ Technol Manage 10(3):412–426
5. Casten T, Ayres R (2005) Recycling energy: growing income while mitigating climate change. Report, recycled energy development, Westmont, IL, Oct. 18. Available online at: http://www.recycled-energy.com/_documents/articles/tc_energy_climate_change.doc. Accessed 27 Oct 2011
6. Marinova M, Beaudry C, Taoussi A, Trépanier M, Paris J (2008) Economic assessment of rural district heating by bio-steam supplied by a paper mill in Canada. Bull Sci Technol Soc 28(2):159–173
7. Rezaie B, Rosen MA (2012) District heating and cooling: review of technology and potential enhancements. Appl Energy 93:2–10
8. Kharseh M, Nordell B (2011) Sustainable heating and cooling systems for agriculture. Int J Energy Res 35(5):415–22
9. Dincer I, Rosen MA. Thermal energy storage: systems and applications, 2nd ed. Wiley, West Sussex
10. Rosen MA, Dincer I (1997) On exergy and environmental impact. Int J Energy Res 21(7):643–54
11. Rosen MA, Dincer I (1999) Exergy analysis of waste emissions. Int J Energy Res 23(13):1153–1163
12. Rosen MA, Dincer I, Kanoglu M (2008) Role of exergy in increasing efficiency and sustainability and reducing environmental impact. Energy Policy 36(1):128–137
13. Rosen MA, Tang R, Dincer I (2003) Effect of stratification on energy and exergy capacities in thermal storage systems. Int J Energy Res 28(2):177–193
14. Nußbicker-Lux J, Bauer D, Marx R, Heidemann W, Müller-Steinhagen H (2009 June 14–17) Monitoring results from German central solar heating plants with seasonal thermal energy storage. EFFSTOCK 2009; Stockholm, Sweden, June 14–17. EFFSTOCK
15. Schmidt T, Nussbicker J, Raab S (2005) Monitoring results from German central solar heating plants with seasonal storage. ISES 2005 Solar World Congress
16. Lottner V, Mangold D (2000) Status of seasonal thermal energy storage in Germany. Terrastock 2000, 8th international conference on thermal energy storage, August 28–September 1, 2000; Stuttgart, Germany
17. Fisch N, Kübler R (1997) Solar assisted district heating-status of the projects in Germany. Int J Sustain Energy 18(4):259–270

18. Zhai H, Dai Y, Wu J, Wang R (2009) Energy and exergy analyses on a novel hybrid solar heating, cooling and power generation system for remote areas. Appl Energy 86(9):1395–1404
19. TuTiempo.net Historical Weather: Friedrichshafen, year 2006. Available on line at: www.tutiempo.net/en/Climate/Friedrichshafen/109350.htm. Accessed 15 Oct 2011
20. Rezaie B, Reddy BV, Rosen MA (2012) Assessment of the utilization of thermal energy storage in district energy systems. Int J Energy Environ Econ 20(5):395–414

Chapter 13
Recent Developments in Solar-Powered Micro CHP Systems

Muhyiddine Jradi and Saffa Riffat

Abstract Over the last two decades, the world has exhibited an unprecedented increase in the energy resources demand due to the huge technological and industrial developments accompanied by a tremendous population growth. The fluctuations in the conventional fossil fuel prices and the global warming problem are urging the need for switching towards renewable energy resources. With the buildings and residential sector contributing to a large portion of energy consumption, micro-scale combined heat and power systems (CHP) tend to be an effective solution to satisfy heating and electricity needs for buildings and residential accommodations. Taking advantage of the decentralized production and the capability of being driven by renewable energy resources, micro CHP systems are presented as a feasible substitute to the central production stations especially in rural and developed areas. The current work provides a comprehensive overview for the recent developments in the field of micro CHP systems. Research studies regarding micro CHP systems applications in buildings and residential accommodations are reviewed. Moreover, recent options for micro CHP prime movers are reviewed and compared in terms of the technology development, performance, environmental and economic impacts. Different applications of solar organic Rankine systems in the residential sector are presented including small-scale electricity production and reverse osmosis desalination systems. Discussions are concentrated on micro CHP systems driven by organic Rankine cycle (ORC) which provides more durability and reliability in operation and reduces maintenance levels and safety concerns. In addition, recent studies dealing with solar ORC micro CHP systems are examined. The current work doesn't only add to the literature on micro CHP systems but also provides recommendations for future design and development of ORC solar-powered micro CHP systems including working fluid selection and solar collector technology used.

Keywords Combined heat and power · Micro-CHP · Solar energy · Organic Rankine cycle · Working fluid

M. Jradi (✉) · S. Riffat
Department of Architecture and Built Environment, Faculty of Engineering, University of Nottingham, University Park, Nottingham NG7 2RD, UK
e-mail: mehyojradi.25@hotmail.com

S. Riffat
e-mail: saffa.riffat@nottingham.ac.uk

I. Dincer et al. (eds.), *Progress in Sustainable Energy Technologies: Generating Renewable Energy,* DOI 10.1007/978-3-319-07896-0_13,

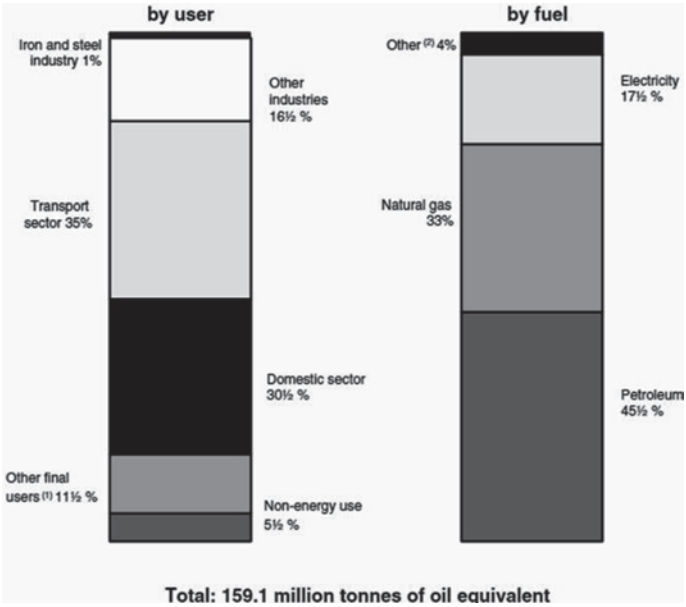

Fig. 13.1 Final energy consumption in 2010 in UK [1]

13.1 Introduction

Due to the technological advancement, the high rate of population growth and the rapid urbanization, the demand for energy resources has been increasing drastically in an unprecedented manner in all life fields including electric power generation, domestic energy use and transportation. Final energy consumption in UK has increased by 4.4% in 2010. Figure 13.1 shows that the transportation sector contributes to about 36% of the final energy consumed in UK in 2010, followed by the domestic sector with 30% [1]. Petroleum remains the main fuel consumed with about 45% in 2010. In addition, heat and electricity account for 63% of the final energy consumption in the UK [2]. The sharp fluctuations in the conventional fossil fuel prices have a severe effect on the overall economic growth with major energy sector security risks [3]. In parallel, the increase in the consumption of conventional energy resources is always accompanied by considerable emissions of pollutants and toxic gases. The increase of greenhouse gases concentration in the atmosphere has altered the whole global climate resulting into the catastrophic global warming problem.

As a response, there is an urgent need for a total change in the energy generation and consumption patterns based on sustainable, energy efficient and environmental friendly energy resources. Such new energy resources include solar energy, wind energy, biomass energy and waste heat. Switching towards renewable energy resources can help saving the environment as well as fostering the rural development,

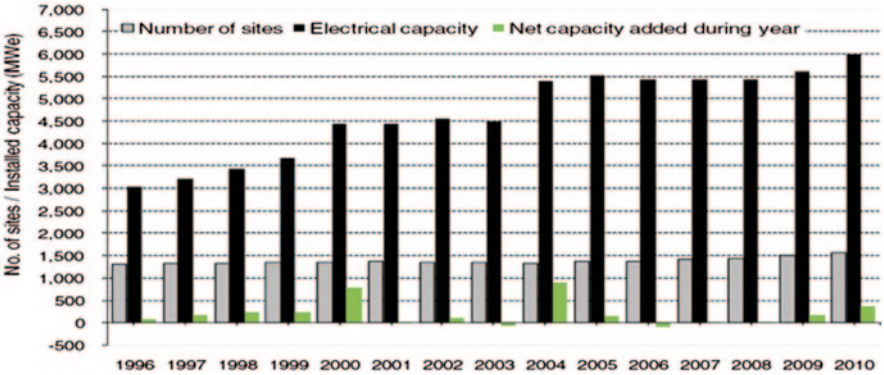

Fig. 13.2 Installed CHP capacities in UK [8]

the economic growth and the technological innovation [4]. Installed generation capacity from renewable resources in UK has increased by 15% with 9,202 MW at the end of 2010 [5]. However, the contribution of renewable energy-based electricity is still only 6.8% of the overall generation. In addition, 1,212 ktoe of heat from renewable sources was produced in 2010 with an increase of 17%. The combined heat and power generation system (CHP) is a flexible technology which can help in saving the environment, achieving energy security and flourishing the economic growth. CHP systems offer the possibility of being driven by clean and renewable energy resources such as solar thermal energy, biomass combustion and waste heat. This process is very cost effective for both industrial and residential consumers and can save up to 35% on the primary energy [6]. Furthermore, CHP generation provides variety of products including steam and hot water, process heating, electricity, direct mechanical drive, cooling and dehumidification, and thus it allows more rational use of fuel energy. The European Directive 2004/8/EC provides a framework for the development of efficient combined heat and power systems to achieve primary savings in the internal energy market [7]. Totally, the installed capacity of CHP systems in the EU is over 100 GW with 22% in Germany and 9% in each of Netherlands and Poland. Denmark leads in terms of CHP systems share in electricity production with nearly 46%, where 30% of the electricity produced in the Netherlands, Latvia and Finland comes from CHP systems. CHP capacity in UK increased by 7% between 2009 and 2010 from about 5,614 to 5,989 MW as shown in Fig. 13.2. Sixty-eight percent of the CHP systems installed in UK run on natural gas, where renewable energy driven CHP systems increased to 6% of the total installed CHP systems in 2010. As shown in Table 13.1, the UK market is dominated by medium-scale CHP systems with capacity ranging between 100 kW and 1 MW. CHP systems operating in UK have saved the economy nearly 12.98 $MtCO_2$ of carbon emissions in 2010 [8].

Table 13.1 CHP installations in UK by capacity and size range [8]

	2006	2007	2008	2009	2010
Number of schemes	*1,363*	*1,414*	*1,434*	*1,495*	*1,568*
Less than 100 kWe	462	456	457	448	462
100–999 kWe	643	686	705	766	806
1–9.9 MWe	187	202	201	209	231
10 MWe and above	71	70	71	72	69
Total capacity (MWe)	*5,432*	*5,438*	*5,449*	*5,614*	*5,989*
Less than 100 kWe	29	29	28	28	29
100–999 kWe	165	179	181	195	204
1–9.9 MWe	705	733	709	725	773
10 MWe and above	4,532	4,497	4,530	4,666	4,984

13.2 Micro CHP Systems

Various energy uses in buildings contribute to about half of the UK's overall energy consumption as well as half of the carbon dioxide emissions to the atmosphere [9]. Large amount of the energy consumed in buildings is utilized for heating including hot water, process heating and space heating, and the majority of buildings especially in Western Europe are heated using central heating systems or plants working on fuel oil or natural gas [10]. Electricity needs for these buildings are supplied by centralized power stations. However, about 50 % of the energy produced in these central stations is lost as waste heat, in addition to the losses in the power transport through the high voltage transmission lines and in the transformers. Thus only 35–45 % of the energy produced by these stations is available for the final user consumption. Moreover, such centralized large-scale systems need very high capital and investment costs and exhibit complex designs and operation schemes requiring high levels of maintenance. Due to their large-scale production, centralized energy plants operate mostly on fossil fuels and thus hinder the evolution and the integration of renewable energy resources which are mostly suitable for small-scale systems. In addition, large scale energy production systems need vast land areas to be built and are characterized with very high environmental footprint of energy production with high amount of CO_2 emissions. Therefore, micro-scale combined heat and power systems within the size range of 1–10 kWe, tend to be the most effective mean to satisfy heating and electricity needs for buildings and residential accommodations as well as achieving energy security supply and reducing greenhouse gas emissions. Domestic buildings, residential dwellings, commercial buildings, offices, schools and hospitals are all suitable applications for micro CHP systems, where electricity is generated and supplied at the end user point without any transmission losses and the waste heat is used for hot water and space heating. This decentralized production of heat and electricity can offset the problem of electricity shortages especially in rural areas and regions where the electric grid is not continuous or even not available.

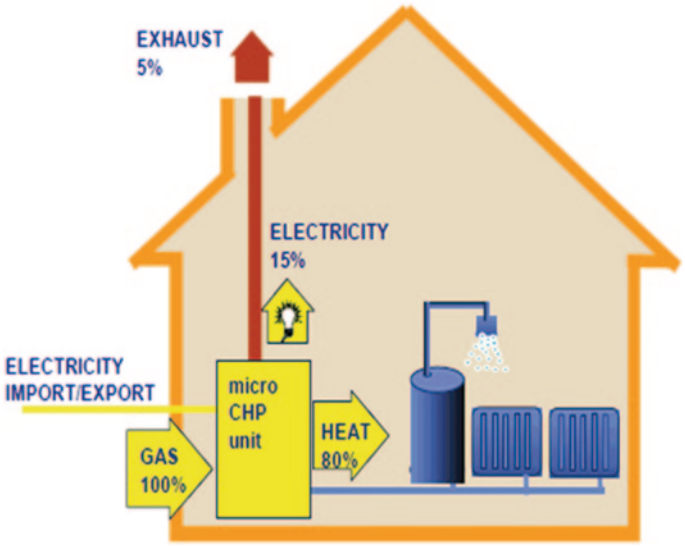

Fig. 13.3 Energy flows within micro CHP system [11]

The UK Government's energy strategy addresses micro CHP systems as a key element to attain carbon mitigation and supply security objectives with plenty of environmental, social and economic benefits [13]. In addition, the Government has decreased the VAT from 17.5% to only 5% for buildings to install micro CHP systems, aiming that by 2050 micro CHP systems would supply 30–40% of the electricity needs in UK [12]. Micro CHP systems possess high degree of reliability since electricity is generated and supplied directly at the end user site with an overall 80–85% conversion of gas to useful heat and 10–15% electrical efficiency. Energy flows within a micro CHP system are demonstrated in Fig. 13.3 [11]. In overall, the efficiency of micro CHP systems can reach twice that of central stations and on-site boilers. Thus a CHP system can fulfill the building heating and electrical needs with less fuel consumption allowing around 25% savings in total energy costs compared to condensing boilers in UK with a reduction of 2.5 tonnes of CO_2 emissions per year. The capability of driving a micro CHP system by solar thermal energy, biomass combustion, waste heat and other clean energy resources allows attaining diversity and security in energy supply as well as decreasing pollutants and gas emissions. The annual CO_2 emission savings due to the installation of different types of micro CHP systems compared to grid electricity and on-site boilers are shown in Fig. 13.4. In addition, micro CHP systems are extremely flexible and responsive with low maintenance level required and low noise and vibration levels.

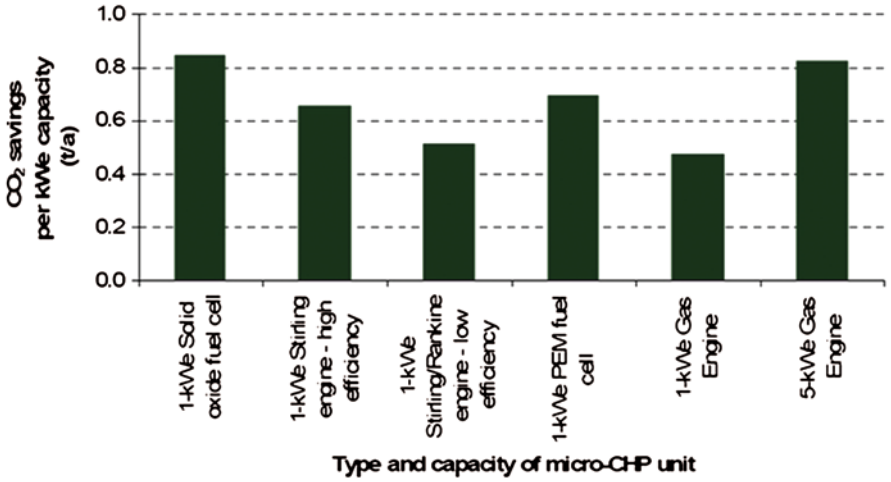

Fig. 13.4 Annual micro CHP CO_2 savings compared to grid electricity and boiler alternatives [12]

13.3 Applications of Micro CHP Systems in Buildings

Considerable amount of research have been conducted in the field of micro CHP to investigate the feasibility of operating such systems for domestic and residential applications. Valkiainen et al. [14] reported that micro CHP systems applicability in buildings is governed by the electrical efficiency of the system, installation space demanded, emissions and level of noise, system flexibility and reliability and the components cost. Another study was performed by D'Accadia et al. [15] who claimed that the future of small scale domestic CHP systems is mainly linked to the technology utilized and the matching between energy costs and electrical and thermal load profiles. A domestic micro CHP system of maximum load capacity of 1 kWe and 2 kWth was presented by Arsalis et al. [16]. The proposed system is based on the HT-PEMFC fuel cell technology and is able to fulfill electrical and heating needs for a typical Danish family. In addition, many researchers have examined the design and operation of micro CHP systems in residential applications and aimed to optimize the performance as well as the overall electrical and the thermal efficiency of the system [17–19]. Briguglio et al. [20] investigated a low temperature 5 kW fuel cell-based micro CHP system for residential applications. An electrical and thermal analysis was performed and the results showed that an overall efficiency of 85 % can be attained with stack cooling and good insulation. Another study was carried out by De Paepe et al. [10] who examined the possibility of using micro CHP systems in residential buildings. They evaluated five micro CHP systems with capacities less than 5 kW and found that micro CHP systems if well sized can save energy cost and reduce gas emissions.

The feasibility of using CHP systems in clustered dwellings in Sweden and Baltic was examined by Bernotat et al. [21]. They found that micro CHP systems

effectiveness is directly proportional to the heat demand in the area of application. Ren et al. [22] compared gas engine and fuel cell micro CHP systems for residential buildings and found that fuel cell systems offer a better option in such small scale applications. In 2003, a 1 kW gas engine micro CHP system, known as "ECOWILL", was revealed by Honda [23]. The system is suitable for residential applications and allows savings of about 500 $ on the energy bill per year with 20% less CO_2 emissions. More than 90 thousand systems were sold in the last 6 years. Recently, Baxi Group presented the "Baxi Ecogen" 1 kW micro CHP Stirling-based system for domestic and residential use in UK, which can save up to 600 £ while reducing the emissions by nearly 40% per year [6]. All of these improvements and developments raise an urgent need for a low-cost and effective micro CHP system for residential and building applications.

13.4 Micro CHP Systems Technologies

There is a range of different generating technologies which can be considered as prime movers for micro CHP applications. In general, all the technologies are based on a conversion process from chemical energy within the fuel to a driving useful energy in the form of heat and/or electricity under the effect of a heating source. This heat source can be provided through the combustion of a conventional fossil fuel or via a renewable energy resource depending on the technology and the application considered. These technologies can be divided into two categories, combustion based technologies (Stirling engine, micro turbine engine, Rankine cycle engine and reciprocating engine) and electrochemical based technologies (fuel cells) [24]. Some of these micro-generation technologies are available commercially including reciprocating and micro turbine small-scale engines, while others are still in the research and development stages with very limited commercial systems finding their way to the market including organic Rankine micro-systems and fuel cells based systems. Table 13.2 provides an assessment of the main micro-CHP prime movers listing their main advantages and disadvantages when employed in micro CHP applications. In addition, the table compares micro CHP technologies based on their electrical and overall efficiency, lifetime, investment costs, system capacity, noise and emission levels, part load efficiency and various types of fuel harnessed.

Reciprocating Engines

Reciprocating engines or known as piston-driven internal combustion engines are classed into two main types, compression ignition and spark ignition engines. Generally, reciprocating micro CHP system consists of a spark ignition reciprocating engine and a generator connected to it. Reciprocating engines can be fueled by diesel oil, natural gas or gasoline, and it is more suited for large applications [28].

Table 13.2 Assessment and comparison of different micro-CHP technologies [25–27]

Micro-CHP technology	Reciprocating engines	Micro turbines	Stirling engines	Fuel cells	Rankine engines
Advantages	Efficient part load performance High flexibility and operational reliability Short start-up time required	Compact size and flexible design Low maintenance levels Moderate output heat temperature	Low noise and emission levels Suitable for domestic applications due to their low power to heat ratio Possibility to be run by renewable resources	High electrical efficiency Long lifetime period Low operation noise and emission levels High output temperature	High flexibility and simple design Low system cost Low operational pressure and temperature for ORC systems Wide range of fuels utilized including biomass and solar energy resources
Disadvantages	Large number of moving parts High mechanical vibration and acoustic noise levels High emissions rate	Inefficient part load performance Unsuitable for intermittent use and frequent start/stop applications	Require long start-up time High investment costs Limited adaptability variable output	Very high capital and investment costs Need for efficient hydrogen storage techniques Complex design and operation	Relatively low electrical efficiency More research and commercial development required in the field of organic cycle applications
Capacity (kwe)	Up to 2000	20–400	1–100	Up to 2000	Up to 2000
Electrical efficiency	22–27%	25–30%	10–28%	25–63%	15–38%
Overall efficiency	70–80%	70–80%	>85%	50–80%	>85%
Lifetime (h)	20,000–50,000	5000–40,000	10,000–30,000	10,000–65,000	30,000–50,000
Fuels used	Diesel, natural gas, propane, biogas, landfill gas	Propane, natural gas, distillate oil, biogas	Bio-fuels, waste heat, solar energy	Hydrogen, methanol, natural gas, propane	Natural gas, bio-fuels, biomass, solar energy, geothermal energy, waste heat
Electrical to thermal ratio	0.5–1	0.4–0.7	0.15–0.4	0.5–2	0.15–0.4
Output heat temperature (°C)	80–200	120–350	Up to 85	Up to 1000	Up to 100
Part load efficiency	High	Low	Moderate	Very high	Moderate
Footprint (sqft/kWe)	0.062–0.47	0.18–0.42	3–6.5	0.5–2	<0.1
Noise level	High	Moderate	Moderate	Low	Moderate
Installation costs ($/kWe)	1100–2200	2400–3000	9000	5000–7700	430–1100
NO_x emissions (lb/MWh)	3–33	0.4–2	1.7	<0.02	1.8

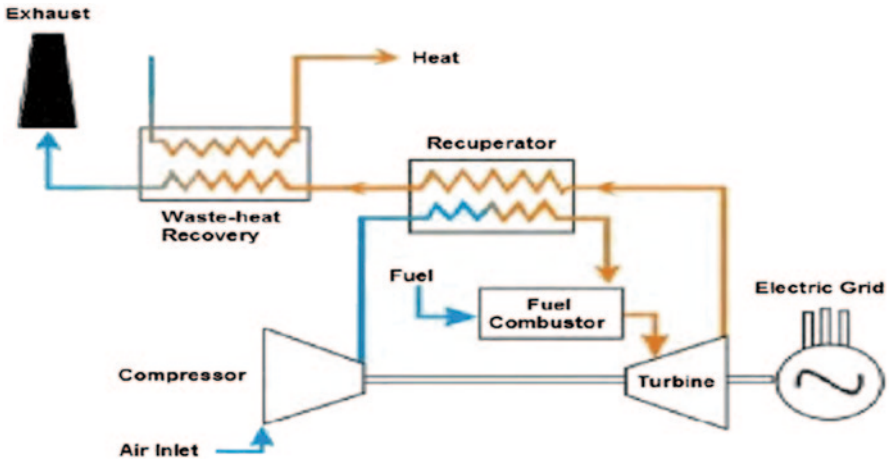

Fig. 13.5 Micro turbine CHP system [30]

The fuel–air mixture is compressed and ignited inside the engine's cylinder and the resulting hot gas is expanded to drive the generator and produce electricity. In addition, heat is recovered from the hot exhaust and the engine's coolant. Recently, there have been different micro CHP units available in the market including the 4.7 kWe Ecopower unit, Honda's 1 kWe Ecowill and the 5.4 kWe Dachs from the German supplier Senertec. Generally, reciprocating micro CHP systems have a total (thermal and electrical) efficiency of about 80 % [29]. However, reciprocating engine systems are very noisy and needs frequent maintenance in addition to the high level of nitrogen oxides emissions which make them unattractive for small residential applications [12].

Micro Turbines

Micro turbine CHP system consists generally of a generator, combustion chamber, recuperator, compressor and turbine connected together by a shaft as shown in Fig. 13.5. In a micro turbine, the heated and compressed air–fuel mixture is burned in the combustion chamber. The exhaust hot gas then expands in the turbine to drive the generator and produce electricity [30]. Heat from the system is recovered from the hot exhaust gas with a heat recovery system. Micro turbine systems are most applicable for 25–250 kWe commercial and industrial applications and can use variety of fuels including natural gas, biogas, diesel and propane with longer maintenance cycles and lower emissions compared to the reciprocating systems. However, and due to their low electrical efficiency and inflexibility to load profile changes, micro turbine systems applications in the residential and building sector are very limited.

Stirling Engines

Stirling engine is initially a reciprocating engine with a closed cylinder where fuel combustion takes place in a separate combustion chamber, thus it is known as a closed-cycle piston external combustion engine [28]. The Stirling micro CHP system has a closed cycle engine where the working gas is perpetually contained in the cylinder and undergoes four processes, heating, expansion, cooling and compression. This is accomplished through a temperature difference attained between an external heating source and an external heat sink on the other side. Generally, the working gas is air, helium or hydrogen and the heating source could be a renewable source such as bio-fuels combustion and solar energy. Stirling micro CHP systems provide higher flexibility, lower emissions and are quieter in their operation compared to internal combustion systems. However, small scale Stirling CHP systems tend to be more expensive and have low electrical efficiencies in the range of 10–15 % [12]. Several Stirling micro CHP units were recently introduced to the market including Sunachine unit of 3 kWe maximum output and the Whispergen 1 kWe unit [24].

Fuel Cells

Basically, a fuel cell micro CHP system consists of a fuel cell stack with cathode, anode and electrolyte, a fuel reformer for fuel preparation and a power conditioner to transform *DC* to *AC* electricity. Hydrogen fuel at the anode combines with the atmospheric oxygen at the cathode in an electrochemical reaction to produce electricity with water and heat as the only bi-products. Different types of fuel cells are used as the basis for micro CHP systems in residential applications including solid oxide fuel cells (SOFC), polymer electrolyte fuel cells (PEFC) and proton exchange membrane fuel cells (PEMFC). PEFC have small dimensions with lower costs compared to other fuel cells but with lower electrical efficiency [20]. SOFC operates at very high temperatures up to 1000 °C due to their hard ceramic-based electrolyte. SOFC micro CHP systems can use natural gas as a fuel and can reach a very high electrical efficiency up to 55 %. PEMFC systems have low operating temperatures and they can meet shifts in power demands. In general, fuel cell micro CHP systems are very quiet and provide high levels of reliability, modularity and rapid adaptability to load changes, but with very high investment costs compared to other technologies. Lately, several fuel cell micro CHP units were developed including the 4.6 kWe Vaillant PEMFC unit and the 1 kWe Sulzer Hexis SOFC unit [24].

Rankine Engines

Generally, Rankine engines converts heat into useful work based on the thermodynamic Rankine cycle. The cycle consists of a closed loop where heat is supplied to

the working fluid from an external source. The cycle comprises four main components as shown in Fig. 13.6, evaporator, pump, turbine and condenser. The working fluid is pumped from lower to higher pressure and then heated to become a dry saturated vapor in the evaporator using an external source of heat. Then the vapor passes through the turbine to decrease its temperature and pressure. Finally, the wet vapor is condensed back to a liquid in the condenser at constant temperature. Rankine systems can be divided into two categories, steam Rankine systems with water as the working fluid and organic Rankine systems which use an organic fluid instead of water. Due to their durability, cost effectiveness, high levels of safety and simplicity, micro CHP systems with organic Rankine cycle (ORC) have received increasing attention for domestic and buildings applications. In addition, such systems offer the possibility of utilizing heat from low-temperature sources as biomass combustion, waste heat and solar energy. ORC-based micro CHP systems are still in the phase of study and development and many companies are working on developing such systems but currently very limited units are available commercially.

13.5 Solar Driven ORC-Based Micro CHP Systems

Based on the technologies screening presented in the preceding section, Stirling engines and Rankine engines tend to be the most applicable technologies for micro CHP systems in buildings based on their acceptable efficiencies, flexibility and low emissions. Reciprocating engines provide high operating efficiencies but with high emissions and high maintenance costs. Micro turbine CHP systems are inflexible to the load variation with low efficiency limiting the possibility of implementation in building applications. In addition, Fuel cell technology in micro CHP systems is still in the research and development phases and is still lacking the economic feasibility due to the high investment costs. On the other hand solar driven Stirling engines need very high quality heat which can be attained only with large concentrators with high investment costs. Therefore, Rankine-based engines provide the best viable and effective technology for micro CHP systems in the residential applications, especially the organic Rankine systems which have received significant attention in the last few years.

Solar Driven ORC Applications

Solar driven ORC systems have received increased attention due to the advantage presented by the ORC cycle and the raising need for decentralized heat and power systems for residential buildings. A low temperature 1.5 kWe micro ORC system for electricity production was presented by Nguyen et al. [32] with low electrical efficiency of about 4.3 % using n-pentane working fluid. Similar system was investigated by Cong et al. [33] by using solar energy as the heat source and attaining

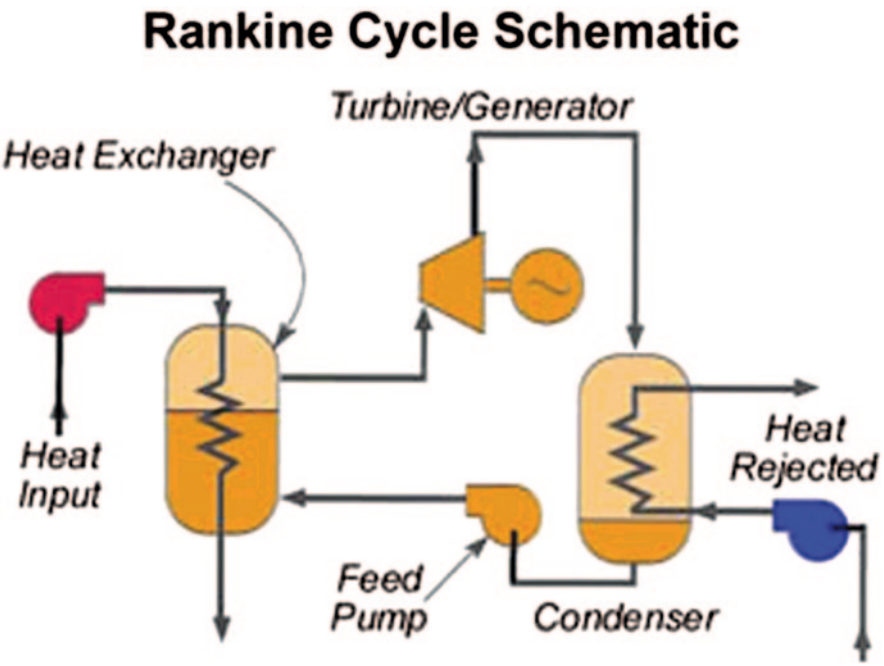

Fig. 13.6 Typical Rankine cycle schematic [31]

maximum thermal efficiency of 20 %. In addition, Bao et al. [34] proposed a novel low temperature auto-cascade solar ORC system shown in Fig. 13.7, with a zeortopic mixture isopentane as a working fluid. Two solar collectors and two expanders were used in the system and it was shown that the main factors affecting the system performance are the fluid mixture composition and the outlet temperature of the first solar collector.

One successful application for the solar organic Rankine cycle is in driving desalination fresh water production systems especially the reverse osmosis technique. A basic schematic for a solar driven ORC reverse osmosis system is shown in Fig. 13.8. One main reason for considering the ORC as an applicable technology for driving reverse osmosis systems is the possible useful coupling between the ORC system turbine and the saline water high pressure pump. Kosmadakis et al. [35] presented a two stage reverse osmosis ORC system and reported acceptable overall system efficiency with a good amount of fresh water produced. Another 2 kWe low temperature solar ORC for a reverse osmosis desalination system was examined by Manolakos et al. [36]. They reported an efficiency of 4 % using R134a as the working fluid and evacuated tube solar collectors. Similar study was conducted by Wang et al. [37] who investigated a solar desalination reverse osmosis system with a solar driven ORC. An overall system efficiency of 4.2 and 3.2 % was attained using evacuated tube and flat plate solar collectors respectively.

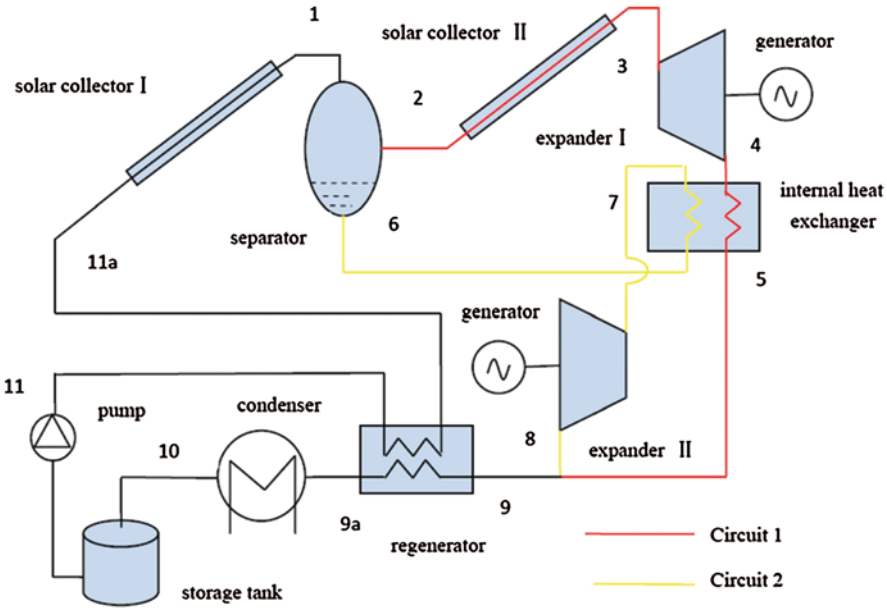

Fig. 13.7 Low temperature auto-cascade solar ORC system [34]

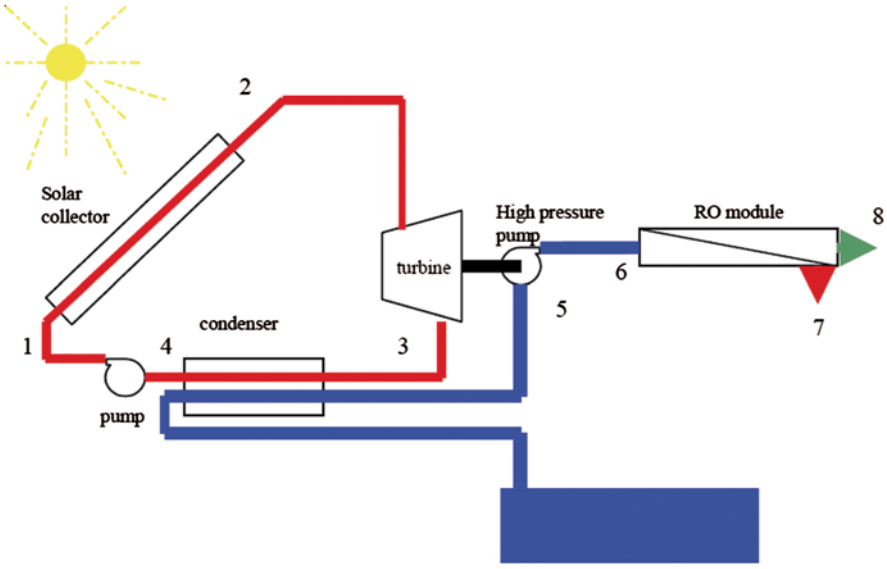

Fig. 13.8 Schematic of a reverse osmosis system powered by a solar-heated ORC [38]

Solar ORC Micro CHP Systems

Systems based on the organic Rankine cycle have received increasing attention in the recent years in the field of micro-scale power generation and heating in residential and building applications [39]. When employed in micro-scale systems, organic Rankine cycle has many advantages compared to the ordinary steam cycle due to the fact of using an organic fluid as the main driver instead of water. Generally, organic fluids have lower boiling points compared to water and hence provide the possibility for organic Rankine systems to be driven by low-grade heat sources including biomass, solar energy and geothermal heat. Moreover, ORC-based systems operate at lower pressure and temperature compared to steam systems, providing more simplicity, durability and controllability to the system and reducing high maintenance and operational costs and safety concerns [9]. In addition, organic fluids employed in micro CHP systems provide higher turbine efficiency in full and partial loads with no concerns regarding erosion or corrosion problems due to the thermodynamic characteristics of the fluid [40].

The majority of the presented information in the literature regarding Rankine based systems deal with large-scale steam Rankine cycle systems for central power plants. However, there are recent interesting studies investigating the applicability and the performance of ORC micro CHP systems in the residential and buildings sector. Yagoub et al. [41] presented a hybrid solar-natural gas small-scale ORC CHP system for an office-building with a 25 kW solar collectors thermal capacity and a 1.5 kW electrical turbine-generator unit. The maximum overall utilization efficiency attained was 17 % using HFE-301 as a working fluid, and the system was able to provide about 30 % of the building electricity demand. Recently, a solar driven ORC micro CHP system was proposed by Ksayer [42] to fulfill electricity and hot water needs for a typical dwelling. The maximum electric power generated by the system was about 2.25 kWe with about 200 l of hot water at 60 °C per day. However, the authors recommend additional research and development for the system especially due to the large volume of the storage tank used (5 m^3) and the large surface area of the solar collectors considered (about 100 m^2). Several improvements to the system design include an electrical accumulator for sunny hours and a proper selection for the working fluid and the type of the solar collector integrated. Similar study was conducted by Facao et al. [43] who investigated a 5 kWe solar driven micro CHP system with an organic Rankine cycle. As shown in Fig. 13.9, the proposed system consists of two circuits, a primary circuit where the working fluid expands in the turbine and then passes to the condenser, and a secondary circuit where the fluid is heated by the solar collector, with a heat exchanger for heat transfer between both circuits. Facao et al. [43] reported that the system electrical generation efficiency is directly proportional to the temperature output from the solar collector and can attain about 22 % in the case of 230 °C working fluid temperature. Therefore, based on the advantages presented for the organic Rankine cycle in small-scale systems and the satisfactory successful applications of micro CHP units, the design and development of a low-cost and effective solar ORC micro CHP system for residential

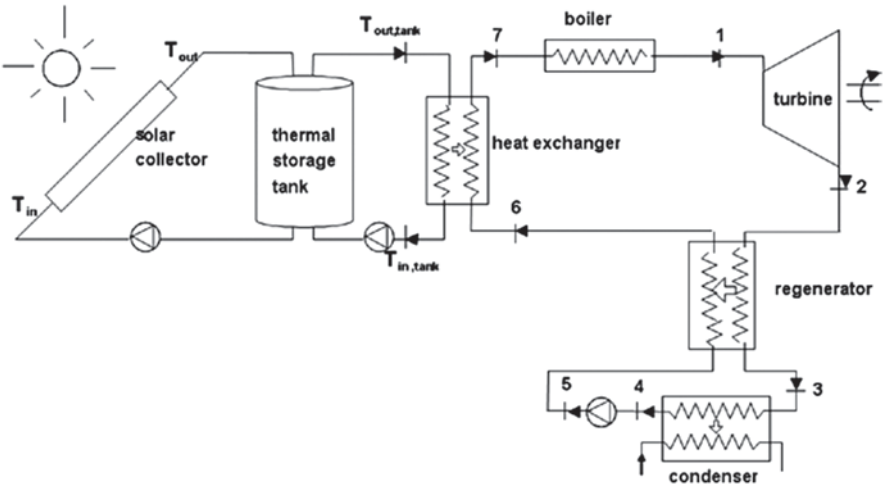

Fig. 13.9 Solar driven ORC micro CHP system [43]

applications is a favorable and a wise decision. This new micro CHP system can provide electricity and heating demands with an acceptable overall efficiency, low investment costs and with environmental friendly operation.

Working Fluid Selection

The selection of the working fluid for the ORC-based systems has been one of the main research lines in the field of organic Rankine cycles in the recent years. This is based on the direct relation between the properties and the characteristics of the working fluid and the system performance, overall efficiency and the impact on the environment. Generally, a suitable working fluid for an ORC system must have some desirable chemical, physical, environmental, economic and safety Characteristics. These include low specific volume, non-flammability, environmentally friendly, low viscosity, high thermal conductivity, low critical temperature and pressure, good thermal stability and non-toxicity. In addition, the heat source nature and temperature play the basic role in the selection of the most suitable working fluid in each application. Numerous investigations were carried out to study the performance of different working fluids for ORC systems owing to improve the cycle operation and efficiency. Tchanche et al. [44] studied the fluid selection for low temperature solar ORC system with temperatures less than 90 °C. Based on the investigations results, they recommended the use of R134a as the most favorable fluid, followed by R152a, R290, R600 and R600a. Rayegan et al. [39] developed a procedure to compare different ORC working fluids under similar conditions and reported that R245fa and R245ca are the most suitable for solar ORC low temperature

applications. Similar study carried out by Saleh et al. [45] has shown also that R245fa and R245ca could provide the best power generating ability with high economic efficiency for low-temperature solar ORC systems. On the other hand, some researchers examined the use of hydrofluoroethers (HFE) working fluids instead of the HFC and HCFC fluids for the ORC systems. Tsai et al. [46] performed an environmental risk assessment of HFE fluids. They concluded that HEF fluids could be an applicable substitute to HFC and HCFC fluids in the ORC systems due to their environmental friendly aspect especially HFE-7000, HFE-7100, HFE-7200 and HFE-7500. In spite of many research works and studies regarding the working fluid selection, there is still no fluid identified as the best recommended fluid for all the applications. This is mainly due to the interdependence between the cycle design, working conditions, heat input source and selection of the optimal fluid.

Solar Collector Selection

In addition to the selection of the optimal working fluid for the desired ORC application, the choice of the solar collector is a focal point in designing the solar driven CHP system. There are various types of solar collectors in the market with different properties and sizes. According to their working temperature and motion, solar collectors are categorized into stationary solar collectors including flat plate collectors, vacuum tube collectors and compound parabolic collectors, and concentrating collectors including parabolic trough collectors, linear Fresnel reflecting collectors, parabolic dish and central receivers. In general, stationary solar collectors have the same solar radiation intercepting and absorbing areas, whereas concentrating solar collectors tend to have larger intercepting area focusing the radiation towards smaller absorbing receiver to increase the heat flux [47]. Concentrating solar collectors have many advantages over stationary ones including the ability to heat the working fluids to a very high temperature, less heat losses and higher collector efficiency. However, compared to stationary collectors, concentrating solar collectors have higher costs, require high level of maintenance and intercept very small portion of diffuse radiation. Kalogirou [47] presented a comprehensive screening shown in Table 13.3, for different solar collector types with their working temperature ranges and concentration ratios.

Thus, the main factors to be taken into account when selecting a suitable solar collector for the desired CHP system include the solar collector efficiency and the operating temperature, the collector's cost and the possibility of integrating the collector in the architectural design of the building. Based on all these factors and since the operating temperature of the working heat transfer fluid is in the range of 100–200 °C for the low-temperature solar domestic CHP [24], the combined parabolic solar collectors with evacuated tubes present a feasible and applicable technology along with compact medium temperature solar thermal concentrators including parabolic troughs and linear Fresnel reflectors. CPC solar collector has high working efficiency in the range of 100–200 °C operating temperatures [48]

Table 13.3 Solar collector types [47]

Motion	Collector type	Absorber type	Concentration ratio	Indicative temperature range (°C)
Stationary	Flat plate collector	Flat	1	30–80
	Evacuated tube collector	Flat	1	50–200
	Compound parabolic collector	Tubular	1–5	60–240
Single-axis tracking	Linear Fresnel reflector	Tubular	10–40	60–250
	Parabolic trough collector	Tubular	15–45	60–300
	Cylindrical trough collector	Tubular	10–50	60–300
Two-axis tracking	Parabolic dish reflector	Point	100–1000	100–500
	Heliostat field collector	Point	100–1500	150–2000

Note: Concentration ratio is defined as the aperture area divided by the receiver/absorber area of the collector

with an acceptable cost and less required maintenance compared to other concentrating collectors. In addition, it provides a wide range of solar radiation interception with the ability to collect both direct and diffuse radiation without the need for an expensive solar tracking system, making it a viable and attractive option for the solar driven ORC–CHP system. Micro CHP applications which require heating the working fluid to a temperature in the range of 80–250 C can't be feasibly assisted by the traditional non-concentrating collectors such as flat plat collectors and vacuum solar tubes. Therefore, the use of medium solar thermal concentrators including parabolic troughs and linear Fresnel concentrators provides a wiser option and can enhance the operation of such applications, taking advantage of the solar reflective surfaces and the compact absorbing receiver line within the concentrator. Solar concentrators allow focusing direct light beam and thus attaining higher thermal efficiency with less convective losses compared to non-concentrating collectors.

Conclusions

As a conclusion, there is no doubt that micro CHP systems are attracting the interest in both industrial and research fields especially in the last decade. Based on the literature review presented, solar driven micro CHP systems based on the organic Rankine cycle is a promising technology and has large potential in various fields especially in building applications. The concerns regarding the negative environmental impacts of the current energy consumption and production patterns and the aims to achieve efficient and secure energy sector raises the need for such clean

and effective CHP systems. Based on the fact that the residential sector contributes to a considerable portion of the overall energy use, a micro-scale solar driven CHP system of 1–10 kWe capacity can fulfill the building's electricity and heating demands with an efficient, clean and environmentally friendly performance. A comprehensive review regarding micro CHP systems with the recent developments and innovations is presented in this paper. Successful applications of micro CHP systems in building and residential accommodations are examined. In addition, a critical comparison and assessment of different micro CHP prime movers is provided. Discussions are concentrated on solar powered micro CHP systems based on the organic Rankine cycle with different developments and applications.

On the other hand, in spite of all the economic and environmental benefits provided by the solar driven micro CHP systems, this technology is still in its preliminary research and development stages with no real steps for commercial demonstration and implementation. The current research paper not only adds to the growing body of literature on micro CHP systems but also serves as a basis for future development of micro-scale solar driven CHP systems. Based on the presented review of the current status of micro-CHP systems, it is shown that will be wise decision to learn from the successful experience of large and medium scale units and shift to develop and commercialize more efficient and compact micro-scale CHP units in the upcoming years. Special consideration should be given to solar ORC-based micro CHP systems with careful selection of the expander, the solar collector and the working fluid employed. This paper is an introductory work for further detailed theoretical and experimental investigation of an innovative solar ORC-based micro CHP system to be carried out at the University of Nottingham. New type scroll expander modified from an HVAC-compressor will be tested and integrated as a vital part of the ORC system striving to improve the overall performance while employing different types of fluids especially the environmentally friendly HFE-7000 and HFE-7100. In the next phase of the work, a complete system model will be developed and accurate dynamic simulations will be carried out aiming for the optimized coupling between the solar collector system and the ORC unit under specific climate and operational conditions. The robust simulation model will allow predicting the thermal and electrical performance of the system different components including the ORC cycle, the expander and the solar concentrator. A complete technical, economic and environmental assessment will be performed to investigate the feasibility of using such solar ORC-based micro-CHP system to provide electrical and thermal demands for a residential application under the Middle East conditions taking into account the environmental and the economic aspects of the project. The new developed solar-driven ORC-based micro CHP system will fulfill the thermal needs and part of the electric demands of a residential application. The new system will present itself as an attractive substitute for centralized heat and electricity production systems with an efficient and environmentally friendly operation accompanied with an acceptable cost and low maintenance level.

Nomenclature Subscript and Superscripts

e	electrical
th	thermal

Acronyms

AC	Alternating Current
CHP	Combined Heat and Power
CPC	Compound Parabolic Collector
DC	Direct Current
HFE	Hydrofluoroether
ORC	Organic Rankine Cycle
PEFC	Polymer Electrolyte Fuel Cell
PEMFC	Proton Exchange Membrane Fuel Cell
SOFC	Solid Oxide Fuel Cell
VAT	Value Added Tax

References

1. Digest of UK energy statistics (DUKES) (2011) Chapter 1: Energy. http://www.decc.gov.uk/assets/decc/11/stats/publications/dukes/2303-dukes-2011-chapter-1-energy.pdf. Accessed 25 July 2014
2. UK Energy Research Center (UKERC) (2011) Combined heat and power. http://www.ukerc.ac.uk/support/tiki-index.php?page=CHP. Accessed 12 June 2014
3. Li T, Tang D, Li Z, Du J, Zhou T, Jia Y (2012) Development and test of a Stirling engine driven by waste gases for the micro-CHP system. Appl Therm Eng 33–34:119–123
4. Qiu G, Liu H, Riffat S (2011) Expanders for micro-CHP systems with organic Rankine cycle. Appl Therm Eng 31:3301–3307
5. Digest of UK energy statistics (DUKES) (2011) Chapter 7. Renewable sources of energy. http://www.decc.gov.uk/assets/decc/11/stats/publications/dukes/2309-dukes-2011-chapter-7-renewable-sources.pdf. Accessed 23 July 2014
6. Combined Heat and Power Association (CHPA). (2011) Micro CHP. http://www.chpa.co.uk/micro-chp_190.html. Accessed 27 June 2014
7. Directive 2004/8/EC of the European Parliament and of the Council (2004) Official J Eur Union L52:50–60
8. Digest of UK energy statistics (DUKES) (2011) Chapter 6: CHP. http://www.decc.gov.uk/assets/decc/11/stats/publications/dukes/2308-dukes-2011-chapter-6-chp.pdf. Accessed 23 July 2014
9. Liu H, Shao Y, Li J (2011) A biomass-fired micro-scale CHP system with organic Rankine cycle (ORC)—thermodynamic modelling studies. Biomass Bioenergy 35:3985–3994
10. De Paepe M, D'Herdt P, Mertens D (2006) Micro-CHP systems for residential applications. Energy Convers Manage 47:3435–3446
11. Harrison J (2004) Micro combined heat & power (CHP) for housing. 3rd International conference on sustainable energy technologies. Nottingham, UK
12. Kuhn V, Klemes J, Bulatov I (2008) MicroCHP: overview of selected technologies, products and field test results. Appl Therm Eng 16:2039–2048

13. Department of Trade & Industry (DTI) (2003) Energy white paper, our energy future. TSO ISBN 0-10-157612. http://webarchive.nationalarchives.gov.uk/+/http://www.berr.gov.uk/files/file10719.pdf. Accessed 22 June 2014
14. Valkiainen M, Klobut K, Leppäniemi S, Vanhanen J, Varila R (2002) Micro CHP systems based on PEM fuel cell. Status report [only in Finnish]. VTT Tiedotteita-Meddelanden-Research Notes: 2055, Finland: VTT Chemical Technology, Espoo ISBN 951-38-5804-9
15. D'Accadia M, Sasso M, Sibilio S, Vanoli L (2003) Micro-combined heat and power in residential and light commercial applications. Appl Therm Eng 23:1247–1259
16. Arsalis A, Nielsen M, Kær S (2011) Modeling and parametric study of a 1 kWe HT-PEMFC-based residential micro-CHP system. Int J Hydrogen Energy 36:5010–5020
17. Obara S (2006) Dynamic characteristics of a PEM fuel cell system for individual houses. Int J Hydrogen Energy 30:1278–1294
18. Georgopoulos N (2002) Application of a decomposition strategy to the optimal synthesis/design and operation of a fuel cell based total energy system. M.S. Thesis, Virginia Tech, Blacksburg, VA, USA
19. Hawkes AD, Leach MA (2007) Cost-effective operating strategy for residential micro-combined heat and power Energy 32:711–723
20. Briguglio N, Ferraro M, Brunaccini G, Antonucci V (2011) Evaluation of a low temperature fuel cell system for residential CHP. Int. J Hydrogen Energy 36:8023–8029
21. Bernotat K, Sandberg T (2004) Biomass fired small-scale CHP in Sweden and the Baltic states: a case study on the potential of clustered dwellings. Biomass Bioenergy 27:521–530
22. Ren H, Gao W (2010) Economic and environmental evaluation of micro CHP systems with different operating modes for residential buildings in Japan. Energy Build 42:853–861
23. Takahiro K (2008) Development strategies toward promotion and expansion of residential fuel cell micro-CHP system in Japan, Osaka Gas Co. http://www.igu.org/html/wgc2009/papers/docs/wgcFinal00801.pdf. Accessed 23 May 2014
24. Aoun B (2008) Micro combined heat and power operating on renewable energy or residential building. Ph.D. Thesis, Center for Energy and Processes, Mines ParisTech
25. Sustainable Energy Authority of Ireland (SEAI) (2006) New technologies for CHP applications. http://www.seai.ie/Publications/Your-Business-Publications/New-Technologies-final.pdf. Accessed 11 July 2014
26. US Department of Energy (DOE) (1999) Review of combined heat and power technologies. http://www1.eere.energy.gov/manufacturing/distributedenergy/pdfs/chp_review.pdf. Accessed 28 June 2014
27. US Environmental Protections Agency (EPA) (2008) Catalog of CHP technologies. http://www.epa.gov/chp/documents/catalog-of-%20chp-tech-entire.pdf. Accessed 6 July 2014
28. Alanne K, Saari A (2004) Sustainable small-scale CHP technologies for buildings: the basis for multi-perspective decision-making. Renew Sustain Energy Rev 8:401–431
29. Aabakken J (2006) Power technologies energy data book, NREL. http://www.nrel.gov/analysis/power-databook/docs/pdf/db-chapter02-engine.pdf. Accessed 12 June 2014
30. Communities for Advanced Distributed Energy Resources (CADER) (2011) Micro turbine CHP system cycle. http://www.cader.org/microturbines.html. Accessed 26 June 2014
31. Nichols B (2011) Thermodynamic power cycles. http://www.barber-nichols.com/capabilities/engineering_capabilities/thermodynamic_power_cycles/default.asp. Accessed 29 Apr 2014
32. Nguyen V, Doherty P, Riffat S (2001) Development of a prototype low temperature Rankine cycle electricity generation system. Appl Therm Eng 21:169–181
33. Cong CE, Velautham S, Darus A (2005) Sustainable power: solar thermal driven organic Rankine cycle. Proceedings of the International Conference on Recent Advances in Mechanical and Materials Engineering, Kuala Lumpur, Malaysia 20:68–77
34. Bao J, Zhao L, Zhan W (2011) A novel auto-cascade low-temperature solar Rankine cycle system for power generation. Solar Energy 85:2710–2719
35. Kosmadakis G, Manolakos D, Kyritsis, S, Papadakis G (2010) Design of a two stage organic Rankine cycle system for reverse osmosis desalination supplied from a steady thermal source. Desalination 250:323–328

36. Manolakos D, Papadakis G, Kyritsis S, Bouzianas K (2007) Experimental evaluation of an autonomous low-temperature solar Rankine cycle system for reverse osmosis desalination. Desalination 203:366–374
37. Wang XD, Zhao L, Wang JL, Zhang WZ, Zhao X Z, Wu W (2010) Performance evaluation of a low temperature solar Rankine cycle system utilizing R245fa. Solar Energy 84:353–364
38. Garcia-Rodriguez L, Delgado-Torres A (2007) Solar-powered Rankine cycles for fresh water production. Desalination 212:319–327
39. Rayegan R, Tao YX (2011) A procedure to select working fluids for Solar Organic Rankine Cycles (ORCs). Renew Energy 36:659–670
40. Oberngerger I (2000) Biomass CHP plant based on an ORC process. Realized EU demonstration project in Admont/Austria, in meeting of IEA Bioenergy, TASK 19. Biomass Combustion
41. Yagoub W, Doherty P, Riffat S (2006) Solar energy-gas driven micro-CHP system for an office building. Appl Therm Eng 26:1604–1610
42. Ksayer E (2011) Design of an ORC system operating with solar heat and producing sanitary hot water. Eng Proc 6:389–395
43. Facao J, Palmero-Marrero A, Oliveira A (2009) Analysis of a solar assisted micro-cogeneration ORC system. Int J Low Carbon Technol 3:254–264
44. Tchanche BF, Papadakis G, Lambrinos G, Frangoudakis A (2009) Fluid selection for a low-temperature solar organic Rankine cycle. Appl Therm Eng 29:2468–2476
45. Saleh B, Koglbauer G, Wendl M, Fischer J (2007) Working fluids for low-temperature organic Rankine cycles. Energy 32:1210–1221
46. Tsai WT (2005) Environmental risk assessment of hydrofluoroethers (HFEs). J Hazard Mater A119:69–78
47. Kalogirou SA (2004) Solar thermal collectors and applications. Prog Energy Combust Sci 30:231–295
48. Brunold S, Frey R, Frei U (1994) A comparison of three different collectors for process heat applications\2 Proceedings of optical materials technology for energy efficiency and solar energy conversion XIII. Proc of SPIE 2255:107–118

Chapter 14
Evaluation of Transient Behavior of a Single-Effect Absorption Chiller

Aghil Iranmanesh and Mozaffar Ali Mehrabian

Abstract This paper deals with a lumped-parameter dynamic simulation of a single-effect LiBr–H_2O absorption chiller. In the majority previous studies, thermodynamic properties of LiBr–H_2O solution were taken from some approximate relations causing the results to be somewhat inaccurate. These relations were used to solve simultaneous differential equations involving the continuity of species constituting the LiBr–H_2O solution, momentum equations and energy balances. To diminish the effect of these approximate relations on the results, in this study the thermodynamic properties were taken from the EES software. By making a link between EES and MATLAB softwares, the simultaneous differential equations were solved in MATLAB environment and this process was continued until the convergence criterion was satisfied. Moreover, this paper considers the effect of quality on the concentration of solution at the exits of generator and absorber. This effect was ignored in the previous works. In other words, the concentrations of solution at the generator and absorber were not assumed to be equal with the corresponding concentration at the exit of those components in this paper.

Keywords Absorption chillers · LiBr–H_2O · Single-effect · Transient behavior

14.1 Introduction

Nowadays, researchers are prompted to reconsider the absorption refrigeration systems because of the increasing anxiety on the depletion of ozone layer and global warming. Absorption systems use the working fluids not dangerous to the environment and the input energy to the absorption chiller is heat, rather than mechanical work. Different heat sources can be applied for the absorption chillers such as solar and geothermal energy as well as waste heat released from industrial machines.

A. Iranmanesh (✉)
Department of Mechanical Engineering, Ferdowsi University of Mashhad, Mashhad, Iran
e-mail: iranmanesh.aghil@gmail.com

M. A. Mehrabian
Department of Mechanical Engineering, Shahid Bahonar University of Kerman, Kerman, Iran
e-mail: ma_mehrabian@yahoo.com

I. Dincer et al. (eds.), *Progress in Sustainable Energy Technologies: Generating Renewable Energy,* DOI 10.1007/978-3-319-07896-0_14,

Many works were done on the steady-state and dynamic simulation of absorption chillers so far. Jeong et al. [1] developed the dynamic simulation of a steam-driven LiBr–H_2O absorption heat pump for recovering low-grade waste heat. Storage terms with thermal capacities and solution mass storage were assumed to be constant in this model. The solution and vapor mass flow rates were determined using the pressure differences between the vessels. Time step and heat transfer coefficients in the simulation were assumed to be constant. Sugano et al. [2] developed a dynamic model of the absorption chiller driven by hot water and this model was used for controlling the system in part load applications. Transient behavior of a single-effect absorption chiller using ionic liquids was studied by Cai et al. [3]. Several relations were used to predict the thermodynamic properties of ammonia–water solution causing the results to be erroneous. Furthermore, the concentrations of solution at the exit of the absorber as well as the generator were assumed to be equal to the concentration inside the absorber and generator respectively. A dynamic model of a small single-effect absorption chiller on the basis of external and internal steady-state enthalpy balances was developed by Kohlenbach and Ziegler [4]. The results obtained from the simulation were compared with the experimental data.

This study deals with the dynamic analysis of a single-effect absorption chiller by considering the effect of quality on the solution concentration. Dynamic approach can be applied for controlling purposes. The fourth order Range–Kutta method is selected to solve the simultaneous equations deduced from continuity, momentum, and energy balances. The results inferred from the dynamic analysis are compared with the data from the steady-state condition. Obtaining major parameters such as coefficient of performance, second law efficiency, and … as a function of time are the other objectives of this research.

14.2 Formulation of the Dynamic Model

Governing Equations

The schematic diagram of a single-effect LiBr–H_2O absorption chiller is illustrated in Fig. 14.1. Each main component is characterized by a single pressure, temperature, and concentration. Several assumptions are made to simplify the simulation:

- The amount of heat diffusion in the flow direction is negligible.
- Neither the generator releases any heat to the surroundings nor the evaporator receives any heat from the surroundings.
- The refrigerant at the exit of the evaporator is assumed to be at the state of saturated vapor.
- The refrigerant at the exit of the generator is assumed to be at the state of superheated vapor.

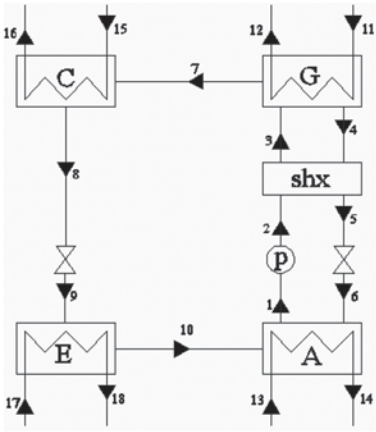

Fig. 14.1 Schematic diagram of a single-effect LiBr–H_2O absorption chiller

- The concentration of solution leaving the generator and absorber is different from the concentration inside the generator and absorber respectively.
- The input work of the pump is negligible.
- There is no pressure loss in the pipes.
- The fluid temperature at the exit of each component is the same as the temperature inside that component.

The governing equations for the dynamic analysis are:

Mass continuity:

$$\frac{d(M_i)}{dt} = \dot{m}_{in} - \dot{m}_{out} \tag{14.1}$$

Continuity of LiBr and water species:

$$\frac{d}{dt}(M_A Z_A) = \dot{m}_6 X_{LG} - \dot{m}_1 X_{LA} \tag{14.2}$$

$$\frac{d}{dt}(M_G Z_G) = \dot{m}_3 X_{LA} - \dot{m}_4 X_{LG} \tag{14.3}$$

Momentum:

$$\frac{d\dot{m}_i}{dt} + \frac{1}{2} f_i \frac{\dot{m}_i |\dot{m}_i|}{\rho_i A_i D_i} = \frac{A_i}{L_i}(\Delta P) \tag{14.4}$$

Energy balance:

$$\frac{d}{dt}(M_i h_i) = \dot{m}_{in} h_{in} - \dot{m}_{out} h_{out} \pm Q_i \tag{14.5}$$

The concentration of solution at the exit of the absorber and generator is a function of the quality and solution concentration of generator and absorber respectively:

$$X_{LG} = \frac{Z_G}{(1 - Qu_G)} \tag{14.6}$$

$$X_{LA} = \frac{Z_A}{(1 - Qu_A)} \tag{14.7}$$

Now, Eqs. (14.2) and (14.3) lead to:

$$\frac{d}{dt}(M_A Z_A) = \dot{m}_6 \frac{Z_G}{(1 - Qu_G)} - \dot{m}_1 \frac{Z_A}{(1 - Qu_A)} \tag{14.8}$$

$$\frac{d}{dt}(M_G Z_G) = \dot{m}_3 \frac{Z_A}{(1 - Qu_A)} - \dot{m}_4 \frac{Z_G}{(1 - Qu_G)} \tag{14.9}$$

Z stands for the concentration of solution at the generator and absorber. X_L is the concentration of solution at the exit of the absorber and generator. As the quality approaches to zero, the amount of Z will become equal to X_L.

The following equations can be applied for the expansion valves and the pump:

$$\frac{1}{2}\xi_1 \frac{1}{\rho_i A_{V_1}^{\ 2}} \dot{m}_i \left|\dot{m}_i\right| = P_{V_1}^{\ in} - P_{V_1}^{\ out} \tag{14.10}$$

$$\Delta P = a_0 + a_1 \dot{m}_i + a_2 \dot{m}_i^{\ 2} \tag{14.11}$$

Where ξ_1 is the expansion valve friction factor and assumed to be constant. The smallest cross-sectional area of the expansion valve is indicated by A_V. a_0, a_1, and a_2 can be obtained from the characteristic curve of the pump. To solve the simultaneous differential equations, a trial and error process is needed to calculate the pressure, temperature, and quality of the main components. In the second stage, the properties at other state points of the cycle can be obtained from the initial conditions. These amounts are used to solve the simultaneous differential equations and the amounts of parameters at the next step can be calculated. This process is repeated until the convergence criterion is satisfied.

The second law efficiency represents the reversible performance of the cycle and is defined as the ratio of total exergy taken from the system to the total exergy given to the system [5] (Tables 14.1, 14.2 and 14.3) (Figs. 14.2, 14.3, 14.4, 14.5, 14.6, 14.7, 14.8, 14.9, 14.10, 14.11, 14.12, 14.13):

$$\eta = \frac{\Delta E_{taken}}{\Delta E_{given}} = 1 - \frac{\Delta E_{loss}}{\Delta E_{given}} = 1 - \frac{\sum \Delta E_1 + \sum \Delta E_2 + \sum \Delta E_V}{\Delta E_{3eva} + \Delta E_{3gen_1} + \sum \Delta E_p} \tag{14.12}$$

Table 14.1 Typical set of input data

ε_{shx}	UA_A	UA_C	UA_E	UA_G	$\dot{m}_{11}$	T_{11}	$\dot{m}_{13}$	T_{13}	$\dot{m}_{15}$	T_{15}	$\dot{m}_{17}$	T_{17}
0.64	1.8	1.2	2.25	1.00	1.00	100	0.28	25.0	0.28	25	0.4	10.0

Table 14.2 Output data from steady-state analysis (Ref. [6])

COP	Q_A	Q_C	Q_G	Q_E	Q_{shx}
0.720	14.039	11.213	14.678	10.574	3.06

14.3 Validation

To run the computer code, several initial conditions were assumed. The results obtained from the dynamic simulation were compared with the steady-state results since the initial conditions at the first step were assumed to be the same (Table 14.1). However, the results show a good agreement between the steady-state and dynamic results.

Conclusions

Several initial conditions were considered to study the dynamic simulation of a single-effect absorption chiller. Firstly, the pressure difference between the generator and absorber is higher than the steady-state value (Figs. 14.12 and 14.13). As the pressure difference between the generator and absorber decreases, $\dot{m}_1$ will increase according to the characteristic curve of the pump (Fig. 14.11). On the contrary, $\dot{m}_6$ will decrease according to Eq. (14.10). M_G decreases while an increase in M_A is observed in spite of increasing the amount of $\dot{m}_1$ and decreasing $\dot{m}_6$ (Figs. 14.3 and 14.11). Although $\dot{m}_1$ is increasing, its rate of increase is still lower than $\dot{m}_6$, leading to an in increase in M_A and a decrease in M_G. The effect of $\dot{m}_7$ and $\dot{m}_{10}$ on $M_A$and M_G can be ignored because of their small amounts. Rich solution leaves the generator at the higher rate in comparison with weak solution. In spite of that, an increase in Q_G leads to an increase in X_{LG} (Figs. 14.6 and 14.8). A decrease in the generator pressure and an increase in X_{LG} leads to an increase in T_G according to Duhring diagram (Lee et al. [7]). Absorbing the refrigerant at a higher rate leads to a decrease in Qu_A and an increases in Q_A (Figs. 14.7 and 14.8). An increase in $Q_G$and a decrease in Q_E reduce the coefficient of performance and the second law efficiency (Figs. 14.8, 14.9, and 14.10).

Table 14.3 Thermodynamic properties of state points corresponding to input data (Ref. [6])

	h	$\dot{m}$	P	Qu	T	XL
1	85.8	0.0500	0.679	0.000	32.9	56.7
2	85.8	0.0500	7.347	–	32.9	56.7
3	147.0	0.0500	7.347	–	63.2	56.7
4	221.2	0.0455	7.347	0.000	89.4	62.4
5	153.9	0.0455	7.347	–	53.3	62.4
6	153.9	0.0455	0.679	0.006	44.7	62.4
7	2644.6	0.0045	7.347	–	76.8	0.0
8	167.2	0.0045	7.347	0.000	39.9	0.0
9	167.2	0.0045	0.679	0.064	1.5	0.0
10	2503.4	0.0045	0.679	1.000	1.5	0.0
11	418.9	1.0000	–	–	100.0	–
12	404.2	–	–	–	96.5	–
13	104.8	0.2800	–	–	25.0	–
14	154.9	–	–	–	37.0	–
15	104.8	0.2800	–	–	25.0	–
16	144.8	–	–	–	34.6	–
17	42	0.400	–	–	10.0	–
18	15.6	–	–	–	3.7	–

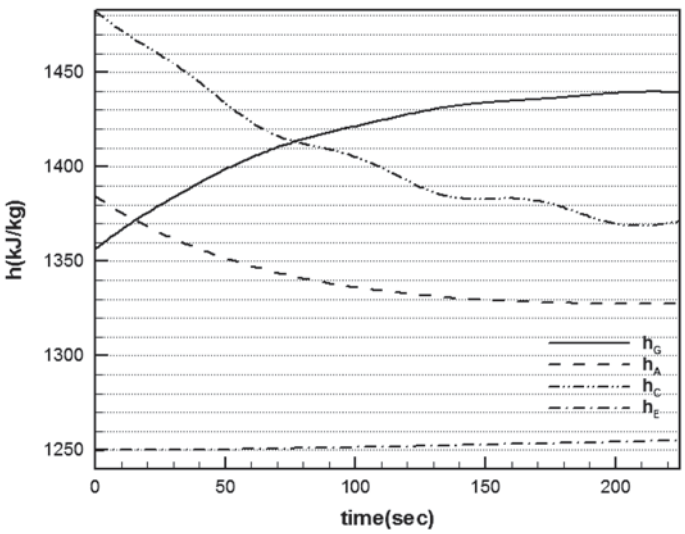

Fig. 14.2 Variation of the enthalpy of components versus time

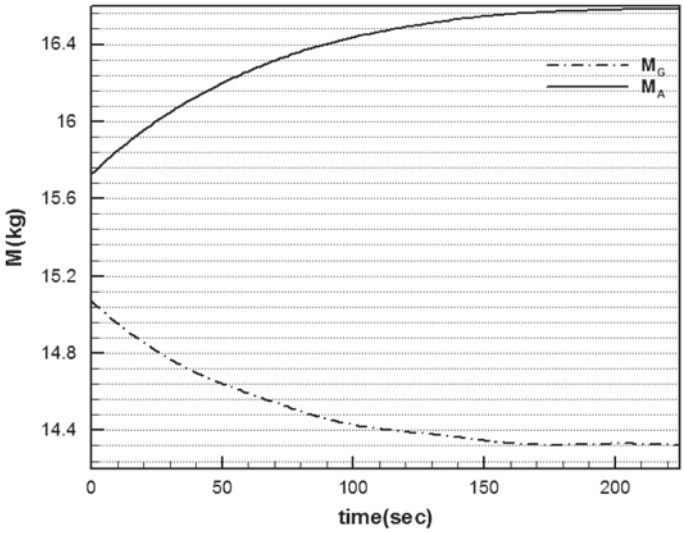

Fig. 14.3 Variation of the mass of solution in the generator and absorber versus time

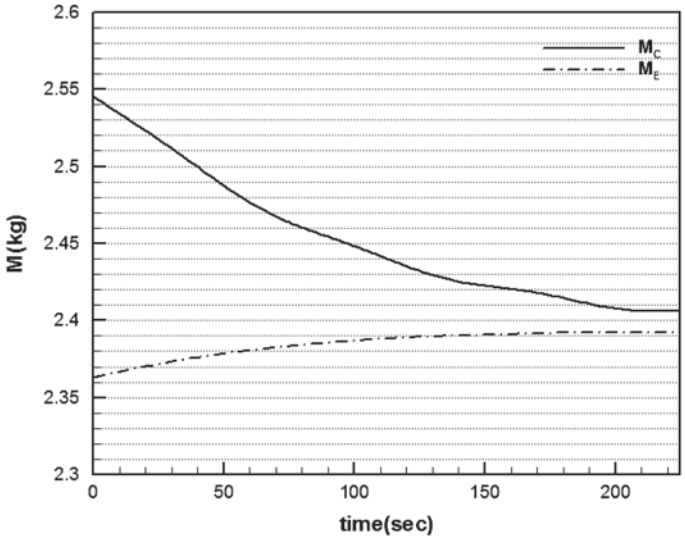

Fig. 14.4 Variation of the mass of refrigerant in the condenser and evaporator versus time

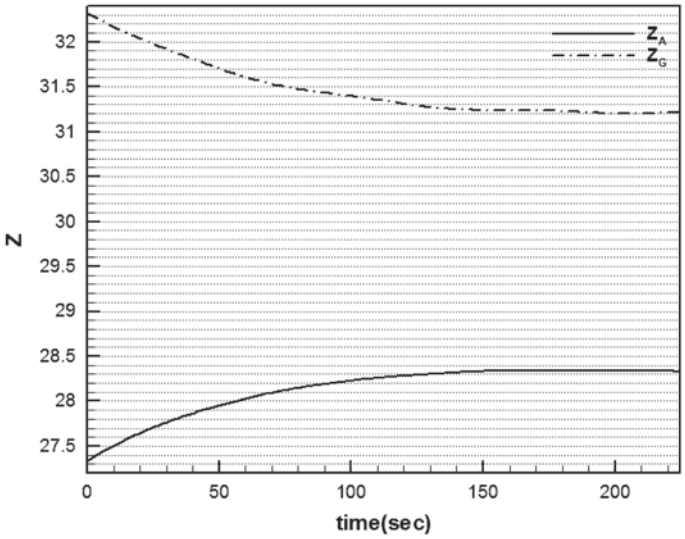

Fig. 14.5 Variation of the concentration of solution in the absorber and generator versus time

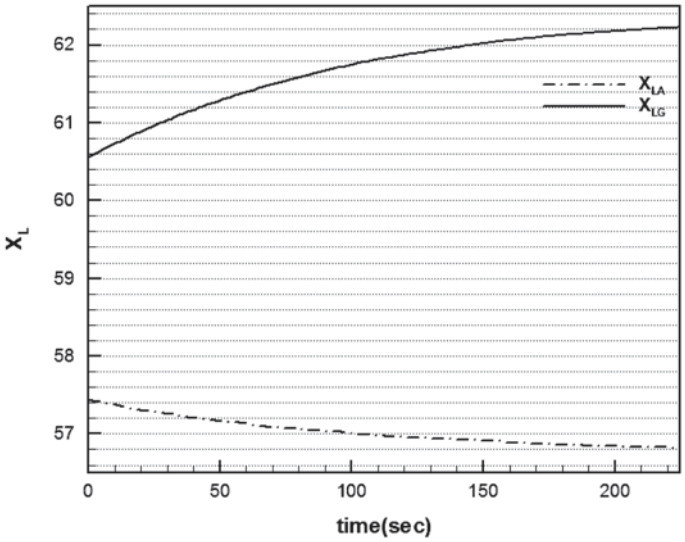

Fig. 14.6 Variation of the concentration of the solution at the exit of the absorber and generator versus time

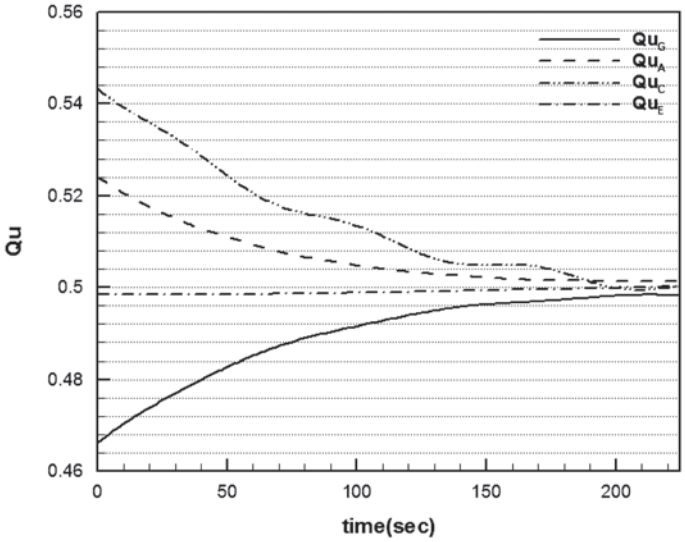

Fig. 14.7 Variation of the quality of components in the absorption system versus time

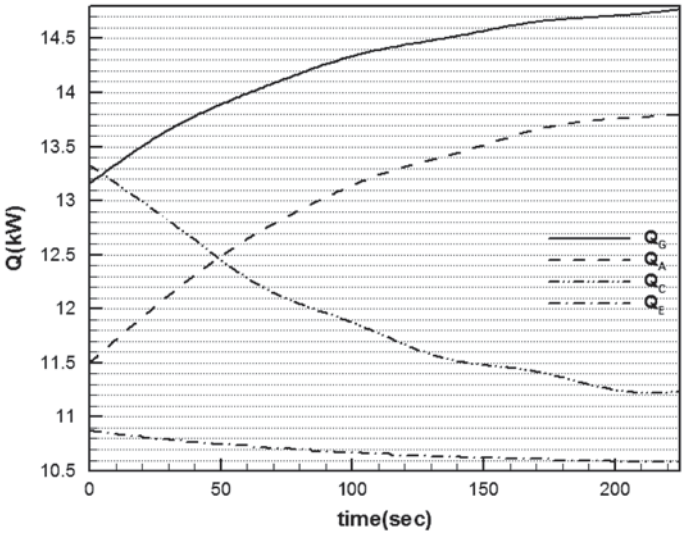

Fig. 14.8 Variation of the heat transfer rate of components versus time

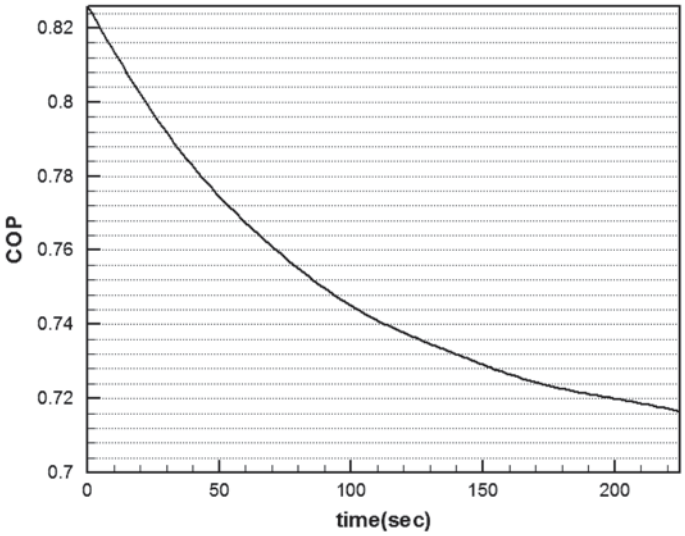

Fig. 14.9 Variation of the coefficient of performance of the cycle versus time

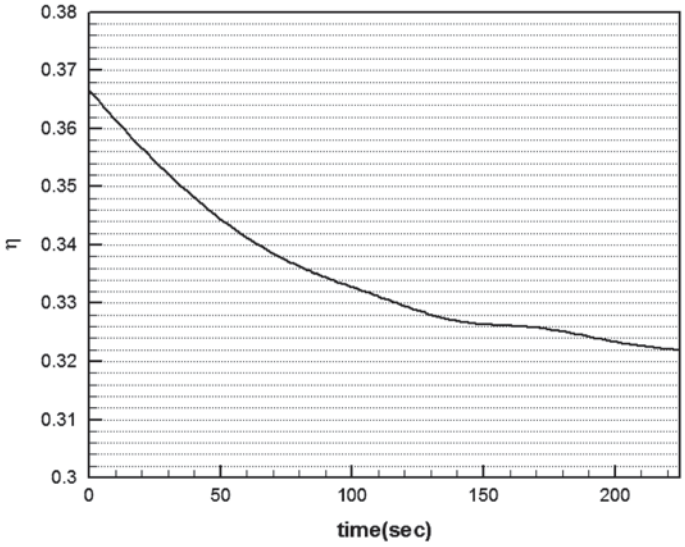

Fig. 14.10 Variation of the second law efficiency of the cycle versus time

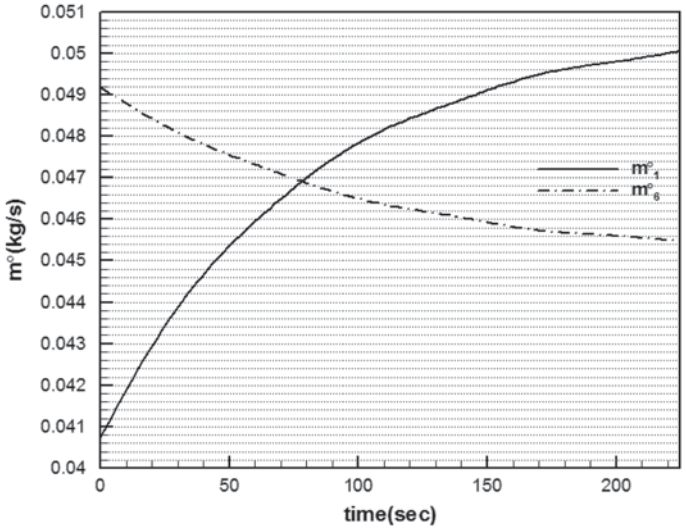

Fig. 14.11 Variation of the mass flow rate of solution at the exit of the generator and absorber versus time

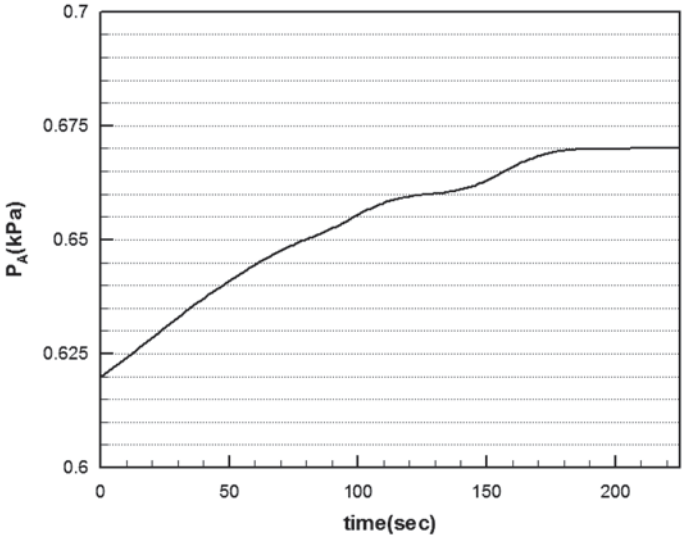

Fig. 14.12 Variation of the absorber pressure versus time

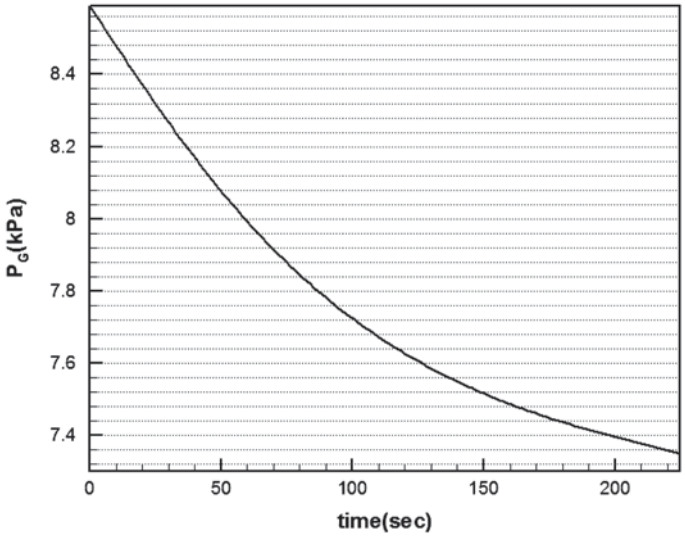

Fig. 14.13 Variation of the generator pressure versus time

Nomenclature

A	Absorber
G	Generator
C	Condenser
E	Evaporator
shx	Solution heat exchanger
P	Pump
M	The amount of mass in each component, kg
t	Time, s
$\dot{m}$	Mass flow rate between components, kg/s
L	Liquid
Z	Concentration of solution at the absorber and generator
X_L	Concentration of solation at the exit of generator and absorber
f	The pipe friction factor
ρ	Density, kg/m^3
A	The pipe cross-sectional area, m^2
D	Pipe diameter, m
L	Pipe length, m
P	Pressure, kPa
Q	Heat transfer rate, kW
h	Enthalpy, kJ/kg
Qu	Quality
ξ	The expansion valve friction factor

A_v	The smallest cross-sectional area of the expansion valve, m^2
η	Second law efficiency
ΔE	Exergy difference, kJ
T	Temperature, °C
UA	Conductance, kW/K
COP	Coefficient of performance

References

1. Jeong S, Kang BH, Karng SW (1998) Dynamic simulation of an absorption heat pump for recovering low grade waste heat. Appl Therm Eng 18(1–2):1–12
2. Sugano N, Saito K, Kawai S, Nisiyama N, Honma R, Wakimizu H (1994) Simulation and experimental research of dynamic characteristics of single-effect absorption refrigerators driven by waste hot water. Trans JSME (B) 60(576):290–296
3. Cai W, Sen M, Paolucci S (2007) Dynamic modeling of an absorption refrigeration system using ionic liquids. ASME International Mechanical Engineering Congress and Exposition, Seattle
4. Kohlenbach P, Ziegler F (2008) A dynamic simulation model for transient absorption chiller performance, part I: the model. Int J Refrig 31(2):217–225
5. Mehrabian MA, Shahbeik AE (2004) Thermodynamic modeling of a single-effect LiBr–H_2O absorption refrigeration cycle. Proc. IMechE Part E 219:261–273
6. Herold KE, Radermacher R, Klein SA (1996) Absorption chillers and heat pumps. CRC Press, Boca Raton
7. Lee HR, Koo KK, Jeong S, Kim JS, Lee H, Oh YS, Park DR, Baek YS (2000) Thermodynamic design data and performance evaluation of the water + lithium bromide + lithium iodide + lithium nitrate + lithium chloride system for absorption chiller. Appl Therm Eng 20(8):707–720

Chapter 15
Combined Effect of Global Warming and Buildings Envelope on the Performance of Ground Source Heat Pump Systems

Mohamad Kharseh, Lobna Altorkmany, Mohammed Al-Khawaja and Ferri Hassani

Abstract Heating and cooling systems as well as domestic hot water account for over 50% of the world's energy consumption. Due to their high thermal performance, ground source heat pump systems (GSHP) have been increasingly used to reduce energy consumption. The thermal performance of GSHP systems strongly depends on the temperature difference between indoor and ground operation temperature. This temperature difference is a function of mean annual air temperature and energy demand for heating and cooling over the year. The thermal load of a building, on the other hand is influenced by the thermal quality of the building envelope (TQBE) and outdoor temperature. Over the time, there is a change in heating and cooling load of buildings due to two reasons; improving the comfort requirements and outdoor temperature change. The overall aim of the current work is to study the impact of climatic changes in combination with TQBE on driving energy of GSHP. This was achieved by comparing the driving energy of the GSHP for different global warming (GW) scenarios and different TQBE. Under climate conditions of selected cities (Stockholm, Roma, and Riyadh), the current study shows that GW reduces the driving energy of GSHPs in cold climates. In contrast, GW increases the driving energy of GSHPs in hot climates. Also it was shown that buildings with poor TQBE are more sensitive to GW. Furthermore, the improvement of TQBE reduces the driving energy more in cold climates than in hot or mild climates.

M. Kharseh (✉) · M. Al-Khawaja
Faculty of Engineering, Qatar University, 2713 Doha, Qatar
e-mail: Kharseh@qu.edu.qa

M. Al-Khawaja
e-mail: Khawaja@qu.edu.qa

L. Altorkmany
Department of Engineering Sciences and Mathematics, Luleå University of Technology, 97187 Luleå, Sweden
e-mail: loal@ltu.se

F. Hassani
Department of Mining Metals and Materials Engineering, McGill University, Montreal, QC H3A 2A7, Canada
e-mail: ferri.hassani@mcgill.ca

I. Dincer et al. (eds.), *Progress in Sustainable Energy Technologies: Generating Renewable Energy,* DOI 10.1007/978-3-319-07896-0_15,

Keywords Heat pump · GSHP · Global warming · Heating and cooling load

15.1 Introduction

Human activities that are based on burning fossil fuel are very likely the cause of ongoing global warming (GW) and, therefore, reducing fossil energy consumption has become an urgent issue. Heating and cooling systems of buildings as well as hot water consumption account for a considerable part of the global energy consumption. The thermal load of building strongly depends on the thermal quality of the building envelope (TQBE) and prevailing weather conditions. Thus, increasing the performance of heating/cooling systems and also improving the TQBE can play a significant role in saving energy and the environment. With regard to increasing the performance of H/C systems, the performance of ground source heat pump systems (GSHP), compared to conventional systems, has made such systems increasingly common in commercial, institutional and residential buildings [1–4]. Yet, studies have been conducted to show the impact of improving the TQBE in reducing the thermal load of buildings.

The performance of GSHP strongly depends on the operation ground temperature. The annual mean air temperature and the ratio of heating to cooling load (RHC), which is affected by GW [5–12] and by the TQBE, determine the operation ground temperature. Hence, the ongoing warming and improving the TQBE have a direct impact on the RHC and ground operating temperature and, consequently, on the performance of GSHPs. By assuming a fixed TQBE it was shown that GW reduces and increases driving energy of GSHPs in cold and hot climates respectively [5].

In the current study, the impact of improving the TQBE in combination with three different scenarios of GW on the driving energy of GSHPs was investigated in three different climate conditions. The GW scenarios were selected to represent no climate change, a mild and a fast climate change projection over the next 50 years:

i. No climate change
ii. Slow scenario, with a warming rate of $\varepsilon = 0.2\,^{\circ}C/10$ years,
iii. Fast scenario, with a warming rate of $\varepsilon = 0.5\,^{\circ}C/10$ years.

The different levels of TQBE were selected based on the fact that they represent (A) standards TQBE imposed under current building regulations, (B) poorer TQBE than those standards imposed under current building regulations, and (C) better TQBE than those standards imposed under current building regulations. The cities were selected so that they represent hot climate (Riyadh), temperate climate (Rome), and cold climate (Stockholm).

The overall objective was to find out how GW in combination with change in the thermal quality of the building envelope affects:

- The heating and cooling load of buildings
- Thermal performance of existing GSHP system
- Driving energy of existing GSHP system.

Table 15.1 Specifications of ground heat exchanger design

Ground temperature (°C)	Mean air temperature	Pipe outer diameter	0.1 (m)
Borehole type	Coaxial	Outer pipe wall thickness	0.004 (m)
Configuration (Stockholm–Rome)	2: 1 × 2, line	Outer pipe conductivity	0.4 (W/m K)
Configuration (Riyadh)	3: 1 × 3, line	Inner pipe conductivity	0.22 (W/m K)
Borehole space	10 (m)	Pipe inner diameter	0.05 (m)
Borehole depth	100 (m)	Inner pipe wall thickness	0.0046 (m)
Borehole diameter	0.11 (m)	Filling conductivity	0.6 (W/m K)
Flow rate	0.002 (m^3/s)	Ground thermal conductivity	2.5 (W/m K)
Contact resistance	0 (m K/W)	Ground heat capacity	2.1 (MJ/m^3 K)

15.2 Outline of GSHP System

Due to its high thermal performance, GSHPs have been introduced as an important option for reducing energy consumption. At the beginning of 2010 the totally installed GSHP capacity in the world was 50,583 MW producing 121,696 GWh/year [13]. In the US GSHPs have been promoted and shown as an important measure to reduce the greenhouse gas emissions [14].

GSHPs essentially refer to a combination of a heat pump and a system for exchanging heat with the ground.

Such systems move heat from the ground to heat buildings in the winter or alternatively, to cool them in the summer. This heat transfer process is achieved by circulating a heat carrier (water or a water–antifreeze mixture) between a ground heat exchanger (GHE) and heat pump. The GHE is plastic pipes installed vertically or horizontally under the ground surface. In the current study, two different configurations of vertical GHE 100 m deep were considered, see specifications in Table 15.1.

The temperature difference between the ground and the conditioned space is referred to as temperature lift. This temperature plays a major role in determining the coefficient of performance (COP = delivered energy/driving energy) of GSHPs. A smaller temperature lift results in a better COP. More specifically, extracting heat from a warmer ground during the heating season and injecting heat into a colder ground during cooling season leads to a better COP. Figure 15.1 shows the COP of heating and cooling machine as a function of fluid temperature for supply temperature of 35 and 10 °C, respectively [1–3].

15.3 Thermal Quality of Building Envelope and Thermal Load

The thermal quality of building envelope (TQBE) refers to the performance of the building shell as a barrier to unwanted heat transfer between the interior of the building and the outside environment. The TQBE plays the fundamental role in

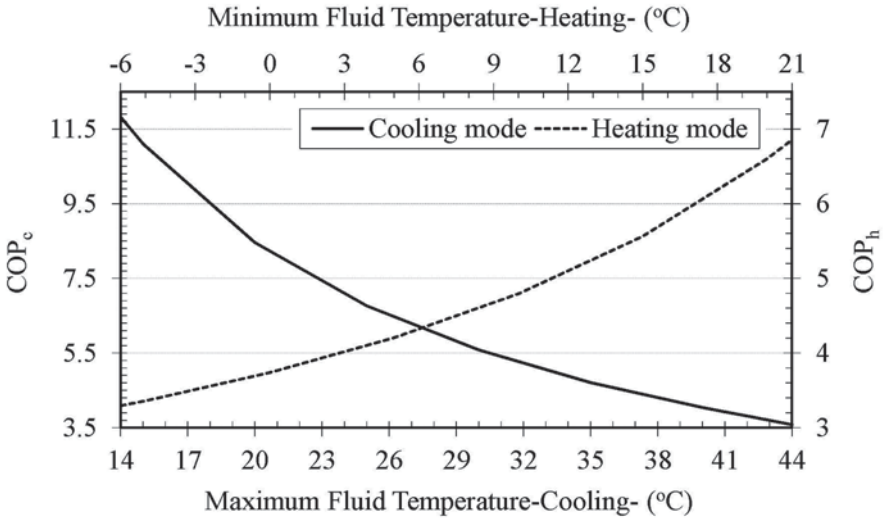

Fig. 15.1 Coefficient of performance (COP) as a function of fluid temperature [3, 4]

determining the thermal load of building and, consequently, determines the RHC. For instance, high TQBE can reduce heat losses from building to the point where internal heat gain and passive solar heat gain can offset a large fraction of the remaining heat loss. The TQBE depends on three factors: (1) insulation level of the exterior wall, ceiling, and floor; (2) thermal properties of windows; and (3) air tightness of the envelope.

Of the 150 million residential dwellings in the 15 EU Member States, approximately 72 % were built before 1972. Most of these buildings were built to standards that required far poorer TQBE than those imposed under current building regulations [15]. The maximum permitted heating load for new residential buildings, in Germany for instance, under the 1995 regulations was 65–100 kWh/m^2 year, while the actual average heating requirement of existing buildings is estimated to be 220 kWh/m^2 year [16]. This difference was attributed to the fact that the majority of existing buildings were built before 1995. Hence, there is a big potential for reducing energy use in buildings by improving the thermal characteristics of buildings. Recent reports by the Intergovernmental Panel on Climate Change (IPCC) have outlined broad strategies for reducing energy use in buildings and the related environmental implications.

It has been shown that different improvement measures of the TQBE (including increased insulation level and improving thermal properties of windows) result in different energy saving rates. Improving TQBE in a wide variety of US climates might lead to energy savings of 30–75 % [6–8]. Hamada et al. show under climate conditions of Japan, Finland, Germany, and Canada the energy saving due to improving the TQBE compared to the same house built according to the conventional standards is likely to fall between 30 and 40 % [9]. Under climate conditions of

Ankara, Demirbilek et al. show that a reduction in heating load of 45 % could be fulfilled by reorienting the facing of buildings (relative to the Sun) and increasing the insulation level of exteriors, floors and roofs of buildings [10]. Florides showed that using low-emissivity double glazing windows alone could reduce the cooling load by 24 % [11]. In cold-climate countries around the world, improving the TQBE could lead to a reduction in the heating load by 10 %.

In addition to reducing the heating load of buildings, improving the TQBE might affect the cooling load of a building as follows:

In cold climates, e.g. Nordic countries, where the internal heat gain dominates the cooling load of a building, insulating the exterior walls results in increasing cooling load of buildings [10, 12]. In addition to increased internal comfort requirements and internal heat gain, this might give a sufficient explanation for the increased need for mechanical cooling equipment in Nordic countries.

In hot climates, where the external heat gain dominates the cooling load of a building, increased insulation levels have greatly reduced buildings' heating and cooling loads compared to the same house built according to a lower insulation level [16, 17].

- However, in temperate climates either the internal or the external load may dominate the cooling load of a building, the effect of an increased level of insulation is less clear.

Simultaneously, improving the TQBE in new buildings using foam products for insulation (which have a relative low heat capacity), results in reducing thermal mass of the building envelope. Accordingly, the opportunity to use passive heating and cooling by shifting thermal loads on a time scale of hours has been reduced. Increasing thermal mass of building envelopes using phase-change materials (PCM) for example, has been a subject of considerable interest in the last decade. Kuznik et al. show that using a proper thickness of PCM wallboard improves the thermal inertia of buildings and thereby decreases temperature fluctuation inside the buildings [18]. However Florides et al. show that increasing thermal masses of walls and roofs utilizing night ventilation is not enough for lowering the house temperature to acceptable limits during summer [11].

15.4 Methodology

As shown in Table 15.2, in the current study three buildings (in three different cities) of the same size and geometry, but different TQBE are used.

The calculation process may be divided into five steps:

1. Determine the heating and cooling load for each building and three different GW scenarios,
2. Design the GHE to satisfy the heating and cooling load using Earth energy design model (EED) [19],

Table 15.2 Specifications of studied buildings in selected cities

		Stockholm	Rome	Riyadh
Indoor temperature (°C)	Winter	21	22	23
	Summer	23	24	25
Average base temperature (°C)	Heating	17.5	19	20
	Cooling	20	21	23
Building area (m^2)			150	
Building volume (m^3)			450	
Window to wall ratio (%)			15	
Ventilation flow rate (m^3/s)			0.12	
Wall U-value (W/m^2 K)	Poorer	0.3	0.7	1.5
	Current	0.15	0.5	1.1
	Better	0.09	0.3	0.8
Window U-value (W/m^2 K)	Poorer	1.75	3	3.5
	Current	1.25	2.5	3
	Better	0.9	2	2.5
Total heat loss coefficient (W/m^2 K)	Poorer	74	151	265
	Current	45	115	203
	Better	30	79	154

3. Estimate the corresponding COP by using Fig. 15.1,
4. Determine the corresponding electrical input energy (i.e., driving energy) by dividing the heating and cooling load by system's COP, and
5. Compare the driving energy for each assumed TQBE and each GW scenario.

These steps were repeated for each selected city, i.e. Stockholm, Rome, and Riyadh. The climate data can be found using METEONORM model [20].

Determination of the Heating and Cooling Load

The estimation of the heating and cooling load is difficult because of the dynamic influences of parameters such as occupancy patterns, building operating schedules and climatic conditions. However, the degree-hours (DH) method is a common method used to estimate the heating/cooling load of a building [5, 21–26]. The DH method does not explicitly take into account the effect of the sun on the cooling load of a building. This fault represents major inherent deficiencies of the DH method and results in a lower estimation of the cooling load.

Another available method that can be used to estimate the thermal load of buildings is the overall thermal transfer value (OTTV) method. OTTV is a measure of heat exchange between the outdoor and indoor environments through the external envelope of a building, which is typically used to determine the cooling load of buildings [27–29]. Unfortunately, OTTV has its inherent deficiencies, such as using the monthly average temperature in defining the cooling season. In addition, the need for air-conditioning takes place mostly during daytime in summer, while OTTV does not take this into consideration. Other deficiencies of OTTV have been

discussed by following reference [30]. Namely, the OTTV method may not truly reflect the thermal performance of the building envelope.

Therefore, in the current study, a new method that can be used to calculate the thermal load of buildings was developed. This new method, which is a combination of the OTTV and DH methods, proportionately expresses the thermal load of the building as a function of the thermal quality of the building envelope; temperature difference between indoor and outdoor; and number of heating/cooling hours as shown (see below). The heating load is:

$$Q_h = \sum_{i=1}^{N} \left[(K_{tot} + \rho C_p \cdot m_v) \cdot (T_{inh} - T_o) - A \cdot q_{in} \right]_j \tag{15.1}$$

The cooling calculation is more complex, as the walls receive different amounts of solar radiation at different orientations (i.e., different azimuth angle). Therefore, the general procedure is to calculate the thermal load due to conduction and solar effect on the wall and window with the same orientation and then add the thermal load due to internal heat gain and ventilation as follows:

$$Q_c = \sum_{i=1}^{M} \left[\begin{array}{l} \sum_{j=1}^{4} \left[K_j \cdot (T_o - T_{inc}) + (A_{w,j} \cdot U_w \cdot \alpha \cdot R_{so} + A_{f,j} \cdot SC_j \cdot SF_j) \cdot avg(I_t)_j \right] + \\ \rho C_p \cdot m_v \cdot (T_o - T_{inc}) + A \cdot q_{in} \end{array} \right] \tag{15.2}$$

Where K_j represents the total heat loss coefficient of the wall (opaque surface and fenestration) of direction j (W/K), see Eq. (15.5); T_{inh} and T_{inc} is indoor design temperature for heating and cooling season, respectively (°C). N is the number of hours provided that T_o (outdoor temperature) $\leq T_{bh}$ (base temperature of heating season), Eq. (15.7), and M is the number of hours provided that $T_o \geq T_{bc}$ (base temperature of cooling season), Eq. (15.8). m_v is the average air exchange rates (m^3/s); ρC_p is the volumetric thermal capacity of air (J/m^2 K); $A_{w,j}$ and $A_{f,j}$ is area of the opaque walls and fenestration with direction j, respectively, (m^2); U_w and U_f is the U-value of the opaque wall and fenestration, respectively, (W/m^2 K); q_{in} is internal thermal load (W/m^2); SC_j is the shading coefficient of fenestration (defined as the ratio of solar heat gain of the fenestration to solar heat gain of the standard reference glass); SF_j, solar factor for that orientation; α is absorption coefficient of the opaque wall surface; R_{so} is outside surface resistance (m^2 K/W). $avg(I_t)_j$ is average solar intensity per square meter falling on vertical surface with direction j, (W/m^2). This value can be calculated by using the available solar energy per square meter on the horizontal surface and incident angle of the wall surface as follows. The incident angle of vertical surface with direction j, θ_{ji}, is [31]:

$$\begin{aligned} \cos\theta_{ji} = & -\sin\delta_n \cdot \cos\varphi \cdot \cos\gamma_j + \cos\delta_n \cdot \sin\varphi \cdot \cos\gamma_j \cdot \cos\omega_i \\ & + \cos\delta_n \cdot \sin\gamma_j \cdot \sin\omega_i \qquad\qquad \omega_i < Ws \end{aligned} \tag{15.3}$$

This way, the average solar intensity per square meter falling on vertical surface with direction j is:

$$avg(I_t)_{ji} = \mathrm{SE_i} \cdot \cos\,\theta_{ji} \tag{15.4}$$

Here δ is declination angle on the day number n of the year, φ is location latitude, γ_j is azimuth angle of surface with direction j, w is hour angle at hour i; W_{sn} is the hour angle of the sunrise on day number n of the year. SE_i is available solar energy on horizontal surface at hour i (W/m^2), which can be taken from a local weather station or using METEONORM [20].

The magnitude of the total heat loss coefficient of the building wall of direction j depends on size, design, geometry, and the thermal performance of the external building shell as follows:

$$K_j = A_{w,j} \cdot U_w + A_{f,j} \cdot U_f \tag{15.5}$$

Thus, the total heat loss coefficient of the building shell, K_{tot}, is:

$$K_{tot} = \sum_{j=1}^{4} K_j = \sum_{j=1}^{4} A_{w,j} \cdot U_w + A_{f,j} \cdot U_f \tag{15.6}$$

The base temperature, T_b, depends on both the thermal quality of the building's envelope and use of building. A low value of T_b implies a highly insulated building [5, 25]. In this work, we have derived equations that can be used to estimate the base temperature of the heating and cooling seasons as follows:

$$T_{bh} = T_{inh} - \frac{A \cdot q_{in}}{K_{tot} + \rho C_p \cdot m_v} \tag{15.7}$$

$$T_{bc} = T_{inc} - \frac{A \cdot q_{in}}{K_{tot} + \rho C_p \cdot m_v} \tag{15.8}$$

It is important to mention that in the last equation, the effect of solar energy on the base temperature of the cooling season was not considered. Namely, the base temperature of the cooling season is a bit lower than that calculated using Eq. (15.8), but in the current study the T_{bc} will be calculated using Eq. (15.8).

In the above calculations the following assumptions were made:

- The opaque surface and fenestration in all orientations have the same thermal properties (i.e., all walls have the same outside surface resistance and absorption coefficient; windows have the same shading coefficient and solar factor in all directions.
- The external surfaces of buildings have the cardinal directions (i.e. N, W, S, and E).
- The reduction in heating load due to solar gain is not considered in heating calculation, which is the common approach in heating calculations.

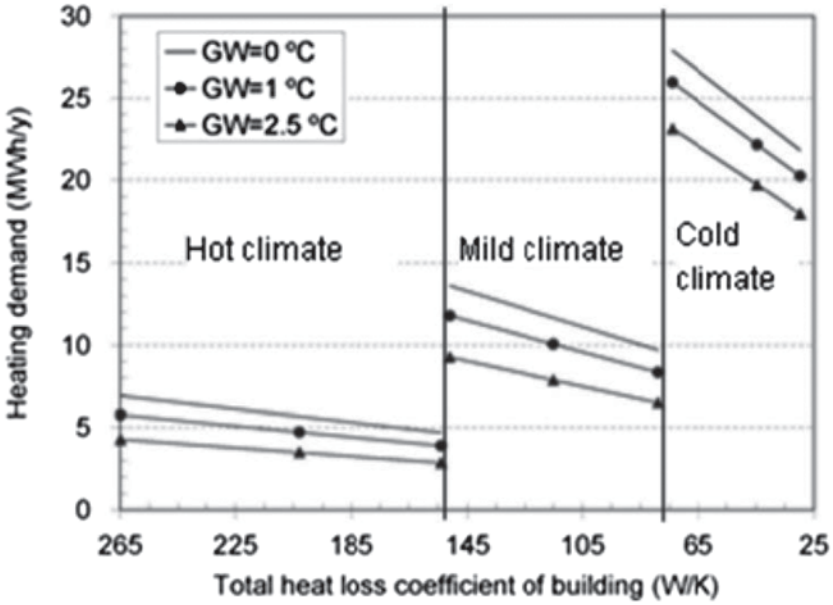

Fig. 15.2 Impact of GW and TQBE on heating load in three different climate categories

It is also important to mention that due to the fact that most residential buildings are high-rise (multiple storeys), the roof area is therefore small compared with the external wall area. In addition, most roofs of no skylight area have a lower U-value than the walls and hence, there is no solar heat gain through the roof and the heat conduction tends to be small. Consequently, heat gain/loss through the roof and floor is generally small compared with external walls. Therefore and for simplicity, only thermal transfer through walls was considered in the current study [28], $m_v = 0.12 m^3/s$, SC = 0.87, SF = 0.7, $\alpha = 0.75$, $R_{os} = 0.044$, and $q_{in} = 4$, which are reasonable [27, 28].

In this way the heating and cooling load was calculated for three different climate categories, three TQBE, and three different GW scenarios. The results are illustrated in Figs. 15.2 and 15.3.

The monthly heating share of the annual heating load was calculated by dividing the heating load of every month by the annual heating load. The monthly cooling share of the annual cooling load was calculated by dividing the cooling load of every month by the annual cooling load.

The calculations show that the monthly share of heating and cooling is changed due to increasing ambient air temperature (i.e., GW). As shown, monthly share of annual heating load increases during cold months and decreases during warmer months. This is considered as having a negative impact on GSHP performance. In contrast, the monthly share of the annual cooling load decreases during the warm months, while it is increasing during colder months. This is considered as having a positive impact on GSHP performance.

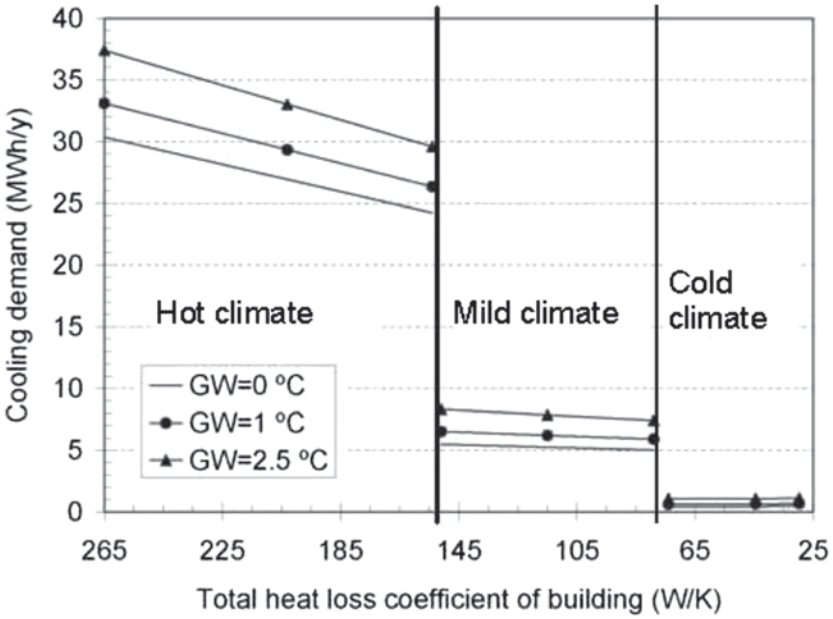

Fig. 15.3 Impact of GW and TQBE on cooling load in three different climate categories

Impact of Global Warming on Ground Temperature

Projections of future climatic conditions are usually described by different scenarios. These include uncertainties that must be taken into account in the interpretation of the results. As is mentioned above, in the current study it was assumed that the ambient air temperature will increase linearly over the next 50 years following two different scenarios i.e. a slow and a fast climate change projection. This assumption, i.e. linear increase of the global temperature, does not have a significant impact on the mean change in the ground temperature [32]. Based on these assumptions, Kharseh derived an equation that expresses the mean changes in ground temperature [33].

Figure 15.4 shows the mean changes of ground temperature versus the depth below ground surface due to changes in ambient air temperature.

Thus, if the warming rate follows the worst scenario then the mean change of ground temperature in 2060 over 100 m below the surface is ~0.8 °C. Consequently, today's performance of GSHP systems will not be the same in the future due to the increasing ground temperature. Furthermore, Fig. 15.4 reveals that shallow borehole systems will be more affected since the influence of GW on ground temperature is dampened by the depth below surface.

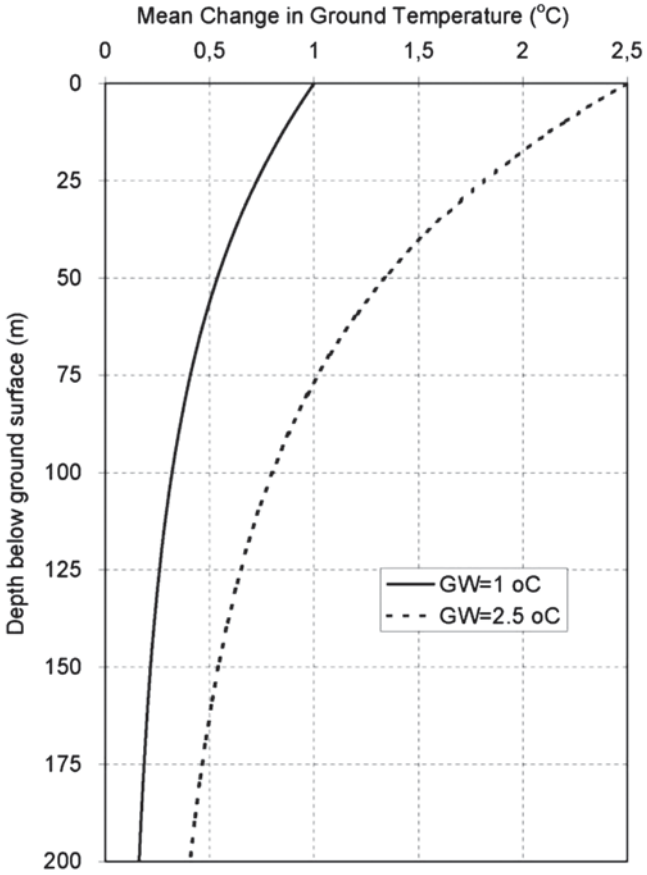

Fig. 15.4 Mean change of ground temperature after 50 years due to GW as a function of the depth. λ = 2.5 W/m K, C = 2.1 MJ/m^3 K

Driving Energy of GSHP System

The driving energy of the GSHP system to meet the heating/cooling load, which are illustrated in Figs. 15.2 and 15.3, was determined using Eq. (15.9):

$$E = \frac{Q_h}{cop_h} + \frac{Q_c}{cop_c} \tag{15.9}$$

In order to design GHE and consequently find out the COPh, and COPc, the EED model was used as follows, taking into consideration the assumptions in Table 15.1, [19]:

Table 15.3 The calculated coefficient of performance

City	K_{tot}	Performance	GW (°C)		
			0	1	2.5
Stockholm	74	COPh	3.60	3.66	3.74
		COPc	15.00	15.00	15.00
	45	COPh	3.68	3.73	3.83
		COPc	15.00	15.00	15.00
	30	COPh	3.73	3.79	3.88
		COPc	15.00	15.00	15.00
Rome	151	COPh	5.17	5.32	5.56
		COPc	8.59	8.14	7.53
	115	COPh	5.27	5.41	5.66
		COPc	8.60	8.19	7.63
	79	COPh	5.37	5.51	5.76
		COPc	8.63	8.23	7.72
Riyadh	265	COPh	10.00	10.00	10.00
		COPc	4.31	4.12	4.01
	203	COPh	10.00	10.00	10.00
		COPc	4.51	4.35	4.10
	154	COPh	10.00	10.00	10.00
		COPc	4.67	4.52	4.29

- Set the borehole depth at 100 m.
- Assume a value of COP for heating and cooling using Fig. 15.1.
- The resulting fluid temperatures (obtained using EED) were used to recalculate COP. This new value of COP is reused in EED.
- Repeat the last step until good matches between the maximum, minimum temperature and COP are reached.

The results are presented in Table 15.3 and are illustrated in Fig. 15.5. It can be seen that improving the TQBE results in reduced driving energy. Also, the GW has a positive and negative effect in cold and hot climates respectively.

Figure 15.6 shows the change in driving energy of GSHP system as a result of change in ambient air temperature of one degree. It can be seen that poorly insulated houses are more affected by climatic changes. Furthermore it can be seen that the GW has a positive effect in cold climates and a negative effect in hot climates.

Figure 15.7 shows the changes in driving energy of a GSHP system due to reducing the total heat loss coefficient of a building envelope by one unit (W/K), i.e. improving the TQBE. It can be seen that the benefit of improving the TQBE is the greatest in a cold climate and smallest in a mild climate. In addition, GW reduces the benefit of improving TQBE in cold climates, which is the opposite case in hot climate.

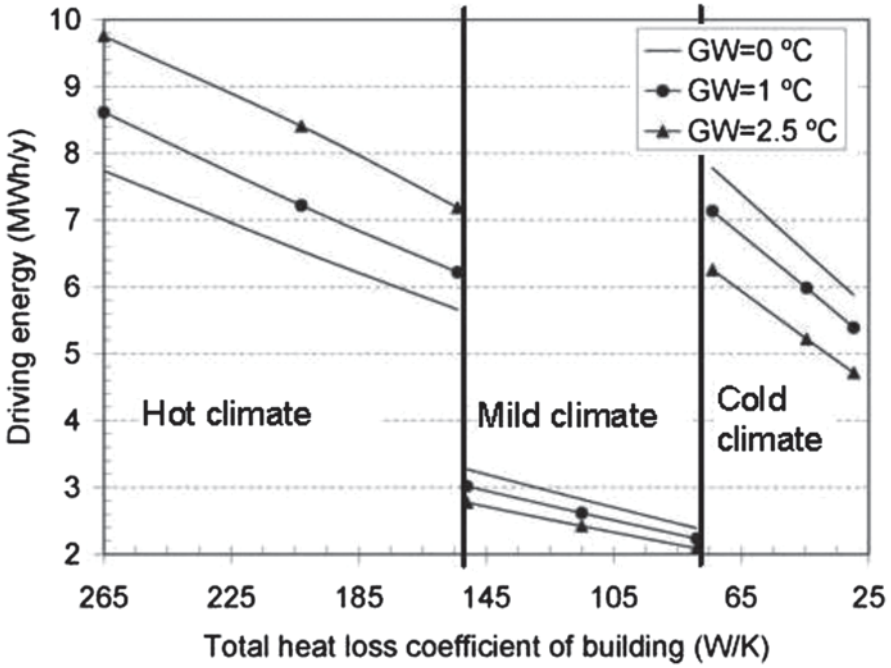

Fig. 15.5 Driving energy of GSHP as a function of GW and total heat loss coefficient of building envelope

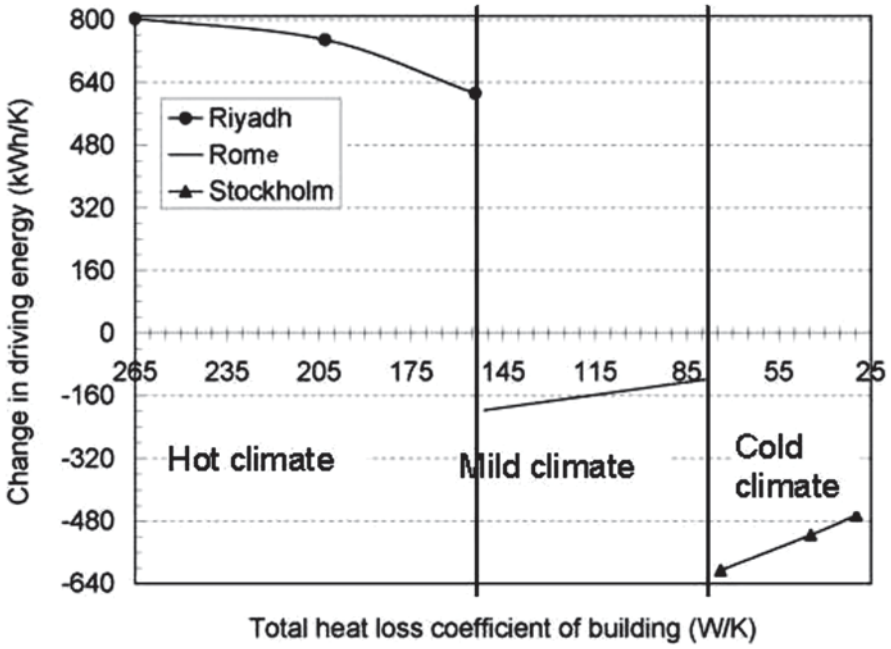

Fig. 15.6 Average changes in driving energy of GSHP (kWh) due to increasing the ambient air temperature by one degree (K)

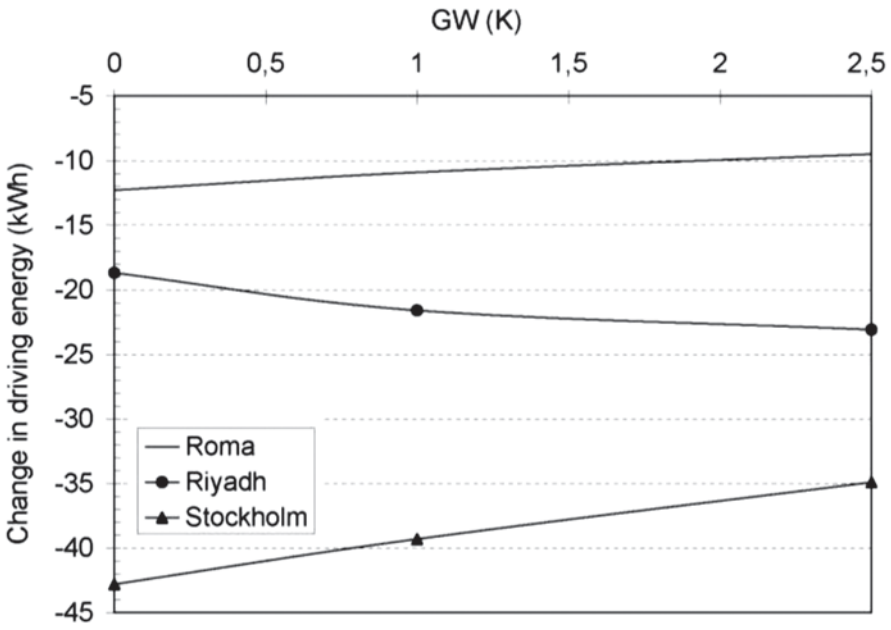

Fig. 15.7 Average reduction in driving energy of GSHP (kWh) due to reducing the total heat loss coefficient of buildings envelope one unit (W/K)

Conclusions

Performed calculations of the heating and cooling load, Figs. 15.2 and 15.3, show that;

- It is obvious that the ongoing warming reduces the heating load considerably more in cold regions than in warmer regions.
- Conversely, the effect of warming on the cooling load in hot climate is larger compared to the colder areas.
- Improving the TQBE always reduces the heating load, while varies for the cooling load. That is to say, improving TQBE reduces the cooling load in hot regions, while the effect is reversed for the cold areas.
- The rate change in cooling load due to improving TQBE in a hot climate is greater than that in a mild climate. In a cold climate, the cooling load tends to increase slightly with the improved TQBE.

Calculations show that due to GW, the monthly share of the annual heating load increases during cold months and decreases during warmer months. This is considered to have a negative impact on GSHP performance. In contrast, the monthly share of the annual cooling load decreases during the warm months, while it increases during colder months. This is considered to have a positive impact on GSHP performance. It is worth mention that similar results have been achieved by following reference [5].

The calculation of driving energy of a GSHP system, Fig. 15.5 shows that

- Improving the TQBE leads to reducing the driving energy of a GSHP system at different rates in different climates. In other words, the benefit of improving the TQBE is the greatest in a cold climate and smallest in a mild climate.
- Increasing the ambient air temperature increases the driving energy in hot regions, while GW decreases the driving energy in cold regions.
- It is obvious that buildings of poor TQBE are more sensitive to GW, Fig. 15.6.
- GW has a more significant impact on the driving energy in hot and cold regions compared with temperate regions, see Fig. 15.6.
- GW reduces the benefits of improving the TQBE in a cold climate, while it is the opposite case in a hot climate. Improving the TQBE has considerable impact on driving energy in hot and cold regions compared with temperate regions, see Fig. 15.7.

Nomenclature

$A_{f,j}$	fenestration area with direction j (m^2)
$avg(I_t)_j$	average solar intensity per square meter falling on vertical surface with direction j (W/m^2)
$A_{w,j}$	opaque walls area with direction j (m^2)
COPc	coefficient of performance of cooling mode (dimensionless)
COPh	coefficient of performance of heating mode (dimensionless)
E	required driving energy of the GSHP (MWh)
K_j	total heat loss coefficient of the wall (opaque surface and fenestration) of direction j (W/K)
K_{tot}	total heat loss coefficient of building shell (W/K)
M	number of hours provided that $T_o \geq T_{bc}$
m_v	average air exchange rates (m^3/s)
N	number of hours provided that $T_o \leq T_{bh}$
Q_c	cooling load (MWh)
Q_h	heating load (MWh)
q_{in}	internal thermal load (W/m^2)
R_{so}	outside surface resistance (m^2 K/W)
SC_j	shading coefficient of fenestration with direction j
SE_i	available solar energy on horizontal surface at hour i (W/m^2)
SF_j	solar factor for direction j
T_{bc}	base temperature of cooling season (°C)
T_{bh}	base temperature of heating season (°C)
T_{inc}	indoor design temperature for season (°C)
T_{inh}	indoor design temperature for heating season (°C)
T_o	outdoor temperature (°C)
U_f	U-value of the fenestration (W/m^2 K)
U_w	U-value of the opaque wall (W/m^2 K)
W_{sn}	hour angle of the sunrise on day number n of the year
A	building floor area (m^2)
ρC_p	volumetric thermal capacity of air (J/m^2 K)

Greek Symbols

α absorption coefficient of the opaque wall surface
γ_j azimuth angle of surface with direction j
δ declination angle on the day number n of the year
ε global warming rate (°C/s)
θ_{ji} incident angle of vertical surface with direction j
φ location latitude angle
φ location latitude
ω hour angle at hour i

Acronyms

DH degree-hours
EED Earth energy design model
GSHP ground source heat pump system
GW global warming
OTTV overall thermal transfer value
TQBE The thermal quality of building envelope

References

1. Hepbasli A (2005) Thermodynamic analysis of a ground-source heat pump system for district heating. Int J Energy Res 29:671–687
2. Kharseh M (2009) Reduction of prime energy consumption in the Middle East by GSHP systems. Licentiate Thesis, Luleå University of Technology
3. Kharseh M, Nordell B (2011) Sustainable heating and cooling systems for agriculture. Int J Energy Res 35:415–422
4. De Swardt CA, Meyer JP (2001) A performance comparison between an air-source and a ground-source reversible heat pump. Int J Energy Res 25:899–910
5. Kharseh M, Altorkmany L, Nordell B (2011) Global warming's impact on the performance of GSHP. Renew Energy 36:1485–1491
6. Rudd A, Kerrigan P, Ueno K (2004) What will it take to reduce total residential source energy use by up to 60 %. ACEEE Summer Study on Energy Efficiency in Buildings 1:293–305
7. Gamble D, Dean B, Meisegeier D, Hall J (2004) Building a path towards zero energy homes with energy efficient upgrades. ACEEE 1:95–106
8. Holton JK (2002) Base loads (lighting, appliances, DHW) and the high performance house. ASHRAE Trans 108 (Part 1):232–242
9. Hamada Y, Nakamura M, Ochifuji K, Yokoyama S, Nagano K (2003) Development of a database of low energy homes around the world and analyses of their trends. Renew Energy 28:321–328
10. Demirbilek FN, Yalciner UG, Inanici MN, Ecevit A, Demirbilek OS (2000) Energy conscious dwelling design for Ankara. Build Environ 35:33–40
11. Florides GA (2002) Measures used to lower building energy consumption and their cost effectiveness. Appl Energy 73:299–328
12. Kharseh M, Altorkmany L (2012) How global warming and building envelope will change buildings energy use in central Europe. Appl Energy 97:999–1004

13. Lund JW, Freeston DH, Boyd TL (2010) Direct utilization of geothermal energy 2010 worldwide review. World Geotherm Congress 2010:1–23
14. L'Ecuyer M (1993) The potential of advanced residential space conditioning technologies for reducing pollution and saving consumers money, Report of the US Environmental Protection Agency. EPA 430-R-93-004
15. Gaterell MR (2005) The impact of climate change uncertainties on the performance of energy efficiency measures applied to dwellings. Energy Build 37:982–995
16. Harvey LDD (2009) Reducing energy use in the buildings sector: measures, costs, and examples. Energy Efficiency 2:139–163
17. Huang J, Hanford J, Yang F (1999) Residential heating and cooling loads component analysis. LBNL-44636
18. Kuznik F (2008) Optimization of a phase change material wallboard for building use. Appl Therm Eng 28:1291–1298
19. Blomberg T, Claesson J, Eskilson P, Hellström G, Sanner B (2000) Earth energy designer. Blocon, 2.0
20. METEONORM (2004) Global meteorological database for engineers, planners and education. Meteotest Genossencschaft, V7.0.22.8
21. Papakostas K, Mavromatisb T, Kyriakisa N (2010) Impact of the ambient temperature rise on the energy consumption for heating and cooling in residential buildings of Greece. Renew Energy 35:1376–1379
22. Durmayaz A, Kadioglu M, Sen Z (2000) An application of the degree-hours method to estimate the residential heating energy requirement and fuel consumption in Istanbul. Energy 25:1245–1256
23. Guttman NB, Lehman RL (1992) Estimation of daily degree-hours. J Appl Meteorol 31:797–810
24. Kadioglu M, Sen Z (1999) Degree-day formulations and application in Turkey. J Appl Meteorol 38:837–846
25. Christenson M, Manz H, Gyalistras D. (2006) Climate warming impact on degree-days and building energy demand in Switzerland. Energy Convers Manage 47:671–686
26. Jiang F (2009) Observed trends of heating and cooling degree-days in Xinjiang Province, China. Theor Appl Climatol 97:349–360
27. Wong SL, Wan KKW, Li DHW, Lam JC (2010) Impact of climate change on residential building envelope cooling loads in subtropical climates. Energy Build 42:2098–2103
28. Lam JC, Tsang CL, Li DHW, Cheung SO (2005) Residential building envelope heat gain and cooling energy requirements. Energy 30:933–951
29. Lam JC (2000) Energy analysis of commercial buildings in subtropical climates. Build Environ 35:19–26
30. Yik FWH, Wan KSY (2005) An evaluation of the appropriateness of using overall thermal transfer value (OTTV) to regulate envelope energy performance of air-conditioned buildings. Energy 30:41–71
31. Duffie JA, Beckman WA (2006) Solar engineering of thermal processes, 3 edn. Wiley, Malden
32. Lachenbruch AH, Marshall BV (1986) Changing climate: geothermal evidence from permafrost in the Alaskan Arctic. Science 234:689–696
33. Kharseh M (2014) Ground response to global warming. Submitted

Chapter 16
Concentrated Solar Power: A Vision for Rajasthan

Nishant Aggarwal and Dinesh Khanduja

Abstract Different technologies for solar thermal power plants making use of concentrating solar energy systems are:

- Parabolic troughs,
- Central receivers (towers) and
- Parabolic dishes.

A project of solar trough field combined with a gas fired combined cycle power plant (Integrated Solar Combined Cycle—ISCC) in Rajasthan for the generation 140 MW will have annual abatement of 714,400 t of CO_2 emissions, use of primary fuel (LNG), overcome dust problems, solar energy collected by the solar field during the day will be stored in the storage system and then dispatched after sunset, additional capacity of 100–150 MW can reduce electricity problems, 24 h operation facility and supply of both heat and electricity at least prices. The ISCC will operate as base load plant with and expected plant load factor of 80 %. It will have 35 MW capacity solar thermal block of parabolic trough and 105 MW combined cycle block using natural gas. The ISCC plant will comprise a solar field to support a 35–40 MW solar thermal plants combined cycle power block involving two gas turbines of 70 MW connected to the Heat Recovery Steam Generator (HRSG) and a steam turbine of 70 MW connected to both HRSG. The project will be the first of its kind in the world where solar thermal energy will be integrated into combined cycle power block. This project could easily decrease both electricity charges as well as installation charges of the power plant in India.

Keywords Parabolic troughs · Central receivers · Parabolic dishes · CO_2 emissions · Heat exchanger · Steam turbine · Climate and cost conditions

N. Aggarwal (✉) · D. Khanduja
Mechanical Department, NIT, Kurukshetra, Haryana, India
e-mail: nishant.aggarwal.nitk@gmail.com

D. Khanduja
e-mail: dineshkhanduja@yahoo.com

I. Dincer et al. (eds.), *Progress in Sustainable Energy Technologies: Generating Renewable Energy,* DOI 10.1007/978-3-319-07896-0_16,

16.1 Introduction

In solar thermal power plants the incoming radiation is tracked by large mirror fields which concentrate the energy towards absorbers. They, in turn, receive the concentrated radiation and transfer it thermally to the working medium. The heated fluid operates as in conventional power stations directly (if steam or air is used as medium) or indirectly through a heat exchanging steam generator on the turbine unit which then drives the generator. To make solar high flux, with high energetic value originating from processes occurring at the sun's surface at black-body-equivalent temperatures of approximately 5800 K usable for technical processes and commercial applications, different concentrating technologies have been developed or are currently under development for various commercial applications. Such solar thermal concentrating systems will undoubtedly provide within the next decade a significant contribution to efficient and economical, renewable and clean energy supply.

The solar thermal technologies comply with the prime objectives and key research, technology, and demonstration actions because their developments will enhance the deployment of solar energy systems for bulk electricity production and the conservation of fossil energy, consequently preserving the environment in particular with respect to their high potential to contribute to the reduction of the CO_2 emissions, they reduce the generating costs of solar power plants, and thus contribute to ensure durable and reliable energy services at affordable costs in the medium- to long-term range, to the quality of life, health, safety (including working conditions) and job creation. The erection of such plants at undeveloped areas can create new opportunities of industrial fabrication, of assembling and of operation and maintenance.

Since 1985 nine parabolic trough-type solar thermal power plants in California have fed more than 8 billion kWh of solar-based electricity into the Southern Californian grid, demonstrating the soundness of the concept. A recent expertise of the World Bank has shown solar thermal cost reductions below 6 US cents/kWh after the year 2010, convincing the Global Environment Facility (GEF) to support barrier removal and market introduction of solar thermal power in developing countries. India, Egypt, Morocco and Mexico have now applied within the GEF Operational Programme for about 50 million US-$ GEF grant for each project to cover their incremental costs of solar thermal power projects.

Parabolic Trough Systems

Trough systems use linear concentrators of parabolic shape with highly reflective surfaces, which can be turned in angular movements towards the sun position and concentrate the radiation onto a long-line receiving absorber tube [1, 2]. The absorbed solar energy is transferred by a working fluid, which is then piped

to a conventional power conversion system. The used power conversion systems [5] are based on the conventional Rankine-cycle/steam turbine generator or on the combined cycle (gas turbine with bottoming steam turbine).

Technology Shortages Parabolic trough systems have the following technology shortages [1, 2]:

- The upper process temperature is currently limited by the heat transfer thermal oil to 400 °C.
- The heat transfer thermal oil adds extra costs of investment and of operating and maintenance.
- Depending on national regulations, environmental constraints from ground pollution by spillage of thermal oil could occur.
- Some absorber tubes are still object of early degradation; reasons are the risk of breakage of absorber envelope glass tubes with loss of vacuum insulation and degradation of the absorber tube selective coating.
- High winds may break mirror reflectors at field corners.
- Low-cost and efficient energy storage systems have not been demonstrated up to now.
- The direct steam generation trough technology is still in a developmental stage.

Central Receiver Systems

Central receiver systems use heliostats to track the sun by two axes mechanisms following the azimuth and elevation angles with the purpose to reflect the sunlight from many heliostats oriented around a tower and concentrate it towards a central receiver situated atop the tower [1, 2]. This technology has the advantage of transferring solar energy very efficiently by optical means and of delivering highly concentrated sunlight to one central receiver unit, serving as energy input to the power conversion system.

In spite of the elegant design concept and in spite of the future prospects of high concentration and high efficiencies, the central receiver technology needs still more research and development efforts and demonstration of up-scaled plant operation to come up to commercial use. Its main attraction consists in the prospect of high process temperatures generated by highly concentrated solar radiation to supply energy to the topping cycle of any power conversion system and to feed effective energy storage systems able to cover the demand of modern power conversion systems. The solar thermal output of central receiver systems can be converted to electric energy in highly efficient [5] Rankine-cycle/steam turbine generators, in Brayton-cycle/gas turbine generators or in combined cycle (gas turbine with bottoming steam turbine) generators. Grid-connected tower power plants are applicable up to about 200 MW solar-only unit capacity.

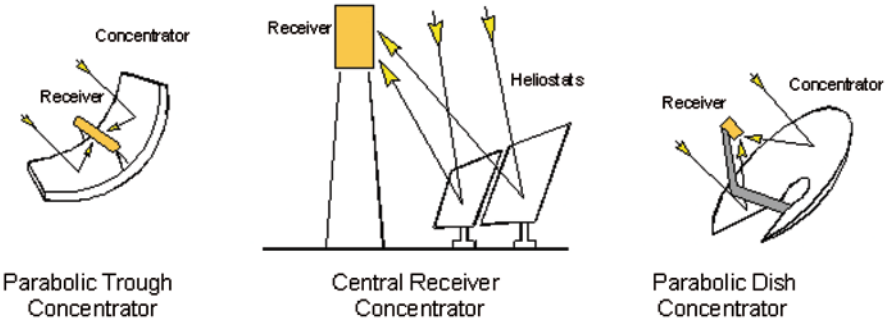

Fig. 16.1 Schematic diagram of three concepts of concentrating solar thermal electricity generation: (a) Parabolic trough, (b) Central receiver (tower), (c) Parabolic dish [6]

Technology Shortages Central receiver systems have the following technology shortages [1, 2]:

- No successful scaled-up central receiver plants are available for commercial demonstration up to now, although more than six experimental and pilot demonstration central receiver plants were successfully operated world-wide since 1981.
- Not yet verified is the good potential projected for the improvement of solar system performance and for cost reductions.
- Not yet verified are projections of the installed plant capital costs, operation and maintenance costs, electricity costs, solar subsystem performance, operational characteristics and of the annual plant availability.
- The industrial demonstration of volume production of heliostat components is still missing.

Parabolic Dish Systems

Dish systems use parabolic reflectors in the shape of a dish to focus the sun's rays onto a dish-mounted receiver at its focal point [1, 2]. In the receiver a heat-transfer medium takes over the solar energy and transfers it to the power conversion system, which may be mounted in one unit together with the receiver (e.g. receiver/Stirling engine generator unit) or at the ground. Due to its ideal optical parabolic configuration and its two axes control for tracking the sun, dish collectors achieve the highest solar flux concentration, and therefore the highest performance of all concentrator types in terms of peak solar concentration and of system efficiency. These collector systems are restricted to unit capacities of some 10 KW for geometrical and physical reasons. The dish technology is applicable to off-the-grid power generation, i.e. at remote places or at island situations. Dish systems may optionally be arranged in large dish arrays in order to accumulate the power output from the KW capacity up to the MW range. It requires some more continued R&D activities and demonstration before start of market introduction (Fig. 16.1).

Technology Shortages Parabolic dish systems have the following technology shortages [1, 2]:

- The electricity output of single dish/Stirling unit is limited to small ratings of e.g. 25 KW due to geometric and physic reasons (exception: Australian big dish designed for use of a 50 KW steam engine or turbine generator).
- Large-scale deployment has not yet occurred.
- No commercial demonstration has been performed up to date.
- Not yet demonstrated or verified are projections of capital costs, operation and maintenance costs, electricity costs, system performance and of the annual plant availability over the long run.
- The predicted potential for improvements of solar system performance and of cost reductions is still to be verified.
- Hybrid systems have inherent low-efficient combustion and have to be proven.
- No adequate energy storage system is applicable or available.
- The establishment of industrial large volume production of dish components and Stirling engines is needed for entry into appropriate market segments.

16.2 Goals for Research & Development (R&D)

There are the following main goals for solar thermal power plants [1–3]:

- Of highest importance is the erection of large solar thermal power plants having at least units of equivalent solar capacities of 10 MW or even more favourable 100 MW to ensure a significant contribution to the environmentally safe electricity production in the country.
- Essential objectives of R&D activities concern the development of improved and optimized components and subsystems. In essence, the most important features and cost-reducing items considered are the qualification and demonstration of direct steam generation for parabolic troughs, the reliable utilization of volumetric air and molten salt receiver techniques for central receiver systems, the hybrid operation of saturated steam central receiver systems and of the hybrid operation of dish/Stirling systems.
- The integrated hybrid solar/fossil solutions (ISCCS plants) have to be followed up. They link proven solar thermal and conventional technologies through optimized integration of solar thermal energy into fossil-fired power plants, particularly into combined cycle power stations. Such applications are not only door openers for solar applications, but in fact represent a most realistic strategy.
- Finally, an effective answer to the problematic issue of energy storage systems is obligatory. As a short-term goal, guaranteed electricity delivery from a buffer storage or short-period storage capacity is advisable, and as a long-term objective solar-only operation from large storage capacities (Fig. 16.2) (Tables 16.1, 16.2, 16.3 and 16.4).

Fig. 16.2 Rajasthan physical map

Table 16.1 Climatological conditions

Parameters	Values
Sunshine hour	Annual daily average 8 h
Ambient temp	20–33 °c
Relative humidity	54–26 %
Concentration of dust	< 300 μg/m^3

16.3 Study Area

Environmental Issues Coal plants usually have emissions of 900–1100 kg CO_2/MWh and oil plants around 600–700 kg CO_2/MWh, while CSP plants 10–50 kg CO_2/MWh. Starting with 1400 million t of carbon dioxide per year in the year 2000, the emissions are reduced to 350 Mt/y in 2050, instead of growing to 2300 Mt/y (Fig. 16.3).

Assumed that 1 € = Rs. 65 and 1 K = 1000 Units (Fig. 16.4)

Table 16.2 Computed solar radiation (kWh m^{-2} day^{-1}) at different arid station in Rajasthan

Station	Winter (Dec–Feb)	Summer (March–May)	Monsoon (Jun–Sep)	Post monsoon (Oct–Nov)	Annual average	Annual total (kWh m^{-2} $year^{-1}$)
Jodhpur	4.92	6.93	6.43	5.52	5.92	2160
Bikaner	4.67	7.33	7.27	5.38	6.16	2250
Jaisalmer	4.84	7.36	7.39	5.52	6.27	2290
Barmer	4.92	7.36	6.82	5.57	6.16	2250
Hanumangarh	4.20	6.33	6.10	5.60	5.55	2025

Table 16.3 Cost analysis [4]

Year	Installed capacity (MW)	Installation cost (€/KW)	Electricity cost (€/KW)	Installation cost (Rs./KW)	Electricity cost (Rs./KW)
2006	1918	2000–3000	0.10–0.16	130−195 K	6.5–104
2010	4498	1500–2000	0.08–0.12	97.5−130 K	5.2–6.5
2020	30000	1000–1500	0.06–0.09	6.5−97.5 K	3.9–5.85

Table 16.4 Land requirement

CSP capacity (MW)	Land requirement (km^2)
30	0.9
250	3.1
1000	12.3
6000	74.2

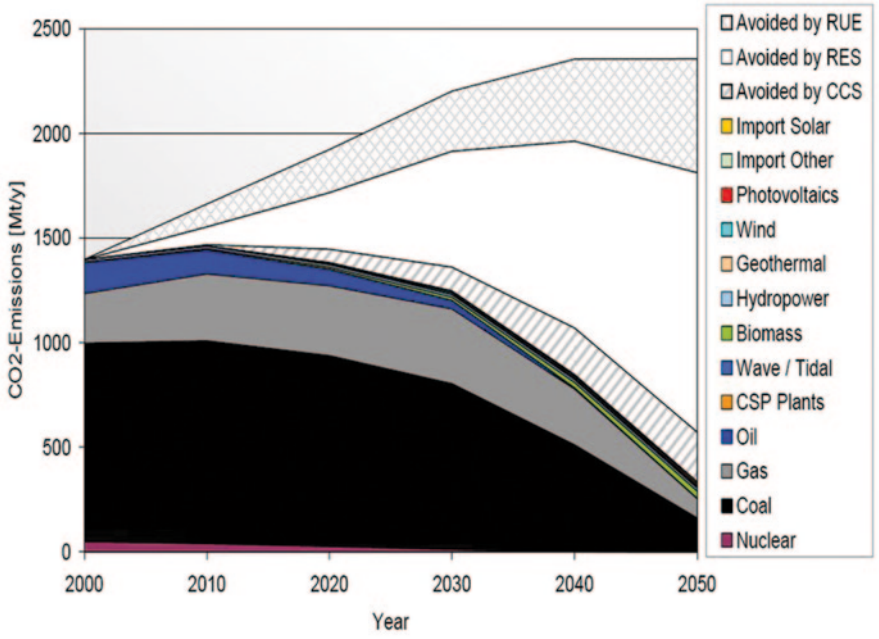

Fig. 16.3 The emission of CO_2 by various plants in all countries

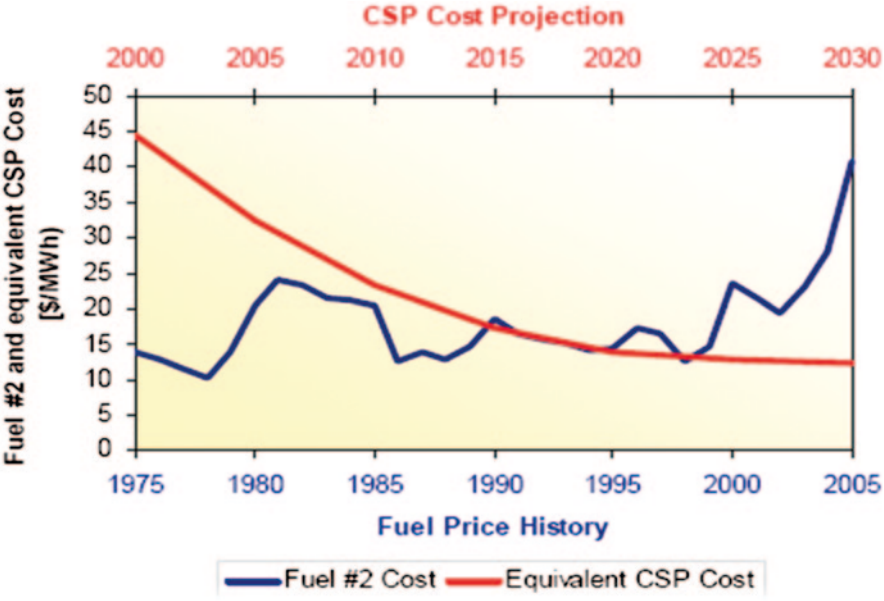

Fig. 16.4 Historical prices of fuel oil #2 and cost of equivalent solar energy from concentrating solar power projected for a comparative time span of 30 years

16.4 Results and Discussions

Solar Radiation > 6.0 kw/m^2 day avg.

Solar irradiation in Rajasthan ranges between 5.8 and 6.4 kWh/m^2/day on average for the year. It is more than sufficient levels (2,000 kWh of sunlight radiation per m^2 annually) for operating a solar thermal plant.

A project of solar trough field combined with a gas fired combined cycle power plant (Integrated Solar Combined Cycle—ISCC) in Rajasthan for the generation 140 MW will have following major points:

1. The operation of plant will result in an annual abatement of 714,400 t of CO_2 emissions, as compared to a hard coal power plant of average efficiency in Rajasthan (e.g. Suratgarh).
2. The primary fuel for the gas turbine LNG (Liquefied Natural Gas) can be used.
3. Problem of dust can be overcome by cleaning concentrated once a week by water or air jets.
4. Solar energy collected by the solar field during the day will be stored in the storage system and then dispatched after sunset.

It will be based on the integrated operation of the parabolic trough solar plant with a combined cycle gas turbine using fossil fuels such as Naphtha, fuel oil or low sulphur heavy stock (LSHS). The ISCC will operate as base load plant with and

expected plant load factor of 80 %. It will have 35 MW capacity solar thermal block of parabolic trough and 105 MW combined cycle block using natural gas. The ISSC plant will comprise a solar field to support a 35–40 MW solar thermal plants combined cycle power block involving two gas turbines of 70 MW connected to the Heat Recovery Steam Generator (HRSG) and a steam turbine of 70 MW connected to both HRSG. The steam turbine will receive the steam from the waste heat recovery boiler as well as from a solar field of approximately 220,000 m^2 parabolic trough collectors. A central building will have a central microprocessor control system that monitoring and controls all operations. The project will be the first of its kind in the world where solar thermal energy will be integrated into combined cycle power block.

Conclusions

1. Solar thermal power plant based on parabolic trough system is most suitable power plant for Rajasthan. It produces cheapest electricity among all solar plants.
2. In the near future of around 2020, the net electricity charges in India would decrease by 25 % and net installation charges of the power plant would decrease by 33.33 %.
3. Least land requirement would be there for the given 140 MW installation capacity.
4. Higher cost of installation can be overcome with mass production of concentrators and saving the cost of elimination of CO_2.
5. The provision of an additional capacity of 100–150 MW will reduce the electricity shortage in state.
6. They can be installed in hybrid applications to allow for 24-h operation.
7. Remote applications (from 10 KW installed capacity) which can be used to provide heat and electricity in small villages.
8. The plant will have 35 MW capacity solar thermal block of parabolic trough and 105 MW combined cycle block using natural gas.
9. The plant will be the first of its kind in the world where solar thermal energy will be integrated into combined cycle power block.

References

1. Becker M, Meinecke W (eds) (1992) Solar thermal technologies, comparative study of central receiver, parabolic trough, parabolic dish and solar chimney power plants (in German). Springer, Berlin
2. Chavez JM, Kolb GJ, Meinecke W (1993) In: Becker M, Klimas P (eds) Second generation central receiver technologies, a status report. C. F. Müller, Karlsruhe

3. Meinecke W, Bohn M (1995) In: Becker M, Gupta B (eds) Solar energy concentrating systems, applications and technologies. DLR C. F. Mueller, Heidelberg
4. Cohen GE, Kearney DW, Kolb GJ (1999) Final report on the operation and maintenance improvement program for concentrating solar power plants. SANDIA Report SAND99-1290, June 1999
5. Stine WB, Diver RB (1994) A compendium of solar dish/stirling technology. SANDIA Report SAND93-7026 UC-236, January 1994
6. www.powerfromthesun.net. Accessed 18 Jan 2014

Chapter 17
Dynamic Exergy Analysis of a Solar Ejector Refrigeration System with Hot Water Storage Tank

Hooman Golchoobian, Ali Behbahaninia, Majid Amidpour and Omid Pourali

Abstract A dynamic model is proposed to use in investigating the exergy analysis of a solar ejector refrigeration system using R141, for office air conditioning application for a building in Tehran. Classical hourly outdoor temperature and solar radiation model in a hot summer day were used to provide basic data for analysis. To improve the efficiency of the system a hot water storage tank is used and analyzed dynamically. The results show that dynamic analysis is confidently more useful than analysis in a constant condition. This method is more completed because it can present efficiency of the system components at each time. The components have different efficiencies at different days and hours. Collector has the highest level of irreversibilities and ejector is in the next step. Irreversibilities at the first and the last hours of working-time are higher. In addition, using the hot water storage tank decreased auxiliary heating in the afternoon.

Keywords Solar ejector refrigeration system · Exergy · Dynamic analysis · Storage tank

17.1 Introduction

Ejector refrigeration is a thermally driven technology that has been used for cooling applications for many years. In their present state of development they have a lower COP than vapor compression systems but offer advantages of simplicity and no moving parts. Their greatest advantage is their capability to produce refrigeration using waste heat or solar energy as a heat source at temperatures above 80 °C.

H. Golchoobian (✉) · A. Behbahaninia · M. Amidpour · O. Pourali
Mechanical Engineering Faculty, K.N. Toosi University of Technology, Tehran, Iran
e-mail: h.golchoobian@gmail.com

M. Amidpour
e-mail: amidpour@kntu.ac.ir

O. Pourali
e-mail: o.pourali@kntu.ac.ir

I. Dincer et al. (eds.), *Progress in Sustainable Energy Technologies: Generating Renewable Energy,* DOI 10.1007/978-3-319-07896-0_17,

The idea of solar ejector refrigeration system was advanced by Srinivasa Murthy et al. [1] and M. Sokolov et al. [2, 3]. After that numerical and experimental works were done for the system optimization which has been reported in literatures by B. Zhang et al. [4] and K. Chunnanond et al. [5]. Lots of experimental studies by S. Aphornratana et al. [6], B. J. Huang et al. [7], A. Selvaraju et al. [8], A. Selvaraju et al. [9], I. W. Eames et al. [10] and T. Sankarlal et al. [11] were done on this system for analyzing the effect of operation conditions such as the generator temperature, evaporator temperature, and condenser temperature, geometrical condition of nozzle, research about refrigerant and collector selection, on the performance of system. Using numerical method for ejector simulating is presented by E. D. Rogdakis et al. [12] who tried to improve the system performance. A. Arbel et al. [13], X. J. Zhang et al. [14] and J. L. Yu et al. [15] combined the system with different refrigeration system to improve the performance. For improving this system through the exergy analysis method nothing important is done except one article by Pridasawas [16] that researcher analyzed the solar ejector refrigeration components by exergy method in a constant weather and radiation condition. The results of exergy analysis of the system in a constant solar radiation are not close to a real system condition. Moreover not using storage tank in the system and its analysis is another disadvantage of previous researches.

The aim of this article is analyzing the components of solar ejector refrigeration system in a dynamic situation. To improve the efficiency of the system a hot water storage tank is used and analyzed dynamically. Dynamic exergy analysis of components based on weather solar radiation variation in a selected day is done and the results are discussed.

17.2 System Description and Assumptions

The solar ejector refrigeration system is shown in Fig. 17.1. It comprises of two loops, one is solar collection loop which is the main energy source of ejector refrigeration system and the other is ejector refrigeration loop which supplies useful cooling to the user. In the power subsystem, the refrigerant flows through the generator, the ejector, the condenser and the circulating pump, and finally flows back to the generator to supply high pressure motive fluid to the ejector. In the refrigeration subsystem, the refrigerant flows through the ejector, the condenser, the expansion valve, the evaporator, and then back to the suction of the ejector to supply the required cooling capacity.

The exergy analysis of the solar-driven ejector refrigeration system was performed assuming the following conditions.

- Evacuated tubular solar collector is used.
- R141 is used as the refrigerant for the refrigeration cycle.
- Water is used as the heating medium between the solar collector and the generator.
- The cooling capacity is 5 kW.

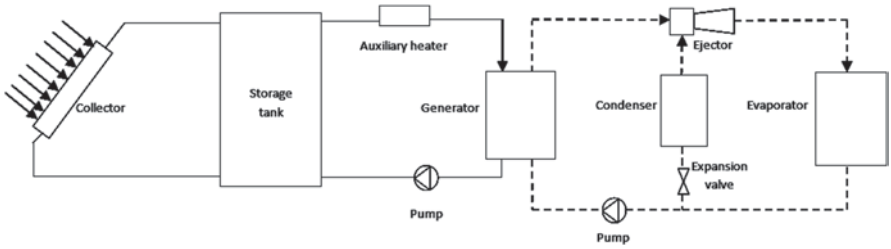

Fig. 17.1 Schematic diagram of solar ejector refrigeration system

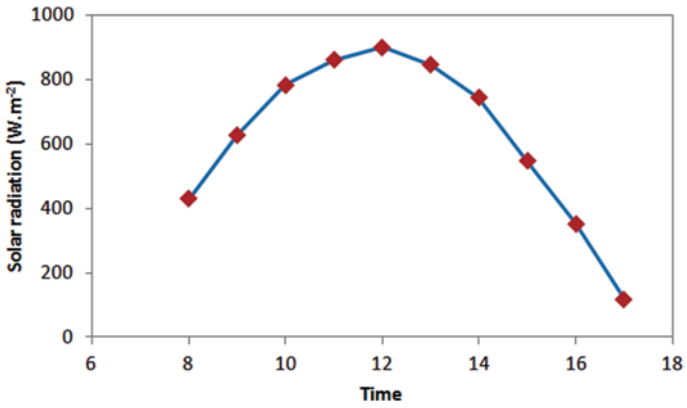

Fig. 17.2 Solar radiation during the selected day

- The generating temperature is 85 °C.
- The condensing temperature is 35 °C.
- The evaporation temperature is 8 °C.
- The pump efficiency is assumed to be 25 %,
- The total efficiency of the ejector is assumed to be 70 %.

For performing dynamic exergy analysis of the system, solar radiation in a selected day of Tehran is required. This is presented in Fig. 17.2.

17.3 Mathematical Model and Performance Criteria

A flat plat solar collector with double glass cover is selected. The efficiency of collector is calculated from Eq. (17.1).

$$\eta = F_R(\tau\alpha)_e - F_R U_L \frac{(T_i - T_a)}{1} \tag{17.1}$$

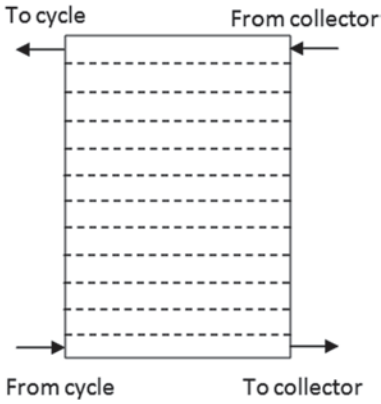

Fig. 17.3 Storage tank

A storage tank is used for energy saving. In Fig. 17.3 inlets and outlets of tank is shown. For analyzing the tank temperature, 12 fully mixed parts are considered. For temperature stratified water tank, having a variable inlet design, a collector control function F_i^C is defined to identify which node receives water from the collector; The equations for tank analysis is the same as the equations were used by E. M. Kleinbach et al. [17]. The liquid returning from the load can be controlled in a similar manner with a load return control function F_i^L. Along with the above given control functions, and taking into account of the axial heat conduction between nodes, an energy balance on node i can be expressed as:

$$\begin{aligned} m_i C_p \frac{\partial T_{s,i}}{\partial t} &= (UA)_i \left(T_a - T_{s,i}\right) + F_i^C F_{CO} m_C C_p \left(T_{c_r} - T_{s,i}\right) \\ &\quad + F_i^L F_{AU} C_p m_L \left(T_{L_r} - T_{s,i}\right) + \lambda A \Delta x \frac{\partial^2 T_{s,i}}{\partial x^2} + Q_{in} \end{aligned} \tag{17.2}$$

Equation (17.2) gives the heat balance on node i. The first term on the right side of the equation expresses the heat loss from the layer of the node to the surrounding; the following three terms denotes the heat gain from the collector circulation, heat utilized by load and the heat conduction between nodes, respectively. The last term refers to the heat exchange caused by fluid flow either by the upward or downward motion, from neighboring nodes. The heat conduction term in Eq. (17.2) can be expanded in the following form by using the central difference scheme:

$$\lambda A \Delta x \frac{\partial^2 T_{s,i}}{\partial x^2} = \lambda A \frac{T_{s,i+1} + T_{s,i-1} - 2T_{s,i}}{\Delta x} \tag{17.3}$$

For the convenience of computer programming, the expressions of Q_{in} for interior points can be combined into a compact form by the use of a special symbol Max(), which stands for the largest of the quantities contained within it. Thus:

$$Q_{in} = Max(m_{m,i},0)C_p(T_{s,i-1} - T_{s,i}) + Max(-m_{m,i},0)C_p(T_{s,i} - T_{s,i+1}) \quad (17.4)$$

Where '$m_{m,i}$' denotes the net flow in the storage tank as a resultant of the collector down-flow and the load up-flow streams. Energy balance equations are written for each part and by solving 12 equations together at any time with considering initial and boundary conditions, the temperature analysis of tank is completed. Programming is done in Matlab.

The energy balance at the mixing point of the ejector can be written as Eq. (17.5).

$$\left(m_g + m_e\right)\cdot h_S = m_e \cdot h_g + m_g \cdot h_3 \quad (17.5)$$

The mass ratio or so called the entrainment ratio can be written as the Eq. (17.6).

$$\omega = \frac{m_e}{m_g} = \sqrt{\left(\eta_N.\eta_D\right)\cdot\left(\frac{h_3 - h_{4,is}}{h_{6,is} - h_S}\right)} - 1 \quad (17.6)$$

Neglecting the work input to the pump, the thermal COP of the ejector refrigeration system is defined as the ratio between cooling capacity and necessary heat input, as shown in Eqs. (17.7) and (17.8).

$$COP_{ERS} = \omega\frac{\left(h_9 - h_8\right)}{\left(h_3 - h_1\right)} \quad (17.7)$$

$$COP_{SERS} = COP_{ERS}\,\eta_{col} \quad (17.8)$$

A second law analysis calculates the system performance based on exergy, which always decreases, owing to thermodynamic irreversibility. The exergy loss, thus, provides a very important criterion to evaluate the thermodynamic performance of a system. Exergy is defined as Eq. (17.9).

$$E = m\left[(h - h_0) - T_0(s - s_0)\right] \quad (17.9)$$

Exergy input, output and exergy efficiency of solar collector can be calculated by Eqs. (17.10) to (17.14).

$$E_{c,r} = f\sigma T_{sun}^4 + (1-f)\sigma T_p^4 - \sigma T_{sc}^4 \quad (17.10)$$

$$E_{c,h} = Q_{ava}\left(1 - \left(\frac{T_{ref}}{T_{sc}}\right)\right) \quad (17.11)$$

$$E_{c,in} = E_{c,r} + E_{c,h} \quad (17.12)$$

$$E_{c,out} = Q_u \left(1 - \left(\frac{T_{ref}}{T_{sc}}\right)\right) \tag{17.13}$$

$$\varepsilon_{col} = \frac{E_{c,out}}{E_{c,in}} \tag{17.14}$$

Exergy input, output and exergy efficiency of generator can be calculated by Eqs. (17.15) to (17.17).

$$E_{g,in} = E_7 - E_8 \tag{17.15}$$

$$E_{g,out} = E_1 - E_5 \tag{17.16}$$

$$I_g = E_{g,in} - E_{g,out} \tag{17.17}$$

Exergy input, output and exergy efficiency of condenser can be calculated by Eqs. (17.18) to (17.20).

$$E_{c,in} = E_3 - E_4 \tag{17.18}$$

$$E_{c,out} = Q_c (1 - T_0 / T_c) \tag{17.19}$$

$$I_c = E_{c,in} - E_{c,out} \tag{17.20}$$

Exergy input, output and exergy efficiency of evaporator can be calculated by Eqs. (17.21) to (17.23).

$$E_{ev,in} = E_2 - E_6 \tag{17.21}$$

$$E_{ev,out} = Q_{ev} \left(1 - \frac{T_{ev}}{T_0}\right) \tag{17.22}$$

$$I_{ev} = E_{ev,in} - E_{ev,out} \tag{17.23}$$

Exergy input, output and exergy efficiency of ejector can be calculated by Eqs. (17.24) to (17.26).

$$E_{ej,in} = E_1 + E_2 \tag{17.24}$$

$$E_{ej,out} = E_3 \tag{17.25}$$

$$I_{ej} = E_{ej,in} - E_{ej,out} \tag{17.26}$$

Exergy input, output and exergy efficiency of expansion valve can be calculated by Eqs. (17.27) to (17.29).

$$E_{ex,in} = E_4 \tag{17.27}$$

$$E_{ex,out} = E_6 \tag{17.28}$$

$$I_{ex} = E_{ex,in} - E_{ex,out} \tag{17.29}$$

Exergy input, output and exergy efficiency of pump can be calculated by Eqs. (17.30) to (17.32).

$$E_{p,in} = W_p \tag{17.30}$$

$$E_{p,out} = E_{out,flow} - E_{in,flow} \tag{17.31}$$

$$I_p = E_{p,in} - E_{p,out} \tag{17.32}$$

17.4 Results and Discussions

For finding storage tank outlet temperature several heat transfer equations should be solved in parallel mode. These equations are solved by programming in Matlab. The outlet temperature of storage tank in a typical day is presented in Fig. 17.4. As it is shown in Fig. 17.4 the storage tank outlet temperature is 90 °C at 8 a.m. It's because of starting collector cycle at the average of 50 min sooner than refrigeration cycle. The inlet temperature of generator should be 90 °C. So auxiliary heating is needed to compensate.

Collector efficiency is calculated for a day and the result is presented in Fig. 17.5. It's clear from the figure that collector efficiency changes by time. Early hours of morning and late hours of afternoon are the hours that collector is so inefficient and the efficiency of the whole system decreases.

Irreversibilities of components are calculated dynamically in the defined period and results are shown in Fig. 17.6. Collector has the highest irreversibility with 52% and ejector with 19% is in the next step. Heat transfer through a finite temperature difference, mixing of materials at different states, friction in the flow of fluids, are the most important reasons of irreversibilities in ejector.

As noted previously about the two types of COPs, they are calculated at different hours of the day and the results are presented in Fig. 17.7.

Exergetic efficiency of the system is presented in Fig. 17.8. Input exergy of the system is in collector, auxiliary heater and pump. Output exergy of evaporator is the useful exergy of the system. The collector has high efficiency at noon and the most of necessary energy of the system can be supplied from collector.

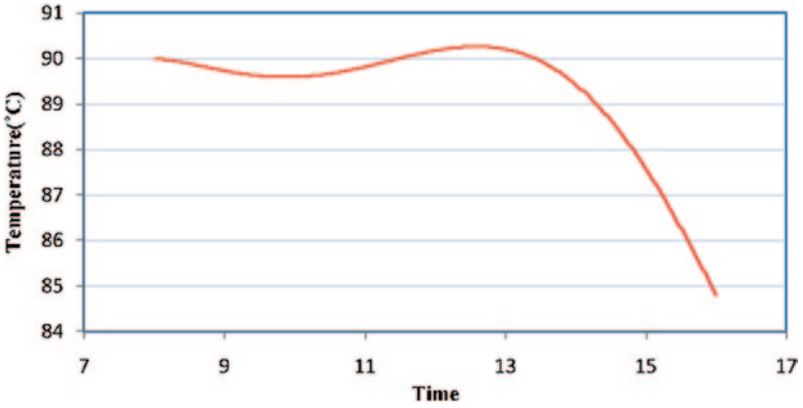

Fig. 17.4 Storage tank outlet temperature in a day

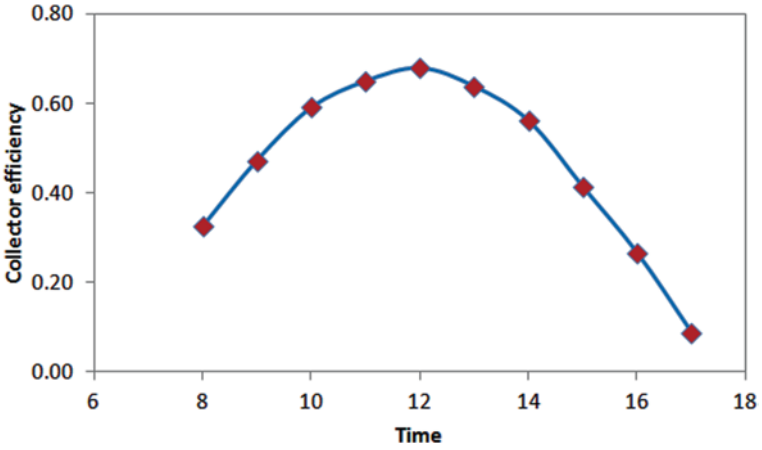

Fig. 17.5 Collector efficiency

Conclusions

The results show that dynamic analysis is confidently more useful than analysis in a constant condition. This method is more completed because it can present the efficiency of components of the system at each time. As the results present components have different efficiencies at different days and hours. Collector has the highest level of irreversibilities and ejector is in the next step. Irreversibilities at the first and the last hours of working-time are higher. It's because of low efficiency of the collector in these hours. In addition, using the hot water storage tank decreased auxiliary heating in the afternoon.

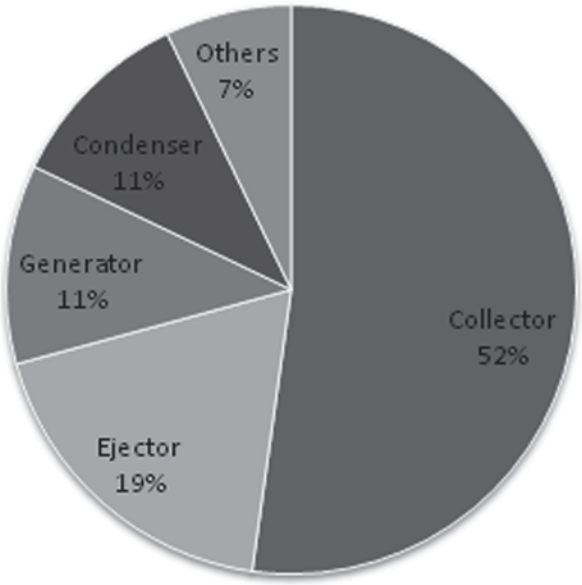

Fig. 17.6 Average irreversibilities in components of the system

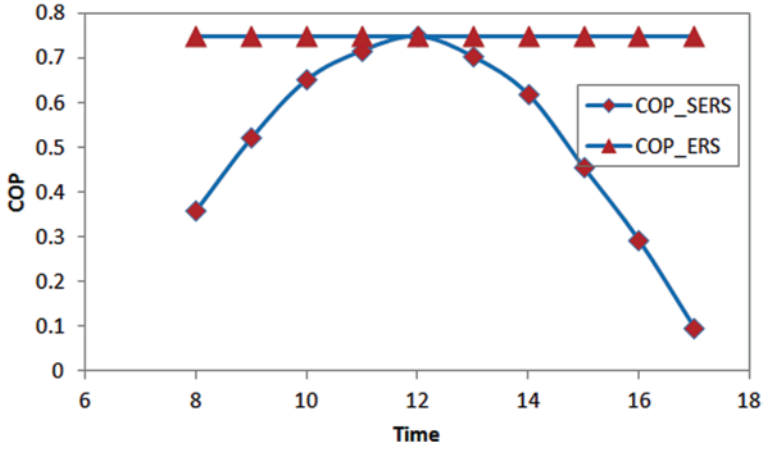

Fig. 17.7 COP variation during the day

Nomenclature

A	Area, m^2
C_p	Specific heat at constant pressure, J kg^{-1} K^{-1}
COP	Coefficient of performance
E	Exergy, W

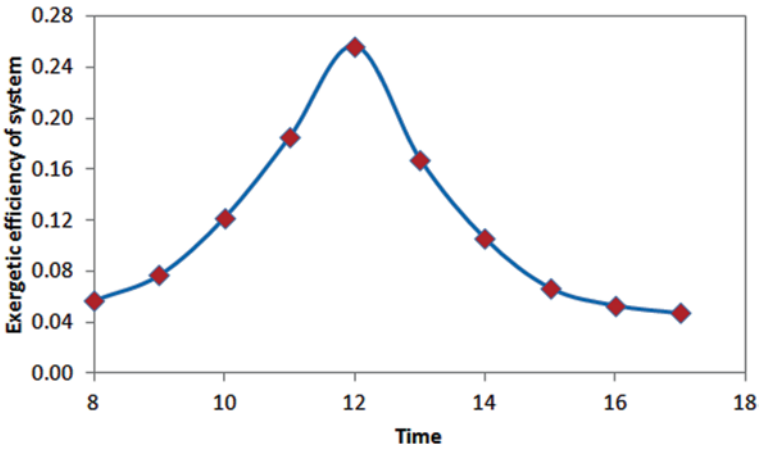

Fig. 17.8 Exergetic efficiency of the system during the day

F_R	Collector heat removal factor
h	Enthalpy, kJ kg^{-1}
I	Solar radiation, W m^{-2}
m	Mass flow rate, kg s^{-1}
Q	Heat, W
s	Entropy, kJ kg^{-1} K^{-1}
T	Temperature, K
U_L	Heat loss coefficient, W m^{-2} K^{-1}
UA	Loss coefficient-area product, W K^{-1}
W	Power, W

Greek letters

λ	Heat conduction coefficient, W m^{-1} K^{-1}
ε	Exergy efficiency
σ	Stefan–Boltzmann constant
η	Efficiency
$(\tau\alpha)_e$	Effective transmittance absorbance product
ω	Mass ratio

Subscripts

a	Ambient
c	Condenser
col	Collector
ev	Evaporator
ej	Ejector
ERS	Ejector refrigeration system
ex	Expansion valve

g	Generator
i	I'th node in the stratified tank
L	Load
p	Pump
S	Storage tank
SERS	Solar ejector refrigeration system

References

1. Srinivasa Murthy S, Balasubramanian R, Krishna Murthy MV (1991) Experiments on vapour jet refrigeration system suitable for solar energy applications. Renew Energy 1(5/6):757–768
2. Sokolov M, Hershgal D (1993) Optimal coupling and feasibility of a solar-powered year-round ejector air conditioner. Solar Energy 50(6):507–516
3. Sokolov M, Hershgal D (1993) Solar-powered compression-enhanced ejector air conditioner. Solar Energy 51(3):183–194
4. Zhang B, Shen SQ (2002) Development of solar ejector refrigeration system. In: Proceedings of the 1st international conference on sustainable energy technologies
5. Chunnanond K, Aphornratana S (2004) Ejectors: applications in refrigeration technology. Renew Sustain Energy Rev 8:129–155
6. Aphornratana S, Eames IW (1997) A small capacity steam-ejector refrigerator: experimental investigation of a system using ejector with movable primary nozzle. Int J Refrig 20(5):352–358
7. Huang BJ, Petrenko VA, Samofatov IYA, Shchetinina NA (2001) Collector selection for solar ejector cooling system. Solar Energy 71(4):269–274
8. Selvaraju A, Mani A (2004) Analysis of an ejector with environment friendly refrigerants. Appl Therm Eng 24:827–838
9. Selvaraju A, Mani A (2006) Experimental investigation on R134a vapour ejector refrigeration system. Int J Refrig 29:1160–1166
10. Eames IW, Ablwaifa AE, Petrenko V (2007) Results of an experimental study of an advanced jet-pump refrigerator operating with R245fa. Appl Therm Eng 27:2833–2840
11. Sankarlal T, Mani A (2007) Experimental investigations on ejector refrigeration system with ammonia. Renew Energy 32:1403–1413
12. Rogdakis ED, Alexis GK (2000) Design and parametric investigation of an ejector in an air-conditioning system. Appl Therm Eng 20:213–226
13. Arbel A, Sokolov M (2004) Revisiting solar-powered ejector air conditioner-the greener the better. Solar Energy 77:57–66
14. Zhang XJ, Wang RZ (2002) A new combined adsorption-ejector refrigeration and heating hybrid system powered by solar energy. Appl Therm Eng 22:1245–1258
15. Yu JL, Ren YF, Chen H, Li YZ (2007) Applying mechanical subcooling to ejector refrigeration cycle for improving the coefficient of performance. Energy Convers Manage 48:1193–1199
16. Pridasawas W, Lundqvist P (2004) An exergy analysis of a solar-driven ejector refrigeration system. Solar Energy 76:369–379
17. Kleinbach EM, Beckman WA, Klein SA (1993) Performance study of one-dimensional models for stratified thermal storage tanks. Solar Energy 50(2):155–166

Chapter 18
Combined Photovoltaic Solar Cell—Fuel Cell System: Powering a Dormitory Building

Fehmi Gorkem Uctug and Betul Akyurek

Abstract The feasibility analysis of installing a combined photovoltaic solar cell—fuel cell system for a dormitory building was realized. The idea was to produce energy for day-time consumption via the solar cells, and then using the excess electricity produced via the solar cells for electrolysis so that the hydrogen produced can be utilized in a proton exchange membrane fuel cell in order to provide power for night-time. The annual electricity requirement of the chosen dormitory building was estimated as 50,961.04 kWh, whereas the actual consumption was learned to be 52,037.18 kWh via the electricity bills provided by the dormitory administration. The day and night time electricity requirements of the building were calculated for each month and it was found that the month with the highest energy consumption during the day is December whereas the month with the highest energy consumption during the night is January. The system was designed so that it could meet the day-time energy requirement during December and the night-time energy requirement during January. Such a system was calculated to require a solar cell installation area of 1315 m^2. The costs of solar cell, electrolyzer and fuel cell systems and any other auxiliary equipment were obtained from various manufacturers' websites and the total required investment was calculated as $ 887,000. Breakeven periods were calculated in order to have a general idea regarding the feasibility of the combined system. Initially, the breakeven period of this particular combined system was found to be at least 97 years, which is very high. Then, it was considered to sell the excess electricity, that was not consumed either by the building or the electrolyzer, produced during the day-time in the months other than December to the local grid, as allowed by Turkish Law #6094, at a rate of $ 0.13 per kWh. In that case, the breakeven period was found to decrease almost to 19 years, rendering the investment moderately feasible in the long term.

Keywords Hybrid system · Fuel cells · Solar energy · Feasibility · Incentive schemes

F. G. Uctug (✉) · B. Akyurek
Energy Systems Engineering Department, Bahcesehir University, Ciragan Caddesi Osmanpasa Mektebi Sokak No: 4–6, 34353 Besiktas, Istanbul, Turkey
e-mail: gorkem.uctug@eng.bahcesehir.edu.tr

B. Akyurek
e-mail: btlakyurek@gmail.com

I. Dincer et al. (eds.), *Progress in Sustainable Energy Technologies: Generating Renewable Energy,* DOI 10.1007/978-3-319-07896-0_18,

18.1 Introduction

Efficient production and utilization of energy is a crucial concept in modern world, not only because it favors economical stabilization, but it also helps prevent environmental pollution, and the combination of these two facts is essential for sustainable development. In developed countries, buildings are responsible for the consumption of approximately 40% of all commercial energy supplied as processed fuels or electricity [1, 2]. For thousands of years, mankind has tried to improve the energy efficiency of buildings via simple methods such as choosing the ideal geographic location or by using appropriate building and insulating materials depending on the climate. As the technology developed, the measures to minimize energy loss have become more complex. However, it was the 1973 global energy crisis that triggered a worldwide pursuit in designing buildings with better energy utilization, by incorporating energy efficiency and renewable energy resources [3]. Since then, many countries adopted laws and regulations on how to use energy more efficiently and energy efficiency in residential and commercial buildings have become a common area of interest [4–8]. Above-mentioned laws and regulations impose certain targets and deadlines regarding both residential and commercial buildings with the aim of reaching specified energy consumption limits. For instance, in Turkey the Energy Efficiency Law came into effect in 2005, aiming to minimize the high level of energy intensity so as to achieve productive and effective use in every field of energy, prevention of wasteful expenditure and protection of the environment. This law, which was revised recently in January 2011, comprises the principals and procedures in order to increase the energy efficiency in industrial, building and transport sectors. With this law, Turkey aims to accomplish an energy saving of 30% in the next decade [9]. Hence, it is clear that energy efficiency in any type of building, whether small-scaled ones like houses or larger ones like dormitories or hotels, must be improved. In order to achieve this goal, home-owners, tenants and building managers must take suitable actions. Therefore, the solution must satisfy energy-related, environmental and financial aspects of the problem. In cases where it would not be possible to reduce the energy consumption, the proper action would be decreasing the environmental impact of the energy used in the buildings, in other words, producing energy via environmentally friendly methods such as photovoltaic solar cells or fuel cells.

Photovoltaic Solar Cells and Fuel Cells Photovoltaic (PV) conversion is the direct conversion of sunlight into electricity without any heat engine to interfere. PV cells are designed to transfer the energy contained in individual photons penetrating the panel to electrons that are channeled into an external circuit for powering an electric load. The function is achieved both through the layout of molecular structure at the microscopic level, and the arrangement of conductors at the edge of the cell at the macroscopic level. PV solar cells are simply designed systems with little maintenance requirement. Their power outputs can range from mW to MW level, making them suitable for various applications such as water pumping, remote buildings, solar home systems, communications, satellites and space vehicles, reverse osmosis plants, and for even power plants [10]. The solar cell works in three steps: (i) Photons

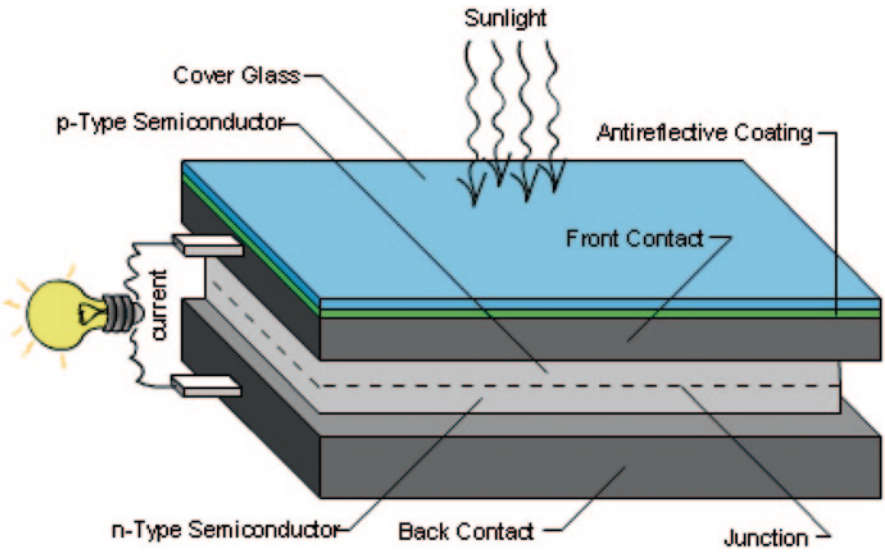

Fig. 18.1 Basic working principle of a photovoltaic solar cell [12]

in sunlight hit the solar panel and are absorbed by semiconducting materials, such as silicon. (ii) Electrons are knocked loose from their atoms, causing an electric potential difference. Current starts flowing through the material to cancel the potential and this electricity is captured. Due to the special composition of solar cells, the electrons are only allowed to move in a single direction. (iii) An array of solar cells converts solar energy into a usable amount of direct current electricity [11]. Figure 18.1 below shows the basic working principle of a photovoltaic solar cell.

Fuel cells can simply be described as electrochemical devices that convert the energy of a chemical reaction directly into electrical energy. Like commercial batteries, fuel cells have anode and cathode parts, in which oxidation and reduction reactions take place, respectively. However, unlike batteries fuel cells do not have limited lifespan, in theory a fuel cell can operate continuously as long as fresh fuel is supplied. Most common fuel cell fuel is hydrogen, whose exothermic oxidation results in an electric current passing through a load which is connected between the positive and the negative terminals of the fuel cell. Fuel cells can be classified according to different criteria, however the most common approach is to classify them according to the type of electrolyte, which is the material that allows the flow of ions from one electrode to the other, but prevents the flow of electrons. There are five main types of fuel cells, with many further sub-types. These main types are as follows:

- Proton Exchange Membrane Fuel Cell (PEMFC)
- Alkaline Fuel Cell (AFC)
- Phosphoric Acid Fuel Cell (PAFC)
- Molten Carbonate Fuel Cell (MCFC)
- Solid Oxide Fuel Cell (SOFC)

Table 18.1 Applications of PEMFC with a variety of power requirement [14]

Level of power	Applications
>1 MW	Local distributed power generation
100 kW—1 MW	Large transportation vehicles such as naval ships and buses; small portable or stationary power stations
10 kW—100 kW	Transportation vehicles such as cars; back-up power for medium-sized communication station
1 kW—10 kW	Transportation vehicles such as motorcycles and utility vehicles; underwater platform; uninterrupted power supply; residential power system
100 W—1 kW	Simple riding devices such as bicycles, scooters and wheelchairs; backpack power; uninterrupted power supply for small services
10 W—100 W	Portable power such as for emergency working power supply and military equipment; battery replacements; lighting; signal light power
<10 W	Small portable electronics such as cell phones

Amongst these types, PEMFC is a popular and commonly-preferred due to its high energy density per unit volume, ease of operation and maintenance and possibility of low-temperature operation. Although PEMFCs are not available for combined heat and power production purposes, they can be utilized for a variety of applications such as residential power, portable applications and transportation [13]. Table 18.1 above shows the utilization of PEMFC systems in various applications with a wide range of power requirements [14].

As indicated above, hydrogen is the most common fuel cell fuel and hydrogen can be produced through different methods. One of these methods is electrolysis, in which an electric current dissociates water into hydrogen and oxygen, a process that is the exact reverse of a fuel cell reaction. Producing hydrogen via electrolysis obviously requires another power source to provide the electric current, and using the electricity obtained via PV technology would lead minimal carbon footprint. Therefore, from an environmentally-friendly point of view, a combined photovoltaic solar cell—proton exchange membrane fuel cell (PVSC-PEMFC) would be an ideal choice for residential power supply. Examples of providing the power required for electrolysis via PVSC systems can be found in the available literature, albeit in the design stage, for instance in Spain, Saudi Arabia and Brazil [15–17]. The work presented in this paper is inspired by these studies involving the use of PVSC-electricity for hydrogen production via electrolysis. Figure 18.2 below shows the energy supply system designed in this particular work in a simplified manner [18].

18.2 Methodology

In this work, the availability of a hypothetical combined PVSC-PEMFC system for powering an actual dormitory building was analyzed in terms of feasibility. The general idea was to provide at least the maximum possible entire day-time energy requirement of the building via the PVSC system, and the excess electricity not

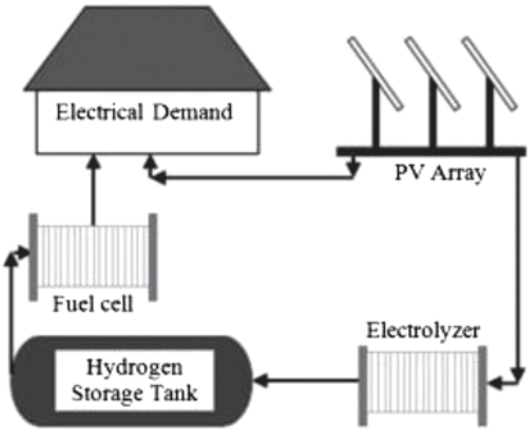

Fig. 18.2 Schematic of a typical solar-hydrogen system [18]

used during the day would be utilized for electrolysis in order to produce hydrogen. Hydrogen would then be oxidized during the night in a PEMFC system so as to meet the night-time electricity requirement partially or totally. The total cost of the combined system was calculated and the income was accepted as the annual cost of electricity produced by the PVSC and PEMFC system, which can be considered as an opportunity cost since the dormitory building would not be consuming grid power anymore. The main variable in our financial model was the surface area that would be allocated for PVSC installation. We kept this particular variable between two limits. The lower limit was the area required for PVSC installation so that the entire day-time energy requirement of the building could be met via the PVSC system in all months; whereas the upper limit was the area required for PVSC installation so that the entire night-time energy requirement of the building could be met via the PEMFC system which is powered by the H_2 produced via the excess PVSC electricity, again in all months. The individual steps of the method can be described as follows:

Determining the Electricity Requirement of the Dormitory Building

In order to be able to determine the capacity of the PVSC and PEMFC systems to be designed, the first step was to calculate the electricity demand of the building. During the initial stages of the study, official electricity billing information was not available; therefore the electricity consumption of the building was approximated. Even when the billing information became available, the approximation approach still proved to be beneficial as the day-time and night-time electricity requirements were required separately in order to be able to design the PVSC system. One of the authors of this paper, Ms. Betul Akyurek, had been a resident of the analyzed dormitory building between years 2009 and 2011; therefore her experience on the

Table 18.2 Approximated monthly electricity consumption characteristics of the dormitory building, classified as day-time and night-time

Months	Day-time (kWh)	Night-time (kWh)	Total (kWh)
January	2239.2	3885.36	6124.56
February	1997.76	3613.2	5610.96
March	2117.52	3441.2	5558.72
April	1833.6	3068.2	4901.8
May	1877.28	3056.2	4933.48
June	918.6	1428.64	2347.24
July	486.64	607.34	1093.98
August	436.64	582.14	1018.78
September	970.64	1471.48	2443.12
October	1949.52	3495.6	5445.12
November	2228.4	3410.88	5639.28
December	2276.4	3567.6	5844
Annual Sum (kWh)			50,961.04

daily habits and the lifestyle of the residents provided valuable insight during determining the electricity consumption characteristics of the building, as presented in Table 18.2 above. The analyzed dormitory building had approximate basal dimensions of 30×30 m, and nearly 60 residents when fully occupied. Table 18.2 was prepared by considering the approximate power ratings and durations of use of several electrical equipments such as refrigerators, washing machines, dishwashers, television sets, computers, etc. that are available for the residents. The details of this approach can be found elsewhere [19].

The billing information was shared with us only days before the completion of this work, and the actual electricity consumption of the building in year 2010 was learned to be 52,037.18 kWh. The percentage relative error (%RE) in our calculations regarding the annual electricity consumption of the building can be found as:

$$\%RE = \left(52{,}037.18 - 50{,}961.04\right) / 52{,}037.18 \times 100 = 2.1\% \tag{18.1}$$

As can be seen above, the approximation used in this study produced very accurate results; hence the remaining part of our work, which was based on the data given in Table 18.2, can be regarded to be trustworthy.

Calculating the Costs of the PVSC System

The PVSC system was designed so that it can meet the day-time energy requirement when the load is at its maximum at least, in other words during the month of December, when the electricity consumption reaches a peak value of 2276.4 kWh. Obviously, assuming constant electricity production rate for a PVSC system would be an unrealistic assumption, as the duration of solar radiation changes significantly from month to month. Hence, the average solar radiation periods were deemed nec-

Table 18.3 Average durations of solar radiation for Istanbul region of Turkey [20]

Months	Duration of solar radiation (hours)
January	103
February	115
March	165
April	197
May	273
June	325
July	365
August	343
September	280
October	214
November	157
December	103

essary so that the minimum and maximum power ratings of the entire PVSC system can be determined. This information was obtained from the website of the Turkish State Meteorological Service, and tabulated in Table 18.3 above.

In order to obtain an electric energy of 2276.4 kWh, the PVSC system must have a minimum total power rating of:

$$2276.4\ \text{kWh} / 103\ \text{h} = 22.1\ \text{kW} \tag{18.2}$$

Information regarding the power ratings and surface area values of commercial PVSC systems was available elsewhere [19]. In that study, the average power rating of a typical single-module PVSC system suitable for residential applications is given as 180 W (0.18 kW) whereas the surface area is given as 1.32 m^2. Hence, the minimum number of required modules and minimum allocated building surface area were found as:

$$22.1\ \text{kW} / (0.18\ \text{kW} / \text{module}) = 122.8 \approx 123\ \text{modules} \tag{18.3}$$

$$123\ \text{modules} \times 1.32\ \text{m}^2 / \text{module} = 162.4 \approx 162\ \text{m}^2 \tag{18.4}$$

The entire PVSC system was designed so that an area of at least 162 m^2 would be allocated to PVSC installation. Therefore in all months, excess electricity could be produced during the day and then utilized in the electrolysis system. The average price of the PVSC system was also obtained as $ 604.82 per module from the work of Uctuğ [19].

Calculating the Costs of the PEMFC and Electrolyzer Systems

The PEMFC system was designed via a similar approach to the one used for the design of the PVSC systems. This time the aim was to create a system which is capable of meeting the entire night-time energy demand of the dormitory building

when the load is at its highest, namely in the month of January. Hence, the system had to be capable of providing an electrical energy of 3885.36 kWh in the month of January. If the total active (what is meant by "active" is the total number of hours during which dormitory residents will effectively operate electrical equipment) night-time hours during January in the region of Istanbul are assumed to be 7 h/day, the required power rating of the PEMFC system can be calculated as:

$$3885.86\ \text{kWh} / (31 \times 7)\ \text{h} = 17.9 \approx 18\ \text{kW} \tag{18.5}$$

where 31 indicates the number of days in January. The typical cost of a 18-kW PEMFC system was obtained from the work of Jeong as $ 23,540 [21]. The hydrogen (H_2) requirement of the PEMFC system was obtained from the website of Ballard® as 1.15 kg/h, leading to a monthly H_2 production rate of 250 kg. The cost of an electrolyzer system with such capability, together with the cost of the auxiliary equipment such as purifiers, storage tanks and pumps was estimated as $ 261,000 [22–24]. It must be indicated that, while the PEMFC system may not work at full capacity all times, i.e. the entire night-time energy requirement of the building may not be met via the PEMFC system at all times due to the lack of hydrogen, the system was designed so that it can meet the entire night-time energy demand if necessary.

Calculating the Breakeven Period as an Indication of Feasibility

The final step was to calculate the breakeven point. In order to accomplish this goal, firstly the cost of electricity produced via PVSC and PEMFC systems was calculated. Since there would be no expense in regards to grid power consumption anymore (partly or totally, depending on the month and PVSC area), this cost figure was considered as an income in the shape of opportunity cost for the dormitory management. Once the cost was obtained, the total capital investment made on the PVSC, PEMFC and the electrolyzer systems was divided by the annual income to determine the breakeven period in terms of years. Hence, straight depreciation technique was used. The cost of electricity for residential buildings in Turkey was taken as approximately $ 0.1/kWh.

Before proceeding with the results, the costs of several systems used in this design study can be found in Table 18.4.

18.3 Results and Discussion

Capital Investment Costs

As indicated in the " Methodology" section, the minimum surface area that needed to be allocated for PVSC installation so that the entire day-time energy requirement of the building could be met via PVSC electricity in all months was found as

Table 18.4 Costs of PVSC, PEMFC and electrolyzer systems

System	Cost ($)
PVSC	604.82 (per module) 458.20 (per m^2)
PEMFC	23,540
Electrolyzer	261,000

162 m^2. Via a similar approach, the maximum surface area that needs to be allocated for PVSC installation so that the PVSC electricity can provide sufficient H_2 production via electrolysis to meet the night-time energy requirement of the building via the PEMFC in all months was found as 1315 m^2. In other words, the PVSC installation area, which is the main variable in this study, was varied between 162 and 1315 m^2. Whereas 162 m^2 is a realistic value for roof area of a residential building with approximate basal dimensions of 30×30 m, it is not realistic to allocate a total area of 1315 m^2 only by making use of the roof. Therefore it was assumed that part of the building's exterior surface area was also allocated for PVSC installation. This is not an uncommon approach and one example can be found in Fanney's work (2001) [25]. For a combined energy production system involving 162 m^2-PVSC unit together with an 18 kW PEMFC unit, the required capital investment was calculated as $ 358,800 whereas a combined system involving a 1315 m^2 PVSC unit together with an 18 kW PEMFC unit was estimated to cost approximately $ 887,000. Both capital investment values also include the costs of the electrolyzer and other auxiliary equipment.

Annual Incomes and Breakeven Periods

The minimum and maximum incomes were calculated for each month and the results of these calculations can be seen in Figs. 18.3 and 18.4 below:

If the values provided on a monthly basis in Figs. 18.3 and 18.4 are summed, the minimum annual income can be found as $ 2870. Similarly, the maximum annual income can be found as $ 6721. Therefore, the breakeven periods for minimum and maximum investments were calculated as follows:

$$\text{Breakeven period for minimum investment} = (\text{capital investment}) / (\text{annual income}) = 358{,}800 / 2870 = 125.01 \approx 125 \text{ years} \quad (18.6)$$

$$\text{Breakeven period for maximum investment} = (\text{capital investment}) / (\text{annual income}) = 887{,}000 / 6721 = 131.97 \approx 132 \text{ years} \quad (18.7)$$

As the results above indicate, the breakeven periods in the minimum and maximum investment cases are very long, rendering the investment infeasible. In Table 18.5

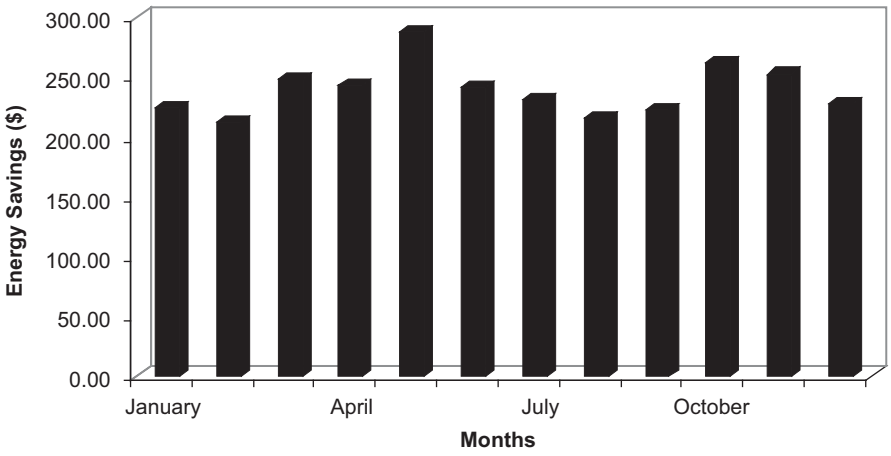

Fig. 18.3 Minimum monthly energy savings (for a 162 m^2 PVSC + 18 kW PEMFC system)

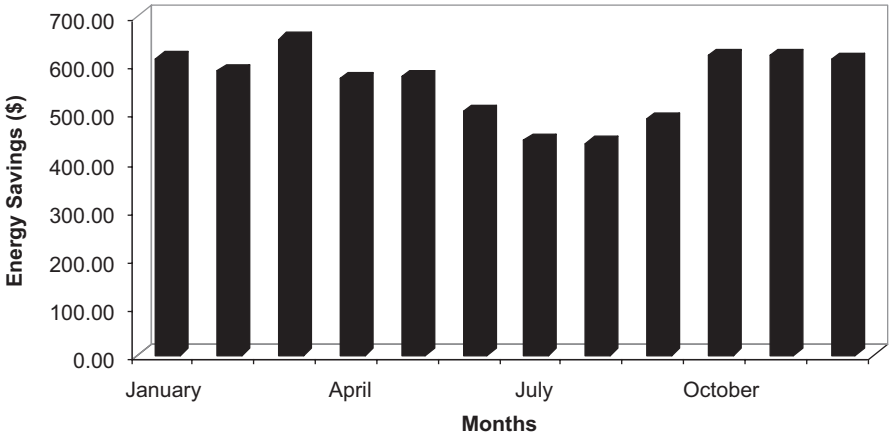

Fig. 18.4 Maximum monthly energy savings (for a 1315 m^2 PVSC + 18 kW PEMFC system)

below, the total annual income, total capital investment and breakeven periods as functions of allocated PVSC area can be found:

Data tabulated in Table 18.5 indicate that the shortest possible breakeven periods are calculated as 97.2 years for allocated PVSC areas of 400 and 500 m^2, and even at these values the investments appear to be infeasible with unacceptably long breakeven periods. At this stage, one final alternative approach was decided to be evaluated. As of January 2011, Turkish Law 6094 allows small-scale (< 500 kW) private entities to sell electricity produced via renewable resources back to the local network at variable rates, the rate being determined by the type of energy produc-

Table 18.5 Annual income, total capital investment and breakeven period as functions of allocated PVSC area

Area (m^2)	Annual income ($)	Total capital investment ($)	Breakeven period (years)
162	2869.84	358,798.93	125.0
200	3198.26	376,176.60	117.6
300	4062.96	421,996.30	103.9
400	4810.99	467,816.00	97.2
500	5285.52	513,635.69	97.2
600	5630.74	559,455.39	99.4
700	5936.23	605,275.09	102.0
800	6146.83	651,094.79	105.9
900	6344.58	696,914.48	109.8
1000	6455.13	742,734.18	115.1
1100	6560.27	788,553.88	120.2
1200	6649.96	834,373.57	125.5
1300	6717.43	880,193.27	131.0
1315	6721.00	887,066.23	132.0

tion method. Solar based electricity via PVSC systems can be sold at a rate of $ 0.13 per kWh [26]. If this opportunity could be exploited, it might have been possible to achieve more feasible results. Therefore a final model was created that considers the excess electricity that was not consumed during day-time hours be sold back to the local network. The results can be found in the following sub-section.

Breakeven Periods After Selling the Excess Electricity to the Local Network

This calculation was performed only for the case of maximum PVSC installation, i.e. 1315 m^2 PVSC area. In this approach, firstly the difference between the maximum possible energy production rate of the combined PVSC-PEMFC system and the actual energy consumptions were calculated for each month. The sum of these differences corresponded to the excess electricity that can be sold. One sample calculation for the case of January was performed as follows:

$$\text{Maximum power rating of the PVS Csystem} = 1315\ \text{m}^2 / (1.32\ \text{m}^2 / \text{module}) \times (0.18\ \text{kW} / \text{module}) = 179.32\ \text{kW} \tag{18.8}$$

$$\text{Energy production via PVSC system in January} = 179.32\ \text{kW} \times 103\ \text{h} \approx 18,470\ \text{kWh} \tag{18.9}$$

where 103 is the total duration of solar radiation in hours for Istanbul region in the month of January (see Table 18.3).

$$\text{Electricity consumed for } H_2 \text{ production} = 3885.36 / 0.24 \approx 16189 \text{ kWh} \tag{18.10}$$

where 3885.36 is the night-time electricity consumption of the building during January in kWh (see Table 18.2) and 0.24 is the efficiency of the electrolyzer system based on the LHV value of H_2 and assuming an operational PEMFC efficiency of 60% [27].

$$\text{Excess electricity} = 18470 - (16189 + 2239.2) = 41.8 \text{ kWh} \tag{18.11}$$

where 2239.2 is the day-time electricity consumption of the building during January in kWh (see Table 18.2).

$$\text{Excess electricity income} = 41.8 \text{ kWh} \times 0.13\$ / \text{kWh} = \$5.43 \tag{18.12}$$

Results of the entire set of the calculations can be found in Table 18.6 below.

With this approach, the combined system not only provides the entire day-time and night-time energy requirement of the dormitory building, but also enables the administration to sell the excess electricity back to the local network. The total annual income via this approach can be calculated as follows:

$$\text{Total annual income} = 50961.04 \times 0.1 + 41908.70 = \$47005.34 \approx \$47,000 \tag{18.13}$$

where 50,961.04 is the total annual electricity consumption of the building in kWh (19,332.2 + 31,628.4, also see Table 18.2) and 0.1 is the cost of grid electricity in $/kWh.

Hence, the breakeven period for the combined PVSC-PEMFC system with the option of selling the excess electricity can be calculated as:

$$\$887,000 / \$47,000 / \text{year} = 18.9 \approx 19 \text{ years} \tag{18.14}$$

To sum up, the possibility of selling the excess electricity decreased the breakeven period from 132 to 19 years for the case of maximum initial investment. The percentage change can be calculated as 86%, which is a very significant value. These results indicate that, despite the possibility of producing environmentally sustainable energy, a combined PVSC-PEMFC system may still not be economically feasible, especially due to the high cost of PVSC modules and the electrolyzer unit. However, if the excess electricity can be sold back to the local network, the investment is paid off within 20 years. Our results prove that the reasoning behind

Table 18.6 Monthly income from selling excess electricity

Months	Day-time Energy (kWh)	Night-time Energy (kWh)	Electrolyzer Energy (kWh)	Total energy production (kWh)	Excess electricity (kWh)	Income ($)
January	2239.2	3885.36	16,188.92	18,469.96	41.8	5.43
February	1997.76	3613.2	15,042.89	20,621.8	3581.15	465.55
March	2117.52	3441.2	14,328.47	29,587.8	13,141.81	1708.44
April	1833.6	3068.2	12,774.72	35,326.04	20,717.72	2693.30
May	1877.28	3056.2	12,724.76	48,954.36	34,352.32	4465.80
June	918.6	1428.64	5947.88	58,279	51,412.52	6683.63
July	486.64	607.34	2528.55	65,451.8	62,436.61	8116.76
August	436.64	582.14	2423.63	61,506.76	58,646.49	7624.04
September	970.64	1471.48	6131.23	50,209.6	43,107.73	5604.00
October	1949.52	3495.6	14,553.29	38,374.48	21,871.67	2843.32
November	2228.4	3410.88	14,200.57	28,153.24	11,724.27	1524.15
December	2276.4	3567.6	14,853.05	18,469.96	1340.51	174.27
Total	19,332.2	31,628.84				41,908.70

Turkish Law #6094 is logical and such financial incentives might really encourage potential investors.

Conclusions

In this study, the feasibility analysis of a combined photovoltaic solar cell-proton exchange membrane fuel cell system in order to power a dormitory building was performed. The general idea was to provide at least the maximum possible entire day-time energy requirement of the building via the solar cell system, and the excess electricity not used during the day would be utilized for electrolysis in order to produce hydrogen. Hydrogen would then be oxidized during the night in the fuel cell system so as to meet the night-time electricity requirement partially or totally. The minimum investment was calculated to require a solar cell installation surface of 162 m^2 with an approximate capital of $ 358,800 whereas the maximum investment was calculated to require a solar cell installation surface of 1315 m^2, costing almost $ 887,000. The breakeven periods on the initial investment was found to range between 97 and 132 years, meaning that installing a combined solar cell-fuel cell system would not be an economical option. However, after considering the possibility of selling the excess electricity back to the local network, as allowed by Turkish Law #6094, the breakeven period of the maximum investment decreased to 19 years.

Future works on this topic should consider the fact that according to Turkish Law #6094, the agreement between the state and the investors will valid for ten years after the signing of the contract and at the end of the tenth year, a new pricing agreement will be made, whose details are yet uncovered. Hence, for a breakeven period greater than ten years, the annual income after the tenth year would actually

be different. However, due to the unavailability of information on this matter, it was assumed that the local network would buy the electricity at the same rate throughout the period of this particular financial analysis.

Nomenclature

PEMFC Proton-exchange membrane fuel cell
PVSC Photovoltaic solar cell

References

1. Laustsen J (2008) Energy efficiency requirements in building codes, energy efficiency policies for new buildings International Energy Agency. http://www.iea.org/g8/2008/Building_Codes.pdf. Accessed 27 Feb 2012
2. Perez-Lombard L, Ortiz J, Pout C (2008) A review on buildings energy consumption information. Energy Build 40:394–398
3. Hunn B (1996) Fundamental of building energy dynamics. The MIT Press, London
4. Dixon RK, McGowan E, Onysko G, Scheer R.M (2010) US energy conservation and efficiency policies: challenges and opportunities. Energy Policy 38:6398–6408
5. Hamza N, Greenwood D (2009) Energy conservation regulations: impacts on design and procurement of low energy buildings. Build Environ 44:929–936
6. Lee WL, Yik FWH (2004) Regulatory and voluntary approaches for enhancing building energy efficiency. Prog Energy Combust Sci 30:477–499
7. Ekins P, Lees E (2008) The impact of EU policies on energy use in and the evolution of the UK built environment Energy Policy 36:4580–4583
8. Wiel S, Egan C, Cava MD (2006) Energy efficiency standards and labels provide a solid foundation for economic growth, climate change mitigation, and regional trade. Energy Sustain Dev 10:54–63
9. Balat M (2010) Security of energy supply in Turkey: challenges and solutions Energy Convers Manag 51:1998–2011
10. Parida B, Iniyan S, Goic R (2011) A review of solar photovoltaic technologies. Renew Sustain Energy Rev 15:1625–1636
11. Vanek FM, Albright LD (2008) Energy systems engineering: evaluation and implementation. McGraw-Hill, USA
12. http://www.oxford-royale.co.uk. Accessed 1 March 2012
13. Hoogers G (2003) Fuel cell technology handbook. CRC Press, USA
14. Li X (2008) Principles of fuel cells. Taylor and Francis Group, New York
15. Contreras A, Carpio J, Molero M, Veziroglu TN (1999) Solar-hydrogen: an energy system for sustainable development in Spain. Int J Hydrog Energy 24:1041–1052
16. Almogren S, Veziroglu TN (2004) Solar-hydrogen system for Saudi Arabia. Int J Hydrog Energy 29:1181–1190
17. Do Sacramento EM, Sales AD, Lima LC de, Veziroglu TN (2008) A solar-wind hydrogen system for the Ceara state in Brazil. Int J Hydrog Energy 33:5304–5311
18. Shabani B, Andrews J (2001) An experimental investigation of a PEM fuel cell to supply both heat and power in a solar-hydrogen RAPS system. Int J Hydrog Energy 36:5442–5452
19. Uctug FG, Yukseltan E (2012) A linear programming approach to household energy conservation: efficient allocation of budget. Energy Build doi:10.1016/j.enbuild.2012.02.020
20. http://www.mgm.gov.tr/index.aspx. Accessed 21 Nov 2011
21. Jeong KS, Soo-oh B (2002) Fuel economy and life cycle cost analysis of a fuel cell hybrid vehicle. J Power Sources 105:58–65

22. http://pdf.directindustry.com/pdf/ballard–22779.html. Accessed 28 Nov 2011
23. Pyle W, Healy J, Cortez R (1994) Solar hydrogen production by electrolysis. J Home Power 39:32–38
24. http://rebresearch.com/Electrolyzer_and_MR_costs.pdf. Accessed 29 Nov 2011
25. Fanney AH, Dougherty, BP, Davis MW (2001) Measured performance of building integrated photovoltaic panels. J Sol Energy Eng Spec Issue: Sol Thermochem Process 123:187–193
26. Baris K, Kucukali S (2012) Availability of renewable energy sources in Turkey: current situation, potential, government policies and the EU perspective. Energy Policy 42:377–391
27. Petrucci RH (1989) General chemistry. Macmillan, New York

Chapter 19
Investigation of a Combined Air Source Heat Pump and Solar Thermal Heating System Within a Low Energy Research Home

Jennifer White, Mark Gillott and Rebecca Gough

Abstract Over 75 % of the energy consumption of an average UK home can be attributed to space heating and hot water production (Department of Energy and Climate Change 2009). As such, it is important to develop and install efficient low carbon systems, integrated into buildings with high thermal performance, in order to reduce overall energy demand.

To date, testing of Air Source Heat Pump (ASHP) technology in the UK climate has been limited. This study investigates the performance of a combined Panasonic Aquarea 9 KW ASHP and Hoval SolKit® solar thermal collector (STC) within a thermally efficient inhabited research home, in order to assess the ability of the system to deliver heating and hot water requirements.

The testing period extends from 4th July 2011 to 29th February 2012. Initial results indicate that the ASHP and STC combined system is able to deliver the required levels of heating and hot water in order to meet the requirements of the occupants, with reduced bills as compared to traditional heating systems. Indoor temperatures have been maintained at a stable comfortable level, alongside minimal or no reliance on an auxiliary immersion heater for hot water.

An average coefficient of performance (COP) of 3.99 has been calculated for the dataset, exceeding the desired industry target COP of 3 but falling slightly below the manufacturer expected efficiency of 4.1. The COP fell below both values for a significant number of individual days, leading to questions over the consistency of the system efficiency. It should also be noted that the test period coincided with an unseasonable mild winter in the UK.

Whilst a single renewable technology source is unlikely to provide the energy levels required to heat an average UK home throughout an entire year, the combined system installed in the test house performs favourably when compared to

J. White (✉) · M. Gillott
University of Nottingham, Nottingham, UK
e-mail: laxjw3@nottingham.ac.uk

M. Gillott
e-mail: mark.gillott@nottingham.ac.uk

R. Gough
Loughborough University, Loughborough, UK
e-mail: r.gough@lboro.ac.uk

I. Dincer et al. (eds.), *Progress in Sustainable Energy Technologies: Generating Renewable Energy,* DOI 10.1007/978-3-319-07896-0_19,

conventional non-renewable heating and hot water systems. In the context of previous research, this study does show positive results and demonstrates that an ASHP/STC combined system may be a suitable installation in a UK home.

Keywords Air source heat pump · Solar thermal collector · Energy efficiency · Renewable energy sources

19.1 Introduction

The UK Government has set ambitious targets relating to energy efficiency and carbon emissions, and has allowed a relatively short time-scale for measures to be implemented to deliver them. In 2008, the UK adopted the Climate Change Act [2], and the national aim to reduce carbon emission levels to 80 % below 1990 levels by 2050 is still in force.

Energy consumption within UK buildings accounts for approximately 40 % of the total UK carbon emissions [3], in line with similarly developed countries. The Building Research Establishment estimates that up to 30 % of UK carbon emissions emanate from domestic housing stock [4], with the average UK household producing approximately 6 t of carbon dioxide each year [5]. Therefore, developing ways to improve the energy performance of new and existing homes will clearly have a direct positive contribution towards the achievement of wider national energy and carbon reduction targets.

Many renewable energy technologies are included in the Renewable Heat Incentive [6], a Government initiative which aims to encourage the installation of lower energy systems. STC's are included in the scheme, but at present ASHPs are excluded due to the limited research undertaken as to their ability to function effectively in the UK climate. The opportunity to study a combined system within a UK research context is therefore both timely and relevant to providing further background to ASHP performance.

19.2 BASF House Case Study

Due to the increased awareness of the need to design homes that are more sustainable in terms of construction and operation, several research projects are ongoing at academic institutions throughout the UK. At the University of Nottingham, the Creative Energy Homes Project located on the University Park campus provides a facility for the in-situ testing of housing design, materials and technologies. The development of six houses has been possible through collaboration between the Department of Architecture and Built Environment and a number of industrial sponsors. This paper focuses on the BASF Research House, which is situated within this development.

The house was designed by Derek Trowell Architects and completed in June 2008. The main target of the design brief was to minimise energy demands and carbon emissions whilst providing an affordable house that would appeal to potential occupants [7]. A second key aim was to achieve a cost effective build with a short construction period that would be attractive to housing developers.

The principles of Passivhaus standards were utilised during the design process, alongside a target to achieve Code Level 4 of the Code for Sustainable Homes. These aspirations resulted in the property achieving a space heating requirement of less than 15 KWh/m^2/annum at the design stage (through use of dynamic EDSL TAS modelling rather than PHPP methodology). Elements such as small floor area (100 m^2), an entrance lobby/buffer space to the north elevation, a double height sunspace to the south elevation, and creation of a natural ventilation stack effect through use of a central stairwell and windows in the sunspace and north facing roof ridge, enable this level of heating demand to be achieved [8].

The walls at ground floor level were formed using polystyrene form-work filled with concrete (ICF), whilst prefabricated timber insulated sandwich (SIPS) panels were utilised in the first floor and roof construction. These materials provide relatively low thermal mass, but did allow a short build period to be achieved (25 weeks). To improve the thermal efficiency of the construction materials, micro-encapsulated wax phase change material (PCM) boards were incorporated into the ceilings of the south facing rooms of the house. Double glazed doors and windows were installed throughout the property [9].

Equal importance was placed on the performance of the construction elements and installed systems within the design of the property. A water conservation and rainwater harvesting system and earth air heat exchanger were incorporated into the wider design strategy. In addition, space heating and hot water heating was originally served by a combined biomass and solar thermal collector (STC) system.

The efficiency of the biomass boiler was found to be compromised as it was oversized for the property, so this was replaced with an air source heat pump (ASHP) in July 2010. The combined system under consideration therefore comprises of a single phase Panasonic ASHP and Hoval SolKit® STC. The system can be supported by a secondary source of hot water in the form of an immersion heater, should there be times when the STC cannot meet the demands of the occupants.

19.3 Field Investigation

The combined ASHP and STC system was evaluated for a period dating from July 2011 to February 2012. The system configuration is shown in Fig. 19.1.

Environmental conditions and mechanical/engineering systems within the BASF house are continually monitored using integrated sensors and equipment provided by Cool Planet/WebBrick©. The data files generated from this system relating to internal air temperatures, heating system temperatures, energy flow, power input

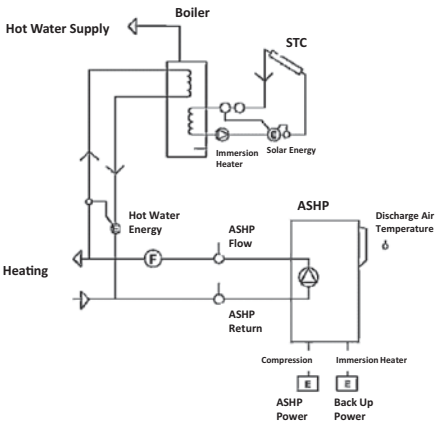

Fig. 19.1 System configuration of combined ASHP & STC heating system [10]

and solar hot water supply were used in the analysis of the ASHP/STC performance and energy contribution. External temperature, external humidity and solar radiation measurements were obtained from a weather station situated on campus in the vicinity of the research house. Table 19.1 summarises the data utilised in the system evaluation.

19.4 Results & Discussion

Evaluation of Hot Water Production

The hot water needs of house occupants are served by the combined solar thermal collector (STC) and air source heat pump (ASHP) system, with an immersion heater to provide back-up support when required. There are many factors that can have an impact upon the efficiency of a solar thermal collector (STC), including solar radiation levels, cloud cover, wind speed and direction and external temperature. The position, size and orientation of the solar array will also affect performance. As Fig. 19.2 shows, during the time period studied a distinct trend can be observed between amount of hot water delivered by the solar collector and the level of available solar energy. During the winter months, when less solar energy can be utilised, the STC is able to produce lower amounts of hot water. The reverse situation is apparent during the summer months, with high levels apparent from July to October, less production in November to January, and a steady increase again during February.

When the STC provides lower levels of hot water, support is required from the ASHP, and potentially the immersion heater, in order to fulfil system and occupant demands. Therefore, the contributions from each source will vary depending on seasonality and temperature. The data in Fig. 19.3 confirms this theory, with

Table 19.1 Data used within system evaluation

Parameter	Source	Units
ASHP flow	Webbrick system	°C
ASHP return	Webbrick system	°C
Solar flow	Webbrick system	°C
Solar return	Webbrick system	°C
Living space temperature	Webbrick system	°C
Bedroom 1 temperature	Webbrick system	°C
Bedroom 2 temperature	Webbrick system	°C
Bedroom 3 temperature	Webbrick system	°C
Total flow ASHP	Webbrick system	l/s
ASHP power input	Webbrick system	Wh
ASHP hot water flow	Webbrick system	n/a
Solar energy	Webbrick system	kWh
External temperature	Weather station	°C
External humidity	Weather station	%
Solar radiation	Weather station	W/m^2

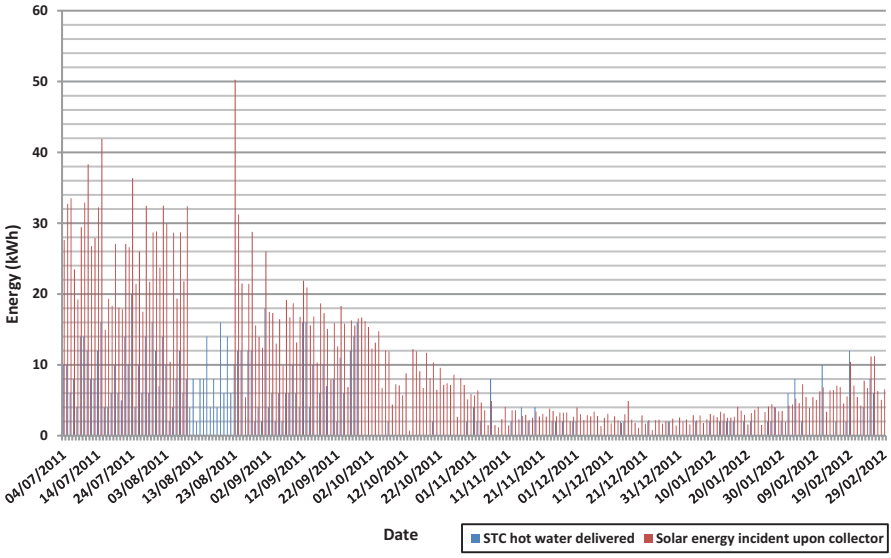

Fig. 19.2 Solar thermal collector hot water delivery vs available solar energy

high levels attributable to the STC in the summer months (68 % of total hot water production). More reliance was placed on the ASHP in the winter period, with the ASHP providing 86 % of hot water requirements. The ASHP is also able to provide a more consistent known amount of water, as it less sensitive to external influences as compared to the STC.

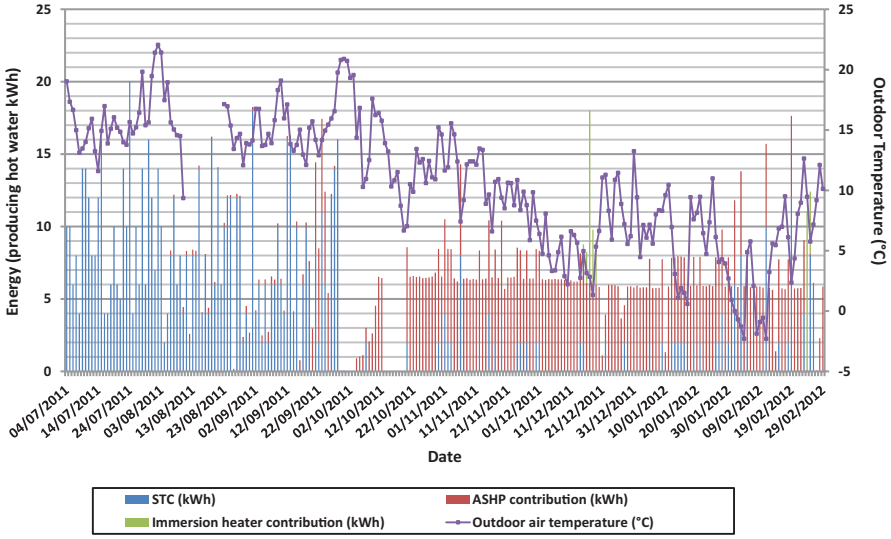

Fig. 19.3 Contribution of each source to hot water supply vs ambient outdoor temperature

The immersion heater was utilised only occasionally during the period of study, on six days in total. In December, the system was switched on for four days, but this was due to routine testing and was not in response to user demand. The ASHP failed for a four day period in February 2012. The immersion heater was required for the first two days as there was no contribution from the STC due to poor weather conditions. However, the STC did provide a large amount of hot water during the final two days of the system failure, meaning that the immersion heater could be switched off.

One limitation of the ASHP system is that, at very low temperatures, it may not be able to supply all hot water and heating needs. The coldest conditions within the study period were experienced in the first two weeks of February, with the coldest single point temperature recorded on the 11th February at −7.3 °C. On this occasion, and others where the temperature dropped below 0 °C, the immersion heater was not required. This suggests that the combined STC and ASHP system can fulfil the hot water and heating demands of the occupants throughout all seasons.

It should be noted that the winter of 2011–2012 was considerably milder than previous years, with the annual average temperature being 10.7 °C, compared with 8.8 °C and 9.9 °C in 2010/11 and 2009/10 respectively [11]. Indeed, in December 2010, the average minimum temperature was −4 °C, whilst the same average was 3.4 °C in December 2011 [12]. Such variation in climate could impact significantly on the performance of the combined STC and ASHP system, suggesting that an extended evaluation throughout further heating seasons should be undertaken to fully validate the observed results.

Evaluation of Space Heating Performance

In terms of space heating requirements, the ASHP component of the combined system is solely responsible for maintaining a comfortable internal temperature of approximately 20 °C. The coefficient of performance (COP) is considered by industry to be the primary indicator of performance. This is the ratio between the heat provided at the heat sink and energy required, and can be calculated using the following equation Eq. (19.1):

$$COP = \frac{Energy\ Produced\ by\ the\ System}{Energy\ Consumed\ by\ the\ System} = W\frac{Qin}{Qin} = \frac{Qin}{Qin - Qout} \tag{19.1}$$

where Q_{in} *(W)* is equal to total heat input and Q_{out} *(W)* is equal to total heat output.

The energy produced by the system (E) is a function of the mass flow rate (M), specific heat capacity (C) and the difference between return and supply temperatures (ΔT), as defined in Eq. (19.2):

$$E = M\ x\ C\ x\ \Delta T \tag{19.2}$$

The mass flow rate of the working fluid (M) can be found using Eq. (19.3):

$$M\ (kg/s) = Density\ (kg/m^3)\ x\ Volume\ Flow\ Rate\ (m^3/s) \tag{19.3}$$

The ASHP system utilises a mixed working fluid, which consists of 25 % glycol and 75 % water. The temperature of the fluid will affect the density, and so a value must be calculated for each temperature within an 18–50 °C working range at 0.10 °C intervals. The density of the separate solutions is first calculated Eq. (19.4).

$$\rho_1 = \frac{\rho_0}{(1 + \beta(\Delta T)}} \tag{19.4}$$

where ρ_1 equals final density (kg/m^3), $\rho_0$indicates initial density (kg/m^3), β represents the volumetric temperature expansion coefficient (m^3/m^3 °C), and ΔT is equivalent to the required hot water temperature minus the cold water supply temperature (°C or K). The values for each fluid component are then combined using Eq. (19.5):

$$\rho = (\%W\ \text{x}\ \rho_w) + (\%G\ \text{x}\ \rho_G) \tag{19.5}$$

where ρ equals combined fluid density (kg/m^3), %W and %G refer to the water and glycol ratio within the working fluid, and ρ_w and ρ_G relate to the water and glycol densities (kg/m^3).

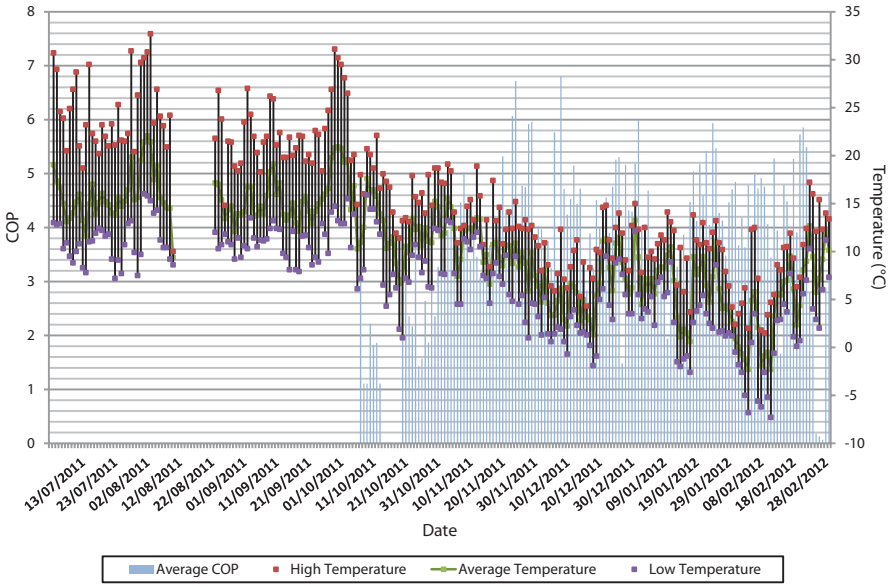

Fig. 19.4 ASHP function (COP) vs External temperature data

The data collected for the ASHP system shows that no heating was required within the BASF house from July 2011 to early October 2011. This is due to the high performance of the highly insulated building fabric. When external temperatures began to decrease in October 2011, the ASHP was required to function in order to achieve comfortable internal temperatures. This trend can be seen in Fig. 19.4.

The manufacturer specification [13] states that, for a 9 KW system, the ASHP should produce a COP of 4.1 at temperatures above 7 °C, and 2.5 at temperatures below −7 °C. Whilst the average calculated COP system for the period when the ASHP was utilised (October 2011–February 2012) is 3.99, Fig. 19.5, shows that there were a number of days when temperatures were above 7 °C when the COP fell below the published COP of 4.1.

Mean COP for each day does not appear to relate directly to external temperature. COP was below 4.1 for 88 of the 146 days within the research period, meaning that it performed to the manufacturer suggested efficiency for only 40 % of the time. The level of performance cannot be attributed solely to low external temperatures, as on 4 of the 7 days when mean external temperatures fell to below 0 °C, the COP remained above 4.1.

The 11th February 2012 was the sole day within the test period with a mean external temperature of below −7 °C, and COP remained relatively high at 3.45. Several cold days were experienced (temperature range of −1.8 °C to −7.3 °C) between 1st and 11th February 2012, and COP values within this period ranged from 3.45 to 4.92. Therefore, even at low external temperatures, the ASHP performed well in relation to manufacturer expected efficiency levels.

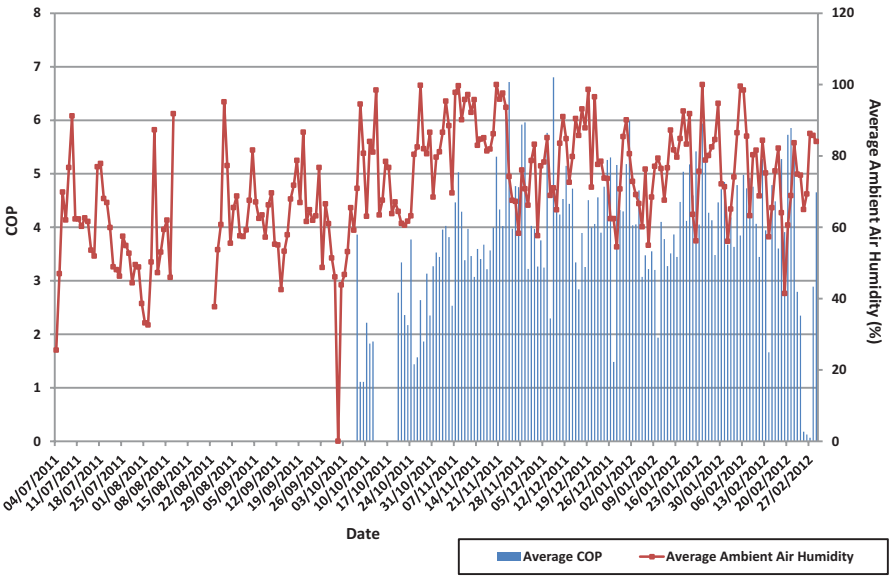

Fig. 19.5 ASHP Function (COP) vs External Humidity Data

COP values ranged from 1.11 (recorded on two days when external temperatures were above 10 °C), to a maximum of 6.80 (achieved on a day with a mean external temperature of 6.8 °C). Therefore, within the study data, there appears to be no obvious correlation between external temperature levels and ASHP efficiency, or between mean external humidity and COP (Fig. 19.5). However, the overall average COP for the period when the ASHP was functioning does largely meet manufacturer system performance guidelines.

Other factors may be contributing to the ASHP COP levels, such as those associated with internal heat distribution systems. Figures 19.6, 19.7, 19.8 and 19.9 represent the internal temperature levels present in several areas of the house during the testing period.

During the summer months, when there is no requirement for the ASHP, the internal temperatures throughout the house show greater variation than later in the year when the system functions to regulate the air temperature supplied. Whilst there are differences in temperatures throughout different space within the property, levels within each room remain consistent and maximum and minimum values are similar for each day. Also, as seen in Fig. 19.10, the mean internal temperature does not vary with external temperature variation, suggesting that the ASHP is providing a comfortable living environment for the occupants throughout the heating season.

In terms of comparative system heating costs, an estimation has been undertaken between the ASHP and other fuel sources that could be utilised in the BASF house. This is based on energy cost and CO^2 emission data obtained from the Energy Saving Trust [14]. The BASF house, largely due to efficient design and renewable energy systems integrated into the building, has an annual heating cost of

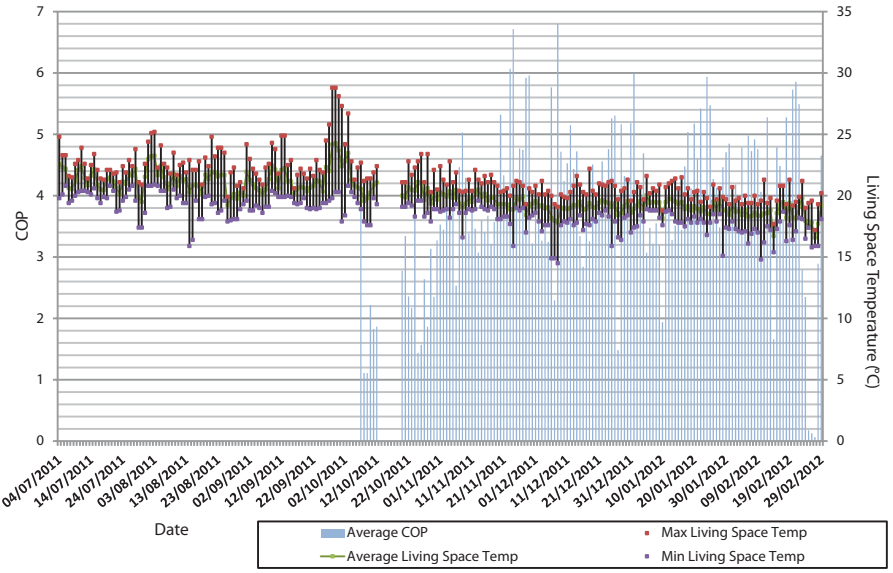

Fig. 19.6 ASHP function (COP) vs internal ground floor temperature data

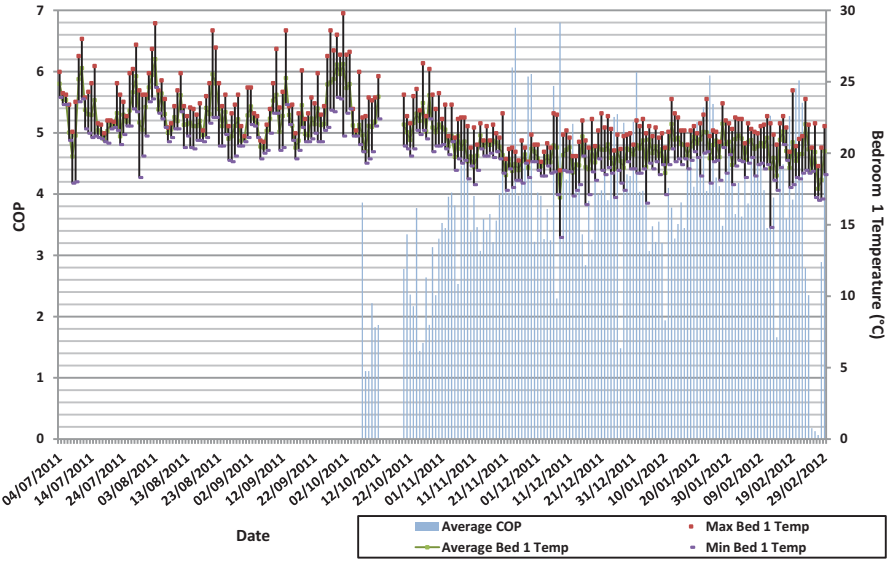

Fig. 19.7 ASHP function (COP) vs internal bedroom 1 temperature data

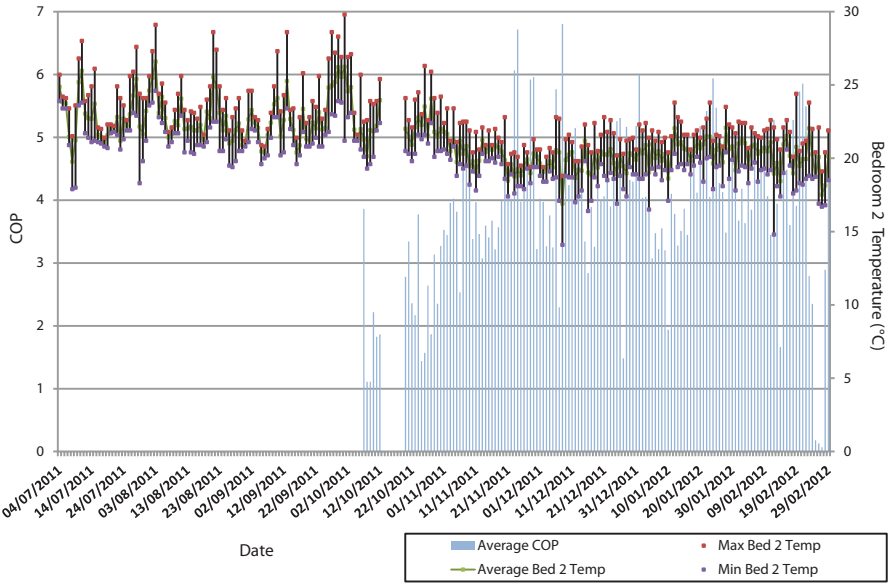

Fig. 19.8 ASHP function (COP) vs internal bedroom 2 temperature data

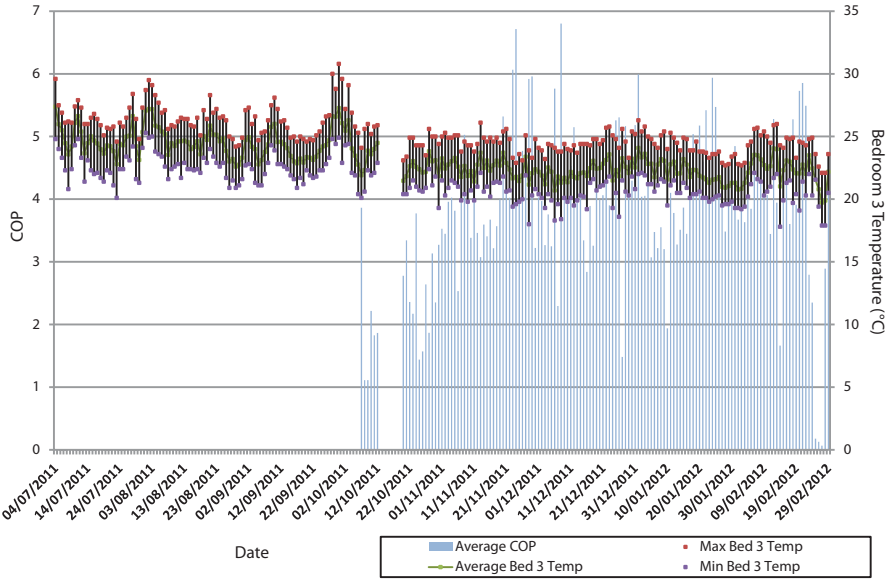

Fig. 19.9 ASHP function (COP) vs internal bedroom 3 temperature data

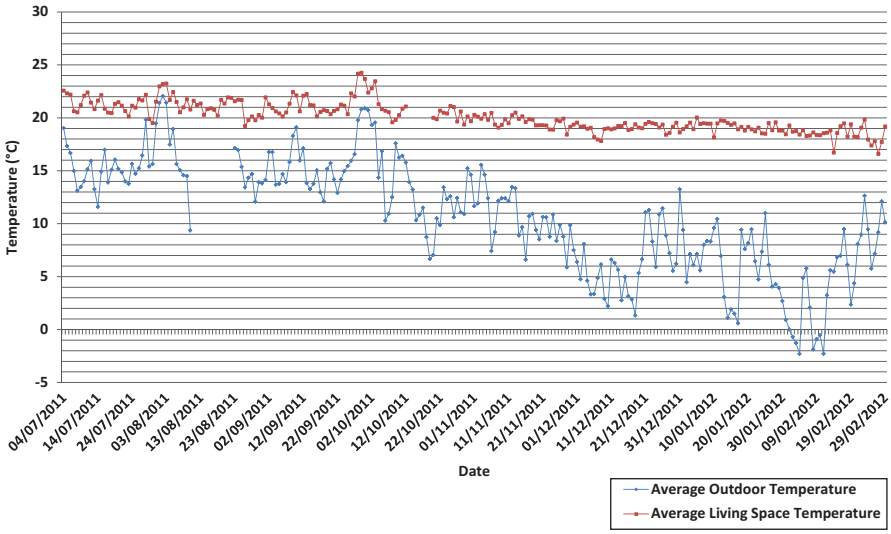

Fig. 19.10 Mean external temperature vs mean internal temperature

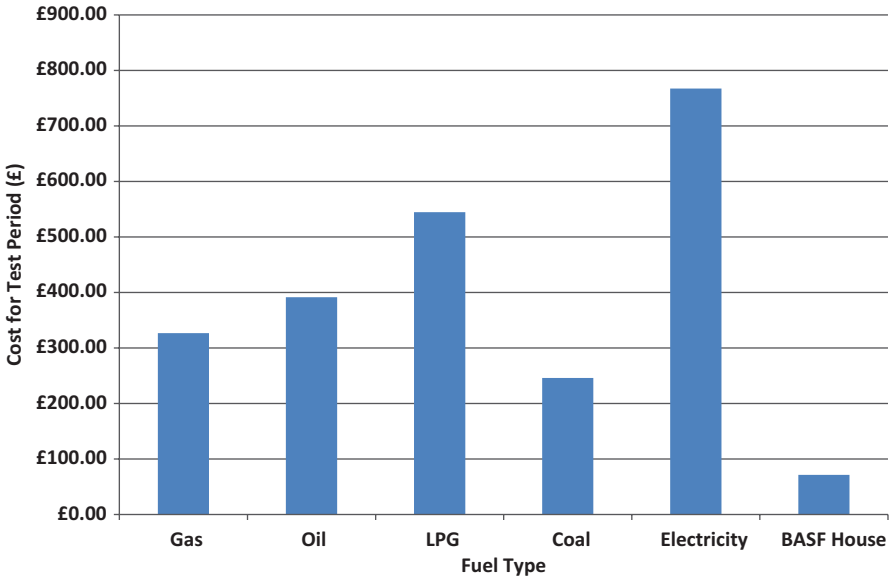

Fig. 19.11 Annual energy consumption for average UK home vs BASF house

approximately £112 and CO^2 emissions of 408kgCO^2. Both values are considerably lower than those of average homes utilising more conventional fuel sources, as demonstrated in Figs. 19.11 and 19.12.

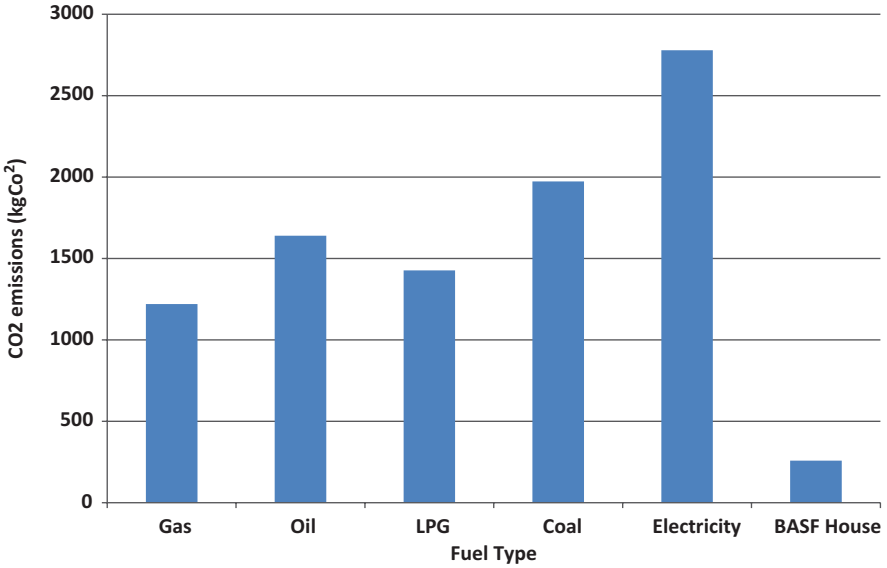

Fig. 19.12 Annual CO^2 emissions for average UK home vs BASF house

Conclusions

It is widely accepted that there is a need to integrate renewable energy technology into new and existing homes in order to reduce energy demands of the overall housing stock, and therefore UK total energy consumption. The use of an ASHP for space and water heating purposes is a viable option, although further evaluation would be beneficial in order to fully assess performance in the UK climate. This study has provided valuable research into the use of an ASHP and STC combined system, and in conjunction the two renewable systems do meet the hot water and space heating demands of the BASF house occupants during the study period.

However, the COP of the ASHP did fluctuate independently of external temperature and humidity levels, suggesting that the position of the space heating radiators could be affecting system efficiency. The mean COP for the entire research period, at 3.99, was comparative to that included in manufacturer guidance (COP of 4.1). Heating and energy bills and emissions associated with the heating systems were also exceptionally low, due to the renewable systems and efficient thermal design of the house.

Therefore, whilst the research undertaken during this study may be limited due to the mild conditions encountered during the winter of 2011–2012 in the UK, it has enabled a positive contribution to be made in terms of evidence relating to the viability of ASHP heat pump installation in new build and existing housing.

Nomenclature

ASHP	Air Source Heat Pump
C	Average Water Specific Heat Capacity, kj/kgK
CO^2	Carbon Dioxide
COP	Coefficient Of Performance
ΔT	Temperature Difference,°C or K
E	Energy, kWh
ρ_1	Final Density of Working Fluid, kg/m^3
ρ_0	Initial Density of Working Fluid, kg/m^3
ρ_w	Density of Water, kg/m^3
ρ_G	Density of Glycol, kg/m^3
Q_{out}	Total Heat Output, W
Q_{in}	Total Heat Input, W
M	Mass Flow Rate, kg/s
η	System Efficiency, %
β	Volumetric Temperature Expansion Coefficient, m^3/m^3°C
%W	Percentage of Water in Working Solution, %
%G	Percentage of Water in Working Solution, %
STC	Solar Thermal Collector

References

1. DECC (Department of Energy and Climate Change) (2009) The UK low carbon transition plan. National strategy for climate and energy. HMSO, London
2. DECC (Department of Energy and Climate Change) (2008) The Climate Change Act 2008. HMSO, London
3. MacKenzie F, Pout C, Shorrock L, Matthews A, Henderson J (2010) Energy efficiency in new and existing buildings—comparative costs and CO2 savings. BRE Trust, Watford
4. Utley JI, Shurrock LD (2008) Domestic energy fact file. BRE Trust, Watford
5. CLG (Communities and Local Government) 2008. Code for sustainable homes: setting the standard in sustainability for new homes. CLG: London
6. DECC (Department of Energy and Climate Change) (2011) Renewable heat incentive. HMSO: London
7. Gillott M, Rodrigues LT, Spataru C (2010) Low-carbon housing design informed by research. Proc Inst Civil Eng—Eng Sustain 163(ES2):77–87
8. BASF.2008. Building a sustainable future. The BASF house—UK project. BASF Plc.: Cheadle
9. Rodrigues LR (2009) An investigation into the use of thermal mass to improve comfort in UK housing. PhD Theses. University of Nottingham, Nottingham
10. Gough R (2012) Investigation into low carbon heating systems for the UK domestic sector. Dissertation, University of Nottingham, Nottingham
11. TuTiempo (2012) http://www.tutiempo.net/en/Climate/NOTTINGHAM-WATNALL/33540.htm, Accessed 13 March 2012
12. Met Office (2012) http://www.metoffice.gov.uk/climate/uk/stationdata/suttonboningtondata.txt. Accessed 13 March 2012
13. Airconwarehouse (2012) http://www.airconwarehouse.com/acatalog/Panasonic-Aquarea-Brochure-Airconwarehouse.pdf. Accessed 13 March 2012
14. Energy Saving Trust (2011) http://www.energysavingtrust.org.uk. Accessed 13 March 2012

Chapter 20
A Solar Water Heater for Subzero Temperature Areas

Naeem Abas, Nasrullah Khan and Ishtiaq Hussain

Abstract There is a general consensus that prevailing Energy Crises 2050 will lead towards a serious shortage of fossil fuels in near future. Avoiding Global warming and energy crises are two major challenges to be faced in the coming decade. In this scenario, synthetic refrigerants are well known to create global warming and ozone depletion phenomena. Among natural refrigerants, CO_2 having favourable properties in terms of heat transfer and thermodynamics, has been chosen as refrigerants in this study. This paper presents an optimal design and implementation of CO_2 based solar water heater using evacuated glass tubes for low insulation area like Gilgit-Baltistan. The performance of designed/fabricated system has been measured using Thermosyphon arrangements. Several parameters, i.e. header design, filling pressure and temperature, height of tank, heat exchanger design, pipe size and its material, of this self-sustained energy free system have been thoroughly studied. Further, they have been optimized for the best performance.

Keywords Energy crises · Thermosyphon · Solar water heater · heat transfer

20.1 Introduction

Prevailing energy crisis 2050, as a view point; there is immense need to explore and develop new sustainable energy options for increasing population and energy needs on planet earth. This fragile planet has bundle of options for its energy survival but requires a thirst to tap it fully. Efforts have to be carried out to discover the hidden treasures of energy. Nature helps us by providing unending sources of energy in the

N. Abas (✉) · N. Khan
Department of Electrical Engineering, COMSATS Institute of Information Technology, Park Road Chak Shehzad, Islamabad, Pakistan
e-mail: naeemk56@yahoo.com

N. Khan
e-mail: nasrullahk@yahoo.co

I. Hussain
National Center for Physics, Islamabad, Pakistan
e-mail: ishtiaq.hussain@ncp.edu.pk

I. Dincer et al. (eds.), *Progress in Sustainable Energy Technologies: Generating Renewable Energy,* DOI 10.1007/978-3-319-07896-0_20,

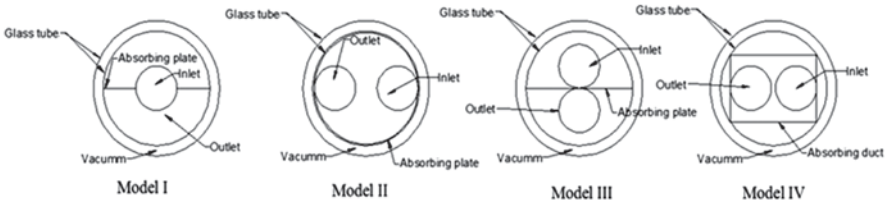

Fig. 20.1 Cross section of models with different shapes of absorbing tube

form of sun, wind, geothermal and oceans. A lot of work has already been done on converting available sunlight into energy and power using Solar PV, concentrators, collectors, & water heaters [1].

Evacuated glass tubes (EGTs) have emerged as new technological trend in the market of solar water heaters across the globe. These tubes significantly have high efficiency and low manufacturing cost [2] EGT are made of two concentric borosilicate glasses with one end sealed are widely used in modern EGT solar water heaters. The outer glass is transparent that allows the incident solar flux to pass through the glass and reaches to second layer of glass tube that has special selective coating inside to absorb solar radiations. Vacuum thermally insulate the inner and outer glass tube, resulting in higher temperature in the inner glass tubes and ambient temperature in the outer glass tube.

Heat collection and transfer from inside of EGT is a major design challenge in today's high temperature and high pressure solar water heating systems. Cabanillas in 1995 measured the heat flux distribution on EGT, revealed that 57 % of total solar insulation falls on top half while remaining on lower half with minimum intensity on side of the EGT. Yong Kim (2006) [3] performed an experimental study on four of different shapes of absorber tubes inside the EGT as shown in Fig. 20.1.

All models were tested at incident angle 0°, 30° and 60° for beam radiations. Results show that model 2 is optimal for whole day performance. All models were tested at incident angle 0°, 30° and 60° for beam radiations. Results show that model 2 is optimal for whole day performance (Table 20.1).

These calculations on a single evacuated glass tube were made by considering the effect of beam radiation only and neglecting shadowing effect and diffuse radiations which are 33 % of total solar flux. These models were again experimentally tested using 3 tubes and he considered this time effect of shadow and diffuses radiations. Experimental results were quite different from previous attempt. He observed that model 3 is 18.5 % more efficient than model 2 and 28.7 %, 26.9 % more efficient than model 1 and model 4 respectively. He suggested that model III has given best performance for whole day results. Keeping in view the above results a new shape of absorber tube was designed and implemented on U shaped heat pipe.

If the arrangement of EGTs is such that the distance between the centers of the 2 tubes is same as the outer diameter, then results of shading effect are optimal. Michel Hayek in 2011 [4] experimentally proved that heat pipe based collectors have 15–20 % higher efficiency than water in glass tubes solar collectors.

Table 20.1 Efficiencies of different models of EGT absorber shape [3]

Design Model	Efficiency			Average
	0°	30°	60°	η
Model 1	55.1	51.1	33.9	48.03
Model 2	63.2	63.2	63.2	63.20
Model 3	65.2	58.5	45.4	56.00
Model 4	58.1	61.9	44.0	54.66

For a radiation level of 1000 kWh/year/m^2 an evacuated glass tube solar water heater (ETSWH) can collect annually 28 % more energy [5] than flat plate solar water heater (FPSWH). In ETSWH for transfer of collected heat two methods are used, direct fluid flow and heat pipe system. Heat pipe system have several advantages over direct fluid flow as they act as thermal diode, hold up high pressure and freezing, and have higher efficiency than direct flow method. However the ETSWH have higher initial costs than FPSWH. In present system U shaped heat removal heat pipes with two input and output manifold are used.

CO_2 is an old natural refrigerant used by Thaddon S.C low in 1866 [6] and was later replaced by CFC and HFC. CO_2 has low critical temperature 31.1 C and pressure 7.38 MPa. The heat transfer and transport properties are attractive and favorable as a working fluid in sub-zero region with low solar insulation. CO_2 being non-toxic non-flammable [7] having high vapor pressure and volumetric refrigeration capacity enables smaller system size.

X.R Zhang and his colleagues in 2004 conducted a feasibility study on Solar Powered Rankin Cycle using CO_2 as working fluid (SCRS) and they showed that CO_2 could be efficiently used as working fluid in trans critical state with higher efficiency. Later in 2007 X.R Zhang and his co research workers experimentally investigated the performance of supercritical CO_2 as working fluid in evacuated glass tube (EGTs) solar collectors with liquid CO_2 pump. The results show that thermal efficiency of SCRS is 65–70 % which is higher when water is used as working fluid in EGTs and power generation efficiency is (8.78–9.45 %) also more than Photovoltaic [1, 6].

Numerous work has been done by Rieber [8] Ochner [9] and J Jeong [10]. H. Yamaguchi in 2009 [11] with his team performed an experimental study on thermosyphon based SWH using CO_2 as working fluid. They used EGT with U shape heat removal tubes of stainless steel material. In present experimental study heat removal tubes of copper are used to take advantage of thermal conductivity of copper which is 28 times higher than stainless steel.

Adnan Shariah proposed [12] an optimal design for thermosyphon based SWH using TRNSYS software. He showed that with appropriate selection of design parameters solar fraction may be improved 10–25 %. Adnan Shariah with his simulation results showed that the height of up riser in thermosyphon system is same as length of storage water tank. This optimization is adopted in present experimental study.

In FPSWH the input and output ports are different datum levels executing a natural circulation in expected direction, while in ETSWH the reverse thermosyphon

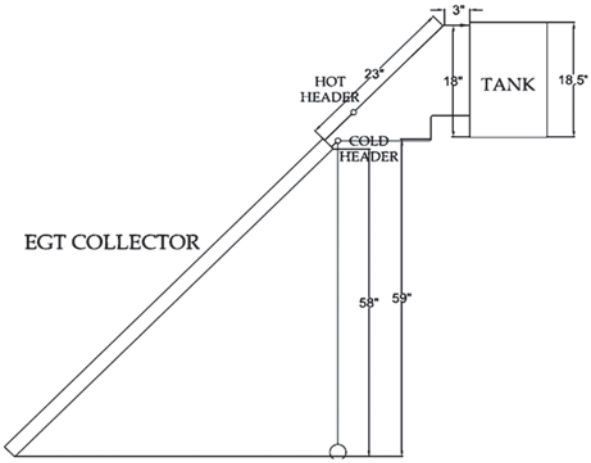

Fig. 20.2 Layout of CO_2 Thermosyphon solar water heater

is major issue to be addressed. Redpath in 2011 after a series of extensive work on thermosyphon based ETSWH and their associated problems, proposed that 5° inclination in header and from horizontal may block the reverse thermosyphon significantly which is opted in presents test rig [5, 7].

Gilgit-Baltistan is located on north side of Pakistan with average 16 MJ/m^2 solar insolation level. CO_2 exhibits critical point at 31.1 °C and 73 bar pressure. The high pressure constraint was achieved by filling the system at 70 bar and high temperature will be achieved by mild solar sunshine.

20.2 Experimental Setup

Layout of ETSWT using CO_2 as working fluid with optimized design based on natural convection of CO_2 is shown in Fig. 20.2. The density difference property of CO_2 will ensure the flow of CO_2 after gaining heat from EGT collector to storage water tank. The system consists of a series of EGTs as heat collecting source, two manifolds (headers) and heat exchanger passing through storage tank as shown in Fig. 20.3.

Heat collecting unit consist of 16 borosilicate glass, three layers coated evacuated glass tubes of dimension 1800*58*48 mm. EGTs have absorbance range 0.90–0.92 and a vacuum of 5*10^{-3} Pa. These tubes are mounted on a purpose built aluminum stand with rubber support on top and bottom.

For flow of high pressure CO_2, U shaped copper tubes of wall thickness of 1 mm having tube length 3200 mm are fixed inside the EGT with wooden cork as shown in Fig. 20.3. The wooden corks are sealed with silicon to with stand with high temperature and to avoid heat loss in open air. Stainless steel tubes were mainly used in previous several experiments conducted by H. yamaguchi, X.R. Zhang and their colleagues. As copper has higher thermal conductivity and heat transfer properties

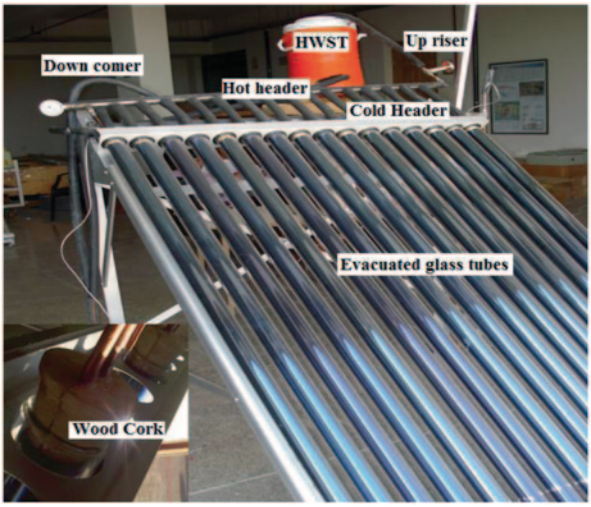

Fig. 20.3 Experimental test rig of ETSWH using CO_2 as working Fluid

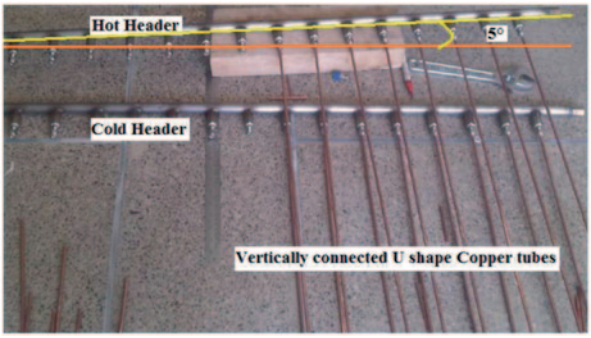

Fig. 20.4 Parallel headers U shape copper tubes

as compared to stainless steel. The U shaped copper loops have length 1750 mm down to bottom of evacuated glass tube connected in vertical mode.

20.3 Header Design

Two headers of length namely cold and hot, made of stainless steel are used in this setup. The hot header is at little higher datum level than cold header as shown in Fig. 20.4. Reverse Thermosyphon a major hurdle in Thermosyphon based solar water heaters, following arrangement has been adopted as shown in Fig. 20.4.

1. Hot header is at higher datum level then cold header hence supporting buoyancy forces.
2. Cold and hot headers are at an angle 5°, stopping reverse flow.

3. U shaped copper tubes are connected to headers in vertical arrangement so that upper portion is at higher temperature gradient than lower.
4. Aluminum fin in semicircle shape is used.

A heat exchanger of copper tube having length of 20 feet in helical shape is placed inside the hot storage tank of capacity 25 L. The output of hot header is connected to heat exchanger through up-riser. Buoyancy forces resulting from heat collected inside the EGT move CO_2 to hot storage tank where is exchanges heat with water and cold CO_2 is again feed to system through down comer.

20.4 Co_2 Filling System

A CO_2 cylinder having capacity of 7 kg with hand operated valve is used for filling of CO_2 in the U shaped heat removal tubes. The cylinder is connected to main heat removal circuit through high pressure 3 way stainless steel valve and a short hose of length 9.52 mm. Stainless steel valve has withstand high pressure ability up to 6000 PSI. The 3 way SS valve has ability to discharge pressure in open air accumulated in short hose during filling of CO^2 in system, hence ensuring safety. The amount of CO_2 to be charged in system, holds a key importance. In existing system the charged amount is 1.428 kg at pressure 60 bar initially. 2 glycerin filled pressure and temperature gauges of size ¼ inches made by WIKI Germany having measuring capacity of 250 bar and 350 °C were installed in test rig.

20.5 Results and Discussion

Serpentine Heat Removal Tubes

Initially the copper heat removal tubes were connected in serpentine arrangement in EGT collector as shown in Fig. 20.5. The system was filled with CO_2 at pressure 40 bar and was made exposed to bright sunshine. The temperature and pressure are plotted in Fig. 20.6.

The temperature and pressure inside the heat removal tube increased but no heat transfer was found in this arrangement. The CO_2 gas was filled at different pressure ranging from 40 to 70 bar, but thermosyhpon did not occur in any of the case.

Parallel Heat Removal Tubes

U shaped heat removal tubes were connected in parallel arrangement with hot and cold header as shown in Fig. 20.2. CO_2 was filled in system at −5 °C and different

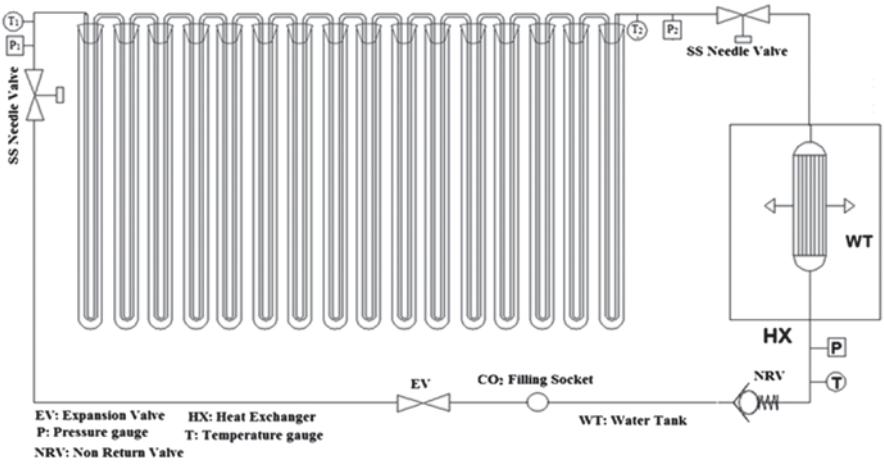

Fig. 20.5 Layout of serpentine heat removal arrangement

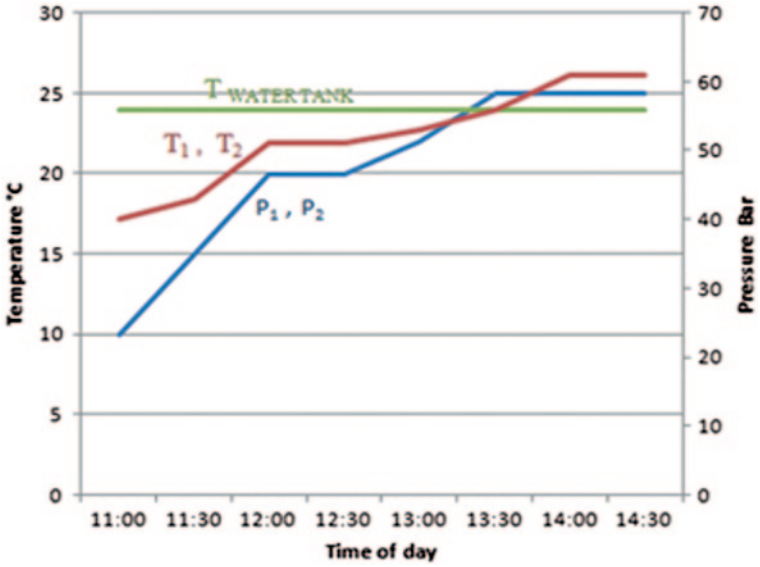

Fig. 20.6 Temperature pressure graph of serpentine arrangement

pressure ranging from 40 to 70 bars. The termsyphon got successful at minimum pressure from 65 to 70 bars. A successful temperature difference $\Delta T = 10\,°C$ was achieved. During initial experiments, non return valves (NRV) were used to stop reverse thermosyphon but due to dry ice blockage NRV got damage causing a permanent blockage in line (Fig. 20.7).

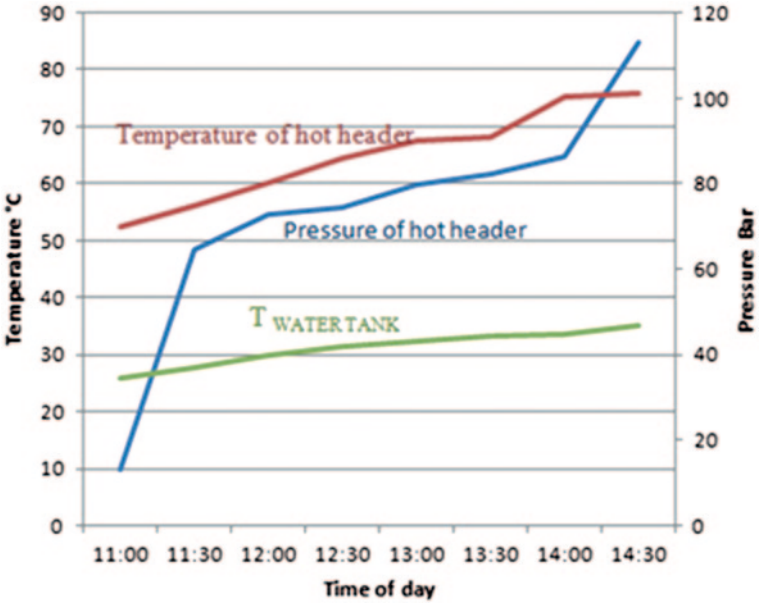

Fig. 20.7 Temperature pressure graph of parallel arrangement

Conclusions

The EGTs using CO_2 as working fluid were tested on parallel and serpentine arrangement for thermosyphon operation. It was found that EGTs can only work with parallel heat removal arrangement. The optimal Thermosyphon design consists of hot hheader at higher datum than cold header. To improve efficiency and to stop reverse thermosyphon, it is recommended that hot header should be an inclination 5° or more and U shaped heat removal tubes may be connected to headers in parallel arrangement with semicircle aluminum fin. Non return valves provide permanent blockage hence must not be used in system. The height of up-riser is approximately same as length of water tank.

References

1. Zhang X-R, Yamaguchia H, Unenoa D, Fujimab K, Enomotoc M, Sawadad N (2006) Analysis of a novel solar energy-powered Rankine cycle for combined power and heat generation using supercritical carbon dioxide. Renew Energy 31:1839–1854
2. Morrision GL, Budihardjo I, Behnia M (2004) Measurement and simulation of flow rate in a water-in-glass evacuated tube solar water heater. Sol Energy 78:257–267
3. Kim Y, Seo T (2007) Thermal performances comparisons of the glass evacuated tube solar collector with shapes of absorber tube. Renew Energy 32:772–798

4. Hayek M, Assaf J, Lteif W (2006) Experimental investigation of the performance of evacuated tube solar collectors under eastern Mediterranean climate conditions. Energy Procedia 6:618–626
5. Redpath DAG, Lo SNG, Eames PC (2011) Experimental Investigation and optimisation study of a direct expansion thermosyphon heat-pipe evacuated tube solar water heater subjected to a northern maritime climate. Int J Ambient Energy 31(2):91–100
6. Yamaguchi H, Zhang X-R, Fujima K, Enomoto M, Sawada N (2006) Solar energy powered Rankine cycle using supercritical CO_2. Appl Therm Eng 26:2345–2354
7. Chen Y, Pridasawas W, Lundqvist P (2010) Dynamic simulation of a solar driven carbon dioxide transcritical power system for small scale combined heat and power production. Solar Energy 84:1103–1110
8. Rieberer R (2005) Naturally circulating probes and collectors for ground-coupled heat pumps. Int J Refrig 28:1308–1315
9. Ochsner K (2008) Carbon dioxide heat pipe in conjunction with a ground source heat pump (GSHP). Appl therm Eng 28:2077–2082
10. Jeong SJ, Lee KS (2010) An experimental study of a carbon dioxide-filled thermosyphon for acquisition of low-temperature waste energy. Int J Energy Res 34:454–461
11. Yamaguchi H, Zhang X-R, Sawada N, Suzuki H, Ueda U (2009) Experimental study on a solar water heater using supercritical Carbon dioxide as working fluid. Proceeding of the ASME 2009, 3rd International Conference of Energy Sustainability, San Francisco, California, USA
12. Shariah A, Shalabi B (1997) Optimal design for a thermosyphon solar water heater. Renew Energy 11:351–361

Chapter 21
Modeling of the Heliostat Field in Central Receiver Systems for A Given Input Power

Pouyan Talebizadeh, Mozzafar Ali Mehrabian, Morteza Abdolzadeh and Mohammad Reza Azmi

Abstract The aim of this paper is to model the heliostat field in central receiver solar power plant (CRSPP) for a given input power. An in-house computer program is developed based on the vector geometry to select an individual heliostat and calculate its characteristic angles at any time of the day, any day of the year and any location on earth. This program is also used for open loop control of the heliostat field. To find the layout of heliostat field, the radial staggered configuration is used for the heliostat field as one of the best configurations used so far. Then, the locations of heliostats are determined and the efficiency of each heliostat is calculated in order to find the most efficient heliostats in the field. The heliostats with higher efficiency (more than 80 %) are chosen to be located in the field. Then, by calculating the input power of each heliostat supplied to the receiver, the absorbed heat power by the receiver is calculated. Consequently the minimum number of heliostats with their locations is determined for a specific heat power. The results show that for a 20 MWt (thermal power) CRSPP, 294 heliostats are needed which result in a heliostat layout with 86.45 % total efficiency.

Keywords Central receiver system · Heliostat layout · Input power

P. Talebizadeh (✉)
Amirkabir University of Technology, Tehran, Iran
e-mail: talebizadeh.pouyan@aut.ac.ir

M. A. Mehrabian
Faculty of Mechanical Engineering,
Shahid Bahonar University of Kerman, Kerman, Iran
e-mail: ma_mehrabian@alum.mit.edu

M. Abdolzadeh
Faculty of Mechanical Engineering,
Kerman graduate university of technology, Kerman, Iran
e-mail: m.abdolzadeh@kgut.ac.ir

M. R. Azmi
Islamic Azad University-Science and Research Branch, Tehran, Iran
e-mail: mohamadrezaazmi@yahoo.com

I. Dincer et al. (eds.), *Progress in Sustainable Energy Technologies: Generating Renewable Energy,* DOI 10.1007/978-3-319-07896-0_21,

21.1 Introduction

The central receiver solar power plant (CRSPP) is known as one of the least expensive power plants to produce solar electricity on a large scale. In CRSPP, the solar radiation is reflected by the surrounding heliostat field onto a receiver, and then in the receiver the energy is converted into thermal power to generate electricity. The surrounding heliostat field has a significant cost contribution in CRSPP, almost 50 % of the total cost and 40 % of the total losses is assigned to the heliostat field. Therefore, the design and optimization of heliostat field layout are very important [1]. The idea of CRSPP was first discussed in 1956 by Baum et al. [2]. He planned to use 1300 mirrors and put them on the wagons and turned the wagons around a boiler.

Lipps and Vant-Hull [3] studied four categories of heliostat arrangement for 100 MW power plant. They introduced a cell model to establish an array of representative heliostats. They showed that N-S staggered configuration is suitable for the southern field; however, a radial staggered configuration can be used universally. Collado and Turegano [4] presented a procedure for evaluating the annual energy produced by a defined heliostat field as a product of annual energy per mirror and annual average mirrors per unit area. They presented an analytical function for the blocking factor as one of the main parameters in the optimization process in a radial staggered configuration which allows establishing the necessary radial increment between consecutive rows that verifies a fixed blocking factor.

Siala and Elayeb [5] presented the graphical method for a no-blocking radial staggered layout and introduced a mathematical formulation for the method. They divided the field into certain groups to increase the efficient use of land. They showed that the method is a simple one when compared to cell-wise procedure, making it more suitable for preliminary design of heliostat fields. Collado [6] introduced a simplified procedure to define a large number of heliostat coordinates through basically two parameters, i.e. a simplified blocking factor and an additional security distance throughout the field. He determined the layout of heliostat field for a constant blocking factor and height of the tower in Almeria, Spain. He compared his work with the previous cell wise method. Zhihao Yao et al. [7] modeled a 1 MW solar thermal central receiver system in China which is under construction. They developed a software tool[1] for heliostat field layout design and performance calculation and simulated the whole central receiver system in the TRNSYS plant model. In their work which is based on energy balance, they presented the mathematical procedure for calculating the absorbed power in the receiver. Xiudong Wei et al. [8] developed a new method for the design of the heliostat field layout for solar power tower. They considered the efficiency factor as the product of the annual cosine efficiency and the annual atmospheric transmission efficiency of heliostat and showed that the results are as good as considering the annual interception efficiency.

[1] Heliostat Field Layout Design (HFLD)

The purpose of this study is to design a surrounding heliostat field for a given input power on the receiver. In this procedure, the heliostats characteristic angles are determined to track the sun each moment which can be used for open loop control of the heliostat field. Then, the coordinates of each heliostat are found and their efficiencies are calculated and the best locations for placing the heliostats are predicted. Then, by calculating the produced power by the high efficient heliostats, the minimum number of heliostats for a given input power is determined. At last, the distribution of the heliostats is found for a 20 MWt CRSPP. Note that in the previous works, the heliostat layout was considered as one unit when the produced power was calculated. However, in this paper every heliostat is considered individually and therefore the input power of the heliostat field is the summation of the input power of each heliostat.

21.2 Mathematical Modelling

To define the layout of heliostats for a radial staggered configuration, some assumptions are made to determine the locations of heliostats [4]. Only the two heliostats that are next to each other in front row are considered to calculate the blocking factor and to develop the model. Shading is ignored because blocking has a more pronounced effect on the layout of heliostat field [9]. It is also assumed that the azimuth angle of the normal vector of the heliostat surface is the same as that of the unitary vector pointing to the tower from the center of the heliostat. With these assumptions, the radial increment between consecutive and staggered rows (ΔR) is defined as [4]:

$$\Delta R = \left[\left(\frac{cos\omega}{cos\varepsilon_T} \right) \left(1 - \frac{(1-f_b)wr}{2wr - (\sqrt{1+wr^2} + ds)} \right) \right] \times LH \tag{21.1}$$

where f_b is the blocking factor, i.e., the ratio of the heliostat area free of blocking to the total area of the heliostats, wr is the width–height ratio of the heliostat, LH is the height of the heliostat, and $ds \times LH$ is any additional security distance between adjacent heliostats in the same row. ω is the incidence angle of the sunrays onto the heliostat surface and ε_T is the elevation angle of the tower unit vector pointing from the center of heliostat surface to the receiver. ω and ε_T are shown in Fig. 21.1.

For determining ω and ε_T, an algorithm is developed based on the vector geometry to pick an individual heliostat and calculate its characteristic angles at any time of the day and any day of the year. As shown in Fig. 21.2, the unit vector along the reflected ray heading to the sun is shown by $\vec{s}$, the unit vector along the reflected ray heading to the receiver is shown by $\vec{r}$ and the unit vector along the reflected ray normal to the reflective plane is shown by $\vec{m}$.

The unit vector $\vec{m}$ determines the orientation of the mirror plane with respect to the sun and should be found in such a way that the reflected ray strikes the receiver.

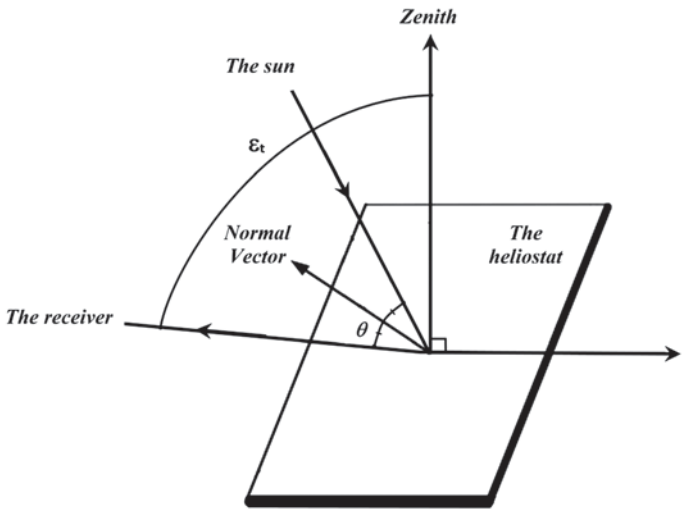

Fig. 21.1 The characteristic angles of the heliostat

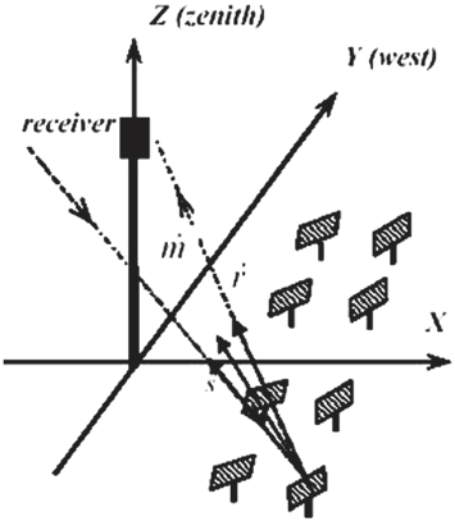

Fig. 21.2 Unit vector $\vec{s}$, $\vec{r}$ and $\vec{m}$ in the main coordinate system [10]

The unit vector $\vec{r}$ is a function of heliostat position with respect to receiver. If X, Y and Z are the coordinates of the heliostat center, the components of $\vec{r}$ are defined as follows:

$$r_x = -\frac{X}{\sqrt{X^2 + Y^2 + (THT - Z)^2}} \tag{21.2}$$

$$r_y = -\frac{Y}{\sqrt{X^2 + Y^2 + (THT - Z)^2}} \tag{21.3}$$

$$r_z = \frac{H - Z}{\sqrt{X^2 + Y^2 + (THT - Z)^2}} \tag{21.4}$$

The unit vector $\vec{s}$ can be defined in terms of three angles: latitude φ, solar hour angle ω, and solar declination angle δ. The components $\vec{s}$ are defined as follows [11]:

$$s_x = -\cos(\omega)\sin(\varphi)\cos(\delta) + \cos(\varphi)\sin(\delta) \tag{21.5}$$

$$s_y = \sin(\omega)\cos(\delta) \tag{21.6}$$

$$s_z = \cos(\omega)\cos(\varphi)\cos(\delta) + \sin(\varphi)\sin(\delta) \tag{21.7}$$

The definition of ω and δ are given in [12]. From the laws of reflection we have:

$$\vec{r} \times \vec{m} = \vec{m} \times \vec{s} \tag{21.8}$$

Therefore, the components of unit vector $\vec{m}$ are derived as follows [11]:

$$m_x = \frac{|s_z + r_z|}{s_z + r_z}(s_x + r_x) \times \frac{1}{\sqrt{(s_x + r_x)^2 + (s_y + r_y)^2 + (s_z + r_z)^2}} \tag{21.9}$$

$$m_y = \frac{|s_z + r_z|}{s_z + r_z}(s_y + r_y) \times \frac{1}{\sqrt{(s_x + r_x)^2 + (s_y + r_y)^2 + (s_z + r_z)^2}} \tag{21.10}$$

$$m_z = |s_z + r_z| \times \frac{1}{\sqrt{(s_x + r_x)^2 + (s_y + r_y)^2 + (s_z + r_z)^2}} \tag{21.11}$$

where the vectors $\vec{r}$, $\vec{m}$ and $\vec{s}$ are in hand, ω is defined as:

$$\cos\omega = \vec{s}.\vec{m} \Rightarrow \omega = \cos^{-1}(s_x m_x + s_y m_y + s_z m_z) \tag{21.12}$$

If the unit vector $\vec{k}$ is defined as [0 0 1], ε_T is calculated as follows:

$$cos\varepsilon_T = \vec{k}.\vec{r} \Rightarrow \varepsilon_T = cos^{-1}(r_z) \tag{21.13}$$

Figure 21.3 displays a schematic view of the locations of heliostats in the radial staggered configuration where the diameter of the heliostat (the length of the inner segment in the circles) is:

$$DH = \sqrt{LH^2 + wr^2 LH^2} = \sqrt{1 + wr^2} \times LH \tag{21.14}$$

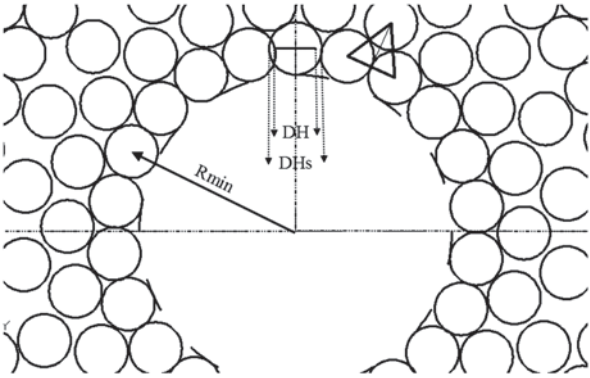

Fig. 21.3 The schematic view of the locations of the heliostat

This diameter plus the security distance (the diameter of the circles) will be:

$$DHs = (\sqrt{1 + wr^2} + ds) \times LH \tag{21.15}$$

As an approximation to the minimum increment of the radius between consecutive rows,

$$\Delta R \min \approx DHs \cos 30^{\circ} \tag{21.16}$$

Then, the constant azimuth angle increment used in a zone which is also the azimuth angle of the tower unit vector would be [6]:

$$\Delta\alpha_T = 2tan^{-1}((DHs/2)/Rzone) \tag{21.17}$$

Where $Rzone$ is the radius used for generating the first row of such heliostat zone. This azimuth increment will be conserved in the later outward rows in the same zone. So, adjacent heliostats in the same row become more separated from each other as the radius of the heliostat field increases. This will be continued until it would be possible to place one extra heliostat between them. Then, it should be necessary to start a new zone beginning with the first row, at a new $Rzone$, in which the adjacent heliostat circles would be tangent to each other again.

Given the first row and the azimuth increment for a zone, the problem is now to derive each local ΔR in the successive (staggered) rows with fixed blocking factor. Now, the position of the heliostats can be defined with $Rzone$, ΔR, α_T. On the other hand, the values of ω and ε_T can be found if the location of heliostats are known. So, an iterative process is scheduled, which is fed with $\Delta R_{\min}$ as the first approximation.

After determining the coordinates of all heliostats, the local heliostat field efficiency η_f as a parameter to find the best locations for placing the heliostats should be calculated. It will be defined as the products of cosine efficiency, the spillage factor (f_{sp}) i.e. the fraction of the energetic spot reflected by the heliostat which hits onto the receiver surface and the attenuation factor (f_{at}) i.e. the attenuation of

the reflected beam as it travels from the heliostat to the receiver. Therefore, η_f is defined as:

$$\eta_f = \cos\omega \cdot f_b \cdot f_{sp} \cdot f_{at} \tag{21.18}$$

According to [13], f_{at} for a clear day (23 km visibility) is calculated as follows:

$$f_{at} = 0.99326 - 0.1046S + 0.017S^2 - 0.002845S^3 \tag{21.19}$$

Where S is the distance from heliostat to the receiver in kilometers. The process of calculating f_{sp} is given in [4]. A computer code has been developed using Matlab software to determine the location of each heliostat by iteration and then calculate the efficiency of each heliostat. The total efficiency of the surrounding heliostat field is the average of the efficiencies of all heliostats.

For calculating the input power on the receiver, the input power of each heliostat is determined and the dissipations of the receiver are subtracted from it. According to [4], the input power of each heliostat supplied to the receiver per unit area of mirror is calculated as follows:

$$P_{m,A} = I \cdot \rho \cdot \cos\omega \cdot f_{sp} \cdot f_{sb} \cdot f_{at} \quad (W/m^2) \tag{21.20}$$

where ρ is the reflectivity coefficient, I (W/m^2) is the direct solar irradiation at the design point and f_{sb} is the fraction of area free of shadows and blocking. Due to the more pronounced effect of f_b on the layout of heliostat field, f_{sb} is assumed to be equal to f_b.

According to [14], some other efficiencies should be considered as follows:

$$P_{tot,A} = P_{m,A} \cdot \eta_{ave} \cdot \eta_R \cdot \eta_{sto} \quad (W/m^2) \tag{21.21}$$

where η_{ave} is the field availability performance factor which includes maintenance, outages, etc. and is set to 0.99, which would correspond to commercial plant predictions [15]. Furthermore, in the solar two project [15], the receiver efficiency η_R was defined as the quotient of absorbed power/incident power on the receiver which was determined as 88 % and the same value is incorporated in this study [15]. η_{sto} is the storage tank efficiency which is about 99 % for the molten salt storage tanks [14].

Therefore, the heat power onto the receiver by each heliostat is evaluated by:

$$Q_{inc} = P_{tot,A} \times A_h \quad (W) \tag{21.22}$$

Where A_h is the area of the heliostats and is equal to $wr \cdot LH^2$. At last, the produced power of all heliostats is determined as follows:

$$\dot{Q}_{inc,tot} = \sum_{i=1}^{n} \dot{Q}_{inc,i} \quad (W) \tag{21.23}$$

Table 21.1 The constant parameters used in this paper

f_b	0.95	A_a	25 m^2
LH	SQRT(120)	A_r	40 m^2
ρ	0.888	ε	0.88
wr	1	$R_{\min}$	65 m
ds	0.3	I	950 W/m^2
α	0.97	THT	130 m
Fraction of mirror area in heliostat	0.9583	Standard deviation of sun shape	2.51 mrad

where n is the number of heliostats.

The net absorbed heat power of the receiver is defined as [7]:

$$\dot{Q}_{net} = \alpha \dot{Q}_{inc,\,tot} - \dot{Q}_{conv} - \dot{Q}_{emi} \quad (W) \tag{21.24}$$

where α is the absorbtion coefficient of the receiver. $\dot{Q}_{conv}$ is the convection loss which is defined as follows [7]:

$$\dot{Q}_{conv} = hA_r(T_w - T_A) \quad (W) \tag{21.25}$$

h is the combined forced and natural convection coefficient which is found in [7] and A_r is the area of the receiver.

$\dot{Q}_{emi}$ is the radiation loss and can be calculated as follows:

$$\dot{Q}_{emi} = \sigma \varepsilon A_a (T_w^{\,4} - T_A^{\,4}) \quad (W) \tag{21.26}$$

where σ (5.67×10–8 W/m^{2}K^4), ε is the emissivity and A_a is the receiver aperture area.

In Table 21.1, the values of constant parameters which are used in the design of the heliostat layout are listed [6].

21.3 Results and Discussion

In this section, the validation of the code is studied first and then the layout of heliostat field is discussed. At the end, the layout of heliostat field for a specific input power is determined and a 20 MWt CRSPP is modeled.

For the validation, the results of the computer code are compared with the results of Collado [6]. Figure 21.4 displays the distribution of the surrounding heliostat field achieved in this paper in comparison with Collado for Almeria, Spain. As it is shown the two sets of results are in excellent agreement with each other.

Note that the process of determining ΔR for the present work is based on the vector geometry and the aim of this paper is doing the same process for Kerman, Iran for a constant input power in order to study the feasibility of constructing a CRSPP in this area.

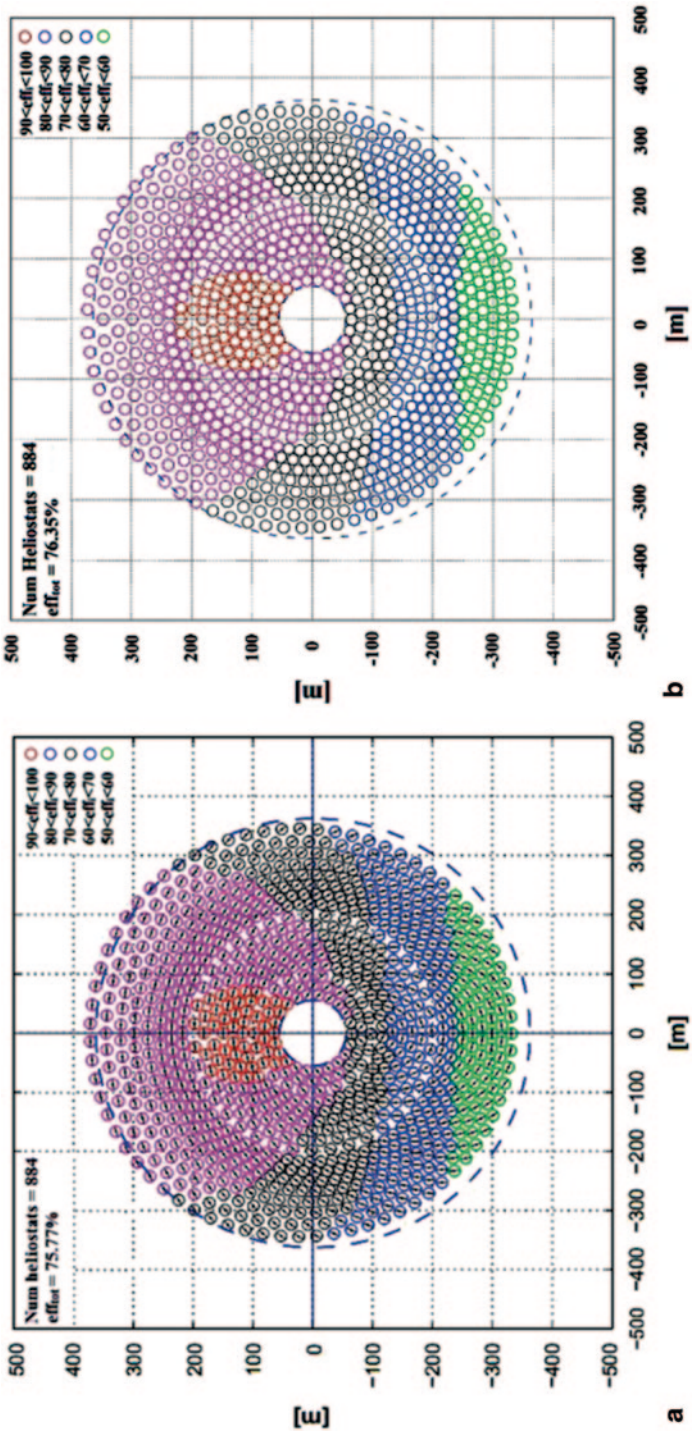

Fig. 21.4 The distribution of the surrounding heliostat field in Almeria, Spain

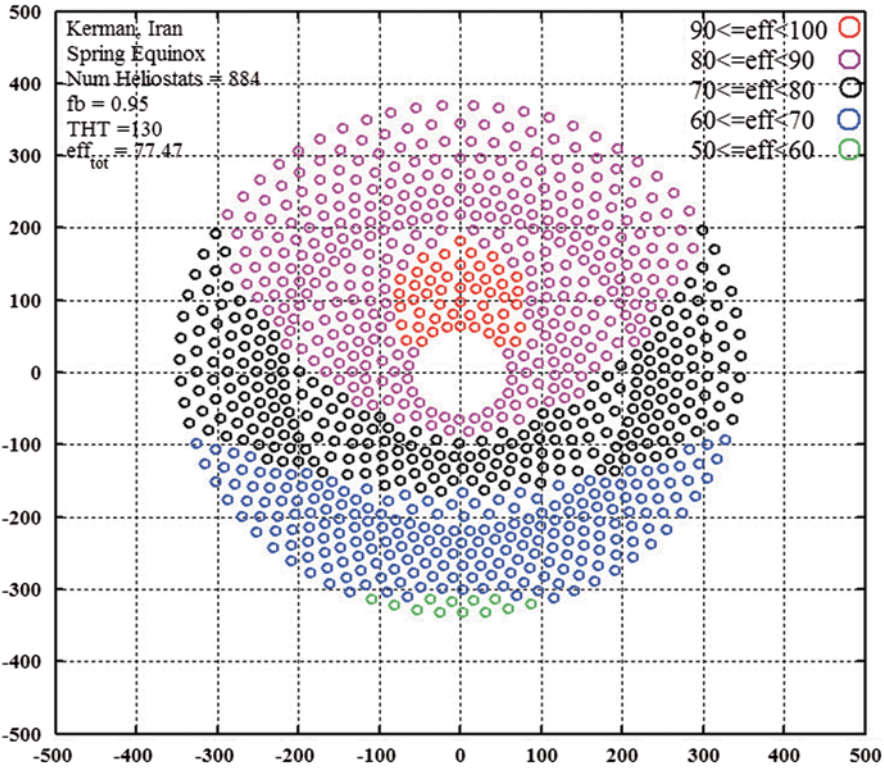

Fig. 21.5 The distribution of the surrounding heliostat field in Kerman, Iran for the spring equinox

After verifying the code, finding the layout of heliostat field is done for Kerman, Iran with the latitude of 30.28°. Figure 21.5 displays the distribution of heliostats with their efficiencies for the spring equinox (March 21) at noon. According to [6], spring equinox is defined as the design point. Note that in Figs. 21.5, 21.6, 21.7 and 21.8, the radius of heliostats does not match with the distance between them.

As it is shown in Fig. 21.5, the higher efficiency belongs to the heliostats on the north axis, near the tower, because Kerman is in the north hemisphere like Almeria. However, the total efficiency of the surrounding heliostat field is higher in Kerman than Almeria due to the higher solar intensity in this area. The mirror density is higher at the south of the tower and is decreased slowly toward the west/east sides (because of symmetry), and finally approaches to the lowest level at the north of the tower.

Figure 21.6 shows the layout of the heliostats with the efficiencies more than 90%. It should be mentioned that when the heliostats with the efficiencies more than 90% (51 heliostats) are considered, only 3.07 MW heat power can be collected on the receiver.

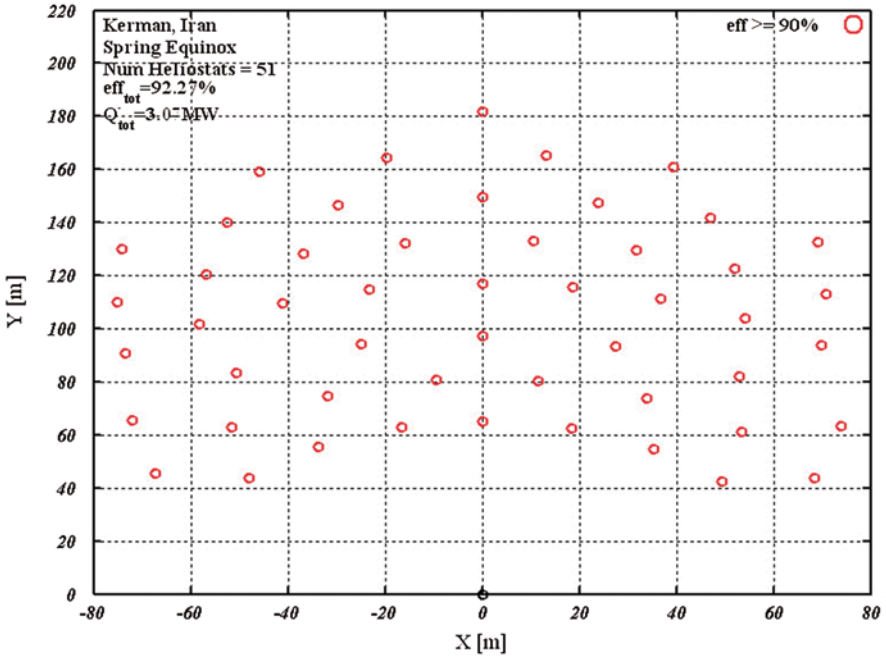

Fig. 21.6 The heliostat layout for heliostats with efficiencies more than 90 %

Note that the difference between present study and Zhihao et al. [7] in the calculation of absorbed heat power is that in this study, the absorbed heat power of individual heliostats are first calculated and then added to each other to calculate the total absorbed heat power, however, Zhihao et al. [7] considered a constant cosine efficiency and a constant attenuation efficiency for all the heliostat field and due the variation of this parameter from one heliostat to another, the process in this study is more accurate than Zhihao et al. [7]. In addition, some other efficiencies (η_{ave}, η_R and η_{sto}) are also considered in this paper.

In Fig. 21.7, the distribution of the heliostats with the efficiencies more than 80 % is illustrated. As shown in this figure, with 409 heliostats having efficiencies more than 80 %, almost 27.7 MW absorbed heat power is collected on the receiver.

Note that in Figs. 21.6 and 21.7, eff_{tot} is the average of the efficiencies of the heliostats.

In the process of modeling the heliostat layout, as mentioned before, first the heliostats with higher efficiencies are chosen to be located in the field. The aim of this study is to find the best heliostat layout that can provide 20 MW absorbed heat power on the receiver. So, for this purpose, heliostat with higher efficiencies are located one by one (from the heliostat with the highest efficiency to the lowest one) and their input power are calculated and add to each other until the total input power is equal to 20 MW. Then, the computer code is stopped and the distribution of the heliostats is found.

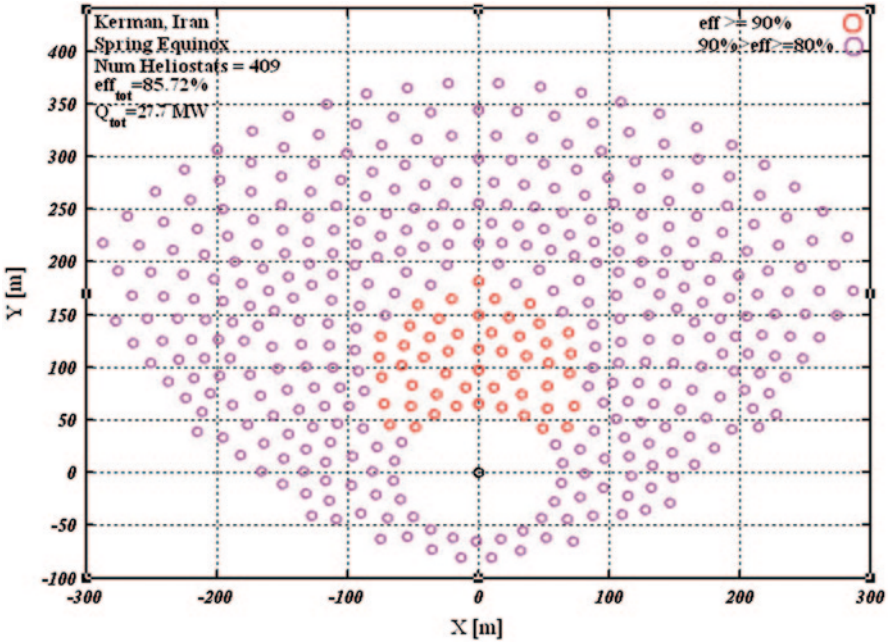

Fig. 21.7 The heliostat layout for heliostats with efficiencies more than 80 %

The distribution of the heliostat field for a plant with 20 MW input power is displayed in Fig. 21.8. As shown in this figure, with 294 heliostats and the present method, the total efficiency of the heliostat layout is 86.54 %. With the same method, the distribution of the heliostat field for different given input power can be modeled.

Conclusions

In this paper, the design and modeling of a surrounding heliostat field for a Central Receiver Solar Power Plant is carried out for Kerman, Iran. The vector geometry is used for calculating the characteristic angles and the cosine efficiency of the heliostats. Then by considering a constant-in-time blocking factor for a radial staggered configuration, the distribution of the heliostats is introduced and the efficiencies of the heliostats is calculated in order to select the heliostat with higher efficiencies. Therefore, the areas with more efficient heliostats are selected. Then, the design is repeated for the heliostat layout under the condition of constant absorbed power for finding the minimum number of heliostats. For this purpose, more efficient heliostats are considered and the absorbed power of these heliostats is calculated. Due

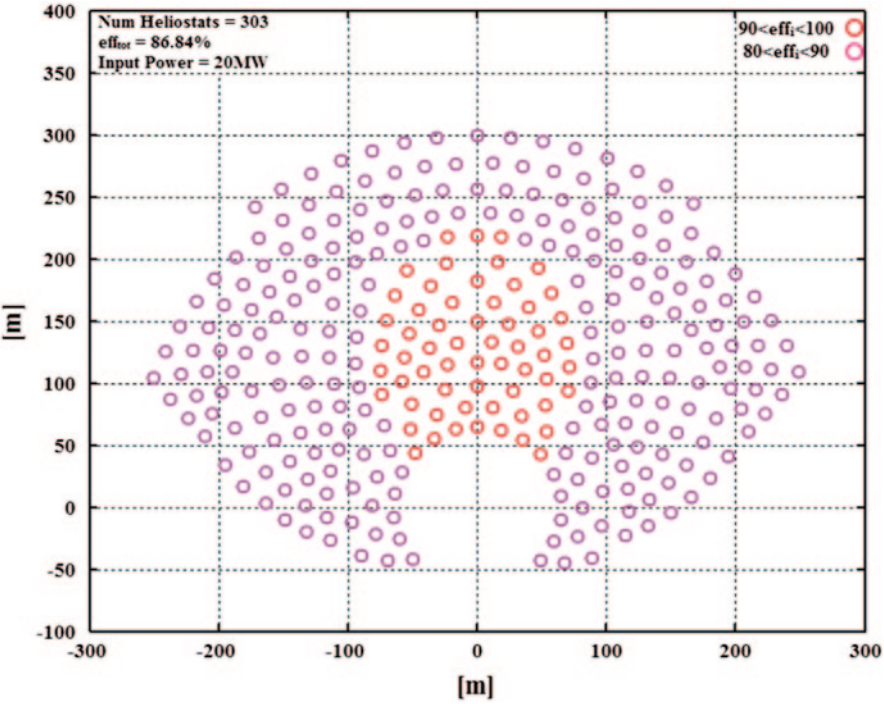

Fig. 21.8 The distribution of the surrounding heliostat field for a 20 MWt CRSPP

to the high cost of the surrounding heliostat field and also less dissipation of the energy, the optimum design of the surrounding heliostat field is very important.

Nomenclature

A_a	The receiver aperture area (m^2)
A_h	Area of the heliostat (m^2)
A_r	The area of the receiver (m^2)
A_{tot}	Total area (m^2)
DH	This diameter of the heliostat (m)
DHs	This diameter of the heliostat plus the security distance (m)
ds	The security distance–heliostat height ratio
eff_{tot}	The total efficiency of the surrounding heliostat field (%)
f_{at}	The attenuation factor
f_b	The blocking factor
f_{sb}	The Shadow-blocking factor
f_{sp}	the spillage factor
h	The combined force and natural convection coefficient ($W/m^2\,^\circ C$)
I	the direct solar irradiation at the design point (W/m^2)

$\vec{k}$	k unit vector [0 0 1]
LH	Height of the heliostat (m)
$\vec{m}$	The unit vector along the reflected ray normal to the reflective plane
n	Number of heliostats
$p_{tot,A}$	The total input power of each heliostat per unit mirror area (W/m^2)
PH	Spillage function
$\dot{Q}_{conv}$	The convection loss (W)
$\dot{Q}_{emi}$	The radiation loss (W)
$\dot{Q}_{inc}$	The heat power onto the receiver by each heliostat (W)
$\dot{Q}_{inc,tot}$	The produced power of all heliostats (W)
$\dot{Q}_{net}$	The net absorbed heat power of the receiver (W)
R_{zone}	The radius of each heliostat zone (m)
$\vec{r}$	The unit vector along the reflected ray directed to the receiver
S	The distance from heliostat to the receiver (km)
$\vec{s}$	The unit vector along the reflected ray directed to the sun
T_a	The ambient temperature (˚C)
T_w	The mean receiver wall temperature (˚C)
THT	Height of the tower (m)
wr	Width height ratio
X	The X coordinate of the heliostat center
Y	The Y coordinate of the heliostat center
Z	The Z coordinate of the heliostat center

Greek Symbols

ΔR	The radial increment between consecutive and staggered rows (m)
ΔR min	The minimum radial increment between consecutive and staggered rows (m)
$\Delta\alpha_{\mathrm{T}}$	Constant azimuth angle increment
α	The absorption coefficient of the receiver
Δ	Solar declination angle (˚)
ε	Emissivity
ε_T	The elevation angle (˚)
η_{ave}	The field availability performance factor
η_f	The local heliostat field efficiency
η_R	The receiver efficiency
η_{sto}	The storage tank efficiency
η_{tra}	The tracking error
θ	The incidence angle (˚)
ρ	The reflectivity coefficient
σ	Stephan-Boltzmann constant ($5.67 \times 10–8$ W/m^{2}K^4)
σ_r	The dispersion of the effective sun shape on the receiver
φ	Latitude (˚)
ω	Solar hour angle (˚)

References

1. Kolb GJ, Jones SA, Donnelly MW (2007) Heliostat cost reduction study SAND 2007–3293
2. Baum VA, Aparasi RR, Garf BA (1957) High power solar installation. Sol Energy 1:6–12
3. Lipps FW, Vant-Hull LL (1975) A cell wise method for the optimization of large central receiver systems. Sol Energy 20:505–516
4. Collado FJ, Turegano JA (1989) Calculation of the annual thermal energy supplied by a defined heliostat field. Sol Energy 42:49–65
5. Siala FMF, Elayeb ME (2001) Mathematical formulation of a graphical method for a no-blocking heliostat field layout. Renew Energy 23:77–92
6. Collado FJ (2009) Preliminary design of surrounding heliostat fields. Renew Energy 34:1359–1363
7. Zhihao Y, Zhifeng W, Zhenwu L, Xiudong W (2009) Modeling and simulation of the pioneer 1 MW solar thermal central receiver system in China. Renew Energy 34:2437–2446
8. Xiudong W, Zhenwu L, Zhifeng W, Weixing Y, Hongxing Z, Zhihao Y (2010) A new method for the design of the heliostat field layout for solar tower power plant. Renew Energy 35(9):1970–1975
9. Falcone PK (1986) A handbook for solar central receiver design. SAND86–8009, Albuquerque
10. Talebizadeh P, Mehrabian MA, Abdolzadeh M (2011) The process of designing surrounding heliostat field for a central receiver solar power planet the 10th international conference on sustainable energy technologies (SET), Kumburgaz, Istanbul, Turkey
11. Talebizadeh P, Mehrabian MA, Rahimzadeh H (2013) The optimization of heliostat layout in central receiver solar power plants. J Energy Eng (in press)
12. Duffie JA, Beckman WA (1982) Solar engineering of thermal processes. Wiley, New York
13. Vittitoe CN, Biggs F (1978) Terrestrial propagation loss, paper presented at the American section international solar energy society meeting, August, Denver, Colorado
14. Collado FJ (2008) Quick evaluation of the annual heliostat field efficiency. Sol Energy 82(3):79–84
15. Pacheco JE, Reilly HE, Kolb GJ, Tyner CE (2000) Summary of the solar two: test and evaluation program. Alburquerque (NM), SANDIA Labs: SAND2000–0372 C

Chapter 22
Single Pass Solar Air Heater Without Absorber

Raheleh Nowzari and Loay Aldabbagh

Abstract The single pass solar air heater is constructed and tested for thermal efficiency at a geographic location of Cyprus in the city of Famagusta. The length and the width of the collector are 150 and 100 cm respectively. The distance between the cover glass, 0.4 cm in thickness, and the bottom of the collector, is 3 cm. The absorber plate was replaced by fourteen steel wire mesh layers, 0.2×0.2 cm in cross section opening, and they were fixed in the duct parallel to the glazing. The distance between each set of wire mesh layers is 0.5 cm to reduce the pressure drop. The wire mesh layers were painted with black before installing them into the collector. The obtained results show that as the mass flow rate increases, the efficiency of the system will also increase. The temperature difference (ΔT) between the inlet and outlet air through the system increases as the mass flow rate decreases. The maximum ΔT (45.8 °C) is achieved at the flow rate of 0.011 kg/s. The range of the mass flow rate used in this work is between 0.011 and 0.04 kg/s. It is also found that the maximum efficiency obtained for the single pass air collector is 53.01 % for the mass flow rate of 0.04 kg/s.

Keywords Single Pass · Solar air heater · Wire mesh layers · Thermal Efficiency

22.1 Introduction

Solar air heater is a simple device that heats air by utilizing solar energy from the sun. Its wide range of applications involves drying of agricultural products, such as seeds, fruits, vegetables and space heating [1]. Also, solar air heaters are used as pre heaters in industries and as auxiliary heaters in buildings to save energy during winter times[2] Conventional solar air heaters mainly consist of a panel, insulated hot air ducts, a glass cover and air blowers if it is an active system. The panel consists

R. Nowzari (✉)
Mechanical Engineering Department, Istanbul Aydin University,
Florya, Istanbul, Turkey
e-mail: raheleh298@yahoo.com

L. Aldabbagh
Mechatronics Engineering Department, College of Engineering, Mosul University, Mosul, Iraq
e-mail: loayaldabbagh@uomosul.edu.iq

I. Dincer et al. (eds.), *Progress in Sustainable Energy Technologies: Generating Renewable Energy,* DOI 10.1007/978-3-319-07896-0_22,

of an absorber plate which is placed inside the hot air duct. The hot air duct is made from either wood or other metallic and non-metallic materials. This is thermally insulated from the bottom and all the sides are also insulated. A glass or plastic cover is fixed above the absorber plate to form a passage for air flows. There are different factors affecting the air heater efficiency, these include collector length, collector depth, type of the absorber plate, glass cover, wind speed, inlet temperature, etc. Among all, the collector glass cover and the absorber plate shape factor are the most important parameters in the design of any type of air heater [3]. The heat transfer coefficient between the air stream and the absorber plate is an important factor in solar air heaters. The air heater will have low thermal efficiency as a result of a low heat transfer coefficient between the absorber plate and the air flow. A solution to this problem is to modify the absorber plate. Different adjustments on the absorber part of the air heater were done by researchers to increase the thermal efficiency of the solar systems. Using fin on the absorber plate [4], adding porous material inside the collector [5], or making a cross-corrugated absorber plate [6] are the samples of these modifications. The thermal performance of a single and double pass solar air heater with fins attached and using steel wire mesh layers as absorber plate was investigated experimentally by A.P. Omojaro and Aldabbagh [3]. For the single pass solar air heater, they were used seven steel wire mesh layers and the range of the air mass flow rate was between 0.012 and 0.038 kg/s. Also the distance between the glass and the bottom of the collector, was 7 cm. According to their study the maximum efficiency obtained for this single pass air heater was 59.62 % for air mass flow rate of 0.038 kg/s. To achieve high thermal efficiencies and reducing heat losses from the cover, a novel solar air collector of pin-fin integrated absorber was designed by [7]. In their design the gap between the glazing and the absorber plate was 5 cm. According to their experimental results, the average thermal efficiency of pin-fin arrays collector reaches 50–74 % compared to the solar transmittance of 83 % for the glazing, for the air volume flow rate of 19 m^3/h. The investigations on a packed bed solar air heater having its duct packed with blackened wire screen matrices of different geometrical parameters (wire diameter and pitch) were performed by Mittal and Varshney [8] and their resulting values of effective efficiency clearly indicate that the thermal gain of packed bed collectors is relatively higher as compared to smooth collectors, although the pressure drop across the duct increases significantly. A single-glazed solar matrix air collector was tested by Kolb et al. [9].

Their collector consists of two parallel sheets of black galvanized industrial woven, fine-meshed wire screens made of copper. Their results show that at the duct height of 4 cm and mass flow rate of 0.04 kg/s, the thermal efficiency of the solar air heater is around 70 %. Ho-Ming Yeh et al. [10] has designed a solar air heater in which the absorber plate was constructed with fins and the fins have been attached by the baffles to create turbulence and extend the heat transfer area. In their work, the distance between the second glass and the absorber plate was 5.5 cm and they were found that the collector efficiency of baffled solar air heaters is larger than that of flat plate heaters without fins and baffles. The thermal performance of cross-corrugated solar air collectors was studied by [6]. The cross-corrugated collectors

consist of a wavelike absorbing plate and a wavelike bottom plate, which are crosswise positioned to form the air flow channel. In their study, the mass flow rate ($\dot{m}$) changes in the range of 0.001–0.25 kg/m^2 s. Their results show that the efficiencies of collectors increase monotonically and dramatically with $\dot{m}$, therefore, to achieve a better thermal performance of the solar air collectors it is essential to maintain a higher air mass flow rate. Several configurations of copper screen meshes were investigated experimentally by [5]. They were found that the overall heat transfer depends on porosity and surface area density.

The aim of this study is to investigate experimentally the efficiency of a single pass solar air heater with porous media acting as an absorber plate. The height of duct is fixed at 3 cm. The porous media in this system consists of steel wire mesh layers arranged in a way to give low pressure drop across the collector.

22.2 Experimental Set-Up and Equipment

The experimental work on the single pass solar air heater was conducted at a geographic location of Cyprus in the city of Famagusta. The schematic view of the constructed single pass air collector is shown in Fig. 22.1. The collector length and width were 150 and 100 cm respectively. The distance between the glass cover and the bottom of the collector, duct height, was 3 cm. The frame of the solar collector was made from plywood of 1.8 cm in thickness and the whole frame was painted with black. To minimize the heat losses, the sides and bottom of the frame were insulated with 3 cm thick Styrofoam. Normal window glass of 0.4 cm thickness was used as glazing. Fourteen steel wires mesh layers, 0.2×0.2 cm in cross section opening and 0.025 cm in diameter, were fixed in the collector parallel to the glazing. The wire meshes are actually the ordinary wire screens which everyone uses on the windows in order to prevent the winged insects to enter the house. The wire meshes which are used in our collector are similar to the ones which were used by [3, 4, 11]. The arrangement of the wire mesh layers is as follows:

Six wire mesh layers were attached to each other, as one matrix, and placed at the bottom of the collector, five more layers were attached with each other and placed at the middle and the last three meshes were connected to each other and located on top of the other layers. The distance between the three sets of wire meshes were fixed to be 0.5 cm. Moreover, 0.5 cm spacing was left between the cover and the upper layers. In order to increase the absorptivity of the wire mesh layers, they were painted with matt black before being installed into the system. There was no need for absorber plate since the wire mesh layers were acting as an absorber plate and as a result the cost of the solar air heater were reduced significantly because the wire mesh is really cheap and it is always available in the market. In addition, the new arrangement of the wire mesh layers in the collector which gives high porosity, $\Phi = 0.83$, will reduce the pressure drop through the collector. In order to get a

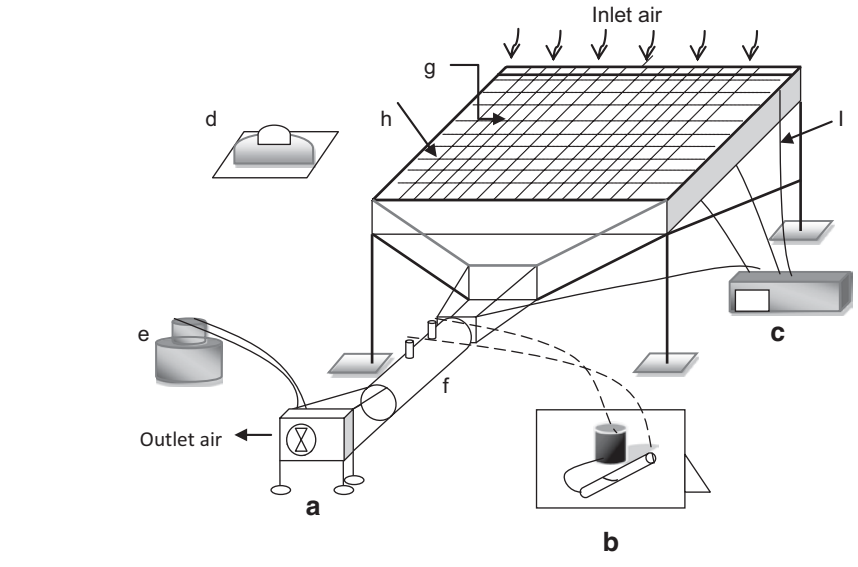

(1)

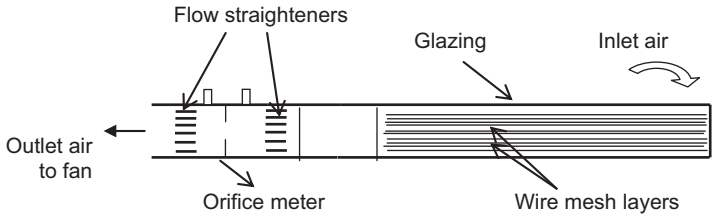

(2)

a. Centrifugal Fan
b. Inclined manometer (θ =15 °)
c. Digital Thermometer
d. Pyranometer
e. Speed controller
f. Orifice meter
g. Wire mesh layers
h. Glass cover
I. Thermocouple

Fig. 22.1 Schematic assembly of the single pass solar air heater(1), side view of the SAH (2)

uniform flow through the orifice meter, two flow straighteners, made from plastic straw tubes of 0.46 cm in diameter and 2 cm length, were fixed before and after the orifice meter. The orifice meter was designed according to Holman J.P. [12] and installed in the pipe with diameter of 8 cm. The pipe was placed between the converging section of the collector and the single inlet Centrifugal fan. The fan type was OBR 200 M−2 K. The pressure difference through the orifice was calculated by using an incline tube manometer of 15° angle. In order to increase the accuracy of the inclined manometer, a low density fluid such as alcohol (803 kg/m^3) was used in the tests. Different air mass flow rates can be achieved by using a speed controller.

The speed controller was connected to the fan to allow the user to adjust the speed on the desired value. The air was entered to the collector through 1×100 cm^2 opening made on the top side of the glazing as shown in Fig. 22.1. T-type thermocouples were used to measure the air temperatures at the inlet, outlet, and different places inside the solar collector. Three thermocouples were located at the beginning of the pipe, before the orifice meter, in order to measure the outlet temperature, Tout, of the air. The inlet temperature (ambient temperature), T_{in}, was measured by three more thermocouples which were placed underneath the collector. A Ten-channel Digital Thermometer (MDSSi8 Series digital, Omega, ±0.5 °C accuracy) was used to record the temperature readings. Three thermocouples were also placed at the top, middle and bottom of the glazing and the bed (inside the wire mesh layers) to record their temperatures at different hours of the day. The incident solar radiation on the collector glazing was measured hourly with an Eppley Precision Spectral Pyranometer (PSP). An instantaneous solar radiation meter model HHM1 A digital Omega, 0.25% basic dc accuracy with the resolution of ±0.5% from 0 to 2800 Wm^{-2} was coupled to the PSP. The solar collector was faced toward south in order to receive the maximum radiation and its tilt angle was fixed at 39.5° according to the geographical location of Cyprus (35.125 °N and 33.95 ° Elongitude).

The tests were started at 8 AM and ended at 5 PM. The outlet and inlet temperatures of the air, the ambient temperature, the bed and the glazing temperatures were recorded hourly at each experiment. Also the solar radiation and the incline tube manometer reading were read as well. Wind speed and humidity values were taken hourly from the Northern Cyprus Department of Meteorology's webpage.

22.3 Uncertainty Analysis

The uncertainty of the air mass flow rate and the thermal efficiency are demonstrated in this section. The mass flow rate ($\dot{m}$), is calculated by Eq. (22.1),

$$\dot{m} = \rho Q \tag{22.1}$$

where, ρ is the density of air and Q is the air volume flow rate. The pressure difference at the orifice, which is measured from the inclined tube manometer, is used to find the volume flow rate.

The fractional uncertainty, $\omega_{\dot{m}}/\dot{m}$, for the mass flow rate is calculated according to [12, 13]:

$$\frac{\omega_{\dot{m}}}{\dot{m}} = \left[\left(\frac{\omega_{T_{air}}}{T_{air}} \right)^2 + \left(\frac{\omega_{\Delta P}}{\Delta P} \right)^2 \right]^{1/2} \tag{22.2}$$

where, T_{air} is the film air temperature between the outlet and inlet.

The ratio of energy gain to solar radiation incident on the collector plane is the efficiency of solar collector, η, and is:

$$\eta = \frac{\dot{m} c_P (T_{out} - T_{in})}{I A_c} \tag{22.3}$$

where, $\dot{m}$ is the air mass flow rate, c_p is the specific heat of the fluid and AC is the area of the collector. According to Eq. (22.3), the fractional uncertainty for efficiency, ω_η/η, is a function of $\Delta T, \dot{m}$ and I. c_p, and A_C are considered to be constant.

$$\frac{\omega_\eta}{\eta} = \left[\left(\frac{\omega_{\dot{m}}}{\dot{m}} \right)^2 + \left(\frac{\omega_{\Delta T}}{\Delta T} \right)^2 + \left(\frac{\omega_I}{I} \right)^2 \right]^{1/2} \tag{22.4}$$

For the single pass air heater, the mean value of all variables for each day was calculated separately. Then, the mean value (of the variable mean values) for all the days was obtained separately and used to calculate the fractional uncertainty. The mean values of ΔT, T_{in}, T_{out}, T_{air}, $\dot{m}$, solar intensity, and the efficiency were found to be 21.22 °C, 33.8 °C, 55 °C, 44.4 °C, 0.026 kg/s, 711.37 W/m^2 and 44.48 %, respectively, through the all days of the experiment. The fractional uncertainty of the mass flow rate and the efficiency are found to be 0.0035 and 0.0093, respectively.

22.4 Results and Discussion

The performance analysis of the single pass solar air heater is done experimentally in the city of Famagusta, 35.125 °N and 33.95 °E longitude, which is located in Cyprus. The tests are performed in summer time during 13 to 23 August 2011 with clear sky condition. The thermal efficiency of the solar air heater with wire mesh layers as absorber plate and small duct height of 3 cm, at different mass flow rates is studied. The mass flow rate of the air was varied from 0.011 to 0.04 kg/s.

The solar intensity versus standard local time of the day for different days and various mass flow rates are shown in Fig. 22.2a. The highest daily solar radiation obtained with single pass solar air collector, which was at the mass flow rate of 0.016 kg/s (day 2), was 1018.5 W/m^2 at 13:00 h and the average solar intensity through that particular day was about 735 W/m^2.The mean solar intensity for each day is calculated and it is found that all mean averages are within the close range and it shows that a stable amount of solar radiation measured for each day of the experiment. The mean average solar intensity for all the days of the experiment was 711.4 W/m^2.

The inlet ambient temperature, Tin, versus time of the day for all the days in which the experiment was carried out is presented in Fig. 22.2b. In general, the input temperature was found to be increasing from the morning to evening with little fluctuation during some of the days.

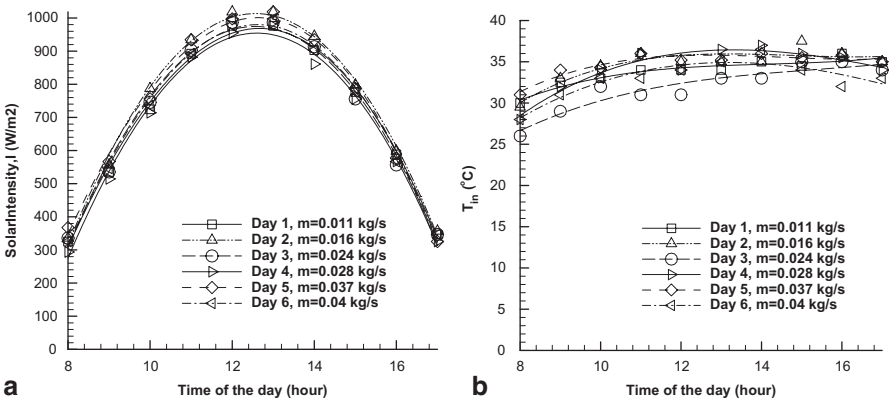

Fig. 22.2 Solar intensity versus time of the day (**a**), ambient temperatures versus time of the day (**b**), for different mass flow rates of air at different days

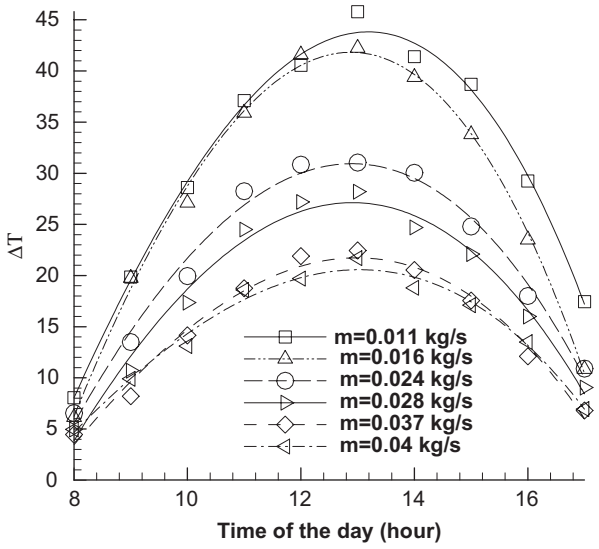

Fig. 22.3 The outlet and inlet air temperature difference (ΔT) versus time of the day for various mass flow rates

The temperature differences, $\Delta T = T_{out} - T_{in}$, versus time of the day for different air mass flow rates are shown in Fig. 22.3. In general, ΔT decreases with increasing air mass flow rate. Moreover, the temperature difference was increasing from morning to a peak value at noon and then was decreasing in the afternoon until sunsets, in a similar manner as the solar radiation. The maximum temperature difference was about 45.8 C at 13:00 h and it was obtained at the minimum mass flow rate of 0.011 kg/s. L.B.Y. Aldabbagh et al. [11] was investigated a single pass solar air heater with ten wire mesh layers as absorber plate. They were found that the maximum value of ΔT was around 27 °C at the mass flow rate of 0.012 kg/s.

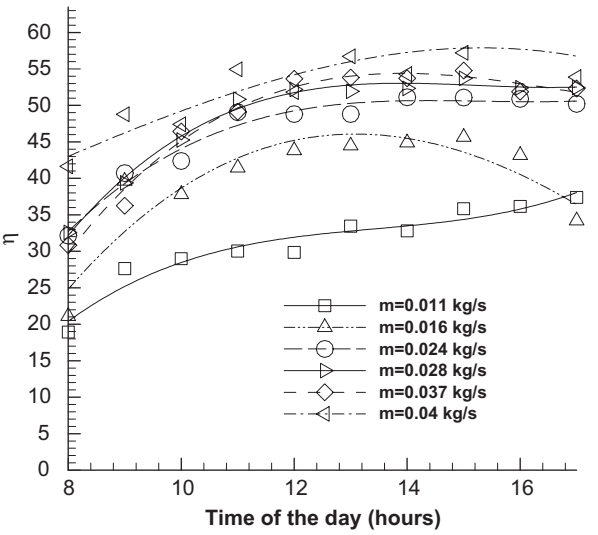

Fig. 22.4 Efficiency versus time for different mass flow rates of air

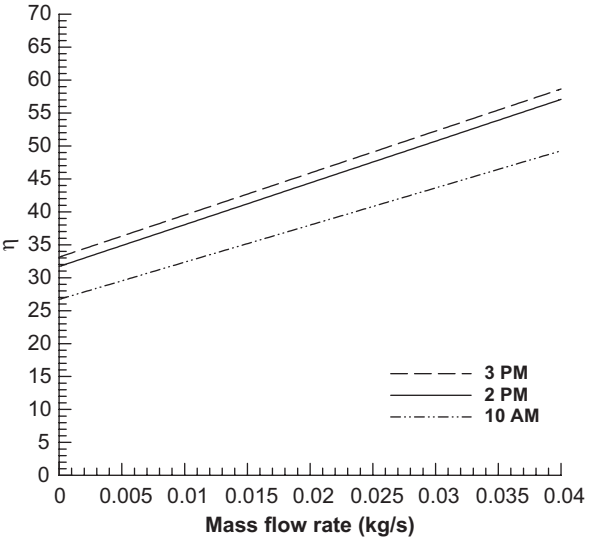

Fig. 22.5 Variation of thermal efficiency for different mass flow rates at 10 AM, 2 PM and 3 PM

Efficiency versus time of the day at different mass flow rates of air for the single pass air heater is shown in Fig. 22.4. As the behavior of inlet air temperature, the efficiency for most of the cases was found to be increased with the standard local time of the day from morning until 13:00 PM with slight decrease in the afternoons. The continued increase in the efficiency, not following the solar intensity curve, is due to the increase in the inlet air temperature and the energy stored in the wire mesh layers. The maximum value of the efficiency was about 56.73% and it was occurred at 13:00 h for the mass flow rate of 0.04 kg/s. The thermal efficiency

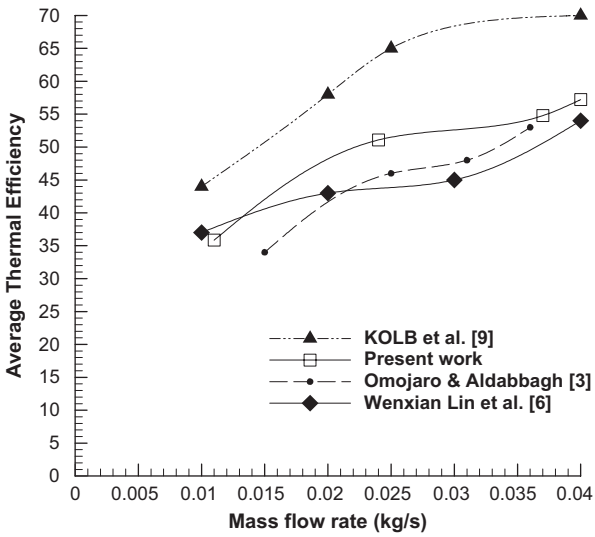

Fig. 22.6 Comparison of the average thermal efficiency of the present study with the other published data

increased as the air mass flow rate was increased (Fig. 22.5). The thermal efficiency of the single pass solar air heater as a function of mass flow rate for 10:00 AM, 2:00 PM and 3:00 PM are shown in Fig. 22.5. El-Sebaii et al. [14] Indicated that the thermal efficiency increases with increasing the mass flow rate until a typical value of $\dot{m} = 0.05$ kg/s beyond which the increase in thermal efficiency becomes insignificant. [14, 15] recommended to operate the system with or without the packed bed, with the mass flow rate of 0.05 kg/s or lower to have a lower pressure drop across the system and a reasonably high thermal efficiency, more than 70%.

The comparison of the average thermal performance of the present work with other types of SAHs is shown in Fig. 22.6. Kolb A. et al. [9] was tested a single-glazed solar matrix air collector and they were found that the at the duct height of 4 cm and mass flow rate of 0.04 kg/s, the thermal efficiency of the solar air heater is around 70%. According to Wenxian Lin et al. [6] who studied the thermal performance of cross-corrugated solar air collectors, the efficiency of collector increases monotonically and dramatically with $\dot{m}$. As it mentioned in the literature, [3] investigated the performance of the single and double pass solar air heater with fins and steel wire mesh as absorber. The maximum average efficiency which was obtained from their work was 59.62% for mass flow rate of 0.038 kg/s.

Comparison of the results of a packed bed collector with those of a conventional collector shows a substantial enhancement in the thermal efficiency. Generally, increasing the spacing between the bed and the glass cover reduces the average flow velocity and decreases the heat transfer coefficient. Moreover, using small depth channel will also reduce the pumping power. But on other hand the porous media, increase the pressure drop, which becomes important at high volume flow rates of air. Hence, the spacing of the pass channel has a significant effect on the performance of the solar air heater. The effect of changes in the channel depth on the

thermal efficiency, with and without the porous media was studied by [16, 17]. They recommended building collector with an upper channel depth of 3.5 cm and lower channel depth of 7 cm. [14] recommends using the same height for both upper and lower channel to give higher temperature output when porous media is used along with it. The proposed model in this study has an average thermal efficiency higher than the other models proposed by [6, 3].

Conclusion

The thermal performance of the single pass solar air heater was investigated experimentally at a geographic location of Cyprus in the city of Famagusta. The obtained results were compared with the published results. The results of the study showed that the maximum efficiency which can be reached by the proposed solar air heater with the porous media instead of an absorber plate and the duct height of 3 cm, was 53.01 % for the air mass flow rate of 0.04 kg/s. It was found that increasing the mass flow rate has opposite effect on the temperature differences. The thermal efficiency increased as the air mass flow rate increased but, the temperature difference between the inlet and outlet air, ΔT, decreased due to increasing the mass flow rate. Also it was seen that as the solar intensity, I, increases during a day the temperature differences also increases. The measured average solar intensity for all the days of the experiment was 711.4 W/m^2 and the input temperature was found to be increasing from the morning to evening with little fluctuation.

Nomenclature

c_P	Specific heat of air, kJ/kg.K
E	East
$\dot{m}$	Mass flow rate of air, kg/s
N	North
ΔP	Pressure difference, N/m^2
Q	Volume flow rate, m^3/s
T_{in}	Inlet temperature of air, °C
T_{out}	Outlet temperature of air, °C
ΔT	Temperature difference (T_{out}–T_{in}), °C

Greek Letters

ρ	Density, kg/m^3
η	Thermal efficiency
I	Intensity of solar radiation, W/m^2
Φ	Porosity
$\omega_{\dot{m}}$	Uncertainty for the mass flow rate
ω_{η}	Uncertainty for the thermal efficiency

References

1. Akpinar EK, Sarsilmaz C, Yildiz C (2004) Mathematical modeling of a thin layer drying of apricots in a solar energized rotary dryer. Int J of Energy Res 28:739–752
2. Qenawy AM, Mohamad AA (2007) Analysis of high efficiency solar air heater for cold climates, 2nd Canadian solar buildings conference, 2007, Calgary, June 10–14
3. Omojaro AP, Aldabbagh LBY (2010) Experimental performance of single and double pas solar air heater with fins and steel wire mesh as absorber. Appl Energy 87:3759–3765
4. El-khawajah MF, Aldabbagh LBY, Egelioglu F (2011) The effect of using transverse fins on a double pass flow solar air heater using wire mesh as an absorber. Sol Energy 85:1479–1487
5. Tian J, Kim T, Lu TJ, Hodson HP, Queheillalt DT, Sypeck DJ et al (2004) The effects of topology upon fluid flow and heat transfer within cellular copper structures. Int J Heat and Mass Transfer 47:3171–3186
6. Wenxian L, Wenfeng G, Tao L (2006) A parametric study on the thermal performance of cross-corrugated solar air collectors. Appl Thermal Eng 26:1043–1053
7. Donggen P, Xiaosong Z, Hua D, Kun Lv (2010) Performance study of a novel solar air collector. Appl Thermal Eng 2010(30):549–560
8. Mittal MK, Varshney L (2006) Optimal thermohydraulic performance of a wire mesh packed solar air heater. Sol Energy 80:1112–1120
9. Kolb A, Winter ERF, Viskanta R (1999) Experimental studies on a solar air collector with metal matrix absorber. Sol Energy 65:91–98
10. Ho-Ming Y, Chii-Dong H, Chi-Yen L (2000) Effect of collector aspect ratio on the collector efficiency of upward type baffled solar air heaters. Energy Convers Manage 41:971–981
11. Aldabbagh LBY, Egelioglu F, Ilkan M (2010) Single and double pass solar air heaters with wire mesh as packing bed. Energy 35:3783–3787
12. Holman JP (1989) Experimental methods for engineers. McGraw-Hill, New York
13. Esen H (2008) Experimental energy and energy analysis of a double-flow solar air heater having different obstacles on absorber plates. Build Environ 43:1046–1054
14. El-Sebaii AA, Aboul-Enein S, Ramadan MRI, El-Bialy E (2007) Year round performance of double pass solar air heater with packed bed. Energy Convers Manage 48:990–1003
15. Ramadan MRI, EL-Sebaii AA, Aboul-Enein S, El-Bialy E (2007) Thermal performance of a packed bed double-pass solar air heater. Energy 32:1524–1535
16. Sopian K, Supranto WRW, Daud, MY, Othman BY (1999) Thermal performance of the double-pass solar collector with and without porous media Renew Energy 18:557–564
17. Sopian K, Alghoul MA, Ebrahim MA, Sulaiman MY, Musa EA (2009) Evaluation of thermal efficiency of double-pass solar collector with porous–nonporous media Renew Energy 34:640–645

Chapter 23
An Alternative Energy Concept: A Solar Power Plant with a Short Diffuser

Sandro Nizetic and Neven Ninic

Abstract This paper elaborates an alternative energy concept involving a solar power plant with a short diffuser. The main physical part of the proposed alternative energy source is a gravitational vortex (convective vortices) that can be thought of as a heat engine. A solar power plant with a short diffuser could produce electricity without carbon dioxide emissions by transforming the available solar energy into useful mechanical shaft work. The proposed concept is similar to the solar chimney power plant concept, but without a chimney of limited height; in that sense, the design is closer to the atmospheric vortex engine concept. Specific details about the proposed alternative solution, previous research outcomes and planned future research work will be discussed in this paper.

Keywords Convective vortex · Experimental setup · Solar power plant · Simulation chamber

23.1 Introduction

The idea for the proposed solar power plant with a short diffuser, Ninic and Nizetic [1] was inspired by the fact that the solar chimney concept proposed by Schlaich [2, 3] has a chimney of limited height, which yields a relatively low overall efficiency for the solar chimney power plant. The main advantage of the solar chimney power plant concept is the possibility of achieving carbon-free electricity production by utilization of the available solar energy. Several case studies have been performed [4–7] and they showed that solar chimney power plant technology is even now a viable option for specific geographic locations. Another alternative energy concept was proposed by Michaud [8, 9]. Namely, Michaud's first proposed concept was an atmospheric vortex engine, which could also produce electricity. The

S. Nizetic (✉) · N. Ninic
Faculty of Electrical Engineering, Mechanical Engineering and Naval Architecture, University of Split, Rudjera Boskovica 32, 21000 Split, Croatia
e-mail: snizetic@fesb.hr

N. Ninic
e-mail: neven.ninic@fesb.hr

I. Dincer et al. (eds.), *Progress in Sustainable Energy Technologies: Generating Renewable Energy,* DOI 10.1007/978-3-319-07896-0_23,

main part of the Michaud concept is the gravitational vortex (convective vortices), which is the source of the available mechanical work. In a physical sense, convective vortices are similar to the heat engine concept because in both cases, heat input must be ensured and the outcome of the system is useful mechanical (shaft) work. This kind of approach is elaborated in detail in Nizetic [10]. An advantage of the Michaud concept is the fact that industrial waste heat or even low-temperature heat could be used as a heat source. Hence, the solar power plant with a short diffuser (or a modified solar chimney power plant) combines the advantages of the two previously mentioned concepts. It is obvious that the gravitational vortex is the most important part of the proposed concepts and that the research efforts should be focused on the vortex. However, only a few theoretical models exist in which convective vortices are used as source of useful mechanical shaft work. First, an elementary theoretical model of convective vortices was developed by Ninic and Nizetic [11] and further developed in Nizetic [12]. Michaud also performed energy calculations for his concept, and the first CFD analysis of his concept was performed by a group of researchers at the University of Western Ontario (the part of the simulation results can be found in [9]. Research on the nature and behavior of convective vortices is still in progress; conducting this research is necessary before technical realization of the concept can occur.

The objective of this paper is to elaborate the specific characteristics of the proposed solar power plant with a short diffuser and to briefly discuss previous and future research on this intriguing topic.

23.2 The Concept of a Solar Power Plant with a Short Diffuser

The proposed solar power plant with a short diffuser consists of five main parts, i.e., Fig. 23.1, collector S, short diffuser D, gravitational vortex GVC (airflow), nozzles N and diffuser deflector F (which is used to direct the descending airflow). The surrounding air is heated as it passes through the solar collector. In the central part of the plant, solar energy is transformed by a gravitational vortex into useful shaft work, which is then used to drive the turbine, i.e., for electricity production. Nozzles are used only in the beginning stage, before the stationary regime, to make the air denser after the turbines, i.e., to establish an air downdraft. The most sensitive part of the proposed concept is the specific flow object GVC (gravitational vortex-convective vortices). According to Fig. 23.1, the physical structure of the GVC consists of the heated airflows UF (flow from the solar collector) and the cooled descending airflow DF in the central section of the gravitational vortex. From a theoretical perspective, the maximal height of the gravitational vortex is the troposphere level because the updraft force vanishes there.

The influential factor for the achieved gravitational vortex height is the working potential of the air, i.e., the CAPE value (Convective Available Potential Energy,

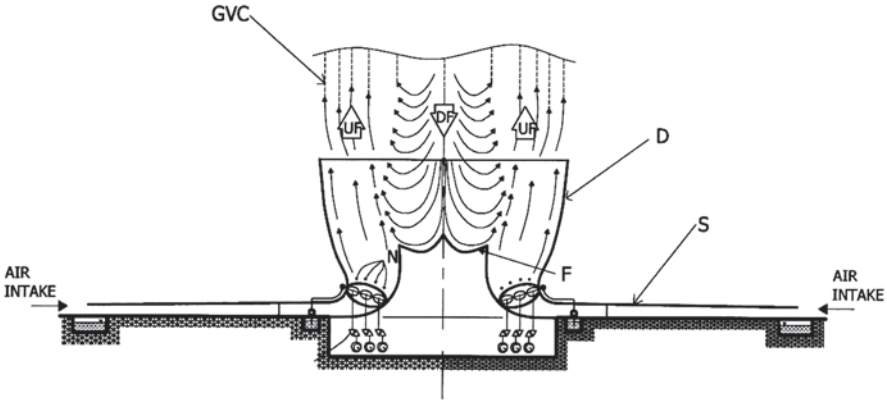

Fig. 23.1 A solar power plant with a short diffuser Nizetic [12]

Renno et al. [13], which depend, in general, on the surrounding air conditions. The Carnot heat-to-work efficiency of the convective vortices when acting as heat engines is approximately 22.0% compared with the maximal troposphere level and the average temperatures of the heat source and the sink.

Renno [13] developed a general approach for determination of the heat-to-work efficiency of natural convective vortices, such as tornadoes, dust devils and waterspouts, and for estimation of the other important vortex physical parameters. Using the available partial experimental data for the natural convective vortices, Renno calculated that the heat-to-work efficiency of natural convective vortices ranges from 5% for weak dust devils to 20% for intense hurricanes (it is obvious that the calculated values are in accordance with the Carnot efficiency). In terms of the magnitude, the heat-to-work efficiency of the convective vortices is not high, but the potential in the surrounding atmosphere for mechanical work production is enormous (Michaud [14]). More-specific details regarding the solar power plant concept with a short diffuser can be found in [1].

23.3 Theoretical Modeling of the Gravitational Vortex and the Experimental Approach

According to previous research [10–12, 15–17] the elementary theoretical model of the gravitational vortex for the solar power plant concept is proposed as a three-layer model [11]. In [11], an important conclusion is drawn regarding the fact that the descending cooled airflow may be the key for the maintenance (and also genesis) of the convective vortices in the surrounding atmosphere. This conclusion has also been confirmed by other researchers who have studied the meteorological aspect of natural convective vortices [18, 19]. From that point of view, a new proposal for the

Fig. 23.2 Convective vortices simulation chamber details

theoretical model should include the descending cooled airflow in the central part of the GVC flow structure. The previously mentioned model will be further developed as a new theoretical model for the proposed solar power plant with a short diffuser. Hence, future research work will be focused on the articulation of the physical model with descending cooled airflow and on development of the mathematical model. Finally, CFD simulations are also planned to confirm the important data and to provide the basis for possible further experimental research.

An important part of the research on convective vortices involves the experimental approach. In the Department of Thermodynamics of the Faculty of Electrical Engineering, Mechanical Engineering and Naval Architecture, University of Split, the convective simulation chamber was developed with donations from the *Carslberg* Croatia d.o.o., according to the suggestions from the T.P. Grazulis [20], Fig. 23.2. A simulation chamber will be used for the experimental research on the general convective vortices characteristics, which are important for validation of the assumptions of the proposed convective vortices theory models. In addition to the proposed convective vortices theoretical models (which are acting as heat engines), there is also a meteorological aspect that can be found in Renno [13, 21]. The meteorologist researchers do not deal with the possible utilization of the convective vortices for mechanical work production.

Conclusions

It is obvious that research about alternative energy concepts with convective vortices serving as heat engines has potential. Continuous research on this topic should occur. Natural convective vortices, such as dust devils, tornadoes, and waterspouts prove that it is possible to generate and maintain the convective vortices in the surrounding atmosphere. Hence, the engineering challenge is to try to simulate nature. As expected, this is not easy work, but it is possible. One engineering challenge will be to produce and maintain the artificially produced convective vortices, i.e., to restrain the powerful convective vortices. Finally, it can be concluded that alternative energy concepts with convective vortices, such as a solar power plant with a short diffuser, has a future, but only if we provide a serious and continuous research effort, as previously mentioned.

Acknowledgements The author would like to thank the Croatian Ministry of Science, Education and Sports (research project 023–0231751-3011) and the *Carlsberg Croatia d.o.o*. for funding this project.

References

1. Ninic N, Nizetic S (2007) Solar Power plant with short diffuser. Patented invention, PCT/HR2007/000037-(WO/2009/060245)
2. Schlaich J (1995) The Solar Chimney. Edition Axel Menges, Stuttgart
3. Haff W, Friedrich K, Mayr G, Schlaich J (1983) Solar chimneys: Part I: principle and construction of the pilot plant in Manzanares. Int J Sol Energy 2(1):3–20
4. Dai YJ, Huang HB, Wang NRZ (2003) Case study of solar chimney power plants in Northwestern regions of China. Renew Energy 28:1295–1304
5. Frederick, NO, Reccab MOJ (2006) The potential of solar chimney for application in rural areas of developing countries. Fuel 85:2561–2566
6. Nizetic S, Ninic N, Klarin B (2008) Analysis and feasibility of implementing solar chimney power plants in the mediterranean region. Energy 33:1680–1690
7. Ketlogetswe C, Fiszdon JK, Seabe NO (2008) Solar chimney power generation project—the case for botswana. Renew Sustain Energy Rev 12:2005–2012
8. Michaud LM (1975) Proposal for the use of a controlled Tornado-like vortex to capture the mechanical energy produced in the atmosphere from solar energy. Bull Am Meteorol Soc 56(5):530–534
9. Louis M. Michaud (2008) http://vortexengine.ca/cfd.shtml. Accessed on the 12 Feb 2012
10. Nizetic S (2011) Technical utilisation of convective vortices for carbon-free electricity production: a review. Energy 36:1236–1242
11. Ninic N, Nizetic S (2009) Elementary theory of stationary vortex columns for solar chimney power plants. Sol Energy 83(4):462–476
12. Nizetic S (2010) An atmospheric gravitational vortex as a flow object: improvement of the three-layer model. Geofizika 27(1):1–20
13. Renno N, Ingersoll AP (1996) Natural convection as a heat engine: a theory for CAPE. J Atmos Sci 53:572–585
14. Michaud LM (1995) Heat to work conversion during upward heat convection, Part I: carnot engine method. Atmos Res 39:157–178.

15. Ninic N (2006) Available energy of the air in solar chimneys and the possibility of its ground-level concentration. Sol Energy 80:804–811
16. Ninic N, Juric Z, Nizetic S (2006) Thermodynamical aspect of definitions “CAPE” and “TCAPE”. Geofizika 23(2):143–154
17. Nizetic S (2014) Analytical approach for estimating the pressure drop potential in convective vortex heat engines. Trans Can Soc Mech Eng 38(1):81–91
18. Markowski PM, Straka JM (2003) Rasmussen E.N. Tornado genesis resulting from the transport of circulation by a downdraft idealized numerical simulations. Am Meteorol Soc 95:795–823
19. Bluestein HB (2005) A review of ground-based, mobile, W-band Doppler-radar observations of tornadoes and dust devils. Dynam Atmos Oceans 40:163–188
20. Website: http://www.tornadoproject.com/tornproj/tornproj.htm. Accessed on the 18 Jan 2012
21. Renno N (2008) A thermodynamically general theory for convective vortices. Tellus 60 A 66:688–699

Chapter 24
Production of Renewable Hydrogen by Aqueous-Phase Reforming of Glycerol Over Ni-Cu Catalysts Derived from Hydrotalcite Precursors

Pablo Tuza, Robinson L. Manfro, Nielson F. P. Ribeiro and Mariana M. V. M. Souza

Abstract Ni-Cu catalysts derived from hydrotalcite-like compounds were prepared and evaluated in aqueous-phase reforming of glycerol. The catalysts were characterized by chemical composition, textural analysis, crystalline structure and reducibility. The reaction was carried out in a batch reactor with solution of 10 wt. % glycerol, at 250 and 270 °C. A maximum glycerol conversion of 60 % was achieved at 270 °C. In the gas phase, the H_2 selectivity was always higher than 80 % and formation of CO was very low (< 3 %) at 250 °C. The addition of Cu decreased the formation of methane. H_2 is consumed during the reaction at 270 °C, mainly for Cu-containing catalysts, with simultaneous formation of propylene glycol in the liquid phase. Acetol, lactic acid and acetaldehyde were also formed in the liquid phase, at both temperatures.

Keywords Hydrogen · Glycerol · Reforming · Catalysts · Hydrotalcites

24.1 Introduction

Renewable energy sources are becoming increasingly important because of depleting of petroleum reserves and mounting environmental concerns associated with fossil fuel utilization. In this sense, the use of hydrogen as an alternative energy carrier has been largely encouraged over the last years. Nowadays nearly 95 % of

M. M. V. M. Souza (✉) · P. Tuza · R. L. Manfro · N. F. P. Ribeiro
Escola de Química, Universidade Federal do Rio de Janeiro (UFRJ), Centro de Tecnologia, Bloco E, sala 206, CEP, 21941–909 Rio de Janeiro, Brazil
e-mail: mmattos@eq.ufrj.br

P. Tuza
e-mail: pableim@yahoo.es

R. L. Manfro
e-mail: robinson@eq.ufrj.br

N. F. P. Ribeiro
e-mail: nielson@eq.ufrj.br

I. Dincer et al. (eds.), *Progress in Sustainable Energy Technologies: Generating Renewable Energy,* DOI 10.1007/978-3-319-07896-0_24,

the world hydrogen is produced from fossil fuels [1], thus, it is necessary to find renewable sources to produce hydrogen. Biomass is a promising source for hydrogen production due to the carbon neutral nature with environmental benefits.

Gasification and steam reforming have been widely investigated for conversion of biomass to hydrogen, but these processes involve high temperatures and many side reactions, which decrease the hydrogen selectivity [2, 3]. Aqueous-phase reforming (APR) for production of hydrogen, first developed by the Dumesic group [4], is an advantageous technology for feedstocks such as sugars, alcohols and polyols, because it is carried out at low temperatures, reducing the cost of the process and minimizing undesirable decomposition reactions. Moreover, it produces H_2 and CO_2 in a single reactor with low levels of CO, which is important for fuel cell applications [5].

Several biomass-derived oxygenated compounds have been used in APR process, such as methanol, sorbitol, glycerol, ethyleneglycol, and ethanol [4–7]. Glycerol is of particular interest because it is obtained as a by-product of biodiesel production by transesterification of vegetable oils or animal fats. The transesterification reaction produces approximately 110 kg of glycerol per ton of biodiesel [8]. With increase in production of biodiesel, an excess of glycerol is expected in the world market and therefore, it is essential to find useful applications for glycerol. One of the promising ways to utilize this diluted glycerol from biodiesel plants is to produce hydrogen. The hydrogen generation by APR of glycerol takes place according to the Eq. (24.1):

$$C_3H_8O_3 + 3H_2O \rightarrow 3CO_2 + 7H_2 \tag{24.1}$$

Noble metal catalysts are commonly used to carry out the APR at small scales because they are more active and less susceptible to carbon deposition than non noble metal catalysts [4, 6]. However, large scale reforming processes use Ni-based catalysts that are far cheaper and more available than noble metals. A good catalyst for APR process has to be active in the cleavage of C–C bonds and water-gas shift reaction, but has to inhibit the cleavage of C–O bond and methanation reactions [4, 5, 9].

Ni shows a good activity for C–C scission, but it also exhibits high rates of methanation [5]. Cu, on the other hand, is inactive for C–C bond cleavage but has high activity for water-gas shift reaction, thus favoring the selectivity to hydrogen. In the present work Ni and Cu were selected to be included in catalyst formulations applied to glycerol reforming in order to obtain high activity and selectivity to hydrogen.

Hydrotalcite-like compounds (HTLCs) or layered double hydroxides, also known as anionic clays, have a lamellar structure with alternating positively charged mixed metal hydroxide sheets and negatively charged interlayer anions along with water molecules [10]. Thermal treatments of HTLCs give a stable, high surface area, homogeneous mixture of oxides with very small crystal size, which by reduction results in high metallic dispersion. Ni-Mg-Al mixed oxides prepared from hydrotalcite precursors have been successfully used as catalysts for various reactions, including reforming and oxidation of methane [11, 12] and ethanol reforming [7].

On the other hand, hydrotalcite-derived Cu-Mg-Al catalysts exhibit high activity for water-gas shift reaction [13]. Ni-Cu-Mg-Al catalysts derived from hydrotalcites have not been investigated in APR of glycerol yet.

In this context, the objective of this work is to study Ni-Cu catalysts prepared from hydrotalcite precursors in aqueous-phase reforming of glycerol for hydrogen production. The effect of the Cu loading (0–20 wt %) on the catalytic activity for reforming reaction and hydrogen selectivity was investigated, correlating with structural and morphological properties of the catalysts. By-products formed in liquid phase were identified and the main reaction routes were proposed.

24.2 Experimental

Catalyst Preparation

Hydrotalcite-like compounds were prepared by coprecipitation method at room temperature. An aqueous solution containing appropriate amounts of nitrate precursors (Al/(Ni + Cu + Mg + Al) = 0.25 and [Ni + Cu + Mg + Al] = 1.5 M) was added dropwise to a vigorously stirred solution containing Na_2CO_3 and NaOH (CO_3^{2-}/Al^{3+} = 0.375 and OH^-/Al^{3+} = 6.3). The gel formed was aged for 18 h at 60 °C. The resulting solid was filtered, washed with distilled water (70 °C) until pH 7 and dried overnight at 100 °C.

The Ni, Cu, Mg, Al-mixed oxides were produced by calcination of HTLCs under flowing air (60 mL min^{-1}), using a heating rate of 10 °C min^{-1}, from room temperature to 500 °C and keeping at this temperature for 2 h.

The NiO loading in calcined samples was always 20 wt % and CuO loading was varied between 0 and 20 wt %. The samples will be referred to as Ni, Ni5Cu, Ni10Cu and Ni20Cu, according to CuO loading.

Catalyst Characterization

The chemical composition of the synthesized samples was determined by X-ray fluorescence (XRF) using a Rigaku (RIX 3100) spectrometer.

X-ray powder diffraction (XRD) patterns were recorded in a Rigaku Miniflex II X-ray diffractometer equipped with a graphite monochromator using CuKα radiation (40 kV). The measurements were carried out with speed of 2° min^{-1} and over the 2θ range of 5° and 90°.

The textural characteristics, such as BET specific area and pore volume (BJH method), were determined by N_2 adsorption-desorption at − 196 °C in a Micromeritcs ASAP 2000. Prior to the analysis the samples were outgassed for 24 h at 200 °C.

The reducibility of the catalysts was analyzed by temperature programmed reduction (TPR), carried out in a microflow reactor operating at atmospheric pressure.

The samples were firstly dehydrated at 150 °C under flowing Ar before the reduction. A mixture of 1.53 % H_2/Ar flowed at 30 mL min^{-1} through the sample, raising the temperature at a heating rate of 10 °C min^{-1} up to 1000 °C. The outflowing gases were detected by thermal conductivity detector (TCD).

Catalytic Tests

The reactions of APR of glycerol were carried out in an autoclave batch reactor of 600 mL with 450 rpm of agitation, using 400 mg of catalyst in 250 mL of 10 wt. % glycerol solution. Before the reaction, the reactor was purged with He to remove the air inside. The catalytic tests were performed at 250 and 270 °C, resulting in autogeneous pressures of 38 and 52 atm, respectively.

The catalysts were reduced ex situ under 75 mL min^{-1} of 20 % H_2/N_2 up to 1000 °C, using a heating rate of 10 °C min^{-1}.

Gas products were analyzed online by gas chromatography (GC −1000), equipped with a Hayesep D column and TCD. The products detected in the gas phase were H_2, CH_4, CO_2 and CO. The selectivity to these products was calculated without considering water.

In the liquid phase glycerol and by-products were quantified by a Shimadzu HPLC with Aminex HPX 87 H column, using 0.005 M H_2SO_4 as eluent at 0.6 mL min^{-1}, and both UV and refractive index detectors. Conversion was calculated based on the moles of glycerol in the feed. Some liquid by-products were identified by gas chromatography-mass spectrometry (GC-MS) using a Shimadzu QP2010 instrument with DB5 column.

24.3 Results and Discussion

Catalyst Characterization

The chemical composition of the synthesized samples is presented in Tables 24.1 and 24.2. The composition of the as-synthesized samples is similar to those of the gel of synthesis, indicating an approximately complete incorporation of the cations in HTLC structure. The nickel loading of the sample without copper is slightly lower than the nominal value, which can be due to a small loss of nickel during washing.

The XRD patterns of HTLC precursors (Fig. 24.1a) exhibit characteristic planes of a well-crystallized HT in carbonate form (JCPDS 411428). The absence of other phases suggests that both Ni^{2+} and Cu^{2+} have isomorphically replaced Mg^{2+} cations in the brucite-like layers [7, 14]. A clear improvement in the orderliness of the layer was noted with decreasing copper content, as indicated by both the increase in intensity and sharpness of (110) and (113) reflections, observed around 60 and

Table 24.1 Chemical composition, structural and textural characteristics of the as-synthesized samples

Sample	Al/(Ni+Cu+Mg+Al)[a] (molar)	a (Å)	c (Å)	S_{BET} (m^2/g)	V_{PORE} (cm^3/g)
Ni	0.26 (0.25)	3.053	23.59	46.4	0.106
Ni5Cu	0.28 (0.25)	3.055	23.49	42.1	0.167
Ni10Cu	0.25 (0.25)	3.059	23.29	60.5	0.152
Ni20Cu	0.24 (0.25)	3.064	23.20	62.0	0.145

[a] The values in parentheses are nominal values

Table 24.2 Chemical composition, textural characteristics of the calcined catalysts and Ni particle sizes of the reduced catalysts

Sample	NiO[a] (wt %)	CuO[a] (wt %)	MgO (wt %)	S_{BET} (m^2/g)	V_{PORE} (cm^3/g)	Ni particle size (nm)[b]	D[c] (%)
Ni	16.7 (20)	–	57.8	260.0	0.308	28.8	3.5
Ni5Cu	19.1 (20)	5.3 (5)	48.0	211.3	0.480	9.4	10.7
Ni10Cu	19.2 (20)	11.3 (10)	44.8	203.4	0.416	9.8	10.3
Ni20Cu	19.4 (20)	22.5 (20)	33.7	118.4	0.325	14.3	7.0

[a] The values in parentheses are nominal values
[b] Calculated by the Scherrer equation using (200) plane of Ni
[c] Dispersion of Ni metal particles

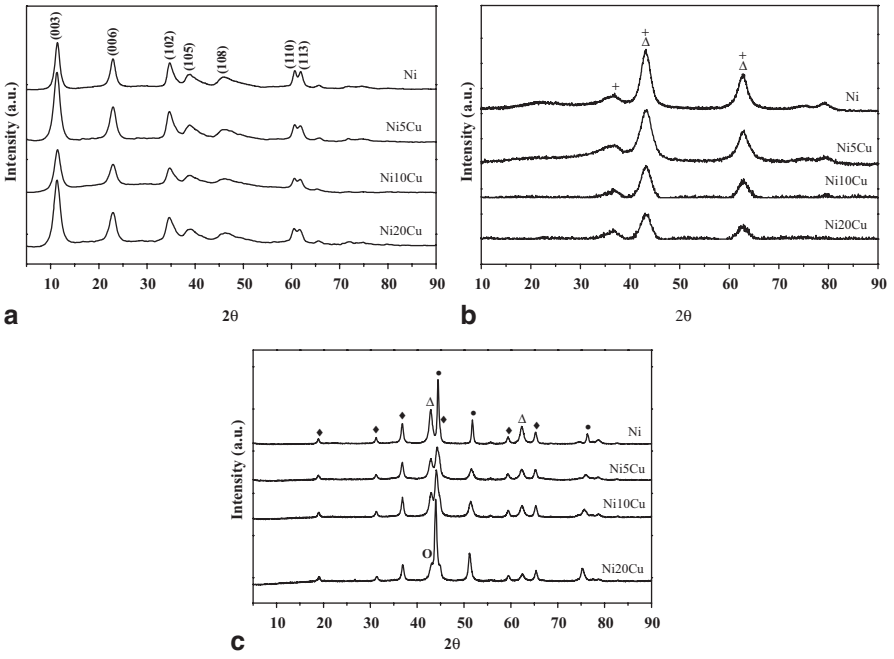

Fig. 24.1 XRD patterns of the as-synthesized HTLCs (**a**), and catalysts after calcination (**b**) and reduction (**c**). Phases: Δ MgO, + NiO, ● Ni, ♦ spinel phases, O Cu^0

62°, respectively. This effect was expected due to Jahn-Teller distortion at higher concentrations of copper, leading to poor long-range ordering [15].

The lattice parameters a (cation-cation distance in the brucite-like layer) and c = 3c' (thickness of one brucite-like layer and one interlayer) were calculated based on the rhombohedral structure of hydrotalcites, as shown in Table 24.1. The lattice parameter a increases with copper content since the ionic radius of Cu^{2+} (0.73 Å) is larger than that of Mg^{2+} (0.65 Å) [14]. There is also a decrease of the parameter c with increasing copper content, which can be associated with a decrease in the interlayer distance, as suggested by Chmielarz et al. [16].

After calcination at 500 °C, the characteristic peaks of HT structure disappear and XRD patterns (Fig. 24.1b) show the presence of poorly crystallized MgO periclase phase at 42.9° and 62.3° (JCPDS 45946). The presence of NiO is only evidenced by the very small peak at 37.2°, since the other peaks of this phase are overlapped with MgO at 43.3° and 62.9° (JCPDS 471049). On the other hand, whatever the Cu content, no crystalline Cu-containing phase evolved and no well-defined spinel phase was noted. These results indicate that most of Ni, and Cu and Al oxides are well dispersed in MgO matrix, forming a solid solution, in accordance with the literature [15]. Kovanda et al. [17] reported that $CuAl_2O_4$ spinel was formed from Cu-Mg-Al hydrotalcites only after calcination above 800 °C. The lines of MgO are broader in the sample of lower Mg content, indicating a decrease in the size of the MgO crystal or an increase of the Al^{3+} incorporation in MgO since the ionic radius of Al^{3+} (0.54 Å) is smaller than those of Mg^{2+} (0.65 Å) and Ni^{2+} (0.72 Å) [18]. Moreover, the reflections of MgO-solid solution are shifted towards wider 2θ angles than in pure MgO, which also indicates the presence of foreign ions in the oxide lattice [19].

XRD analysis of the catalysts was also carried out after reduction at 1000 °C (Fig. 24.1c). The reduction caused the formation of Ni^0, with reflections at 44.5°, 51.9° and 76.4° (JCPDS 4850), showing that ex situ activation was successful in reducing the active nickel phase. Metallic nickel is formed by the reduction of NiO and Mg-Ni-O solid solution [7]. It can also be observed the formation of spinel phases (MAl_2O_4 with M = Mg, Ni or Cu) and a small contribution of Cu0 at 43.3° for the sample with higher Cu loading (Ni20Cu).

The Ni particle sizes were calculated by the Scherrer equation, using the peak at 2θ = 51.9°, which corresponds to the (200) plane of Ni fcc. The results are shown in Table 24.2, together with the corresponding Ni dispersion, estimated according to Anderson [20]. The use of HTLC precursors results in high dispersion of metal particles, as already observed by other authors [7, 18, 21]. The addition of copper greatly improved the Ni dispersion, which can be related to the increased reducibility of nickel in presence of copper, as will be shown by TPR.

Textural characteristics of the as-synthesized samples (Table 24.1) showed that samples with higher amount of copper have larger BET surface areas, which is coherent with previous results [13]. Adsorption-desorption isotherms of nitrogen for all HTLCs (not shown) exhibited the type IV pattern with a broad hysteresis loop, characteristic of mesoporous materials. There was an increase in surface area and pore volume after calcination, as shown in Table 24.2, which can be related to

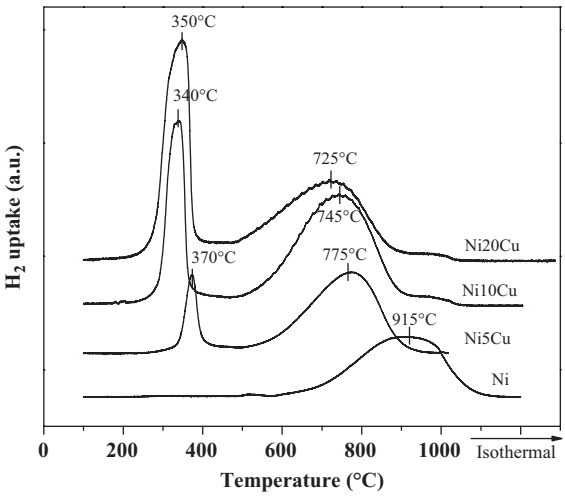

Fig. 24.2. TPR profiles of the catalysts

the destruction of the layered structure (as observed by XRD). The surface areas of the Cu-containing samples after calcination are smaller than the Ni sample, which Kovanda et al. [17] related to the low sintering temperature of the copper oxides.

TPR profiles of the catalysts are displayed in Fig. 24.2. The sample without Cu showed only one reduction peak at 915 °C, which can be associated either to the reduction of Ni species on Mg-Ni-O solid solution or to the reduction of $NiAl_2O_4$ spinel phase formed at temperatures higher than 800 °C during TPR analysis. The Cu-containing samples exhibited two reduction peaks, one at low temperatures (340–370 °C), associated with the reduction of Cu^{2+} to Cu^0, and another at high temperatures (725–775 °C), related to reduction of Ni species. The low-temperature peak shifts to lower temperatures as the amount of Cu increases, suggesting that a large amount of Mg stabilizes a large amount of Cu in the solid solution, decreasing the reducibility of Cu^{2+} component [17]. On the other hand, the increase in Cu content decreased the reduction temperature of Ni species, which was attributed by Ashok et al. [22] to the spillover of hydrogen produced by Cu, accelerating the nucleation of the Ni metal.

Table 24.3 shows the reduction degrees of CuO and NiO, calculated by integration of the first and second TPR peaks, respectively, considering the reduction of Cu^{2+} to Cu^0 and Ni^{2+} to Ni^0. The addition of Cu increased the reducibility of Ni^{2+} species, in accordance with Ashok et al. [22]. Another possibility is that the second reduction peak also corresponds to the reduction of copper in spinel phase (shown by XRD) and, in this case, the reduction of copper species would be 100 % with an incomplete reduction of nickel species.

Table 24.3 Reduction degrees of CuO and NiO calculated from temperature-programmed reduction results

Catalyst	CuO[a] (%)	NiO[b] (%)
Ni	–	72.5
Ni5Cu	79.1	100
Ni10Cu	94.5	100
Ni20Cu	80.3	100

[a] calculated by integration of the first reduction peak
[b] calculated by integration of the second reduction peak

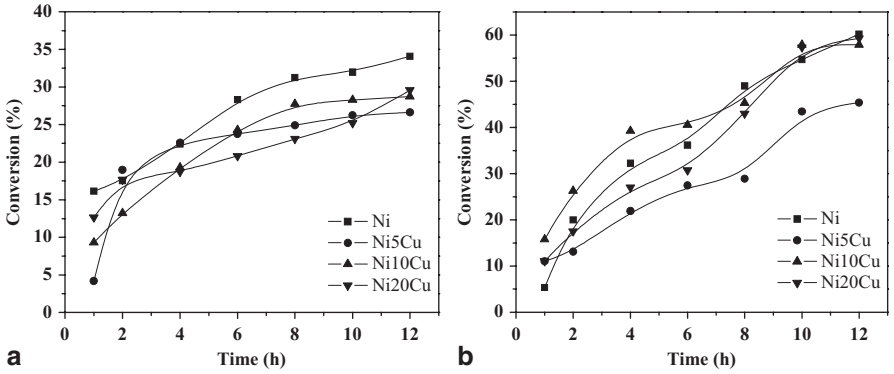

Fig. 24.3. Glycerol conversion as a function of time on stream for aqueous-phase reforming of 10 wt. % glycerol solution at 250 (**a**) and 270 °C (**b**)

Catalytic Tests

The glycerol conversion of the Ni-Cu catalysts for aqueous-phase reforming at 250 and 270 °C is displayed in Fig. 24.3. At 250 °C, the conversions increased with time up to about 6–8 h, while at 270 °C they increased continuously up to 10 h. The glycerol conversion increased by increasing the reaction temperature for all catalysts, as similarly observed in a previous study [23]. At 250 °C, Ni catalyst provided the best performance, starting at 16 % of conversion and ending at approximately 34 % after 12°h of reaction. The conversions with the copper containing catalysts were not much different from the Ni catalyst, with conversion of around 28 % after 12 h. At 270 °C, all catalysts reached 59 % of conversion, except Ni5Cu that showed a maximum conversion of 45 %.

The gas product distribution of the APR of glycerol at 250 °C is shown in Fig. 24.4. H_2, CO_2, CH_4, and CO were the only reaction products identified in the gas phase. The Ni5Cu and Ni10Cu catalysts showed the best performance in terms of hydrogen production, with H_2 selectivity of about 90 %, which remained practically constant during 12°h of reaction. The H_2 selectivity for the other catalysts was about 80 %. In relation to CO_2, Ni5Cu exhibited the lowest selectivity, 3 % in

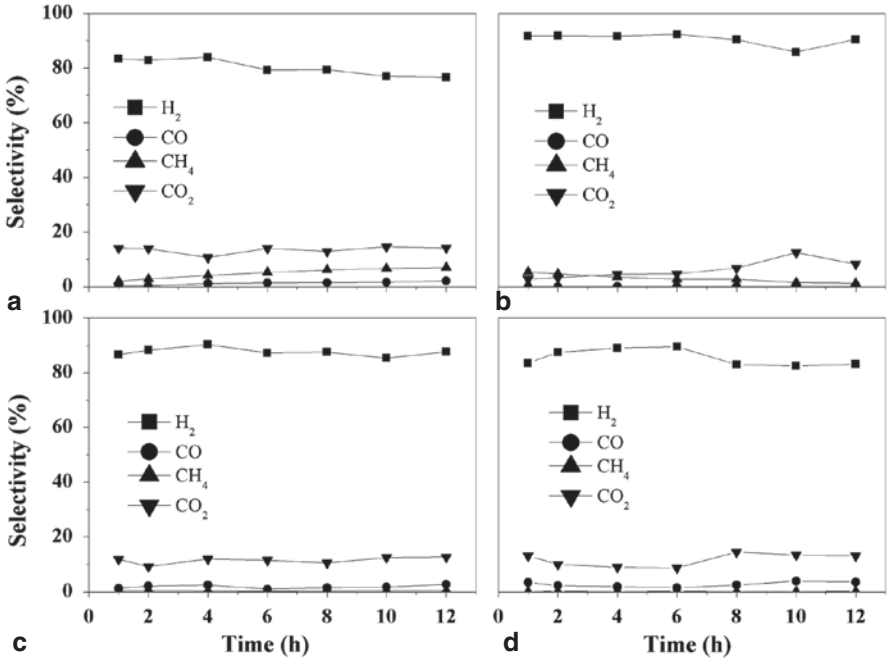

Fig. 24.4 H_2, CH_4, CO_2 and CO selectivities as a function of time on stream for aqueous-phase reforming of 10 wt. % glycerol solution at 250 °C with (**a**) Ni, (**b**) Ni5Cu, (**c**) Ni10Cu and (**d**) Ni20Cu catalysts

the beginning of the reaction and 8 % at the end. The other catalysts presented CO_2 selectivity of approximately 15 %, increasing to 30 % for Ni10Cu in the last hour. CO selectivities were always below 3 % and the maximum CH_4 selectivity was 7 % for Ni catalyst.

The higher selectivity of Ni5Cu and Ni10Cu catalysts for production of hydrogen may be related to the lower Ni particle size. The lower Ni particle size decreases the number of clusters with multiple nickel atoms that are necessary for CO dissociation, thus resulting in higher H_2 selectivity [23]. This effect is the same as the addition of Sn to nickel catalysts reported by the Dumesic group [9]. Wawrzetz et al. [24] showed that H_2 and CO_2 formation decreased in APR of glycerol with increasing Pt particle size.

The aqueous-phase reforming of glycerol produces primarily H_2 and CO_2, according to reaction (1). The H_2 selectivity obtained by Shabaker et al. [9] in APR of glycerol using Ni-Sn catalyst was 64 %, at 265 °C, with 30 % of CO_2. In the present study, the H_2 selectivity varied between 80–90 %, while CO_2 was in the range of 5–30 %, showing that H_2/CO_2 ratio was much higher than the stoichiometry of the reforming reaction, which indicates that the reaction is not purely APR. Different side reactions are occurring with glycerol in the liquid phase, as will be shown later.

It can be seen from Fig. 24.4 that the formation of CO is very low, indicating that the low temperature favors the water-gas shift reaction (Eq. 24.2), since Ni has a moderate activity and Cu is one of the most active metals in this reaction [25]. Although it is well known that Ni catalysts have high activity in methanation reactions of CO and CO_2 (Eq. 24.3–24.4) [5], the CH_4 formation was not significant in the present study. The addition of Cu decreased the activity for methanation reaction, since Cu is not active for this reaction [26].

$$CO + H_2O \rightarrow CO_2 + H_2 \tag{24.2}$$

$$CO + 3H_2 \rightarrow CH_4 + H_2O \tag{24.3}$$

$$CO_2 + 4H_2 \rightarrow CH_4 + 2H_2O \tag{24.4}$$

The main products detected in liquid phase for APR of glycerol at 250 °C were lactic acid, acetol (hydroxyacetone) and acetaldehyde. The formation of lactic acid is related to dehydrogenation of glycerol (Eq. 5), as proposed by Ramirez-López et al. [27]. Acetol is produced by dehydration of glycerol (Eq. 6), as already observed by many authors [24, 28–30]. Acetaldehyde can be formed from dehydration of ethylene glycol (Eq. 8), which is produced by decarbonylation/dehydrogenation of glycerol (Eq. 7) [29]. Lactic acid was produced at higher concentrations (11–13 gL^{-1}) than acetol (2–4 gL^{-1}) or acetaldehyde (4–5 gL^{-1}). The high concentration of these by-products shows that formation of H_2 by these side reactions is significant, justifying the high H_2 selectivities found (Fig. 24.4).

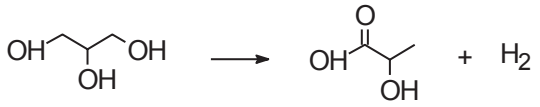

(24.5)

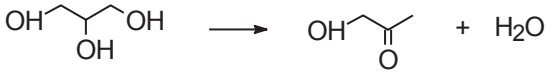

(24.6)

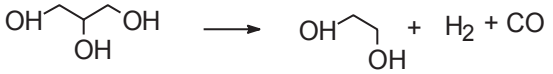

(24.7)

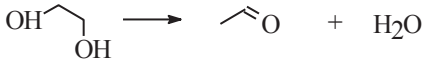

(24.8)

Figure 24.5 presents the product distribution for APR of glycerol at 270 °C. Ni catalyst generated an initial H_2 selectivity close to 90 %, which decreased to approximately 75 % after 4 h of reaction, and remained constant until the end of the reaction. CO_2 selectivity increased from 4 to 19 % in 8 h of reaction and then decreased

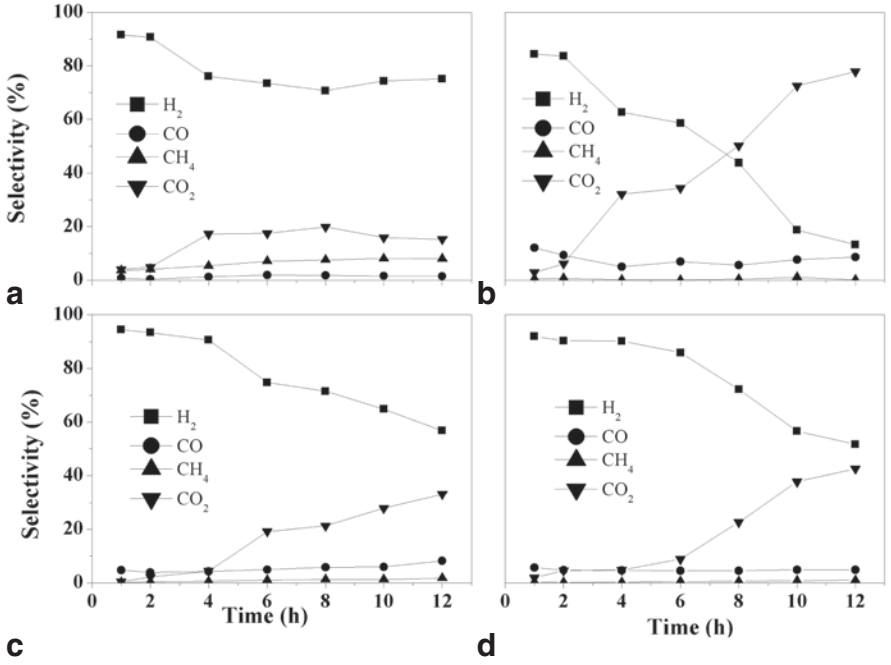

Fig. 24.5. H_2, CH_4, CO_2 and CO selectivities as a function of time on stream for aqueous-phase reforming of 10 wt. % glycerol solution at 270 °C with (**a**) Ni, (**b**) Ni5Cu, (**c**) Ni10Cu and (**d**) Ni20Cu catalysts

to 15 %. This catalyst produced little CO, around 2 % after 12°h of reaction. However, methane production was greater under these conditions, reaching a selectivity of 8 %.

Reactions performed with Ni10Cu and Ni20Cu catalysts presented H_2 selectivity initially around 92 % and decreased to approximately 53 % after 12°h of reaction. Formation of CO_2 was below 2 % in the beginning of the reaction, increasing to 33 and 42 % for Ni10Cu and Ni20Cu, respectively. Noteworthy is the product distribution for Ni5Cu catalyst: the H_2 selectivity decreased from 85 to 13 % after 12°h of reaction, while CO_2 increased from 3 to 78 %. The CO selectivity was approximately 5 % for Ni10Cu and Ni20Cu catalysts, and reached 9 % for Ni5Cu. The CH_4 selectivity remained below 1 % for all Cu-containing catalysts.

The distribution of products at 270 °C followed the same trend for all catalysts: H_2 production decreased with time, while CO_2 increased, but this tendency is more pronounced for Cu catalysts, especially Ni5Cu. Hydrogen produced by APR can be consumed in the hydrogenation of products from dehydration of glycerol, as acetol, 3-hydroxypropanal [24], pyruvaldehyde and acetaldehyde [29].

The main products detected in liquid phase for APR of glycerol at 270 °C were lactic acid, acetol, acetaldehyde and also propylene glycol. Propylene glycol comes from hydrogenation of acetol (Eq. 9) [24, 28, 31]. The production of lactic acid was

higher for Ni catalyst (achieving 19 gL^{-1}), while acetol formation increases with Cu content: from 3 gL^{-1} for Ni catalyst to 22 gL^{-1} for Ni20Cu, at the end of the reaction. Small traces of other liquid by-products were detected by GC-MS, mainly for Cu-containing catalysts at long reaction times: 1,2 butanediol, cyclopentanone, 2,5 hexadione and 4-hydroxy −3-hexanone.

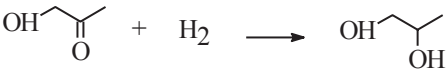

(24.9)

Propylene glycol was formed at higher concentrations on Cu-containing catalysts, which agrees with many authors [31–33], who showed that Cu is a better catalyst than Ni for hydrogenolysis of glycerol to propylene glycol. Meher et al. [34] showed specifically that Cu/Zn/Al mixed-oxide catalysts derived from hydrotalcite precursors have high activity in glycerol conversion to propylene glycol. Moreover, the production of propylene glycol increases with reaction time, while the H_2 selectivity decreases, confirming the occurrence of hydrogenation reactions.

Conclusions

Ni-Cu catalysts derived from hydrotalcite-like compounds showed great potential to be used in aqueous-phase reforming of glycerol, with good activity and high selectivity to hydrogen. Ni5Cu catalyst showed the best performance in the conversion of glycerol at 250 °C, with production of the largest amount of hydrogen. However, this catalyst provided the least desirable performance at 270 °C because of low conversion and almost total consumption of hydrogen. The consumption of H_2 is related to hydrogenation of acetol, formed by dehydration of glycerol, producing propylene glycol. Lactic acid and acetaldehyde were also formed in liquid phase, besides small traces of heavier by-products.

Acknowledgement The authors thank Núcleo de Catálise/COPPE/UFRJ for providing the FRX, BET analysis and also GC-MS; Angela Rocha for helping with GC-MS; and CNPq for the financial support granted to carry out this work.

References

1. Dunn S (2002) Hydrogen futures: toward a sustainable energy system. Int J Hydrog Energy 27:235–264
2. Huber GW, Iborra S, Corma A (2006) Synthesis of transportation fuels from biomass: chemistry, catalysts, and engineering. Chem Rev 106:4044–4098
3. Adhikari S, Fernando SD, Haryanto A (2009) Hydrogen production from glycerol: an update. Energy Conv Manage 50:2600–2604

4. Cortright RD, Davda RR, Dumesic JA (2002) Hydrogen from catalytic reforming of biomass-derived hydrocarbons in liquid water. Nature 418:964–967
5. Davda RR, Shabaker JW, Huber GW, Cortright, RD, Dumesic JA (2005) A review of catalytic issues and process conditions for renewable hydrogen and alkanes by aqueous-phase reforming of oxygenated hydrocarbons over supported metal catalysts. Appl Catal B 56:171–186
6. Shabaker JW, Davda RR, Huber GW, Cortright RD, Dumesic JA (2003) Aqueous-phase reforming of methanol and ethylene glycol over alumina-supported platinum catalysts. J Catal 215:344–352
7. Cruz IO, Ribeiro NFP, Aranda DAG, Souza MMVM (2008) Hydrogen production by aqueous-phase reforming of ethanol over nickel catalysts prepared from hydrotalcite precursors. Catal Comm 9:2606–2611
8. Behr A, Eilting J, Irawadi K, Leschinski J, Lindner F (2008) Improved utilisation of renewable resources: new important derivatives of glycerol. Green Chem.10:13–30
9. Shabaker JW, Huber GW, Dumesic JA (2004) Aqueous-phase reforming of oxygenated hydrocarbons over Sn-modified Ni catalysts. J Catal 222:180–191
10. Cavani F, Trifiró F, Vaccari A (1991) Hydrotalcite-type anionic clays: preparation, properties and applications. Catal Today 11:173–301
11. Basile F, Basini L, D'Amore M, Fornasari G, Guarinoni A, Matteuzzi D, Del Piero G, Trifiro F, Vaccari A (1998) Ni/Mg/Al anionic clay derived catalysts for the catalytic partial oxidation of methane: residence time dependence of the reactivity features. J Catal 173:247–256
12. Tsyganok AI, Tsunoda T, Hamakawa S, Suzuki K, Takehira K, Hayakawa T (2003) Dry reforming of methane over catalysts derived from nickel-containing Mg–Al layered double hydroxides. J Catal 213:191–203
13. Ferreira KA, Ribeiro NFP, Souza MMVM, Schmal M (2009) Structural transformation of Cu–Mg–Al mixed oxide catalysts derived from hydrotalcites during shift reaction. Catal Lett 132:58–63
14. Dussault L, Dupin JC, Dumitriu E, Auroux A, Guimon C (2005) Microcalorimetry, TPR and XPS studies of acid–base properties of NiCuMgAl mixed oxides using LDHs as precursors. Thermochimica Acta 434:93–99
15. Kannan S, Dubey A, Knozinger H (2005) Synthesis and characterization of CuMgAl ternary hydrotalcites as catalysts for the hydroxylation of phenol. J Catal 231:381–392
16. Chmielarz L, Kustrowski P, Rafalska-Łasocha A, Majda D, Dziembaj R (2002) Catalytic activity of Co-Mg-Al, Cu-Mg-Al and Cu-Co-Mg-Al mixed oxides derived from hydrotalcites in SCR of NO with ammonia. Appl Catal B 35:195–210
17. Kovanda F, Jirátová K, Rymes J, Kolousek D (2001) Characterization of activated Cu/Mg/Al hydrotalcites and their catalytic activity in toluene combustion. Appl Clay Sci 18:71–80
18. Takehira K, Shishido T, Wang P, Kosaka T, Takaki K (2004) Autothermal reforming of CH4 over supported Ni catalysts prepared from Mg–Al hydrotalcite-like anionic clay. J Catal 221:43–54
19. Fornasari G, Gazzano M, Matteuzzi D, Trifiró F, Vaccari A (1995) Structure and reactivity of high-surface-area Ni/Mg/Al mixed oxides. Appl Clay Sci 10:69–82
20. Anderson JR (1975) Structure of metallic catalysts. Academic Press New York
21. Shishido T, Sukenobu M, Morioka H, Furukawa R, Shirahase H, Takehira K (2001) CO_2 reforming of CH4 over Ni/Mg–Al oxide catalysts prepared by solid phase crystallization method from Mg–Al hydrotalcite-like precursors. Catal Letters 73:21–6
22. Ashok J, Subrahmanyam M, Venugopal A (2008) Hydrotalcite structure derived Ni-Cu-Al catalysts for the production of H2 by CH4 decomposition. Int J Hydrog Energy 33:2704–2713
23. Manfro RL, Costa AF, Ribeiro NFP, Souza MMVM (2011) Hydrogen production by aqueous-phase reforming of glycerol over nickel catalysts supported on CeO_2. Fuel Proc Technol 92:330–335

24. Wawrzetz A, Peng B, Hrabar A, Jentys A, Lemonidou AA, Lercher JA (2010) Towards understanding the bifunctional hydrodeoxygenation and aqueous phase reforming of glycerol. J Catal 269:411–420
25. Grenoble DC, Estadt MM, Ollis DF (1981) The chemistry and catalysis of the water gas shift reaction: 1. The kinetics over supported metal catalysts. J Catal 67:90–102
26. Vannice MA (1977) The catalytic synthesis of hydrocarbons from H2/CO mixtures over the Group VIII metals: V. The catalytic behavior of silica-supported metals. J Catal 50:228–236
27. Ramírez-López CA, Ochoa-Gómez JR, Fernández-Santos M, Gómez-Jiménez-Aberasturi O, Alonso-Vicario A, Torrecilla-Soria J (2010) Synthesis of lactic acid by alkaline hydrothermal conversion of glycerol at high glycerol concentration. Ind Eng Chem Res 49:6270–6278
28. Miyazawa T, Kusunoki Y, Kunimori K, Tomishige K (2006) Glycerol conversion in the aqueous solution under hydrogen over Ru/C + an ion-exchange resin and its reaction mechanism. J Catal 240:213–221
29. King DL, Zhang L, Xia G, Karim AM, Heldebrant DJ, Wang X, Peterson T, Wang Y (2010) Aqueous phase reforming of glycerol for hydrogen production over Pt–Re supported on carbon. Appl Catal B 99:206–213
30. Pompeo F, Santori G, Nichio NN (2010) Hydrogen and/or syngas from steam reforming of glycerol: study of platinum catalysts. Int J Hydrog Energy 35:8912–8920
31. Dasari MA, Kiatsimkul PP, Sutterlin WR, Suppes GJ (2005) Low-pressure hydrogenolysis of glycerol to propylene glycol. Appl Catal A 281:225–231
32. Nakagawa Y, Tomishige K (2011) Heterogeneous catalysis of the glycerol hydrogenolysis. Catal Sci Technol 1:179–190
33. Yuan Z Wang J, Wang L Xie W, Chen P Hou Z, Zheng X (2010) Biodiesel derived glycerol hydrogenolysis to 1,2-propanediol on Cu/MgO catalysts. Bioresour Technol 101:7088–7092
34. Meher LC, Gopinath R, Naik SN, Dalai AK (2009) Catalytic hydrogenolysis of glycerol to propylene glycol over mixed oxides derived from a hydrotalcite-type precursor. Ind Eng Chem Res 48:1840–1846

Chapter 25
Effects of Pyrolysis Conditions on Structural Ingredients and Functional Groups of Hybrid Poplar

Hanzade Haykiri-Acma and Serdar Yaman

Abstract In this study, thermal behavior and the functional group distributions of structural ingredients of biomass were investigated under pyrolytic conditions. An energy-forestry tree (hybrid poplar) was used as biomass material. Macromolecular ingredients in this biomass such as holocellulose (hemicellulosics + celluloses) and lignin were isolated chemically using several analytical techniques. Thermal analysis, X-ray Diffraction (XRD), X-ray Fluorescence (XRF), BET surface area, Fourier Transform Infrared Spectroscopy (FTIR), and Scanning Electron Microscopy (SEM) techniques were applied to specify the biomass and its ingredients.

Pyrolysis of biomass was carried out in a horizontal tube furnace from ambient to 600 °C with a heating rate of 10 °C/min under nitrogen flow of 100 mL/min. In this way, biochars were produced at different temperatures, and the effects of pyrolytic conditions on the structural ingredients and the distribution of the functional groups were interpreted.

It was found out that the physical and chemical analysis results as well as the thermal decomposition characteristics of holocellulose, lignin, and extracted biomass are highly different from those of the main biomass sample. In addition, the obtained biochars contain large amounts of aromatic and ether type structures. Also, it was also determined that the aromatic bands get stronger with increasing pyrolysis temperature. Besides, carbonyl bands disappeared as temperature increases. It was also revealed that the lignin contains many functional groups, of which methoxyl groups were the most apparent functionalities. On the other hand, the calorific value of the produced biochars tended to increase with increasing pyrolysis temperature.

Keywords Hybrid poplar · Pyrolysis · Cellulosics

H. Haykiri-Acma (✉) · S. Yaman
Chemical and Metallurgical Eng. Faculty, Department of Chemical Engineering,
Istanbul Technical University, 34469 Maslak, Istanbul, Turkey
e-mail: hanzade@itu.edu.tr

S. Yaman
e-mail: yamans@itu.edu.tr

I. Dincer et al. (eds.), *Progress in Sustainable Energy Technologies: Generating Renewable Energy,* DOI 10.1007/978-3-319-07896-0_25,

25.1 Introduction

The efficient usage of renewable energy resources to meet the growing energy need has become increasingly important. From this point of view, the energy potential of biomass that is one of the important renewable energy resources must be evaluated properly. In fact, biomass is a fuel that is cheap, abundant, renewable, sustainable, and there is no foreign dependency in contrast to nature of the fossil fuels.

Although biomass has a great potential all over the world, most of the biomass species have some undesirable characteristics such as high moisture content, low density, and low calorific value. Hence, direct burning of biomass as a fuel is not preferable for these reasons, and some secondary fuels that can be obtained from biomass by thermal processes including pyrolysis, gasification or liquefaction may be much more reasonable [1]. In this way, derived-fuels that have superior characteristics than the parent biomass species can be obtained, and accordingly the energy potential of biomass could be evaluated efficiently.

On the other hand, biomass has a heterogeneous structure that is mainly comprised of several macromolecular ingredients. That is, hemicellulosics, celluloses, and lignin account for most of the organic matrix, while some others such as proteins, lipids, extractive matter, etc. are available as well. In this content, the apparent thermal behavior of given biomass species during the thermal conversion processes is highly dependent on the individual thermal behaviors of these ingredients. Besides, some interactions are generally taken place among the thermal characteristics of individual ingredients, leading synergistic variations in thermal properties that cannot be predicted. Thus, some investigations were carried out in order to identify the thermal behavior of such ingredients under specified conditions of thermal conversion processes [2, 3]. For this purpose, macromolecular ingredients in biomass were isolated from the main sample.

Besides, the conditions applied during the thermal conversion processes play an important role on the type and the distributions of the products obtained. In case of high temperatures and long residence times, the yields of the gaseous products are relatively high, while low temperatures favor the formation of solid residue [4, 5]. In addition, inorganics found in the sample may show catalytic effects during the thermal processes that makes it much more complex.

25.2 Materials and Method

Hybrid poplar was selected as the biomass material for this study, because of the fact that it is a very fast growing tree, and accordingly a number of investigations on this special biomass material make it so popular in the domain of energy from biomass.

Hybrid poplar samples were provided from Turkish forestry sector, and first allowed to stand in open containers in laboratory for 1-week to get air-dried sample.

Then, the particle size of the air-dried samples was reduced to −250 μm by milling with equipment that is suitable for chopping and shredding of leafy materials. The proximate analysis and the calorific value determination of the sample were performed according to ASTM standards.

Structural analysis and the isolation of the macromolecular ingredients in biomass were conducted by analytical techniques according to the following procedures. In order to remove the extractives and to obtain extractives-free samples, benzene-ethyl alcohol extraction procedure was applied according to ASTM D1105 standard. The extractives-free bulk (extracted sample) was used as feedstock to isolate each of holocellulose and lignin. Isolation of holocellulose, which is the sum of hemicellulosics and cellulose forms, was performed with the mixtures of $NaClO_2$, acetic acid, and water. Whereas, the isolation of lignin was carried out by van Soest method in which extractives-free sample was treated with 72 vol % sulphuric acid to hydrolyze the cellulosics and to isolate the lignin [6]. The content of acid insoluble lignin which is called as "Klason Lignin" was found by drying and ashing of the neutralized bulk.

Thermal analyses were performed by TA Instruments SDTQ600 model thermogravimetric analyzer with a differential scanning calorimetry detector. The biomass sample weighing approximately 10 mg was heated up to 600 °C with a heating rate 10 °C/min under the nitrogen flow of 100 mL/min, and it was kept at the final temperature for 10 min. The curves of TG, DTG, DTA, DSC could be obtained from these experiments.

Appropriate conditions for the pyrolysis experiments of the main sample (untreated whole sample) and its ingredients in horizontal tube furnace were determined using the results taken from the DTG curve, considering the thermal decomposition characteristics. Consequently, the pyrolysis experiments in horizontal tube furnace were also carried out from ambient to 600 °C. The flow rate of nitrogen through the furnace and the heating rate were fixed at 100 mL/min and 10 °C/min, respectively.

X-Ray Diffraction (XRD) analysis was performed using a Panalytical X'Pert Pro PW 3040/60 model X-Ray diffractometer with a Cu X-ray (1,54060 A° wavelength) target under the condition of 40 kV and 40 mA. The X-Ray Fluorescence analysis was performed to measure the elemental composition of materials. For this purpose, the biomass sample and its structural components were characterized by a Thermo Scientific NITON XL3t model XRF analysis instrument.

FTIR analyses were done by Perkin Elmer Spectrum One instrument with an interval of frequency between 650 and 4000 cm^{-1}. On the other hand, BET surface area measurements were performed by Quantachrome NOVA1200 instrument.

25.3 Results and Discussion

The results from the proximate analysis, calorific value measurement, and the compositional analyses for the original hybrid poplar are given in Table 25.1. Basing on the data in Table 25.1, it is likely to say that hybrid poplar is a typical woody

Table 25.1 Analysis results of hybrid poplar

Moisture (%)	Volatiles (%)	Ash (%)	Fixed Carbon (%)	HHV[a] (MJ/kg)	Extractives (%)	Holocellulose (%)	Lignin (%)
8.9	76.1	3.2	11.8	17.1	5.4	74.2	20.4

[a] *HHV* higher heating value

biomass species with high volatiles and low ash and fixed carbon contents. On the other hand, the most part of the biomass matrix is comprised of holocellulose which indicates the existence of high potential for high thermal reactivity during thermal conversion processes. Besides, lignin that is the unique aromatic major ingredient in biomass is not as abundant as the holocellulose.

Comparison of the DTG curves of the main sample and its ingredients such as extracted sample, holocellulose, and lignin can be seen from Fig. 25.1. It is obvious from Fig. 25.1 that the extracted sample has the highest thermal reactivity. Some criteria including the maximum rate of decomposition (R_{max}) and its temperature ($T_{R\text{-}max}$) have been taken into account to evaluate the thermal reactivity. For instance, the pyrolysis of the main sample gave a (R_{max}) value of 1.13 mg/min at 370 °C. The volatile matter release started at 225 °C and reached the maximum value at 370 °C, and ended at 405 °C.

The isolated holocellulose had a (R_{max}) value of 0.99 mg/min at 328 °C. The volatile matter release started at 190 °C and reached the maximum value at 328 °C, and ended at 370 °C. Besides, lignin is thermally much more stable than cellulose during pyrolysis, and this means lower thermal reactivity. Accordingly, (R_{max}) for lignin was determined as 0.28 mg/min at 175 °C. The volatile matter release started at 120 °C and reached the maximum value at 175 °C, and ended at 310 °C.

When structural components were evaluated among themselves, it was observed that extracted sample had the highest (R_{max}). On the other hand, the lowest ($T_{R\text{-}max}$) temperature belonged to holocellulose with a value of 328 °C. This shows the high thermal reactivity of the hemicellulosics and celluloses that form the holocellulose content, and this is in accordance with literature [1, 2]. In fact, the high oxygen content in such ingredients is responsible for the high thermal reactivity during decomposition even at low temperatures.

Besides, these decomposition runs in thermogravimetric analyzer produced different char yields from the samples. That is, the char yields for the main sample, extracted sample, holocellulose, and lignin were 18.6, 17.0, 23.0, and 37.2 wt%, respectively. This confirms the fact that holocellulose content mainly contributes to the formation of volatiles, while lignin mainly contributes to the formation of solid product called as char.

The analysis results for the pyrolyzed sample in tube furnace at 600 °C are given in Table 25.2. The moisture contents in these residues indicate the fact that they are very attractive to fix moisture form the surrounding. That is, the applied thermal process was capable of elimination all of the moisture content form these samples. However, moisture uptake took place from the surrounding especially during the removal of the residues from the furnace and storing them in sample

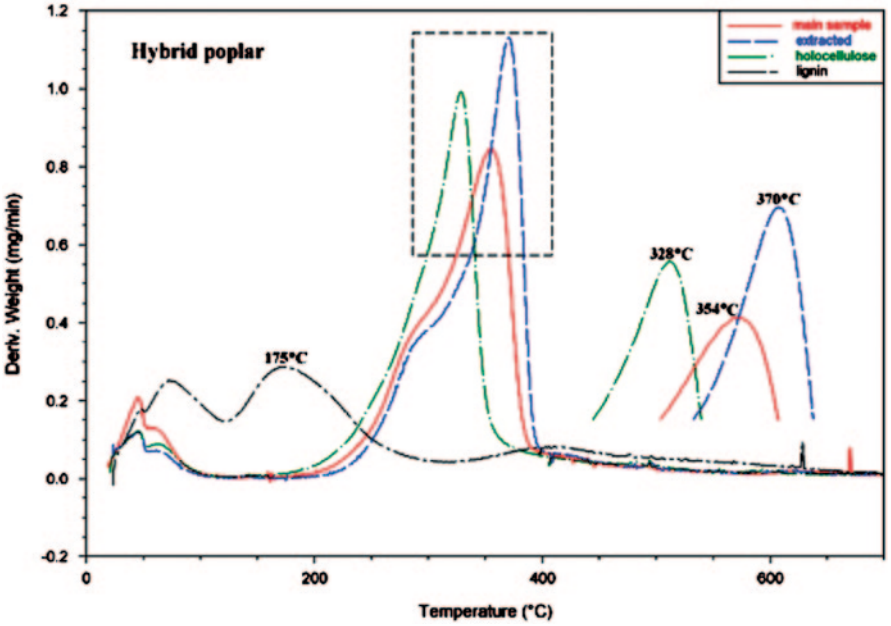

Fig. 25.1 DTG curves for main sample, extracted sample, holocellulose, and lignin

container. Besides, serious decreases took place in the volatile matter contents. However, the most striking variation occurred in the fixed carbon contents that in case of extracted sample, the increase in fixed carbon reached 616%.

Figure 25.2 shows the FTIR spectra of the samples. The interpretation of the FTIR spectrum of the main sample is that there exist one broad band at 3335 cm^{-1}, and strong bands at 1736, 1652, 1594, 1507, 1455, 1423, 1373, 1240, 1158, 1123, 1109, 1031, 698 cm^{-1}, and moderate bands at 2919, 2849, 897 cm^{-1}. The broad band originates from –OH stretching, and the strong bands at 1742–1620 cm^{-1} can be assigned to C=O vibrations in carbonyl groups, mainly ketones and

Table 25.2 Analysis results for pyrolyzed samples

Sample	Moisture (%)	Volatiles (%)	Ash (%)	Fixed carbon (%)	HHV[a] (MJ/kg)	Increase in fixed carbon (%)
Main sample	4.5	13.6	9.3	72.6	31.6	515
Extracted sample	4.5	16.6	9.8	69.1	30.3	616
Holocellulose	7.4	15.6	8.6	68.4	28.8	360
Lignin	5.0	10.0	13.5	71.5	29.3	156

[a] *HHV* higher heating value

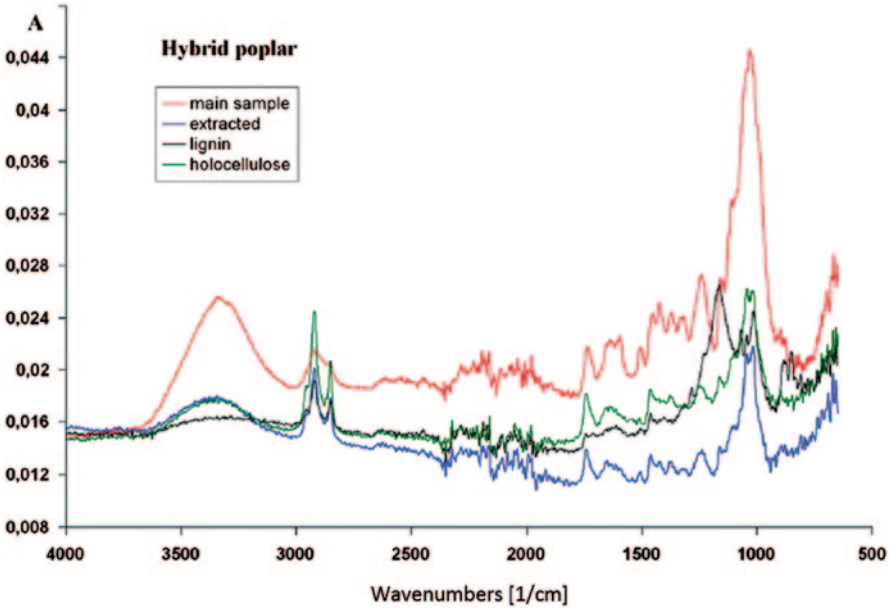

Fig. 25.2 FTIR spectra for hybrid poplar and its structural components

esters. 1594, 1507, 1455 cm^{-1} bands can be assigned to aromatic C = C streching vibration, while 1423 and 1373 cm^{-1} bands are resulted from the existence of $–CH_2$ and $–CH_3$ bending of aldehydes and ketones. The band at 1240 cm^{-1} may be assigned to C–O vibrations in carboxylic acids and derivatives. Bands at 1158, 1123, 1109, 1031 cm^{-1} form as a result of the presence of C–O–C stretching vibrations of ether type structures. The band at 698 cm^{-1} may be ascribed to C–H bending or deformation vibrations in olefinic or aromatic structures. The moderate bands at 2919 and 2849 cm^{-1} are the evidence of C–H stretching of methyl and methylene groups, which are expected from hemicellulose, cellulose and lignin. The strong bands predict that carbonyl groups, aromatic and ether type structures, and carboxyl groups are the most significant functional groups in hybrid poplar. The medium bands can be attributed to the methyl methylene groups of holocellulose and lignin.

In case of lignin, the strong bands reveal the fact that the saturated and unsaturated ether structures were very common in the structure. On the other hand, the moderate bands are the evidence of the carbonyl and metoxyl groups as well as the aromatic structures. As to the FTIR spectrum of holocellulose, the strong bands predict the abundance of methyl, methylene, carbonyl groups, olefinic, aromatic and ether type structures, while the moderate bands belong to alcohols, phenols, and carboxylic acids. Thermal treatment of hybrid poplar caused some variations in functional group distribution. The intensities of the peaks changed and the bands representing the aromatic structure became more apparent in comparison to the

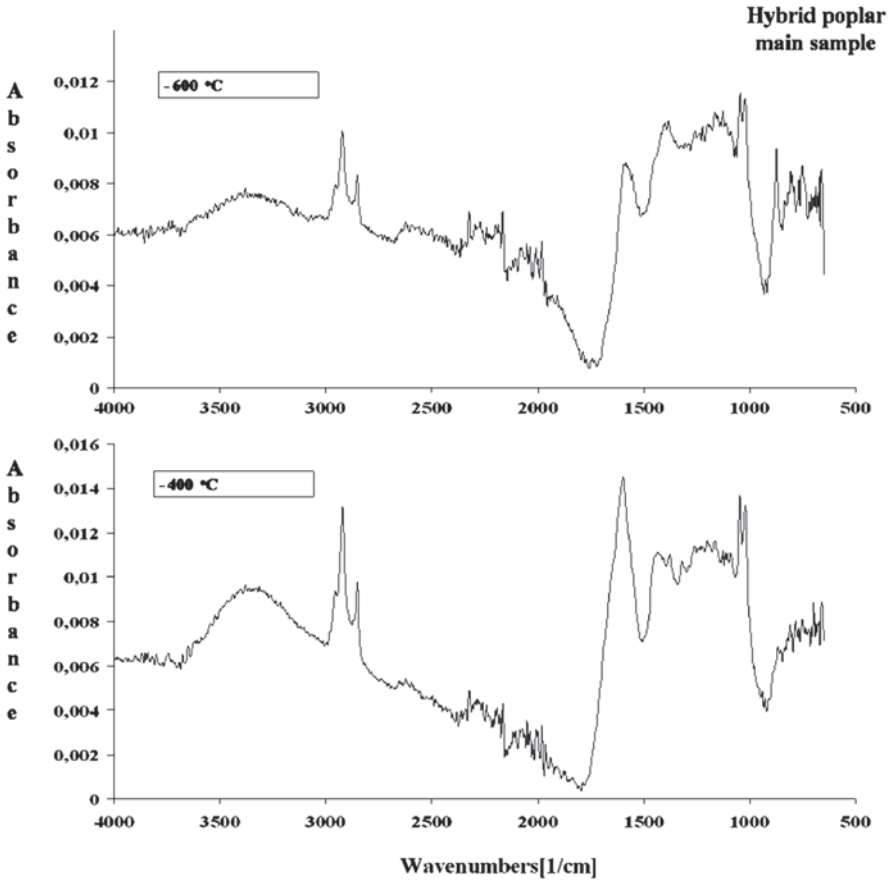

Fig. 25.3 FTIR spectra of thermally treated main sample at 400 and 600 °C

untreated main sample. FTIR spectra for the treated main sample at 400 and 600 °C are given in Fig. 25.3.

Table 25.3 presents the results of the surface areas determined according to BET approach for both the thermally untreated and pyrolyzed samples. It is evident from the results in Table 25.3 that thermal processing enhanced the surface area not only for the main sample but also for all the components of the biomass sample. These increases in surface area are closely related to the elimination of an important part of the volatiles, leading a much more porous structure and a larger surface area. SEM micrographs showing the differences in the textural properties of the pyrolyzed samples can be seen from Fig. 25.4.

Removal of the extractives from the biomass and further treatments to isolate holocellulose and lignin led to morphological changes. From these images, it can be concluded that the main sample has a more leafy structure than the extracted sample. The isolated holocellulose and lignin lost their porosity, and relatively more

Table 25.3 BET surface area results

Sample	Surface area (m^2/g)
Main sample (Untreated)	12.9
Main sample (Pyrolyzed)	236.9
Extracted sample (Untreated)	8.5
Extracted sample (Pyrolyzed)	480.1
Holocellulose (Untreated)	0.6
Holocellulose (Pyrolyzed)	12.7
Lignin (Untreated)	0.5
Lignin (Pyrolyzed)	158.0

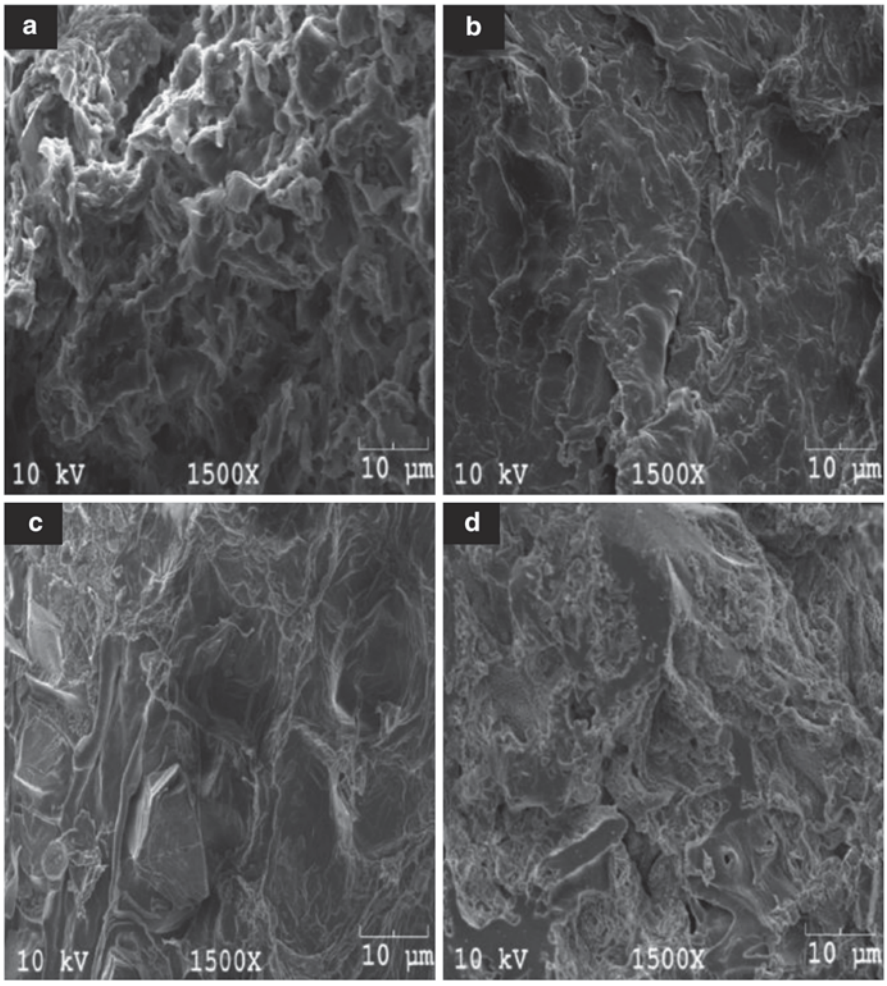

Fig. 25.4 SEM micrographs of pyrolyzed samples **a** main sample, **b** extracted sample, **c** holocellulose, **d** lignin

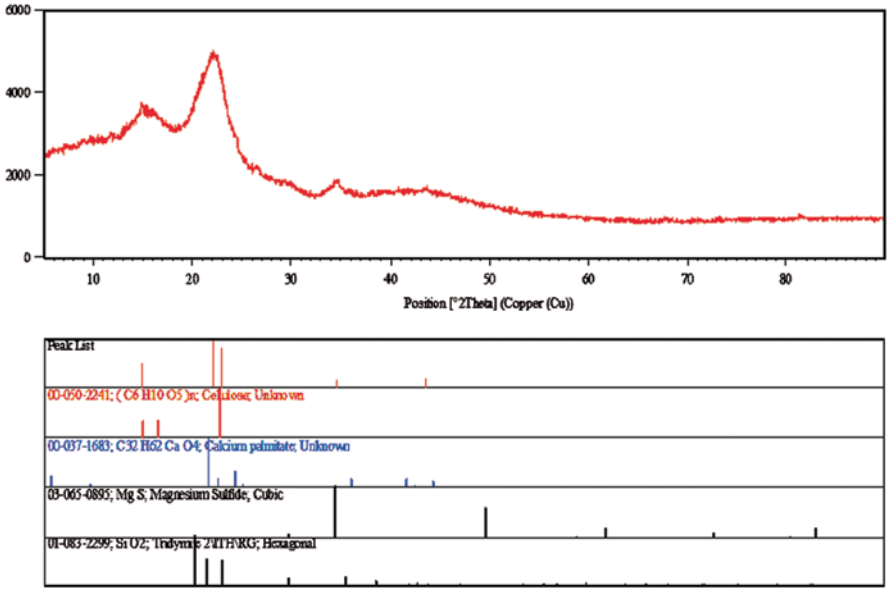

Fig. 25.5 XRD pattern for untreated main sample

smooth surfaces obtained. This is also evident from the low surface areas of these ingredients.

Mineralogical investigations of the samples were conducted by XRD and XRF techniques. Figure 25.5 and Table 25.4 represent the main phases found in the main sample and in its components. The presences of calcium, silicon, magnesium, and potassium compounds were detected in these analyses. More detailed results can be found in XRF results given in Table 25.5. The concentrations of calcium, magnesium, and silicon in the main sample are relatively higher than that for the other inorganics. Whereas, others like chlorine and sulfur were also abundant in holocellulose and lignin, respectively.

Conclusions

Hybrid poplar that is one of the important biomass energy resources have been investigated regarding the thermal reactivity and the physical/chemical characteristics. For this purpose, not only the main sample but also its isolated ingredients such as extracted sample, holocellulose, and lignin were subjected to pyrolysis, and the effects of the applied thermal process on thermal reactivity and the other properties were interpreted.

It was found out that the obtained biochars contain large amounts of aromatic and ether type structures. Also, aromatic bands were determined to increase with

Table 25.4 Comparison of the XRD results of the samples

Hybrid proplar	Main sample	$(C_6H_{10}O_5)n$; Cellulose	$C_{32}H_{62}Ca0_4$; Calcium palmitate	Mg S; Magnesium Sulfide	SiO_2; Tridymite	
	Extracted	Si O_2; Silicon Oxide	$C_{12}H_{10}CaO_8H_2O$; Calcium 1 -phenol-4-sulfonate hydrate	$(C_6H_{10}O_5)n$; Cellulose	$C_{16}H_{16}O_2$; 4.4-Dimethoxystilbene diDimethoxystilbene	K_2S Potassium Sulfide
	Holocellulose	$Mg(H_2O)_6(ClO_2)_2$; Aqua Magnesium Chlorate	$C_{12}H_8Cl_2$; Dichlorobiphenyl	$C_{32}H_{62}CaO_4$; Calcium palmitate		
	Lignin	$K_2S_2O_7$; Potassium Sulfate	$Mg_3S_2O_8(OH)_2$; Magnesium Sulfate Hydroxide			

Table 25.5 XRF results

Sample		Hybrid poplar		
	Main sample	Extracted	Hollocellulose	Lignin
Cd	0,009	0,008	0,008	0,015
Pd	0,003	0,004	0,004	<LOD
Ag	0,004	0,003	<LOD	<LOD
Zn	0,049	0,042	0,019	0,063
Cu	0,030	0,025	0,029	<LOD
Ni	<LOD	0,019	<LOD	<LOD
Fe	0,414	0,536	0,374	1,366
Cr	0,195	0,266	0,271	0,206
Al	<LOD	<LOD	<LOD	<LOD
P	<LOD	<LOD	<LOD	<LOD
Si	1,218	1,681	0,867	<LOD
Ca	7,919	10,130	7,925	2,475
K	<LOD	<LOD	<LOD	<LOD
Cl*	0,363	0,446	12,081	<LOD
S*	0,626	0,533	0,306	30,765
Mg	3,923	<LOD	<LOD	<LOD
Total	14,753	13,693	21,884	34,89

increasing pyrolysis temperature. Besides, carbonyl bands disappeared as temperature increases. It was also revealed that lignin contains many functional groups, of which methoxyl groups were the most apparent functionalities. On the other hand, the calorific value of the produced biochars tended to increase with increasing pyrolysis temperature.

References

1. Klass DL (1998) Biomass for renewable energy, fuels, and chemicals. Academic Press, San Diego. ISBN: 978-0-12-410950-6
2 Haykiri-Acma H, Yaman S Kucukbayrak S (2010) Comparison of the thermal reactivities of isolated lignin and holocellulose during pyrolysis. Fuel Process Technol 91:759–764
3. Haykiri-Acma H, Yaman S, Kucukbayrak S (2011) Burning characteristics of chemically isolated biomass ingredients Energ Convers Manage 52: 746–751
4. Kandiyoti R, Herod A, Bartle K (2006) Solid fuels and heavy hydrocarbon liquids: thermal characterization and analysis. Elsevier, London. ISBN: 978-0-08-044486-4
5. Higman C, Van der Burgt M (2008) Gasification—2nd ed. Elsevier, Oxford. ISBN: 978-0-7506-8528-3
6. Van Soest PJ (1963) Use of detergents in the analysis of fibrous feeds. II. a rapid method for the determination of fiber and lignin. J Associ Offi Anal Chemist 46: 829–835

Chapter 26
Contribution for Solar Mapping in Algeria

Abdeladim Kamel, Hadj Arab Amar, Chouder Aissa, Cherfa Farida, Bouchakour salim and Kerkouche Karim

Abstract In the present paper, a solar mapping methodology is presented. The work was carried out for the major part of Algeria; a sample of data covering 50 sites over the whole country was considered. However, due to the lack of radiometric data that are essential for this study, data obtained from simulation were used. Kriging method was chosen in order to perform different interpolations trough Surfer ® software, it will allow us to prepare the Grid file necessary to get to the last step, which is the establishment of solar map for the whole Algerian country.

Keywords Solar mapping · radiometric data · kriging method · Surfer ® software

26.1 Introduction

According to its geographical location, Algeria holds one of the highest solar potential. Indeed, following an assessment by the satellites, the German Aerospace Center (DLR) concluded that Algeria has the largest solar potential in the Mediterranean basin: 169,440 TWh/year. Sunshine duration on almost all the country is over 2000 h/year and can reach 3900 h in the Highlands and the Sahara. The daily

A. Kamel (✉) · H. A. Amar · C. Aissa · C. Farida · B. salim · K. Karim
Centre de Développement des Energies Renouvelables Route de l'observatoire, BP. 62, 16340 Bouzaréah, Algiers
e-mail: k_abdeladim92@cder.dz

H. A. Amar
e-mail: a.hadjarab@cder.dz

C. Aissa
e-mail: aissachouder@gmail.com

C. Farida
e-mail: f.cherfa@cder.dz

B. salim
e-mail: s.bouchakour@cder.dz

K. Karim
e-mail: k.kerkouche@cder.dz

I. Dincer et al. (eds.), *Progress in Sustainable Energy Technologies: Generating Renewable Energy,* DOI 10.1007/978-3-319-07896-0_26,

energy obtained on a horizontal surface is about 5 kWh on most of the national territory, about 1700 kWh/m^2/year for the North and 2263 KWh/m^2/year for the South, [1–8].

The availability of large amounts of solar radiation in Algeria means that it would be possible to consider solar energy as a potential source of energy for different applications in the form of individual photovoltaic solar modules or systems such Concentrated Solar Power (CSP).

However, the knowledge of the potential solar of the region is crucial for the sizing of different solar systems before their installation at a particular location.

Measurement of the solar global radiation is limited to a few stations over a country like Algeria, with a huge area 2,381,741 km^2, where it is necessary to have several tens of stations providing radiation measurement in order to quantify in an objective way the solar potential.

The purpose of this study is to present a methodology leading us to draw up the Algerian solar map i.e. Plotting maps by region or for the whole country, note that works were undergone in the past, [1,7]. Therefore, we must possess a maximum of data including measured ones through the considered area in the study in order to make objective interpolations using appropriate methods, this task can be performed thanks to the SURFER ® software.

Simulated data of 50 sites representing the country from North to South and from East to West were used in order to establish our solar map.

Meanwhile, measured data recorded on 6 sites where used in order to validate those simulated, the average of recordings in some cases reaches 10 years of measurements.

26.2 Data Used

Global irradiation received on horizontal plane monthly average has been used for this study [9], a set of 50 sites across the country representing different climates and areas of the country was considered.

In Table 26.1, are given the coordinates of the different sites involved in this study. Thus, for more flexibility, four areas were considered [7].

- Zone 1 ($33° \leq \text{latitude} < 37°$): It extends from the Mediterranean coast to the Highlands.
- Zone 2 ($30° \leq \text{latitude} < 33°$): It mainly includes the North of the Sahara desert.
- Zone 3 ($24° \leq \text{latitude} < 30°$): It represents the centre of the Sahara.
- Zone 4 ($18° \leq \text{latitude} < 24°$): It consists of the extreme Southern region of Algeria and the Hoggar and Tassili mountains (Fig. 26.1).

Table 26.1 Preliminary list of sites considered in the study

	Station	Latitude (deg.)	Longitude (deg.)	Altitude (m)
ZONE I				
1	Skikda	36,87	6,95	9
2	Annaba	36,83	7,82	4
3	Jijel	36,83	5,78	2
4	Bejaïa	36,75	5,08	9
5	Alger	36,72	3,25	25
6	Miliana	36,32	2,23	750
7	Constantine	36,28	6,62	687
8	Sétif	36,18	5,42	1081
9	Chlef	36,16	1,35	112
10	Bordj Bou Arreridj	36,07	4,77	928
11	Mostaganem	35,88	0,12	137
12	Oum El Bouaghi	35,88	7,12	889
13	M'sila	35,67	4,50	441
14	Oran	35,63	−0,62	99
15	Mascara	35,60	0,30	474
16	Batna	35,55	6,18	1040
17	Tébessa	35,43	8,13	813
18	Boussaâda	35,33	4,20	461
19	Tiaret	35,25	1,43	1127
20	Sidi Bel Abbes	35,18	−0,65	486
21	Méchria	34,93	−0,43	1149
22	Tlemcen	34,93	−1,32	810
23	Saida	34,87	0,15	770
24	Maghnia	34,82	−1,78	426
25	Biskra	34,80	5,73	81
26	Djelfa	34,68	3,25	1144
27	El Kheiter	34,15	0,07	1000
28	Laghouat	33,77	2,93	767
29	El Bayadh	33,68	1,02	1305
30	El Oued	33,37	6,88	70
31	Touggourt	33,12	6,07	69
ZONE II				
32	Hassi R'mel	32,93	3,28	764
33	Ain sefra	32,75	−0,60	1072
34	Ghardaïa	32,38	3,82	450
35	Ouargla	31,92	5,40	141
36	Hassi Messaoud	31,67	6,15	143
37	Bechar	31,63	−2,25	806
38	El Golea	30,57	2,90	398
39	Béni Abbes	30,13	−2,17	498
ZONE III				
40	Timimoun	29,25	0,23	284
41	In Aménas	28,05	9,63	562

Table 26.1 (continued)

	Station	Latitude (deg.)	Longitude (deg.)	Altitude (m)
ZONE I				
42	Adrar	27,88	−0,28	264
43	Tindouf	27,67	−8,13	402
44	In Salah	27,2	2,47	293
45	Aoulef	26,97	1,08	290
46	Illizi	26,5	8,43	559
47	Djanet	24,55	9,47	1054
ZONE IV				
48	Tamanrasset	22,78	5,52	1378
49	Bordj Badji Mokhtar	21,33	0,95	398
50	In Guezzam	19,57	5,77	411

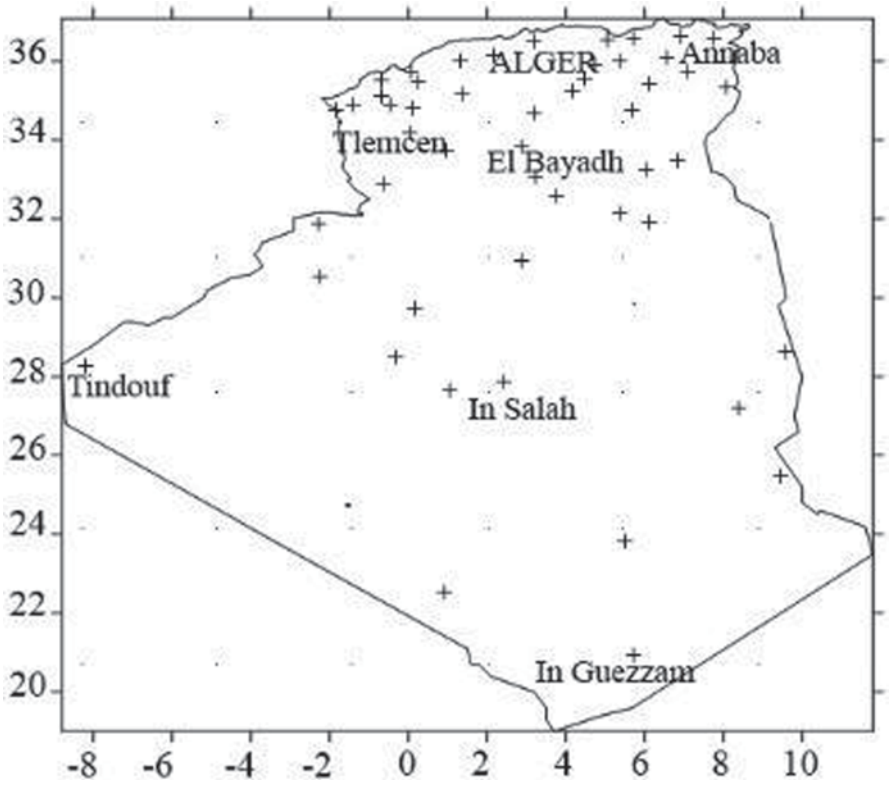

Fig. 26.1 Spatial distribution of 50 considered sites

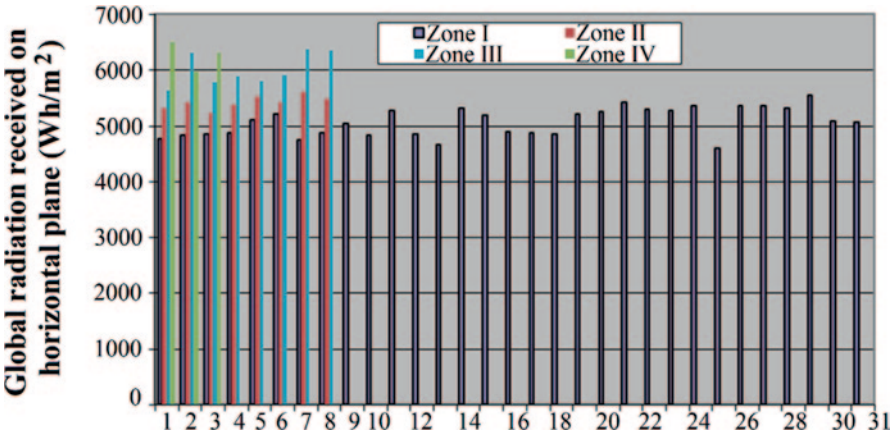

Fig. 26.2 Yearly average of global radiation received on horizontal plane by zone

26.3 Data Analysis

Yearly Average

Yearly and monthly and data of the global irradiation received on horizontal plane were obtained through simulation [9], in Fig. 26.2, are shown the yearly average of global radiation received on horizontal plane for different sites considered by zone. We can notice that the global irradiation is greater in the Southern region (Zone IV), with values ranging between 6 and 7 kWh/m^2 for some cases, if we go toward North (Zone I), the values decrease, with values going below 5 kWh/m^2.

Monthly Average

The monthly average evolution of global radiation for the different sites considered are given in Figs. 26.3, 26.4, 26.5 and 26.6 respectively for zones I, II, III, IV. We notice the same seasonal pattern for all sites considered with a maximum in summer and a minimum in winter. The maximum value was recorded in Illizi with a value exceeding 8 kWh/m^2 in July.

In order to check the accuracy of the data that we have used, the relative error was calculated by using the following relation:

$$E_{Ri} = \left| \frac{Xest_i - Xmeas_i}{Xmeas_i} \right| \tag{26.1}$$

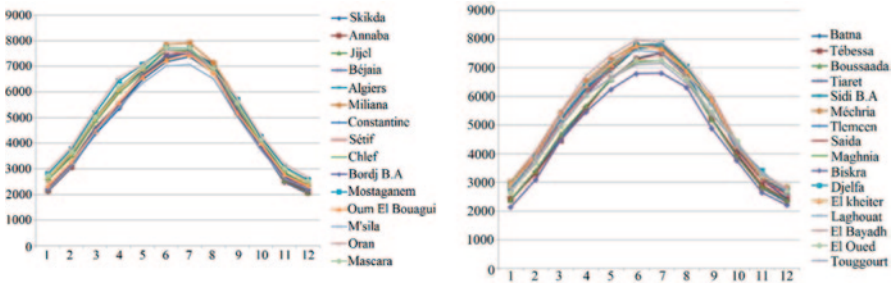

Fig. 26.3 Monthly average of global radiation received on horizontal plane (zone I)

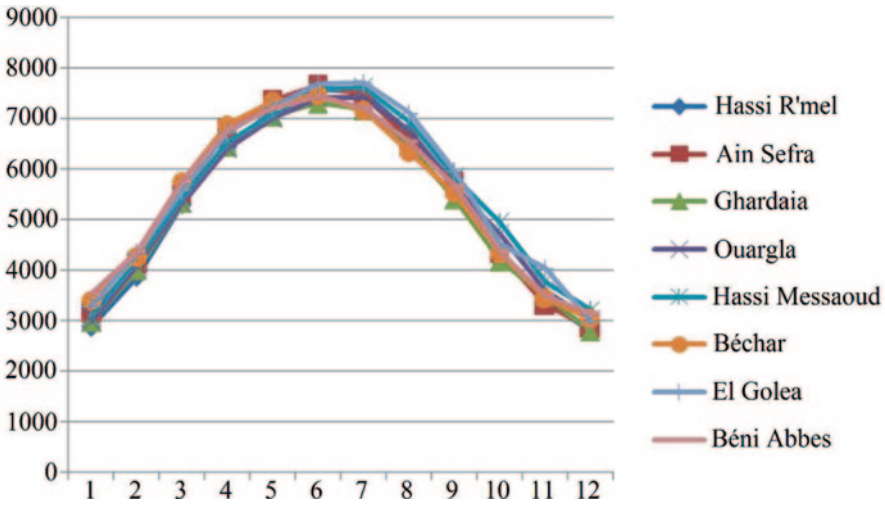

Fig. 26.4 Monthly average of global radiation received on horizontal plane (zone II)

$Xest_i$: is the estimated parameter

$Xmeas_i$: is the measured parameter

Results show that simulated data we have used agree well in almost all cases, in Table 26.2 are given error relative representing the relative errors obtained comparing estimated to measured data concerning global radiation parameter.

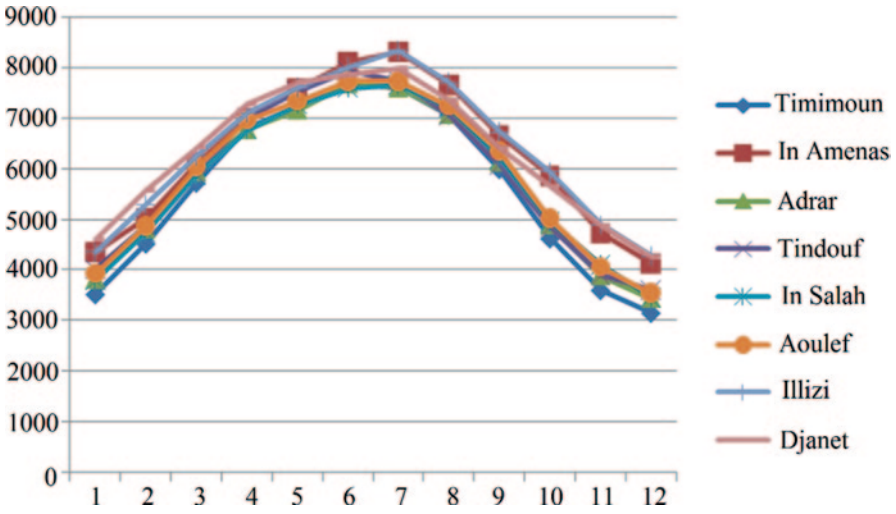

Fig. 26.5 Monthly average of global radiation received on horizontal plane (zone III)

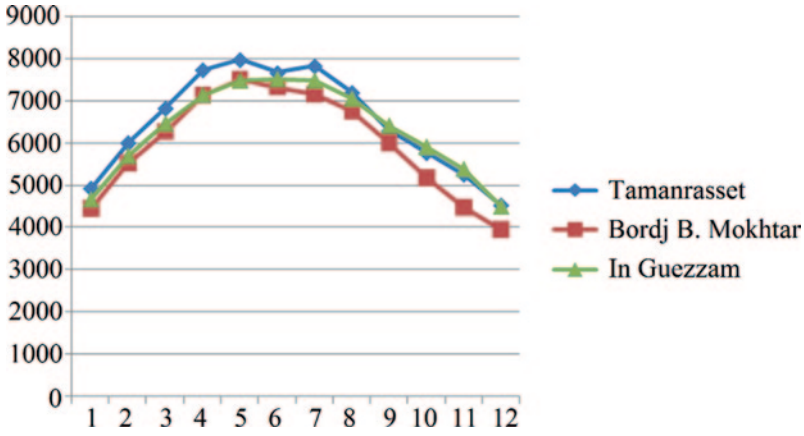

Fig. 26.6 Monthly average of global radiation received on horizontal plane (zone IV)

Table 26.2 Monthly relative error values (%)

	Jan	Feb	Mar	Apr	May	Jun	Jun	Aug	Sep	Oct	Nov	Dec
Algiers	4.2	1.0	2.5	4.7	6.2	5.0	7.5	11.1	7.9	7.9	9.8	11.9
Bouzaréah	1.4	6.7	5.2	26.6	6.8	10.6	16.4	10.2	11.1	6.0	4.5	5.5
Oran	25.5	12.4	7.2	15.4	19.1	22.4	5.0	5.4	0.0	8.0	0.8	8.9
Ghardaïa	23.9	20.7	12.0	7.8	1.6	5.5	0.6	1.9	7.0	13.5	18.2	24.0
Béchar	4.1	10.0	3.9	0.6	1.9	2.7	0.2	5.7	8.8	13.0	10.1	3.1
Tamanrasset	7.6	3.8	3.3	0.4	7.0	2.4	2.8	0.9	2.1	2.1	1.3	12.4

26.4 Solar Cartography

After obtaining global irradiation on horizontal plane from different simulations, interpolations were established thanks to SURFER ® software, using Kriging method [1], therefore results were given in a "Grid" file.

After finishing with the interpolation, the output files (. Grd) were used in order to draw up the map for the mesh that we have chosen for our case the region ranges approximately from −9 to 12° East West longitudes and from 19 to 37° of North latitudes.

In Fig. 26.7, is shown the preliminary annual Algerian solar map for the global irradiation received on horizontal plane for the whole country.

We can see that the south region of the country has a greater solar potential than other regions

Conclusions & Perspectives

A solar mapping method was presented in this study, the layout was done for the region covering the whole National territory, and a data set including 50 sites was considered.

However, it should be noted that these maps need to be used with some caution since the treatment was done using simulated data.

Nevertheless, more accurate maps can be established if the measured data will be available in the future.

Deeper work is planned at moment in order to estimate global radiation from meteorological data for the existing stations across the country, the obtained results will be then compared to measured data in order to validate the models used, once validated, these data can then be used to redraw again the map covering the entire Algerian territory. The same work can be extended to other radiometric parameters such as global radiation received on an inclined angle, diffuse, direct…etc

Afterward, it will be interesting to install radiometric stations and start measurement campaign in some sites in different locations in order to compare data obtained from measurement to those given by our maps. This step is essential and will give more credibility to the obtained results.

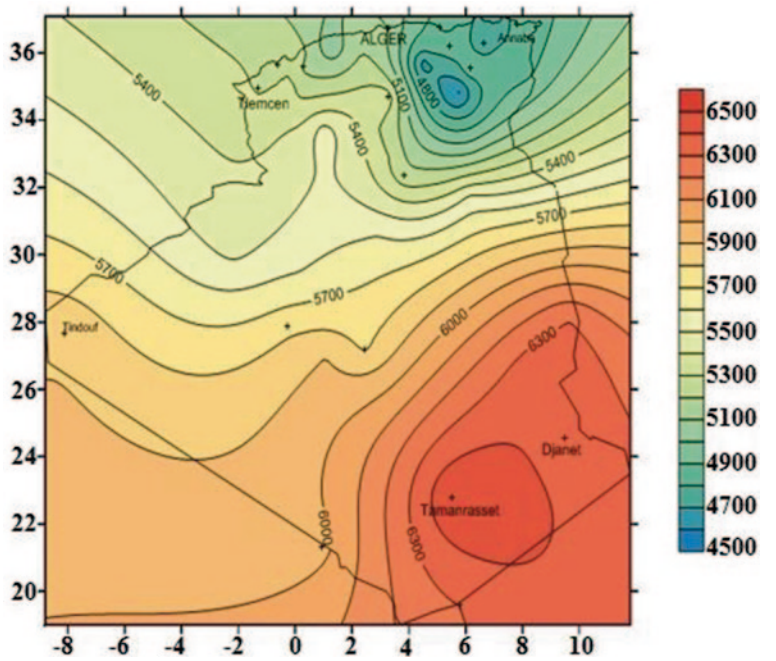

Fig. 26.7 Yearly average of global radiation received on horizontal plane

Acknowledgement Authors would like to thank, MM. Gaira Kacem, Benkaciali Said from URAER and my colleague Yaïche Mohamed Réda for providing measured data for the site of Ghardaïa

References

1. Abdeladim K (2004) Cartographie éolienne-solaire de certaines régions de l'algérie. Technical rapport, Algeirs
2. CDER (2012) Algeria. http://www.cder.dz. Accessed 10 Mar 2012
3. (2007) Energy & Mines Book. http://www.mem-algeria.org. Accessed 26 Dec 2007
4. Hadj arab A, Ait driss B, Amimeur R, Lorenzo (1995) Photovoltaic systems sizing for algeria. Sol Energ 54(2):99–104
5. Mahmah B, Harouadi F, Benmoussa H, Chader S, Belhamel M, M'Raoui A, Abdeladim K, Cherigui A, Etievant C (2009) Medhysol: Future federator project of massive production of solar hydrogen. Int J Hydrog Energ 34(11):4922–4933
6. Mefti A, Bouroubi MY, Khellaf A et (1999) Analyse critique du modele de l'atlas solaire de l'algerie. Rev Energ Renouv 2:69–85
7. Mefti A, Bouroubi MY, Adane A (2003) Generation of hourly solar radiation for inclined surfaces using monthly mean sunshine duration in Algeria. Energy Conversion Manage 44(19):3125–3141
8. Stambouli AB (2011) Algerian renewable energy assessment: the challenge of sustainability Energy Policy 39(8):4507–4519

Chapter 27
Experimental and Theoretical Investigations of Performance of Psychometric Humidification and Dehumidification Solar Water Desalination System Coupled with an Evacuated Tube Solar Collector

Mahmoud Shatat, Saffa Riffat, Yijun Yuan and Abdulkarym Mayere

Abstract There is an acute scarcity of potable water in many parts of the world, and especially in the Middle East region. Important advances have been made in solar desalination technology but their wide application is restricted by relatively high capital and running costs. Until recently, solar concentrator collectors have usually been employed to distill water in compact desalination systems. Currently, it is possible to replace these collectors by the more efficient evacuated tube collectors, which are now widely available on the market at a similar price.

This paper describes the results of experimental and theoretical investigations of the operation of a novel small scale solar water desalination technology using the psychometric humidification and dehumidification process coupled with a heat pipe evacuated tube solar collector with an aperture area of about 1.73 m^2. A number of experimental tests were carried out using a laboratory rig to investigate its water production capacity. Solar radiation (insolation) during a spring term in the Middle East region was simulated by an array of halogen floodlights. A synthetic brackish water solution was used for the tests and its total dissolved solids (TDS) and electrical conductivity were measured before and after the distillation process.

M. Shatat (✉) · S. Riffat · A. Mayere
Institute of Sustainable Energy Technology, University of Nottingham,
Nottingham NG7 2RD, UK
e-mail: mahmoodshatat@hotmail.com

Y. Yuan
ISAW technology Corporation, Ningwei Town, Xiaoshan District,
Hangzhou, China
e-mail: yuanyijunc@msn.com

S. Riffat
e-mail: saffa.riffat@nottingham.ac.uk

A. Mayere
e-mail: abdulkarym@hotmail.com

I. Dincer et al. (eds.), *Progress in Sustainable Energy Technologies: Generating Renewable Energy,* DOI 10.1007/978-3-319-07896-0_27,

A mathematical model was developed to describe the system's operation. A computer program using the Engineering Equation Solver software was written to solve the system of governing equations to perform the theoretical calculations of the humidification and dehumidification processes. The experimental and theoretical values for the total daily distillate output were found to be closely correlated. The test results demonstrate that the system produces about 11.50 kg/m^2.day of clean water with high desalination efficiency. Following the experimental calibration of the mathematical parameter model, it was demonstrated that the performance of the system could be improved to produce a considerably higher amount of fresh water. A water quality analysis showed that levels were well within the World Health Organization guidelines for drinking water. Further research is being performed to improve the performance of the installation.

Keywords Solar desalination · Humidification · Dehumidification

27.1 Introduction

Many countries in the world, and especially in Africa and the Middle East region, suffer from a shortage of fresh water. There are extensive R & D activities to find new and feasible methods to produce drinking water with the use of renewable energy technologies [1]. Conventional desalination systems are operated with fossil fuel which is becoming very expensive and which produces environmental pollution. In spite of these problems, it is likely that seawater desalination in large scale heat and power plants will continue to play a very important role in providing fresh water for domestic and industrial use in areas of high population density in the Middle East region, However, such the plants is not economically viable in remote areas, even those near a coast, and an electricity supply can also be lacking. The development of alternative, compact, small scale water desalination systems is imperative for the population in such areas [1, 2].

Thermal solar energy water desalination has proved to be a viable alternative method to produce fresh water from saline water [3] in remote locations, as also have conventional humidification and dehumidification solar desalination systems and basin solar stills with a relatively large footprint area. Such technologies would also contribute to reducing global warming.

Solar stills have been widely investigated but their disadvantages include relatively low performance due to excessive heat loss to the surrounding area and increasing reductions in efficiency because of scaling and the accumulation of salt impurities [4]. The maximum thermal efficiency of solar stills is about 25 % and the average distillate output capacity is 1.5–3.0 L/m^2/day [5]. Humidification and dehumidification desalination systems coupled with solar concentrator or flat-plate solar water collectors have also been thoroughly investigated. Yuan and Zhang [6] studied a closed circulation solar desalination unit with humidification and dehumidification and focused on analysing water production and system performance

by investigating the effect of the cooling water flow rate, the feed water rate and the structural dimensions. Similarly, Mohamed and El-Minshawy [7] and Eames et al. [8] described the theoretical and experimental investigation of a small scale solar powered barometric desalination system. Comparing the results with the given theory, they showed that the production rate of fresh water depended on three main factors, namely, the heat exchanger effectiveness of the condenser, solar insolation and pressure. Mohamed and El-Minshawy [9] studied the same concept using geothermal energy. Gude et al. [10] studied low temperature desalination using solar collectors of area 18 m^2 augmented by thermal energy storage of 3 m^3 volume; their work included the theoretical and experimental investigation of water production of 100 L/day. Hou and Zhang [11] proposed a hybrid desalination process in a multi-effect humidification–dehumidification system heated by solar collectors and showed that the distilled water output ratio was increased by 2–3 when the rejected water was reused. In this study, they maximized condenser heat recovery through composite curves and found that there is an optimum value for the water to air flow rate ratio, but they did not take the effect of the humidifier inlet temperature and the solar collector efficiency into account.

Two solar desalination units of different size but both utilizing the concept of humidification and dehumidification were constructed in Jordan by Farid et al. [12] and Alhallaj et al. [13]. They found that the effect on heat and mass transfer coefficients of the water flow rate is more significant than the air flow rate. A water desalination system using low grade solar energy was studied by Al Kharabsheh and Goswami [3]. Garg et al. [14] tested an MEH solar system to provide continuous hot water to a desalination unit over a 24 h period by system modeling based on solving heat and mass transfer equations. The result showed that the rate of distilled water production varied linearly as a function of water temperature at the humidifier. Similarly Muller-Holst et al. [15] had studied a small scale thermal seawater desalination apparatus and showed that the water productivity depended on the magnitude of the thermal energy utilized in the evaporation process.

Utilizing this previous research on HD technology in a compact unit coupled with solar collectors, this paper describes a novel process that is more affordable because it has a very small energy input. It uses the hybrid Psychometric Energy Process Desalination system based on the humidification and dehumidification principle with a new special membrane and an evacuated solar collector. This paper also describes the experimental and theoretical calculations of the system. Unlike most previous experimental and simulation work that was restricted to steady state operation at a fixed value of insolation, this work will describe the experimental results and the mathematical model of the Psychometric process with evaporation and condensation for transient numerical simulations as insolation varies over the whole daylight period and the model is extended to the overnight period. Furthermore, it shows that carrying out such experimental investigations will no longer restricted to a specific solar insolation region because the light solar simulator in the Sustainable Energy Laboratories at Nottingham University makes it possible to simulate solar insolation conditions anywhere in the world.

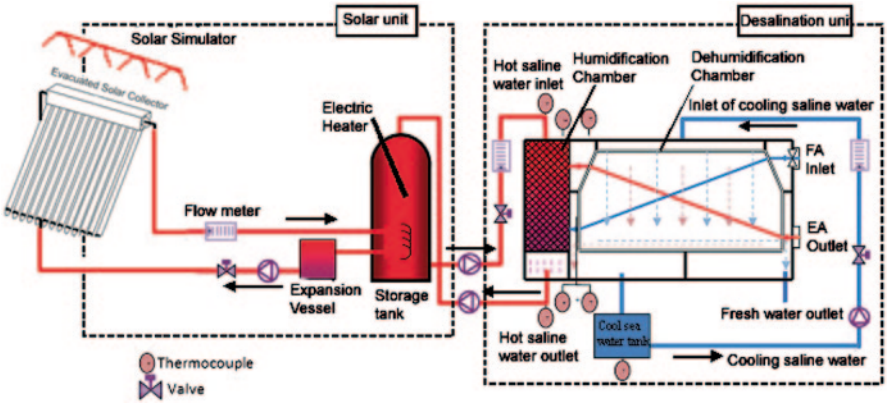

Fig. 27.1 Schematic diagram for the desalination rig test

27.2 System Description

A novel water desalination system was designed and manufactured at the Institute of Sustainable Energy Laboratories at Nottingham University. This system employs the concept of humidification and dehumidification based on the pyschrometric energy process using a special membrane to convert the saline water into fresh water. Figure 27.1 provides schematic diagrams of the desalination process and system components. This system includes the water desalination unit, evacuated solar collector, storage tank, circulation pumps, air fan and auxiliary components. The desalination unit consists of the humidification chamber, which contains an evaporation core (E-core) where evaporation takes place, and the dehumidification chamber, which contains an evaporation-condensation core (E/C-Core) where both evaporation and condensation takes place for energy recycling and water production respectively. The key innovation is the re-use of the psychrometric energy created by the condensing of the moisture in the carrier gas: a little thermal energy is supplied to the humidification and dehumidification process. The HDD system could be one-stage, or multiple stages. Figure 27.4 presents a schematic diagram of a one-stage solar HDD process. The Evaporation Core (E-Core) inside the humidifier is made from packing materials of cellular paper with a specific area of 450 m^2/m^3 volume while the evaporation condensation (E/C) core contains a special membrane of a plastic heat exchanger with two channels; the evaporation channel has a hydrophilic surface and the condensation channel has a hydrophobic surface. This makes the condensation and evaporation process in the E/C core very efficient.

The desalination unit is connected to a 120 L storage tank through the humidifier with a circulation pump and flow meter regulator to adjust the mass flow rate of hot water. This storage tank is fully insulated with foam insulation materials to reduce the heat losses and to keep the system running during the night utilizing the heat stored from solar energy during the day. The water inside the storage tank is heated by a helical copper tubular heat exchanger fixed inside the storage tank as shown

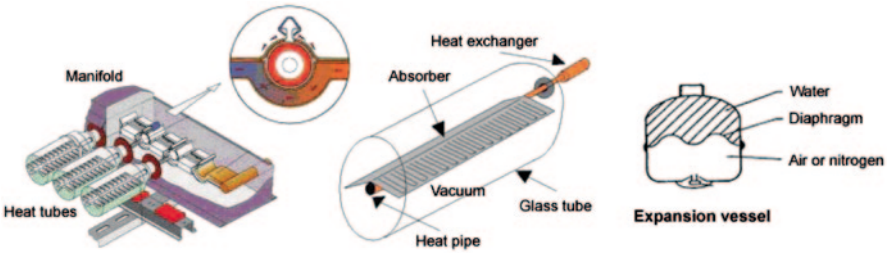

Fig. 27.2 Evacuated solar collector manifolds and heat tubes assembly

in Fig. 27.1; the outer diameter of copper pipe is 22 mm and the total length of heat exchanger is 5.73 m with 6 turns. The inlet and outlet of heat exchanger are connected, respectively, to the outlet and inlet of the manifold at the top of evacuated solar collector so that these form a closed loop and an electrical pump circulates the water in the loop.

The copper manifold header pipe of the collector is a long horizontal cylinder with a volume of approximately 0.45 L. The header pipe also contains 20 small cylindrical heat pipe housing ports, as shown in Fig. 27.2 [16]. The axis of each housing port is perpendicular to the flow direction in the header pipe. In the solar collector, the head of each evacuated tube heat pipe is inserted into a separate housing port and the heat from the heater pipes is transferred to the flow inside the header pipe through the walls of the housing ports. The thermal contact between the heads of the heat pipes and the housing ports is provided by using a special metallic glue compound. An expansion vessel is also incorporated into system in order to prevent the possibility of system damage due to an increase in pressure. The vessel has two halves: one half connects directly to the water system while the second, separated by a special diaphragm, contains air. As pressure rises and the volume increases, the diaphragm is displaced. In addition, the fluid pressure in the solar collector manifold is monitored by a pressure gauge—Bar 100XKPA, 0.60 psi—as illustrated in Fig. 27.2.

A solar sunlight simulator of the application of artificial radiation in the form of comprising of an array of 30 halogen floodlights significantly extends the range of insolation values in the experiment. The floodlights are evenly spaced on a frame installed above and in parallel to the evacuated tubes, as shown in Fig. 27.3. The array is divided into three groups and is connected to the grid via a 3-phase transformer, which enables the level of the radiation flux to be gradually regulated. The maximum electrical power consumed by each floodlight is 400 W. A pyronometer with sensitivity of 17.99×10^{-6} Volts/W/m^2 measures the radiation flux at 20 different locations on the surface of the evacuated tubes and in the spaces between them. The results were averaged as presented in Fig. 27.6. The test rig is also equipped with a metered cylinder tank, circulation pumps and a set of K-type thermocouples to measure the temperature of the water circulating in the heated circuit and the temperature of the saline water at several points in the system. An anemometer device measures air flow velocity and water flow meters measure the flow of the saline hot

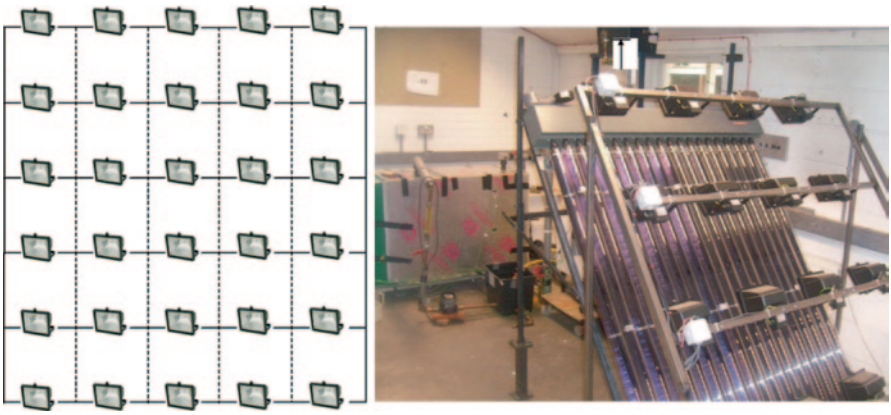

Fig. 27.3 Solar simulator with desalination rig

water, the cooling water and the fluid inside the solar collector manifold. In addition, humidity sensors measured the relative humidity at various locations in the rig.

27.3 Working Principle

In the proposed system, high efficiency is gained through a solar collector heat exchanger immersed in the water storage tank. First, the energy absorbed by the solar collector is utilized to increase the temperature of the liquid which is continuously circulating in the closed solar collector manifold–heat exchanger loop. Heat is then transferred to the saline water in the storage tank via the immersed tubular heat exchanger. The temperature of the saline water in the tank increases gradually and then the saline hot water is sprayed into the humidification chamber to humidify the incoming air. This humidified air enters the dehumidification chamber and is cooled by the incoming seawater, while the seawater is pre-heated to recover heat. The moisture condenses as pure water at the base of the chamber, and the dehumidified air is discharged to the outside, as illustrated at Fig. 27.4.

The process of humidification and dehumidification goes through four stages. (27.1) The outside air at point 1 gets humidified in the evaporation chamber of the E/C core to become point 2; the energy required is supplied from the latent heat of water condensation in the condensation channel so that most of the energy needed for desalination is reused. (27.2) Air at point 2 passes through E-core to get humidified further to become point 3. (27.3) Air at point 3 passes the condensing chamber of the E/C core to get dehumidified. (27.4) The air is discharged as exhaust, leaving the condensed water produced through the condensation channel to be collected in the metering cylinder.

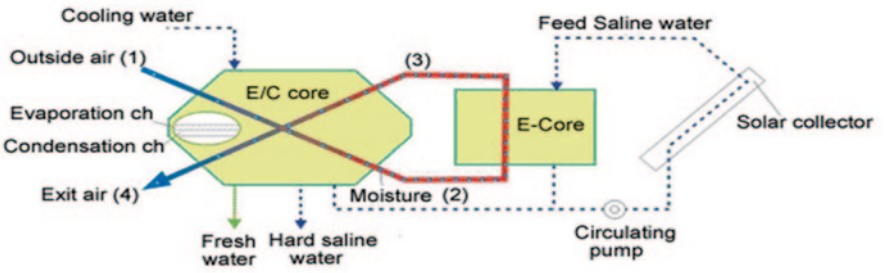

Fig. 27.4 Schematic diagram of water desalination process behaviour

27.4 Experimental Test Procedure

All experimental parameters, such as temperature, air flow, water flow, solar isolations and relative humidity, were measured and recorded using a data logger (DT500). Temperatures were recorded using K-type thermocouples with an accuracy of 0.1 °C. To ensure that all the sensors provided approximately the same reading, they were exposed to the ambient temperature and compared to a mercury-in-glass thermometer with ± 1 division accuracy. They were also immersed in a hot water bath and the same readings were obtained. The accuracy of the thermometer was checked with a handheld digital thermometer which has 0.1 °C accuracy.

Prior to the experiments, the solar desalination system was assembled so that all its sections were horizontal and covered by thermo-insulation materials of thickness 100 mm, as shown in Fig. 27.3. The heat conduction coefficient for the insulation material is 0.023 W/mK. The synthetic brackish water with a high level of total dissolved solids (TDS) and electrical conductivity was prepared and used to fill the storage tank.

The system was tested in conditions simulating a typical spring semester in the Middle East region. For this, information on the variation of the solar radiation during Spring 2004 was used, as shown in Fig. 27.5. The voltage level of electrical power supplied to floodlights was changed every 20 min using the floodlight irradiation measurement results presented in Fig. 27.6.

The fluid mass flow rate through the collector was kept at 180 kg/h, as recommended by the manufacturer. The tests were repeated several times and the water that condensed during the experiments were collected into a metering cylinder and measured after a 24 h period (daylight and unheated periods). An analysis of the water quality was also performed at the end of the experiments.

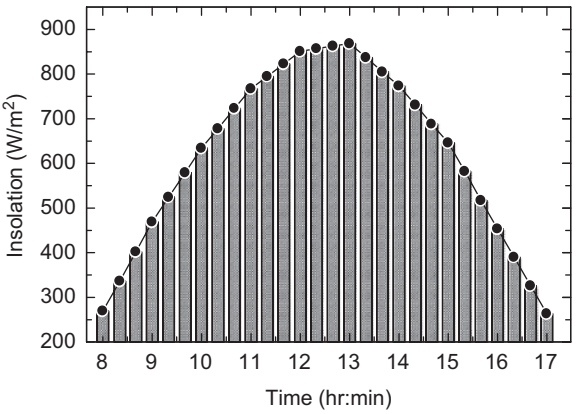

Fig. 27.5 Solar insolation variation in the Middle East region

27.5 Mathematical Model

The mathematical model discussed here shows the energy and mass conservation equations written for each part of the system. Figure 27.4 above illustrates the behaviour of the humidification and dehumidification processes for the whole system when it is connected with the solar collector. In building the model, the following assumptions were made:

- the thermo-physical properties of brackish water are identical to those of pure water;
- the effect of non-condensable gases released from water when it is heated or expanded can be neglected;
- the system is diabetic so heat losses are negligible at this stage;
- the system processes work under steady state conditions;
- the system has a controlled volume, thus air mass flow rate is constant; and

The model was used to simulate and predict the water production of the desalination system over a 24 h period, based on a heat supply during a light day with variable solar isolations (W/m^2) during daylight hours.

The energy conservation equations can be expressed as follows:

Input Energy

The consumed energy in the system can be defined as a combination of the energy required by the solar collector and the electric heater in addition to the auxiliary components, such as circulation pumps and air fan, and it can be expressed as in Eq. 27.1.

$$\dot{Q}_{input} = \dot{Q}_{hum} + \dot{Q}_{aux} \tag{27.1}$$

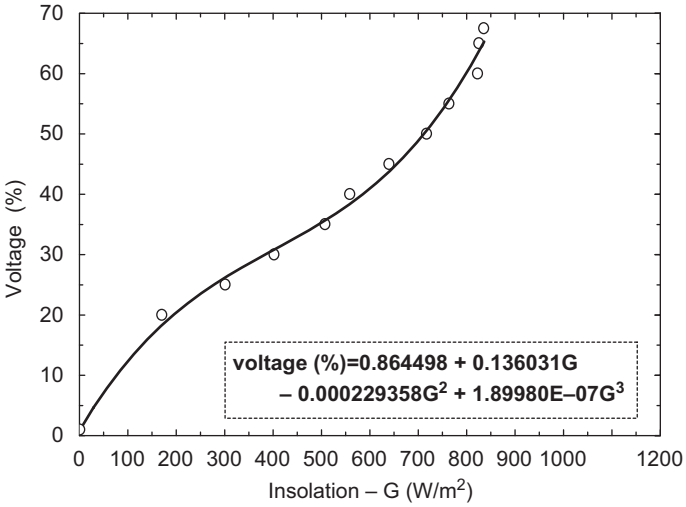

Fig. 27.6 Radiation level versus transformer voltage calibration results

where:

$\dot{Q}_{hum}$ is the supplied energy at the humidifier chamber and $\dot{Q}_{aux}$ is the auxiliary energy required by circulation pumps and fans in the system.

The supplied energy to the humidifier:

$$\dot{Q}_{hum} = \dot{m}_{w,h} C_p (T_{h,i} - T_{h,o}) \tag{27.2}$$

$$\dot{Q}_{hum} = \dot{Q}_{col} + \dot{Q}_{heater} - \Delta \dot{Q}_{losses} \tag{27.3}$$

where:

$\dot{m}_{w,h}$ is mass flow rate of hot water sprayed into humidifier, C_p is specific heat capacity of water, $T_{h,i}$ and $T_{h,o}$ are the temperatures of water at inlet and outlet of humidifier respectively.

The output energy

The output energy can be expressed in terms of the condensation energy, which equals the latent heat of condensation shown in Eq. 27.4

$$\dot{Q}_{out} = h_{fg} \; x \; W_p \tag{27.4}$$

where:

h_{fg} is the latent heat of condensation, which is equal to 2,400 KJ/Kg (approximately) and W_p, which is the amount of produced potable water. It can be expressed as in Eq. 27.5:

$$\dot{W}_p = \dot{m}_a (\omega_3 - \omega_4) \tag{27.5}$$

where $\dot{m}_a$ is the mass flow rate of air and ω_3 and ω_4 are the specific humidity of the water at inlet and outlet of dehumidification chamber, respectively.

In this stage, it was assumed that the heat losses in the desalination unit are negligible (the diabetic wall condition).

The dependence of the magnitude of the latent heat water condensation from current temperatures were determined as proposed by Cooper [17].

$$h_{fg}(T) = 1000 * \left[3161.5 - 2.40741\ (T_{h,i} + 273)\right] \tag{27.6}$$

The heat capacity of water is defined as a function of its temperature as suggested by Eames et al. [8].

$$C_p = 1000 * [4.2101 - 0.0022T + 5x10^{-5}T^2 - 3\ x\ 10^{-7}T^3] \tag{27.7}$$

In these equations h_{fg} is measured in J/kg, T in °C and C_p in J/kg °C

Solar Collector Efficiency

The solar collector efficiency can be defined in terms of the inlet and outlet fluid temperatures of the collector manifold, the area of the collector, and mass flow rate. This was suggested by Yuan and Zhang [6], as in Eq. 27.8.

$$\eta_i = \frac{\dot{m}_c C_p (T_{SCi} - T_{SCo})}{\bar{G} A_{col}} \tag{27.8}$$

The efficiency of the evacuated solar collector used can be also represented by Eq. 27.9 [18].

$$\eta_i = 0.84 - 2.02\frac{T_m - T_a}{\bar{G}} - 0.0046\ \bar{G}\left[\frac{T_m - T_a}{\bar{G}}\right]^2 \tag{27.9}$$

where:

T_m = mean collector temperature, $\frac{(T_{sci} + T_{sco})}{2}$ [°C].

T_a = ambient air temperature [°C].

$\bar{G}$ = Solar irradiance [W/m^2]

Storage Tank

In this model, a water storage tank including an immersed heat exchanger tube is connected to the system in order to keep the system running for 24 h, including the nighttime period. A completely mixed storage tank is assumed.

The energy balance equation for the storage tank with solar collector heat exchanger can be suggested by Eqs. 27.10 and 27.12 [19].

$$M_s C_{ps} \frac{dT_s}{dt} = \dot{Q}_{col} - \dot{Q}_{losses} - \dot{Q}_{humd} \tag{27.10}$$

$$M_s C_{ps} \frac{dT_s}{dt} = \dot{m}_{w,h} C_p (T_{h,o} - T_s) + \dot{m}_c C_{pc} (T_{sci} - T_{sco}) \tag{27.11}$$

where:

$\dot{m}_{w,h}$, $\dot{m}_c$ is mass flow rate of hot water sprayed in the humidifier, and through solar collector, respectively. C_p, C_{pc} is specific heat capacity of water.

$T_s = T_{h,i}$ and $T_{h,o}$, which are the temperatures of the water at inlet and outlet of humidifier.

27.6 Results and Discussions

Solar insolation for Middle East in the spring period was simulated using a sunlight simulator covering an evacuated solar collector, as shown in Figs. 27.3 and 27.5, and the water inside the storage tank was heated through a heat exchanger. The system was investigated under several conditions with various air and hot water mass flow rates. The data sets from the conducted experiments were collected and analysed and the developed mathematical model was programmed using Engineering Equation Solver Software [20] to perform the theoretical and experimental calculations.

The solar simulator at the Institute of Sustainable Energy and Technology has been designed in compliance with the British Standards in that the maximum measured difference in insolation should not exceed 50 W. The preliminary experiments using the solar simulator found that the measured efficiency of the evacuated solar collector was 69 %, which was in a good agreement with the calculated efficiency diagram provided by the manufacturer. After that, several tests were carried out using a 2.2 kW electric heater immersed in the storage tank to simulate an amount of solar insolation equivalent to a day in the Middle East. These were based on the experimental output efficiency of the solar collector carried out previously in order to reduce the heating time and to prolong the period of the system's productivity.

A synthetic saline water solution was prepared at the university lab, put into the storage tank and heated to a temperature of 50 °C. Then the desalination unit was operated with the heater continuing to work in order to achieve heat input into the system equivalent to Middle East insolation. After 75 min, the heat source was switched off and the system continued to work by utilizing the stored heat in the water inside the storage tank. The maximum hot water temperature achieved within 75 min of starting the circulation process to the desalination unit was 57 °C, as shown in Fig. 27.7.

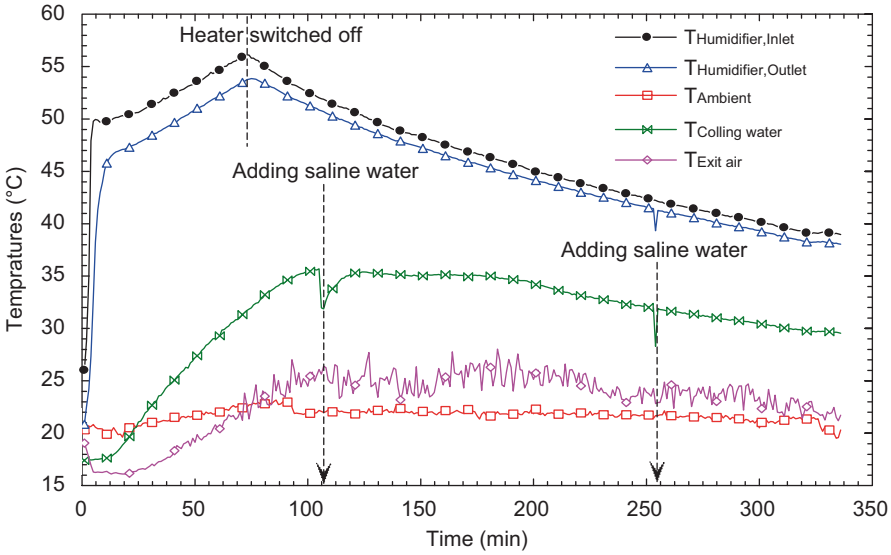

Fig. 27.7 Temperature variations in the desalination unit

Figure 27.7 presents the temperature variations inside the desalination system at different locations. It can be seen that the maximum temperature difference between the inlet and the outlet of humidifier achieved during the hot water circulation process was between 2 and 5 °C degrees. Also measured was the relative humidity of the air at the top of humidifier (point 3) and the exhaust air (point 4) and it was seen that, when the desalination system reached the steady state after 30 min of hot water circulation, the air at the top of the humidifier became fully saturated and the humidity sensors got wet and faulty. To overcome this problem, dry and wet bulb temperature sensors were then used to calculate the relative humidity and ensure that the air at point 3 had become completely saturated. Figure 27.9 presents the variations of relative humidity in the system. Experimentally, it was proved that the relative humidity achieved at point 3 was 97–100 % and the relative humidity of the exhaust air at point 4 was 85–92 %.

The fresh air in the desalination unit goes through two processes, namely evaporation and condensation. Normally, a constant mass of air is supplied from the fan. As the air temperature increases, the air becomes less dense at constant volume; hence more mass is supplied as the temperature increases. Air velocity was measured using an anemometer placed in an existing circular duct of diameter 115 mm and a relatively constant air velocity of between 2.2 and 2.35 kg/min was measured during the operation of the system, as shown in Fig. 27.8. Meanwhile, it was noted that the exhaust air humidity at the outlet of the humidification and dehumidification chamber was dependent on the temperature of the inlet hot water in the humidification chamber; this is reasonable since the temperature of humidifier hot water

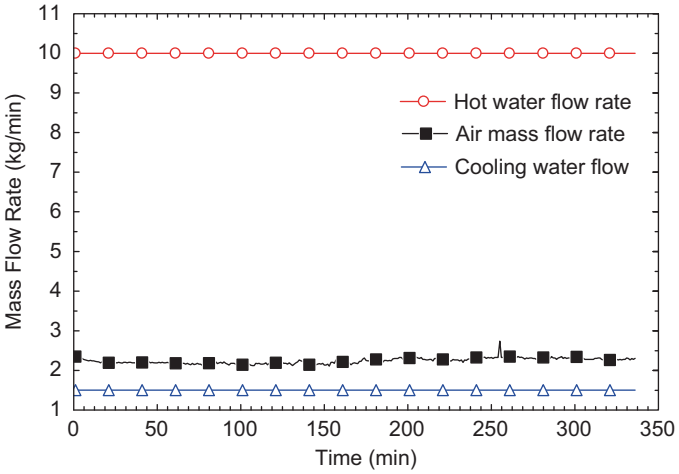

Fig. 27.8 Mass flow rates for hot water, cooling water, and air mass

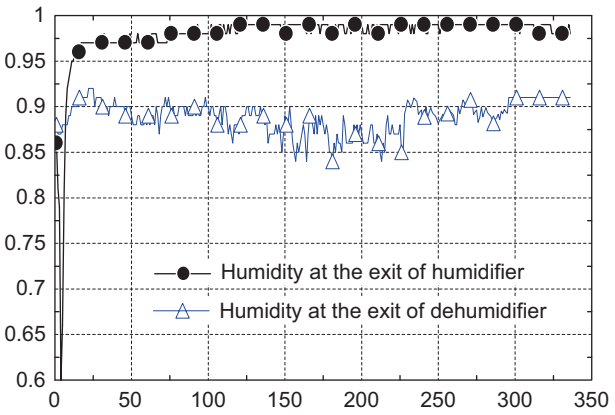

Fig. 27.9 Relative humidity at the humidifier and dehumidifier

affects the exhaust air temperature at the dehumidification chamber. The mass flow rates at the hot water inlet and of the recycling cooling water were also measured and the results are shown in Fig. 27.8. Various hot water mass flow rates were optimized experimentally and it was noted that the higher the mass flow rate the greater was both the water productivity and the coefficient of performance (COP), see Fig. 27.10. As shown in Fig. 27.8, the cooling water flow rate was set at 1.5 kg/min throughout the experiment. It might be expected that the cooling water temperature should increase rapidly due to its gain of latent heat from condensation, but it was observed that the increase in temperature was steady. This indicates that the latent heat of condensation was being effectively utilized through the evaporation channel of the E/C-Core.

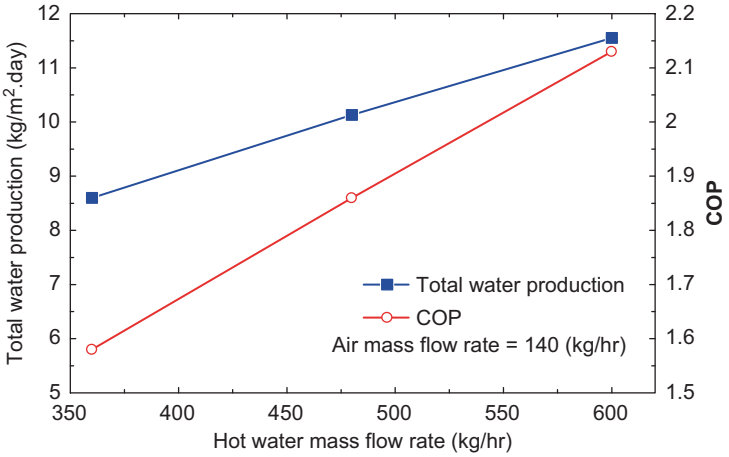

Fig. 27.10 Hot water mass flow rates and COP against water productivity

Further experiments will be conducted with different mass flow rates of cooling water and the achieved optimal mass flow rates ratios of hot water to air flow in order to achieve the optimal water production with the minimum heat input.

Water Production

During the experiment, most time was utilized in heating the saline water in the storage tank before the circulating pump was switched on. It was observed that the production of clean water started within 5 min of this event, as shown in Fig. 27.7. The rate of fresh water production was in direct proportion to the temperature of the hot water at the inlet to the humidifier, as shown in Fig. 27.12. Figure 27.13 presents the water production as a function of time, and shows that the highest fresh water production was achieved when the maximum hot water temperature of 57 °C was reached. The total cumulative water production was found to measure 23.11 kg for the period of operation, 08.00–17.00 h, as illustrated in Fig. 27.13. At the end of this time period, the temperature in the storage tank was 39 °C.

The calculated coefficient of performance (COP) of 2.13 was good and it could have been more if the system had been left to work at temperatures less than 39 °C. However, it is recommended that the system should be operated at temperatures above 40 °C due to advantages in water quality and quantity, as explained in the next section. The total distilled water produced per the area of the solar collector was 11.5 Kg/m^2.day, which is higher than that of conventional stills or stills coupled with solar collectors.

The mathematical model described above was used to calculate the dynamics of production of the distilled water in the system, as shown in Fig. 27.11. It can be seen

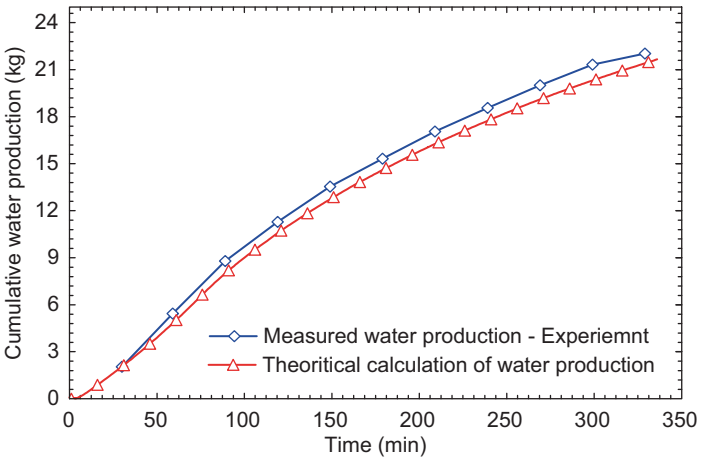

Fig. 27.11 Experimental and theoretical simulation of water production

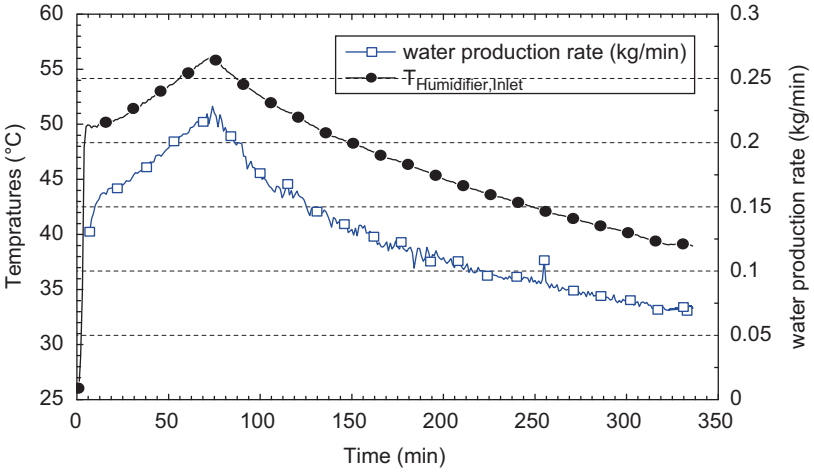

Fig. 27.12 The effect of hot water inlet to the humidifier on the water production rate

that the there is a small difference between the experimental and theoretical values of the amount of the distillate produced. This is probably caused by the fact that the magnitude of heat losses and the sensible heat of the distillate were not taken into account during the calculations. However the predicted overall amount of fresh water produced (21.35 kg) was in a good agreement with the experimental values obtained (23.11 kg). Although the model requires considerable refinement, it can be applied for the preliminary calculations of the system and for the determination of its design dimensions.

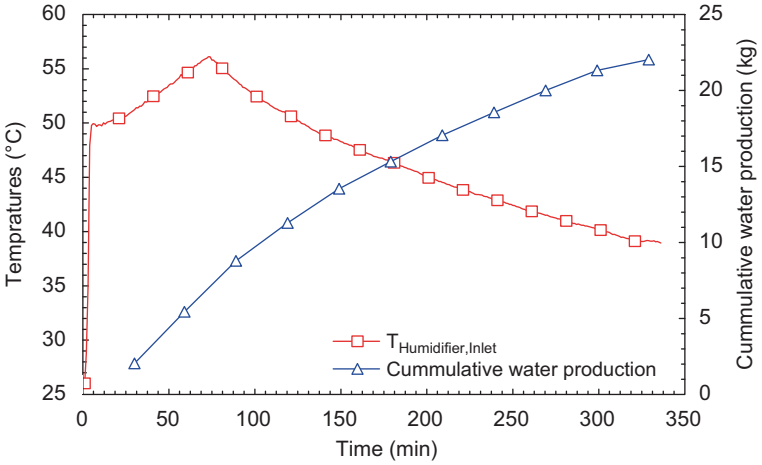

Fig. 27.13 Cumulative water production versus hot water

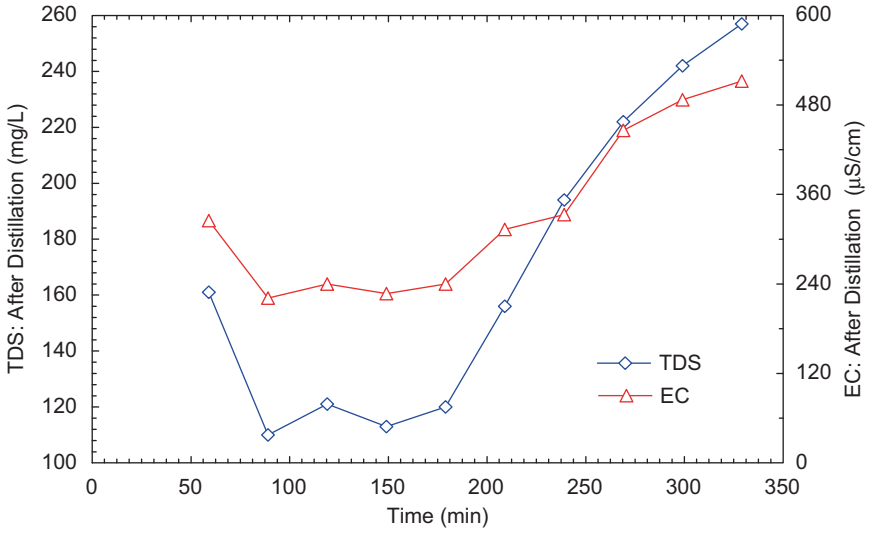

Fig. 27.14 Water quality analysis for TDS and EC for all water product

Water Quality

Generally thermal water desalination processes produce high water quality and this was confirmed by the analysis conducted in the experiment. Water quality parameters for the total dissolved solids (TDS) and electrical conductivity (EC) were measured every 30 min during the water production; as the results are presented in Fig. 27.14. The WHO drinking water guidelines [21], state that water with

TDS of less than 500 mg/L is considered to be acceptable. the TDS of prepared synthetic brackish water was above 2000 mg/L and TDS of produced fresh water was between 110 and 260 mg/L, which is well within the WHO drinking water guidelines. However, it was noticed that the higher the inlet water temperature the lower were the TDS concentrations and the better was the water quality. Hence it is recommended that the system should be operated at temperatures greater than 40 °C in order to achieve better water quality.

Conclusions

The production of fresh water of the tested system was found to be 11.5 kg/m^2.day for typical insolation during springtime in the Middle East. This is higher than that of conventional solar distillation systems such as solar stills coupled with a solar collector. Running in summer with higher solar insolations, the system could produce up to 20 kg/m^2.day. The experimental tests and theoretical simulation proved that, when the system is operated at a higher temperature (70–80 °C), this 20 kg of fresh water would be of high quality. This requires around 1.73 m^2 aperture area of evacuated solar collector. Hence, operating the system at a high temperature eliminates the need for post treatment of the distillate. Furthermore, the proposed mathematical model of the system provided an acceptable accuracy in predicting the amount of water produced. The quality of the fresh water produced by the system is well within the range defined by the World Health Organization guidelines for satisfactory drinking water. The evacuated solar collector provided 69 % efficiency for heating water. It can be concluded that the cost of running this solar powered system is much cheaper than those operated by electricity from the grid and it is estimated that the capital cost payback period is 6 years.

Nomenclature

$\dot{Q}_{hum}$	The supplied energy at the humidifier chamber (KJ)
$\dot{Q}_{aux}$	The auxiliary energy (KJ)
$\dot{Q}_{col}$	Solar collector input energy (KJ)
$\dot{Q}_{heater}$	Electrical heater input energy (KJ)
C_p	Specific heat capacity of water (J/kg.K)
$T_{h,i}$	Temperature of water at inlet humidifier (°C)
$T_{h,o}$	Temperature of water at outlet humidifier (°C)
T_a	Ambient air temperature (°C)
T_m	Mean collector temperature, (°C)
T_{SCi}	Solar collector inlet temperature (°C)
T_{SCo}	Solar collector outlet temperature (°C)
$\dot{m}_{w,h}$	Mass flow rate of hot water sprayed into the humidifier (kg/hr)
$\dot{m}_a$	Mass flow rate of air (kg/hr)

ω	Humidity ratio
Wp	Distillate output (kg)
Acol	Solar collector area (m^2)
$\bar{G}$	Daily average insolation (W/m^2)
hfg	Latent heat of vaporization of water (J/kg)
ηi	Solar collector efficiency

Abbreviations

COP	Coefficient of performance
TDS	Total dissolved solids (mg/L)
EC	Electrical conductivity (μS/cm)
WHO	World health organization
HD	Humidification and dehumidification process
MEH	Multi effect humidification
MED	Multi effect distillation

Acknowledgments The authors would like to gratefully acknowledge that this research was partially supported by the Institute of Sustainable Energy Technology, University of Nottingham and by the IDB's PhD scholarship.

References

1. Buros OK (1999) The ABCs of desalting. USA International Desalination Association, Massachusetts
2. Gleick PH (1998) The worlds water: the biennial report of fresh water resources (1998–1999). Island Press, Washington
3. Al-Kharabsheh S, Goswami D Yogi (2003) Analysis of an innovative water desalination system using low-grade solar heat. Desalination 156(1–3):323–332
4. Abkr A, Ismail F (2005) Theoretical and experimental investigation of a novel multistage evacuated solar still. ASME J Sol Energy Eng 127(3):381–385
5. Solar Distillation, Practical Action Technology Challenging Poverty. http://practicalaction.org/practicalanswers/product_info.php?products_id=165 Accessed 26 Nov 2011
6. Yuan G, Zhang H (2007) Mathematical modeling of a closed circulation solar desalination unit with humidification-dehumidification. Desalination 205(1–3):156–162
7. Mohamed A, El-Minshawy N (2011) Theoretical investigation of solar humidification–dehumidification desalination system using parabolic trough concentrators. Energy Convers Manage 52(10):3112–3119
8. Eames IW, Maidment GG, Lalzad AK (2007) A theoretical and experimental investigation of a small-scale solar-powered barometric desalination system. Appl Therm Eng 27(11–12):1951–1959
9. Mohamed A, El-Minshawy N (2009) Humidification–dehumidification desalination system driven by geothermal energy. Desalination 249(2):602–608
10. Gude VG, Nirmalakhandan N et al (2012) Low temperature desalination using solar collectors augmented by thermal energy storage. Appl Energy 91(1):466–474
11. Hou S, Zhang H (2008) A hybrid desalination process of a multi effect humidification dehumidification and basin type unit. Desalination 220:552–557

12. Farid M, Nawayseh N, Al-Hallaj S, Tamimi, A (1995) Solar desalination with humidification/dehumidification process: studies of heat and mass transfer, Proc., Conference: SOLAR 95, Hobart, Tasmania, 1995, pp. 293–306
13. Al-Hallaj S, Farid MM et al (1998) Solar desalination with a humidification-dehumidification cycle: performance of the unit. Desalination 120(3):273–280
14. Garg HP, Adhikari RS, Kumar R (2003) Experimental design and computer simulation of multi-effect humidification (MEH)-dehumidification solar distillation. Desalination 153(1–3):81–86
15. Müller-Holst H, Engelhardt M et al (1999) Small-scale thermal seawater desalination simulation and optimization of system design. Desalination 122(2–3):255–262
16. Thermomax vacuum solar thermal tubes. http://www.hi-valley.com/solar.htm. Accessed 15 Jan 2012
17. Cooper PI (1969) The absorption of radiation in solar stills. Sol Energy 12(3):333–346
18. MAZDON® HP200, Evacuated Tube Solar Energy Collector, Technical Reference & Installation Manual Domestic Hot Water. http://www.solarthermal.com. Accessed 31 Dec 2011
19. Buzás J, Farkas I et al (1998) Modelling and simulation aspects of a solar hot water system. Math Comput Simul 48(1):33–46
20. Introduction to Engineering Equation Solver software. http://www.fchart.com/ees/ees.shtml. Accessed 27 Jan 2012
21. WHO/EU drinking water standards comparative table, Water treatment & Air Purification and other Supporting Information. http://www.lenntech.com/WHO-EU-water-standards.htm. Accessed 17 Dec 2011

Chapter 28
Optimal Siting of Offshore Wind Farms

Salman Kheirabadi Shahvali, Seyed Hadi Nourbakhsh and Hamed Ganjavi Shakouri

Abstract The goal of this study is finding the best location for constructing an offshore wind farm with respect to investment and operation costs and technical limitations. Wind speed, sea depth and distance between shore and wind farm are three major factors that affect the optimal solution. In other researches in this field, turbine installation technology is considered a fixed parameter. But it shaped 24 % of overnight costs and can bias the project against impossibility. In this study, installation technology is reckoned in three different types related to water depth. At first, a linear relation was assumed between transmission costs, average wind speed and distance from shore. By use of linear regression and value of R-Square, two relations fitness was shown. Then, by considering the sea depth in wind turbine installation technology, investment cost and environmental aspects of wind farm distance from the shore, we designed the basic structure of the model. Finally, we executed the model in Kish island offshore parts and found the right place for constructing a wind farm in order to meet the island electricity demand. Also, it was found that the most important factor in determining the average cost of production is the wind speed and can largely compensate for the additional costs imposed by the selecting an appropriate location.

Keywords Wind turbine · Offshore wind farm · Turbine installation · Persian Gulf

S. K. Shahvali (✉) · S. H. Nourbakhsh
Faculty of Industrial Engineering, University of Tehran, 2nd Campus of technical college, above Jalale ale Ahmad St, Kargar Shomali St, Tehran, Iran
e-mail: Salman.Shahvali@ut.ac.ir

S. H. Nourbakhsh
e-mail: nourbakhsh@ut.ac.ir

H. G. Shakouri
School of Industrial and Systems Engineering, Engineering College University of Tehran, Tehran, Iran
e-mail: hshakouri@ut.ac.ir

I. Dincer et al. (eds.), *Progress in Sustainable Energy Technologies: Generating Renewable Energy,* DOI 10.1007/978-3-319-07896-0_28,

28.1 Introduction

Nowadays the surging demand for electrical energy has became one of the main concerns of countries. Generating electricity from available sources with the lowest cost is the most important step in responding to this demand proliferation.

In recent years due to the increasing costs of various aspects of environmental pollution, clean energy resources has became important for many industrial, commercial and research centers.

The use of wind energy compared to other clean energy sources has the highest annual growth [1]. Wind turbines convert the mechanical energy of this natural phenomenon to electricity.

These Turbines have the lowest use of fossil fuels between other electricity production methods and nearly use no water in production stages. The contamination rate of this technology is nearly zero and its availability in many parts of the world is another advantage of it. Nowadays, China, United States and European countries have largest capacity of installed wind turbines, and for example Denmark and Portugal supply 21 and 18% of their electricity requirement from wind [2]. However, according to the predictions, this is only a small part of the world's installed capacity of wind turbines.

In recent years, there has been a special attention to offshore turbines. The main advantage of this kind of turbines are ability of producing at least several MW, not disturbing the sound of blades, higher efficiency than other turbines and the higher speed of wind at sea than on land. On the other hand, multi-megawatt turbines have less average cost and can reduce costs up to 15%. But in these turbines the problem is noise pollution and breaking the sound barrier [3]. Of course this problem is not important in offshore areas.

28.2 Background

For the first time professor Heronemus, University of Michigan discussed turbines with large size in water and suspended [4]. But since the mid-nineties and after the attention of commercial companies, this plan was not feasible. After that this plan became important for many scientific and commercial centers and then optimization issues were discussed. For example Kuhn started to optimize the turbines according to economic issues and their foundations [5].

In the other research they have studied the ways related to wind energy in Netherland, researchers sought to design a large-scale turbine with high reliability and reducing the costs and for this purpose they used recorded information between 1997 and 2003 and a published a comprehensive report. The notable point in this research is studying the effect of burnout turbines [6]. So an article has studied offshore turbines depreciation specially. This research examines ten European countries and studies the reduction of turbines electricity generation during lifespan [7].

Finding a perfect place for offshore wind farm building is one of the favorite problems investigated with optimization techniques. According to the initial investment, turbine life, maintenance costs and transmission costs, by implementing a mathematical programming, levelized cost of electricity is calculated, compare it in different points and finally the optimal point is found.

Unlike many researches have been done for onshore turbines siting, we can only find few researches about offshore location optimizing. We can mention a joint research in university of Hawaii and Pittsburg. In this study an innovative algorithm is used to find the optimal point and its objective function is defined to minimum the costs [8].

In other article, Genetic Algorithm is used to find the optimal point between existing locations around Jeju Island in South Korea due to the high number of these points. In this study, considering the upper limit for depth and distance to the beach, they were seeking for a place with the highest wind speed between candidate places [9].

In all researches, tower installation technology has been fixed, and in all cases the installation method is the same. But since a large share of the cost is related to turbine installation, about 24 % of total costs [10] and because it can change according to water depth, we consider its effect in our optimization model.

28.3 Modeling

Objective Function In optimization projects like this, the important part is defining the objective function. The purpose of this article is to minimize average cost of electricity generation. Therefore according to Eq. (28.1), it is necessary to estimate the total cost and levelized cost of electricity generation during the project. The cost can be divided into four parts: turbines, installation, transmission and maintenance; just the last case is variable cost. To obtain total electricity generation we should multiply the average power of used turbines in number of hours in project life, number of turbines and their capacity.

$$CPU = \frac{PVC}{E_{out}} \tag{28.1}$$

$$\min z = \frac{C^{turbine} + C_h^{install} + C_d^{transit}}{8760 * \bar{P} * N_{farm} * Ca_{turbine}} \tag{28.2}$$

Turbine Cost In objective function Eq. (28.2), the cost of turbine $C^{turbine}$ is the purchase costs of turbines determined according to the type, capacity and number of turbines. The price of turbines can be extracted from companies' website or can be cited to similar studies. This cost is related to turbine equipment and converting mechanical energy to electricity and is unrelated to the location and installation method of turbines, so turbine costs are the same in offshore and onshore farms.

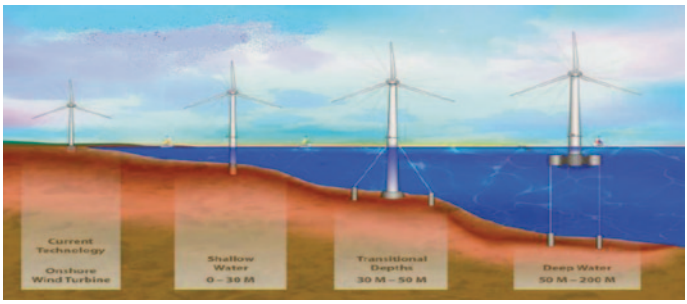

Fig. 28.1 Turbine installation technology in different depths

Installation Cost In previous projects, it is assumed that sea depth is divided to 3 parts. As seen in Fig. 28.1 these parts are: Shallow (depths with less than 30 m height from the seabed), Transitional depths (for ship traffic with depths between 30 and 50 m) and Deep (places with more than 50 m depth) [11].

According to the sea depth, turbines installation technology is variable and can influence on initial costs. About deep sea area, the several years of experiences in technologies being used in oil and gas wells have been utilized in the most of the researches to determine the turbine installation technology and total costs. For example we can name a research done in Netherland with tri-floater [12] or another research done in National Renewable Energy Library (NREL that was named (TLP) and was made from a column and floating tank [13]. Both of these studies have been performed for turbines with a capacity of 5 MW. Another point is that for places above 200 m depth, there is no possible way to install turbines with existing technology. So the cost depends upon the sea depth (h) and is called $C_h^{install}$ in objective function and is calculated according to the number of turbines and their capacity.

$$\text{If } 0 < h < C1 \text{ then } Y1 = 1 \tag{28.3}$$

$$\text{If } C1 < h < C2 \text{ then } Y2 = 1 \tag{28.4}$$

$$\text{If } C2 < h < C3 \text{ then } Y3 = 1 \tag{28.5}$$

$$\sum Yi = 1;\ i = 1, 2, 3 \tag{28.6}$$

In Eq. (28.3) to Eq. (28.6), h represents the depth and Yi are dummy variable (Zero or One). The first related to shallow waters and its upper limit is C_1 that is determined according to the technology. C_2 is the upper limit of current ability to install turbines in transitional depth and C_3 is related to deep waters. Eq. (28.6) is added to ensure that in each place only one installation method is used.

Transmission Cost The main problem in transmission cost is distance to the beach. In this case because of environmental issues, there is no possibility to install

turbines to a distance of 5 nautical miles (about 9 km) so these restrictions should be imposed [13].

Transmission cost, $C_d^{transit}$ includes the cost of power cable and voltage converter stations and it is a function of distance to destination. Of course distance has a great effect on transmission costs but since the distance is directly proportional to the depth, this cost is various from point to point. Due to the limitations listed about distance to the beach, the constraints are given below.

$$d < d_U \tag{28.7}$$

$$d_L < d \tag{28.8}$$

In Eq. (28.7) and Eq. (28.8) the variable "d" is the distance to the beach and "d_L" is the lower limit determined due to environmental issues and "d_U" as the upper limit is determined according to technical issues.

Operating Cost This case is about variable costs and is calculated according to the amount of electricity generation and therefore it has been brought out of the denominator in Eq. (28.1). $C_h^{O\&M}$ is called maintenance cost and it is related to repair costs due to failures and periodic visits. This cost is related to distance and technology used in the installation of towers but since both of them are related to sea depth, this can be defined base on it.

Turbine Power The most important factor in determining the turbine power is speed and intensity of wind in the region. The produced power is related with cubic of speed.

$$p = \frac{E}{\Delta t} = \frac{1}{2} pAV^3 \tag{28.9}$$

In Eq. (28.9), "P" is the produce power that is calculated according to watt. Moreover, "V" is wind speed based on meter/second and "A" is the wind swept area and "$\boldsymbol{\rho}$" is the passing air density [14].

Wind speed changes from height to height, affect capacity factor and determines generated electricity in the year. The given wind speed recorded at weather stations are also usually in different heights and due to the turbine height and Hellman exponent, we can calculate the wind speed (Eq. 28.10).

$$V_{he} = V_{ref} * \left(he / he_{ref}\right)^a \tag{28.10}$$

In this case, "V" is wind speed, "he" is height and "ref" is the profile of source station and "a" is Hellman exponent that is define according to the weather condition and in stable condition is 0.143 [15]. So with the average speed at the desired height for all points we can calculate the average electricity generation per year. As

Eq. (28.9) shows the produced energy is related to the cubic of wind speed and has a great effect on the average amount of electricity cost. To calculate the produced power we use Eq. (28.11).

$$P = K * e * DRA * DRT * A * V^3 \tag{28.11}$$

In this case "K", "e", DRA and DRT respectively refer to coefficient of units, the efficiency of wind turbines and coefficient of air density that is defined due to the height and the average temperature in the region. "A" is the cross-section that rotors sweep the wind (swept area). V^3 is average of cube of wind speed [16].

Calculating the Average Power In order to calculate the average power, we need to find out the efficiency of the turbine that is determined in two ways: First, defines directly in turbine's specifications by the manufacturer. Second, defines according to the speed, nominal power and cross-section and replace them in Eq. (28.9). Then according to the turbine's specification like efficiency and cross-section, characteristics of the region like average wind speed, temperature and height, and using the Table 28.1 and replace them in Eq. (28.11), the average power is calculated.

28.4 Running the Model and Results

The installed capacity of wind power in Iran at the end of 2010 is 92 MW that preliminary studies have shown an estimated practical wind power potential of at least 6,500 MW [17]. Also there is no multi-megawatt or offshore wind turbine in Iran. Because Kish is one of the largest islands in south of Iran and is a demanding area of electricity, Also according to this point that it is a commercial offshore island, it is a good case for this kind of electricity. So in this paper the required parameters for Kish Island is estimated and the model has been implemented.

To assess the parameters, we need to acquire the required amount of capital, maintenance and other costs. Price, life time and other turbines costs are obtainable from different companies, which the average of several companies should be calculated or we can use related articles.

Installation and Maintenance Costs Installation and maintenance costs for a normal farm, according to the sea depth are mentioned in appendix (Tables 28.1 and 28.2). It is noteworthy that in all estimated parameters, it is supposed costs change linear and other intervals are obtained with interpolation.

Transmission Cost This cost relates to sea depth and farm location distance to the shore. But as mentioned before, since distance has the main effect and these two factors increase in one direction, in this study transmission cost estimated base on distance. The table of costs is extracted according to an article studied the optimum transmission voltage [18]. This research has specified that for distances over 90 km,

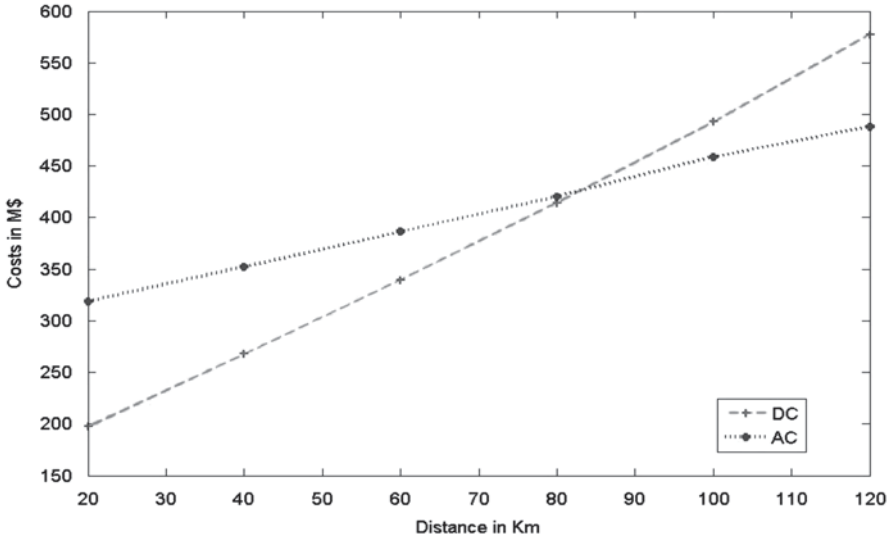

Fig. 28.2 Plot transmission cost against the distance

DC power is suitable. So the AC transmission method is cheaper for our studied interval. Also the transmission voltage has supposed 150 kV.

As shown in Table 28.3, with increasing distance, the costs increase. These numbers are related to lifespan of 20 years and converting the costs to present time and base on million dollars. In order to use this model, we should be able to get the cost as a function of distance. First we plotted these two variables against each other in Fig. 28.2. This plot shows a linear relationship between them.

Then we used linear regression model that was fitted well. Using SPSS software, we determined cost function base on the distance and the results are given in appendix Table 28.4 to Table 28.6. Using these tables, the model can be estimated as Eq. (28.12).

$$C_d^{\text{transit}} = 116.624 + 3.784 * d \tag{28.12}$$

Wind Speed According to wind data at synoptic stations located in Persian Gulf, whatever we get away from the beach to the sea, the average wind speed will increase [19]. So productivity level and annual electricity generation will increase but the costs will increase with increasing distance and depth. The purpose of this section is to find a balance for these 3 variables in order to optimize the interactions with the aim of minimizing the average cost. In addition, these projects should be implemented on a large scale considering the number and size of turbines because large turbines have higher efficiency. So the transmission costs and preparation are optimized [13].

In this study it is supposed that we are looking for a farm with 100 turbines of 5 MW, the total capacity of 500 MW. According to the above and after replacing the nominal speed of a turbine with the capacity of 5 MW (12 m/s) and other characteristics of a turbine in Eq. (28.11), the efficiency was obtained 0.367. Then replacing other parameters, the result for the selected turbines was 2891.09. If we multiply this number in the average of cube of wind speed, the result will be productive capacity of each turbine base on watt.

In this section, stretching the coast to Kish Island and Kish to Sirri Island is considered. Kish Island is located 18 km away to the nearest beach of Iran at 23.30 latitude and 53.59 longitudes and Sirri Island (25.53 latitude and 54.29 longitudes) is located 87 km away from Kish.

According to the latest report of the meteorological organization the following data has been recorded: In Sirri Island the average wind speed is 8.8 knots and station height of 4.4 m. In Kish Island the average wind speed is 6.2 knots and station height of 30 m and in nearest coasted station to Kish (Bandar Lengeh the average wind speed in the height of 22.7 is 5.3 knots [19].

We considered 3 points and a linear change of wind speed along the path then fitted a regression line that results are given in appendix Table 28.7 to 28.9. So using Eq. (28.13), we can calculate the wind speed of all points at 80 m height base on the distance.

$$V_d = 3.166 + 0.035 * d \tag{28.13}$$

Objective Function The objective function of this case can be represented as Eq. (28.14) that is designed to minimize the cost of per unit of energy in constructing a wind farm with capacity of 500 MW and transmission to Kish. To obtain this cost, we suppose that the lifespan of this project is 20 years and then calculate the costs base on present time. Denominator is total electricity generation during 19 years of farm (suppose constructing the farm takes 1 year).

$$\frac{C^{turbine} + C_h^{install} + C_{d-Kish}^{transit}}{Hr * 2.89109 * N * N_{farm} * V_d^3} + C_h^{O\&M} \tag{28.14}$$

In Eq. (28.14), $C^{turbine}$ and $C_h^{install}$ respectively refer to purchase costs and installation costs that is defined due to the depth and the type of technology. $C^{transit}_{d\text{-}Kish}$ is the cost of electricity transmission to the source (Kish Island). In the denominator, N, H_r, N_{farm} and V^3_d respectively refer to farm lifespan, total hours of a year, number of turbines and the cube of average of wind speed (base n distance to the shore. About the depth of the region, according to the map of Persian Gulf, because the average depth form Kish Island to the shore is 20 m, we supposed it as a shallow region.

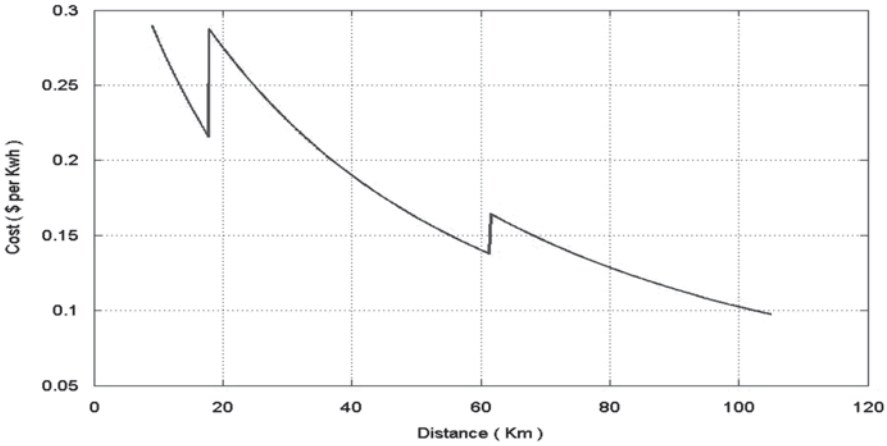

Fig. 28.3 Average cost per kWh in different distances

In this project, the region from Kish Island to 43.5 km toward Sirri Island is supposed as transitional depth and the rest of the path to Sirri that has the depth of 140 m is supposed as deep waters. This division is done assuming linearity of water depth changes.

$C_h^{O\&M}$ is maintenance costs per kWh that as mentioned before is related to sea depth and classified in three classes calculating required parameters and replacing them in the equation, the objective function will be obtained.

Results Solving the programmed model with computer, the last studied point(the coast of Sirri Island) will be the optimum point with the production cost of about 0.097 $ per kWh. According to the pollution costs of other power generation methods in Iran, this technology can be one of the options to replace fossil power plants. Figure 28.3 shows the average cost per unit of energy (CPU). As seen in this figure, with the change of technology, costs will increase suddenly and with increasing the wind speed, the costs will be offset and will be less than the minimum of technology cost.

According to Fig. 28.3, the important factor in determining the average cost, is the wind speed, because although alternative technology will increase the initial costs, transmission and maintenance costs, but according to the wind speed and related production, these increases will be compensated and the overall costs will decrease.

In Fig. 28.4, the change in total cost and total energy is displayed. According to this, the costs change linear but the electricity generation change conversely and increase cubically. So shortly after the change in technology, the imposed costs will compensation.

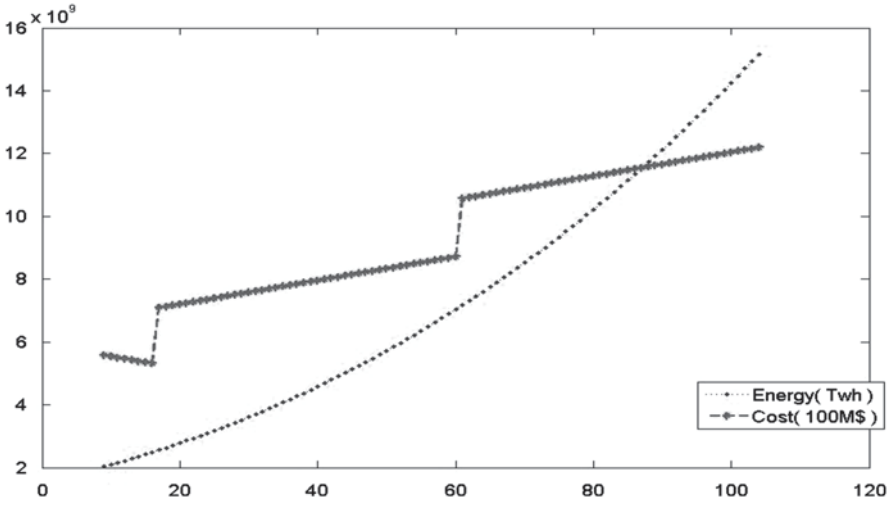

Fig. 28.4 Total energy production and total costs

The average cost per kWh for all the points is 0.17 $. However, wind turbines are mentioned as a new progressing technology and it is expected that production costs will decrease greatly in future years [11].

Conclusions

In this article, the best place for offshore turbines installation in desired region according to limitations and with the aim of reducing the costs was studied. The variables of wind speed, distance to the desired point and water depth were used for modeling. It was found that transmission cost changes as linearly. Then, the technological and environmental constraints were introduced. After optimal balance of costs and according to water depth and distance and electricity generation that depend upon regional wind speed, an objective function was defined.

In the last section, estimating the desired parameters for Kish Island, the model was run. The cost per kWh, including other costs and investment value was calculated, it was 0.097 $. According to the pollution costs and comparing with other methods, these kinds of turbines should be considered as an available and competitive method. On the other hand and according and according to the results of the present article, the most important factor in determining the average cost is the wind speed.

Appendix

Table 28.1 Turbine costs. (adapted from [13])

Turbine size	5 MW
Number of turbine	100
Farm capacity	500 MW
Turbines cost ($)	308,244,000
Rotor diameter (m)	128
Hub height (m)	80
Nominal speed (m/s)	12

Table 28.2 Operation and Maintenance and Installation costs. (adapted from [13, 20, 21])

	Shallow water	Transitional water	Deep water
Turbine capacity	5 MW	5 MW	5 MW
Sea depth (m)	<30	Between 30 and 80	>80
Installation cost ($)	992,000	2,880,000	4,690,000
Foundation type	Mono-pile	Tri-floater	Tension-leg
Operation and maintenance cost (kWh)	0.015	0.016	0.018

Table 28.3 Sensitivity analysis of Transit cost. (adapted from [18])

Distance to shore (for 500 MW) (km)	AC (M$)	DC (M$)
20	197.29	318.68
40	267.92	352.63
60	339.69	386.54
80	414.13	420.45
100	492.74	458.70
120	577.28	488.32

Table 28.4 Mode summery

R	R Square	Adjusted R Square	Std. Error of Estimate
0.999a	0.999	0.999	5.38946

Table 28.5 ANOVA

Model	Sum of squares	df	Mean square	F	Sig
Regression	100,234.605	1	100,234.605	3450.858	0.000
Residual	116.185	4	29.046		
Total	100,350.790	5			

Table 28.6 Regression coefficient

Model	B	Std. Error	Standard Coefficients	t	Sig.
(Constant)	116.624	5.017		23.244	0.000
Distance	3.784	0.64	0.999	58.744	0.000

Table 28.7 Mode summery

R	R Square	Adjusted R Square	Std. Error of Estimate
0.99	0.99	0.993	0.16446

Table 28.8 Regression coefficient

Model	Sum of squares	df	Mean square	F	Sig.
Regression	7.714	1	7.714	265.226	0.038
Residual	0.27	1	0.027		
Total	7.741	2			

Nomenclature

A	Wind swept (m^2)
d	Distance (km)
h	Depth (m)
he	Height (m)
P	Produced power (watt)
V	Wind speed (m/s)

Greek Symbols

ρ	Density (kg/m^3)

Subscript and Superscripts

a	Hellman exponent
C	Cost
DRA	Coefficient of air density for height
DRT	Coefficient of air density for temperature
E	Efficiency
Hr	Total hours of a year
K	Coefficient of units
MW	Megawatt
N	Life span

Acronyms

AC	Alternating current
CPU	Cost per unit (of energy)
DC	Direct current
NREL	National renewable energy library
PVC	Presented value cost
TLP	Tension-leg platform

References

1. World Wind Energy Association (2011). http://www.wwindea.org/home. Accessed 12 March 2011
2. World Wind Energy Report 2010 (2011) World Wind Energy Association http://www.windea.org/home/images/stories/pdfs/worldwinenergyreport2010s.pdf. Accessed 30 April 2011
3. Malcolm D, Hansen A (2002) WindPACT Turbine Rotor Design Study. National Renewable Energy Laboratory, Colorado
4. Heronemus W (1972) Pollution-free energy farm offshore winds. 8th Annual Conference and Exposition Marine Technology Society, Washington DC
5. Kuhn M (1998) Structural and economic optimization of bottom-mounted offshore wind energy converters. Delft University of Technology: Institute for Wind Energy, The Netherlands
6. Hendriks H, Zaaijer M (2004) DOWEC: executive summary of public research activities. ECN, Petten
7. Barthelmie R (2004) ENDOW (efficient development of offshore wind farms): modeling wake and boundary layer interactions article. Wind Energy 7:225–45
8. Ozturk U, Norman B (2004) Heuristic methods for wind energy conversion system positioning. Electr Power Sys Res 70(3):179–85
9. Lee K-H, Jun S-O, Pak K-H, Lee D-H, Lee K-W, Park J-P (2010) Numerical optimization of site selection for offshore wind turbine installation using genetic algorithm. Current Applied Physics 10:302–306
10. Elkinton C, Manwell J, McGowan G (2006) Offshore Wind Farm Layout Optimization (OWFLO) project: an introduction. American Institute of Aeronautics and Astronautics, USA
11. Musical W, Butterfield S (2004) Future for offshore wind energy in the united states. Energy Oceans Conference, Palm beach, Florida
12. Bulder B, Henderson A (2002) Studie naar haalbaarheid van en randvoorwaarden voor drijvende offshore wind turbines. Stichting Energieonderzoek centrum. TNO-Bouw, Nederland
13. Musical W, Butterfield S, Boone A (2004) Feasibility of floating platform systems for wind turbines. 23th ASME Wind Energy Symposium Conference, Reno, Nevada
14. Bagiorgas H, Assimakopoulos M, Theoharopoulos D, Matthopoulos D, Mihalakakou G (2007) Electricity generation using wind energy conversion systems in the area of Western Greece. Energy Convers Manage 48(5):1640–1655
15. Zaman H, Shakouri GH (2010) A simple nonlinear mathematical model for wind turbine power maximization with cost constraints. Energy, Power and Control (EPC-IQ) 1st International Conference on, Basrah: IEEE
16. Saghafi M (2003) Wind energy and its usage in agriculture. University of Tehran, Tehran
17. Global Wind Energy Council (2011) http://www.gwec.net/index.php?id=173. Accessed 24 March 2011
18. Kling W, Hendriks R, Vailati R (2007) HVDC connection of offshore wind farms to the transmission system. Trans Energy Convers 22(1):37–43
19. Iran Meteorological Organization Site (2011) http://www.irimo.ir/english/statistics/mapindex.asp. Accessed 21 June 2011
20. Rademakers L (2003) Assessment and optimization of operation and maintenance of offshore wind turbines. European Wind Energy Conference, Madrid, Spain
21. Jaqcuemin J, Traylor H, Muir N, Cordle A, Baldoc N, Devaney L (2009) Effective turbulence calculations using IEC 61400-1 edition 3: researching consensus through dialogue and action. http://www.gl-garradhassan.com/. Accessed 22 June 2011

Chapter 29
An Investigation into a Small Wind Turbine Blade Design

Sayem Zafar, Mohamed Gadalla and Seyed M. Hashemi

Abstract A small wind turbine blade was designed to be aerodynamically efficient, economical and easy to be manufactured. Aerodynamic analysis was conducted using commercially available software. The aerodynamic analysis suggested laminar flow airfoils to be the most efficient airfoils for such use. Blade geometry was determined after calculating baseline geometric values to have low weight and drag while yielding maximum torque. The blade span was constrained such that the complete wind turbine can be roof-top mountable. The blade was designed without any taper or twist to comply with the low cost and ease of manufacturing requirements. For low cost and favorable strength to weight ratio, fiberglass-epoxy was used as the blade material. Computer simulated structural test results suggested that skin thickness of 1 mm of fiberglass-epoxy can sustain the loads on the blade. The wind turbine blade produces 3.1 N lift with 6.3 N.m torque at 4 m/s wind speed. Since it uses a relatively inexpensive material, fiberglass-epoxy, the cost of the blade is low. Fiberglass-epoxy is also easy to work with hence it contributes towards manufacturing ease. Overall, the research was successful in designing a wind turbine blade that is easy to be manufactured, economical and has high torque.

Keywords Wind Turbine · Airfoil · Small wind turbine blade · Structural analysis

M. Gadalla (✉) · S. Zafar
Department of Mechanical Engineering, American University of Sharjah, Sharjah, United Arab Emirates
e-mail: mgadalla@aus.edu

S. Zafar
e-mail: szafar@aus.edu

S. M. Hashemi
Department of Aerospace Engineering, Ryerson University, 350 Victoria Street, M5B 2K3 Toronto, ON, Canada
e-mail: smhashem@ryerson.ca

I. Dincer et al. (eds.), *Progress in Sustainable Energy Technologies: Generating Renewable Energy,* DOI 10.1007/978-3-319-07896-0_29,

29.1 Introduction

Global reliance on energy has increased many folds over the last few decades and it continues to do so, at an alarming rate. In order to meet the growing energy demand, natural resources are being depleted faster than they can be replenished. Destruction of natural resources can be associated not only to global increase in energy demand but also to our heavy reliance on non-renewable sources of energy. To ensure the stability of global climate and natural resources, it is required to move towards renewable energy sources that have minimal environmental side effects.

Due to the advancements made in aerospace sciences during the last century, a feasible way to generate renewable energy is through wind. Wind energy generation is environmentally friendly as it has a minimal environmental impact with no hazardous emission. Although there are many different ways to generate electricity through wind but none is more efficient than capturing wind energy using horizontal-axis wind turbine. A horizontal axis wind turbine is a wind turbine in which the axis of the rotor's rotation is parallel to the wind stream and the ground [1]. The purpose of the rotor is to convert the linear motion of the wind into rotational energy that can be used to drive a generator. Rotors are comprised of a finite number of blades. For modern wind turbines, the blades are aerodynamically shaped to produce highest lift possible, which converts to higher torque values resulting in increased power generation. In other words, efficient blade design can significantly increase the power output of a wind turbine. Based on the size and possible power output, the turbine blade under design is classified as "small wind turbine" blade [2].

Aerodynamics plays an important role in determining the efficiency of a wind-turbine blade as this is where the kinetic energy in the wind, transforms into mechanical energy. An efficient wind turbine blade is one that produces high lift with relatively low drag for a desired range of Reynolds's number. NACA 63-series airfoil has been used for low Reynolds number, laminar flow cases [3]. Natural Laminar Flow (NLF) airfoil series were developed by NASA to have improved aerodynamic efficiency aiming to increase the lift-to-drag ratio of the wing [4,5]. Laminar-flow airfoils are designed so that the majority of the flow experienced by the airfoil is laminar as the separation point is reached further aft on airfoil, ultimately reducing negative effects caused by flow separation [6]. Also, due to their large regions of laminar flow they produce less drag than other airfoils at low speed. The natural-laminar-flow (NLF) airfoils are considered a great way to reduce drag [7]. Laminar flow airfoil permits start up at lower wind speeds, increasing the startup torque and thus improving the overall performance of the turbine. For small wind turbine blade, the optimal pitch angle appears to be between 15 to 20° [8].

Amongst the airfoils suitable for small wind turbine applications, NACA 6-series were deemed most feasible because of designed low drag values [9]. NACA 6-series airfoils also had an added advantage of manufacturing ease since thickness does not play a significant role on the angle of zero lift [10]. NACA 63 airfoils are

used in wind turbine blades because of their good lift characteristics and availability of two-dimensional aerodynamic characteristics [11]. NACA 63-series airfoil yields effective HWAT (Horizontal Axis Wind Turbine) blade. When comparing general aviation airfoils, NACA 63-425 appears to be the most efficient airfoil for wind turbine use [12]. The loads experienced by a wind turbine blade, namely aerodynamic, gravitational and inertial forces are to be studied when designing the wind turbine blade [13]. Due to the experience gained from aircraft engineering, new light weight composites are available that can be used for the wind turbine blade. For small wind turbine blade, fiber composites appear promising as they are easy to manufacture and have relatively low cost [14]. Structural data for fiber glass reinforced with epoxy appears to be promising material for the wind turbine blade. Fiber glass reinforced with epoxy gives high strength with low weight while it is inexpensive compared to carbon composite [3]. The governing equations for lift and drag yield the total torque generated by the wind turbine blade [15].

This paper presents the design and structural analysis of a small wind turbine blade. The blade is to produce highest power possible with the ability to start producing torque at relatively low wind speeds. It was also desired that the wind turbine blade should not have complex geometry so that it would be easy to manufacture without the help of complex machinery and have low manufacturing cost. Also included is the structural analysis of the wind turbine blade and how it can be conducted using *ANSYS Workbench*.

29.2 Blade Design

The aim of this paper was to design an efficient wind turbine blade to be able to produce highest power possible with the ability to start producing torque at relatively low wind speeds. Wind turbine blade is of importance since it is where the wind interacts with the wind turbine. The blade converts the kinetic energy of the wind into rotational energy subsequently into electricity. It was also desired that the wind turbine blade should not have complex geometry so that it would be easy to manufacture without the help of complex machinery. Design considerations were studied and analysis was performed to achieve the optimal design for the blade.

Airfoil Selection

The airfoil is critical to the blade design as it affects the aerodynamics of the blade. Aerodynamics plays the most important role in the design of a wind turbine blade as it determines the total lift and drag hence the overall power production capability of the blade. The analysis was conducted using yearly average wind speeds, of 4 m/s, for city of Toronto [16]. Airfoil selection was mainly determined by the need to achieve optimal aerodynamic efficiency for a wide range of blade's operating

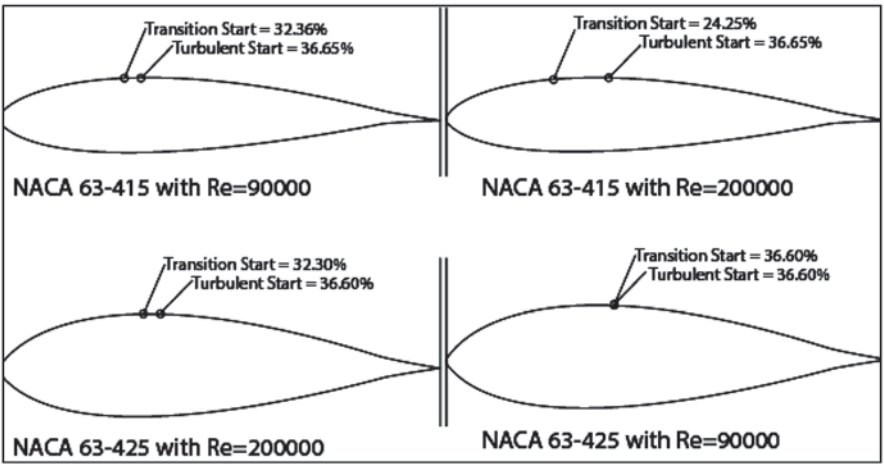

Fig. 29.1 Flow separation point comparison for different airfoils with respect to increment in Reynolds's number

conditions. In order to have a blade that rotates in the presence of the slowest wind speed, it was desired to have a high lift to drag ratio and comparability high C_{Lmax}. Pitching moment effect was considered to be negligible because of small geometry of the blade and low operating Reynolds number.

One of the safety consideration needs to be incorporated in the design is the blade's ability to not exceed the designed maximum operating rotational speed. In order to achieve that requirement, blade has to stall at extremely high wind speeds. High speed stall can be achieved by having a relatively thin airfoil for the blade. For low thickness airfoils, the flow separation point starts traveling towards the leading edge as the wind speed increases, stalling the blade hence reducing the total lift. Figure 29.1 shows the *DesignFOIL* software data depicting the flow separation with respect to Reynolds's number for two different thicknesses of the airfoil. For low thickness airfoil, flow separation point starts moving closer to the leading edge, than compared to the thicker airfoil, as the Reynolds's number increases. The airfoil had to be thin enough to stall at high wind speeds yet thick enough not to cause a sudden stall.

Considering the requirements for the wind turbine blade and reviewing the literature, it was concluded that NACA 63 series natural laminar flow airfoils are the ones best suited for the role. With the above described considerations, handful of airfoil was selected to conduct further analysis. Aerodynamic analysis was conducted, using *JavaFOIL*, on NACA 63 series airfoils to single out the most suitable airfoil.

The wind turbine airfoil was required to have a high C_L over wide range of wind speeds and angles. This wide range of high lift bucket is required to yield high lift with the changes in wind directions and speed. To find out the best available airfoil, a number of selected laminar flow airfoils were tested using *JavaFOIL* to determine the range of high lift bucket for a variety of angle of attacks. The analysis was done

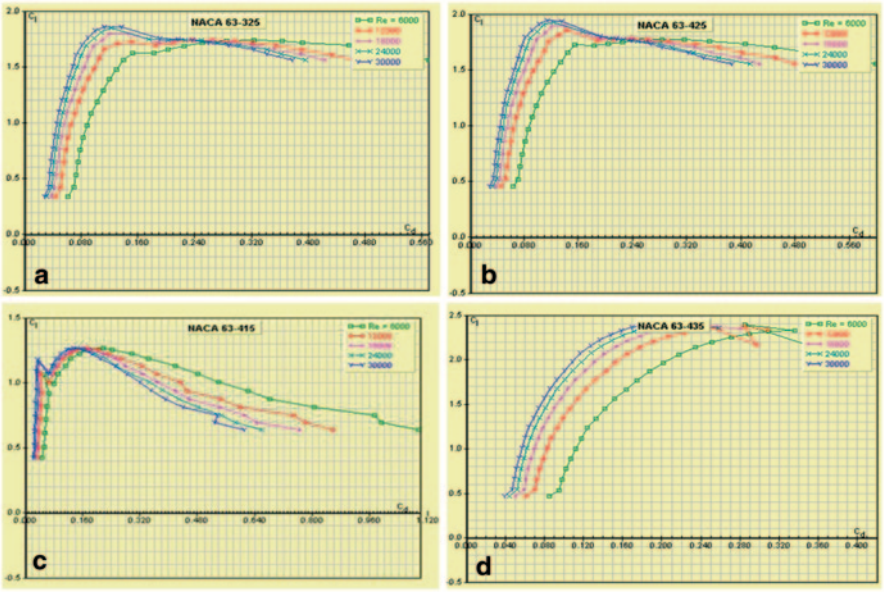

Fig. 29.2 L/D comparison for four different NACA 63 series airfoils

under Reynolds's number conditions calculated for the wind speeds the blade would experience. The wind speeds used are from 2 m/s to 9 m/s.

Figure 29.2, above, describes the lift to drag ratio of NACA 63-415, NACA 63-325, NACA 63-425 and NACA 63-435 under different Reynold's number conditions. It can be seen from the figures that NACA 63-425 seems to have a high and consistant L/D ratio compared to the others. NACA 63-435 airfoil has low L/D for initial angles and it changes significantly with the change in angle of attack. Because of the high wind speed stall consideration, an airfoil with lower thickness was preferred. NACA 63-415 has low L/D ratio and it starts loosing lift quickly as the angle of attack changes. NACA 63-325 has a relatively good high lift bucket with stable performance but the lift is lower than the ones found for NACA 63-425 airfoil. The *JavaFOIL* analysis concluded and agreed favorably with the literature to use NACA 63-425 as the most appropriate general aviation airfoil for small wind turbine blade.

An optimal installed angle of attack was required to be calculated for the wind turbine blade. It is the angle of attack at which the airfoil produces the highest L/D ratio. The find that out, L/D ratio for NACA 63-425 were plotted against angle of attack for different Reynolds's number. Figure 29.3 shows the L/D variation with respect to angle of attack. It can be seen from the Fig. 29.3 that at 7°, the airfoil yields the highest L/D ratio. It is to be noted that the pitch angle of the blade mounted on the turbine would be different than the installed angle of attack. Optimal pitch angle calculation is out of the scope of this paper hence not discussed.

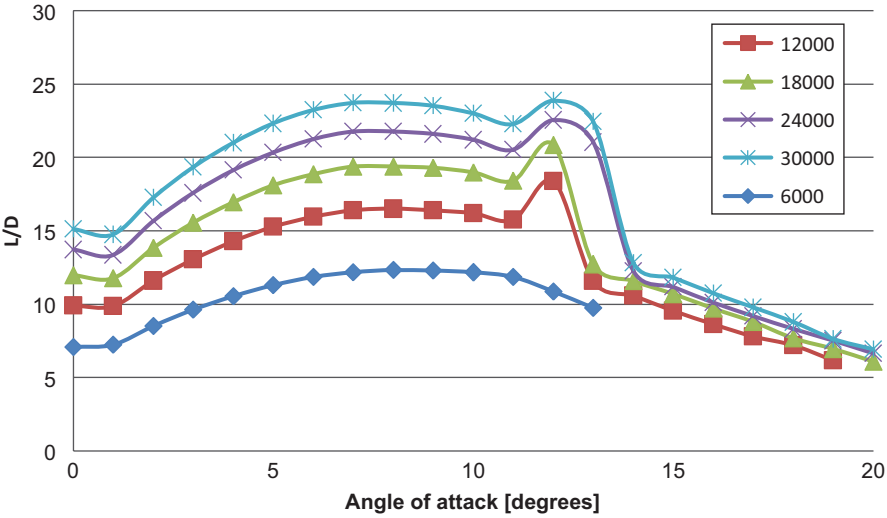

Fig. 29.3 Change in NACA 63-425 airfoil's L/D ratio with respect to angle of attack

Blade Geometry

The wind turbine blade is designed to be used for small turbines which are likely to be used as personal turbines at homes or farms. The blade span, *b*, was chosen so that the total wind turbine height would come around 6 m. Such height would make it convenient for wind turbine to be installed for urban or rural use. Since aspect ratio, AR, relates the blade span with chord, it was the first parameter determined. Aspect ratio is a ratio between the blade span squared to the planform area of the blade. An aerodynamic trend was found leaning towards high aspect ratio because of being an efficient way to reduce drag. Values found in the literature suggested a range of 8 to 10 for sail plane wings [3]. The equation that relates aspect ratio to other geometric parameters is as follows;

$$\mathrm{AR} = \frac{b^2}{S} \tag{29.1}$$

It was desirable to have high lift values at the tip since most of the torque, in a turbine blade, is produced there. Unlike the wings or large wind turbine blades, a small wind turbine blade can have the same chord length at the tip since it would be structurally possible to sustain high bending and centrifugal force values. For small wind turbine blades under low operating speeds, the power output difference is small compared to the twisted blade [17]. A rectangular, non-twisted blade was also desirable because such geometry would reduce the manufacturing cost and eliminate the manufacturing complexity.

Once the aspect ratio AR and span, b, values are known, planform area, *S*, was determined using Eq. 29.1. Planform area helped determined the chord 'c' using Eq. 29.2

$$S = c.b \tag{29.2}$$

Material

The material required for the turbine blade had to be strong enough to sustain the bending yet light enough to have low start-up speed. To achieve that, it was desired to use inexpensive and light weight material with high strength. Another important factor for the blade material was its stiffness. The effect of the stiffness on the material determines the magnitude of deflection under the load or its resistance to elastic deflection. It is important to have low stiffness since a highly deflected blade would require a greater clearance from the wind-turbine stand and would result in lower torque readings because of changed angles. Composites tend to show the desired characteristics of low density with high strength and stiffness [18]. With the described requirements, composites were studied because of their high strength to weight ratios and transparency to electromagnetic waves. Metals were deemed inefficient for the design as they have a very high potential to interfere with radio and television reception [2]. Material's strength, weight, cost and availability were simultaneously analyzed to get an inexpensive, high performance blade. Timber blades have been installed and tested on a small wind turbine [19]. The use of timber blades, in a small wind turbine, is demonstrated and tested for durability and strength. The low cost timber blades helped in reducing the cost yet yielded the desired strength and aerodynamic strength to be used as a wind turbine blade.

29.3 Results and Discussion

After careful consideration and conducting airfoil analysis using *JavaFOIL* and *DesignFOIL*, it was decided to use NACA 63-425 airfoil for the blade. It has a wide range of angle of attack at which it can yield high lift. It also has favorable lift coefficient for wide range of Reynolds's number which would result in steady turbine operations. Table 29.1 shows the calculated values of the blade geometry. Aspect ratio 'AR', was chosen to be 6 since a lower value would result in a higher drag while greater values would result in a decreased chord. Decreased chord would result in a lower total lift hence the turbine would produce low power output. Since the span was initially fixed at 1.52 m, the planform area was calculated to be 0.25 m^2 while chord came out to be 0.27 m. The rotor disk area was 7.52 m^2. Figure 29.4 shows the CAD drawing of the designed wind turbine blade in isometric view.

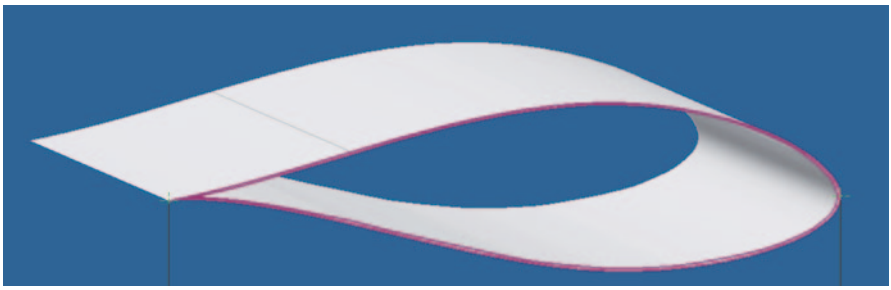

Fig. 29.4 Isometric view of the designed blade using NACA 63-425 airfoil

Table 29.1 Blade geometry values

Parameter	Value
Airfoil	NACA 63-425
Aspect ratio—*AR*	6
Span—b	1.52 [m]
Planform area—S	0.25 [m^2]
Chord	0.27 [m]
Rotor area—A	7.54 [m^2]
Material	E-fibreglass-epoxy
Surface area	1.71 [m^2]

Table 29.2 Typical properties of E-fiberglass-epoxy at room temperature

Property	Values
Density	1950 kg/m^3
Poisson ratio	0.22
Ultimate tensile strength—longitudinal	724 MPa
Ultimate tensile strength—transverse	70.3 MPa
Ultimate compressive strength—longitudinal	476 MPa
Ultimate compressive strength—transverse	227 MPa
Young's modulus—longitudinal	29 GPa
Young's modulus—transverse	12.6 GPa
Shear modulus	3.5 GPa

The chosen material for the wind turbine blade was E-fibreglass-epoxy. It was chosen over carbon-fibre because of its lower cost. E-fibreglass-epoxy is easy to manufacture for the desired shape while it also provides the required strength. Some structural properties of E-fibreglass-epoxy are listed in Table 29.2 [3].

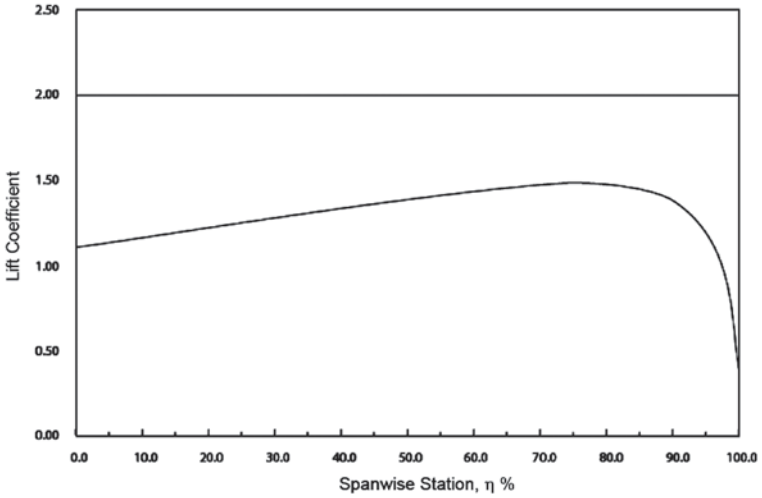

Fig. 29.5 Lift coefficient distribution along the span of the designed blade

Lift

3-D lift coefficient was of the utmost concern since 3-D aerodynamics deals with the span wise effect on the airfoil's aerodynamic coefficients. Lift is particularly important since lift coefficient does not remain the same for a finite structure. Since a blade is a structure of finite length with airfoil cross-sections, a pressure difference between the lower and upper sides is created, producing lift. At the tips, air flows around the tips from the lower side to the upper side because of the difference in pressure. This phenomenon causes a flow component in the span wise direction, affecting the chord-wise streamline. Because of the disturbance, airfoil lift coefficient is not the same as that of the whole blade. Using *Roskam* software, lift coefficient was determined for the entire blade as shown in Fig. 29.5.

The governing equations used to solve the problem come from the standard vortex-lattice theory. The law of Biot-Savart was used to get the flow field around a finite straight vortex line, one of the basic vortex segments needed for the lattice [20]. These vortices induce a flow field in the air, and their strength was determined by the boundary conditions that no air flows through the wings. The forces acting on each vortex segment can be determined by employing the Kutta-Jukovski theorem. Once the lift coefficient was determined, total lift generated by the blade was determined using Eq. 29.3

$$L = \int_{root}^{tip} \frac{\rho}{2} c V_0^2 (C_L) dr. \tag{29.3}$$

Table 29.3 The table shows the result of blade analysis

Parameter	Value
Free-stream velocity—V_0	4 m/s
Density—ρ	1.229 kg/m^3
Lift coefficient—C_L	1.3
Drag coefficient—C_D	0.174
Lift—L	3.18 N
Drag—D	0.43 N
Torque—Q	6.3 N.m
Material thickness	1E-3 m
Material volume	1.71E-3 m^3

Since the wing is of rectangular geometry, the integral can be solved to determine the total lift on the wing.

Drag

Subsonic airfoils experience drag due to different reasons. The dominant drag for low subsonic speed wing is induced drag, which is due to the lift component. The other form of drag is the parasite drag, which exist because to the skin friction plus a small viscous pressure separation. Since the parasitical drag component is relatively small with the pressure separation factor even smaller, tip leakage for the finite blade can be considered negligible. This consideration allows for the use of the same profile drag coefficient for the blade, as for the airfoil.

$$C_D = C_d + C_L{}^2 K \tag{29.4}$$

where;

$$K = \frac{1}{\pi EAR} \tag{29.5}$$

Using the airfoil analysis software, *JavaFOIL*, parasite drag coefficient was determined for the desired conditions. Once the parasite drag coefficient was known, induced drag was calculated using the lift coefficient to determine the overall drag coefficient. Using the Eq. 29.6, total drag on the blade was calculated using $e = 0.83$.

$$D = \int_{root}^{tip} \frac{\rho}{2} c V_0^2 (CD) dr \tag{29.6}$$

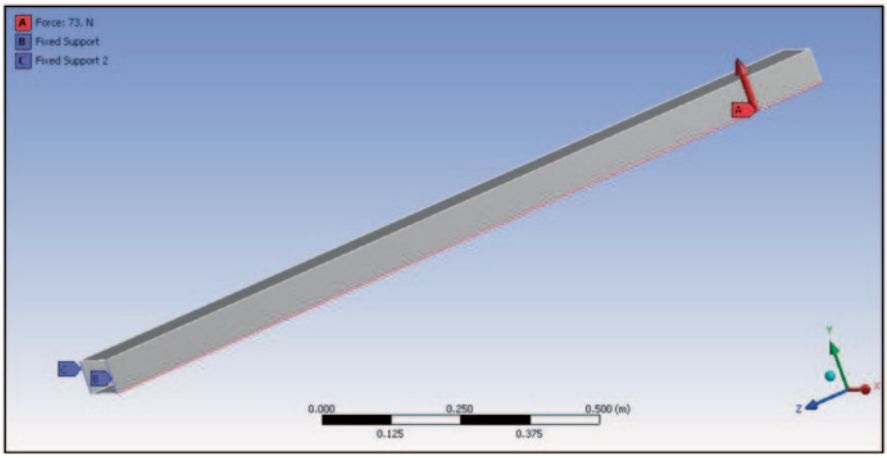

Fig. 29.6 Wind turbine blade box design and test conditions in ANSYS Workbench

Torque

With the aerodynamic parameters known, the next step was to find out the total power generated by the blade. Equation 29.7 suggests that in order to figure out the power generated by the blade, toque, Q, needs to be determined which is described in Eq. 29.5;

$$Q = \int_{root}^{tip} r \frac{\rho}{2} C V_0^2 (C_L \cos \Phi - C_D \sin \Phi) dr \tag{29.7}$$

The equation yields result for the torque produced by the blade. Power is a product of torque and angular speed. Torque can be calculated while angular speeds can be measured by running the tests under different wind conditions (Table 29.3).

Stress Analysis

Stress analysis was conducted on the turbine blade to determine the structural design for the most favourable performance. In order to keep the weight and cost of the blade as low as possible, it was required to keep the fiberglass thickness to a minimum. The structural analysis was conducted to find the thickness value that would give blade the desired strength yet make it light enough to start under low wind speeds. In other words, the blade has to be strong enough to sustain steady aerodynamic loads yet light enough to start under low speeds. It is to be noted that a skin thickness of less than 1 mm, for the given geometry and material, is not

Table 29.4 Test conditions and results of stress analysis on the designed turbine blade

Material volume	1.71E-3 m^3
Material thickness	1E-3 m
Weight	32 N
Maximum designed wind speed	9 m/s
Lift at maximum wind speed	16 N
Total applied test load	73 N
Maximum stress	44 MPa
Maximum deflection	1.5 mm

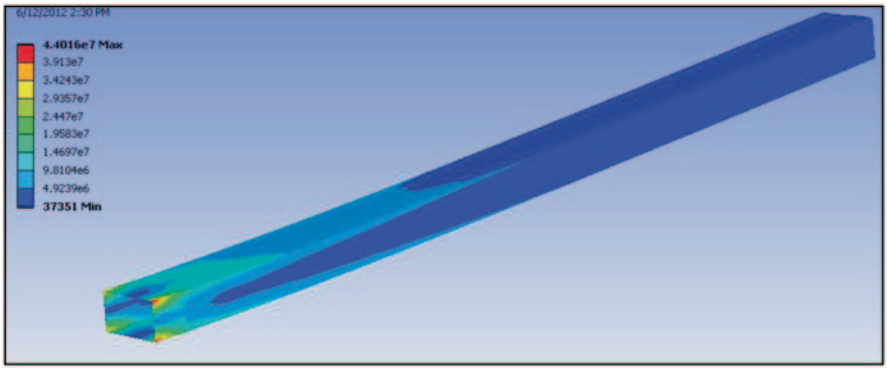

Fig. 29.7 Blade loading test to determine equivalent stress for optimal thickness

feasible. Firstly, it is difficult to manufacture secondly, a thinner surface would bend under its own weight hence the turbine blade would appear squeezed.

A wind turbine blade box was tested, using *ANSYS Workbench* software with a 1 mm thickness of E-fibreglass-epoxy aligned longitudinally along the span. A wind turbine blade box is a rectangular beam of 1 mm thickness, used to simulate the structure of the wind turbine blade. Forces are applied at a spanwise corner line of the box to simulate the effect of lift and weight at quarter chord line. Both, lift and weight, were added up and applied in the same direction. The turbine blade box was fixed from one end replicating the attachment to the turbine hub. Figure 29.6 shows the design and test conditions of the test.

Unlike the wing of an aircraft under cruise condition, only a fraction of lift causes the bending to the blade since most of the force is converted into torque. In order to get a conservative design to ensure reliability and durability under strong wind conditions, the blade was tested for the total lift force and weight. Maximum possible lift and bending were considered which the blade would experience under high winds. Test conditions for structural analysis of the blade are are tabulated below in Table 29.4.

Figure 29.7 shows the equivalent stress experienced by the blade under maximum load condition of 73 N. The tested design uses E-fiberglass-epoxy, longitudinally aligned span wise, and has a thickness of 1 mm. The maximum equivalent

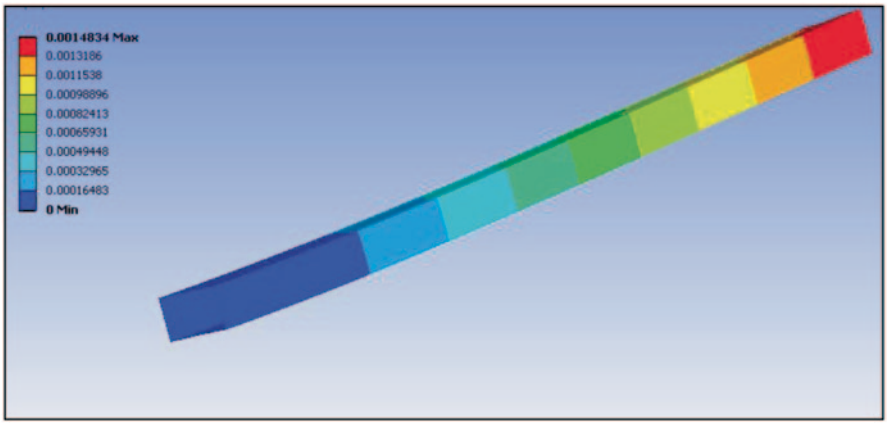

Fig. 29.8 Blade bending test to determine maximum tip deflection

stress was 44 MPa which is far below the ultimate strength of the used material shown in Table 29.2. The test concluded that the designed blade comprehensively sustained the expected loading. Although maximum stress experienced by the blade falls far below the ultimate stress value of E-fiberglass-epoxy, the blade's structural design cannot be further optimized because of the manufacturing constrains discussed earlier.

Figure 29.8 shows the tip deflection test result after applying total load of 73 N on the blade with single layer of E-fiberglass-epoxy. The figure shows the maximum tip deflection value of 1.5 mm. It was important to get the maximum tip deflection value since the blade has to clear the stand at which the turbine is mounted. The value is considered reasonable since any structure around the blade would be farther away.

Conclusion

This paper was aimed at presenting an aerodynamically efficient small wind turbine blade which is economical to produce and easy to manufacture. Design, material and manufacturability considerations were incorporated in the study to determine a blade design which can be produced at relatively low price. A span of 1.5 m was chosen to enable the wind turbine to be used in urban areas. The designed wind turbine blade has NACA 63-425 airfoil which comes out to be the most efficient NACA airfoil for small wind turbine use. Aerodynamic forces were calculated using available techniques and software. Lift, drag and torque values were calculated to be 3.18 N, 0.43 N and 6.3 N.m respectively for an average wind speed of 4 m/s. E-fiberglass-epoxy was used as the blade material since it is transparent to electromagnetic waves, easy to manufacture and relatively

inexpensive compared to other composites. Structural testing was done using *ANSYS* software for the blade skin thickness of 1 mm under the maximum designed load of 73 N. The skin thickness of 1 mm was used since it is the lowest thickness that the blade can be manufactured with. The results showed that the blade experienced 44 MPa equivalent stress while tip deflected 1.4 mm. The results were deemed adequate since the equivalent stress was below the ultimate strength of E-fiberglass-epoxy. The tip deflection was also acceptable since a low deflection would allow a turbine stand to be mounted conveniently. The structural integrity of the blade appears to be satisfactory. Even if the material strength reduces overtime due to cyclic fatigue or environment, the blade will not fail. The study was successful in presenting a blade design that is aerodynamically efficient while being easy and inexpensive to manufacture.

Nomenclature

A	Rotor disk area
AR	Aspect Ratio
b	Blade span
c	Airfoil chord
C_d	Airfoil drag coefficient
C_D	Blade drag coefficient
C_l	2-D lift coefficient
C_L	3-D lift coefficient
D	Drag
e	Wing span efficiency factor
L	Lift
Q	Blade Torque
r	Radius/distance from rotor hub
Re	Reynolds number
S	Blade planform area

Greek Letters

α	angle of attack
Φ	Pitch angle
ρ	Density

Subscripts

V_0	Free stream velocity

References

1. David D Horizontal axis wind turbine. http://www.daviddarling.info/encyclopedia/H/AE_horizontal-axis_wind_turbine.html. Accessed 24 Nov 2009

2. Clarke S (2009) Electricity generation using small wind turbines at your home or farm. Government of Ontario, Ontario. http://www.omafra.gov.on.ca/english/engineer/facts/03-047.htm#neighbourly. Accessed Oct 2009
3. Raymer D (1999) Aircraft design: a conceptual approach. AIAA, Ohio
4. McGhee RJ, Viken JK, Pfenninger W, Beasley WD (1984) Experimental results for a flapped NLF Airfoil with high L/D ratio. NASA TM-85788
5. Sinha SK, Ravande SV (2006) Drag reduction of natural laminar flow airfoils with a flexible surface deturbulator. San Francisco: 3rd AIAA Flow control conference
6. Hansen JR, Garber S. (2003) The wind and beyond: a documentary journey into the history of aerodynamics in America. Volume 1: the ascent of the airplane in America. NASA, Washington
7. Fujino M, Yoshizaki Y, Kawamura Y (2003) Natural-laminar-flow airfoil development for a lightweight business jet. J Aircr 40:609–615
8. Singh RK, Ahmed MR (2012) Blade design and performance testing of a small wind turbine rotor for low wind speed applications. Renew Energy 50:812–819
9. Smetana FO (1997) Introductory aerodynamics and hydrodynamics of wings and bodies: a software based approach. AIAA, Reston (AIAA Education series)
10. Abbott IH, VonDoenhoff AE (1959) Theory of wing sections, Including a summary of airfoil data. Dover Publications, Mineola
11. Timmer WA (2009) An overview of NACA 6-digit airfoil series characteristics with reference to airfoils for large wind turbine blades. Florida: 47th AIAA aerospace sciences meeting including The New Horizons Forum and Aerospace Exposition
12. Rooij RV, Timmer N (2004) Design of airfoils for wind turbine blades. Delft University of Technology, Delf
13. Hau E (2006) Wind turbines: fundamentals, technologies, application, economics. Springer, Berlin
14. Clausen PD, Wood DH (1999) Research and development issues for small wind turbines. Renew Energy 16:922–927
15. Burton DST (2004) Wind energy: handbook. Wiley, Sussex
16. http://toronto.weatherstats.ca/. Accessed 4 Sept 2009
17. Lanzafame R, Messin M (2009) Design and performance of a double-pitch wind turbine with non-twisted blades. Renew Energy 34:1413–1420
18. Budynas RG, Richard B, Nisbett JK (2010) Shigley's mechanical engineering design, 9th edn. McGraw Hill, New York
19. Mishnaevsky L Jr, Freere P, Sinha R, Acharya P, Shrestha R, Manandhar P (2011) Small wind turbines with timber blades for developing countries: materials choice, development, installation and experiences. Renew Energy 36:2128–2138
20. Hansen MO (2008) Aerodynamics of wind turbines. James & James, London

Chapter 30
Hydrogen Production by Reforming Clathrate Hydrates Using the in-Liquid Plasma Method

Andi Erwin Eka Putra, Shinfuku Nomura, Shinobu Mukasa and Hiromichi Toyota

Abstract Clathrate hydrates, which were formed from methane and cyclopentane, were decomposed by plasma at atmospheric pressure. Methane hydrate was synthesized by injecting methane into shaved ice in the reactor at a pressure of 7 MPa and a temperature of 0 °C. In addition, cyclopentane hydrate was formed by adding surfactant into cyclopentane-water emulsion at 0.1 MPa and a temperature of 0 °C. The process of plasma decomposition of clathrate hydrates has been carried out by irradiating high frequency plasma at the tip of the electrode in clathrate hydrates. 2.45 GHz MW oven and 27.12 MHz RF irradiation were used. This study results gas production that its content identified by gas chromatograph. High purity of hydrogen would be extracted from clathrate hydrate using the in-liquid plasma method.

Keywords Hydrogen production · Clathrate hydrates · The in-liquid plasma

30.1 Introduction

Clathrate hydrates are formed by the presence of constituent molecules such as CH_4, CO_2, and even cyclopentane as liquid hydrocarbon within the cavity of lattice water. Clathrate hydrates are formed by the exothermic reaction with a combination of

A. E. E. Putra (✉)
Department of Mechanical Engineering, Hasanuddin University, Indonesia,
Jalan Perintis Kemerdekaan Km. 10, Tamalanrea, 90245, Makassar, Indonesia
e-mail:erwinep@eng.unhas.ac.id

S. Nomura · S. Mukasa · H. Toyota
Department of Engineering for Production and Environment,
Ehime University, Japan, 3 Bunkyo-Cho, 790-8577, Matsuyama, Ehime, Japan
e-mail: nomura.shinfuku.mg@ehime-u.ac.jp

S. Mukasa
e-mail: mukasa.shinobu.me@ehime-u.ac.jp

H. Toyota
e-mail: toyota@ehime-u.ac.jp

I. Dincer et al. (eds.), *Progress in Sustainable Energy Technologies: Generating Renewable Energy,* DOI 10.1007/978-3-319-07896-0_30,

pressure and temperature accordingly. Clathrate hydrates, mainly methane hydrate, which are estimated exist stable and abundant in the seabed and permafrost at low temperature and high pressure are the source of untapped energy. Methane hydrate is categorized as cubic structure I (sI) with the ideal composition of $CH_4.5.75H_2O$ has the pressure phase equilibrium of 2.3 MPa at 0 °C with the content of ice—liquid water—hydrate and cyclopentane hydrate as cubic structure II (sII) 7.7 °C at atmospheric pressure [1]. Therefore, cyclopentane hydrate is generally preferred in experimental laboratory to identify the mechanism of hydrate formation in oil production pipelines [2, 3] and it also applied to the thermal energy storage for air conditioning system [4].

Because of the potential for being economically viable, methane hydrate has been exploited for the recovery of natural gas through dissociation process. One of the hydrate dissociation process is the involving of heating hydrate fields through thermal stimulation at above hydrate equilibrium temperature. Thermal stimulation method is typically by injecting hot water (steam and hot brine) into hydrate fields. Unfortunately, this method requires high production costs due to high-energy losses during the injection of hot water. On the other hand, the use of high frequency waves is irradiated directly to hydrate fields can be more rapidly than the hot water injection [5].

The other application of hydrate technologies for the storage and transportation of hydrocarbon fuels, mainly natural gas, has been investigated. This is because large amount of gas so that they can facilitate the transportation of natural gas [6], and hydrate storage and transport processes became feasible at low pressure [7, 8, 9].

The potential energy source mentioned above can support the availability of fuel gas. However, the release of methane and carbon dioxide into the atmosphere should be considered as a major contribution to global warming. Therefore, as the response to the environmental impact of fossil fuels, hydrogen which is currently used extensively in the chemical industry can be optimized as environmentally energy. Generally, the need of commercial hydrogen is produced by steam methane reforming.

The other process that could be applied to hydrogen industry is plasma generation technology because its high temperature of more than 1000 K may accelerate the reaction rate. On the other hand, a technology for generating plasma in liquid by radio frequency (RF) or microwave (MW) irradiation has been conducted to produce 70–80 % of hydrogen at atmospheric pressure from waste oil and n-dodecane [10, 11]. RF irradiation could be easy to generate plasma in the water at high pressure [12] and to produce hydrogen, oxygen, and hydrogen peroxide from water [13].

In this study, high frequency plasma decomposition of clathrate hydrates at atmospheric pressure consist of methane hydrate and cyclopentane hydrate is conducted. This process is a first step towards the ultimate goal to produce hydrogen from hydrate fields with in-liquid plasma method. The in-liquid plasma makes it possible to stimulate plasma into hydrate fields using transmission cable to connect the power generation in the floating board and the electrode in hydrate fields. The in-liquid plasma method is easily generated with a high localized temperature at high pressure where the plasma exist mostly around the tip of the electrode. That's way this method is considered suitable for this purpose.

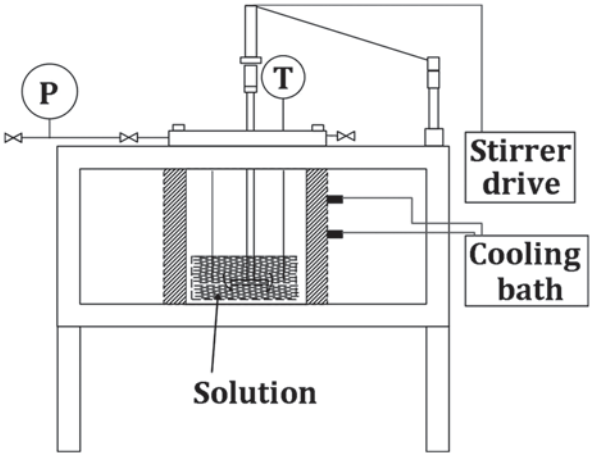

Fig. 30.1 The structure of the clathrate hydrates formation apparatus

30.2 Experimental Procedures

Clathrate Hydrates Formation

Figure 30.1 depicts the experimental equipment used in this research. The volume of the reaction vessel is 400 mL with a height of 140 mm and an inner diameter of 60 mm. The maximum pressure is 15 MPa, and the temperature of the reactor casing is maintained by an ethylene glycol cooling medium. A magnetic stirrer with a diameter of 40 mm and a gas injection tube are positioned 30 mm from the reactor bottom.

Methane hydrate formation has been synthesized by injecting pressurized methane into shaved ice in the formation reactor. one hundred grams of shaved ice were put into the formation reactor that had been cleaned with water. The air in the reactor was then purged by decompression using an aspirator and substituted with methane. The temperature of the cooling bath was kept constant at 0 °C, the methane was pressurized to about 7 MPa and the stirrer was activated to agitate the solution at 400 rpm. The temperature of clathrate hydrates formation was monitored by a thermocouple placed at at 30 mm from the reactor bottom. The temperature and pressure during the process was recorded every 15 minutes.

In addition, 33.5 gm of cyclopentane were dissolved into 146.5 gm of water with 0.2 gm of surfactant. The solution composition is $C_5H_{10}.17H_2O$ and it categorized as cubic structure II (sII). Then, cyclopentane (CP) hydrate was injected into the reactor at atmospheric pressure and was cooled by an ethylene glycol cooling medium at 2 °C. The solution was stirred at 120 rpm during the formation. Hydrate crystal grains are added to the solution when its temperature reaches about 2 °C in order to trigger the formation of hydrates.

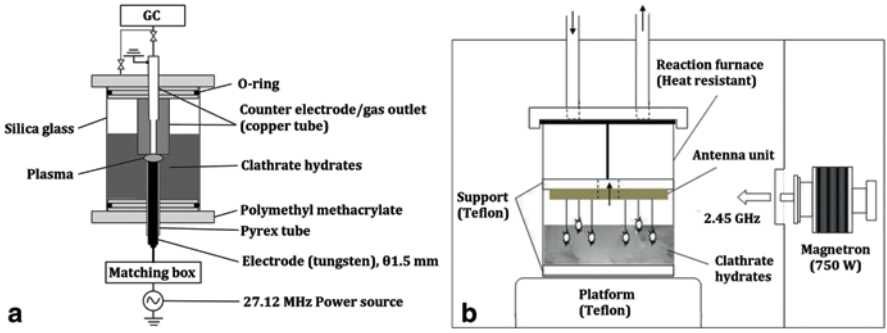

Fig. 30.2 Experimental apparatus for decomposition of clathrate hydrates

Plasma Decomposition of Clathrate Hydrates

27.12 MHz radio frequency plasma and 2.45 GHz MW plasma were used to decompose clathrate hydrates, as shown in Fig. 30.2. Before plasma generated at the tip of the electrode decomposed clathrate hydrates in the reactor vessel at atmospheric pressure, Helium was injected into the reactor vessel to expel air.

27.12 MHz Radio Frequency Plasma Decomposition

A transparent silica glass pipe was used as the reactor vessel with an inner diameter of 55 mm, a thickness of 2 mm, and a height of 85 mm. An electrode consisting of 2 mm of a tungsten rod protruding from a silica glass tube with an outer diameter of 6 mm and a thickness of 1.5 mm as dielectric substance was inserted from the bottom of the reactor and connected to a 27.12 MHz RF power source (T161–5766LQ, Thamway) via a matching box (T020–5766M, Thamway). Additionally, a copper tube was inserted from the top of the reactor to a distance of 4 mm from the lower electrode that served not only as a counter electrode but also as gas outlet as well. Thirty grams of clathrate hydrates were poured into the reactor vessel. The generation of RF plasma in clathrate hydrates was conducted at 150 W at atmospheric pressure. The power values were calculated by subtraction of the reflected power from the forward power. The reflected power was kept constant at the lowest possible level.

2.45 GHz MW Plasma Decomposition of Clathrate Hydrates

The microwave oven was used as a MW source to generate the in-liquid plasma. Fifty grams of clathrate hydrates was placed below the tip of the antennas in the reactor vessel. The reactor vessel was irradiated by microwaves from the magnetron received by antennas. Then, plasma is generated at the tip of antennas.

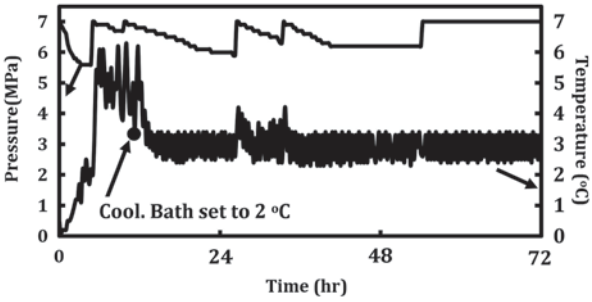

Fig. 30.3 Pressure and temperature along methane hydrate formation. (adapted from [15])

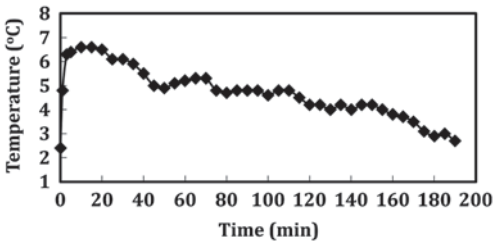

Fig. 30.4 The cyclopentane hydrate formation at atmospheric pressure. (adapted from [16])

A gas chromatograph (Shimadzu 8 A) with a column temperature 60 °C (6 min hold) to 160 °C and Helium as the carrier gas was used to identify the contents of product gases.

30.3 Results and Discussion

Methane hydrate began to be formed immediately after the stirrer was activated at the beginning of the process, which was characterized by the pressure drop to approximately 5.6 MPa and an increase in temperature to approximately 2 °C. This was due to an exothermic reaction, as shown in Fig. 30.3. The methane was pressurized to 7 MPa with a corresponding increase in temperature to approximately 6 °C. The formation of methane hydrate then occurred continuously from the melting ice. The remaining ice was melted to form hydrates by a change in the temperature of cooling bath to 2 °C after the stirrer was stopped. Pressurization with methane to 7 MPa was performed in several times. After the methane hydrate formation process was complete, when the formation pressure was constant at 7 MPa, it was reduced rapidly to atmospheric pressure. The further cooling of the hydrate is required to prolong the completion of hydrate dissociation [14].

Figure 30.4 shows temperature along cyclopentane hydrate formation at atmospheric pressure. The adding of the hydrate crystal grains triggers the hydrate formation that is characterized by an increase in the solution temperature to about 7 °C. The cyclopentane hydrate formation is complete when the solution temperature remained constant at about 2 °C.

Fig. 30.5 Photo of the high frequency plasma decomposition of clathrate hydrates. **a** 2.45 GHz MW plasma decomposition. **b** 27.12 MHz RF plasma decomposition

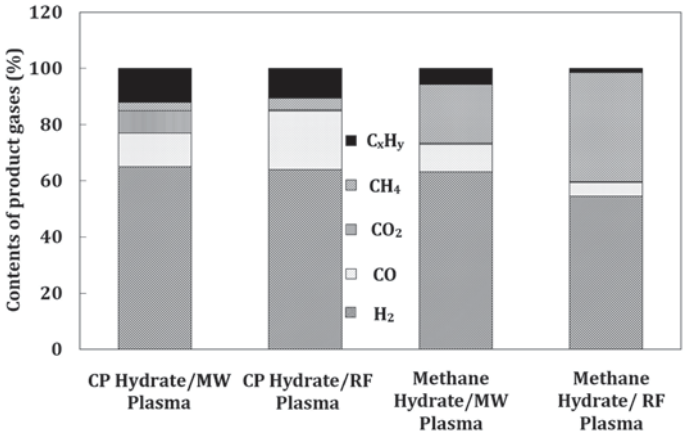

Fig. 30.6 Content of product gases from clathrate hydrate decomposition. C_xH_y consists of C_2H_2, C_2H_4

Clathrate hydrates decomposed by the plasma into the product gases. The product gases are hydrogen (H_2) and carbon monoxide (CO) as the main products, and byproducts are carbon dioxide, methane, carbon (C), and C_2-hydrocarbon. Carbon was found adhered in the reactor walls, the antennas/counter electrodes, and in the remnant of solution as shown in Fig. 30.5.

At plasma decomposition of methane hydrate, the significant methane content in the product gases was identified as the unconverted methane release. It was found about 21 % in the MW plasma and 39 % in the RF plasma as shown in Fig. 30.6.

Table 30.1 Basic reactions for clathrate hydrates

Reactions	DH (kJ/mol)
Methane hydrate	
$CH_4 \cdot 6H_2O \rightarrow CH_4(g) + 6H_2O$	53.5
$CH_4 + H_2O \rightarrow 3H_2 + CO$	206.16
$CO + H_2O \rightarrow H_2 + CO_2$	-41.2
Direct decomposition	
$CH_4 \rightarrow 2H_2 + C\ (s)$	74.87
Cyclopentane hydrate	
$C_5H_{10} \cdot 17H_2O \rightarrow C_5H_{10} + 17H_2O$	82.3
$C_5H_{10} + 5H_2O \rightarrow 10H_2 + 5CO$	952.95
$CO + H_2O \rightarrow H_2 + CO_2$	-41.2
Direct decomposition	
$C_5H_{10} \rightarrow 5H_2 + 5\ C\ (s)$	76.45

The composition of the methane hydrate is $CH_4.6H_2O$ [17, 18] and it also refers to the hydrate number of Handa [1]. In addition, dissociation enthalpy of methane hydrate (ΔH) in this study is 53.5 kJ/mol [18].

First, methane hydrate dissociated by plasma, and then some of water is turned into the steam by evaporation and the reaction of steam methane reforming results H_2, CO, CO_2 as shown in Table 30.1. In addition, H_2, C and light hydrocarbon as byproduct were resulted from direct decomposition of methane. Similarly, dissociation enthalpy of cyclopentane hydrate is 82.3 kJ/mol [19] and the reaction of plasma decomposition of cyclopentane hydrate is also shown in Table 30. The direct decomposition of cyclopentane also produced the light hydrocarbon as a byproduct.

27.12 MHz RF plasma decomposition of clathrate hydrates resulted the highest H_2/CO mole ratio for methane hydrate and the lowest mole ratio of H_2/CO for cyclopentane hydrate as shown in Fig. 30.7. In addition, enthalpy of H_2 formation from methane hydrate is lower than that from cyclopentane hydrate as shown in Fig. 30.8.

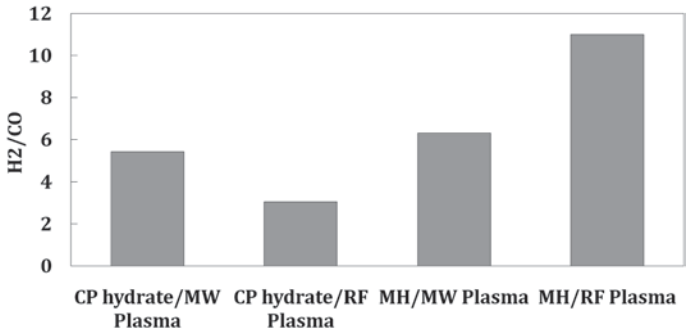

Fig. 30.7 The mole ratio of H_2/CO In the product gases from clathrate hydrate decomposition

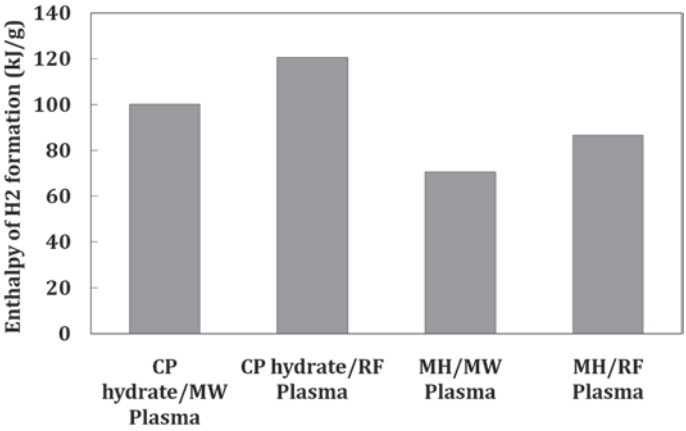

Fig. 30.8 Net amount of energy used for clathrate hydrate decomposition

Conclusions

Experiments producing hydrogen with 2.45 GHz MW plasma using a conventional MW oven and 27.12 RF plasma were conducted and the following results were obtained.

1. The purity of hydrogen from cyclopentane hydrate was 65 % for both sources of plasma and it was 63 % and 55 % from methane hydrate using 2.45 GHz MW plasma and 27.12 RF plasma, respectively.
2. The amount of unconverted methane from methane hydrate decomposition were found to be 21 % in the MW plasma and 39 % in the RF plasma in the product gases.
3. Clathrate hydrates have a great potential as a source of hydrogen because of the high mole ratio of H_2/CO in the product gases and the low enthalpy of hydrogen formation.

References

1. Sloan ED, Koh CA (2008) Clathrate hydrates of natural gases 3th edn. FL: CRC Press-Taylor & Francis Group, New York
2. Aspenes G, Dieker LE, Aman ZM, Høiland S, Sum AK, Koh CA, Sloan ED (2010) Adhesion force between cyclopentane hydrates and solid surface materials. J Colloid Interface Sci 343:529–536
3. Brown CJ, Ni X. (2010) Evaluation of rate of cyclopentane hydrate formation in an oscillatory baffled column using laser induced fluorescence and energy balance. Chem Eng J 157:131–139
4. Nakajima M, Ohmura R, Mori YH (2008) Clathrate hydrate formation from cyclopentane-in-water emulsions. Ind Eng Chem Res 47:8933–8939

5. Dong-Liang L, De-Qing L, Shuan-Shi F, Xiao-Sen L, Liang-Guang T, Ning-Sheng H (2008) In situ hydrate dissociation using microwave heating: preliminary study Energy Convers Manage 49:2207–2213
6. Gudmundsson JS, Andersson V, Levik OI (1997) Gas storage and transport using hydrates. Offshore Mediterranean conference, Ravenna. 19–21 March 1997
7. Stern LA, Circone S, Kirby SH, Durham WB (2001) Anomalous preservation of pure methane hydrate at 1 atm. J Phys Chem B 105:1756–1762
8. Gudmundsson JS, Børrehaug A. (1996) Frozen hydrate for transport of natural gas. 2nd International conference on natural gas hydrate, Toulouse, France. 2–6 June 1996
9. Giavarini C, Maccioni F (2004) Self-preservation at low pressures of methane hydrates with various gas contents. Ind Eng Chem Res 43:6616–6621
10. Nomura S, Toyota H, Tawara M, Yamashita H, Matsumoto K (2006) Fuel gas production by microwave plasma in liquid. Appl Phys Lett 88(23):231502-1-231502-3
11. Nomura S, Toyota H, Mukasa S, Yamashita H, Maehara T, Kawashima A (2009) Production of hydrogen in a conventional microwave oven. J Appl Phys 106:073306-1-073306-4
12. Nomura S, Mukasa S, Toyota H, Miyake H, Yamashita H, Maehara T, Kawashima A, Abe F (2011) Characteristics of in-liquid plasma in water under high pressure than atmospheric pressure. Plasma Sources Sci Technol 20:034012
13. Mukasa S, Nomura S, Toyota H, Maehara T, Yamashita H (2011) Internal conditions of a bubble containing radio-frequency plasma in water. Plasma Sources Sci Technol 20:034020
14. Giavarini C, Maccioni F (2004) Self-preservation at low pressures of methane hydrates with various gas contents. Ind Eng Chem Res 43:6616–6621
15. Putra AEE, Nomura S, Mukasa S, Toyota H (2012) Hydrogen production by radio frequency plasma stimulation in methane hydrate at atmospheric pressure. Int J Hydrog Energy 37:16000–16005
16. Nomura S, Putra AEE, Mukasa S, Yamashita H, Toyota H (2011) Plasma decomposition of clathrate hydrates by 2.45 GHz microwave irradiation at atmospheric pressure. Appl Phys Expr 4(6):066201–1–3
17. Circone S, Kirby SH, Stern LA (2005) Direct measurement of methane hydrate composition along the hydrate equilibrium boundary. The J Phys Chem B 109:9468–9475
18. Anderson GK (2004) Enthalpy of dissociation and hydrate number of methane hydrate from the Clapeyron equation. The J Chem Thermodyn 36:1119–1127
19. Zhang Y, Debenedetti PG, Prud'homme RK, Pethica BA (2004) Differential scanning calorimetry studies of clathrate hydrate formation. The J Phys Chem B 108:16717–16722

Chapter 31
Facilitation of Wind Energy Conversion System Selection as Distributed Generation in Household/Commercial and Agricultural Sectors; Case Study of Iran

Arash Hatami and Hamed Shakouri Ganjavi

Abstract Distributed generation is an approach to power generation by low capacity systems. In this paper small wind turbines are investigated as distributed generation systems used to satisfy household/commercial and agricultural sectors demand. This paper explains a decision-making process during which consumers can easily define appropriate Wind Energy Conversion System (WECS), considering economical accordance by the amount of power consumption and climate condition of installation place. Rotor diameter and turbine hub height are distinguished as two main parameters affecting WECS, referring to consumption rate and climate circumstances of the place. Mathematical relation between Cost Per Unit (CPU) of generated power and these two, is determined with high correlation coefficient which will be applied during the process to easily nominate different WECSs. Having the amount of costs paid by a family per 1 kWh of electricity consumption, WECS characteristics can be conveniently specified using this relation. To examine the influence of each of the above parameters and increasing the validity of the results, turbines with different rated powers and hub heights, are used in four regions with various geographical circumstances.

Keywords Distributed generation · Small wind turbines · Wind energy conversion system

A. Hatami (✉) · H. Shakouri Ganjavi
Department of Industrial and Systems Engineering, Collage of Engineering
University of Tehran, Tehran, Iran
e-mail: ahatami@alumni.ut.ac.ir

H. Shakouri Ganjavi
e-mail: hshakouri@ut.ac.ir

I. Dincer et al. (eds.), *Progress in Sustainable Energy Technologies: Generating Renewable Energy,* DOI 10.1007/978-3-319-07896-0_31,

31.1 Introduction

Manufacturing products, providing services to increase human welfare and satisfying safe life, requires energy consumption. Electrical energy is actually one of the most important types of energy. During population growth and development of human societies, great generation of the electrical energy is inevitable. It is expected that the world electricity usage will reach 32,922 terawatt hours in the year 2035 (approximately two times the amount used in the year 2008) [1]. Therefore, in order to respond to the increase in power demand, countries must develop generation methods and relevant facilities.

In some energy-related literatures, various methods for power generation are categorized into two sets based on primary energy, fossil or renewable energies, used as generation method. Exhaustibility of fossil resources and environmental pollutions has led to extension of electricity generation by renewable primary energy. In this realm, power generation using renewable energy is divided to two categories as hydro and non-hydro. This paper focuses on wind power generation as non-hydro renewable energy. As a fact, non-hydro renewable energies comprise about 5% of global power generating capacity and supply about 3.4% of global electricity generation [2].

The use of wind machines for utilization of the wind speed is not only new, but also reaches as far back as the Chinese in 2000 B.C., in irrigation water pumps and windmills for grinding grains. However, among these energy sources, wind is becoming the world's fastest growing renewable energy source due to its worldwide acceptance as a clean source of energy and having such attributes as security of supply, biodiversity concerns, potential for distributed generation, ecological awareness and other socio-economic factors [3]. Besides, as wind can generate power near load centres, it eliminates the transmission loss in the lines through rural and urban areas [4, 5]. According to World Wind Energy Association, the world wind power capacity reached 196,630 MW in 2011 after a nearly exponential growth for 5 years [6]. It is expected that wind energy, will have a 4.9% share in meeting the world electricity demand until the year 2030 [7]. Furthermore, Modern wind power industry has witnessed huge progress in the past 30 years due to the R&D efforts [8]. For instance, installed wind power capacity in China increased from 2599 MW in 2006 to 44,733 MW in 2011or in the U.S. this is from 11,575 MW in 2006 to 40,180 MW in 2010 [9]. So, it is anticipated that the renewable share in electricity generation will reach 16% in the year 2035 from 1% in the year 2008 [5].

To sum up, nowadays utilization of this form of energy is expanded all over the world and developing countries are carrying out major research to extend this generation method. According to World Wind Energy Association's (WWEA) report, installed capacity dispersion of the world wind turbines until the year 2009, exhibited 25% of the total installed capacity of wind power in Asia [6]. Among the continents, Europe has the largest share in increasing wind power capacity to 48% [6].

As researchers have attended climate changes and the resulting wind speed changes over various seasons of a year, there has been created opportunities to extend wind turbine applications and to develop various types such as vertical and

horizontal axis wind turbines. On the other point of view, considering generation or consumption scale, wind turbines are categorized into two types, small and large turbines. Both are being served and operated by homeowners and small enterprises. In recent years, power generated by small scale wind turbines is increased. Therefore, sales has been grown averagely 40 % per year, since the energy crisis of the 1970s [10].

Among the literatures published in different fields relevant to wind power utilization so far, there are some discussing economic aspects of wind energy conversion system (WECS) and output cost analysis. Some others, have concentrated on efficiency of WECS assessing factors effecting on it [11, 12]. But this paper tries to present a decision-making process so as to easily choose a WECS according to consumer preferences. Against manufacturer brochures which present specific amounts as the WECS characteristics, this process can help consumer to define these amounts according to a three variables mathematical relation developed between cost per unit of generated power (CPU) and both parameters hub height (H) of wind turbine and rotor diameter (D). On the other hand, as defining amount af the both parameters will be done considering consumption rate (affected by D) and climate conditions (affected by H), the defined WECS has more conformity to consumer preferences rather than the one defined by manufacturer. Since the WECS selected by consumer has accordance with the power supply needed and is self-agreeable as well, especially economically, this paper can help anyone serving wind power generation systems. In the following, first an introduction is provided for the well-known wind power literature and some transparent statistics of wind energy developments are investigated. Section 2 describes the methodology through which, general information, wind energy potential of Iran, decision-making process and Weibull parameters of wind speed for four selective locations are surveyed. Latest sub-sections are allocated to estimation of turbine power and way of CPU calculation. In section 3, derivation of mathematical equation based on impressed factors is completely defined. In order to sensitivity analysis and guarantee accuracy in calculations, various hub heights and rated power of wind turbines are used for locations having different climates. Finally, conclusion and groundwork of future research is depicted.

31.2 Methodology Description

Overview

As mentioned, this paper investigates wind power generation using small wind turbines considering existing wind potential in Iran. On the other hand, considering the aspect of wind turbine utilization for satisfying electrical energy demand in household/commercial and agricultural sectors, this paper has special attention to distributed generation realm and present techno-economic analysis as an experimental practice to present a process in order to ease small wind turbines utilization.

As a general rule, wind turbines served to generate electricity are divided into three categories (i.e. small, medium, and large sized) based on the power generation. Small sized wind turbines can generate power up to 10 kw, while that ranges from 10 to 100 kw for medium ones. Large sizes are able to generate more than 100 kw [13]. Consequently, since the turbines applied for supplying the electricity needs of the household/commercial and agricultural sectors are able to generate at most the power of 10 kw, they are regarded as small sized. Large sized turbines are not recommended for this sector due to economic aspects. In fact, they cause more installation costs, while supplying only a portion of the electrical energy required by each family. Therefore, the kind of turbine utilized for these sectors needs to be in correspondence with families' income and the reasonable level of required power. A convertor is commonly used to transform electricity generated by turbine from direct current (DC) to alternative current (AC). Furthermore, an energy storage system is attached to the turbine to save extra generated energy to eliminate power shortage when there is virtually no wind blowing. However, in order to ensure a permanent electricity supply for the consumer, it is necessary to attach an energy storage system, such as a battery, to the WECS. The essential role of the storage system is to remedy the wind fluctuation and then to ensure balance between unpredictable wind turbine power generation and the consumer demand [14, 15]. Therefore, in this paper it is assumed that a WECS comprises all parts including turbine generator, convertor and storage system.

Generally, the quantity of electricity generated by wind turbines in a particular region depends on turbine characteristics and geographical conditions and climate of the region [16, 17]. Turbine characteristics include turbine rated power, rotor diameter, and the height of turbine hub. Geographical conditions regards the amount of sunlight, heat radiation, height from sea level, and the extent of rugged areas in a given region or generally all the parameters influencing wind speed in the region [18]. In fact, all of the above attributes are parameters affecting total energy generated by WECS. Among literatures published in this field, in some issues economic analysis of WECS and/or sensitivity analysis of total output energy from the WECS are reflected [19, 20]. In some others, roles of several components of WECS in the extent of wind speed utilization is considered [21, 22]. But in this paper, fundamental parameters affecting CPU are distinguished and a simple process is introduced as well, to select a WECS which supplies regular amount of consumed power and is economically desirable.

Decision-Making Process

This process, as a draft of the paper contribution demonstrated by Fig. 31.1, is discussed in order that consumers can nominate different WECSs and select the one having the best consistency. It includes a step by step procedure that each step requires information from the former. This process is described in the order as below.

Step 1: Calculating CPU from the bill: As usual, the total price and amount of consumed power are written in the bill. So, consumer is able to calculate CPU of electricity that has been consumed, by dividing the first one to the second.

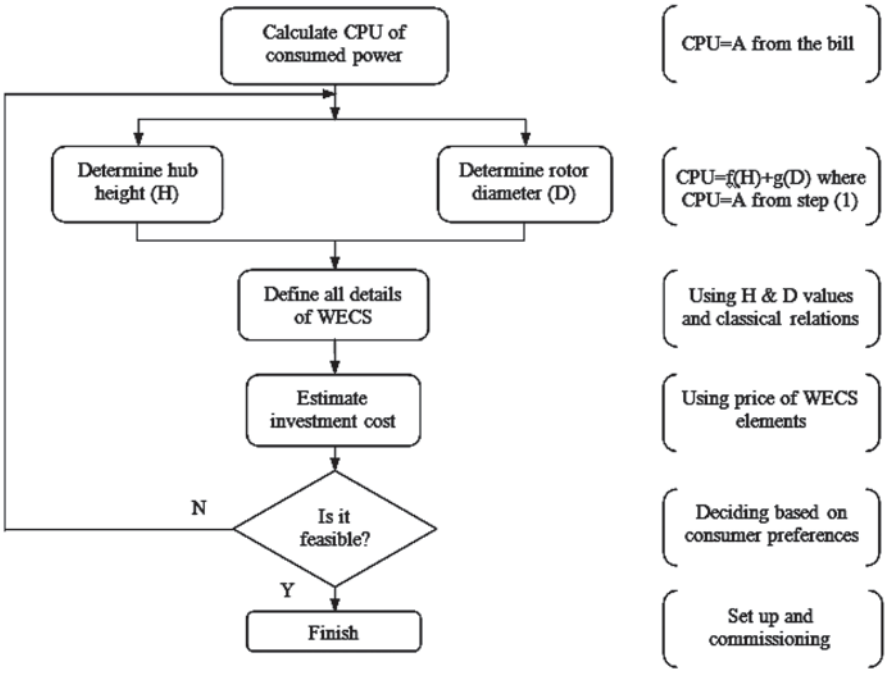

Fig. 31.1 Schematic of design-making process for defining WECS

Step 2: Determining H and D: these parameters are symbols of hub height and rotor diameter of wind turbine, respectively. Since some classical equations should be used to determine CPU, an easy relation between CPU and two parameters H and D is determined in this step. These two parameters are distinguished as the basic factors affecting CPU. According to CPU analysis rather than different values of H and D for four locations with distinctive wind energy potential, the relation is estimated with high correlation coefficient. Therefore, H and D could be evaluated using this relation whenever the value of CPU is known. Estimation of this relation and performed analysis are described completely in section 3.

Step 3: Defining WECS properties: having the amount of H and D and using some classical equations which are presented in the final sub-sections of Sect. 2, characteristics of WECS are achievable. In fact, we nominate a WECS in this step and define its characteristics considering values of the both parameters using classical equations. The mentioned characteristics are system element's properties such as turbine size, storage capacity and so on. Furthermore, system attributes consist of output energy, capacity factor and other information.

Step 4: Determining investment cost: using technical information of WECS, market prices of each system elements could be achievable. Therefore, investment cost could be determined based on costs of wind turbine, storage system, convertor, cables and all things required to set up the system.

Step 5: Feasibility check: in this step, consumer verifies all aspects of nominated WECS in order to conform to their favorite criteria. So, WECS is nominated technically through step 2 and 3 and consumer doesn't have any role to select technical information of WECS. This work will be done referring to economics, taking into account other factors such as generator size or occupied space, vibration and produced noises or even system warranty.

Step 6: Final decision: if nominated WECS properties meet consumer preferences, this process will be finished and WECS is then prepared to set up. If not, another WECS is nominated, going back to step 2 so as to define other values for H and D and all the above steps will be repeated.

It should be noticed that the two equations, in fact, configures a surface in 3D space which exhibits numerous points. But not all the points could be selected, since small wind turbines have standard range of rotor diameters and hub heights. Consequently, there will be a set of distinct H and D values, every pair of which specifies a WECS.

Arriving at the end of the process, since characteristics of selected WECS have been defined based on the amount of power used by consumer and climate circumstances of the place of living, WECS will be adapted technically and economically. In this respect, it should be considered that the process is not functioned as minimizing CPU, enhancing efficiency of generation system or optimizing any of system parameter. In fact, this process suggests different WECS considering CPU value calculated from the bill and helps consumer to choose their favourite generation system using the relation as an applicable tool.

Wind Parameters Estimation

The country of Iran has an area of 1,648,195 km^2, with a population of about 77 million based on the latest census in 2009, 53 million of which live in the urban areas and 24 million in the rural [23]. Having rich fossil resources, this country is a member of OPEC (Organization of Petroleum Exporting Countries) and a major exporter of both oil and natural gas to all over the world. The share of oil and natural gas of Iran, based on energy structure of the country, is 44 and 54 % of the total energy, respectively [5].

The ecological and geographical circumstances have caused beneficial condition in utilization of renewable energies. Nowadays, power generation from renewable sources such as hydro, solar and wind is performed noticeably. In special, in the wind power generation field, with regards to the wind energy classification carried out by America's energy department, in the 7th ranking of this classification many of Iran's wind sites situated in the 800–2000 (W/m^2) range [24]. Referring to different benefits of wind power energy and availability of its preconditions in Iran, establishment and development of wind power stations have salient growth. For example in recent years, Iran's wind capacity was estimated at about 6500 MW [25]. This potential has resulted in many political advantages due to power generation

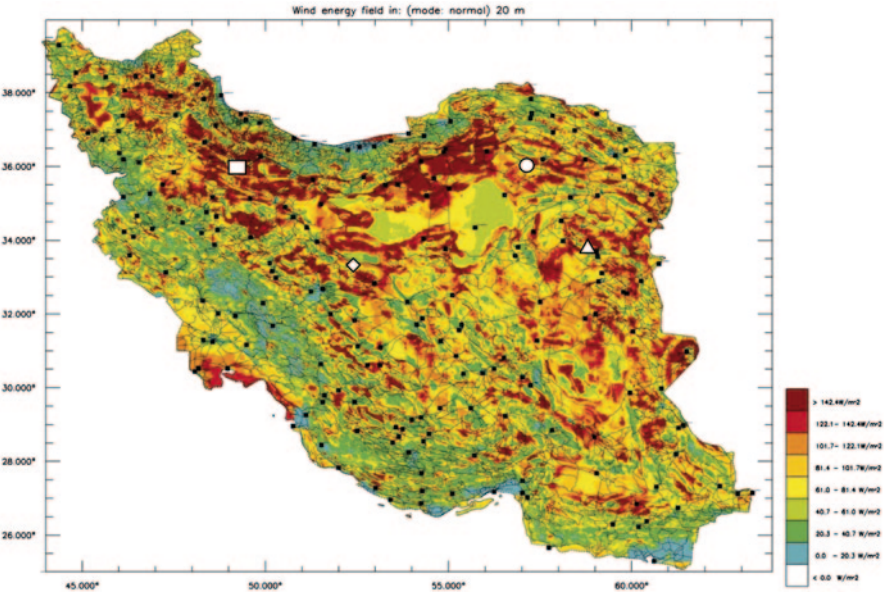

Fig. 31.2 IRAN Wind Atlas demonstrating wind potential at 40 m height [40]. Applied symbol □, ○, ◊ and Δ refer to Jarandagh, Hadadeh, Morche-Khort and Nehbandan respectively

and supplying to the national or international networks and has created job opportunities in the country.

Due to changes in wind speed in different areas, Weibull distribution is used for estimation of wind energy potential. Studies in the past matched the Weibull distribution and experimental data closely [26, 27]. In order to estimate Weibull parameters, as shape and scale, and also gaining high precision in calculations, four locations with various climates and geographical conditions are nominated. These are named as Morche-Khort, Jarandagh, Nehbandan and Hadadeh that are at Esfahan, Ghazvin, Khorasan-e-Jonoubi and Semnan provinces, respectively. In Fig. 31.2 which demonstrates wind atlas of Iran at 40 m height, position of these locations is obvious.

According to the information gained from an anemometer installed in the height of 10 m above the sea level, Weibull parameters are determined with respect to Eqs. 31.1–31.4 [28]. Average wind speed in locations, reported monthly and annually, is presented in Table 31.1.

$$k = \frac{\left\{n.\sum_{i=1}^{n}\left(\ln(v_i).\left(\ln\left\{\ln\left[\frac{1}{1-\frac{1}{n+1}}\right]\right\}\right)\right)\right\} - \left\{\sum_{i=1}^{n}\ln\left(\ln\left[\frac{1}{1-\frac{1}{n+1}}\right]\right).\sum_{i=1}^{n}\ln(v_i)\right\}}{\left\{n.\sum_{i=1}^{n}\left(\ln(v_i)^2\right)\right\} - \left\{\sum_{i=1}^{n}\ln(v_i)\right\}^2} \tag{31.1}$$

Table 31.1 Average wind speed of the four location at 10 M height

	Jarandagh	Nehbandan	Hadadeh	Morche-Khort
January	1.11	0.93	1.21	3.92
February	2.02	3.58	2.78	5.18
March	4.62	5.92	5.34	7.01
April	7.22	4.09	4.78	4.98
May	5.23	2.3	1.89	3.08
June	4.52	2.99	0.84	2.41
July	3.97	3.8	1.02	0.44
August	3.73	5.56	3.46	3.07
September	5.74	7.13	7.19	4.94
October	7.04	6.03	5.75	5.54
November	3.60	3.25	3.87	3.20
December	2.18	1.12	2.48	3.14
Annual	4.25	3.89	3.38	3.91

Table 31.2 Value of Weibull distribution of wind speed at the four locations

	Jarandagh	Nehbandan	Hadadeh	Morche-Khort
k	1.91	1.69	1.5	1.44
c	6.12	5.68	5.12	6.07

$$c = e^{\left(\bar{w} - \frac{\bar{v}}{k}\right)} \tag{31.2}$$

$$\bar{v} = \frac{1}{n}\sum_{i=1}^{n} \ln\left\{\ln\left[\frac{1}{\left(1-\frac{i}{n+1}\right)}\right]\right\} \tag{31.3}$$

$$\bar{w} = \frac{1}{n}\sum_{i=1}^{n} \ln(v_i) \tag{31.4}$$

In Eqs. 31.1 and 31.2, "v_i" stands for the wind speed of i^{th} members of total gained data as "n". Symbols "k" and "c" regard shape and scale parameters of wind speed Weibull distribution, respectively. Considering above equations, values of parameters "k" and "c" are calculated as mentioned in Table 31.2.

Turbine Power Calculation

Turbine power generally refers to the amount of electrical energy that can be generated by a turbine in a specific time interval. Wind speed is a fundamental element that has a direct relationship with turbine power (i.e. the more powerful the

blowing winds are, the more potential has the turbine to generate electricity). Turbine size also affects its throughput power as to the length of blades. Long blades have broader touching surface exposed to the blowing winds and hence the rotation speed enhances. Considering what mentioned above, the power of a turbine can be calculated by Eq. 31.5 with regards to the wind speed and the touching surface the wind has with the blades [39].

$$P = \frac{E}{\Delta t} = \frac{1}{2}\rho A V^3 \tag{31.5}$$

In Eq. 31.5, "P" is the generated power, calculated on the basis of watt (w), "V" is the speed of wind blow and "A" stands for the area where the wind turbine blades cover. According to what is shown in Fig. 31.2, this area is formed by rotation of turbine blades in a circular mode; furthermore, "ρ" regards air density which in this paper is equal to 1 and also is assumed to be fixed for different heights. This assumption leads the error of estimating wind blow to decrease to lower than 5 % [29]. So, Eq. 31.5 is rewritten to result in Eq. 31.6.

$$P = 0.3925 D^2 V^3 \tag{31.6}$$

Note that in Eq. 31.6, "D" indicates the diameter of turbine rotor which is equivalent to the diameter of the area supported by the rotation of turbine blades, exposing to the blowing winds.

Other attributes of a wind turbine are rated power (P_r), minimum wind speed at which the turbine can generate electricity (V_i), maximum wind speed at which the turbine is able to generate the greatest rate of energy by its maximum power (V_0), and rated speed (V_r). Notice that, the reduction in throughput power of turbine in intense winds prevents blades from rotating appropriately. Thus, the turbine efficiency and the power generated decrease. In many literatures, "P_r" is used for estimating generated power from wind turbine [20, 30]. But referring to determination of energy generated by WECS using wind speed, taking into account variability of wind speed, it is better that "$\bar{P}$" resulting from "$\bar{V}$", apply in this way. So, to calculate "$\bar{P}$" according to Eq. 31.6, "$\bar{V}^3$" should be calculated based on Eq. 31.7 [31].

$$\bar{V^3} = \left[\frac{\Gamma\left(1-\frac{3}{k}\right)}{\Gamma^3\left(1+\frac{1}{k}\right)}\right]\bar{V^3} \tag{31.7}$$

Where "Γ" stands for a Gamma function and "$\bar{V}^3$" is the third power of average wind speed. According to what mentioned in Eqs. 31.1–31.4, "$\bar{V}$" is a function of Weibull parameters of the wind speed. Therefore, Eq. 31.7 is rewritten to result in Eq. 31.8.

$$\bar{V^3} = c^3\Gamma\left(1+\frac{3}{k}\right) \tag{31.8}$$

Since the quantity of Gamma function in Eq. 31.8 equals to 2 approximately, "$\bar{P}$"can be calculated using the Eq. 31.9 which can be rewritten by substituting "$\bar{V}^3$" from Eq. 31.6.

$$\bar{P} = 0.785 D^2 c^3 \tag{31.9}$$

According to Eq. 31.9, "$\bar{P}$" is influenced by the scale parameter of Weibull distribution and rotor diameter.

Evaluation of CPU

The CPU is an underlying element in choosing a WECS, which attracts an especial attention since it looks for exploiting small wind turbines for household/commercial and agricultural consumptions. To calculate the CPU, first present value of WECS costs and then the total amount of generated power should be determined. In most papers dealing with this issue, "P_r" is used to calculate the amount of power generated and the CPU, as well [16, 30]. But since calculating the power generated from the turbine is done based on wind speed, which is a variable, it is better to use "$\bar{P}$" as an appropriate criteria. In fact, wind speed varies due to geographical circumstances of installation region and also the hub height of turbine, during day and night hours. It can be inferred from Eq. 31.6 that the variability of wind speed results in variability of power generated by turbine; consequently, using "P_r" to estimate the CPU, which is not influenced by changes in WECS, cannot be justified logically. The CPU is calculated according to Eq. 31.10:

$$CPU = \frac{PVC}{E_{out}} \tag{31.10}$$

In Eq. 31.10, PVC stands for the Present Value of WECS Cost and "E_{out}" indicates total output energy from the wind turbine, which is calculated as follows.

Total output of electrical energy is defined as Eq. 31.11, based on the maximum capacity of the turbine and the amount of energy that it can generate.

$$\bar{E}_{out} = C_f \bar{E} \tag{31.11}$$

In Eq. 31.11, "C_f" is turbine capacity factor and "$\bar{E}$" regards the average amount of energy that can be generated or average output energy. The capacity factor of a wind turbine represents the actual energy output for the given system and conditions as a proportion of a rated power output over an entire rate [32]. Value of this factor is variable in the range from 10 to 50 % and in modern wind machines this will reach 20–35 % [33]. The capacity factor of each wind turbine can be calculated using Eq. 31.12 [34].

$$C_f = \frac{\exp\left(-\left(\frac{V_i}{c}\right)^k\right) - \exp\left(-\left(\frac{V_r}{c}\right)^k\right)}{\left(\frac{V_r}{c}\right)^k - \left(\frac{V_i}{c}\right)^k} - \exp\left(-\left(\frac{V_o}{c}\right)^k\right) \tag{31.12}$$

In Eq. 31.12, "k" and "c" are the parameters of wind speed Weibull distribution and "V_i", "V_r" and "V_o" refer to minimum, rated, and maximum speed of the wind, respectively.

For the 20 year life cycle assumed in this paper, the average output energy, "$\bar{E}$", considering "$\bar{P}$" should be defined according to the investigation period as shown in Eq. 31.13.

$$\bar{E} = 20 \times 365 \times 24 \times \bar{P} \tag{31.13}$$

In order to define CPU, it is necessary to calculate PVC of WECS. Present value technique is one of the most important and premium techniques for assessing projects economically. To specify PVC, all costs relevant to WECS should be categorized first and then each one should be determined individually. These are divided into purchasing, accessories, establishment, and set up costs. Of course, operational and maintenance costs are incurred during the utilization. Therefore, PVC is calculated according to the Eq. 31.14 [16], in which, "t" shows the life cycle (20 years) and "i" is the index of interest rate which equals to 15 %.

$$PVC = I + C_{omr}\left[\frac{(1+i)^t - 1}{i(1+i)^t}\right] - S\left[\frac{1}{(1+i)^t}\right] \tag{31.14}$$

Each of the cost types used in (14) and the assumptions are explained below.

"I": Investment costs including equipment and facilities' (turbine, converter, and battery) costs, execution costs (to establish the whole system), and connection costs (i.e. the expenditure for connecting cables and so on) which are considered as a fixed portion of wind price (30 %).

"C_{omr}": encompasses operational and maintenance costs of utilizing WECS in the given period. It is calculated as a percentage of turbine annual cost (which can be specified by division of turbine price by its useful life).

"S": regards scrap value that the whole WECS has at the end of its life. Scrap value is specified based on a fixed portion of establishment and purchase costs of turbine (10 %).

Therefore, by clarifying values of both PVC and "E_{out}", amount of CPU of a WECS is accessible.

In the next section, methodology of determination and evaluation of mathematical equations that demonstrate relation between CPU and rotor diameter and also hub height is explained.

Table 31.3 Specifications of five small wind turbines

Pr (kw)	D (m)	Vi (m/s)	Vr (m/s)	Vo (m/s)
2	1.5	2.1	12	40
3	2	2.1	12	40
5	3.	1.2	12	60
7	3.2	2.1	12	65
10	4	2.1	12	65

31.3 Mathematical Relation

The purpose of this section is development of a relation with the help of which all characteristics of WECS will be defined, attending families' income influence on payment for CPU. According to Eq. 31.10, CPU depends on PVC, on one hand and "E_{out}" on the other hand. PVC is influenced by physical characteristics of WECS, whose most important part is the wind turbine. Total output of the electrical energy is calculated due to the average energy which is generated by average power of turbine depending on rotor diameter and Weibull distribution scale parameters of wind speed according to Eq. 31.9. In other words, it can be stated that the CPU depends on two parameters, turbine rotor diameter, used to specify turbine size, and Weibull distribution scale parameter of wind speed. As the scale parameter is a function of the height from the sea level, its value varies by different heights based on Eq. 31.15 [11]:

$$c_2 = c_1 \left(\frac{h_2}{h_1} \right)^{\frac{1}{7}} \tag{31.15}$$

In Eq. 31.15, "c_1" pertains to the quantity of scale parameter of wind speed distribution in the height "h_1" = 10 "m" and "c_2" refers to the same issue in the height "h_2" which should be calculated. Therefore, changes in the rotor diameter and the hub height cause changes in PVC and "E_{out}" and finally CPU.

Recognizing the equation, relation between CPU and hub height is first determined considering changes in hub height, assuming rotor diameter to be fixed. For sensitivity analysis of estimation, five various turbines (with various rotor diameters and hub heights) at each four locations are employed (Tables 31.4, 31.5, 31.6 and 31.7). Specifications of the turbines are summarized in Table 31.3 [35–38].

CPU is reduced considering the results demonstrated by Figs. 31.3, 31.4, 31.5 and 31.6, which reflect behavior of CPU affected by increasing the value of H for four locations, assuming rotor diameter to be fixed. Referring to each curve of these figures, a four degree polynomial approximation can be concluded. This approximation is so efficient that it provides a higher correlation coefficient for this relation, compared with the other approximations (≈1). In order to reduce error in estimation, because of noticeable distance between curves drawn for H = 4, the relation is formulated for H ≤ 3.2 m. Thus, result of this propriety can be showed as Eq. 31.16.

Table 31.4 Calculation of CPU for the location Jarandagh

Rated power	H_{hub} (m)	D (m)	C (m/s)	k	Vi	Vr	Vo	Cf	$\overline{P}$(w)	$\overline{E}$(kw)	E_{out} (kw)	PVC (€)	CPU (€/kw)	CPU (Rial/kw)
2	10	1.5	6.1	1.91	1.2	12	40	0.260	404.9	70931.7	18449.7	6022.0	0.3264	5548.8
	12		6.3					0.272	437.8	76696.5	20897.2		0.2882	4899.0
	15		6.5					0.288	481.7	84393.3	24311.1		0.2477	4211.0
	18		6.7					0.301	520.8	91252.1	27483.5		0.2191	3724.9
	20		6.8					0.309	544.9	95467.0	29489.9		0.2042	3471.5
3	10	2	6.1	1.91	1.2	12	40	0.260	719.8	126100.9	32799.5	10189.2	0.3107	5281.1
	12		6.3					0.272	778.2	136349.3	37150.6		0.2743	4662.6
	15		6.5					0.288	856.4	150032.6	43219.6		0.2358	4007.8
	18		6.7					0.301	925.9	162226.0	48859.5		0.2085	3545.2
	20		6.8					0.309	968.7	169719.2	52426.4		0.1944	3304.0
5	10	3	6.1	1.91	1.2	12	60	0.260	1619.4	283726.9	73798.8	13287.9	0.1801	3061.0
	12		6.3					0.272	1751.1	306785.9	83588.8		0.1590	2702.5
	15		6.5					0.288	1926.8	337573.4	97244.2		0.1366	2323.0
	18		6.7					0.301	2083.4	365008.5	109933.9		0.1209	2054.8
	20		6.8					0.309	2179.6	381868.1	117959.4		0.1126	1915.0
7	10	3.2	6.1	1.91	1.2	12	65	0.260	1842.6	322818.2	83966.7	17150.0	0.2042	3472.2
	12		6.3					0.272	1992.3	349054.1	95105.5		0.1803	3065.5
	15		6.5					0.288	2192.3	384083.5	110642.3		0.1550	2635.1
	18		6.7					0.301	2370.4	415298.6	125080.3		0.1371	2330.9
	20		6.8					0.309	2479.9	434481.0	134211.6		0.1278	2172.3
10	10	4	6.1	1.91	1.2	12	65	0.260	719.8	126100.9	32799.5	32628.0	0.9948	16911.1
	12		6.3					0.272	778.2	136349.3	37150.6		0.8783	14930.5
	15		6.5					0.288	856.4	150032.6	43219.6		0.7549	12833.9
	18		6.7					0.301	925.9	162226.0	48859.5		0.6678	11352.5
	20		6.8					0.309	968.7	169719.2	52426.4		0.6224	10580.1

Table 31.5 Calculation of CPU for the location Nehbandan

Rated power	H_{hub} (m)	D (m)	C (m/s)	k	Vi	Vr	Vo	Cf	$\overline{P}$(w)	$\overline{E}$(kw)	E_{out} (kw)	PVC (€)	CPU (€/kw)	CPU (Rial/kw)
2	10	1.5	5.7	1.69	1.2	12	40	0.260	323.7	56706.3	14739.1	6022.0	0.4086	6945.8
	12		5.8					0.271	350.0	61314.9	16619.4		0.3623	6159.9
	15		6.0					0.285	385.1	67468.2	19231.2		0.3131	5323.3
	18		6.2					0.297	416.4	72951.4	21649.0		0.2782	4728.8
	20		6.3					0.304	435.6	76321.0	23174.3		0.2599	4417.6
3	10	2	5.7	1.69	1.2	12	40	0.260	575.4	100811.2	26202.8	10189.2	0.3889	6610.6
	12		5.8					0.271	622.2	109004.3	29545.6		0.3449	5862.7
	15		6.0					0.285	684.6	119943.4	34188.9		0.2980	5066.5
	18		6.2					0.297	740.2	129691.4	38487.2		0.2647	4500.6
	20		6.3					0.304	774.4	135681.8	41198.7		0.2473	4204.4
5	10	3	5.7	1.69	1.2	12	60	0.260	1294.7	226825.2	58956.4	13287.9	0.2254	3831.6
	12		5.8					0.271	1399.9	245259.6	66477.7		0.1999	3398.1
	15		6.0					0.285	1540.4	269872.7	76925.0		0.1727	2936.6
	18		6.2					0.297	1665.6	291805.7	86596.1		0.1534	2608.6
	20		6.3					0.304	1742.5	305284.1	92697.2		0.1433	2436.9
7	10	3.2	5.7	1.69	1.2	12	65	0.260	1473.0	258076.7	67079.3	17150.0	0.2557	4346.3
	12		5.8					0.271	1592.8	279051.0	75636.9		0.2267	3854.6
	15		6.0					0.285	1752.6	307055.2	87523.5		0.1959	3331.1
	18		6.2					0.297	1895.0	332010.0	98527.1		0.1741	2959.1
	20		6.3					0.304	1982.6	347345.4	105468.8		0.1626	2764.3
10	10	4	5.7	1.69	1.2	12	65	0.260	575.4	100811.2	26202.8	32628.0	1.2452	21168.6
	12		5.8					0.271	622.2	109004.3	29545.6		1.1043	18773.6
	15		6.0					0.285	684.6	119943.4	34188.9		0.9543	16223.9
	18		6.2					0.297	740.2	129691.4	38487.2		0.8478	14412.0
	20		6.3					0.304	774.4	135681.8	41198.7		0.7920	13463.4

Table 31.6 Calculation of CPU for the location Hadadeh

Rated power	H_{hub} (m)	D (m)	C (m/s)	k	Vi	Vr	Vo	Cf	$\overline{P}$(w)	$\overline{E}$(kw)	E_{out} (kw)	PVC (€)	CPU (€/kw)	CPU (Rial/kw)
2	10	1.5	5.1	1.5	1.2	12	40	0.249	237.1	41533.3	10340.5	6022.0	0.5824	9900.3
	12		5.3					0.259	256.3	44908.8	11623.9		0.5181	8807.2
	15		5.4					0.271	282.1	49415.6	13401.9		0.4493	7638.8
	18		5.6					0.282	305.0	53431.7	15043.9		0.4003	6805.0
	20		5.7					0.288	319.1	55899.6	16078.1		0.3745	6367.3
3	10	2	5.1	1.5	1.2	12	40	0.249	421.4	73836.9	18383.2	10189.2	0.5543	9422.6
	12		5.3					0.259	455.7	79837.8	20664.7		0.4931	8382.3
	15		5.4					0.271	501.4	87849.9	23825.6		0.4277	7270.2
	18		5.6					0.282	542.2	94989.6	26744.7		0.3810	6476.7
	20		5.7					0.288	567.2	99377.1	28583.4		0.3565	6060.1
5	10	3	5.1	1.5	1.2	12	60	0.249	948.2	166133.1	41362.1	13287.9	0.3213	5461.4
	12		5.3					0.259	1025.3	179635.0	46495.6		0.2858	4858.4
	15		5.4					0.271	1128.2	197662.3	53607.5		0.2479	4213.9
	18		5.6					0.282	1219.9	213726.6	60175.5		0.2208	3753.9
	20		5.7					0.288	1276.2	223598.6	64312.6		0.2066	3512.4
7	10	3.2	5.1	1.5	1.2	12	65	0.249	1078.9	189022.5	47060.9	17150.0	0.3644	6195.2
	12		5.3					0.259	1166.6	204384.7	52901.7		0.3242	5511.2
	15		5.4					0.271	1283.7	224895.8	60993.5		0.2812	4780.0
	18		5.6					0.282	1388.0	243173.4	68466.4		0.2505	4258.3
	20		5.7					0.288	1452.1	254405.5	73173.4		0.2344	3984.4
10	10	4	5.1	1.5	1.2	12	65	0.249	421.4	73836.9	18383.2	32628.0	1.7749	30173.1
	12		5.3					0.259	455.7	79837.8	20664.7		1.5789	26841.7
	15		5.4					0.271	501.4	87849.9	23825.6		1.3695	23280.7
	18		5.6					0.282	542.2	94989.6	26744.7		1.2200	20739.7
	20		5.7					0.288	567.2	99377.1	28583.4		1.1415	19405.6

Table 31.7 Calculation of CPU for the location Morche-Khort

Rated power	H_{hub} (m)	D (m)	C (m/s)	k	Vi	Vr	Vo	Cf	$\overline{P}$(w)	$\overline{E}$(kw)	E_{out} (kw)	PVC (€)	CPU (€/kw)	CPU (Rial/kw)
2	10	1.5	6.1	1.44	1.2	12	40	0.326	395.0	69207.4	22562.2	6022.0	0.2669	4537.4
	12		6.2					0.337	427.1	74832.0	25209.9		0.2389	4060.9
	15		6.4					0.350	470.0	82341.7	28850.3		0.2087	3548.5
	18		6.6					0.362	508.2	89033.8	32187.3		0.1871	3180.6
	20		6.7					0.368	531.7	93146.2	34278.2		0.1757	2986.6
3	10	2	6.1	1.44	1.2	12	40	0.326	702.3	123035.3	40110.5	10189.2	0.2540	4318.5
	12		6.2					0.337	759.3	133034.6	44817.5		0.2273	3864.9
	15		6.4					0.350	835.5	146385.3	51289.4		0.1987	3377.2
	18		6.6					0.362	903.4	158282.3	57221.8		0.1781	3027.1
	20		6.7					0.368	945.2	165593.3	60939.1		0.1672	2842.5
5	10	3	6.1	1.44	1.2	12	60	0.326	1580.1	276829.5	90248.7	13287.9	0.1472	2503.0
	12		6.2					0.337	1708.5	299327.9	100839.4		0.1318	2240.1
	15		6.4					0.350	1879.9	329367.0	115401.1		0.1151	1957.5
	18		6.6					0.362	2032.7	356135.2	128749.1		0.1032	1754.5
	20		6.7					0.368	2126.6	372584.9	137112.9		0.0969	1647.5
7	10	3.2	6.1	1.44	1.2	12	65	0.326	1797.8	314970.4	102682.9	17150.0	0.1670	2839.3
	12		6.2					0.337	1943.9	340568.6	114732.8		0.1495	2541.1
	15		6.4					0.350	2139.0	374746.4	131300.8		0.1306	2220.5
	18		6.6					0.362	2312.8	405202.7	146487.9		0.1171	1990.3
	20		6.7					0.368	2419.6	423918.8	156004.0		0.1099	1868.9
10	10	4	6.1	1.44	1.2	12	65	0.326	702.3	123035.3	40110.5	32628.0	0.8135	13828.7
	12		6.2					0.337	759.3	133034.6	44817.5		0.7280	12376.3
	15		6.4					0.350	835.5	146385.3	51289.4		0.6362	10814.7
	18		6.6					0.362	903.4	158282.3	57221.8		0.5702	9693.4
	20		6.7					0.368	945.2	165593.3	60939.1		0.5354	9102.2

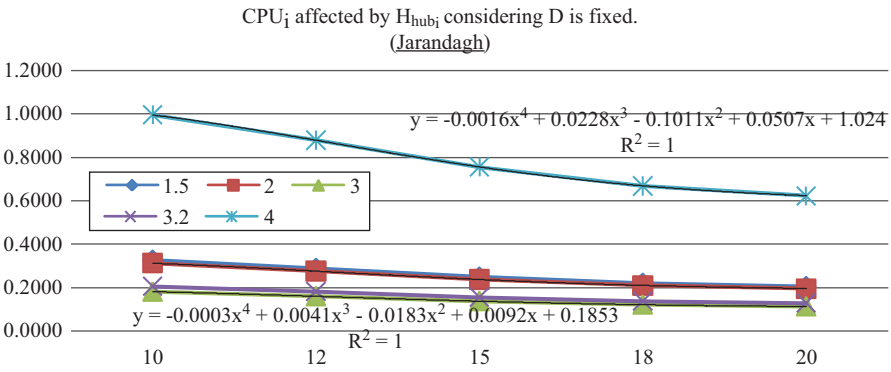

Fig. 31.3 CPUi affected by Hi considering D to be fixed for the locations Jarandagh, Nehbandan, Hadadeh and Morche-Khort respectively

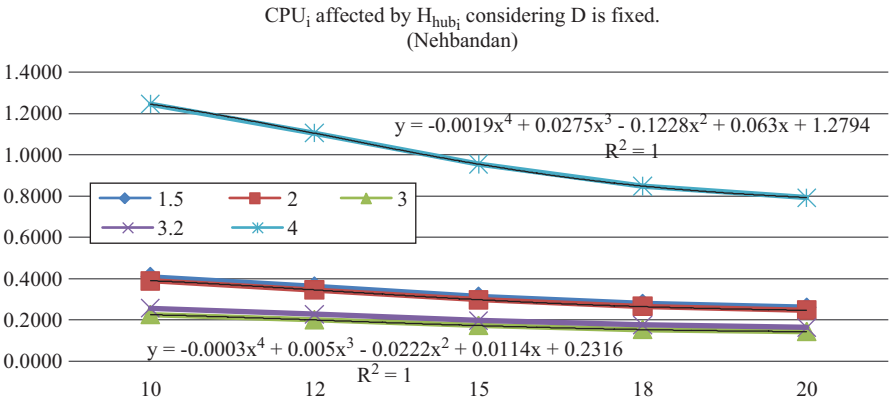

Fig. 31.4 CPUi affected by Hi considering D to be fixed for the locations Jarandagh, Nehbandan, Hadadeh and Morche-Khort respectively

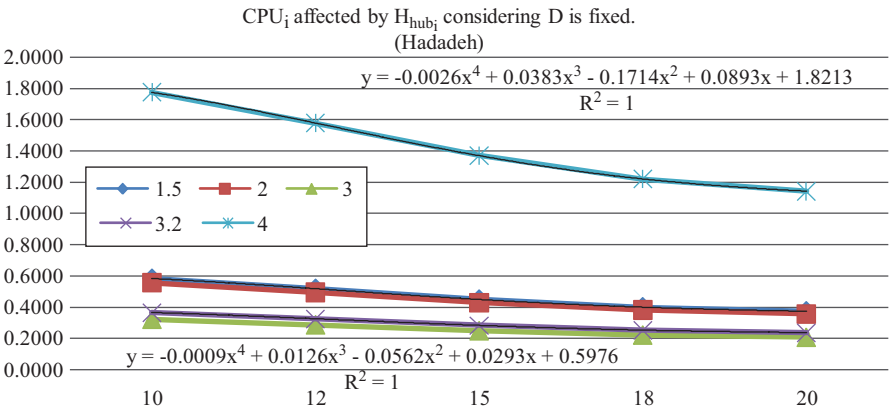

Fig. 31.5 CPUi affected by Hi considering D to be fixed for the locations Jarandagh, Nehbandan, Hadadeh and Morche-Khort respectively

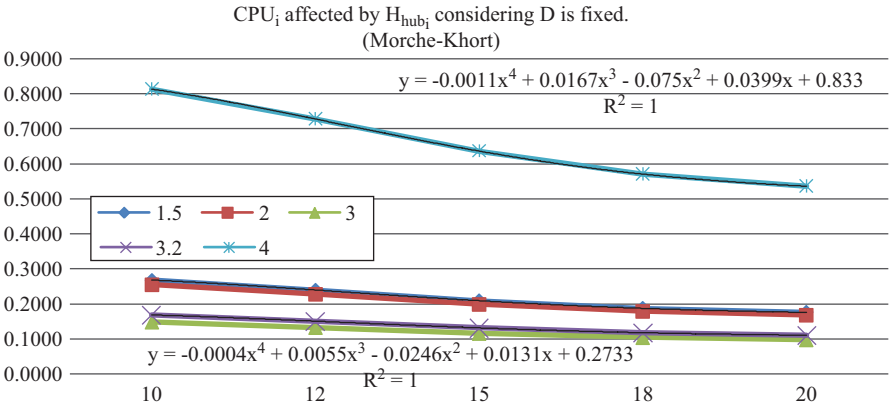

Fig. 31.6 CPUi affected by Hi considering D to be fixed for the locations Jarandagh, Nehbandan, Hadadeh and Morche-Khort respectively

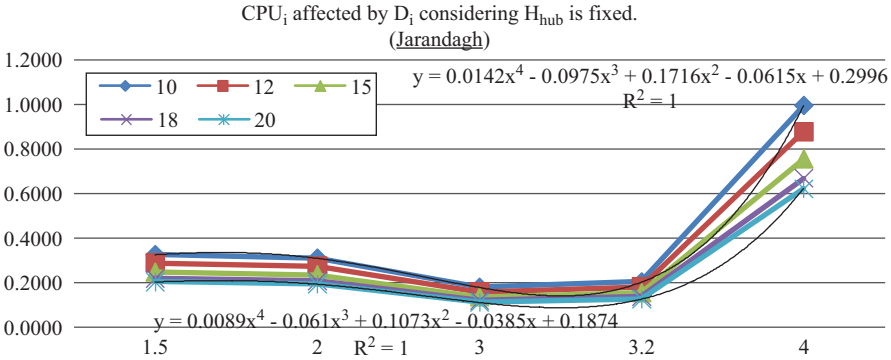

Fig. 31.7 CPUi affected by Di considering H to be fixed for the locations Jarandagh, Nehbandan, Hadadeh and Morche-Khort respectively

$$CPU = -0.0005H^4 + 0.0068H^3 - 0.0302H^2 + 0.0156H + 0.319 \qquad (31.16)$$

Now, the formula is derived for different Rotor diameters. Results are shown in Figs. 31.7, 31.8, 31.9 and 31.10. To define the relationship between CPU and rotor diameter, four degree polynomial relations led to better approximations (with correlation coefficient approximately equal to 1). The relation of this step is depicted by Eq. 31.17.

$$CPU = 0.142D^4 - 0.097D^3 + 0.157D^2 - 0.0612D + 0.2981 \qquad (31.17)$$

Therefore, CPU separately relates to both Eqs. 31.16 and 31.17. On the other hand, if one of the two is considered to be fixed, each of the equations can be usable.

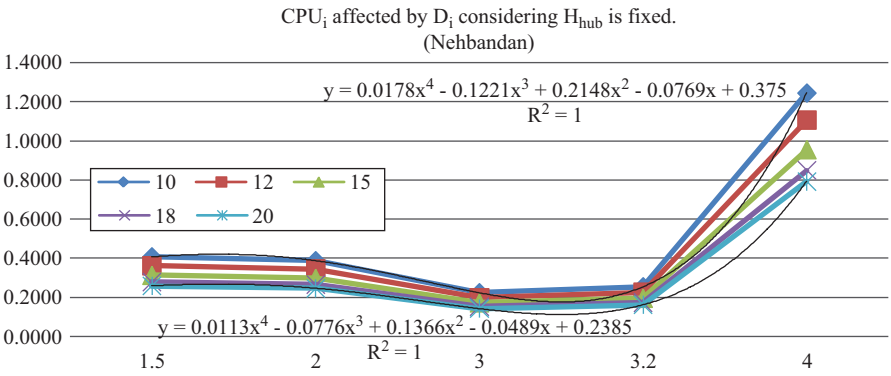

Fig. 31.8 CPUi affected by Di considering H to be fixed for the locations Jarandagh, Nehbandan, Hadadeh and Morche-Khort respectively

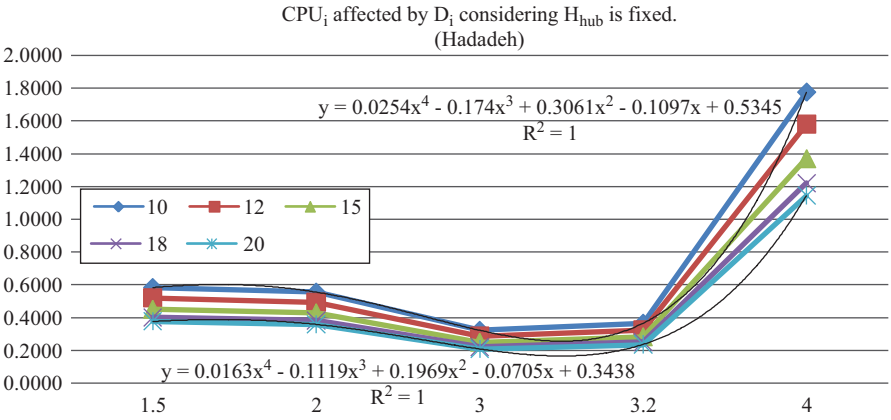

Fig. 31.9 CPUi affected by Di considering H to be fixed for the locations Jarandagh, Nehbandan, Hadadeh and Morche-Khort respectively

But for investigating CPU behaviour versus the two parameters concurrently and estimation of the relation, we have applied the mathematical laboratory software, MATLAB. First, this investigation is performed for each of the locations, whose results are exhibited in Figs. 31.11, 31.12, 31.13 and 31.14. These four figures are respectively presented with statistical details including correlation coefficient (r-square) and sum of them duo to error (SSE) as follows.

As it is clear, variation in value of CPU in relation to each of the parameters, considering value of the other parameter to be fixed, is showing precisely the same manner related to Figs. 31.3, 31.4, 31.5, 31.6, 31.7, 31.8, 31.9 and 31.10 for every locations.

Since value of CPU is in change by the two parameters for every installation locations, it is necessary to define an equation including the three variables CPU,

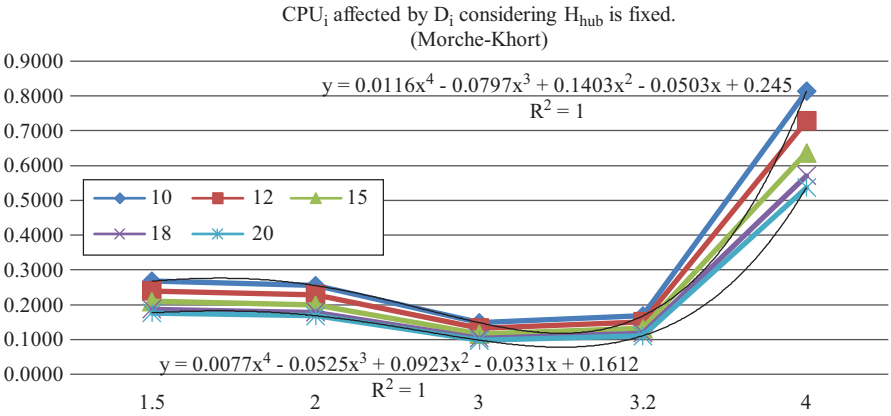

Fig. 31.10 CPUi affected by Di considering H to be fixed for the locations Jarandagh, Nehbandan, Hadadeh and Morche-Khort respectively

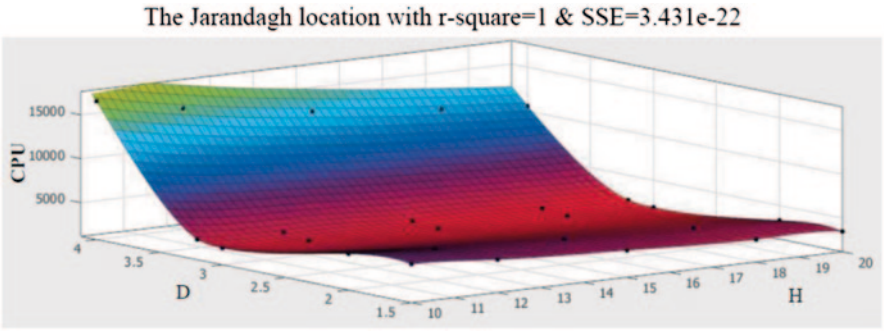

Fig. 31.11 CPUi affected by Di considering H to be fixed for the locations Jarandagh, Nehbandan, Hadadeh and Morche-Khort respectively

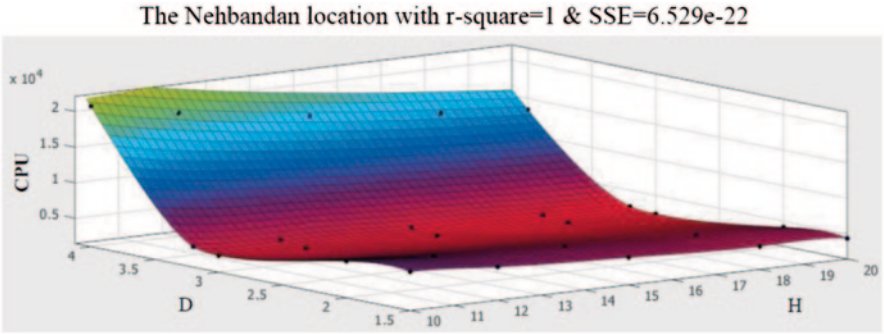

Fig. 31.12 CPUi affected by Di considering H to be fixed for the locations Jarandagh, Nehbandan, Hadadeh and Morche-Khort respectively

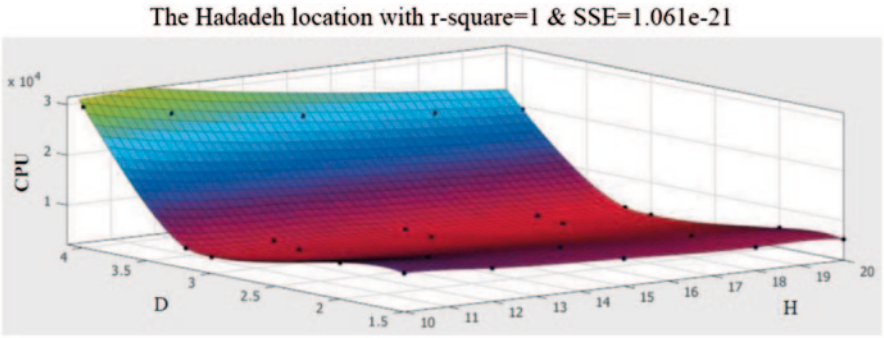

Fig. 31.13 CPUi affected by Di considering H to be fixed for the locations Jarandagh, Nehbandan, Hadadeh and Morche-Khort respectively

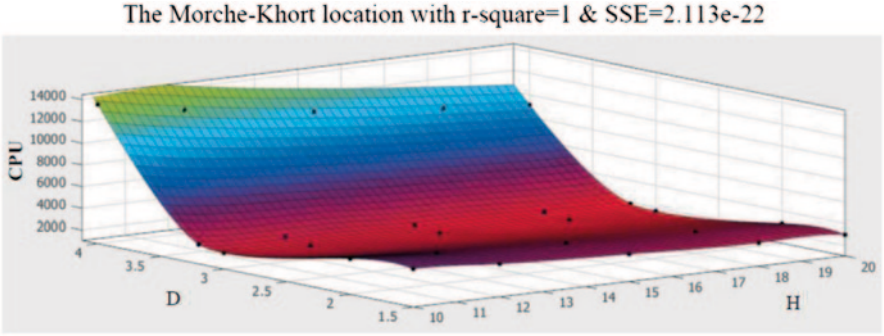

Fig. 31.14 CPUi affected by Di considering H to be fixed for the locations Jarandagh, Nehbandan, Hadadeh and Morche-Khort respectively

D and H. It should be said that because of noticeable distance between points for H = 4 comparing to each other's and the resulting decrease in estimation error, the relation is formulated for H ≤ 3.2 m. Using the MATLAB software, the equation regarding the most conformity (r-square = 0.99999 and FitStdErr = 0.35917932) is defined as below.

$$\ln(CPU) = a_1 + a_2 D_2 + a_3 D(\ln(D)) + a_4 D^3 + a_5 (\ln(D))^2 + a_6 H^{0.5} + a_7 \ln(H) + a_8 \left(\frac{\ln(H)}{H}\right) \tag{31.18}$$

$a_1 = 0.40896$
$a_2 = 8.38018$
$a_3 = -4.00601$
$a_4 = 0.32861$
$a_5 = -27.78753$

$a_6 = 0.22034$
$a_7 = -1.50483$
$a_8 = -4.1781$

Therefore, defining characteristics of WECS, first the cost of each kWh of electricity consumed by family is substituted by CPU. This cost is calculated for each family by dividing total consumed power price on the bill by quantity of consumed units. Then, using this value as CPU, the hub height and rotor diameter can be determined using Eq. 31.18 in relation to each other. Placing value of CPU in this equation, gives us some reasonable values for the both parameters regarding standard range of these parameter values for small wind turbines. Having these values and referring to mentioned equations, other technical information of a specific WECS and also its investment cost, for each pair of the parameter values, will be easily determined.

This relation is very suitable and valuable because of preparing necessary data for establishment of a WECS for each consumer. Besides, this is usable for other applications of wind turbines and can help consumers, as an analytical tool, to be informed about appropriate details of WECS. Also, referring to the last column of Tables 31.3, 31.4, 31.5 and 31.6 difference between CPU of power generated using wind turbines and the cost of power generated by hydro power plants without subsidy (in minimum 750–800 Rials per kWh) is too little. Of course, this can be reduced by increasing rotor diameter and hub height of wind turbine.

Due to elimination of transmission, distribution of electricity and maintenance costs, using small wind turbines in suburb of a city or in rural areas is economically efficient. Furthermore, if wind turbine is installed on the roof of tall buildings, cost of hub height and following the PVC of WECS can be decreased. Considering these facts, generating power using wind turbines is more feasible compared to non-renewable power plants and it can take the place of central power plants extension, even as distributed generation.

Consequence

It is necessary to extend utilization of renewable energies due to mortality of fossil fuels and environmental pollution. A type of energy that can be used for power generation is wind energy. This paper that is developed in realm of utilization of small wind turbines to distributed generation power required in household/commercial and agricultural sectors, presents a decision-making process to technically define characteristics of WECS and other criteria affecting it. Generally, two factors affecting CPU are identified as turbine attributes and climate conditions of installation location. Analyzing total energy output of WECS and CPU of generated power, rotor diameter and hub height are clarified as the main parameters influencing CPU. Mathematical relation between CPU versus rotor diameter and hub height as an essential tool to apply the process, is derived according to the analysis performed for four locations having different geographical and climate conditions with correlation

coefficient ≈1. Using this relation by substituting CPU of power consumed by family and defining distinct values of both rotor diameter and hub height of turbine, all information of different WECS related to each pair of the values, will be accessible and ultimately suitable WECS will be chosen by consumer regarding economical and other criteria. Besides, this relation is usable for each WECS contented by large wind turbines. Furthermore, comparing the calculated CPU by the CPU of power generated using current power plants, it is clear that employing WECS is economically and logically feasible. This is highlighted when WECS is established for supplying power required for rural residential or suburb gardens, which costs of transmission and distribution are removed.

Nomenclature

C	Scale parameter of Weibull distribution
K	Shape parameter of Weibull distribution
H	Hub height
D	Rotor diameter
P	Generated power
V	Wind speed
A	Area covered by rotating wind turbine blades
Cf	Turbine capacity factor
E	Generated energy
I	Investment cost
Comr	Operation, maintenance and repair costs
S	Scrap value
Ln	Natural logarithm function

Greek Symbols

P	Air density
Γ	Gamma function
Δ	Change

Subscript and Superscripts

N	Amount of total data
I	Sample member of total data
R	Rated quantity (ex: rated power)
M	Minimum quantity (ex: minimum generated power)
O	Maximum quantity (ex: maximum generated power)
Out	Output energy

Acronyms

WECS	Wind Energy Conversion System
CPU	Cost Per Unit
Exp	Exponential function
PVC	Present Value of WECS Cost

References

1. Bagheri Moghaddam N, Sayyed MM, Masoud N, Enayat AM, Hami Y (2011) Wind energy status of Iran: evaluating Iran's technological capability in manufacturing wind turbines. Renew Sustain Energy Rev 15:4200–4211
2. REN21 (2007) Global status report. www.ren21.net. Accessed10 Sept 2009
3. Seyit AA, Güler Ö (2010) Evaluation of wind energy investment interest and electricity generation cost analysis for Turkey. Appl Energy 87:2574–2580
4. Gokcek M, Mustafa SG (2009) Evaluation of electricity generation and energy cost of wind energy conversion systems (WECSs) in Central Turkey. Appl Energy 86:2731–2739
5. International Energy Agency (IEA) (2010) World energy outlook. OECD/IEA, Paris
6. World Wind Energy Association (WWEA) (2010) World wind energy report 2009. World Wind Energy Association, Bonn
7. Global Wind Energy Council (GWEC) (2010) Global wind energy outlook. Greenpeace International Amsterdam
8. Joselin herbert GM, Iniyan S, Sreevalsan E, Rajapandian S (2007) A review of wind energy technologies. Renew Sustain Energy Rev 11(6):1117–1145
9. Gong Li, Jing Shi (2012) Applications of bayesian methods in wind energy conversion systems. Renew Energy 43:1–8
10. American Wind Energy Association (AWEA) report (2002) The US Small Wind Turbine Industry, Roadmap. American Wind Energy Association, Colorado
11. Olayinka Ohunakin S, Joshua Ojolo S, Babatunde Ogunsina S, Rufus Dinrifo R (2012) Analysis of cost estimation and wind energy evaluation using wind energy conversion systems (WECS) for electricity generation in six selected high altitude locations in Nigeria. Energy Policy 48:594–600
12. Vlad C, Munteanu I, Iuliana BA, Ceangă E (2010) Output power maximization of low-power wind energy conversion systems revisited: possible control solutions Energy Convers Manage 51(2):305–310
13. Bansal RC, Bhatti TS, Kothari DP (2002) On some of the design aspects of wind energy conversion systems. Energy Convers Manage 43:2175–2187
14. Wenjuan Du, Wang HF, Cheng S, Wen JY, Dunn R (2011) Robustness of damping control implemented by energy storage systems installed in power systems. Int J Electric Power Energy System 33(1):35–42
15. Kaldellis JK (2008) Integrated electrification solution for autonomous electrical networks on the basis of RES and energy storage configurations. Energy Convers Manage 49(12):3708–3720
16. Bagiorgas HS, Assimakopoulos MN, Theoharopoulos D, Matthopoulos D, Mihalakakou GK (2007) Electricity generation using wind energy conversion systems in the area of Western Greece. Int J Energy Convers Manage 48(5):1640–1655
17. Abdelkafi A, Masmoudi A, Krichen L (2013) Experimental investigation on the performance of an autonomous wind energy conversion system. Electr Power Energy Syst 44(1):581–590
18. Clarke S (2003) Electricity Generation Using Small Wind Turbines at Your Home or Farm. Ministry of Agriculture Food and Rural Affairs. http://www.omafra.gov.on.ca/english/engineer/facts/03–047.htm. Accessed May 2011
19. Ahmed Shata AS, Hanitsch R (2008) Electricity generation and wind potential assessment at Hurghada; Egypt. Renew Energy 33:141–148
20. Rehman S (2004) Prospects of wind farm development in Saudi Arabia. Renew Energy 30(3):447–463
21. Naci CA (2003) Energy output estimation for small-scale wind power generators using weibull-representative wind data. J Wind Eng Ind Aerodyn 91:693–707
22. Rehman S, Halawnai TO, Mohandes M (2003) Wind power cost assessment at twenty locations in the kingdom of Saudi Arabia. Renew Energy 28:573–83

23. Statistical Centre of Iran (2010) http://www.amar.org.ir/Default.aspx?tabid=260. Accessed May 2011
24. Ghorashi AH, Rahimi A (2011) Renewable and non-renewable energy status in Iran: art of know-how and technology-gaps. Renew Sustain Energy 15:729–736
25. Fadai D (2007) The feasibility of manufacturing wind turbines in Iran. Renew Sustain Energy 11:536–542
26. Poje D, Cividini B (1988) Assessment of wind energy potential in Croatia. Solar Energy 41:543–554.
27. Madlener R, Latz J (2013) Economics of centralized and decentralized compressed air energy storage for enhanced grid integration of wind power. Appl Energy J 101(1):299–309
28. AL-Fawzan MA (2000) Methods for estimating the parameters of the weibull distribution. king abdulaziz city for science and technology, Saudi Arabia
29. Barber DA, Court A, Hewson EW (1977) Wind characteristics, Wind Energy Over the United States. Final Report; Wind Energy Mission Analysis, ERDA Contract AT (04–3)-1075, Lockheed-California Company; Chapter 3
30. Ahmed Shata AS, Hanitsch R (2006) Evaluation of wind energy potential and electricity generation on the coast of mediterranean sea in Egypt. J Renew Energy 31:1183–1202
31. Gupta BK (1986) Weibull parameters for annual and monthly wind speed distributions for five locations in India. J Sol Energy 37(6):469–471
32 Crawford RH (2009) Life cycle energy and greenhouse emissions analysis of wind turbines and the effect of size on energy yield. Renew Sustain Energy Rev 13:2653–2660
33. El-Mallah A, Soltan AM (1989) A nomogram for estimating capacity factors of wind turbines using site and machine characteristics. Sol Wind Technol 6:633–635
34. Lenzen M, Munksgaard J (2002) Energy and CO2 life cycle analyses of wind turbines—review and applications. Renew Energy 26:339–362
35. Talon turbine prices, http://www.magnet4sale.com/Wind-Power/Talon wind turbine prices (in $). Accessed May 2011
36. Turbine Prices, http://www.allsmallwindturbines.com/all prices of related turbines (in €). Accessed May 2011
37. Proven turbine prices, http://www.provenenergy.com/Wind turbine characteristics and Proven price list (in GBP). Accessed May 2011
38. Fortis turbine prices, http://www.fortiswindenergy.com/eng/prices.asp Fortis prices of complete systems for utility (in €). Accessed May 2011
39. Sahin AZ, Aksakal A (1998) Wind power energy potential at the north-eastern region of Saudi Arabia. J Renew Energy 14:435–440
40. Renewable Energy Organization of Iran (SUNA) (2010) http://www.suna.org.ir/fa/ationoffice/windenergyoffice/windatlasmap. Accessed May 2011

Chapter 32
An Integrated Monitoring Framework for Geothermal Space-Heating Systems in Residential Buildings, Fort McMurray

Xinming Li, Tanzia Sharmin, Hasan Ufuk Gökçe, Mustafa Gul, Mohammed Al-Hussein and David Morrow

Abstract Energy saving is a significant factor in heating system design. Geothermal systems are considered as an effective means to save energy and reduce potential environmental footprint through eliminating greenhouse effects. This paper presents a proposed integrated monitoring framework developed to use geothermal heating systems efficiently. The proposed framework includes a systematic approach to understanding geothermal systems, which is tested on a real-life project in Fort McMurray, Alberta, Canada, where heating is the major contributor to energy consumption. This project utilizes a geothermal system as the main heating system. The main challenges in the case study are that (1) a geothermal system in this project is not designed as cooling system to recover heat from buildings in summer and (2) Fort McMurray has extreme dry-cold weather. To overcome these challenges, the proposed geothermal system is combined with solar systems, drain water heat recovery (DWHR) systems, and conventional electric or natural gas energy for space-heating. In addition, a make-up air system is also installed to improve indoor air quality.

H. U. Gökçe (✉) · X. Li · T. Sharmin · M. Gul
Department of Civil and Environmental Engineering Hole School of Construction, University of Alberta, Edmonton, Canada
e-mail: ufuk.gokce@eos-energy-solutions.de; ufuk@ualberta.ca

T. Sharmin
e-mail: tanzia@ualberta.ca

X. Li
e-mail: xinming1@ualberta.ca

M. Gul
e-mail: mustafa.gul@ualberta.ca

M. Al-Hussein
NSERC Industrial Research Chair in the Industrialization of Building Construction, Department of Civil and Environmental Engineering Hole School of Construction, University of Alberta, Edmonton, Canada
e-mail: malhussein@ualberta.ca

D. Morrow
Hydraft Development Services Inc., Edmonton, Canada
e-mail: david.morrow@shaw.ca

I. Dincer et al. (eds.), *Progress in Sustainable Energy Technologies: Generating Renewable Energy,* DOI 10.1007/978-3-319-07896-0_32,

This paper first researches geothermal systems in the context of energy saving and then compares typical geothermal system practices with the proposed strategy. The advantages of such an integrated design are intuitively clear after comparing the typical usage of geothermal system and the usage in the proposed integrated system. It is concluded that this strategy can extend the lifetime of a geothermal system, provide significantly more energy, and become more energy efficient. The research results will be validated through monitoring systems, data collection, and thermal energy calculations.

Since this is a multi-disciplinary long-term project with a long period, sensors are used to monitor the integrated heating system performance. The resulting data is analyzed to justify the proposed integrated system through estimating thermal energy generated by each heating system, and evaluating the efficiency of each system. Thermocouple and pressure sensors have been located and systems are still being monitored. However, additional sensors to monitor temperature difference and pipe flow rate are still required. Therefore, this paper suggests a new design of monitoring which incorporates additional sensors. After data collection and calculations are completed, the thermal energy generated by each system and Coefficient of Performance (COP) of the heat pumps are determined. Calculations and equation derivations are specified in this paper. Ultimately, this paper demonstrates the essential future of the proposed system and suggests adjustments for future heating system designs in order to improve energy efficiency.

Keywords Geothermal · Integrated systems · Energy efficient · Monitoring · Thermal energy generation

32.1 Introduction

Around 47% of ground thermal energy is absorbed from the sun [1]. This thermal energy stored in the ground displays in diverse ways. More specifically, the earth surface temperature fluctuates, while the ground temperature at shallow depth remains constant for years [2]. The main part of the geothermal system,the geothermal underground heat exchanger or ground loop, uses this shallow ground as an energy resource and water fluid as the transport medium. The underground temperature is warmer than the outside air temperature in winter, but cooler than the outside air temperature in summer. Water flows through a buried piping arrangement, storing heat, and releasing it into the soil under the building site. A low-power circulating pump circulates the fluid. In winter, a geothermal system can extract enough heat from shallow ground to provide heating for houses. In summer, the system is reversed to transfer heat out of the building through using cooler ground as a heat sink [3].

Underground heat exchangers can be further configured as either open loop or closed loop. Open loop directly uses surface or underground water sources as a heat source. Normally, this operation can be completed with lower costs and less

loss during heat transfer. However, space limits usage of the open loop, and water usually causes corrosion later in the system [4]. The closed loop circulates water through its pipe, which can be installed either vertically or horizontally. The vertical closed loop is widely used since it is not limited by surface area. However, in this system, initial excavation costs are generally high [4]. In this paper, the case study uses a closed loop underground heat exchanger due to space limitations.

Geothermal systems also have two other components: a heat pump and distribution system. The heat pump is operated based on a vapor-compression refrigeration cycle [5, 6]. During this cycle, the pump effectively raises heat from the lower temperature in the earth source to a higher temperature through using electrical power input to drive the compressor. The lifespan of these mechanical parts can be around 50 years [7]. Heat pumps are usually evaluated by the coefficient of performance (COP). According to previous research, geothermal heat pumps have higher COP than regular heat pumps, such as air-source heat pumps [8, 9]. The COP of heat pumps is found to be in the range of 2.7–3.4 [10].

Geothermal energy is a reliable, abundant, and renewable resource. According to IGSHPA [7], preheating water from a ground loop can save 50 % in heating fees, decrease the repair fee, and reduce energy consumption by 20–50 %. Geothermal systems also reduce operating costs and CO_2 emissions when compared to traditional heating systems. More specifically, using geothermal energy reduces the dependence on fuel and eliminates CO_2 emissions [11]. According to previous research, in 2001, annual energy savings in fuel oil equaled 170 million barrels (25.4 million tons) and 24 million tons in carbon emissions to the atmosphere [12]. In 2010, the quantity of annual energy increased due to the proper use of geothermal energy (renewable resources). At this time, the annual energy savings equaled 268 million barrels (40 million tons) of fuel oil, which amounted to saving 38 million tons of carbon and eliminating 123 million tons of carbon dioxide emission annually when compared to fuel oil [13]. Compared to conventional Heating Ventilation Air Conditioning (HVAC) equipment, ground source heat pumps can consume upto 50 % less energy [1]. In terms of their usage in Canada, the high-temperature geothermal areas are predominantly located in the western part of the country, while geothermal heat pumps (GHPs) are now used in all Canadian provinces. Geothermal heat pumps are estimated to save around 600 million kWh (2160 TJ/year) of energy, and around 200,000 t in greenhouse gas emissions annually [12]. Due to these substantive cost savings, geothermal systems are expected to play an important role in heating in the future. The project analyzed in this paper is located in Fort McMurray, Alberta, in the western part of Canada, which has dry and extremely cold weather in winter.

Thermal energy is mainly used by space heating (20–23 %), geothermal heat pumps (32–12 %), and bathing and swimming(30–42 %). Thermal energy is also distributed to greenhouse and open-ground heating, industrial process heat, aquaculture pond and raceway heating, agricultural drying, snow melting and cooling [11, 12]. As suggested by these statistics, space heating requires a large amount of energy. Therefore it is essential to research space heating to increase energy savings in the future. Furthermore, the geothermal energy classified by source temperature is used for power production and also cooling or heating systems. High temperature

sources above 150 °C contribute to power production, while moderate temperatures between 90 and 150 °C and low temperatures below 90 °C are suitable for space heating or cooling [14]. The project presented in this paper uses low temperature sources for space heating.

This paper introduces an integrated monitoring framework for geothermal space-heating systems in residential buildings. These two residential buildings, called "Stony Mountain Plaza," are located in Fort McMurray, Alberta, Canada. The entire project is designed based on the principles of energy saving, high efficiency, and low operation cost. It was designed by modular construction in order to reduce construction cost and cycle time. This project utilizes a geothermal system as the main heating system. Ten geothermal vertical loops with a depth of 140 feet are installed under each building with a 5 inch borehole and 3/4 inch high density polyethylene (HDPE). It is important to note that a geothermal system is not designed as a cooling system to recover heat from buildings in summer and the extreme dry-cold weather in Fort McMurray consumes a large amount of energy for heating. To overcome these challenges, an integrated system is proposed to assist the geothermal system, including solar systems, drain water heat recovery systems, and boilers. A significant number of researchers have investigated geothermal systems; however, the number of integrated systems which use several sources is limited, and none are comparable to the integrated system investigated in this project.

Solar energy is a clean and renewable resource, and an essential component of sustainable energy in the future [15]. Radiant light and heat from the sun is a large amount of energy that can be utilized to heat water, space and so on. Energy can be collected by photovoltaic panels and solar thermal collectors. This energy could provide heat to the building as direct heating energy or store spare energy in summer in the earth, thus assisting the geothermal system. Another energy source used in this case study is drain water, due to the fact that most energy used to heat the residence transfers directly to wastewater. Drain water heat recovery extracts heat for free from the wastewater. Drain water travels down carrying away valuable energy with it. This system can recollect half of the energy and utilize it to preheat or heat cold water travelling to the water heater. Based on previous data, heating costs could be saved by up to 40 % [16], greenhouse gas emissions would be reduced, and in our project, the efficiency of the geothermal system would increase. Boilers are used in generating heat for residential purposes through heating water to a preset temperature and circulating that fluid throughout the home. Natural gas is widely used as an important energy resource, especially in Fort McMurray which has sufficient natural gas storage underground. This resource fuels boilers to generate energy and heat water, which can be used for various processes and heating applications. Make-up air is a large air handler usually located on the roof which absorbs outside fresh air into the building without circulating it. Not only does the air handler improve the indoor air quality but it also reduces the work load of the HVAC system and saves money on energy consumption. The main function of air handler is to balance the indoor air pressure through replacing the air that is released by exhaust systems. In addition, incoming cold air can be preheated by a heating loop, which reduces the heat transmission losses for the roof and diminishes the necessity to improve indoor temperature.

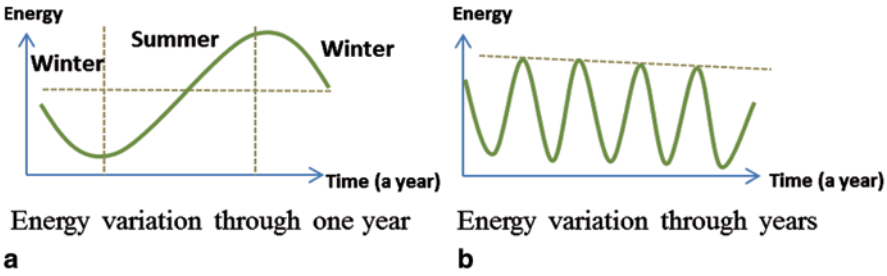

Fig. 32.1 Underground energy distribution by using geothermal as heating and cooling

The entire project is based on the concept of energy efficiency. Through analyzing the data obtained from monitoring, the efficiency of the individual systems, and how the systems work together can be displayed. As a result of this research, engineers are expected to obtain a valuable resource with which they can make further adjustments to heating systems.

32.2 Typical Practice for Geothermal System

Geothermal energy is a sustainable and renewable resource. This energy is cost-effective, reliable, and environmentally friendly. The main challenge of geothermal system is to keep annual energy balanced. Normally, the geothermal heat exchanger works in both winter and summer to make the energy absorbed equivalent to that rejected. Figure 32.1a shows the energy variance in the field over 1 year. The geothermal loop extracts heat from the earth when it is in heating mode in winter and the energy decreases. During summer, the field temperature rises because energy is transferred from the building back to the earth. Figure 32.1b demonstrates how energy in the field fluctuates and the wave range remains relatively consistent (sometimes a slight decrease is observed) throughout the year if the geothermal system works efficiently.

Unlike typical practice, the geothermal system in Stony Mountain Plaza, Fort McMurray is not designed to be a cooling system in summer, since heating is more necessary than cooling. The next section introduces the proposed strategy for this project.

32.3 Integrated Heating System

Since the geothermal system is not designed as cooling system in the Stony Mountain Plaza project, the temperature of the geothermal field decreases gradually, negatively impacting the geothermal system's efficiency. Figure 32.2 demonstrates how underground energy fluctuates under these conditions. As shown in Fig. 32.2a

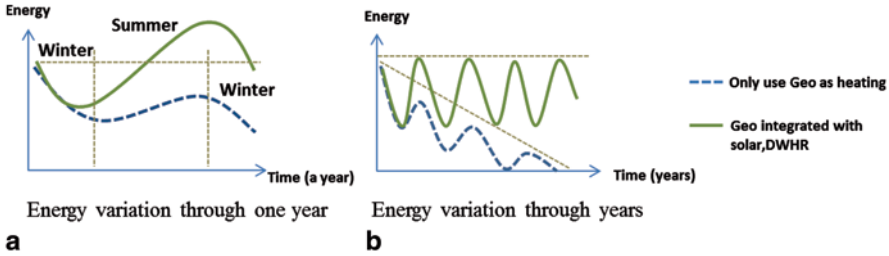

Fig. 32.2 Underground energy distributions by using integrated geothermal system

with the dotted line, if the heating mode is on in winter, the energy decreases, followed by only a slight increase in summer due to the characteristics of the earth's surface. Thus as years pass, the geothermal system may decline in effectiveness.

To address this challenge, solar and Drain Water Heat Recovery (DWHR) systems can be used to rebuild the geothermal system. This process involves directly injecting heat generated by a solar system into a geothermal loop. The DWHR recycled heat from drain water can also serve the geothermal loop and heat the building. Therefore, energy from both solar and intermittent drain water can be collected to recover the heat in the field. The aim of this approach is to use the integrated heating system to achieve long-term maintenance of the geothermal system. The long-term maintenance of this system is visually represented in Fig. 32.2a and b through converting the dotted lines into solid lines.

As demonstrated by the above discussion, combining the geothermal system with solar, drain water, and natural energy extends the lifetime of the geothermal system and provides significantly more thermal energy than an independent heating system. Coordinating these four main systems is expected to be energy efficient and provide thermal energy with a limited budget, space, and energy resources. The following sections provide a more detailed discussion of the integrated heating system for this project.

32.4 Heating System Schematic

Based on the previous analysis, the buildings under investigation are designed to be served by integrated systems,including the geothermal system, solar energy, drain water heat recovery, and conventional electric or natural gas energy, with limited space and budget. The geothermal system is the main heating system used in this project. The solar system directly transfers energy to the geothermal field, while the recovered heat from drain water will be delivered to the geothermal field, which links to water to water heat pumps. In addition to these energy sources, boilers are

designed to provide additional heat to the building through burning natural gas. To operate pumps in each water loop as driving power, electricity is also necessary. Once these systems are combined together, the temperature of the water storage tank is increased to a set point which satisfies the tenants' requirements. Figure 32.3 depicts the heating system schematic. It visually displays how the solar system, drain water heat recovery system, geothermal system, and boilers connect with the water tank and supply heat to the building.

32.5 Monitoring the Building Heating System

The objectives of monitoring are to estimate energy generation from each heating system and evaluate the heating efficiency of each system. The study has been designed to measure temperature, pressure, and/or water flow rate in the pipe to obtain results which will be discussed later in this paper.

The temperature and pressure sensors have already been placed in the basement to monitor each system. In Fig. 32.3, the TXX shows the location and tag of the temperature sensor, while the RXX represents the location and tag of the pressure sensor. Data is collected every 20 s. This process is illustrated in the paragraphs below, which discuss the data collection for the geothermal loop as an example.

Geothermal Loop

Ten underground geothermal loops serve as heat exchangers under each building. Four water to water heat pumps which gather heat from the drain water and solar system are located in the basement. On one side of the geothermal heat pump, a circulating water pipe connects to the geothermal underground loop, drain water heat recovery system, and solar system. On the other side of the heat pump, a water tank links to the heat pump through the supply water pipe and return water pipe. The set point temperature of the tank is 40 °C, which determines the temperature boundary to turn the heat pump and boiler 'on' or 'off'.

The locations of sensors are shown in the 3D model of the geothermal loop (Fig. 32.4). Table 32.1 displays the types of data which can be collected by monitoring the geothermal system, while Table 32.2 provides an example of database interface. Thermal energy generated from the underground geothermal loop and heat pump can be estimated independently if sufficient data has been collected. Furthermore, after data collection it is possible to obtain COP of the heat pump. Through utilizing the same method, the thermal energy generated from each part of the heating system can be calculated. The following section details these thermal calculations.

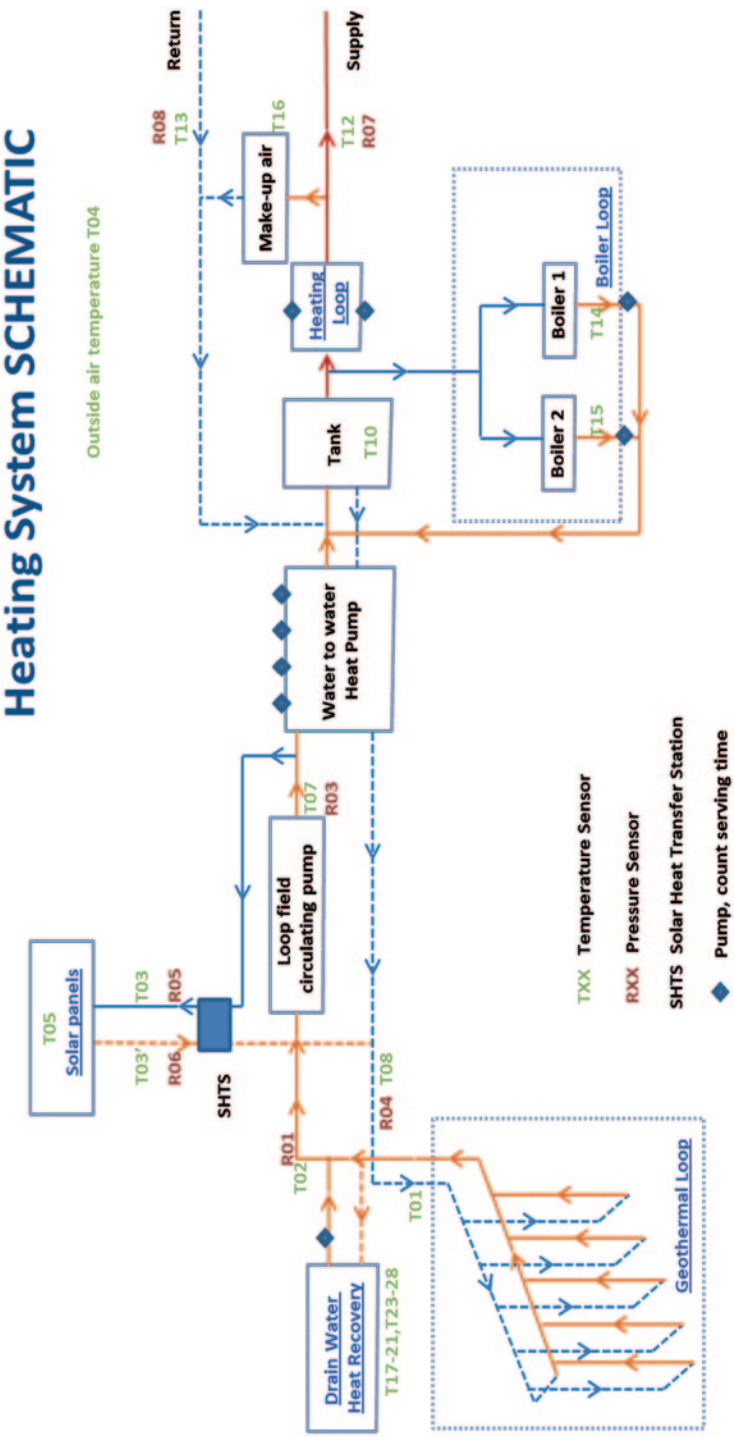

Fig. 32.3 Heating system schematic with sensor locations

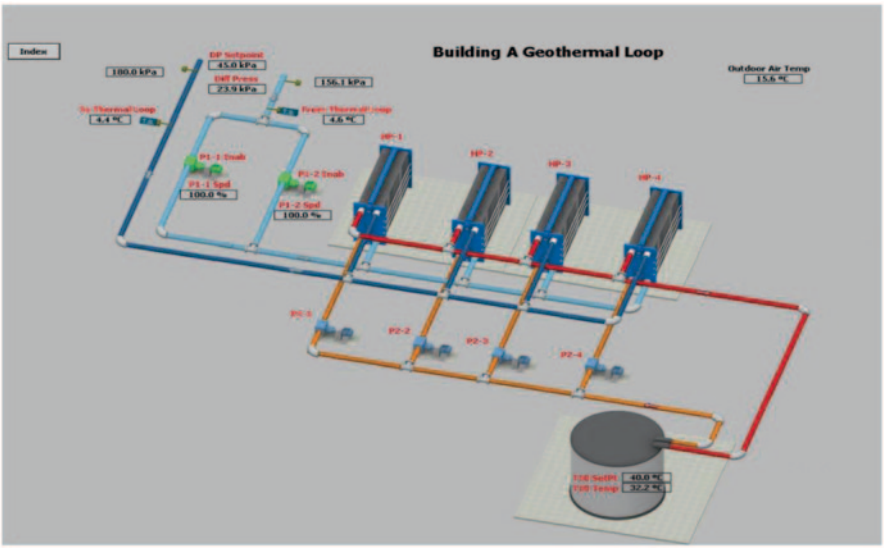

Fig. 32.4 3D model of geothermal loop

32.6 Data Calculation

Data calculation, including thermal calculations and the co-efficient of performance (COP) for the heat pump is provided in this section.

Thermal Calculation

Referring to the specific heat equation ($Q = CM \cdot \Delta t$), thermal energy loss or gain in the water pipe can be calculated through using the specific heat, mass and temperature difference. Since mass can be replaced by other figures ($M = \rho V = \rho RT$), the specific heat equation can be further derived to obtain Eq. (32.1).

$$Q = CM \cdot \Delta t = C\rho V \cdot \Delta t = C \cdot \rho RT \cdot \Delta t \tag{32.1}$$

Where:

Q thermal energy, J
C specific heat, J/Kg °C
M mass of water flow within a period of time, kg
Δt temperature difference, °C
ρ density, kg/m^3
V volume, m^3
R flow rate, m^3/s
T time, s

Table 32.1 Monitoring the geothermal system

Data Collection	
Temperature to geo loop –return (T01)	Tank temperature (T10)
Temperature from geo loop –supply (T02), after DWHR	Serving time for each water-to-water heat pumps (1–4)
Supply pressure/ temperature (R03/T07), after DWHR	Serving time for each pumps (P2-1 ~ 4)
Return pressure/temperature (R04/T08), after Solar	Outside air temperature (T04)
Pressure/temperature difference	
Additional Data Required	
Flow rate	Temperature supply from geo loop
Electric demand for heat pump	Temperature supply and return from HP

In this project, serving time (T) is provided by each of the operation pumps and specific heat remains constant, so the temperature difference between the supply and return pipes that connect to each heating system, along with the flow rate are required for monitoring.

Cop of Heat Pump

The co-efficient of performance (COP) is the ratio of heat supplied and work consumed by the heat pump (IGSHPA 2009). The heating capacity in Eq. (32.2) is the sum of heat extracted from the ground and the electric demand of the heat pump. Based on Eq. (32.1) and (32.2), Eq. (32.3) can be derived as follows. (1 Btu = 1,055.05585 J)

$$\begin{aligned} \mathrm{COP} &= \frac{Heating\ Capacity(Btu/hr)}{Electric\ Demand \cdot 3.412\left(\frac{Btu/hr}{kW}\right)} \\ &= \frac{Heat\ Extracted\ From\ Ground\left(\frac{Btu}{hr}\right) + Electric\ Demand \cdot 3.412\left(\frac{Btu/hr}{kW}\right)}{Electric\ Demand \cdot 3.412\left(\frac{Btu/hr}{kW}\right)} \end{aligned} \tag{32.2}$$

$$\begin{aligned} \mathrm{COP} &= \frac{\sum_1^n \frac{CM \cdot \Delta t_{ii}}{1055}\left(\frac{Btu}{hr}\right) + Electric\,Demand \cdot 3.412\left(\frac{Btu/hr}{kw}\right)}{Electric\,Demand \cdot 3.412\left(\frac{Btu/hr}{kw}\right)} \\ &= \frac{\sum_1^n c\rho \cdot R_i \cdot T_i \cdot \Delta t_i\left(\frac{Btu}{hr}\right) + Electric\,Demand \cdot 3.412\left(\frac{Btu/hr}{kw}\right)}{Electric\,Demand \cdot 3.412\left(\frac{Btu/hr}{kw}\right)} \end{aligned} \tag{32.3}$$

Table 32.2 Sample of data—geothermal system

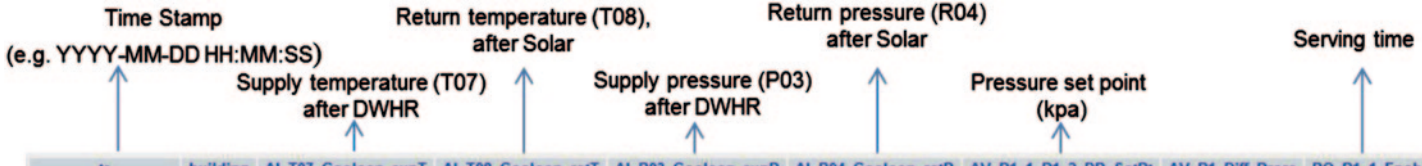

ts	building	AI_T07_Geoloop_supT	AI_T08_Geoloop_retT	AI_R03_Geoloop_supP	AI_R04_Geoloop_retP	AV_P1_1_P1_2_DP_SetPt	AV_P1_Diff_Press	BO_P1_1_Enab
2012-03-29 12:08:02	1	1.94047725200653	2.17324829101562	198.106491088867	174.111206054688	45	24.1449737548828	1
2012-03-29 12:08:23	1	1.91753208637238	2.25543427467346	198.134201049805	174.302001953125	45	23.7471923828125	1
2012-03-29 12:08:44	1	1.83755123615265	2.27524161338806	198.015670776367	174.155364990234	45	23.6182708740234	1
2012-03-29 12:09:05	1	1.7989901304245	2.26917219161987	197.738693237305	173.791763305664	45	23.9398803710938	1
2012-03-29 12:09:26	1	1.83308088779449	2.23848581314087	198.014083862305	173.768051147461	45	24.0802154541016	1
2012-03-29 12:09:48	1	1.87712979316711	2.19292259216309	197.311508178711	173.429351806641	45	23.9037322998047	1
2012-03-29 12:10:11	1	1.81729555130005	2.19070553779602	197.019317626953	173.103103637695	45	23.9162139892578	1
2012-03-29 12:10:33	1	1.75148868560791	2.20040941238403	197.85124206543	173.600357055664	45	24.15966796875	1
2012-03-29 12:10:54	1	1.69328987598419	2.18652606010437	196.998199462891	173.115081787109	45	23.8435363769531	1

Once all data has been collected, the COP can be estimated. If the COP of the heat pump is not high enough, then natural gas should be considered as it is less expensive than electricity. Ultimately, using boilers for heating is less expensive than applying a heat pump. Furthermore, CO_2 emissions should be considered when a power station creates electricity and boilers generate heat.

32.7 Future Research

Based on the above equation derivation, it is essential to obtain the temperature difference and flow rate for supply and return pipes for each part, since the serving time can be read from operation pumps. In order to conduct further energy efficiency analysis, a new chart is designed which incorporates the recommended locations of additional sensors in the basement.

Figure 32.5 demonstrates the design of additional sensors, including those measuring temperature (in rectangle) and flow rate (in oval shape). The drain water heat recovery system can be measured roughly with sensors on the main heating loop or monitored with sensors on each specific portion. If sensors are only installed on the main heating loop, then final calculations can roughly assume that all units serve tenants equally. To improve accuracy, additional sensors are required to monitor each portion. The sensor locations are provided in Fig. 32.6.

This research is a 4 year project, and at the time of publication, systems are still under monitoring. After all data has been collected, the researchers will be able to estimate the percentage of energy supporting the geothermal system from solar energy, DWHR, and boilers.

Conclusions

The integrated heating system presented in this paper is suitable for buildings in Fort McMurray. The advantages of such an integrated design are intuitively clear after comparing the typical usage of geothermal systems and the real usage of the integrated system. It is concluded that this strategy can extend the lifetime of the geothermal system, provide significantly more energy, and improve energy efficiency. These results are expected to be proved by the ongoing monitoring system, data collection, and thermal energy calculations. To estimate the amount of energy generated from each system, the temperature difference in the pipes and flow rate are crucial data. In response to these requirements, a new design to monitor the integrated system is provided and will be implemented in near future. Since it is a long-term project, data collection will take place in future phases. After all data collection, the thermal energy generation distribution can be easily evaluated, and adjustments can be made to the future heating system design in order to observe the benefits of increased energy production and efficiency.

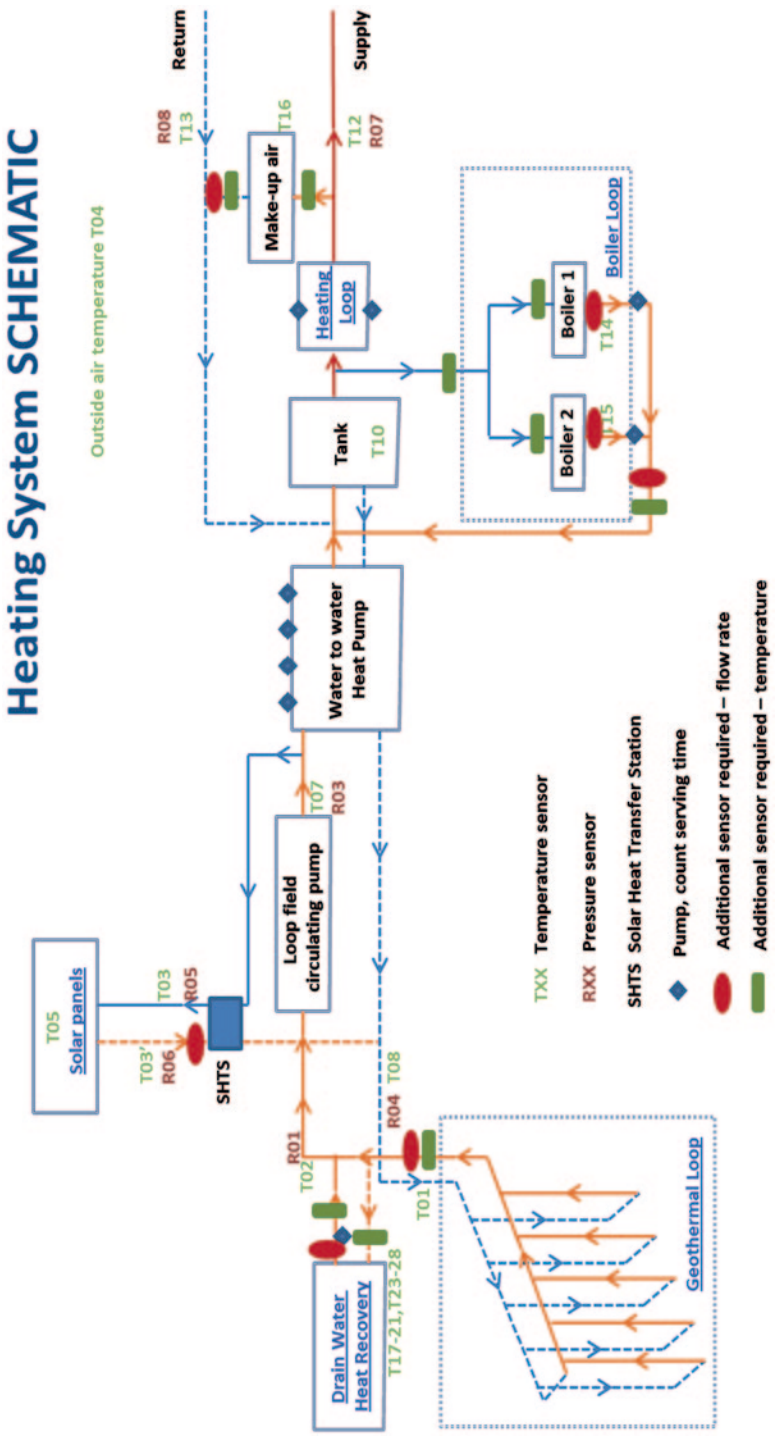

Fig. 32.5 Design of additional sensors' location

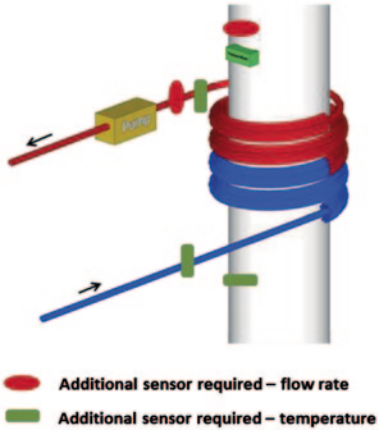

Fig. 32.6 Sensors' location for DWHR portion

Acknowledgement This research has been developed within the scope of the "Stony Mountain Plaza" project in Fort McMurray, Alberta, Canada. It is a multi-disciplinary research project within University of Alberta. The authors would like to thank all of the contributors who provided this research opportunity, especially in terms of access to the associated research and data. The authors would also like to thank the IT partners, including Al Rifai A., Singh G., and Ganev V. who provided technical content for this project.

References

1. Cooperman A, Dieckmann J, Brodrick J (2012) Residential GSHPs. J ASHRAE 54(4):72–79
2. IGSHPA (International Ground Source Heat Pump Association) (2009) Ground source heat pump residential and light commercial design and installation guide. Oklahoma State University, Engineering Technology, Stillwater, Oklahoma 74078
3. Natural Resources Canada (2012) Earth energy, ground-source/geothermal heat pumps, geoexchange. http://www.nrcan.gc.ca/home/. Accessed May 2012
4. Geothermal heat pump consortium Inc.http://bge.apogee.net/ces/library/tcwshp.asp. Accessed April 2012
5. Banks D (2008) An introduction to thermogeology: ground source heating and cooling. Blackwell
6. Lund J, Bertani R (2010) Worldwide geothermal utilization 2010. Geothermal Resources Council Annual Meeting 2010 34(1):182–185
7. IGSHPA (International Ground Source Heat Pump Association) Oklahoma, Ground Source Heat Pump., http://www.igshpa.cn/htdocs/pages.asp?id=12. Accessed April 2012 Geothermal Heat Pump Design Manual, Application guide, AG31-008, Staunton, Virginia USA
8. Wang E, Fung AS, Qi C, Leong WH (2012) Performance prediction of hybrid solar ground-source heat pump system. J Energy Build 47:600–611
9. Kim E, Lee J, Jeong Y, Hwang Y, Lee S, Park N (2012) Performance evaluation under the actual operating condition of a vertical ground source heat pump system in a school building. J Energy Build 50:1–6
10. Bakirci K, Ozyurt O, Comakli K, Comakli O (2011) Energy analysis of a solar-ground source heat pump system with vertical closed-loop for heating applications. J Energy 36:3224–3232
11. Lund JW, Freeston DH (2001) World-wide direct uses of geothermal energy 2000. J Geothermics 30:29–68

12. Lund JW, Freeston DH, Boyd TL (2005) Direct application of geothermal energy: 2005 worldwide review. J Geothermics 34:691–727
13. Gerber* L, Maréchal F (2011) Defining optimal configurations of geothermal systems using process design and process integration techniques. J Appl Therm Eng 43:29–41
14. Ratlamwala TAH, Dincer I, Gadalla MA (2012) Thermodynamic analysis of an integrated geothermal based quadruple effect absorption system for multigenerational purposes. J Thermochimica Acta 535:27–35
15. Ozgener O, Hepbasli A (2007) A review on the energy and exergy analysis of solar assisted heat pump systems. J Renew Sustain Energy Rev 11:482–496
16. Cooperman A, Dieckmann J, Brodrick J (2011) Drain water heat recovery. J ASHRAE 53(11):58–64

Chapter 33
Characterization of Heat Transport Processes in Geothermal Systems

Heiko Huber and Ulvi Arslan

Abstract The Institute of Materials and Mechanics in Civil Engineering has performed a research program supported by the Federal Ministry of Economics and Technology (BMWi) from 2010 till 2012. The main objective of this research program is titled "experimental investigation for the verification of a Finite-Element-Multiphase-Model for heat transport processes in the ground" whereby the subsoil is analyzed as a three-phases-model with separate consideration of conduction, convection and their subsequent interaction.

Extensive experimental field tests as well as laboratory tests were conducted at the Technical University Darmstadt. In addition to the extensive field tests a geothermal laboratory device has been developed. With the help of this device the heat transport processes in different geological and hydrogeological conditions can be simulated. Furthermore, it is possible to determine the increase of the effective thermal conductivity of a line source with rising groundwater flow velocities. The ratio of conductive and convective energy transport to the whole transported energy can be investigated in laboratory. After all the different types of heat transport processes in geothermal systems can be characterized clearly. With the extensive geothermal data of the laboratory tests common numerical programs can be verified and optimized. Therefore, all measured data will be reconsidered by numerical back analysis. Detailed description of the laboratory apparatus and first results of the numerical sensitivity and back analysis will be given in this paper.

Keywords Geothermics · Field tests · Laboratory device · Numerical back analysis

H. Huber (✉)
CDM Smith Consult GmbH, Neue Bergstraße 13, 64665 Alsbach, Germany
e-mail: Heiko.huber@cdmsmith.com

U. Arslan
Institute of Materials and Mechanics in Civil Engineering, Technical University Darmstadt (TUD), Petersenstraße 12, 64287 Darmstadt, Germany
e-mail: arslan@iwmb.tu-darmstadt.de

I. Dincer et al. (eds.), *Progress in Sustainable Energy Technologies: Generating Renewable Energy,* DOI 10.1007/978-3-319-07896-0_33,

33.1 Introduction

In times of global warming renewable energies are getting more important. Geothermal energy is the auspicious renewable energy in the field of geotechnical engineering.

Geothermal energy is thermal energy stored below earth's surface. Although geothermal energy is one of the youngest types of an economic use of renewable energy sources, it is certainly auspicious. While other renewable energy sources depend on environmental conditions, geothermal energy originates in the earth's interior with constant gain. This underground heat generation is caused mostly by the radioactive decay of persistent isotopes. On average, the temperature increases 0.03 °C m^{-1} of depth, which is called geothermal gradient. Therefore 99 % of Earth is hotter than 1,000 °C, while 99 % of the remaining 1 % is even hotter than 100 °C. At depths of about 1 km temperatures of 35–40 °C can be achieved. Objective of geothermal engineering is to use that energy potential with suitable systems extracting or inserting heat energy from or into the ground through heat transfer.

For the design of smaller geothermal systems the geothermal, geological and hydrogeological values can be estimated according to common literature. For the design of complex geothermal systems the subsoil has to be modelled with numerical approaches based on the Finite-Element-Method (FEM) or the Finite-Difference-Method (FDM) using values evaluated in laboratory or in situ. In saturated soils, especially in areas of groundwater flow, the energy transport of the fluid phase (conduction and convection) and the solid phase (conduction) and their interaction has to be considered separately for a proper numerical modelling of geothermal systems. Even in case of low groundwater flow velocity of about 10^{-7} m s^{-1} the role of the convective heat transport cannot be neglected, as described by [1, 2].

Available monitored data of the ratio of heat energy transported by convection to the entire transported heat energy in dependence of the groundwater flow velocity is insufficient [3]. For the optimization of the modelling of geothermal systems a sufficient database of groundwater flow influenced geothermal systems is essential. With help of this database numerical modelling programs for geothermal purpose can be verified.

For a better understanding of the geothermal heat transfer processes like conduction, convection, radiation and their interaction a large scale geothermal laboratory device has been invented and developed at the Technical University Darmstadt.

33.2 Laboratory Device

Assembling

To investigate the different types of heat transport mechanisms in detail a large scale laboratory device has been developed at the Technical University Darmstadt [4] (Fig. 33.1).

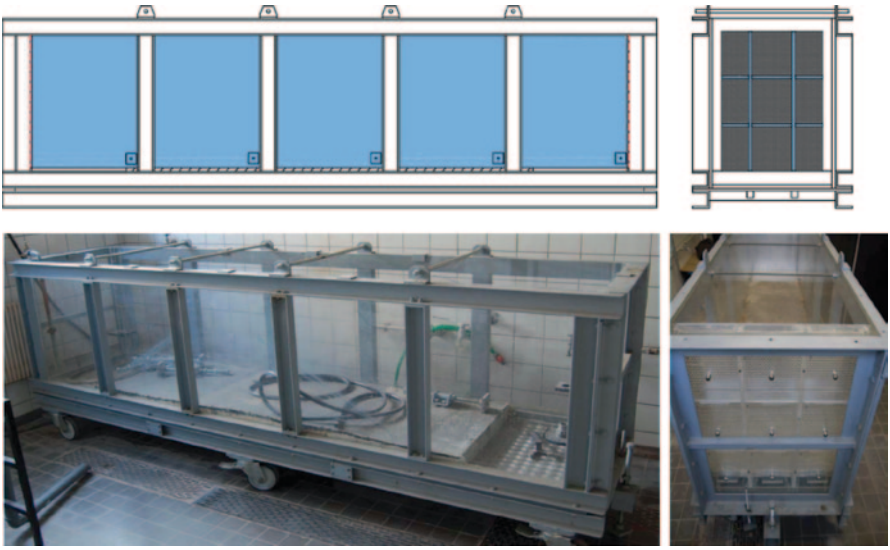

Fig. 33.1 Large scale laboratory device

The laboratory device is constructed in a large scale with outer dimensions of 312/76/90 cm (L/W/H) and inner dimensions of 297/64/71 cm (L/W/H). The construction is very massive with an acryl glass wall of 1.5 cm supported by a steel frame in a U80 shape placed vertically every 50 cm and horizontally at the top and the bottom. The apparatus is covered by an acryl glass plate. Every wall, the bottom and the cover plate as well as its connections are waterproof up to a high pressure.

The device can be filled with different kind of water saturated soil. With its massive construction confined water even of high pressure can be simulated.

At the borders of the device a connection for the water inlet and water outlet is installed. At the outside of the device the water inlet is connected to a water supply tank of adaptable height.

The water outlet is connected to a hydraulic pipeline, which is also variable in its installation height. Inside of the device the water inlet and outlet are enlarged to diffusors of a perforated metal plated and a geotextile being installed 13.3 cm from each border. The diffusors spread the water flow uniformly over the whole section of the device. According to the chosen difference in height ΔH between the hydraulic head of the water supply tank and the pipelines at the water outlet different flow velocities of the water running through the device can be regulated according to the permeability of the installed soil in consideration of Darcy's law.

At about one third of the length of the device (83.3 cm) a line source is installed vertically. This line source is constructed by a copper tube with an outer diameter of 1.8 cm, which is filled with silicon oil surrounding a heating element. With help of this line source a thermal load can be applied to the installed soil steady or transient in time.

The laboratory device is thermally isolated with different layers of Styrofoam. A constantly tempered fluid is circulating in copper tubes between these different layers of Styrofoam. Therefore, a chosen constant temperature can be applied to the device.

Measuring System

The laboratory device is equipped with an extensive measuring system. The hydraulic head of the water supply tank, the water outlet pipelines and different points of the inside of the laboratory device is monitored with 12 water standpipes. To be able to compare the different hydraulic heads the water standpipes are gathered next to each other in a water harp.

At the water inlet and the water outlet the mass flow is measured constantly with flowmeters. At the water outlet the whole section of the device is divided into nine chambers of the same area with separated water outlets. The mass flow through these nine chambers can be measured separately. Therefore, the homogeneity of the water flow over the whole section of the device can qualitatively be verified.

After all, 33 temperature sensors Pt 100 are installed in or at the laboratory device to determine constantly the development of temperature over time. Two Pt 100 are installed at the water inlet and the water outlet to measure the temperature of the flowing water. One sensor is installed inside of the line source to guarantee an accurate thermal load. Thirty Pt 100 are located in a horizontal section in the middle of the height of the device. According to an expected symmetric temperature plume 28 of the sensors in the soil are installed at one side of the symmetric axis. Two of them are installed mirrored to the symmetry axis to verify the expected symmetry.

According to a performed sensitivity analysis the sensors are located next to the line source in direction of the temperature plum, beside and behind the line source. The influence of the convective heat transport can be determined by comparing the temperature development of the sensors before the line source with the sensors behind the line source. A drawing of the arrangement of the measuring system is given in (Fig. 33.2).

Experimental Results

After all 42 scenarios with different geological conditions like coarse and fine sands as well as different hydro-geological conditions like confined and unconfined groundwater with different Darcy velocities were performed. Some of the results are given in the following. Temperature development of chosen temperature sensors in the experiment numbered Sz 3a 4 are shown in (Fig. 33.3). In Sz 3a 4 a constant thermal load of 23.3 W m^{-1} was set to the line source for 2 days, which was installed in uniform, loose coarse sand. The groundwater was confined with an over pressure of about 0.3 m and a Darcy velocity of 0.45 m d^{-1} was applied.

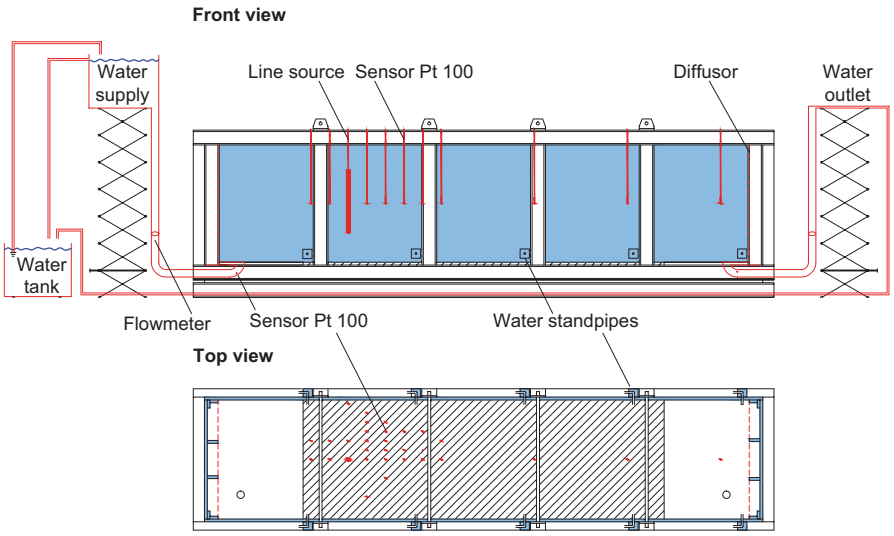

Fig. 33.2 Arrangement of the measuring system

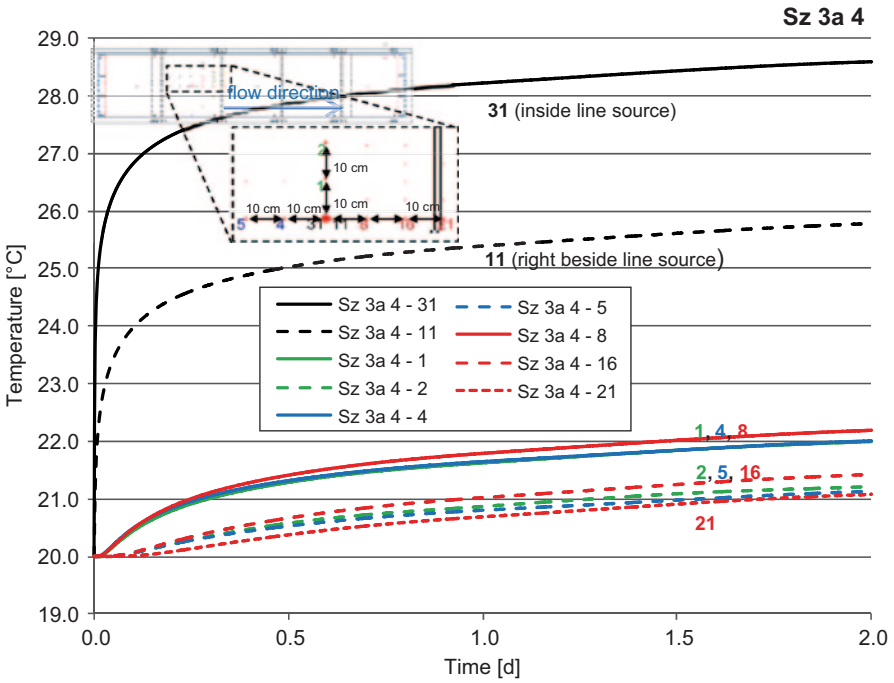

Fig. 33.3 Temperature development over time of chosen temperature sensors in Sz 3a 4

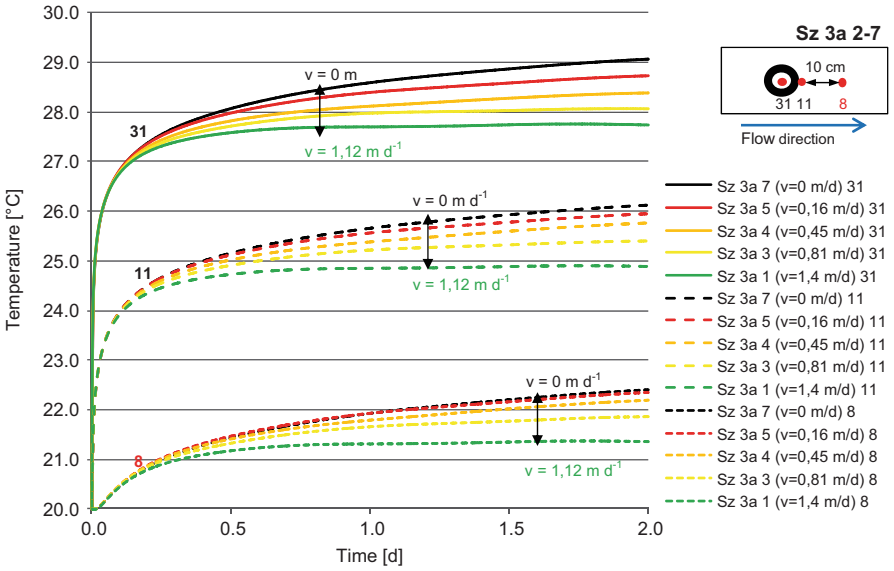

Fig. 33.4 Temperature development over time of chosen sensors in Sz 3a 2–Sz 3a 7

Starting from a tempered level of the whole device of 20 °C, the temperature inside the line source (31) increases to about 28.5 °C after 2 days. Right beside the line source (11) an increase of the temperature to about 25.8 °C after 2 days can be determined. The temperature sensors (1), (4) and (8), with a distance of 10 cm to the line source show a temperature increase of about 2°K after two days. The temperature sensors numbered (2), (5) and (16) with a distance of 20 cm to the line sources show an increase of the temperature of about 1.2°K, while the sensors numbered (21) with a distance of 30 cm to the line source show an increase of 1.1°K. The slope of the temperature increase of the red marked sensors in groundwater flow directions (8), (16) and (21) is parallel to each other with an amount of about 0.31°K d^{-1}. The green marked temperature sensors (1) and (2), which are located beside the line source, are parallel to each other, too, but with a lower slope of about 0.28°K d^{-1}. The blue marked temperature sensors (4) and (5), being located before the line source in groundwater flow direction, show the smallest slope of about 0.25°K d^{-1}. This difference in the slopes of the sensors before, beside and behind the line source is caused due to the convective heat transport.

In those scenarios Sz 3a 2–Sz 3a 7 the Darcy velocity was varied between 0 and 1.12 m d^{-1}, while all other values were kept constant. Therefore the variation of the temperature development inside the laboratory device depending on the Darcy velocity was investigated. The temperature development over time of the temperature sensors inside the line source (31), right beside the line source (11) and in a distance of 10 cm to the line sourced in groundwater flow direction for the scenarios Sz 3a 2–Sz 3a 7 is shown in (Fig. 33.4). A strong correlation between the

Darcy velocity and the slope of the temperature increase can be determined. The higher the Darcy velocity, the smaller is the slope of the temperature increase and therefore the smaller is the absolute temperature of the sensors after 2 days of the test. While the temperature of the sensor inside the line source (31) rises in Sz 3a 7 ($v = 0$ m d^{-1}) to a value of about 29.1 °C after two days, the temperature of the same sensor rises to a value of only 27.2 °C in Sz 3a 2 ($v = 1.12$ m d^{-1}). This trend can also be determined for the temperature sensors numbered (11) and (8). The higher Darcy velocity causes a high dispersion of the applied heat energy of the line source. This high thermal dispersion leads to a larger spatial extension of the temperature plume by lower temperatures inside the plume.

33.3 Numerical Back Analysis

The gathered experimental geothermal laboratory data was back analyzed by numerical methods. The developed numerical model, the sensitivity analysis and the results of the back analysis are given in the following.

Model Description

The numerical back analysis was performed with FEFlow, a finite-element-method based code for combined transient heat and transient flow transport simulation. The laboratory device was simulated as a two dimensional, horizontal, water saturated problem. The simulation area was divided into more than 130,000 three-noded triangles with a higher density of elements inside and right beside the line source and at the borders of the simulation area. The duration of the simulation was chosen according to the performed scenarios to two days, each. The automatic time stepping control scheme was chosen as the predictor-corrector Adams-Bashforth/Trapezoid rule.

The modeling area was simulated with three different materials. Material 1 defines the water saturated soil inside the laboratory apparatus, material 2 and material 3 describes the line source simulated as a copper tube (material 2), which is filled with silicon oil (material 3). As initial conditions the temperature of the whole laboratory device was set to 20 °C and the hydraulic head was set 0.3 m above the height of the laboratory device. As boundary conditions the hydraulic head of the diffusors were defined constant and the temperature of the border and the diffusors were set constant. The properties of the three materials were chosen according to performed laboratory tests and where varied in bandwidths (Table 33.1).

While most of the values of the water saturated sand (material 1) were determined in laboratory, the values of the copper tube (material 2) and the silicon oil (material 3) were chosen due to common literature. The thermal conductivity and the permeability of the silicon oil were chosen very high to guarantee a fast distribution of the temperature inside the line source. The thermal conductivity of the

Table 33.1 Properties of the materials 1–3

	Unit	Bandwidth	Standard value	Remark
Water saturated soil (material 1)				
Thermal conductivity of solid λ_S	W m^{-1} K^{-1}	2.5–6.0	3.85	Determined in laboratory
Thermal conductivity of fluid λ_F	W m^{-1} K^{-1}	0.597	0.597	Determined in laboratory
Vol. heat capacity of solid c_S	MJ m^{-3} K^{-1}	1.0–2.5	1.73	Determined in laboratory
Vol. heat capacity of fluid c_F	MJ m^{-3} K^{-1}	4.18	4.18	Determined in laboratory
Porosity n	–	0.4–0.5	0.46	Determined in laboratory
Permeability k	m s^{-1}	$3.8 \cdot 10^{-3}$	$3.8 \cdot 10^{-3}$	Determined in laboratory
Dispersivity α_L/α_T	m/m	0/0–0.25/0.025	0/0	According to common literature
Darcy velocity v	m d^{-1}	0–0.46	0.155	Determined in laboratory
Copper tube (material 2)				
Thermal conductivity of solid λ_S	W m^{-1} K^{-1}	0.05–0.07	0.056	According to common literature
Vol. heat capacity of solid c_S	MJ m^{-3} K^{-1}	0.03–300	3.45	According to common literature
Porosity n	–	0	0	According to common literature
Permeability k	m s^{-1}	$1.0 \cdot 10^{-20}$	$1.0 \cdot 10^{-20}$	According to common literature
Silicon oil (material 3)				
Thermal conductivity of fluid λ_F	W m^{-1} K^{-1}	5–100	100	According to common literature
Vol. heat capacity of fluid c_F	MJ m^{-3} K^{-1}	1–40	10	According to common literature
Porosity n	–	1	1	According to common literature
Permeability k	m s^{-1}	1	1	According to common literature

copper tube was chosen very small, to simulate the heat transfer from the flowing silicon oil to the copper tube and from the copper tube to the water saturated sand with flowing groundwater.

Sensitivity Analysis

The influence of every single material property was investigated with help of a numerical sensitivity analysis. While all other properties were set to the standard value one property was varied between the chosen bandwidth according to (Table 33.1). The results of the sensitivity analysis are summarized in (Figs. 33.5, 33.6, 33.7 and 33.8).

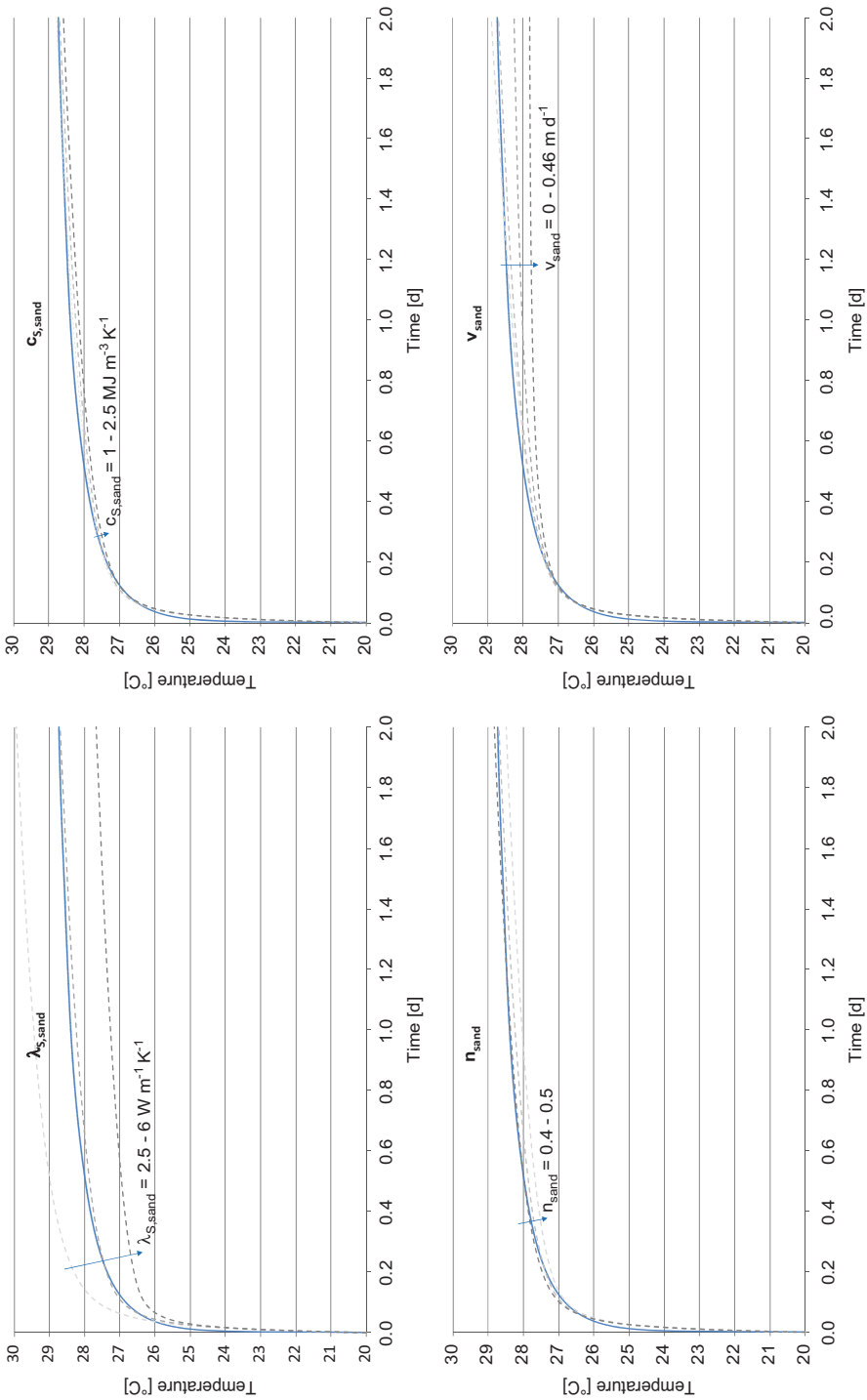

Fig. 33.5 Sensitivity analysis—variation of λ_S, c_S, n and v of material 1 (sand)

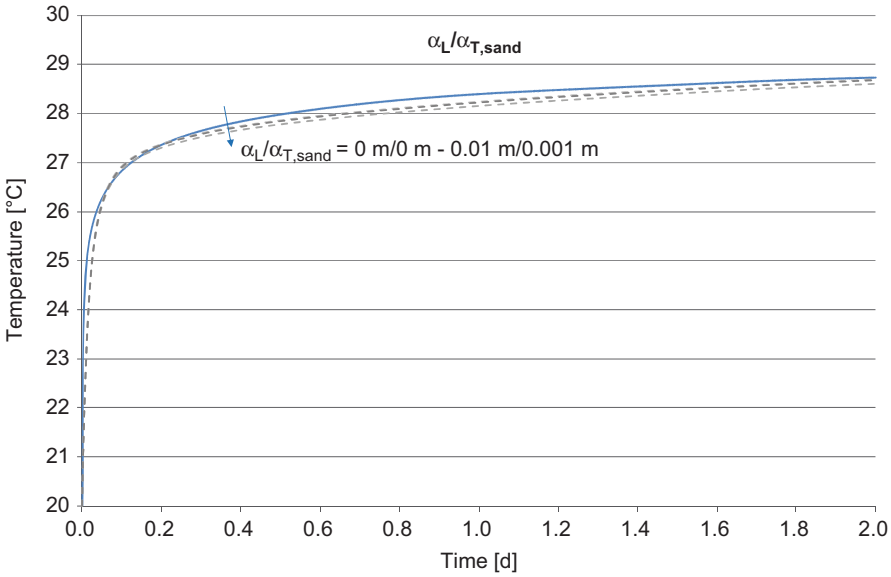

Fig. 33.6 Sensitivity analysis—variation of α_L and α_T of material 1 (sand)

The continuous blue line is the temperature development of the temperature sensor inside the line source (31) gathered in the experiment numbered Sz 3a 5.

A variation of the thermal conductivity λ, the heat capacity c and the porosity n of the water saturated sand leads to a parallel displacement of the temperature, with only small variation of the temperature slope. The slope of the temperature increase without a parallel displacement changes depending on the simulated Darcy velocity v (Fig. 33.4).

A variation of the thermal dispersivity of the water saturated sand leads only to a small parallel displacement of the slope of temperature increase. This is caused due to the small dimensions of the laboratory device. The thermal dispersivity only affects the temperature development in field experiments with larger dimensions (Fig. 33.6).

A variation of the thermal conductivity λ of the copper tube and the silicon oil leads to a parallel displacement of the temperature with only small variation of the temperature slope. A variation of the heat capacity of the copper tube and the silicon oil leads to a displacement of the temperature increase at the beginning of the thermal load. Due to a higher heat capacity the temperature retains longer inside the line source. This leads to higher temperatures at the beginning of the experiment (Figs. 33.7 and 33.8).

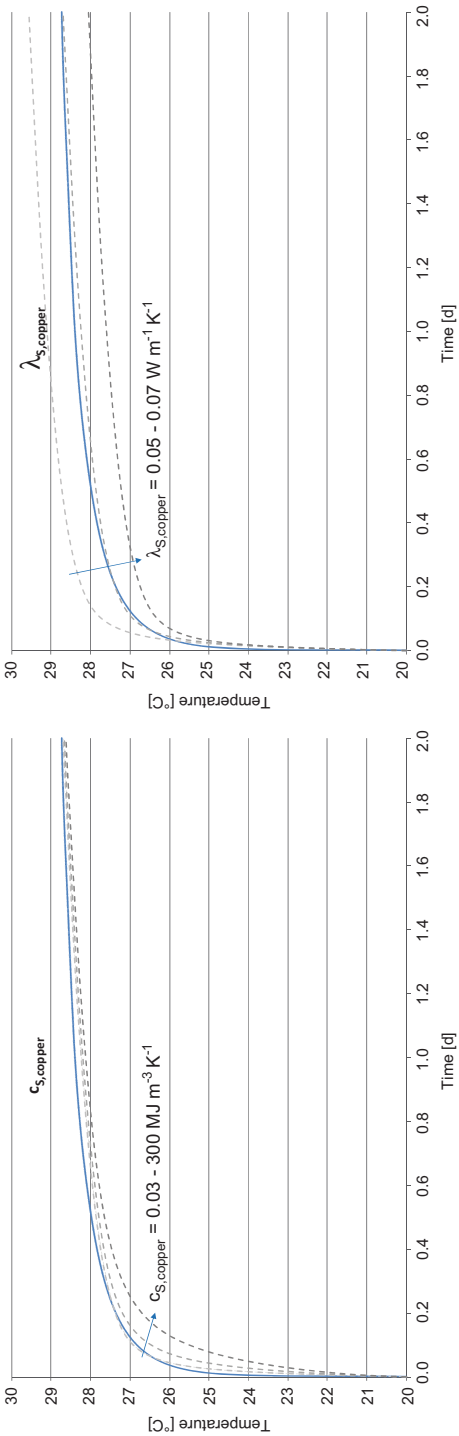

Fig. 33.7 Sensitivity analysis—variation of c_S and λ_S of material 2 (copper)

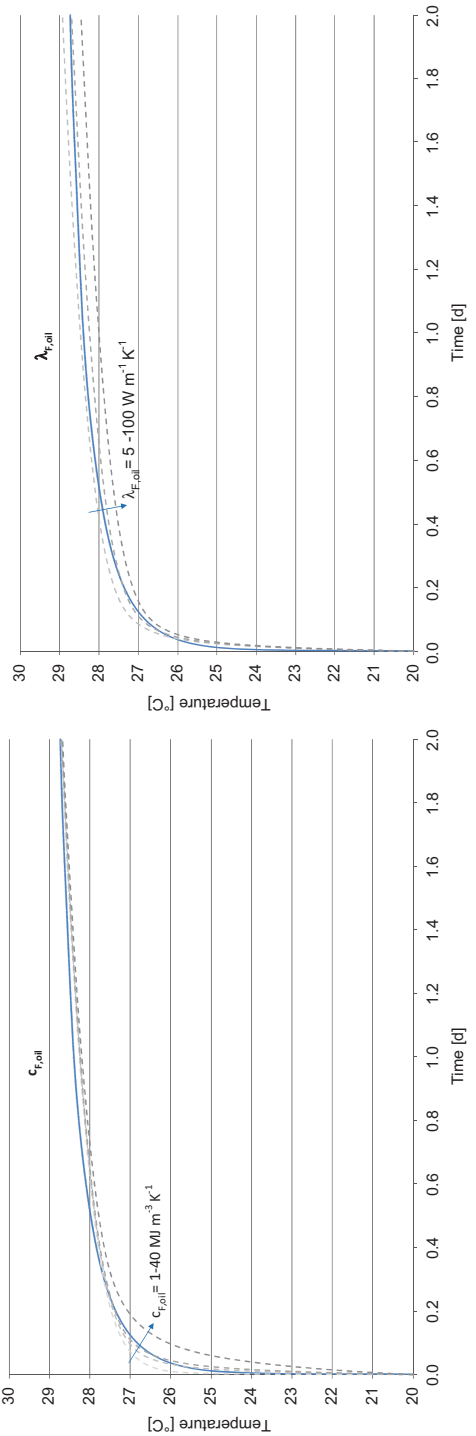

Fig. 33.8 Sensitivity analysis—variation of c_F and λ_F of material 3 (oil)

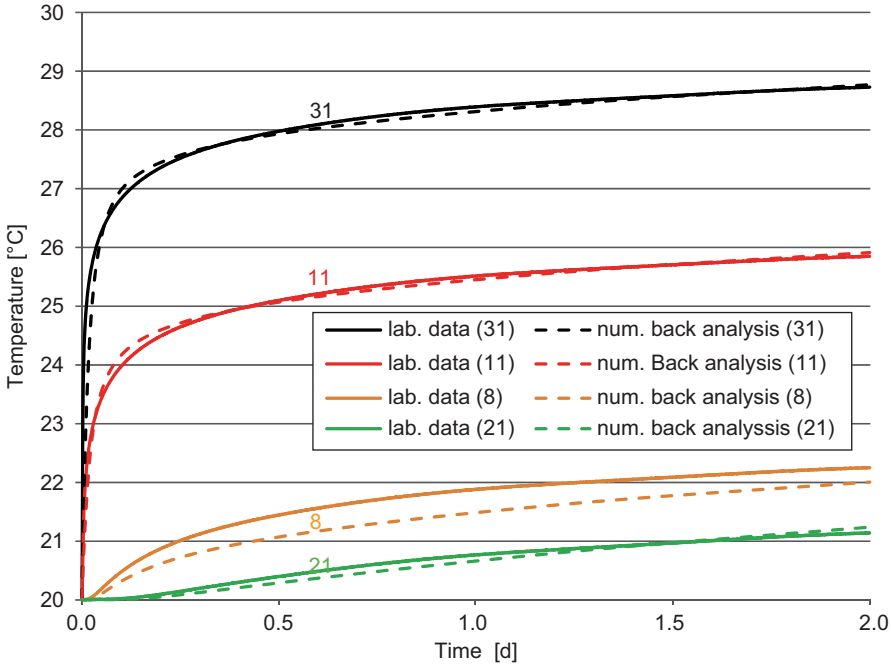

Fig. 33.9 Comparison of the experimental laboratory data with the data from the numerical back analysis of Sz 3a 5

Results

With the help of the sensitivity analysis the best fitting parameters to the laboratory data of the scenario Sz 3a 5 were found, whereby a Darcy velocity of 0.155 m d^{-1} and a constant thermal load of 23.3 W m^{-1} were applied. A comparison of the experimental laboratory data (continuous line) and the numerical back analysis (dashed line) for scenario Sz 3a 5 inside the line source (31), right beside the line source (11) as well as 10 cm (8) and 30 cm away from the line source in groundwater flow direction is given in (Fig. 33.9).

After all, a good fit of the numerical back analysis to the experimental laboratory data was achieved and the numerical model was calibrated for the scenario Sz 3a 5. To validate the numerical model the scenario Sz 3a 7–Sz 3a 10 were back analyzed. In the experimental laboratory scenarios of Sz 3a 7–Sz 3a 10 all geological and hydro geological values were kept constant, while only the thermal load applied on the line source was varied between 14.8 W m^{-1} (Sz 3a 8) and 40.1 W m^{-1} (Sz 3a 9). Due to the variation of the constant thermal load the temperature inside the line source (31) increases to values of 26–36 °C after two days.

A comparison of the experimental laboratory data (continuous lines) and the numerical back analysis (dashed lines) for the scenario Sz 3a 7–Sz 3a 10 inside the line source (31) is shown in (Fig. 33.10). After all a good fit of the numerical back

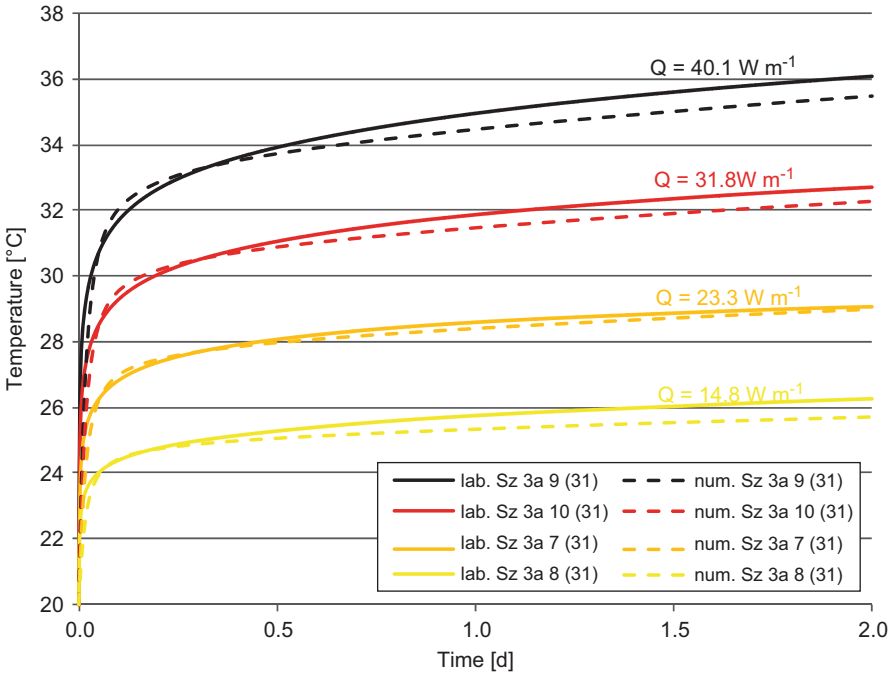

Fig. 33.10 Comparison of the experimental laboratory data and the numerical back analysis of Sz 3a 7–Sz 3a 10

analysis to the experimental laboratory data was achieved. The numerical model was validated.

Conclusion

With the help of the developed geothermal laboratory device data of high accuracy was gathered. In more than 40 scenarios different geological and hydro geological values were varied.

With the gathered data the modeling of geothermal energy transport processes with current numerical programs can be verified and improved. In future work all the results of the laboratory experiments will be compared to the performed geothermal field test [5]. Therefore the numerical model can also be validated for in-situ experiments. With help of this validated model geothermal systems can be optimized.

References

1. Pannike S, Kölling M, Panteleit B, Reichling J (2006) Auswirkung hydrogeologischer Kengrößen auf die Kältefahnen von Erdwärmesondenanlagen in Lockersedimenten, Grundwasser—Zeitschrift der Fachsektion Hydrogeologie 1/2006
2. Katsura T, Nagano K, Hori S, Okawada T (2009) Investigation of groundwater flow effect on the thermal response test result. Proceedings of 11th Energy Conservation Thermal Energy Storage Conference. Stockholm, 15–17 June 2009
3. Glück B (2008) Simulationsmodell „Erdwärmesonden“ zur wärmetechnischen Beurteilung von Wärmequellen, Wärmesenken und Wärme-/Kältespeichern. Rud. Otto Meyer-Umwelt-Stiftung, Hamburg
4. Huber H, Arslan U, Stegner J, Sass I (2011) Experimental and numerical modelling of geothermal energy transport. Proceedings 13th International Conference of the International Association for Computer Methods and Advances in Geomechanics (IACMAG 2011), Melbourne, Australia 9–11 May 2011, Vol. 1, pp 455–459
5. Huber H, Arslan U (2012) Geothermal field tests with groundwater flow, Proceedings thirty-seventh workshop on geothermal reservoir engineering, Stanford University, California, 30 Jan–1 Feb 2012

Chapter 34
The Prospects for Geothermal Application in Algeria

Benziada Mébrouk

Abstract Algeria is favorably positioned in terms of geothermal resources for low and medium enthalpy. The northern Algeria is characterized by complex geology and alpine-type volcanism in the Mio-Pliocene-Quaternary, while the South has a structure much simpler and more regular. More than 200 springs are identified on the territory of Algeria with temperatures of 68 °C in the West, 40 °C at the Center, 96 °C in the East and 60 °C in the South. Geothermal reservoirs are relatively interesting and diverse. They occur both north and south and consist of dolomite tlemcians in the west, carbonate formations in the East and Albian sandstones in the Sahara. Today, geothermal resources of Algeria are used in spas, heating greenhouses and irrigation. Others use successful applications made by including geothermal heat buildings (heating and air conditioning), drying fruits and vegetables, aquaculture, desalination of seawater and brackish water algae production blue green (spirulina) in fish farms. Such applications reduce dependence upon fossil resources (oil). They are very reliable and cost-effective and suitable for the sustainable development of the environment.

Keywords Thermal station · Heating greenhouses · Irrigation · Heating and air conditioning

34.1 Introduction

Algeria belongs to the Mediterranean basin and the Sahara occupies the major part of the country. Algeria located between Morocco and Tunisia with it forms the Maghreb (Fig. 34.1). The springs are much more abundant in the Tellian Atlas, with a very intense foldbelt, as in the Saharan Atlas, structures are much simpler and more regular.

B. Mébrouk (✉)
Centre Développement Energies Renouvelables, Route de l'Observatoire BP62, Bouzaréah, Alger 16340, Algérie
e-mail: m_benziada@yahoo.fr

I. Dincer et al. (eds.), *Progress in Sustainable Energy Technologies: Generating Renewable Energy,* DOI 10.1007/978-3-319-07896-0_34,

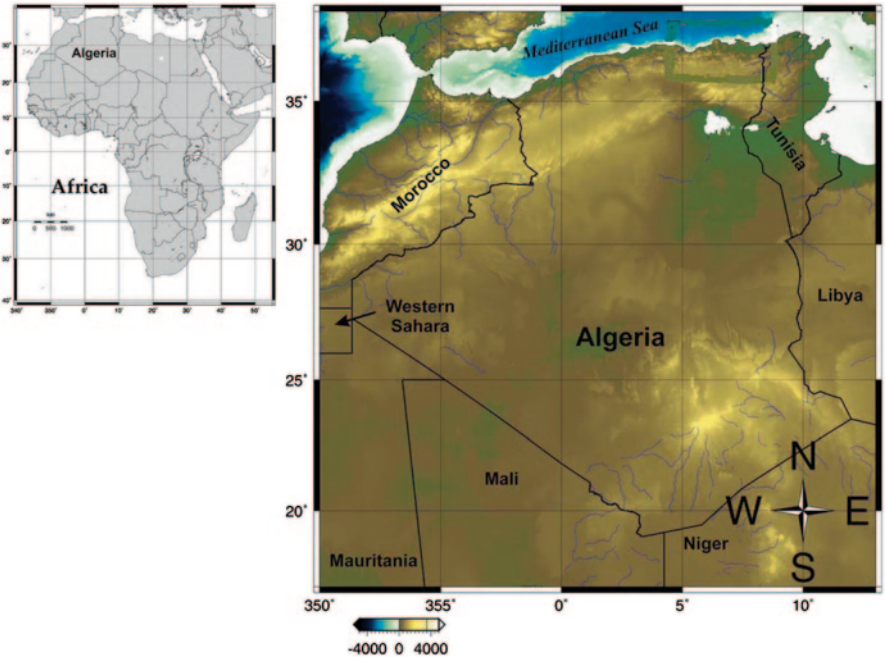

Fig. 34.1 Localization of Algeria in Africa [2]

The aim of this paper is to mention the prospects of geothermal applications in Algeria. In the case of this overview, we will only geothermal called "low and medium temperature" for agricultural applications, district heating and commercial applications.

34.2 Geological Units of Northern Algeria

The Alpine Algerian crust is made of sound geologic domains known from South to North as (Fig. 34.2):

1. The Atlasic Foreland,
2. The External Tellian Zone,
3. Internal Zone, i.e. Kabylian Zone, and
4. Magmatic and Sedimentary Formations, called Post Nappes (post Miocene tectonics), outcropping in the whole northern Algeria [1].

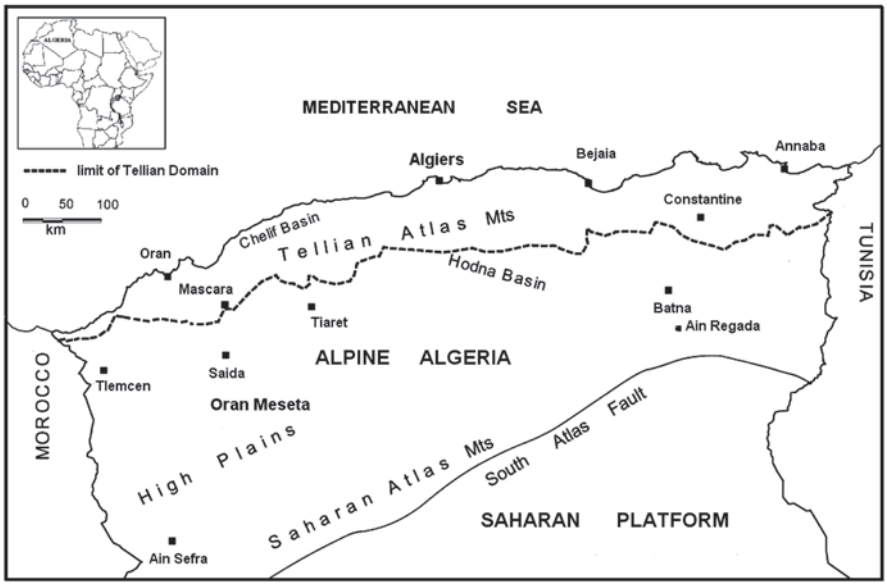

Fig. 34.2 Geological units of Northern Algeria

34.3 Geothermal Resource in Algeria

Geothermal resources are various low temperatures. They are located in northern Algeria and northern Sahara.

In the north, the reservoirs are complex and discontinuous. They consist of facies (limestone, sandy limestone and sandstone) of the Mesozoic and south, a continuous tank is composed mainly of sandstone [2].

He was appointed tablecloth Albian.

The distribution of thermo-mineral waters, in Algeria, is very irregular. These sources are increasing in number gradually as one approaches from the east. This distribution seems to follow that of the ore deposits. Thus it has about 20 mineral springs in the region of Oran, about 40 in the Algiers and 150 in the region of Constantine.

In the North, in part including the Saharan Atlas to the sea, emerging more than 200 hot springs. The water temperature varies between 22 and 98 °C and mineralization total dissolved salt varies between 4 and 10 g/l. The tanks are typically at depths between 1500 and 2500 m.

South, the water Albian covers an area of 600,000 km^2. It is semi-free in the western and captive and warm only in the eastern part. The roof of the aquifer to the east is located between 1000 and 2600 m, the average temperature of water is 60 °C and an operating rate of 4 m^3/s, the water Salinity is 3 g/approx.

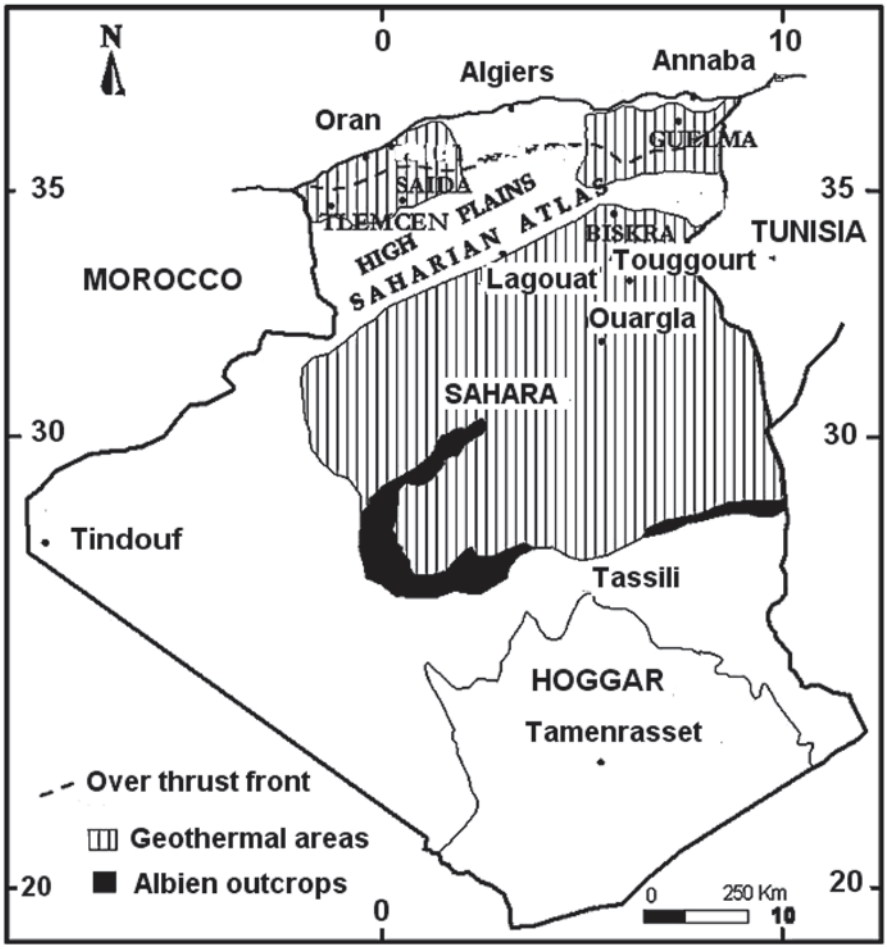

Fig. 34.3 Main geothermal area [2]

The geothermal potential to dewatering, by summing the total flow of the hot springs flow from operating Albian aquifer is over 700 MW (Fig. 34.3).

34.4 Results and Discussion

Map of hot springs (Fig. 34.4) shows that Northern Algeria has low energy resources with temperatures of emergence varies between 30 °C in the West and 98 °C in the East. Spatial analysis of thermal springs is to interest and importance of the

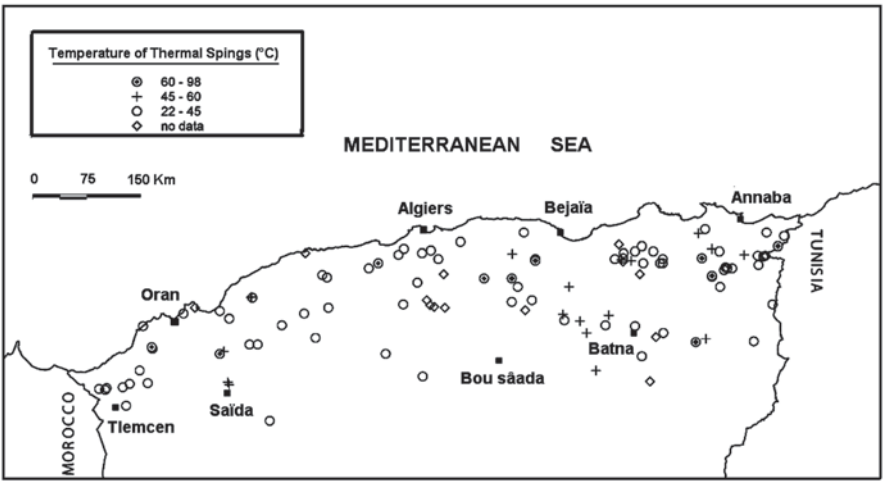

Fig. 34.4 Map of the temperature thermal springs in North of Algeria

Table 34.1 Possible uses of the waters Albian

Temperature (°C)	Possible uses
70	Refrigeration
60	Farming of animals
50	Mushroom heating greenhouses
40	District heating
30	Fermentation
20	Fish

geothermal resources for the thermal applications. The resources of very low enthalpy in shallow aquifers provide many opportunities for the direct applications.

Type use in northern Algeria:

100 < T °C > 70 Heating and cooling of the habitat, food drying.
70 < T °C > 30 Heating of greenhouses and irrigation.
30 < T °C > 20 Fish.

Direct Uses Currently the thermal waters of the Albian though are mainly used for balneology. Importance should be given to these valuable resources. The fields of application are diverse (Table 34.1):

Applications of Geothermal Energy in Algeria Installation between 1993 and 1997 of 18 greenhouses in the region and Ouargla Touggourt for the Production of tomatoes and melons in any season. For aquaculture: raising catfish in the area and Guelma Khenchla. This water may be used for agriculture (greenhouse heating) and heating. The Thermal constructions air conditioning and heating.

In order to integrate the use of geothermal energy in agriculture, the National Organization of Irrigation and Drainage (ONID) Algeria intends to implement in the south, a farm using geothermal energy to of admission into the traditions of agriculture. This experience, to multiplex interests, will, among others, to develop agriculture in the deep south, and the fight against corrosion and scale in a manner that plague disturbing the water infrastructure of the country. The first experiment, led by the ONID, will be the use of geothermal energy in the production of early potatoes from the Albian boreholes in the southern region (Ouargla and El Oued).

Production of the Spirulina in Algeria Algeria is one of the few countries in the world where we cultivate spirulina, an algae rich, which has become a resource of strategic importance. It is at the stage of craft production and experimental. It is in the region of Tamanrasset spirulina that is grown in a pool of 20 m^2 and produces 20 kg of dry spirulina per year. Four months after seeding the basin, we can already harvest spirulina.

Spirulina is blue-green algae and therefore is actually classified as Cyanobacteria (Table 34.2). It is a simple, one-celled form of algae that grows in warm freshwater environments. Even though Spirulina is distantly related to the kelp algae, it is not a sea plant. The freshwater ponds and lakes it favors are notably more alkaline than ordinary lakes and cannot sustain any other forms of microorganisms. Spirulina is much like terrestrial plants except that it does not have a cellulose cell wall.

Spirulina is an algae that is characterized by a high protein, fat, carbohydrate and eleven other vitamins (A, B1, B12, etc.). This is a type of algae that thrives in alkaline lakes in the desert and near the old craters of volcanoes. Spirulina needs a brackish and a temperature variation between 35 and 40 °C. Its harvest per square meter can reach up to 10 g. Spirulina had attracted industrialists who had managed to manufacture products with this alga parapharmaceutical, food for livestock and fish raised in aquariums. Spirulina is a food resource of plant quality, which was used by cattle ranchers, to prevent mad cow disease. In Algeria, pending the establishment of production units and processing of the algal species, we are content with the market and to export unprocessed despite low production.

The world market demand is increasing. Culture of spirulina in Algeria is able to encourage the creation of small businesses as part of youth employment, the Algerian Sahara.

Agriculture The two main applications of geothermal energy in agriculture and fish farming are the greenhouse. The cultures in greenhouses are an attractive option because energy requirements are high. With regard to fish farming, an increase in temperature a few degrees and all its maintenance at a constant level produced an increase in the metabolism in fish and shellfish. In the field of manufacture of food products, temperatures between 40 and 100 °C are used to dehydrate fruits and vegetables. From 60 °C, the heated air can be used to dry agricultural products, pea sounds and wood.

Industry The frost of large industrial buildings can be achieved by a moderate temperature geothermal resource, but most hot water needs or steam industry between

Table 34.2 Class and genera of micro-algae cultured in aquaculture

Class	Genus	Examples of application
Cyanophycea	Spirulina	PL, BP, BS, MR

PL penacid shrimp larvae, *BP* bivalvae molluse postlarvae, *BS* brine shrimp (Artemia), *MR* marine rotifers (Brachionus)

100 and 200 °C. If the geothermal resource is less than 100 °C, it will be used to preheat iron water, whose temperature will result in raised by means of a heat pump. Many processes require large amounts of hot water, such as pulp and paper, textile washing, extraction of chemicals or evaporation of concentrated solutions.

Thus it is easy to see, Algeria contains an abundance of thermo-mineral sources of various compositions and meet all the needs of modern therapeutics. It is highly probable that most of these radioactive sources are: education, barely sketched, can believe it. It is therefore obvious that most inhabitants of Algeria could find, there, in the colony, mineral waters they need.

Conclusions

Geothermal deserves a mobilization of all public and private actors with a concrete action plan. And a gradual substitution of a non-renewable energy by renewable energy for heat production in the various fields is a scalable solution that meets an expectation for the future. Geothermal energy produces clean electricity at low cost, background peak World production of oil, global demand for electricity ever increase, the fight against pollution and energy independence. The geothermal energy has many advantages. I think the time has come interest in geothermal energy both defensive, clean and full of promise.

References

1. ENEL Etude de reconnaissance géothermique Constantinois oriental (1982) Report prepared for the Society National Electrical and Gaz Direction Renewables Technicals, Algiers, Algeria
2. Saibi H (2009) Geothermal resources in Algeria. Renew Sustain Energy Rev 13:2544–3552

Chapter 35
Thermal Interactions of Vertical Ground Heat Exchangers for Varying Seasonal Heat Flux

Seama Koohi-Fayegh and Marc A. Rosen

Abstract A numerical finite volume method in a two-dimensional meshed domain is used to evaluate the temperature response in the ground surrounding multiple borehole systems. The effect of installing ground heat exchangers and the temperature rise in the ground over a period of five years is considered. A transient periodic heat flux is assumed on the borehole wall reflecting the annual variation of heat storage/removal in the ground. The annual variation of heat flux on the walls of the boreholes for a building in Belleville, IL is considered and bin data are used with a typical heat pump.

Keywords Geothermal energy · Vertical ground heat exchangers · Ground temperature · Numerical analysis · Bin method · Periodic heat flux

35.1 Introduction

One potential hindrance to the sustainability of geothermal energy systems is the thermal loss from the system itself, which can affect adjacent systems and the surrounding ground. Some studies show that interference effects are present in some installed geothermal systems, indicating that there may be limits to their proximity and density. Further, the migration of thermal plumes away from these systems may cause temperature rises in nearby temperature-sensitive ecosystems (e.g., aquatic organisms in a watersheds, rivers and lakes) where small temperature differences are important [1].

Analytical and numerical thermal studies have been reported of geothermal heat exchangers, including single ground boreholes modeling [2–26]. The approaches vary in how they evaluate heat conduction in the ground and couple heat transfer inside and outside the boreholes. A limitation to most previous studies is the assumption of a constant and uniform heat input to the ground from the borehole,

M. A. Rosen (✉) · S. Koohi-Fayegh
Faculty of Engineering and Applied Science, University of Ontario Institute of Technology 2000 Simcoe Street North, Oshawa, ON L1H 7K4, Canada
e-mail: Marc.Rosen@uoit.ca

S. Koohi-Fayegh
e-mail: Sima.Kouhi@uoit.ca

I. Dincer et al. (eds.), *Progress in Sustainable Energy Technologies: Generating Renewable Energy,* DOI 10.1007/978-3-319-07896-0_35,

modeled as a cylinder or a line source of heat, e.g., in modelling interacting borehole systems, Koohi-Fayegh and Rosen [27] evaluate numerically the temperature response in the soil surrounding multiple boreholes, assuming a constant heat flux from the borehole wall.

Koohi-Fayegh and Rosen [28–29] address this shortcoming in part by analysing analytically and numerically the thermal interaction among boreholes with varying heat input to the ground along the borehole. But, they do not account for the annual heat flux variation with annual heating and cooling loads. Here, consequently, the long-term performance of multiple vertical ground heat exchangers is investigated to determine their interactions and the migration of thermal plumes away from them. A numerical finite volume method in a two-dimensional meshed domain is used to evaluate the temperature rise in the ground surrounding multiple borehole systems. A sinusoidal boundary condition on the borehole wall is used in determining heat flux from it, based on bin data and building load calculations for a typical building in Belleville, IL. The temperature rise in the ground caused by ground heat exchangers is dependent on the heat flux from the heat exchanger to the ground. In this study, boundary conditions of the U-tube configuration in a typical borehole is simplified by considering only a heat flux from the borehole wall, and we correlate the climate annual periodic variations with the heat flux at the wall of the borehole.

35.2 Analysis

A building in Belleville, IL is considered, with simplified heating and cooling loads respectively expressible as

$$\dot{q}_{HL} = 32.7 - 2.7T_o \tag{35.1}$$

$$\dot{q}_{CL} = 2.7T_o - 52.3 \tag{35.2}$$

where $\dot{q}$ is in kW and outside temperature T_o is in °C. The building is assumed to be used the same way all day and internal heat gains by people, equipment, lights, etc. are taken to be constant throughout the day. The balance point for this building is approximately 13 °C for heating and 19 °C for cooling.

Heat pump efficiency varies with soil temperature and therefore bin summaries are needed to calculate heat pump power consumption and capacity for several values of soil temperature throughout the year. Table 35.1 shows an example of heat pump performance variation with soil temperature. The numbers of hours that temperatures occur in 23 2.8-Celsius-degree bins for each month in Belleville, IL are used to estimate energy consumption patterns for cooling and heating equipment at different times of the year [30]. The bin method is performed with the load profiles expressed by Eqs. (35.1) and (35.2) and the heat pump performance. The heat pump integrated capacity and the rated electric input are calculated separately for each

Table 35.1 Typical heat pump heating and cooling capacities at an air flow rate of 2.8 m^3/s

Soil temperature (°C)	Heating capacity (kW)	Total power input (kW)	Cooling capacity (kW)	Total power input (kW)
	At indoor dry bulb temperature 21 °C		At indoor dry bulb temperature 24 °C	
3	39.9	16.6	57.8	18.9
6	45.1	17.4	56.3	19.2
8	50.4	18.3	54.9	19.6
11	53.9	18.8	53.4	19.9
14	57.4	19.3	51.9	20.3
17	61.0	19.9	50.5	20.6

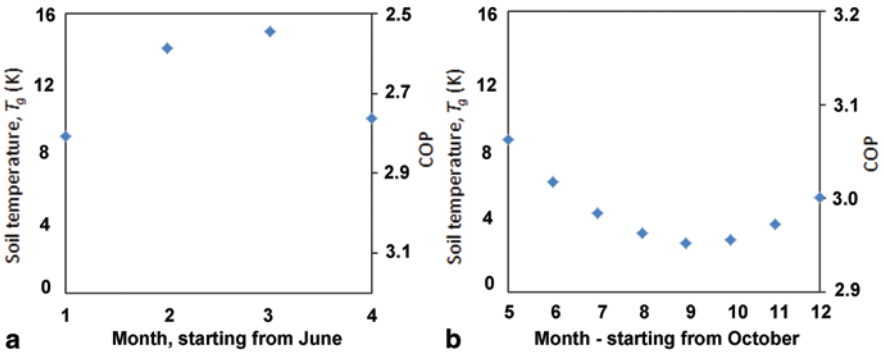

Fig. 35.1 Transient soil temperature in response to heat injection (**a**) and extraction (**b**)

month and by month based on the average monthly temperature (see Fig. 35.1). These average temperatures are obtained with an iterative procedure assuming a transient profile for soil temperature and correcting it to the results after the first-year simulation until the assumption for the soil temperature leads to the same soil temperature in the simulation.

Using the bin method, the variation of heating and cooling loads of the building throughout the year are determined (see Fig. 35.2). The heating and cooling loads of the building are not balanced throughout the year; there are 8 months of heating (red bars) and 4 months of cooling (blue bars). To balance the amount of heat that is stored in the ground, the size of the ground heat exchanger is designed based on the cooling load and supplemental heat in the form of electrical resistance is required when the heating load from the ground heat exchanger is not met.

The average temperature of the ground depends on how the cycle of the heat storage removal starts the first time the system starts to operate. Here, it is assumed that the heat is stored in the ground during the 4-month cooling season through two vertical boreholes of 200 m length. The heat flux from the borehole wall (see Fig. 35.3) demonstrates that the monthly cooling load variation is sinusoidal. Note that due to the unbalanced climate of this area, the heat stored in the ground in the

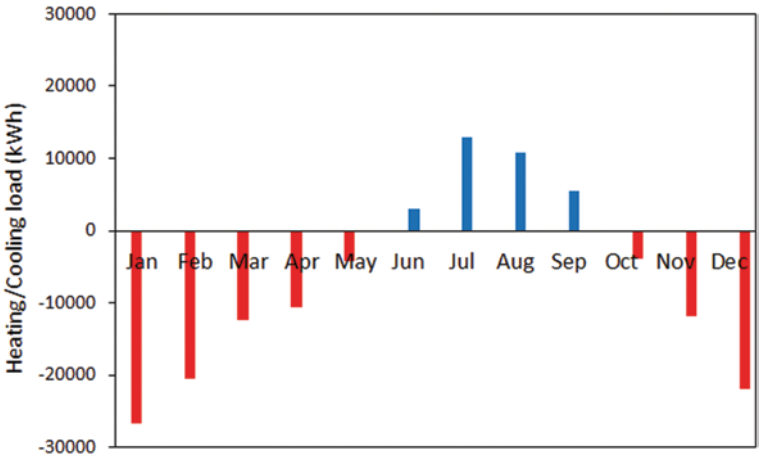

Fig. 35.2 Variation of building heating and cooling loads throughout the year

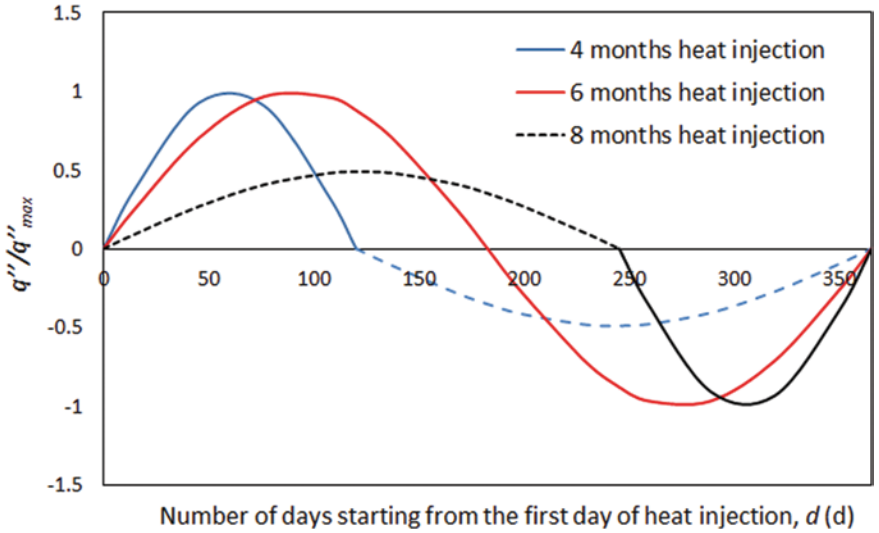

Fig. 35.3 Typical balanced heat injection and extraction profiles

cooling season only covers part of the total heating load in the 8-month heating season, so in the heating months a curve is chosen that achieves the same heat removal from the ground over its period as the heat stored in the ground in the cooling season. That is,

$$\int_0^{day_{sr}} q''_{storage}\, d(day) + R_s \int_{day_{sr}}^{365} q''_{removal}\, d(day) = 0 \tag{35.3}$$

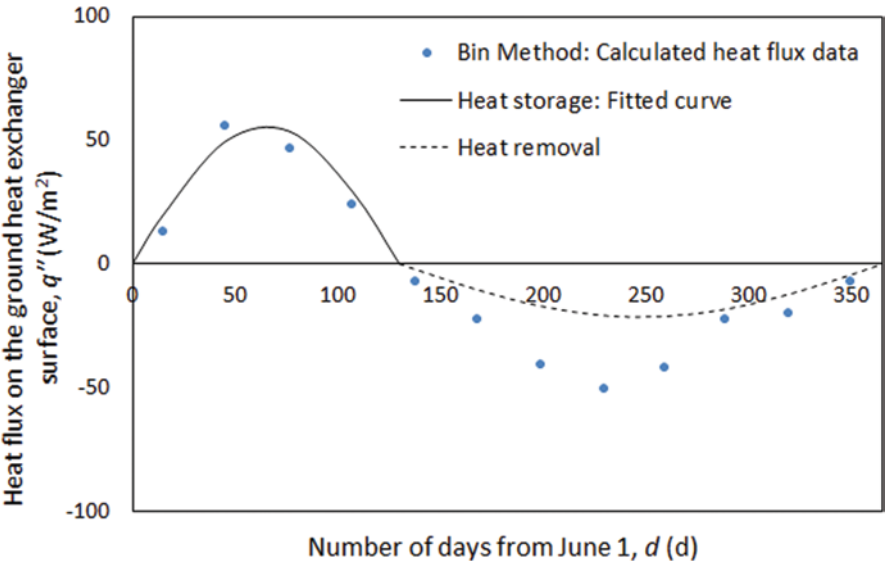

Fig. 35.4 Variation of heat flux on the ground heat exchanger wall

where R_s is the ratio of heat extraction to heat injection to the soil, which reflects heat loss. Starting from the first day of heat storage in the ground, d_{sr} is the last day of heat injection and the start of heat removal from the ground. With Eq. (35.3), a sinusoidal curve is chosen that represents the heat injection or extraction based on the data from the building load analysis (straight lines in Fig. 35.3), and the other mode of operation (heat extraction or injection) can be defined based on Eq. (35.3) that results in a balanced system that collects all the heat that it injects into the ground (dotted lines in Fig. 35.3). Three typical heat injection and extraction profiles are shown in Fig. 35.3 where a naturally balanced profile (6 months heat injection and 6 months heat extraction) is compared with two systems with unbalanced heat injection and extraction needs where one mode of heat injection or extraction is balanced according to Eq. (3) (dotted lines).

The following heat flux profiles for heat injection and extraction are chosen for the current unbalanced system where the system injects heat into the ground for 130 days. The amplitude of the heat extraction profile is chosen so that the system is balanced (Eq. 35.5). Substituting the number of days (d) from June (start of cooling season), this correlation yields q'' (in kW) (see Fig. 35.4) for heat storage and removal, respectively, as follows:

$$q''(d) = 55.9 \ \sin\left(\frac{d}{130}\pi\right) \text{for heat storage} \tag{35.4}$$

$$q''(d) = -0.70 \times 53.7 \ \sin\left(\frac{d-130}{235}\pi\right) \text{for heat removal} \tag{35.5}$$

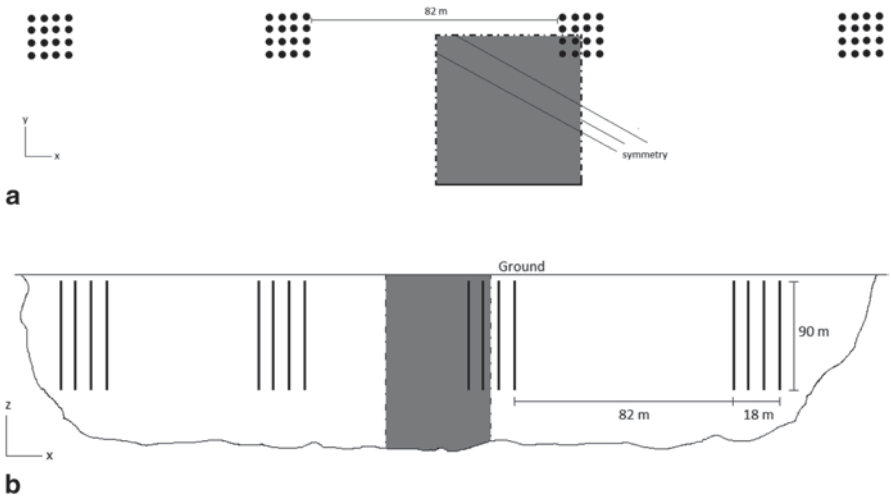

Fig. 35.5 Solution domain: **a** horizontal cross section (*xy*), and **b** horizontal cross section (*xz*)

The amplitude of the sinusoidal heat injection profile in Eq. (35.4) is chosen assuming an average heat injection of 11 W/m. At $R_s = 0.7$, the system has collected all the heat that was stored in the ground. To model the heat exchanger system and assess the effects of a periodic variation of heat flux on the borehole wall, the fitted curve for the cooling season in Fig. 35.4 and the curve for heat removal from the ground resulting in the same amount of heat removal from the ground via Eqs. (35.4) and (35.5) are used as boundary conditions on the borehole wall.

A two-dimensional model of transient heat conduction in the ground around multiple ground heat exchangers is developed. A domain of several borehole systems (spaced 100 m apart and each with 16 vertical boreholes at 6-meter distances) is considered (Fig. 35.5). Conduction is assumed to be the dominant mode of heat transfer in the ground. The general heat conduction equation in cylindrical coordinates is used, with α denoting the ground thermal diffusivity and T the ground temperature. Analytical and numerical approaches are used to calculate the temperature profiles of the ground around the boreholes starting time at t.

35.3 Numerical Approach

After building the geometric model and defining the cell size and type with the GAMBIT software, the software can automatically generate a meshed model which consists of nodes and unstructured computational triangular cells, as shown in Fig. 35.6. A larger size mesh is used in areas with lower temperature gradients, and the region nearest to the boreholes, where the temperature gradient is the higher, is meshed more finely (see Fig. 35.6). The necessary parameters including the material thermal properties as well as the boundary conditions are defined in

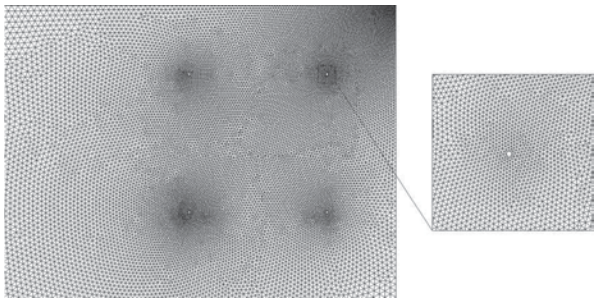

Fig. 35.6 Triangular mesh used for the solution domain

FLUENT. In the numerical approach, the transient governing integral equations for the conservation of energy are solved with a control volume method to perform the numerical simulations of heat transfer in the borehole domain. The heat transfer symmetry about the system shown in Fig. 35.5a is utilized. The gray area is the solution domain, the results of which can be replicated to the other areas due to their symmetry. Here, the farfeild representing the undisturbed ground is selected far enough from the boreholes to ensure the boundary temperature is maintained consistently at the value of the far-field temperature over the concerned time. This permits examination of the migration of thermal plume to the undisturbed ground where ecosystems might be affected.

The discretization in unstructured meshes can be developed from the basic control volume technique where the integral form of the energy conservation equation is used as the starting point:

$$\int_{CV} div\left[grad\left(T\right)\right]dV = \int_{CV} \frac{1}{a}\frac{\partial T}{\partial t}dV \tag{35.6}$$

Here, ΔV is the volume. Integration of Eq. (35.6) over a time interval from t to $t+\Delta t$ gives:

$$\int_{t}^{t+\Delta t}\int_{CV} div\left[grad(T)\right]dVdt = \int_{t}^{t+\Delta t}\int_{CV} \frac{1}{a}\frac{\partial T}{\partial t}dV\,dt \tag{35.7}$$

Using a fully implicit formulation, Eq. (35.8) is discretized in the following form:

$$a_P T_P = \sum_{all\ surfaces} a_{nb}T_{nb} + a_P^0 T_P^0 \tag{35.8}$$

where a_P, a_P^0 and a_{nb} are temperature coefficients which are calculated based on the geometric characteristics of each control volume and the time step in the numerical solution. Equation (35.8) is solved iteratively at each time level before moving to the next time step to yield updated values of temperature.

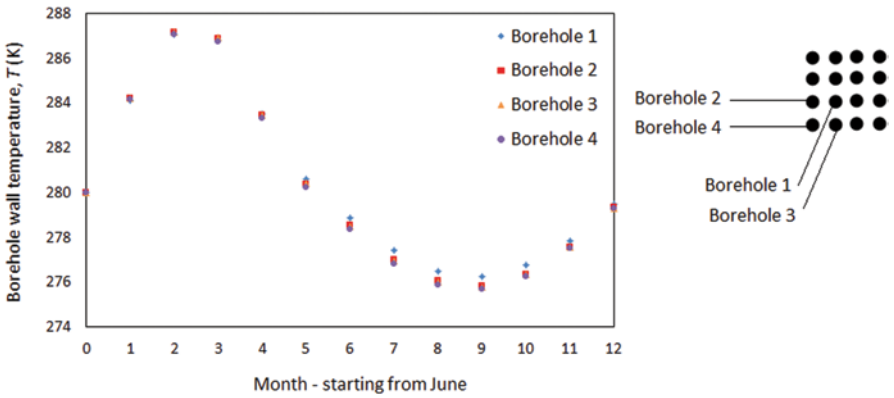

Fig. 35.7 Annual temperature variations of the borehole wall

For numerical heat transfer calculation, a uniform initial temperature of 282 K (the undisturbed ground temperature) is assumed over the entire borefield. There is no heat flux across the symmetry plane which results in zero normal gradients of temperature at a symmetry plane. At the outer edge of the domain, a constant far-field temperature condition equal to the initial temperature is applied (288 K). The periodic heat flux on the borehole wall determined with Eqs. (35.4) and (35.5) is assumed. Time is subdivided into 8760 time steps of 3600s which equals a time period 12 months. Typical geometric and thermal characteristics for the borehole and the surrounding ground (assumed dry clay) are used ($k = 1.5$ W/m K, $c = 1381$ J/kg K, $\rho = 200$ kg/m^3).

35.4 Results and Discussion

The annual temperature variations of the borehole wall for the four boreholes are shown in Fig. 35.7. It is seen that the temperature response of the borehole wall for the different borehole placements is small (<0.2%). Comparing with Fig. 35.4, it is observed that the temperature variation of the borehole wall has some similarities to the transient variation of the heat flux with its maximum and minimum values being in the second and ninth months, respectively.

Figure 35.8 shows the temperature contours in the soil surrounding the boreholes over one year. It is seen that the maximum temperature occurs in the soil immediately outside of the borehole wall and when the heat flux is at its maximum, and that the thermal plume from the system reaches its furthest extent at the end of Month 10. The temperatures for the two symmetry lines which intersect in the center of the system (Fig. 35.5a) are shown in Fig. 35.9. Figure 35.9 shows the soil temperature outside the borefield on the two symmetry lines that intersect in the centre of the borefeild: one that goes towards another borefield (symmetry $y=0$) and one

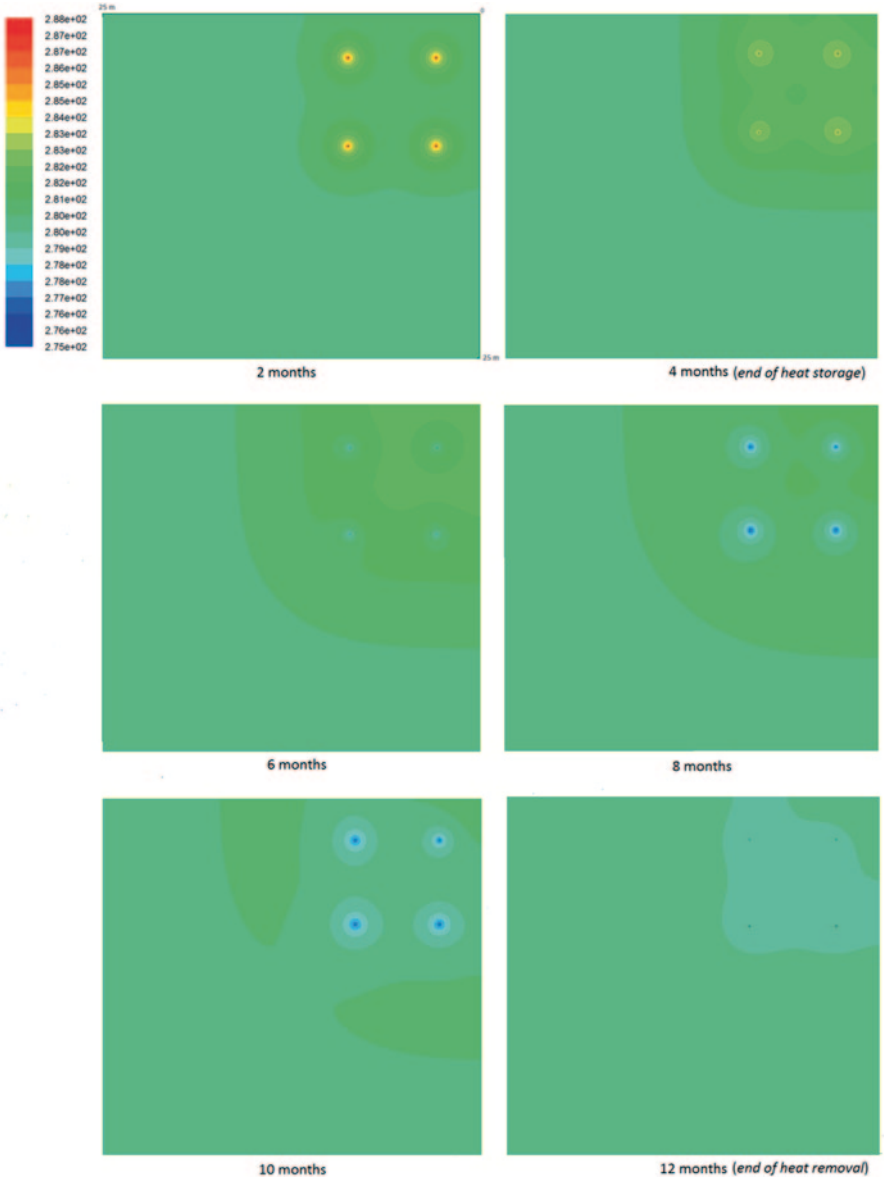

Fig. 35.8 Temperature contours in the soil surrounding the boreholes in Year 1

that goes towards farfield (symmetry $x=0$). It is seen that considering temperature rises of no more than 0.2 °C in the soil, the thermal plume in the soil caused by the system extends about 10 m from the outer edge of the borefield ($x=9$ m) and does not have any interaction with its neighbour system. It can be concluded that, if the borehole spacing and the distance of neighbour borehole systems are kept at

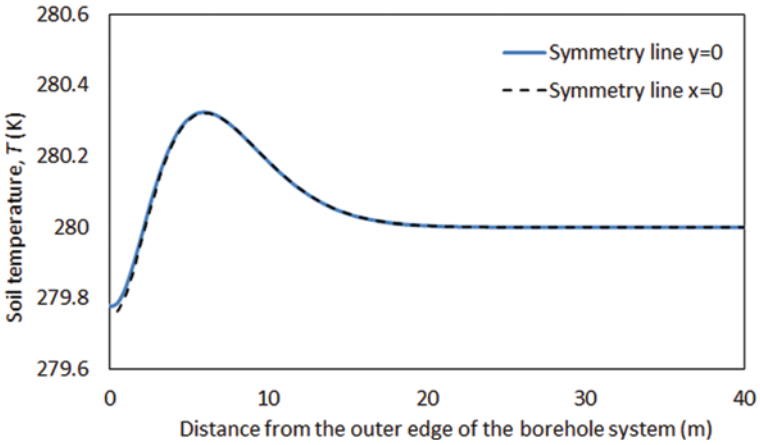

Fig. 35.9 Soil temperature outside the borehole field after 10 months of system operation

a certain distance, for a certain amount of heat flux, here given in Eqs. (35.4) and (35.5), there should not be any thermal interaction between neighbouring systems nor should there be any thermal plume flowing away from the system. It is also observed in Fig. 35.9 that the temperature of the soil is reduced by about 0.2 °C at the borefield boundary, followed by a temperature rise of 0.3 °C in the 10-meter region outside of the borefield. The temperature rise is due to heat conduction in the soil which, extends to about 10 m outside the borefield even after the heat exchanger heat injection phase. When the heat extraction phase begins at the beginning of the fifth month, the temperature of the soil immediately beyond the borehole wall reduces to about 4 °C and, therefore, the direction of the heat conduction in the soil changes towards the borefield resulting in a temperature drop in the borefield and around it. Figure 35.10 shows borehole wall temperatures for Borehole 1 and Borehole 4 during a three-year period of heat storage and removal. It is seen that the temperatures of the borehole walls fall on the same path every year. It can be concluded that for a balanced system where borehole spacing, system spacing and the heat flow rate per unit area are kept at the recommended values and there is no temperature rise or fall after the first year of system performance, there should not be any accumulation of heat in the long term if the same heat storage and removal pattern is followed every year. Even the smallest amounts of temperature rise or fall in the soil after the first year operation can result in unacceptable temperature changes in the long term (Fig. 35.11). Figure 35.11 shows the effect of the minor temperature reduction in the soil after the first year operation over five years. It is seen that the temperature at the borehole walls reduces every year and it is estimated that this pattern can affect the heat pump operation over the system's lifetime.

The temperature contours in the soil surrounding the boreholes at the end of every year in a five-year period are unchanged if all the heat is stored in the ground is collected through the ground heat exchanger. In our case, a small amount of extra

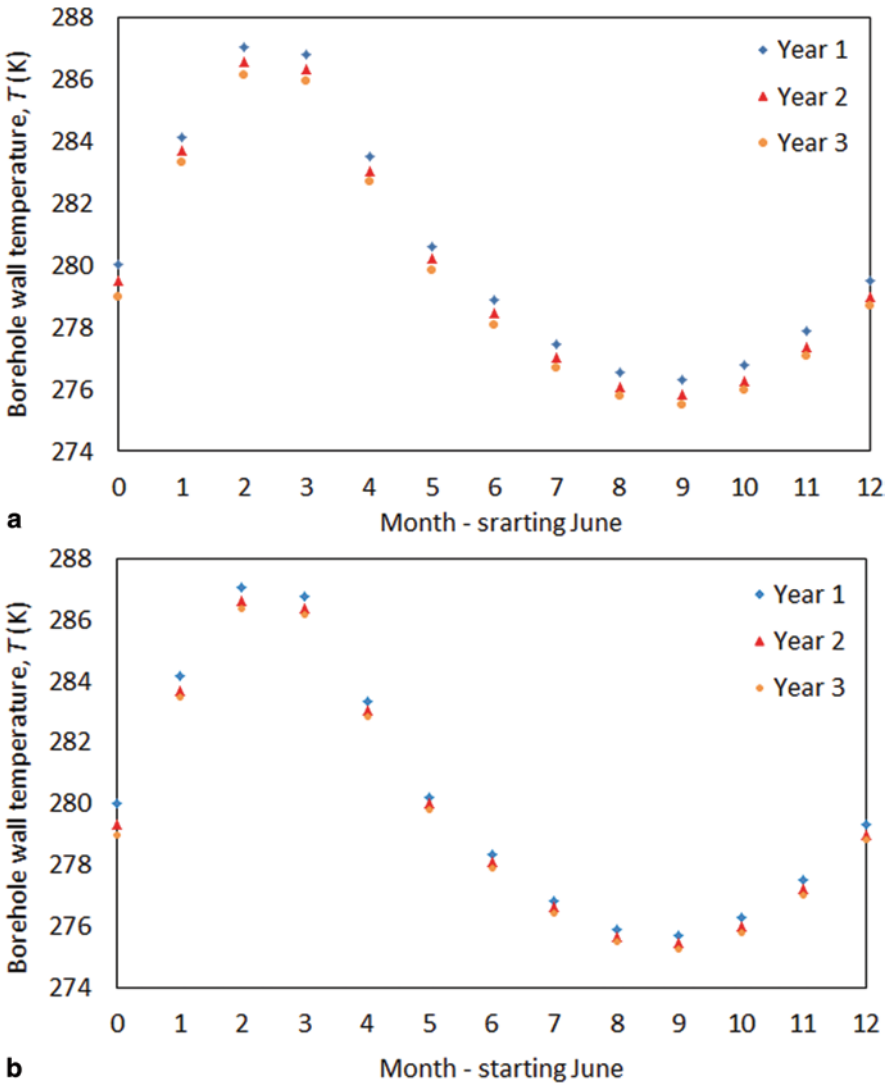

Fig. 35.10 Borehole wall temperatures: **a** Borehole 1, **b** Borehole 2

heat is also collected which causes a slight temperature reduction in the soil at the end of the each year. It can be concluded that excess heat storage or removal, which in some cases can be noticed after the first year operation, can cause a temperature rise or reduction in the long term and affect the sustainability of the system. This effect is also noticed by Wang et al. [31], who observed slightly more heat extraction from than injection into the borehole heat exchanger than required to keep the heat storage and removal in the ground balanced, and a corresponding annual reduction in the temperature of the borehole heat exchanger (0.8 °C after 15 years).

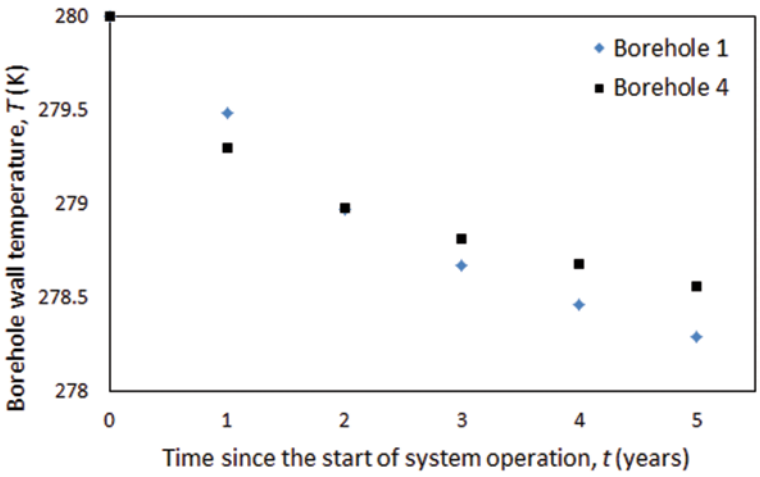

Fig. 35.11 Borehole wall temperatures of Borehole 1 and Borehole 2 over five years of system operation

Conclusions

A numerical finite volume method in a two-dimensional meshed domain is used to evaluate the temperature response in the soil surrounding multiple borehole systems. The heating and cooling loads of a building in Belleville, IL are evaluated as a case study in order to formulate an annual profile for heat injection/extraction to/from the soil. For a balanced heat injection and extraction with the ground, it is shown that there is no temperature increase or decrease in the soil surrounding the system, if the borehole spacing and the heat injection/extraction rate are within acceptable limits. Any temperature rise or decrease in the soil surrounding the ground heat exchanger after the first year operation needs to be compensated for during the second year for the sustainable system operation.

Nomenclature

α temperature coefficient
$\dot{q}$ heat load, kW
q'' heat flux at borehole wall, W/m^2
R_s ratio of heat extraction to heat injection
T temperature, K
t time, s
V volume, m^3
z axial coordinate, m

Greek Letters

α thermal diffusivity, m^2/s

Subscripts

nb node number of the adjacent cell
P centroid *P*

Superscripts

CL cooling load
HL heating load
n discretization step designation in time
o outside

Acknowledgments Support provided by the Ontario Ministry of Environment through its Best in Science program and by the Natural Sciences and Engineering Research Council of Canada is gratefully acknowledged.

References

1. Fisheries and Oceans Canada, Ontario-Great Lakes Area (DFO-OGLA), Fish Habitat and Fluctuating Water Levels on the Great Lakes, August 2009
2. Zeng HY, Diao NR, Fang Z (2003) Efficiency of vertical geothermal heat exchangers in ground source heat pump systems. J Therm Sci 12(1):77–81
3. Zeng HY, Diao NR, Fang Z (2003). Heat transfer analysis of boreholes in vertical ground heat exchangers. Int J Heat Mass Transf 46(23):4467–4481
4. Jun L, Xu Z, Jun G, Jie Y (2009) Evaluation of heat exchange rate of GHE in geothermal heat pump systems. Renew Energy 34:2898–2904
5. Eskilson P (1987) Thermal analysis of heat extraction boreholes. Doctoral thesis, Department of Mathematical Physics, University of Lund, Lund, Sweden
6. Hellström G (1991)Ground heat storage: Thermal analyses of duct storage systems. Doctoral thesis. Department of Mathematical Physics, University of Lund, Lund, Sweden
7. Hart DP, Couvillion R (1986) Earth coupled heat transfer. National Water Well Association, Dublin
8. Lamarche L, Beauchamp B (2007). A new contribution to the finite line source model for geothermal boreholes. Energy and Build 39(2):188–198
9. Kavanaugh SP (1995) A design method for commercial ground-coupled heat pumps. ASHRAE Trans 101(2):1088–1094
10. Kavanaugh SP (1985) Simulation and experimental verification of vertical ground coupled heat pump systems. Doctoral Thesis, Oklahoma State University, USA
11. Kavanaugh SP (1992) Simulation of ground-coupled heat pumps with an analytical solution. Proceedings of the ASME International Solar Energy Conference, Solar Engineering, New York, 1, 395–400
12. Hikari F, Ryuichi I, Takashi I (2004) Improvements on analytical modeling for vertical U-tube ground heat exchangers. Geotherm Resour Counc Trans 28:73–77
13. Zeng HY, Diao NR, Fang Z (2002) A finite line-source model for boreholes in geothermal heat exchangers. Heat Transf Asian Res 31(7):558–567
14. Diao NR, Zeng HY, Fang ZH (2004) Improvement in modeling of heat transfer in vertical ground heat exchangers. HVAC & R Res 10(4):459–470
15. Yang, Shi WM, Liu G, Chen Z (2009) A two-region simulation model of vertical U-tube ground heat exchanger and its experimental verification. Appl Energy 86:2005–2012

16. Bandyopadhyay G, Gosnold W, Mannc M (2008) Analytical and semi-analytical solutions for short-time transient response of ground heat exchangers. Energy and Build 40:1816–1824
17. Bernier M, Pinel A, Labib P, Paillot R (2004) A multiple load aggregation algorithm for annual hourly simulations of GCHP systems. HVAC & R Res 10(4):471–487
18. Yavuzturk C (1999) Modeling of vertical ground loop heat exchangers for ground source heat pump systems. Doctoral thesis, Oklahoma State University, USA
19. Yavuzturk C, Spitler JD (2001) Field validation of a short time step model for vertical ground-loop heat exchangers. ASHRAE Trans 107(1):617–625
20. Yavuzturk C, JD Spitler, SJ Rees (1999) A transient two-dimensional finite volume model for the simulation of vertical U-tube ground heat exchangers. ASHRAE Trans 105(2):465–474
21. Muraya NK (1995) Numerical modeling of the transient thermal interference of vertical U-tube heat exchangers. PhD Thesis, College Station, Texas A & M University, Texas, USA
22. Rottmayer SP, Beckman WA, Mitchell JW (1997) Simulation of a single vertical U-tube ground heat exchanger in an infinite medium. ASHRAE Trans 103(2):651–658
23. Lee CK, Lam HN (2008) Computer simulation of borehole ground heat exchangers for geothermal heat pump systems. Renew Energy 33:1286–1296
24. Li Z, Zheng M (2009) Development of a numerical model for the simulation of vertical U-tube ground heat exchangers. Appl Therm Eng 29(5–6):920–924
25. Fang ZH, Diao NR, Cui P (2002) Discontinuous operation of geothermal heat exchangers. Tsinghua Sci and Technol 7(2):194–197
26. He M, Rees S, Shao L (2009) Simulation of a domestic ground source heat pump system using a transient numerical borehole heat exchanger model, Proceedings of the 11th International Building Performance Simulation Association Conference, Glasgow, Scotland, 607–614
27. Koohi-Fayegh S, Rosen MA (2012) Examination of thermal interaction of multiple geothermal storage and heat pump systems. Appl Energy 97, 962–969
28. Koohi-Fayegh S, Rosen MA (2011) A Numerical Approach to Assessing Thermally Interacting Multiple Boreholes with Variable Heating Strength, Proc. 1st World Sustainability Forum
29. Koohi-Fayegh S., Rosen MA (2012b) Thermally Interacting Multiple Boreholes with Variable Heating Strength, Proc. eSim Conference, Halifax, Nova Scotia, in press
30. USAF (1978) Engineering weather data. Department of the Air Force Manual AFM 88–29. U.S. Government Printing Office, Washington, D.C
31. Wang E, Fung AS, Qi i, Leong WH (2012). Performance prediction of a hybrid solar ground-source heat pump system Energy and Build 47: 600–611

Chapter 36
Environmentally Friendly Systems: Earth Heat Pump System with Vertical Pipes for Heat Extraction for Domestic Heating and Cooling

Saffa Riffat, Siddig Omer and Abdeen Omer

Abstract Geothermal heat pumps (GSHPs), or direct expansion (DX) ground source heat pumps, are highly efficient renewable energy technology, which use the earth, groundwater or surface water as heat sources when operating in heating mode or as heat sink when operating in cooling mode. They are receiving an increasing interest because of their potential to reduce primary energy consumption and thus reduce emissions of the GHGs. The main concept of this technology is that it utilises the lower temperature of the ground, which approximately remains relatively stable throughout the year, to provide space heating, cooling and domestic hot water for buildings. The main goal of this study is to stimulate the uptake of the GSHPs. Recent attempts to stimulate alternative energy sources for heating and cooling of buildings has emphasised the utilisation of the ambient energy from ground source and other renewable energy sources. The purpose of this study, however, is to highlight the fact that use of the GSHPs as an environmental friendly technology able to provide efficient utilisation of energy in the buildings sector in an attempt to promote using of the GSHPs for heating and cooling. The paper presents experimental and theoretical results of the DX GSHPs carried out at the Department of Architecture and Built Environment in the University of Nottingham. The study highlights the potential energy cost saving that could be achieved through the use of ground energy sources. It also focuses on the optimisation and improvement of the operation conditions of the heat cycle and performance of the DX GSHP. It is concluded that the direct expansion of the GSHP, combined with the ground heat exchanger in foundation piles and the seasonal thermal energy storage could play a major role reducing building energy needs.

Keywords Heat pump · Direct expansion GSHPs · Ground source · Performance of GSHP · Seasonal energy storage · Efficiency

A. Omer (✉) · S. Riffat · S. Omer
Department of Architecture and Built Environment, Faculty of Engineering,
University of Nottingham, Nottingham NG7 2RD, UK
e-mail: abdeenomer2@yahoo.co.uk

S. Riffat
e-mail: saffa.riffat@nottingham.ac.uk

S. Omer
e-mail: siddig.omer@nottingham.ac.uk

I. Dincer et al. (eds.), *Progress in Sustainable Energy Technologies: Generating Renewable Energy,* DOI 10.1007/978-3-319-07896-0_36,

36.1 Introduction

It well documented that, globally buildings are responsible for approximately 40 % of the total world annual energy consumption [1]. Most of this energy is for the provision of lighting, heating, cooling and air conditioning. An increase in awareness of the environmental impact of CO_2, NO_x and CFCs emissions triggered a renewed interest in environmentally friendly cooling and heating technologies. Under the 1997 Montreal Protocol, governments agreed to phase out chemicals used as refrigerants that have the potential to destroy stratospheric ozone. It was therefore considered desirable to reduce energy consumption in order to decrease the rate of depletion of world energy reserves as well as the pollution to the environment.

One way of reducing building energy consumption is to design buildings, which are more efficient in their use of energy for heating, lighting, cooling and ventilation. Passive measures, particularly natural or hybrid ventilation rather than air-conditioning, can dramatically reduce primary energy consumption [2]. Therefore, promoting innovative renewable energy applications including the ground source energy may contribute to preservation of the ecosystem by reducing emissions at local and global levels. This will also contribute to the amelioration of environmental conditions by replacing conventional fuels with renewable energies that produce no air pollution or GHGs. An approach is needed to integrate renewable energies in a way to achieve high building performance standards. However, because renewable energy sources are stochastic and geographically diffuse, their ability to match demand is determined by the adoption of one of the following two approaches [3]: the utilisation of a capture area greater than that occupied by the community to be supplied, or the reduction of the community's energy demands to a level commensurate with the locally available renewable resources. Ground source heat pump (GSHP) systems (also referred to as geothermal heat pump systems, earth-energy systems and GeoExchange systems) have received considerable attention in recent decades as an alternative energy source for residential and commercial space heating and cooling applications. The GSHP applications are one of three categories of geothermal energy resources as defined by ASHRAE [4] and include high-temperature (>150 °C) for electric power production, intermediate temperature (<150 °C) for direct-use applications and GSHP applications (generally (<32 °C). The GSHP applications are distinguished from the others by the fact that they operate at relatively low temperatures.

The term "ground source heat pump" has become an inclusive term to describe a heat pump system that uses the earth, ground water, or surface water as a heat source and/or heat sink. The GSHPs utilise the thermal energy stored in the earth through either a vertical or horizontal closed loop heat exchangers buried in the ground. Although, geographically, this energy has local concentrations, its distribution globally is widespread. The amount of heat that is, theoretically, available between the earth's surface and a depth of 5 km is around 140 × 1024 J/day [5]. Only a fraction of this (5 × 1021 J) can be regarded as having economic prospects, and only about 10 % of this is likely to be exploited by the year 2020 [6]. Three main techniques are used to exploit the heat available: geothermal aquifers, hot dry rocks and ground

source heat pumps. However, only the ground source heat pumps are considered in this study because the other previous two are expensive. Many geological factors impact directly on site characterisation and subsequently the design and cost of the GSHP systems. The geological prognosis for a site and its anticipated rock properties influence the drilling methods and therefore the system cost [7]. Other factors that are important to system design include predicted subsurface temperatures and the thermal and hydrological properties of strata [8].

The purpose of this study is to examine the effectiveness of ground source heat pump (GSHP) use for building space heating in a given geographical conditions and assess the potential energy saving cost. A demonstration facility was developed as part of this study and extensive measurements that will assist future GSHP systems designs and aid reducing uncertainty were performed, in order to draw a wider picture on the capability and potential of ground source heat pumps to meet the energy needs of buildings.

36.2 Performance of Ground Sources Heat Pump

The performance of the heat pump depends on the performance of the ground loop and vice versa. Some of the factors that may affect performance of the GSHP include:

- The underground pipes/boreholes may create undesirable hydraulic connections between different water bearing strata.
- Undesirable temperature changes in the aquifer that may result from the operation of a GSHP.
- Other issue that may need to be taken into consideration is the pollution of groundwater that might occur from leakage of additive chemicals used in the system.

Efficiencies of the GSHPs can be high because the ground maintains a relatively stable temperature allowing the heat pump to operate close to its optimal design point. In contrary in air source heat pumps, the air temperature varies both throughout the day and seasonally such that air temperatures, and therefore efficiencies, are lowest at times of peak heating demand. Heat pump efficiencies improve as the temperature differential between 'source' and demand temperature decreases, and when the system can be 'optimised' for a particular situation. The relatively stable ground temperatures moderate the differential at times of peak heat demand and provide a good basis for high performance.

The refrigerant is circulated directly through the ground heat exchanger in a direct expansion (DX) system but most commonly GSHPs are indirect systems, where a water/antifreeze solution circulates through the ground loop and energy is transferred to or from the heat pump refrigerant circuit via a heat exchanger. This application will only consider closed loop systems. The provision of cooling, however, will result in increased energy consumption and the efficiency it is supplied with.

For electrically driven heat pump the steady state performance at a given set of temperatures could be assessed in terms of the coefficient of performance (COP). It is defined as the ratio of the heat delivered by the heat pump and the electricity supplied to the compressor [9]:

$$\text{COP} = \text{heat output (kWth)/electricity input (kWel)} \qquad (36.1))$$

36.3 System Analysis, and Experimental Test Rig and Measurements

This section describes the details of the prototype GSHP test rig, details of the construction and installation of the heat pump, heat exchanger, heat injection fan and water supply system. It also, presents a discussion of the experimental tests being carried out.

The construction of the experimental rig was undertaken in three steps. The first step included drilling three boreholes (each 30 m deep, and diameter 143 mm), digging out the pit and the connection of the manifolds and preparation of coils. Holes were grouted with bentonite and sand. The pipes were laid and tested with nitrogen. The pit was backfilled and the heat pump was installed. The second part involved setting up of the main experimental rig: construction and installation of the heat injection fan, water pump, heat exchangers, expansion valve, flow meters and the electricity connections. The third stage was the connection of the heat pump and measuring transducers.

The schematic of the test rig that was used to support the two ground-loop heat exchangers is shown in Fig. 36.1. The test rig consisted of two main loops: heat source loop and evaporation heat pump. The 3 boreholes, each 30 m deep were used to provide sufficient energy for the heat pump. The closed-loop systems were connected to wells, and the ground-loop heat exchangers were connected to the heat pump.

The measurements of the different parameters have been carried out during the testing period using the data logger (DT 500). The following parameters were measured:

1. Indoor air temperature and relative humidity values
2. Pit temperature for all boreholes
3. Vapour temperature
4. Condenser temperature
5. Compressor outlet temperature and
6. Heat exchanger temperature.

The system monitored for a period of two-year during which the data were analyzed to assess the effect of the various parameters on the performance of the GSHP. Energy input and output of the system are calculated in order to assess the COP of the system.

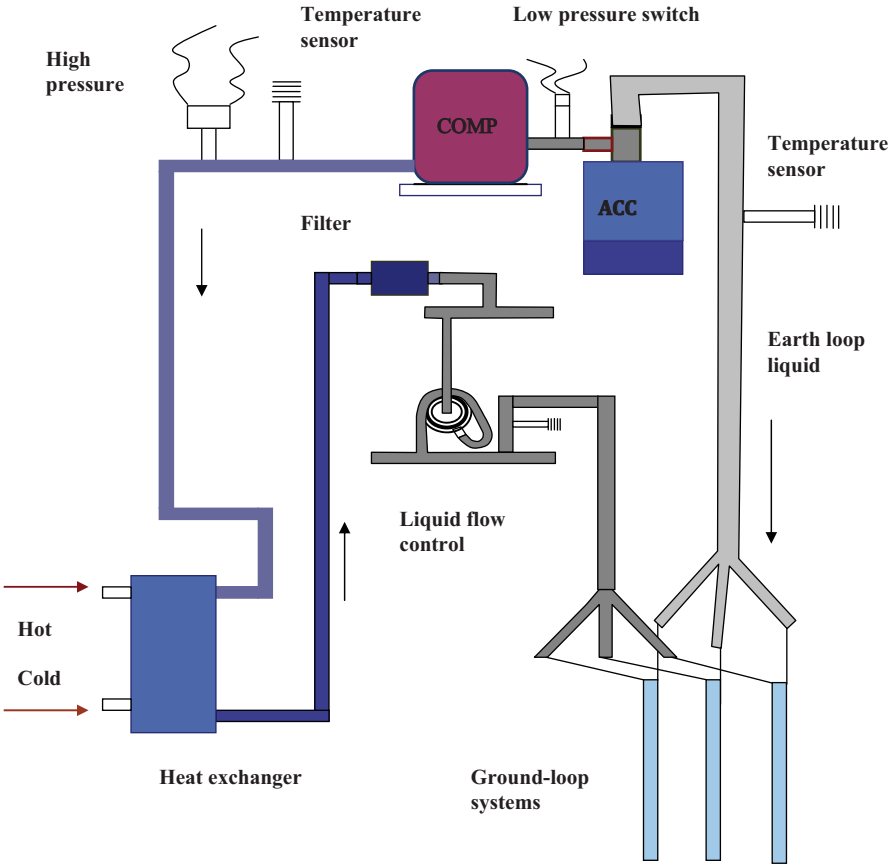

Fig. 36.1 Details of the experimental GSHP rig

Two different control mechanisms for the supply of energy from the heat pump for space heating were tested. From March until July, the supply of energy from the heat pump to the space heating system was controlled by a thermostat mounted in the room. From August, an alternative control using an outside air temperature sensor was used in order to reduce the need for the auxiliary heating. This is because the amount of energy the auxiliary heater is using will have a large effect on the cost of the system. This resulted in the heat pump operating more continuously in cold weather, and considerably less use of the auxiliary heater has been made. Using the outdoor air temperature sensor, results in the return temperature being adjusted for changes in the outdoor temperature and good prediction of the heating requirement. Very stable internal temperatures were maintained. The same periods of the year have been compared, using the room temperature sensor and an outdoor air temperature sensor. The operating conditions were not identical, but the average 24-h temperatures for the two periods were quite similar at 9.26 and 9.02 °C respectively.

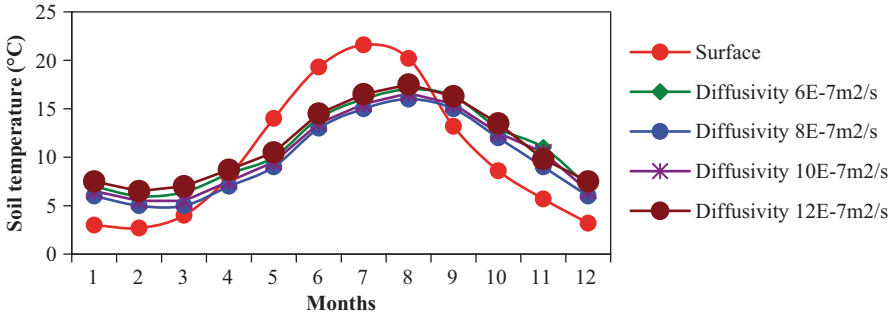

Fig. 36.2 Variation of the temperature of ground at depth 1 m for different thermal diffusivity

36.4 Results and Discussions

Thermal Behaviour of the Ground

From Eq. (36.2]), it can be inferred that the wave amplitude decreases exponentially with depth [10]:

$$Ax = As\ e^{-x\sqrt{\frac{\Pi}{365\alpha}}} \tag{36.2}$$

Where:

Ax is the thermal wave amplitude at the depth x (°C)

In addition, the phase lag decreases linearly with the depth.

$$t - to = ½\sqrt{\frac{365}{\alpha\Pi}}x \tag{36.3}$$

The Eq. (36.2 and 36.3) can be used to deduce the ground temperature at any depth depending on the surface temperature of the soil (mean temperature and amplitude) and of the physical properties of the soil profile: conductivity (k), density (ρ) and specific heat (c), grouped in the apparent thermal diffusivity (α) considering a homogenous soil [11, 12]:

$$\alpha = k / \rho c \tag{36.4}$$

Thus, the soil properties and depth determine the damping and the phase lag of the temperature wave. The greater the depth to which the pit is excavated and the lower the apparent thermal diffusivity of the soil, the greater the stability inside it and the less the external variations will be perceived. Figures 36.2, 36.3, 36.4 and 36.5 are

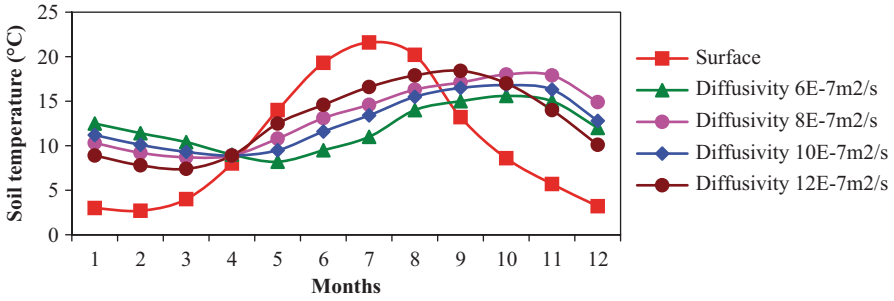

Fig. 36.3 Variation of temperature of ground at depth 3 m for different thermal diffusivity

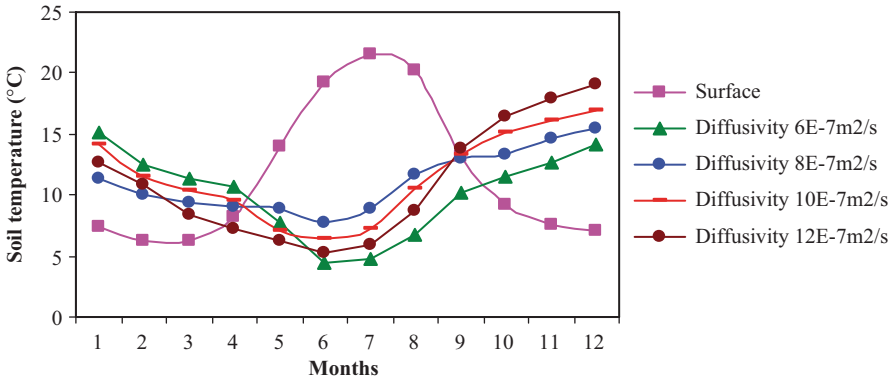

Fig. 36.4 Variation of the temperature of ground at depth 5 m for different thermal diffusivity

examples in which it can be seen how temperature varies with the depth and thermal diffusivity of an ideal surface temperature of 12 °C, annual amplitude of 10 °C and phase lag of 20 days.

As well as damping the amplitude and phase lag of temperature wave, the oscillations also reduce with depth although this effect is not shown in Eq. 36.3. Figures 36.6–36.7 show experimental data of the ground temperature, where it can be seen how the daily variations recorded decrease as depth increases. The stability of earth temperatures with respect to daily cycles and the phase lag of the annual wave make the ground a useful heat source in winter and a means of cooling in summer.

$$T(x,t) = (T_m - k) A_s \, e^{-x\sqrt{\frac{\Pi}{365\alpha}}} \cos\left[\frac{2\Pi}{365}\left(t - t_o - \frac{x}{2}\sqrt{\frac{365}{\Pi\alpha}}\right)\right] \tag{36.5}$$

The measured temperatures of the ground loops start at the winter—14 °C are the mixed output of all ground loops (situated at 1 m and 1.7 m and two levels in between) as shown in Fig. 36.8. The surface temperature from 2 m onwards the

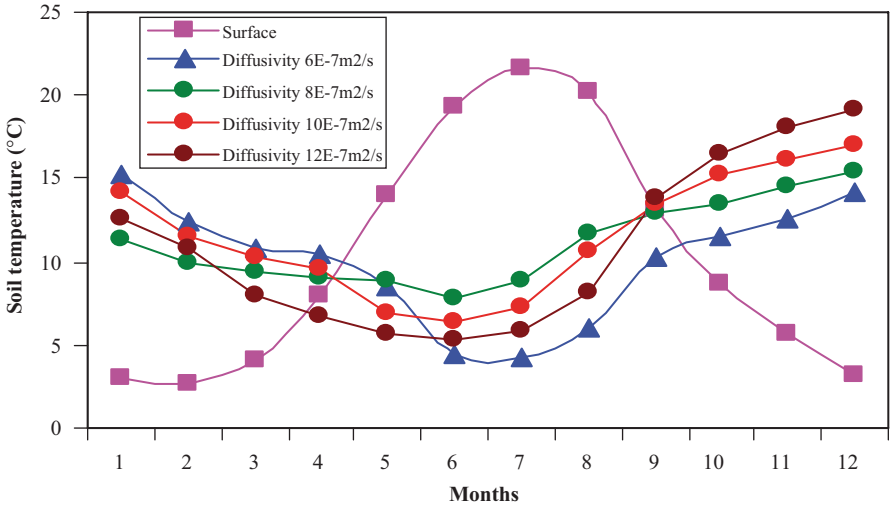

Fig. 36.5 Variation of the temperature of ground at depth 7 m for different thermal diffusivity

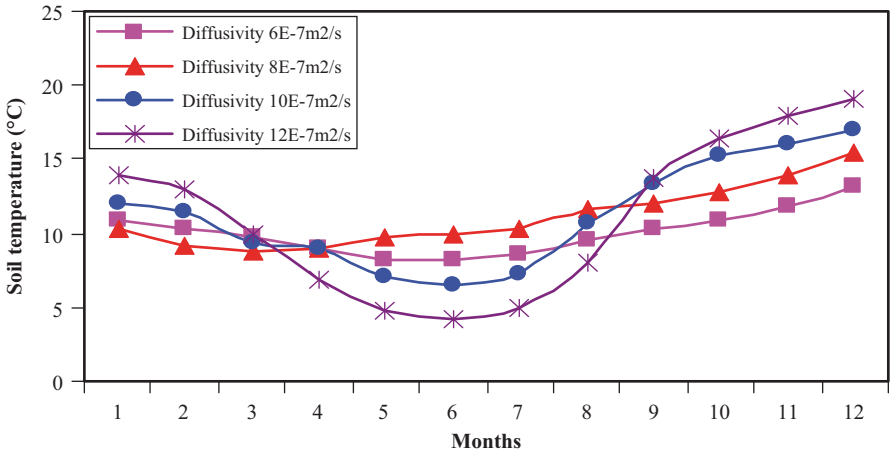

Fig. 36.6 Temperature of ground at depth 9 m for different thermal diffusivity

recorded temperatures for the more recent set of measurements were slightly lower than those from the earlier, whilst the 1 m measurement was higher. This suggests that the surface temperature may have an influence, probably through conduction within the copper pipe, on the temperature recorded at the first metre depth, but that this effect becomes negligible at lower depths.

There are lots of disturbing factors affecting measurements. Surface topography, vegetation and hydrological conditions affect also to the subsurface temperature. Below surface the temperature profile is being disturbed by changes in groundwater conditions. From the measurements it has been found out that daily variation of

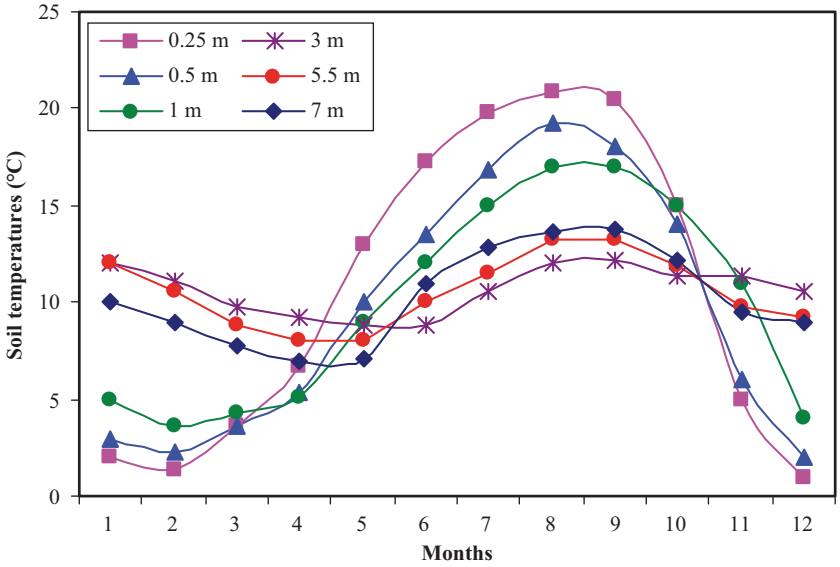

Fig. 36.7 Experimental soil temperatures at various depths

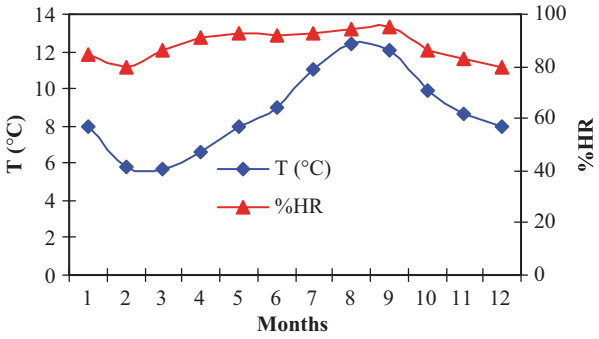

Fig. 36.8 Experimental temperature and relative humidity values for the air inside the pit at an average depth of 3 m

surface temperature can be seen in the depth of 2 m and annual variation of surface temperature can be seen in the depth of 20 m. Rapid temperature changes are therefore not conveyed very deep so the temperature reconstructions from boreholes do not show rapid temperature changes, but they show how the temperature has varied during decades and centuries.

Performance of the GSHP

Figure 36.9 shows the summary results of the data collected, at specific periods of the tests. Temperature T_1, T_2, T_3, T_4, T_5 and T_6 shown in Fig. 36.9 indicate Heat

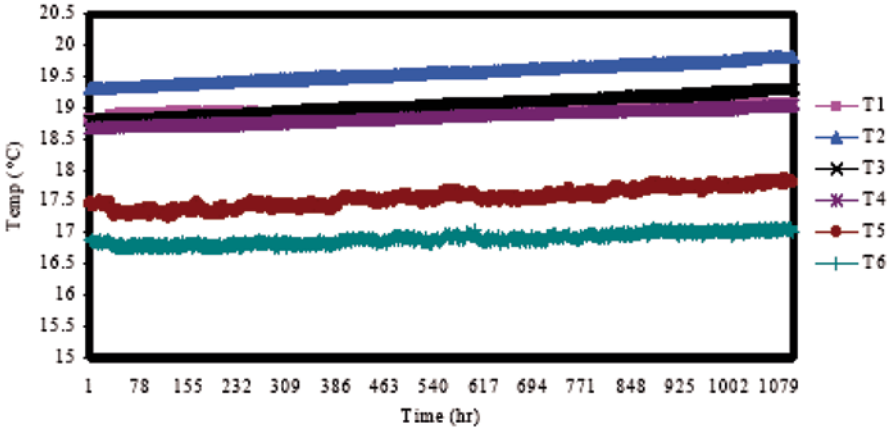

Fig. 36.9 Variation of temperatures for a period of 6 days for the GSHP system

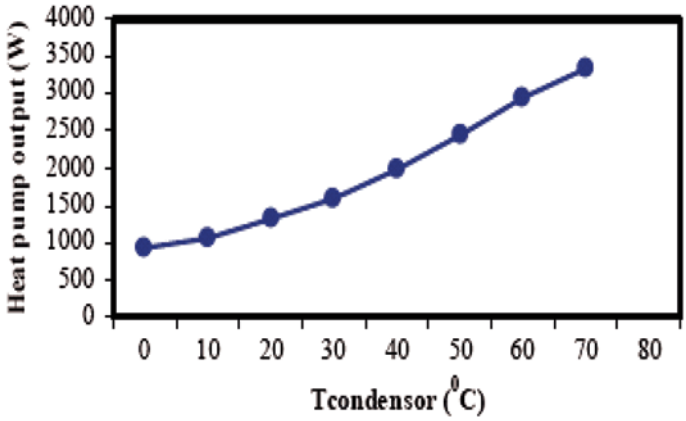

Fig. 36.10 Variation of heat pump output with condenser temperature

exchanger temperature out let, compressor outlet temperature, condenser outlet temperature, vapour temperature, indoor air temperature, and pit temperature respectively.

The performance of the heat pump is inversely proportional to the difference between the condensation temperature and the evaporation temperature (the temperature lift). These are stable operating conditions, but not true steady state conditions. At output temperatures greater than 40 °C, the heat pump was providing heating to the domestic hot water. The variation is largely due to variations in the source temperatures (range 0.2 to 4.3 °C). These results indicate that the system performance meets the specified rating for the heat pump of 2.5 kW at an output temperature in the range of 45 (older systems) and 65 °C (newer systems).

Figure 36.10 shows the daily total space heating from the heat pump and the auxiliary heater for the two heating control systems versus condenser temperature.

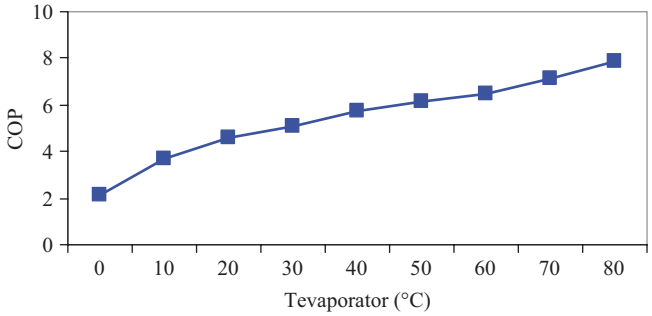

Fig. 36.11 Heat pump performance vs evaporation temperature (°C)

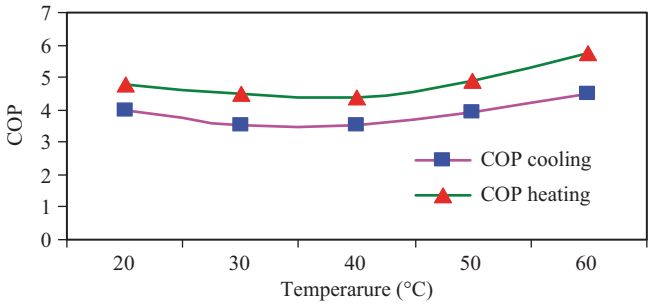

Fig. 36.12 COP Vs condenser temperatures for different applications (°C)

Figure 36.11 shows the COP of heat pump as a function of the evaporation temperature. As can be seen, the theoretical measured is strongly dependent on the temperature lift. It is important not only to have as high a source temperature as possible but also to keep the sink temperature (i.e., heating distribution temperature) as low as possible. In practice, the achievable heat pump COP is lower than the ideal COP because of losses during the transportation of heat from the source to the evaporator and from the condenser to the room and the compressor. However, technological developments are steadily improving the performance of the heat pumps.

Figure 36.12 shows COP of the ground source heat pump for different applications, and show that this increases slightly with condenser temperatures. As expected, the achievable COP is lower in cooling mode than in heating mode.

Over its first year of operation, the ground source heat pump system has provided 91.7 % of the total heating requirement of the room and 55.3 % of the domestic water-heating requirement, although only sized to meet half the design-heating load. The heat pump has operated reliably and its performance appears to be at least as good as its specification. The system has a measured annual performance factor of 3.16. The system is quiet and unobtrusive and achieved comfort levels.

Additionally, the heat pump did not reduce the useful space in the laboratory, and there are no visible signs of the installation externally (no flue, vents, etc.).

However, the performance of the heat pump system could also be improved further by eliminating unnecessary running of the integral distribution pump. It is estimated that reducing the running time of this pump, which currently runs virtually continuously, would increase the overall performance factor to 3.43. This would improve both the economics and the environmental performance of the system. More generally, there is still a potential for improvement in the performance of the heat pump, and seasonal efficiency for ground source heat pumps of 4.0 might be possible. It is also likely that unit cost will fall as production volumes increase.

The ground source heat pump (GSHP) systems have been identified as one of the best sustainable energy technologies for space heating and cooling in residential and commercial buildings. The GSHPs for building heating and cooling are extendable to more comprehensive applications and can be combined with the ground heat exchanger in foundation piles as well as seasonal thermal energy storage from solar thermal collectors. Heat pump technology can be used for heating only, or for cooling only, or be 'reversible' and used for heating and cooling depending on the demand. Reversible heat pumps generally have lower COPs than heating only heat pumps. They will, therefore, result in higher running costs and emissions and are not recommended as an energy-efficient heating option. The GSHP system can provide 91.7% of the total heating requirement of the building and 55.3% of the domestic water-heating requirement, although only sized to meet half the design-heating load. The heat pump can operate reliably and its performance appears to be at least as good as its specification. The system has a measured annual performance factor of 3.16. The heat pump system for domestic applications could be mounted in a cupboard under the stairs and does not reduce the useful space in the house, and there are no visible signs of the installation externally (no flue, vents, etc.).

The performance of the heat pump system could also be improved by eliminating unnecessary running of the integral distribution pump. It is estimated that reducing the running time of this pump, which currently runs virtually continuously, would increase the overall performance factor to 3.43. This would improve both the economics and the environmental performance of the system. More generally, there is still potential for improvement in the performance of heat pumps, and seasonal efficiencies for ground source heat pumps of 4.0 are being achieved. It is also likely that unit costs will fall as production volumes increase. By comparison, there is little scope to further improve the efficiency of gas- or oil-fired boilers. The need for alternative low-cost energy has given rise to the development of the GSHP systems for space cooling and heating in residential and commercial buildings. The GSHP systems work with the environment to provide clean, efficient and energy-saving heating and cooling the year round. The GSHP systems use less energy than alternative heating and cooling systems, helping to conserve the natural resources. The GSHP systems do not need large cooling towers and their running costs are lower than conventional heating and air-conditioning systems. As a result, GSHP systems have increasingly been used for building heating and cooling with an annual rate of increase of 10% in recent years.

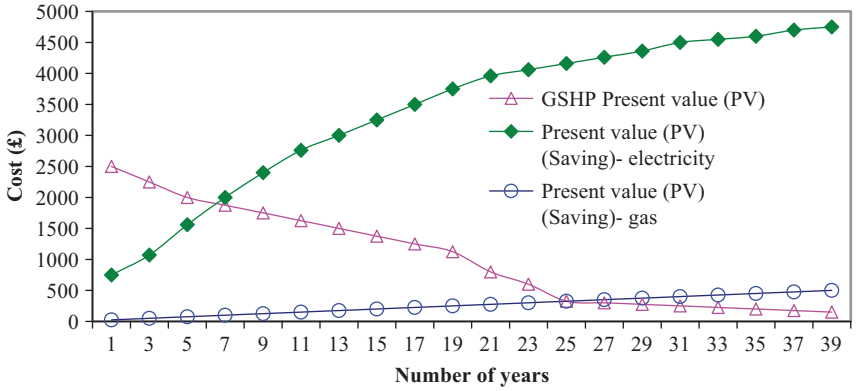

Fig. 36.13 Comparison of present values of different energy sources

36.5 Cost Analysis of the GSHPS

The most important first step in the design of a GSHP installation is the calculation of the building's heat load, its related energy consumption profile and the domestic hot water requirements. This will allow accurate sizing of the heat pump system. This is particularly important because the capital cost of a GSHP system is generally higher than for alternative conventional systems and economies of scale are more limited. Oversizing will significantly increase the installation cost for little operational saving and will mean that the period of operation under part load is increased. Frequent cycling, on the other hand, reduces equipment life and operating efficiency. Conversely if the system is undersized design conditions may not be met and the use of top-up heating, usually direct acting electric heating, will reduce the overall system efficiency

The discounted payback period (DPP) is a method of comparing alternative investments or for evaluating a single investment in payback analysis. Payback period is the time required for the total accumulated savings or benefits of a system to offset investment costs. Since the time value of money must be considered in payback computations, all the costs must be discounted to calculate the discounted payback period. Payback is achieved when the total accumulated present value (PV) savings are enough to offset the total PV costs of an alternative. The discounted payback period is simply the total elapsed time between the point when the savings begin to accrue and the point at which payback will occur.

Figure 36.13 shows the discounted payback period of the combination of GSHP and gas heating system about 5.5 years for electric heater heating system and 25 years comparing gas-fired condensing boiler system.

However, in terms of the number of year of discounted payback period, the combined GSHP and gas heating system is less attractive compared with an electric heater heating system and gas-fired condensing boiler, with the payback period of 5.5 years and 25 years respectively.

The choice of horizontal or vertical system depends on the land area available, local ground conditions and excavation costs. As costs for trenching and drilling are generally higher than piping costs it is important to maximise the heat extraction per unit length of trench/borehole. The piping material used affects life, maintenance costs, pumping energy, capital cost and heat pump performance. Both gas-fired and oil-fired systems are likely to have higher annual servicing costs than those for the heat pump system. The performance of the heat pump system could also be improved by eliminating unnecessary running of the integral distribution pump. This would improve both the economics and the environmental performance of the system. More generally, there is still potential for improvement in the performance of heat pumps and seasonal efficiencies for the DX GSHPs. It is also likely that unit costs will fall as production volumes increase. The GSHPs can provide an energy-efficient, cost-effective way to heat and cool building facilities.

Conclusions

The installation and operation of a geothermal system may be affected by various factors. These factors include, but are not limited to, the field size, the hydrology of the site the thermal conductivity and thermal diffusivity of the rock formation, the number of wells, the distribution pattern of the wells, the drilled depth of each well, and the building load profiles. The performance of the heat pump system could also be improved by eliminating unnecessary running of the integral distribution pump. This would improve both the economics and the environmental performance of the system.

The results of soil properties investigation have also demonstrated that the moisture content of the soil has a significant effect on its thermal properties. When water replaces the air between particles it reduces the contact resistance. Consequently, the thermal conductivity varied from 0.25 W/m/K for dry soil to 2.5 W/m/K for wet soil. However, the thermal conductivity was relatively constant above a specific moisture threshold. In fact, where the water table is high and cooling loads are moderate, the moisture content is unlikely to drop below the critical level. In Nottingham, where the present study was conducted, soils are likely to be damp for much of the time. Hence, thermal instability is unlikely to be a problem. Nevertheless, when heat is extracted, there will be a migration of moisture by diffusion towards the heat exchanger and hence the thermal conductivity will increase.

Long measurements have shown that, the net energy exchange in the soil after 1 year of operation was only 3 % of the total cold energy charged. This shows that there was no acute soil temperature change after the whole year operation of the GSHP system. Therefore, the system is feasible technically and the operation mode is reasonable.

Nomenclature

A	area, m^2
c_p	specific heat, J/kg°C
E	Energy (kJ)
$\dot{E}$	Energy flow rate (kW)
Ex	Specific exergy (kJ/kg)
Ex	Exergy (kJ)
$\dot{E}x$	Exergy flow rate (kW)
h	heat transfer coefficient, $W/m^2°C$
h	Specific enthalpy (kJ/kg)
m	Mass (kg)
$\dot{m}$	Mass flow rate (kg/s)
P	Pressure (kPa)
Q	Heat (kJ)
$\dot{Q}$	Heat transfer rate (kW)
s	Specific entropy (kJ/kg-K)
S	Entropy (kJ/K)
$\dot{S}$	Entropy flow rate (kW/K)
t	Time (s)
T	Temperature (K)
W	Work (kJ)
$\dot{w}$	Work transfer rate (kW)

Greek Symbols

α	Mass ratio of the refrigerant sent to the HPE
Δ	Change
ρ	Density, kg/m^3
η	Energy efficiency
Ψ	Exergy efficiency

Subscript and Superscripts

ch	Chemical
cv	Control volume
dest	Destruction
en	Energy
ex	Exergy
gen	Generation
in	Inlet stream
ke	Kinetic
out	Outlet stream
pe	Potential
ph	Physical
°	Standard state
0	Reference state

Acronyms

BPRV	Back Pressure Regulated Valve
COP	Coefficient of Performance
EES	Engineering Equation Solver
EV	Expansion Valve
f	surrounding fluid
GHG	Greenhouse Gas
HPE	High Pressure Evaporator
LP	Low Pressure Evaporator
RH	Relative Humidity
RI	Relative Irreversibility
SI	Sustainability Index
SMER	Specific Moisture Extraction Ratio
VLE	Vapor-liquid Equilibrium

References

1. Riffat SB, Boukhanouf R, Srivastava NC (2002), N.C. Design and modelling of an adsorption system for heating and cooling applications. Proceedings of the 1st International Conference on Sustainable Energy Technologies, pp 70–78, Porto, Portugal, 12–14 June 2002
2. ASHRAE (1995) Commercial/Institutional ground source heat pump engineering manual. American Society of heating, Refrigeration and Air-conditioning Engineers, Inc, Atlanta
3. Kavanaugh S, Rafferty K (1997) Ground source heat pumps; design of geothermal systems for commercial and institutional buildings. American Society of heating, Refrigeration and Air-conditioning Engineers, Inc, Atlanta
4. Austin WA, Yavuzturk C, Spitler JD (2000) Development of an in situ system and analysis procedure for measuring ground thermal properties. ASRAE Trans 106(1):365–379
5. Fetter CW (1981) Determination of the direction of ground-water flow. Ground Water Monitor Rev 1(3):28–31
6. Isiorho SA, Meyer JH (1999) The effects of bag type and metre size on seepage metre measurements. Ground Water 37(3):411–413
7. Freeze RA, Cherry A (1989) Guest editorial—what has gone wrong. Ground Water 27(4):20 (July–August 1989)
8. Eggen G 1990 Ground temperature measurements. Kluwer Academic Publishers, Oslo
9. Abdeen MO (2014) Cleaner and greener energy technologies: sustainable development and environment. Stand Glob J Sci Res 1(1):012–021 (UK, February).
10. Abdeen MO (2014) Soil thermal properties and the effect of groundwater on the closed loops. J Environ Sustain Energy Environ Res 3(1):34–52 (Pakistan)
11. Abdeen MO (2014) Low energy building design: heating, ventilation and air conditioning. Cooling India Magazine 9(11):63–76 (India February)
12. Abdeen MO (2014) Chapter 1: Geothermal energy systems, technology, geology, greenhouse gases and environmental pollution control. In: J Yang (ed) Geothermal energy, technology and geology. NOVA Science Publishers, Inc., New York, pp 1–46

Chapter 37
Thermal Response Test Analysis for an Energy Pile in Ground-Source Heat Pump Systems

Chun Kwong Lee and Hong Nam Lam

Abstract A thermal response test (TRT) analysis for a cylindrical energy pile (CEP) was carried out in order to determine the thermal properties of the materials in different regions of the system being modelled. Sample test data were generated by using a three-dimensional numerical model of the CEP. Various combinations of the materials inside and outside the CEP were investigated. It was found that the thermal properties of both the CEP and the surrounding soil could be determined with sufficient accuracy. This was important as the effective thermal properties of the CEP depended on the design of the CEP which could be very difficult to determine by other means. Another study was made to explore the possibility of assuming a homogeneous material outside the pipes with the adoption of equivalent thermal properties determined from the TRT analysis so that an analytical modeling approach could be employed. A comparison of the simulation results was made for the CEP based on the specified thermal properties of the various regions with those for the case in which the equivalent thermal properties was used. By applying a cooling-dominated annual periodic load profile, it was found that the simulated temperature of the fluid leaving the CEP could differ substantially. This meant that the assumption of a homogeneous material outside the pipes could lead to erroneous results.

Keywords Ground-source heat pump · Energy pile · Thermal response test analysis · Parameter estimation

37.1 Introduction

Ground-source heat pump (GSHP) systems have been used in Europe and USA [1] for many years due to their better energy efficiency in providing heating in winter. The ground is used to exchange heat with the surrounding by circulating a fluid

C. Kwong Lee (✉) · H. Nam Lam
Department of Mechanical Engineering, University of Hong Kong, Pokfulam Road, Hong Kong, China
e-mail: a8304506@graduate.hku.hk

H. Nam Lam
e-mail: hn.lam.hku@hku.hk

I. Dincer et al. (eds.), *Progress in Sustainable Energy Technologies: Generating Renewable Energy,* DOI 10.1007/978-3-319-07896-0_37,

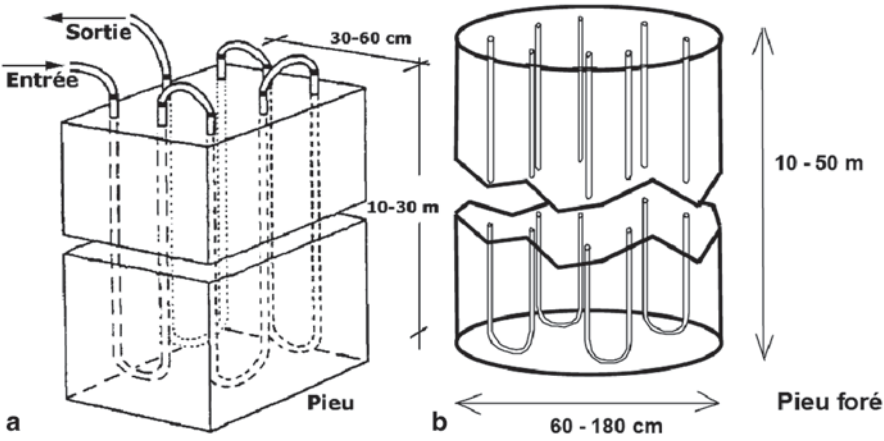

Fig. 37.1 General energy pile arrangement for (**a**) hammer precast pile and (**b**) cast-in-place pile (extracted from Pahud [2])

around the U-tubes installed in a vertical ground heat exchanger borefield. However, the drilling of deep boreholes is costly which will incur in a high initial cost. This hinders the wide application of such systems. To improve the situation, the U-tubes can be installed in concrete piles as energy piles. In this way, the initial cost can be substantially reduced. Figure 37.1 shows the common configuration of the energy piles according to Pahud [2]. The use of energy piles grows rapidly in Europe [3] with Austria being one of the countries having the earliest installations. This reflects the economic benefits of employing the energy piles. Reported installations include the applications in the Zurich Airport [4, 5], a house in UK [6], a college in London [7], a multi-storey building in Tokyo [8] and a three-storey building in Sapporo [9].

One main difficulty in adopting the energy piles is the proper modelling of their performance in view of the wide variety of concrete pile design for meeting primarily different structural requirements. A more popular way involves the use of numerical methods to calculate the heat transfer around an energy pile [10–12]. These methods usually employ very fine grids to discretise the regions both inside and outside the energy pile. This results in a very long computation time for performance simulation. Pahud et al. [4] modified the DST model [13] which was previously developed for a closely-packed borefield and applied it to an energy pile system. Analytical modelling methods are also developed. These include the application of the cylindrical source model from Carslaw and Jaeger [14] to small diameter steel piles [15], the application of the line source model from Ingersoll et al. [16] to each pipe in an energy pile by assuming a homogeneous media around the pipes [17], a solid cylindrical source model from Man et al. [18] and a ring-coil source model from Cui et al. [19]. The latter two models also assume homogeneous media both inside and outside the energy pile, the justifications for which have yet to be provided.

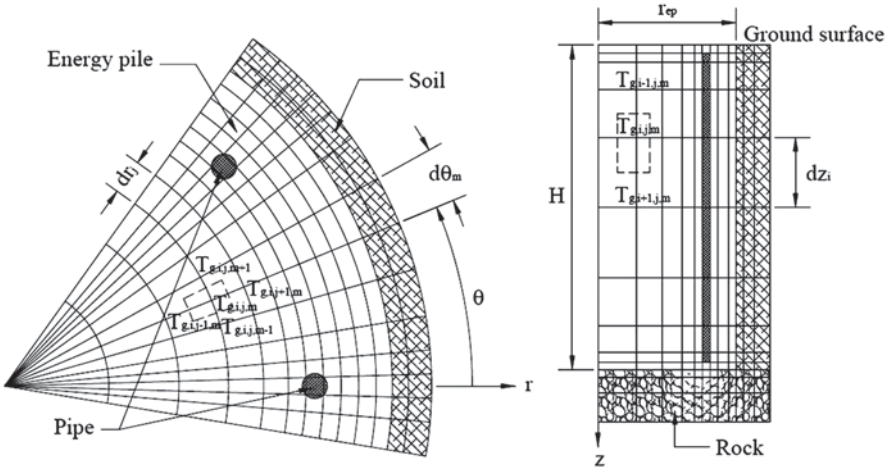

Fig. 37.2 Discretisation scheme for the CEP

In view of the above limitations, a simplified three-dimensional numerical model was developed in Fortran by the authors [20] of a cylindrical energy pile (CEP) similar to the one shown in Fig. 37.1b which avoided the use of very fine grids around the pipes and the allowance of individual specification for the thermal properties in the various regions. It was found that both the thermal properties inside and outside the CEP within the pile depth affected the performance of the CEP. Hence, the precise determination of these thermal properties is important. A thermal response test (TRT) analysis [21] is commonly used in GSHP systems to calculate the ground thermal properties and the thermal resistance of a borehole ground heat exchanger. In this study, a similar analysis is made on a CEP to investigate the possibility of estimating the various thermal properties accurately. Besides, another study is made to predict the errors incurred if the material outside the pipes is assumed to be homogeneous in order to justify the applicability of the analytical approach employed by Bozis et al. [17].

37.2 Methodology of Analysis

Figure 37.2 shows the discretisation scheme used for the numerical model based on the cylindrical coordinate system. Each pipe in the CEP is represented by a sector column with the sector circumscribed by the pipe radius and being equally-distant from the centre of the energy pile. The CEP is assumed to be installed on top of a rock layer and surrounded by soil. The fluid temperatures along the pipes and the temperature inside and outside the CEP are calculated by using an iterative method for each time step according to the pipe connection configuration. Groundwater

Table 37.1 Summarised thermal properties used for the various regions

Material	Thermal conductivity (W/m-K)	Thermal diffusivity (10^{-7} m^2/s)	Volumetric heat capacity (kJ/m^3-K)
Heavy sand (5 % water)	2.20[a]	13.48[a]	1,632
Light sand (5 % water)	1.40[a]	10.13[a]	1,382
Granite	3.00[a]	12.38[a]	2,423
Concrete, made with gravel, dry	1.28[b]	6.612	1,936[b]

[a] Based on mean values of ranges indicated in ASHRAE [22]
[b] Based on values from Bejan [23]

flow effect is not accounted for, and the heat transfer from the pipe to the outside is assumed to be purely conductive.

Sample TRT data are generated using the selected model. TRT analyses are then carried out on the generated test data in order to determine thermal properties of the materials in the various regions. To enhance the appropriateness of the analyses, some practical values for the actual materials are employed. According to the previous study, the performance of the CEP is not sensitive to the thermal properties of the rock layer. Hence, only granite is selected for the rock. The interior of the CEP mainly consists of concrete with steel reinforcement. The effective thermal properties of the pile are then calculated from

$$k_{ep} = \alpha k_s + (1-\alpha)k_c \tag{37.1}$$

$$\rho c_{ep} = \alpha \rho c_s + (1-\alpha)\rho c_c \tag{37.2}$$

Here, α is the volume ratio of the steel in the energy pile. Eqs. (1 and 2) are used to obtain indicated figures only, as the precise determinations are much more complex which depend on the configuration of the steel framework in the CEP. It also highlights the importance of predicting the thermal properties inside the CEP through a TRT analysis, as there is no other easy way to find them. Nevertheless, the indicated figures provide a reasonable approximation for use in the analyses. By using different values of α, the thermal properties of the energy pile can be adjusted accordingly. Finally, two types of soil, namely heavy sand and light sand, are considered so that the effects of the thermal properties of the soils and the energy pile on the precision of the TRT analyses can be investigated. Table 37.1 summarises the information of the thermal properties used to generate the TRT data. Four cases, each with different combinations for the materials, are analysed as follows:

a. Heavy sand with 5 % by volume of steel reinforcement in the energy pile;
b. Heavy sand with 2 % by volume of steel reinforcement in the energy pile;
c. Light sand with 5 % by volume of steel reinforcement in the energy pile;
d. Light sand with 2 % by volume of steel reinforcement in the energy pile.

A test period of five days is adopted for each set of the TRT data. A continuous constant load is applied to the CEP, and the fluid temperature leaving the CEP

Table 37.2 Parameter values used for the energy pile

Parameter	Value	Parameter	Value
Radius of energy pile (m)	0.5	Pipe-to-pile centre distance (m)	0.4
Pipe outer radius (m)	0.016	Pipe inner radius (m)	0.013
Length of energy pile (m)	40.0	Pipe thermal conductivity (W/m-K)	0.4
Fluid thermal conductivity (W/m-K)	0.614	Fluid density (kg/m^3)	1000.0
Fluid dynamic viscosity (kg/m-s)	0.00086	Fluid specific heat capacity (kJ/kg-K)	4.19
Fluid mass flow rate (kg/s)	0.2	Number of pipes in energy pile	8
Peak applied load (W)	4000.0	Undisturbed ground temperature (^{o}C)	20.0

($T_{f,o}$) is used as the recorded data. In view of the small discretisation sizes used, the simulation time step is taken as one minute to enhance the convergence of the iterations, but the TRT data are recorded hourly. The other parameters used for the CEP are given in Table 37.2. All the pipes are assumed to be equally-spaced in the energy pile and connected consecutively in a single circuit such as the one shown in Fig. 37.1a.

The simplex method from Nelder and Mead [24] is selected as the parameter estimation algorithm in the TRT analysis. As the performance of the CEP is insensitive to the thermal properties of the rock layer, only the thermal conductivities and volumetric heat capacities for the regions inside the CEP and the surrounding soil are predicted. The corresponding values for the rock layer are then taken as the arithmetic mean between the predicted values for the two regions. In view of the fact that two volumetric heat capacities have to be determined simultaneously, a mean-quad-difference (*MQD*) as defined below is employed for minimisation:

$$MQD = \frac{\sum_{1}^{N_{data}} (T_{f,o,test} - T_{f,o,sim})^4}{N_{data}} \tag{37.3}$$

where N_{data} is the number of results in each set of the test data. At least three trials are made for each case with different initial guessed values for the simplex points. The same methodology for setting the initial simplex points and the criteria for iteration completion as briefed in another previous study [25] is adopted. The only main difference is that with the adoption of a quad difference, the second criterion for iteration completion is changed to the case when the minimum *MQD* is less than $5 \times 10–^{13}$ ^{o}C^4.

To determine if the assumption of a homogeneous material outside the pipes is appropriate, another TRT analysis is made using the same test data but with the adoption of the same thermal properties in all the regions outside the pipes. An equivalent thermal conductivity and volumetric heat capacity can be determined. The equivalent thermal properties are then used in the numerical model for a ten-year dynamic simulation, and the results are compared with those based on the specified thermal properties in the various regions. An annual periodic load

Table 37.3 Predicted thermal properties in different regions

	Predicted thermal properties (Error) (soil/energy pile)	
Case	Thermal conductivity [W/m-K (%)]	Volumetric heat capacity [kJ/kg-K (%)]
A	2.184 (0.71)/3.926 (0.26)	1,658 (1.59)/2,013 (0.40)
B	2.185 (0.70)/2.337 (0.14)	1,659 (1.68)/1,963 (0.36)
C	1.369 (2.21)/3.931 (0.37)	1,450 (4.91)/2,006 (0.75)
D	1.358 (3.00)/2.346 (0.51)	1,475 (6.76)/1,947 (1.17)

approximated by a sine curve is employed with the ratio of the peak cooling/heating load being 4:1. A twelve-hour daily operating schedule is also employed.

37.3 Results and Discussion

TRT Analysis Assuming Different Thermal Properties in the Various Regions

Table 37.3 summarised the predicted thermal properties in the various regions and the percentage errors incurred for the four cases investigated. The errors were absolute values with reference to the information shown in Table 37.1. The corresponding values calculated according to Eqs. (1&2) for the thermal properties inside the CEP were 3.916 W/m-K and 2,021 kJ/kg-K for Cases A&C, and 2.334 W/m-K and 1,970 kJ/kg-K for Cases B&D respectively. It could be observed that the predicted thermal properties were close to the specified values. The largest percentage errors occurred for the light sand in Cases C&D with a higher value for the volumetric heat capacity. It was not surprising as the performance of the CEP was less sensitive to the volumetric heat capacity. The predicted thermal properties inside the CEP agreed very well with the specified ones. This was extremely helpful as it was not easy to determine them by other methods. This also highlighted the significance of the TRT analysis on the CEP.

TRT Analysis Assuming Same Thermal Properties in the Various Regions

Table 37.4 showed the corresponding equivalent thermal properties determined for the four cases investigated by assuming a homogeneous media outside the pipes based on the trial with the lowest *MQD*. Clearly, the MQD_{min} reflected the discrepancy between the specified thermal properties inside and outside the CEP. Consequently, the MQD_{min} was the lowest for Case B and highest for Case C. Nevertheless, these values were much higher than the corresponding ones obtained by assuming different thermal properties in the various regions which usually did not exceed 10^{-12} °C[4]. The equivalent thermal properties did not necessarily fall between

Table 37.4 Predicted equivalent thermal properties

Case	Thermal conductivity (W/m-K)	Volumetric heat capacity (kJ/kg-K)	MQD_{min} (°C^4)
A	2.527	2,231	2.568×10^{-3}
B	2.168	1,961	1.615×10^{-5}
C	2.020	2,015	5.842×10^{-2}
D	1.753	1,829	1.446×10^{-2}

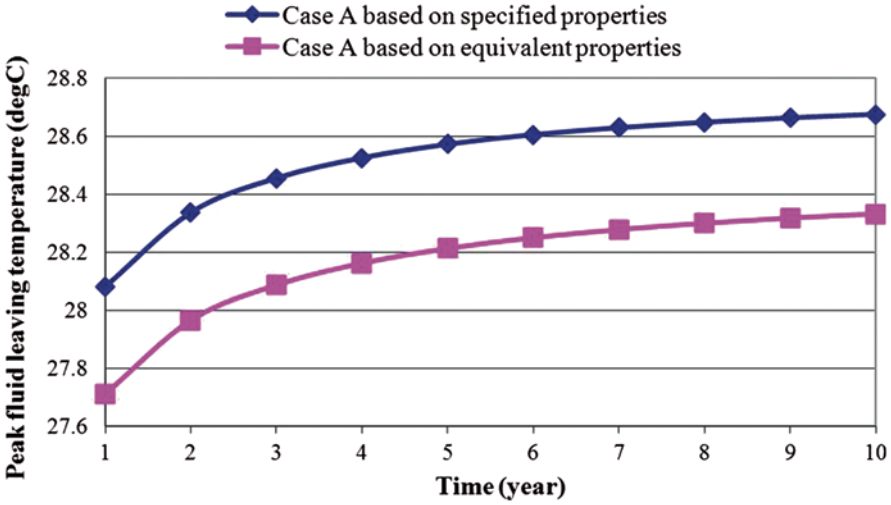

Fig. 37.3 Comparison of the peak fluid temperature leaving the CEP based on specified and equivalent thermal properties for Case A

the corresponding values for the soil and the energy pile. It seemed that the volumetric heat capacities influenced the prediction of the equivalent thermal conductivity and vice versa.

Figures 37.3, 37.4, 37.5, 37.6 compared the variation of the peak temperature of the fluid leaving the CEP ($T_{f,\,o,max}$) based on the specified and the equivalent thermal properties under a cooling-dominated annual periodic load for ten years for the different cases investigated. Except for Case B, the adoption of the equivalent thermal properties under-estimated the simulated $T_{f,\,o,max}$. The errors for the cases with the heavy sand were lower than those with the light sand, and the discrepancy was the largest for Case C which reached 1.59 °C after ten years. This was very substantial. The error also reached 1.13 °C for Case D. This implied that the effect of the thermal properties inside the CEP was more significant when the thermal conductivity of the soil was lower. Indeed, the maximum difference in the simulated $T_{f,\,o,max}$ did not exceed 0.35 °C when the heavy sand was used. Nevertheless, the assumption a homogeneous media outside the pipes and consequently the adoption of the analytical modelling approach could lead to erroneous results and the simplified numerical model for the CEP should be employed.

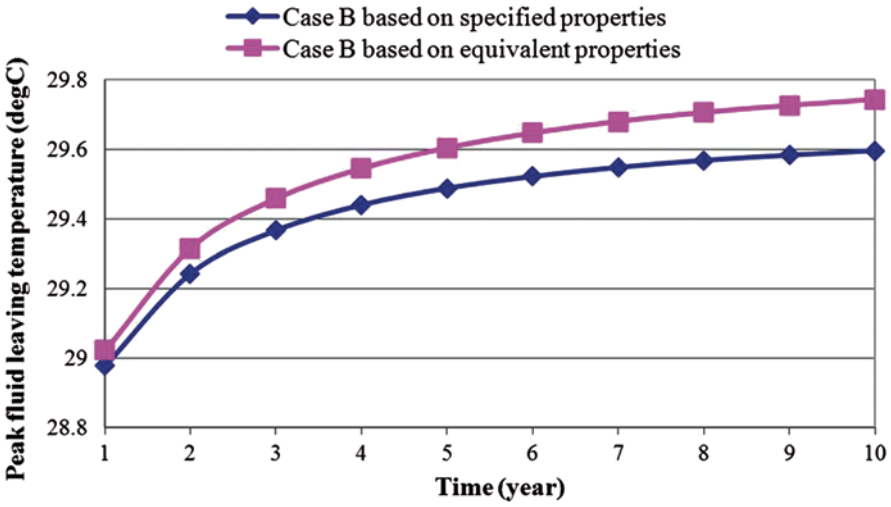

Fig. 37.4 Comparison of the peak fluid temperature leaving the CEP based on specified and equivalent thermal properties for Case B

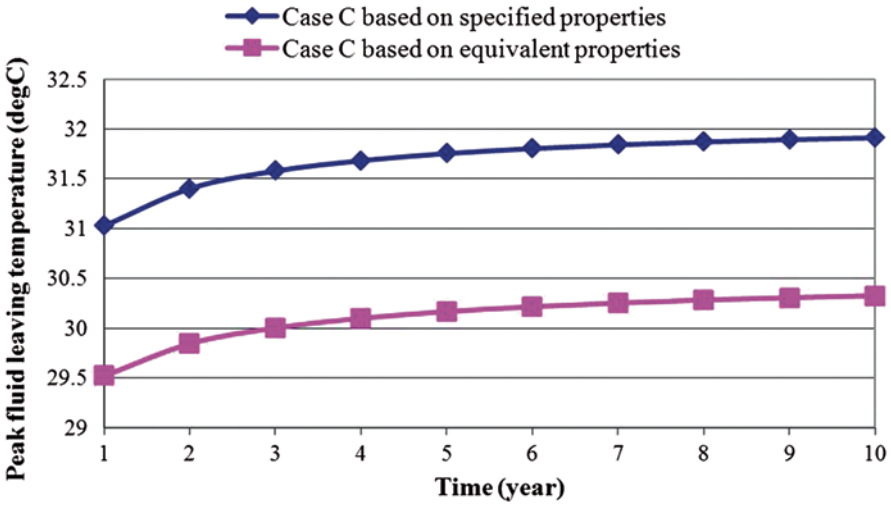

Fig. 37.5 Comparison of the peak fluid temperature leaving the CEP based on specified and equivalent thermal properties for Case C

Conclusions

A thermal response test (TRT) analysis was performed for a cylindrical energy pile (CEP) for determining the thermal properties of the material inside the CEP and those of the surrounding soil. A simplified three-dimensional numerical model of the

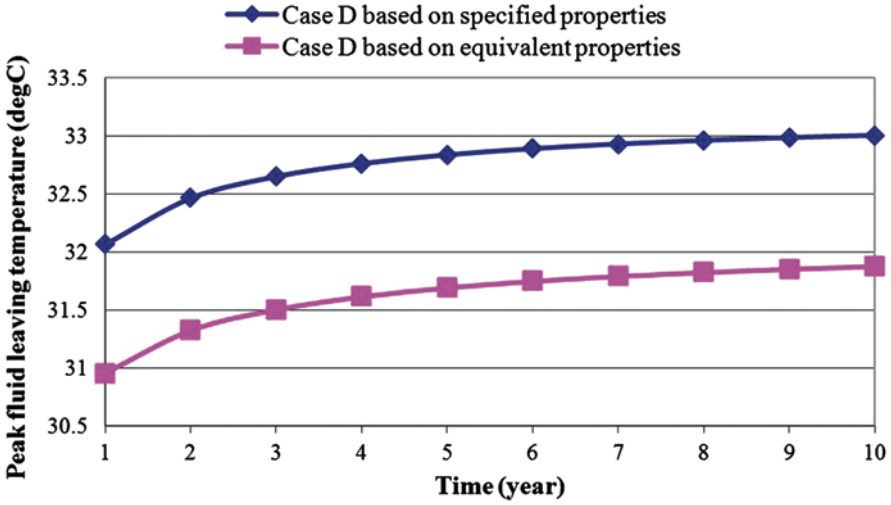

Fig. 37.6 Comparison of the peak fluid temperature leaving the CEP based on specified and equivalent thermal properties for Case D

CEP was employed to generate sample TRT data for five days. A parameter estimation technique was used to predict the thermal conductivities and the volumetric heat capacities in the various regions. Four cases, each with different combinations of the materials inside and outside the CEP, were investigated. It was found that the thermal properties of both the CEP and the surrounding soil could be determined with sufficient accuracy. The percentage errors incurred in the predicted volumetric heat capacities were higher than the corresponding thermal conductivities in each case. This was due to the lower sensitivity of the CEP performance to the volumetric heat capacities. Nevertheless, they were still acceptably small, especially for the thermal properties inside the CEP. This was important as the effective thermal properties of the CEP depended on the design of the CEP which could be very difficult to determine by other means. This also highlighted the significance of the TRT analysis.

Another study was made in which a TRT analysis was carried out with the assumption of a homogeneous material outside the pipes in the numerical model. An equivalent thermal conductivity and volumetric heat capacity were predicted for each case. These equivalent thermal properties were then used to perform long-term dynamic simulations for ten years, and the results were compared with those based on the specified thermal properties in the various regions under a cooling-dominated annual periodic load with a daily operating schedule of twelve hours. It was found that the simulated temperature of the fluid leaving the CEP could differ substantially, with a consequent discrepancy reaching 1.59 °C for Case C after ten years. The errors were smaller when heavy sand with a higher thermal conductivity was used as the soil. That meant that the assumption of a homogeneous material outside the pipes and the adoption of an analytical approach could lead to erroneous results, and the simplified numerical model for the CEP should be employed instead.

Nomenclature

c	Specific heat (kJ/kg-K)
dr	Ground grid separation in the radial direction (m)
$d\theta$	Ground grid separation in the circumferential direction (radian)
dz	Ground grid separation in the vertical direction (m)
H	Length of the energy pile (m)
k	thermal conductivity (W/m-K)
MQD	Mean-quad-difference as defined in Eq. (37.3) ($°C^4$)
N_{data}	Number of results in each set of TRT data
r	Measurement in the radial direction (m)
T	Temperature (°C)
z	Measurement in the vertical direction (m)

Greek Symbols

α	Volume ratio of steel in the energy pile
θ	Measurement in the circumferential direction (radian)
ρ	Density (kg/m^3)

Subscript and Superscripts

c	Concrete
ep	Energy pile
f	Circulating fluid
g	Ground including all regions outside the pipes
i	Discretisation designation in the vertical direction
j	Discretisation designation in the radial direction
m	Discretisation designation in the circumferential direction
max	Maximum
min	Minimum
o	Outlet
s	Steel
sim	Simulated value
test	Test value

Acronyms

CEP	Cylindrical Energy Pile
GSHP	Ground-source Heat Pump
TRT	Thermal Response Test

Acknowledgement The authors would like to gratefully acknowledge the funding support provided to this research work by the Research Grants Council of Hong Kong under the General Research Fund for Project Number 713710.

References

1. Spitler JD (2005) Ground-source heat pump system research-past, present and future. HVAC & R Res 11(2):165–167
2. Pahud D (2002) Geothermal energy and heat storage. SUPSI-DCT-LEEE, Laboratorio di Energia, Ecologia ad Economia
3. Brandl H (2006) Energy foundations and other thermo-active ground structures. Geotechnique 56(2):81–122
4. Pahud D, Formentin A, Hubbuch M (1999) Heat exchanger pile system of the dock midfield at the zurich airport—detailed simulation and optimization of the installation, final report. Swiss Federal Office Energy, Switzerland
5. Pahud D, Hubbuch M (2007) Measured thermal performances of the energy pile system of the dock midfield at Zurich Airport. Proceedings of European Geothermal Congress 2007, Unterhaching Germany
6. Suckling T, Cannon R (2004) Energy piles for pallant house, Chichester, UK. Ground Eng 37(7):27–29
7. Bourne-Webb PJ, Amatya B, Soga K, Amis T, Davidson C, Payne P (2009) Energy pile test at Lambeth College, London: geotechnical and thermodynamic aspects of pile response to heat cycles. Geotechnique 59(3):237–248
8. Sekine K, Ooka R, Yokoi M, Shiba Y, Hwang S (2007) Development of a ground-source heat pump system with ground heat exchanger utilizing the cast-in-place concrete pile foundations of building. ASHRAE Transactions 113(1):558–566
9. Hamada Y, Saitoh H, Nakamura M, Kubota H, Ochifuji K (2007) Field performance of an energy pile system for space heating. Energy Build 39(5):517–524
10. Gao J, Zhang X, Liu J, Li K, Yang J (2008) Thermal response and ground temperature of vertical pile-foundation heat exchangers: a case study. Appl Therm Eng 28(17–18):2295–2304.
11. Laboui L, Nuth M (2006) Numerical modeling of some features of heat exchanger piles. Geotechnical Spec Publ 153:189–194
12. Morino K, Oka T (1994) Study on heat exchanged in soil by circulating water in a steel pile. Energy Build 21(1):65–78
13. Hellstrom G (1991) Ground heat storage. thermal analysis of duct storage systems: part I theory. Doctoral Thesis, Department of Mathematical Physics, University of Lund, Sweden
14. Carslaw HS, Jaeger JC (1959) Conduction of heat in solids. Claremore Press, Oxford
15. Katsura T, Nagano K, Narita S, Takeda S, Nakamura Y, Okamoto A (2009) Calculation algorithm of the temperatures for pipe arrangement of multiple ground heat exchangers. Appl Therm Eng 29(5–6):906–919
16. Ingersoll LR, Zobel OJ, Ingersoll AC (1954) Heat conduction: with engineering, geological and other applications. University of Wisconsin Press, Madison
17. Bozis D, Papakostas K, Kyriakis N (2011) On the evaluation of design parameters effect on the heat transfer efficiency of energy piles. Energy Build 43(4):1020–1029
18. Man Y, Yang H, Diao N, Liu J, Fang Z (2010) A new model and analytical solutions for borehole and pile ground heat exchangers. Int J Heat Mass Transf 53(13–14):2593–2601
19. Cui P, Liu X, Man Y, Fang Z (2011) Heat transfer analysis of pile geothermal heat exchangers with spiral coils. Appl Energy 88(11):4113–4119
20. Lee CK, Lam HN (2013) A simplified model of energy pile for ground-source heat pump systems. Energy 55:838–845
21. Austin WA (1998) Development of an In-situ system for measuring ground thermal properties. Master Thesis, Oklahoma State University
22. ASHRAE (2003) ASHRAE Handbook: heating, ventilation and air-conditioning applications. ASHRAE, Atlanta
23. Bejan A (1993) Heat transfer. Wiley, New York
24. Nelder JA, Mead R (1965) A simplex method for function minimization. Comp J 7(1):308–313
25. Lee CK, Lam HN (2011) Determination of groundwater direction in thermal response test analysis for geothermal heat pump systems. HAVC & R Res 17(6):991–999

Chapter 38
Thermal Performance Comparison Between Longitudinal and Lateral Hollow Plate Fin Heat Sinks

M. F. Ismail, M. A. Zobaer and M. T. H. Khan

Abstract Micro heat sinks are being widely used in electronics cooling. Perforations in micro heat sinks have proven to give better heat transfer than a solid ones. A numerical investigation is conducted in this study for three-dimensional fluid flow and convective heat transfer from hollow fins with longitudinal and lateral perforation. Incompressible air as working flu id is modeled to calculate the fluid flow parameters. Temperature field inside the fins is obtained by solving Fourier law of heat conduction equation. Flow and heat transfer characteristics are presented for Reynolds numbers from 70 to 234 based on the fin thickness. Numerical simulation is validated with the published experimental results of the previous investigators and good agreement is observed. Results show that the fins with lateral perforations have better heat transfer enhancement and but higher pressure drop.

Keywords Micro heat sink · Longitudinal and lateral perforations · Pressure drop · Heat transfer enhancement

38.1 Introduction

Heat removal from small electronic equipments has been a major concern along with the advancement of micro and nano structures. Several heat transfer enhancement techniques has been adopted for better performance of heat sinks. To increase heat transfer rate between a primary surface and the surrounding fluid extended surfaces (fins) are frequently used in heat exchanging devices. Porosity, slots or perforations as a heat transfer enhancement technique was successfully employed by Sahin et al. [1].

M. F. Ismail (✉)
Department of Mechanical Engineering, University of British Columbia, Vancouver, Canada
e-mail: farhadananda.128@gmail.com

M. A. Zobaer
Department of Mechanical Engineering, Bangladesh University of Engineering and Technology (BUET), Dhaka, Bangladesh

M. T. H. Khan
Industrial and Systems Engineering, Wayne State University, Detroit, MI, USA

I. Dincer et al. (eds.), *Progress in Sustainable Energy Technologies: Generating Renewable Energy,* DOI 10.1007/978-3-319-07896-0_38,

Sparrow et al. also conducted a numerical study to find out heat transfer enhancement by introducing strip fins. The optimization of fin size is of great importance as the demand for light weight, compact, and economical fins are on the rise. Sparrow et al. [2] experimentally determined heat transfer coefficient on an upstream facing surface that was contained a regular array of holes. El-Sayed et al. [3] experimentally investigated to determine the optimal position of fin array for turbulent heat transfer, fluid flow and pressure drop in longitudinal rectangular fin array for three different orientations of tested models: (1) parallel flow, (2) impinging flow, and (3) reverse impinging flow in the flow field. Molki et al. [4] showed that perforated plate attached to a duct has a better heat transfer performance than a simple solid baffle p late attached to the same duct wall. Dorignac et al. [5] experimentally determined convective heat transfer on a multi perforated plates and proposed an empirical relation for heat exchange at windward surface of a perforated flat plate.

Ismail et. al. [6] numerically compared fins with various types of perforations. In our study, hollow fins with two square perforation arranged in two different configuration are analyzed. Pressure drag co-efficient and pressure drop due to perforation are also considered as these parameters are responsible for the effective and efficient cooling performance of heat sinks. For this consideration, three-dimensional turbulent flu id flow and convective heat transfer around an array of solid and perforated fins are analyzed numerically. The perforations are arranged in two ways for comparison: longitudinally, along the fin length with their cross section perpendicular to the fluid flow direction and laterally, a long the fin width with their cross section parallel to the flu id flow direct ion. Boundary conditions, governing equations and computational domain o f this study are the same as used by Shaeri et al. [7]

Nomenclature

A	Area	Nu	Nusselt number
CP	Pressure drag coefficient	Pr	Prandtl number
D	Fin thickness	Re_L	Reynolds number
HP	Perforation height	h	Convection heat transfer coefficient
WP	Perforation width	λ	Fluid thermal conductivity
L	Fin length	μ	Fluid kinematics viscosity
V	Fin volume	ρ	Fluid density
u_{in}	Inlet velocity		

38.2 Problem Description

Typical bluff plate model is shown in Fig. 38.1. The airflow is considered to be steady and laminar with constant properties. Moreover, air velocities are such that forced convection is dominant for heat transfer mechanism between fins and ambient air and in the perforations. Fin material is assumed to be aluminum with thermal

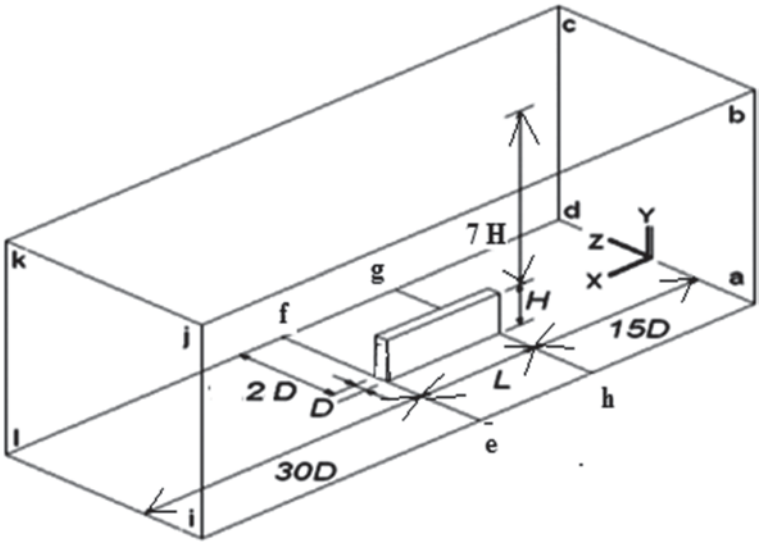

Fig. 38.1 Computational domain showing the solid fin [6]

conductivity of 202 Wm^{-1} K^{-1}. Such fins are widely used for heat removal from heating surfaces. Fins having the length (L), height (H) and thickness (D) equal to 24, 12 and 4 mm, respectively are assumed for this study. Each perforation has equal height (H_P) and width (W_P) of to 2.25 mm and their length is equal to the fin's length.

The fin's thickness is used as the characteristic length for the Reynolds number. The investigations are made for Reynolds number $Re = (\rho vD)/\mu$ in the range of 70 to 234. This range of Reynolds number covers velocity range of 0.3–1 m/s. These velocities are chosen such that the flow inside the perforations should also be laminar. Due to uniform air flow parallel to the fins and symmetry, computations are made for one fin instead of array of fins. Figure 38.1 shows the computational domain which is similar to the domain used by Shaeri et al., [7].

38.3 Numerical Method

Physical Model

Physical model and governing equations for the three dimensional steady state incompressible fluid flow are the same as used by Shaeri et al., [7]. For calculation of temperature field in the fin's surfaces and perforation's walls, conjugate problem of Fourier's steady state heat conduction equation with convection in the fluid are solved simultaneously. The domain used in the present study is illustrated in

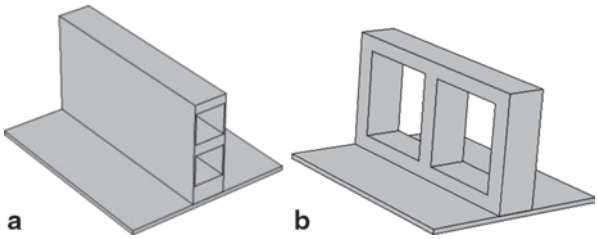

Fig. 38.2 Fins used in the present study **a** Fins having longitudinal perforation, and **b** lateral perforation

Fig. 38.1. The plane *abcd* is inlet boundary, where steady flow condition is considered for all variables using $u_{in} = u_{\infty}$, and $T_{in} = T_{\infty}$. Free stream temperature is assumed to be 25 ˚C and the base plane *efgh*, has a constant heat flu x of 4500 w/m^2. The rest of the planes i.e. *adeh* and *fgil* are assumed to be adiabatic. The plane *ijkl* is considered as exit boundary. For present computation, the effect of radiation heat transfer is neglected. It consists of an entrance region, an exit plane and the upper free stream surface that are planes *abcd*, *ijkl* and *bckj*, respectively.

These planes should be sufficiently far from the fin surfaces so that the results become independent of the boundary positions. For this reason some tests were performed for obtaining an appropriate distance from the fin surfaces that can be found in the study of Shaeri et al. [7]. In the present study, the length of computational domain is chosen 15D upstream, 30D downstream, 7H in Y direction and 3.5D in Z direction. Figure 38.2a, b show the hollow fins having two perforations. The solution must be independent of grids. Several grid configurations are studied to ensure that the solutions are grid independent and the test is shown in Table 38.1. From the table it is observed that 175,000 mesh elements are sufficient for the numerical simulation.

Validation of the Numerical Simulation

To validate the present numerical model experimental results of Nakamura et al. [8] are considered in this study for validation. At first heat transfer from a low-profile block is investigated and Fig. 38.3 shows the comparison between the experimental study and the present study. From the study of Nakamura et al. the following correlation can be obtained for the laminar flow condition-

$$\mathrm{Nu} = 0.59\mathrm{Pr}^{1/3}(Re^*)^{0.5} \tag{38.1}$$

Table 38.1 Mesh sensitivity test for Reynolds number 250

No of elements	Friction coefficient	Nusselt no.
70,520	0.014	2.98
97,397	0.017	3.19
170,596	0.021	3.2
276,188	0.022	3.21
589,237	0.023	3.21

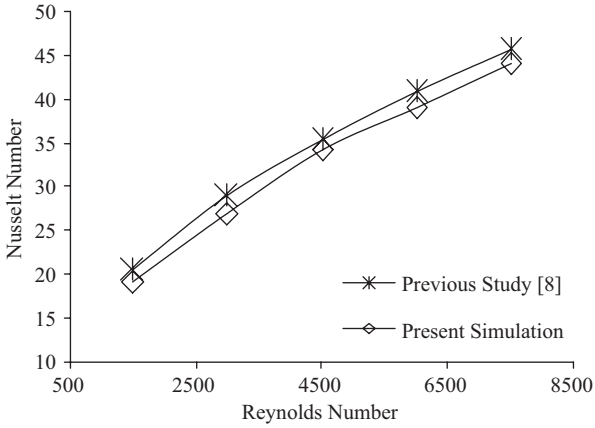

Fig. 38.3 Comparison between previously published study [8] and present numerical results: variation of Nusselt Number at various Reynolds Number

$$\mathrm{Re}^{*} = \frac{\rho u_{\infty} L}{\beta^{2} \mu} \tag{38.2}$$

Where, Nu = Nusselt number, Pr = Prandtl number and Re* = modified Reynolds number, u_{∞} = free stream velocity, L = reference length, β = opening ratio, μ = viscosity of the fluid. For the validation the value of opening ratio was assumed as 0.8. Free stream temperature was assumed as 22 ˚C and a constant heat flux of 187 W/m^2 was applied at the base of the block. The velocity range of the study of [8] was 0.24–0.72 ms^{-1}.

From Fig. 38.3, good agreement is observed with the comparison of the results of Nakamura et al. [8]. Therefore, current numerical results are reliable.

38.4 Result and Discussion

The present analysis of flow field and convection heat transfer for conjugate problem is carried out for Re_D = 70–234. From Fig. 38.4, it can be noted that the fin with lateral perforation yields higher Nusselt number than the fin with longitudinal perforation. The drag force that acts on the faces of perforated fins differs with that of acting on the surfaces of solid fin. The drag force has two components, one is related to surface shear stress as the friction drag and another is due to a pressure differential in the flow direction resulting from wake format ion as form or pressure drag. Figures 38.5–38.7 show variation of friction, form and total drag coefficient in t he flow direction respectively. According to the Fig. 38.5 lateral perforations produces more form drag. It is mentioned that the wake formed behind the perforated fins are larger compared to longitudinally perforated fins. Based on Fig. 38.6 fin with longitudinal perforations has higher value of the friction drag with respect to fin with lateral perforation. The increase in friction is due to increase in the fin contact area with the fluid for longitudinal perforation Fig. 38.7 shows that the sum

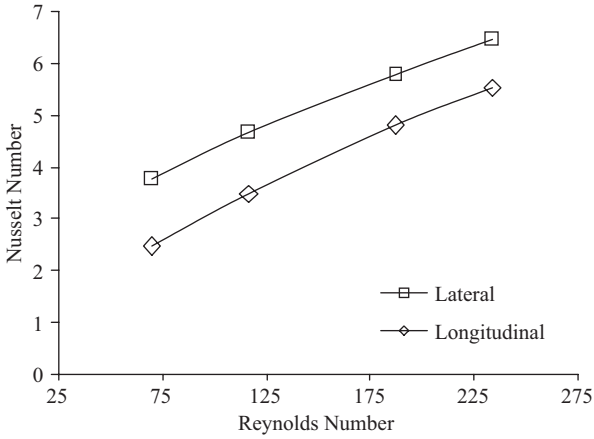

Fig. 38.4 Nusselt Number variation at various Reynolds Number

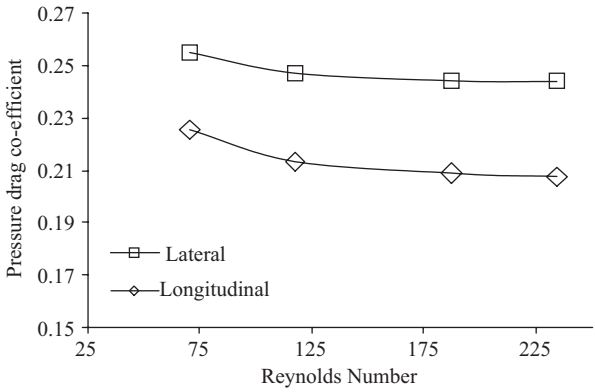

Fig. 38.5 Variation of pressure drag coefficient at different Reynolds Number

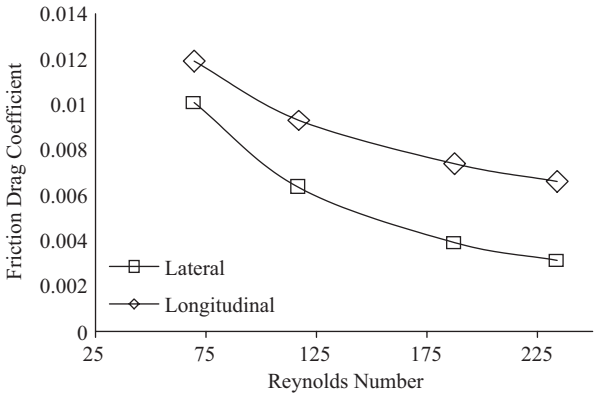

Fig. 38.6 Variation of friction drag coefficient at different Reynolds Number

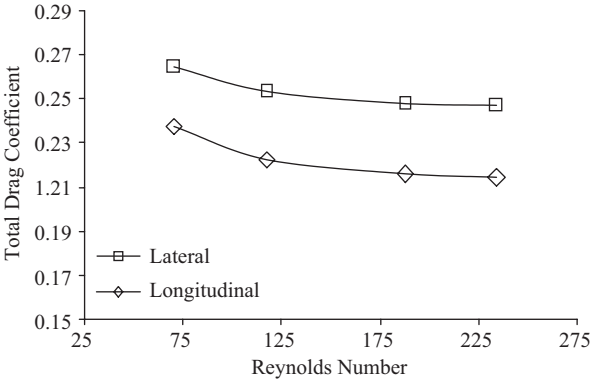

Fig. 38.7 Variation of total drag coefficient at different Reynolds Number

of the friction and form drag i.e. total drag force for laterally perforated fin is greater than the longitudinal one. It can be seen from the Figs. 38.5–38.7 that drag coefficient decrease in all case with an increase in Reynolds number. Figure 38.8 shows flow path lines at 5 mm height from the base (top view). It is noted that for lateral perforation some flow recirculation is observed but for the longitudinal perforated fins there is not any recirculation of flow. Rather it is seen that some flow passes through the perforated channels. There are some flow separations are also observed.

Conclusions

Thermal performance of fins with two types of perforation i.e. lateral and longitudinal having same fin volume is numerically investigated in this paper. From the analysis it is found that lateral perforated fins have higher heat removal rate in comparison with longitudinal perforated ones. But the drag force is higher in case of the lateral one. So pumping power consumption rate is lower for the longitudinal perforation. So while selecting perforated heat sinks, designer should keep in mind these things that which types of perforations should be used at that particular application.

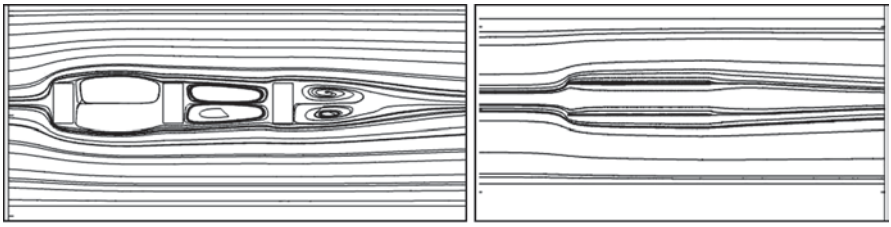

Fig. 38.8 Flow path lines at 5 mm height from the base (*top view*) at Reynolds Number 130: **a** lateral perforated fin, **b** longitudinal perforated fin

References

1. Sahin B, Demir A (2008) Performance analysis of a heat exchanger having perforated square fins. Appl Therm Eng 28:621–632
2. Sparrow EM, Carranco Ortiz M (1982) Heat transfer coefficients for the upstream face of a perforated plate positioned normal to an oncoming flow. Int J Heat Mass Transfer 25(1):127–135
3. El-Sayed SA, Mohamed ShM, Abdel-latif AA, Abouda AhE (2004) Experimental study of heat transfer and fluid flow in longitudinal rectangular fin array located in different orientations in fluid flow. Exp Therm Fluid Sci 29:113–128
4. Molki M, Hashemi-Esfahanian A (1992) Turbulent convective mass transfer downstream of a perforated baffle blockage. Int J Heat Fluid Flow 13:116–123
5. Dorignac E, Vullierme JJ, Broussely M, Foulon C, Mokkadem M (2005) Experimental heat transfer on the windward surface of a perforated flat plate. Int J Therm Sci 44:885–893
6. Ismail MF Effects of perforations on the thermal and fluid dynamic performance of a heat exchanger. IEEE transactions on components, packaging and manufacturing technology (in press). doi:10.1109/TCPMT.2013.2240766
7. Shaeri MR, Yaghoubi M (2009) Thermal enhancement from heat sinks by using perforated fins. Energy Convers Manage 50:1264–1270
8. Nakamura H, Igarashi T (2004) Forced convection heat transfer from a low-profile block simulating a package of electronic equipment. J Heat Transf 126(3):463–470

Chapter 39
Model-Based Analysis of Singapore's Energy System

Markus Wagner, Karl Schoensteiner and Thomas Hamacher

Abstract Sustainable energy production and usage will become important key factors in future energy systems. In particular, Singapore as one of the world's most densely populated countries with a high standard of living, needs a long-term concept for its energy use. Besides the high oil consumption of the industrial sector, power generation, which is nearly fully based on gas and oil, causes a high demand of fossil fuels. This leads not only to high CO_2 emissions but also to a significant import dependency on neighboring countries. Renewable energy sources and a more efficient conversion of energy are necessary for sustainable economic growth.

The analysis of Singapore's energy system is carried out by using the mathematical optimization model TIMES (The Integrated MARKAL (Market Allocation) EFOM (Energy Flow Optimization Model) System). This optimization model acts as an economic model generator for local, national or multi-regional energy systems. After modeling Singapore's energy system as a network consisting of processes (power plants, electric vehicles etc.) and commodities (energy carriers, passenger kilometers etc.), it is cost-optimized regarding to a defined objective function. Furthermore, various boundary conditions (energy prices, policies etc.) are taken into consideration.

Based on the TIMES calculations, different scenarios for energy generation, conversion and consumption are analyzed and assessed on the basis of primary energy demand, final energy demand and CO_2 emissions. The special focus is on Singapore's passenger transportation and the integration of different kinds of electric vehicles (battery electric vehicles, fuel cell electric vehicles). In order to show the effects on final energy supply, the existing stock of power plants in Singapore is enhanced by alternative technologies of power generation (solar, coal and nuclear energy).

M. Wagner (✉) · K. Schoensteiner · T. Hamacher
Institute for Energy Economy and Application Technology (IfE),
Technische Universität München, Arcisstr. 21, 80333 Munich, Germany
e-mail: markus.wagner@tum.de

K. Schoensteiner
e-mail: karl.schoensteiner@tum.de

T. Hamacher
e-mail: thomas.hamacher@tum.de

I. Dincer et al. (eds.), *Progress in Sustainable Energy Technologies: Generating Renewable Energy,* DOI 10.1007/978-3-319-07896-0_39,

By this, the necessity of a holistic approach for the development of a sustainable energy system is shown.

Keywords Urban energy modeling · TIMES · Renewable energies · Electromobility · CO_2 emissions

39.1 Introduction

Energy supply is influenced by different economic, environmental and technological factors. Rising energy prices, CO_2 emission targets, development of new and improvement of existing power plants lead to complex challenges for future energy systems. By enabling the user to display the actual situation and the future development in a region, energy models show the impacts of certain decisions and their effects. Consequently, energy modeling is a central tool for planning future energy systems. This paper analyzes the energy system of Singapore based on a TIMES model.

Singapore is an island in South-East Asia. With over 7200 people per km^2 it is one of the world's most densely populated countries [1]. Total population of Singapore counts 5.1 million people. The country has no indigenous natural resources and its renewable energy potential is very limited. Therefore, energy is a valuable good. Singapore's energy supply changed significantly in the last decade. In 2000, over 80 % of electricity was produced by oil fired power plants, while the rest was generated by gas power plants. Today, power generation from natural gas dominates Singapore's grid mix with 80 % share of total generation [2]. However, Singapore is highly dependent on gas imports from its neighboring countries Malaysia and Indonesia [3]. High prices of natural gas result in expensive electricity. The situation could be improved by diversification of fuel sources (e.g. construction of a LNG terminal) and usage of additional power generation technologies. Another promising approach is to reduce energy consumption. Therefore, the industry, the residential, the building and the transport sector are investigated. A special focus is set on the transport sector.

The model was created within the project TUM CREATE (Technische Universität München Campus for Research Excellence and Technological Enterprise), which is a research programme founded by the National Research Foundation (NRF) of Singapore. Involved partners are Technische Universität München (TUM) and Nanyang Technological University (NTU). The aim is to develop innovative technologies und future transportation concepts [4].

In a first step, the energy model is explained in detail. After this, an overview about the examined scenarios is given. Based on these, the simulated results for Singapore as a whole are presented. To discuss the integration of different kinds of electric vehicles, each scenario analyzes energy consumption and CO_2 emissions. Finally, the key findings are composed.

39.2 Methodology

Optimization Model TIMES TIMES is an acronym for The Integrated MARKAL EFOM System and was developed by the Energy Technology Systems Analysis Programme (ETSAP) within the International Energy Agency (IEA). It acts as an economic model generator for local, national or multi-regional energy systems. That means that TIMES generates a model based on the input data provided by the user. TIMES can be used for estimating the development of energy systems over a long-range time horizon consisting of specific time periods. Besides the analysis of the overall energy system of a region, certain sectors can be studied in detail (electricity sector, transportation sector etc.).

In order to cost-optimize the system—providing energy services according to minimum global cost—predictions for demands of energy services are essential (passenger kilometers, electricity for air-conditioning etc.). Furthermore, the user is supposed to provide data of existing and future technologies in each sector (power plants, cars etc.) as well as data of present and future sources and potentials of primary energy supply for each modeled region.

TIMES combines the preferences of the two bottom-up energy system models MARKAL and EFOM and provides, furthermore, various new features. MARKAL contributes the concept of the so-called Reference Energy System (RES) and the equilibrium properties. In TIMES prices, quantities, supply and demand are in equilibrium. In addition, TIMES takes over the detailed modeling of energy flows on the technology level from EFOM [5].

To define scenarios in TIMES, different input parameters are needed: energy demands, potentials of primary energy sources, settings of policies as well as technical and economic parameters.

Demand curves are received by identifying suitable demand drivers in several regions such as population growth or gross domestic product (GDP). The values of these drivers for Singapore have to be derived from external sources and models (IEA, Energy Market Authority (EMA), Energy Market Company (EMC) etc.).

Besides the demand, supply curves of primary energy and materials are a necessary component of a scenario. These curves can be available as steps, which represent the potential of a resource at particular costs. On the other hand, supply curves can be modeled as an aggregate potential for the model horizon or as an annual potential, for instance.

In order to consider emissions of pollutants or emission taxes and emission restrictions, policy settings may be an important part when defining a scenario in TIMES. In addition, certain policy settings could limit the construction of nuclear power plants and support electricity generation by solar photovoltaics (PV).

As a last point concerning the development of scenarios, techno-economic parameters for transformation of primary energy resources into energy services are needed. This is achieved by modeling technologies or processes (power plants, refineries etc.) which convert commodities into other commodities (emissions, fuels etc.). For the optimization, TIMES can choose between available modeled

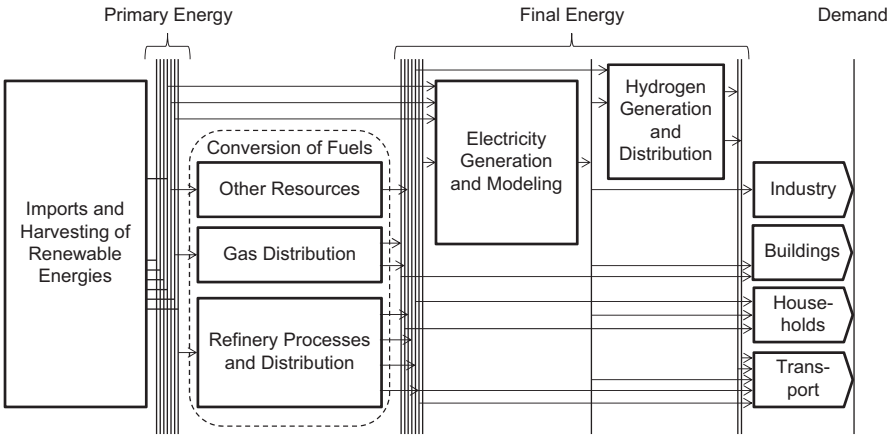

Fig. 39.1 Reference Energy System of Singapore implemented in TIMES

technologies, whereas some technologies may be mandatory. The optimization aims to achieve an economic deployment of technologies in the model periods considered [5].

TIMES uses three types of objects to build up a Reference Energy System. The Singaporean energy system is reduced to a network diagram consisting of [5]:

- Processes (technologies) transform commodities into other commodities. For example, processes are mining or import processes of primary energy sources, power plants or refineries which produce electricity or fuels for end-use demand devices, such as households or cars.
- Commodities comprise energy carriers, materials, energy services and emissions. Commodities are produced by processes and are consumed by other processes.
- Commodity flows connect processes and commodities. They are associated with specific processes and represent inputs or outputs of these processes.

Figure 39.1 shows the RES based on the developed TIMES model for Singapore. The resolution in this example is quite rough to give the best possible overview about the entire model. Boxes represent processes and technologies, while commodities and commodity flows are symbolized by vertical lines and horizontal lines between commodity lines and process boxes.

In the above RES there are four sectors (industry, buildings, households, transport) which are characterized by a specific final energy demand. The energy carriers for covering the final energy demand have to be provided by the additional processes and technologies presented in the diagram. Examples include generation (gas power plant, oil power plant, refinery etc.) and distribution of electricity or fuels. In order to make the final energy available for subsequent processes, a process for importing and harvesting of energy carriers is needed [5].

All following calculations and results are derived from the developed TIMES model for Singapore. After cost-optimizing the whole system, outcomes for prices, capacities, activities, emissions, energy flows etc. are available for each process. Thus, additional results for characterizing the energy system of Singapore can be calculated (primary energy consumption, final energy consumption, installed capacity etc.).

The model horizon covers the time period until the year 2059, while the results are given for the model years 2000, 2010, 2020, 2030, 2040 and 2050. The reasons for choosing this timeframe are on the one hand the opportunity for validation with existing data and on the other hand the prediction of possible future developments in Singapore. Most of the results are calculated on an annual basis.

Future Scenarios In order to give the best assessment of possible future developments in the Singaporean traffic sector, several scenarios were defined. In 2010, passenger transportation in Singapore was mainly supplied by private cars (42%) and the Mass Rapid Transport (MRT) system (24%). The remaining share of passenger transport performance was divided up into buses (19%), taxis (9%) and motorcycles/scooters (6%) [6]. Due to significant investments in public transport, e.g. doubling of the MRT network till 2020, it is assumed that its modal split—percentage of passengers using public transportation—will rise in future years [7]. On the basis of predictions of the Singaporean population growth, the demand of passenger and commodity transport will be increasing in the examined time period. The aim of this investigation is to show the impacts of different technologies in the transport and energy sector on Singapore's overall energy system.

Therefore, four different vehicle scenarios describe future trends in transportation. The ICE (internal combustion engine) scenario does not introduce new vehicle technologies but simulates efficiency improvements of internal combustion engines. In other scenarios, conventional vehicles are substituted step by step by new technologies. While battery electric vehicles (BEV) become the dominant technology in the BEV scenario, fuel cell electric vehicles (FCEV) dominate in the FCEV scenario. As hydrogen production influences the efficiency and the final energy demand significantly, hydrogen generation by steam reforming (REF) and by electrolysis (ELY) are studied.

With the intention of making statements about the overall influence of CO_2 emissions and import dependency, the examination of final energy conversion into passenger kilometers (Pkm)/ton kilometers (Tkm) is not sufficient. For resilient results, conversion of primary energy to final energy has to be taken into consideration. While options for the production of conventional fuels are limited and very similar to each other, generation of electricity is highly dependent on the power plant stock. Therefore, four scenarios for Singapore's future power generation were designed. Each of the scenarios is named after the main sources of electricity. Singapore's grid mix showed significant changes in the past. In 2000, electricity was generated by around 80% by oil power plants and 20% by gas power plants. Since then, generation was more and more based on combined cycle gas turbines (CCGT). Today, electricity generation from gas has a total share of 78.7%, while petroleum products supply 18.7% of Singapore's electricity needs [2].

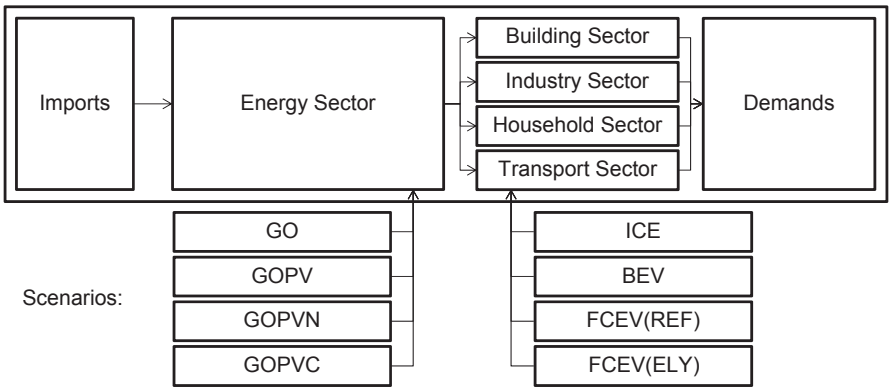

Fig. 39.2 Structure of the energy model and influencing scenarios

The Gas-Oil scenario (GO scenario) projects today's power generation to future periods. While gas will remain the main source of electricity generation, it is assumed that the decommissioning of oil power plants in Singapore will continue in future years. The existing capacity of coal power plants, which amounts 160 MW in 2012, is seen as constant in future model years. Other sources of electricity are not included in the GO scenario. The development and integration of PV is a key element in Singapore's energy policy [8]. Consequently, the GO scenario is extended by PV as an additional source of electricity. According to official calculations, PV potential per year is set to 7 TWh in the medium term and to 14 TWh in the long term [9]. However, photovoltaic systems alone cannot lower Singapore's import dependency, as explained in the next section. Therefore, the GOPV scenario (Gas-Oil-Photovoltaics scenario) is expanded by nuclear power plants (GOPVN—Gas-Oil-Photovoltaics-Nuclear scenario) and coal power plants (GOPVC—Gas-Oil-Photovoltaics-Coal scenario) as new types of power generation technologies. For both scenarios a stepwise expansion of new generation technologies is assumed, up to a total installed capacity of nuclear and coal power plants of 7 GW.

Figure 39.2 gives an overview how the energy model is varied by the above discussed scenarios. The resulting energy models are the basis for the examination. The results are presented in the next section.

39.3 Results and Discussion

Overall Energy System In a first step, consequences of the scenarios on Singapore's overall energy system are investigated.

Table 39.1 shows the results for all possible combinations of scenarios for primary energy demand (PED) and CO_2 emissions in the model year 2050. As the biggest technological difference between the scenarios appears at the end of the model horizon, the latest model year is chosen to assess the results.

Table 39.1 Primary energy demand and CO_2 emissions in Singapore in 2050

Scenario		ICE	BEV	FCEV	FCEV
				Steamreforming	Electrolysis
Gas Oil	PED (TWh)	279.2	272.7	273.1	285.9
	CO_2 (Mt)	63.4	62.5	62.6	65.5
Gas Oil PV	PED (TWh)	256.0	249.6	249.9	262.7
	CO_2 (Mt)	58.8	58.1	58.0	60.9
Gas Oil PV Nuclear	PED (TWh)	313.2	312.1	307.5	329.8
	CO_2 (Mt)	44.9	42.9	44.0	44.9
Gas Oil PV Coal	PED (TWh)	268.7	263.2	262.7	277.4
	CO_2 (Mt)	72.9	73.1	72.2	77.2

The large effects of the selected framework of power generation technologies on Singapore's import dependency and ecology are demonstrated. An integration of PV leads to a significant reduction in primary energy demand and CO_2 emissions. However, the limitation of the PV potential in Singapore to 14 TWh (annual contribution to the electricity generation) results in a continuing high import dependency on natural gas. This could be further reduced by additional alternative power plant technologies. The integration of nuclear power plants leads to lower CO_2 emissions and a much higher primary energy demand. This effect is caused by relatively low energy efficiencies of nuclear power plants compared to gas power plants. Though, it serves the purpose of reducing import dependencies on neighboring countries by importing uranium. Another approach to do so is the integration of coal fired power plants. Compared to the GOPV scenario, an increase of primary energy demand is seen here as well: CCGT are substituted by coal power plants with lower efficiency factors. Another negative aspect is the increase of CO_2 emissions caused by previous mentioned lower efficiencies and higher specific emissions of coal compared to natural gas.

As shown in the above table, the effect of the transport scenarios on primary energy demand and CO_2 emissions is limited compared to changes in the generation mix. This is mainly caused by one fact. The share of transportation on overall energy demand is rather small. In 2010, the modeled primary energy demand for passenger and commodity transportation sums up to 24 TWh, while the overall primary energy demand of Singapore amounts 211 TWh. In the following section, it can easily be seen that this will not change much in future model years.

Summing up, energy generation has large impacts on future developments. Singapore's primary energy demand will increase compared to 2010, driven by higher demand in the industrial sector and economic growth. Import dependencies on neighboring countries will decline due to efficiency measurements and diversification of energy sources. The impact of chosen generation technologies on CO_2 emissions is even more remarkable. Only the integration of nuclear power plants leads to a reduction of CO_2 emissions in the long term. The impact of the transportation

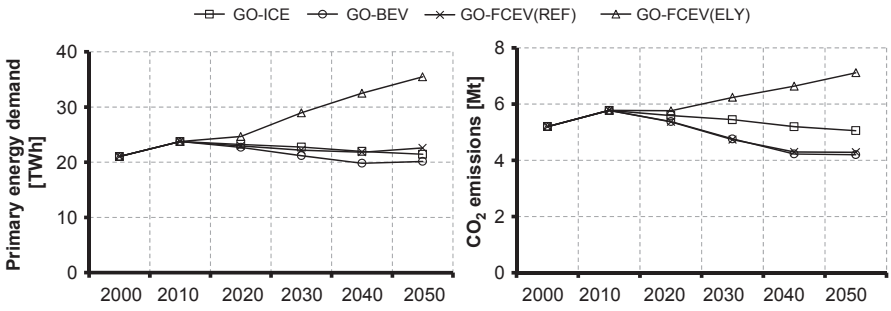

Fig. 39.3 Primary energy demand and CO_2 emissions in the transport sector on the basis of the GO scenario

sector is very limited. To discuss the feasibility of electric vehicle integration in Singapore, the transport sector is considered separately in the next section.

Transportation Sector First, the different transport scenarios are analyzed associated with the GO scenario, which represents future developments in the electricity sector based on the existing technologies oil and gas.

Figure 39.3 displays the future primary energy demand and CO_2 emissions in Singapore.

Except for fuel cell electric vehicles which are supplied by hydrogen gained from electrolysis, primary energy demand decreases as from 2010. Least primary energy is demanded in the battery electric vehicle scenario. This is caused by higher energy efficiencies of battery electric vehicles compared to conventional vehicles and fuel cell electric vehicles. However, the relatively high efficiency factor of steamreforming results in the second highest overall efficiency of the FCEV(REF) scenario up to 2040. In contrast, when hydrogen is produced by electrolysis, the bad efficiencies of this process and the electricity generation result in the highest primary energy demand of all scenarios.

Summing up, differences in primary energy demand between conventional vehicles and innovative vehicle technologies are relatively low. This is caused by a permanent improvement of internal combustion engines with regard to efficiency measurements, hybridization as well as the high efficiencies in the supply pathways of fossil fuels.

Similar to primary energy demand, CO_2 emissions decline in all vehicle settings except the FCEV(ELY) scenario from 2010 on. This is a remarkable development with regard to the rising passenger transportation demand from 25 billion Pkm in 2010 to 40 billion Pkm in 2050. In the ICE scenario there is a reduction in overall CO_2 emissions from 5.8 Mt in 2010 to 5.1 Mt in 2050. In the BEV scenario and the FCEV(REF) scenario there is even a decline to 4.2 Mt in 2050. The similar results are quite plausible, because both technology settings are indirectly based on natural gas. The higher efficiency of electric batteries compared to fuel cells in the BEV scenario are compensated by lower efficiencies of CCGT power plants compared to steam reforming. Like in the assessment of primary energy demand, most CO_2 is

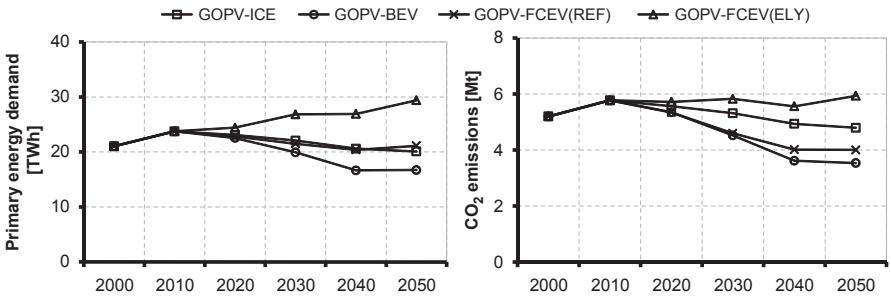

Fig. 39.4 Primary energy demand and CO_2 emissions in the transport sector on the basis of the GOPV scenario

emitted in the fuel cell electric vehicle scenario, which is based on hydrogen generated by electrolysis.

The existing conventional power generation mix, based on oil and gas, limits the achievements in energy efficiency and carbon dioxide reduction when integrating electric vehicles. In the long term, only the BEV scenario leads to the desired savings in primary energy demand compared to the ICE scenario. In case of the FCEV scenarios, even more energy is needed and Singapore's dependency on natural gas imports is rising. CO_2 emissions in the BEV scenario are with 4.2 Mt in 2050 about 17% lower than in the ICE scenario. In the FCEV(REF) scenario, nearly the same emissions like in the BEV scenario are reached. In the case that hydrogen is generated by electrolysis, CO_2 emissions will rise by 40% to 7.1 Mt in 2050. One significant advantage of all innovative scenarios compared to the conventional vehicle scenario (ICE) is that local emissions can be avoided.

Before other generation technologies are integrated into Singapore's energy system, it has to be stated that the electricity demand in the BEV and FCEV(ELY) scenario is with 9.1 and 18.6 TWh in 2050 far higher than in the ICE and FCEV(REF) scenario (3.2 and 3.3 TWh). This characteristic has to be noted when new generation capacities are integrated into Singapore's grid mix up to a certain capacity or energy level, as this results in different specific CO_2 emissions and efficiencies in every scenario.

In the GOPV scenario, the existing power plant technologies are enhanced by photovoltaics. The results for primary energy demand and CO_2 emissions of this scenario associated with the transport settings are presented in Fig. 39.4.

First, primary energy demand declines for almost all scenarios. This is caused by the fact, that photovoltaics are powered by solar radiation and do not require any type of energy imports. The more electricity is used in each transport scenario, the higher the efficiency improvement. Primary energy demand in the ICE scenario is reduced from 21.4 TWh (GO-ICE) to 20.1 TWh in 2050, while primary energy demand in the BEV scenario decreases from 20.2 TWh (GO-BEV) to 16.7 TWh caused by the higher share of electricity in total final energy consumption. Consequently, changes in the FCEV(REF) scenario and the ICE scenario are only moderate, while the largest efficiency improvements can be seen in the FCEV(ELY) scenario, which

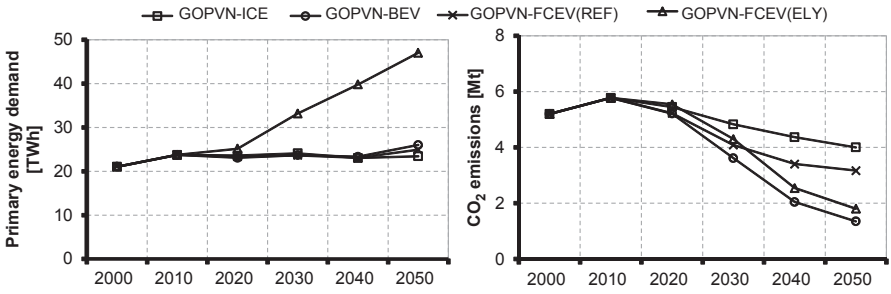

Fig. 39.5 Primary energy demand and CO_2 emissions in the transport sector on the basis of the GOPVN scenario

has the highest electricity need. In this scenario primary energy demand of the transport sector is reduced by 17% in 2050 by the integration of PV.

Solar PV is an emission-free generation technology. Therefore, the overall CO_2 emissions of the transport sector are reduced in every scenario. Just like in the GO scenario, CO_2 emissions are lowest with the BEV technology setting, followed by FCEV(REF) and the ICE technology setting. Most emissions are caused in the FCEV(ELY) scenario. The more electricity is consumed, the higher is the reduction in emissions. For instance, in the FCEV(ELY) scenario CO_2 emissions in 2050 are reduced by 17% compared to the gas and oil powered generation mix.

Summing up, photovoltaic integration results in a significant reduction in primary energy demand and CO_2 emissions in electricity generation. This has a large impact on transport technologies which consume much electricity. Therefore, the attraction of the BEV and the FCEV(ELY) scenario rises. In the BEV scenario carbon dioxide emissions in the transportation sector are reduced by 27% and primary energy demand declines by 17% in 2050 compared to the ICE scenario. The high electricity demand of electrolysis causes even larger improvements in the FCEV(ELY) scenario. Yet, primary energy demand and carbon dioxide emissions are much higher than in the other scenarios. As electricity demand is only a minor part of final energy consumption in the FCEV(ELY) scenario and the ICE scenario, there are only little changes in energy demand and CO_2 emissions compared to the Gas-Oil scenario.

Figure 39.5 shows the effects of an additional integration of nuclear power plants in Singapore

For every scenario an increase in primary energy demand can be seen. This comes from a lower energy efficiency of nuclear power plants compared to gas power plants. Just like in the examinations above, transport settings with a high demand of electricity are affected more by these developments. The most energy efficient scenario in 2050 is the ICE scenario. Compared to the GOPV generation mix, primary energy demand rises only by 14%, in contrast to the BEV scenario (primary energy demand rises by 56%) and the FCEV(ELY) scenario (primary energy demand rises by 62%). It is important to say, that this increase is mainly caused by imports of uranium. The dependency on natural gas from neighboring countries is reduced by 75% compared to the GOPV scenario.

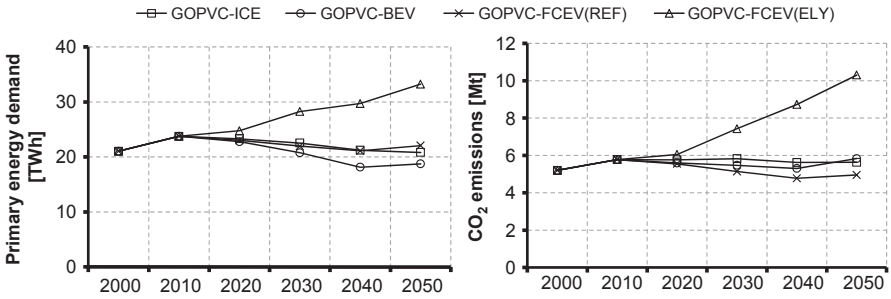

Fig. 39.6 Primary energy demand and CO_2 emissions in the transport sector on the basis of the GOPVC scenario

As Fig. 39.5 shows, the additional integration of nuclear power plants leads to significant changes in the CO_2 emissions of the different transportation scenarios. There is a reduction of CO_2 emissions for all scenarios. Especially in the BEV and the FCEV(ELY) scenario, carbon dioxide emissions decline by 63 % and 70 % in 2050. In the transport scenarios which are mainly characterized by fossil fuels, reduction of emissions is much less.

Summing up, with a high percentage of carbon free power generation, innovative vehicle technologies, which are directly (BEV) or indirectly (FCEV(ELY)) supplied by electricity, can lead to a significant reduction in CO_2 emissions compared to vehicles which are supplied by fossil fuels.

Finally, the different transport scenarios are discussed on the basis of a grid mix which is mainly influenced by oil, gas, PV and hard coal power plants (GOPVC) (Fig. 39.6).

Similar to the GOPVN scenario, there is a rise in primary energy demand of all transport settings compared to the GOPV scenario. This is due to a lower energy efficiency of coal power plants compared to CCGT. Nevertheless, the BEV scenario remains the most efficient scenario, followed by the ICE and FCEV(REF) scenario. The highest primary energy demand results in the FCEV(ELY) scenario.

The GOPVC scenario causes the highest emissions of CO_2 in Singapore. This affects the transportation sector. The FCEV(REF) scenario has the lowest CO_2 emissions per Pkm. While the BEV scenario has the second lowest emission factor until 2040, it is undercut in 2050 by the ICE scenario, as power generation leads to higher CO_2 emissions. Emissions in the FCEV(ELY) scenario nearly double emissions in the FCEV(REF) scenario, due to the high demand of electricity for hydrogen generation.

Conclusions

This paper investigates the effects of an integration of electric vehicles in Singapore depending on different kinds of electricity generation.

Only when electromobility is seen in the context of an overall energy system, it is possible to assess the consequences of an integration of electric vehicles in Singapore. After comparison of four different transportation scenarios (dominance of conventional vehicles, battery electric vehicles and fuel cell electric vehicles based on hydrogen generated by steam reforming or electrolysis) in combination with four different power generation technology settings (Gas-Oil, Gas-Oil-Photovoltaics, Gas-Oil-Photovoltaics-Nuclear, Gas-Oil-Photovoltaics-Coal) specified results are achieved.

The overall efficiency of electric vehicles is highly dependent on the efficiency of power generation. Concerning primary energy demand, significant reductions are only achieved when the shares of renewable energies and power plant efficiencies are high. If efficiency of generating electricity is low, fuel cell electric vehicles based on hydrogen generated by steam reforming and conventional vehicles will require less primary energy than vehicles with higher electricity consumption.

As electric vehicles and fuel cell electric vehicles are locally emission-free, they offer advantages concerning air quality and dirt compared to internal combustion engine based vehicles. However, concerning total emissions, a more specific assessment is necessary. Total emissions for transportation in the BEV and FCEV(REF) scenario based on a GO, GOPV or GOPVN grid mix are less than in the ICE scenario. Caused by their high electricity demand, vehicles in the FCEV(ELY) scenario need a nearly emission-free power generation to achieve lower emissions than conventional vehicles.

Based on the predicted developments for commodity prices and vehicle technologies, battery electric vehicles and fuel cell vehicles will be more expensive than conventional vehicles. Singapore's strong governmental intervention in the transportation sector, which leads to relatively high costs of private transportation and a very young vehicle fleet, offers perfect surroundings for a fast integration of electric vehicles.

Electromobility is a very interesting approach to influence Singapore's future energy system in terms of efficiency and ecology. However, it is important to stress that the transport sector's contribution is limited and highly dependent on the way how final energy is produced. Therefore, a general statement which kind of electromobility would be the best solution for Singapore is not possible. As shown in the paper, the optimal result can only be achieved by the development of a holistic approach.

References

1. Singapore Department of Statistics (DOS) (2012) Key annual indicators. http://www.singstat.gov.sg. Accessed 20 June 2012
2. Energy Market Authority (EMA) (2011) Energising our nation—Singapore energy statistics 2011. Singapore
3. Asia Pacific Energy Research Centre (APERC) (2011) APEC energy overview 2010. Tokyo, Japan

4. TUM CREATE Ltd. (2012) About. http://www.tum-create.com.sg/. Accessed 20 June 2012
5. Loulou R, Labriet M (2007). ETSAP-TIAM: the Times Integrated Assessment Model Part I: Model Structure. Springer, Berlin
6. Land Transport Authority (LTA) (2012) Facts & figures. http://www.lta.gov.sg. Accessed 20 June 2012
7. Land Transport Authority (LTA) (2008) LTMASTERPLAN Singapore
8. Energy Market Authority (2011) Statement of Opportunities Singapore
9. Luther J, Aberle A, Reindl T, Mhaisalkar S, Koh K, Jadhav N, Zhang, J, Yao K (2011) Solar energy technology primer: a summary. National Climate Change Secretariat and National Research Foundation, Singapore

Chapter 40
Analysis of a Combined Power and Heating Thermodynamic System Driven by Low Temperature Heat Source

Jianzhong Song, Xiaosong Zhang, Can Yang and Qikuang Yao

Abstract Nowadays, the power shortage becomes more serious. The new methods of producing electricity power have been paid more and more attentions to. All over the world, the low temperature heat source is very abundant, such as the geothermal energy, solar energy and industrial waste heat. In this paper, a combined power and heating thermodynamic system powered by low temperature heat source based on ORC (organic Rankine cycle) was proposed. The system consists of a heat source system, a screw expander, a hot water generator, a condenser and a feed pump. And the fluid R245fa was selected as the working fluid. From the low temperature heat source, firstly the electricity power and secondly the heating power ware gained. The cycle performance of the system was studied at the typical working condition. And some key factors to the system are analyzed. Also, the experiment system was set up, and the experimental performance of the system was studied under the typical working condition. In the period of the experiment, the low temperature heat source is the heat collected from solar. The performance comparison based on the simulation results and the experimental results was done. Also, the actual effects of some factors were analyzed to improve the system.

Keywords Power generation · Heating · Screw expander · ORC · Low grade heat

J. Song (✉) · X. Zhang · C. Yang · Q. Yao
School of Energy and Environment, Southeast University,
Nanjing, China
e-mail: strongangel@126.com

X. Zhang · J. Song
Changshu Applied Technology, Academy of Southeast University,
Changshu, China
e-mail: rachpe@seu.edu.cn

C. Yang
e-mail: yangcan070122@163.com

Q. Yao
e-mail: yaokey22@163.com

I. Dincer et al. (eds.), *Progress in Sustainable Energy Technologies: Generating Renewable Energy,* DOI 10.1007/978-3-319-07896-0_40,

40.1 Introduction

With the rapid expansion of the modern society, the power demand is continuously increasing. And the power shortage becomes more serious. Meanwhile, large number of power is produced by the combustion of fossil fuels like coal, oil and nature gas. And it's well known that the reserves of fossil fuels are limited. Also, the gas coming from the combustion will result in serious environmental pollution problem. So, the applications of concerting renewable energies (solar energy, wind energy, biomass and geothermal energy) to electricity become more and more important, and have attracted more attention. At the same time, the low-temperature heat can be gained more easily from various renewable energies. So, the technologies have been developed and the efficiencies are improving.

There are some cycles using in the low-temperature thermal power generation, such as organic Rankine cycle, Stirling cycle and Kalina cycle. And the organic Rankine cycle (ORC) shows great flexibility, high safety in recovering low-grade heat [1], it has a great potential to become competitive with fossil fuels (especially natural gas) based power systems. And many researchers do researches on the cycle, the working fluids, the system performance, and so on. For example, Hung et al. [2–4] mainly studied the working fluids which are more suitable in the range of low temperature. Liu [5] examined the influence of working fluids on the performance of ORC cycle for waste heat recovery system. Goswami [6] proposed a new combined power/refrigeration cycle utilizing ammonia and water, and the overall thermal efficiency reached 23.54%. Manolakos et al. [7, 8] designed and built a low-temperature solar organic Rankine cycle system for reverse osmosis desalination in Greece, and R134a was selected as the working fluid. The maximum power generation was about 2.05 kW which was quiet enough to drive the RO unit, and the overall system efficiency was about 4%. Nguyen et al. [9] developed a small-scale Rankine cycle system designed to generate electricity from low temperature heat. It uses n-pentane as the working fluid and it was capable of delivering 1.5 kW of electricity with a thermal efficiency of 4.3%. Zhang et al. [10] did the theoretical analysis of a solar energy-powered Rankine cycle which utilizing CO_2 as the working fluid. The electricity power efficiency and heat power efficiency were as high as 11.4 and 36.2% based on the simulation, respectively.

In this study, a combined power and heating thermodynamic system powered by low temperature heat source based on ORC (organic Rankine cycle) was proposed. And the experimental system was set up. Power is produced by expansion of a high pressure vapor through an expander and heating comes from the expander exhaust.

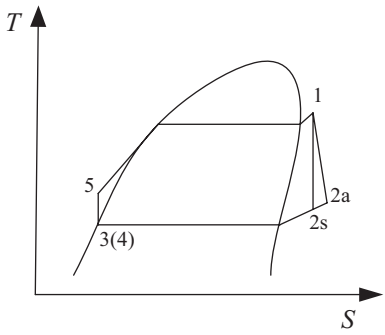

Fig. 40.1 Typical T-s process diagram

40.2 System Description and Thermal Analysis

A typical low-temperature heat Rankine cycle system consists of the following components: (1) vapor generation/evaporator, (2) expander/turbine, (3) generator, (4) condenser/cooler, (5) storage tank, (6) working fluid pump. The typical T–s process diagram is shown in Fig. 40.1, and it is contains of following processes:

1-2a (2s): the saturated or superheated vapor fluid at high pressure expands to the low pressure; where 2a means the state of the actual work condition, 2s means the state of the ideal work condition;

2a (2s)-3(4): heat rejection through the cooler/condenser, the expander exhaust is cooled down to liquid phase by water or air. Then the liquid fluid flows into the storage tank, from where the liquid is pumped into the evaporator;

3(4)-5: The working fluid in the storage tank is pumped to a high pressure by the feed pump;

5-1: The high pressure liquid fluid is heated in the vapor generator, where the phase change takes place.

The system operation can be described briefly below. The pump pumps the working fluid to the vapor generator at a high pressure level. In the vapor generator, the working fluid is heated by the low temperature heat sources and the phase changes from liquid to vapor. The generated vapor flows into the expander and produces power there, and the generated shaft work drives the generator. And then, the expander exhaust flows to the cooler/condenser, where the heating power can be gained. Then condensed working fluid flows into the storage tank and is pumped to high pressure. Again the fluid is pumped into the vapor generator, and a new cycle begins. The flow diagram of the proposed system is shown in Fig. 40.2. In the experimental system, a screw expander was utilized and the condensation was divided into two parts: a cooler (water heater) and a condenser. High temperature heating power can be gained from the cooler while the low temperature heating power can be gained from the condenser. In this study, hot water can be gained from the cooler, and only this part of heat was taken into the calculation.

From the Fig. 40.1 the thermal process of the system is very clear. All the heat input of the system is the heat gained in the vapor generator. And the power output

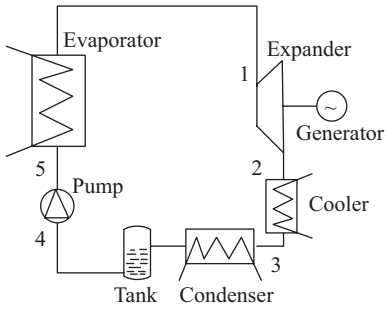

Fig. 40.2 Flow diagram of the system

consists of the shaft work and the heating power. So the electricity efficiency η_{E} and system efficiency η_{T} can be defined as:

$$\eta_{\mathrm{T}} = \frac{W_E + Q_H - W_P}{Q_W} \tag{40.1}$$

$$\eta_{\mathrm{E}} = \frac{W_E - W_P}{Q_W} \tag{40.2}$$

Where, Q_W is the heat quantity absorbed by R245fa in the vapor evaporator; Q_H is the heat quantity obtained from the cooler (water heater); W_E is the power output obtained from the expander; W_P is the power consumed by the feed pump. And these parameters can be defined as (in Fig. 40.2):

$$W_{\mathrm{E}} = m\left(h_2 - h_1\right) \tag{40.3}$$

$$W_{\mathrm{P}} = m\left(h_5 - h_4\right) \tag{40.4}$$

$$Q_{\mathrm{W}} = m\left(h_1 - h_5\right) \tag{40.5}$$

$$Q_{\mathrm{H}} = m\left(h_3 - h_2\right) \tag{40.6}$$

From Eqs. (40.3) to (40.6), $\dot{m}$ is the mass flow rate of R245fa in the cycle loop. h is the enthalpy of the working fluid at each state point.

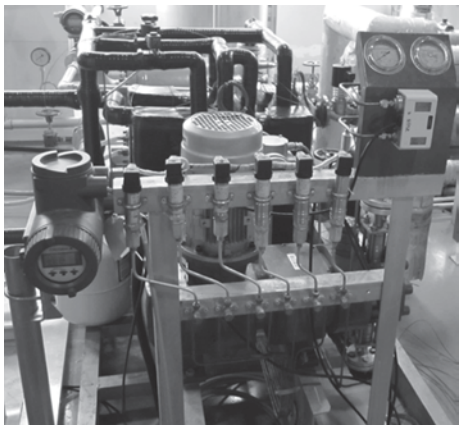

Fig. 40.3 Photo of the experimental system

Table 40.1 Vapor generator, cooler and condenser characteristics

	Vapor generator	Cooler	Condenser
Manufacturer	Alfa Nova	Alfa Nova	Alfa Nova
Dimensions, L × w × h, mm	150 × 111 × 526	167 × 111 × 526	190 × 111 × 526
Heat transfer area, m^2	2.448	2.754	3.264
Fluids, hot/cold	Heat transfer oil/ R245fa	R245fa/Water	R245fa/Water
Type	Counter flow	Counter flow	Counter flow

40.3 Experimental Setup

With the work done above, an experimental system was designed and set up. Figure 3 shows the experimental system. The experimental system is mainly comprised of a vapor generator, a cooler, a water cooled condenser, a fluid storage tank, a feed pump, a screw expander, transducers and data acquisition system. In the experiment, an oil heater was selected as the low-temperature heat source. The heat transfer oil was heated in the heater and pumped into the vapor generator. The power was produced from the expander, and it's measured by a power meter. Also, the heating power was gained from the cooler, a plate heat exchanger where the water was heated by the working fluid from the expander outlet. The characteristics of these heat exchangers were shown in Table 40.1. And a pump is used in the experimental system to feed the liquid working fluid, which can adjust the capacity in the range of 0–100 % during operation. This diaphragm metering pump can provide a maximum operating pressure of 2 MPa and flow rate of 320 L/h. Meanwhile, T-type thermocouples and pressure transmitters were installed at different positions to measure the temperatures and pressures. The mainly properties measured include: R245fa temperatures at the inlets and outlets of the vapor generation, cooler and the condenser; R245fa pressure at the inlet and outlet of the expander. Also, a mass flow

meter was used to measure the flow rate of R245fa. All the output signals of the experimental data were transported through the data acquisition system and recorded as functions of time in the computer.

40.4 Results and Discussion

In this section, both the simulation results and the experimental results were presented. The system performances under different working conditions were studied. In order to study the effect of the parameter changes on the cycle performance, only one parameter changed at a time during the simulation. For all simulations, the following system specifications were assumed. The inlet temperature of water loop of the condenser was 25 ˚C, and the mass flow rate of the R245fa was 0.1 kg/s. The efficiency of the expander and the pump were assumed to be 0.7 and 0.8. For the simulation results, the power output mainly means the power output of the expander, and the efficiency of belt transmission system and the generator were not taken into account.

The effect of the expander inlet pressure on the system performance was investigated with the expander inlet temperature was changed from 80 to 130 ˚C. And the pressure of condenser was constant at 0.2 MPa with the temperature of 30 ˚C. It's assumed that R245fa at the inlet of the expander was under the saturation condition, and the temperature of R245fa at inlet of condenser was 45 ˚C. The simulation results were shown in Fig. 40.4 and Fig. 40.5. It can be seen from Fig. 40.4 that with the increase of the pressure, both the power output and the heating power gained of per unit mass were increased. And the final electricity would be gained with the low value by considering the belt transmission efficiency and the electricity generator efficiency. And it is also clear from the curves of Fig. 40.5 that the system efficiency and the power output efficiency increase with the rise of expander inlet pressure. Cause of the pressure at the outlet of the expander was constant, the expansion ratio rises. So more absorbed heat power was changed into power in the expander. Also, the temperature of the expander exhaust was higher with the higher inlet pressure. That means more heat power can be gained.

Actually, it's hard to make R245fa at the expander inlet keeping with the saturation condition. So, the effects of degree of superheat on the system performance ware studied. Figure 40.6 shows the effect of expander inlet temperature on the system performance. And the effects of degree of superheat on the system performance can be gained. In the simulation work, the expander inlet temperature varied from 80 to 130 ˚C while the expander inlet pressure was set at 0.8 MPa, 1.0 MPa, 1.0 MPa and 1.2 MPa. It's shown clearly that the values of the total system efficiency increased rapidly with the increase of expander inlet temperature at each pressure level. However, the power output efficiency kept nearly the same values while the values of the power output increased. Because when the expander inlet temperature grew, the value added of heat absorbed in the vapor generator was larger than that of the power output. In other words, superheating the working fluid can improve

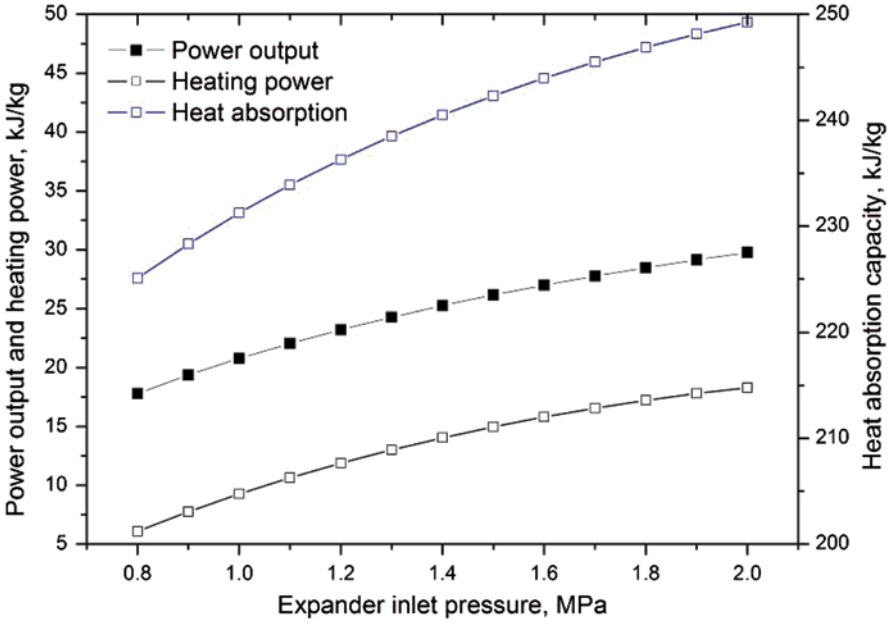

Fig. 40.4 Effect of expander inlet pressure on power output, heating power and heat absorption per unit mass

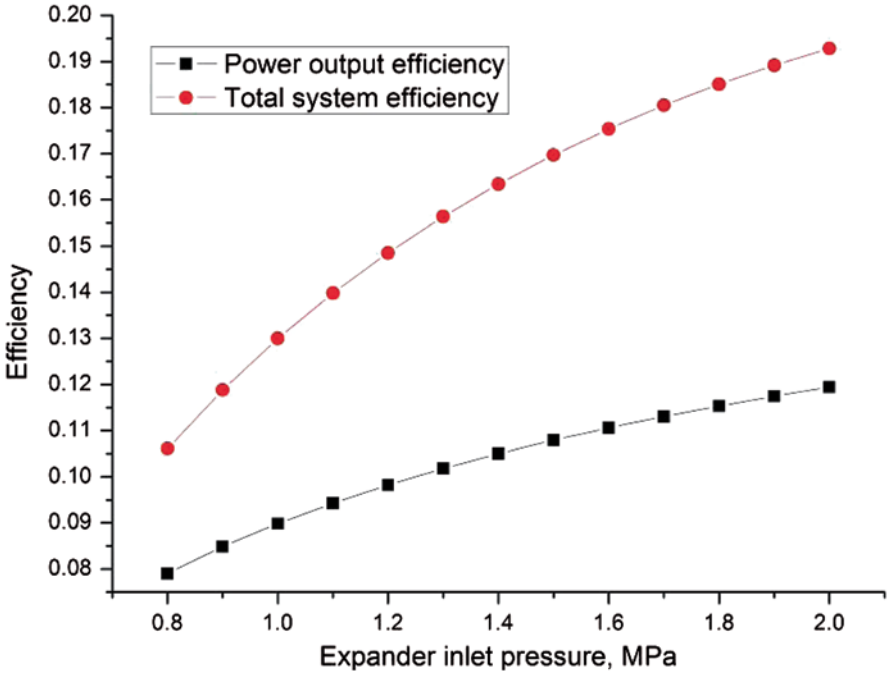

Fig. 40.5 Effect of expander inlet pressure on the cycle performance

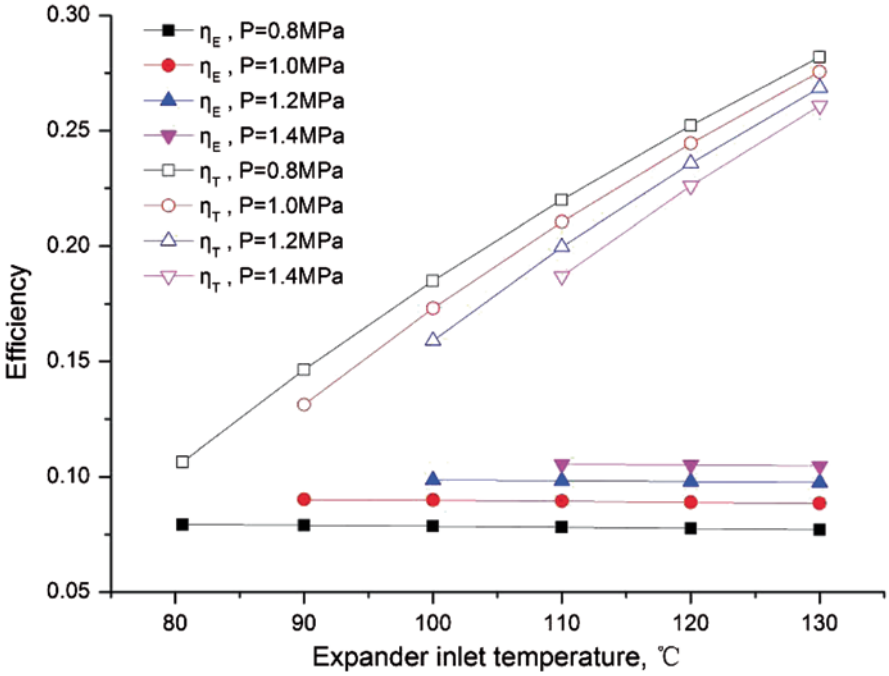

Fig. 40.6 Effect of expander inlet temperature on the system performance

the values of power output, but of no use to the power output efficiency. Also it's shown that when the expander inlet temperature was fixed, the total system efficiency reduces while the power output efficiency increased. Figure 40.7 shows the variation tendency of power output, heating power and heat absorption per unit mass when the expander inlet temperature was fixed at 130 ˚C. The power output increases while the heating power and heat absorption reduce rapidly. That results in the variation tendency of the power output efficiency and the system efficiency.

Also, there were some experimental results gained while the expander inlet pressure was in the range of 0.8–0.9 MPa. And the electricity power output from the single phase synchronous generator was measured and recorded. The heating power was the heat of the hot water which was transferred from the cooler (hot water heat exchanger). The mass flow rate of R245fa was 0.1kg/s and the heat resource temperature was changed from 95 to 120 ˚C. The measured expander inlet temperature changed from 80 to 110 ˚C. And the water inlet temperature of condenser was 25 ˚C. The outlet temperature of condenser was 25.7 ˚C with the pressure of 0.2 MPa. And the averaged measured values of the parameters of the expander inlet and outlet at steady state were shown in Table 40.2.

The performance of the system depended on the experiment was shown in Fig. 40.8. The power output depended on the calculated enthalpy difference of R245fa measured parameters at the expander inlet and outlet. The electricity power output was the electricity power measured by the wattmeter. There were differences

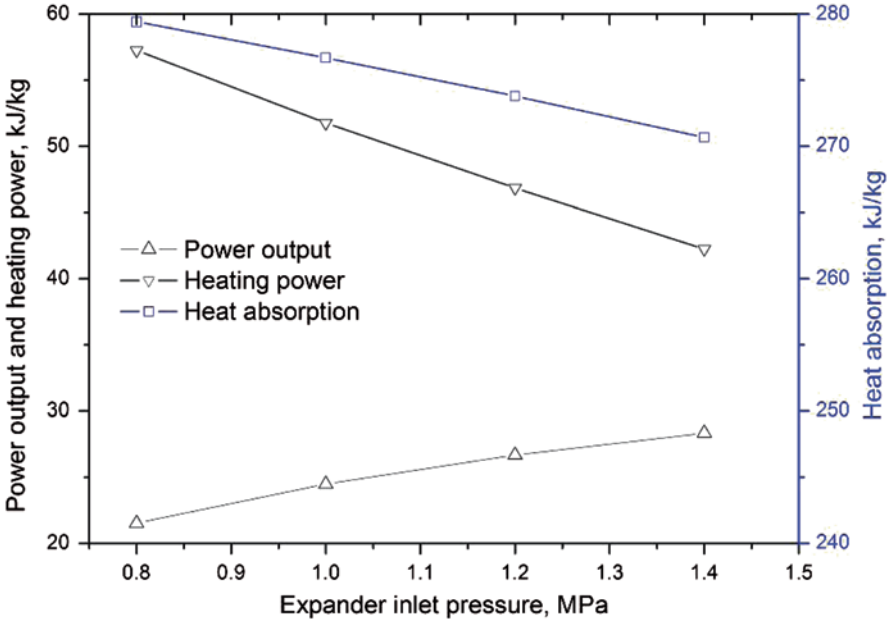

Fig. 40.7 Variation tendency of power output, heating power and heat absorption per unit mass

Table 40.2 Measured values of inlet and outlet parameters of expander

Heat source temperature, T_h (°C)	Inlet of expander		Outlet of expander	
	T(°C)	P (MPa)	T(°C)	P (MPa)
120	107.43	0.86	86.46	0.28
110	100.11	0.85	80.57	0.3
100	88.56	0.83	71.62	0.31
95	80.55	0.8	63.77	0.31

between them because of the belt transmission efficiency, generator efficiency and the heat transfer between the expander and the surroundings. Heat transfer occurred can reduce the capacity of expander power output, especially when the expander inlet temperature is high. With the increase of the expander inlet temperature, the electricity power output, the system efficiency and electricity output efficiency all increased. It showed the same variation tendency compared to the simulation results.

Conclusions

Analysis of a combined power and heating system using R245fa as the working fluids was carried out based on both the theoretical and experimental results. A parameter study of such a combined system was performed. The results showed

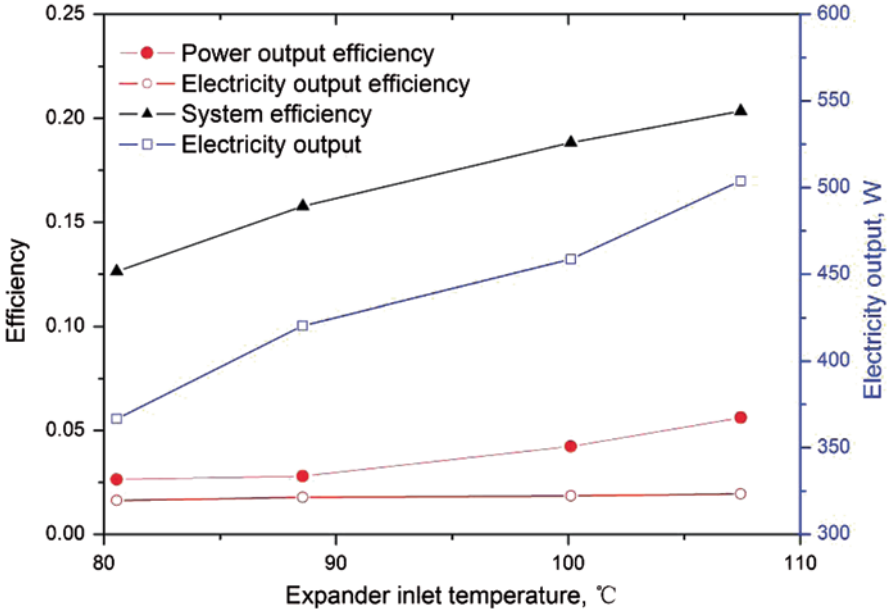

Fig. 40.8 Effect of expander inlet temperature on system experimental performance

that the higher expander inlet pressure may lead the higher power output and the better system performance while R245fa was in saturation condition at the expander inlet. And superheating the working fluid at the expander inlet was useless to the power output efficiency but useful for the system efficiency and the values of power output. So, it may be a good choice for the system utilizing in the waste heat recovery. However, the degree of superheating is not the larger the better. It needs to be synthetically considered with the system pressure level, the heat sources, the system safety, and so on. And the experimental results mainly showed the effect of expander inlet temperature on the system performance. The electricity power output was affected by some factors, the transmission efficiency, the generator efficiency, the expander efficiency, heat loss of expander, and so on.

Nomenclature

H	Specific enthalpy (kJ/kg)
$\dot{m}$	Mass flow rate of R245fa (kg/s)
P	Pressure (MPa)
T	Temperature (˚C)
T_h	Heat source temperature (˚C)
W_E	Power output from the expander (W)
W_P	Power consumed by the feed pump (W)
Q_H	Heat power output from the cooler (W)
Q_W	Heat absorption from the low temperature heat source (W)

L The length of the heat exchanger (mm)
W The width of the heat exchanger (mm)
H The height of the heat exchanger (mm)

Greek letters

η_T Total system efficiency
η_E Power output efficiency

Subscripts

1 Inlet of expander
2 Outlet of expander
3 Outlet of the cooler
4 Outlet of condenser
5 Outlet of feed pump

Acknowledgements This work was financially supported by the Twelfth 5-year Science and Technology Support Plan of China (No. 2011BAJ03B05, NO.2011BAJ03B14).

References

1. Sternlicht B (1982) Waste energy recovery: an excellent investment opportunity. Energy Convers Manage 22:361–373
2. Hung TC, Shai TY, Wang SK (1997) A review of Organic Rankine Cycles (ORCs) for the recovery of low-grade waste heat. Energy 22(7):661–667
3. Hung TC, Wang SK, Kuo CH (2010) A study of organic working fluids on system efficiency of an ORC using low-grade energy sources. Energy 1:1–9
4. Hung T-C (2001) Waste heat recovery of organic Rankine cycle using dry fluids. Energy Convers Manage 42:539–553
5. Liu B-T, Chien K-H, Wang C-C (2004) Effect of working fluids on organic Rankine cycle for waste heat recovery. Energy 29:1207–1217
6. Goswami DY, Vijayaraghavan S, Lu S, Tamm G (2004) New and emerging developments in solar energy. Solar Energy 76:33–43
7. Manolakos D, Papadakis G, Mohamed ES et al (2005) Design of an autonomous low-temperature solar Rankine cycle system for reverse osmosis desalination. Desalination 183:73–80
8. Manolakos D, Papadakis G, Kyritsis S et al (2007) Experimental evaluation of an autonomous low-temperature solar Rankine cycle system for reverse osmosis desalination. Desalination 203:366–74
9. Nguyen VM, Doherty PS, Riffat SB (2001) Development of a prototype low temperature Rankine cycle electricity generation system. Appl Therm Eng 21:169–81
10. Zhang XR, Yamaguchi H, Uneno D (2006) Analysis of a novel solar energy-powered Rankine cycle for combined power and heat generation using supercritical carbon dioxide. Renew Energy 31:1839–1854

Chapter 41
A Comparative Life Cycle Assessment of Compressed Natural Gas and Diesel Powered Refuse Collection Vehicles

Syed Ahmed, Lars Rose, Mohammed Hussain, Kourosh Malek, Robert Costanzo and Erik Kjeang

Abstract Consumers and organizations worldwide are searching for low-carbon alternatives to conventional gasoline and diesel vehicles to reduce greenhouse gas (GHG) emissions and their impact on the environment. A comprehensive technique used to estimate overall cost and environmental impact of vehicles is known as life cycle assessment (LCA). In this article, a comparative LCA of diesel and compressed natural gas (CNG) powered heavy duty refuse collection vehicles (RCVs) is conducted. The analysis utilizes real-time operational data obtained from the City of Surrey in British Columbia, Canada. The impact of the two alternative vehicles is assessed from various points in their life. No net gain in energy use is found when a diesel powered RCV is replaced by a CNG powered RCV. However, significant reductions (about 24 % CO_2-equivalent) in GHG emissions are obtained. Moreover, fuel cost estimations based on 2011 price levels and a 5 year lifetime for both RCVs reveal that considerable cost savings may be achieved by switching to CNG vehicles. Thus, CNG RCVs are not only favorable in terms of reduced climate change

E. Kjeang (✉) · S. Ahmed · L. Rose · M. Hussain · K. Malek
Mechatronic Systems Engineering, School of Engineering Science, Simon Fraser University, 250-13450 102 Avenue, Surrey, BC V3T 0A3, Canada
e-mail: ekjeang@sfu.ca

L. Rose · K. Malek
National Research Council, 4250 Wesbrook Mall, Vancouver, BC V6T 1W5, Canada

L. Rose
Materials Engineering Department, University of British Columbia, 309-6350 Stores Road, Vancouver, BC V6T 1Z4, Canada

K. Malek
Chemistry Department, Simon Fraser University, 8888 University Drive, Burnaby, BC V5A 1S6, Canada

R. Costanzo
Engineering Department, City of Surrey, 14245-56 Avenue, Surrey, BC V3X 3A2, Canada

I. Dincer et al. (eds.), *Progress in Sustainable Energy Technologies: Generating Renewable Energy,* DOI 10.1007/978-3-319-07896-0_41,

impact but also cost effective compared to conventional diesel RCVs, and provide a viable and realistic near-term strategy for cities and municipalities to reduce GHG emissions.

Keywords Life cycle assessment (LCA) · Compressed natural gas (CNG) · Refuse collection vehicle (RCV)

41.1 Introduction

Rising oil prices and growing environmental concerns are driving research into alternative, cleaner, and more efficient ways of producing and using energy. According to Natural Resources Canada (2008), the transportation sector is the largest source of greenhouse gas (GHG) emissions in Canada, accounting for more than one-third of Canada's total GHG emissions. Additionally, criteria air contaminants (CAC) from the transportation sector are posing significant environmental and health risks for Canadians, particularly for about 80 % of the population who live and/or work in urban areas [1].

In order to minimize the impact of emissions from the transportation sector, consumers and organizations are seeking viable low-carbon alternatives to conventional gasoline and diesel vehicles. The compressed natural gas (CNG) powered vehicle is a viable alternative to conventional gasoline and diesel powered vehicles and can significantly reduce emissions from the transportation sector. Two studies of CNG and gasoline engines have shown significant reductions of all combustive emissions [2, 3]. However, Aslam et al. observed an increase in NO_x emissions [4]. This increase in NO_x despite significant reductions in other emissions is also observed in studies comparing CNG to diesel fuel [5–7]. A possible explanation for the increase in NO_x is given by Nylund et al. who argue that if no special measures are taken, NO_x emissions will be higher than for diesel engines [8]. CNG engines need to operate in a lean-burn operation or in stoichiometric combustion in combination with a three-way catalyst to reduce emissions.

However, to validly evaluate and assess the energy, emissions, and economic effects of alternative fuels and vehicle technologies, a holistic or comprehensive approach has to be considered. The approach, often referred to as life cycle approach, or life cycle assessment (LCA), must include all the steps required to produce a fuel, to manufacture a vehicle, and to operate and maintain the vehicle throughout its lifetime including disposal and recycling at the conclusion of its life cycle. This particular approach provides a better understanding of alternative choices in fuels and vehicle technologies and makes informed selections for the long-term possible. Conversely, without a life cycle approach, false conclusions can be drawn, particularly for alternative vehicle technologies that employ fuels with distinctly varied primary energy sources and fuel production processes. Numerous studies have been conducted on alternative vehicle technologies from the life cycle perspective, often estimating fuel cycle emissions and energy use associated with various transporta-

tion fuels and technologies. On the topic of comparative LCA, fuel cell vehicles are compared with conventional vehicles [9–14] and electric vehicles [15]. Others have done a comparative LCA of different hydrogen production pathways [16, 17].

LCAs comparing CNG to diesel vehicles have concluded different results partially due to locale specific data. Comparing CNG and diesel light duty vehicles, [18, 19] have done an LCA study showing higher efficiency and reduction of CO_2 emissions for CNG and a 13 % reduction of life cycle energy consumption for diesel compared to gasoline. However, if the diesel fuel is derived from natural gas (FT diesel), an increase in energy demand offsets any GHG reduction in vehicle usage. Previous studies on comparative LCA of heavy duty CNG and diesel vehicles were focused on transit buses [20–23]. Karman found significant reductions of CO_2 emissions for vehicles in the city of Beijing, China when switching to CNG, but stressed the importance of locale specific data for an LCA [21]. Kliucininkas et al. found a higher environmental impact for CNG compared to diesel in Kaunas, Lithuania due to a higher consumption of CNG per traveled distance with related upstream emissions [22]. Ryan and Caulfield found a significant decrease of all pollutants except CO in CNG buses compared to diesel buses on the Euro V norm in Dublin, Ireland [23]. Ally and Pryor compared CNG, diesel, and H_2 fuel cell and showed that CNG required more energy per distance traveled and slightly higher GHG emissions compared to diesel [20]. However, vehicles driven by CNG showed lower emissions related to smog, acidification, and soil/water contamination (NO_x, CO, SO_2, and non-methane volatile organic compounds) for Western Australia. On presenting LCA impacts, Kliucininkas et al. used “milli ecopoints” (mPt) per km traveled [22]. One point is interpreted as one thousandth of the annual environmental load (damage) of one average European inhabitant. Sorensen has monetized (in Euros) the environmental, social, and other impacts[24]. However, the majority of LCAs present their findings in the quantity of greenhouse gases and pollutants per kilometre traveled for vehicles as well as energy consumed to evaluate efficiency.

The current state of LCA studies of heavy duty vehicles as relating to refuse collection vehicles (RCVs) is however largely absent. Therefore, there is a significant need to conduct LCA studies of RCVs and evaluate the results in light of existing studies on transit buses that also employ heavy duty engines. Interestingly, there are conflicting reports of the climate change (or global warming) impact with respect to GHG emissions from CNG and diesel buses. Karman showed a small decrease of GHG emissions of CNG [21] while Ally and Pryor showed an increase [20]. Our current LCA on RCVs will be presented in the context of these transit bus studies to show how a reduction of GHG emissions and climate change impact can be achieved by switching from diesel to CNG RCVs.

The present study involves a municipal organization in British Columbia, Canada, known as the City of Surrey (hereafter referred to as the City). The City has about 300 vehicles in its engineering vehicle fleet, ranging from light duty passenger and commercial vehicles to rangers (pickups), heavy duty commercial vehicles, buses, and RCVs. The City became interested in finding viable low-carbon alternative fuel vehicles to replace incumbent gasoline and diesel vehicles in order to meet or exceed its goal of reducing GHG emissions from fleet vehicles by 20 %

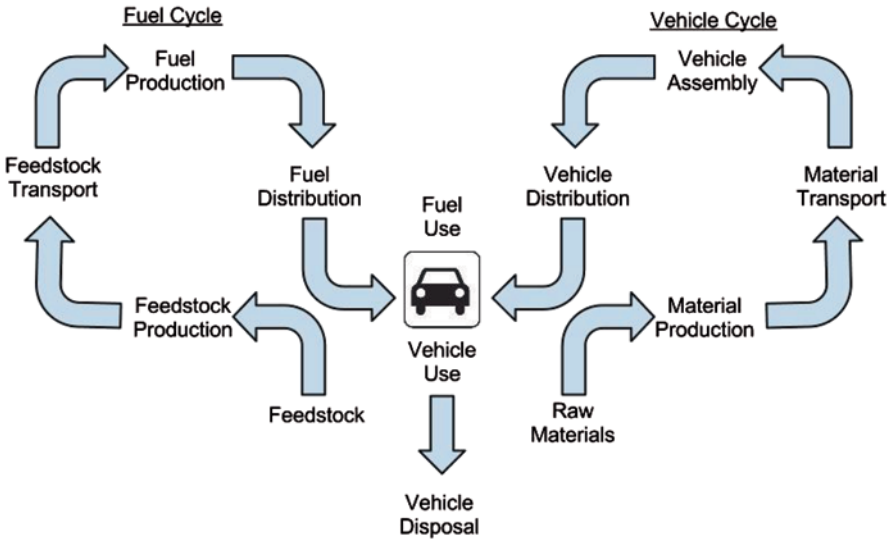

Fig. 41.1 Typical life cycle of a vehicle technology

by the year 2020. In this regard, the City wants to undertake a holistic or pragmatic approach that can assess low-carbon alternative fuel vehicles from various points in their life cycle. In an attempt to assess viable low-carbon alternative fuel vehicles, this study focuses on heavy duty RCVs powered by CNG as a potential replacement of the diesel powered RCVs presently operated in the City.

The objective of the present study is to conduct a life cycle analysis of a CNG powered RCV and compare it with a diesel powered RCV, utilizing the reliable and real-time operational data provided by the City and its contractor. The findings of this study will enable decision-makers to make an informed selection of CNG vehicles over conventional diesel vehicles based on realistic estimations of life cycle emissions, cost, and energy use.

41.2 Life Cycle Assessment Methodology

The methodology used to assess different vehicle technologies from various points in their life cycle is often referred to as life cycle assessment (LCA). LCA is a 'cradle-to-grave' approach of assessing systems or technologies by compiling an inventory of relevant inputs and outputs, assessing the potential environmental impacts associated with identified inputs and outputs, and interpreting the results of inventory and impact phases to help make informed decisions [25].

A typical life cycle of a vehicle technology is shown in Fig. 41.1. The life cycle can be classified into two major categories: the fuel cycle and the vehicle cycle. In the fuel cycle, the following stages result, starting from the feedstock production

where energy is used and greenhouse gases are released. At this stage in CNG production, for example, the associated input of energy to extract natural gas and the emissions output related to the extraction are accounted for. As for diesel, the extraction of crude petroleum is considered. Next in the fuel cycle is feedstock transport, in which the associated costs of transportation are documented. As with our example, natural gas is transported to gas processing facilities via pipelines or tank trucks requiring energy as well as producing emissions. Conversion of crude oil feedstock to practical fuels is a very energy intensive step of the fuel cycle, generating significant amounts of emissions. However, natural gas purification results in significantly less energy use and emissions. Lastly, the fuel needs to be transported for use by the vehicle. Emission and energy use associated with fueling trucks are thus accounted for in the fuel distribution stage. In this LCA, the fuel cycle shares similar inputs and outputs with the vehicle cycle at the "Fuel Use" stage (Fig. 41.1).

Both the production and operation of the vehicle need to be accounted for in the LCA. The materials that are extracted from the earth required to produce the vehicle are accounted for in the "Vehicle Material Production" stage. In the standard RCV internal combustion engine and fuel storage systems, aluminum and steel are needed for production. These materials can be extracted from the ground or from old vehicles via recycling. The LCA accounts for the energy required for these operations as well as emissions generated. Next, these materials are transported to RCV assembly plants where energy is required for production with emissions correlating directly to RCV production. Further emissions are produced and energy is required for the transport of the RCVs to end users and for disposal or recycling at the end of its lifetime.

An LCA of a vehicle technology can be relatively laborious and time and data intensive. As one can see from observing the fuel pathway from resource extraction and the stages of vehicle production from raw materials above, much time can be spent in gathering the inventory data itself. Consequently, it may be advantageous to use established tools that can access the necessary data from databases and assist with the main analysis. The scope at any stage can branch out to secondary or tertiary energy and environmental effects; therefore one must also list the assumptions and boundaries of the analysis to give the reader the scope of the LCA conducted. The following sections will elaborate more on the tool employed and the assumptions made in the present study.

41.3 Description of Analysis

As mentioned in the previous section, a complete LCA of a vehicle technology should consider all the steps of the fuel cycle and the vehicle cycle shown in Fig. 41.1. It can be conducted either by developing custom-made in-house models or using existing LCA tools developed by various organizations. According to the United States Environmental Protection Agency there are about 30 LCA tools developed for different applications [26]. Among them, two LCA tools were developed

in North America for transportation applications: GHGenius and GREET. While GHGenius is a complete LCA package for various fuels and vehicle technologies, GREET (the Greenhouse gases, Regulated Emissions, and Energy use in Transportation model developed by Argonne National Laboratories) is mainly a fuel cycle model for different vehicle technologies. Recently, the developers of GREET also released its vehicle cycle model for light duty vehicles; however, the vehicle cycle model for heavy duty trucks is yet to be released [27, 28]. Therefore, in the present study, GHGenius is selected to conduct a complete comparative LCA study of CNG and diesel powered RCVs. The following subsections provide a brief overview of the GHGenius model and summarize the key assumptions pertaining to the present study.

GHGenius

GHGenius is a Canadian life cycle modeling tool for transportation fuels and vehicle technologies developed and maintained by Natural Resources Canada. The model complies with ISO 14040 and 14044 standards for LCA. It is a derivative of the life cycle emissions model (LEM) developed by Delucchi [29]. It has more than 200 vehicle, fuel, and feedstock combinations and predicts life cycle energy use and emissions for the past, present, and future years using historical data or correlations for changes in energy and process parameters. Additionally, it has economic tools incorporated to estimate cost effectiveness of different fuel and vehicle combinations [30, 31].

Some of the salient features of GHGenius compared to other LCA tools include the availability of a comprehensive Canadian database in the model, inclusive of all the steps of the life cycle in the model starting from raw material acquisition to end-use, and generation of much more detailed output from model simulations. In addition to light duty vehicles, provisions are available for heavy duty vehicles suitable for the RCV analysis. Hence, GHGenius is selected as a primary life cycle analysis tool for this study. The main methodology and assumptions used by GHGenius in the context of the present study are explained in the following subsections [31–33].

GHG Emissions and Energy Projections

In GHGenius, GHG emissions are calculated in terms of grams of pollutant per kilometre of vehicle travel. GHG emissions can then be displayed in terms of grams of equivalent CO_2 emissions using the Intergovernmental Panel on Climate Change 100 year global warming potential (GWP) [34]. The IPCC GWP is a relative measure of how much heat each gas contributes to climate change as compared to the standard carbon dioxide. The GWP for methane and nitrous oxide is 21 and 310 respectively for 100 years. The greenhouse gases included in the calculation of grams of CO_2-equivalent emissions are carbon dioxide (CO_2), methane (CH_4), and nitrous

oxide (N_2O). The sum of grams of CO_2-equivalent at various points of the life cycle is then added to the grams of CO_2 released during the operation of the vehicle. In the end, results are provided for the total life cycle GHG emissions from the usage and production of the vehicle and fuel.

GHGenius estimates the total energy used during the life cycle in joules per kilometre driven. It aggregates data on the energy use during the fuel distribution, fuel production, feedstock recovery, and transmission stages. As for the fuel use stage, it uses parameters such as the vehicular efficiencies in litres per kilometre driven for each fuel (diesel and natural gas in our study) and the heating values in megajoules per litre to calculate the amount of energy required for operation. The sum total of energy used by each vehicle can then be displayed in total joules per kilometre traveled.

On the topic of emission standards and data, the standards for light duty passenger cars are normalized by vehicle driving distance, g/km; however, for heavy duty vehicles, standards are defined by engine energy output, g/kWh. Emission certification is performed by running stand-alone engines on an engine dynamometer. The emission standards adopted in 2000 in the USA and Canada are similar to those in Europe known as the "Euro Norm" for heavy duty vehicles [8]. Euro Norm ranges from "Euro I Norm" to "Euro VI Norm" which is the strictest. In the present case, both CNG and diesel engines are evaluated under Euro V Norm emission standards [35, 36]. Using data on these engines and diesel emissions made available by Environmental Canada, GHGenius utilizes MOBILE6.2C to obtain adjustment factors to convert the certified levels to real world conditions. In addition, GHGenius allows user input of fuel consumption and percentage of highway driving for further flexibility. The GHGenius Manual Volume 1 in Section 47.17 and 47.23 details the MOBILE6.2C data on heavy duty diesel and CNG engines, respectively [37, 38].

GHG Impact Assessment

GHGenius can assess the cost effectiveness of alternative fuels and vehicles compared to conventional fuels and vehicles. This calculation is particularly useful in comparing vehicle related GHG reduction strategies with fuel related strategies on a common basis. The function to calculate cost effectiveness integrates the relative costs of alternative fuels and vehicles with the estimated GHG emissions. As a result, the cost effectiveness function estimates costs in terms of GHG emissions reduction ($ per unit CO_2-equivalent) achieved by an alternative fuel/vehicle technology using the following equation:

$$E_C = \frac{\left(\sum_{y=1}^{n} \frac{P}{F}\left\{VKT_y\left(\left(F_a FCR_a\right) - \left(F_c FCR_c\right)\right)\right\}\right) + \left(P_a - P_c\right) + \frac{P}{A} OM + C_o}{VKT_t\left(GHG_c - GHG_a\right)} \tag{41.1}$$

where, $\sum_{y=1}^{n}$ is the sum of the annual terms for the economic lifetime of n years at an assumed discount rate; $\frac{P}{F}$ and $\frac{P}{A}$ are factors to calculate the present value of a future cost and the present value of a series of future constant annual costs assuming an economic lifetime n and a discount rate i; F_a and F_c are the consumer fuel prices of the alternative and conventional fuel per litre excluding taxes ($/L); FCR_a and FCR_c are the fuel consumption ratings of the vehicle using alternative and conventional fuel (L/km); VKT_y and VKT_t are vehicle kilometres traveled per year and total traveled over the economic lifetime of the vehicle (km); P_a and P_c are the purchase prices of the alternative and conventional vehicles excluding taxes; GHG_a and GHG_c are life cycle greenhouse gas emission factors for the alternative and conventional fuels (CO_2-equivalent g/km); OM are the constant annual non-fuel operating and maintenance costs over the life ($); and C_0 are other costs ($).

The result of the cost effectiveness function can be a positive or negative number. If the cost effectiveness calculation results in a positive number, the alternative fuel (CNG in the present study) powered vehicle costs more than the conventional fuel (diesel) powered vehicle per unit GHG emissions reduced. Alternatively, if negative cost effectiveness results from the model, the alternative fuel powered vehicle has a lower life cycle cost per unit GHG emissions reduced compared to the conventional fuel powered vehicle. Further details on the cost effectiveness parameters are available in [33].

Goal, Scope, and Assumptions

The scope of the present LCA is consistent with the scope of GHGenius including all parts of the fuel cycle: feedstock production and recovery, leaks and flaring, feedstock transport, fuel production, fuel storage and distribution, and fuel dispensing at retail level. In its scope it includes on the vehicle cycle: vehicle operation, vehicle assembly and transport, and emissions from materials manufacturing. The functional metrics used to describe the results are (1) energy used (per km of travel), (2) greenhouse gases emitted (in CO_2-equivalent per km), (3) combustive emissions generated (per km), and (4) cost effectiveness as described above. These four functional metrics are utilized to indicate the anticipated categorical impact of the different vehicles on (1) resource use (energy efficiency), (2) climate change, (3) air quality, and (4) economic viability, respectively. Other LCA impact categories such as ozone depletion, acidification, eutrophication, human health, and land use are beyond the scope of this comparative LCA. The contributions of each phase of the complete fuel and vehicle life cycles will be analyzed. The system boundaries and assumptions are:

- The secondary energy and environmental effects are not quantified. For instance, energy use and associated emissions during the production of crude oil

Table 41.1 RCV data collected from the City of Surrey and its contractor

In-use city fuel consumption (L/h)	12
Tare mass (kg)	15,000
Maximum mass (kg)	23,300
Stops per day	1400
Range requirement (km)	100
Average daily distance travelled(km)	54
Maximum operational lifetime (years)	5
Capital cost of diesel RCV ($CDN)	220,000
Capital cost of CNG RCV ($CDN)	260,000

and natural gas are quantified, but the energy used and emissions produced in the manufacturing of equipment required for oil and gas exploration and extraction and the material used in the construction of a refinery are not quantified.

- A penalty of 0.35 % on fuel economy is applied for every 1 % increase in vehicle mass for the CNG RCV [39].
- The lifetime of the diesel and CNG RCVs is assumed to be 5 years based on data obtained by the City of Surrey and the non-fuel costs of operation and maintenance are assumed to be equal.
- Emissions associated with the materials manufacture and assembly are a function of the mass of the vehicle and spectrum of materials in the vehicle.
- The fraction of city driving is assumed to be one, implying no highway driving for RCVs.
- The crude oil price is assumed to be equivalent to the average crude oil price of April 2011 ($ 122 US per 0.159 m^3 crude oil) plus a distribution and retail cost of $ 0.055 CDN per litre (currency exchange rate 1.04 $US/$CDN) [40, 41]. Diesel and CNG fuel prices as of April 2011 are used ($ 0.93 CDN per litre and $ 4 CDN per GJ, respectively).

41.4 Data Collection

A significant portion of any life cycle analysis requires collection of reliable data. The quality of data has a profound impact on the quality of the results predicted or estimated by an LCA tool. GHGenius has access to data for Canada from reports produced by Statistics Canada, Natural Resources Canada (NRCan), Environment Canada, and the National Energy Board for the production of power, crude oil, refined petroleum products, and natural gas. Additionally, GHGenius allows the user to provide data for certain steps in the process to provide the highest degree of flexibility possible in the model without compromising the quality of the results predicted.

In the present study, considerable time is invested to collect reliable real-time data for the different stages of the life cycle of diesel and CNG RCVs. The data collected from the City and its contractor on the RCVs is tabulated in Table 41.1. The in-use city diesel fuel consumption is calculated based on the reported RCV

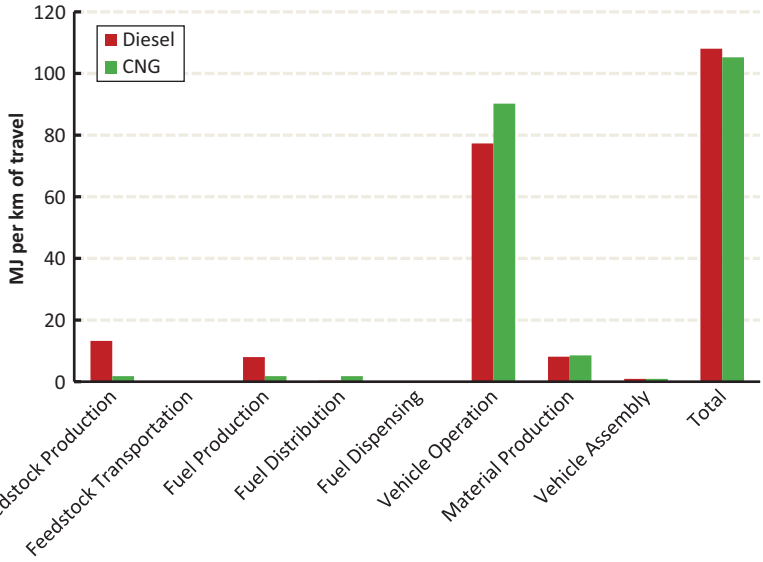

Fig. 41.2 Estimated energy use during different life cycle stages of diesel and CNG RCVs

operational time of 9 h per day, making 1400 stops along the way, and requiring 12 L/h. The average RCV speed is estimated to 6 km/h, including the idling time at each stop, based on the average daily driving distance of 54 km. The relatively demanding and energy-intensive duty cycle in the present case features more frequent stops than in other reports [42], underlining the importance of collecting data specifically for each project directly from the source. The lifetime of an RCV in terms of distance traveled is calculated based on the daily trip distance multiplied by the days used per year for the projected lifetime of 5 years.

The CNG consumption is calculated on a relative basis to the diesel engine. The energy efficiency of the Cummins Westport CNG engines modeled in GHGenius is 86–87% of that of a diesel engine. Consequently, an additional approximate 16% of fuel energy is required to achieve the same distance with a CNG motor as with a diesel motor.

41.5 Results and Discussion

The GHGenius LCA modeling framework combined with the assumptions listed above and the data collected from the City of Surrey is employed to estimate the energy use, emissions, and cost of the diesel and compressed natural gas (CNG) powered heavy duty refuse collection vehicles (RCVs) over the complete life cycle of their production and operation. Figure 41.2 shows the estimated energy use of diesel and CNG powered RCVs. The x-axis represents the various stages of the

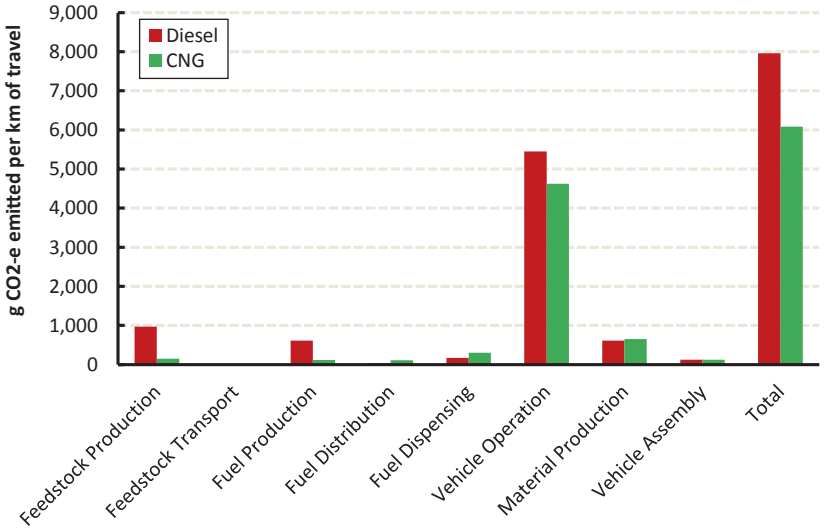

Fig. 41.3 Equivalent CO_2 emissions during different life cycle stages of diesel and CNG RCVs

fuel and vehicle cycles, while the y-axis represents energy use as a function of distance traveled by an RCV for its total lifespan of 90,000 km. Interestingly, it is found that the energy use during fuel/vehicle operation of a CNG powered RCV is approximately 17% higher than the diesel powered RCV for the fixed lifetime of both RCVs. This result is comparable to [20] in the cases where primary energy demand is higher for CNG. This increase is due to the low energy density of CNG fuel compared to diesel fuel. However, there is negligible difference (about 3%) in the total energy use during the complete life cycle of both RCVs, implying no net gain in energy use by replacing a diesel powered RCV with a CNG powered RCV. This is because of higher energy use during crude oil extraction (feedstock recovery stage) and fractional distillation (fuel production stage) of diesel fuel compared to the CNG fuel, which in turn offsets the lower energy use of diesel powered RCV during fuel/vehicle use stage. However, the main advantage of CNG based vehicles is the reduction of overall GHG and particulate emissions.

The equivalent CO_2 emissions during different life cycle stages of diesel and CNG powered RCVs is shown in Fig. 41.3. It can be seen that the total life cycle GHG emissions emitted by a CNG powered RCV are about 24% less than for the diesel powered RCV; in other words, replacing a diesel powered RCV with a CNG powered RCV results in a significant reduction of GHG emissions. Also, it can be seen that the vehicle operation stage (fuel use) is the single largest contributor to GHG emissions for both RCVs, accounting for 70–75% of total GHG emissions. CNG is essentially methane, which comprises the highest hydrogen-to-carbon ratio of all hydrocarbons. Diesel, in contrast, comprises a mix of predominantly carbon-rich compounds as a result of fractional distillation of petroleum. When the two are combusted in an internal combustion engine, methane produces less carbon

dioxide, carbon monoxide, and other carbon-containing emissions. Moreover, the GHG emissions in the diesel fuel cycle (feedstock and fuel production) are significantly higher than those of CNG due to the relatively energy-intensive petroleum extraction and fractional distillation processes known to release significantly more emissions than the extraction and purification of natural gas. Notably, GHG emissions from refuse collection fleets can be reduced significantly by CNG RCV implementation.

In a previously published study, showed 70 grams per mile (44 g/km, or 2.5%) reduction of CO_2-equivalent life cycle emissions for the case of a CNG transit bus versus a diesel bus operated in Beijing, China [21]. Further analysis shows that at the vehicle operation stage, CO_2-equivalent emissions increased (48 g/km, or 3.6%) due to high CH_4 emissions by the CNG bus. However, upstream emissions of diesel fuel were higher. In the presently employed version of GHGenius, when comparing RCVs, a much higher (1880 g/km, or 24%) reduction is obtained over the full life cycle. Notably, the total GHG emissions of the CNG and diesel trucks in our study (6080 and 7960 g/km) are approximately 3.6x and 4.6x higher than those of the CNG and diesel buses in Karman's work (1700 and 1740 g/km), as a result of the higher fuel consumption for RCVs. The higher relative GHG emissions reductions in our study is mainly from the vehicle operation phase where recent advances in CNG engine technology are expected to improve the environmental value proposition of such vehicles. Moreover, methane emissions from CNG vehicle operation are less significant in the present version of GHGenius. The type of diesel fuel considered for the comparison also influences the results. Due to the energy-intensive sulfur removal process, the ultra-low sulfur diesel (ULSD) used in our work requires significantly more energy upstream than the low-sulfur diesel (LSD) used by [21]. The present work compares ULSD to CNG because this has become a standard in the USA and Canada. In addition, several other parameters may contribute to the difference, such as percentage of city and highway driving, vehicle range, and fuel economy, all of which were recently revised in the simulation of GHGenius version 3.19a employed here.

In a similar study on CNG and diesel buses in Australia, Ally and Pryor showed 25% higher overall GHG emissions for CNG than diesel [20]. In a subsequent report, a breakdown of the LCA shows unusually high emissions from the CNG vehicle operation phase compared to other studies [43]. This can be attributed to two different technologies for heavy duty CNG engine operation. The Australia buses are Mercedes-Benz CNG OC 500LE with CNG engines that are run under lean-burn combustion conditions. The buses available in Canada from which GHGenius utilizes its data are based on Cummins Westport ISL-G CNG engines, which burn at stoichiometric conditions. Pelkmans et al. showed that CNG engines that run at stoichiometric conditions produce less carbon dioxide than those run at lean-burn conditions [44]. Overall, as indicated by our results, recent improvements in CNG internal combustion engines enable significant GHG emission reductions compared to incumbent diesel and gasoline engines. Based on conditions for the City of Surrey, selection of a new CNG RCV over a diesel RCV is estimated to reduce GHG emissions by 169 t (metric tons) during its 5-year lifetime. It is noteworthy

that the net impact per vehicle is more significant for RCVs than for most other municipal fleet vehicles due to their high energy requirements.

Figure 41.4 shows criteria air contaminant (CAC) emissions during different stages of the diesel and CNG powered RCV life cycle. CAC emissions include carbon monoxide (CO), nitrogen oxides (NO_x), volatile organic compounds (VOC), sulphur oxides (SO_x), and particulate matter (PM). As pointed out earlier, CAC emissions are posing significant environmental, health, and economic risks for our communities and citizens. For instance, according to Canadian Medical Association (CMA) predictions, there were 306 premature deaths in British Columbia due to CAC pollution in 2008, and related economic damages of over $ 900,000 CDN [45]. It can be seen from Fig. 41.4 that replacing a diesel powered RCV with a CNG powered RCV results in a considerable reduction in total CAC emissions, ranging from 21 % reduction in VOC emissions (Fig. 41.4c) to 44 % reduction in NO_x and SO_x emissions (Fig. 41.4b, 41.4d). While SO_x and PM are mainly reduced at the feedstock and fuel production stages, the CO, NO_x, VOC, and PM emissions are significantly reduced at the fuel dispensing and vehicle operation stages where a positive net impact on local, urban air quality can be achieved. At the location of vehicle deployment, a 54 % reduction in overall CAC emissions can be obtained. This calculation by GHGenius includes recent advances of diesel exhaust treatment via particulate traps to control PM emissions [46]. Thus, replacing diesel with CNG powered RCVs would lead to cleaner air in urban areas.

The cost effectiveness calculations integrate information on the relative costs of the CNG fuel and vehicle with GHG emissions results produced by GHGenius to arrive at the cost of GHG emission reductions. The calculations include the lifetime vehicle and fuel costs, including the purchase price, operation, and maintenance. In Fig. 41.5, a negative value is present indicating a net cost savings of the alternative CNG powered RCV relative to the conventional diesel powered RCV. In other words, CNG powered RCV saves $ 650 and 330 CDN per tonne of CO_2 reduced with and without consideration of diesel tax, respectively. It is noteworthy that both the federal and provincial governments in Canada offer significant tax incentives for using CNG in commercial vehicles. For instance, the Harmonized Service Tax (HST) in British Columbia is fully refunded for users of CNG vehicles [47]. However, the entire tax on diesel fuel is estimated to $ 0.30 CDN per litre($ 0.04 and 0.26 CDN per litre federal and provincial excise tax, respectively) [48]. Therefore, both scenarios (with and without diesel tax) are considered in the cost effectiveness calculations. Figure 41.6 shows the lifetime fuel cost of diesel and CNG fuels based on a 5 year lifetime, excluding tax. It can be seen that significant fuel cost savings on the order of $ 100,000 CDN per vehicle can be achieved by switching to CNG. Besides the tax incentives on using natural gas from governments, the operational cost reduction on fuel offers the consumers and organizations the best incentive to switch to CNG powered vehicles. Additionally, diesel engines with modern emission limits tend to wear sooner than engines built several decades ago. At the same time, the durability of CNG based engines has improved significantly as a result of the increasing interest in these engines and the resulting development activities worldwide [49]. As a consequence, the robustness of CNG engines is approximately

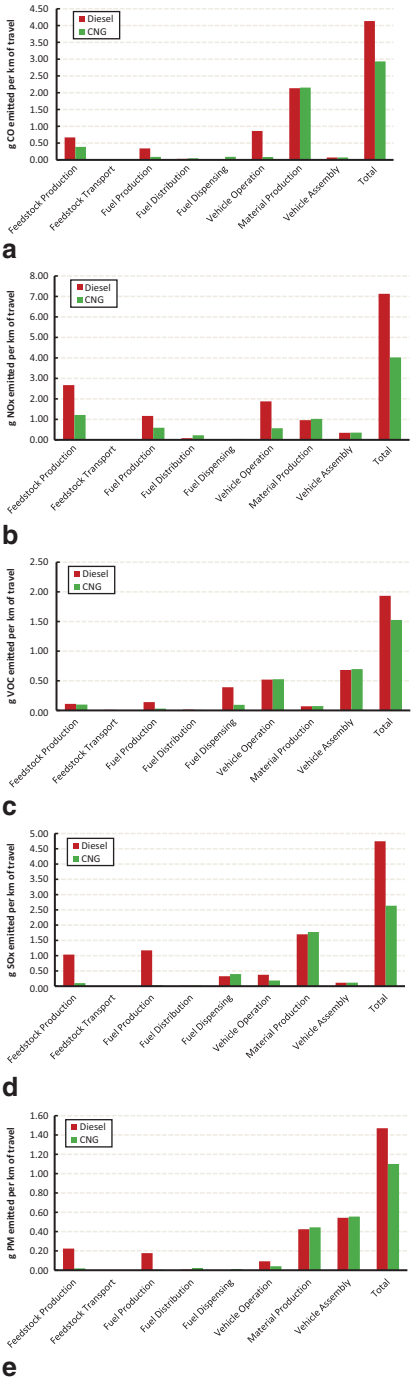

Fig. 41.4 Criteria air contaminant (CAC) emissions during different life cycle stages of diesel and CNG RCVs: **a** CO, **b** NO_x, **c** VOC, **d** SO_x, and **e** PM

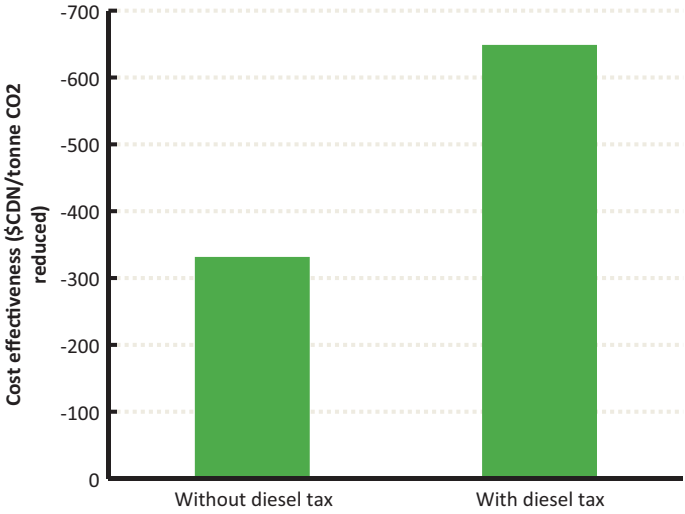

Fig. 41.5 Cost effectiveness of replacing a diesel powered RCV with a CNG powered RCV

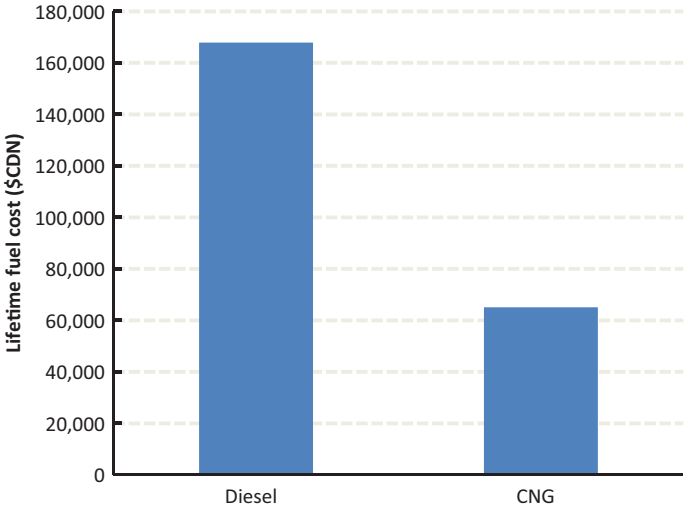

Fig. 41.6 Lifetime fuel cost of diesel and CNG powered RCVs

on par with diesel engines. CNG combustion based RCV pilot projects at various municipalities worldwide have shown that this can be achieved [50].

The GHGenius results mentioned above realistically demonstrate the benefits of using CNG RCVs versus conventional diesel RCVs. While the predictions for emissions and cost savings are expected to be reliable and consistent with other studies

done elsewhere, one may consider the uncertainties in conducting life cycle analysis mainly originating from the accuracy and appropriateness of the data used as input. GHGenius is sensitive to the quality of the data it uses. The models are kept updated by identifying trends and avoiding outliers as well as incorporating data from Statistics Canada with each release of new information. Specific data utilized in GHGenius is regionalized across Canada and in some cases generalized for North America. GHGenius developers acknowledge gaps in data, e.g., N_2O emissions related to feedstock production. Sensitivity analysis of new modules incorporated into the model are usually performed with respect to other LCA models such as GREET. GHGenius also includes a Monte Carlo simulator that can evaluate the sensitivity of different input parameters simultaneously. With respect to the crude oil price used (April 2011), major price variations in both diesel and CNG fuels are known to occur and the cost effectiveness of CNG RCVs is expected to vary accordingly. In the present case of comparing CNG with diesel fuel, GHGenius provides a reliable platform to carry out the LCA.

Conclusions

A comparative life cycle analysis of diesel and CNG powered RCVs is conducted based on conditions relevant to a Canadian city. The study uses the most reliable and real-time operational data obtained from a municipal organization, providing services to Surrey, the second largest city in British Columbia, Canada. Using GHGenius, a life cycle analysis tool, the potential impact of replacing a modern diesel powered RCV with a new CNG powered RCV is assessed from various stages in their life cycle. It is found that there is no net energy savings in replacing a diesel powered RCV with a CNG powered RCV. However, CNG powered RCVs result in significant GHG reductions compared to diesel powered RCVs, estimated to 24% based on the full life cycle. The CNG vehicle therefore has lower impact on climate change than the diesel vehicle. Moreover, CNG powered RCVs produce considerably less CAC emissions, which in turn enables locally improved urban air quality with a related potential reduction in health care costs associated with diseases caused by harmful CAC emissions. Additionally, the CNG powered RCV is found to be cost effective in terms of tonnes of CO_2 reduced. Thus, CNG powered RCVs not only reduce the GHG and CAC emissions, but also provide significant cost savings over their lifetime.

Alternative propulsion systems exist. Powered by a fuel cell (FC), a hybrid combination of a fuel cell and batteries (HFC), or batteries alone (EV), electric motors may be used for propulsion. The fuel for the fuel cells, hydrogen, can be produced from natural gas, electrolysis, crude oil, or as a by-product of chlorine production. Batteries in a HFC are recharged by the fuel cell. However, the batteries in an EV are charged from the grid. In addition to these more developed technologies, hydraulic hybrid has come into the market recently, for example by Autocar's introduction of the E3 hydraulic hybrid RCV [51]. Data for LCA analysis of these technologies

in an RCV are not readily available. In the framework of the LCA presented here, these technologies (FC, HFC, EV, and other hybrid concepts) can potentially be favorable to the CNG vehicle if the environmental impact of the production of the alternative drivetrain capacity does not offset the benefits of the more efficient vehicle usage. However, with respect to the goal of zero emissions, the FC, HFC, and EV are seen as the most likely long-term options for operation of refuse collection fleets. FC and HFC vehicles for this class of heavy duty vehicle with a usage pattern that involves a large number of stops per day and fast acceleration following each stop still have to be developed to be operational with the same reliability as diesel vehicles today. It can be predicted that EVs represent the favorable option in terms of both emissions during operation and overall emissions during the vehicle life cycle. However, battery-powered RCVs face the same challenges, but the first prototypes of battery powered RCVs are being tested. The results of this work suggest that using CNG powered RCVs can improve the operational economy and reduce overall emissions with an immediate impact. Combining hybrid battery electric and the CNG internal combustion engine technologies in an RCV is another interesting option that will be investigated in our future work.

Acknowledgements The authors gratefully acknowledge funding from the Pacific Institute for Climate Solutions (PICS) and the City of Surrey. Furthermore, City of Surrey employees Curtis Rhodes and Gord Simmonds and Emterra employees Ed Walsh and Nevil Davies are acknowledged for their aid and helpful discussions. The authors also acknowledge Don O'Connor, $(S\&T)^2$ Consultants Inc., for technical support related to the use of GHGenius.

References

1. Transport Canada- Policy, Research and Statistics (2006) Report on transportation in Canada, 2006. http://www.tc.gc.ca/eng/policy/anre-menu.htm. Accessed 3 April 2012
2. Jang C, Lee J (2005) Experimental investigation of the effects of various factors on the emission characteristics of low-emission natural gas vehicles. Proc Inst Mech Eng 219:825–832
3. Zhang CH, Xie YL, Wang FS, Ma ZY, Qi DH, Qiu ZW (2011) Emission comparison of light-duty in-use flexible-fuel vehicles fuelled with gasoline and compressed natural gas based on the ECE 15 driving cycle. Proc Inst Mech Eng 225:90–98
4. Aslam MU, Masjuki HH, Kalam MA, Abdesselam H, Mahlia TMI, Amalina MA (2006) An experimental investigation of CNG as an alternative fuel for a retrofitted gasoline vehicle. Fuel 85:717–724
5. Jayaratne ER, Ristovski ZD, Meyer N, Morawska L (2009) Particle and gaseous emissions from compressed natural gas and ultra-low sulphur diesel-fuelled buses at four steady engine loads. Sci Total Environ 407:2845–2852
6. Kathuria V (2004) Impact of CNG on vehicular pollution in Delhi: a note. Trans Res Part D 9:409–417
7. Ravindra K, Wauters E, Tyagi SK, Mor S, Van Grieken R (2006) Assessment of air quality after the implementation of compressed natural gas (CNG) as fuel in public transport in Delhi. India Environ Monit Assess 115(1–3):405–417
8. Nylund NO, Erkkila K, Lappi M, Ikonen M (2012) Transit bus emission study: comparison of emissions from diesel and natural gas buses, 2004. http://www.vtt.fi/inf/pdf/jurelinkit/VTT-Nylund.pdf. Accessed 26 July 2012

9. Collela WG, Jacobson MZ, Golden DM (2005) Switching to a U.S. hydrogen fuel cell vehicle fleet: the resultant change in emissions, energy use, and greenhouse gases. J Power Sources 150:150–181
10. Granovskii M, Dincer I, Rosen MA (2006) Life cycle assessment of hydrogen fuel cell and gasoline vehicles. Int J Hydrogen Energy 31:337–352
11. MacLean HL, Lave LB (2003) Life cycle assessment of automobile/fuel options. Environ Sci Tech 37:5445–5452
12. Pehnt M (2001) Life-cycle assessment of fuel cell stacks. Int J Hydrogen Energy 26:91–101
13. Pehnt M (2003) Assessing future energy and transport systems: the case of fuel cells Part I: methodological aspects. Int J Life Cycle Assess 8:283–289
14. Zamel N, Li X (2006) Life cycle analysis of vehicles powered by a fuel cell and by internal combustion engine for Canada. J Power Sources 155:297–310
15. Cuenca R, Formento J, Gaines L, Marr B, Santini D, Wang M (2012) Total energy cycle assessment of electric and conventional vehicles: an energy and environmental analysis. Argonne National Laboratory, ANL/ES/RP-9638, 1998. http://dx.doi.org/10.2172/627823. Accessed 25 July 2012
16. Row J, Raynolds M, Woloshyniuk G (2002) Life cycle value assessment (LCVA) of fuel supply options for fuel cell vehicles in Canada. Pembina Institute. http://infohouse.p2ric.org/ref/37/36488.pdf. Accessed 3 April 2012
17. Spath PL, Mann MK (2012) Life cycle assessment of hydrogen production via natural gas steam reforming. NREL (National Renewable Energy Laboratory) Technical Report, NREL/TP-570-27637, 2001. http://www-pord.ucsd.edu/~sgille/mae124_s06/27637.pdf. Accessed 3 April 2012
18. Weiss MA, Heywood JB, Drake EM, Schafer A, AuYeung FF (2012) On the road in 2020. Report MIT EL 00-003, Energy Laboratory, Massachusetts Institute of Technology, Cambridge, MA, 2000. http://web.mit.edu/mitei/lfee/programs/archive/publications/2000-03-rp.pdf. Accessed 22 April 2012
19. Weiss MA, Heywood JB, Schafer A, Natarajan VK (2003) Comparative assessment of fuel cell cars. Report MIT LFEE 2003-001, Laboratory of Energy and the Environment, Massachusetts Institute of Technology, Cambridge, MA, 2003. http://web.mit.edu/mitei/lfee/programs/archive/publications/2003-01-rp.pdf. Accessed 22 April 2012
20. Ally J, Pryor J (2007) Life-cycle assessment of diesel, natural gas and hydrogen fuel cell bus transportation systems. J Power Sources 170:401–411
21. Karman D (2006) Life-cycle analysis of GHG emissions for CNG and diesel buses in Beijing. EIC Climate Change Technology, 2006 IEEE, pp 1–6
22. Kliucininkas L, Matulevicius J, Martuzevicius D (2012) The life cycle assessment of alternative fuel chains for urban buses and trolleybuses. J Env Manage 99:98–103
23. Ryan F, Caulfield B (2010) Examining the benefits of using bio-CNG in urban bus operations. Trans Res Part D 15:362–365
24. Sorensen B (2004) Total life-cycle assessment of PEM fuel cell car. Proc. of the 15th World Hydrogen Energy Conf., Yokohoma, Japan, 2004. http://ptech.pcd.go.th/p2/userfiles/consult/5/LCA%209.pdf. Accessed 22 April 2012
25. Scientific Applications International Corporation (SAIC) (2012) Life cycle assessment: principles and practice, U.S. Environmental Protection Agency, 2006. nepis.epa.gov/Exe/ZyPURL.cgi?Dockey=P1000L86.txt. Accessed 3 April 2012
26. U.S. Environmental Protection Agency (2011) http://www.epa.gov/nrmrl/lcaccess/. Accessed 9 May 2011
27. Wang M, Wu Y, Elgowainy A (2012) Operating manual for GREET: version 1.7. Center for Transportation Research, Energy Systems Division, Argonne National Laboratory, November 2005, Revised in February 2007. http://greet.es.anl.gov/publication-ycrv02rp. Accessed 3 April 2012
28. Wang M (2012) Overview of GREET Model Development at Argonne. Center for Transportation Research, Argonne National Laboratory, GREET User Workshop, Argonne, IL, June 25–26, 2007. http://www.transportation.anl.gov/pdfs/TA/419.pdf. Accessed 3 April 2012

29. Delucchi MA (2012) Lifecycle energy use, greenhouse gas emissions, and air pollution from the use of transportation fuels and electricity. Institute of Transportation Studies, University of California, Davis, 1998. http://www.its.ucdavis.edu/publications/2002/UCD-ITS-RR-02-02.pdf. Accessed 2 April 2012
30. Natural Resources Canada's GHGenius Model 3.19a (2005) http://www.ghgenius.ca/downloads.php. Accessed 9 May 2011
31. (S&T)^2 Consultants Inc. (2006) Introduction to lifecycle analysis and GHGenius, Natural Resources Canada, January 24, 2006. http://www.ghgenius.ca/reports/IntroductionToGHGenius.pdf. Accessed 22 April 2012
32. O'Connor D (2010) Life cycle assessment and GHGenius, GHGenius Workshop, December http://www.ghgenius.ca/reports/GHGeniusDec2010Workshop.pdf. Accessed 3 April 2012
33. (S&T)^2 Consultants Inc. (2005) Documentation for Natural Resources Canada's GHGenius model 3.0, September 15, 2005. http://www.ghgenius.ca/reports/DocumentationforExcelGHGenius.pdf. Accessed 22 April 2012
34. Intergovernmental Panel on Climate Change (IPCC) (2007) IPCC Fourth Assessment Report: Climate Change, 2007. http://www.ipcc.ch/publications_and_data/ar4/wg1/en/ch2s2-10-2.html. Accessed 30 March 2012
35. Cummins Westport (2012) Description of Cummins Westport Products http://cumminsengines.com/assets/pdf/4103878.pdf. Accessed 27 Aug 2012
36. U.S. EPA-Environmental Protection Agency (2012) http://www.epa.gov/otaq/regs/hd-hwy/ncp/420r12004.pdf. Accessed 13 Sept 2012
37. (S&T)^2 Consultants Inc. (2012) GHGENIUS MODEL 4.01, VOLUME 1, MODEL BACKGROUND AND STRUCTURE, 2012. http://www.ghgenius.ca/reports/GHGeniusManualVol1.pdf. Accessed 27 July 2012
38. (S&T)^2 Consultants Inc. (2012) GHGENIUS MODEL 4.01, VOLUME 2, DATA AND DATA SOURCES, 2012. http://www.ghgenius.ca/reports/GHGeniusManualVol2.pdf. Accessed 26 July 2012
39. Cheah L, Evans C, Bandivadekar A, Heywood J (2012) Factor of two: halving the fuel consumption of new US automobiles by 2035, Appendix E, 2007. http://hdl.handle.net/1721.1/42918. Accessed 22 April 2012
40. Bloomberg Energy & Oil Prices (2011) www.bloomberg.com/energy/2011/04/19. Accessed 21 April 2011
41. Fogt R (2011) Online Conversion. www.onlineconversion.com. Accessed 21 April 2011
42. Blohm T, Anderson S Ricardo R (2004) Hybrid refuse truck study. Virtual product Design Conference, Huntington Beach, CA, 2004. http://www.kerstech.com/PDFs/Hybrid%20Refuse%20Truck%20Feasibility%20Study.pdf. Accessed 22 April 2012
43. Ally J (2012) Life Cycle Assessment (LCA) of the Hydrogen Fuel Cell, Natural Gas, and Diesel Bus Transportation Systems in Western Australia, 2008. http://www.crest-au.com/docs/alt_LCAreport.pdf. Accessed 30 July 2012
44. Pelkmans L, De Keukeleere D, Lenaers G (2001) Emissions and fuel consumption of natural gas powered city buses versus diesel buses in real-city traffic. Urban Transport VII, Transaction: The Built Environment, 2001, 52
45. Geduld J (2012) No breathing Room: National Illness Costs of Air Pollution, Summary Report. Canadian Medical Association, 2008. www.cma.ca. Accessed 27 July 2012
46. Natural Resources Canada (2008) Energy Use Data Handbook. http://oee.nrcan.gc.ca/publications/statistics/handbook10/pdf/handbook10.pdf. Accessed 22 April 2012
47. Government of British Columbia (2011) Harmonized State Tax & Natural Gas. British Columbia Website. http://www.hstinbc.ca/building_the_economy/industry_specific/natural_gas. Accessed 25 April 2011
48. Department of Finance Canada (2011) Backgrounder on Oil and Gas Prices, Taxes and Consumers. Dept. of Finance, 2006. http://www.fin.gc.ca/toc/2006/gas_tax-eng.asp. Accessed 25 April 2011
49. Cummins Westport (2012) Description of Cummins Westport Products. http://www.cumminswestport.com/products/islg.php. Accessed 2 April 2012

50. Gordon D, Burdelski J, Cannon JS (2003) Greening garbage trucks: new technologies for cleaner air. INFORM, Inc., New York, 2003. http://www.informinc.org/reportpdfs/st/GreeningGarbageTrucks.pdf. Accessed 4 April 2012
51. Loveday E (2012) Autocar launches E3 hydraulic hybrid garbage truck, 2011. http://green.autoblog.com/2011/05/12/autocar-launches-e3-hydraulic-hybrid-garbage-truck/. Accessed 6 Aug 2012
52. Pax S (2011) Lifecycle analysis: moving from black-box to transparency. Environmental Leader, 2011. http://www.environmentalleader.com/2011/04/12/lifecycle-analysis-moving-from-black-box-to-transparency/. Accessed 12 April 2011

Chapter 42
Anaerobic Treatment and Biogas Production of Raw Leachate from Fresh Market Waste Composting by an Anaerobic Hybrid Reactor

Chinnapong Wangnai, Pratin Kullavanijaya and Somboon Pitayarangsarit

Abstract Raw leachate discharged from composting process is considered as a promising feedstock for biogas production with high potential for renewable bioenergy recovery. In order to prevent environmental concerns relating to the composting disposal, anaerobic digestion could be a good practice for treatment and utilizing the wastewater derived from fresh market waste composting facilities. The aim of this study was to examine an anaerobic hybrid reactor performance on organic content reduction and biogas production from the raw leachate. The preliminary study included the examinations on leachate characteristics and biochemical methane potential (BMP) assay. In the pilot study, a 200-liter anaerobic hybrid reactor with a combination of an upflow sludge bed reactor and a filter reactor was setup and was operated semi-continuously with the raw leachate collected from a fresh market waste composter as feedstock. The prior test results showed that the leachate contains high COD and BOD as 34,500 and 14,775 mg L^{-1}, respectively. An extensive data on BMP tests indicated that the leachate could be anaerobically digested and generated biogas with the conversion rate as 0.48 L g^{-1} of COD removed of fed leachate. Average methane content in the biogas was approximately 60 %. Similar results were achieved in an observation of the anaerobic hybrid reactor performance for 100 days. The reactor was operated efficiently with hydraulic retention time higher than 10 days and maximum organic loading rate as 8 g COD L^{-1} day^{-1}. However, H_2S content in the biogas was higher than 5000 ppm which required further H_2S clean-up before utilizing biogas as an alternative fuel.

C. Wangnai (✉) · P. Kullavanijaya
Pilot Plant Development and Training Institute, King Mongkut's University of Technology Thonburi (Bang Khun Thian), 49 Soi Thian Thale 25, Tha Kham, Bang Khun Thian, Bangkok 10150 Thailand
e-mail: chinnapong@pdti.kmutt.ac.th

S. Pitayarangsarit
TCM Environment Co., Ltd., 1 Moo 10, Soi Watmahawong, Samrong, Phrapradaeng, Samutprakarn 10130 Thailand

I. Dincer et al. (eds.), *Progress in Sustainable Energy Technologies: Generating Renewable Energy,* DOI 10.1007/978-3-319-07896-0_42,

Keywords fresh market waste · composting leachate · anaerobic hybrid reactor · biogas

42.1 Introduction

In Thailand, fresh market waste is considered as a major component in municipal solid wastes (more than 60 %) refer to the latest survey report of the Pollution Control Department [1]. As the waste contains mainly discarded or rotten fruits and vegetables with high organic content, it is normally collected and disposed in landfill sites and needs a lot of budget for proper operation and maintenance. Composting the fresh market waste with an application of rotary drum reactor is an alternative waste management to gain benefit from this waste with an outcome as fertilizer or soil conditioner [2]. A biomass digesting system designed and built for municipal solid wastes composting by TCM Environment limited company is one of the high-rate rotary drum composter. The TCM biomass digester is operated with appropriate conditions for aerobic and thermophilic biodegradation in order to accelerate conversion of the fresh market waste to compost as 24 hour-batch process. This could significantly decrease organic solid waste loading to the waste disposal facilities. However, a large amount of raw leachate discharged from the composting process may cause environmental concerns regarding its high strength organic and inorganic compositions. For a good practice in waste management, this raw leachate required further treatment to meet the standards of discharged wastewater.

Anaerobic digestion of organic matter has been studied and applied as a practical method for treatment of biodegradable waste and to produce biogas which can be used as a combusting fuel for decades. The design and performance of the anaerobic digestion reactors are relied on various feedstock characteristics and operating conditions. High-rate anaerobic reactors; namely, anaerobic filter reactor (AF), anaerobic fixed-film reactor (AFF) [3,4] and upflow anaerobic sludge blanket (UASB) [5] have been studied and developed for treatment and energy recovery from high strength wastewater from agro-industry. Although the efficiency of these reactors is impressive, the troublesome of each reactor is found differently. Supporting material installation, construction cost, and clogging are the main drawbacks for AF and AFF reactors. The UASB reactor has been reported to be unsuitable for high particulate-containing wastewater which could inhibit granular sludge formation and the sludge methanogenic activity. Furthermore, high flow rate of wastewater feeding could continuously cause active sludge washout [6]. To solve these problems, anaerobic hybrid reactors (AHR) with a combination of key features of different anaerobic reactor systems into a single reactor have been studied in treating various industrial wastewaters, municipal

waste and leachate [7–12]. Regarding various fresh market waste characteristics which can be observed from country to country, optimum operating conditions for composting systems are relatively different. Therefore pilot-scale studies for treating raw leachate are required to obtain suitable design criteria. The object of this study was to examine a pilot-scale AHR performance on organic matter reduction and biogas production from the raw leachate discharged from an accelerated rotary drum composter.

42.2 Material and Methods

Characterization of Raw Leachate In order to investigate consistency of the raw leachate characteristics, discharged liquid samples from six batch-operations of the TCM biomass digester were collected and analyzed for basic parameters required for biogas plant operation as values of pH, chemical oxygen demands (COD), total alkalinity (ALK), and total volatile fatty acids (VFA) according to Standard Methods [13] and modified titration method [14]. Furthermore, composite leachate from the prior characteristics test was analyzed for other parameters relating to anaerobic digestion performance, namely biological oxygen demands (BOD), total Kjeldahl nitrogen (TKN), total phosphorus and solids content.

Biochemical Methane Potential Assay Studies on biochemical methane potential (BMP) were carried out by applying serum vial technique modified from previous works [15–17]. Sludge from a full-scale biogas plant treating palm oil mill effluent was used as test inoculum. The test was performed under controlled and reproducible conditions in 120-mL glass bottles with working volume of 65 mL. Each bottle was filled with the inoculum and substrate at a ratio of 1:2 and was purged with gas mixture of 70 % N_2 and 30 %CO_2 before sealing. The triplicate controlled and test serum vials were stored in an incubator at 37 °C. Biogas production was measured daily by method of water displacement [18]. The methane accumulated in the headspace of the closed vials was measured by thermal conductivity gas chromatography (Shimazu 14B) with Porapak-N column. Cumulative methane yields derived from neglecting background gas from controlled vials were plotted against incubating time in order to estimate biochemical methane potential of the raw leachate.

Pilot-Scale Anaerobic Hybrid Reactor Study This study was carried out with a pilot scale stainless steel anaerobic digester with a total volume of 200 L. The reactor was designed to run as a plug-flow system. 750 pieces of plastic media "bio-ball" with approximately 90 % void volume were packed inside the upper part of the reactor-packed bed zone, while the bottom part was set as a sludge bed zone. Figure 42.1 shows schematic flow sheet of the pilot-scale AHR used in this study.

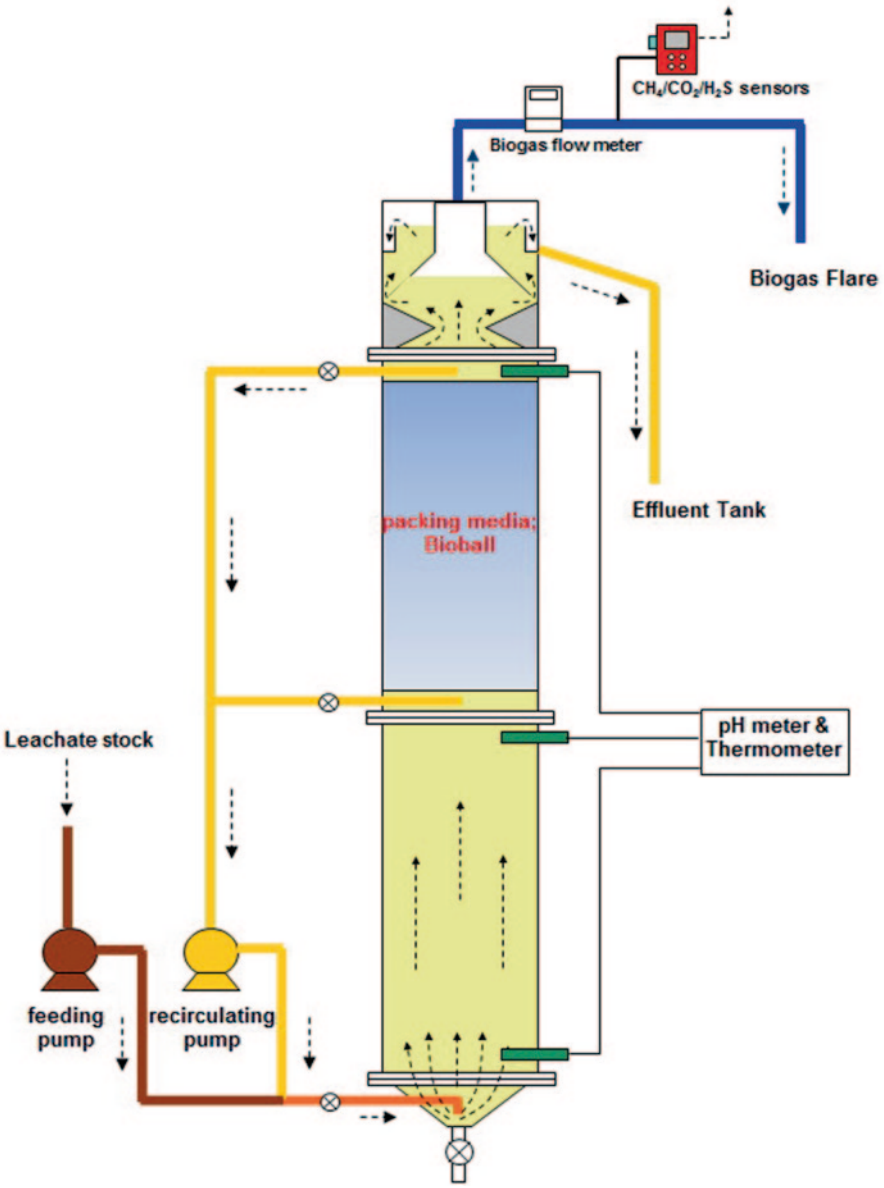

Fig. 42.1 Schematic diagram of the anaerobic hybrid reactor

42.3 Results and Discussion

Study on Characterization of Raw Leachate and Feedstock Data for preliminary study on raw leachate discharged from the high-rate rotary drum digester daily fed with fresh market waste indicate that the basic parameters were unlikely stable

Table 42.1 Basic characteristics of raw leachate (unit in mg L^{-1}; except pH)

Sample #	pH	ALK	VFA	Total COD	Soluble COD	% Soluble COD
I	4.37	1103	6096	39,890	19,087	48
II	4.20	1152	8607	40,673	26,927	66
III	4.87	3662	9876	38,420	22,120	58
IV	5.42	3490	6536	28,687	16,880	59
V	5.81	6267	10,445	39,007	25,187	65
VI	5.93	3732	5970	29,397	13,357	45
Mean	5.10	3234	7922	36,012	20,593	57
SD	0.73	1927	1986	5458	5137	9

Table 42.2 Characteristics of composite leachate used as feedstock

Parameter	Unit	Value
pH	–	5.06
ALK	mg L^{-1}	3250
VFA	mg L^{-1}	7500
Total COD	mg L^{-1}	34,500
Soluble COD	mg L^{-1}	23,190
BOD	mg L^{-1}	14,775
TKN	mg L^{-1}	1870
TP	mg L^{-1}	975
Sodium	mg L^{-1}	730
Potassium	mg L^{-1}	2830
Chloride	mg L^{-1}	670
Sulfate	mg L^{-1}	940
TS	mg L^{-1}	25,750
SS	mg L^{-1}	10,940
VS	mg L^{-1}	17,730
VSS	mg L^{-1}	9344
VS/TS	%	69

(Table 42.1). All leachate samples were acidic and contained high organic content with total COD concentrations varied between 28,687–40,673 mg L^{-1}. Hence, the mean soluble COD was 20,593 mg L^{-1} and was 57% of the total COD so that this waste is promising to use as feedstock for biogas production. However, alkalinity values were significantly variable with standard deviation as high as 61.4%. It could be explained that the fluctuation was related to variation on the mixture of meat and fish scraps and discarded fruits and vegetables loaded to the composter.

Therefore, composite leachate from 6-consecutive batchs composting was prepared to use as this research feedstock. The physical properties of the composite wastewater as determined are listed in Table 42.2. In comparison with other studies [19, 20], the COD concentration of this compost leachate was significantly higher than the COD contents of leachate from garden waste composting facilities and leachate from market refuse; 34,500, 7200, and 1152 mg L^{-1}, respectively. On the other hand, COD composition of the leachate from municipal compost manufacturing plant [12] was higher as 80,000 mg L^{-1}. Regarding nutrient require-

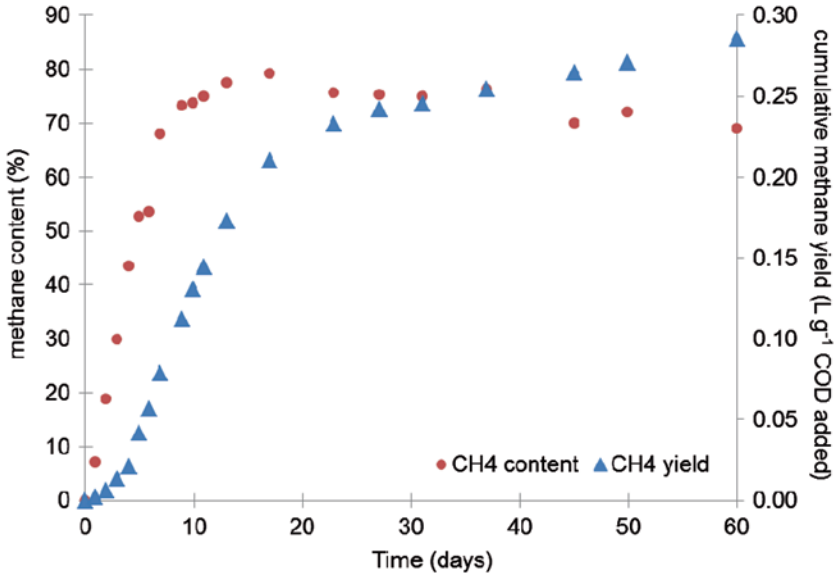

Fig. 42.2 Cumulative methane yields from the BMP test of composite leachate

ments for anaerobic digestion, general COD:N ratio of 20:1 and 50:1 were reported [21, 22], while the composite leachate in this study contained COD:N value of 18:1.

Study on Biochemical Methane Potential of Raw Leachate The biochemical methane potential is presented in term of methane yield. The results of cumulative methane yield and methane content are presented in Fig. 42.2. Data from the BMP assay show that the composite leachate was converted to biogas in drastically high rate during the first 20 days of incubation with the highest methane composition of 80%. The rate of biogas production was gradually decreased subsequently whilst percentages of methane content in the biogas produced was varied in the range of 70–75. The maximum cumulative methane yield was determined at approximately 0.29 L g^{-1} COD added after 60 days of the observation. Compared with the high-strength pressed off leachate from the organic fraction of municipal solid waste [23], the cumulative methane yield for the fresh market composting leachate was slightly higher. Nevertheless, the methane production of the pressed liquor reached its final state within 2 weeks.

Study on The Pilot-Scale Anaerobic Hybrid Reactor Performance The pilot-scale AHR was operated with semi-continuous feeding mode for 100 days. Various HRTs were applied to the AHR with relatively changes in OLRs, presented in Fig. 42.3. The relative variations of pH, buffering capacity and accumulating VFA are showed in Fig. 42.4. The reactor pH slightly varied during the study. On the contrary, alkalinity and VFA were significantly increased when the operating HRT was shorter than 10 days. In this experiment, the operating alkalinity varied from

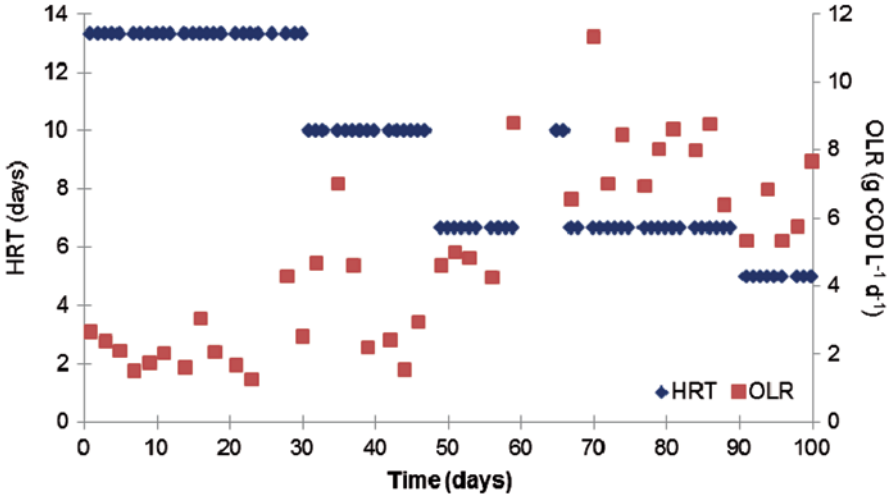

Fig. 42.3 Variations of OLR and HRT during the pilot-scale operation

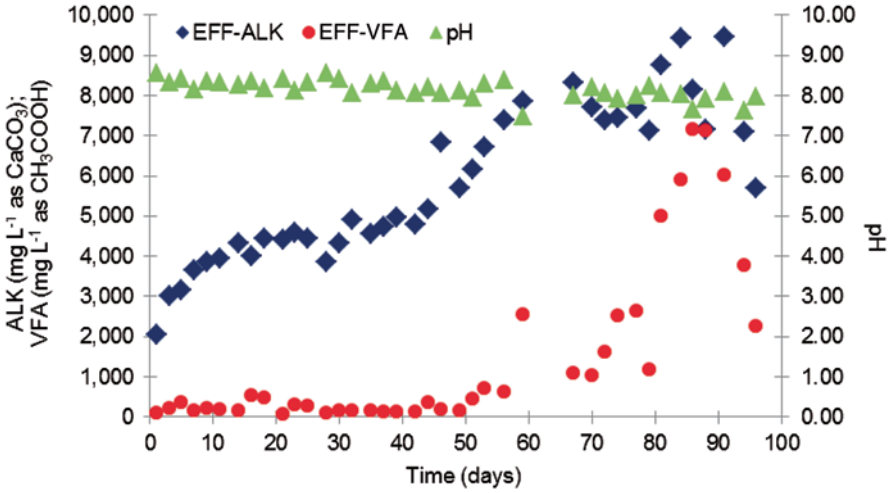

Fig. 42.4 Variations of pH, ALK and VFA during the pilot-scale operation

2050–9460 mg L^{-1} as $CaCO_3$, which was higher than general value ranging from 1000–5000 mg L^{-1} as $CaCO_3$ in a steady anaerobic digester. It could be explained that the increasing alkalinity was relied on the high alkalinity of the inlet leachate. On the other hand, the dramatic increment of the VFA was possibly affected by the operating OLR greater than 6 g COD L^{-1} day^{-1}. This incident could be clarified as an effect of COD overloading, while increasing VFA was not being satisfactory

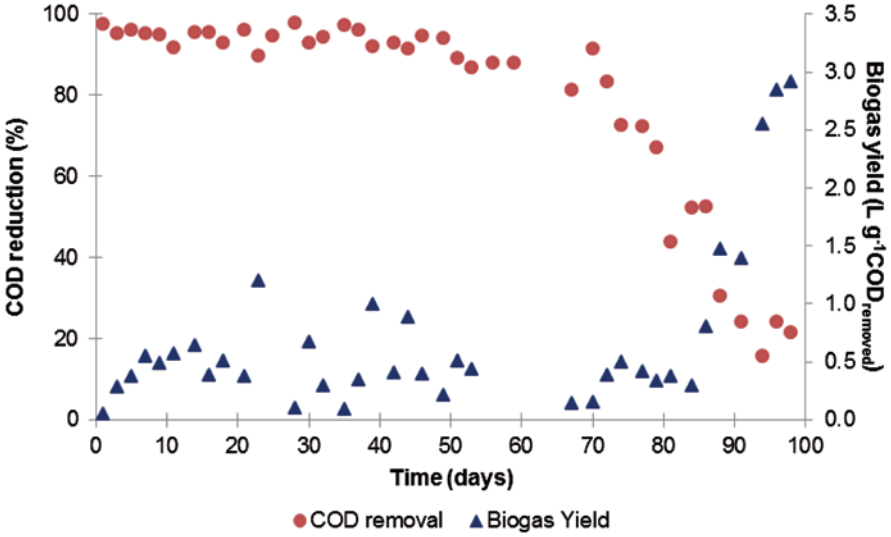

Fig. 42.5 Variations of COD removal efficiency and biogas yield during the pilot-scale operation

compensated by an increased in alkalinity. The accumulated VFA concentration as higher than 7000 mg L^{-1} caused significant drop of alkalinity during day 86 and 100, when the reactor ultimately failed.

The performance of the AHR reactor was monitored in terms of organic removal efficiency and biogas yield as shown in Fig. 42.5. Similar to the results from the other work [12], the average COD removal performance of the pilot-scale reactor was approximately 95%. However, the COD reduction decreased sharply when OLR increased from 6.5 to 8.0 g COD L^{-1} day^{-1} and HRT was deducted from 10 to 7 days. Furthermore, the removal efficiency drastically declined lower than 40% when the reactor was fed at 5 days HRT. It is strongly believed that COD loading shock and washout of microorganisms were the cause of this significant drop of the organic removal performance.

The reactor performance can also be discussed in term of biogas production over COD removed. The biogas yield was independent on OLR and HRT at the initial stage. The mean value of biogas yield during day 1–80 was approximately 0.44 L g^{-1} COD removed. Nevertheless, the biogas yield revealed an unclearly upward trend when the AHR operated with the lowest HRT as 5 days during day 85–100. It was hypothesized that the higher flow rate of the influent according to short HRT operation increased mixing level of organic particulates, which normally settled at the bottom part of the reactor, with both suspended-growth and attached growth microorganisms. Therefore, the unbalance of inlet COD and COD converted to biogas existed and the overrated biogas yields were calculated.

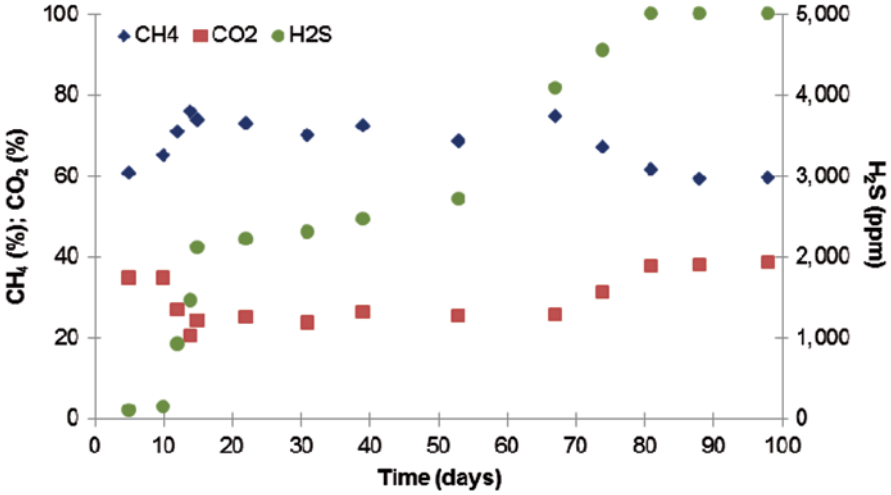

Fig. 42.6 Variations of biogas composition during the pilot-scale operation

In addition, the shorten HRT operation affected compositions of the biogas generated during this pilot-scale study (Fig. 42.6.). The percentage of methane gas decreased gradually from over 70 to 60. Meanwhile, hydrogen sulfide (H_2S) content stepwise increased from 100 to 2500 ppm when the HRT was decreased to 10 days. The H_2S level as high as 5000 ppm could be found when the reactor experienced unsteady-state with operating HRT of 5 days. The high concentration of VFA and COD accumulated in the reactor during the last stage of this study could be toxic to methanogenic microbes. In contrast, the excess VFA and COD were a favor for sulfate-reducing bacteria (SRB) in competing with methane forming microbes for carbon source. Consequently, the predominant SRB generated by-product gas with high content of H_2S.

Conclusions

The preliminary characteristics test results showed that the raw leachate from fresh market composting by the high-rate rotary drum digester contains high COD and BOD as 34,500 and 14,775 mg L^{-1}, respectively. Further study on biochemical methane potential of the composite leachate indicated that it could be anaerobically digested and generated biogas with the conversion rate as 0.48 L g^{-1} of COD removed of inlet leachate. The mean methane content in the biogas was approximately 60 %. The maximum cumulative methane yield was determined at approximately 0.29 L g^{-1} COD added after 60 days of the study. Similar results were achieved in

the investigation of the pilot-scale anaerobic hybrid reactor performance for 100 days. It could be concluded that the reactor was operated efficiently with hydraulic retention time longer than 10 days and maximum organic loading rate of 8 g COD L^{-1} day^{-1}. However, H_2S content in the biogas was higher than 5000 ppm which required further H_2S clean-up before utilizing biogas as an alternative fuel. These results suggested that the anaerobic hybrid reactor could be applied as a practical leachate treatment and biogas production system.

Nomenclature

AHR	anaerobic hybrid reactor
ALK	total alkalinity (mg L^{-1} as $CaCO_3$)
BMP	biochemical methane potential (L g^{-1} COD added)
BOD	biological oxygen demands (mg L^{-1})
COD	chemical oxygen demands (mg L^{-1})
CH_4	methane
CO_2	carbon dioxide
H_2S	hydrogen sulfide
HRT	hydraulic retention time (days)
OLR	organic loading rate (g COD L^{-1} day^{-1})
TKN	total Kjeldahl nitrogen (mg L^{-1})
TP	total phosphorus (mg L^{-1})
TS	total solids (mg L^{-1})
SS	suspended solids (mg L^{-1})
SD	standard deviation
VFA	volatile fatty acids (mg L^{-1} as CH_3COOH)
VS	volatile solids (mg L^{-1})
VSS	volatile suspended solids (mg L^{-1})

Acknowledgement This work was accomplished with the financial and technical support from National Science and Technology Development Agency (NSTDA) via industrial technology assistance program (iTAP) and TCM Environment Co., Ltd.

References

1. PCD. Municipal solid wastes survey report (2009) http://www.pcd.go.th/info_serv/waste_wastethai48_53.html. Accessed 2 Feb 2012
2. Zhu B, Zhang R, Gikas P, Rapport J, Jenkins B, Li X (2010) Biogas production from municipal solid wastes using an integrated rotary drum and anaerobic-phased solids digester system. Bioresour Technol 101(16):6374–6380
3. Tanticharoen M, Bhumiratana S (1995) Waste treatment plants. Narosa Publishing House, New Delhi
4. Daryapurkar RA, Kaul SN (1991) Experience with full-scale anaerobic fixed film reactor. J Environ Sci Health (Part A Environ Sci Eng Toxicol) 26(3):317–333
5. Lettinga G (1995) Anaerobic digestion and wastewater treatment systems. Antonie van Leeuwenhoek. 67:3–28 (Int J Gen Mol Microbiol)

6. Lettinga G, Velsen Van AFM, Hobma S, Zeeuw De W, Klapwijk A (1980) Use of the upflow sludge blanket reactor concept for biological wastewater treatment, especially for anaerobic treatment. Biotechnol Bioeng 22:699–734
7. Lo KV, Liao PH, Gao YC (1994) Anaerobic treatment of swine wastewater using hybrid UASB reactors. Bioresour Technol 47:153–157
8. Borja R, Banks CJ, Khalfaoui B, Martin A (1996) Performance evaluation of an anaerobic hybrid digester treating palm oil mill effluent. J Environ Sci Health (Part A) 31(6):1379–1393
9. Surarak B, Wangnai C, Chaiprasert P, Tanticharoen M (1998) Performance of an anaerobic hybrid reactor combining a filter and a sludge bed. Proceedings for the 10th Annual general meeting of Thai society for biotechnology for a self-sufficient economy, 25–27 November 1998, Sol Twin Towers Hotel, Bangkok, Thailand: 94–102
10. Najafpour GD, Zinatizadeh AAL, Mohamed AR, Isa MH, Nasrollahzadeh H (2006) High-rate anaerobic digestion of palm oil mill effluent in an upflow anaerobic sludge-fixed film bioreactor. Process Biochem 41:370–379
11. Mokhtarani N, Bayatfard A, Mokhtarani B (2012) Full scale performance of compost's leachate treatment by biological anaerobic reactors. Waste Manage Res 30(5):524–529
12. Rajabi S, Vafajoo L (2012) Investigating the treatability of a compost leachate in a hybrid anaerobic reactor: an experimental study. World Acad Sci Eng Technol 61:1175–1177
13 APHA, AWWA, WPCF (2012) Standard methods for the examination of water and wastewater, 22nd edn. American Water Works Association
14. Anderson GK, Yang G (1992) Determination of bicarbonate and total volatile acid concentration in anaerobic digesters using a simple titration. Water Environ Res 6(6):53–59
15. Owen W, Stuckey D, Healy J Jr, Young L, McCarty P (1979) Bioassay for monitoring biochemical methane potential and anaerobic toxicity. Water Res 13:485–492
16. Smolders GJF, van der Meij J, van Loosdrecht MCM, Heijnen JJ (1994) Model of the anaerobic metabolism of the biological phosphorus removal process: stoichiometry and pH influence. Biotechnol Bioeng 43(6):461–470
17. Moller HB, Sommer SG, Ahring BK (2004) Methane productivity of manure, straw and solid fractions of manure. Biomass Bioenerg 26:485–495
18. Esposito G, Frunzo L, Liotta F, Panico A, Pirozzi F (2012) Bio-methane potential tests to measure the biogas production from the digestion and co-digestion of complex organic substrates. The Open Environ Eng J 5:1–8
19. Mukherjee SN, Kumar S (2007) Leachate from market refuse and biomethanation study. Environ Monit Assess 135:49–53
20. Tyrrel SF, Seymour I, Harris JA (2008) Bioremediation of leachate from a green waste composting facility using waste-derived filter media. Bioresour Technol 99:7657–7664
21. Gray NF (1989) Biology of waste water treatment. Oxford University Press, New York
22. Gerardi MH (2003) The microbiology of anaerobic digesters. Wiley, New York
23. Nayono SE, Winter J, Gallert C (2010) Anaerobic digestion of pressed off leachate from the organic fraction of municipal solid waste. Waste Manage 30:1828–1833

Chapter 43
A First Experimental Survey on the Urban Heat Island in Padua (Italy)

Marco Noro, Renato Lazzarin and Filippo Busato

Abstract The Urban Heat Island effect concerns the higher air temperature in urban environment with respect to the rural one. This phenomenon is well known by hundreds of years, but it has been experimentally studied only in the last few decades and in large metropolis. Very different possibilities concerning the measurements are possible (fixed ground based meteorological stations, "transept" measurements, satellite-based infrared sensors), with different difficult and quality of the data measured.

The paper reports on the experimental results obtained by a research group of the University of Padua (Italy) in 2010 and 2011 springs-summers in Padua city. The main thermo-hygrometric variables (dry-bulb temperature, relative humidity, global solar radiation) have been measured along some different paths fixed in advance. The paths have been selected in order to cross different zones of the fabric of the city: urban, sub-urban and rural. The high number of "transepts" implemented in different time bands during the day and after the sunset allows to characterize the phenomenon in different meteorological conditions. The results indicate a presence of the UHI in urban zones of the city up to 5 °C.

This work is intended to be developed during 2012 by the research group of the Department of Management and Engineering of the University of Padua, in cooperation with Co.Ri.La. (Venice) in the European Project "UHI – Development and application of mitigation and adaptation strategies and measures for counteracting the global Urban Heat Islands phenomenon" (3CE292P3). The paper reports the analysis of data recorded by two fixed meteorological stations (in the centre and out of Padua) during the period 1994–2011, that show some increase in the UHI effect

M. Noro (✉) · R. Lazzarin
Department of Management and Engineering, University of Padua,
stradella San Nicola, 336100, Vicenza, Italy
e-mail: marco.noro@unipd.it

R. Lazzarin
e-mail: renato@gest.unipd.it

F. Busato
3F Engineering, via del Giglio 40/A, 35133 Padova, Vicenza, Italy
e-mail: filippo.busato@gmail.com

I. Dincer et al. (eds.), *Progress in Sustainable Energy Technologies: Generating Renewable Energy,* DOI 10.1007/978-3-319-07896-0_43,

during this period. Some guidelines concerning the choice of the experimental measurements settings are supplied by the Authors. The future measurements will be used also to calculate some outdoor comfort index and to verify how the latter will change modifying some characteristic parameters (buildings placement, thermal properties, trees presence, etc.) by a simulation model.

Keywords Urban Heat Island · Padua · Outdoor thermal comfort · Experimental measurements

43.1 Introduction

Urban environment is characterized by some typical features: high density of population and buildings, high energy consumption and shortage of green areas. A main consequence is the Urban Heat Island phenomenon (UHI) that is the systematic higher air temperature of urban environment with respect to rural one. The main outcomes are [8]:

- a deterioration of the summer outdoor climate conditions;
- an increase of energy consumptions;
- an increase of polluting emissions.

There is a lot of literature on the UHI effect: some authors [2–7, 14, 21] studied the urban canyons, while Montavez [12] evaluated the effect of thermal properties of the building materials. Other authors studied the impact of absence of green areas in the cities, substituted by waterproof surfaces that limit the evapotranspiration effect [23, 6]. Also the effect of the minor albedo of building surfaces has been evaluated by Akbari [1].

Urban Heat Island effect results from a lot of causes that interact each other, in function of the particular situation of every city. Briefly, the main factors effecting the phenomenon are:

- the structure of urban canyons that effect the infrared radiation heat exchange capacity of the urban surfaces toward the sky;
- the albedo of the urban surfaces that increase the heat absorbed by buildings, pavements, roads and roofs;
- the anthropogenic heat caused by heat engine exhausted and chillers condensation heat;
- the greenhouse effect that is amplified by the higher pollutants concentration in urban atmosphere;
- the shortage of green areas that increases the sensible heat exchange with air and decreases the evaporative cooling effect due to evapotranspiration of trees and grass.

UHI has been studied worldwide (Athens, London, Berlin, Vancouver, Montreal, New York, Tokyo, Hong Kong) since sixties of the past century [22]. In Italy, some studies have been conducted recently in Bologna [24], Milan [3, 20], Florence

Table 43.1 Main instrumentation used during 2010 and 2011 campaigns of measurement by the research group of the Department of Environmental Agronomy and Crop Productions of the University of Padua

Instrument	Model	Characteristics
Thermo-hygrometer	Vaisala HMP -45C	Range: T: (−40÷60 °C) RH: (0÷100 %) Accuracy: T: ±0,2 °C RH: ±2 % (0÷90 %) ±3 % (90÷100 %)
Satellite receiver	Garmin 16-HVS GPS	Accuracy: 15 m in mod. standard GPS 3–5 m in mod. differential GPS
Pyranometer	Kipp & Zonen CM5	–
Datalogger	Campbell Scientific CR3000	–

[17–19]. In the Veneto Region, in the North East of Italy, the University of Padua is conducting a study of the Padua city's UHI since 2010. In the next two paragraphs it will be described the main results of the 2010 and 2011 campaigns of measurement; following paragraph will describe the first activities done and the ones programmed in the next future in charged to the Authors' research group.

43.2 Experimental Measures During 2010

The research group of the Department of Environmental Agronomy and Crop Productions of the University of Padua has done two experimental campaigns of measurements during 2010 [5] and 2011 [16] in order to collect data to evaluate the spatial variability of the UHI in the city of Padua. In 2010 the chosen transept (18 km long) started and finished in Legnaro (rural zone outside Padua), crossing the city centre. The main variables measured by a mobile station mounted on a car (Table 43.1) have been dry bulb air temperature and relative humidity, solar global radiation on the horizontal, wind speed. The measurements have been conducted both during day and night, preferably with stationary weather conditions (no wind, clear sky), in July and August 2010. Data acquisition has been done with the following procedure:

- acquisition (once a second) of the geographical coordinates by the GPS;
- distance calculus (once a second); if ≥100 m save the data, otherwise continue to reach the threshold;
- calculus and saving of the half path geographical coordinates, to which measurements are referred;
- calculus of the average and standard deviation on 100 m for the main variables measured: temperature (°C), relative humidity and global radiation (W m^{-2});
- calculus of the average and standard deviation of water vapor partial pressure (kPa) and absolute humidity (g_v m^{-3}).

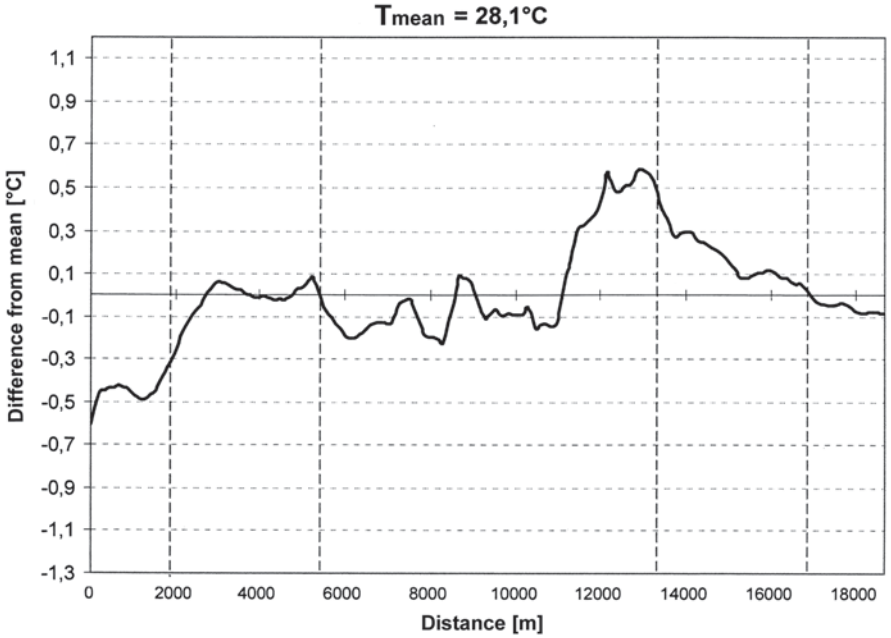

Fig. 43.1 Mean deviations for the air temperature; vertical lines depict the boundary between rural (first and last sectors), sub-urban (second and forth sectors) and urban (central) environment (07/07/2010 daily transept)

Data have been acquired during 9 days, some of which in double sessions: one daily session (during 12am−1.30pm in order to minimize boundary conditions variation such as solar radiation) and one nightly session (between 3 and 5 h after the sunset in order to investigate the phenomenon during its potentially maximum magnitude [15]). Also the discomfort index HUMIDEX [9] has been calculated in order to investigate the combined effect of high air temperature T (°C) and humidity (water vapor partial pressure e, hPa):

$$H = T + \frac{5}{9} \cdot (e - 10) \tag{43.1}$$

The main results of the 2010 campaign of measurements are reported:

- data logged during daily sessions are more affected by boundary conditions (mainly solar radiation and wind velocity) than nightly ones, so data understanding is more difficult;
- generally speaking, daily sessions did not point out any relevant heat island effect in Padua. It is noteworthy the higher air temperature of sub-urban zones with respect to rural ones, but without the typical "bell-shaped" form. In nearly all the graphs there is a local minimum after 8000 m, corresponding to a shaded road with the presence of some water and green areas (the Riviere). Figure 43.1

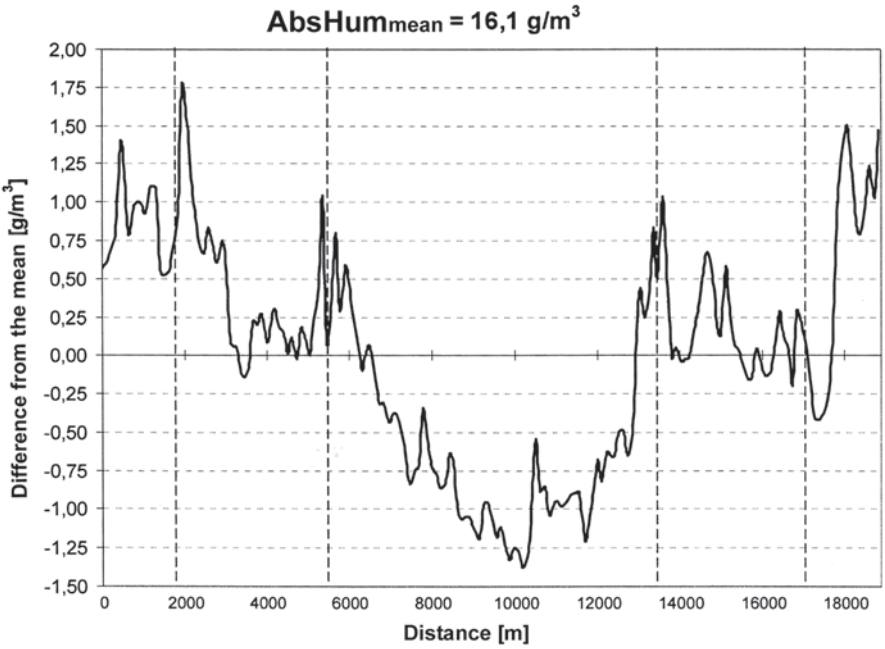

Fig. 43.2 Absolute humidity variation during the 07/13/2010 daily transept

is an example of this behavior. The humidity ratio graphs do not depend on the temperature unlike the relative humidity ones; they show some particular situation along the transept (presence of water and/or green areas), but it is evident the presence of a gradient directed from the countryside to the city centre (Fig. 43.2). So differences in humidity ratio between rural and urban zones are evident during the day because of the higher evapotranspiration effect of the formers.

Nightly transepts show a more regular and accurate behavior of the variables thanks to more stable atmospheric conditions (lower convective currents, wind velocity and shading). 2 °C urban heat island effect is depicted by Fig. 43.3. Absolute humidity variation during the transept is less evident than during the day; it is always caused by higher evapotranspiration effect in rural zones. This effect is present also locally inside the urban zone, for example between 10th and 11th kilometer, Fig. 43.4; this is viale Manzoni that is very near to the town walls, surrounded by green areas: there is a local minimum of air temperature and a local maximum of humidity. HUMIDEX index variation during the nightly transept shows "evident discomfort"[1] values (Fig. 43.5);

[1] $H<27$: no discomfort; $27 \leq H < 30$ noticeable discomfort; $30 \leq H < 40$ evident discomfort; $40 \leq H < 55$ dangerous discomfort; $H \geq 55$ heat stroke probable.

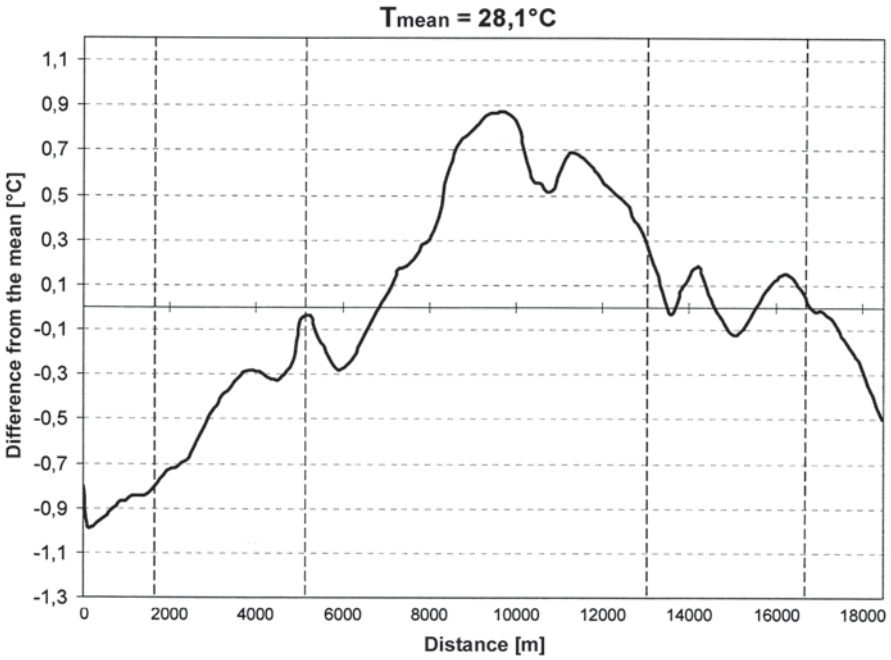

Fig. 43.3 Mean deviations for the air temperature during of the 07/15/2010 nightly transept

- Authors of the study reports the particular behavior of Prato della Valle, in the centre of the city: this is an area with a lot of water flows and green zones, so it would be expected a decrease in nightly temperature while there is a maximum (around 10,000 m in Fig. 43.5). The cause is that the transept pass along the perimeter and not inside the square. In this case the spatial influence of the green is very limited and it is suggested a deeper investigation on this zone.

43.3 Experimental Measures During 2011

The second campaign of measurements by the research group of the Department of Environmental Agronomy and Crop Productions has been done with the same instrumentation (Table 43.1) but with a different transept [16]. In this case it has been chosen a longer path (50 km, always starting and ending in the countryside) in order to cross the six homogeneous zones of the 2005 Padua town-planning scheme:

- A: zone with historical and artistic buildings;
- B: zone partially or totally built, different from A;

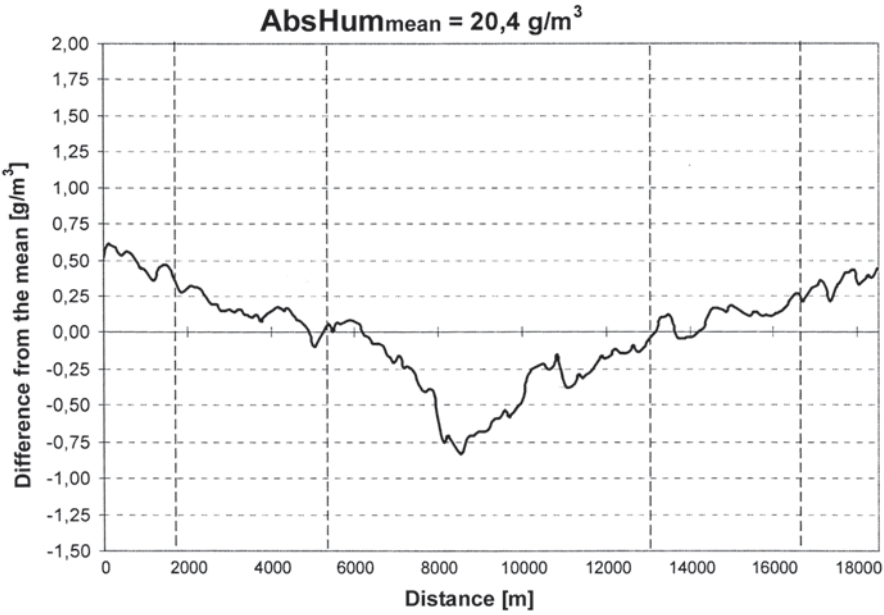

Fig. 43.4 Absolute humidity variation during the 07/15/2010 nightly transept

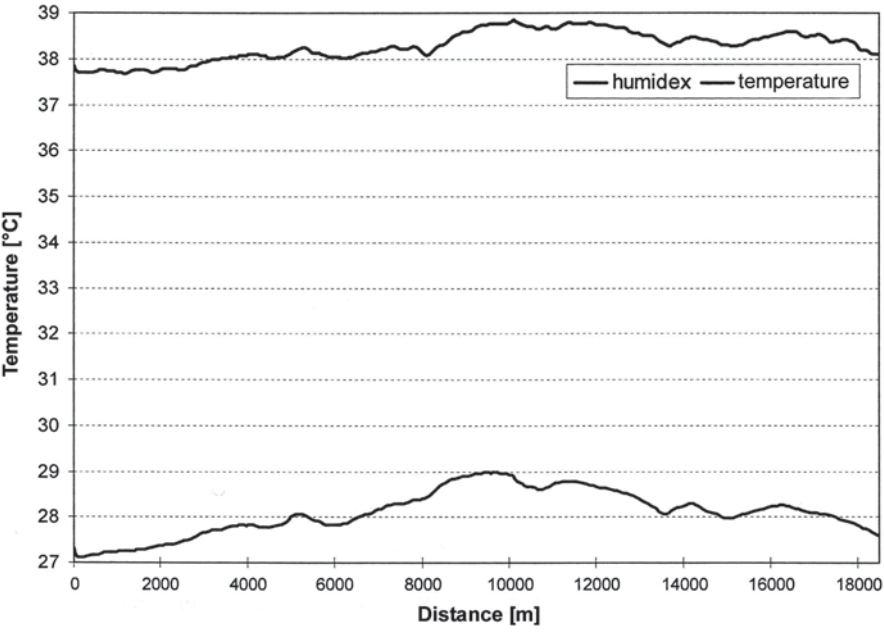

Fig. 43.5 HUMIDEX index (*top curve*) and d.b. temperature (*bottom curve*) during the 07/15/2010 nightly transept

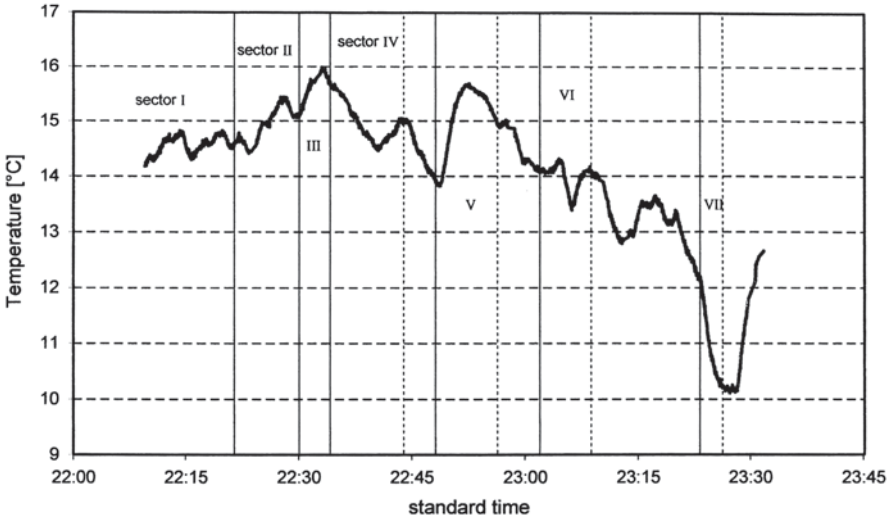

Fig. 43.6 Temperature variation during the 04/05/2011 nightly transept

- C: zone for new buildings or partially built but with lower size and house density than B;
- D: zone for new industrial or similar buildings;
- E: zone for agricultural purpose;
- F: zone for common interest buildings.

Each of the 13 transepts effectuated during April-May 2011 period has been split in seven "sectors", characterized by the preponderance of one or two of the aforementioned zones. Daily and nightly transepts have been conducted mostly in stable meteorological conditions. Temperature data have been corrected with ARPAV (Veneto Environment Protection Regional Agency) meteorological station data in order to compensate temperature difference between starting and ending of the session. This is shown in Fig. 43.6 that refers to a nocturnal transept with clear sky and no wind. Urban heat island effect is about 5 °C at 11pm, that is the difference between III-V sectors (typical of F and A zones) and VII sector (F zone), corrected by 0.7 °C measured by ARPAV meteorological station.

Relative and specific humidity behavior shows, like the previous 2010 campaign of measurements, a higher water content in the air in rural zones with respect to urban ones (Fig. 43.7).

Daily morning sessions show a very limited heat island effect, in the order of 1 °C considering the aforementioned correction (Fig. 43.8). Humidity ratios instead vary more considerably, because solar radiation has a greater available surface to cause the evapotranspiration phenomenon in rural zone, increasing the latent heat quota (Fig. 43.9).

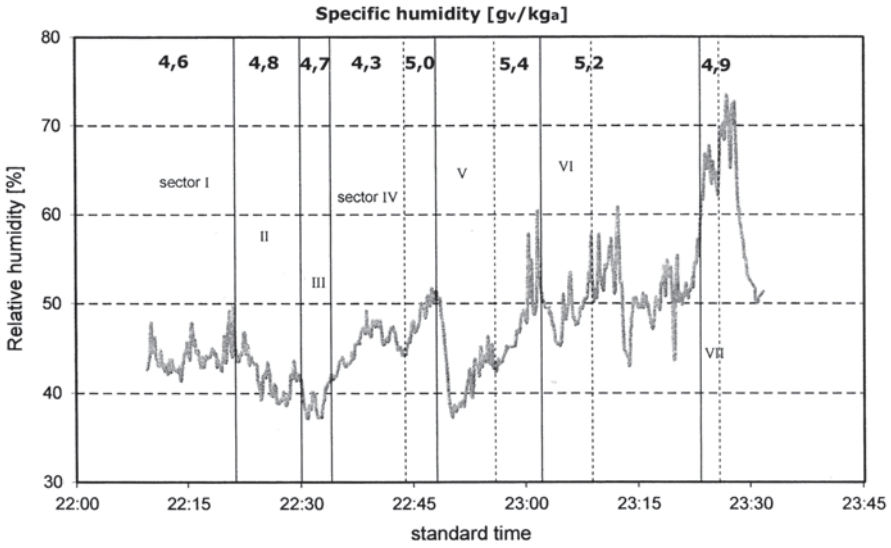

Fig. 43.7 Relative and specific humidity variation during the 04/05/2011 nightly transept

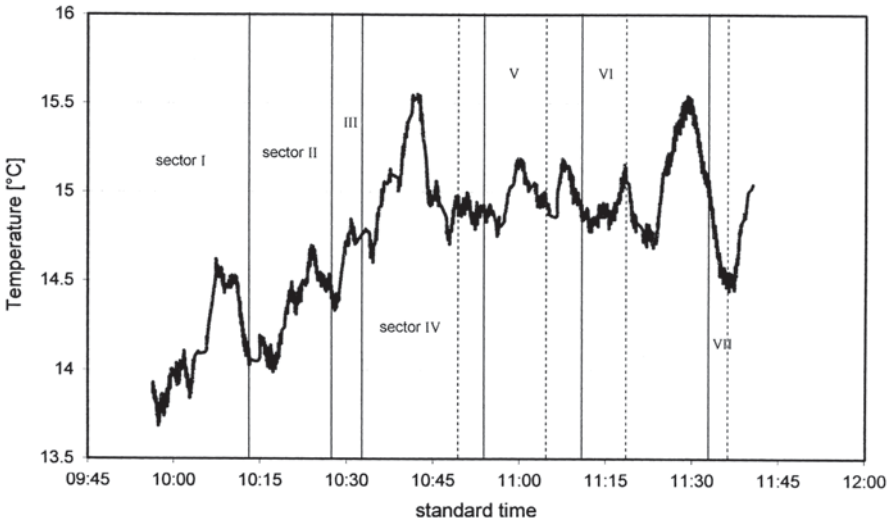

Fig. 43.8 Temperature variation during the 04/14/2011 daily transept

Authors' analysis then has been directed to the study of the roads and sectors crossed with the transept. For the former it has not been possible to identify a "hotter" road, because of the necessity of "micro" scale measurements, very influenced by variation of boundary conditions (solar radiation, wind speed, anthropogenic

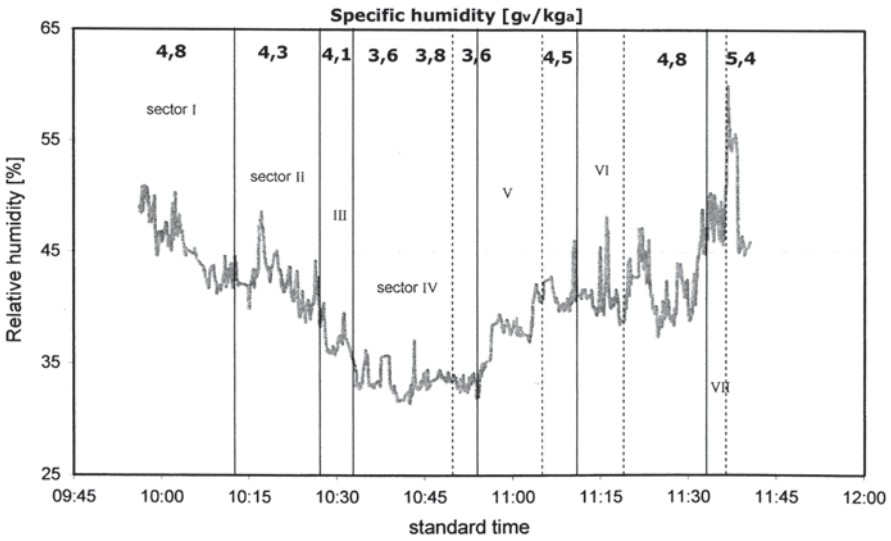

Fig. 43.9 Relative and specific humidity variation during the 04/14/2011 daily transept

heat, etc.). For the latter it has been possible to state that sector V (historic centre, A zone) is the hottest during all the nightly transepts done in stable meteorological conditions. Other transepts have stated that sector III is the hottest: this is a zone of the city where recently new bus and tram stations have been built near the existing railway station, with a great increase in urban impervious surfaces.

Finally, the two studies here reported [5, 16] have stated the presence of the urban heat island effect in Padua, quantifiable in 1–5 °C in function of time of the day and meteorological conditions.

43.4 European Project "UHI": Data Analysis and Experimental Measurements

European Project "UHI – Development and application of mitigation and adaptation strategies and measures for counteracting the global Urban Heat Islands phenomenon" (3CE292P3) started in May 2011. The main objectives of the project are to improve knowledge of the UHI effect, to set up a transnational network to monitor the phenomenon and to define mitigation and adaptation strategies to be implemented in town planning plans. The project involves the Emilia-Romagna Region ARPA, Veneto Region, Co.Ri.La. (a research centre on venetian environment) and other research centers, universities and municipality of the Central Europe (Wien, Prague, Lubjana, etc.). The research group of the Department of Management and Engineering (University of Padua), to whom the Authors of the present paper belong, cooperates with Co.Ri.La. in the Project.

Meteorological Data Analysis

After a very wide review on the causes, the bioclimatic factors producing the intensity of the phenomenon and the impact on the climate change (soon available on http://www.eu-uhi.eu/), a first activity in the Work Package 5 has been the collection and analysis of historic meteorological data of the main cities participating the Project (Padua for the Veneto Region). Data supplied by ARPAV concern hourly mean values of air temperature and wind velocity at 2 m above the ground along the period 10/01/1993–03/31/2012. Starting from these data, the monthly mean values of minimum, maximum and average temperatures, quantity of rainfall, population, Heating and Cooling Degree Days have been calculated.

Heating Degree Days (HDD) is calculated by Eurostat method:

$$\begin{aligned} HDD &= \sum (18 - T_m) \quad \text{if} \quad T_m \le 15^{\circ}\text{C} \\ HDD &= 0 \quad \text{if} \quad T_m > 15^{\circ}\text{C} \end{aligned} \tag{43.2}$$

where T_m is the mean daily temperature and the sum is extend to the whole year.

Cooling Degree Days (CDD) is calculated similarly:

$$\begin{aligned} CDD &= \sum (T_m - 18{,}3) \quad \text{if} \quad T_m \ge 18.3^{\circ}\text{C} \\ CDD &= 0 \quad \text{if} \quad T_m < 18.3^{\circ}\text{C} \end{aligned} \tag{43.3}$$

Two ARPAV meteorological stations have been considered: the Orto Botanico (city centre) and Legnaro (countryside). Average of daily mean values and of daily minimum values are respectively 0.5 and 1.5 °C higher in the former with respect to the latter. It can be deduced that urban heat island in Padua is mainly a nocturnal phenomenon. Such a difference in temperatures is present every month but is more evident in summer (2 °C in July, Fig. 43.10).

Furthermore, Fig. 43.10 shows that, despite difference between daily maximum temperatures of the two stations is meanly null along the period 1994–2011, this is the result of the compensation of the negative difference of the first period (1994–2000) and the positive difference of the following one. This trend (increasing of maximum daily temperatures in urban zones with respect to rural ones) can be read as the presence of a daily heat island effect as well. This could explain the increasing trend of CDD in urban zone of the city (Fig. 43.11).

Concerning Padua population, it is decreased in 1980–2000 period and then slightly increased. It should be considered that, while increase of population increases the UHI effect [13], the opposite is not true (for example impervious surfaces do not vary significantly).

The WP 5 of the Project asks also for the analysis of data of a “very hot” week during 2011 summer (a series of 7 days characterized by high temperatures, clear sky and wind velocity lower than 5 m s^{-1}). It has been chosen the 18–24 August

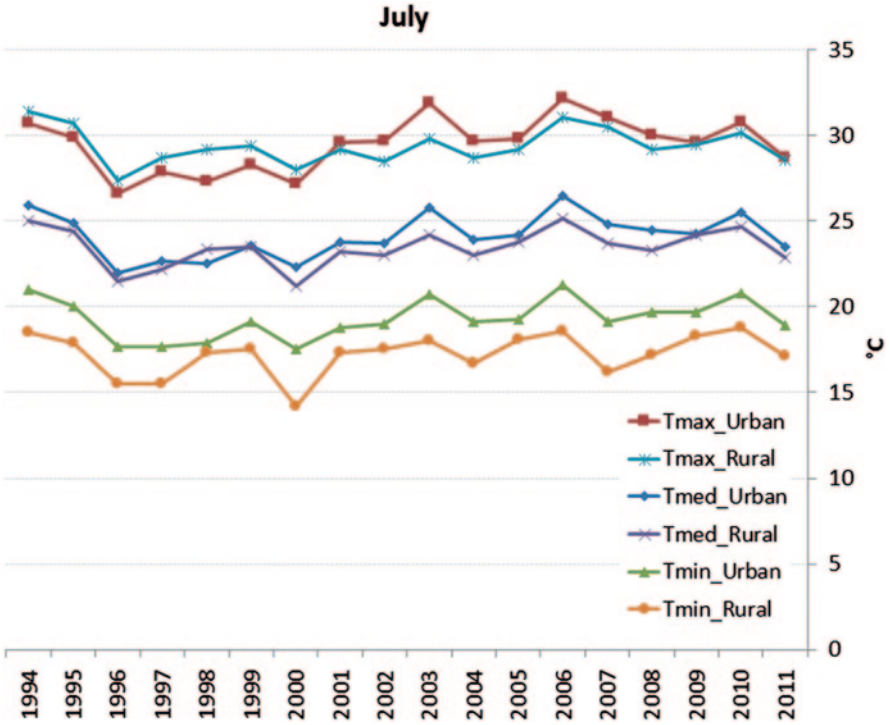

Fig. 43.10 Yearly mean values of the daily average, minimum and maximum temperatures in the period 1994–2011 (data collected from the Orto Botanico (urban) and Legnaro (rural) ARPAV meteorological stations)

2011 week (Fig. 43.12): it shows the presence of the UHI effect (2–4 °C) during nightly hours, before sunrise (between 4am and 5am).

Experimental Measurements in the UHI Project

During 2012 summer the research group of the Department of Management and Engineering will conduct some experimental measurements in order to:

- study the presence of the UHI effect also in smaller city than metropolis, like Padua;
- give some useful indication, based on the data collected, for the city planning.

A new transept has been studied (22 km), measuring air temperature, relative humidity, wind velocity and global solar radiation. In some characteristic sites it will be measured the net radiation on the six directions as well (North, South, East, West, Bottom, Up) for the calculus of mean radiant temperature. The main idea is to calculate some outdoor comfort index (HUMIDEX, PET, SET*) [10, 11] and to investigate the possible causes of the UHI effect.

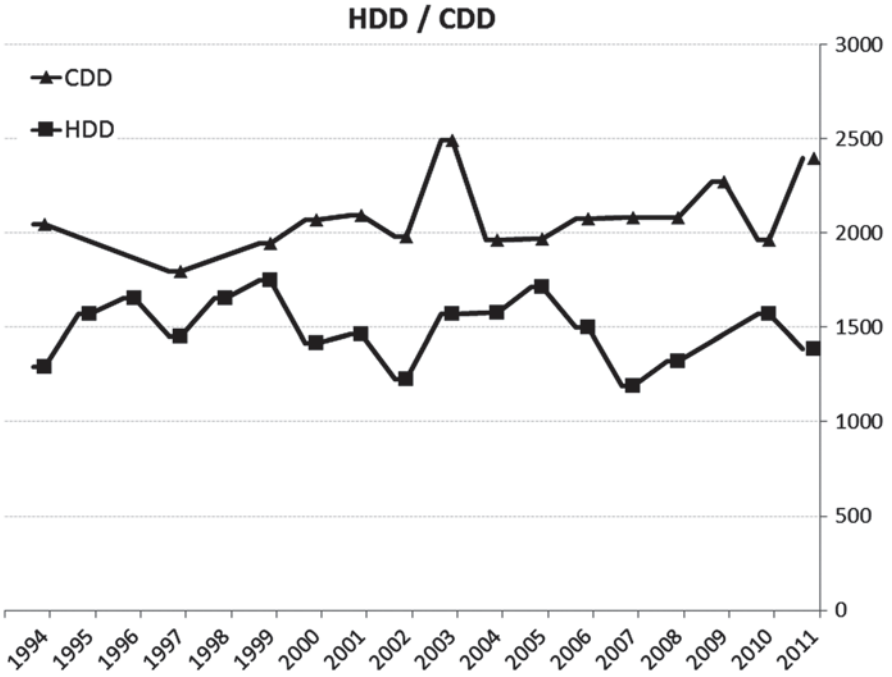

Fig. 43.11 HHD and CDD trends in the urban zone (Orto Botanico ARPA meteorological station) along the period 1994–2011. Some values are estimated because of data missing (for this reason it was not possible to have the rural data trends as well)

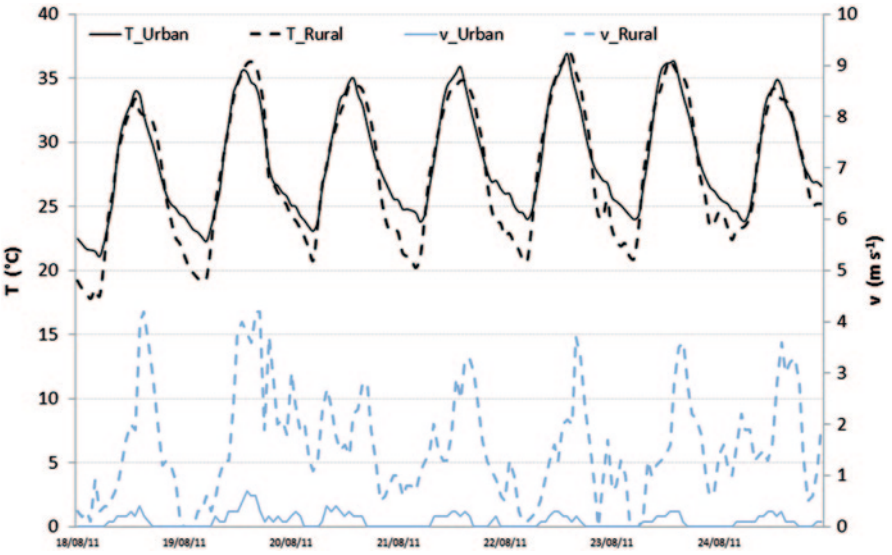

Fig. 43.12 Air temperature and wind velocity at 2 m measured by the two ARPAV meteorological stations during the 18–24 August 2011 week

A session of measurement will be conducted as follow:

1. set of all the sensors and data logger;
2. starting the transept, synchronizing all the watches;
3. stopping at one characteristic site. Continuing the data acquisition of the variables, from the appropriate point (not too near buildings walls or pavement, not exposed to direct solar radiation, etc.) the net radiation on the six previous directions will be measured. Main metadata will be taken as well:
   - distance and dimension of buildings, green areas, etc. by the use of photos, Google maps, etc.;
   - prevalent use of the territory;
   - kind of surfaces (green, built, water);
   - height of trees and buildings;
   - presence of anthropogenic heat sources (traffic, condensers and/or cooling towers, etc.);
4. points 2) and 3) will be repeated till the end of the transept.

The main objectives of this campaign of measurements are to investigate the presence of UHI effect in Padua and to highlight some possible correlations between the main variables (the ones just described). This will be used in order to do some simulations with the Rayman software [10, 11] in order to understand how the outdoor comfort depends on the characteristic of the site. For example, it will be possible to understand how mean radiant temperature or comfort indexes will vary modifying distance between buildings, emissivity of surfaces, etc, giving some useful information to the city planner.

Conclusions

Urban Heat Island effect is well known but studied especially in metropolis. Very few studies have been conducted in Italy and none in Veneto Region. The paper reports on the first results of some campaigns of measurement by the University of Padua. They show the presence of a not negligible effect, above all during nightly hours. The paper reports also on the first and future activities in the UHI Project (Central Europe 2007/2013) which involve the research group of the Authors.

Nomenclature

CDD	Cooling Degree Days
e	water vapor partial pressure (hPa)
H	Humidex index
HDD	Heating Degree Days
PET	Physiologically Equivalent Temperature (°C)
RH	Relative Humidity
SET*	Standard Effective Temperature (°C)
T	Temperature (°C)

Subscript and Superscripts

m mean

Acronyms

ARPAV Agenzia Regionale Prevenzione Ambientale Veneto (Veneto Environment Protection Regional Agency)
d. b. dry bulb
GPS Global Position System
UHI Urban Heat Island

Acknowledgement Data of the first paragraphs of the paper are based on the experimental campaigns of measurements conducted by the research group of the Department of Environmental Agronomy and Crop Productions of the University of Padua by Prof. Andrea Pitacco, Mr. Davide Pedroni and Mr. Marco Di Gilio [5, 16].

Thanks to ARPAV, Mr. Pierpaolo Campostrini and Mr. Matteo Morgantin (Co.Ri.La.) and to Mr. Matteo Sottana for the use of meteorological data.

References

1. Akbari H, Konopacki S (2005) Calculating energy-saving potentials of heat-island reduction strategies. Energy Policy 33(6):721–756
2. Arnfield J (2003) Two decades of urban climate research: a review of turbulence, exchanges of energy and water, and the urban heat island. Int J Climatol 23:1–26
3. Bacci P, Maugeri M (1992) The urban heat island of Milan. Il Nuovo Cimento C 15(4):417–424. doi:10.1007/BF02511742
4. Corburn J (2009) Cities climate change and urban heat island mitigation: localising global environmental science Urban Stud 46:413–427
5. Di Gilio M (2010) Studio sulla variabilità spaziale dei parametri termo-igrometrici nel territorio di padova. M.D. thesis, University of Padua, (Italy)
6. Imhoff ML, Zhang P, Wolfe RE, Bounoua L (2010) Remote sensing of the urban heat island effect across biomes in the continental USA. Remote Sens Environ 114(3):504–513
7. Landsberg HE (1981) The urban climate. International Geographic Series, vol 28. Academic, New York
8. Lazzarin R (2011) Le isole di calore nelle aree urbane (Urban heat islands in urban areas). Casa&Clima 34:34–40
9. Masterton JM, Richardson FA (1979) Humidex, a method of quantifying human discomfort due to excessive heat and humidity, CLI 1–79. Environment Canada, Atmospheric Environment Service, Downsview, Ontario
10. Matzarakis A, Rutz F, Mayer H (2007) Modelling radiation fluxes in simple and complex environments—application of the RayMan model. Int J Biometeorol 51:323–334
11. Matzarakis A, Rutz F, Mayer H (2010) Modelling radiation fluxes in simple and complex environments—basics of the RayMan model. Int J Biometeorol 54:131–139
12. Montavez JP, Rodriguez A, Jimenez JI (2000) A study of the urban heat island of Granada. Int J Climatol 20(8):899–911
13. Oke TR (1973) City size and the urban heat island. Atmos Environ 7:769–779

14. Oke TR (1981) Canyon geometry and the nocturnal urban heat island: comparison of scale model and field observations. J Climatol 1:237–254
15. Oke TR (1982) The energetic basis of the urban heat island. Quart J Royal Meteorol Soc 108:1–24
16. Pedroni D (2011) Study of the urban heat Island in the city of padova and suburbs. M.D. thesis, University of Padua, (Italy)
17. Petralli M, Prokopp A, Morabito M, Bartolini G, Torrigiani T, Orlandini S (2006) Ruolo delle aree verdi nella mitigazione dell'isola di calore urbana: uno studio nella città di Firenze. Rivista Italiana di Agrometeorologia 1:51–58
18. Petralli M, Massetti L, Orlandini S (2009) Air temperature distribution in an urban park: differences between open-field and below a canopy. The seventh. International Conference on Urban Climate, Yokohama, Japan
19. Petralli M, Massetti L, Orlandini S (2011) Five years of thermal intra-urban monitoring in Florence (Italy) and application of climatological indices. Theor Appl Climatol 104:349–356. doi:10.1007/s00704-010-0349-9
20. Picot X (2004) Thermal comfort in urban spaces: impact of vegetation growth. Case study: Piazza della Scienza, Milan, Italy. Energy Build 36:329–334. doi:10.1016/j.enbuild.2004.01.044
21. Santamouris M (ed) (2001) Energy and climate in the urban built environment. James & James, London, p 407
22. Santamouris M (2007) Advances in building energy research: v. 1. Earthscan Ltd., London. ISBN-13: 978–1844073894
23. Takebayashi H, Masakazu M (2007) Surface heat budget on green roof and high reflection roof for mitigation of urban heat island. Build Environ 42(8):2971–2979
24. Zauli Sajani S, Tibaldi S, Scotto F, Lauriola P (2008) Bioclimatic characterisation of an urban area: a case study in Bologna (Italy). Int J Biometeorol 52:779–785. doi:10.1007/s00484-008-0171-6

Chapter 44
Microwave Enhanced Pyrolysis Of Gumwood

Kaiqi Shi, Tao Wu, Jiefeng Yan, Haitao Zhao, Philip Hall and Edward Lester

Abstract Microwave pyrolysis of biomass has gained increasing interests due to the fact that microwave heating provides a volumetric heating and instant heating at improved heating efficiencies compared with conventional heating techniques. In this study, microwave-enhanced pyrolysis of gumwood was carried out at 500 ℃ with silicon carbide as a microwave absorber. Conventional pyrolysis of gumwood was also studied under the same temperature conditions as that of microwave-enhanced pyrolysis. The yields of pyrolytic products, morphology of bio-char, and composition of bio-oil and bio-gas are analyzed by using Scanning Electron Microscope, Gas Chromatograph/Mass Spectrum and Gas Chromatograph respectively. The yields of pyrolytic bio-oil and bio-gas under microwave heating are 8.52 and 73.26 wt.% respectively, which are higher than the products obtained via conventional methods under similar operating conditions. In microwave-enhanced pyrolysis, numerous carbon nano tubes (CNTs) are formed on the surface of the bio-char. The bio-oil obtained by microwave pyrolysis has simpler constituents compared with conventional pyrolytic bio-oil. The proportions of syngas (H_2+CO) and methane (CH_4) in the gas product produced under microwave-enhanced pyrolysis are 62.52 and 22.41 vol.% respectively, which are higher than that of gas product from

T. Wu (✉) · K. Shi · J. Yan · H. Zhao · P. Hall
Division of Engineering, The University of Nottingham Ningbo China,
No.199 Taikang East Road, Ningbo 315100, China
e-mail: tao.wu@nottingham.edu.cn

K. Shi
e-mail: kaiqi.shi@nottingham.edu.cn

J. Yan
e-mail: jiefeng.yan@nottingham.edu.cn

H. Zhao
e-mail: haitao.zhao@nottingham.edu.cn

P. Hall
e-mail: philip.hall@nottingham.edu.cn

E. Lester
School of Chemical and Environmental Engineering,
The University of Nottingham, Nottingham NG7 2RD, UK
e-mail: edward.lester@nottingham.ac.uk

I. Dincer et al. (eds.), *Progress in Sustainable Energy Technologies: Generating Renewable Energy,* DOI 10.1007/978-3-319-07896-0_44,

conventional pyrolysis. It is clear that microwave-enhanced pyrolysis has shown the potential as an alternative method for biomass conversion.

Keywords Microwave · Biomass · Pyrolysis · Syngas

44.1 Introduction

The use of fossil fuels in meeting human being's primary energy demand increased significantly in the past two decades and the projected use of fossil fuels will still increase. However, the utilization of fossil fuels under conventional ways is believed to be the major cause of global warming. It is therefore of particularly importance to find clean and abundant alternative energy sources.

There are many types of alternative energy sources, such as solar energy, geothermal energy, wind power, hydropower, and biomass energy. Biomass is biological materials derived from living or recently living organisms and their wastes. It is considered as one of the sustainable replacements for fossil fuels. The use of biomass as an energy source has some significant environmental advantages due to its zero net emission of CO_2. Currently there are some technologies being used for the conversion of biomass into heat and power, chemicals and many other value-added materials [1]. Biomass pyrolysis is one of the most commonly adopted thermo-chemical processes for the conversion of biomass. It is usually conducted at 450–550 ℃ in which biomass is rapidly heated in the absence of oxygen [2, 3]. In such a process, biomass is converted to solid, liquid and gaseous products. Comparing with other biomass conversion technologies, such as combustion and bio-refining, pyrolysis of biomass has many advantages, such as reducing the volume of waste and the potential to recover value added products [4]. In recent decades, novel pyrolysis technologies have been gaining increasing interests [5, 6]. Numerous efforts have been made to find optimized operating conditions for existing pyrolysis processes and to develop non-conventional conversion technologies by adopting innovative heating methods or catalyst for the improvement of the yields and quality of desired products. Fast pyrolysis system is one of the technologies that have been developed to produce bio-oil from various biomass sources. The techno-economic feasibility study of a fluidized bed pyrolysis technology has shown promising potentials [7].

However, there are still some drawbacks of pyrolysis of biomass. Conventional pyrolysis is carried out by heating the materials via conduction, convection and radiation. This method has some constraints in terms of heat transfer resistance, heat losses to surrounding, low efficiency in the use of heat supplied to biomass materials, damage to reactor walls due to continuous electrical heating [8]. Another drawback of such is low heating rate in electric/gas furnace which results in long heating duration which causes undesired or secondary reactions to occur, which subsequently result in the increase in non-condensable gases, causing the decrease of bio-oil yield [8–10]. Bio-oil obtained from conventional pyrolysis exhibits very complex constituents. The portion of light aromatic compounds in bio-oil is around 10.7 wt.% [11], which makes the bio-oil very difficult to be used as a fuel or a feedstock. Furthermore,

polycyclic aromatic hydrocarbon (PAH) compounds, the highly cancerogenic substances, also exist in the bio-oil from electric/gas furnace pyrolysis of carbonaceous materials [12], which may need some extra caution when it is handled.

Microwave (MW) technology has been considered as a mild and controllable heating technology, allowing simple and rapid processing of materials [13]. Microwave heating provides a volumetric heating and instant heating at improved heating efficiencies compared with conventional heating techniques [14]. During microwave heating process, electromagnetic energy is transferred into thermal energy [15]. Compared with conventional heating methods, due to the volumetric heating, more uniform temperature distribution can be achieved via MW heating and the undesired secondary reactions may be avoided. As a result, better control of the heating process and more desired products can be obtained [15]. More importantly, since heat is transformed by microwave energy within feedstock internally, the large size materials, such as wood block and straw bale, can be handled [3, 16]. Furthermore, apart from serving as an alternative heating method, microwave can also cause specific molecular activations, affecting Arrhenius pre-exponential factor [17]. Therefore, it is an energy efficient method for chemical processing and has become widely accepted [18].

In recent years, microwave pyrolysis of biomass has been gaining increasing interests and become one of the research focuses attracting widespread concern [19–26]. There are many advantages of microwave enhanced pyrolysis of biomass over conventional pyrolysis, which include high heating rate and short heating time needed to reach a desired high temperature that may take hours using conventional heating methods [12]. Even a low microwave input power can achieve a high yield of bio-oil [27, 28]. The composition of liquid product obtained from microwave pyrolysis is highly aromatized and the hazardous PAH content was not detected [29, 30], indicating that the microwave oil had a low toxic risk. Besides, the oxygen content of bio-oil obtained via microwave-enhanced pyrolysis was lower than that of bio-oil produced via electric heating methods [10, 31]. In brief, microwave assisted pyrolysis is a new fast pyrolysis technology for biomass processing [31], which is very promising due to its unique features such as high efficiency, energy saving, selective, less polluting, easy to control and so on [22].

In this study, both of microwave enhanced pyrolysis and conventional pyrolysis of gumwood are carried out under the same temperature level to reveal the difference between the two pyrolysis methods.

44.2 Experimental

Gumwood was obtained from Huzhou, China. It was grinded into a size smaller than 212 μm. Silicon carbide (SiC) was employed as a microwave absorber, the size of which is larger than 212 μm. Dichloromethane (CH_2Cl_2) was used as a solvent for pyrolytic bio-oil collecting. Proximate and ultimate analyses of gumwood are shown in Table 44.1.

Table 44.1 Proximate and ultimate analyses of gumwood

Properties		Gumwood
Proximate analysis (wt.%)	Moisture content	2.1
	Volatile matter	86.0
	Fixed carbon	11.8
	Ash content	0.1
Ultimate analysis[a, b] (wt.%)	Carbon	47.1
	Hydrogen	6.3
	Oxygen[c]	43.5
	Nitrogen	2.1
	Sulfur	1.0

[a] Dry basis
[b] Ash free basis
[c] By difference

The experiments were carried out in a drop tube furnace and a multi-mode cavity microwave system, respectively. In microwave enhanced pyrolysis system, microwave power was selected at 300 W and pyrolysis temperatures were set up at 500 °C for 30 min. SiC was employed as microwave absorber with the mass ratio to biomass of 20:1. Nitrogen (N_2) with a flow rate of 100 mL/min was applied to create an oxygen-free atmosphere. Solid, liquid and gas products were collected. Conventional pyrolysis was also carried out in a drop tube furnace at the same temperature and N_2 flowrate as in the microwave enhanced pyrolysis system.

The solid pyrolytic products, bio-char, were characterised using a Scanning Electron Microscope (SEM, Hitachi S-4800). The liquid products, bio-oil, were analyzed using a Gas Chromatograph/Mass Spectrum (GC/MS, Thermo ISQ). The gas products, bio-gas, were analyzed with Gas Chromatograph (GC, Agilent 6890).

44.3 Results and Discussion

The yields of pyrolytic bio-char, bio-oil and bio-gas are listed in Table 44.2. It is clear that more bio-oil and bio-gas are obtained via microwave enhanced pyrolysis of gumwood, which are 8.52 and 73.26 wt.%, respectively. Due to the volumetric and instant heating of microwave induced pyrolysis, the inner temperature of gumwood is higher than that under conventional heating condition, which leads to fast decomposing process of biomass. Therefore, the yields of pyrolytic bio-oil and bio-gas via microwave method are higher than the pyrolytic products via conventional pyrolysis.

The SEM images of gumwood bio-chars prepared by microwave enhanced pyrolysis and conventional pyrolysis are shown in Fig. 44.1. It is clear that there are numerous ball shape stuff of nano-scale fibers on the surface of microwave enhanced pyrolytic bio-char. However, conventional pyrolytic bio-char only has some irregular small particles on its surface.

Table 44.2 Pyrolysis products yields

Methods	Bio-char (wt.%)	Bio-oil (wt.%)	Bio-gas[a] (wt.%)
Microwave pyrolysis	18.22	8.52	73.26
Conventional pyrolysis	29.68	5.73	64.59

[a] By difference

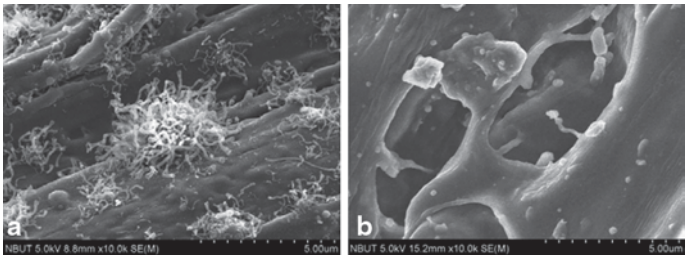

Fig. 44.1 SEM micrographs of bio-chars obtained via microwave pyrolysis (**a**), and conventional pyrolysis (**b**)

Table 44.3 EDS of microwave pyrolytic bio-char

Elements	Contents (wt.%)	Element	Contents (wt.%)
C	91.82	Ca	0.24
O	6.69	Ti	0.16
Si	0.29	Fe	0.02
Cl	0.03	Cu	0.34
K	0.19	Zn	0.22

According to Energy Disperse Spectroscope (EDS) of nano fibers shown in Table 44.3, the content of carbon reaches as high as 91.82%. These nano materials are mostly formed by carbon and could be considered as Carbon Nano Fibers (CNFs). The CNFs are grown from pyrolysed round particles (PRPs), as shown in Fig. 44.2, without the use of specific catalysts, substrates and source gases. The fact that diameter sizes of PRPs and CNFs are all around 100 nm, reveals that CNFs are formed from PRPs.

Bio-oils obtained by microwave pyrolysis and conventional pyrolysis were analyzed by using GC/MS to show their constituents. Figure 44.3 shows the GC graphs of various bio-oils. Microwave pyrolytic bio-oil has fewer constituents than conventional pyrolytic bio-oil. Therefore, the upgrading of microwave enhanced pyrolytic bio-oil is slightly easier compared with conventional pyrolytic bio-oil.

It can be seen from Table 44.4 that the microwave enhanced pyrolysis of gumwood generates more than conventional methods. The High Heating Value (HHV) of main pyrolytic fuel gases, such as H_2, CO and CH_4, are calculated and listed in Table 44.5. The total HHV of microwave enhanced pyrolytic fuel gas is 3021.31 kcal/m^3, 30% higher that via conventional method. It is clear that microwave pyrolytic bio-gas has a potential to be used directly as a fuel gas.

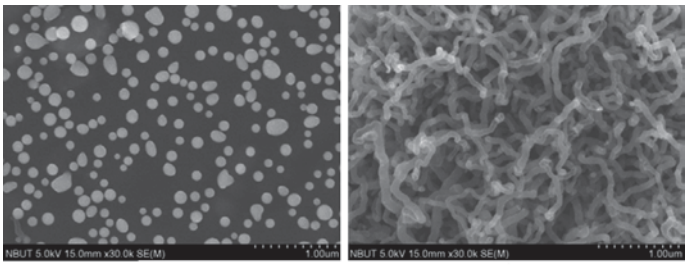

Fig. 44.2 SEM micrographs of pyrolysed round particles and carbon nano fibers

Table 44.4 GC analysis of bio-gas

Bio-gas	Microwave pyrolysis (vol.%)	Conventional pyrolysis (vol.%)
H_2+CO	62.52	46.32
CO_2	22.41	46.62
CH_4	13.48	10.94
C_2H_6	0.52	0.98
C_2H_4	0.99	1.94
CxHy	0.09	1.20

Table 44.5 High heating value of main fuel bio-gas

Bio-gas	HHV (kcal/m^3)	
	Microwave pyrolysis	Conventional pyrolysis
H_2+CO	1808.39	1332.26
CH_4	1212.92	984.37
Total	3021.31	2316.63

Conclusions

By comparing the pyrolytic products of microwave enhanced pyrolysis and conventional pyrolysis of Gumwood, it is evident that microwave enhance pyrolysis of biomass has many advantages over conventional pyrolysis in terms of the yield of gas and liquid product and their physical and chemical properties. The bio-oil and bio-gas obtained by microwave pyrolysis have better potential to be used as fuel resources due to their better quality compared with those obtained via conventional methods. Apart from these, microwave enhanced pyrolysis of char can result in the formation of bio-char containing nano carbon fibers which might be of some significance if the formation of such nano structure can be controlled.

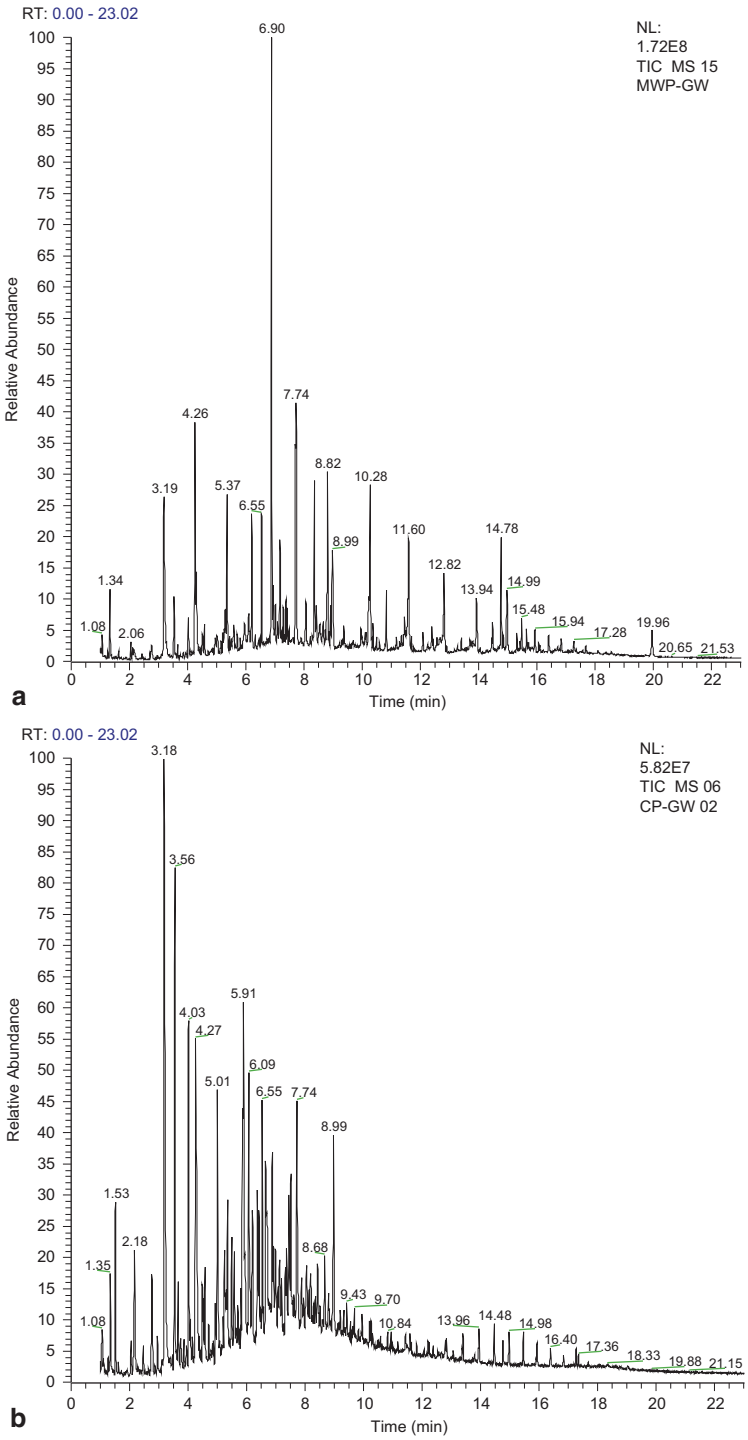

Fig. 44.3 GC/MS analysis of bio-oils obtained by microwave pyrolysis (**a**), and conventional pyrolysis (**b**)

Acknowledgment Ministry of Science and Technology of China (Grant No. 2008DFA61600), Bureau of Science and Technology of Ningbo City (Grant No.2008B10048) and Ningbo Municipal Innovation Team on WEEE Recycling Technologies (Grant No. 2012B82011) are acknowledged for the financial support to this study. The University of Nottingham Ningbo China is also appreciated for providing Scholarship to PhD students involved in this work.

References

1. Budarin VL et al (2009) The preparation of high-grade bio-oils through the controlled, low temperature microwave activation of wheat straw. Bioresour Technol 100(23):6064–6068
2. Scott DS, Piskorz J (1984) The continuous flash pyrolysis of biomass. Can J Chem Eng 62(3):404–412
3. Zhao X et al (2010) Microwave pyrolysis of corn stalk bale: a promising method for direct utilization of large-sized biomass and syngas production. J Anal Appl Pyrolysis 89(1):87–94
4. Baysar A, Johnson KJ, Kuester JL (1988) Microwave heating applications in thermochemical biomass conversion. In: Bridgwater AV, Kuester JL (eds) Research in thermochemical biomass conversion. Springer, Netherlands, pp 680–695
5. Yang H et al (2006) Pyrolysis of palm oil wastes for enhanced production of hydrogen rich gases. Fuel Process Technol 87(10):935–942
6. Tu W-K et al (2009) Products and bioenergy from the pyrolysis of rice straw via radio frequency plasma and its kinetics. Bioresour Technol 100(6):2052–2061
7. Islam MN, Ani FN (2000) Techno-economics of rice husk pyrolysis, conversion with catalytic treatment to produce liquid fuel. Bioresour Technol 73(1):67–75
8. Bridgwater AV (1999) Principles and practice of biomass fast pyrolysis processes for liquids. J Anal Appl Pyrolysis 51(1–2):3–22
9. Domínguez A et al (2008) Bio-syngas production with low concentrations of CO_2 and CH_4 from microwave-induced pyrolysis of wet and dried sewage sludge. Chemosphere 70(3):397–403
10. Tian Y et al (2011) Estimation of a novel method to produce bio-oil from sewage sludge by microwave pyrolysis with the consideration of efficiency and safety. Bioresour Technol 102(2):2053–2061
11. Rofiqul Islam M, Haniu H, Rafiqul Alam Beg M (2008) Liquid fuels and chemicals from pyrolysis of motorcycle tire waste: product yields, compositions and related properties. Fuel 87(13–14):3112–3122
12. Kwak T-H et al (2006) Environmental aspects of gasification of Korean municipal solid waste in a pilot plant. Fuel 85(14–15):2012–2017
13. DE C, WH S (1996) Microwave processing of materials. Annu Rev Mater Sci 26:299–331
14. Appleton TJ (2005) Microwave technology for energy-efficient processing of waste. Appl Energy 81(1):85–113
15. Thostenson ET, Chou TW (1999) Microwave processing: fundamentals and applications. (Composites Part A): Appl Sci Manuf 30(9):1055–1071
16. Miura M (2004) Rapid pyrolysis of wood block by microwave heating. J Anal Appl Pyrolysis 71(1):187–199
17. Hoz de la, Diaz-Ortiz AA, Moreno A (2005) Microwaves in organic synthesis. Thermal and non-thermal microwave effects. Chem Soc Rev 34(2):164–178
18. Gronnow MJ (2005) Energy efficiency in chemical reactions: a comparative study of different reaction techniques. Org Process Res Dev 9(4):516–518
19. Antonakou E (2006) Evaluation of various types of Al-MCM-41 materials as catalysts in biomass pyrolysis for the production of bio-fuels and chemicals. Fuel 85(14–15):2202–2212
20. Chen Mq (2008) Catalytic effects of eight inorganic additives on pyrolysis of pine wood sawdust by microwave heating. J Anal Appl Pyrolysis 82(1):145–150

21. Salema AA, Ani FN (2011) Microwave induced pyrolysis of oil palm biomass. Bioresour Technol 102(3):3388–3395
22. Jiang J, Ma X (2011) Experimental research of microwave pyrolysis about paper mill sludge. Appl Therm Eng 31(17–18):3897–3903
23. Koberg M et al (2011) Bio-diesel production directly from the microalgae biomass of nannochloropsis by microwave and ultrasound radiation. Bioresour Technol 102(5):4265–4269
24. Omar R et al (2011) Characterization of empty fruit bunch for microwave-assisted pyrolysis. Fuel 90(4):1536–1544
25. Zhao X et al (2011) Microwave pyrolysis of straw bale and energy balance analysis. J Anal Appl Pyrolysis 92(1):43–49
26. Du Z (2011) Microwave-assisted pyrolysis of microalgae for biofuel production. Bioresour Technol 102(7):4890–4896
27. Domínguez A (2007) Conventional and microwave induced pyrolysis of coffee hulls for the production of a hydrogen rich fuel gas. J Anal Appl Pyrolysis 79(1–2):128–135
28. Fernández Y et al (2008) Obtaining synthesis gas by heat treatment in microwave biomass and biogas. Obtención de gas de síntesis por tratamiento térmico en microondas de biomasa y biogás 65(534):103–109
29. Domínguez A et al (2005) Investigations into the characteristics of oils produced from microwave pyrolysis of sewage sludge. Fuel Process Technol 86(9):1007–1020
30. Huang YF et al (2008) Total recovery of resources and energy from rice straw using microwave-induced pyrolysis. Bioresour Technol 99(17): 8252–8258.
31. Miura M et al (2001) Microwave pyrolysis of cellulosic materials for the production of anhydrosugars. J Wood Sci 47(6):502–506

Chapter 45
Improving Operating Efficiency of Installed Capacity in a Power and Water Cogeneration Plant

Farayi Musharavati

Abstract Over the years, power and water cogeneration plants have become popular in the gulf region. This is because of the perceived potential for the technology to drastically reduce the unit costs of freshwater and power. While potential benefits of such installations have been realized, additional benefits can be accrued by critically examining the operating performances of installed capacity. In this study, potentials for improving plant operating efficiencies in cogeneration power/water production plants are investigated. Unlike the usual thermodynamics approach, it is shown that by implementing more effective and more efficient methods and techniques in the day-to-day operations of power/water cogeneration plants the potential to reduce the unit costs of water and electricity exist. However, this potential is subject to local and/or regional power and water regulatory market valuations. The approach under taken is to analyze and identify improvements in operating practices that affect; primary fuel utilization, non-fuel variable production costs, and non-fuel operation and maintenance costs. The underlying logic is that by improving plant performances in areas mentioned above, improvements in plant operating efficiencies can be realized. The discussions in this study unfolds by analyzing plant operating efficiencies for improvement options. Relationships between operational practices, their effects and influences on overall plant operating efficiencies are discussed. Estimates of operating efficiency best practice measures in power/water cogeneration plants are used to assess and evaluate the potential for efficiency improvements in power/water cogeneration plants. The results of case study shows that by improving plant operating efficiencies through more effective and more efficient operational practices, production operations can realize significant savings in fuel utilization, reductions in non-fuel variable production costs and reductions in operation and maintenance costs.

Keywords Plant operating efficiency · Installed capacity · Cogeneration plants · Production costs · Operation and maintenance costs · Fuel utilization · Plant availability · Plant capabilities

F. Musharavati (✉)
Department of Mechanical and Industrial Engineering,
Qatar University, PO Box 2713, Doha, Qatar
e-mail: farayi@qu.edu.qa

I. Dincer et al. (eds.), *Progress in Sustainable Energy Technologies: Generating Renewable Energy,* DOI 10.1007/978-3-319-07896-0_45,

45.1 Introduction

Cogeneration is the simultaneous production of more than one useful form of energy from the same energy source [1]. In cogeneration power/water production plants the generated heat is used in the production of freshwater from seawater through the desalination process. Such plants have become a common practice in arid and semi-arid regions, for example the gulf region. This is because it is generally perceived that cogeneration power/water production is a cost effective plant design that can reduce production costs in separate power and water production facilities. While this is true, sub-optimal plant operating practices may raise the costs of power and water production. In competitive bulk power and water markets, incurred costs may be regulated or, in the worst case scenario, partially shouldered to consumers [2]. Albeit, the position taken in this study is that costs of production (and hence the per unit costs of power and water) in power/water production plants can be further reduced by improving plant operating efficiencies. A case study of a cogeneration power/water production plant (hereinafter called the generating company) in the State of Qatar will be used as an example in the discussions that follow. In order to put the discussions in this paper into perspective, it is important to briefly describe the business model for power and water production in the State of Qatar.

Background

The generating company (power/water cogeneration plant) is one among the largest joint stock companies in the Gulf Region. It owns and operates a number of power plants and desalination stations to meet the power and water consumption needs. The generating company produces water and power and sells these products to a transmission and distribution company. While the generating company is a private limited, the government holds significant shares in power generation and water production. In addition, the power/water transmission and distribution company is also under the control of the government. Although the issues of privatizing the transmission and distribution company have been discussed, the issue of bulk market valuations and competitive bidding in bulk power and water markets is relatively less significant in the current power and water supply issues to consumers in the Gulf Region. At present, the probability of economic risk that may be incurred in the power generation and water production processes is relatively low since the government has large shares in both the fuel (natural gas) supply company and the transmission and distribution company (water and electricity). Since there are many power/water production plants in the gulf region, the move to privatize power generation and water supply may catalyze the emergence of highly competitive power bidding and bulk power markets locally and/or regionally. Such a move will further increase the need to improve plant operating efficiencies.

The general consensus world over is that power and water are among the most important elements that support the development of national economies. Therefore,

one of the risks of the generating company lies in its ability to deliver power and water capacities as agreed upon by the transmission and distribution company. Consequently, the generating company has a pre-determined load factor and power/water generation schedule that was mutually agreed upon when the plant was commissioned. This agreement lasts for the life of the generating company and any inability of the generating company to deliver as per schedule incurs penalties from the transmission and distribution company. Therefore, 'management control' in the generating company need to ensure that optimal power and water production capacities are maintained as per agreement.

The generating company controls more than 70 % of all water capacity and more than 60 % of all power capacity in Qatar. Power capacities are met through a number of cogeneration power/water production stations. The discussions in this paper are based on a case study analysis of one of the cogeneration power and water production stations. In the case study natural gas is used as a primary fuel in the cogeneration power/water production plant. This fuel represents around 70 % of the generating company's total cash costs. Therefore, the issue of optimal fuel utilization plays a significant role in the day-to-day operations and performances of the generating company. On a positive note, natural gas fuel acquisition for the generating company is guaranteed since the fuel supply comes from a government owned organization.

Both power and water are heavily subsidized through the transmission and distribution company in Qatar. Currently, power and water are provided at no cost to Qatari nationals, which make up about 13 % of Qatar's population, and at a subsidized price to expatriates. As such, utility management in both the generating and transmission distribution companies may not recognize the need to continuously improve operating practices as long as prescribed targets are met. It is also possible for the power and water production activities to be done under suboptimal conditions. Therefore, methods and techniques for continuously improving operating practices are vital to the existence and perpetual survival of power and water production operations.

In general, cogeneration power/water production plant operating practice can be fine-tuned towards optimal efficiencies through best practice. However, the plant operating statistics for most non-private cogeneration power/water production plants are far from best practice efficiencies. Some of the reasons for this anomaly emanate from the following observations: (a) there are very few regulatory incentives for utility management to focus on promoting high operating performances that can compete in the global market place, and (b) there is very little regulatory enforcement to speed up management's focus on improving operating efficiencies [3]. As a result, most non-private cogeneration power and water production plants continue to implement old sub-optimal practices as long as they make 'profit'. While this may be true for some organizations, the importance of moving towards "best practice" in power/water cogeneration plants cannot be ignored. There is, therefore, an inherent need to explore, investigate and identify non-capital innovative ways for improving operating efficiencies of installed capacity in power/water cogeneration plants.

Aims and Objectives

The aim of this study is to explore, analyze, examine and determine the potentiality of improving operating efficiencies of installed capacity in power/water cogeneration plants. Such improvements have ripple effects that impact on cogeneration power/water production costs and subsequent reductions in the per unit cost of both power and water production. The presented argument is that continuous improvement actions on operational practices in cogeneration plants can achieve milestones in upgrading non-private cogeneration power/water production plant performances towards global efficiency frontiers. Such an achievement has the added advantage of further reducing the unit costs of power and water. In the following analysis, performance based measures were used to assess the relative operating performances of cogeneration power and water production plants. A case study of an existing cogeneration power/water production plant was used to illustrate how changes in operational practice can result in improvements in operating performances.

The case study plant in this study consists of a gas cycle coupled to a multi-stage flash (MSF) distillation process. A comparative performance based approach was used to show the gap between current operations in the case study cogeneration plant and the potential improvements towards higher plant operating performances and hence towards a more competitive power/water cogeneration industry. More specifically, it is shown that by implementing more effective and more efficient operational methods and techniques the potential to further reduce unit costs of water and power exists.

In order to achieve the stated aim, the approach taken in this study is to explore, investigate, analyze and identify opportunities and initiatives for improving operating practices that affect; fuel utilization, variable costs as well as operation and maintenance costs. Relative comparison of actual plant statistics in the generating plant with statistics of a reference plant were used to determine the potential improvements and potential savings that can be realized by implementing best practice.

45.2 Theoretical Review

Cogeneration Modes and Configurations

Although cogeneration power and water production plants are generally perceived to be cost-effective, flexibility in operations is one of the most important characteristics in competitive bulk power and water production markets. Flexibility is usually determined by the intrinsic thermodynamic design of a plant configuration. Flexibility is also linked to the power/water ratio of a given power/water plant configuration.

In the public literature, a number of different types of configuration classifications have been discussed. Common configuration classifications include; (i) configurations based on the implemented thermodynamic cycle [4], and (ii) configurations based on the desired cogeneration mode [5]. In the later, the classifications are based on whether the cogeneration mode is serial or parallel. In parallel cogeneration, power is produced by supplying part of the produced steam to a steam turbine for power generation while the other part of the steam is supplied to the water desalination process. In such parallel arrangement, the total energy consumption is almost equivalent to that required when using separate sources of steam for power generation and for water desalination. Albeit, an advantage of the parallel arrangement is that the plant configuration is highly flexible in operations particularly when compared to the serial cogeneration mode.

Unlike the parallel cogeneration mode, the series cogeneration mode produces power and water in 'two stages'. In the first stage, the supplied steam undergoes expansion in a steam turbine to produce power. In the second stage, the steam is supplied to the water desalination process. Therefore, the series cogeneration mode requires relatively less total energy consumption in comparison to the parallel cogeneration mode. These parallel and serial cogeneration modes represent extremes of the cogeneration power and water production configurations. On a scale of 0–1, the digit 0 may be used to represent the series cogeneration mode while the digit 1 represents the parallel cogeneration mode. Such a scale can be used to relatively compare operating performances of alternative plant configurations in terms of; (a) flexibility in operations, and (b) flexibility in plant energy use.

Other plant configuration classifications are based on the implemented thermodynamic cycle. The common ones include: steam thermal cycles, gas cycles and combined cycles all coupled to a water desalination process [4]. Common desalination processes include multi-stage flash (MSF) distillation, multi-effect distillation (MED) and reverse osmosis (RO). The optimization analysis of such plant configuration has been discussed by many authors including [4, 5, 6]. Of interest to the present study is the inferred observation that satisfactory optimization analysis can be achieved through the following methods; (a) evaluating design specifications of the various elements and components that will constitute a desired configuration, and (b) by optimizing design and operating parameters and conditions of a given plant configuration [4]. Since the analysis presented in this paper is based on installed capacity, the latter method of analysis was adopted.

Design Parameters

Power to water ratio is a plant design characteristic usually determined by the implemented cogeneration technology in a given plant [4]. Thus, power to water ratios achieved in various cogeneration technologies depends on plant design [7]. It has been shown that different plant designs are associated with a specific range of power to water ratios [5, 6, 7, 8]. For example, it has been shown that extraction turbine

systems can give power to water ratios between 8 and 15 MW/MIGD, back pressure turbine systems can give between 3 and 6 MW/MIGD and gas turbine systems can give between 8 and 20 MW/MIGD.

While operations can be configured to produce power/water ratio as per plant design, operational practice and changes in power/water requirements can result in sub-optimal operating conditions. A number of issues can lead to sub-optimal operating conditions including; (i) variations in the demand of power and water either by time of the day or month of the year, (ii) general increase in population, and (iii) rapid growth and development of the various industries. These variations often require fine tuning of operations in installed capacity. In other circumstances, large variations may even require a corresponding change in the plant design or plant design parameters. Each of the changes made may be associated with changes in operating and energy efficiencies. The changes made may also have a bearing on the energy consumption in the plant. As such, it is necessary for operators to implement informed decisions in order to avoid sub-optimal performance.

In [5, 9], it was observed that the plant utilization factor declines as the power to water ratio is increased. Moreover, it has also been shown that achieving the desired power to water ratio depends on a number of factors including; fuel acquisition efficiency, cost of fuel allocated to the water desalination process, power and water sales, capital costs, local as well as regional requirements in the case of an existing bulk power and water market [10]. If characteristics of the power demand in power/water cogeneration plant vary with time, auxiliary boilers are required to provide supplementary fuel for energy in order to keep water production at a constant level. Another important significance of the power to water ratios lies in that fuel savings tend to increase with decreasing power to water ratio [7].

Energy Conservation

In the public literature, energy conservation methods and techniques have been discussed by many authors including [11]. Energy use issues discussed in this paper include; energy in installed capacity, operations and general plant utility management practices. Good plant management practices include: effective repairing of leaks (natural gas and compressed air); maintaining optimum combustion efficiency, as well as maintenance of pipe and equipment insulation. Best operational practices include: retrofits and/or replacement of production or auxiliary equipment, upgrades of process-specific equipment such as; new boilers, heat exchangers, economizers, and process control instrumentation. Overall efficiency for boilers are mainly determined by (a) combustion efficiency, and (b) structural and other losses. Combustion efficiency can be affected by excess air, exhaust temperature, burner tip and deflector replacements. Improvements in these areas include using newly developed and more efficient burners, as well as automatic combustion control [12]. Structural improvements to minimize heat losses due to radiation and

convection from surfaces, openings and from blowdown in boilers can also be carried out in order to conserve energy.

Energy Consumption

In cogeneration power/water production using the multi-stage flash (MSF) desalination process, the MSF is energy intensive [13]. The value and the cost of the thermal energy supplied to the MSF process depends on the method of supplying this energy. Steam can be supplied directly from fuel operated auxiliary boilers (FOABs) or from waste heat recovery boilers (WHRBs) associated with gas turbine power generation. In the case study plant, both FOABs and WHRBs are used. The use of FOABs to produce relatively low-pressure and temperature steam to drive the MSF process is, thermodynamically, wasteful. The thermal energy supplied to operate an MSF unit is in the form of relatively low-pressure steam to the brine heater (heat input section). The saturation temperature of this steam should be only few degrees above the top brine temperature (TBT). The TBT temperature depends on the method applied for treatment of seawater [14, 15].

45.3 Method of Analysis

Case Study

A case study of a power/water cogeneration plant was used to compare plant design characteristics with actual plant performance data. The gas turbine cycle used in the generating company is a constant flow cycle with a constant addition of heat energy. The Brayton power cycle is the ideal thermodynamic cycle that approximates the operation of a gas turbine cycle in the case study. Figure 45.1 depicts the open, or simple cycle, characteristic of a typical gas turbine installed in the case study plant. The gas cycle is composed of a compact set formed by a compressor, a combustion chamber and a gas turbine connected to an electric generator.

In Fig. 45.1, air is compressed from point 1 to point 2 via an axial flow compressor. Fuel and an ignition source are subsequently added resulting in combustion and ultimately the addition of heat to the system between points 2 and 3. Work is then extracted by the turbine between points 3 and 4 due to the expansion of hot combustion gases. Since the work produced by the turbine exceeds the work consumed by the compressor between points 1 and 2, useful work is produced and is used to turn an electrical generator. The hot exhaust gases from the power generation gas turbine section are used in the waste heat recovery boiler section as a heat source to generate steam required in the distillers. Waste heat recovery boilers operate under two conditions: the unfired condition and

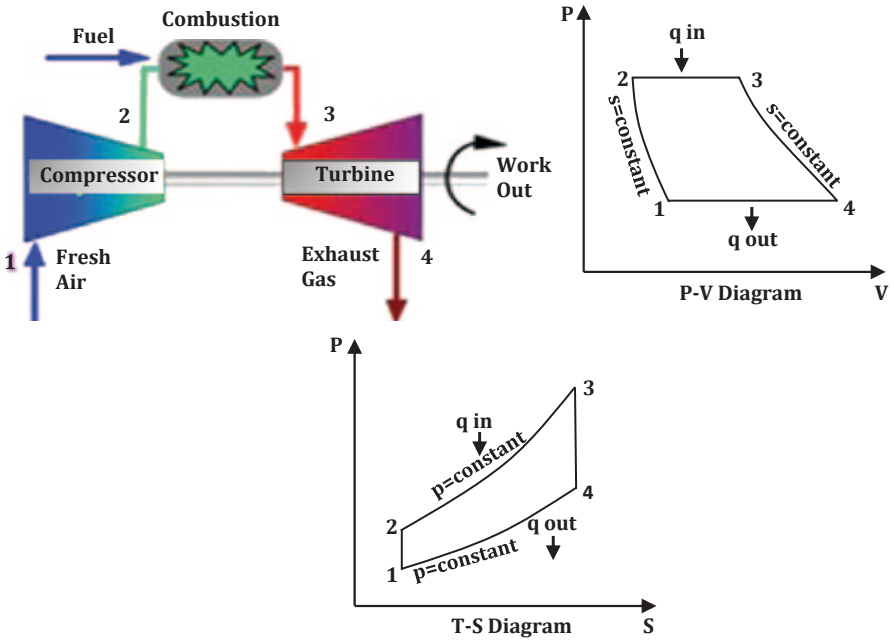

Fig. 45.1 Simplified cycle of the implemented gas turbine

the fired one. For normal operating conditions, 160 t/h dry saturated steam is supplied at 15 bars, while the feed water temperature is maintained at 140 °C. Auxiliary boilers are also available to produce steam of similar properties to that produced by the waste heat recovery boilers. However, the steam capacity of the auxiliary boilers is limited to 80 t/h when supplied with feed water at 140 °C. The auxiliary boiler efficiency ranges from 85 to 86 %. A simplified schematic for the multi-stage flash (MSF) desalination process is shown in Fig. 45.2. The MSF plant consists of the following major sections: Distillation, heat input section, heat recovery section and the heat rejection section. The MSF distillation process was designed to produce a total of 216,000 m^3/day of distilled water with a top brine temperature of 91 °C or 270,000 m^3/day with a top brine temperature of 112 °C.

The heat input section consists of the brine heater, where thermal energy is supplied. In the heat recovery section the heat of condensation is transferred to the brine, and thus pre-heats the recirculated brine in stages 1–14. In the heat rejection section, the heat of condensation is partly transferred to the make-up stream and mostly to sea water cooling stream in stages 15 and 16. The MSF has two operating conditions; one with a top brine temperature of 91 °C when polyphosphate type-chemicals are used for scale inhibition and the other with a top brine temperature of 112 °C when Belgard-EV is used for scale inhibition. The design parameters for the MSF are shown in Table 45.1.

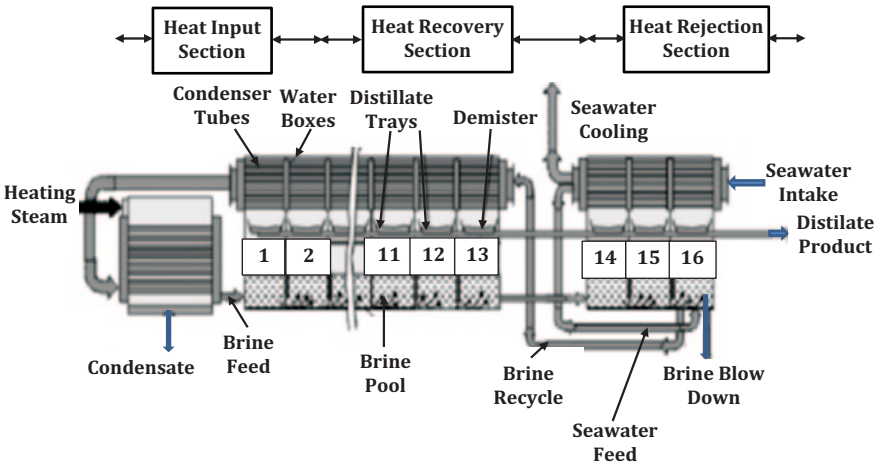

Fig. 45.2 Simplified schematic for the multi-stage flash (MSF) desalination process

Table 45.1 Design parameters of the multi-stage flash distillation plant

Operating mode	MODE 1	MODE 2
Top brine temperature (°C)	9	112
Total Distillate output (m^3/day)	216,000	270,000
Distillate conductivity (max) (µS/m at 25 °C)	5500	5500
High purity distillate normal output for each distiller (m^3/day)	160	160
High purity distillate max. output for each distiller (m^3/day)	1600	1600
High purity distillate conductivity (max.) (µS/m at 25 °C)	220	220
Total sea water for all purpose (m^3/h at 38 °C)	30,000	27,000
High pressure steam consumption (kg/h at 15 bar)	2805	2805
Low pressure steam consumption, t/h at saturated conditions	113	127
Gained output ratio	6.3	7.1

Plant Operating Efficiency

The operating efficiency of an organization can be measured in many ways. A number of aspects can be considered in evaluating the operating efficiency. Common categories of operating efficiency that are related to operational practices include; fuel acquisition efficiency, plant operating efficiency and capital efficiency.

Fuel acquisition is a significant aspect in determining the marginal and variable costs of power/water cogeneration plants. Since fuel acquisition practices are fully under the control of utility management changes, fuel procurement practices affect plant operating efficiencies. Fuel is the largest component of variable power production costs. The generating company uses natural gas as the primary fuel that drives the gas turbine cycle. Fuel acquisition for the generating company is quite simplified since the natural gas comes from a government owned organization. Therefore, fuel acquisition is guaranteed in the current business model of the

generating company. Since capital efficiency is outside the scope of this paper, the remaining discussions are focused on plant operating efficiency.

Although there are many ways of defining plant operating efficiencies, the discussions in this paper will revolve around operating practices that affect a number of aspects that define plant operating efficiency. Such aspects include: non-fuel variable costs, non-fuel operating costs, and maintenance costs. In the following analysis, data on the aspects mentioned above were collected from the generating company for analysis. The approach used in the analysis was to develop estimates of efficiency frontier references for key measures of the various aspects that define plant operating efficiencies. The potential improvements were then evaluated by comparing actual plant operating data against the reference data. The key statistics for the concepts under study were ordered into quartiles. The mean value of the "best practices" quartile for each key statistic was then calculated and used as the "efficiency frontier reference" for the sake of comparison. Potential savings were then estimated using actual plant statistic deviations from the frontier references.

Data Collection

Design parameter data were collected from reference plant operation manuals for comparison with actual plant data in the case study. Actual performance of the case study were analyzed using operational data for 1 year operation period for maximum continuous rating (MCR). MCR is defined as the maximum output that a plant is capable of producing continuously under normal conditions over a year. Under ideal conditions, the actual output could be higher than the MCR [15]. Data collected included; mass flow rates, pressures and temperatures of system components, gross power generated, net power generated, power consumed, desalinated water production, and seawater consumption.

45.4 Results and Discussions

Plant Operating Performance

Case study plant performances are summarized in Figs. 45.3 and 45.4. The energy generated ranges from 240,000 to 460,000 MWH. Water production varied between 3,000,000 and 4,800,000 m^3 per month. The power to water ratio ranged between 51.6 and 151.3 kWh/m^3.

Plant capabilities and availabilities are characteristics of the cogeneration power and water production plant. Plant availability statistics are usually a function of maintenance planning and implemented strategies. In this study, the only aspect of capability discussed is the flexibility of the cogeneration power and water production plant in terms of possible power to water ratios and in terms of

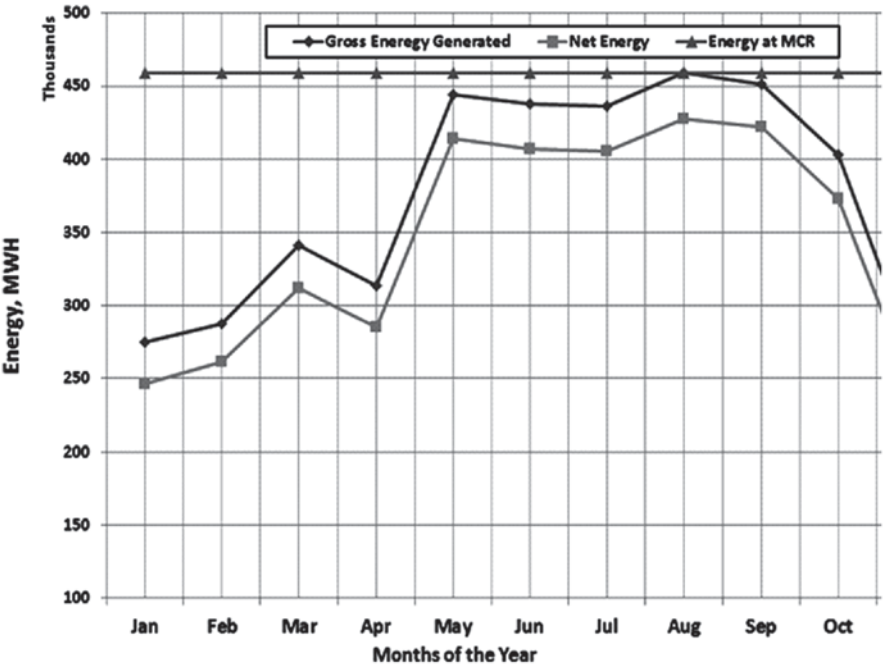

Fig. 45.3 Variations of energy generated in the case study plant for a one year operation

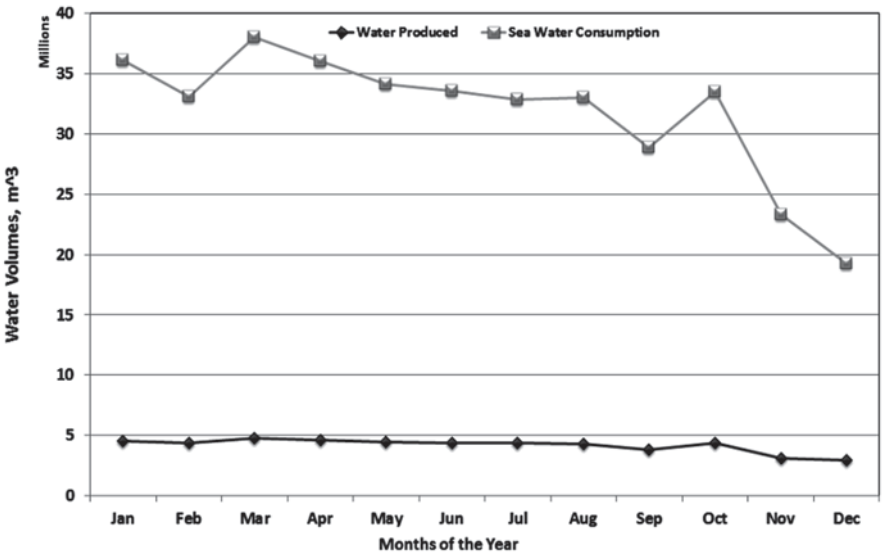

Fig. 45.4 Variations of water produced in the case study plant for a one year operation

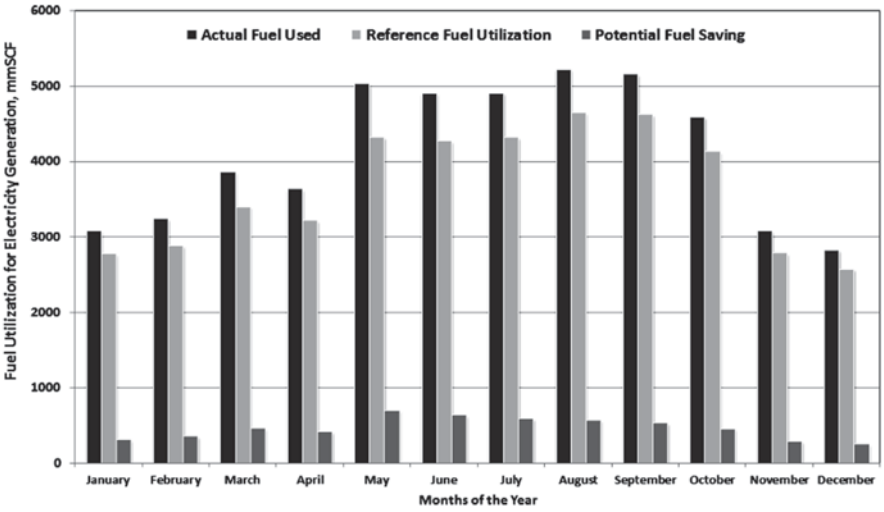

Fig. 45.5 Distribution and comparison of fuel utilization in power generation for one year operation

the ability to deliver varying capacities. In general, cogeneration power and water production plants are less flexible than single purpose plants due to the economic pressure to maximize the combined production of water and power. Therefore, the design of cogeneration power and water production plants may reduce the plant flexibility which ultimately results in indirect penalties [5]. In addition, cogeneration plants usually have a lower availability factor since any incident interrupting the output of one of the two products may lead to a disturbance or stoppage in the production of the other, thus increasing the cost per unit products. On the other hand, plant capabilities can be considered to be a measure of a given plant's ability to generate power or produce water over a range of required percentages within the confines of the plant design limits.

Fuel Utilization

A comparison of the fuel utilization distribution in power generation for 1 year operation for the reference and actual plant data are shown in Fig. 45.5.

The potential fuel savings (i.e. reference—actual) is also shown in Fig. 45.5. This potential savings represent non-capital-intensive potential improvements in operating efficiencies by continuously positioning operational practice towards best practice. The represented potential savings can be gained through effective repairing of leaks (natural gas and compressed air); maintaining optimum combustion efficiency, appropriate maintenance practices and optimal strategies for utilizing key equipment, pipes and equipment insulation.

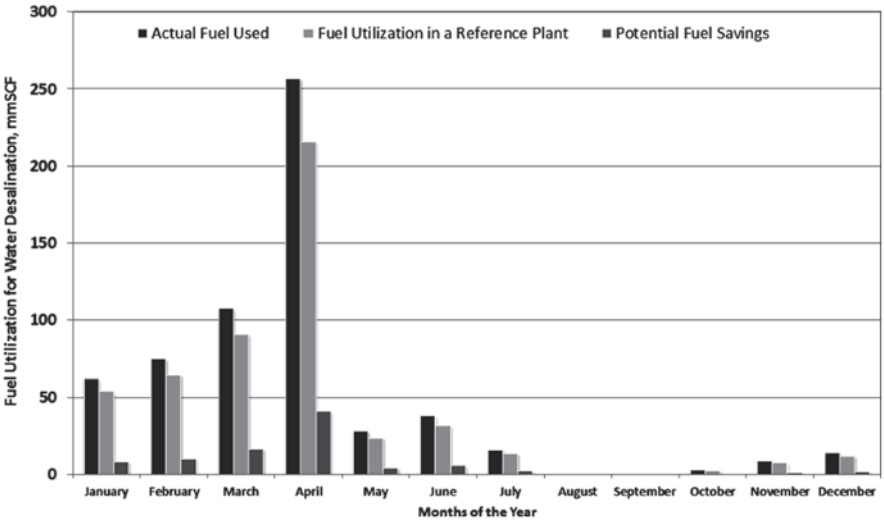

Fig. 45.6 Distribution and comparison of fuel utilization in water desalination for 1 year operation

A comparison of the fuel utilization distribution in water desalination for one year operation for the reference and actual plant data are shown in Fig. 45.6. The potential fuel savings (i.e. reference—actual) are also shown. This potential savings represent non-capital-intensive potential improvements in operating efficiencies by continuously positioning operational practice towards best practice. Basic operational practices for gaining the represented potential savings include; retrofits and/or replacement of production and auxiliary equipment, upgrades of process-specific equipment such as new waste heat boilers, economizers, and process control instrumentation.

The data analyses presented in the previous paragraphs have examined a cogeneration power and water production plant in a bid to explore whether there is potential for improving operating efficiencies and thus reducing fuel utilization. By setting reference performances and comparing them with actual plant operating data, the analysis shows that the case study plant has an annual potential fuel saving of: 93 mmSCF on the water delination side and 5596 mmSCF on the power generation side thus amounting to a total of 5689 mmSCF fuel savings.

Operation and Maintenance Costs

A comparison of the non-fuel variable operation and maintenance (O & M) costs distribution for one year operation of the water desalination side are shown in Fig. 45.7. The potential cost savings (i.e. actual—reference) are also shown in Fig. 45.7. Figure 45.7 does not include fixed operation and maintenance costs. The potential savings represent the potential improvements in operating efficiencies by

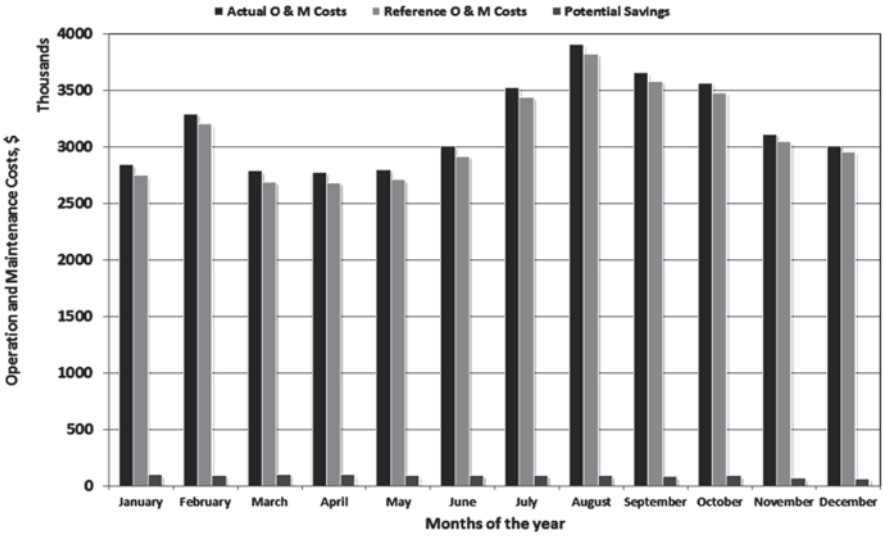

Fig. 45.7 Comparison and distribution of variable operation and maintenance costs for water desalination

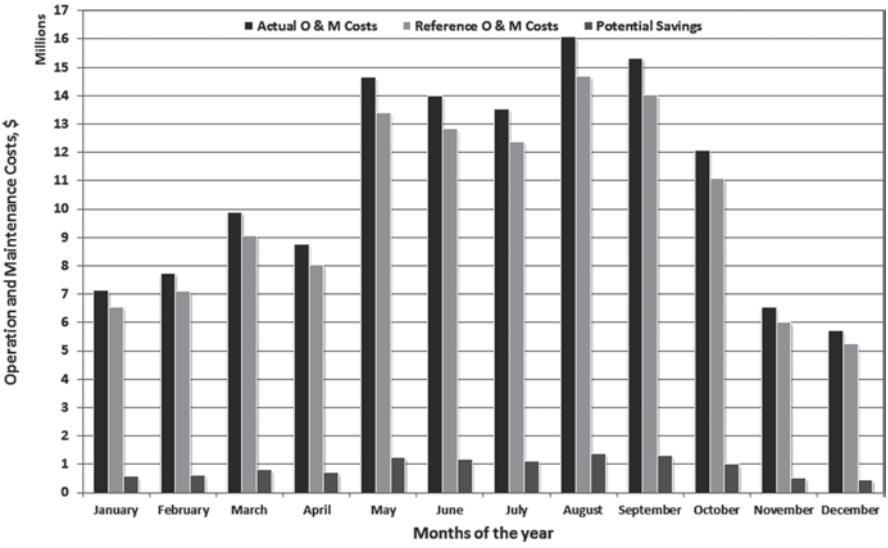

Fig. 45.8 Comparison and distribution of variable operation and maintenance costs for power production

continuously positioning operational practice towards best practice. The total potential savings in variable costs for 1 year operation amounts to $ 1,002,291/year.

A comparison of the variable operation and maintenance costs distribution for 1 year operation of the power generation side are shown in Fig. 45.8.

The statistics for fuel utilization has shown that the case study plant has an annual potential fuel saving of 93 mmSCF on the water delination side and 5596 mmSCF on the power generation side thus amounting to a total of 5689 mmSCF fuel savings. For a 10 year period, these savings amount to a total of 56,890 mmSCF. The data analyses for operation and maintenance costs presented in this section have examined a cogeneration power and water production plant in a bid to explore whether there is potential for improving operating efficiencies and thus reducing production costs. By setting reference performances and comparing them with actual plant operating data, the analysis shows that the generating company has an annual potential cost savings of $ 1,002,291 on the water desalination side and $ 4,456,113 on the power generation side, thus amounting to a total of $ 5,458,404. In 10 years these savings could accumulate to a total of $ 54,584,040. These calculations include only variable operation and maintenance costs (non-fuel costs) that can be gained by improving operating efficiencies of installed capacity.

Concluding Remarks

In this study, the importance of power/water cogeneration plants as alternative and cost effective means of providing both water and power simultaneously has been discussed. It is generally believed that power/water cogeneration plants have the potential to drastically reduce the unit costs of freshwater and power. Consequently, a number of thermodynamic and thermo-economic investigations on power/water cogeneration plants have been discussed by many authors. While progress has been made in terms of thermodynamic design and efficiencies, the contribution of this study was to explore, investigate analyze and identify other substantial benefits that can be accrued by critically examining the operating performances and practices in installed capacity of power/water cogeneration plants. Since most of the operational practices are generally under the control of "utility management" in various plants, the discussions in this study will be helpful to plant operators, supervisors and utility managers.

It has been shown that potential for improving operating efficiencies exist in power/water cogeneration plants results in significant improvements in the production costs. The focus of the presented analysis was to establish reasonable efficiency frontiers for comparing the performance of power/water cogeneration plants with reference statistics. In this way, a given power/water cogeneration plant can be analyzed in order to evaluate and compare power generating and water production operating efficiencies. To this end, a case study of an existing power/water cogeneration plant has revealed that changing the way a plant is operated results in positioning plant operations towards best practice. This may lead to the realization of potential savings, and improvements in operating performances. The overall effects of positioning power/water production cogeneration towards best practice lies in the overall reduction of the unit costs of water and electricity.

However, this potential is subject to bulk local and/or regional power and water regulatory market valuations.

Acknowledgements This paper was made possible by a UREP award [UREP09-076-2-020] from the Qatar National Research Fund (a member of The Qatar Foundation). The statements made herein are solely the responsibility of the author[s].

References

1. Kanoglua M, Dincer I (2009) Performance assessment of cogeneration plants. Energy Convers Manage 50(1):76–81
2. Goudarzi L, Roberts BF (2012) ESC Electric Utility Analysis Report, Economic Sciences Corporation. http://www.econsci.com/euar9703.html. Accessed July 2012
3. Ferreira EM, Balestieri JAP, Zanardi M A (2010) Optimization analysis of dual purpose systems. Desalination 250:936–944
4. Al-Mutaz IS, Al-Namlah AM (2004) Characteristics of dual purpose MSF desalination plants. Desalination 166:287–294
5. Hamed OA (2005) Overview of hybrid desalination systems—current status and future prospects. Desalination 186:207–214
6. Hamed O A, Al-Sofi MAK, Imam M, Mustafa G M, Ba-Mardouf K, Al-Washmi H, (2000) Thermal performance of multi-stage distillation plants in Saudi Arabia. Desalination 128:281–292
7. Mussati FS, Aguirre PA, Scenna NJ (2003) Dual-purpose desalination plants (Part II. pptimal configuration). Desalination 153:185–189
8. Mussati FS, Aguirre PA, Scenna NJ (2005) Optimization of alternative structures of integrated power and desalination plants. Desalination 182:123–129
9. Mussati FS, Barttfeld M, Aguirre PA, Scenna NJ (2008) A disjunctive programming model for superstructure optimization of power and desalting plants. Desalination 222:457–465
10. Ionita IC (2002) Engineering and economic optimization of energy production. Int J Energy Res 7:697–715
11. Pramanik D (2000) Study of thermal efficiency of steam boilers at sugar mills. In: National Seminar on Energy audit, conservation and cogeneration for sugar industries, National Sugar Institute, Kanpur, 26 Dec 2000
12. Gacem Y, Taleb S, Ramdani A, Senadjki S, Ghaffour N (2012) Physical and chemical assessment of MSF distillate and SWRO product for drinking purpose. Desalination 290:107–114
13. Khawajia AD, Kutubkhanaha IK, Wieb J (2008) Advances in seawater desalination technologies. Desalination 221(1–3):47–69
14. Al-Rawajfeh AE, Fath HES, Mabrouk AA (2012) Integrated salts precipitation and nanofiltration as pretreatment of multistage flash desalination system. Heat Transf Eng 33(3):272–279
15. IESO (2012) http://www.ieso.ca/imoweb/marketdata/. Accessed 25 July 2012

Chapter 46
Simulation, Modeling and Analysis of Water/Power Ratios for a Dual Purpose Water and Power Production Plant

Luma M. Diab and Farayi Musharavati

Abstract In dual purpose power and water (DPPW) production plants two challenges are often encountered; (a) maintaining operations that meet a desired water production/demand ratio or power production/demand ratio, and (b) meeting the desired water to power ratio. Although these problems are usually implied in the implemented plant design and technology, operational issues play an important role in fine tuning operations towards optimal performance. In addition, operational practices have a bearing on energy consumption and operating efficiencies. In this study, a simulation based approach is used to provide data for handling the fine tuning of operations towards desired targets. To this end, numerical simulation is used to determine the relationships between total water/power demand and total water/power produced. In order to reduce the specific energy consumption of the plant, investigations on the design and operating features of the DPPW production plants were carried out. An existing DPPW production plant was used as a case study. The investigation proceeded by focusing on identifying the optimal production operation strategies that, if implemented, can reduce energy consumption in the production of water and power. Discrete event simulation was used to experiment with a number of feasible plant configurations and strategies for producing power and water. Water to power ratios were used to compare the effectiveness of the feasible production operation strategies through simulation experiments. For each configuration, average values of the simulated data (i.e. both water and power) were determined and used to calculate water to power ratios. Simulation results show that different plant configurations and different operational strategies and practices affect the water to power ratios. This allows engineers and operators to select plant configurations, operational strategies and practices that give them the desired water to power ratios

F. Musharavati (✉) · L. M. Diab
Department of Mechanical and Industrial Engineering,
Qatar University, PO Box 2713, Doha, Qatar
e-mail: farayi@qu.edu.qa

L. M. Diab
e-mail: Luma_diab89@windowslive.com

I. Dincer et al. (eds.), *Progress in Sustainable Energy Technologies: Generating Renewable Energy,* DOI 10.1007/978-3-319-07896-0_46,

with respect to demand scenarios. Therefore, simulation is an effective tool in identifying opportunities for tuning operations to meet desired production requirements.

Keywords Simulation modeling · Numerical simulation · Discrete event simulation · Dual purpose power and water (DPPW) production · Desalination · Water/power ratios

46.1 Introduction

Power and water production are among the most important factors that facilitate the developmental process of a national economy [1]. To date, dual purpose power and water production plants have been accepted as one of the feasible solutions for providing freshwater and electricity in arid and semi-arid regions. Consequently, a lot of research has been done to improve, upgrade and advance the thermodynamic efficiencies of the various technologies used in dual purpose power and water production plants [2–5]. Unlike most of these research attempts that focus more on capital intensive projects, the research presented in this study aims to identify non-capital intensive initiatives for improving operating performances. More specifically, this study focusses on using general purpose simulation as a tool for providing process plant data for fine tuning operations to desired targets and improved operating efficiencies.

In the operations of DPPW production plants, two challenges are often encountered, namely; (1) meeting the desired or an optimal water to power ratio, and (2) maintaining operations that meet either a desired or an optimal water production/demand ratio or power production/demand ratio. Problems associated with these challenges usually arise as consequences of operational issues and practice. As such, these challenges can be addressed by identifying and implementing; (a) suitable plant configurations, and (b) optimal production operation strategies. Implementing suitable plant configurations allows operators to engineer plant performance towards optimum water to power ratios. On the other hand, implementing optimal production operation strategies often results in significant improvements in operating and energy efficiencies. In this study, the challenges mentioned above are addressed through a simulation based approach. A case study of an existing DPPW production plant in Qatar was used to identify optimization initiatives for improving operating efficiencies and reducing production costs in the operations of dual purpose water and power production plants.

A number of possible configurations and arrangements of the DPPW production systems can be achieved in practice. For case study plant considered in this study, power generation is driven by gas turbines and thermal energy from their exhaust are used to generate low-to-medium pressure steam in waste heat recovery boilers. Steam is routed directly to the brine heater of a multi-stage flash (MSF) distillation plant. Auxiliary boilers are used in order to achieve higher yields.

The power to water ratios produced by various conventional DPPW production systems depends on plant design [6]. It has been shown that different plant designs are associated with a specific range of power to water ratios. For example, extraction turbine systems can give between 8 and 15 MW/MIGD, back pressure turbine system can give between 3 and 6 MW/MIGD and gas turbine systems can give between 8 and 20 MW/MIGD. The significance of the power to water ratios lies in that fuel savings tend to increase with decreasing power to water ratio [6]. In practice, the demand of power and water varies either by time of the day, month of the year and also by the general increase in population as well as the growth and development of the industry. These variations often require fine tuning of operations within design limits. In other circumstances, large variations may require a corresponding change in the plant design or plant design parameters. Each of the changes made may be associated with changes in operating and energy efficiencies. The changes made may also have a bearing on the energy consumption in the plant. As such it is necessary for operators to make informed decisions. One way of availing decision information is to use simulation.

The aim of this study is to use simulation to identify, evaluate and assess optimization initiatives for improving operating efficiencies and reducing production costs in DPPW production plants. Simulation models can then be used to explore and investigate the performance of the plant operations under different conditions and scenarios. In order to achieve the aim mentioned above, the following specific objectives will be addressed:

- To model and simulate the relationship between total water (power) demands and total water (power) produced in a bid to characterize production-demand scenarios
- To model and simulate production operations strategies in order to identify optimal operating strategies based on the power to water ratios.

In the analysis, improvements on operating efficiencies were based on; (i) analyzing energy savings related to an optimal match of the power to water ratio, and (ii) identifying optimal operating scenarios, states and parameters for improving operating efficiencies. Achieving such improvements often translate into reducing consumption of primary fuel and fresh water utilizations in power and water production plants while at the same time meeting the electricity and desalinated water requirements for consumers. In addition, implementation of the results of this study can go a long way in positioning an organization towards operational excellence. This would also allow the organization to benchmark and or compare its operations with the highest industry standard on operational efficiency. Moreover, improving operational efficiencies usually involves adopting flexible organization structures that allow for a network flow of information. This would also involve other stakeholders, such as the suppliers, distributors and customers along the supply chain. The remainder of this paper is organized as follows; simulation methods used in this paper are described, followed by an outline of the results of the simulation based study and finally concluding remarks are discussed.

46.2 Methodology

Modeling is the creation of a simplified representation of a complex system with the goal of providing predictions of the system's performance measures. Plant models were designed to capture materials flow.

Numerical Simulation

Numerical simulation modeling for water balance analysis was based on the following equation, after [7]:

$$SC_k = SC_{k-1} + \sum_{i=1}^{N} D_K^i + W_{B_K} - W_K, \quad where\ K = 1,\ 2,\ \ldots.\ K \tag{46.1}$$

where:

SC_k Total contents of reservoir at period k, m^3—similarly this is denoted as total water consumption (m^3/month) giving us the annual total

RC Reservoir capacity, m^3—this is found by flow rate (m^3/hr) × 24 h/day × 30 days/month

D_K^i Output of distillation unit i during interval k—for the case study we have distillate flow rate + flow rate of number of high purity distillates

W_{B_K} Brackish water production during period k, m^3/h

W_K Total water demand, m^3/h—similarly this is equivalent to total water production (m^3/h) for our case.

An assumption obtained from key personnel at the case study was that the daily production = daily demand.

In applying the model represented in Eq. (46.1), the brackish water production constraint was ignored since only seawater was being used in the case study plant. Consequently, the modified equation is shown in Eq. (46.2).

$$SC_k = SC_{k-1} + \sum_{i=1}^{N} D_K^i + - W_K, \quad where\ K = 1,\ 2,\ \ldots.\ K \tag{46.2}$$

Simulation Modeling

Simulation modeling is a common method for analyzing complex systems. It creates a simplified representation of a system under study. Then one can start experimenting with the system, keeping in mind prescribed set of goals, such as improved system design, cost–benefit analysis, and sensitivity to design parameters. Experimentation consists of generating system scenarios and observing system behavior over time [8].

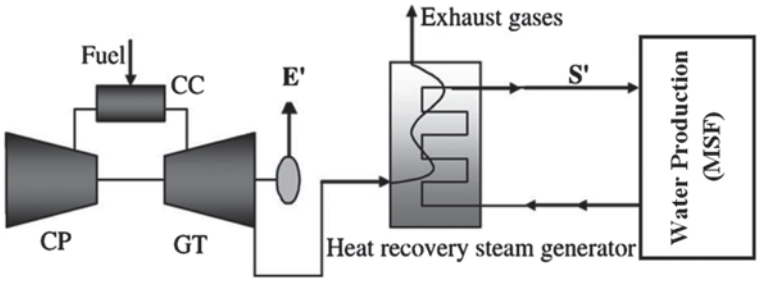

Fig. 46.1 Simplified configuration of the case study plant proposed by Ferreira et.al [3]

The working simulation tool for the models in this study is ARENA. ARENA is a simulation environment consisting of module templates, built around SIMAN language. ARENA provides a module-oriented simulation environment to model practically any scenario involving the flow of transactions through a set of processes. Since ARENA generates correct SIMAN code and checks the model for syntactic errors (graphical and textual), a large amount of initial debugging takes place automatically. In this study, ARENA software was used to simulate process system operations and conduct "*what-if*" analysis in a bid to identify the most suitable production operations strategy [9]. ARENA simulation model was created in order to simplify the overall processes into sub processes and components. Simulation modeling and simulation experiments using ARENA software were applied primarily to identify relationships between various production operations strategies and the intricate interactions among the power and water production activities.

Case Study

A case study of an existing DPPW production plant in Qatar was used in the analysis. The basic configuration of the case study plant is shown in Fig. 46.1. The power production side consists of a compressor (CP), combustion chamber (CC) and a gas turbine (GT), while the water production side is based on the multistage flash (MSF) distillation process.

The compressor compresses incoming air to a high pressure which is then mixed with natural gas and burnt in the combustion chamber to produce high pressure and high velocity gas which in turn is used as mechanical energy to drive the compressor and the electrical generator. The hot exhaust gases from the power generation gas turbine section is used in the waste heat boiler section as a heat source to generate the steam required for the distillers. The case study plant operates with 14 gas turbines, 12 waste heat recovery boilers and 10 auxiliary boilers.

The simplified structure of the MSF desalination plant is shown in Fig. 46.2. The plant consists of the following principal sections: (i) heat input section-which consists of the brine heater, where thermal energy is supplied; (ii) heat recovery

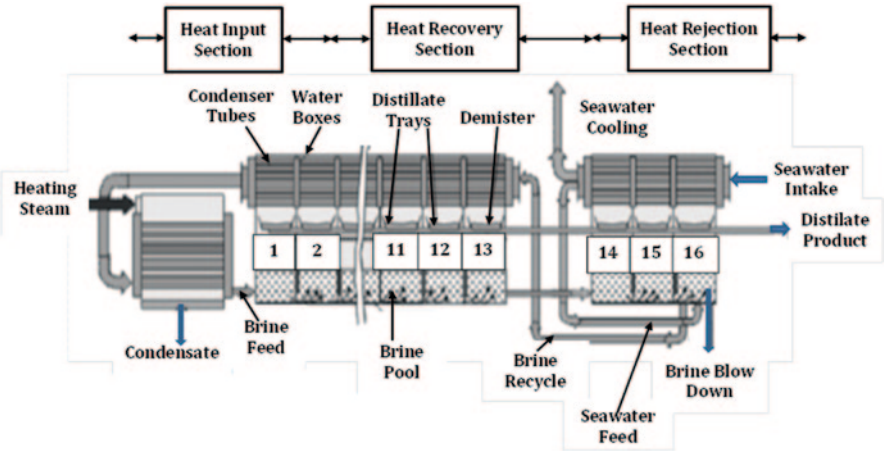

Fig. 46.2 Simplified structure of the MSF desalination plant

section-where heat of condensation is transferred to the brine, and thus pre-heats the recirculated brine in stages 1 through 14; and (iii) heat rejection section-where heat of condensation is partly transferred to the make-up stream and mostly to sea water cooling stream, through stages 15 and 16.

The distillation unit has two operating modes: mode 1, 85–100 % of 18,000 m^3/day at a top brine temperature of 91 °C; and mode 2, 70–100 % of 22,500 m^3/day at a top brine temperature of 112 °C.

Simulation Experiments

In the power and water production simulation experiments, a quasi-experimental design was used [10]. This approach focuses on comparing the results of the current situation (control experiment) with "*what-if*" scenarios. In the case study plant, power generation is driven by gas turbines and thermal energy from their exhaust is used to generate low-to-medium pressure steam through the waste heat recovery boilers. In this set-up, steam is routed directly to the brine heater of the distillation plant. Auxiliary boilers are usually used for higher yields. Although it is flexible (within the plant design parameters), the power to water ratio produced depends on operational practice. However, fuel savings increase with decrease in the power to water ratio. Therefore, an optimal power to water ratio is often sought in practice.

Since the case study plant will always produce both water and electricity, operational differences have an influence on the power to water ratio. Alternatively, a desired power to water ratio can be achieved by optimizing the feasible production operation strategies implied by the plant design. Such operational strategies have a bearing on the unit cost of either water or electricity as well as primary energy consumption. An important observation in such plants is that the influence of energy

efficiency improvements of installed capacity is less compared to the influence based on plant design changes or retrofit/re-design issues.

Water desalination processes are energy intensive and their coupling with power plants should result in appreciable cost saving when compared with separate single purpose power generation and desalination installations. The average specific fuel consumption for the case study plant was calculated to be 306 NM^3/MWH. The specific energy consumption of the water desalination process can be reduced either by use of innovative modifications in conventional power cycles and/or by reducing the irreversibility of the multi-stage flash (MSF) process through improvements in the design and operating features of the distillers.

In experimenting with the power/water production ratios, several configurations of the installed capacity can be simulated. For example, the case study plant usually operates with a duplicate "standby" line. This arrangement enables smooth production of the required power and water capacities in a bid to meet the fluctuating demands for water and electricity. Simulation experiments can then be used to mimic different couplings of the available gas turbines, compressors and heat recovery boilers as well as auxiliary boilers. These different couplings were assumed to represent different operational states in the dual purpose power and water production plant.

The focus of this investigation was on operational issues assuming that the design issues are satisfied, in the plant design, based on thermodynamic analysis. More specifically, this investigation focused on identifying the optimal production operation strategies within the limits of the general plant design that in turn can reduce energy consumption in the production of water and power. Further, simulation modeling was used to experiment with a number of feasible plant configurations (assuming retrofits in plant designs) for the sake of comparison. Since the "entities" for simulation of power and water production strategies are different, water production and power production units were treated separately in simulation models created in AREANA simulation software. Figures 46.3 and 46.4 depict the simulation models that were used for "*what-if*" analysis experiments for water and power production. Data was collected from runs of the simulation models based on the simulation models presented in Figs. 46.3 and 46.4.

46.3 Results and Discussion

Production–Demand Ratios

Numerical simulation was used to determine the relationship between total water or power demand and total water or power produced. To minimize the per unit cost of electricity production and water desalination, two important selections must be accounted for at a certain time interval: namely, electricity and water demands. In order to satisfy electricity generation and freshwater production demands, the optimal

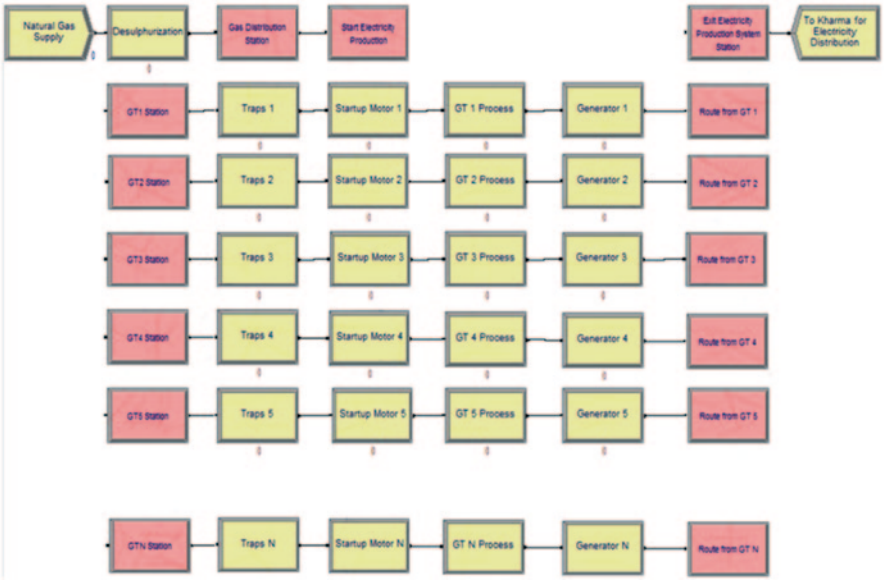

Fig. 46.3 Arena simulation model for experimenting with various electricity production operation strategies in the case study plant

unit configuration and operating conditions are solved as implied in the mathematical model. The benefit of modeling such a system via mathematical descriptions is that the process can be optimized in such a way that the operating factors of cost will be minimized, while simultaneously considering the various constraints.

The power produced and power demand patterns for the case study are shown in Fig. 46.5 while Fig. 46.6 shows the patterns of the water produced and water demanded. While the patterns in Fig. 46.5 and 46.6 shows that the case study plant adequately meets the demand pattern (i.e. the production to demand ratios are always more than 1), the differences in the power/water produced and power/water demand can be streamlined through improved operating practices that aim to optimize production with respect to demand. Such practices would also aim at reducing surplus, which if not leased or not consumed in the plant would constitute an opportunity lost.

Figure 46.7 shows the relationships between power produced, estimated power demand and the power used in the case study plant.

From Fig. 46.7 it can be observed that the total power used in-house is about 8 times less (on average) to the power generated. The power used in-house is also fairly constant, which can be considered to be good since energy improvements can be levelized in the whole plant. Figure 46.7 also shows that the power produced exhibits variational differences particularly in the months May, June, July, August and October. This variation is related to the climatic variation for which the said months are during summer time according to Doha climate. During this time, more power is needed for air-conditioning and cooling.

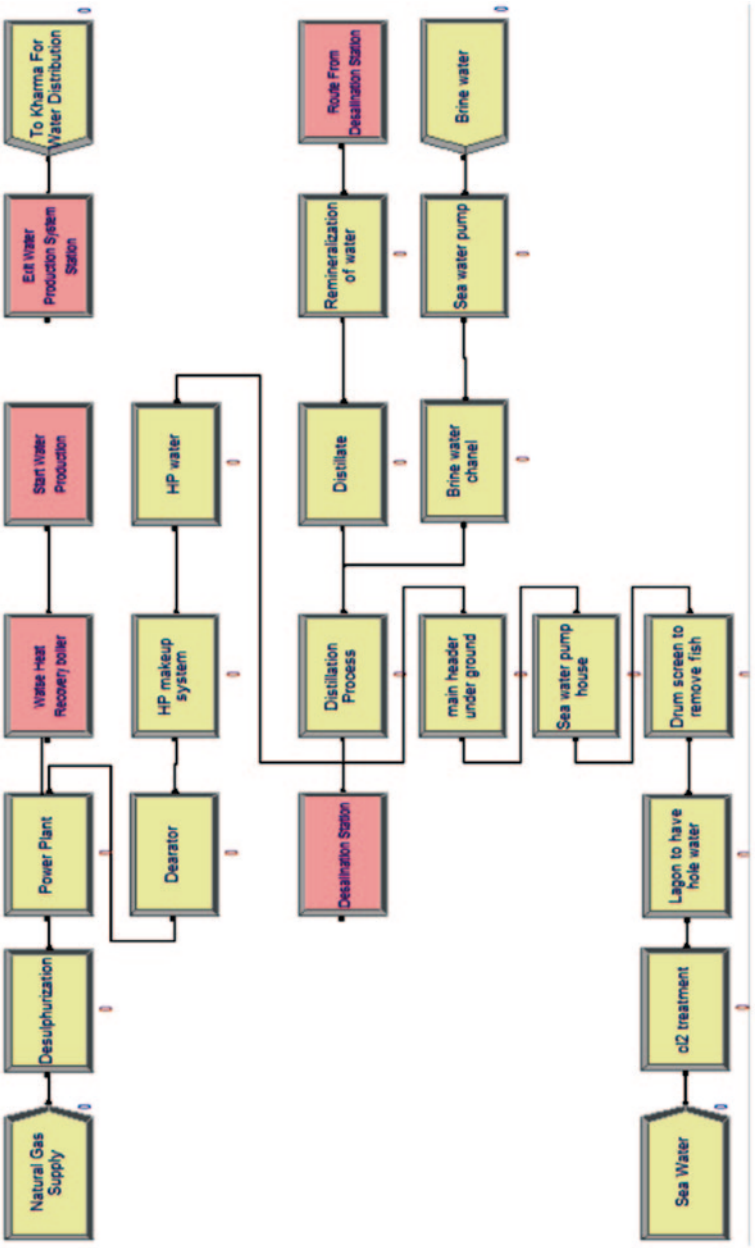

Fig. 46.4 Arena simulation model for experimenting with various water production operation strategies in the case study plant

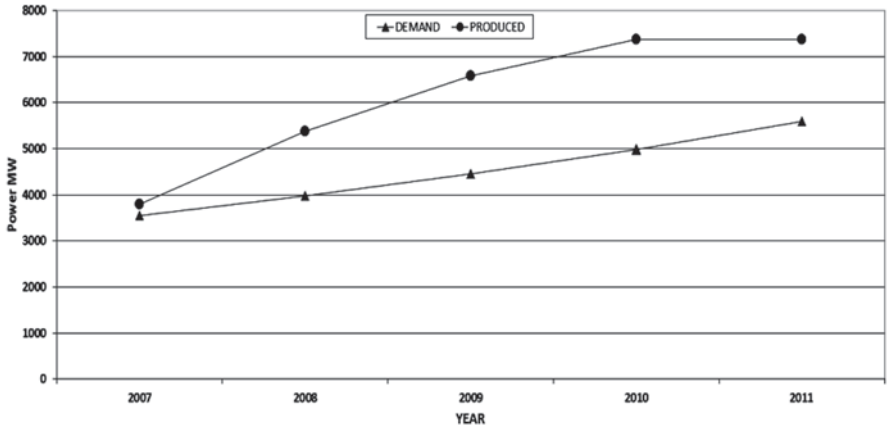

Fig. 46.5 Comparison of power produced and power demand

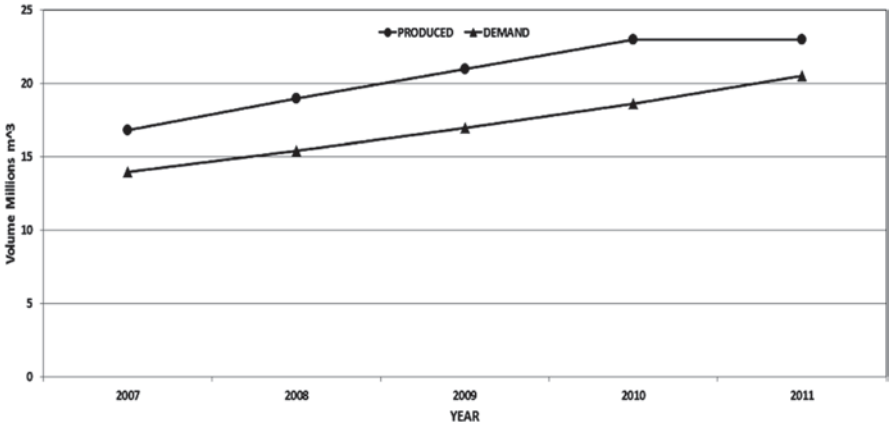

Fig. 46.6 Comparison of water produced and water demand

Figure 46.8 shows a comparison of the water demand and water produced for a period of one month. Figure 46.8 also shows that the water produced exhibits variational differences with particularly low demands in the months of November and December. Ideally, the total water produced must be greater than the total water consumption. From Fig. 46.8, it can be observed that the production volumes are always greater than the demand. Although this is generally regarded as the desired situation it conflicts with lean concepts such as waste of over production and waste of inventory. As such, it was recommended that a further investigation be conducted in order to come up with an optimal water production/demand ratio based on certain policies that may be considered practical regarding the supply of freshwater. Such policies should also include the distribution factors and scenarios from the water distribution company.

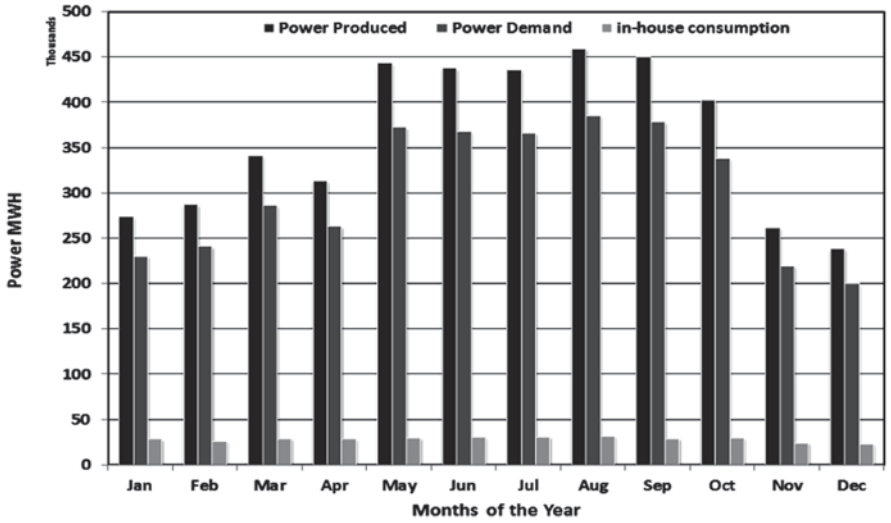

Fig. 46.7 Relationships between power produced, power demand and the power used in the case study plant

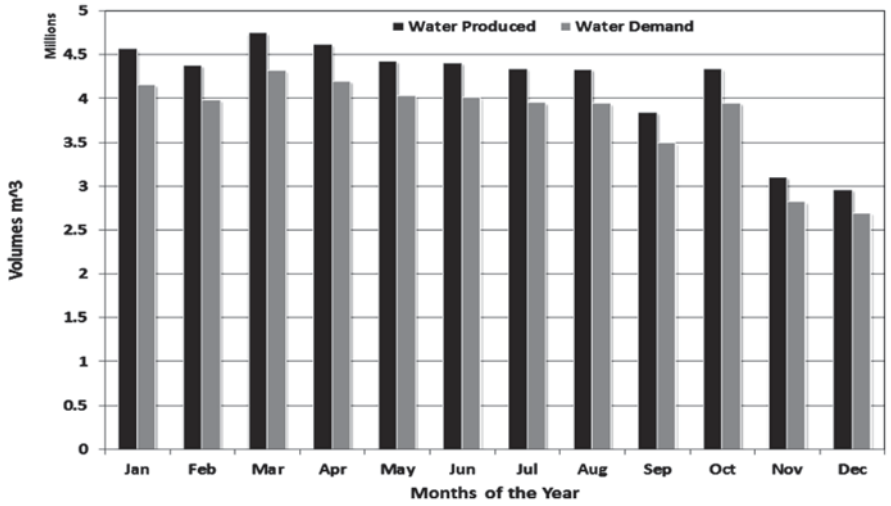

Fig. 46.8 Comparison of water production and water demand for a period of 1 year

Figure 46.9 shows a comparison of fuel gas consumption for the power generation side and the water desalination side. From Fig. 46.9, it can be observed that the fuel consumed in the power generation side far exceeds that used in the water production side. Figure 46.10 shows that 99% of natural gas consumed in the case study is used for power generation. Thus more natural gas (fuel) consumption is allocated to the power generation side than in the water desalination process. It can

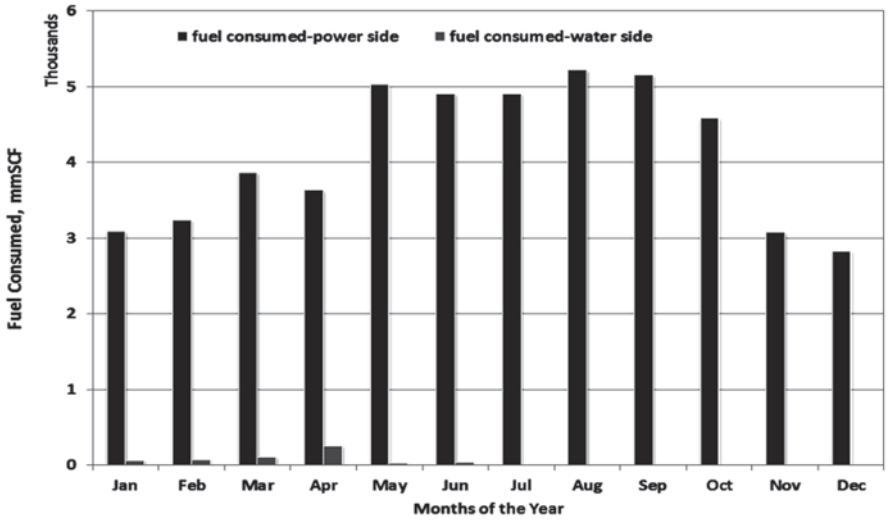

Fig. 46.9 A comparison of fuel gas consumption for the power generation side and the water desalination side

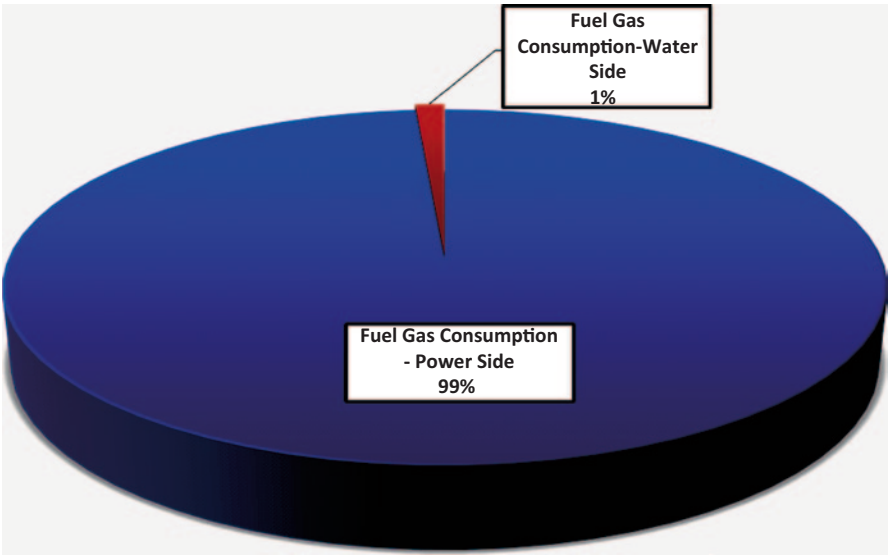

Fig. 46.10 Relative percentage consumption of natural gas in the case study plant

also be noted from Fig. 46.10 that relatively very small natural gas fuel is used in the months; May, June, July, August, September, October November and December.

Data and information from numerical simulations suggest that the case study plant is capable of providing the required amounts of both power and water. Of concern are the surplus that is implied in the various graphical illustrations shown

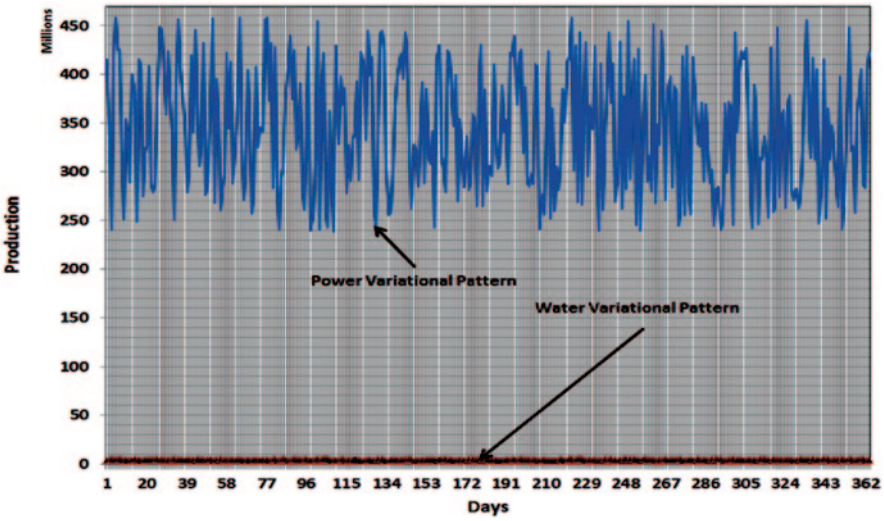

Fig. 46.11 Comparison of power and water production for a simulated run length of 365 days

in this section. The variational differences shows that a wide range operational scenarios and practices are implemented in the case study in a bid to optimize the production/demand ratios. However, the actual dynamics involved in the matching of demand and production are more complicated than implied in the previous discussions. This is because the case study plant is only one of the many plants that supply water and power to the State of Qatar. In addition, the case study business model is complicated by the fact that after the case study generates power and produces water, these commodities are sent to a transmission and distribution company which operates independently. Since these two organizations operate separately, they could be optimized individually. However, the decoupling between these organizations means that each of them have different pull system objectives even though they share the same products. To avoid sub-optimal operations implied in the individually optimized operations, it is necessary for the two organizations to operate within an integrated value optimization framework. Such a framework will go a long way in streamlining operations so that the production quantities are commensurate with demand quantities. The integrated approach also has the ripple effect of reducing the per unit costs of both power and water. Figure 46.11 shows the variational power and water production for a length of 365 days. These variation patterns seem to indicate that the case study plant changes the production (of water or electricity) based on random or fluctuating demands. The random and larger variations in power demands can be explained by the fact that it is easier to estimate demands in water than electricity. However, it is difficult to conclude whether the demand is specific to the case study plant or some of it is used for supporting production from other plants under the corresponding company or some of the power is leased (since frequent leasing is part of the case study business model).

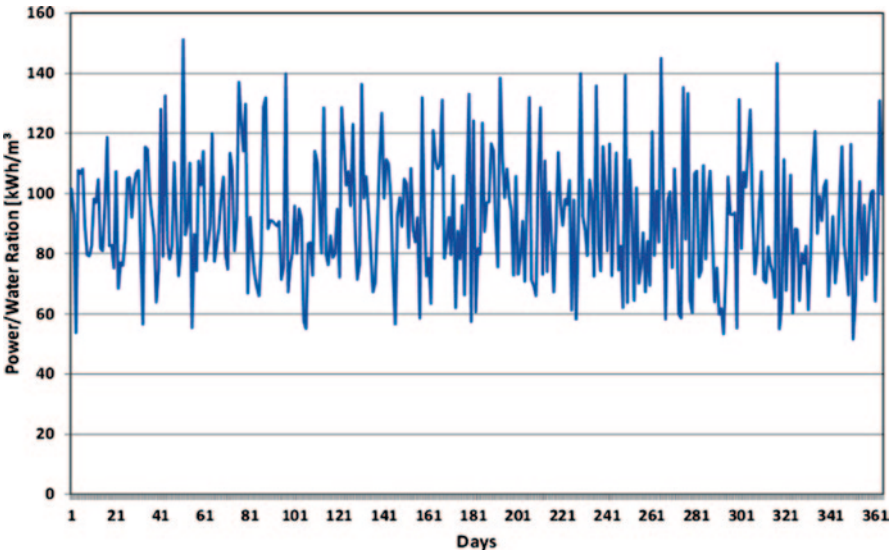

Fig. 46.12 Variation of the power to water ratio for a simulated run length of 365 days

Figure 46.12 shows a simulated plot of the power to water ratio for a simulated run length of 365 days. From Fig. 46.12 it can be inferred that theoretically (i.e. based on simulated data) the power to water ratio can range from a minimum of 51 to 151.26 kWh/m^3, although it is acknowledged that the figure 46.151.26 kWh/m^3 is generally beyond practical design of the case study plant. Although the power to water ratio figures are simulated figures, they seem to indicate that the case study plant strategy is to meet the high demands of water. On the other hand, the fuel plant allocation (see Fig. 46.9) seems to indicate a strong presence of power production in the case study plant. Albeit, these facts are very difficult to put into context because the case study plant is only one of the four plants under companies that produce water and electricity for the population in Qatar. The true context of the simulated data can be further developed by focusing the study on all dual purpose power and water production plants and how they relate to the issues of power and water demands in the State of Qatar.

From the literature review, it was found that by operating at wide range of top brine temperatures, improvements in energy consumption can be realized in the desalination process [11]. In addition, the installed configuration of the desalination plant has an influence on energy consumption. In essence, dual-purpose power desalination plants are used to reduce the production cost of both electricity and water. Various combinations of power-desalination systems can be implemented to satisfy both power and water demands regardless of optimal polices. The preference of one scheme over another depend on many factors such as: the required power to water ratio, the cost of fuel energy charged to the desalting process, electricity sales, capital costs, and local requirements.

Table 46.1 Comparison of water to power ratios for different alternative plant configurations

	Alternative configuration	Water/Power ratios	Rank
1	Gas turbine connected to MSF desalination system—control experiment (i.e. setup in the case study plant)	0.013	4
2	Extraction/condensation steam turbine coupled to MSF desalination system	0.031	5
3	Combined cycle gas turbine with backpressure steam turbine coupled to MSF desalination system	0.011	2
4	Backpressure steam turbine coupled to MSF desalination system	0.012	3
5	Combined cycle gas turbine with extraction/condensation steam turbine coupled to MSF desalination system	0.010	1

The power to ratios were used in the simulation experiments with the various configurations mentioned in the previous paragraph. Simulation models for these experiments were configured based on the experimental arena models shown in Figs. 46.3 and 46.4. Water and power production statistics were simulated for a simulation length of 365 days. For each configuration, average values of the simulated data (i.e. both water and power) were determined and used to calculate the water to power ratios for the five configurations. The results are shown in Table 46.1.

Based on the water to power ration, alternative (5) (i.e. Combined cycle gas turbine with extraction/condensation steam turbine coupled to MSF) seems to be a better choise as the optimal configuration for dual purpose power and water production plants. This configuration performs better than the case study plant (alternative (1) in Table 46.1).

Concluding Remarks

A lot of research has been done to improve, upgrade and advance the thermodynamic efficiencies of the various technologies used in dual purpose power and water production plants. This study has contributed to the perpetual goal of reducing the per unit cost of power and water produced from dual purpose power and water production plants by investigating ways, methods, and mechanisms of improving the operating efficiency of installed capacities. Although major upgrades would require at least retrofits or plant redesign, the major issues tackled in this paper are more to do with improving operational practice by observing and using data and information from simulations. The underlying theme was that by improving the operating efficiencies, the overall gain will translate to reductions in production costs, in particular reductions in per unit cost of both water and electricity produced in dual purpose water and power production plants.

A case study was used to illustrate how simulated data and information can be used to fine tune operations as well as identify optimization initiatives for; (a) improving operating efficiencies, and (b) reducing production costs in dual purpose

power and water production plants. Opportunities for improving operating efficiencies related to plant configurations, parameter optimization as well as power and water production strategies were identified through numerical simulations and simulation modeling techniques. Numerical simulations have pointed out that there is surplus production of both water and power in the case study plant. Although the actual reasons for this surplus could not be determined through simulations, identifications of surplus production indicates the need for further investigations. In some cases, surplus could be produced as part of the production strategies. However, it has been indicated that in such cases, the minimum amounts of surplus as per design or operational issues should be scientifically determined to avoid unnecessary costs, energy consumptions as well as to conserve energy.

Evaluations and comparative analysis of operational states and scenarios were based on the water to power and power to water ratios. The obtained results indicate that optimal production operations strategies depend on the water to power or power to ratio targets. If a plant is designed to achieve a specific water to power or power to water ratio then process parameters must be optimized accordingly and an operational strategy drafted to achieve the target water to power or power to water ratio. This is important since operational practice may deviate plant performance away from optimal performance. Although this approach is desirable, it should be noted that costs have an influence on the implemented plant configuration. Top brine temperature has also been identified as one of the limiting factors in reducing energy consumption in the desalination units. For the case study plant configuration, this limitation can be addressed through retrofits or plant re-designs to incorporate other issues such as new and/or improved seawater pre-treatment. Based on the investigations recorded in this study, the following future work is recommended:

a. To carry out a detailed parametric study using process simulation method in order to appraise the physical behavior of dual purpose power and water production plants
b. To carry out a detailed thermodynamics and in-depth thermo-economic analysis of different configurations of power/water ratios in dual purpose power and water production plants
c. To develop an integrated value optimization framework for the production-distribution system (production and distribution) systems in order to leverage improvements in operating efficiencies with an added advantage of reducing the per unit cost of power and water production

Nomenclature

SC_k Total contents of reservoir at period k
RC Reservoir capacity
D_K^i Output of distillation unit *i* during interval *k*
W_{B_K} Brackish water production during period *k*
W_K Total water demand

Acronyms

DPPW	Dual Purpose Power and Water
MSF	Multi-stage Flash
CP	compressor
CC	combustion chamber
GT	gas turbine
E´	Electric energy production
S´	Thermal energy production

Acknowledgment This report was made possible by a UREP award [UREP09-076-2-020] from the Qatar National Research Fund (a member of The Qatar Foundation). The statements made herein are solely the responsibility of the author[s].

References

1. Little AW, Green A (2009) Successful globalization, education and sustainable development. Int J Educ Dev 29:166–174
2. Al-Mutaz IS, Al-Namlah AM (2004) Characteristics of dual purpose MSF desalination plants. Desalination 166:287–294
3. Ferreira EM, Balestieri JAP, Zanardi MA (2010) Optimization analysis of dual purpose systems. Desalination 250:936–944
4. Luo C, Zhang N, Lior N, Lin H. (2011) Proposal and analysis of a dual-purpose system integrating a chemically recuperated gas turbine cycle with thermal seawater desalination. Energy 36: 3791–3803
5. Mussati, FS, Aguirre PA, Scenna NJ (2003) Dual-purpose desalination plants. Part II. optimal configuration. Desalination 153:185–189
6. Hamed OA, Al-Sofi MAK, Imam M, Mustafa GM, Ba-Mardouf K, Al-Washmi H (2000) Thermal performance of multi-stage distillation plants in saudi arabia. Desalination 128:281–292
7. Uche J, Serra L, Valero A (2001) Thermoeconomic optimization of a dual-purpose power and desalination plant. Desalination 136: 147–158
8. Kelton W, Sodowski R, Swets N (2006) Simulation with ARENA, 5th edn. McGraw-Hill, New York
9. Altiok T, Melamed B (2007) Simulation modeling and analysis with ARENA. Elservier
10. Leedy PD, Ormrod JE (2005) Practical research, planning and design, 8th edn. Pearson/ Prentice Hall, Upper Saddle River
11. Hamed OA, Mustafa GM, Ba Mardouf K, Al Washmi H Prospects of improving energy consumption of the multi-stage flash distillation process. Proceedings of the Fourth Annual Workshop on Water Conservation in the Kingdom, Dhahran, 23–25 April

Index

I. Dincer et al. (eds.), *Progress in Sustainable Energy Technologies: Generating Renewable Energy,* DOI 10.1007/978-3-319-07896-0,